

Springer Aerospace Technology



Antonio Viviani  
Giuseppe Pezzella

# Aerodynamic and Aerothermodynamic Analysis of Space Mission Vehicles



Springer

**Springer Aerospace Technology**

More information about this series at <http://www.springer.com/series/8613>

Antonio Viviani • Giuseppe Pezzella

# Aerodynamic and Aerothermodynamic Analysis of Space Mission Vehicles



Springer

Antonio Viviani  
Department of Aerospace and Mechanical  
Engineering  
Second University of Naples – SUN  
Aversa, Italy

Giuseppe Pezzella  
Fluid Dynamics Laboratory  
Centro Italiano Ricerche  
Aerospaziali – CIRA  
Capua, Italy

ISSN 1869-1730  
Springer Aerospace Technology  
ISBN 978-3-319-13926-5  
DOI 10.1007/978-3-319-13927-2

ISSN 1869-1749 (electronic)  
ISBN 978-3-319-13927-2 (eBook)

Library of Congress Control Number: 2014958028

Springer Cham Heidelberg New York Dordrecht London  
© Springer International Publishing Switzerland 2015

This work is subject to copyright. All rights are reserved by the Publisher, whether the whole or part of the material is concerned, specifically the rights of translation, reprinting, reuse of illustrations, recitation, broadcasting, reproduction on microfilms or in any other physical way, and transmission or information storage and retrieval, electronic adaptation, computer software, or by similar or dissimilar methodology now known or hereafter developed.

The use of general descriptive names, registered names, trademarks, service marks, etc. in this publication does not imply, even in the absence of a specific statement, that such names are exempt from the relevant protective laws and regulations and therefore free for general use.

The publisher, the authors and the editors are safe to assume that the advice and information in this book are believed to be true and accurate at the date of publication. Neither the publisher nor the authors or the editors give a warranty, express or implied, with respect to the material contained herein or for any errors or omissions that may have been made.

Printed on acid-free paper

Springer International Publishing AG Switzerland is part of Springer Science+Business Media ([www.springer.com](http://www.springer.com))

*In loving memory of my parents, Domenico  
and Giovanna.*

*Also, I dedicate this book to my beloved  
Teacher and Mentor, Prof. Luigi G.  
Napolitano, late but never forgotten  
Educator, Master of Science and Innovator.*

***Antonio Viviani***

*To my wife Maria Grazia and my son  
Giandomenico for all their love and  
understanding.*

***Giuseppe Pezzella***



# Preface

In the last four decades, man's capacity to endeavor further into space and accomplish more sophisticated missions has increased dramatically. Earth orbiting satellites are launched on a nearly daily basis and interplanetary probes are sent every year to other planets in the Solar System.

Spacecrafts are launched reasonably often to the International Space Station (ISS) and successful re-entry of a space vehicle has become commonplace.

At the end of the orbital phase, the spacecraft enters the Earth/Planet atmosphere and then flies to the landing site to complete its mission; as a result, spacecrafts have to be sufficiently decelerated from their high speed, (ranging from 8 to 12 km/s for the Earth), during the atmospheric descent safely landing on the Earth/Planet surface at a predefined velocity.

This issue is very challenging for an entry vehicle: the spacecraft's velocity is hypersonic while the atmosphere is essentially stagnant. Therefore, the substantial deceleration of the spacecraft causes a strong shock wave to form in front of it, with an intense heating and pressure increasing of the gases surrounding the space vehicle. As a consequence, upon entry into an atmosphere, a spacecraft encounters a highly complex thermochemical fluid environment where, due to flow temperatures reaching thousands of kelvin, convective and radiative heat transfer towards the spacecraft are very significant. Moreover, at super-orbital velocity, the radiative heat flux becomes greater than the convective one and ablation occurs on the heat shield.

This required a detailed study of several disciplines such as, for example: *aerodynamic loads, aerodynamic heating, vehicle stability, guidance, navigation and control, and landing characteristics*.

With that in mind, this book intends to provide a detailed state of the art on different themes of *hypersonic aerodynamics and aerothermodynamics*, by considering different space vehicle aeroshapes useful for different space mission objectives, e.g., Crew Return Vehicle (CRV), Crew Exploration Vehicle (CEV), Sample Return Vehicle (SRV), and Flying Test Bed (FTB).

For instance, the first chapter provides the basics of hypersonic aerodynamics and aerothermodynamics. A number of hypervelocity key topics are discussed in detail. For example, this chapter shows that most of the re-entry vehicle energy must be dissipated in the form of heat, but no vehicle made of the actual materials can absorb more than a small fraction of this heat energy and still survive. This critical design issue is also clearly described in Chap. 2 where it is explained how, for a successful landing, most of the energy loss must heat the gas flowing around the body, rather than the body itself, and why an understanding of the mechanism of heat transfer at hypersonic speeds is essential for the desirable objective of a safe land. Chapter 1 points out also that almost all critical heat transfer problems for a spacecraft that arise in penetrating a planetary atmosphere occur in the continuum flow regime. In fact, in the decisive portion of the trajectory, the flowfield past a blunt-nose body (body of revolution or wing leading edge) generally exhibits a distinct bow shock wave, a shock layer of dissociated and ionized hot gas between the shock and the body surface, and a boundary layer over the surface, across which the gas temperature drops sharply to its value at vehicle surface. Then, aerodynamic coefficients sign and conventions are described with care. Finally, discussion about fluid dynamics characteristics numbers for hypersonic aerodynamics and aerothermodynamics is also reported and ends the chapter.

The second chapter provides the mathematical model to assess the descent flight trajectory and the corresponding aerothermal loading environment the spacecraft has to withstand during re-entry. Indeed, this chapter shows that heat energy is transferred to the vehicle by conduction and diffusion of chemical species in the boundary layer, and by radiation from the hot gas in the shock layer near the nose, mostly in the ultraviolet to near-infrared range of the spectrum; that heat energy is also radiated away from the surface, mostly in the infrared to far-infrared, where the gas in the shock layer is very nearly transparent (e.g., wall radiative cooling). Then, a discussion about thermal protection system (TPS) concepts to shield the spacecraft from the intense heat of atmospheric entry is also provided. So, several engineering relationships to evaluate in a rather simple way both convective and radiative (from flow to surface) heat flux at vehicle stagnation point are provided in the chapter. Such a heat flux estimation formulas are fundamental in the early design phase where quickly evaluations are mandatory.

After the discussion of fundamentals of hypersonic aerodynamics and aerothermodynamics, vehicle aerodynamic design can be focused on spacecraft aeroshape definition. This is the topic of the third chapter. Here, aeroshape design guidelines, which help research scientists and engineers to assess the best vehicle aeroshape to choose to successfully accomplish the space mission once known requirements and constraints, are provided and emphasized. Therefore, several figures of merit for ballistic and lifting body are discussed and investigated in detail. For example the pitch dumping design issue is argued with care.

Starting from Chap. 4 (and up to Chap. 7), this book focuses on phase-A design practices, in a realistic loading scenario, of several vehicle concepts, ranging from capsules, lifting-bodies, and winged-bodies, to develop research flying test beds.

For instance, Chap. 4 provides computational fluid dynamics (CFD) analyses of the flow field past a CRV proposed for the recovery of astronauts from the ISS. A number of engineering-based design analyses has been also carried out and presented in this chapter to address a preliminary vehicle design. A numerical study has been conducted to assess the effects of thermo-chemical modeling and surface catalyticity on the design of a CRV re-entering from Low Earth Orbit (LEO). Therefore, the effects of complexity of some state-of-the-art chemical models, kinetics of reactions, vibrational relaxation, and wall reaction mechanism on vehicle aerothermodynamics and aerodynamics, and on some flow field features are addressed. In particular, the effects of finite rate chemistry are highlighted by comparing vehicle aerodynamic performances and some flow features evaluated by means of both perfect gas and reacting gas models. In this framework, several Euler and Navier–Stokes computations have been performed both in trajectory-based and space-based design approaches. Then, results have been compared to establish the model influence on aerodynamic (lift, drag, pitching moment, and trim angle of attack) and aerothermodynamic (convective heat flux distribution on the vehicle forebody heat shield) performances. Moreover, the role played by surface catalyticity on vehicle thermal loading is pointed out in Chap. 4. Hence, a possible Earth-entry scenario, with the associated aeroheating environment, for the proposed capsule-type vehicle, is reported and analyzed by accounting for real gas effects, experienced along the atmospheric descent. Finally, numerical results and their comparison with flight data and wind tunnel data are emphasized.

The fifth chapter focuses on thermochemical non-equilibrium CFD analyses carried out for the development of the aerodynamic database of an unmanned lifting vehicle, re-entering from LEO, and addresses particular design issues, such as shock wave boundary layer interaction (SWIBLI) and shock-shock interaction (SSI). For example, the IXV aerodynamic analysis, carried out for the whole flight scenario, is discussed. This aerodynamic analysis, namely AEDB tool, relies on computational fluid dynamics, wind tunnel test, and engineering-based design data generated during the project phases, from rarefied flow conditions, to hypersonic continuum flow and up to reach subsonic speeds regime. In particular, databasing activities are developed in the light of a build-up approach. This means that all aerodynamic force and moment coefficients are provided by means of a linear summation over certain number of incremental contributions such as, for example, effect of sideslip angle, aerodynamic control surface effectiveness, etc. The AEDB tool provides the IXV aerodynamics with control effectiveness throughout the flight speed regimes from subsonic, transonic, supersonic up to hypersonic and high altitude; rarefied atmospheric effects are also provided. Further, the effect of mission requirements and constraints on the aeroshape evolution history is also provided in detail.

In Chap. 6, the attention moves on winged re-entry vehicles suitable for both manned and unmanned mission to and from LEO. A sub-orbital mission scenario is addressed too. The chapter deals with aerodynamic and aerothermodynamic analysis of several winged vehicles which consist of reusable flying test beds. Several design approaches, ranging from engineering-based to CFD analyses, have been addressed to assess the vehicle aerothermal performances. To this end,

aerodynamic results for a wide range of free stream conditions, including reacting and non-reacting flow, and different angles of attack, have been provided and compared. Vehicle aerodynamic database in build-up approach is emphasized.

Chapter 7 deals with aerodynamic and aerothermodynamic design of an SRV. As the next step of the exploration of our Solar System, the sample-return mission is expected to play an important role, since precise investigation of soil samples in laboratories leads us to much further understanding about planets, asteroids, comets and so on. For simplicity of the spacecraft system and reduction of mission cost, it is necessary to establish the technology of super-orbital re-entry in which a small re-entry capsule carrying the sample of a target celestial body enters the Earth's atmosphere directly from the interplanetary trajectory at super-orbital velocity. In this chapter, an overview of the analysis approach, typically followed within SRV design, has been done. The chapter provides a systematic survey that would be required for the preparation of ambitious sample return projects. In fact, some indications concerning main design topics to be addressed in designing such a kind of vehicle for planetary exploration are recognized. For instance, numerical simulations have been carried out for a super-orbital re-entry capsule to determine both aerodynamic and aerothermodynamic performances in the framework of an entirely passive Earth entry vehicle. The capsule enters into the Earth's atmosphere directly from the hyperbolic Earth-return trajectory. Therefore, the atmospheric entry speed of the capsule is over 12 km/s, so that a very strong bow shock wave is generated around the capsule, whereby the shock layer gas is much more highly heated than the case of a "normal" Earth orbital re-entry. Hence, it is predicted that radiative heat flux will be stronger in the super-orbital re-entry than in the Earth orbital re-entry. To make the effective design of the TPS within the highly limited weight, it is important to make more accurate estimation of aerodynamic heating and to reveal the contribution of the radiative heat flux. Indeed, thermochemical non-equilibrium flow modeling cannot be avoided. In fact, intensity of radiation is strongly dependent on vibrational, electron and electronic temperatures. In particular, in the Chap. 7 we assess the aerodynamic performances and stability of a SRV along the whole re-entry – path, the capsule aerothermal environment and heat shield ablation, as well. Design results, presented in this chapter, refer to both numerical and engineering-based analysis. Engineering-based design has been applied to assess flow field regime and capsule aerodynamics, while Navier–Stokes simulations have been performed to evaluate the flow field past the capsule, the effects of heat shield mass blowing, and to made plasma radiation analysis. Design results are presented and discussed.

After design applications focused on entry flight, the book moves attention to the needs of the early phase of a space mission: the launch. For instance, in Chap. 8, launcher aerodynamic and aerothermodynamic design activities at phase-A level are described. The goal is to describe how it is possible to address the preliminary aerodynamic and aerothermodynamic data bases of both expendable and semi-reusable launch vehicles at earlier design stage. To this aim, different design approaches as engineering methods and CFD are detailed. The flight scenario with the corresponding loading environment is defined and analyzed for some

reusable launcher boosters. Then, the chapter describes how the joint use of wind tunnel testing and CFD is a powerful tool, able to provide high quality data as input for performances evaluations as well as launcher control and sizing. In fact, the building of detailed aerodynamic and aerothermodynamic databases require a very important number of computations and experimental test campaigns for each flight regime the launcher experiences during the ascent. So, examples of numerical and experimental efforts are provided as well.

Finally, the Appendix A: A Manned Space Mission to Mars deals with the aerodynamic analysis of innovative unusual CEV concepts, suitable for a manned Mars entry, aiming to support design studies of planetary entry systems. In this framework, two lifting body configurations have been analyzed so far. Several fully 3D computational fluid dynamics analyses, both for perfect gas model and for non-equilibrium reacting gas mixture model, have been performed. The flowfield environment past the exploration vehicle for an assigned Mars entry scenario has been addressed. To this end, a wide range of flow conditions, including different angles of attack, various Mach numbers and Reynolds numbers, have been investigated. A number of fully 3D Navier–Stokes and Euler CFD computations of the hypersonic flowfield past two lifting body vehicles have been performed for several freestream conditions of a proposed Mars entry loading environment. Results reported in this chapter are useful for providing numerical data for further understanding the fluid dynamics process, as those of high enthalpy flow and vehicle shape effects, involved in the design analysis of lifting body vehicle for the exploration of Mars.

October 2014  
Naples, Italy

Antonio Viviani  
Giuseppe Pezzella



# Contents

<b>1</b>	<b>Basics of Hypersonic Aerodynamics and Aerothermodynamics .....</b>	<b>1</b>
1.1	Introduction .....	1
1.2	Hypersonic Flow Key Points .....	2
1.2.1	Strong Bow Shock .....	3
1.2.2	Importance of Temperature/Aerodynamic Heating .....	3
1.2.3	Blunt Aeroshapes to Reduce Heat Transfer .....	4
1.2.4	Surface Pressure Estimation .....	5
1.2.5	High-Temperature Effects .....	6
1.2.6	Viscous Interaction .....	7
1.2.7	Entropy Gradient .....	8
1.2.8	Thin Shock Layer .....	9
1.2.9	Engine–Airframe Integration .....	9
1.2.10	Control and Stability Issues .....	10
1.3	Re-entry from Orbit .....	11
1.4	Typical Hypersonic Flowfield Features Past a Vehicle in Continuum Flow Regime .....	16
1.4.1	Fluid Flow Governing Equations .....	21
1.4.2	Flow Characteristics Related to the Change of $M_\infty$ .....	25
1.4.3	Shock Relations .....	27
1.4.4	Method of Characteristics .....	31
1.4.5	High-Temperature Effects .....	33
1.4.6	Viscous Interaction .....	47
1.5	Spacecraft Aerodynamic Coefficients .....	50
1.5.1	Reference Coordinate System .....	50
1.5.2	Conventions for Aerothermodynamic Data .....	59
1.6	Simplified Aerodynamic Analysis .....	62
1.6.1	Low-Order Method Aerodynamics .....	63
1.6.2	Newtonian Impact Flow Theory .....	64
1.6.3	Modified Newtonian Flow Theory .....	70
1.6.4	Flat Plate Hypersonic Aerodynamics .....	72
1.6.5	Sphere Hypersonic Aerodynamics .....	77

1.6.6	Cylinder Hypersonic Aerodynamics .....	79
1.6.7	Sharp/Blunt Cone Aerodynamics .....	80
1.6.8	Tangent-Wedge and Tangent-Cone Methods .....	82
1.6.9	Flat Plate Theory and Spacecraft Hypersonic Aerodynamic Characteristics .....	85
1.6.10	Panels Method Aerodynamics .....	91
1.6.11	Surface Inclination Methods and Aeroshape Aerodynamic Design: The Pressure Methods Selection Rationale .....	97
1.7	Hypersonic vs. Subsonic Aerodynamics .....	105
1.7.1	Aerodynamic Drag .....	105
1.7.2	Aerodynamic Lift .....	106
1.7.3	Planform Features .....	107
1.8	Entry Flight and Aeroheating .....	110
1.8.1	Stand-off Distance .....	112
1.8.2	Aerodynamic Heating .....	114
1.9	Basics of Space Vehicle Design .....	117
1.10	Dimensional Analysis .....	121
	References .....	124
<b>2</b>	<b>Fundamentals of Atmospheric Entry .....</b>	<b>127</b>
2.1	Introduction .....	127
2.2	Initial Specific Energy for Some Entry Missions .....	128
2.3	Equations for Planar Flight .....	128
2.3.1	Ballistic Entry .....	135
2.3.2	Equilibrium Gliding Entry .....	140
2.3.3	Skip Entry .....	143
2.3.4	Cross-Range Maneuvers .....	150
2.4	Heat Transfer for Perfect Gas and Chemically Reacting Flows .....	154
2.4.1	Fourier's Law and Convective and Diffusive Heat Transfers .....	155
2.4.2	Heat Transfer for Perfect Gas Flows .....	157
2.4.3	Skin Friction Coefficient and Reynolds Analogy .....	162
2.4.4	Total Entry Heat Load .....	167
2.4.5	Entry Heating Rate .....	168
2.4.6	Heat Transfer for Chemically Reacting Flows .....	172
2.4.7	Film Coefficient Approach .....	173
2.5	Stagnation-Point Heating .....	174
2.5.1	Stagnation-Point Heat Transfer for Perfect Gas Flow .....	178
2.5.2	Stagnation-Point Heat Transfer for Chemically Reacting Gas .....	189
2.5.3	Engineering Methods and Stagnation-Point Heating Assessment .....	199
2.6	Free Molecular Heating .....	204

2.7	Entry Corridor .....	207
2.7.1	Velocity–Flight-Path Angle Map .....	207
References .....		210
<b>3</b>	<b>Some Preliminary Considerations on Entry Vehicle Design .....</b>	<b>211</b>
3.1	Introduction .....	211
3.2	Overview of Evolution of Hypersonic Vehicle Configuration .....	212
3.2.1	Hypersonic Vehicle Powered by Scramjet Engine .....	218
3.3	Overview of Entry Vehicle Design Philosophy .....	221
3.3.1	Hypersonic Lift-to-Drag Ratio and Vehicle Ballistic Coefficient .....	229
3.3.2	Ballistic Coefficient and Vehicle Volume Factor and Fineness Ratio .....	230
3.3.3	Hypersonic Trim Lift-to-Drag Ratio and Vehicle Volumetric Efficiency .....	235
3.4	Spacecraft with High-Pressure Drag Configurations .....	238
3.5	Ballistic Entry Vehicle Design .....	244
3.5.1	Aeroshell Cone Angle .....	246
3.5.2	Aeroshell Base Diameter .....	246
3.5.3	Aeroshell Nose Radius .....	247
3.5.4	Aeroshell Corner Radius .....	249
3.5.5	Blunt Bodies Dynamic Instability .....	252
3.6	Lifting Entry Vehicle Design .....	265
3.6.1	Example of Design Study for Low Earth Orbit Return ...	270
3.6.2	Example of Design Study for a High-Speed Earth Return from a Comet .....	271
3.7	Maneuvering Systems for Entry Vehicles .....	278
3.7.1	Aerodynamics of the Maneuver .....	278
3.7.2	Control System Characteristics .....	279
3.8	Vehicle Stability in Longitudinal and Lateral–Directional Flight .....	280
3.8.1	Static Stability in Longitudinal Flight .....	280
3.8.2	Effect on Stability Due to Shift in CG Position .....	283
3.8.3	Hypersonic Flight Stability and Control Issues .....	284
3.8.4	Static Stability in Lateral–Directional Flight .....	288
3.8.5	Vertical Tail Design .....	289
3.8.6	The Hypersonic Directional Stability Problem .....	290
3.9	An Example of Design for Glide Re-entry Vehicles .....	294
3.10	Spatuled-Body Configuration .....	308
3.10.1	An Introduction to Waverider Configuration Design: The Inverse Design Method .....	313
3.10.2	Osculating Cone Waveriders .....	313
3.10.3	Wedge and Cone-Derived Waveriders .....	315

3.11	Vehicle Aerodynamic Heating and Skin Temperature .....	317
3.11.1	Convective Heat Transfer and the Eckert's Reference Temperature Method .....	322
3.11.2	The Eckert's Reference Temperature Method and Flat Plate Aeroheating .....	329
3.11.3	Thermal Protection Techniques .....	330
3.12	A Look to the Computational Fluid Dynamics Effort During Design .....	331
3.12.1	Flow Physics .....	333
3.13	Aero thermal Regimes and Vehicle Design .....	343
3.13.1	Flow Regimes .....	344
3.13.2	Thermochemical Flow Regimes .....	363
	References .....	365
<b>4</b>	<b>Analysis of an Apollo-Shaped Crew Return Vehicle .....</b>	<b>367</b>
4.1	Introduction .....	367
4.2	Overview of Flow and Chemistry Coupling Within LEO Re-entry Scenario .....	370
4.3	Heat Shield Surface Catalytic Effects .....	373
4.4	The Apollo-Like CRV Concept and the LEO Re-entry Flight Scenario .....	377
4.4.1	Vehicle Concept Overview .....	377
4.4.2	Description of Design Approach and Used Tools .....	379
4.5	Mathematical Formulation and Numerical Solution .....	385
4.5.1	Flowfield Governing Equations .....	385
4.5.2	Numerical Technique .....	392
4.5.3	The Computational Grid Domain .....	392
4.6	Model Validation .....	394
4.6.1	Test Article Geometry and Computational Domain .....	394
4.6.2	Test Conditions and Engineering Analysis .....	395
4.6.3	CFD Results .....	396
4.7	CRV Design Analysis .....	399
4.7.1	Re-entry Flight Scenario .....	399
4.7.2	Appraisal of the Aeroheating Loading Environment .....	401
4.7.3	CRV Computational Flowfield Analysis .....	405
4.8	CRV Aerodynamic Analysis .....	417
4.8.1	Engineering Assessment of CRV Aerodynamics .....	421
4.8.2	Numerical Assessment of CRV Aerodynamics .....	429
4.9	CRV Aero thermodynamic Features .....	438
4.9.1	CRV Zero-Lift Aero thermodynamics .....	438
4.9.2	CRV AoA Aero thermodynamics .....	441
4.9.3	CRV High-Altitude Aero thermodynamics .....	444
4.10	Reliability of Numerical Study .....	446
	References .....	454

<b>5 Lifting-Body Vehicles .....</b>	457
5.1 Introduction .....	457
5.2 Historical Background .....	459
5.3 IXV Trade-Off Objectives and Logic .....	471
5.3.1 The Capsule Class .....	478
5.3.2 The Wing–Body Class .....	479
5.3.3 The Lifting-Body Class .....	480
5.4 IXV Vehicle Description and Configuration Rationale .....	480
5.5 IXV Top Level Drivers .....	483
5.6 IXV Project Background .....	485
5.7 IXV Mission Requirements and Description .....	487
5.7.1 Mission .....	489
5.7.2 System .....	489
5.7.3 TPS and Hot Structures .....	490
5.7.4 Dependability .....	490
5.7.5 ATD .....	491
5.7.6 Innovative Materials and Concepts for TPS&HS .....	491
5.7.7 HMS .....	491
5.7.8 GNC .....	491
5.8 WTT and CFD Data Comparisons with IXV Nominal Trajectory ..	492
5.9 Results of WTT Campaigns .....	495
5.9.1 ONERA S4ma Test Highlights .....	496
5.9.2 DLR H2K Test Highlights .....	498
5.9.3 DNW-SST Test Highlights .....	499
5.9.4 FOI T1500 Test Highlights .....	504
5.9.5 IXV and HEG Wind Tunnel .....	513
5.10 Results of CFD Analysis .....	515
5.11 Aerodynamic Analysis .....	535
5.11.1 General Inputs for Aerodynamic Data Set Generation ..	535
5.11.2 Reference Coordinate System and Aerodynamic Sign Conventions .....	536
5.11.3 IXV Aerodynamic Model and Database Development ..	537
5.11.4 Formulation of the Aerodynamic Database .....	538
5.11.5 Aerodynamic Database Development .....	542
5.11.6 Free Molecular and Transitional Flow Regimes .....	542
5.11.7 Continuum Flow Regime .....	547
5.11.8 Elevator Effectiveness on Longitudinal Coefficients .....	555
5.11.9 Sideslip Angle Effects on Longitudinal and Lateral–Directional Actions .....	562
5.11.10 Ailerons Effect on Lateral–Directional Actions .....	563
5.11.11 Aerodynamic Database Accuracy .....	566
References .....	569

<b>6</b>	<b>Winged Re-entry Vehicles .....</b>	571
6.1	Introduction .....	571
6.2	Vehicles Description .....	578
6.3	Flight Scenario and Flow Regime Assessment .....	580
6.3.1	Rarefied-Transitional Regimes .....	582
6.3.2	Viscous Interaction Regime .....	583
6.3.3	Real Gas Regime .....	584
6.3.4	Laminar-to-Turbulent Transition .....	587
6.4	Design Approach and Used Tools .....	589
6.5	Aerodynamic Characterization .....	598
6.5.1	ORV Aerodynamic Reference Parameters .....	598
6.5.2	Reference Coordinate System and Aerodynamic Sign Conventions .....	598
6.5.3	Inputs for ORV Aerodynamic Database Generation .....	600
6.5.4	ORV Aerodynamic Model .....	602
6.5.5	Formulation of the Aerodynamic Database .....	603
6.5.6	Process of Development of the Aerodynamic Database ..	606
6.6	Low-Order Methods Aerodynamic Results .....	607
6.6.1	HPM Results for Rarefied and Transitional Flow Conditions .....	607
6.6.2	HPM Results for Continuum Flow Condition .....	611
6.7	CFD-Based Aerodynamic Results .....	626
6.8	Aerodynamic and Aerothermodynamic Appraisal of the FTB-X Vehicle Concept .....	644
6.8.1	Vehicle Configuration .....	644
6.8.2	Analysis Method and Used Tools .....	646
6.8.3	Vehicle Aerodynamic Appraisal .....	648
6.8.4	FTB-X Aerodynamics in Rarefied and Transitional Flow Conditions .....	648
6.8.5	FTB-X Aerodynamics in Continuum Flow Conditions ..	653
6.8.6	Vehicle Aero thermal Environment .....	671
6.8.7	FTB-X Re-entry Flight Mechanics Performance and Effects of Air Rarefaction .....	684
6.9	Aerodynamic Data Uncertainties .....	687
6.9.1	Formulation of the Aerodynamic Database Uncertainty ..	687
6.9.2	Aerodynamic Database Uncertainty and WTT Measurements .....	689
6.9.3	Aerodynamic Database Uncertainties and CFD Data .....	690
6.9.4	Aerodynamic Database Uncertainties and Flight Data .....	690
6.9.5	Orbiter and X-33 Aerodynamic Uncertainties .....	692
6.9.6	FTB-X Aerodynamic Uncertainty Model .....	695
	References .....	699

<b>7 Analysis of Sample Return Capsules .....</b>	703
<b>7.1 Introduction .....</b>	703
<b>7.2 Design Process for Sample Return Spacecrafts .....</b>	706
<b>7.2.1 Requirements and Constraints .....</b>	707
<b>7.2.2 Similarity and Scaling .....</b>	707
<b>7.2.3 Overview of SRV Design Analysis .....</b>	713
<b>7.2.4 Shock Layer Condition .....</b>	721
<b>7.3 Spacecraft Reference Configuration and Re-entry Flight Scenario .....</b>	725
<b>7.4 Aerodynamic and Aerothermodynamic Performance Analysis .....</b>	728
<b>7.4.1 Flowfield Governing Equations .....</b>	729
<b>7.4.2 Loading Scenario and Air Mixture Composition .....</b>	733
<b>7.4.3 Flight Regime Overview and Flow Simulation Modeling .....</b>	738
<b>7.4.4 Computational Domains, Boundary Conditions, and Solution Convergence .....</b>	741
<b>7.5 Numerical Results .....</b>	745
<b>7.6 SRV Aerodynamics .....</b>	760
<b>7.6.1 Engineering-Based Aerodynamic Results of SRV .....</b>	761
<b>7.6.2 CFD-Based Aerodynamics of SRV .....</b>	764
<b>References .....</b>	765
<b>8 Launchers: Present and Future .....</b>	767
<b>8.1 Introduction .....</b>	767
<b>8.2 Launcher Aerodynamic Analysis .....</b>	768
<b>8.2.1 Aerodynamic Conventions for Launchers .....</b>	768
<b>8.2.2 Aerodynamic Coefficients and Vehicle Design .....</b>	770
<b>8.2.3 Aerodynamic Analysis of Launchers .....</b>	772
<b>8.2.4 Quick Design Approach for External Loading Characterization .....</b>	775
<b>8.3 Examples of Quick Aerodynamic Design Analysis of Launchers .....</b>	776
<b>8.3.1 The VSB-30 Launcher .....</b>	776
<b>8.3.2 The Vega Launcher .....</b>	779
<b>8.3.3 The Next-Generation Launcher Vehicle (NGLV) .....</b>	781
<b>8.3.4 The Future Launchers Preparatory Program Concepts .....</b>	787
<b>8.4 Pre-projects Phases: Uncertainties in Databases .....</b>	825
<b>8.4.1 Uncertainties Due to CFD Level of Physical Model and Code Validation .....</b>	826
<b>8.4.2 Uncertainties Due to Launcher Shape Representation in Early Program Phases .....</b>	827
<b>8.4.3 Uncertainties Due to Limited Computation Points .....</b>	828
<b>8.5 Developments Phases: The Challenges for Precise CFD .....</b>	828

8.6	Example of Navier–Stokes Computations for a Development Phase .....	829
8.6.1	Aerodynamic Design of an Ariane 5 Liquid Flyback Booster .....	829
8.6.2	The Ariane 5 Geometry for Wind Tunnel Testing .....	842
8.6.3	CFD Contribution to the Aerodynamic Appraisal of the Vega Launcher .....	845
8.7	Developments Phases: Uncertainties in Databases .....	858
8.7.1	Local Loading of Protrusions and Interstages Cavities ...	859
8.8	Numerical Solution and Grid Convergence Analyses.....	863
	References .....	865
	<b>Appendix A: A Manned Space Mission to Mars.....</b>	869
A.1	Introduction .....	869
A.2	The Trip to Mars and Return .....	869
A.3	Vehicle Configuration Selection .....	871
A.4	Methodology Analysis and Used Tools .....	874
A.4.1	Engineering-Based Design Analysis.....	874
A.4.2	CFD-Based Design Analysis .....	876
A.5	Aerodynamic Analysis .....	879
	References .....	887
	<b>Index .....</b>	889

# List of Boxes

The Perfect Gas Model .....	22
Flow Species Internal Energy and Degrees of Freedom .....	36
The Compressibility Factor for a Two- and Four-Species Mixture .....	43
Mass Fraction and Mole Fraction Relationship .....	45
Aerodynamic Force Analysis .....	53
Derivation of Newtonian Sine-Squared Law .....	65
Energy and Heat .....	110
The Velocity Ellipse .....	122
The Apollo Re-entry .....	146
The Nusselt Number and the Fourier's Law .....	157
The Adiabatic Wall Temperature, $T_{aw}$ .....	160
The Body-Averaged Skin Friction Coefficient for Laminar Flow on a Flat Plate .....	165
Skin Friction Coefficient and Heat Transfer Estimate .....	167
Stagnation-Region Flowfield Properties .....	174
The Stagnation-Point Velocity Gradient Evaluation .....	179
Stagnation Region Heat Transfer Estimate .....	183
The Heat Flux at the Stagnation Point of a Sphere .....	191
The Stagnation-Point Heat Flux for Different Relationships .....	201
Thermal Accommodations Coefficient for a Non-ideal Surface .....	206
Vehicle Mass Characteristics and Ballistic Coefficient .....	231
Some Design Highlights of Huygens, Marsnet, and Rosetta Spacecrafts .....	247
Dynamics Stability and Blunt Body Wake .....	253
Dynamics During Entry .....	255
Dynamic Stability and Vehicle Design Considerations .....	261
Lifting Entry by the Center of Gravity Offset .....	266
Blunt Bodies Versus Slender Bodies Entry Load Directions .....	268
Typical Force and Moment Characteristics of a Hypersonic Vehicle .....	286
Orbiter Longitudinal Aerodynamic Characteristics at Hypersonic Speed .....	296
Lift-to-Drag Ratio in Landing Approach for High-Speed Vehicles .....	302

The Surface Temperature at the Stagnation Point of the Shuttle Orbiter .....	319
The Eckert's Reference Temperature Method and Cone Aeroheating .....	324
Real Gas Flow Physics for Blunt Body Capsules .....	338
The Knudsen Number in Terms of Reynolds and Mach Numbers .....	346
Orbital Transfer by Aerocapture .....	352
Orbiter Aerodynamics and Aerothermodynamics in Transitional Flow Conditions .....	355
Zero Lift Drag Coefficient of an Apollo-Like Capsule .....	422
Axial Coefficient of an Apollo-Like Capsule .....	424
Normal Coefficient of an Apollo-Like Capsule .....	426
An Example of Aerodynamic Trade-Off .....	615

# Chapter 1

## Basics of Hypersonic Aerodynamics and Aerothermodynamics

### 1.1 Introduction

Generally speaking, the re-entry flight of blunt bodies—either ballistic or lifting—takes place in an extreme and yet not completely known environment, named *hypersonic regime*.

The term *hypersonic* is used to distinguish flowfield phenomena and problems appearing at flight speeds which are greater enough than the usual supersonic speeds. The appearance of new characteristic features in hypersonic flowfields justifies the use of a new term, different from the well-established one *supersonic*.

These characteristically hypersonic features, as discussed later, may be roughly divided into those of hydrodynamic nature, which arise because the flight Mach number is large, and those of a physical or chemical nature, which arise because the energy of the flow is very large [1]. Anyway, there is a conventional rule of thumb that defines hypersonic aerodynamics as those flows where the Mach number is greater than 5, according to the flow regime classification summarized in Fig. 1.1.

However, this is no more than just a rule of thumb; rather hypersonic flow is best defined as *that regime where certain physical flow phenomena become progressively more important as the Mach number is increased to higher values*.

In some cases, one or more of these phenomena may become important above Mach 3, whereas in other cases they may not be compelling until Mach 7 or higher [2].

Anyway, basics of hypersonic flows, especially for what concerns aerodynamics and aerothermodynamics of a vehicle traveling at such a high speed, will be discussed in detail hereinafter.

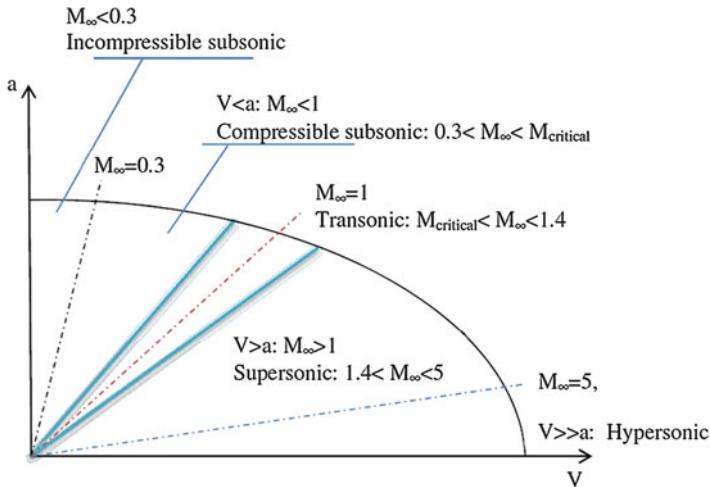


**Fig. 1.1** Ellipse of motion regimes

## 1.2 Hypersonic Flow Key Points

As the objective of this book is studying vehicles operating in very high-speed flow conditions, namely, hypersonic regime,<sup>1</sup> in the present chapter, several key features of the hypersonic regime will be discussed and analyzed.

Today hypersonic vehicles are commonplace. They include missiles, launch vehicle, and entry bodies. Nevertheless, there is no exact statement defining the start of the hypersonic flow regime. Conventionally, in aerodynamics, a flow is in *hypersonic regime* if the Mach number  $M$  is greater than 5 [2].

Anyway, this is just a simple definition. More in detail it could be said that hypersonic flow regime arises [3]:

1. For Mach numbers at which supersonic linear theory fails
2. When  $\gamma$  is no longer constant and we must consider temperature effects on fluid properties
3. For Mach number from 3 to 5, where Mach 3 might be required for blunt bodies causing large disturbances to the flow and Mach 5 might be the starting point for more highly streamlined bodies powered by scramjet engines

---

<sup>1</sup>Since the 1950s the flight at extreme high speed has been explored and utilized with the advent of missiles and spacecraft. Examples are the development of the Mach 25 Mercury, Gemini, and Vostok manned orbital spacecraft of the 1960s; the historic Mach 35 Apollo spacecraft, which returned men from the moon starting in 1969; and, finally, Space Shuttle re-entry flights since 1981. The flight at extreme high speeds such as those of vehicle returning from space is called hypersonic flight, and the aerodynamic and gas dynamic characteristics of such a flight are classified under the label of hypersonic aerodynamics.

Therefore, one more accurate definition should be:

The hypersonic flow is the regime where specific physically phenomena become more and more predominant as Mach number increases.

Indeed, ten key points can be accounted for:

1. Strong bow shocks are commonplace.
2. Temperature and aerodynamic heating become important.
3. Blunt shapes are commonplace.
4. In many cases vehicle surface pressure can be estimated fairly easily.
5. High-temperature effects become important.
6. Viscous interaction between outer flow and the boundary layer region may be critical.
7. Entropy gradients become important.
8. Thin shock layer may be established.
9. Engine-airframe integration may be critical.
10. Control and stability issues lead to different aeroshapes.

Some comments on these key points are in order.

### ***1.2.1 Strong Bow Shock***

The high enough speeds and angle of incidence at which travel hypersonic vehicles lead to strong bow shock waves to form ahead of vehicles because of flow disturbances cannot work their way upstream<sup>2</sup>; rather, at some finite distance from the body, the disturbance waves pile up and coalesce, forming a strong wave in front of the body [3].

### ***1.2.2 Importance of Temperature/Aerodynamic Heating***

If one were to follow the trend set by supersonic aerodynamics, a typical hypersonic body would be an extremely slender body with a sharp leading edge. The sharp leading edge would no doubt reduce the drag. However, in hypersonic flow, one cannot ignore the heat transfer to the body [3].

This is easily illustrated considering the relationship between stagnation temperature ( $T_0$ ) and static temperature ( $T_\infty$ ):

$$\frac{T_0}{T_\infty} = 1 + \frac{\gamma - 1}{2} M_\infty^2 \quad (1.1)$$

---

<sup>2</sup>Note that information about the presence of the body attempts to be transmitted to the surrounding flow via molecular collision; that is, the information is propagated upstream at approximately the local speed of sound. However, the vehicle travels at usual more speed, at hypersonic speed.

Because of viscous dissipation (i.e., friction between adjacent fluid layers) caused by the no-slip boundary condition at wall, the boundary layer is also a region of very high temperatures. Therefore, the high-temperature fluid in the boundary layer will transfer heat to the body until the temperature gradient at the wall is zero (i.e., adiabatic wall,  $T_{aw}$ ):

$$T_{aw} = T_e \left( 1 + r \frac{\gamma - 1}{2} M_\infty^2 \right) \quad (1.2)$$

where  $r$  is the recovery factor.

Equations (1.1) and (1.2) highlight that the temperature value at vehicle wall can reach prohibitive levels as Mach number is higher and higher. For example, the limit for aluminum structure is around Mach 2, which was the Concorde's cruise Mach number. The SR-71 is made of titanium, and temperature limits the speed to slightly over Mach 3. Therefore, this means that within hypersonic configuration design, aeroheating and, hence, viscous effects represent critical concerns. Also, unlike normal airplane aerodynamics, hypersonic vehicles fly at very high altitudes, and the Reynolds number may be so low that the flow is laminar. Thus laminar flows are often of interest. This is important because the heat transfer is much lower when the flow is laminar. In fact, being able to estimate the transition location from laminar to turbulent flow conditions with certainty is a critical requirement in hypersonic vehicle design [3].

### 1.2.3 Blunt Aeroshapes to Reduce Heat Transfer

Since round shapes have lots of drag, why do we see such highly rounded shapes? The answer is the heat transfer. Using similarity techniques, Van Driest showed that the stagnation region wall heating rate  $\dot{q}_0$  is proportional to the square root of the edge velocity gradient  $\left(\frac{du_e}{dx}\right)_{sp}$  [4]. De Jarnette et al. show the relationship between the velocity gradient and the stagnation-point radius  $R$  to be as follows [5]:

$$\left(\frac{du_e}{dx}\right)_{sp} = \frac{V_\infty}{R} \sqrt{1.85 \frac{\rho_\infty}{\rho_e}} \quad (1.3)$$

and

$$\dot{q}_0 \propto \sqrt{\left(\frac{du_e}{dx}\right)_{sp}} \propto \frac{1}{\sqrt{R}} \quad (1.4)$$

It is obvious from the previous equation that a sharp nose ( $R \rightarrow 0$ ) would never survive the stagnation-point heating. Therefore, all hypersonic vehicles require blunt

leading edges. In fact, all manned vehicles present an almost flat leading edge ( $R \rightarrow \infty$ ) in order to minimize the heat transfer rate, Eq. (1.4), thereby maintaining a survivable atmosphere inside the vehicle; also the high drag helps reduce the velocity to enable a soft touchdown.

Thus, we need a nose or leading edge radius large enough for the tip not to melt. H. Julian Allen and A.J. Eggers, Jr., at NASA Ames did the analysis that showed that blunt bodies were required to survive entry from orbit [6].

### 1.2.4 Surface Pressure Estimation

In many cases surface pressures are relatively easy to estimate at hypersonic speeds [3]. At supersonic speed we have a local relation for two-dimensional flows relating surface slope and pressure:

$$C_p = \frac{2\theta}{\sqrt{M^2 - 1}} \quad (1.5)$$

This relation, however, is not particularly useful in most cases on actual aircraft configurations.

In comparison, hypersonic rules are useful. The most famous relation is based on the concepts of Newton. Although Newton was wrong for low-speed flow, his idea does apply at hypersonic speeds.

The idea is that the oncoming flow can be thought of as a stream of particles, which lose all their momentum normal to a surface when they *hit* the surface.

This leads to the famous relation:

$$C_p = 2\sin^2\theta \quad (1.6)$$

Here  $\theta$  is the angle between the flow vector and the surface. Thus, you only need to know the geometry of the body locally to estimate the local surface pressure. Also, particles impact only the portion of the body facing the flow, as shown in Fig. 1.2.

The rest of the body is in a *shadow*, and the  $C_p$  is zero [3].

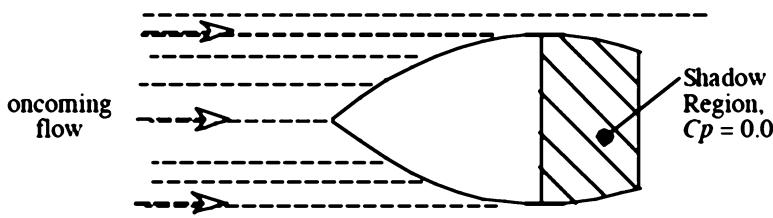


**Fig. 1.2** Shadow sketch, showing region where  $C_p$  is zero

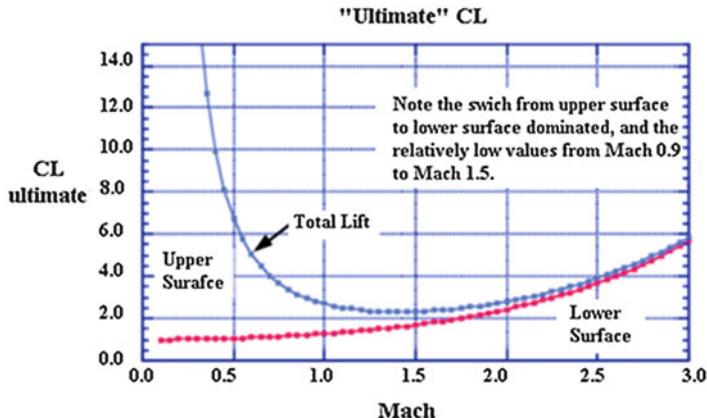


**Fig. 1.3** The “ultimate  $C_L$ ” plot (showing the dominance of the lower surface at hypersonic speeds)

Two key observations come from the Newtonian rule. First, the Mach number does not appear! Second, the pressure is related to the square of the inclination angle and not linearly as it is in the supersonic formula, i.e., Eq. (1.5). This illustrates how the situation in hypersonic flow is significantly different than the linearized flow models at lower speed. This figure also shows how the situation changes from low speed to high speed.

Moreover, let us look at the “ultimate” lift plot in Fig. 1.3. Here the lower surface pressure is taken equal to the stagnation value, and the upper surface is taken equal to the vacuum value. We can see that at low speeds the lift is generated on the upper surface, while at high speed the lift is almost completely generated on the lower surface.

### 1.2.5 High-Temperature Effects

As Mach number becomes hypersonic, the air behind a strong shock wave cannot be approximated as a perfect gas because temperature overcomes a threshold. For example, Fig. 1.4 is a plot of temperature behind a normal shock wave as a function of free-stream velocity, for a vehicle flying at a standard altitude of 52 km [see Eq. (1.1)] [3].

Two curves are shown: the upper curve, which assumes a calorically perfect non-reacting gas with the ratio of specific heats  $\gamma = 1.4$  and which gives an unrealistically high value of temperature, and the lower curve, which assumes an equilibrium chemically reacting gas and which is usually closer to the actual situation.

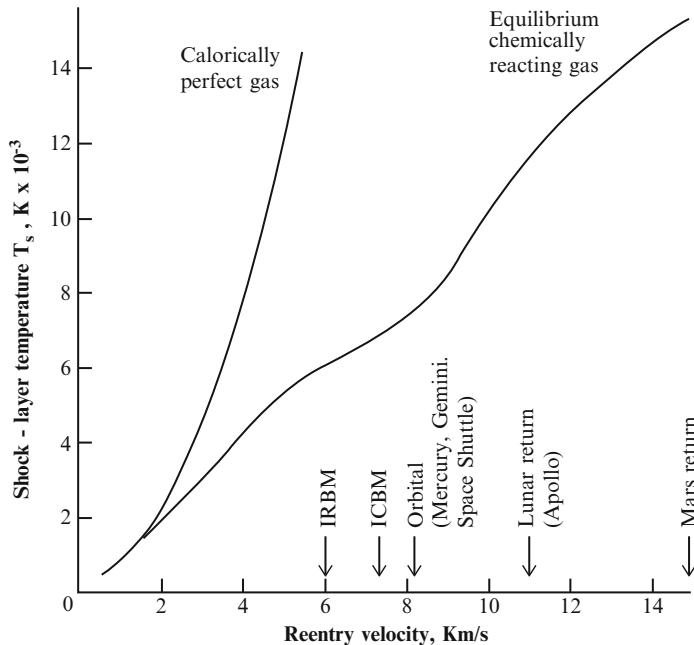


**Fig. 1.4** Temperature behind a normal shock wave as a function of free-stream velocity at a standard altitude of 52 km

So, two important points are assessed:

1. By any account, the temperature in the nose region of a hypersonic vehicle can be extremely high, for example, reaching approximately 11,000 K at a Mach number of 36 (e.g., Apollo re-entry).
2. The proper inclusion of chemically reacting effects is vital to the calculation of an accurate shock layer temperature; the assumption that  $\gamma$  is constant and equal to 1.4 is no longer valid.

### 1.2.6 Viscous Interaction

It is known that for a constant pressure process, an increase in temperature results in a lower density. Therefore, to maintain the same mass flow in the higher-temperature boundary layer associated with supersonic flows, the boundary-layer thickness will have to increase [3].

It has been shown using similarity techniques that

$$\frac{\delta}{x} \propto \frac{M_\infty^2}{\sqrt{Re_x}} \quad (1.7)$$

Hence, for a given Reynolds number, a hypersonic ( $M_\infty \gg 1$ ) boundary layer will be significantly thicker than a supersonic boundary layer, thus effecting the outer inviscid flowfield past the vehicle.

This interaction between the boundary layer and the outer flowfield region is called viscous interaction.

### 1.2.7 Entropy Gradient

Consider a blunt nose wedge, as sketched in Fig. 1.5 [3]. At hypersonic Mach numbers, the shock layer over the blunt nose is thin, with a small shock-detachment distance,  $d$ . In the nose region, the shock wave is highly curved. Recall that the entropy of the flow increases across a shock wave, and the stronger the shock, the larger the entropy increase. A streamline passing through the strong, nearly normal portion of the curved shock near the centerline of the flow will experience a larger entropy increase than a neighboring streamline which passes through a weaker portion of the shock further away from the centerline.

Hence, starting from the nose region, an “entropy layer” flows downstream, along the body for large distances from the nose, as shown in Fig. 1.5. In this layer a strong entropy gradient is achievable. The boundary layer along the surface grows inside this entropy layer and is affected by it. Since the entropy layer is also a region of strong vorticity, as related through Crocco’s theorem from classical compressible flow, this interaction is sometimes called a *vorticity interaction*:

$$T \nabla s - (\nabla \times \mathbf{V}) \times \mathbf{V} = \nabla H \quad (1.8)$$

where  $T$  is the temperature,  $s$  is the entropy,  $\mathbf{V}$  is the flow velocity, and  $H$  is the total enthalpy.

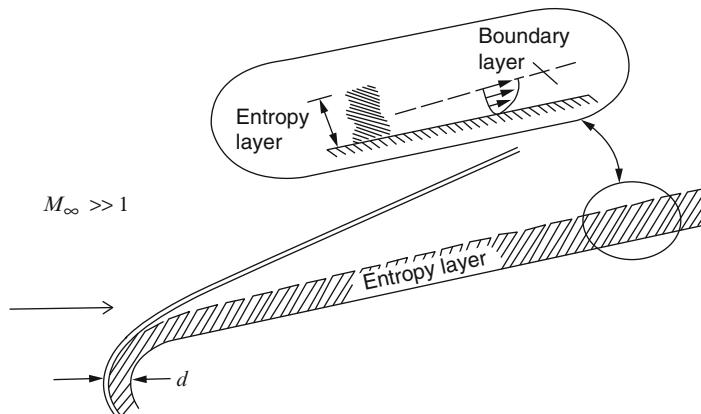


**Fig. 1.5** The entropy layer

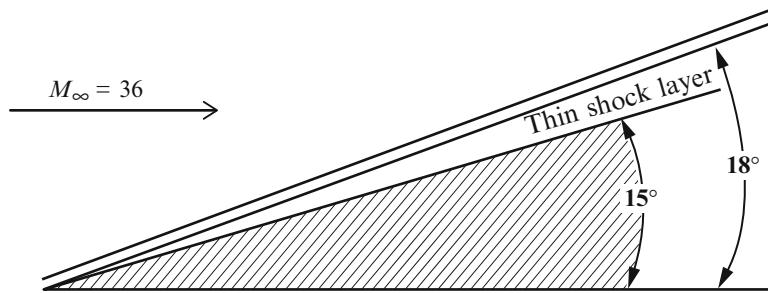


**Fig. 1.6** Thin hypersonic shock layer

The entropy layer causes analytical problems when we wish to perform a standard boundary-layer calculation on the surface, because there is a question as to what the proper conditions should be at the outer edge of the boundary layer.

### 1.2.8 Thin Shock Layer

The flowfield between the shock wave and the body is defined as the shock layer, and for hypersonic speeds this shock layer is thin. Let us consider, for example, a wedge of  $15^\circ$  semi-angle in a flow at  $M_\infty = 36$ . Applying the standard oblique shock theory, for a perfect gas with  $\gamma = 1.4$ , the shock-wave angle will be only  $18^\circ$ , as shown in Fig. 1.6. If chemically reacting effects are included, real gas hypothesis applies and the shock-wave angle will be even smaller. It is a basic characteristic of hypersonic flows that shock waves lie close to the body and that the shock layer is thin. At high Reynolds numbers, where the shock layer is essentially inviscid, this characteristic can be used to theoretical advantage, leading to a general analytical approach called *thin shock layer theory*. A thin shock layer approaches the fluid dynamic model postulated by Isaac Newton in 1687; such *Newtonian theory* is simple and straightforward and is frequently used in hypersonic aerodynamics for approximate calculations aiming to estimate the pressure distribution over the surface of a hypersonic body.

As drawback some physical complications arise, such as the merging of the shock wave itself with the boundary layer, and such phenomenon becomes important at low Reynolds numbers [3].

### 1.2.9 Engine–Airframe Integration

Any air-breathing hypersonic vehicle will have a highly integrated engine and airframe. It will be hard to tell exactly what counts as the vehicle and what counts as the propulsion system.

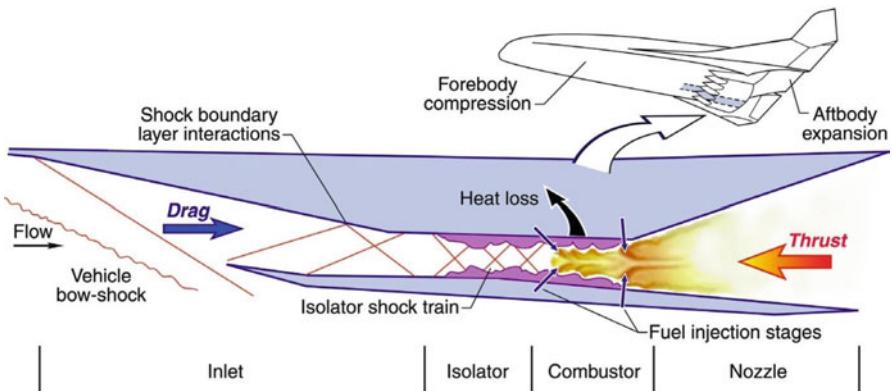


**Fig. 1.7** Example of engine–airframe integration for a hypersonic aircraft

This is exemplified in the concepts developed for recent aerospace planes. In these concepts the propulsion is at least in part provided by a scramjet engine, which obtains thrust with a combustion chamber in which the flow is supersonic. Figure 1.7 shows this concept [2]. The entire forebody of the vehicle underside is used as an external inlet to provide flow at just the right conditions to the engine. The entire underside afterbody is the exhaust nozzle.

### 1.2.10 Control and Stability Issues

Hypersonic flight presents major challenges to airframe and control system designers. High velocity can cause a hypersonic vehicle to be highly sensitive to changes in flight conditions (e.g., Mach number and angle of attack) that can result in instability or weakly damped transient oscillations of the airframe. The design problem is further compounded by the fact that hypersonic aerodynamic parameters, as predicted from ground tests or theoretical computational methods, do not reflect the actual flight parameters; there are significant uncertainties in the parameter values required for airframe and control system design.

Consequently, conventional techniques do not always lead to a design that is stable and at the same time robust to parameter uncertainties [2, 3].

It appears that a key reason for instability at hypersonic speeds is that the center of pressure *CoP* position (without active control) remains constant irrespective of the angle of attack,  $M$ , and altitude. Hence, stability augmentation due to moment arm effect through shift in *CoP* position (as in the case of subsonic and low supersonic speeds) does not occur at hypersonic speeds. Thus, without active control, a hypersonic vehicle is likely to be lightly damped or even unstable. Active

control provides for stability and rapid damping of the transients (following a disturbance) by changing the *CoP* position in a controlled way. In fact, active control can often make a vehicle stable even when the static stability margin indicates instability.

With uncertain aerodynamics and the fact that *CoP* position remains fixed, it is clear that a hypersonic vehicle would require an active and robust (insensitive to parameter uncertainties) control to accomplish stable sustained flight. Moreover, if a hypersonic vehicle is expected to demonstrate desirable flight qualities over a large flight envelope (in terms of  $M$  and altitude), then an adaptive control scheme needs to be implemented.

Because of the engineering difficulty and performance costs associated with conventional aerodynamic control of hypersonic vehicles, several alternative approaches have been proposed based on solely internal systems. One of these is a moving mass intended to effect control by shifting the center of gravity (*CG*) position axially and laterally. However, the extent, speed, and precision of movements of the weights may not be sufficient to confer stability nor indeed provide the control required to maintain the angle of attack at a value to achieve the desired lift force. Moreover, precision control of angle of attack is necessary for many high-speed air-breathing propulsion systems to operate satisfactorily.

### 1.3 Re-entry from Orbit

A typical descent trajectory followed by a spacecraft returning from low Earth orbit (LEO) is close to those reported in the altitude–velocity map Fig. 1.8 [7].

Thus, during descent, a re-entry vehicle encounters several flow regimes so that its aerodynamic performances and inertial and aerothermal loading conditions as well change accordingly. This suggests having some insights on such flow regimes.

Let us start considering, as reported in Fig. 1.8, the variety of flow regimes and thermochemical phenomena encountered in the nose region by an orbital re-entry vehicle [7]. As shown, at the beginning of the atmospheric re-entry, the space vehicle encounters *free molecular flow* conditions up to about 120 km altitude. Then the vehicle flies through *transitional flow* regime up to reach *continuum flow* conditions at about 70 km altitude, where spacecraft velocity ranges from 7 to about 5 km/s.

When considering from subsonic to supersonic vehicles, the fluid is studied as a continuum, but for hypersonic regime, it is not always possible to apply such hypothesis. The rarefied upper atmosphere cannot be treated as such, and the effect of individual molecules on the vehicle must be considered. Indeed, consider a flowfield where the number density of particles and hence the intermolecular collision frequency is high. The relaxation time for a particle moving through such flowfield will be short and the associated relaxation distance small. If this relaxation

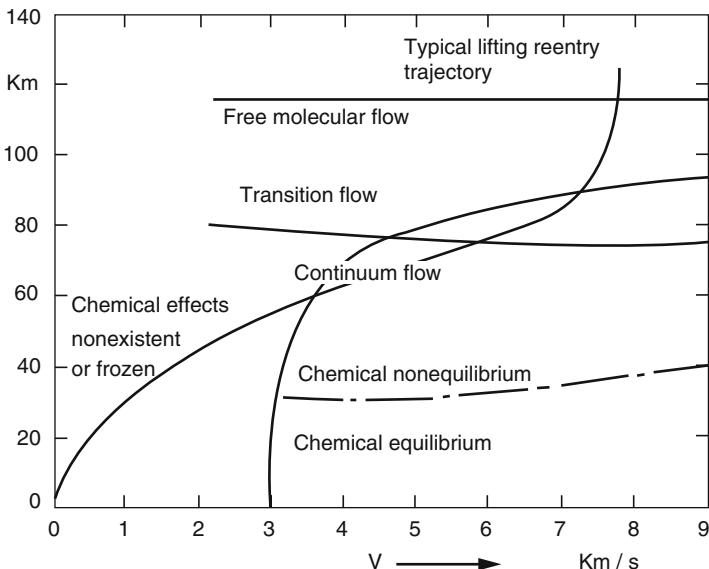


**Fig. 1.8** Stagnation-point flow regimes for re-entry vehicle

distance is small compared to the characteristic dimension of the flowfield, the macroscopic properties can be considered to vary continuously, and the gas can be treated as a *continuum*.

In contrast, a rarefied flowfield will have a long relaxation time and hence a longer relaxation distance. If this relaxation distance is not small compared to the characteristic flowfield dimension, the state of the individual particles and their interaction with other particles and the boundaries must be considered.<sup>3</sup>

One measure of the relaxation distance in a gas is the *molecular mean free path* between collision,  $\lambda$  [m], defined as follows [8]:

$$\lambda = \frac{1}{\sqrt{2}} \pi \sigma^2 n \quad (1.9)$$

where  $n$  [number of molecules/m<sup>3</sup>] is the *number density of the gas* and  $\sigma$  [m] the *effective diameter of gas particles*.

The mean free path depends only upon the number density of the gas,  $n$ , which is a function of the altitude. Though the effective diameter of the gas particles,  $\sigma$ , depends upon the temperature of the gas, the variation of  $\sigma$  is not a significant factor as the density.

---

<sup>3</sup>This is the case when the molecular mean free path (i.e., the distance a molecule travels between collisions) can become as large as the scale of the vehicle itself.

In order to quantify the relative importance of treating the fluid as a collection of particles vis-à-vis a continuum, a nondimensional parameter named *Knudsen number*,  $\text{Kn}$ , defined as

$$\text{Kn}_n = \frac{\lambda}{L_{\text{ref}}} = \frac{\text{mean free path}}{\text{characteristic flowfield dimension}} \quad (1.10)$$

is used.

Thus, free molecular flow occurs when Knudsen number is much greater than 1, i.e.,  $\lambda \gg L_{\text{ref}}$ .

When the density is low, i.e., at high altitudes, the mean free path is large (Knudsen number is high) and the flowfield cannot be treated as a continuum. Nevertheless, the Knudsen number can be high also when the characteristic dimension is small, e.g., flow through a shock wave where the characteristic dimension would be the thickness of the shock wave.

So, not only  $\lambda$  is important, but also  $L_{\text{ref}}$  which depends on the particular case studied.

The characteristic length could be a dimension of a flowfield characteristic or of the body. Indeed, for a blunt cone, the base radius may be appropriate. For a lifting body, the mean aerodynamic chord of the lifting surface may be the correct choice. On the other hand, for flows past flat plates, the boundary layer thickness or the distance from the leading edge may be the appropriate characteristic dimension.

Based on the relative importance of the particulate nature of air, quantified by the Knudsen number, three major regimes can be considered [8]:

1. Free molecular flow ( $\text{Kn}_n \gg 1$ ) :  $\frac{M}{Re} > 3$
2. Transition (from free molecular to continuum flow) regime  $3 > \frac{M}{Re}$  and  $\frac{M}{\sqrt{Re}} > 0.01$  ( $Re \gg 1$ )
3. Continuum flow ( $\text{Kn}_n \ll 1$ ) :  $0.01 > \frac{M}{\sqrt{Re}}$

Free molecular flow is dominated by molecule–surface interaction with negligible interaction between incident and reflected particles. Continuum flow, on the other hand, is dominated by intermolecular collisions. In the transition regime between these two extremes, both intermolecular and molecule–surface collisions are important (see Figs. 1.9 and 1.10) [8].

In terms of Mach and Reynolds numbers, continuum flow occurs when  $M/(Re)^{1/2} < 0.01$  and free molecular flow occurs when  $M/Re > 3$  (see Table 1.1), as shown in the *Mach–Reynolds* map in Fig. 1.10 [8].

In free molecular flow conditions, a distinct bow shock does not exist in front of a blunt body, and at altitudes just below the free molecular limit, molecules near the vehicle surface may have a mean velocity different from that of the surface. This is referred to as *velocity slip* condition. If the fluid molecules do not acquire the energy corresponding to the energy of the vehicle surface after one collision, there is lack of *momentum accommodation*. If a temperature discontinuity occurs at the vehicle surface, there is a lack of *thermal accommodation*. In free molecular and

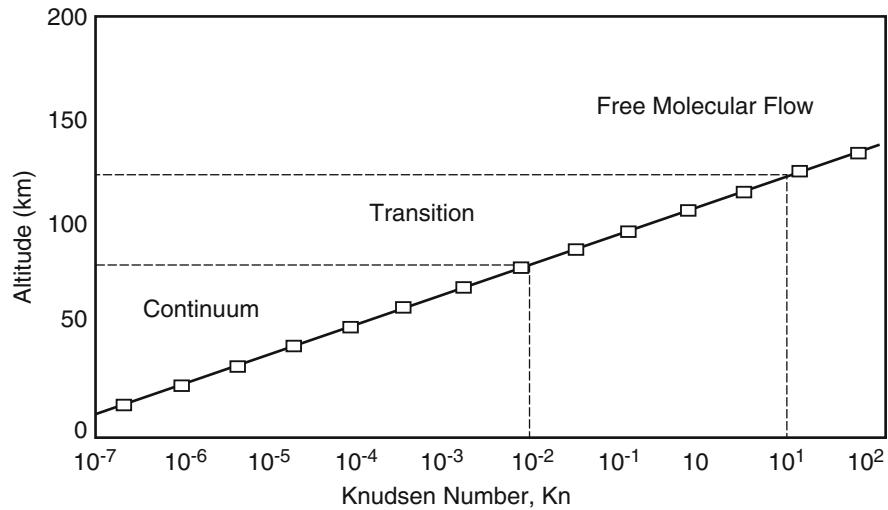


Fig. 1.9 Knudsen number vs. altitude

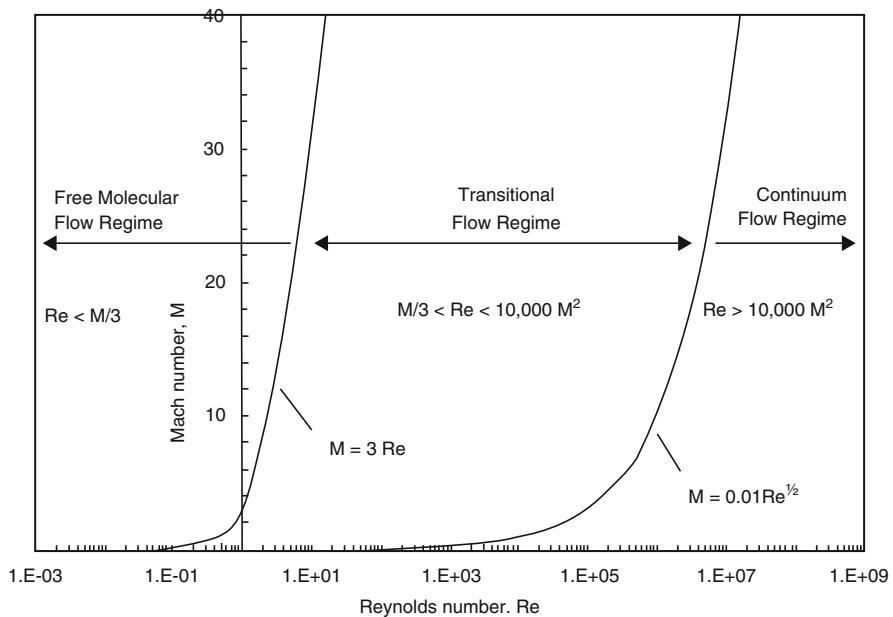


Fig. 1.10 Free molecular and continuum flow regimes based on Mach and Reynolds numbers

**Table 1.1** Free molecular and continuum flow regime boundaries [8]

Flow regime	Anderson (1989) <sup>a</sup>	Regan and Anandakrishnan (1993)
Free molecular	$\text{Kn} \gg 1$	$Re < M/3$
Near free molecular	$\text{Kn} > 1.0$	—
Transitional	$1.0 > \text{Kn} > 0.03$	$M/3 < Re < 10^3 M^2$
Continuum	$\text{Kn} < 0.2$	$Re > 10^3 M^2$

<sup>a</sup>Note the overlap of the continuum and translational flow regimes. Anderson (1989) notes that this region ( $0.03 < \text{Kn} < 0.2$ ) temperature and velocity slip effects (discontinuities) are present at the body surface

near free molecular flows, thermal and momentum accommodation coefficients can be determined experimentally and used to predict *temperature jump* and *velocity slip at the surface*.

The convective heat flux in free molecular flow can be determined from the kinetic theory of gases or obtained from an experimental correlation of Stanton number (St) and thermal accommodation coefficient.

Note that almost all critical heat transfer problems for a spacecraft that arise in penetrating a planetary atmosphere occur in the continuum flow regime.

Thus, for the aim of the present research effort, the regime of interest is the continuum flow ( $K_n \ll 1$ ).

Coming back to Fig. 1.8, we see that at flight conditions below 90 km, the altitude–velocity map highlights that the flight domain separates in two regions. On the left (flight velocities lower than 3 km/s), we have the altitude–velocity plane where chemical effects are nonexistent or frozen.

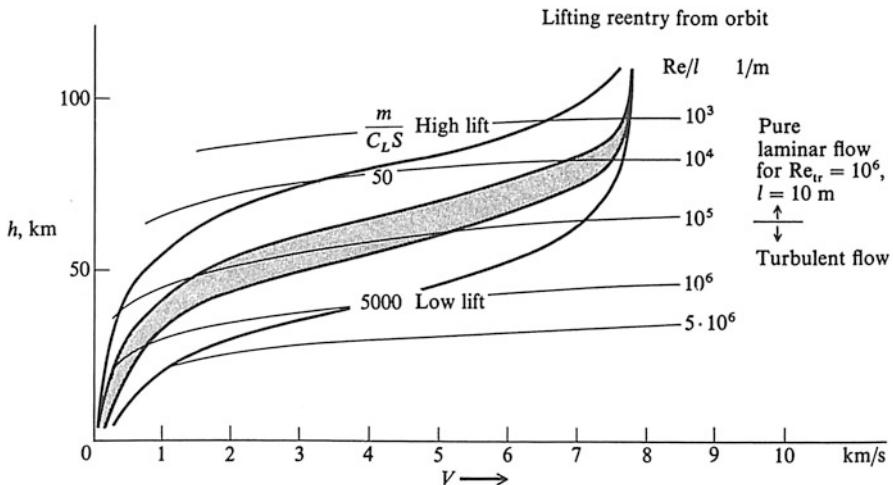
On the contrary, a vehicle flying at velocities larger than 3 km/s experiences flow *dissociations and thermochemical effects*. In particular, Fig. 1.8 highlights that only below about 30 km altitude the flow can be considered in *chemical equilibrium*. Thermochemical nonequilibrium flow conditions will be discussed in detail later when attention will be focused on *high-temperature real gas effects*.

Figure 1.11 shows that the unit Reynolds number  $Re/l$  increases as altitude decreases [3].

$Re/l$  reaches value of about  $10^3 \text{ l/m}$  at very high altitude so that the flow can be considered pure laminar; while at low altitude (says below 50 km)  $Re/l$  is equal to about  $10^6 \text{ l/m}$ , thus confirming that the flow is in turbulent conditions.<sup>4</sup> Thus, the flow regimes encountered by the vehicle cover fully laminar to fully turbulent and free molecular to fully continuum phases, with transitional phases along the way. Note, however, that the position on the altitude–velocity map of those boundaries depends strongly on the kind of re-entry space vehicle (e.g., characteristic length), as will be explained hereinafter in the book.

---

<sup>4</sup>Note that the black strip in Figure 1.11 represents the re-entry envelope of the US Space Shuttle Orbiter, as a reference.



**Fig. 1.11** Typical re-entry trajectory with isolines of Reynolds number

## 1.4 Typical Hypersonic Flowfield Features Past a Vehicle in Continuum Flow Regime

It is in this regime that the vehicle will experience the maximum inertial and aerothermal loads, which drive most aspects of hypersonic vehicle design. Figure 1.12 illustrates a flowfield about a typical hypersonic vehicle.

Therefore, before going into any details, it is useful to examine a very general flowfield that takes place past a typical hypersonic vehicle, as shown in Fig. 1.12 [8].

Based on the local features, the flowfield around the hypersonic body may be divided into three regions:

1. The boundary layer<sup>5</sup>
2. The outer inviscid flow region
3. The wake region

Some comments on above regions are in order.

The boundary layer is the region adjacent to the body surface, dominated by viscous effects and heat conduction. The shearing effect of viscosity causes the velocity to vary from zero at the wall, satisfying the wall boundary conditions, to the outer flow velocity at the edge of the boundary layer (see Fig. 1.13). In subsonic

<sup>5</sup>The aerodynamic boundary layer was first defined by Ludwig Prandtl in a paper presented on August 12, 1904, at the third International Congress of Mathematicians in Heidelberg, Germany. It allows aerodynamicists to simplify the equations of fluid flow by dividing the flow field into two areas: one inside the boundary layer, where viscosity is dominant and the majority of the drag experienced by a body immersed in a fluid is created, and one outside the boundary layer where viscosity can be neglected without significant effects on the solution.

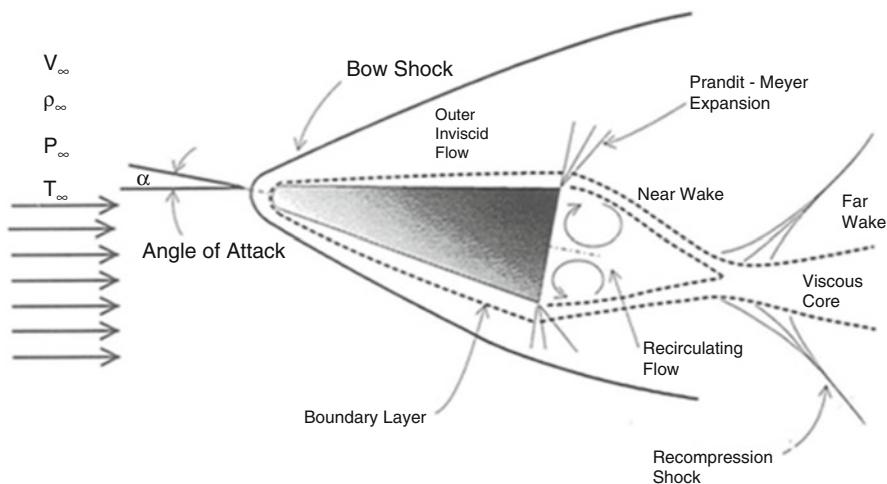


Fig. 1.12 Typical hypersonic body flowfield in continuum regime

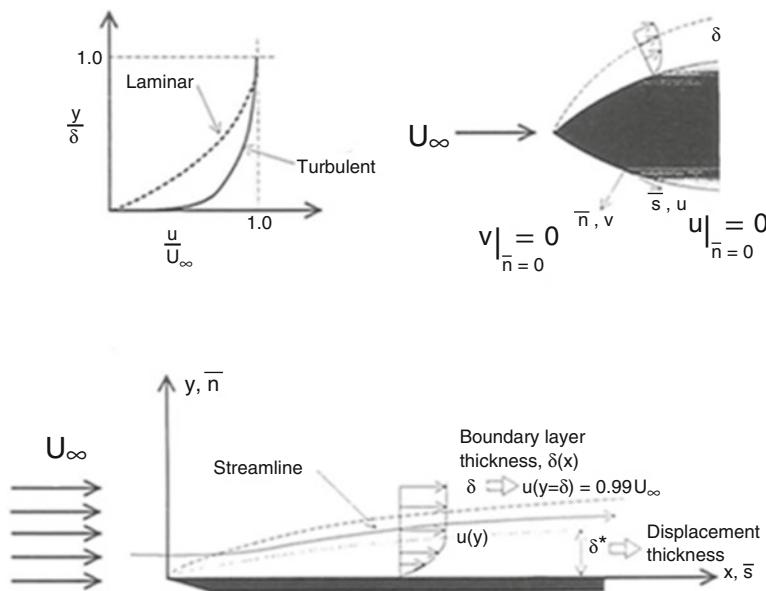


Fig. 1.13 Boundary-layer velocity profiles

regime the boundary-layer thickness  $\delta_{99\%}$  (or  $\delta$ ) is defined as the distance normal to the wall where the local velocity is 99 % of the “free-stream” (or boundary-layer edge) velocity and is related to  $Re$ :

$$\delta \propto \frac{1}{\sqrt{Re}} \quad (1.11)$$

In particular, the velocity profiles in the boundary layer, as shown in Fig. 1.13, are different ranging from laminar to turbulent boundary layer, thus suggesting that both shear stress and heat flux are expected to be greater in the case of turbulent flow [8].

To satisfy the mass conservation equation, the streamlines will be deflected away from the wall because of the slower-moving fluid accumulating near the wall. The amount of deflection of the streamlines outside the boundary layer is called the *displacement thickness*  $\delta^*$ :

$$\delta^* = \int_0^\delta \left( 1 - \frac{\rho}{\rho_e} \frac{u}{u_e} \right) dy \quad (1.12)$$

where the subscript e refers to the conditions at the edge of the boundary layer.

$\delta^*$  is a function of the distance from the leading edge and the velocity profile in the boundary layer. This thickness can exert a major displacement effect on the inviscid flow outside the boundary layer, causing a given body shape to appear much thicker than really is; it is like the flow is disturbed from an “*apparent body*”.

The velocity profile in the boundary layer determines the viscous forces acting on the body. The wall shear stress  $\tau_w$ , [ $\text{kg}/\text{ms}^2$ ], is given by

$$\tau_w = \mu \left( \frac{\partial u}{\partial y} \right)_w \quad (1.13)$$

and the local skin friction coefficient  $C_f(x)$ , nondimensional, reads

$$C_f(x) = \frac{\tau_w}{\frac{1}{2} \rho_e V_e^2} \quad (1.14)$$

Similarly, the temperature must vary from the wall to the outer edge to satisfy the boundary conditions and to account for the temperature rise due to kinetic energy changes (adiabatic) and friction.

The heat transfer rate at the wall may be expressed by Fourier’s law of heat conduction. The wall heat transfer rate  $\dot{q}_w$ , [ $\text{W}/\text{m}^2$ ], and Stanton number  $St$ , nondimensional, are given by

$$\dot{q}_w = -k \left( \frac{\partial T}{\partial y} \right)_w \quad (1.15)$$

$$St = \frac{\dot{q}_w}{\rho_e u_e (h_{aw} - h_w)} \quad (1.16)$$

where  $k$ , [ $\text{W}/\text{mK}$ ], is the thermal conductivity and  $h_{aw}$  and  $h_w$ , [ $\text{J}/\text{kg}$ ], are the adiabatic wall enthalpy (enthalpy for  $\dot{q}_w = 0$ ) and the actual wall enthalpy, respectively.

Recalling Eq. (1.11) it is evident that for high Reynolds number flows, the boundary layer is usually quite thin. Hence, the viscous effects can be assumed to

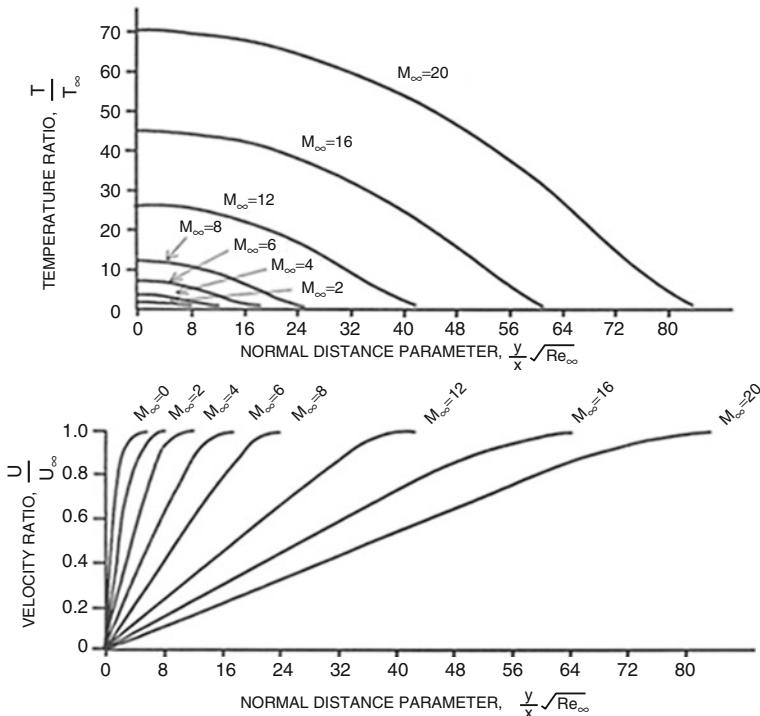


**Fig. 1.14** Temperature and velocity distribution across laminar boundary layers on an insulated flat plate at various Mach numbers

be confined to the boundary layer. For thin boundary layers, the pressure is constant normal to the surface and is assumed to be imposed by the outer flow at the outer edge of the boundary layer (Prandtl's condition).

On the contrary, Eq. (1.8) suggests that the boundary-layer thickness and temperature increase dramatically with high Mach and Reynolds numbers.

This is clearly shown in Fig. 1.14 where temperature and velocity distribution across laminar boundary layer on an insulated flat pale at various Mach numbers are provided. As one can see, the higher the Mach number, the larger the temperature ratio  $T / T_{\infty}$  at lower normal distance parameter  $\frac{y}{x} \sqrt{\text{Re}_{\infty}}$  [8].

The coupling of the energy and the momentum equation is illustrated when comparing the results of the adiabatic (see Fig. 1.14) and nonadiabatic (see Fig. 1.15) wall flows.<sup>6</sup>

<sup>6</sup>When the speed of sound is much greater than the free-stream flow velocity ( $U \ll a$ ), the density may be considered to be a constant (i.e., incompressible flow). In addition, if the coefficient of viscosity and heat conduction are also constant, the energy equation is decoupled from the momentum equation, significantly simplifying the problem. However, this luxury is not afforded in high-speed flow, where the density may no longer be considered a constant.

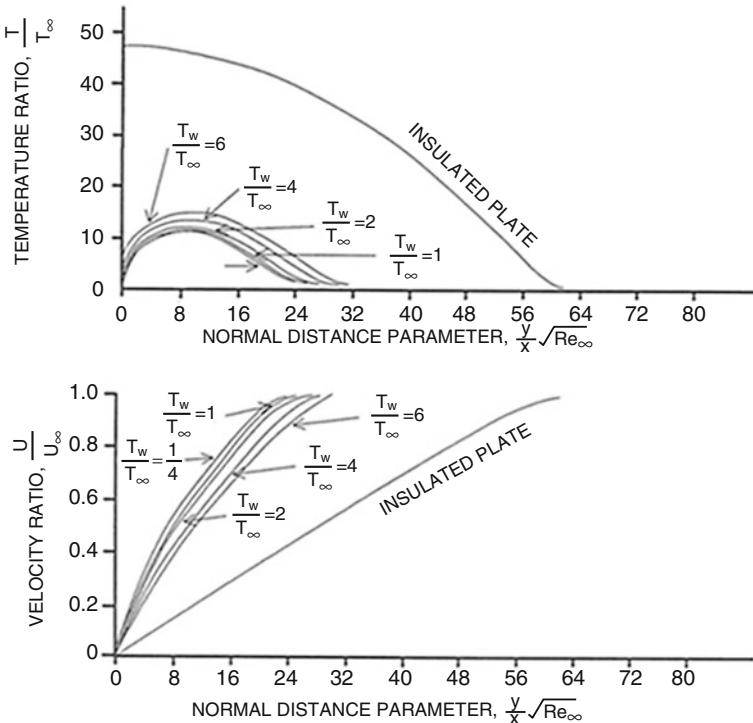


**Fig. 1.15** Temperature and velocity distribution across laminar boundary layer for  $M_{\infty} = 16$  and various wall-to-free-stream temperature ratios

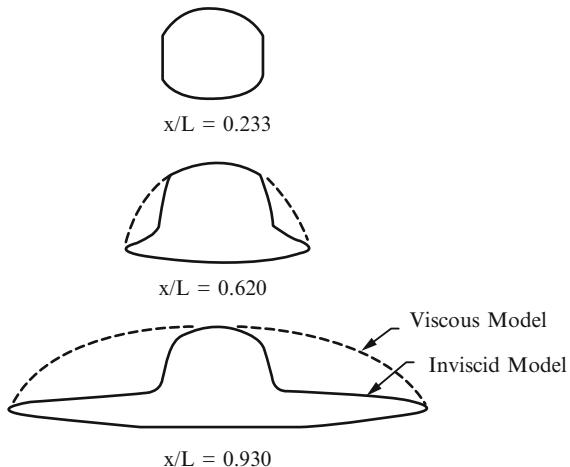
This is illustrated in Fig. 1.15 where temperature and velocity distribution across laminar boundary layer for  $M_{\infty} = 16$  and various wall-to-free-stream temperature ratios is shown [8].

As shown, the boundary layer is much thicker for an adiabatic wall than for a cold wall. Since the shear stress and heat transfer rate are proportional to the velocity and temperature gradients, see Eqs. (1.13) and (1.15), respectively; a thicker boundary layer results in lower shear stress and heat transfer rates at the wall.

The outer flow region, assumed to be inviscid (i.e., viscosity is confined to the boundary layer) and nonconducting, governs the pressure forces acting on the body. The outer flow may be determined independently of the boundary layer by using a fictitious body (i.e., viscous model) that is the original body (i.e., inviscid model) with the displacement thickness  $\delta^*$  superimposed. For instance, this approach was used in the past for the Space Shuttle introducing the HALIS configuration (see Fig. 1.16) and investigating Orbiter aerodynamic performance by carrying out CFD Euler computations only [3].

The inviscid pressure and velocity field determined by means of Euler equations, Eq. (1.25), on such fictitious body will provide the boundary conditions for the outer edge of the boundary layer [2, 3].

**Fig. 1.16** Cross sections of the simplified Orbiter geometry (viscous model equal to HALIS configuration)



The wake region flow is quite complex and is dominated by a recirculating zone behind the separation point (see Fig. 1.12). In addition, the vorticity diffuses from the boundary layer merging with the outer flow. The wake flow determines the base pressure and hence the base drag. In hypersonic separated base flow, a good approximation is  $p_{\text{base}} = p_{\infty}$ . If the flow does not separate, the wake region may be treated as a combination of the boundary layer and outer inviscid flow.

Anyway, a detailed description of the flowfield that takes place past a vehicle at hypersonic speed in continuum flow regime can be obtained by integrating the flowfield governing equations.

#### 1.4.1 Fluid Flow Governing Equations

All fluid flowfields are governed by the following three conservation laws:

1. Conservation of mass: continuity equation
2. Conservation of momentum: Newton's second law of motion
3. Conservation of energy: first law of thermodynamics

These conservation laws in conjunction with a *definition of the fluid* provide the system of equations required to determine the flowfield for a given set of *boundary conditions*.

If the atmosphere around the body is modeled as a continuum, the conservation equations lead to a system of equations based on the bulk properties of air, well known as the *Navier–Stokes* equations.

On the other hand, a rarefied flowfield is described by *Boltzmann* equation, which is based on molecular mechanics. So, a high  $K_n$  indicates the importance of the particulate nature of the fluid and the Boltzmann equation must be adopted, whereas low  $K_n$  permits treatment of the fluid as a continuum and the use of the

Navier–Stokes equation solution. For  $K_n \rightarrow \infty$ , the Boltzmann equation solution converges asymptotically to the Navier–Stokes equation solution.

In combination with a *definition of the gas* and a set of *boundary conditions*, the *Navier–Stokes* equations determine the flowfield past the body. Indeed, for a very wide range of problems, air may be defined as a *perfect gas*. Therefore, the pressure,  $p$  [Pa], reads

$$p = \rho R T \quad (1.17)$$

where  $\rho$  is the density,  $T$  the temperature, and  $R$  the gas constant, while for what concerns boundary conditions at far-field, the condition is that any disturbance caused by the presence of the body should remain finite.

### Explanation Box. The Perfect Gas Model

Consider the air around you as made up of molecules that are in random motion, frequently colliding with neighboring molecules. Imagine that you pick one of these molecules out of the air around you. Examine it closely. You will find that a force field surrounds this molecule, due to the electromagnetic action of the electrons and nuclei of the molecule. In general, this force field will reach out from the given molecule, and will be felt by neighboring molecules, and vice versa. Thus, the force field is called an intermolecular force and is shown in Fig. 1.17.

In this figure, the intermolecular force is sketched as a function of distance away from the particle. At small distance, the force is strongly repulsive, tending to push the two molecules away from each other. However, as we

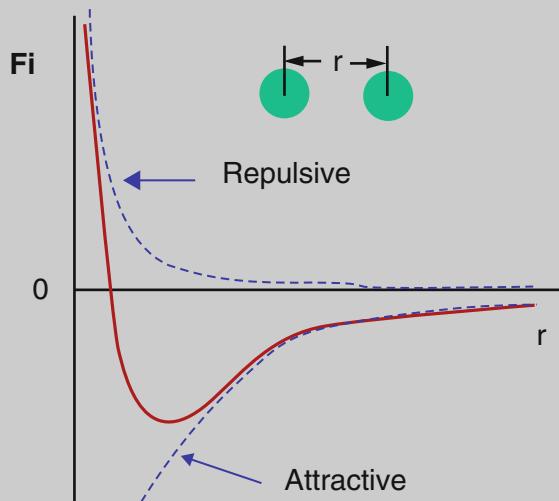


**Fig. 1.17** Intermolecular force diagram

(continued)

move further away from the molecule, the intermolecular force rapidly decreases, becomes a weak attractive force, tending to attract molecules together. At distances approximately ten molecular diameters away from the molecule, the magnitude of the intermolecular force is negligible. In this case we speak about a perfect gas.

A *perfect gas* is both *thermally perfect* and *calorically perfect* [9].

A *thermally perfect gas* is one that obeys the ideal gas equation of state:

$$p = \rho RT$$

For a *calorically perfect gas*, the internal energy depends on temperature:

$$e = c_v T \quad (1.18)$$

with  $c_v$  being constant, namely specific heat at constant volume.

Note, however, that high-temperature real gas effects force the flow to deviate from the perfect gas model. Indeed, dissociated gases can be considered as mixtures of thermally perfect gases, whose molecular species are calorically imperfect.

As will be explained later, the internal energy of a mixture of thermally perfect gases in equilibrium is, with  $Y_i$  being the mass fraction of species  $i$ ,

$$e = \sum_{i=1}^n Y_i e_i \quad (1.19)$$

where the internal energy of a species  $i$  is the summation of translational, rotational, vibrational and electronic energies

$$e_i = e_{\text{trans}_i} + e_{\text{rot}_i} + e_{\text{vibr}_i} + e_{\text{el}_i} \quad (1.20)$$

At the body surface, in general, the velocity normal to a wall (solid, impermeable surface) must be zero. For the tangential velocity, the concept of boundary layer region is applied. In this region viscous effects are predominant and tangential velocity at wall is zero (see Fig. 1.13). Thus,

$$V|_w = 0 \quad (1.21)$$

In addition, the gas temperature at the body surface must match the specified wall temperature ( $T_w$ ). Since the wall temperature will depend upon the heat conduction through the vehicle surface, it will generally not be known *a priori*. When the wall temperature is specified (i.e., fixed wall temperature condition,  $T_w$ ), the flow problem is decoupled from the body internal heat conduction problem

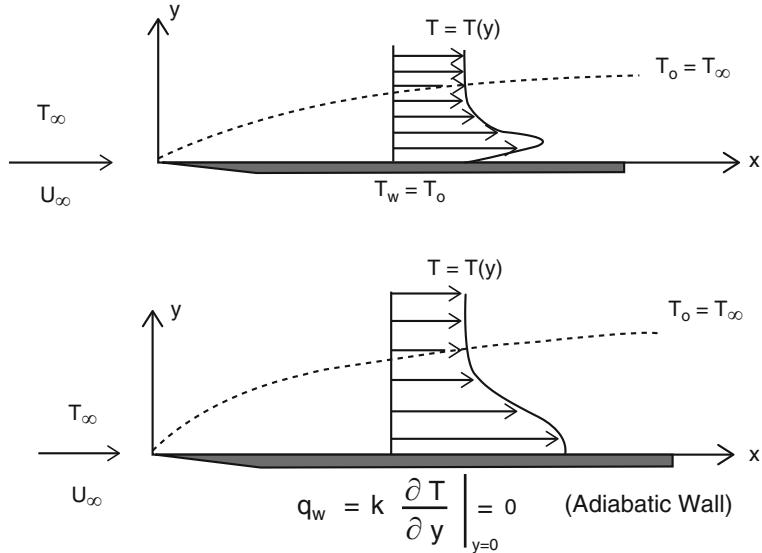


**Fig. 1.18** Boundary-layer temperature profiles

(see Fig. 1.18) [8]. If no conduction through the vehicle wall is present, the condition is called adiabatic wall condition. The specified wall temperature is given by

$$T(x) = T_w(x) \quad (1.22)$$

and the adiabatic wall condition is expressed as

$$\left( \frac{\partial T}{\partial y} \right)_w = 0 \quad (1.23)$$

The Navier–Stokes equations for compressible and unsteady flow read

$$\begin{cases} \frac{\partial \rho}{\partial t} + \nabla \cdot (\rho \mathbf{u}) = 0 \\ \frac{\partial (\rho \mathbf{u})}{\partial t} + \nabla \cdot (\rho \mathbf{u} \times \mathbf{u}) = \nabla \cdot \mathbf{T} + \rho \mathbf{f} \\ \frac{\partial (\rho E)}{\partial t} + \nabla \cdot (\rho E \mathbf{u}) = \nabla \cdot (\mathbf{T} \cdot \mathbf{u}) - \nabla \cdot \mathbf{q} + \rho \mathbf{f} \cdot \mathbf{u} + \rho r \end{cases} \quad (1.24)$$

Here it has denoted by  $\mathbf{T}$  the stress tensor,  $\mathbf{q}$  the vector of heat flux, and finally by  $\mathbf{f}$  and  $r$  the external force field per unit mass and the heat supply per unit mass per unit time, respectively.

The Navier–Stokes equations are a set of coupled, nonlinear, partial differential equations. The equations are a mixed set of elliptic–parabolic equations for steady flow and are hyperbolic–parabolic when the unsteady term is retained.

Neglecting the viscous and the heat transfer terms from the Navier–Stokes equations, a simplified set of equations, called the Euler equations, is obtained:

$$\begin{cases} \frac{\partial \rho}{\partial t} + \nabla \cdot (\rho \mathbf{u}) = 0 \\ \frac{\partial (\rho \mathbf{u})}{\partial t} + \nabla \cdot (\rho \mathbf{u} \times \mathbf{u}) + \nabla p = 0 \\ \frac{\partial (\rho E)}{\partial t} + \nabla \cdot (\rho E \mathbf{u}) + p \nabla \cdot \mathbf{u} = 0 \end{cases} \quad (1.25)$$

Even though the Euler equations are also coupled, nonlinear partial differential equations, they are of a lower order than the Navier–Stokes equations. The unsteady Euler equations are hyperbolic, but the steady state equations change their character from elliptic in subsonic flow ( $M_\infty < 1$ ) to hyperbolic in supersonic flow ( $M_\infty > 1$ ).

### 1.4.2 Flow Characteristics Related to the Change of $M_\infty$

Let now try to get a physical understanding of the reasons for and effects of the change in character of the flow with a change in  $M_\infty$ .

A disturbance (point source) in a fluid creates acoustic waves (i.e., infinitesimal pressure pulses) that radiate spherically with the speed of sound,  $a$ , telegraphing the presence of the source to the flowfield. Figure 1.19 illustrates the propagation of the acoustic waves from a moving source [8]. As a result, when the speed of the source,  $U$ , is less than  $a$ , the acoustic waves will warn the surrounding fluid of the approach of the source.

When the source moves faster than  $a$ , the warnings cannot propagate ahead of the source and are confined to a cone of influence, called the *Mach cone*. In a source-fixed frame of reference, with a uniform flow,  $U$ , past the source, for subsonic flow ( $U < a$ ), the disturbance influences the entire flowfield, while in a supersonic flow

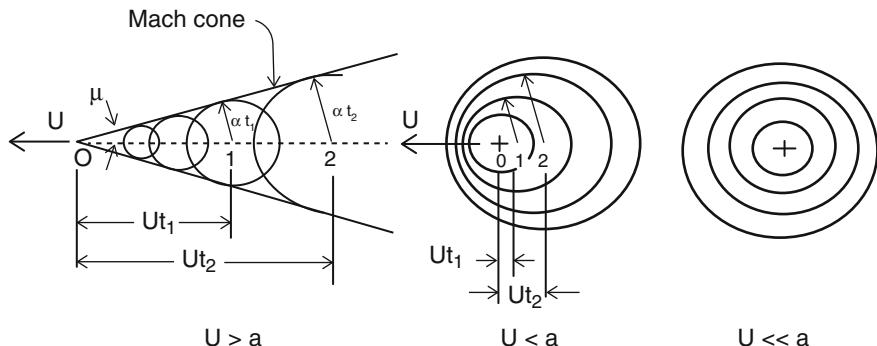


**Fig. 1.19** Wave propagation from a moving source

( $U > a$ ), the influence is limited to a zone demarcated by the Mach lines. The Mach lines are inclined to the local flow by the Mach angle,  $\mu$ , a characteristic angle associated with the Mach number:

$$\mu = \sin^{-1} \left( \frac{1}{M_\infty} \right) \quad (1.26)$$

Hence the subsonic problem will require the boundary conditions to be specified over the entire outer boundary and is called a *boundary value problem*. The supersonic problem, on the other hand, is an *initial value problem*, requiring boundary conditions only at an initial stage with the solution obtained by marching downstream.

The Euler equations may be further simplified for bodies that create only small perturbations to the free-stream. The resultant small perturbations equations are linear, except when  $M_\infty \rightarrow 1$  (transonic) or  $M_\infty \gg 1$  (hypersonic).

A flow that contains both subsonic and supersonic regions is referred to as transonic flow.

Based on the character of the governing equations and the accuracy of some of the approximations, the continuum flow regime may be subdivided into:

- (a) Incompressible flow  $M_\infty \leq 0.3$  (constant  $\rho$ )
- (b) Compressible subsonic flow  $0.3 < M_\infty < 1$
- (c) Transonic flow  $0.8 < M_\infty < 1.2$
- (d) Supersonic flow  $M_\infty > 1$
- (e) Hypersonic flow  $M_\infty > 5$

Figure 1.20 illustrates some of the salient flow features that take place past an airfoil, related to the change of  $M_\infty$  [8].

Since the character of the governing equations changes at  $M_\infty = 1$ , the solution technique must also be modified accordingly. In addition, a strong interaction between the boundary layer and shock waves in transonic flow further complicates any solution process.

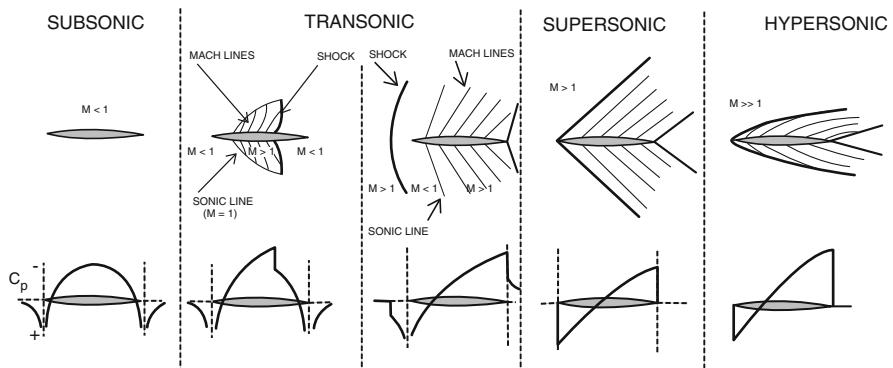


**Fig. 1.20** Continuum flow regimes. Flow characteristics past an airfoil, related to the change of  $M_\infty$

### 1.4.3 Shock Relations

In order to present the hypersonic theory, let us begin from the incompressible subsonic case. It is known that the constant density medium in incompressible flow decouples the momentum and energy equations. Considering an inviscid flowfield, the Euler equation (momentum equation) integrates to yield Bernoulli's equation (valid for irrotational flow, i.e.,  $\boldsymbol{\omega} = \nabla \times \mathbf{V} = 0$ ):

$$\frac{1}{2} \rho V^2 + p = \text{constant} \quad (\text{along a streamline}) \quad (1.27)$$

Increasing  $M_\infty$ , density can no longer be considered a constant and the energy equation for the adiabatic flow of a perfect gas may be written as

$$c_p T + \frac{1}{2} V^2 = c_p T_0 \equiv h_0 = \text{constant} \quad (1.28)$$

where

$$c_p = \frac{f+2}{2} R \quad \text{and} \quad \frac{c_p}{R} = \frac{\gamma}{\gamma-1} \quad (1.29)$$

$$c_p - c_v = R \quad (1.30)$$

$c_p$  and  $c_v$ , [J/kg K], are the specific heats at constant pressure and at constant volume, respectively, and  $f$  the number of active degrees of freedom (dof).

So, the compressible flow momentum equation (sometimes referred to as the compressible flow Bernoulli's equation) becomes, dividing by the density,  $\rho$ , and substituting (1.29) and (1.30),

$$\frac{V^2}{2} + \frac{\gamma}{\gamma-1} \frac{p}{\rho} = \text{constant} \quad (\text{along a streamline}) \quad (1.31)$$

From the (1.31), for an isentropic (adiabatic, inviscid, nonconducting) flow, the relationships between the stagnation conditions and local flow properties are

$$\begin{aligned} \frac{a_0^2}{a^2} &= \frac{T_0}{T} = 1 + \frac{\gamma-1}{2} M^2 \\ \frac{p_0}{p} &= \left(1 + \frac{\gamma-1}{2} M^2\right)^{\gamma/(\gamma-1)} \\ \frac{\rho_0}{\rho} &= \left(1 + \frac{\gamma-1}{2} M^2\right)^{1/(\gamma-1)} \end{aligned} \quad (1.32)$$

where the subscript 0 refers to stagnation conditions.

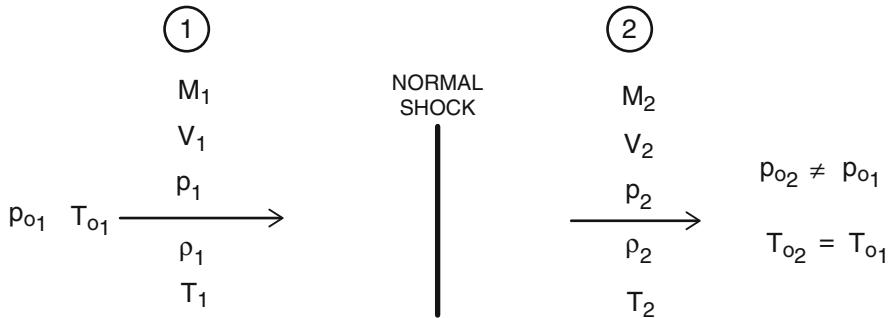


**Fig. 1.21** Flow across a normal shock

Equations (1.32) are valid only in isentropic flows. However, when a supersonic flow is compressed through a shock wave, the process is no longer isentropic. A shock wave is quite thin (of the order of molecular mean free path) and from a macroscopic perspective may be considered to be a discontinuity in the flow.

Without going to the details of demonstration, the flowfield properties behind a normal shock (see Fig. 1.21) may be calculated using the Rankine–Hugoniot relations [8]:

$$\begin{aligned}\frac{p_2}{p_1} &= 1 + \frac{2\gamma}{\gamma+1} (M_1^2 - 1) \\ \frac{\rho_2}{\rho_1} &= \frac{u_2}{u_1} = \frac{(\gamma+1)}{(\gamma-1)} \frac{M_1^2}{M_1^2 + 2} \\ \frac{T_2}{T_1} &= 1 + \frac{2}{(\gamma+1)^2} \frac{(\gamma-1)}{\gamma} \frac{M_1^2 + 1}{M_1^2} (M_1^2 - 1) \\ M_2^2 &= \left(1 + \frac{\gamma-1}{2} M_1^2\right) \Big/ \left(\gamma M_1^2 - \frac{\gamma-1}{2}\right)\end{aligned}\quad (1.33)$$

From the last relation of Eq. (1.33), it can be seen that the flow past a normal shock is always subsonic.

In case of oblique shock, Eq. (1.33) has to be modified in order to take into account for the deflection angle  $\theta$  and shock angle  $\beta$ . When the flow is not normal to the shock, the velocity component normal to the shock is modified as if going through a normal shock, and the component parallel to the shock must be equal on either side of the shock to satisfy the continuity equation.

Since an oblique shock acts as a normal shock to the component of flow normal to it, the normal shock equations, Eq. (1.33), given above may be applied to the oblique shock problem (see Fig. 1.22) [8].  $M_1$  and  $M_2$  are replaced by their normal

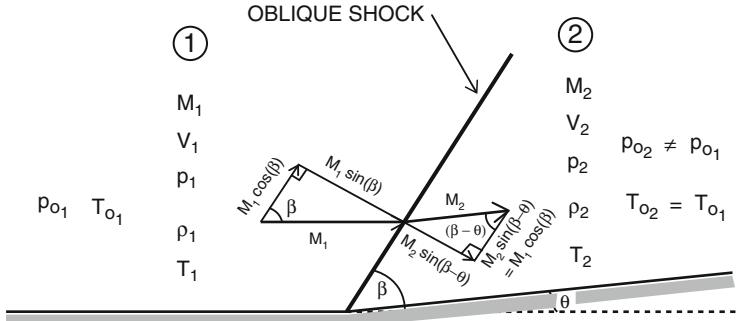


**Fig. 1.22** Flow across an oblique shock

components  $M_1 \sin\beta$  and  $M_2 \sin(\beta - \theta)$ , where  $\beta$  is the shock angle and  $\theta$  is the flow deflection angle. The relationships among the shock angle, deflection angle, and properties across an oblique shock are given in Eq. (1.34):

$$\begin{aligned}
 \frac{p_2}{p_1} &= 1 + \frac{2 \gamma}{\gamma + 1} (M_1^2 \sin^2 \beta - 1) \\
 \frac{\rho_2}{\rho_1} &= \frac{u_2}{u_1} = \frac{(\gamma + 1)}{(\gamma - 1)} \frac{M_1^2 \sin^2 \beta}{M_1^2 \sin^2 \beta + 2} \\
 \frac{T_2}{T_1} &= 1 + \frac{2}{(\gamma + 1)^2} \frac{(\gamma - 1)}{\gamma} \frac{M_1^2 \sin^2 \beta + 1}{M_1^2 \sin^2 \beta} (M_1^2 \sin^2 \beta - 1) \\
 \tan \theta &= 2 \cot \beta \frac{M_1^2 \sin^2 \beta - 1}{M_1^2 (\gamma + \cos 2\beta) + 2} \quad (1.34)
 \end{aligned}$$

Equations (1.34) hold for 2-D case. In the three-dimensional case of a flow past a cone, determining the properties behind the shock is not as simple as the two-dimensional case. Unlike a wedge flow, the properties behind a shock in conical flow are constant along any ray emanating from the vertex of the cone (see Fig. 1.23) [8].

The conical shock angle  $\beta_c$  and the properties behind the shock are tabulated for a range of Mach numbers  $M_\infty$ , cone angles  $\theta_c$ , and ray angles  $\omega$ .

For both two and three-dimensional flow, if the flow deflection angle is too large, an oblique shock solution does not exist and a curved shock, detached from and normal at the leading edge (see Fig. 1.24), is formed [8]. Since the flow behind the normal part of the curved shock will be subsonic, the shape and stand-off distance of the curved shock depends upon the geometry of the body and must be calculated along with the entire flowfield. An additional problem associated with a curved shock is that the entropy increase across the shock varies with the shock angle. Hence, even with a constant entropy free-stream, the flow behind the shock will have an entropy gradient, resulting in complications.

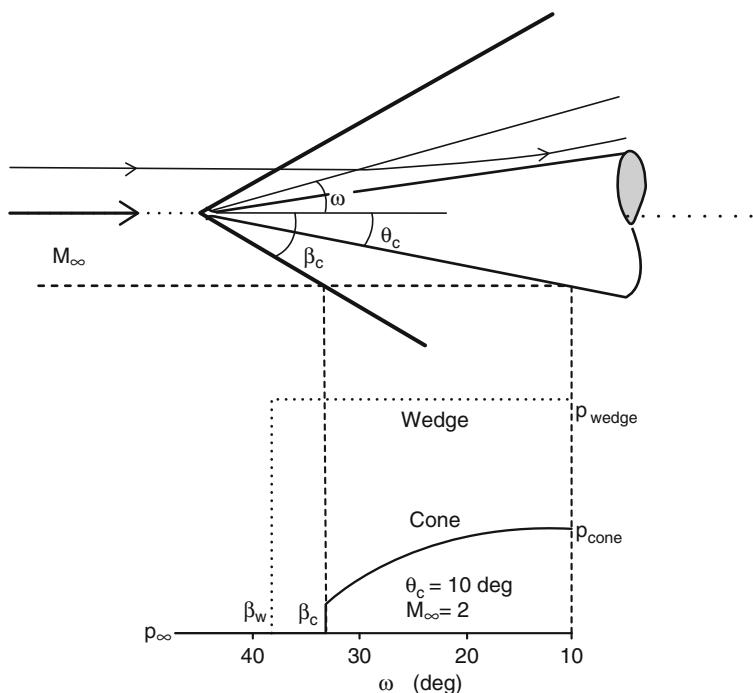


**Fig. 1.23** Supersonic flow over a sharp cone

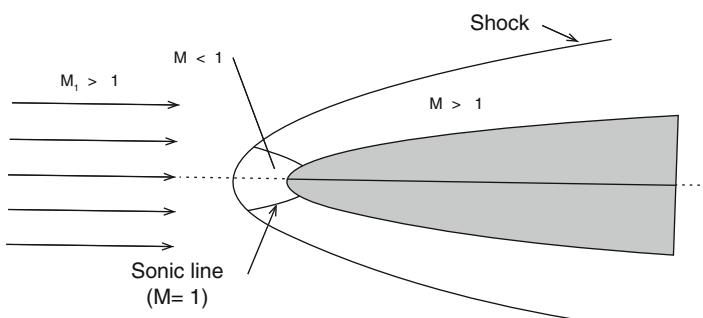
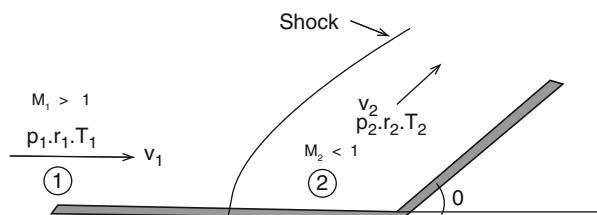


**Fig. 1.24** Example of detached shock

### 1.4.4 Method of Characteristics

When a supersonic flow is expanded by a convex surface (see Fig. 1.25), the flow remains isentropic throughout [8]. The resulting change in the flow direction is related to the Mach number by the *Prandtl–Meyer* function, i.e.,

$$v(M) = \sqrt{\frac{\gamma + 1}{\gamma - 1}} \tan^{-1} \sqrt{\frac{\gamma - 1}{\gamma + 1} (M^2 - 1)} - \tan^{-1} \sqrt{(M^2 - 1)} \quad (1.35)$$

so that  $v = 0$  corresponds to  $M = 1$ . It is also possible to compress a flow isentropically (without creating a shock) by a smooth concave turn. The relationship between the initial Mach number, turning angle  $\theta$ , and the final Mach number is given by

$$v(M_2) = v(M_1) - |\theta| \quad (1.36)$$

for compression and

$$v(M_2) = v(M_1) + |\theta| \quad (1.37)$$

for expansion.

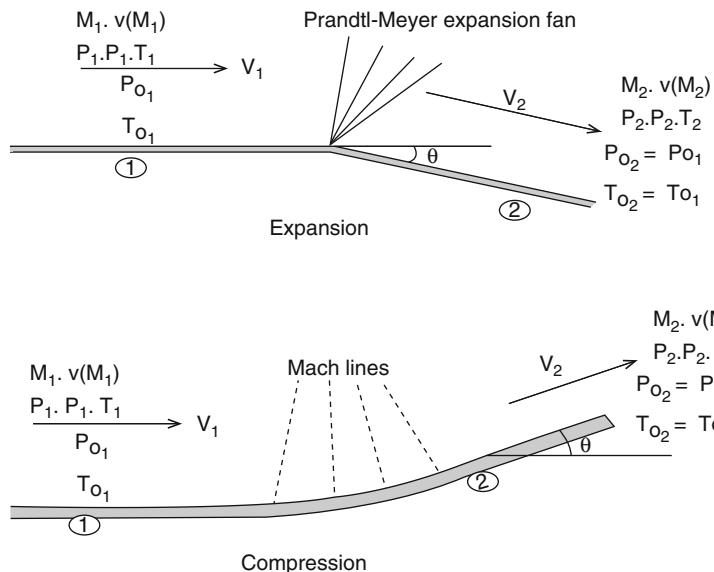


**Fig. 1.25** Isentropic flow processes

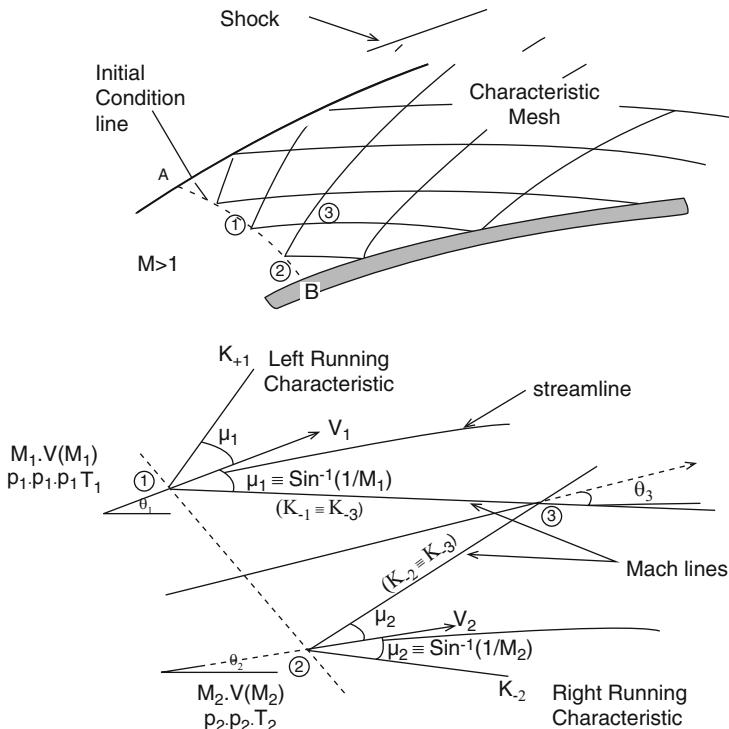


**Fig. 1.26** Method of characteristics

Since the expansion process is isentropic and we are considering only isentropic compression here, the stagnation conditions are unchanged.

Hence, the local flow properties can be determined from Eq. (1.32).

It has been already said that the steady-state Euler equations in supersonic flow are hyperbolic. Therefore, if the flow properties are known at some initial plane (or line for a two-dimensional case), the method of characteristics (MOC) is ideally suited for determining the flowfield downstream of the initial plane (or line) [8].

Refer to Fig. 1.26, let line AB be the initial condition line, i.e., the line along which all of the flow properties are known [8]. It is known that the influence of a generic point on the flow downstream is limited to a cone defined by the Mach lines, Eq. (1.26). These Mach lines are, in fact, the characteristic lines, along which the compatibility parameters  $K$  are constant. Along a right-running characteristic

$$K_- = \text{constant} = \theta - v(M) \quad (1.38)$$

and along a left-running characteristic

$$K_+ = \text{constant} = \theta + v(M) \quad (1.39)$$

where  $\theta$  is the flow direction and  $v$  is the Prandtl–Meyer function [Eq. (1.35)]. It is possible to discretize the problem and consider two neighboring points, labeled 1 and 2 in Fig. 1.26, on AB. The characteristic lines, approximated by straight line segments, emanating from these points intersect at point 3. Hence, point 3 is influenced by both 1 and 2. Since  $K$  must be constant along a characteristic,  $(K_-)_1 = (K_-)_3$  and  $(K_+)_2 = (K_+)_3$ , and we can calculate  $\theta_3$  and  $v_3$ . Proceeding in a like manner from the other points on AB and giving special treatment to the boundaries, the entire flowfield may be charted.

In three-dimensional flow, the Mach lines and characteristic lines would be replaced with characteristic surfaces. Here the geometry gets quite complicated and other numerical techniques are preferred [8].

#### 1.4.5 High-Temperature Effects

In introductory studies of thermodynamics and compressible flow, the gas is assumed to have constant specific heats; hence the ratio  $\gamma = c_p/c_v$  is also constant. This leads to some ideal results for pressure, density, temperature, and Mach number variations in a flow.

The approximation of air as a perfect gas, however, is no more valid when temperature overcomes a threshold. Indeed, let us come back to the example discussed before in paragraph 1.2 when we introduced the high-temperature effects issue. So, let us consider the nose region of an Apollo-like vehicle traveling at  $M_\infty = 36$ , as sketched in Fig. 1.27 [3]. The bow shock wave is normal, or nearly normal, in the nose region. So that the gas temperature behind this strong bow shock wave reaches about 11,000 K.

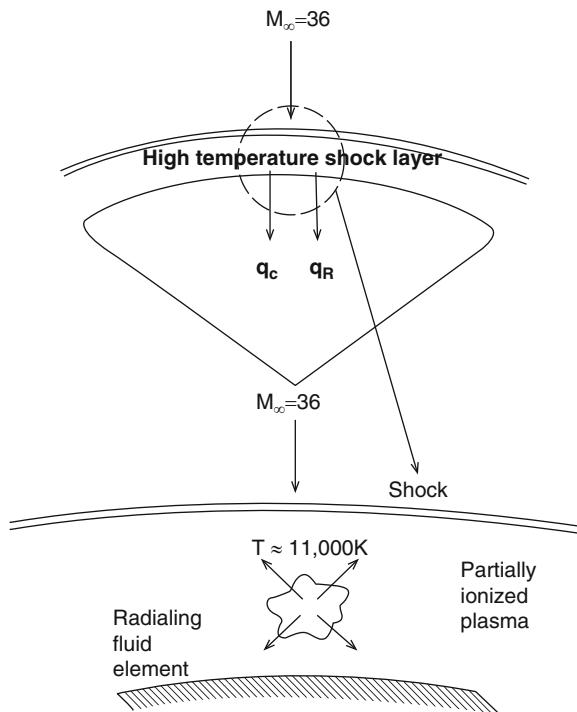
At such high temperature, flow dissociation and ionization occur by means of chemical reactions. Therefore, the gas consists of diatomic and monatomic particles as well as ions and electrons, thus evolving in a “nonideal” fashion. Specifically:

1. The vibrational energy of the flow molecules becomes excited, and this causes the specific heats  $c_p$  and  $c_v$  to become functions of temperature. In turn, the ratio of specific heats,  $\gamma = c_p/c_v$ , also becomes a function of temperature. For air, this effect becomes important above a temperature of 800 K.
2. As the gas temperature is further increased, chemical reactions can occur. For an equilibrium chemically reacting gas,  $c_p$  and  $c_v$  are functions of both temperature and pressure, and hence  $\gamma = f(T, p)$ .

Further, density of air is quite low at high altitudes where characteristic times of chemical reactions and energy exchange will be of comparable order with the characteristic time of the flow or more. Under these conditions, translational, rotational, vibrational, electron temperatures are not essentially equal.

As a consequence, in order to analyze such a re-entry flowfield, thermochemical nonequilibrium modeling cannot be avoided. To understand the behavior of nonequilibrium flows, let us consider a diatomic gas like oxygen or nitrogen, such

**Fig. 1.27** High-temperature shock layer



that the gas mixture will consist of a concentration of atoms and molecules of only one species,  $\text{N}_2$  or  $\text{O}_2$ . Under this hypothesis we can observe that as recognized in Fig. 1.28, for air at 1 atm pressure, around a temperature of 800 K, the vibrational energy of the molecules becomes significant [3]. This is not a chemical reaction, but it does have some impact on the properties of the gas. When the temperature reaches about 2,000 K, the dissociation of  $\text{O}_2$  begins. At the 4,000 K, the  $\text{O}_2$  dissociation is essentially complete; most of the oxygen is in the form of atomic oxygen, O. Moreover, by an interesting quirk of nature, 4,000 K is the temperature at which  $\text{N}_2$  begins to dissociate. When the temperature reaches 9,000 K, most of the  $\text{N}_2$  has dissociated. Coincidentally, this is the temperature at which both oxygen and nitrogen ionization occurs, and above 9,000 K, we have a partially ionized plasma consisting mainly of O,  $\text{O}^+$ , N,  $\text{N}^+$ , and electrons  $e^-$ . There is a region of mild ionization that occurs around 4,000–6,000 K: here, small amounts of NO are formed, some of which ionize to form  $\text{NO}^+$  and free electrons  $e^-$ . In terms of the overall chemical composition of the gas, these are small concentrations; however, the electron number density due to NO ionization can be sufficient to cause the communications blackout during re-entry. With the exception of vibrational excitation, which is not affected by pressure, if the air pressure is lowered, these “onset” temperatures decrease: conversely, if the air pressure is increased, these “onset” temperatures are raised [3].

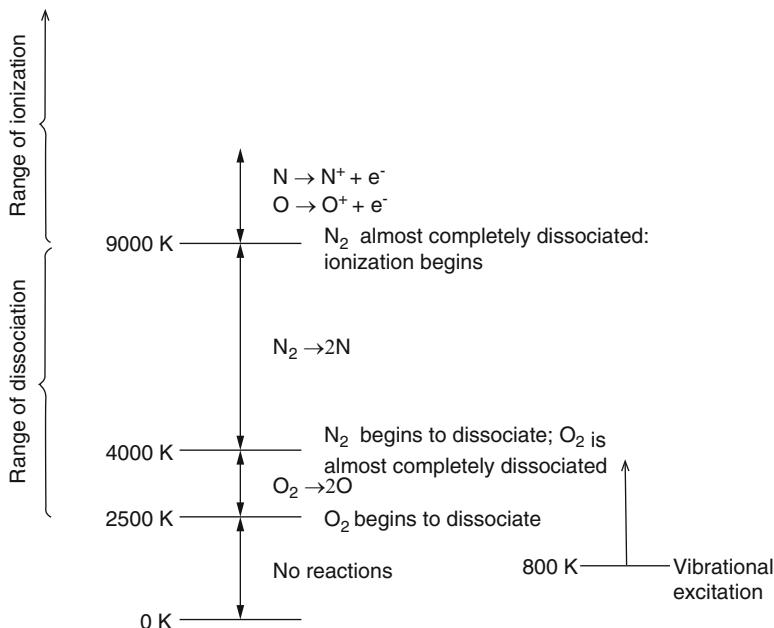


**Fig. 1.28** Ranges of vibrational, dissociation, and ionization for air at 1 atm pressure

All of these phenomena are called high-temperature real gas effects. Indeed, the monatomic gases like atomic oxygen and nitrogen of the reacting mixture in the shock layer, exhibiting fewer degrees of freedom ( $f$ ), have thermodynamic properties different from those of diatomic gases like  $O_2$  and  $N_2$  [see Eqs. (1.29) and (1.30)]. The specific enthalpy  $h$ , [J/kg]; the specific internal energy  $e$ , [J/kg]; and even the gas constant  $R$  for the mixture will depend on the concentrations of the species  $Y_i$  (e.g.,  $Y_{O_2}$ ,  $Y_O$ ,  $Y_{N_2}$ ,  $Y_{NO}$ ,  $Y_{e^-}$ ):

$$\begin{aligned} h &= h(T, Y_i) = h(T, p) \\ e &= e(T, Y_i) = e(T, p) \end{aligned} \quad (1.40)$$

As a result, the gas cannot be approximated even as a thermally perfect gas if the vibrational excitation and chemical reactions take place very rapidly in comparison to the time it takes for a fluid element to move through the flowfield (i.e., fluid residence time  $\tau_f$ ); we have vibrational and chemical equilibrium flow. In this case, since the concentrations depend on both temperature and pressure, Eq. (1.40) becomes

$$\begin{aligned} h &= h(T, p) \\ e &= e(T, p) \end{aligned} \quad (1.41)$$

This situation usually occurs at lower altitudes where a higher density and shorter mean free path result in smaller reaction times. If the opposite is true (i.e.,  $\tau_f \gg \tau_c$ ), we have nonequilibrium flow, which is considerably more difficult to analyze.

### Explanation Box. Flow Species Internal Energy and Degrees of Freedom

The internal energy can be illustrated by considering the degrees of freedom  $f$ , which atoms and molecules have. We do this by means of the simple *dumbbell molecule* model shown in Fig. 1.29 [10]. We see that molecules (and atoms) have:

- Three translational degrees of freedom
- Two rotational degrees of freedom (the energy related to the rotation around the third axis a-a can be neglected)
- Two vibrational degrees of freedom, i.e., one connected to the internal translation movement and one connected to the spring energy

Finally, a part of internal energy pertains to electronic excitation, like ionization, namely, electronic excitation energy.

Thus, a molecule has four parts of internal energy:

$$e = e_{\text{trans}} + e_{\text{rot}} + e_{\text{vibr}} + e_{\text{el}} \quad (1.42)$$

The terms  $e_{\text{trans}}$  (translational energy) and  $e_{\text{el}}$  (electronic excitation energy) apply to both atoms and molecules and the terms  $e_{\text{rot}}$  (rotational energy) and  $e_{\text{vibr}}$  (vibrational energy) only to molecules. Rotational energy  $e_{\text{rot}}$  is fully present already at very low temperatures and in general in

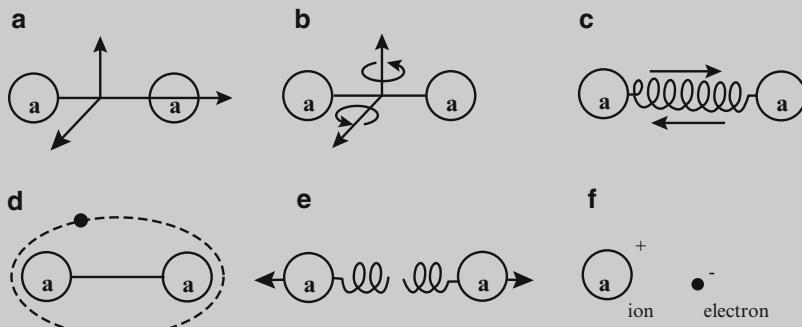


**Fig. 1.29** Schematic of degrees of freedom of a dumbbell molecule and illustration of high-temperature phenomena: (a) translation  $f = 3$ , (b) rotation  $f = 2$ , (c) vibration  $f = 2$ , (d) electron excitation, (e) dissociation, (f) ionization

(continued)

aerothermodynamics is considered as fully excited. Vibrational energy  $e_{\text{vibr}}$  is being excited in air at temperatures above 800 K. Electronic excitation energy  $e_{\text{el}}$ , i.e., energy due to electronic excitation, like ionization, is being excited at very high temperature (larger than 9,000 K).

The principle of equipartition of energy permits us to formulate the internal energy  $e$ ; the specific heats  $c_v$ ,  $c_p$ ; and their ratio  $\gamma = c_p/c_v$  of atoms and molecules in terms of the dof (f), which gives us insight into some basic high-temperature phenomena. We assume excitation of all degrees of freedom (translational, rotational, vibrational) of atoms and molecules. We neglect  $e_{\text{el}}$ , and obtain the general relations, for a species with molecular weight  $m$ ,  $R_0$  being the universal gas constant ( $R = R_0/m$ ):

$$e = \frac{f}{2} \frac{R_0}{m} T; c_v = \frac{f}{2} \frac{R_0}{m}; c_p = \frac{f+2}{2} \frac{R_0}{m}; \gamma = \frac{f+2}{f}; \quad (1.43)$$

which we now apply to the air species.

### Atoms (N, O)

For atoms we obtain ( $f = 3$ )

$$e_{\text{atom}_i} = \frac{3}{2} \frac{R_0}{m_i} T; c_{v_{\text{atom}_i}} = \frac{3}{2} \frac{R_0}{m_i}; c_{p_{\text{atom}_i}} = \frac{5}{2} \frac{R_0}{m_i}; \gamma_{\text{atom}_i} = 1.66\bar{6} \quad (1.44)$$

### Molecules (N<sub>2</sub>, O<sub>2</sub>, NO)

*Molecules with translational and rotational excitation only ( $f = 5$ ):*

$$e_{\text{molec}_i} = \frac{5}{2} \frac{R_0}{m_i} T; c_{v_{\text{molec}_i}} = \frac{5}{2} \frac{R_0}{m_i}; c_{p_{\text{molec}_i}} = \frac{7}{2} \frac{R_0}{m_i}; \gamma_{\text{molec}_i} = 1.4 \quad (1.45)$$

*Molecules with translational, rotational, and partial vibrational excitation:*

The vibrational energy of diatomic molecules reads

$$e_{\text{vibr}} = \frac{R \vartheta_{\text{vibr}}}{e^{\frac{\vartheta_{\text{vibr}}}{T}} - 1} \quad (1.46)$$

and the specific heat

$$c_{\text{vibr}} = R \left( \frac{\vartheta_{\text{vibr}}}{T} \right)^2 \frac{e^{v_{\text{vibr}}}/T}{(e^{v_{\text{vibr}}}/T - 1)^2} \quad (1.47)$$

We find now

$$e_{\text{molec}_i} = \frac{5}{2} \frac{R_0}{m_i} T + e_{\text{vibr}_i}; c_{v_{\text{molec}_i}} = \frac{5}{2} \frac{R_0}{m_i} + c_{v_{\text{vibr}_i}} \quad (1.48)$$

(continued)

$$c_{\text{pmole}_i} = \frac{7}{2} \frac{R_0}{m_i} + c_{v_{\text{vibr}_i}}; \gamma_{\text{molec}_i} = \gamma_{\text{molec}_i}(T) \leq (1.4) \quad (1.49)$$

*Molecules with full vibrational excitation ( $f=7$ ):*

The case of full vibrational excitation of a molecule is hypothetical because the molecule will dissociate before it reaches this state. Nevertheless, Eq. (1.46) and Eq. (1.47) exhibit for large temperatures the limiting cases:

$$e_{\text{vibr}} = RT; c_{v_{\text{vibr}}} = R \quad (1.50)$$

Hence we obtain

$$e_{\text{molec}_i} = \frac{7}{2} \frac{R_0}{m_i} T; c_{v_{\text{molec}_i}} = \frac{7}{2} \frac{R_0}{m_i}; c_{\text{pmole}_i} = \frac{9}{2} \frac{R_0}{m_i}; \gamma_{\text{molec}_i} = 1.285 \quad (1.51)$$

*Molecules with half vibrational excitation (Lighthill gas),  $f=6$ .*

This case with a heat capacity twice as large as that of atoms was proposed by Lighthill in his study of the dynamics of dissociated gases. It yields a good approximation for applications in a large temperature and pressure/density range:

$$e_{\text{molec}_i} = \frac{6}{2} \frac{R_0}{m_i} T : c_{v_{\text{molec}_i}} = \frac{7}{2} \frac{R_0}{m_i}; c_{\text{pmole}_i} = \frac{8}{2} \frac{R_0}{m_i}; \gamma_{\text{molec}_i} = 1.33\bar{3} \quad (1.52)$$

*Molecules with an infinitely large number of degrees of freedom,  $f$ .*

This is a limiting case, which means

$$e_{\text{molec}_i} = \infty; c_{v_{\text{molec}_i}} = \infty; c_{\text{pmole}_i} = \infty; \gamma_{\text{molec}_i} = 1 \quad (1.53)$$

High-temperature gas effects are recognized, as usual, in the altitude–velocity map as in Fig. 1.30 [3].

As one can see, the re-entry trajectory on the altitude–velocity map is superimposed on approximate boundaries for *vibrational excitation*, *oxygen* and *nitrogen dissociation*, *ionization*, and *thermochemical nonequilibrium*.

According to Ref. [3] the 10 and 90 % labels at the top of Fig. 1.30 denote the effective beginning and end of various regions where these effects are important. Therefore, as the velocity becomes larger, vibrational excitation is first encountered in the flowfield, at about 1 km/s. At the higher velocity of about 2.5 km/s, the vibrational mode is essentially fully excited, and *oxygen dissociation* starts. The O<sub>2</sub> dissociation is essentially complete at about 5 km/s, wherein N<sub>2</sub> dissociation commences. This effect covers the shaded region labeled *nitrogen dissociation*.

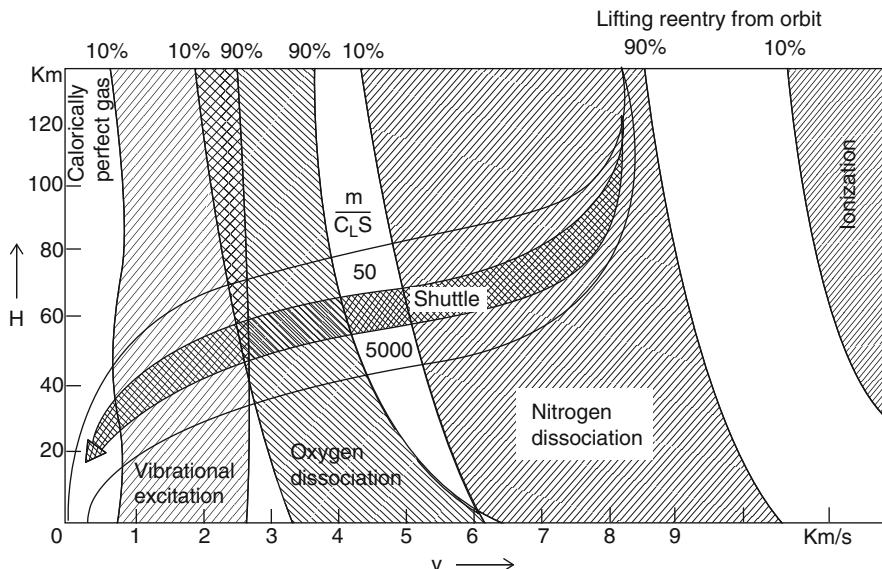


**Fig. 1.30** Altitude–velocity map with superimposed regions of vibrational excitation, dissociation, and ionization

Finally, above 10 km/s, the  $N_2$  dissociation is complete, and ionization begins. It is most interesting that regions of various dissociations and ionization are so separate on the altitude–velocity map, with very little overlap. In a sense, this is a situation when nature is helping to simplify things for us [3].

As a consequence, Fig. 1.30 highlights that the entry flight paths slash across major sections of the altitude–velocity map where chemical reactions and vibrational excitation arise. This clarifies why high-temperature effects are so important to entry-body flows [2, 3, 7, 9, 10]. Figure 1.30 suggests also that there will be an increasing number of species occurring in the different domains along with the descent trajectory.

Indeed, the flow chemical composition can vary spatially and temporally. Moreover, the continual exchange of energy between the transitional and internal degrees of freedom of the flow molecules results in thermal and/or chemical nonequilibrium in the different domains of altitude–velocity map, as recognized in Fig. 1.31 [2, 3].

Figure 1.31 recalls and explains that discussed before about Fig. 1.8. In particular, Fig. 1.31 shows three different regions with chemical and thermal nonequilibrium, namely, **A**, **B**, and **C**. Region **A** deals with *chemical and thermal equilibrium*. **B** refers to *chemical nonequilibrium with thermal equilibrium*. Finally, **C** reports the region of *chemical and thermal nonequilibrium*. So that looking at this chart, one can rapidly assess the thermochemical models to use in the CFD simulation once free-stream conditions are known.

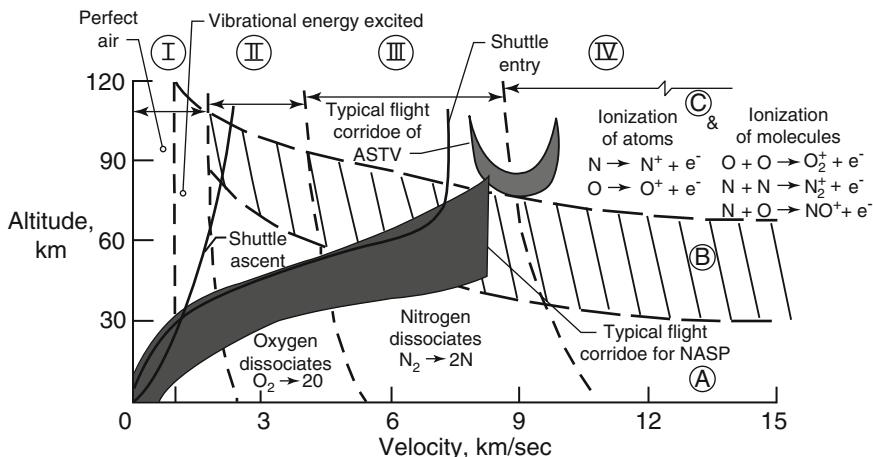


**Fig. 1.31** Flight stagnation region air chemistry for 30.5 cm radius sphere

Note, however, that Fig. 1.31 refers to flight stagnation region air chemistry for 30.5 cm radius sphere. Therefore, the boundaries of A, B, and C regions must be adjusted according to the particular re-entry trajectory in the light of the *binary scaling principle* [3].

The above discussion suggests that high-temperature chemically reacting flows can have an influence on aerodynamic lift, drag, and moments of a hypersonic vehicle. For example, such effects were found to be important for estimating the amount of body-flap deflection necessary to trim the Space Shuttle during high-speed re-entry. However, by far the most dominant aspect of high temperatures in hypersonics is the resultant high heat transfer rates to the surface. Aerodynamic heating dominates the design of all hypersonic machinery, whether it be a flight vehicle, a ramjet engine to power such a vehicle, or a wind tunnel to test the vehicle. This aerodynamic heating takes the form of heat transfer from the hot boundary layer to the cooler surface called convective heating, denoted by  $q_c$  in Fig. 1.27. Moreover, if the aerodynamic shock layer temperature is high enough, the thermal radiation emitted by the gas itself can become important, giving rise to a radiative flux to the surface called radiative heating, denoted by  $q_R$  in Fig. 1.27. For example, for Apollo re-entry, radiative heat transfer was more than 30 % of the total heating. For a space probe entering the atmosphere of Jupiter, the radiative heating will be more than 95 % of the total heating.

Another consequence of high-temperature flow over hypersonic vehicles is the “communications blackout” experienced at certain altitudes and velocities during atmospheric entry, where it is impossible to transmit radio waves either to or from the vehicle. This is caused by ionization in the chemically reacting flow, producing free electrons which absorb radio-frequency radiation. Therefore, the accurate prediction of electron density within the flowfield is important.

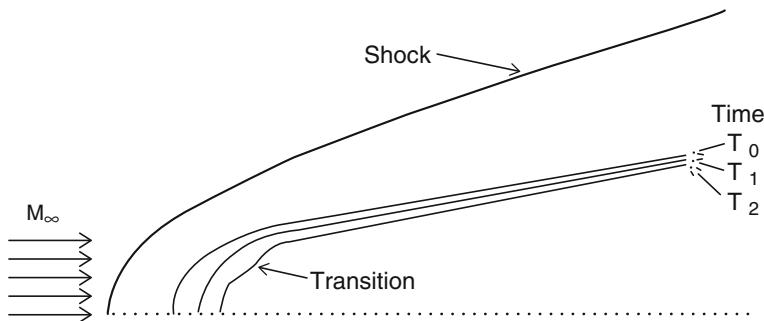


**Fig. 1.32** Nose-tip ablation history

Finally, the high-temperatures real gas effects are important not only to the fluid properties but also to the material properties of the vehicle moving at hypersonic speed. For instance, it is worth noting that the temperatures reached in the region of the stagnation point are much higher than the melting point of most materials; unless some form of active cooling is provided, the stagnation region will ablate. In fact, controlled ablation is a common method of thermal management for these bodies.

The rate of ablation depends on the thermodynamic properties of the heat shield. Not only the presence of the ablated materials in the flowfield will complicate the chemical reaction process, but also the shape of the body itself will be altered, especially in the stagnation regions (see Fig. 1.32) [8].

Hence, the heat transfer rate not only influences the flowfield properties but also governs the rate of change of the shape of the nose tip. Furthermore, as the heat shield vaporizes, or outgases, the process of the gases leaving the surface with a finite velocity alters the boundary conditions and hence the flowfield [8].

#### 1.4.5.1 The Compressibility Factor, $z$

As energy is absorbed by the gas molecules entering the shock layer, the conservation laws and the thermophysics dictate certain changes in the forebody flow. Indeed, a large amount of the energy that would have gone into increasing the static temperature behind the bow shock wave for a perfect gas is used instead to excite the vibrational energy levels or to dissociate the gas molecules and the flow can no longer be considered as *calorically perfect gas*. It is worth noting that the dissociation and ionization reactions are pressure dependent because each particle yields two product particles, and such reactions are inhibited by high pressure. Therefore, higher temperature and, consequently, higher velocity are required to produce the reactions at sea level than at high altitudes where much lower pressures occur.

A multispecies gas can no longer be treated as perfect gas and so new relationships for the thermodynamic properties must be derived, but dissociated air can be treated as a mixture of perfect gas:

$$p_i = \frac{M_i}{V} \frac{R_o}{m_i} T \quad (1.54)$$

where  $M_i$  and  $m_i$  are the mass and molecular weight of the substance  $i$ , respectively.

Then, for Dalton's law,

$$p = \sum_i p_i = \frac{R_o T}{V} \sum_i \frac{M_i}{m_i} \quad (1.55)$$

where the total mass of mixture reads

$$M = \sum_i M_i \quad (1.56)$$

Defining the mass fraction (also known as mass concentration) of substance  $i$ ,

$$Y_i = \frac{M_i}{M} \quad (1.57)$$

Thus,

$$\sum_i Y_i = 1 \quad (1.58)$$

Also, note that

$$Y_i = \frac{M_i}{V} \cdot \frac{V}{M} = \frac{\rho_i}{\rho} \quad (1.59)$$

As a result, accounting for the change in the gas composition, the equation of state becomes

$$\begin{aligned} p &= \frac{R_o T}{V} \sum_i \frac{M_i}{m_i} = \frac{R_o M T}{V} \sum_i \frac{Y_i}{m_i} = \rho R_o T \\ &\times \sum_i \frac{Y_i}{m_i} = \rho R_o T \frac{z}{m_o} = \rho z T \frac{R_o}{m_o} = \rho z R T \end{aligned} \quad (1.60)$$

Therefore, to account for the departure from the thermally perfect equation of state,

$$p = \rho R T = \rho \frac{R_o}{m_o} T \quad (1.61)$$

Due to the chemical reactions in air, the compressibility factor,  $z$ , is introduced:

$$z = \frac{m_o}{\bar{m}} \quad (1.62)$$

where  $R_o$  is the universal gas constant,  $m_o$  is the molecular weight of the gas in the perfect (or reference) state, and  $\bar{m}$  is the mean molecular weight of the gas mixture at the conditions of interest.

 **Explanation Box. The Compressibility Factor for a Two- and Four-Species Mixture**

Evaluate the compressibility factor,  $z$ , in case:

- (a) Binary mixture of O<sub>2</sub> and O
- (b) Mixture of O<sub>2</sub>, N<sub>2</sub>, O, and N

**Case (a)**

This is the case of O<sub>2</sub> mixture dissociation:



The mass balance is

$$\sum_i Y_i = Y_{\text{O}} + Y_{\text{O}_2} = 1$$

Also

$$\sum_i \frac{Y_i}{m_i} = \frac{Y_{\text{O}}}{m_{\text{O}}} + \frac{Y_{\text{O}_2}}{m_{\text{O}_2}} = \frac{2Y_{\text{O}}}{m_{\text{O}_2}} + \frac{Y_{\text{O}_2}}{m_{\text{O}_2}} = \frac{2Y_{\text{O}}}{m_{\text{O}_2}} + \frac{1 - Y_{\text{O}}}{m_{\text{O}_2}} = \frac{1 + Y_{\text{O}}}{m_{\text{O}_2}}$$

Thus, the equation of state becomes

$$\begin{aligned} p &= \frac{R_o M T}{V} \sum_i \frac{Y_i}{m_i} = \rho R_o T \frac{1 + Y_{\text{O}}}{m_{\text{O}_2}} = \rho \frac{R_o}{m_{\text{O}_2}} T (1 + Y_{\text{O}}) \\ &= \rho R T (1 + Y_{\text{O}}) = \rho R T z \end{aligned}$$

Therefore,

$$z = 1 + Y_{\text{O}}$$

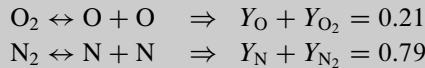
(continued)

Note that the value of  $z$  depends upon the amount of O<sub>2</sub> dissociated in the mixture, so

$$1 < z < 2$$

### Case (b)

Consider an original mixture of 21 % O<sub>2</sub> and 79 % N<sub>2</sub> that is undergoing the following reactions:



Therefore,

$$\begin{aligned} \sum_i \frac{Y_i}{m_i} &= \frac{Y_{\text{O}}}{m_{\text{O}}} + \frac{Y_{\text{O}_2}}{m_{\text{O}_2}} + \frac{Y_{\text{N}}}{m_{\text{N}}} + \frac{Y_{\text{N}_2}}{m_{\text{N}_2}} = \frac{2Y_{\text{O}}}{m_{\text{O}_2}} + \frac{Y_{\text{O}_2}}{m_{\text{O}_2}} + \frac{2Y_{\text{N}}}{m_{\text{N}_2}} + \frac{Y_{\text{N}_2}}{m_{\text{N}_2}} \\ &= \frac{2Y_{\text{O}}}{m_{\text{O}_2}} + \frac{0.21 - Y_{\text{O}}}{m_{\text{O}_2}} + \frac{2Y_{\text{N}}}{m_{\text{N}_2}} + \frac{0.79 - Y_{\text{N}}}{m_{\text{N}_2}} = \frac{0.21 + Y_{\text{N}}}{m_{\text{N}_2}} + \frac{0.79 + Y_{\text{N}}}{m_{\text{N}_2}} \\ \sum_i \frac{Y_i}{m_i} &= \frac{0.21}{32} + \frac{0.79}{28} + \frac{Y_{\text{O}}}{32} + \frac{Y_{\text{N}}}{28} \end{aligned}$$

But

$$\frac{1}{m_{\text{o}}} = \frac{0.21}{32} + \frac{0.79}{28}$$

Thus,

$$m_{\text{o}} \sum_i \frac{Y_i}{m_i} = 1 + \frac{m_{\text{o}}}{32} Y_{\text{O}} + \frac{m_{\text{o}}}{28} Y_{\text{N}} = 1 + 0.898 \cdot Y_{\text{O}} + 1.027 \cdot Y_{\text{N}} = z$$

where

$$\begin{aligned} 1 &< Y_{\text{O}} < 0.21 \\ 0 &< Y_{\text{N}} < 0.79 \end{aligned} \Rightarrow 1 < z < 2$$

So knowing the amount of dissociation of each flow species permits the evaluating of the equation of state

$$p = z(Y_{\text{O}}, Y_{\text{N}}) \rho R T$$

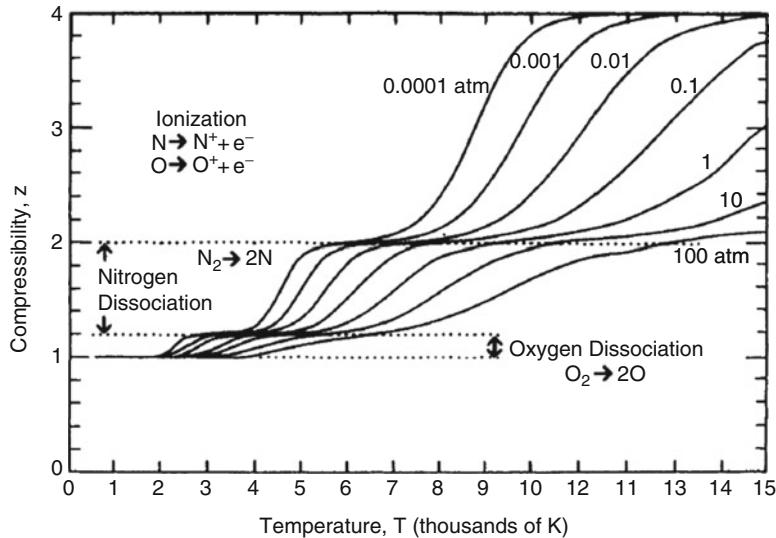


**Fig. 1.33** Compressibility of air as a function of temperature

The compressibility factor for air is presented as a function of temperature and of pressure in Fig. 1.33 [9].

As indicated by the curves presented in Fig. 1.33, the compressibility factor is not influenced by the vibrational excitation and, therefore, is equal to 1.0 until oxygen dissociation begins [9]. Since air contains about 20 % oxygen,  $z$  approaches 1.2 as the oxygen dissociation approaches completion. Similarly,  $z$  approaches 2.0 as the nitrogen dissociation approaches completion and all of the molecules have dissociated into atoms. The ionization process produces further increases in  $z$ .

Note that the ionization reactions occur at very nearly the same temperature and with nearly the same energy changes so that they may be classed together as a single reaction, for the purpose of approximation.

#### Explanation Box. Mass Fraction and Mole Fraction Relationship

The mass fraction,  $Y_i$ , to mole fraction,  $\chi_i$ , relationship reads

$$Y_i = \chi_i \frac{m_i}{m}$$

where  $m_i$  and  $m$  are the molecular weight of species  $i$  and mixture molecular weight, respectively.

(continued)

Indeed, the mole fraction  $\chi_i$  is

$$\chi_i = \frac{\text{number of mole of species } i}{\text{number of mixture mole}} = \frac{N_i}{N} = \frac{M_i}{m_i} \cdot \frac{m}{M} = \frac{M_i}{M} \cdot \frac{m}{m_i} = Y_i \cdot \frac{m}{m_i}$$

where the mixture molecular weight reads

$$m = \sum_i \chi_i m_i$$

As an example, suppose that the gas mixture composition of case b) of the previous explanation box is

$$\chi_N = 0.55$$

$$\chi_{N_2} = 0.20$$

$$\chi_O = 0.25$$

$$\chi_{O_2} \cong 10^{-6}$$

Thus,

$$\begin{aligned} m &= \sum_i \chi_i m_i = \chi_N \cdot m_N + \chi_{N_2} \cdot m_{N_2} + \chi_O \cdot m_O + \chi_{O_2} \cdot m_{O_2} \\ &= 0.55 \cdot 14 + 0.20 \cdot 28 + 0.25 \cdot 16 + 10^{-6} \cdot 32 = 17.30 \end{aligned}$$

$$Y_N = \chi_N \frac{m_N}{m} = 0.55 \frac{14.00}{17.30} = 0.45$$

$$Y_{N_2} = \chi_{N_2} \frac{m_{N_2}}{m} = 0.20 \frac{28.00}{17.30} = 0.32$$

$$Y_O = \chi_O \frac{m_O}{m} = 0.25 \frac{16.00}{17.30} = 0.23$$

$$Y_{O_2} = \chi_{O_2} \frac{m_{O_2}}{m} = 10^{-6} \frac{32.00}{17.30} \cong 0$$

and the compressibility factor reads

$$z = 1 + 0.898 \cdot Y_O + 1.027 \cdot Y_N = 1 + 0.898 \cdot 0.23 + 1.027 \cdot 0.45 = 1.669$$

So,  $1 < z < 2$ , as expected.

### 1.4.6 Viscous Interaction

Recall that by using similarity techniques, it follows that

$$\frac{\delta}{x} \propto \frac{M_\infty^2}{\sqrt{Re_x}} \quad (1.63)$$

Now consider, for example, a supersonic flow past a flat plate with a sharp leading edge at zero angle of attack (see Fig. 1.34) [8].

As said before, the outer inviscid flow may be determined by considering inviscid flow past a fictitious body with a shape of the original body increased by the boundary-layer displacement thickness  $\delta^*$ . In supersonic flow  $\delta^*$  is negligible, and the pressure at the edge of the boundary layer  $p_e(x)$  is the same as the free-stream pressure  $p_\infty$ .

However, in hypersonic flow, where  $\delta$  is much larger, Eq. (1.63), than in supersonic flow, the flow deflection caused by  $\delta^*$  induces a leading edge shock. Associated with this boundary-layer-induced shock, there is an increase in  $p_e(x)$  near the leading edge. This result should not be unexpected since we know that an increase in pressure is associated with an increase in temperature. This induced shock alters the outer region flowfield, which in turn affects the boundary layer, causing higher skin friction and heat transfer rates. This interaction between the boundary layer and the outer inviscid region is called viscous interaction; the two regions can no longer be determined independently. Viscous interaction is more pronounced near the leading edge, where  $d\delta^*/dx$ , and hence the flow deflection, is the greatest. A viscous interaction parameter  $\chi$  allows evaluating the relative importance of the interaction between the inviscid and viscous regions as follows:

$$\chi = M_\infty^3 \sqrt{\frac{C_w}{Re_{x_\infty}}} \quad (1.64)$$

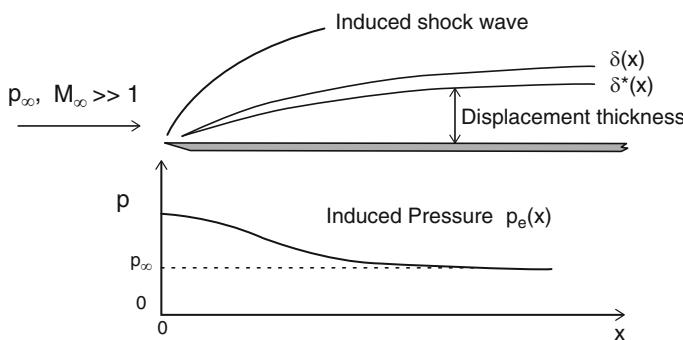


**Fig. 1.34** Boundary-layer-induced shock wave and pressure distribution over a flat plate

where

$$C_w = \frac{\rho_w \mu_w}{\rho_\infty \mu_\infty} \quad (1.65)$$

The subscript w stands for wall.

$C_w$  is the Chapman–Rubesin nondimensional parameter;  $Re_{x_\infty}$  is the Reynolds number based on the distance  $x$  from the leading edge and the free-stream conditions.

In regions of strong viscous interaction ( $\chi \gg 1$ ), the outer inviscid and boundary-layer flows must be solved simultaneously.

If one assumes that the boundary layer acts as slender wedge with an angle equal to the displacement thickness gradient, it can be shown that the ratio of the induced pressure to the free-stream pressure  $p_i/p_\infty$  is proportional to the viscous interaction parameter  $\chi$  for strong interaction ( $\chi > 3$ ). The correlation of induced pressure for an insulated flat plate in air, taken from Hayes and Probstein's classic work, is illustrated in Fig. 1.35 [8].

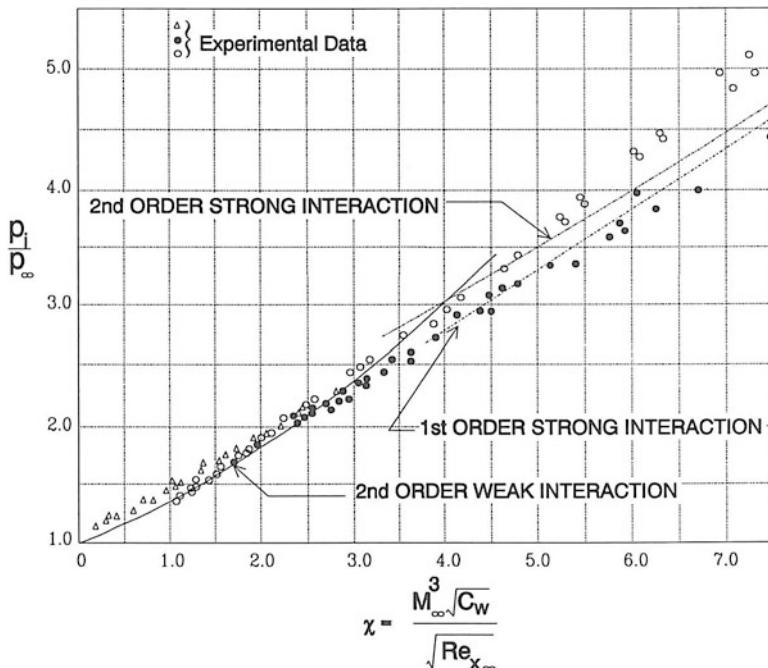


Fig. 1.35 Weak interaction and strong interaction correlation

In subsonic regime the nondimensional parameter  $C_p$  (pressure coefficient) is defined as

$$C_p \equiv \frac{p - p_\infty}{q_\infty} \quad (1.66)$$

where  $q_\infty = \frac{1}{2} \rho_\infty V^2$  is the dynamic pressure.

In hypersonic regime this can be rewritten as

$$C_p \equiv \frac{p - p_\infty}{q_\infty} = \frac{2}{\gamma M^2} \left( \frac{p}{p_\infty} - 1 \right) \approx \frac{2}{\gamma M^2} \frac{p}{p_\infty} \quad (1.67)$$

as for hypersonic flow  $(p/p_\infty) \gg 1$ .

From Fig. 1.35 we see that  $(p_i/p_\infty) \propto \chi$  so we can define a new viscous interaction parameter  $\bar{V}$  as

$$C_p \propto \frac{M_\infty}{\sqrt{Re_{x_\infty}}} \sqrt{C_w} \equiv \bar{V} \quad (1.68)$$

So,  $\bar{V}$  is similar to the Knudsen number for viscous flow.

Another form of viscous-inviscid interaction occurs when a shock wave impinges on a surface and interacts with the boundary layer.

The flow deflection caused by the impinging shock causes local flow separation, and the increased pressure causes the boundary layer to reattach. The reattachment of the boundary layer creates a shock that merges with the reflected shock (see Fig. 1.36) [8].

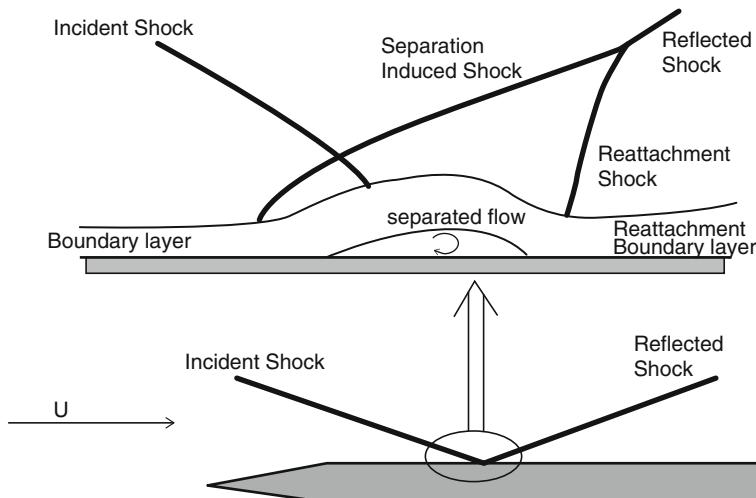


**Fig. 1.36** Boundary-layer/shock-wave interaction

This region of viscous–inviscid interaction is a region of very high heat transfer rates due to the thinner boundary layers caused by the interaction; it has the potential to cause catastrophic failure if not adequately accounted for [8].

## 1.5 Spacecraft Aerodynamic Coefficients

The dynamics of a moving space vehicle are governed mainly by the forces of a gravitational field of some sort of celestial bodies, which could be, for example, a fixed star, a planet, a moon, etc. Other forces and moments are given by propulsion and reaction control systems, which are needed for the ascent to a space orbit or even for leaving the gravitational field of a celestial body as well as for any trajectory maneuvers in space. Finally, space vehicles entering the atmosphere of a celestial body experience forces and moments due to its flight through this atmosphere.

Aerodynamics is concerned with lift and drag of the vehicle as well as with its flyability (trim, static, and dynamic stability) and maneuverability. The aerodynamic discipline delivers on the one hand the aerodynamic shape of the space vehicle and on the other hand the complete set of aerodynamic and aerothermal loads (wall temperature, heat flux, pressure, and skin friction) along the whole flight trajectory.

### 1.5.1 Reference Coordinate System

Aerodynamic data are usually provided in the body reference frames as illustrated in Fig. 1.37. Here the subscript “ $b$ ” indicates the body reference frame (BRF), while “ $w$ ” indicates the wind reference frame (WRF) and “ $s$ ” indicates the stability reference frame (SRF). The pole for the calculation of the moment coefficients is assumed in the vehicle CoG, which is in turn defined usually in the layout reference frame (not reported in figure).

The BRF has the origin placed in the CoG. The  $x$ -axis is parallel to the fuselage reference line (FRL) and is positive toward the vehicle nose. The  $Y_b$  is positive toward the right wing and  $Z_b$  completes the right-handed triad.

The aerodynamic reference axis systems are sets of conventional, right-hand, orthogonal axes with the  $x$ - and  $z$ -axes in the plane of symmetry and with the positive  $x$ -axis directed out of the nose (in the body axis system) or pointing into the component of the wind (in the stability axis system) which lies in the plane of symmetry. This means that the  $X_w$  axis is parallel to the free-stream velocity and directed opposite to it; the  $Z_w$  orthogonal to the  $X_w$ , lying in the vehicle symmetry plane and pointing toward the vehicle bottom; and the  $Y_w$  completing the right-handed triad. Finally, the SRF is obtained from the WRF with a rotation of an angle equal to the sideslip angle  $\beta$  around the  $Z_w$  axis. As an alternative the SRF can be derived from the BRF by rotating around the  $Y_b$  axis of an angle equal to the angle of attack  $\alpha$ .

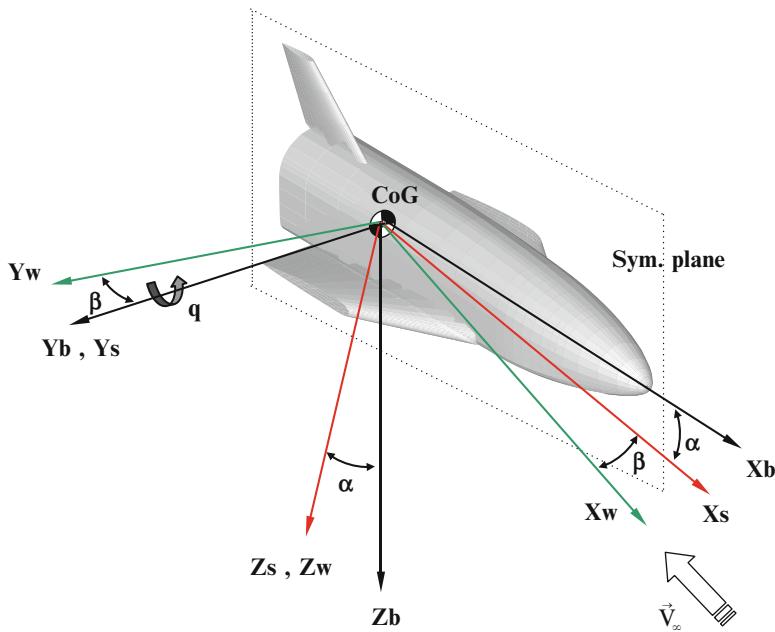


**Fig. 1.37** Aerodynamic reference frames

The rotation matrix to be used to convert quantities from BRF reference frame to SRF is

$$\begin{bmatrix} X \\ Y \\ Z \end{bmatrix}_S = \begin{bmatrix} \cos \alpha & 0 & \sin \alpha \\ 0 & 1 & 0 \\ -\sin \alpha & 0 & \cos \alpha \end{bmatrix} \begin{bmatrix} X \\ Y \\ Z \end{bmatrix}_B \quad (1.69)$$

The rotation matrix to be used to convert quantities from SRF reference frame to WRF is

$$\begin{bmatrix} X \\ Y \\ Z \end{bmatrix}_W = \begin{bmatrix} \cos \beta & \sin \beta & 0 \\ -\sin \beta & \cos \beta & 0 \\ 0 & 0 & 1 \end{bmatrix} \begin{bmatrix} X \\ Y \\ Z \end{bmatrix}_S \quad (1.70)$$

The rotation matrix to be used to convert quantities from BRF reference frame to WRF is

$$\begin{bmatrix} X \\ Y \\ Z \end{bmatrix}_W = \begin{bmatrix} \cos \alpha \cos \beta & \sin \beta & \sin \alpha \cos \beta \\ -\cos \alpha \sin \beta & \cos \beta & -\sin \alpha \sin \beta \\ -\sin \alpha & 0 & \cos \alpha \end{bmatrix} \begin{bmatrix} X \\ Y \\ Z \end{bmatrix}_B \quad (1.71)$$

Finally, in order to perform inverse transformation, it is sufficient to transpose the rotation matrices, being them orthogonal by definition.

Two sets of aerodynamic forces are usually considered in building vehicle aerodynamic database. The first one is defined in the BRF as follows:

1.  $N$ : normal force. Directed opposite to the  $Z_b$  axis
2.  $A$ : axial force. Directed opposite to the  $X_b$  axis
3.  $Y$ : side force. Directed like the  $Y_b$  axis

The second one is defined in the SRF as follows:

1.  $L$ : lift force. Directed opposite to the  $Z_s$  axis
2.  $D$ : drag force. Directed opposite to the  $X_s$  axis
3.  $Y$ : side force. Directed like the  $Y_s$  axis (it coincides with the one previously defined)

The aerodynamic moments will be always defined in the BRF as follows<sup>7</sup>:

1.  $l$ : rolling moment. Directed like the  $X_b$  axis
2.  $m$ : pitching moment. Directed like the  $Y_b$  axis
3.  $n$ : yawing moment. Directed like the  $Z_b$  axis

However, as usual in fluid dynamics, we prefer to manage dimensionless parameters, such as Mach number, Reynolds number, and Knudsen number. So, dimensionless force and moment coefficients are considered.<sup>8</sup>

An aerodynamic force coefficient is defined as

$$\text{Force coefficient} = \frac{\text{Force}}{\text{dynamic pressure} \times \text{reference area}} \quad (1.72)$$

A moment coefficient is defined as

$$\text{Moment coefficient} = \frac{\text{Moment}}{\text{dynamic pressure} \times \text{ref.area} \times \text{ref.length}} \quad (1.73)$$

where

$$\begin{aligned} \text{Dynamic pressure} &= q_\infty = \frac{1}{2} \rho_\infty V_\infty^2 \\ \rho_\infty &= \text{Freestream mass density of fluid} \\ V_\infty &= \text{Freestream fluid velocity} \end{aligned} \quad (1.74)$$

Thus, vehicle aerodynamics is expressed in terms of the following force and moment coefficients<sup>9</sup>:

<sup>7</sup>It is worth noting that, some authors also indicate rolling, pitching and yawing moments with  $M_x$ ,  $M_y$  and  $M_z$ , respectively.

<sup>8</sup>Often it is possible to test a scaled model of a vehicle in a wind tunnel and measure the force and moment coefficients on the model. If the test Mach and Reynolds numbers match those in flight, then the forces and moments can be scaled to flight conditions (if free molecular flow will be encountered in flight, then ground test Knudsen number should match the flight Kn number).

<sup>9</sup>In a wind tunnel test, a calibrated strain gauge balance is used to measure forces and moments.

$$\text{Axial force coefficient} = C_A = \frac{A}{q_\infty S_{\text{ref}}} \quad (1.75)$$

$$\text{Normal force coefficient} = C_N = \frac{N}{q_\infty S_{\text{ref}}} \quad (1.76)$$

$$\text{Side force coefficient} = C_Y = \frac{Y}{q_\infty S_{\text{ref}}} \quad (1.77)$$

$$\text{Rolling moment coefficient} = C_l = C_{m_x} = \frac{l}{q_\infty S_{\text{ref}} L_{\text{ref}}} \quad (1.78)$$

$$\text{Pitching moment coefficient} = C_m = C_{m_y} = \frac{m}{q_\infty S_{\text{ref}} L_{\text{ref}}} \quad (1.79)$$

$$\text{Yawing moment coefficient} = C_n = C_{m_z} = \frac{n}{q_\infty S_{\text{ref}} L_{\text{ref}}} \quad (1.80)$$

The reference length commonly adopted for a winged-body vehicle is the mean aerodynamic chord (mac) defined as

$$\bar{c} = \frac{2}{S_w} \int_0^{\frac{b}{2}} c^2(y) dy \quad (1.81)$$

where  $c(y)$  represents the variation of the wing chord, extended up to the symmetry plane, along with the wind span.

### Explanation Box. Aerodynamic Force Analysis

Aerodynamic forces develop whenever there is relative motion between the fluid and the immersed body.

Appealing to intuition it makes sense that the aerodynamic force,  $A$ , on a body depends on its shape, altitude, velocity, and its attitude, which is its relative position with respect to the flow of the fluid. Therefore, for a given shape and attitude, let us assume that  $A$  depends on the free-stream density (i.e., altitude), the velocity, the size of the body, the viscosity<sup>10</sup>, and also the

---

<sup>10</sup> $A$  depends also on viscosity because the aerodynamic forces are generated in part from body skin friction distributions.

(continued)

speed of sound in the fluid to address also the effect of the compressibility of the airflow<sup>11</sup>:

$$A = f(\rho_\infty, V_\infty, S, \mu_\infty, a_\infty) \quad (1.82)$$

A simple dimensional analysis will lead to the functional form for the aerodynamic force  $A$ .

Then we write

$$A \approx \rho_\infty^\alpha, V_\infty^\beta, l^\gamma, \mu_\infty^\delta, a_\infty^\varepsilon \quad (1.83)$$

where  $\alpha, \beta, \gamma, \delta$ , and  $\varepsilon$  are dimensionless constants. However, no matter what the values of these constants may be, it is a physical fact that the dimensions of the left- and right-hand sides of the equation must match; that is, if  $A$  is a force (say, in Newtons), then the net result of all the exponent and multiplication on the right-hand side must also produce a result with the dimensions of a force.

This constraint will ultimately give us information on the values of  $\alpha, \beta, \gamma, \delta$ , and  $\varepsilon$ .

Indeed, in dimensions, with  $M$  being the mass,  $L$  the length, and  $T$  the time, we express the equivalence

$$MLT^{-2} \approx (ML^{-3})^\alpha \cdot (LT^{-1})^\beta \cdot L^\gamma \cdot (ML^{-1}T^{-1})^\delta \cdot (LT^{-1})^\varepsilon$$

Equating powers, for each quantity, we obtain the system

$$\begin{aligned} M) \quad 1 &= \alpha + \delta \\ L) \quad 1 &= -3\alpha + \beta + \gamma - \delta + \varepsilon \\ T) \quad -2 &= -\beta - \delta - \varepsilon \end{aligned}$$

In terms of  $\delta$  and  $\varepsilon$ , we solve for

$$\begin{aligned} \alpha &= 1 - \delta \\ \beta &= 2 - \delta - \varepsilon \\ \gamma &= 2 - \delta \end{aligned}$$

---

<sup>11</sup>As well-known flow compressibility effects are governed by the free-stream Mach number  $M_\infty = V_\infty/a_\infty$ .

(continued)

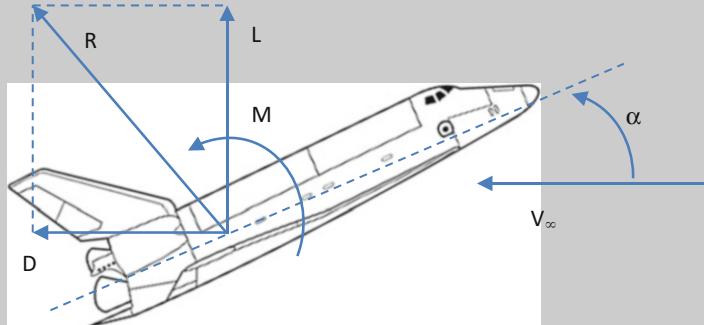
If the effects of viscosity through  $\mu$ , and compressibility through  $a$ , are neglected, we take  $\delta = \varepsilon = 0$  and have the form  $A = C\rho_\infty l^2 V_\infty^2$ . Then, the size of the body can be expressed through a reference area,  $S_{\text{ref}}$ , and the expression for the aerodynamic force is given as

$$A = \frac{1}{2} \rho_\infty V_\infty^2 S_{\text{ref}} C_A \quad (1.84)$$

where  $C_A$  is a certain dimensionless coefficient which uses a function of the shape of the body and its attitude with respect to the relative velocity of the fluid. In this book, the vehicle considered will have a plane of symmetry, and it will invariably operate under symmetric conditions.

In other words, the velocity vector is conveniently described by the angle of attack,  $\alpha$ , which is the angle between the relative velocity vector and a reference line fixed with respect to the vehicle (see figure).

In deriving the equations of motion, it is convenient to resolve the aerodynamic force into two forces: the drag force opposite to the direction of the motion and the lift force orthogonal to it. Hence, we obtain



$$\begin{aligned} D &= \frac{1}{2} \rho_\infty V_\infty^2 S_{\text{ref}} C_D = q_\infty S_{\text{ref}} C_D \\ L &= \frac{1}{2} \rho_\infty V_\infty^2 S_{\text{ref}} C_L = q_\infty S_{\text{ref}} C_L \\ M &= \frac{1}{2} \rho_\infty V_\infty^2 S_{\text{ref}} L_{\text{ref}} C_m = q_\infty S_{\text{ref}} L_{\text{ref}} C_m \end{aligned} \quad (1.85)$$

(continued)

where  $q_\infty$  is the dynamic pressure, while  $C_L$ ,  $C_D$ , and  $C_m$ , called the lift, drag, and pitching moment<sup>12</sup> coefficients, respectively, are functions of the angle of attack.

Now, if we retain the effects of viscosity and compressibility, with  $\delta \neq 0$  and  $\varepsilon \neq 0$ , Eq. (1.83) will take the form

$$A \approx \rho_\infty S V_\infty^2 \left( \frac{\mu_\infty}{\rho_\infty V_\infty l} \right)^\delta \left( \frac{a_\infty}{V_\infty} \right)^\varepsilon \quad (1.86)$$

The ratio  $V_\infty/a_\infty$  is the Mach number,  $M_\infty$ , while the dimensionless quantity  $\frac{\rho_\infty V_\infty l}{\mu_\infty}$  is known as the Reynolds number,  $Re$ .

By comparing Eqs. (1.84) and (1.86), we conclude that Eq. (1.85) for the aerodynamic forces and moment is still valid, but the drag, lift, and moment<sup>13</sup> coefficients are now functions of the angle of attack, the Mach number, and the Reynolds number:

$$\begin{aligned} C_D &= C_D(\alpha, M_\infty, Re_\infty) \\ C_L &= C_L(\alpha, M_\infty, Re_\infty) \\ C_m &= C_m(\alpha, M_\infty, Re_\infty) \end{aligned} \quad (1.87)$$

Of course the same dependence from  $\alpha$ ,  $M_\infty$ , and  $Re_\infty$  applies for the remaining aerodynamic force and moment coefficients (i.e.,  $C_Y$ ,  $C_I$ , and  $C_n$ ).

As a result, Eq. (1.82), written from intuition but not very useful, has cascade to the simple, direct form of Eqs. (1.85) and (1.87), which contain a tremendous amount of information. In fact, Eq. (1.85) says that the lift and drag force and the pitching moment are directly proportional to the dynamic pressure, to the reference surface, to the reference length (moment only), and to the lift, drag, and pitching moment coefficients.

In fact, Eq. (1.85) can be turned around and used as a definition for the lift, drag, and pitching moment coefficients:

---

<sup>12</sup>Note that even though we discussed only about force, also the moment can be considered provided that a reference length is considered.

<sup>13</sup>Moment coefficient depends, of course, on the pole chosen for the moment calculation, usually the vehicle's center of gravity.

(continued)

$$\begin{aligned}
 C_D &= \frac{D}{q_\infty S_{\text{ref}}} \\
 C_L &= \frac{L}{q_\infty S_{\text{ref}}} \\
 C_m &= \frac{M}{q_\infty L_{\text{ref}} S_{\text{ref}}} \tag{1.88}
 \end{aligned}$$

That is, the lift, drag, and pitching moment coefficients are always defined as the aerodynamic lift, drag, and moment divided by dynamic pressure and some reference area and length (moment coefficient only).

To help appreciate the value of the relationships expressed by Eq. (1.87), let us assume that we are given a particular aerodynamic shape, and we wish to measure the drag and how it varies with the different parameters— $\rho_\infty$ ,  $V_\infty$ ,  $S_{\text{ref}}$ ,  $\mu_\infty$ , and  $a_\infty$ —according to Eq. (1.82).

This means that we have to run a set of wind tunnel tests, making measurements of  $D$  where one of the five parameters is varied but the remaining four are held fixed.

So, when we are finished, we end up with five individual stacks of wind tunnel data from which we can (in principle) obtain the precise variation of  $D$  with  $\rho_\infty$ ,  $V_\infty$ ,  $S_{\text{ref}}$ ,  $\mu_\infty$ ,  $a_\infty$ .

This represents, however, a lot of personal effort and a lot of wind tunnel testing at great financial expense.

On the contrary, by dealing with Eq. (1.87), that is, the drag coefficient instead of the drag itself and  $M_\infty$  and  $Re_\infty$  instead of  $\rho_\infty$ ,  $V_\infty$ ,  $S_{\text{ref}}$ ,  $\mu_\infty$ , and  $a_\infty$ , we have ended up with only two stacks of wind tunnel data rather than five we had earlier.

Clearly, by using the dimensionless quantities  $C_D$ ,  $M_\infty$ , and  $Re_\infty$ , we have achieved a great economy of effort and wind tunnel time.

Finally,  $M_\infty$  and  $Re_\infty$  number are powerful quantities in aerodynamics. They are called *similarity parameters*.

Indeed, consider that we have two different flows, say, a red flow and a green flow, over two bodies that are geometrically similar but are of different sizes for the red and green flows.

The red and green flows have different values of  $\rho_\infty$ ,  $V_\infty$ ,  $\mu_\infty$ ,  $a_\infty$ , but they both have the same  $M_\infty$  and  $Re_\infty$ .

Thus, from Eq. (1.87),  $C_L$ ,  $C_D$ , and  $C_m$ , measured in the red flow, will be the same values as the  $C_L$ ,  $C_D$ , and  $C_m$ , measured in the green flow, even though the red and green flows are different flows. In this case, the red and

(continued)

green flows are called dynamically similar flows; hence,  $M_\infty$  and  $Re_\infty$  are called similarity parameters.

Note that it is the concept of dynamic similarity that allows measurements obtained in wind tunnel of a small-scale model of an airplane/spacecraft to be applied to the real airplane/spacecraft in free flight. If in the wind tunnel test (say, the red flow) the values of  $M_\infty$  and  $Re_\infty$  are the same as those for the real airplane/spacecraft in free flight (say, the green flow), then  $C_L$ ,  $C_D$ , and  $C_m$  measured in the wind tunnel will be precisely the same as those values in free flight. The concept of dynamic similarity is essential to wind tunnel testing.

In most wind tunnel test of small-scale models of real airplane/spacecraft, every effort is made to simulate the values of  $M_\infty$  and  $Re_\infty$  encountered by the real airplane/spacecraft in free flight.

Unfortunately, due to the realities of wind tunnel design and operation, this is frequently not possible (i.e., duplication of both the  $M_\infty$  and  $Re_\infty$  number at the same time). In such cases, the wind tunnel data must be “extrapolated” to the conditions of free flight. Such extrapolations are usually approximations, and they introduce a degree of error when the wind tunnel data are used to describe the conditions of full-scale free flight. The problem of not being able to simultaneously simulate free flight value of  $M_\infty$  and  $Re_\infty$  in the same wind tunnel is still pressing today in spite of the fact that wind tunnel testing has been going on for almost 150 years. Among other reasons, this is why there are so many different wind tunnels at different laboratories around the world.

The normal, axial, lift, drag, and moment coefficients for an aerodynamic body can be obtained by integrating the pressure and skin friction coefficient over the body surface from the leading to the trailing edge. For a two-dimensional body,

$$\begin{aligned} C_N &= \frac{1}{c} \left[ \int_0^c (C_{p,l} - C_{p,u}) dx + \int_0^c \left( C_{f,u} \frac{dy_u}{dx} + C_{f,l} \frac{dy_l}{dx} \right) dx \right] \\ C_A &= \frac{1}{c} \left[ \int_0^c \left( C_{p,u} \frac{dy_u}{dx} - C_{p,l} \frac{dy_l}{dx} \right) dx + \int_0^c (C_{f,u} + C_{f,l}) dx \right] \\ C_{mLE} &= \frac{1}{c^2} \left[ \int_0^c (C_{p,u} - C_{p,l}) x dx - \int_0^c \left( C_{f,u} \frac{dy_u}{dx} + C_{f,l} \frac{dy_l}{dx} \right) x dx \right] + \\ &\quad + \frac{1}{c^2} \left[ \int_0^c \left( C_{p,u} \frac{dy_u}{dx} + C_{f,u} \right) y_u dx + \int_0^c \left( -C_{p,l} \frac{dy_l}{dx} + C_{f,l} \right) y_l dx \right] \end{aligned} \quad (1.89)$$

and

$$\begin{aligned} C_L &= C_N \cos \alpha - C_A \sin \alpha \\ C_D &= C_N \sin \alpha + C_A \cos \alpha \end{aligned} \quad (1.90)$$

(continued)

Equation (1.89) emphasized that lift, drag, and moments on an aerodynamic shape stem from the detailed pressure and shear stress distributions on the surface and that measurements and/or calculations of these distributions, especially for complex configurations, are not trivial undertakings. On the other hand, Eq. (1.88) indicates that lift, drag, and moments can be quickly obtained from simple formulas. The bridge between these two outlooks is, of course, the lift, drag, and moment coefficients. All the physical complexity of the flow field around an aerodynamic body is simplicity buried in  $C_L$ ,  $C_D$ , and  $C_m$ .

### 1.5.2 Conventions for Aerothermodynamic Data

The following aerodynamic sign convention (see both Fig. 1.37 and Fig. 1.38 for the stability axis system; directions on the figure are positive as shown) for forces, moments, velocities, and accelerations is adopted:

- Angle of attack ( $\alpha$ ) is positive when free-stream arrives under the pilot.
- Sideslip angle ( $\beta$ ) is positive when free-stream arrives from right side of the pilot.
- Aileron deflection angle ( $\delta_a$ ) is positive when trailing edge down.
- Elevon deflection angle ( $\delta_e$ ) is positive when trailing edge down.
- Body flap deflection angle ( $\delta_{bf}$ ) is positive when trailing edge down.
- Rudder deflection angle ( $\delta_r$ ) is positive when trailing edge down.

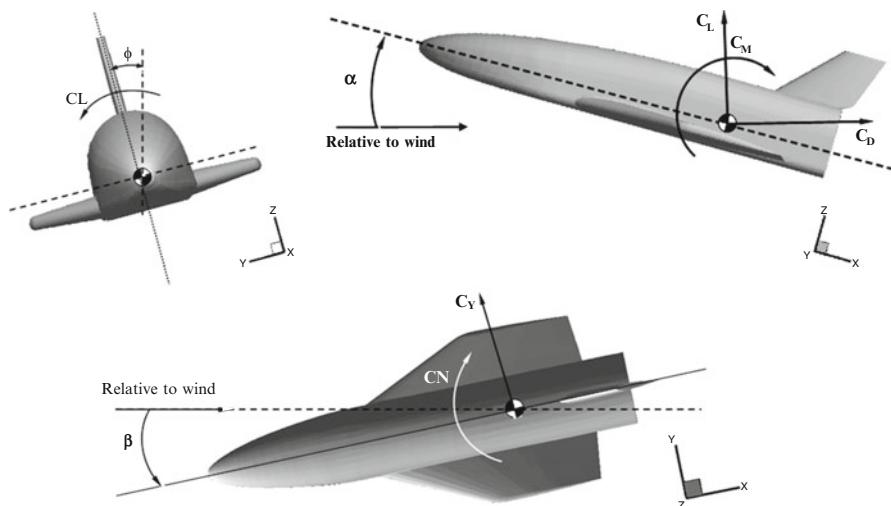


**Fig. 1.38** Aerodynamic sign convention

- Axial force coefficient ( $C_A$ ) is positive when force is pushing in front of vehicle toward the base.
- Normal force coefficient ( $C_N$ ) is positive when force is pushing on belly side of vehicle toward up.
- Side force coefficient ( $C_Y$ ) is positive when force is pushing on left side of vehicle toward the right.
- Rolling moment coefficient ( $C_I$ ) is positive when right wing is down.
- Pitching moment coefficient ( $C_m$ ) is positive when the aircraft puts the nose up.
- Yawing moment coefficient ( $C_n$ ) is positive when right wing is backward.

According to the ISO norm 1151 (1988). It is also the convention usually adopted in Flight Mechanics. Therefore, the static stability conditions for the vehicle are the following:

- Longitudinal static stability:  $C_{m\alpha} < 0$
- Lateral-directional static stability:  $C_{n\beta} > 0; C_{I\beta} < 0$

Vehicle aerodynamic control surface deflections, forces, and hinge moments are summarized and illustrated in Fig. 1.39.

In general, control surface deflection angles are measured in a plane perpendicular to the control surface hinge axis. An exception is the rudder control surface deflections which are measured in a plane parallel to the fuselage reference plane.

Finally, note that in the general case, these coefficients depend on the angle of attack  $\alpha$ ; the angle of yaw  $\beta$ ; the rate of change of  $\alpha$  and  $\beta$ , that is,  $\dot{\alpha}$  and  $\dot{\beta}$ ; the

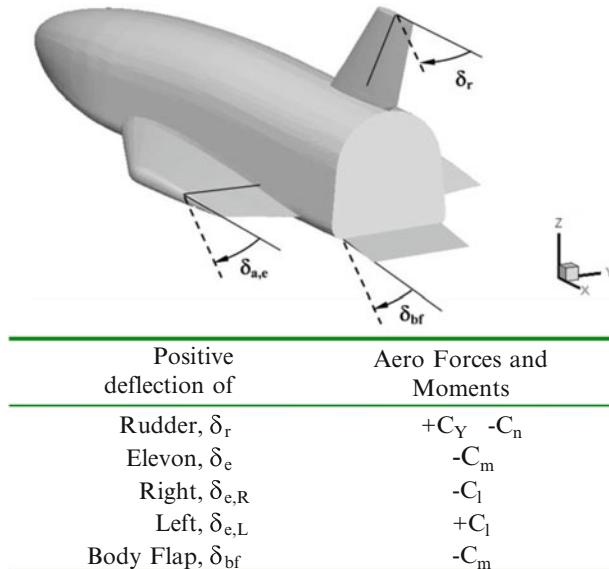


Fig. 1.39 Aerodynamic control surface deflections, forces, and moments

angular velocities for the roll, the pitch and the yaw rotations of the space vehicle, usually denoted by  $p, q, r$ ; and the deflections of the aerodynamic control surfaces.<sup>14</sup>

If linear behavior is present in the considered intervals of  $\alpha, \beta, p, q, r, \dot{\alpha}$ , and  $\dot{\beta}$ , the dependencies of the aerodynamic coefficients are given customarily in linear form,<sup>15</sup> equivalent to the first elements of a Taylor series expansion.

Generally speaking, for the pitching moment coefficient, one gets, for example,

$$\begin{aligned} C_m = C_{m,\alpha=0} &+ \frac{\partial C_m}{\partial \alpha} \alpha + \frac{\partial C_m}{\partial \beta} \beta + \frac{\partial C_m}{\partial \delta_e} \delta_e + \frac{\partial C_m}{\partial \delta_a} \delta_a + \frac{\partial C_m}{\partial \delta_{sb}} \delta_{sb} \\ &+ \frac{\partial C_m}{\partial \delta_{bf}} \delta_{bf} + \frac{\partial C_m}{\partial p^*} p^* + \frac{\partial C_m}{\partial q^*} q^* + \frac{\partial C_m}{\partial r^*} r^* + \frac{\partial C_m}{\partial \dot{\alpha}^*} \dot{\alpha}^* \\ &+ \frac{\partial C_m}{\partial \dot{\beta}^*} \dot{\beta}^* + \text{high order terms} \end{aligned} \quad (1.91)$$

where

$$p^* = \frac{p L_{\text{ref}}}{V_\infty}, \quad q^* = \frac{q L_{\text{ref}}}{V_\infty}, \quad r^* = \frac{r L_{\text{ref}}}{V_\infty} \quad (1.92)$$

are the reduced roll, pitch, and yaw rate.

$$\dot{\alpha}^* = \frac{\dot{\alpha} L_{\text{ref}}}{V_\infty}, \quad \dot{\beta}^* = \frac{\dot{\beta} L_{\text{ref}}}{V_\infty} \quad (1.93)$$

are the reduced rate of change of the angles of attack and sideslip.

$$\delta_e = \frac{\delta_{e,L} + \delta_{e,R}}{2} \quad (1.94)$$

is the elevon deflection.

$$\delta_a = \frac{\delta_{e,L} - \delta_{e,R}}{2} \quad (1.95)$$

---

<sup>14</sup>At high altitudes, due to the low density there, aerodynamic control surfaces are not useful and/or efficient. In such regimes, therefore, flight control is conducted by the thrusters of reaction control systems (RCS).

<sup>15</sup>This linear expansion of  $C_m$  dependencies is commonly used in classical Flight Mechanics. In general these dependencies are due to the configuration and the mission of the flight vehicle considered. Of course, civil and combat aircraft have other relevant dependencies than winged re-entry vehicles or capsules. For demonstration purposes, we write here the typical linear formulation of the force and moment coefficients, including the guidance and control capability through appropriate deflections of the aerodynamic control surfaces as ailerons, speed brake, and body flap.

is the aileron deflection where the subscripts L and R denote the left and right aileron, while  $\delta_{bf}$  and  $\delta_{sb}$  are the body flap and speed brake deflections, respectively.

Flight data, however, suggest that most of the first-order terms can be neglected, except the terms  $\frac{\partial C_m}{\partial \alpha}$ , whereby the static stability is defined, as well as  $\frac{\partial C_m}{\partial \dot{\alpha}^*}$  and  $\frac{\partial C_m}{\partial \dot{q}^*}$ , which stand for the dynamic stability of the longitudinal motion. Therefore, Eq. (1.91) reduces to

$$\begin{aligned} C_m &= C_{m,\alpha=0} + \frac{\partial C_m}{\partial \alpha} \alpha + \frac{\partial C_m}{\partial \delta_e} \delta_e + \frac{\partial C_m}{\partial \delta_a} \delta_a + \frac{\partial C_m}{\partial \delta_{sb}} \delta_{sb} \\ &\quad + \frac{\partial C_m}{\partial \delta_{bf}} \delta_{bf} + \frac{\partial C_m}{\partial q^*} q^* + \frac{\partial C_m}{\partial \dot{\alpha}^*} \dot{\alpha}^* \\ &= C_{m,\alpha=0} + C_{m,\alpha} \alpha + C_{m,\delta_e} \delta_e + C_{m,\delta_a} \delta_a + C_{m,\delta_{sb}} \delta_{sb} + C_{m,\delta_{bf}} \delta_{bf} \\ &\quad + C_{m,q^*} q^* + C_{m,\dot{\alpha}^*} \dot{\alpha}^* \end{aligned} \quad (1.96)$$

where  $(C_{m,\dot{\alpha}^*} + C_{m,q^*})$  is the pitch-dumping derivative.<sup>16</sup>

In a similar manner all the other aerodynamic coefficients can be defined, of course with distinct dependencies.

For instance, for lift and drag, we get

$$C_L = C_{L,\alpha=0} + \frac{\partial C_L}{\partial \alpha} \alpha + \frac{\partial C_L}{\partial \beta} \beta + \frac{\partial C_L}{\partial \delta_e} \delta_e + \frac{\partial C_L}{\partial \delta_a} \delta_a + \frac{\partial C_L}{\partial \delta_{bf}} \delta_{bf} + \frac{\partial C_L}{\partial q^*} q^* + \frac{\partial C_L}{\partial \dot{\alpha}^*} \dot{\alpha}^* \quad (1.97)$$

$$\begin{aligned} C_D &= C_{D,\alpha=0} + \frac{\partial C_D}{\partial \alpha} \alpha + \frac{\partial C_D}{\partial \beta} \beta + \frac{\partial C_D}{\partial \delta_e} \delta_e + \frac{\partial C_D}{\partial \delta_a} \delta_a + \frac{\partial C_D}{\partial \delta_{sb}} \delta_{sb} + \frac{\partial C_D}{\partial \delta_{bf}} \delta_{bf} \\ &\quad + \frac{\partial C_D}{\partial q^*} q^* + \frac{\partial C_D}{\partial \dot{\alpha}^*} \dot{\alpha}^* \end{aligned} \quad (1.98)$$

## 1.6 Simplified Aerodynamic Analysis

Due to the absence of high-performance digital computers, aerodynamic design of hypersonic vehicles developed in the late 1960s and early 1970s by means of low-order design methods, based on Newtonian flow theory.

This early work focused on vehicle aerodynamic performance analysis and comparisons with experimental data, thus developing the vehicle aerodynamic

---

<sup>16</sup>This derivative provides information about dynamic stability of space re-entry vehicles. From experience it is well known that the dynamic behavior of re-entry vehicles can be critical in the vicinity of transonic flow, which means the regime  $0.5 \leq M_\infty \leq 1.5$ . That is in contrast to the dynamic characteristics at higher Mach numbers: in the supersonic and hypersonic Mach number regime, the dynamic derivatives play only a minor role.

database to use by hand in the traditional, segregated design environment, especially during a conceptual design phase.

Indeed, during the early design phase (e.g., phase-A design), low-order methods are typically suitable being able to improve computational speed even if at the expense of fidelity. For example, as will be explained later, panel methods can be used in conjunction with Newtonian flow theory to obtain the hypersonic aerodynamic characteristics of a vehicle with orders of magnitude reduction in computational requirement compared to computational fluid dynamics (CFD). Further, the importance of Newtonian flow theory can be appreciated also considering that the geometry (and/or a part of it) of many common hypersonic vehicles of practical interest such as sphere-cone, blunt biconic, and spherical forebody segments can be also expressed analytically (see hereinafter), thus providing vehicle aerodynamic performance in a closed form approach. This means that rapid simulations of hypersonic aerodynamic and trajectory optimization for conceptual design scope are enabled.

Further, this allows vehicle shape parameters to be directly incorporated into the equations of motion. The resulting unified mathematical framework in both trajectory and vehicle shape allows trajectory optimization methods to be extended to also include vehicle aeroshape. This trajectory optimization methodology substitutes the slower, more general optimization methodology often used in traditional, segregated design environments to account for the wide range of possible design problems and interactions among contributing analysis.

Low-order design method based on Newtonian flow theory, however, has been largely forgotten by the aerospace community in the recent decades. The high-performance computers, now available, allow engineers to perform also in the early-design stage highly reliable CFD simulations. This approach, however, represents a not viable option. In fact, the substantial trial-and-error effort, which characterizes the vehicle conceptual design, becomes prohibitive when considering the computational cost, time effort, and great amount of numerical results provided by CFD analysis.

As a result, the ability of Newtonian flow theory to model general and complex shapes is still desirable and valid design tool.

### **1.6.1 Low-Order Method Aerodynamics**

Hypersonic flow is inherently nonlinear. This is intuitively obvious recalling the important physical aspects of hypersonic, such as high-temperature chemically reacting flows, viscous interaction, entropy layers, etc., previously described. It is difficult to imagine that such complex phenomena could be described by simple linear relationships. Even without these considerations, the basic theory of inviscid compressible flow, when the Mach number becomes large, does not yield aerodynamic theories which are mathematically linear. This is in stark contrast to supersonic flow which, for thin bodies at small angles of attack, can be described by

a linear partial differential equation, leading to the familiar supersonic expression for pressure coefficient on a surface (or streamline) with local deflection angle  $\theta$ :

$$C_p = \frac{2\theta}{\sqrt{M_\infty^2 - 1}} \quad (1.99)$$

This equation is a classic result from inviscid, linearized, two-dimensional, supersonic flow theory. Unfortunately, it is not valid at hypersonic speeds.

Equation (1.99), for a specified free-stream Mach number, gives the pressure coefficient on the surface of a body strictly in terms of the local deflection angle of the surface,  $\theta$ . So  $C_p$  is a function of local variable and not of the global flowfield; thus it does not require a detailed solution of the complete flowfield.

In essence, Eq. (1.99) provides a local surface inclination method for the prediction of pressure distributions over two-dimensional supersonic bodies (in the hypothesis of thin bodies at small angles of attack).

Such simplicity is always welcomed by practicing aerodynamicists who have to design flight vehicles. This leads to the question: although hypersonic aerodynamics is nonlinear, and hence Eq. (1.99) does not hold, are there other methods, albeit approximate, which allow the rapid estimate of pressure distributions over hypersonic bodies just in terms of the local surface inclination angle? In other words, is there a viable *local surface inclination method* for hypersonic applications? The answer is yes; indeed, there are several methods which apply to hypersonic bodies as Newtonian flow theory described hereafter [2, 3, 9].

### 1.6.2 Newtonian Impact Flow Theory

Three centuries ago, Isaac Newton established a fluid dynamic theory which later was used to derive a *law* to compute the force on an inclined plane in a moving fluid. This law states that the force varies as the square of the sine of the deflection angle, the famous Newtonian *sine-squared law*. Experimental investigations carried out by D'Alembert more than a half-century later indicated that Newton's sine-squared law was not very accurate in the subsonic regime and, indeed, the preponderance of fluid dynamic experience up to the present day confirms this finding.

The exception to this is the modern world of hypersonic aerodynamics. Ironically, Newtonian theory, developed 300 years ago for the application to low-speed fluid dynamics, has direct application to the prediction of pressure distributions on hypersonic bodies.

In 1687, Newton in proposition 34 and 35 of his *Principia*, modeled a fluid flow as a stream of particles in rectilinear motion, much like a stream of pellets from a shotgun blast which, when striking a surface, would lose all their momentum normal to the surface but would move tangentially to the surface without loss of tangential momentum.

Thus, consider a stream with velocity  $V_\infty$  impacting on a surface area  $A$  inclined at an angle  $\theta$  to the free-stream, as shown in Fig. 1.40 [3].

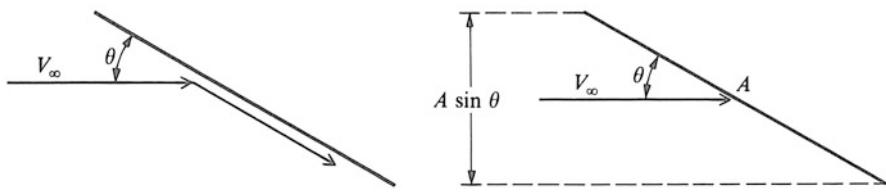


**Fig. 1.40** Schematic for Newtonian impact theory

From this mind, through appropriate consideration and simplex analytical calculations, he obtained the so-called Newtonian sine-squared law for pressure coefficient:

$$C_p = 2\sin^2\theta \quad (1.100)$$

where 2 represents the pressure coefficient at the stagnation point.

#### **Explanation Box. Derivation of Newtonian Sine-Squared Law**

The component of the free-stream velocity normal to the surface implies that the change in normal velocity is

$$V_\infty \sin \theta$$

Therefore, the mass flux incident on a surface area  $A$  is

$$\rho_\infty (V_\infty \sin \theta) A$$

Hence the time rate of change of momentum of this mass flux is mass flow change in normal component of velocity that is

$$(\rho_\infty V_\infty A \sin \theta) (V_\infty \sin \theta) = (\rho_\infty V_\infty^2 A \sin^2 \theta)$$

From Newton's second law, the time rate of change of momentum is equal to the force  $F$  exerted on the surface:

$$F = \rho_\infty V_\infty^2 A \sin^2 \theta$$

or

$$\frac{F}{A} = \rho_\infty V_\infty^2 \sin^2 \theta$$

This force acts along the same line as the rate of change of momentum, i.e., normal to the surface.

(continued)

Newton assumed the stream of particles to be rectilinear, i.e., individual particles do not interact with each other, and have no random motion. Due to this lack of random motion,  $F$  is a force associated only with the directed linear motion of the particles. The static pressure of a gas or liquid on the other hand is due to the purely random motion of the particles. Hence,  $F/A$ , which has the dimensions of pressure, must be interpreted as the pressure difference:

$$\frac{F}{A} = p - p_{\infty}$$

where  $p$  is the surface pressure and  $p_{\infty}$  is the free-stream static pressure. Substituting and simplifying,

$$p - p_{\infty} = \rho_{\infty} V_{\infty}^2 \sin^2 \theta$$

or

$$\frac{p - p_{\infty}}{\frac{1}{2} \rho_{\infty} V_{\infty}^2} = \frac{p - p_{\infty}}{q_{\infty}} = 2 \sin^2 \theta$$

or

$$C_p = 2 \sin^2 \theta$$

This equation is the famous *Newtonian sine-squared law* for pressure coefficient. It states that pressure coefficient is proportional to the sine square of angle between a tangent to the surface and the direction of the free-stream.

So, what does Newtonian pressure coefficient have to do with hypersonic flow? To answer this question, let us consider the shock wave and thin shock layer on a 15° sharp wedge at Mach 36, illustrated in Fig. 1.41 [3]. This figure also shows the streamline pattern over the wedge.

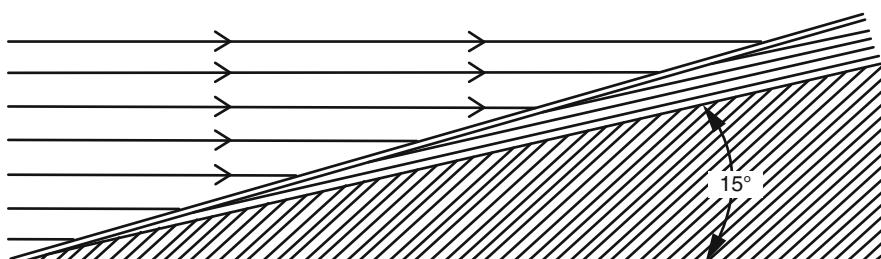


**Fig. 1.41** Streamlines in the thin hypersonic shock layer at  $M_{\infty} = 36$  past a wedge

Here, upstream of the shock wave, the streamlines are straight and parallel to the free-stream direction; downstream of the shock wave, the streamlines are also straight but parallel to the wedge surface inclined at a  $15^\circ$  angle. As the shock wave lies close to the surface at hypersonic speeds, it seems that the incoming flow is directly impinging on the wedge surface and then is running parallel to the surface downstream, i.e., the idea Newton expressed in 1687. Therefore, the geometric picture of hypersonic flowfields has some characteristics which closely approximate Newtonian flow. Equation (1.100) is then a good approximation to compute the surface pressure coefficient in hypersonic flow, where  $\theta$  is taken as the local deflection angle, i.e., the angle between the tangent to the surface and the free-stream. Clearly, Newtonian theory is a *local surface inclination method* where  $C_p$  depends only on the local surface deflection angle; it does not depend on any aspect of the surrounding flowfield. As example, consider Fig. 1.42a, which shows an arbitrarily shaped two-dimensional body [3].

The value of  $C_p$  at the arbitrary point  $P$  is given by  $C_p = 2 \sin^2 \theta$ , computing  $\theta$  as the angle between the free-stream and the local tangent to  $P$ . Now consider a three-dimensional body such as that sketched in Fig. 1.42b [3]. In this case the  $\theta$  angle is computed as the complementary to  $\phi$  angle, where  $\phi$  is the angle between  $\mathbf{n}$  (unit normal vector to the surface at point  $P$ ) and  $\mathbf{V}_\infty$  (velocity vector):

$$\mathbf{V}_\infty \cdot \mathbf{n} = |\mathbf{V}_\infty| \cos \phi = |\mathbf{V}_\infty| \sin \left( \frac{\pi}{2} - \phi \right) \quad (1.101)$$

The vectors  $\mathbf{n}$  and  $\mathbf{V}_\infty$  define a plane, and in that plane the angle  $\theta = \pi/2 - \phi$  is the angle between a tangent to the surface and the free-stream direction. Thus, from Eq. (1.101),

$$\mathbf{V}_\infty \cdot \mathbf{n} = |\mathbf{V}_\infty| \sin \theta$$

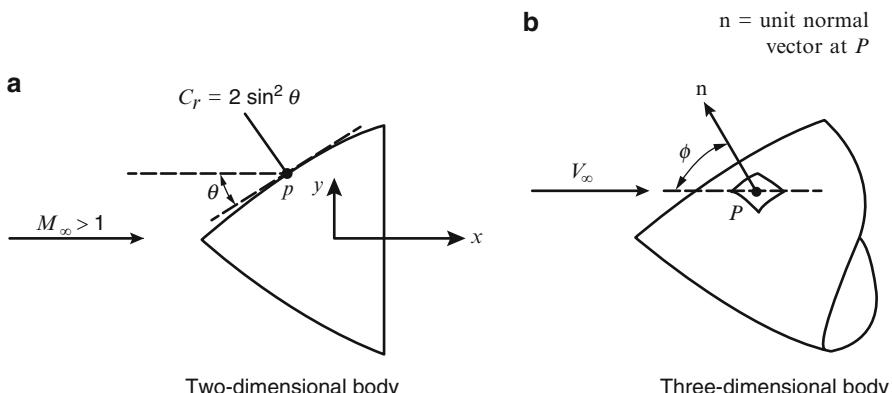


**Fig. 1.42** (a) Geometry for Newtonian applications in two-dimensional flow; (b) geometry for Newtonian applications in three-dimensional flow

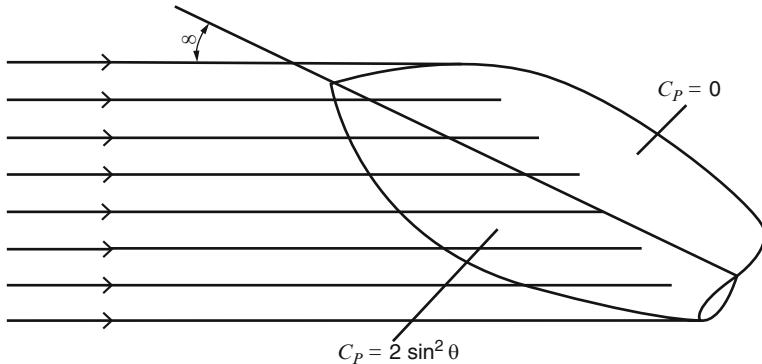


**Fig. 1.43** Region on the leeward side of a body, from Newtonian theory

or

$$\sin \theta = \frac{\mathbf{V}_\infty}{|\mathbf{V}_\infty|} \cdot \mathbf{n} \quad (1.102)$$

In the Newtonian model, the particles in the free-stream impact only on the frontal area of the body; they cannot curl around the body and impact on the back surface.

Hence, for the portion of a body which is not invested by the incident flow, as shown schematically in Fig. 1.43, no pressure is felt [3]. Hence, over this shadow region, it is consistent to assume  $p = p_\infty$ . Therefore,  $C_p = 0$ .

Now let us consider the blunt body sketched in Fig. 1.44.

It is clear that the maximum pressure, hence the maximum value of  $C_p$ , occurs at the stagnation point, where  $\theta = \frac{\pi}{2}$  ( $\varphi = 0$ ). Here Eq. (1.100) predicts  $C_p = 2$ .

This result is in contrast with that obtained for incompressible flow theory where  $C_p = 1$  at the stagnation point. Indeed, the stagnation pressure coefficient increases continuously from 1.0 at  $M_\infty = 0$  to 1.28 at  $M_\infty = 1.0$  up to about 1.84 for  $\gamma = 1.4$  as  $M_\infty \rightarrow \infty$ .

Note that this result that the maximum pressure coefficient approaches 2 at  $M_\infty \rightarrow \infty$  can be obtained independently from the one-dimensional momentum equation.

To this end let us consider a normal shock wave at hypersonic speed, as sketched on Fig. 1.45.

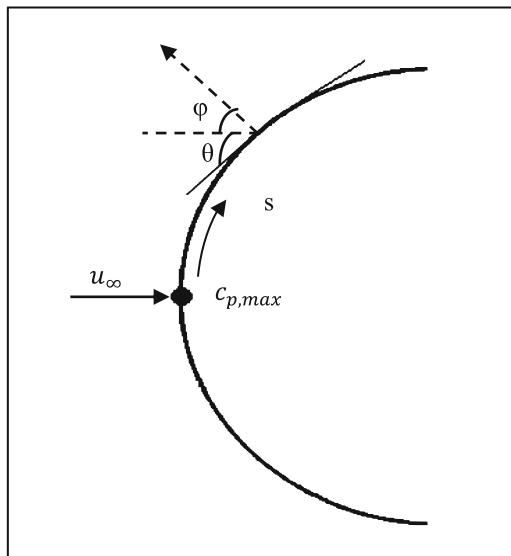
For this flow one-dimensional momentum equation gives

$$p_\infty + \rho_\infty V_\infty^2 = p_2 + \rho_2 V_2^2 \quad (1.103)$$

Recall that across a normal shock wave, the flow velocity decreases,  $V_2 < V_\infty$  (because of the flow behind the normal shock is subsonic).

This change becomes more severe as  $M_\infty$  increases, of course.

Thus, at hypersonic speeds, we can assume that

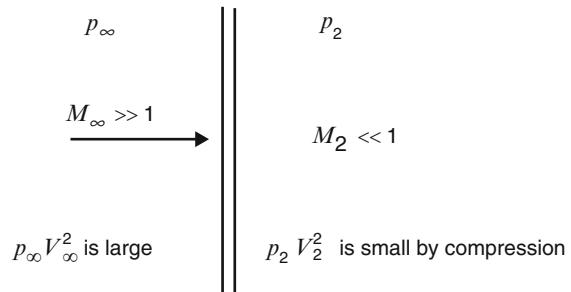


$$c_p = 2 \sin^2 \theta$$

$$c_p = 2 \cos^2 \varphi$$

**Fig. 1.44** Blunt body

**Fig. 1.45** Hypersonic flow across a normal shock wave



$$(\rho_\infty V_\infty^2) \gg (\rho_2 V_2^2) \quad (1.104)$$

and we can neglect the latter term in Eq. (1.103). As a result, Eq. (1.103) becomes, at hypersonic speeds in the limiting case as  $M_\infty \rightarrow \infty$

$$p_2 - p_\infty = \rho_\infty V_\infty^2$$

or

$$C_p = \frac{p_2 - p_\infty}{\frac{1}{2} \rho_\infty V_\infty^2} = 2 \quad (1.105)$$

thus confirming the Newtonian results of Eq. (1.100).

Finally, note that for large but finite Mach numbers, the value of  $C_p$  at a stagnation point is less than 2, as will be explained by modified Newtonian flow theory.

### 1.6.3 Modified Newtonian Flow Theory

Lester Lees proposed a modification to Newtonian theory, writing Eq. (1.100) as

$$C_p = C_{p\max} \sin^2 \theta \quad (1.106)$$

where  $C_{p\max}$  is the maximum value of the pressure coefficient, evaluated at a stagnation point behind a normal shock wave, i.e.,

$$C_{p\max} = \frac{p_{O2} - p_\infty}{\frac{1}{2}\rho_\infty V_\infty^2} \quad (1.107)$$

where  $p_{O2}$  is the total pressure behind a normal shock wave at the free-stream Mach number. It is worth noting also that the stagnation point flow state will be also indicated by the subscript t2 in this book. From the exact normal shock-wave theory, the “Rayleigh Pitot tube formula” gives

$$\frac{p_{O2}}{p_\infty} = \left[ \frac{(\gamma + 1)^2 M_\infty^2}{4\gamma M_\infty^2 - 2(\gamma - 1)} \right]^{\frac{\gamma}{(\gamma-1)}} \left[ \frac{1 - \gamma + 2\gamma M_\infty^2}{\gamma + 1} \right] \quad (1.108)$$

Noting that  $\frac{1}{2}\rho_\infty V_\infty^2 = (\frac{\gamma}{2}) p_\infty M_\infty^2$ , Eq. (1.107) becomes

$$C_{p\max} = \frac{2}{\gamma M_\infty^2} \left[ \frac{p_{O2}}{p_\infty} - 1 \right] \cong 2 - \varepsilon \quad (1.109)$$

where  $\varepsilon = \rho_1/\rho_2$  is the density ratio across the bow shock wave.

Combining Eq. (1.108) and Eq. (1.109), the following one is obtained:

$$C_{p\max} = \frac{2}{\gamma M_\infty^2} \left\{ \left[ \frac{(\gamma + 1)^2 M_\infty^2}{4\gamma M_\infty^2 - 2(\gamma - 1)} \right]^{\frac{\gamma}{(\gamma-1)}} \left[ \frac{1 - \gamma + 2\gamma M_\infty^2}{\gamma + 1} \right] - 1 \right\} \quad (1.110)$$

This relation is plotted in Fig. 1.46 [3].

Note that in the limit  $M_\infty \rightarrow \infty$

$$\begin{aligned} C_{p\max} &\rightarrow \left[ \frac{(\gamma+1)^2}{4\gamma} \right]^{\frac{\gamma}{(\gamma-1)}} \left[ \frac{4}{\gamma+1} \right] \\ &\rightarrow 1.84 \text{ for } \gamma = 1.4 \\ &\rightarrow 2.0 \text{ for } \gamma = 1.0 \end{aligned}$$

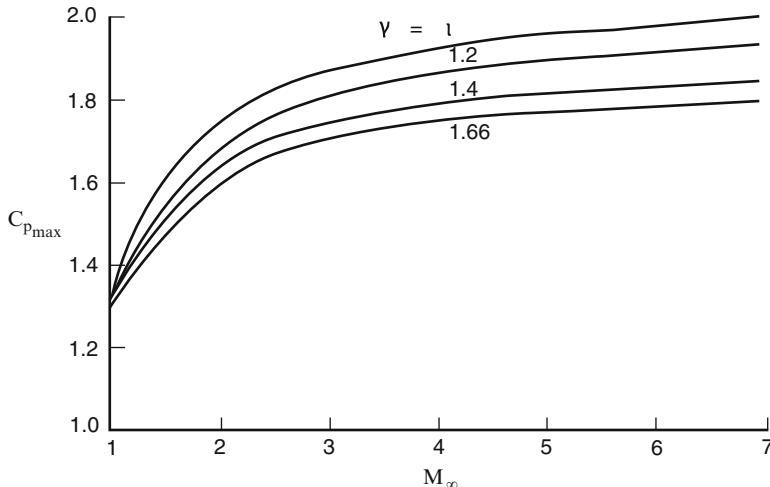


**Fig. 1.46** Variation of stagnation pressure coefficient with  $M_\infty$  and  $\gamma$

Equation (1.106), with  $C_{p\max}$  given by Eq. (1.110), is called the *modified Newtonian law*. This forces the modified Newtonian analysis to be “exact” at the stagnation point, following the  $(\sin^2)$  law for all other vehicle’s areas.

Note that the *modified Newtonian law* is no longer Mach number independent. The effect of a finite Mach number enters through Eq. (1.110).

As both  $M_\infty \rightarrow \infty$  and  $\gamma \rightarrow 1$ , Eq. (1.106) and Eq. (1.110) yield  $C_p = 2\sin^2\theta$ . That is, the *straight Newtonian law* is recovered in the limit as  $M_\infty \rightarrow \infty$  and  $\gamma \rightarrow 1$ .

For the prediction of pressure distributions over blunted-nose bodies, *modified Newtonian*, Eq. (1.106), is considerably more accurate than the *straight Newtonian*, Eq. (1.100).

This is illustrated in Fig. 1.47, which shows the pressure distribution over a paraboloid at Mach 8 [3].

The solid line is derived by a finite-difference solution of the blunt-body flowfield; the solid symbols are the modified Newtonian results from Eq. (1.106) and Eq. (1.110). Note the excellent agreement, particularly over the forward portion of the nose. The dashed line is the straight Newtonian result from Eq. (1.100); it lies 9 % above exact results.

Finally, it is worth to note that combining Eq. (1.106) and Eq. (1.107), the equation for the impact pressure at an aeroshape station can be given considering that

$$C_p = \frac{p - p_\infty}{\frac{1}{2}\rho_\infty V_\infty^2} = C_{p\max} \sin^2\theta = \frac{p_{02} - p_\infty}{\frac{1}{2}\rho_\infty V_\infty^2} \sin^2\theta \quad (1.111)$$

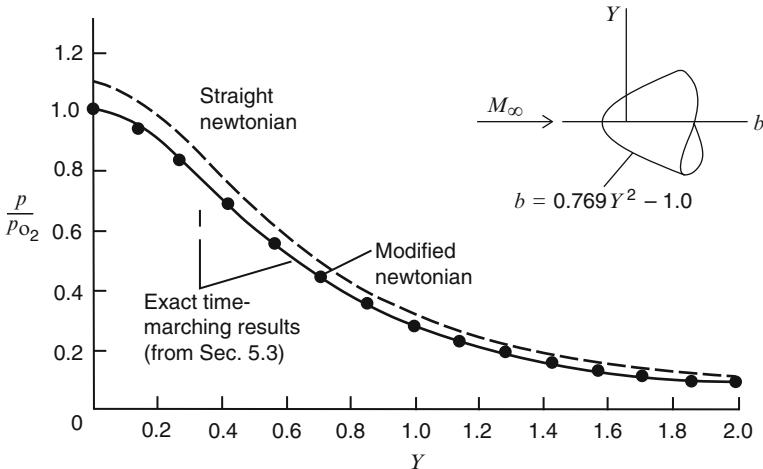


**Fig. 1.47** Surface pressure distribution over a paraboloid at  $M_\infty = 8.0$ ;  $p_{02}$  is the total pressure behind a normal shock wave at  $M_\infty = 8.0$

So,

$$\frac{p - p_\infty}{\frac{1}{2} \rho_\infty V_\infty^2} = \frac{p_{02} - p_\infty}{\frac{1}{2} \rho_\infty V_\infty^2} \sin^2 \theta \rightarrow \frac{p}{p_\infty} = 1 + \left( \frac{p_{02}}{p_\infty} - 1 \right) \sin^2 \theta \quad (1.112)$$

Therefore, once the vehicle surface is defined, the application of this equation is all that is needed to determinate the pressure distribution on the complete vehicle surface.<sup>17</sup>

#### 1.6.4 Flat Plate Hypersonic Aerodynamics

Newtonian theory quickly allows assessing flat plate hypersonic aerodynamics, as sketched in Fig. 1.48 [3]. Here, a two-dimensional flat plate with chord length  $c$  is at an angle of attack,  $\alpha$ , to the free-stream. Since friction is not considered and surface pressure always acts normal to the surface, the resultant aerodynamic force,  $N$ , is perpendicular to the plate, as shown in Fig. 1.48.

For an infinitely thin flat plate, this is a general result which is not limited to Newtonian flow theory or even flow.  $N$  is decomposed into lift (normal to the velocity vector) and drag (in the direction of the velocity vector), denoted by  $L$  and  $D$ , respectively, as shown in Fig. 1.48.

<sup>17</sup>See the evaluation of pressure distribution on the pitch plane of an Apollo-like vehicle provided in Chap. 4.

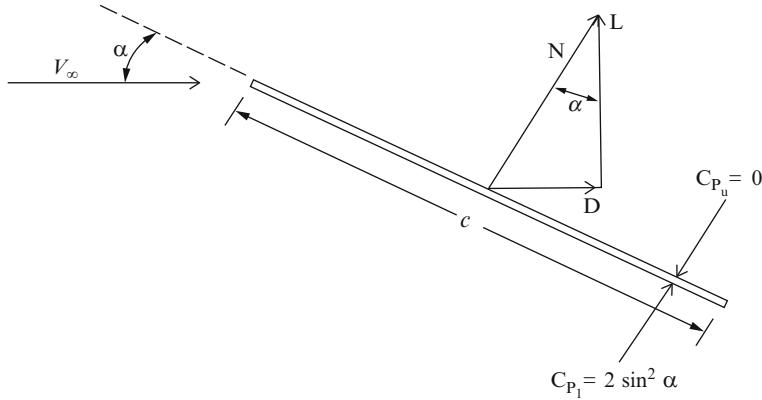


**Fig. 1.48** Flat plate at angle of attack. Illustration of aerodynamic forces

According to Newtonian theory, the pressure coefficient on the lower surface is

$$C_{p_l} = 2 \sin^2 \alpha \quad (1.113)$$

and that on the upper surface, which is in the shadow region, is

$$C_{p_u} = 0 \quad (1.114)$$

Defining the normal force coefficient as  $C_N = N/q_\infty S$  where  $S = (c)$  (1),  $C_N$  is computed by integrating the pressure coefficients over the lower and upper surfaces:

$$C_N = \frac{1}{c} \int_0^c (C_{p_l} - C_{p_u}) dx \quad (1.115)$$

where  $x$  is the distance along the chord from the leading edge. Substituting Eq. (1.113) and Eq. (1.114) into Eq. (1.115), we obtain

$$C_N = (2 \sin^2 \alpha) \quad (1.116)$$

From the geometry of Fig. 1.48, it can be seen that the lift and drag coefficients, defined as  $C_L = L/q_\infty S$  and  $C_D = D/q_\infty S$ , respectively, are given by

$$C_L = C_N \cos \alpha \quad (1.117)$$

and

$$C_D = C_N \sin \alpha \quad (1.118)$$

i.e.,

$$C_L = 2\sin^2\alpha \cos\alpha \quad (1.119)$$

and

$$C_D = 2\sin^3\alpha \quad (1.120)$$

$$C_D = 2\sin^3\alpha \quad (1.121)$$

Finally, the lift-to-drag ratio<sup>18</sup> L/D is given by

$$L/D = \cot\alpha \quad (1.122)$$

The results obtained above for the application of Newtonian theory to an infinitely thin flat plate are plotted in Fig. 1.49, where L/D,  $C_L$ , and  $C_D$  are plotted vs. angle of attack [3].

Thus, the following consideration can be asserted:

1. In the range of  $\alpha$  from  $0^\circ$  to  $15^\circ$ , the variation of  $C_L$  with  $\alpha$  is very nonlinear. This is in direct contrast to the familiar result for subsonic and supersonic flow, where for thin bodies at small  $\alpha$ , the lift curve is a linear function of  $\alpha$  (recall, e.g., that the theoretical lift slope from incompressible thin airfoil theory is  $2\pi$  per radian). This is also in contrast with the results from linearized supersonic theory where for a plate suggests that

$$C_L = \frac{4\alpha}{\sqrt{M_\infty^2 - 1}}$$

As result, the nonlinear lift curve shown in Fig. 1.49 is a graphic demonstration of the nonlinear nature of hypersonic flow.

2. The  $C_L$  curve has a maximum at  $\alpha = 54.7^\circ$ . It is worth to note that the maximum lift coefficient for many practical hypersonic vehicles occurs at angles of attack close to  $\alpha \approx 55^\circ$  and then decreases, reaching zero at  $\alpha = 90^\circ$ . However, the attainment of  $C_{L\max}$  (point A) in Fig. 1.49 is not due to any viscous, separated flow phenomenon analogous to that which occurs in subsonic flow. Rather, in Fig. 1.49, the attainment of a maximum  $C_L$  is purely a geometric effect. Anyway, the angle at which  $C_{L\max}$  occurs can be early quantified differentiating Eq. (1.120) with respect to  $\alpha$  and setting the derivative equal to zero:

---

<sup>18</sup>Note that L/D is one of the most important features of the vehicle aerodynamic performance. In fact, it has a direct impact on cross-range capability and on aero thermal loading alleviation.

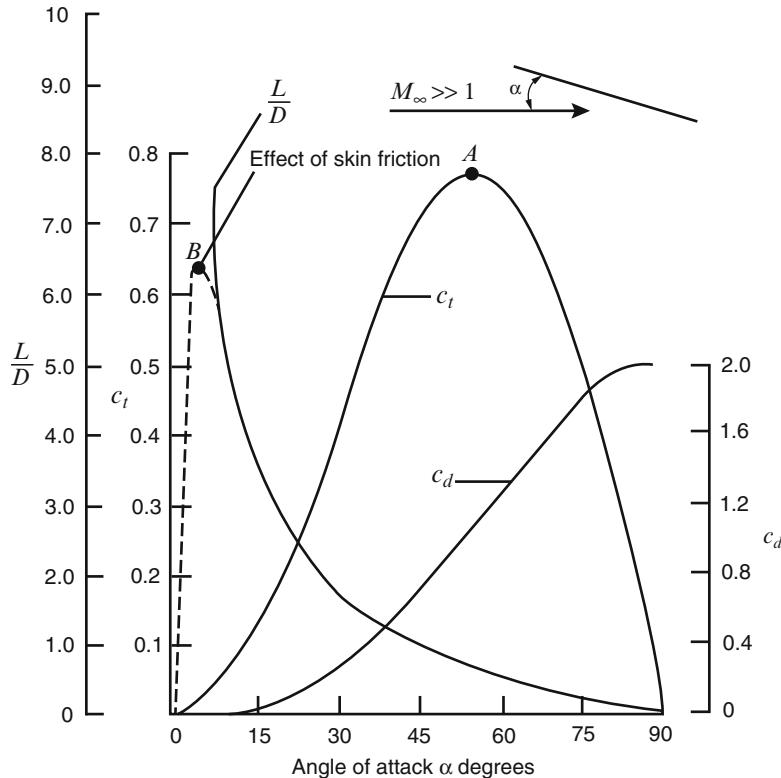


**Fig. 1.49** Newtonian results for a hypersonic aerodynamics flat plate

$$\frac{dC_L}{d\alpha} = \frac{d}{d\alpha} (2\sin^2\alpha \cos\alpha) = 2\sin^2\alpha (-\sin\alpha) + 4\cos^2\alpha \sin\alpha = 0$$

or

$$\sin^2\alpha = 2\cos^2\alpha = 2(1 - \sin^2\alpha)$$

or

$$\sin^2\alpha = \frac{2}{3}$$

Hence,

$$\bar{\alpha} = 54.7^\circ$$

and

$$C_{L\max} = 2\sin^2\bar{\alpha}\cos^2\bar{\alpha} = 0.77$$

3.  $C_D$  monotonically increases from zero at  $\alpha = 0$  to a maximum of 2 at  $\alpha = 90^\circ$ . The Newtonian result for drag is essentially wave drag at hypersonic speeds because we are dealing with an inviscid flow, hence no friction drag. The variation of  $C_D$  with  $\alpha$  is essentially a cubic variation, in contrast to the result from linearized supersonic flow which shows that

$$C_D = \frac{4\alpha^2}{\sqrt{M_\infty^2 - 1}}$$

that is,  $C_D$  varies as the square angle of attack.

Note that the hypersonic result that  $C_D$  varies as  $\alpha^3$  is early obtained from Eq. (1.121) which for small  $\alpha$  becomes

$$C_D = 2\alpha^3$$

4. The value of L/D increases monotonically as  $\alpha$  (curve slope) is decreased. Indeed,  $(L/D) \rightarrow \infty$  as  $\alpha \rightarrow 0$ . This is valid for inviscid hypothesis as, if friction is included,  $D$  becomes finite at  $\alpha = 0$ , and then  $(L/D) \rightarrow 0$  as  $\alpha \rightarrow 0$ .

The solid curve in Fig. 1.49 is the pure Newtonian result; it shows that L/D is infinitely large at  $\alpha = 0$  and monotonically decreases to zero at  $\alpha = 90^\circ$ . The infinite value of L/D at  $\alpha = 0^\circ$  is purely fictional. It is due to the neglect of skin friction. When skin friction is added to the picture, denoted by the dashed curve in Fig. 1.49, the lift-to-drag ratio reaches a maximum value at a small angle of attack (point B) and is equal to zero at  $\alpha = 0$ . (At  $\alpha = 0$ , no lift is produced, but there is a finite drag due to friction; hence,  $(L/D) = 0$  at  $\alpha = 0$ ).

Finally, note that the value of  $(L/D)_{\max}$  and the angle of attack at which it occurs are strictly a function of the zero-lift drag coefficient,  $C_{D_0}$ .

$C_{D_0}$  is simply due to the integrated effect of skin friction over the plate surface at  $\alpha = 0^\circ$ . Indeed, at small angles of attack, the skin friction exerted on the plate should be essentially that at zero angle of attack; hence we can write the total drag as

$$C_D = C_{D_0} + 2\sin^3\alpha$$

This relationship highlights that  $(L/D)_{\max} \propto \frac{1}{\sqrt{C_{D_0}}}$  so that  $(L/D)_{\max}$  decreases as  $C_{D_0}$  increases: the higher the friction drag, the lower is the aerodynamic efficiency. Also, the angle of attack at which maximum (L/D) occurs increases as  $C_{D_0}$  increases.

5. There is yet another interesting aerodynamic condition that holds at  $(L/D)_{\max}$ , derived as follows:

$$C_D = 2\alpha^3 + C_{D_0} = 2C_{D_0} + C_{D_0} = 3C_{D_0}$$

Since the total drag coefficient is the sum of the wave-drag coefficient  $C_{D_w}$  and the friction drag coefficient  $C_{D_0}$ , we can write at  $(L/D)_{\max}$  flight conditions that

$$C_D = C_{D_w} + C_{D_0} = 3C_{D_0}$$

or

$$C_{D_w} = 2C_{D_0}$$

This clearly shows that, for the hypersonic flat plate using Newtonian theory, at the flight conditions associated with  $(L/D)_{\max}$ , wave drag is twice the friction drag.

So, both transonic and hypersonic flow cannot be described by a linear theory. These flows are inherently nonlinear regimes, even angles of attack.

### 1.6.5 Sphere Hypersonic Aerodynamics

Newtonian flow theory can be applied to estimate the hypersonic drag coefficients for a sphere. No lift is expected of course.

Consider a sphere with radius  $R$  immersed in a hypersonic flow.

The aerodynamic force  $d\vec{F}$  acting on a body region of area  $dA$  is given by (see Fig. 1.50)

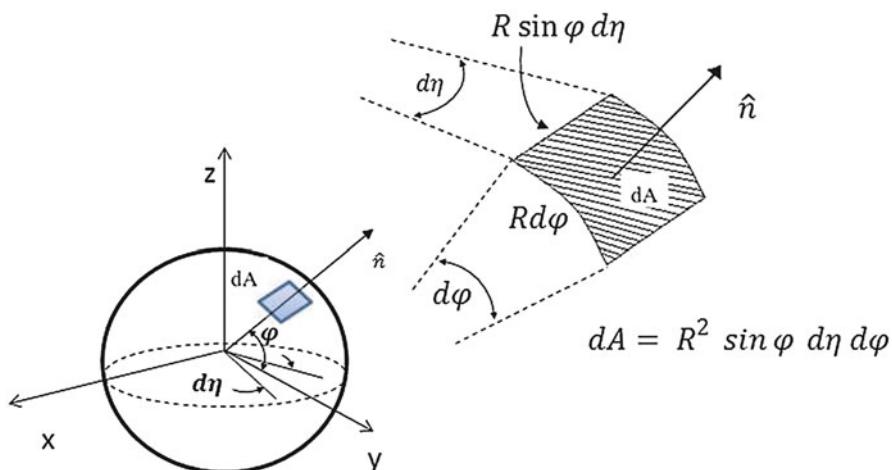


**Fig. 1.50** Infinitesimal element of a sphere

$$d\vec{F} = -q_\infty C_p dA \hat{n} \quad (1.123)$$

Hence, the aerodynamic drag due to  $dA$  is

$$dD = d\vec{F} \cdot \vec{u}_\infty \quad (1.124)$$

or

$$dD = -q_\infty C_p dA \hat{n} \cdot \vec{u}_\infty \quad (1.125)$$

Therefore, the assessment of shape drag at hypersonic velocity follows from the determination of each term in Eq. (1.125). To this end consider an infinitesimal element of the sphere of area equal to  $dA$ , shown in Fig. 1.50. This figure highlights that

$$dA = R^2 \sin \varphi \, d\eta \, d\varphi \quad (1.126)$$

For the theory of *modified Newtonian*,

$$C_p = C_{p\max} \cos^2 \varphi \quad (1.127)$$

Further, Fig. 1.51 suggests that

$$\begin{cases} \hat{n} = -\cos \varphi \hat{i} + \sin \varphi \hat{j} \\ \hat{u}_\infty = \hat{i} \end{cases} \quad (1.128)$$

Therefore,

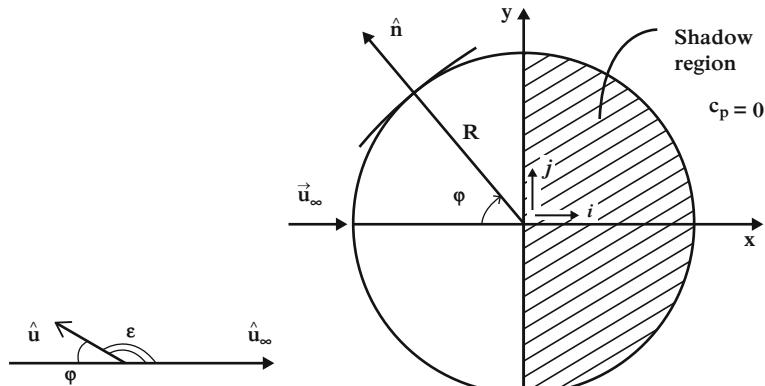


**Fig. 1.51** Section of a sphere (*cylinder*) immersed in hypersonic flow

$$\hat{n} \cdot \vec{u}_\infty = \cos \varepsilon = \cos(180 - \varphi) = -\cos \varphi \quad (1.129)$$

As a result,

$$dD = C_{P\max} \cos^3 \varphi q_\infty dA \quad (1.130)$$

Integrating this expression over the sphere surface, it follows that

$$\begin{aligned} D &= \iint_A dD = C_{P\max} q_\infty \iint_A \cos^3 \varphi dA = \\ &= 2C_{P\max} q_\infty \int_0^\pi \cos^3 \varphi \int_0^{\frac{\pi}{2}} R^2 \sin \varphi d\varphi d\eta = 2\pi R^2 C_{P\max} q_\infty \int_0^\pi \cos^3 \varphi \sin \varphi d\varphi = \\ &= -2\pi R^2 C_{P\max} q_\infty \int_0^\pi \cos^3 \varphi d\cos \varphi = -\left[ 2S_{\text{ref}} C_{P\max} q_\infty \frac{\cos^4 \varphi}{4} \right]_0^{\frac{\pi}{2}} = \\ &= \left[ S_{\text{ref}} C_{P\max} q_\infty \frac{\cos^4 \varphi}{2} \right]_0^{\frac{\pi}{2}} = \frac{S_{\text{ref}} C_{P\max} q_\infty}{2} \end{aligned}$$

Therefore,

$$C_D = \frac{D}{q_\infty S_{\text{ref}}} = \frac{C_{P\max}}{2} = \begin{cases} 1 & \text{for Newtonian theory } (C_{P\max} = 2) \\ \frac{2-\epsilon}{2} & \text{for Modified Newtonian theory} \end{cases} \quad (1.131)$$

where  $S_{\text{ref}}$  is the reference surface and that for a sphere is  $S_{\text{ref}} = \pi R^2$ .

### 1.6.6 Cylinder Hypersonic Aerodynamics

Newtonian flow theory allows addressing cylinder aerodynamics at hypersonic speed. No lift is expected, of course (i.e., because we deal with a symmetric configuration in symmetric flight).

Consider a cylinder with radius  $R$  immersed in a hypersonic flow.

The reference surface is  $S_{\text{ref}} = 2R$ .

Recalling Eq. (1.123),

$$d\vec{F} = -q_\infty C_p dA \hat{n} = -2 \frac{(\hat{u}_\infty \cdot \hat{n})^2}{(\hat{u}_\infty \cdot \hat{u}_\infty)} C_p dA \hat{n} \quad (1.132)$$

Thus,

$$dD = d\vec{F} \cdot \frac{\hat{u}_\infty}{|\hat{u}_\infty|} \quad (1.133)$$

$$q_\infty C_D S_{\text{ref}} = \iint_S - (p - p_\infty) \hat{u}_\infty \cdot d\vec{s} = 2 \int_0^{\frac{\pi}{2}} (p - p_\infty) \cos \phi R d\phi \quad (1.134)$$

$$\frac{p - p_\infty}{q_\infty} = C_p = 2 \cos^2 \phi \rightarrow p - p_\infty = 2 q_\infty \cos^2 \phi \quad (1.135)$$

Substituting into Eq. (1.134), Eq. (1.135) yields

$$q_\infty C_D S_{\text{ref}} = -2 \int_{\frac{\pi}{2}}^0 2 q_\infty \cos^3 \phi R d\phi = -4 R q_\infty \int_{\frac{\pi}{2}}^0 \cos^3 \phi d\phi \quad (1.136)$$

Thus,

$$q_\infty C_D 2 R = -4 R q_\infty \int_{\frac{\pi}{2}}^0 \cos^3 \phi d\phi \quad (1.137)$$

So,

$$\begin{aligned} C_D &= -2 \int_{\frac{\pi}{2}}^0 \cos^3 \phi d\phi = -2 \int_{\frac{\pi}{2}}^0 \cos^2 \phi \cos \phi d\phi \\ &= -2 \int_{\frac{\pi}{2}}^0 (1 - \sin^2 \phi) d\sin \phi = -2 \left[ (\sin \phi) \Big|_{\frac{\pi}{2}}^0 - \frac{1}{3} (\sin^3 \phi) \Big|_{\frac{\pi}{2}}^0 \right] \end{aligned} \quad (1.138)$$

Finally,

$$C_D = -2 \left[ -1 - \frac{1}{3} (-1) \right] = \frac{4}{3} \quad (1.139)$$

according to the Newtonian flow theory.

It is interesting to note that the above results from Newtonian theory do not explicitly depend on Mach number. Of course, they implicitly assume that  $M_\infty$  is high enough for hypersonic flow to prevail; apart from that, the precise value of  $M_\infty$  does not enter the calculations. This is compatible with the Mach number independence principle (i.e., Oswatich principle). In short this principle states that certain aerodynamic quantities become relatively independent of Mach number if  $M_\infty$  is made sufficiently large. Newtonian results are the epitome of this principle.

### 1.6.7 Sharp/Blunt Cone Aerodynamics

For a sharp cone with semivertex angle  $\theta_c$ ,

$$C_D = 2 \sin^2 \theta_c \quad (1.140)$$

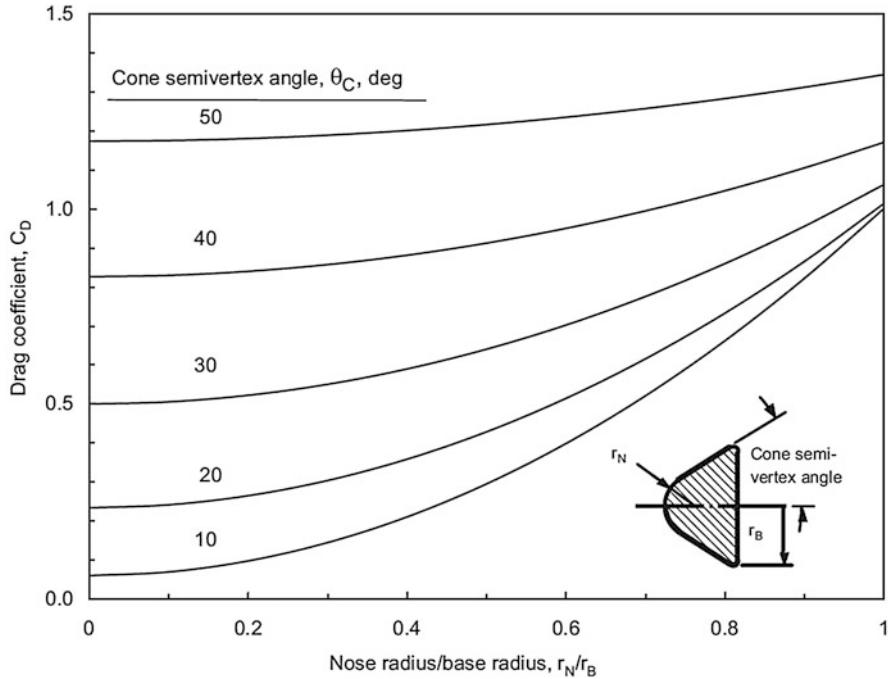


Fig. 1.52 Hypersonic drag coefficient for sphere cones

For a blunt cone with a semivertex angle  $\theta_c$ , nose radius  $R_N$ , and base radius  $R_B$ ,

$$C_D = 2\sin^2\theta_c + \left(\frac{R_N}{R_B}\right)^2 \cos^4\theta_c \quad (1.141)$$

$C_D$  is shown as a function of bluntness ratio  $R_N/R_B$  and the cone semivertex angle in Fig. 1.52 for the case of  $\gamma = 1.4$  [2, 17].

Thus, by exploiting the modified Newtonian theory, the complete zero-lift drag coefficient for blunt cone reads

$$C_D = (2 - \varepsilon) \left[ \frac{1}{2} \left( \frac{R_N}{R_B} \right)^2 (1 - \sin^4\theta_c) + \sin^2\theta_c + - \left( \frac{R_N}{R_B} \sin\theta_c \cos\theta_c \right)^2 \right] \quad (1.142)$$

Note that when  $R_N = R_B$  (and therefore  $\theta_c = 0$ ), the body is a hemisphere and Eq. (1.142) becomes

$$C_D = \frac{2 - \varepsilon}{2} \quad (1.143)$$

the same as that for a sphere, of course. When  $R_N = 0$  the body is a sharp cone and the drag coefficient reads

$$C_D = (2 - \varepsilon) \sin^2 \theta_c \quad (1.144)$$

Compare Eq. (1.144) to Eq. (1.140) recalling Eq. (1.109).

It is clear that small nose radii can be accommodated without substantial drag penalties. This is important since the heat flux at the stagnation point is inversely proportional to the square root of the nose radius. Thus thermal protection can be enhanced without much sacrifice in drag.

Finally, note that the effect of the thermodynamic state of the gas is contained solely in the initial term multiplying the square brackets in Eq. (1.142); recall that in the hypersonic limit

$$\varepsilon = \frac{\gamma - 1}{\gamma + 1} \quad (1.145)$$

Thus at higher temperature where  $\gamma < 1.4$ , the drag coefficient will be larger than the perfect gas value shown in Fig. 1.52.

### 1.6.8 Tangent-Wedge and Tangent-Cone Methods

The Newtonian theory was one of numerically simple techniques known as *impact methods*; the tangent-wedge and tangent-cone methods, presented in this section, are two others.

Let us consider first the tangent-wedge method, applicable to two-dimensional hypersonic shapes, as the one shown in Fig. 1.53 [3].

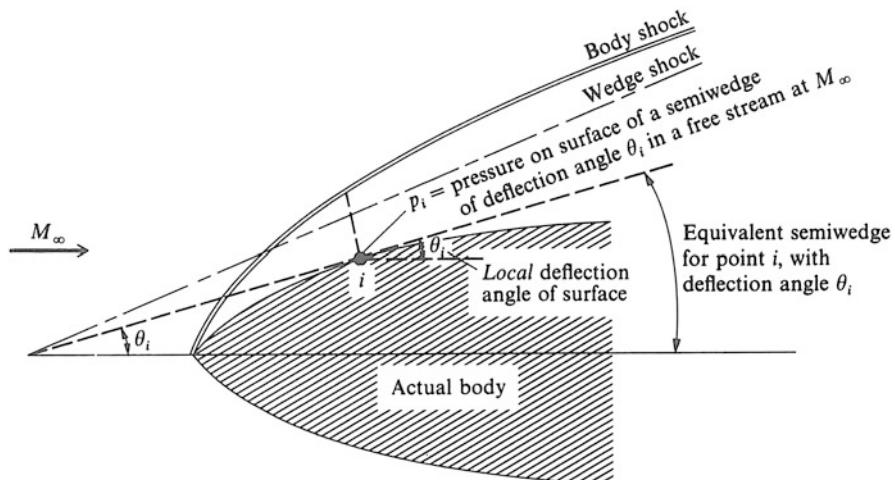


**Fig. 1.53** Illustration of the tangent-wedge method

Assume that the nose of the body is pointed and that the local surface inclination angle  $\theta$  at all points along the surface is less than the maximum deflection angle for the free-stream Mach number. In order to compute the pressure at point  $i$ , the local deflection angle  $\theta_i$  is needed, which is defined by the tangent to the surface. Extruding the tangent as a straight line, an equivalent wedge is obtained, as shown by the dashed line in Fig. 1.53.

The tangent-wedge approximation assumes that the pressure at point  $i$  is the same as the surface pressure on the equivalent wedge. In this way,  $p_i$  is obtained directly from the exact oblique shock relations for a deflection angle of  $\theta_i$  and a Mach number of  $M_\infty$ .

The tangent-cone method, valid for application to axisymmetric bodies, is analogous to the tangent-wedge method and is illustrated in Fig. 1.54 [3].

In this case tangent line can be imagined as the surface of an equivalent cone, with a semi-angle of  $\theta_i$ . The tangent-cone approximation assumes that the pressure at point  $i$  is the same as the surface pressure on the equivalent cone at a Mach number of  $M_\infty$ , that is,  $p_i$ .

Both the tangent-wedge and tangent-cone methods are very straightforward. However, they are approximate methods, not based on any theoretical basis, in contrast to the theoretical basis for Newtonian flow. Nevertheless, the tangent-wedge and tangent-cone methods frequently yield reasonable results at hypersonic speeds. An attempt to explain such good agreement with reality is hereinafter given. Referring to Fig. 1.53, let us consider the equivalent wedge and its shock wave. For the sake of clarity in Fig. 1.55, a detail of the region close to  $i$  point is shown [3].

Drawing a line normal to the surface of the wedge in  $i$ , it can be seen that the wedge shock crosses such line before the body shock does.

In the hypersonic flow across an oblique shock wave on a slender body, the  $y$  component of the flow velocity  $v$  is changed much more strongly than the  $x$

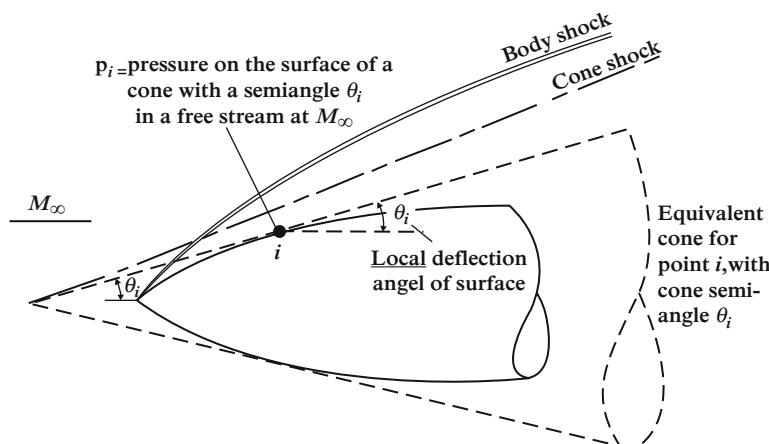
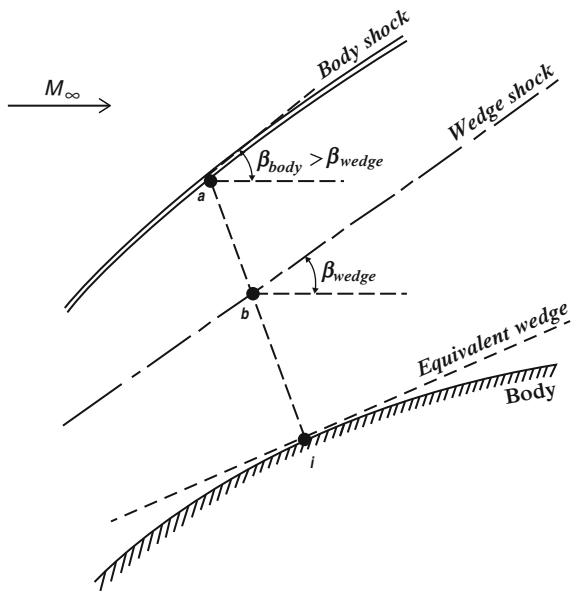


**Fig. 1.54** Illustration of the tangent-cone method

**Fig. 1.55** Segment of a hypersonic shock layer; for use in partial justification of the tangent-wedge method



component,  $u$ . Thus, with reference to the shock geometry shown in Fig. 1.56, in the limit of  $M_\infty$  it follows that [3]

$$\frac{\Delta u}{V_\infty} = \frac{V_\infty - u_2}{V_\infty} \rightarrow \frac{\gamma + 1}{2} \theta^2 \quad (1.146)$$

$$\frac{\Delta v}{V_\infty} = \frac{v_2}{V_\infty} \rightarrow \theta \quad (1.147)$$

From Eqs. (1.146) and (1.147), it is evident that the change of the  $u$  velocity is considerably smaller (order of  $\theta^2$ ) than the change of the  $v$  velocity (order of  $\theta$ ). (Keep in mind that  $\theta$  is a small angle in radians.) As from Euler's equation  $dp = -\rho V dV$ , the previous result implies that the major pressure gradients are normal to the flow. Referring to Fig. 1.55, the principal change in pressure is therefore along the normal line  $ia$ , while changes in the flow direction are second order. Hence, the surface pressure on the body at point  $i$  is dominated by the pressure behind the shock at point  $a$ . Due to the centrifugal force effects, the pressure at point  $i$ ,  $p_i$ , will be less than  $p_a$ . Now, in the tangent-wedge method,  $p_i = p_b$ , where  $p_b$  is the pressure behind the imaginary wedge shock (at point  $b$  in Fig. 1.55). The pressure  $p_b$  is less than  $p_a$  because the imaginary wedge shock angle at point  $b$  is little than the actual body-shock angle at point  $a$  ( $\beta_{body} > \beta_{wedge}$ ). So, the wedge pressure  $p_a$  is a reasonable approximation for the surface pressure  $p_i$  because in the real case the higher pressure  $p_a$  behind the body shock is mitigated by centrifugal effects as approaching the point  $i$ . The same reasoning holds for the tangent-cone method.

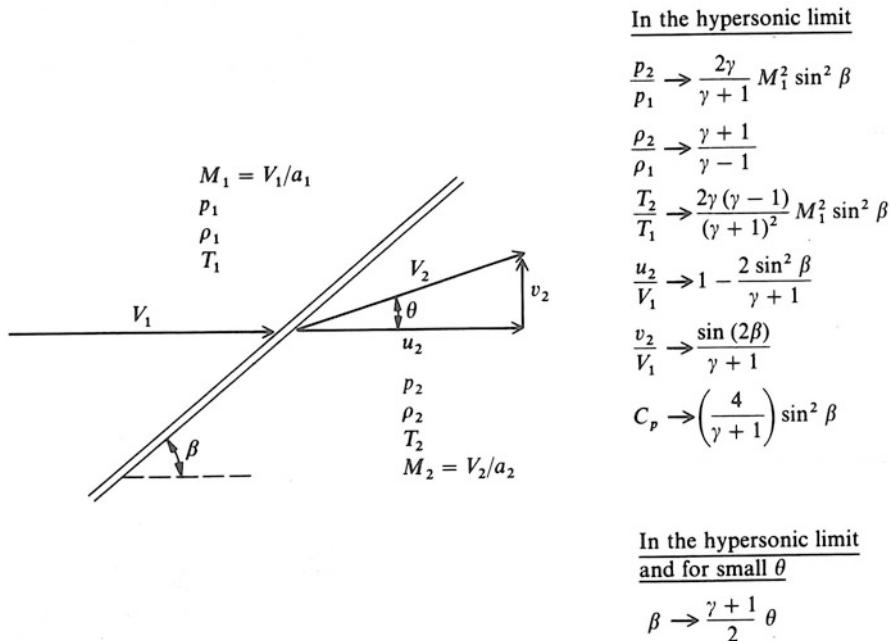


Fig. 1.56 Oblique shock-wave geometry

Results obtained with the tangent-cone method applied to a pointed ogive are shown in Fig. 1.57 [3]. Here, the surface pressure distribution is plotted vs. distance along the ogive. Four sets of results are presented, each for a different value of the parameter defined as the hypersonic similarity parameter  $K = M_\infty (d/l)$ , where  $d/l$  is the slenderness ratio of the ogive. The solid line is an exact result obtained from the rotational method of characteristics, and the dashed line is the tangent-cone result.

It can be seen that very reasonable agreement is obtained, thus confirming the usefulness of the tangent-cone method, albeit its rather weak basis. The same type of agreement is typical of the tangent-wedge method [3].

### 1.6.9 Flat Plate Theory and Spacecraft Hypersonic Aerodynamic Characteristics

Although an infinitely thin plate, by itself, is not a practical aerodynamic configuration, its aerodynamic behavior at hypersonic speeds is consistent with some of the basic characteristics of other typical hypersonic shapes. In other word, flat plate aerodynamics, based on Newtonian flow theory, allows for assessing the aerodynamic characteristics of space vehicles during their flight at hypersonic speed.

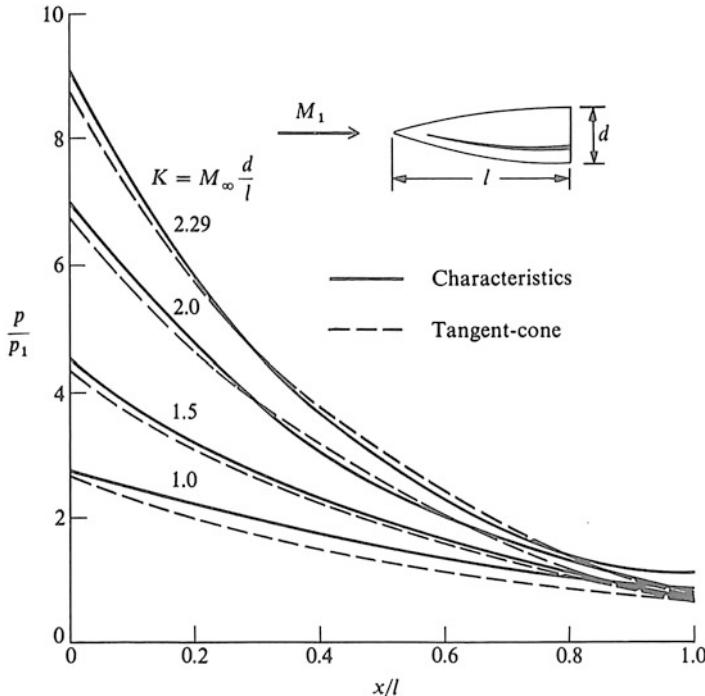


**Fig. 1.57** Surface pressure distributions for ogives of different slenderness ratio  $d/l$

To this end let us consider Eq. (1.121):

$$C_D = 2\sin^3\alpha$$

This equation refers only to the losses due to the shock wave and not from friction too. The full expression of the drag coefficient reads, as stated before,

$$C_D = C_{D_0} + 2\sin^3\alpha$$

where  $C_{D_0}$  is calculated considering experimental date available for the vehicle. For instance, the maximum aerodynamic ratio  $(\frac{L}{D})_{\max}$  is given at small angle of attack (i.e.,  $0^\circ \leq \alpha \leq 20^\circ$ ). For this reason (i.e.,  $\alpha$  small), it can be assumed that

$$\begin{cases} \sin \alpha \cong \alpha \\ \cos \alpha \cong 1 \end{cases}$$

With this assumption Eqs. (1.120) and (1.121) become

$$\begin{aligned} C_L &= 2\alpha^2 \\ C_D &= C_{D_0} + 2\alpha^3 \end{aligned}$$

So, the problem becomes to assess  $C_{D_0}$ . To this end, let us consider that at the maximum aerodynamic ratio, it is known that

$$\frac{d}{d\alpha} \left( \frac{C_L}{C_D} \right) = 0 \rightarrow \frac{d}{d\alpha} \left( \frac{2\alpha^2}{C_{D_0} + 2\alpha^3} \right) = 0$$

which means

$$\alpha = \sqrt[3]{C_{D_0}}$$

and, hence, the maximum aerodynamic ratio reads

$$\left( \frac{C_L}{C_D} \right)_{\max} = \frac{2}{3} \frac{1}{\sqrt[3]{C_{D_0}}}$$

from which one is able to determine  $C_{D_0}$  once the maximum lift to drag is known.

The theory so far described can be appropriately modified to take into consideration that wing span of spacecraft is not constant but rises.

A way to model a wing span is through straight line approach. In this way the planform shape of generic spacecraft can be described by means of small number of lines. In this framework let us asses Space Shuttle and X-34 aerodynamic at hypersonic speed.

### 1.6.9.1 The Space Shuttle Aerodynamics

The top view of the Space Shuttle Orbiter is shown in Fig. 1.58. Due to the symmetry of the shape, only half of the geometry can be considered, as shown in Fig. 1.58b. In this figure Orbiter's half geometry has been modeled with straight lines, where  $(x_1, y_1) = (0; 0)$ ;  $(x_2, y_2) = (19.67; 4.64)$ ;  $(x_3, y_3) = (26.26; 11.2)$ ;  $(x_4, y_4) = (31.18; 11.2)$ ;  $(x_5, y_5) = (32.82; 0)$ .

The mathematical equation of the line between two generic points is

$$y - y_i = \frac{y_{i+1} - y_i}{x_{i+1} - x_i} (x - x_i)$$

Therefore, the normal force coefficient  $C_N$  is given by

$$C_N = \frac{2}{S_{\text{ref}}} \int_0^c (C_{p,l} - C_{p,u}) y \, dx$$

where  $C_{p,u} = 0$  and  $C_{p,l} = 2\sin^2\alpha$  according to the Newtonian flow theory.

As a result,

$$C_N = \frac{1}{S_{\text{ref}}} \int_0^c (2\sin^2\alpha) y \, dx = \frac{674.22}{S_{\text{ref}}} \sin^2\alpha$$

where for the Orbiter  $S_{\text{ref}} = 250 \text{ m}^2$ .

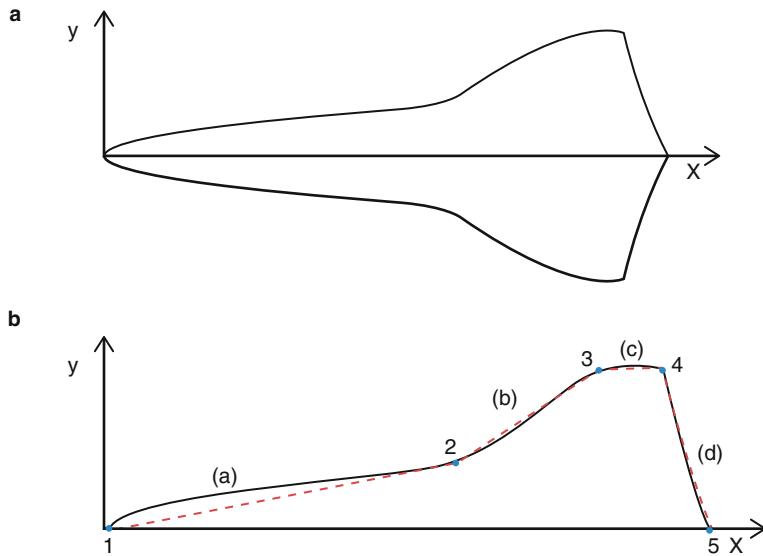


**Fig. 1.58** Planform shape of Space Shuttle Orbiter (a). Half geometry modeled with *straight lines* (b)

So

$$C_N = 2.7 \sin^2\alpha$$

and, then,

$$\begin{aligned} C_L &= k \sin^2\alpha \cos\alpha \\ C_D &= C_{D_0} + k \sin^3\alpha \end{aligned}$$

where  $k = 2.7$ .

With the hypothesis of a small angle of attack (AoA), we have

$$\begin{aligned} C_L &= k\alpha^2 \\ C_D &= C_{D_0} + k\alpha^3 \end{aligned}$$

So that by searching for the AoA which maximizes the lift-to-drag ratio, it follows that

$$\alpha = \sqrt[3]{\frac{2}{k} C_{D_0}}$$

The maximum aerodynamic ratio for the Space Shuttle Orbiter is equal to 1.9. Therefore,

$$C_{D_0} = \frac{\sqrt[3]{4k}}{3\left(\frac{L}{D}\right)_{\max}} = 0.057$$

and one can conclude that for the Orbiter

$$\begin{cases} C_L = 2.7 \sin^2 \alpha \cos \alpha \\ C_D = 0.057 + 2.7 \sin^3 \alpha \end{cases}$$

The comparison with the Orbiter experimental aerodynamic is provided in Fig. 1.59. As one can see, flat plate aerodynamic results compare rather well to experimental data.

### 1.6.9.2 X-34 Launch Vehicle Aerodynamics

The top view and straight lines half geometry model of the X-34 vehicle are shown in Fig. 1.60.

The point coordinates are

$$\begin{aligned} (x_1, y_1) &= (0; 0); & (x_3, y_3) &= (5.72; 1.05); & (x_2, y_2) &= (2.92; 1.05); \\ (x_4, y_4) &= (9.25; 1.85) \end{aligned}$$

So that

$$C_N = \frac{116.13}{S_{\text{ref}}} \sin^2 \alpha$$

where  $S_{\text{ref}} = 33.21 \text{ m}^2$ .

So,

$$C_N = 3.49 \sin^2 \alpha$$

Hence,

$$\begin{cases} C_L = k \sin^2 \alpha \cos \alpha \\ C_D = C_{D_0} + k \sin^3 \alpha \end{cases}$$

where  $k = 3.49$ . Taking into account that for the X-34 vehicle the maximum aerodynamic ratio is equal to 2.237, it yields that

$$\begin{cases} C_L = 3.49 \sin^2 \alpha \cos \alpha \\ C_D = 0.046 + 3.49k \sin^3 \alpha \end{cases}$$

The comparison with X-34 aerodynamic is provided in Fig. 1.61.

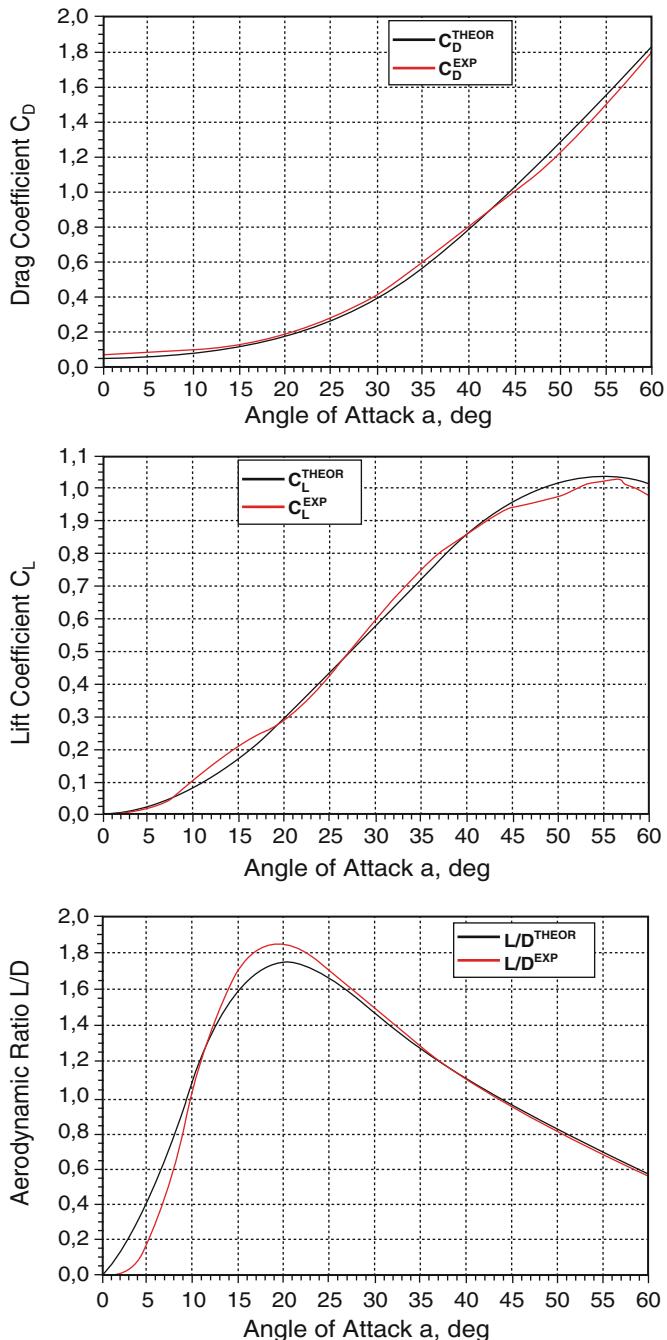


**Fig. 1.59** Aerodynamic drag, lift, and lift-to-drag coefficients of Space Shuttle

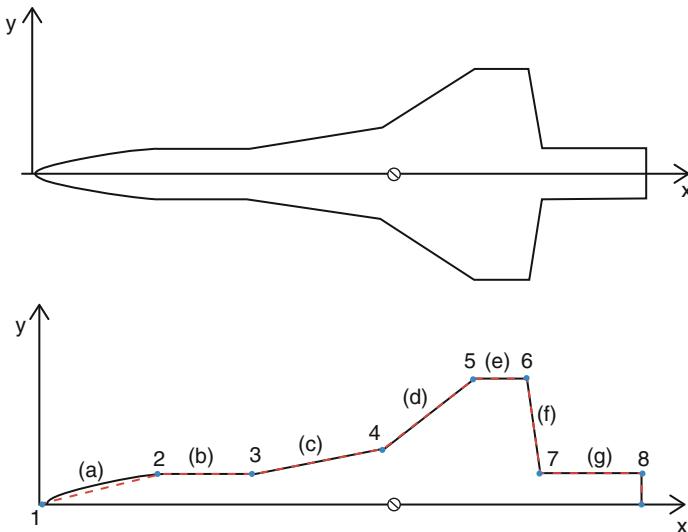


**Fig. 1.60** Planform shape of X-34 and straight lines half geometry model

As one can see, results compare rather well to experimental data available for X-34.

### 1.6.10 Panels Method Aerodynamics

The Newtonian theory, being based on the idea that the shock layer is so thin that the shock practically coincides with the body surface, is locally applicable to every surface point on a smooth body. As a result, a body surface may be subdivided into a number of individual panels, and each one may be treated separately to determine the pressure force acting there, as shown in Fig. 1.62. The total force and moment structure on the whole vehicle surface may then be obtained by summing the contributions of each element of the body surface.

A general element of the body surface is shown in Fig. 1.63.

The station  $i$  denotes a plane normal to the  $x$ -axis of the flight vehicle while station  $i + 1$  denotes the next axial station along the  $x$ -axis (see Fig. 1.62). Rays  $j$  and  $j + 1$  denote longitudinal lines along with the body surface defining the shape of the vehicle. In this coordinate system,  $x$  is measured along the axis of the vehicle generally originating at the nose tip ( $x = 0$ ). The  $x-z$  plane is taken as the symmetry plane of the vehicle with  $z$  measured positive vertically and  $y$  measured positive outboard along the right (starboard) side of the vehicle.

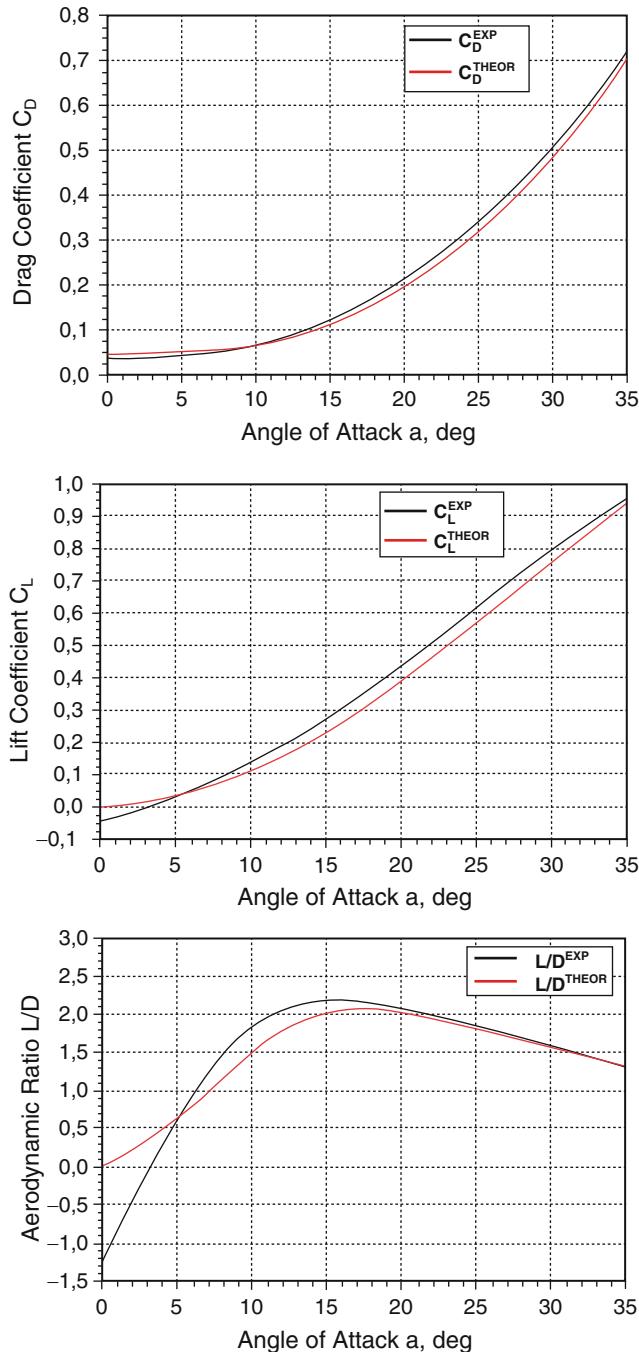


**Fig. 1.61** Aerodynamic drag, lift, and lift-to-drag coefficients of X-34

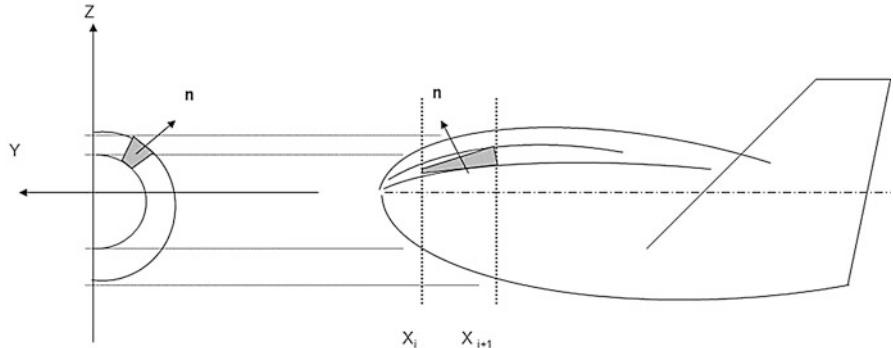


**Fig. 1.62** General illustration of a typical surface element on a flight vehicle

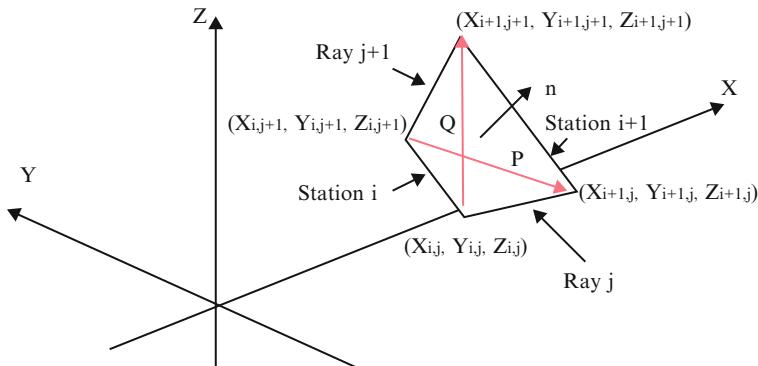


**Fig. 1.63** A general quadrilateral body surface element showing the unit normal vector along with the locations of the four corner points

Recalling Eq. (1.106) the pressure coefficient for each panel reads

$$C_p = \begin{cases} (2 - \varepsilon) \frac{(\vec{V}_\infty \cdot \vec{n})^2}{\vec{V}_\infty \cdot \vec{V}_\infty} & \vec{V}_\infty \cdot \vec{n} < 0 \\ 0 & \vec{V}_\infty \cdot \vec{n} \geq 0 \end{cases} \quad (1.148)$$

Therefore, the pressure distribution on the vehicle surface can be easily evaluated once the unit normal is known.

To this end, Fig. 1.63 suggests that the outward normal vector  $\mathbf{n}$  may be found by forming the cross-product between the vectors  $\mathbf{P}$  and  $\mathbf{Q}$  such that the normal points outward as shown. Thus,

$$\hat{\mathbf{N}} = \vec{\mathbf{P}} \times \vec{\mathbf{Q}} = \left[ (x_{i+1,j} - x_{i,j+1}) \hat{i} + (y_{i+1,j} - y_{i,j+1}) \hat{j} + (z_{i+1,j} - z_{i,j+1}) \hat{k} \right] x \\ x \left[ (x_{i+1,j+1} - x_{i,j}) \hat{i} + (y_{i+1,j+1} - y_{i,j}) \hat{j} + (z_{i+1,j+1} - z_{i,j}) \hat{k} \right] \quad (1.149)$$

Then the normal becomes

$$\widehat{N} = [(y_{i+1,j} - y_{i,j+1})(z_{i+1,j+1} - z_{i,j}) - (y_{i+1,j+1} - y_{i,j})(z_{i+1,j} - z_{i,j+1})]\widehat{i} + [(x_{i+1,j+1} - x_{i,j})(z_{i+1,j} - z_{i,j+1}) - (x_{i+1,j} - x_{i,j+1})(z_{i+1,j+1} - z_{i,j})]\widehat{j} + [(x_{i+1,j} - x_{i,j+1})(y_{i+1,j+1} - y_{i,j}) - (x_{i+1,j+1} - x_{i,j})(y_{i+1,j} - y_{i,j+1})]\widehat{k} \quad (1.150)$$

The unit normal may be obtained by dividing the normal by its magnitude as follows:

$$\widehat{n} = \frac{\vec{N}}{\sqrt{\vec{N} \cdot \vec{N}}} \quad (1.151)$$

The area of the element may be found by

$$A = \frac{1}{2} \left| \vec{P} \times \vec{Q} \right| = \frac{1}{2} \left| \vec{N} \right| \quad (1.152)$$

With this in mind for each surface panel, we have

$$d\vec{F} = \bar{V} C_p q_\infty A \widehat{n} = \bar{V} (2 - \varepsilon) \frac{\left( \vec{V}_\infty \cdot \widehat{n} \right)^2}{\vec{V}_\infty \cdot \vec{V}_\infty} q_\infty A \widehat{n} \quad (1.153)$$

where  $\varepsilon = (\gamma - 1)/(\gamma + 1) = 0.16$  for  $\gamma = 1.4$ . Then, defining the angle of attack  $\alpha$  as the angle between the velocity vector and the i-direction, which defines the  $x$ -axis, we can determine the lift and drag increments acting on the surface element from the following relations:

$$dD = d\vec{F} \cdot \frac{\vec{V}_\infty}{|\vec{V}_\infty|} \quad (1.154)$$

$$dL = \sqrt{d\vec{F} \cdot d\vec{F} - (dD)^2}$$

The differential moment about a reference point, say the origin, due to the differential force on a particular body surface element is given by

$$d\vec{M}_0 = \vec{r} \times d\vec{F} = [(x - x_0)\widehat{i} + (y - y_0)\widehat{j} + (z - z_0)\widehat{k}] \times d\vec{F} \quad (1.155)$$

In this expression the radius vector is measured from the reference point to the centroid of the surface element. The components of the moment about the  $x$ ,  $y$ , and

$z$  axes are defined as the rolling, pitching, and yawing moments of the vehicle, that is,  $l$ ,  $m$ , and  $n$ , respectively. Thus,

$$d\vec{M}_0 = dl\hat{i} + dm\hat{j} + dn\hat{k} \quad (1.156)$$

Summing up the contributions of all the panels provides the complete force and moment description of the vehicle for the flight condition chosen.

One may develop information like spacecraft drag polar and associated moment variations by rotating the vehicle through a number of angles of attack at a particular Mach number and altitude (i.e., vehicle aerodynamic database, AEDB).

The preceding analysis considered forces and moments arising from normal stresses alone (i.e., pressure contribution alone that determines the inviscid AEDB). However, the tangential stresses due to friction (and the corresponding resultant heating) must also be accounted for in the aerodynamic design of an atmospheric entry vehicle. The geometric layout of the body surface panels, the determination of the pressure on each element, and the determination of the velocity component normal to the body surface panels may all be used in an approximate analysis of the skin friction (and heating loads) experienced by the vehicle during the hypersonic portion of the entry descent. The major parameter that forms the basis of the analysis is the Reynolds number based on the local tangential velocity, temperature, and distance from the stagnation point, that is,

$$Re_x = \frac{\rho_e u_e x}{\mu_e} \quad (1.157)$$

The variable  $x$  denotes the distance along the surface of the vehicle measured from the relevant stagnation point (for a body) or stagnation line (for a wing), while  $u$  denotes the tangential component of the free-stream velocity. The subscript  $e$  is introduced to indicate that these are conditions that are experienced at the outer edge of the boundary layer.

In order to evaluate the density and viscosity, the pressure and temperature are required. The pressure on the panel is obtained from the pressure coefficient. The tangential component of velocity on the panel, that is, the inviscid value, may be obtained from the preceding Newtonian analysis and is given by

$$\vec{u} = \vec{V}_\infty - \left( \vec{V}_\infty \cdot \hat{n} \right) \hat{n} \quad (1.158)$$

Similarly, as shown by Rasmussen, one may use the known pressure coefficient to derive the inviscid surface Mach number on the surface, or more accurately, at the outer edge of the viscous boundary layer, as follows [11]:

$$M_e^2 = \frac{2}{\gamma - 1} \left[ \left( \frac{1 + \gamma M_\infty^2}{1 + \frac{\gamma}{2} c_p M_\infty^2} \right)^{\frac{\gamma-1}{\gamma}} - 1 \right] \quad (1.159)$$

The temperature at the edge of the boundary layer may be found by first considering the inviscid adiabatic energy equation on the body streamline as given by

$$h_\infty + \frac{1}{2}V_\infty^2 = h_e + \frac{1}{2}u_e^2 \quad (1.160)$$

The implicit assumption in this equation is that the kinetic energy carried by the normal component of velocity is transformed into thermal energy, just as the normal component of momentum is converted to an increase in pressure in the basic Newtonian flow approximation. In order to find the temperature  $T_e$  from the enthalpy  $h_e$ , it is necessary to use tables or models for the thermodynamic properties of high-temperature air.

As far as skin friction for both laminar and turbulent cases is concerned, the slender, planar body (the panel), being characterized by a constant pressure, allows to use the flat plate Eckert's reference temperature method and Reynolds' analogy approximation. This approach is indeed a suitable method within preliminary design phase.

Reynolds analogy gives for the local skin friction coefficient as

$$C_f(x) = \frac{2Nu_x}{\sqrt[3]{Pr}Re_x} = \frac{2A}{\sqrt[3]{Pr}} \left( \frac{\rho^*}{\rho_e} \right)^a \left( \frac{\mu^*}{\mu_e} \right)^b Re_x^{c-1} \sqrt{3^j} \quad (1.161)$$

since the Nusselt number is given by

$$Nu_x = A \left( \frac{\rho^*}{\rho_e} \right)^a \left( \frac{\mu^*}{\mu_e} \right)^b Re_x^c \sqrt{3^j} \quad (1.162)$$

and  $\rho^*$  and  $\mu^*$  depend on reference temperature  $T^*$ , i.e.,  $\rho^* = \rho(T^*)$  and  $\mu^* = \mu(T^*)$ .

All the coefficients are explained in the following table (Table 1.2).

For the estimations of both density and viscosity ratios, let us consider that the boundary layer has constant pressure across it (Prandtl's condition) so that

$$\frac{\rho^*}{\rho_e} = \frac{T_e z^*}{T^* z_e} \quad (1.163)$$

**Table 1.2** Coefficients for Nusselt evaluation; see Eq. (1.162)

Type of flow	A	a	b	c	j
Laminar	$0.332 Pr^{1/3}$	0.5	0.5	0.5	—
Turbulent	$0.0296 Pr^{1/3}$	0.8	0.2	0.8	—
Flat plate	—	—	—	—	0
Axisymmetric	—	—	—	—	1

where  $z$  is the compressibility factor to account for real gas effects, whereas fitting data for the viscosity yields<sup>19</sup>

$$\frac{\mu^*}{\mu_e} = \left( \frac{T^*}{T_e} \right)^{\frac{2}{3}} \quad (1.164)$$

Therefore,

$$\left( \frac{\rho^*}{\rho_e} \right)^a \left( \frac{\mu^*}{\mu_e} \right)^b = \left( \frac{z^*}{z_e} \right)^a \left( \frac{T^*}{T_e} \right)^{\frac{2}{3}b-a} \quad (1.165)$$

In the case of constant pressure flow over an adiabatic wall<sup>20</sup>, the skin friction coefficient integrated over a specific length of surface  $x$  is given for laminar flow and for turbulent flow as follows:

$$C_{f,\text{laminar}} = 1.328 \left[ 1 - 0.72 \Pr^{1/2} \left( \frac{\gamma_e - 1}{2} \right) M_e^2 \right]^{-0.1835} \sqrt{3^j} Re_c^{-1/2} \quad (1.166)$$

$$C_{f,\text{turbulent}} = 0.0592 \left[ 1 - 0.72 \Pr^{1/3} \left( \frac{\gamma_e - 1}{2} \right) M_e^2 \right]^{-0.6734} \sqrt{3^j} Re_c^{-1/5}$$

### 1.6.11 Surface Inclination Methods and Aeroshape

#### Aerodynamic Design: The Pressure Methods Selection Rationale

Surface impact methods (SIM), such as Newtonian and modified Newtonian flow theories, tangent wedge, and tangent cone shown so far, allow determining the pressure distribution over a complex three-dimensional body in hypersonic flow.

Those methods are simple relationships capable of modeling the inherently nonlinear hypersonic flow. SIM allow rapid estimation of pressure distribution over hypersonic bodies, defined solely in terms of the local surface inclination angle. Although simple techniques, they are useful for hypersonic aerodynamic analysis in the framework of preliminary (conceptual) design phase, primarily due to the speed of computations which characterizes such methods. When a detailed accurate knowledge of the flowfield past the hypersonic vehicle is required, the more sophisticated CFD technique must be used, but at the computational cost that may be three or four orders of magnitude larger than the cost of running a Newtonian analysis.

---

<sup>19</sup>The considered range of temperature and pressure is  $300 \text{ K} < T < 3,000 \text{ K}$  and  $10^{-4} \text{ atm} < P < 10^2 \text{ atm}$ .

<sup>20</sup>This case is perhaps the most conservative one for cruising flight since it presupposes no active cooling.

Thus, Computational fluid dynamics, while providing the most detailed aerodynamic phenomena, is often left for detailing special problem in practical design.

But this technique is cost and time demanding. Therefore, less expensive aerodynamic design analysis as low-order surface impact method is welcome.

Being computationally inexpensive, SIM are suitable for inclusion in a design loop, based on computational methods. This is especially amazing in the framework of aerodynamic design of hypersonic vehicle, for which ground-based testing is limited in size, performance, and cost. Indeed, there are large ranges of computational technique used for aerodynamic design and analysis, with the desired technique generally set by design, analysis, and cost requirements. For example, stability and control studies for systems whose behavior are not well understood will generally require numerous aerodynamic performance estimates around the nominal design especially within a multidisciplinary design optimization (MDO). Indeed, vehicle design is a root-solving optimization process in which a system with optimal characteristics is constructed within the constraints of the problem. So, to perform this root-solving process, disciplinary models or contributing analyses, such as vehicle aerodynamics, are generally connected into a large iterative design process often illustrated using a design structure matrix (DSM), as shown in Fig. 1.64.

The DSM maps the interaction of various contributing analyses and provides a final framework for the MDO of hypersonic vehicles. Therefore, to support this design environment, efficient contributing analysis tools, as SIM, are mandatory. As a consequence, compromises in computational techniques are required, leading to simplified models of the system.

As far as the implementation of SIM is concerned, the vehicle surface must be defined by a system of several planar panels (i.e., panel mesh), where each individual

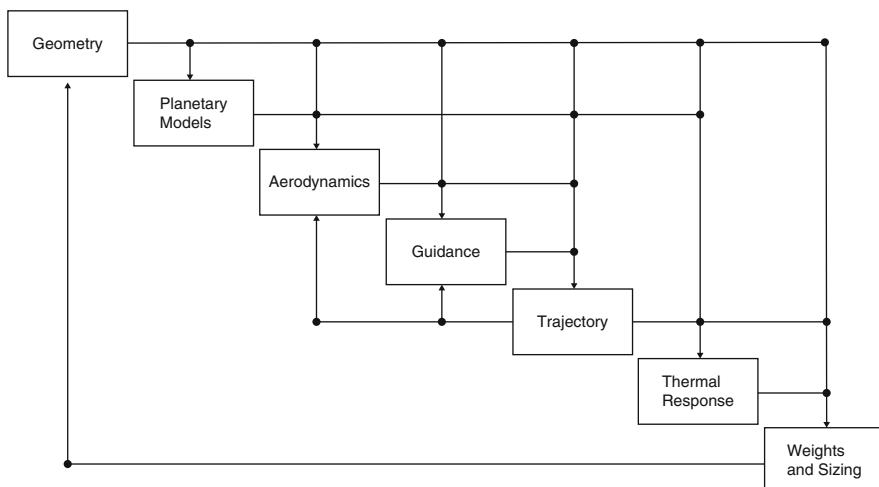


**Fig. 1.64** Design Structure Matrix (DSM) for planetary entry vehicle

element can be analyzed independently as either an impact or shadow flow regime to provide a complete vehicle pressure distribution.

From this pressure aerodynamic forces and moments can be integrated. The only geometric parameter required to obtain the surface pressure from Newtonian theory is the angle the free-stream impact with the mesh element.

To compute aerodynamic forces and moments, the element areas and centroids are also used.

The surface pressure over an impact region is calculated by using the local surface inclination relative to the free-stream. Shadow flow regions are processed as having pressure coefficient equal to zero, equating the surface pressure to the free-stream pressure.

Anyway the methods to be used in calculating the pressure in impact and shadow regions may be specified independently and can be selected by the user; several methods are available (see Table 1.3), some of which previously analyzed [12].

Newtonian, modified Newtonian, tangent-wedge, and tangent-cone methods allow the design of vehicle aeroshape in a relatively simple way.

However, it is not possible to state with any certainty which of the above methods is the best for a given application. All of these methods have their pros and cons, and some intuitive logic is required to select one over the others for a given problem. For example, Fig. 1.65 suggests that in the prediction of the pressure distribution over a typical hypersonic airplane, any distinguishable portions of the fuselage might be treated with the tangent-cone method, whereas the wings might be better treated with the tangent-wedge method.

So, the generic vehicle configuration can be divided into a combination of simple shapes, i.e., cones, cylinders, flat plates, spheres, and wedges, for which

**Table 1.3** Available methods for inviscid analysis

Impact flow	Shadow flow
Modified Newtonian	Newtonian
Modified Newtonian + Prandtl–Mayer	Modified Newtonian + Prandtl–Meyer
Tangent wedge (oblique shock)	Prandtl–Meyer expansion
Tangent-wedge empirical	Inclined cone
Tangent cone	Van Dyke Unified
Inclined cone	$C_p = -1/M_\infty^2$
Van Dyke Unified	Shock expansion (Strip Theory)
Blunt body shear force	Input pressure coefficient
Shock expansion (Strip Theory)	Free molecular flow
Free molecular flow	Dahlem–Buch empirical
Input pressure coefficient	ACM empirical
Hankey flat-surface empirical	
Delta Wing empirical	
Dahlem–Buck empirical	
Blast-wave pressure increments	

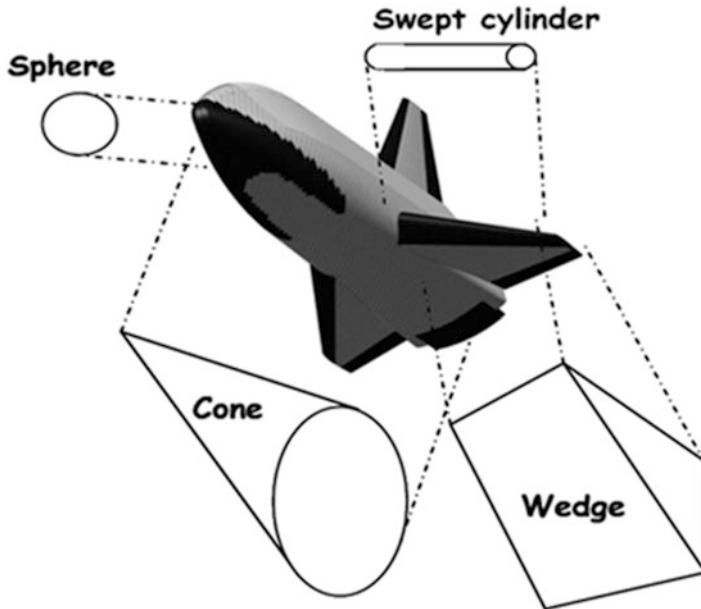


**Fig. 1.65** Design methodology. Representative flow models for a typical hypersonic airplane

analytical solutions are also available. Instead, for surfaces with high inclination angles (greater than the maximum deflection angle for an oblique shock wave at the given  $M_\infty$ ), the Newtonian method is appropriate. Within the boundaries where the Newtonian method holds, for blunt surfaces, modified Newtonian,  $C_p = C_{p\max} \sin^2 \theta$ , is best, whereas classic Newtonian,  $C_p = 2 \sin^2 \theta$ , usually yields better results for slender bodies.

Therefore, the designer must decide which SIM methods are most applicable for a particular configuration and flight regime.

Anyway, a pressure method selection rationale was developed during this study which enables the designer to predict aerodynamic forces and moments with sufficient accuracy for preliminary design of advanced cruise and maneuvering vehicles. Results of work performed during the Aerodynamic Configured Missile (ACM) study indicated that increased aerodynamic prediction accuracy could be realized by separating configurations into three basic parts: nose, body, and aerodynamic surfaces [13, 14]. The dividing line between the nose and body is the point of maximum diameter. Further, it was found that methods yielding lower-pressure predictions were required on the body where three-dimensional flow effects predominate. The tangent-cone method was used for windward body surfaces to accurately predict these flow phenomena. The leeward side pressure measurements on the noncircular and lifting bodies indicated that a new method was needed for negative impact angles. The new method developed was based on experimental data and named ACM empirical. The pressure predictions on the bodies became more

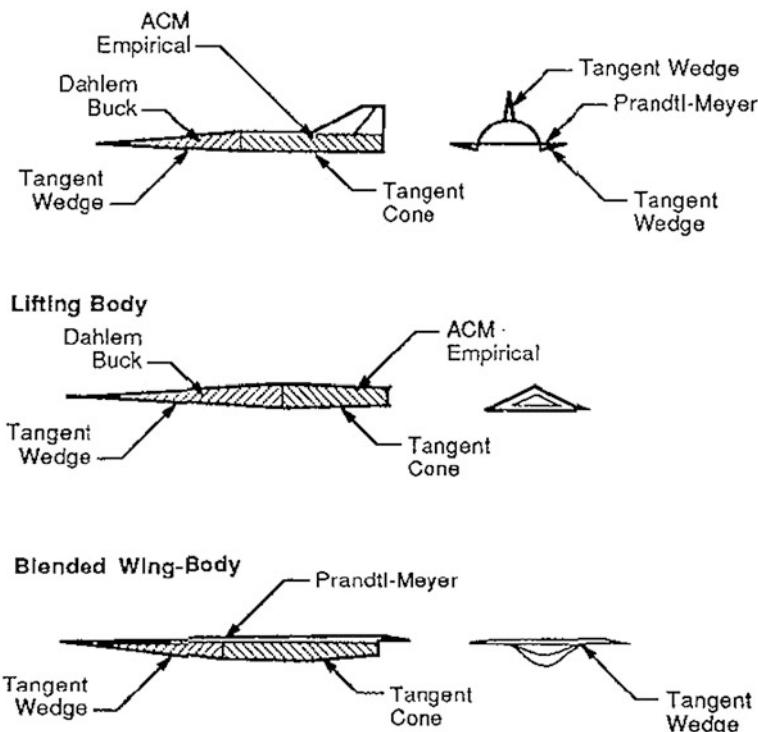


**Fig. 1.66** Pressure methods applied to aero configured missiles

consistent with measured values by using a combination of tangent-cone and ACM empirical. The ACM pressure method rationale is shown in Fig. 1.66 [13].

Tangent wedge was used on the flat undersides of noses to simulate the nearly two-dimensional flow properties. Tangent wedge was also used on the nose of the blended wing-body to simulate carryover lift from the wing, while the Dahlem-Buck method (windward and leeward) was used on circular portions of noses. Tangent wedge was used on the windward side of tails and Prandtl-Meyer on the leeward side, to produce sufficiently high pressures to account for body carryover effects.

The method selection rationale developed during the ACM study was reevaluated for application to more conventional missile configurations. A typical supersonic missile is shown in Fig. 1.67, with the reevaluated method selection rationale [14].

Dahlem-Buck was used on both the windward and leeward surfaces of ogive noses. If the body cross sections were not circular, tangent cone was used on windward surfaces and ACM empirical leeward. Inclined cone was used on windward surfaces of circular bodies, and ACM empirical was again applied to leeward surfaces. Tangent wedge was used on fins not shielded by body parts and tangent cone for those that were shielded. The methods described above formed the basis

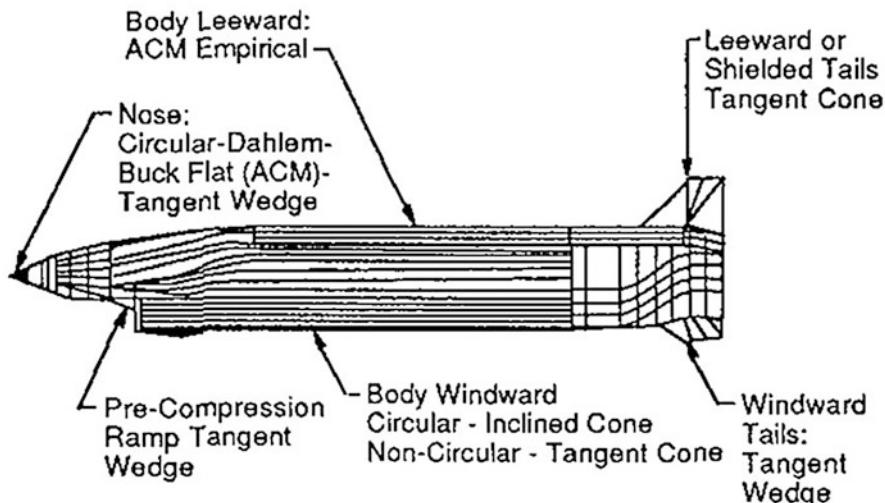


Fig. 1.67 Rational for selection of pressure methods

for the aerodynamic prediction rationale used to study the missile configuration. The flight region of primary interest during the ACM study was high supersonic, Mach 3–5. This rationale was extended to the hypersonic region for this study effort.

For example, Moore and Williams provided a solution rationale for the different vehicle parts as nose, body, and aerodynamic surface [14]. For high hypersonic speeds ( $M_\infty > 8$ ), modified Newtonian is suggested for all impact surfaces, while for all leeward vehicle surfaces, Prandtl–Mayer expansion is appropriate.

Moore and Williams also noted in their work that there was no significant improvement in prediction accuracy by applying a real gas approximation through the use of an effective  $\gamma$  [see Eq. (1.110)]. There was also little change in the overall vehicle pressure distribution when viscous methods were applied, viscous considerations being more critical for estimating vehicle drag.

The prediction of lateral–directional aerodynamic may not be as accurate using the same selection rationale as that for the longitudinal aerodynamics.

Further, in Maughmer et al., three hypersonic configurations were considered: the North American X-15, the hypersonic research airplane (scramjet powered), and the Space Shuttle Orbiter (see Figs. 1.68, 1.69, and 1.70, respectively) [13].

Comparisons were made with both experimental and flight test data, with each vehicle assigned analysis methods in relation to nose, body, and aerodynamic lifting surface. Modified Newtonian was used on all blunt surfaces such as leading and trailing edges. The other methods which dominated the inviscid portion were tangent wedge, tangent cone, and Prandtl–Meyer (shadow regions).

It was concluded that all the longitudinal performance derivatives were of some use at the conceptual design stage. Regions which encounter flow separation required careful consideration. The primary control derivatives for the

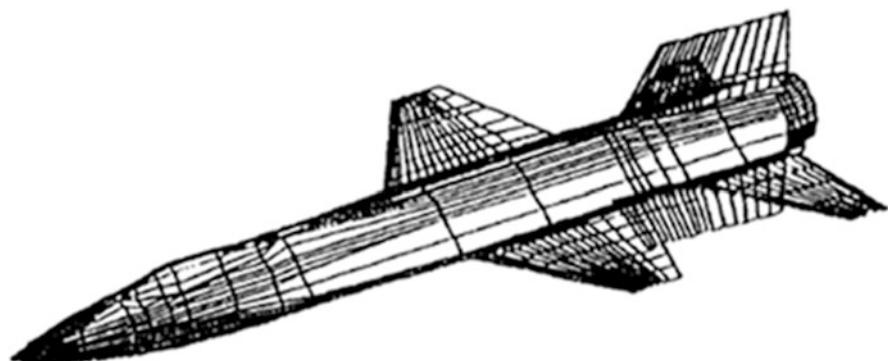


Fig. 1.68 North American X-15 configuration

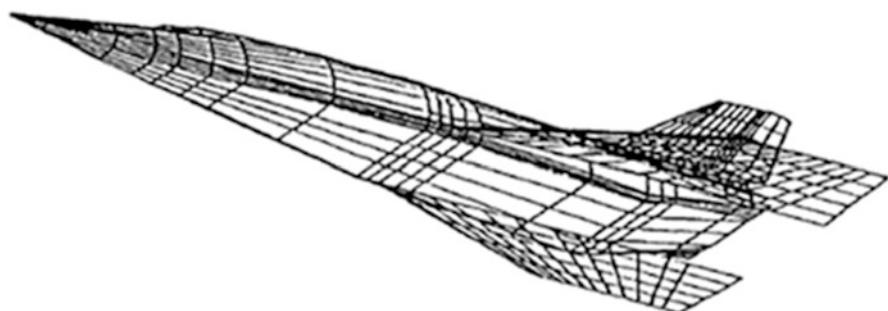


Fig. 1.69 Hypersonic research airplane configuration

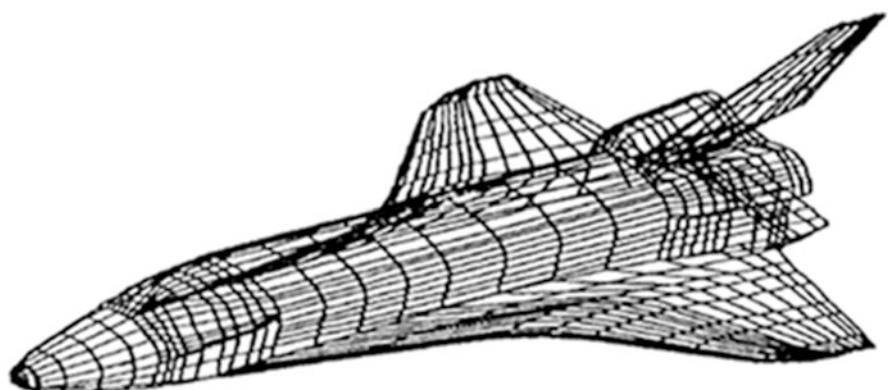
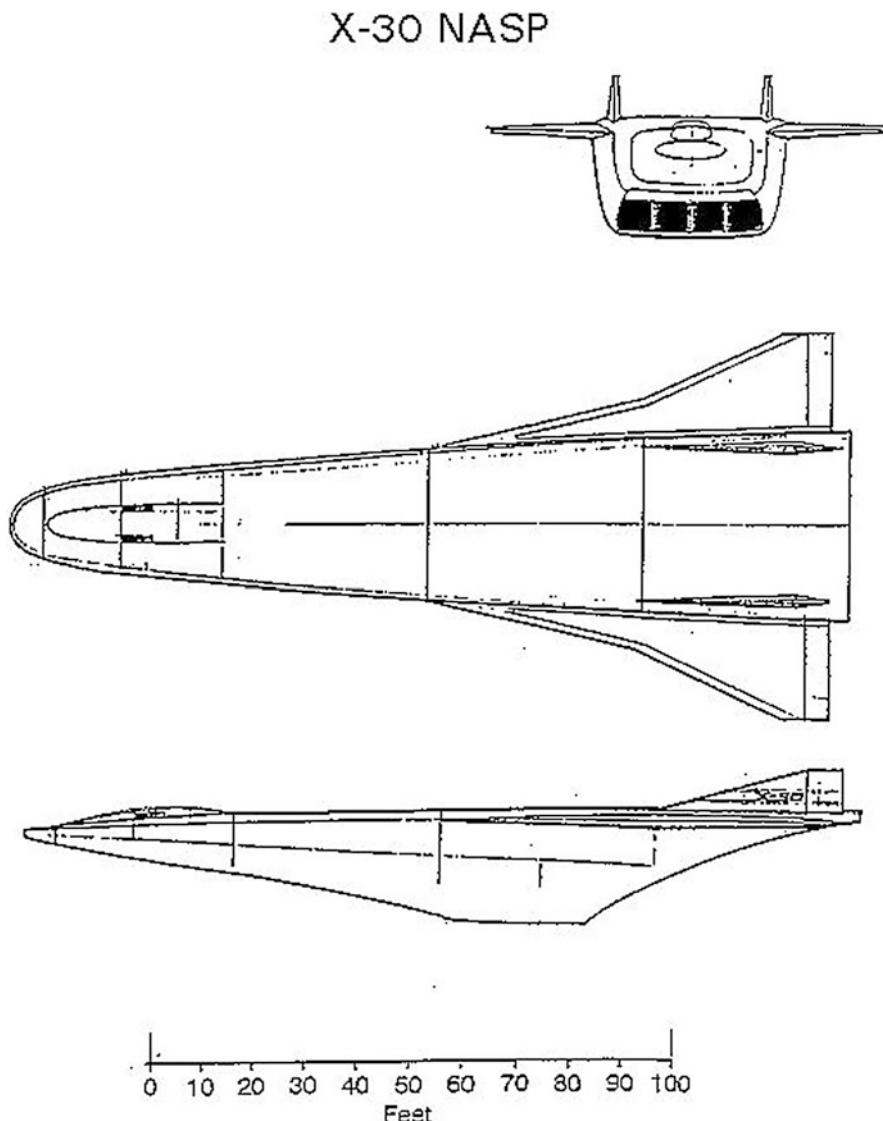


Fig. 1.70 Space Shuttle Orbiter configuration



**Fig. 1.71** X-30 configuration

lateral/directional case also provided reasonable results. Chavez and Schmidt report on the analysis procedure used in the dynamic analysis of a configuration known as the X-30 (NASP, National Aerospace Plane); see [2] (Fig. 1.71).

Newtonian theory was used for determining the pressure distribution over the vehicle forebody and coupled to a one-dimensional model of the scramjet engine. Two-dimensional shock-expansion theory gave the pressure distribution on the X-30 afterbody/nozzle.

In the past, all the local surface inclination methods were embodied in an industry-standard computer program named the “*Hypersonic Arbitrary Body Program*” (*HABP*). This program has been in wide use throughout industry and government since the early 1970s. *HABP* and modified versions, *S/HABP*, is at present the most widely used tool in the preliminary design and analysis of hypersonic vehicles [14].

Finally, it is worth to note that this design approach is a viable option also within vehicle aeroheating analysis.

Then, the vehicle surface is approximated by a system of planar panels; the lowest level of geometry used in the analysis is a quadrilateral element. The pressure acting on each panel is evaluated by user-specified compression-expansion and approximate boundary-layer methods.

An aerodynamic analysis using *S/HABP* demands two types of geometry models—*inviscid* and *viscous*—as shown for the space shuttle Orbiter, the FDLD-7 and X-24C-10D vehicles in Figs. 1.72, 1.73, and 1.74, respectively [13].

*S/HABP* requires a detailed geometric representation of a vehicle in order to accurately predict aerodynamic forces and moments using *inviscid* pressure calculations. For the *viscous* analysis, the code contains a variety of empirically based *viscous* pressure methods. The methods require Reynolds number and surface pressure and temperature for proper execution. A typical *viscous* geometry model contains a series of flat surfaces on which the shear force is determined. The forces calculated from the *inviscid* and *viscous* routines are summed together to determine total vehicle forces.

The *inviscid* and *viscous* analyses require two different grids, and several examples are shown from Figs. 1.72, 1.73, and 1.74 [13]. The *inviscid* geometry models require more detail in areas with high contour variations (noses or leading edges of wings) for accurate pressure calculations. Areas of the vehicles that were flat, such as the sides, were modeled with larger elements. For skin friction calculations, geometrically complex vehicles can be divided into a number of simple plane surfaces without impacting prediction accuracy. Modeling the approximate wetted area of the vehicles is the critical consideration when creating the *viscous* geometries. Definitively, the grid of *viscous* analysis is an approximate representation of the vehicles, while the *inviscid* grid is a more exact representation [13].

## 1.7 Hypersonic vs. Subsonic Aerodynamics

### 1.7.1 Aerodynamic Drag

In subsonic flow, the size of the wake determines the amount of drag. Emphasis in low-speed design is placed on fairing reward to reduce drag. A single wire can produce as much drag as a large fairing.

At hypersonic speed, the base region is in a vacuum and geometric details in the base have little influence on the drag. The stagnation point has the greatest pressure,

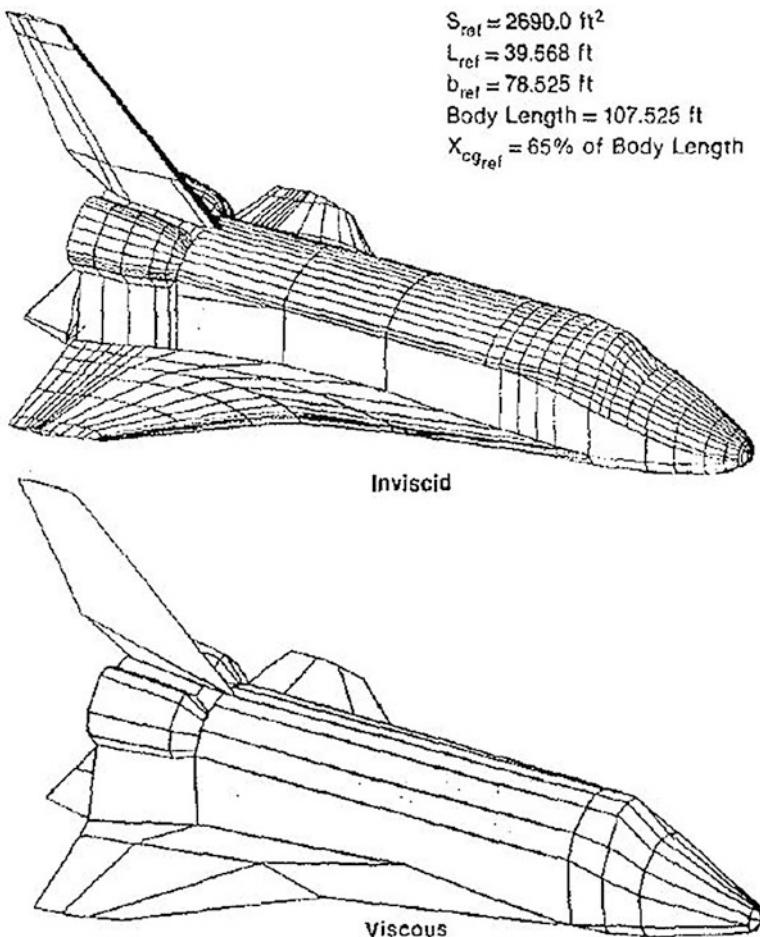


**Fig. 1.72** Space Shuttle analysis geometries

which decreases rapidly as the slope decreases (i.e.,  $C_p = 2 \sin^2\delta$ ). The size of the stagnation region, therefore, determines the drag. A small cylinder possesses the same drag as a large wedge.

Contrasting hypersonic drag characteristics with subsonic: one fairs rearward in subsonics and forward in hypersonics to minimize drag (see Fig. 1.75) [18].

### 1.7.2 Aerodynamic Lift

To generate lift at subsonic speed, a cambered airfoil is placed at a small angle of attack, but with care so as not to separate the flow on the upper surface (i.e.,

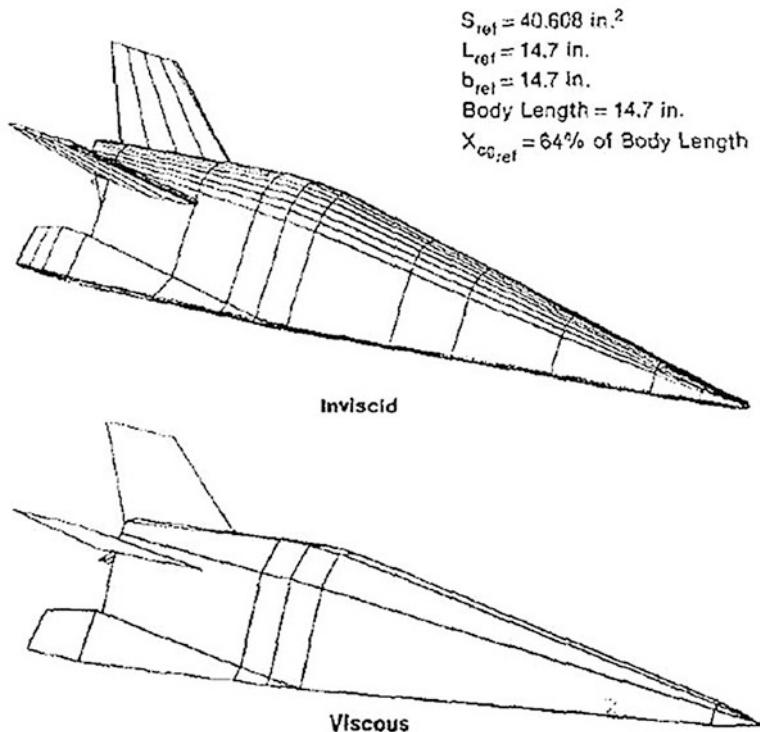


**Fig. 1.73** FDLD-7 analysis geometries

aerodynamic stall). Large suction forces on the upper side dictate the magnitude of the lift, as shown in Fig. 1.76 [18].

At hypersonic speed, little lift is developed from the upper surface so that separation is of little consequence. Only the pressure forces on the lower surface generate lift. Therefore, it is possible to divide the design features in a compatible manner by designing the lower surface (i.e., windsides) for hypersonic flight and the upper surface (i.e., leeside) for subsonic.

### 1.7.3 Planform Features

We know that, at subsonic speeds, a high-aspect-ratio, unswept wing minimizes induced drag (or end effects) and maximizes L/D. At high speeds, large sweep minimizes the leading-edge drag, dictating a low aspect ratio for efficient L/D (see Fig. 1.77) [18]. Hence, a major incompatibility occurs, requiring a compromise or a sophisticated variable sweep design (see Tornado fighter).

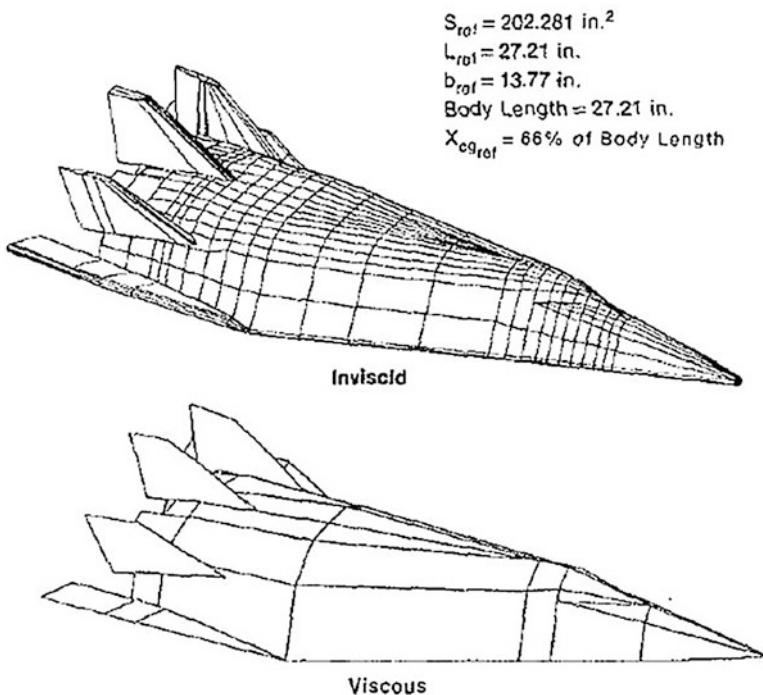


Fig. 1.74 X-24C-10D analysis geometries

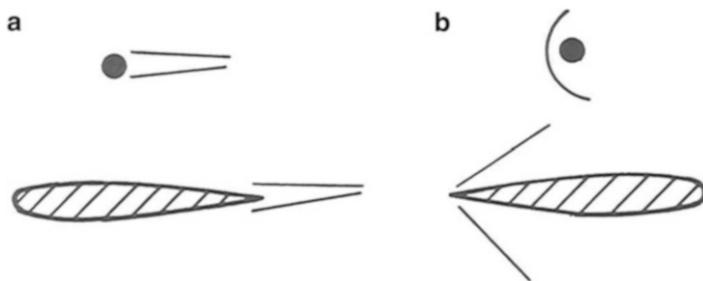
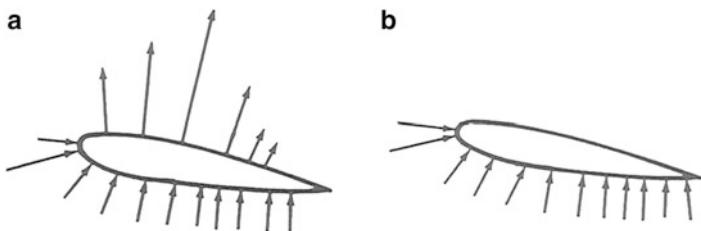


Fig. 1.75 Comparison of aerodynamic drag. (a) Subsonic ( $M \ll 1$ ): equal drag configurations, rearward fairing, size of wake determines the drag. (b) Hypersonic ( $M \gg 1$ ): equal drag configurations, forward fairing, size of stagnation region determines the drag

Another feature of the planform selection is the center of pressure shift that occurs when decelerating from supersonic to subsonic speeds.

Qualitatively, at high speed, the aerodynamic center is at the area centroid for a flat surface (since  $C_p = 2 \sin^2 \delta = \text{const}$  when  $\delta = \text{const}$ ).

At subsonic speeds, the aerodynamic center shifts to the quarter chord, consistent with potential flow theory (see Fig. 1.78) [18]. A delta wing and a top-mounted fuselage can be designed to minimize this shift (i.e., the Space Shuttle) [18].



**Fig. 1.76** Aerodynamic lift. (a) Subsonic ( $M \ll 1$ ): upper surface produces the lift. (b) Hypersonic ( $M \gg 1$ ): lower surface produces the lift

**Fig. 1.77** Comparison of planforms. (a) Subsonic ( $M \ll 1$ ):

$$\text{AR} = b^2/bc = b/c \gg 1.$$

(b) Hypersonic ( $M \gg 1$ ):

$$\text{AR} = b^2/\frac{1}{2}bc = 2$$

$$b/c = 4 \cot \Lambda$$

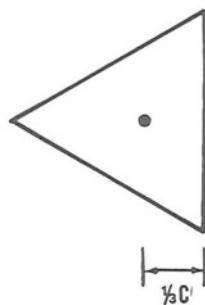
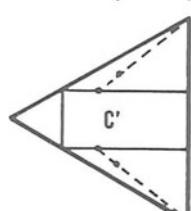
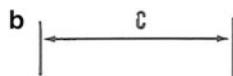
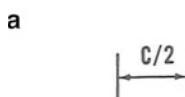
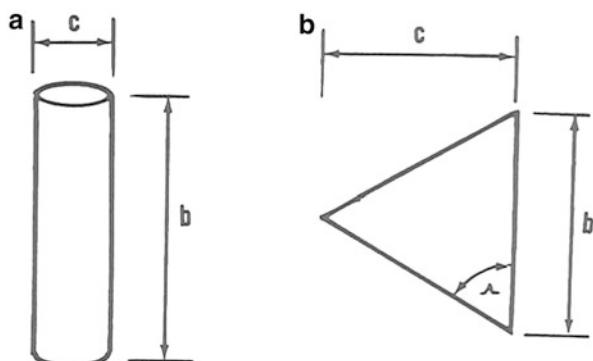


**Fig. 1.78** Comparison of centers of pressure. (a) Subsonic ( $M \ll 1$ ): upper surface, center of pressure at  $c'/2$ . (b) Hypersonic ( $M \gg 1$ ): lower surface, center of pressure at  $\frac{1}{3}c$

The more pointed and slender the body, the weaker the shock wave attached and hence the smaller the wave drag.

## 1.8 Entry Flight and Aeroheating

Originally, the major concern of re-entry was to find a way to survive the aerodynamic heating. Many people believed it to be impossible and coined the label *thermal barrier*, analogous to the *sonic barrier* of the previous generation of scientists who believed that flight beyond the speed of sound was not possible [18].

Their fears may be comprehended by calculating the kinetic energy (KE) of an orbiting vehicle:

$$KE = \frac{1}{2}mV_c^2 \quad (1.167)$$

where  $m$  and  $V_c$  are its mass and velocity, respectively. During re-entry, all this kinetic energy must be dissipated and converted into heat ( $Q$ ) to decelerate the vehicle to landing velocity. Then, the energy balance reads

$$Q = KE = \frac{m}{2g}V_c^2 \rightarrow \frac{Q}{m} = \frac{V_c^2}{2g} \quad (1.168)$$

where  $m$  is the weight of the spacecraft and  $g$  the gravity acceleration.

### Explanation Box. Energy and Heat

The KE of 1 kg of matter hitting the Earth atmosphere with parabolic velocity is  $Q/w = 6.371 \times 10^6 \text{ m} = 1.49 \times 10^4 \text{ kcal/kg}$ .

To melt ice at a pressure of 1 atm and a temperature of 0 °C, we have to transfer 80.4 kcal/kg to it.

To transform the water from 0 °C to steam of 100 °C, we have to add 100 kcal to heat the water, 499 kcal for internal heat, and 40.5 kcal for external heat of vaporization, or a total of 720 kcal/kg.

The above explanation box shows very convincingly that only a very small fraction of the energy to be braked can be absorbed by the vehicle, or the vehicle itself will be destroyed.

Another condition to examine is the stagnation temperature  $T_0$  on the nose of a re-entry vehicle as shown in Fig. 1.79.

The energy equation in this case is given by

$$c_p T_0 = c_p T_\infty + \frac{V_\infty^2}{2} \quad (1.169)$$

**Fig. 1.79** Stagnation temperature on the nose of re-entry vehicle

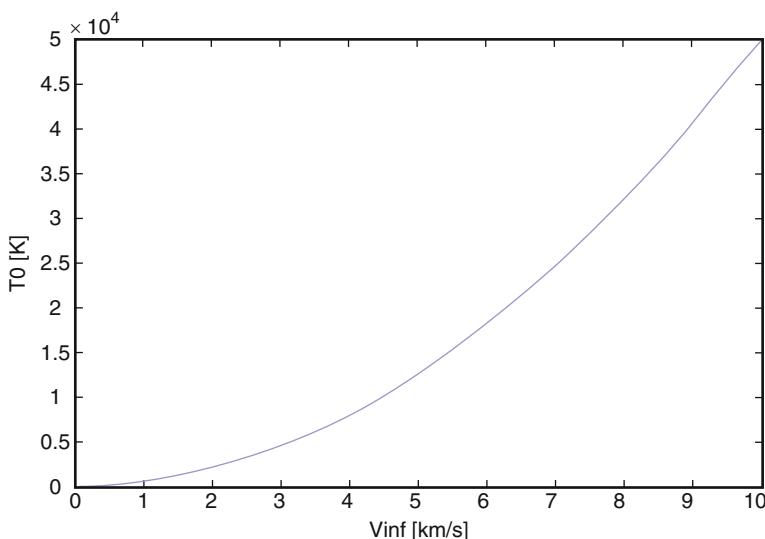
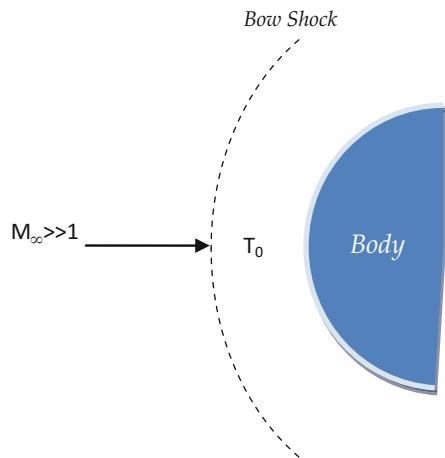


**Fig. 1.80** Diagram of  $T_0$  vs.  $V_\infty$  for  $c_p = 1,000.6 \text{ (m}^2/\text{s}^2\text{K)}$

where  $c_p$  is the specific heat at constant pressure. A hypersonic approximation to this equation is ( $T_0 \gg T$ ):

$$T_0 = \frac{V_\infty^2}{2c_p} \quad (1.170)$$

that is plotted in Fig. 1.80. As shown, the temperatures encountered by the entry vehicle are higher than any material can sustain.

In this case, one concludes that a *thermal barrier* does exist. But this is an erroneous conclusion. Indeed, it was assumed that all the heat energy went into the vehicle.

As will be shown later, aeroshape design investigations (discussed in Chap. 3) suggest making use of blunt-body configurations as they allow maximizing the heat loss in the air surrounding the spacecraft instead of in the vehicle itself. In this case, in fact, a strong bow shock detaches in front of vehicle thus increasing the temperature in the shock layer, especially in the vehicle nose region.

Finally, note that several engineering relationships allow designer to estimate the distance running from the detached bow shock and the vehicle nose, namely, shock stand-off distance.

### 1.8.1 Stand-off Distance

Consider a bluff body in a supersonic flow. When Mach number increases its value, the shock wave is detached to the body, because there isn't a solution to balance equations with an attached shock wave. So near the nose, the shock wave is locally normal to the stagnation streamline (see Fig. 1.81), and in this region we found most severe variation of thermo-fluid dynamic quantity [15].

The distance between shock and body evaluated in the stagnation point is the so-called stand-off distance ( $\Delta$ ). Functionally to satisfy the continuity equation, we see that  $\Delta$  depends essentially by:

- Nose radius of the body, in the stagnation point ( $R_N$ )
- Mach number ( $M$ )
- Specific heats ratio ( $\gamma$ )

It is very important to know  $\Delta$  because it influences both heat flux in the stagnation point and the pressure distribution on the vehicle.

There are several approximated expressions to evaluate  $\Delta$ .

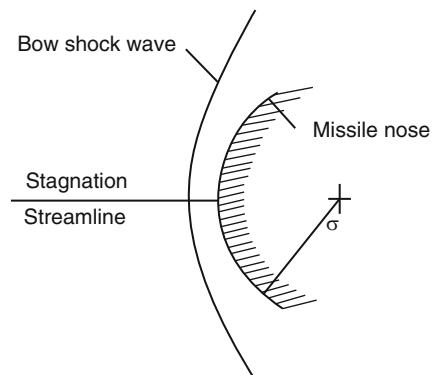


**Fig. 1.81** Stagnation point at the nose of a blunt body

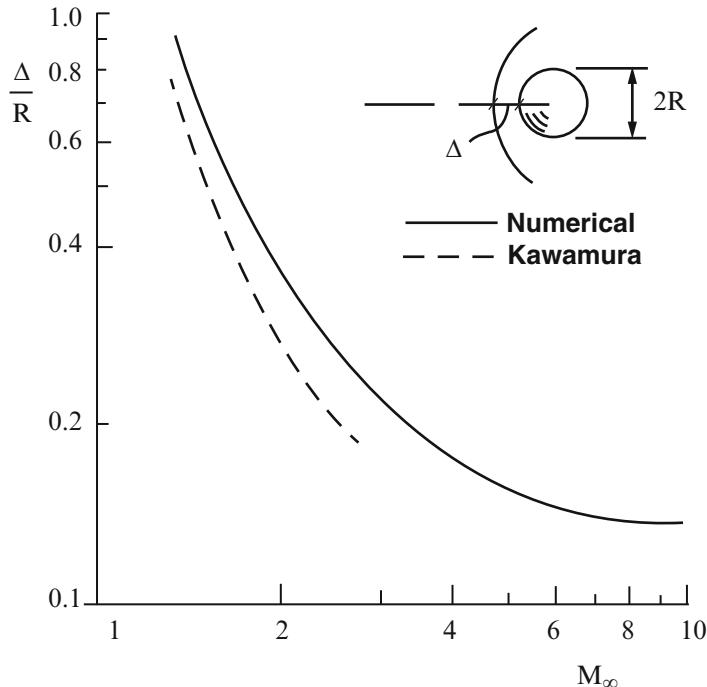


Fig. 1.82 Sphere stand-off distance

For instance, the first one was suggested by Hayes and Probstein [15]. This relationship gives the stand-off distance between a sphere and a bow shock with radius of curvature  $R_s$ :

$$\frac{\Delta}{R_s} = \frac{\frac{\rho_\infty}{\rho_2}}{1 + \sqrt{\frac{8}{3} \frac{\rho_\infty}{\rho_2}}} \quad (1.171)$$

So  $\Delta$  decreases when  $\rho_2/\rho_\infty$  increases and becomes almost a constant for  $M \rightarrow \infty$ , as suggested by Eq. (1.172) and Fig. 1.82 [3]:

$$\lim_{M \rightarrow \infty} \frac{\rho_\infty}{\rho_2} = \frac{\gamma + 1}{\gamma - 1} \quad (1.172)$$

Another relationship to assess the stand-off distance is suggested by Seiff (it is more useful than the first one, because  $\Delta$  is dimensionless by nose radius of the body  $R_N$ ) [3, 15, 16].

It is a simply linear expression between stand-off distance and density ratio:

$$\frac{\Delta}{R_N} = 0.78 \left( \frac{\rho_\infty}{\rho_2} \right) \quad (1.173)$$

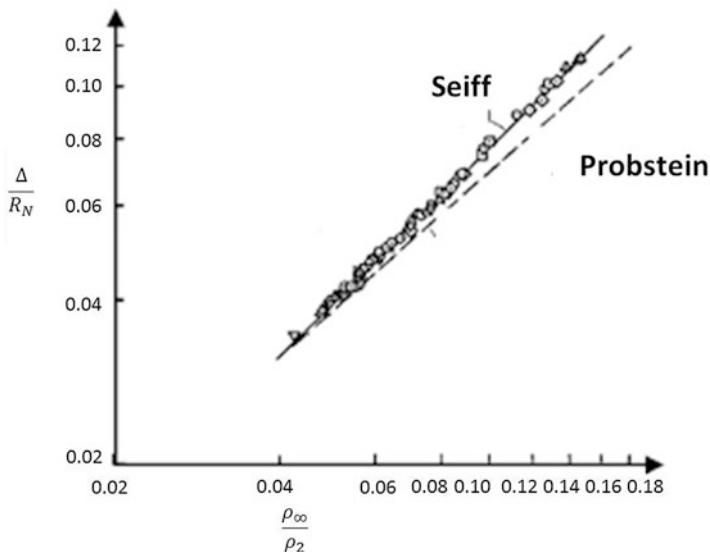


**Fig. 1.83** Difference from Seiff and Probstein relationships for a sphere of radius  $R_N$

Figure 1.83 shows the difference from Seiff and Probstein relationships considering several experimental data collected for a sphere [3].

Finally, the dependence of  $\Delta$  by  $\gamma$  shows like the standoff distance is real gas effects depending: in a chemically reacting gas, with same altitude and velocity, the stand-off distance is nearer to the body, as shown in Fig. 1.84 [3].

Practically, thermochemistry phenomena typical of high temperatures real gas flow absorb energy from the flux, so the temperature downstream the shock wave is lower than the corresponding one in the case of ideal gas; this implies an increment of density (see Fig. 1.85) and a decrement of thickness of the shock layer (see Fig. 1.84) [3].

## 1.8.2 Aerodynamic Heating

During re-entry the deceleration of spacecraft causes a strong shock wave ahead of vehicle. This determines intense heating and pressurizing of the atmospheric gases past the space vehicle. With temperatures surrounding the vehicle in the thousands of kelvin, convective and radiative heat transfer toward the spacecraft is significant.

Bluff shapes have poor aerodynamic lifting performance, and their re-entry trajectories are determined principally by non-lifting ballistic considerations. As a result, the peak heating rates may be very high and ablative TPS are necessary.

For slender vehicle shapes, by virtue of the weaker shock wave, a greater fraction of the total energy dissipated in the boundary layer is transferred to the structure.

**Fig. 1.84** Relative locations of blunt-body bow shock waves for calorically perfect and chemically reacting gases

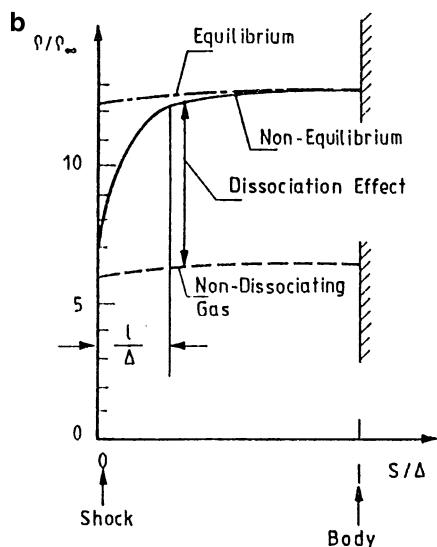
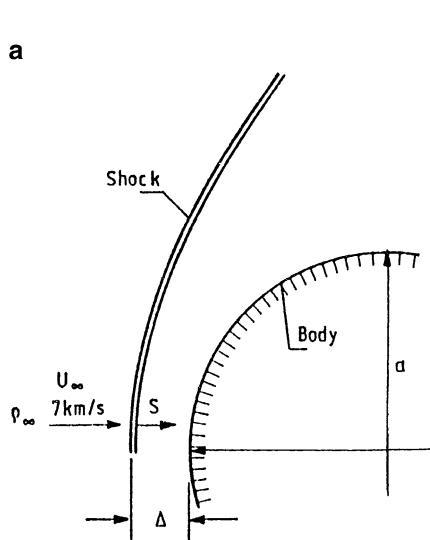
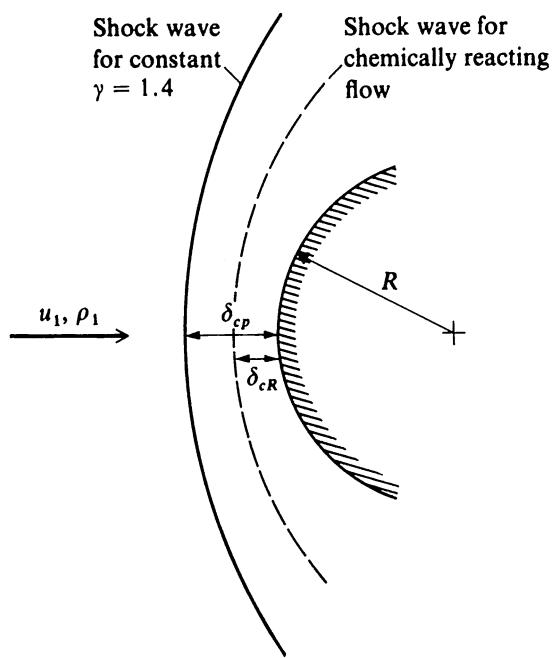


**Fig. 1.85** Flow on a blunt body (a) stand-off distance and (b) stagnation-point profile of density for a dissociating gas

This may not be a disadvantage since greater aerodynamic sophistications may be used to generate an efficient lifting aeroshape which may glide and decelerate over relatively long periods at higher altitude during re-entry, thereby reducing the peak heating rate below that for bluff non-lifting configurations. For slender lifting vehicles with low wing loading, the heating rates may be reduced to sufficiently low values that equilibrium between convective heat input and radiative heat loss can be maintained at temperature low enough that metallic surface construction, without an ablating thermal protection system, can be tolerated.

### 1.8.2.1 Convective Heat Transfer

Convective heat transfer is the transfer of heat from one place to another due to the movement of fluids. The presence of bulk motion of the fluid enhances the heat transfer between the solid surface and the fluid. Convective heat transfer actually describes the combined effects of conduction (heat diffusion), plus heat transfer by bulk fluid flow, a process technically termed *heat advection*. The term convection can refer to transfer of heat with any fluid movement, but advection is the more precise term for the transfer due only to bulk fluid flow.

The process of transfer of heat from a solid to a fluid, or the reverse, requires not only transfer of heat by bulk motion of the fluid but also *diffusion/conduction* of heat through the still boundary layer next to the solid. Thus, this process with a moving fluid requires both diffusion and advection of heat, a summed process that is generally called convection. The convection heat transfer mode is comprised of two mechanisms. In addition to energy transfer due to random molecular motion (diffusion), energy is also transferred by bulk, or macroscopic, motion of the fluid. This motion is associated with the fact that, at any instant, large numbers of molecules are moving collectively or as aggregates. Such motion, in the presence of a temperature gradient, contributes to heat transfer. Because the molecules in aggregate retain their random motion, the total heat transfer is then due to the superposition of energy transport by random motion of the molecules and by the bulk motion of the fluid. It is customary to use the term convection when referring to this cumulative transport and the term advection when referring to the transport due to bulk fluid motion.

Later in the book, several engineering relationships for the assessment of convective heat flux will be provided.

### 1.8.2.2 Radiative Heat Transfer

Modern space exploration missions plan to bring back to Earth extraterrestrial material, to analyze it, and to know something more about the origins of Solar System. During these re-entry flight trajectories, because of the high velocity, the shock layer becomes extremely hot (see Fig. 1.86) [3]. For instance, Fig. 1.86 highlights that at a re-entry velocity of about 11 km/s, the temperature in the shock

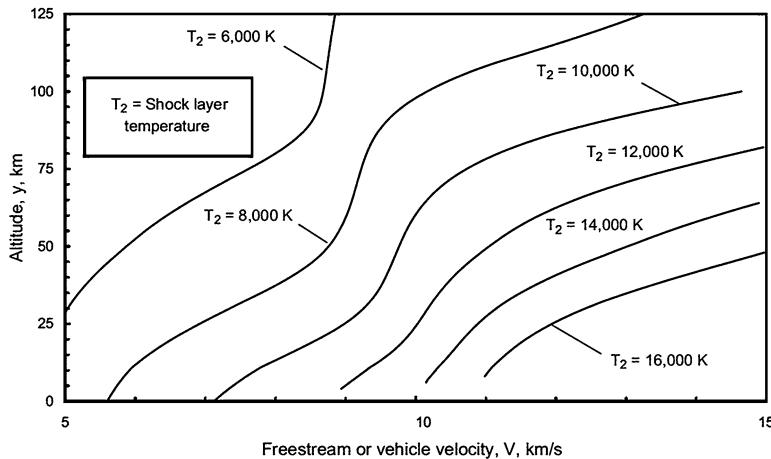


**Fig. 1.86** Shock layer temperature for equilibrium air

layer during descent can range from about 10,000 to 14,000 K for air in equilibrium condition.

Therefore, the radiative heating will become quite significant (Fig. 1.87), and it can exceed the convective heating (e.g., Table 1.4 underlines that space vehicle re-entering at 15 km/s has to withstand to a total integrated heat load ( $Q$ ) made of 61 % and 83 % radiative for flight path angles of  $10^\circ$  and  $50^\circ$ , respectively). The presence of a radiating flowfield has two main effects on the prediction of heating on the forebody of a spacecraft. Firstly, the radiation adds another mode of heat transfer to the vehicle surface. Along with convective heating, radiative heat transfer must also be considered to make an accurate heating prediction. The second effect of radiation in the shock layer is the so-called radiative cooling effect. Some of the emitted energy escapes the shock layer and thus decreases the energy in the flowfield. The lowering of temperatures in the shock layer leads to an increase in the average density. This, in turn, produces a thinner shock layer. The thinner shock layer radiates less, so ultimately radiative cooling reduces some of the effect of radiant heat transfer. It is apparent that the correct modeling of the fluid physics, radiative transfer, and their effects on each other becomes important for accurate heat load predictions [3].

## 1.9 Basics of Space Vehicle Design

The survival of a space vehicle demands for accurate aerodynamic and thermal analyses or in a one word *aero-thermo-fluid-dynamic* analysis of the entry vehicle [17, 18, 19].

**Fig. 1.87** Comparison of radiative and convective stagnation-point heat transfer

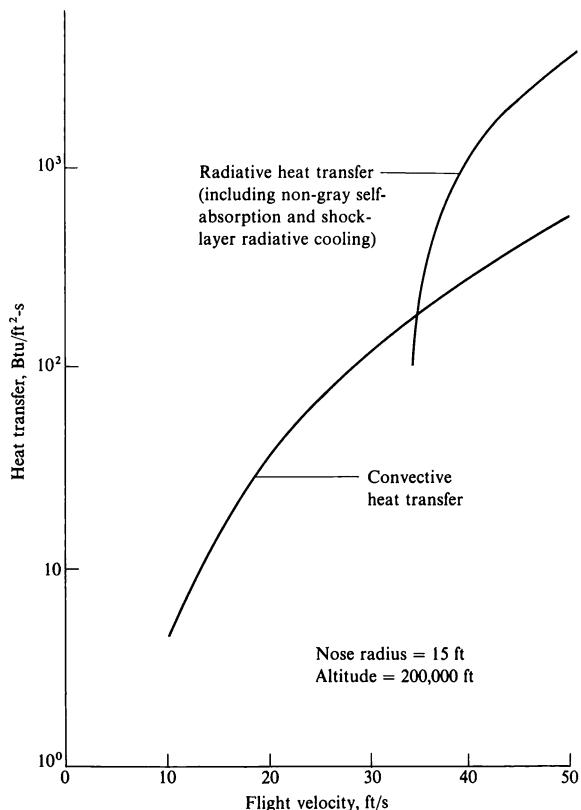


**Table 1.4** Peak stagnation-point heat flux and total heat load for Earth entry spacecraft

Entry vehicle	BP, kg/m <sup>2</sup>	VE, km/s	$\gamma_E$ , deg	$q_{\max} t$ , W/cm <sup>2</sup>	Q, J/cm <sup>2</sup>
Apollo CM, L/D ≈ 0.3	≈500	≈11	–	≈510 <sup>b</sup>	–
Stardust <sup>a</sup>	68.2	12.9	–8.2	856	23,730 <sup>c</sup>
Entry Body, <sup>a</sup> L/D = 0	50	15	–10	1,750	19,340 <sup>d</sup>
Entry Body, <sup>a</sup> L/D = 0	50	15	–50	11,170	20,300 <sup>e</sup>

<sup>a</sup>Results of NASA TRAJ simulation, 1999

<sup>b</sup>Approximately 34 % of the total heat flux is radiative and 66 % is convective

<sup>c</sup>The total heat load is 9 % radiative and 91 % convective

<sup>d</sup>The total heat load is 61 % radiative and 39 % convective

<sup>e</sup>The total heat load is 83 % radiative and 17 % convective

This analysis gives:

- The vehicle *aerodynamic forces* and *moments*, necessary to obtain its free-entry trajectory.
- The time histories of heat fluxes (convective and radiative one, if any), the temperatures, and the integrated heat loads, necessary to design the vehicle TPS.
- The time histories of dynamic pressure, inertial loads, and skin friction coefficient, required for assessment of structural loads and venting environment.

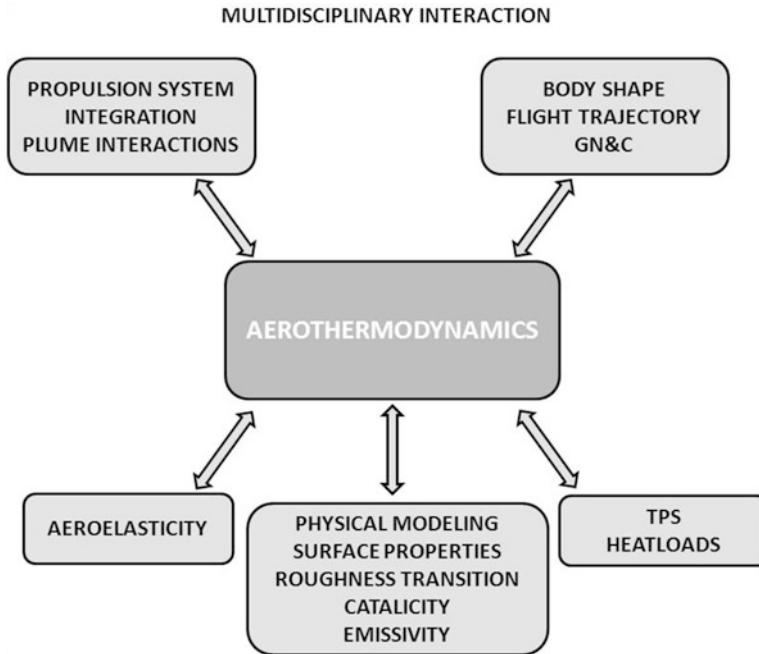


**Fig. 1.88** The multidisciplinary nature of aerothermodynamics

Hence, the *multidisciplinary nature* of aerothermodynamics is evident, as summarized in Fig. 1.88. For example, the aerodynamic forces, the temperatures, and the heat fluxes obtained along nominal trajectories depend on the spacecraft configuration and position of center of gravity; they, in turn, are the final point of an iterative process (*design loop*) that ends only when the trajectory provides a stable and controllable entry flight [19, 20, 21, 22].

Gnoffo et al. in Ref. [2] say about the design process: “*The process of design involves defining and, then, refining and narrowing the boundaries of a design space until a final solution is reached. To achieve an optimum design, the optimum design solution must always remain within the design space as the design space boundaries are narrowed.*”

Generally, the first step in the design process is determining *mission requirements* and *objectives*. An initial shape of the vehicle is determined as a function of a number of parameters such as *landing accuracy requirements*, *payload mass*, *volume*, and the *launch booster payload shroud*. The mass, aerothermodynamic performance of the aeroshape (i.e., aerothermodynamic database), and the flight initial conditions determine an envelope of possible entry trajectories. The initial aerothermodynamic database is generated using low-fidelity methods, such as modified Newtonian for the aerodynamics and engineering correlations for the stagnation-point heating. Using a three-degree-of-freedom (dof) trajectory analysis, an initial design trajectory is generated to meet the mission requirements and

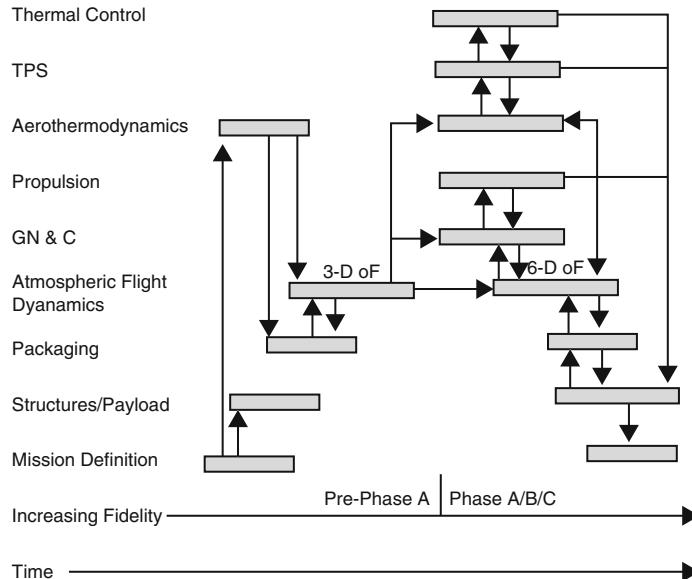


**Fig. 1.89** Design process for a capsule aeroshell

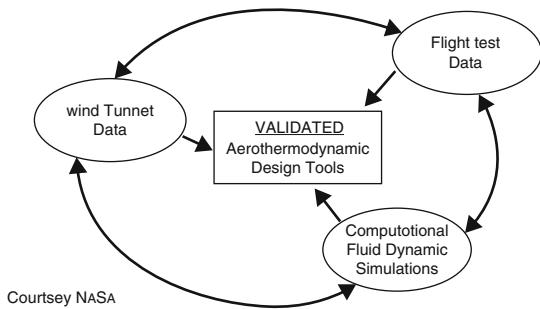
satisfy subsystem constraints, such as *maximum acceleration loads* or *maximum temperature and heating rates* for the TPS. In the next phase, the various discipline and subsystem analyses are highly coupled, and the design process becomes iterative, as described in Fig. 1.89 in the case of the design process of a capsule aeroshell. In this phase, accurate predictions of the aerodynamics and entry heating are required to design the TPS and for 6-dof trajectory analysis [23, 24].

In this framework one of the most useful design tools is computational fluid dynamics (CFD). In fact, aerothermodynamic experimental data, fully representative of the entry flight environment, are not always available in ground-based experimental facilities such as the plasma wind tunnel (PWT) [25, 26].<sup>21</sup> Thus, high-fidelity numerical simulation techniques, such CFD, are mandatory. These methods are computationally intensive and require accurate modeling of relevant physical processes to achieve good results; further, the resources required for a simulation usually increase as the accuracy of the prediction increases [27]. Therefore, to limit costs, high-fidelity aerothermodynamic simulation is only employed in the later stages of the design process, after the design has been significantly refined.

CFD results, however, can be considered acceptable and reliable, only when they are confirmed by both wind tunnel and flight tests, as highlighted by the design cycle in Fig. 1.90 [2].

<sup>21</sup>For example, the full duplication in the same experiment of entry trajectory in the Mach-Reynolds map.

**Fig. 1.90** The correct aerothermodynamic design cycle



All the design considerations outlined above emphasize depending, of course, on the flowfield regime the spacecraft encounters during the atmospheric descent.

## 1.10 Dimensional Analysis

As discussed so far, hypersonic flow conditions past an entry vehicle determine a rather complex flowfield environment [28, 29]. Several physical phenomena arise and may become critical for the survivability of the spacecraft. Therefore, it is fundamental to know the importance relative of critical physical phenomena by comparing them to each other. Thus, useful information can be deduced by forming grouping of parameters as dimensionless ratios [30].

This technique is called *dimensional analysis* and is a very powerful engineering tool. It is an important part of the judgment process necessary to make engineering design decisions and help also eliminate errors in the mathematical model of physical phenomenon under investigation.

The following is a list of such dimensionless ratios, important in Fluid Mechanics, which bear the names of early investigators:

$$\text{Mach number } M = \frac{V}{a} \quad (1.174)$$

$$\text{Reynolds number } \text{Re} = \frac{\rho VL}{\mu} \quad (1.175)$$

$$\text{Prandtl number } \text{Pr} = \frac{\mu c_p}{k} \quad (1.176)$$

$$\text{Lewis number } \text{Le} = \frac{\rho D c_p}{k} \quad (1.177)$$

$$\text{Nusselt number } \text{Nu} = \frac{hL}{k} \quad (1.178)$$

$$\text{Stanton number } \text{St} = \frac{h}{\rho V c_p} \quad (1.179)$$

$$\text{Knudsen number } \text{Kn} = \frac{\lambda}{L} \quad (1.180)$$

The physical interpretation of these dimensionless numbers is in order:

$$\frac{\text{Ordered energy}}{\text{Random energy}} = \frac{\frac{1}{2}mu^2}{\frac{1}{2}m\bar{v}^2} = \frac{u^2}{3RT} = \frac{\gamma}{3} \frac{u^2}{a^2} = \frac{\gamma}{3} M^2$$

Thus, the Mach number  $M$  is a normalized flow speed where the normalizing factor is the speed of sound  $a$ , [m/s], a measure of the compressibility of the fluid, i.e.,

$$M = \frac{V}{a} = \frac{\text{macroscopic speed fluid}}{\text{speed of sound in the fluid}} \quad (1.181)$$

where  $a = \sqrt{\gamma R T}$  (for a perfect gas);  $T$  is the temperature [K];  $\gamma$  is the ratio  $c_p/c_v$ , where  $c_p$  and  $c_v$  are the specific heat at constant pressure and at constant volume, respectively; and  $R$  is the gas constant.

In subsonic flow  $a^2 \gg u^2$ , so that the random energy dominates; at hypersonic speed,  $u^2 \gg a^2$ , ordered energy prevails. That's why impact Newtonian theory is a good but simple model for hypersonic flow. The Mach dimensionless number allows clarifying how the velocity ellipse shown in Fig. 1.1 is obtained.

### Explanation Box. The Velocity Ellipse

The equation of total enthalpy for a steady, adiabatic, and inviscid flow reads

$$H = h + \frac{V^2}{2} = c_p T_0$$

But

$$h = c_p T = \frac{a^2}{\gamma - 1}$$

Hence,

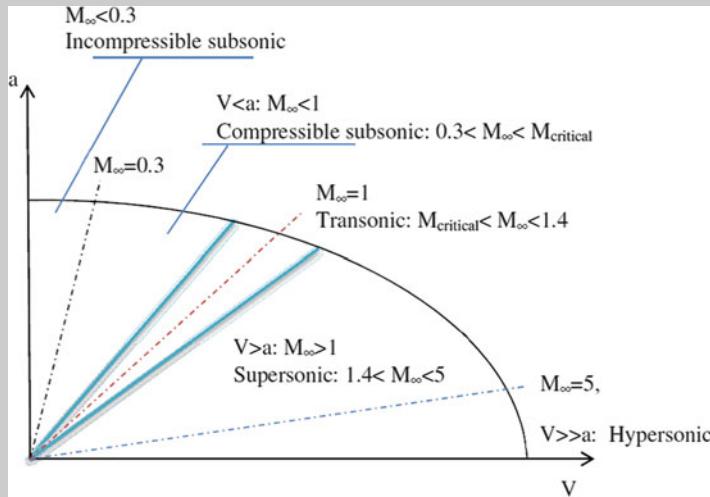
$$\frac{a_o^2}{\gamma - 1} = \frac{a^2}{\gamma - 1} + \frac{V^2}{2}$$

or

$$\frac{a^2}{a_o^2} + \left( \frac{\gamma - 1}{2} \right) \frac{V^2}{a_o^2} = 1$$

(continued)

This is the equation for an ellipse as plotted in Fig. 1.1 and reported below for commodity.



As shown, a limited region of this ellipse contains hypersonic flow. In this region, the term

$$\frac{a}{a_0} \ll 1$$

and can be eliminated from the energy equation.

The Mach number, therefore, ceases to be a significant parameter of the problem. Only  $V_1$  and  $\rho_1$  are useful descriptors of the free-stream. Both  $T_1$  and  $P_1$  are small terms and have little consequence on the numerical outcome. For example, at the stagnation point,

$$\begin{aligned} p_2 &= \rho_1 V_1^2 \\ T_2 &= \frac{V_1^2}{2c_p} \\ \rho_2 &= \frac{p_2}{RT_2} = \frac{\rho_1 V_1^2}{\frac{R}{2c_p} V_1^2} = \frac{2\gamma}{\gamma - 1} \rho_1 \end{aligned}$$

Based upon this simple model, we can deduce information concerning hypersonic aerodynamic characteristics and contrast it with subsonics.

In the figure the critical Mach number is reported. Note that it is the minimum value of the free-stream Mach number for which the local flow becomes supersonic.

The Reynolds number is the ratio of inertia to viscous in the fluid, i.e.,

$$\frac{\text{Inertial force}}{\text{Viscous force}} = \frac{\dot{m}v}{\tau A} = \frac{\rho AV^2}{\mu \frac{V}{L_{\text{ref}}} A} = \frac{\rho VL_{\text{ref}}}{\mu} = Re \quad (1.182)$$

where  $\mu$ , [kg/m/s], is the coefficient of viscosity of the fluid,  $\rho$  is the density [kg/m<sup>3</sup>], and  $L_{\text{ref}}$ , [m], is the characteristic dimension of the flowfield:

$$\frac{\text{Viscous dissipation energy}}{\text{Energy conducted}} = \frac{\tau AV}{\dot{q}A} = \frac{\mu \frac{V^2}{L}}{k \frac{T}{L}} = \frac{\mu c_p}{k} \frac{V^2}{c_p T} = \text{Pr} \frac{M^2}{\gamma - 1} \quad (1.183)$$

$$\frac{\text{Heat diffused}}{\text{Heat conducted}} = \frac{\dot{m}_i H}{\dot{q}A} = \frac{\rho D \frac{\partial C_i}{\partial z} AH}{k \frac{\partial T}{\partial z} A} = \frac{\rho DH}{kT} = \frac{\rho D c_p}{k} \frac{H}{c_p T} = \text{Le} \left( \frac{H}{c_p T} \right) \quad (1.184)$$

$$\frac{\text{Heat convected}}{\text{Heat conducted}} = \frac{hT}{k \frac{T}{L}} = \frac{hL}{k} = \text{Nu} \quad (1.185)$$

The Stanton number is the ratio of the convective heat transfer at the surface to the heat transferred by the heat capacity of the gas:

$$\text{St} \equiv \frac{\text{Convective heat transfer coefficient}}{\rho c_p V} = \frac{\dot{q}}{\rho c_p V (T_f - T_w)} \quad (1.186)$$

$$\frac{\text{No. of collisions with body}}{\text{No. of collisions with another molecule}} = \frac{f_L}{f_\lambda} = \frac{\frac{\bar{v}}{L}}{\frac{\bar{v}}{\lambda}} = \frac{\lambda}{L} = \text{Kn} \quad (1.187)$$

## References

1. Kuchemann D (1978) The aerodynamic design of aircraft. Pergamon, Oxford
2. Bertin JJ, Cummings RM (2003) Fifty years of hypersonics: where we've been, where we're going. *Prog Aerosp Sci* 39:511–536
3. Anderson JD Jr (1989) Hypersonic high temperature gas dynamics. McGraw-Hill Book Company, New York
4. Van Driest ER (1952) Investigation of laminar boundary layer in compressible fluids using the Crocco method, NACA-TN-2597. NACA Report, Washington, DC
5. De Jarnette FR, Hamilton HH, Weilmuenster KJ (1987) A review of some approximate methods used in aerodynamic heating analyses. *J Thermophys Heat Transf* 1(1):5–12

6. Julian Allen H, Eggers AJ Jr (1958) A study of the motion and aerodynamic heating of ballistic missiles entering the earth's atmosphere at high supersonic speeds, NACA report 1381, Moffett Field, California
7. Advisory Group for Aerospace Research and Development (North Atlantic Treaty Organization) (1997) Capsule aerothermodynamics. AGARD-R-808, AGARD, Neuilly sur Seine
8. Regan FJ, Anandakrishnan SM (1993) Dynamics of atmospheric re-entry. American Institute of Aeronautics and Astronautics, Washington, DC
9. Bertin JJ Hypersonic aerothermodynamics, AIAA education series. American Institute of Aeronautics and Astronautics, Inc., Washington, DC
10. Hirschel E, Weiland C (2009) Selected aerothermodynamic design problems of hypersonic flight vehicles. AIAA-Springer, Berlin
11. Rasmussen M (1994) Hypersonic flow. Wiley, New York
12. Viviani A, Pezzella G (2012) Next generation launchers aerodynamics, Research Signpost, Trivandrum – 695 023, Kerala, India
13. Maughmer M, Ozoroski L, Straussfogel D, Long L (1993) Validation of engineering methods for predicting hypersonic vehicle control forces and moments. *J Guidance Control Dyn* 16(4):762–769
14. Moore M, Williams J (1989) Aerodynamic prediction rationale for analyses of hypersonic configurations, AIAA paper 89-0525. McDonnell Douglas Astronautics Company, St. Louis
15. Hayes WD, Probstein RF (1959) Hypersonic flow theory. Academic Press, New York
16. Howe J (1989) Hypervelocity atmospheric flight: real gas flow fields, NASA TM 101055, Moffett Field, California
17. Serraglia F, Valorani M (2011) An optimization tool for the design of SSTO vehicles with combined air-breathing/rocket propulsion. In: Proceedings of the 4th European Conference for Aerospace Sciences (EUCASS) held in Saint Petersburg, Russia, July 4–8, 2011
18. Park C (1997) Evaluation of real-gas phenomena in high enthalpy impulse test facilities: a review. *J Thermophys Heat Transf* 11(1), 10–18. doi: [10.2514/2.6217](https://doi.org/10.2514/2.6217)
19. Livier PA, Habchi SD, Burnell SI, Lingard JS (2003) Computational fluid dynamics prediction of the Beagle 2 aerodynamic database. *J Spacecr Rockets* 40(5):632–638
20. Viviani A, Pezzella G, Cinquegrana D (2006) Aerothermodynamic analysis of an apollo-like reentry vehicle. In: Proceedings of the 14th AIAA/AHI Space Planes and Hypersonic Systems and Technologies Conferences, 6–9 November 2006, Canberra, paper AIAA-2006-8082
21. Viviani A, Pezzella G, Borrelli S (2008) Effect of finite rate chemical models on the aerothermodynamics of Reentry Capsules. In: Proceedings of 15th AIAA International Space Planes and Hypersonic Systems and Technologies Conference, 28 April–1 May 2008, Dayton, OH, paper AIAA-2008-2668
22. Park C (1991) Review of chemical-kinetic problems of future NASA missions. In: Proceedings of AIAA 29th Aerospace science meeting, Reno, NV, 7–10 January 1991, AIAA-91-0464
23. Gupta RN, Yos JM, Thompson RA, Lee KP (1990) A review of reaction rates and thermodynamic and transport proprieties for an 11-species air model for chemical and thermal non-equilibrium calculations up to 30000 K, NASA RP 1232, NASA, Washington DC
24. Sagnier P, Maraffa L (1991) Parametric study of thermal and chemical non-equilibrium nozzle flow. *AIAA J* 29(3):334–343. doi: [10.2514/3.59921](https://doi.org/10.2514/3.59921)
25. Wray K (1962) Chemical kinetics of high temperature. In Riddell FRR (ed) Hypersonic flow research. Progress in aeronautics and rocketry, vol 7. Academic Press, New York, pp 182–204
26. Yamauchi M, Fujii K, Higashino F (1995) Numerical investigation of supersonic flows around a spiked blunt body. *J Spacecr Rockets* 32(1):32–42
27. Sharma SP, Gillispie WD, Meyer SA (1991) Shock front radiation measurements in air, Paper AIAA-91-0573. In: Proceedings of AIAA 29th Aerospace science meeting, Reno, NV, 7–10 January 1991, AIAA-91-0464
28. White FM (1974) Viscous fluid flow. McGraw-Hill, New York
29. Rivell T (2006) Notes on earth atmospheric entry for Mars sample return missions, NASA/TP–2006-213486, Ames Research Center, Moffett Field
30. Hankey WL (1988) Re-entry aerodynamics. American Institute of Aeronautics & Astronautics, Washington, DC

# **Chapter 2**

## **Fundamentals of Atmospheric Entry**

### **2.1 Introduction**

To guide detailed CFD studies of spacecraft aerodynamics and aerothermodynamics, it is useful to first perform mission concept studies to assess as much as possible all the important flowfield phenomena the entry vehicle will face during descent. Such preliminary mission trade-off studies can be performed with the use of simple engineering computational techniques and empirical correlations, discussed in detail in this chapter.

In this framework, we shall look at basic equations of motion of a spacecraft during its approach and entry and note some relationships between trajectory, vehicle parameters, and structural and thermal loads in order to investigate which vehicle characteristics are important in spacecraft aerodynamic and aerothermodynamic design.

In doing that, we shall use when possible analytical and simplified approaches. *Indeed, a recurrent theme in this text is that recourse to all available engineering approach or analytical sophistication is desirable, even essential, prior to critical design and development. However, preliminary design and system feasibility assessment would be virtually impossible without the use of simpler, less accurate techniques.*

Atmospheric entry technology is a highly interdisciplinary area of space vehicle design. This is due to the many different functions that must be satisfied by the atmospheric entry system and to the wide range of flight regimes and conditions encountered during a typical entry.

Basically, the atmospheric entry system must provide controlled dissipation of the combined kinetic and potential energy associated with the vehicle's speed and

altitude at the entry interface. By controlled dissipation, we imply that both dynamic and thermal loads are maintained within acceptable limits during entry.<sup>1</sup>

This requires a carefully designed flight trajectory and often a precision guidance system to achieve the desired results. Control of the vehicle in response to guidance commands implies control of lift and drag throughout the flight. This is a nontrivial task for entry from Earth orbit, because it spans an aerodynamic flight range from subsonic speeds to Mach 25 (i.e., entry by Earth orbit), and even higher speeds are encountered for hyperbolic entry (i.e., entry by interplanetary orbit).

In keeping with our approach, we present the simplest analysis that treats the issues of salient interest to the re-entry vehicle designer.

## 2.2 Initial Specific Energy for Some Entry Missions

To directly sample the atmosphere of a planet or to land on its surface requires the vehicle to decelerate from the entry velocity at arrival to a low descent speed. The amount of energy to be lost in a braking maneuver is very large, and this must be dissipated by heat. Some of this heat passes into the vehicle, but most is given to the atmosphere, and this is necessarily given the total high specific energy. The total specific energy for several planetary missions is given in Table 2.1 [1].

## 2.3 Equations for Planar Flight

Figure 2.1 shows the geometry of atmospheric entry for planar flight over a spherical, nonrotating planet<sup>2</sup> [2].

We take this model to be the simplest one that allows presentation of the important phenomena. We have:

$$\frac{dV}{dt} = -\frac{D}{m} - g \sin \gamma \quad (2.1)$$

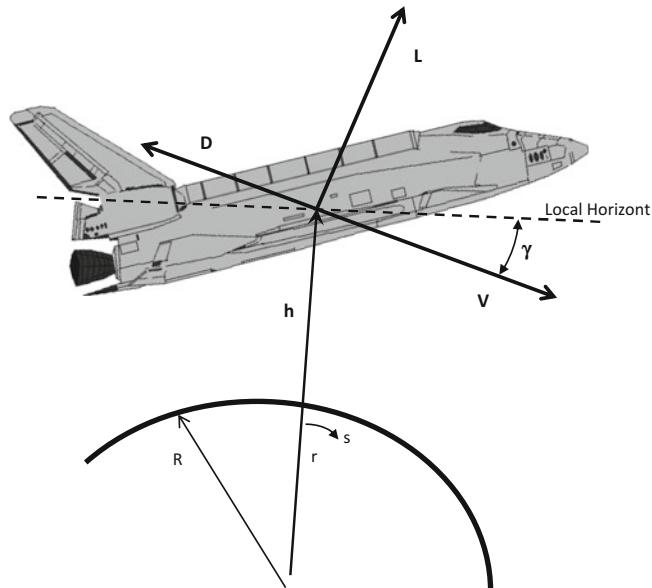
---

<sup>1</sup>It is worth noting that in several hundred missions over more than four decades of manned spaceflight, there has been only one fatal launch accident, the Challenger 51-L mission. Numerous launch abort procedures have evolved, and a variety of these (on-pad, in-flight, and abort-to-orbit) have been exercised in particular cases. In contrast, there have been three missions involving fatal re-entry system failures of one kind or another (Soyuz 1, Soyuz 11, and *Columbia* STS-107) and several other close calls. Though the technology of atmospheric entry is relatively mature, it remains very exacting in its demands, a characteristic deriving in part from the general lack of plausible abort scenarios following a primary system failure.

<sup>2</sup>Aside from the fact that thrust is normally zero for entry flight, the Flight Mechanics are the same as those for launch vehicle performance.

**Table 2.1** Initial specific energy for some atmospheric entry missions

Planet/Moon	Typical entry velocity range $V_e$ km/s	Entry altitude $h_e$ km	Specific energy MJ/kg
Venus	Pioneer 11.5	120	66
	Mercury orbiter 16	120	128
Earth	Suborbital: 6	120	18
	Orbital: 8	120	32
	Lunar return		
	Apollo: 11	120	61
	Mars/comet Return: 13–16.5	120	85–136
Mars	Viking: 4.5	120	10
	Marsnet: 6	120	18
	Mesur: to 8	120	32
Jupiter	Gallileo: 48		1,152
Saturn	25		313
Titan	Huygens: 6	1,000	18
	Aerocapture: 8		32
Uranus	25–26	500	313–338
Neptune	24–27	450	288–365

**Fig. 2.1** Atmospheric entry geometry

$$V \frac{d\gamma}{dt} = \frac{L}{m} - \left( g - \frac{V^2}{r} \right) \cos \gamma \quad (2.2)$$

$$\frac{ds}{dt} = \left( \frac{R}{r} \right) V \cos \gamma \quad (2.3)$$

$$\frac{dr}{dt} = \frac{dh}{dt} = V \sin \gamma \quad (2.4)$$

$$L = \frac{1}{2} \rho V'^2 S C_L \quad (2.5)$$

$$D = \frac{1}{2} \rho V'^2 S C_D \quad (2.6)$$

$$g = g_s \left( \frac{R}{R+h} \right)^2 \quad (2.7)$$

where

$V$  = inertial velocity magnitude

$V'$  = speed relative to planetary atmosphere

$R$  = planetary radius

$h$  = height above surface

$r = R + h$  = radius from planetary center

$s$  = downrange travel relative to nonrotating planet

$\gamma$  = flight-path angle, positive above local horizon

$m$  = vehicle mass

$L$  = lift force, normal to flight path

$D$  = drag force, parallel to flight path

$C_L$  = lift coefficient

$C_D$  = drag coefficient

$\rho$  = atmosphere density

$S$  = vehicle reference area for lift and drag

$g$  = gravitational acceleration

$g_s$  = surface gravitational acceleration

These are the equations for planar flight over a nonrotating spherical planet. They may be integrated forward in time subject to prescribed entry interface conditions ( $r_e$ ,  $V_e$ ,  $\gamma_e$ ), a model for the atmosphere density  $\rho(h)$ , and specified values of the vehicle control parameters  $C_L$  and  $C_D$ . Indeed, this would be essential prior to specification of a flight vehicle configuration and entry trajectory. However, direct numerical integration procedure will produce more accurate results (which incidentally justifies the use of a more sophisticated mathematical and physical model), but at the cost of considerable loss of insight.

Furthermore, the assumption of a nonrotating planet introduces three basic errors. First, equations of motion are valid as written only in an inertial frame; neglect of planetary rotation involves neglect of the centrifugal and Coriolis forces generated by the transformation of the time derivatives to a rotating frame. Predictions of position and, to a smaller extent, velocity relative to the planetary surface will be in error if the rotational effect is omitted.

The atmosphere shares the planetary rotation, which tends to carry the vehicle along with it, thus altering the trajectory. Also, errors are introduced in the aerodynamic modeling of the flight vehicle if the atmosphere-relative velocity  $V'$  is not used.

Finally, planetary rotation aids the re-entry by reducing the initial velocity in the direction of rotation.

To obtain the broader perspective that is possible with an analytical solution, three simplifying assumptions are employed:

1. The atmosphere density<sup>3</sup> is approximated by means the isothermal atmosphere model.
2. The gravitational acceleration  $g$  is assumed constant.
3. In Eq. (2.2) we employ the approximation:

$$\frac{V^2}{r} \approx \frac{V^2}{R} \approx \frac{V^2}{r_e} \quad (2.8)$$

Some comments on these assumptions are in order.

Concerning the first assumption, it is worth noting that prior to any mission involving an entry into the atmosphere, sufficient detail must be known or estimated in order to construct an engineering model of the atmosphere. The model must take account of the extremes of conditions likely to be encountered since this will affect the entry vehicle performance considerably. Even the atmosphere of the Earth has large variability and many unknowns particularly in the upper atmosphere. The derivation of a model atmosphere is the first step leading to the engineering models which contain the extreme variability. Indeed, it follows that using the ideal gas law

$$p = \rho R_{\text{gas}} T \quad (2.9)$$

where  $R_{\text{gas}}$  is the specific gas constant, equal to 288.28 J/Kg/K, and the hydrostatic equation:

$$d\rho = -\rho g dr \quad (2.10)$$

---

<sup>3</sup>Although for numerical calculations a more detailed model such as the U.S. Standard Atmosphere might be employed, such model is inappropriate for analytical work where closed-form results are desired.

we obtain the differential relation

$$\frac{d\rho}{\rho} = - \left( \frac{g}{R_{\text{gas}}} + \frac{dT}{dr} \right) \frac{dr}{T} = -\beta dr \quad (2.11)$$

where  $T$  is the absolute temperature. Therefore, by integrating we have the atmosphere profile

$$\rho(h) = \rho_s e^{-\beta h} \quad (2.12)$$

where

$$h = r - R.$$

$\beta^{-1}$  = scale height, (Eq. 2.12) highlights that the scale height is a measure of the interval in which the density reduces by a factor of  $e$ .

$\rho_s$  = surface density.

With the assumption of isothermal<sup>4</sup> atmosphere (no. 1) and constant gravitational acceleration (no. 2), the scale factor  $\beta$  is constant:

$$\beta = -\frac{1}{T} \left( \frac{g}{R_{\text{gas}}} + \frac{dT}{dr} \right) \quad (2.13)$$

The scale height is therefore a particular characteristic of each planetary atmosphere. Indeed, there are at least eight bodies in our solar system with atmospheres thick enough to use for aerodynamic deceleration of a capsule. These are shown in Table 2.2 with approximate constituents [1]. The constituents of Earth, Mars, and Venus are well established from atmosphere probe missions.<sup>5</sup> However, there remain quite large uncertainties in the models for the other planets. Estimates of the uncertainty are important criteria for aerothermodynamic design since the chemistry and consequent radiative and convective heat fluxes will change with different atmospheric constituents.

Assumption no. 2 follows considering that, for the Earth, with the entry interface altitude commonly taken by convention as 120 km, variations in  $g$  amount to no more than 4 %, an acceptable error at this level of study.

The remaining assumption that variations in  $(l/r)$  are negligible in Eq. (2.2) contributes an error of about 2 % over the entry altitude range of interest for the Earth. This is insignificant in comparison with other approximations thus far employed. In this chapter, we will consistently use  $(1/r_e)$  to replace  $(l/r)$  in Eq. (2.2) and derivations that follow from it.

<sup>4</sup>The Earth's atmosphere contains regions of strong temperature gradient, with resulting substantial variations in scale height. For entry analysis as given here, it is customary to select  $\beta^{-1}$  for the best fit according to some criteria. Recommended value ranges between 6.7 and 7.165 km.

<sup>5</sup>The estimation of constituents is made from remote spectroscopic measurements and from geological time-scale modeling.

**Table 2.2** Some characteristics of Solar System bodies with atmospheres

Planet/moon	Mass (Earth = 1)	Diameter km	Surface gravity (Earth = 1)	Surface pressure Atm	Scale height $\beta^{-1}$ km	Approximate nominal atmosphere
Venus	0.815	12,104	0.9	95.0	5.3	96 % CO <sub>2</sub> 4 % N <sub>2</sub>
Earth	1.0	12,756	1.0	1.0	7.1	78 % N <sub>2</sub> 21 % O <sub>2</sub> 1 % Ar
Mars	0.11	6,786	0.38	0.0078	7.6	97 % CO <sub>2</sub> 3 % N <sub>2</sub>
Jupiter	317.8	142,800				11 % He 89 % H <sub>2</sub>
Saturn	95.2	120,000				80 % He 20 % H <sub>2</sub>
Titan	0.023	5,150	0.138	0.0015	38	87 % N <sub>2</sub> 3 % CH <sub>4</sub> 10 % Ar
Uranus	14.6	50,800				15 % He 85 % H <sub>2</sub>
Neptune	17.2	48,600				19 % He 81 % H <sub>24</sub>

So, in order to take advantage of an analytical approach to the problem of entry particle dynamics, it is worth noting that two independent variable transformations are normally employed in conjunction with the assumptions discussed earlier.

It is customary to eliminate time and altitude in favor of density through the kinematic relation:

$$\frac{d}{dt} = \frac{dr}{dt} \frac{d}{dr} = V \sin \gamma \frac{d}{dr} \quad (2.14)$$

and the density model

$$d\rho = -\rho_s e^{-\beta h} dh \quad (2.15)$$

or

$$\frac{d}{dr} = -\beta \rho \frac{d}{d\rho} \quad (2.16)$$

Thus, with some additional manipulations, Eqs. (2.1) and (2.2) are transformed to yield

$$\frac{d}{d\rho} \left( \frac{V^2}{gr_e} \right) = \left( \frac{SC_D}{m} \right) \left( \frac{1}{\beta} \sin \gamma \right) \left( \frac{V^2}{gr_e} \right) + \frac{2}{\rho \beta r_e} \quad (2.17)$$

$$\frac{d}{d\rho} (\cos \gamma) = \left( \frac{1}{2\beta} \right) \left( \frac{SC_D}{m} \right) \left( \frac{L}{D} \right) - \left( \frac{gr_e}{V^2} - 1 \right) \frac{\cos \gamma}{\rho \beta r_e} \quad (2.18)$$

These are the *reduced planar equations for flight over a nonrotating spherical planet*.

The reduced equations still cannot be integrated directly and thus require further approximations to obtain closed-form results. Nonetheless, they are worthy of some examination at this point.

In reduced form, the dependent variables are the nondimensional energy ( $V^2/gr_e$ ) and  $\gamma$ , with  $\rho$  the independent variable. Because at the entry altitude

$$gr_e = \frac{\mu}{r_e} = \frac{GM}{r_e} = (V_{circ}^2)_e \quad (2.19)$$

it is seen that the entry energy is referenced to the circular velocity at entry altitude.

Specification of entry interface conditions ( $V_e$ ,  $\gamma_e$ ,  $\rho_e$ ) is sufficient to determine a particular trajectory subject to the fixed parameters in Eqs. (2.17) and (2.18).

Trajectory solutions take the form of velocity and flight-path angle as a function of density, the independent variable. The location is obtained, if required, from Eqs. (2.3) and (2.4), with Eq. (2.8) relating altitude to density.

Four parameters control the solution of Eqs. (2.17) and (2.18): *two define the vehicle and two define the relevant planetary characteristics*.

The vehicle parameters are the lift-to-drag ratio L/D and the ballistic coefficient,<sup>6</sup> which is the mass of the vehicle divided by the drag area,  $m/S_{ref}C_D$ .

The planetary entry environment is determined by the radius  $r_e$  and the atmosphere scale height  $\beta^{-1}$ .

The sources of parameter variation can be both natural and artificial. That is, L/D and the ballistic coefficient will vary considerably over the Mach 25 to 0 entry flight regime due to the differing flowfield dynamics. Additionally, however, the vehicle L/D is the primary control parameter available to the trajectory designer for tailoring the entry profile. Substantial mission flexibility can be gained with judicious L/D control. This cannot be modeled in the closed-form results derived from Eqs. (2.17) and (2.18) and offers another reason why detailed trajectory design requires a numerical approach.

Some discussion of the physical significance of the terms in the reduced equations is in order, because in later sections we will obtain approximate solutions based on assuming a flat Earth, no gravity, small flight-path angle, etc.

Equations (2.1), (2.2), (2.3), (2.4), (2.5), (2.6), and (2.7) clearly show the influence of various terms such as lift, drag, and centrifugal force. The physical identity of the various terms is not as clear in the reduced form of Eqs. (2.17) and (2.18).

---

<sup>6</sup>The ballistic coefficient is a measure of the ability of an object to overcome fluid resistance. Typical values for spacecraft will be on the order of 10–100 kg/m<sup>2</sup>. It is shown to be the primary entry vehicle parameter for ballistic entry.

The first term on the right-hand side of Eq. (2.17) is the reduced drag, and the second term ( $2/\rho\beta r_e$ ) is the reduced form of the tangential gravitational component,  $g \sin\gamma$ , in Eq. (2.1). Depending on the vehicle configuration and flight conditions, one of these terms may be dominant.

The first term on the right-hand side of Eq. (2.18) is the reduced lift force. The term ( $g - V^2/r$ ) in Eq. (2.2) gives the net normal force contribution of gravity and centrifugal acceleration. The corresponding term on the right-hand side of Eq. (2.18) is obvious; note, however, that  $gr_e/V^2$  is the gravitational term, whereas “1” is the reduced centrifugal term.

The surface density  $\rho_s$  appears only through Eq. (2.8), which relates density to altitude.

Such simplification yields several possible first-order entry trajectory solutions, classically denoted as:

1. Ballistic entry;
2. Equilibrium glide entry;
3. Skip entry.

These solutions may be adequate within a restricted range of conditions, but most results are approximate only and are primarily suited to initial conceptual design. However, they are very useful in demonstrating the types of trajectories that can exist and the parameters that are important in determining them.

### 2.3.1 *Ballistic Entry*

First-order ballistic entry analysis involves two assumptions in addition to those thus far employed. By definition of ballistic entry, zero lift is assumed. We also employ the approximation

$$\frac{1}{\beta r_e} \cong 0 \quad (2.20)$$

which results in dropping terms in Eqs. (2.17) and (2.18) where  $\beta r_e$  is in the denominator.

Some examination of these assumptions is in order.

The zero-lift approximation is often quite accurate and can be made more so when desired. Entry bodies possessing axial symmetry and flown at zero angle of attack will fly nominally ballistic trajectories.<sup>7</sup> The second approximation is

---

<sup>7</sup>In a practical vehicle, small asymmetries will always produce an offset between the center of mass and the center of pressure. This causes the vehicle, unless it is spherical, to fly aerodynamically

somewhat less valid. Although it is true that  $\beta r_e$  is typically large (approximately 900 for the Earth), this does not justify dropping all terms in Eqs. (2.17) and (2.18) where it appears in the denominator. In particular,  $(2/\rho\beta r_e)$  represents the reduced gravitational force along the trajectory. By omitting it, we assume that the drag force dominates, which is not always true.

The drag is always small and usually comparable to the tangential gravitational force at the entry interface. Toward the end of the entry phase, when the velocity becomes small,  $(2/\rho\beta r_e)$  will again dominate, and neglecting it will lead to inaccuracy.

From the preceding comments, it is seen that our second ballistic entry assumption corresponds to neglecting gravity with respect to drag in Eq. (2.1) and to neglecting the difference between gravitational and centrifugal force in Eq. (2.2). Thus, first-order ballistic entry may be viewed as a zero-g, flat-Earth solution.

In any case, if terms containing  $(1/\beta r_e)$  are dropped and zero lift is assumed, Eq. (2.18) integrates immediately to yield

$$\cos \gamma = \cos \gamma_e \quad (2.21)$$

i.e., the flight-path angle during descent remains constant at the entry value.

The validity of this result is obviously somewhat questionable. Intuition and experience suggest that for shallow entry angles, such as those that are required for manned flight, the vehicle will undergo a lengthy high-altitude deceleration and then, its energy depleted, nose over into a nearly vertical trajectory. Also, the shallow entry angle produces a lengthier entry, with consequently more time for gravity to curve the flight path. Nonetheless, when entry occurs at a reasonably steep angle, the flight path is indeed nearly straight.

Equation (2.17) may be integrated subject to our assumptions to yield

$$V = V_e \exp \left[ \left( \frac{1}{2\beta} \right) \left( \frac{\rho_s}{\sin \gamma_e} \right) \left( \frac{SC_D}{m} \right) \exp(-\beta h) \right] \quad (2.22)$$

for the velocity as a function of altitude and entry flight-path angle.

Of possibly greater interest is the derivative of velocity, the acceleration, which can be shown to have a peak value of

$$a_{\max} = -\frac{\beta V_e^2}{2e} \sin \gamma_e \quad (2.23)$$

It is clear that the maximum deceleration is independent of the physical characteristics of the entry vehicle and depends only on entry speed,  $V_e$ , and flight-path angle,  $\gamma_e$ .

---

trimmed at some angle of attack, inducing a lift force. However, this may be dealt with, by slowly rolling the vehicle during the entry to cancel out any forces normal to the velocity vector. For example, the Mercury spacecraft was rolled at a nominal 15 deg/s rate during re-entry.

The maximum deceleration occurs at altitude

$$H_{\text{crit}} = \frac{1}{\beta} \ln \left[ \left( -\frac{1}{\beta} \right) \left( \frac{\rho_s}{\sin \gamma_e} \right) \left( \frac{SC_D}{m} \right) \right] \quad (2.24)$$

and velocity

$$V_{\text{crit}} = \frac{V_e}{e} \quad (2.25)$$

The vehicle speed at maximum deceleration bears a fixed relationship to the entry speed ( $-61\%$ ), while the corresponding altitude depends on the physical characteristics and flight-path angle but not on the entry speed.

If the altitude of peak deceleration is to be positive, the argument of the logarithm in Eq. (2.24) must be greater than unity. Assuming hypervelocity impact with the ground is to be avoided, the useful range of entry angles is defined by

$$0 < -\sin \gamma_e < \left( \frac{\rho_s}{\beta} \right) \left( \frac{SC_D}{m} \right) \quad (2.26)$$

The ballistic entry results just given should be used with caution. For example, Eq. (2.23) predicts zero peak deceleration for  $\gamma_e = 0$ , a grazing entry. The first-order analysis provides a very poor model of the entry in such a case. The second-order analysis by Chapman summarized in Fig. 2.2, shows that ballistic entry from low circular Earth orbit has an irreducible deceleration load of about 8 g, which occurs for flight-path angles between  $0^\circ$  and  $-1^\circ$  [2].

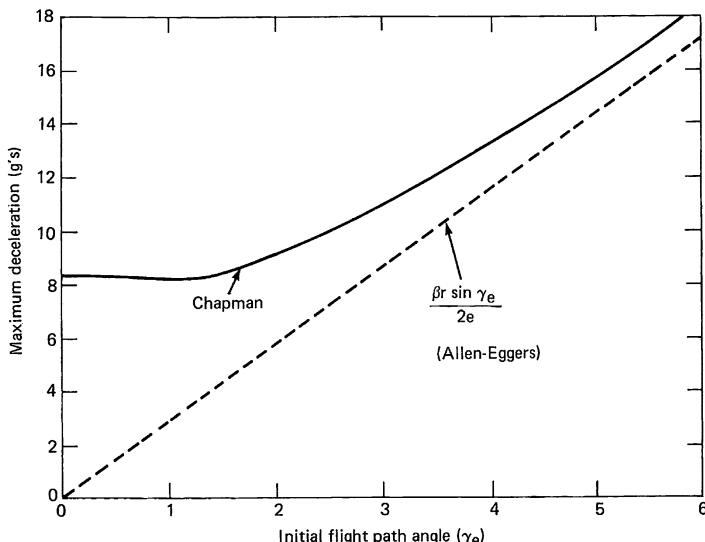
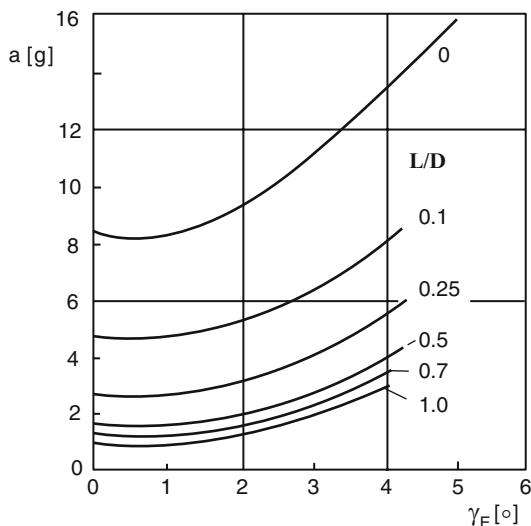


Fig. 2.2 Deceleration loads for ballistic entry from Earth orbit

**Fig. 2.3** Deceleration force versus entry angle as a function of L/D



So, entry at hyperbolic speed is practical only at fairly steep angles and consequently very high deceleration if skipout is to be avoided.

For flight-path angles steeper than about  $5^\circ$ , the theories are in reasonable agreement as to trend, though the first-order theory underpredicts the deceleration by about 1 g.

Thus, due to the limitation in negative “g’s” that mankind can tolerate, manned ballistic re-entry for entry incidences higher than  $4^\circ$  is not possible. Nevertheless, a moderate value of L/D greatly eases the entry dynamic load. For instance, Fig. 2.3 shows the g forces versus entry angle for some low to medium L/D configurations [1]. For zero-entry angle, one could obtain acceptable g forces to the expense of landing accuracy and integrated heat load. It is interesting to note that the g forces reduce rapidly even for low L/D vehicles. The 3 g limit can be obtained with L/D configurations of 0.25 as long as their entry angle is lower than  $3^\circ$  (Apollo has L/D = 0.25 till 0.35). Indeed, lift can be used to reduce the level of deceleration as well as the heating rates during re-entry.

Figure 2.4 shows a typical shallow-angle ballistic entry solution, obtained by numerically integrating Eqs. (2.1, 2.2, 2.3, 2.4, 2.5, 2.6, and 2.7) [2]. The sharp peak in entry deceleration and the rather high value of that peak are characteristic of ballistic entry.

As indicated earlier, the peak is seriously underestimated in this case by Eq. (2.23), which predicts a 3.6 g maximum deceleration.

Note also in Fig. 2.4 the difference between the inertial and Earth-relative entry speed. The Earth-relative (hence atmosphere-relative) speed should be employed for  $V_e$ ; however, the approximations inherent in a first-order solution are such that correcting for atmosphere-relative velocity may not be important. If used, the appropriate correction is

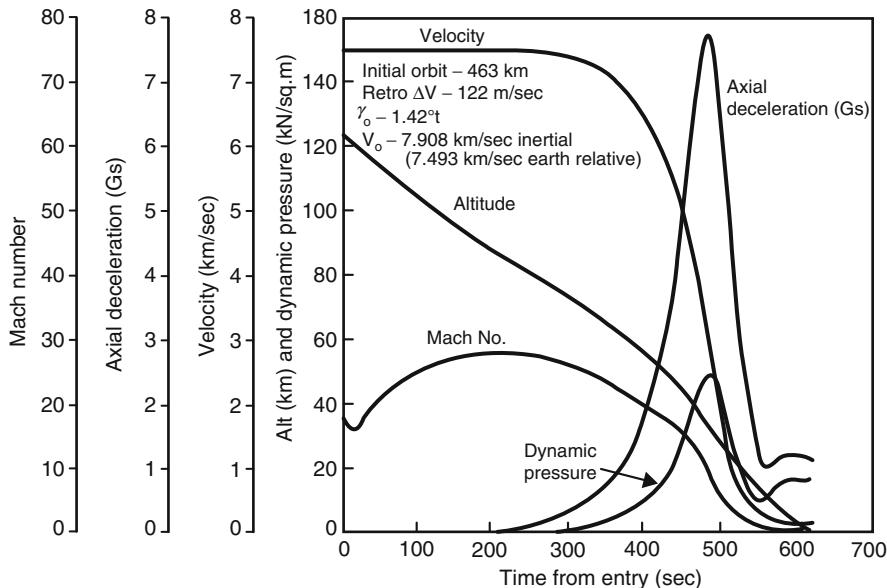


**Fig. 2.4** Typical ballistic entry from Earth orbit

$$V'_e = \left[ 1 - \left( \frac{\omega r_e}{V_e} \right) \cos i \right] V_e \quad (2.27)$$

where

$\omega$  = angular velocity of Earth,  $7.292 \times 10^{-5}$  rad/s

$V_e$  = inertial entry velocity

$V'_e$  = Earth-relative entry velocity

$i$  = orbital inclination

$r_e$  = entry interface radius.

Purely ballistic entry has a somewhat limited range of application; however, within this range, it is quite useful and is widely employed. It is simple to mechanize, requiring little or no guidance beyond stabilization for the deorbit burn, if any. Entry and landing accuracy is determined primarily by the precision to which  $V_e$  and  $\gamma_e$  are controlled, knowledge of the ballistic coefficient, and variations in atmosphere properties. However, relatively large dispersions in the controlling parameters can usually be tolerated without disaster; the technique is quite robust when, again, one is within its range of applicability.

Ballistic entry has seen application to numerous vehicles, including the manned US Mercury spacecraft and Russian Vostok/Voskhod series, as well as unmanned spacecraft, including Discoverer, Pioneer Venus, and Galileo.

### 2.3.2 Equilibrium Gliding Entry

In contrast to ballistic entry, first-order gliding entry analysis assumes that the vehicle generates sufficient lift to maintain a lengthy hypersonic glide at a small flight-path angle. Clearly this is an idealization. Substantial lift is readily obtained at hypersonic speeds, and it is possible to achieve shallow-angle gliding flight over major portions of the entry trajectory. However, a practical vehicle configuration for an extended hypersonic glide will be poorly suited to flight at low supersonic and subsonic speeds as well. Toward the end of its flight, such a vehicle must fly at a steeper angle to maintain adequate airspeed for approach and landing control.

This is readily illustrated by the space shuttle entry. The entry guidance phase is initiated at the entry interface altitude of 120 km with the flight-path angle typically about  $-1.2^\circ$ . It terminates when the shuttle reaches an Earth-relative speed of about 760 m/s (Mach 2.5), at an altitude of approximately 24 km, and a distance to the landing site of about 110 km. This phase of flight covers a total range of roughly 8,500 km, with the average flight-path angle on the order of  $-1^\circ$ . The shuttle's hypersonic glide phase is considerably longer than was the case for preceding manned vehicles. Upon completion of entry guidance, the terminal area energy management (TAEM) phase is initiated. The goal of this procedure is to deliver the orbiter to the runway threshold at the desired altitude and speed for approach and landing.

This phase of flight covers a range of 110 km while descending through 24 km of altitude, at an average flight-path angle of about  $-12^\circ$ , an order of magnitude steeper than that for the hypersonic phase.

The results of this section, although inadequate in the terminal flight regime, may well be appropriate for the major portion of a gliding entry.

In keeping with the small angle assumption noted earlier, we assume  $\sin\gamma \cong \gamma$ ,  $\cos\gamma \cong 1$ , and hence  $d(\cos\gamma)/d\rho \cong 0$ . With these approximations, Eq. (2.18) is reduced to an algebraic equation for energy as a function of density

$$\frac{V^2}{gr_e} = \frac{1}{\left[1 + \left(\frac{r_e}{2}\right)\left(\frac{SC_D}{m}\right)\left(\frac{L}{D}\right)\rho\right]} = \frac{1}{\left[1 + \left(\frac{r_e}{2}\right)\left(\frac{SC_D}{m}\right)\left(\frac{L}{D}\right)\rho_s e^{-\beta h}\right]} \quad (2.28)$$

Equation (2.28) may be differentiated with respect to  $\rho$  and substituted into Eq. (2.17) to solve for the flight-path angle. Consistent with the assumption of small  $\gamma$ , we neglect the tangential component of gravitational acceleration and obtain

$$\sin\gamma \cong \gamma \cong -\frac{2}{\left[\left(\beta r_e\right)\left(\frac{L}{D}\right)\left(\frac{V^2}{gr_e}\right)\right]} \quad (2.29)$$

Note that, although the flight-path angle  $\gamma$  is assumed to be small and its cosine constant,  $\gamma$  is not itself assumed constant.

Equation (2.28) is an equilibrium glide result, where the gravitational force cancels the sum of the centrifugal and lift forces. This is readily seen by noting

the physical identity of the various terms in Eq. (2.18). Of course, the equilibrium is not exact because the derivative term in Eq. (2.18) is not identically zero. For this reason, the trajectory given by Eq. (2.28) is sometimes, and more correctly, referred to as a pseudo-equilibrium glide.

To obtain the acceleration along the trajectory, note from Eq. (2.1)

$$a = \frac{dV}{dt} \cong -\frac{D}{m} = -\left(\frac{V^2}{2}\right)\left(\frac{SC_D}{m}\right)\rho \quad (2.30)$$

where again we neglect the gravitational acceleration along the flight path.

Solving Eq. (2.28) for  $\rho$  and substituting above gives the tangential acceleration,

$$\frac{a}{g} = \left(\frac{V^2}{gr_e} - 1\right) \Big/ \left(\frac{L}{D}\right) \quad (2.31)$$

experienced by the vehicle during the equilibrium glide. Note that the maximum deceleration is encountered as the vehicle slows to minimum speed. Here we see the advantage of even small values of L/D in moderating entry deceleration loads (see Fig. 2.3).

It is seen that the deceleration increases as velocity is reduced and that even moderate L/D can reduce the deceleration significantly. For example, the Gemini capsule with L/D about 0.2 enabled the peak load to be reduced to about 5 g compared to the 8 g of the Mercury ballistic entry along the same initial flight path.

For the shuttle, which flies a major portion of its entry profile with a hypersonic L/D of about 1.1, Eq. (2.31) predicts essentially a 1 g re-entry. These results are consistent with flight experience.

By integrating the velocity along the entry trajectory, the total range of the equilibrium glide is found to be

$$s = \frac{r_e}{2} \left(\frac{L}{D}\right) \ln \left[ \frac{1}{\left(1 - \frac{V^2}{gr_e}\right)} \right] \quad (2.32)$$

Clearly, the greatest range is obtained when entry is performed at the maximum vehicle L/D.

As an example, consider a space shuttle entry at an atmosphere-relative speed of 7.5 km/s with a hypersonic L/D of 1.1 assumed. With these representative values, Eq. (2.32) yields a predicted range of about 8,000 km, in good agreement with flight experience. This may be somewhat fortuitous, because the shuttle in fact uses substantial lift modulation during entry to achieve landing point control. This is shown in Fig. 2.5 for the STS-2 re-entry [2]. Nonetheless, an L/D of 1.1 closely approximates the high-altitude, high-speed portion of the entry, and it is this portion that obviously has the most effect on total range.

Equation (2.32) is of limited utility when the entry speed approaches the reference circular velocity. In this case, the argument of the logarithm is almost

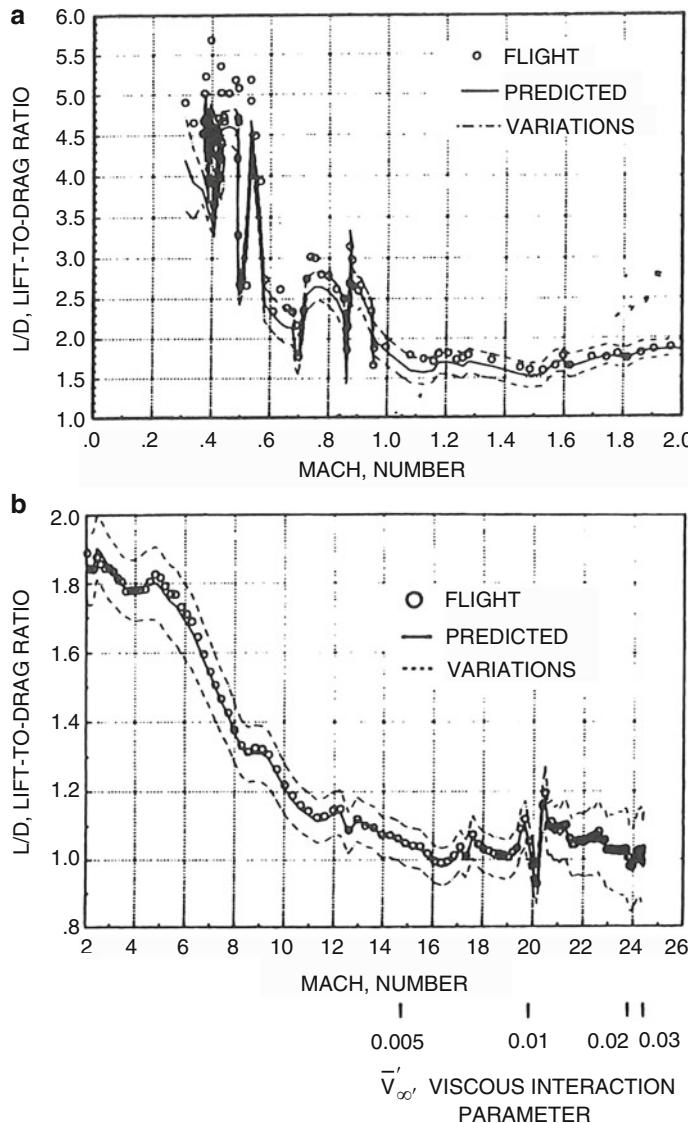


**Fig. 2.5** Lift modulation for STS-2 re-entry

singular and hence extremely sensitive to the value of the entry velocity. This reflects a limitation of the first-order theory rather than any real physical effect. Equation (2.32) is also invalid for the supercircular entry, because the logarithm becomes imaginary in this case.

Figure 2.6 shows an entry trajectory simulation result for the British horizontal take-off and landing (HOTOL) vehicle concept [2]. HOTOL was a mid-1980s design for an unmanned, reusable, single-stage-to-orbit vehicle intended for runway launch and landing.

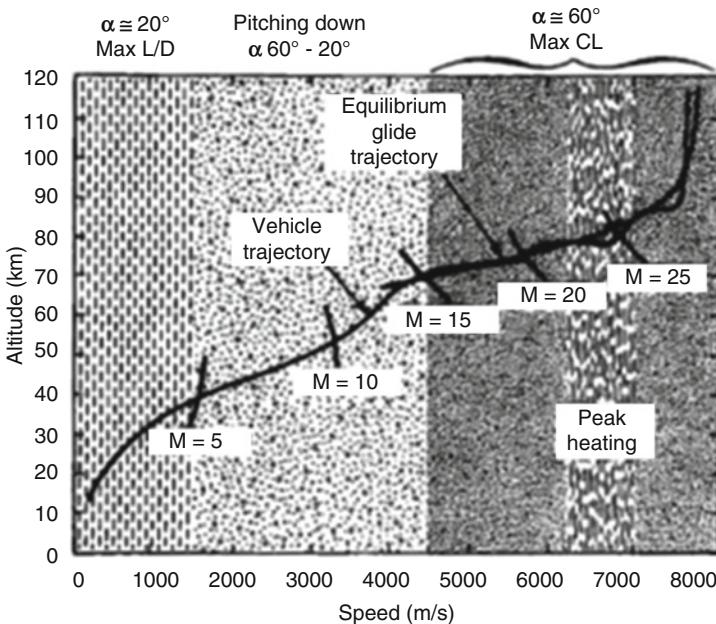


**Fig. 2.6** HOTOL entry trajectory

Because it was to be quite light, it needed to fly a high, shallow-angle gliding entry to minimize peak dynamic and thermal loads. As shown, the result is an entry profile that closely approximates the pseudo-equilibrium glide trajectory during the high-speed portion of the flight.

Finally, note that equilibrium glide is appropriate to entry from orbit since  $V_{\text{circ}}^2 = (gr)_e$ . Therefore, super-orbital entry implies negative lift, i.e., inverted flight. The equilibrium glide is not the only lifting entry of interest since at super-orbital speed, skip trajectories may be used where sufficient energy is lost prior to an exit from the atmosphere at suborbital velocity followed by a second suborbital entry. This is a form of aerocapture and was studied for Apollo. Alternatively the vehicle lift can be used to keep the vehicle in the atmosphere until velocity is suborbital when the vehicle may be rolled 180°. This was adopted for Apollo and was used in ESA studies for the Rosetta lifting capsule.

### 2.3.3 Skip Entry

Gliding entry flight is not restricted to the equilibrium glide condition discussed in the previous section. Of particular interest is the case of supercircular entry with sufficient lift to dominate the gravitational and centrifugal forces. This is essentially the first-order ballistic entry model with lift added. With proper selection of parameters, the so-called skip or skip-glide entry may be obtained.

Consider the high-speed entry of a lifting vehicle at an initially negative flight-path angle. As always, the vehicle and atmosphere parameters are considered constant. With lift dominant over gravity, the flight path will be turned upward ( $d\gamma/dt > 0$ ) so that the vehicle enters the atmosphere, reaches a certain minimum altitude, pulls up, and eventually exits the atmosphere at reduced speed. Provided the exit velocity and flight-path angle are properly controlled, a brief Keplerian phase ensues, followed by a second entry that occurs somewhat downrange from the first, as shown schematically in Fig. 2.7 [2].

This type of trajectory offers considerable flexibility in the control of high-speed entry. For example, at lunar return speeds of about 11 km/s, the kinetic energy to be dissipated is about twice that of a typical low-Earth-orbit entry (i.e., about 60 MJ/kg). This results in a very challenging thermal control problem, especially if the entry is required to occur in a single pass. With the skip entry, however, the vehicle can reduce its velocity sufficiently on its first pass to guarantee Earth capture. The brief suborbital lob allows radiative cooling and is followed by a second entry phase at lower speed.

Skip entry is also useful for range control and allows the vehicle to land in places that could not be reached via a single entry phase.

With the previously mentioned assumptions (0 g, flat Earth) for a first-order model, Eqs. (2.17) and (2.18) are reduced to

$$\frac{d}{dp} \left( \frac{V^2}{gr_e} \right) = \left( \frac{SC_D}{m} \right) \left( \frac{1}{\beta \sin \gamma} \right) \left( \frac{V^2}{gr_e} \right) \quad (2.33)$$

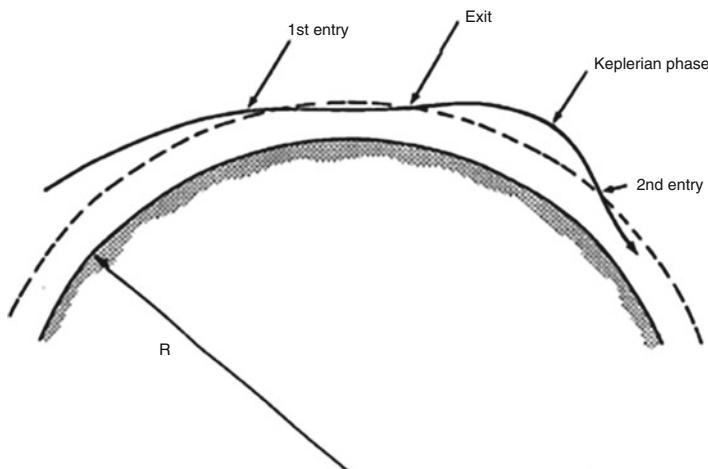


**Fig. 2.7** Skip entry trajectory

$$\frac{d}{d\rho} (\cos \gamma) = \left( \frac{1}{2\beta} \right) \left( \frac{SC_D}{m} \right) \left( \frac{L}{D} \right) \quad (2.34)$$

Assuming, as always, constant ballistic coefficient and L/D, Eq. (2.34) integrates immediately to yield the flight-path angle as a function of density (hence altitude):

$$\cos \gamma = \cos \gamma_e + \left( \frac{1}{2\beta} \right) \left( \frac{SC_D}{m} \right) \left( \frac{L}{D} \right) \rho \quad (2.35)$$

with the approximation  $\rho_e \cong 0$ . Since

$$\frac{dV}{d\gamma} = \frac{dV}{d\rho} \frac{d\rho}{d(\cos \gamma)} \frac{d(\cos \gamma)}{d\gamma} = -\frac{\frac{V^2}{2}}{\left( \frac{L}{D} \right)} \quad (2.36)$$

the velocity as a function of flight-path angle is found to be

$$V = V_e \exp \left[ -\frac{(\gamma - \gamma_e)}{\frac{L}{D}} \right] \quad (2.37)$$

Equations (2.35) and (2.37) constitute the first-order solution for gliding flight with lift large in comparison to other forces and range small with respect to the planetary radius. Though we are discussing skip entry, these approximations are also appropriate to gliding entry at medium or large flight-path angle.

For the skip entry, however, we note that  $\gamma = 0$  defines the pull-up condition.

Equation (2.35) then yields the density at pull-up,

$$\rho_{\text{pullup}} = \rho_{\max} = \frac{2\beta (1 - \cos \gamma_e)}{\left( \frac{SC_D}{m} \right) \left( \frac{L}{D} \right)} \quad (2.38)$$

and Eq. (2.37) gives the corresponding velocity

$$V_{\text{pullup}} = V_e \exp \left( \frac{\gamma_e}{\frac{L}{D}} \right) \quad (2.39)$$

Care must obviously be taken to ensure that the pull-up density corresponds to a positive altitude. Though this is not typically a problem for the Earth, it can be a constraint when considering skip entry at a planet, such as Mars, with a tenuous atmosphere.

Observing that both entry and exit occur at the same defined altitude (and hence the same density, often assumed zero), the exit flight-path angle is simply

$$\gamma_{\text{exit}} = -\gamma_e \quad (2.40)$$

From Eq. (2.37), the exit velocity is then

$$V_{\text{exit}} = V_e \exp \left[ \frac{(2\gamma_e)}{\frac{L}{D}} \right] \quad (2.41)$$

The acceleration along the trajectory is found to be

$$a = \frac{1}{2} \sqrt{1 + \left( \frac{L}{D} \right)^2} \left( \frac{S C_D}{m} \right) \rho V^2 \quad (2.42)$$

Maximum deceleration occurs at a small negative flight-path angle, i.e., just prior to pull-up. However, the value at pull-up ( $\gamma = 0$ ) is nearly the same and is much more easily obtained; hence,

$$a_{\max} \cong a_{\text{pullup}} = \sqrt{1 + \left( \frac{1}{\frac{L}{D}} \right)^2} (1 - \cos \gamma_e) \beta V_e^2 \exp \left( \frac{2\gamma_e}{\frac{L}{D}} \right) \quad (2.43)$$

Taken together, Eqs. (2.41) and (2.43) imply the existence of an entry corridor (see paragraph 2.7), that is an acceptable range of flight-path angles, for supercircular skip entry. The lower (steep entry) bound on  $\gamma_e$  is determined for a given L/D by the acceptable deceleration load. For a manned vehicle, a reasonable maximum might be 12 g, the design limit for the Apollo missions. The upper (shallow entry) bound on  $\gamma_e$  for supercircular entry is determined by the requirement that the exit velocity be reduced to a sufficiently low level to allow the second phase of entry to occur within a reasonable time. The Apollo command module, for example, had battery power for only a few hours after the service module was jettisoned and could not tolerate a lengthy suborbital lob.

### Explanation Box. The Apollo Re-entry

As an example of re-entry flight, consider that Apollo's lunar return was an aerocapture to ground from 11 km/s and achieved this with L/D  $\sim 0.3$  and with 12 g as maximum deceleration design limit.

Suppose that Apollo re-entry must be achieved by supercircular skip re-entry. So, let us determine the re-entry corridor. Thus, using the 12 g acceleration and an atmospheric scale height of 7.1 km, the steepest allowed entry angle is found from Eq. (2.43) to be  $-4.8^\circ$ . Assuming circular exit velocity to be the maximum acceptable (the vehicle will not go into orbit because the flight-path angle is nonzero at the exit interface, which is itself too low for a stable orbit), we find from Eq. (2.41) that the shallowest possible entry is  $-2.9^\circ$ .

(continued)

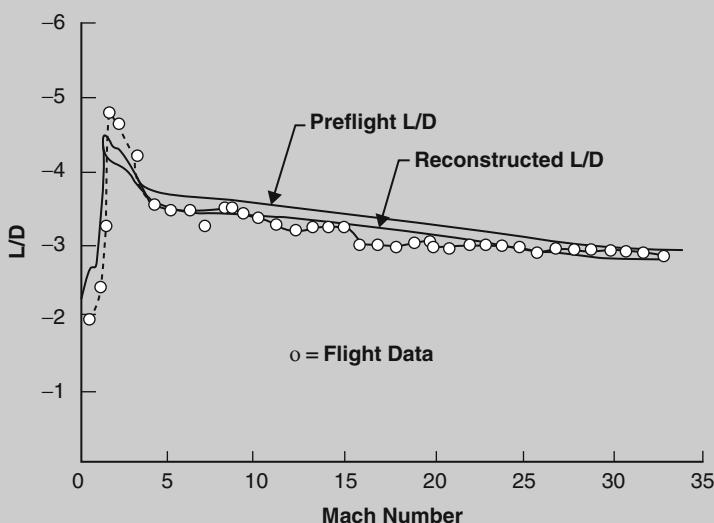


**Fig. 2.8** Apollo spacecraft lift-to-drag ratio

An indication of the accuracy and limitations of the first-order skip entry analysis presented here is obtained by noting that the Apollo 11 entry was initiated at a velocity- and flight-path angle of 11 km/s and  $-6.5^\circ$ , respectively.

The 12 g undershoot (steep entry) boundary was  $-7^\circ$  and the overshoot (shallow angle) boundary was  $-5^\circ$ . The relatively low decelerations for this rather high flight-path angle are due, of course, to the Apollo aerodynamic efficiency (see Fig. 2.3). Indeed, the predicted and actual L/D for the Apollo vehicle is shown in Fig. 2.8 [2].

Anyway, the preceding discussion of entry corridor limits, though relevant, is oversimplified. In addition to errors introduced by the first-order model, other limitations must be considered. The total entry heating load is aggravated by an excessively shallow entry, whereas the heating rate (but not usually the total heat load) is increased by steepening the flight path. Either case may be prohibitive for a particular vehicle and may modify the entry corridor width determined solely from acceleration and exit velocity requirements.

The constant L/D assumption is an unnecessarily restrictive artifact of the analytical integration of the equations of motion. A more benign, and thus safer, entry can be obtained at an initially shallow angle with the lift vector negative, i.e., with the vehicle rolled on its back. Once the vehicle has been

(continued)

pulled into the atmosphere in this manner, it may be rolled over and flown with positive lift to affect the skip. This strategy was employed for the Apollo lunar return.

As implied earlier, a skip entry sequence was possible with the Apollo command module and was initially selected as the nominal entry mode.

Refinement of the entry guidance and targeting philosophy ultimately led to the use of a modulated-lift entry in which a full skipout was avoided in favor of a trajectory that retained aerodynamic control throughout a nominal entry. However, the full skip phase was still available for trajectory control in the event of an off-nominal entry. Because of the conservative aerothermodynamic design of the Apollo vehicle, heating loads were not a factor in entry corridor definition. Coming back to the g-load experienced by astronauts during missions, it is worth noting that the Apollo flights were generally kept to maximum values of less than 8 g. Indeed, the maximum decelerations during re-entry for Apollo 7 through Apollo 17 are summarized in the following table.

This indicates the reason for the magnitude of the ballistic coefficient for operational manned entry vehicles being typically less than around 400 or 500 kg/m<sup>2</sup>.

Flight	Maximum g at re-entry
Apollo 7	3.33
Apollo 8	6.84
Apollo 9	3.35
Apollo 10	6.78
Apollo 11	6.56
Apollo 12	6.57
Apollo 13	5.56
Apollo 14	6.76
Apollo 15	6.23
Apollo 16	7.19
Apollo 17	6.49

In addition, Figs. 2.9, 2.10, and 2.11 show the acceleration history during boost and re-entry for some missions. Figure 2.9 provides the g-level of a typical launch profile of Saturn V.

(continued)

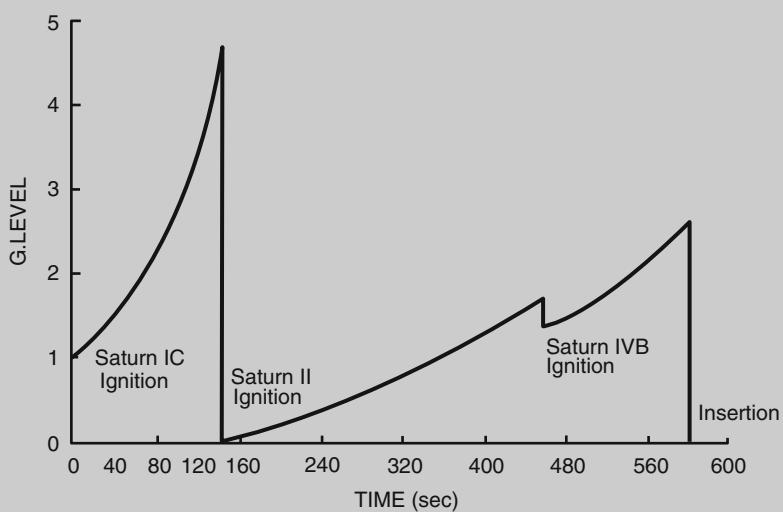


Fig. 2.9 Typical Apollo's launch profile—Saturn V launch vehicle

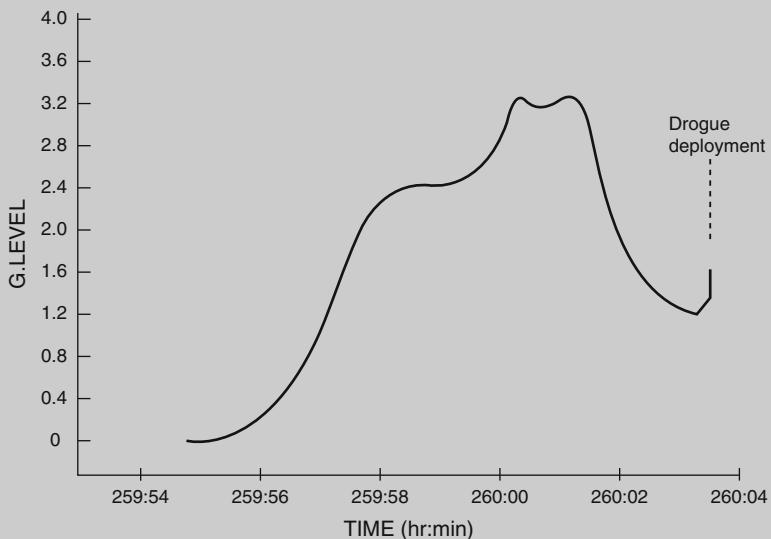
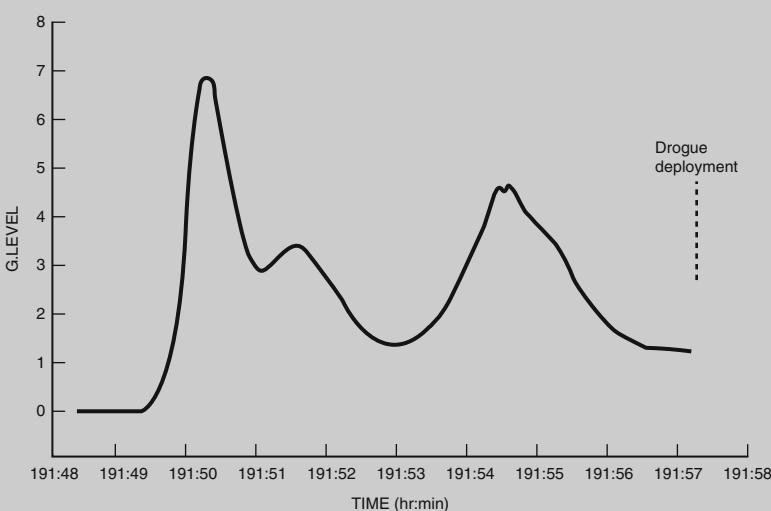


Fig. 2.10 Earth orbital re-entry profile of Apollo 7

(continued)



**Fig. 2.11** Lunar orbital re-entry profile of Apollo 10

As shown, during the first two minutes of ascent flight, the crew experienced a rapid increase of acceleration up to about 5 g followed by a sudden drop down to 0 g just after the first stage (i.e., Saturn 1C) release. After that, the maximum acceleration is equal to about 3 g just before to orbit insertion (i.e., end of launch phase) at  $t \cong 580$  s.

Finally, time histories of g-load recorded for the Apollo 7 and Apollo 10 re-entries are provided in Figs. 2.10 and 2.11, respectively.

### 2.3.4 Cross-Range Maneuvers

Thus far we have assumed that the entry trajectory lies in the plane of the initial orbit. However, if a lifting entry vehicle is banked (lift vector rotated out of the vertical plane defined by  $r$ ,  $V$ ), then a force normal to the original orbit plane (i.e.,  $L_n$ ) is generated and the vehicle flies a three-dimensional trajectory (see Fig. 2.12).

This may be done with both gliding and skip entry profiles as discussed earlier. As with the planar trajectories discussed previously, however, first-order results are available that yield considerable insight into the effect of banking maneuvers. Because cross-range control is often of interest even in the preliminary stages of entry vehicle and trajectory design, we will consider here some results of first-order three-dimensional entry analysis.

It is usually of interest to examine the maximum *footprint*, or envelope of possible landing points, to which an entry vehicle can be steered.

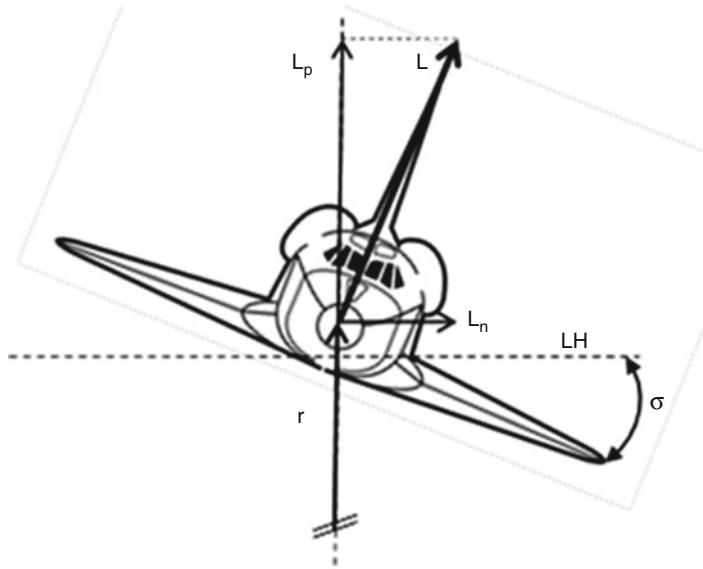


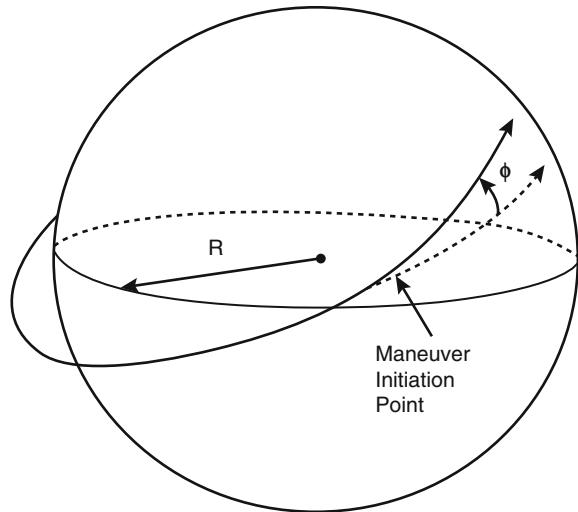
**Fig. 2.12** Lift decomposition due to a roll angle  $\sigma$

In-plane or downrange control for a lifting vehicle is attained through modulation of the lift-to-drag ratio. As seen in Eq. (2.32), maximum range is attained with flight at the highest available L/D. A landing at lesser range can be achieved by flying energy-dissipating maneuvers up and down in the entry plane, or back and forth across the initial plane. Cross-range maneuvers that do not cancel result in a lateral offset of the landing point, at some expense in downtrack range.

As shown in Fig. 2.12, in order to perform a lateral maneuver, a lifting entry vehicle must bank to obtain a turning force normal to the initial plane and, upon attaining the desired heading change, reduce the bank angle again to zero. For maximum lateral range, the bank angle modulation must be performed in such a way that the downtrack range is not unduly reduced, or else the cross-range maneuver will not have time to achieve its full effect. There will thus be an optimum bank angle history that allows the maximum possible cross-range maneuver for a given downrange landing point.

For analytical purposes, the optimum, time-varying, bank angle history must be replaced by an equivalent constant value that provides similar results while allowing integration of the equations of motion. Although justified by the mean value theorem of integral calculus, this procedure renders invalid any consideration of the trajectory history, preserving only the maximum capability information. If in addition we assume an equilibrium glide with small changes in heading angle, results for maximum lateral range may be obtained. To first order, the angular cross range is

**Fig. 2.13** Cross-range entry geometry



$$\phi = \frac{\pi^2}{48} \left( \frac{L}{D} \right)^2 \sin 2\sigma \quad (2.44)$$

where  $\sigma$  = optimum constant bank angle and  $\phi$  = latitude angle attained relative to great-circle equatorial plane of initial entry trajectory.

In terms of distance over the planetary surface, we have

$$s_{\perp} = R\phi \quad (2.45)$$

Figure 2.13 shows the geometry for a cross-range maneuver [2].

The use of  $(L/D)_{\max}$  in Eq. (2.44) implies, as with the planar equilibrium glide, that maximum cross range is achieved with flight at maximum L/D. Note that the Eggers solution yields  $\sigma = 45^\circ$  for the optimum constant bank angle.

This is intuitively reasonable, because it implies that use of the vehicle lift vector is evenly divided between turning ( $\sigma = 90^\circ$ ) and staying in the air ( $\sigma = 0^\circ$ ) long enough to realize the result of the turn. However, Eq. (2.44) overpredicts the cross-range travel that can be achieved with a given vehicle L/D. This is shown in Fig. 2.14, which compares the Eggers solution, the second-order result of Vinh, and the cross range achieved with the true optimal bank angle history [2].

It is seen that, for a vehicle L/D of 1.5 or less (small enough that even the maximum possible cross-range angle remains relatively small), the theories are in reasonable agreement.

As an example, consider the Gemini spacecraft with, as stated previously, an L/D of 0.2. Equations (2.44) and (2.45) yield a maximum cross-range travel of about 52.4 km. This is in excellent agreement with the actual Gemini vehicle footprint data, shown in Fig. 2.15 [2].

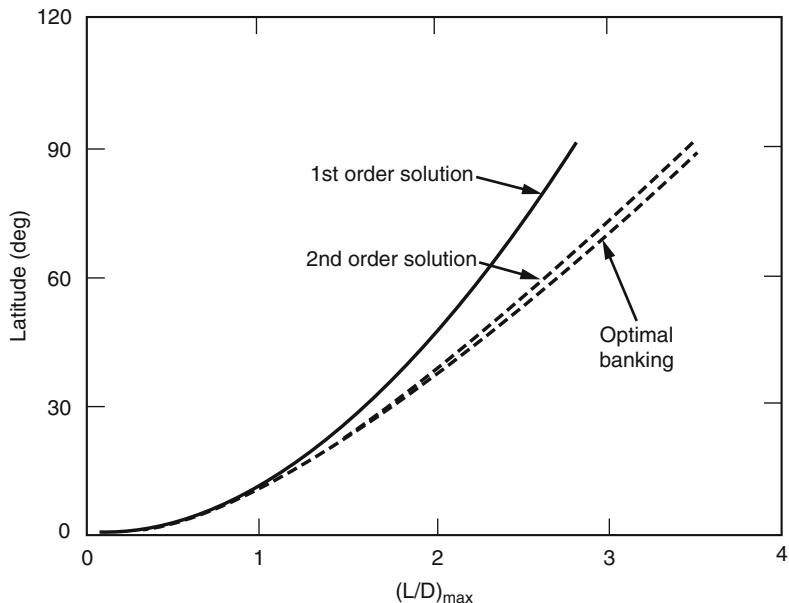


Fig. 2.14 Cross-range capability for varying lift-to-drag ratio

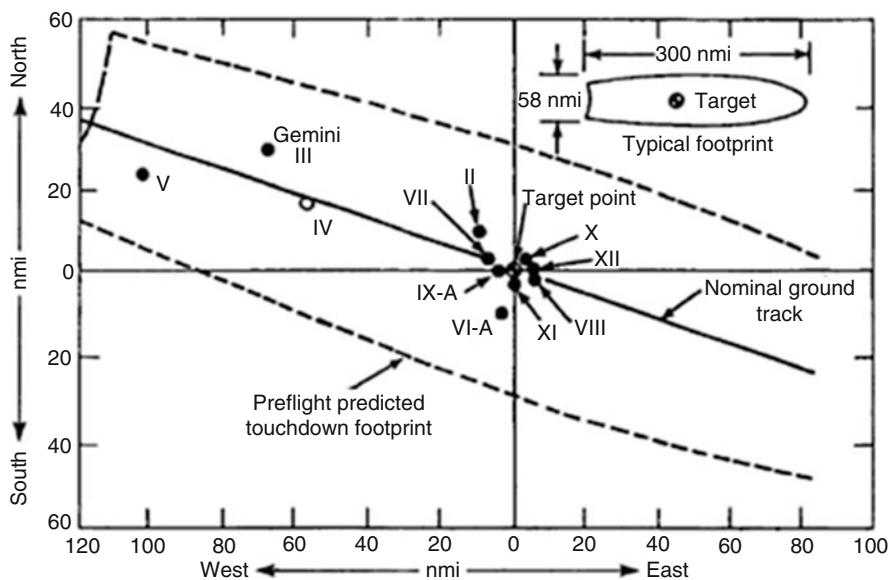


Fig. 2.15 Gemini landing footprint

The shuttle, with its much higher L/D, exhibits correspondingly greater cross-range capability. This allows the shuttle to land routinely at Edwards Air Force Base (34°N latitude) out of a 28.5° inclination orbit. This would be impossible for a low L/D vehicle. The maximum shuttle cross-range capability demonstrated to date has been 1,465 km, very close to the maximum value predicted by Eq. (2.45) for a vehicle with a hypersonic L/D of 1.1.

## 2.4 Heat Transfer for Perfect Gas and Chemically Reacting Flows

In this section, we focus on the basic principles and the derivation of some basic relationships used in heat transfer analysis for planetary entry.

Up to this point, we have considered only the particle dynamics of atmospheric entry, wherein the vehicle is completely characterized by its L/D and ballistic coefficient. This determines the flight trajectory and allows assessment of the vehicle acceleration and dynamic pressure loads, the downrange and cross-range travel, and the sensitivity of these quantities to the entry conditions and vehicle parameters.

On the other hand, of equal importance are the thermal loads imposed on the vehicle during entry. These are of two types: the *heating rate*,  $\dot{q}$ , and the *integrated heat load*,  $Q$ .

The allowed heating rate, either local or body-averaged, is a concern because of the thermal gradient induced from a heat flux according to Fourier's law<sup>8</sup>:

$$\dot{q} = -k \nabla T \quad (2.46)$$

where

$\dot{q}$  = power per unit area, W/m<sup>2</sup>.

$k$  = thermal conductivity, W/mK.

$\nabla T$  = gradient of temperature, K/m.

In materials with a nonzero coefficient of thermal expansion (i.e.,  $\alpha \neq 0$ ), a temperature gradient causes differential expansion and mechanical stress in the vehicle wall material.

The integrated heat load is obviously a concern in that the average vehicle temperature will increase with the energy input. It reads

$$Q = \int_{t_i}^{t_f} \dot{q} dt \quad (2.47)$$

where  $t_i$  and  $t_f$  are the initial and final time of entry flight, respectively.

---

<sup>8</sup>Note that the negative sign indicates that the heat flow is positive in the direction of temperature fall.

Trade-offs between allowed heating rate and integrated heat load are often necessary. Sustained high-energy flight at high altitude (e.g., gliding entry) reduces the instantaneous heating rate but, by extending the duration of the flight, may unacceptably increase the total heat absorbed.

As will be explained in Chap. 3, a more rapid, high-drag entry usually reduces the total energy input at the expense of incurring a very high local heating rate and may in addition result in unacceptable dynamic loads.

Entry vehicle heating results from the dissipation of the initial total (kinetic plus potential) energy through two heat transfer mechanisms, *convection* and *radiation*.

Convective heating occurs when the air, heated by passage through a strong bow shock in front of the vehicle, bathes the wall in a hot fluid stream.

If the air is hot enough, significant thermal radiation will occur as well. Radiative heat transfer is important when the entry velocity is greater than about 10 km/s and may be significant at considerably lower speeds.

Peak aerodynamic heating will usually occur in vehicle stagnation-point regions, such as on a blunt nose or wing/tail leading edges. However, turbulent flow along the vehicle afterbody can under some conditions produce a comparable or greater heat flux. Conversely, delayed onset of turbulence (i.e., turbulent transition at a higher than expected Reynolds number) can produce a substantially cooler aft body flow than expected.

Thermal control is a major entry vehicle design challenge. For instance, the specific kinetic energy that is dissipated during entry from low Earth orbit is about  $3 \times 10^7$  J/kg. This is sufficient to vaporize a heat shield composed of pure carbon ( $h_v = 6 \times 10^7$  J/kg) and equal to half the initial vehicle mass. If this is to be prevented, then the major portion of the entry kinetic and potential energy must be deflected to the atmosphere rather than the vehicle. A good aerothermodynamic design will allow only a few percent of this energy to reach the vehicle, as will be discussed in Chap. 3.

### 2.4.1 Fourier's Law and Convective and Diffusive Heat Transfers

From the theory of viscous fluid flow, it is known that the flowfield about an atmospheric entry vehicle develops a thin boundary layer close to the body to which viscous effects, including skin friction and heat transfer, are confined. In the case of a perfect gas<sup>9</sup> flow, the heat flux to the wall is proportional to the local temperature gradient only

---

<sup>9</sup>The perfect gas equation of state is applicable at pressure below 100 bar and/or temperature above 30 K when intermolecular forces are negligible. For most entry conditions, a perfect gas can be assumed,  $p = \rho RT$ . For a perfect gas, the internal energy is a function of temperature only. Therefore, it immediately follows that  $c_p$  and  $c_v$  are also functions of temperature only. For a calorifically perfect gas,  $c_p$  and  $c_v$  are constant, i.e.,  $\gamma = c_p/c_v$  is constant. The assumption of a perfect gas may not be valid at high-speed flow, i.e., high-temperature real gas flow. In this case,

$$\dot{q}_w = \left( k \frac{\partial T}{\partial y} \right)_w = \left( \rho \alpha c_p \frac{\partial T}{\partial y} \right)_w \quad (2.48)$$

where  $y$  is the coordinate normal to the wall and  $\alpha$  is the thermal diffusivity.

On the other hand, heat transfer in the chemically reacting case is the sum of the Fourier conduction component using the frozen conductivity (i.e., the conductivity that the mixture would possess if no chemical change occurred when a temperature gradient was imposed upon it), that is, the convective heat flux, plus a chemical term dependent on the diffusion of species toward the wall (i.e., diffusive heat flux):

$$\dot{q}_w = \left( k \frac{\partial T}{\partial y} \right)_w + \left( \sum \rho Y_i V_i h_i \right)_w = \left( k \frac{\partial T}{\partial y} \right)_w + \left( D_i \rho \sum h_i \frac{\partial Y_i}{\partial y} \right)_w \quad (2.49)$$

where for the  $i$ th species  $Y_i$  is the mass fraction,  $V_i$  the diffusion velocity,  $h_i$  the dissociation enthalpy, and  $D_i$  the diffusion coefficient.

The temperature and mass fraction gradients are obtained from the boundary-layer flowfield solution, determined from the boundary-layer edge properties and wall conditions. The edge conditions in turn follow from the inviscid solution for the flow over the entry vehicle. The vehicle heat transfer analysis is thus dependent on the detailed knowledge of the flowfield.

The difficulty of obtaining an accurate solution for the high-speed flowfield around an entry vehicle can hardly be overstated. The fluid is a chemically reacting gas, possibly not in equilibrium, probably ionized, and with potentially significant radiative energy transfer. Vehicle surface properties such as roughness and wall catalicity influence the flowfield and heat transfer analysis.

We note in passing that this partially ionized flowfield is the *plasma sheath* that interferes with air-to-ground communication during major portions of entry flight. This was the cause of the well-known *communications blackout*.

The advent of the Tracking Data Relay Satellite System (TDRSS) constellation has at least somewhat alleviated this problem; antennas on the leeward side of the space shuttle can generally complete the link to a TDRSS satellite. However, the roll maneuvers necessary for shuttle landing point control can, and periodically do, disrupt communications during the entry phase.

The entry flight regime is equally demanding of an experimental approach. It is at present impossible to conduct a wind-tunnel experiment that simultaneously provides both Mach and Reynolds numbers appropriate to entry flight.<sup>10</sup> Thus, the space shuttle received the first true test of its performance during its first flight, a potentially hazardous situation, because, unlike its predecessors, the shuttle was not flight tested in an unmanned configuration.

the compressibility factor  $z$  must be accounted for  $p = \rho z RT$ , where  $z$  is a function of temperature and pressure and is available in generalized compressibility charts.

<sup>10</sup>Sometimes, the re-entry trajectory and vehicle dimensions allow for full Mach–Reynolds duplications in wind tunnel, as will be shown for the IXV experimental vehicle.

### 2.4.2 Heat Transfer for Perfect Gas Flows

A recurrent theme in this text is that recourse to all available analytical sophistication is desirable, even essential, prior to critical design and development. However, preliminary design and mission feasibility assessment would be virtually impossible without the use of simpler, less accurate techniques. Accordingly, we rely on an approach to entry heating analysis first given by Allen and Eggers. This approach assumes the primary source of energy input to be convective heating from the laminar boundary-layer flow over the entry vehicle (i.e., perfect gas flow condition only). In this case, the local heating rate as given by Eq. (2.48) may be correlated<sup>11</sup> with the total enthalpy difference across the boundary layer

$$\dot{q}_w = \left( k \frac{\partial T}{\partial y} \right)_w = \left( \frac{k}{c_p} \right) \left( \frac{\text{Nu}_L}{L} \right) (H_{oe} - H_w) = \left( \frac{\text{Nu}_L}{\text{Pr}} \right) \left( \frac{\mu}{L} \right) H_{oe} \left( 1 - \frac{H_w}{H_{oe}} \right) \quad (2.50)$$

where:

$\text{Nu}_L$  = Nusselt number

$\text{Pr} = \mu c_p / k$  is the Prandtl number which is the viscous dissipation to heat conduction ratio

$k$  = thermal conductivity

$\mu$  = fluid viscosity

$c_p$  = fluid heat capacity at constant pressure

$H = V^2/2 + c_p T$  = total enthalpy

$V$  = free-stream velocity

The Nusselt number  $\text{Nu}_L$  is a parameter based on both the fluid properties and on the particular flow situation. The subscript L implies that the Nusselt number is based on an appropriate length scale L for the particular type of boundary-layer flow in question. The choice of length scale obviously varies with the nature of the flow geometry; as we shall see, it will often be a characteristic parameter such as the vehicle nose or wing/tail leading edge radius.

#### Explanation Box. The Nusselt Number and the Fourier's Law

It is both customary and advantageous in fluid dynamics to work in terms of nondimensional parameters. Many nondimensional groups are used in heat

(continued)

---

<sup>11</sup>The Fourier's law is applicable at all y across the layer and, therefore, applies to the stationary gas in a boundary layer next to an isothermal wall, but since the asymptotic gradient is difficult to measure in practice, it is conventional to express the heat flow from the wall to the fluid in the form  $\dot{q}_{\text{conv}} = h_c (T_f - T_w)$

transfer analysis, and we shall now explore some of the relationships between them by looking at the nature of the convective heat transfer coefficient,  $h_c$ . In convection analyses, the appropriate parameter is the Nusselt number, defined as the ratio of convective energy transfer to conductive energy transfer under comparable conditions. For example, in a one-dimensional case, assume a wall is heated by a slab of fluid having thickness  $L$  and mass-averaged temperature  $T_f$ . If the fluid is stagnant, then from Fourier's law the heat flux into the wall is

$$\dot{q}_{\text{cond}} = -k \left( \frac{dT}{dx} \right) = (T_f - T_w) \frac{k}{L} \quad (2.51)$$

whereas if the fluid is moving, convection occurs and the heat flux may then be written according to Newton's law of cooling as

$$\dot{q}_{\text{conv}} = h_c (T_f - T_w) \quad (2.52)$$

where  $h_c$  is the convective heat transfer coefficient or film coefficient. It is not a constant of the fluid but includes the *combined effects of conduction and convection* in the fluid.  $h_c$  is a function of numerous variables such as the transport properties, density, and velocity of the fluid.

The ratio of convective to conductive heat transfer would then be

$$\text{Nu}_L = \frac{\dot{q}_{\text{conv}}}{\dot{q}_{\text{cond}}} = \frac{h_c L}{k} \quad (2.53)$$

Thus, heat transfer at low Nusselt number, of order one, is essentially conductive.

Equation (2.53) allows us to rewrite Newton's law of cooling, Eq. (2.52), in terms of Nusselt number and thermal conductivity

$$\dot{q}_{\text{conv}} = \frac{\text{Nu}_L k}{L} (T_f - T_w) \quad (2.54)$$

In this example,  $L$  was the thickness of the fluid slab. In a more general situation,  $L$  is a characteristic length scale for the particular case of interest.

The Prandtl number is a fluid property, ranging from 0.71 to 0.73 for air below 9,000 K, but is often taken as unity for approximate calculations. The subscripts *oe* and *w* denote local flow conditions at the outer edge (*oe*) of the boundary layer and at the wall (*w*), respectively.

Total enthalpy is conserved for the inviscid flow across the normal shock portion of the bow wave. Because it is this stream that wets the body (i.e.,  $V \gg 1$ ), we have

$$H_{oe} = H = h + \frac{V^2}{2} = c_p T + \frac{V^2}{2} \cong \frac{V^2}{2} \quad (2.55)$$

The unsubscripted parameters denote, as usual, free-stream or approach conditions. The right-hand approximate equality follows from the high-speed, low-temperature nature of the upstream flow.<sup>12</sup>

Multiplying and dividing Eq. (2.50) by  $(\rho V)_{oe}$  yields an equivalent result

$$\dot{q}_w = (\rho V)_{oe} \left( \frac{\text{Nu}_L}{\text{Pr Re}_L} \right) H_{oe} \left( 1 - \frac{H_w}{H_{oe}} \right) = (\rho V)_{oe} St H_{oe} \left( 1 - \frac{H_w}{H_{oe}} \right) \quad (2.56)$$

where

$$St = \frac{\text{Nu}_L}{\text{Pr Re}_L} = \frac{h_c}{c_p(\rho V)_{oe}} \quad (2.57)$$

is the Stanton number, a local heat transfer coefficient which is the ratio of actual energy transfer rate to the energy flux available and  $Re = \rho VL/\mu$  is the Reynolds number which is the ratio of mass flux to viscosity of the flow.

The derivation of Eq. (2.56) makes it clear that the Reynolds number  $Re$  is referenced to the same (as yet unspecified) length scale as the Nusselt number and to boundary-layer edge values of density and velocity.

With Eq. (2.55), Eq. (2.56) becomes

$$\dot{q}_w = \frac{St}{2} (\rho V)_{oe} V_{oe}^2 \left( 1 - \frac{H_w}{H_{oe}} \right) \quad (2.58)$$

Equation (2.58) shows that the heating rate to the body depends on the local wall temperature through the term  $(1 - H_w/H_{oe})$ . Because the flow is stagnant at the wall,  $H_w \cong c_p T_w$  with the equality exact if  $T_w$  is low enough (below about 600 K) that the gas may be assumed calorically perfect. It is a conservative assumption, consistent with other approximations adopted here, to assume the wall to be sufficiently cool that  $H_w/H_{oe}$  is small. The heating rate is then

$$\dot{q}_w = \frac{St}{2} (\rho V^3)_{oe} \quad (2.59)$$

In hypersonic flow, the heat flux is therefore proportional to the cube of the velocity  $(\rho V^3)$ , i.e., in contrast to the drag which is proportional to the square of the velocity  $(\rho V^2)$ . This is the basic reason why heat transfer is so important in hypersonics.

---

<sup>12</sup>For example, assume an entry vehicle at 80 km altitude with  $T = 200$  K,  $V = 6,000$  m/s, and  $C_p = 1,005$  J/kgK. Then,  $V^2/C_p T = 90$ , and the thermal energy content of the air provides a negligible contribution to the total enthalpy.

 **Explanation Box. The Adiabatic Wall Temperature,  $T_{aw}$**

Because of viscous dissipation (i.e., friction between adjacent fluid layers) caused by the no-slip boundary condition (i.e.,  $\vec{V} \cdot \vec{n} = 0$ ), the boundary layer is also a region of very high temperatures. Therefore, the high-temperature fluid in the boundary layer will transfer heat to the body until the temperature gradient at the wall (heat flux) is zero (i.e., adiabatic wall,  $T_{aw}$ ).

So, in practice it is conventional to express the heat flow from the wall to the fluid, Eq. (2.52), in the form

$$\dot{q}_{\text{conv}} = h_c (T_{aw} - T_w) \quad (2.60)$$

$T_{aw}$  can be found by solution of the boundary-layer equations, but in engineering analysis, we introduce the recovery factor  $r$  defining the amount of energy *recovered* as the gas is slowed by friction through the boundary layer

$$T_{aw} = T_e + r \frac{V_e^2}{2c_p} \quad (2.61)$$

while at the outer edge of the boundary layer

$$T_0 = T_e + \frac{V_e^2}{2c_p} \quad (2.62)$$

Therefore,

$$r = \frac{T_{aw} - T_e}{T_0 - T_e} \quad (2.63)$$

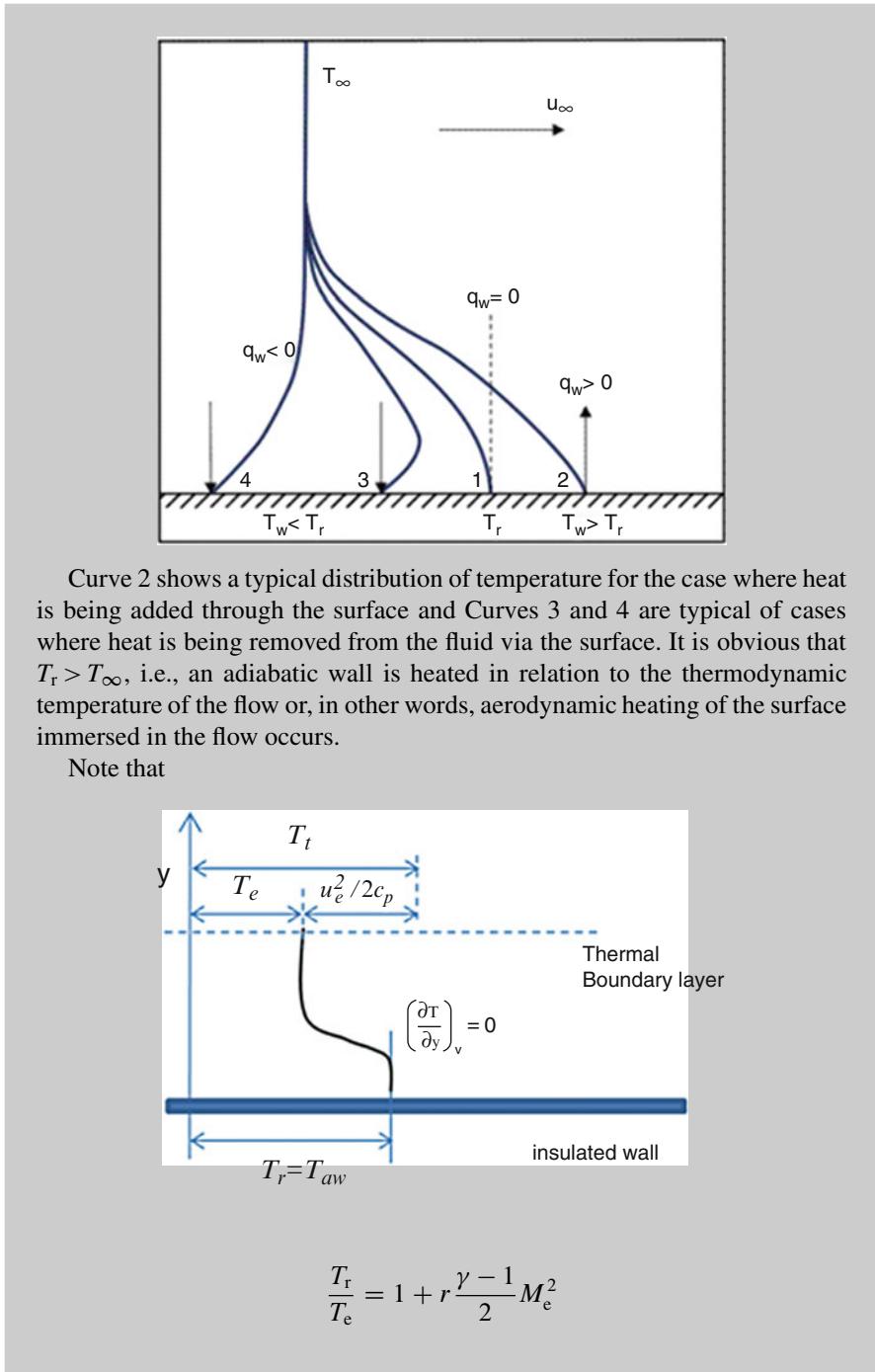
For incompressible laminar flow over a flat plate,  $r = \sqrt{\text{Pr}}$ , and for incompressible turbulent flow over a flat plate,  $r \cong \sqrt[3]{\text{Pr}}$ . These factors are used well into the hypersonic regime and have accuracy compatible with the simplified engineering analysis. We now call  $T_{aw}$  the recovery temperature  $T_r$ .

Now if we change the temperatures to enthalpies, Eq. (2.60) becomes

$$\dot{q}_w = (\rho V)_{oe} St (H_r - H_w) \quad (2.64)$$

It is worth noting that the temperature profile in the boundary layer of a high-velocity gas flow over an adiabatic surface is displayed by the curve 1 in the figure below.

(continued)



(continued)

$$\begin{aligned}\frac{T_{te}}{T_e} &= 1 + \frac{\gamma - 1}{2} M_e^2 \rightarrow \\ \rightarrow T_{te} - T_e &= \frac{\gamma - 1}{2} T_e M_e^2 = \frac{\gamma - 1}{2} T_e \frac{u_e^2}{\gamma R T_e} = \frac{u_e^2}{2 c_p}\end{aligned}$$

and

$$T_r = T_e + r (T_{te} - T_e)$$

while

$$\begin{aligned}\frac{T_r}{T_{te}} &= \frac{T_r}{T_e} \cdot \frac{T_e}{T_{te}} = \left(1 + r \frac{\gamma - 1}{2} M_e^2\right) \cdot \left(\frac{1}{1 + \frac{\gamma - 1}{2} M_e^2}\right) \\ &= \left(1 + r \frac{\gamma - 1}{2} M_e^2 + r - r\right) \cdot \left(\frac{1}{1 + \frac{\gamma - 1}{2} M_e^2}\right) = r + \frac{1 - r}{1 + \frac{\gamma - 1}{2} M_e^2}\end{aligned}$$

### 2.4.3 Skin Friction Coefficient and Reynolds Analogy

Recalling the importance of vehicle aerodynamic and aerothermodynamic performance, it is obvious that a fundamental role is played by air friction at wall. In fact, pressure and shear stress at wall determine aerodynamic force and moment acting on the vehicle, while air friction into boundary layer converts flow energy into heat (i.e., vehicle aeroheating).

In this framework, consider flow over a flat plate where a laminar boundary layer grows due to the viscosity of the fluid. According to the Newton's law of viscosity, the shear stress at any point in the fluid is proportional to the velocity gradient at that point. The constant of proportionality  $\mu$  is called the dynamic viscosity<sup>13</sup> of the fluid. So that the shear stress at wall reads

$$\tau_w = \left(\mu \frac{dV}{dy}\right)_w = \left(\rho v \frac{dV}{dy}\right)_w \quad (2.65)$$

---

<sup>13</sup>In contrast to kinematic viscosity,  $\nu = \mu/\rho$ .

Since the wall asymptotic gradient is difficult to measure as in the heat transfer case, the shear stress at the wall  $\tau_w$  is usually expressed as a function of the local dynamic pressure by introducing the local skin friction coefficient,<sup>14</sup>  $C_f$ ,

$$\tau_w = \frac{1}{2} \rho_e V_e^2 C_f \quad (2.66)$$

where  $C_f$  depends on Reynolds number,  $C_f = C_f(Re)$ .

Now looking at Eqs. (2.48) and (2.65) it is apparent that there is a similarity between the expressions for the heat flux and the shear stress at vehicle wall. Indeed, if the fluid has a kinematic viscosity  $\nu$  equal to its thermal diffusivity  $\alpha$  (i.e., the Prandtl number is unity), dividing  $\tau_w$  by  $\dot{q}_w$  gives

$$\frac{\tau_w}{\dot{q}_w} = \frac{(1/2) C_f \rho_e V_e^2}{St \rho_e V_e (H_r - H_w)} = \frac{\left(\mu \frac{dV}{dy}\right)_w}{\left(k \frac{dT}{dy}\right)_w} = \frac{\mu \frac{V_e}{\delta}}{\frac{k}{c_p} \left(\frac{H_r - H_w}{\delta}\right)} \quad (2.67)$$

if one assumes a linear slope for both velocity and temperature profile in the boundary layer with thickness  $\delta$ .

Rearranging this equation gives

$$\frac{\tau_w}{\dot{q}_w} = \frac{C_f}{2} = \frac{\mu c_p}{k} St = St \quad (2.68)$$

since we supposed  $Pr = 1$ .

As a result, exploiting the Reynolds analogy for laminar boundary-layer flow, we note that

$$St \cong \frac{C_f}{2} \quad (2.69)$$

Therefore, through the Reynolds analogy, one is able to relate the flow parameters to the thermal ones. This is the simple Reynolds analogy mean. This approximation is typically valid to within about 20 %. For example, the Reynolds analogy factor  $2St/C_f$  varies between 1.24 and 1.27 over the subsonic to Mach 16 range for laminar flow over a flat plate.

The usefulness of Reynolds analogy lies in this simple relationship which allows first-order engineering analysis of many viscous flows where heat transfer is of interest. For example, we may use this result to examine the relationships that can be derived between atmosphere, vehicle parameters, and heating in simple trajectory analysis.

---

<sup>14</sup>The momentum transfer of fluid passing a flat plate can be characterized by the skin friction coefficient,  $C_f$ .

For instance, with the Reynolds analogy, Eq. (2.59) becomes

$$\dot{q}_w = \frac{C_f}{4} (\rho V^3)_{oe} \quad (2.70)$$

and we see that for a reasonably cool wall, the gross heat transfer rate is independent of the body temperature.

Integration over the body wall area  $S_w$  gives the total heating rate (power input) to the body

$$Q \cong \frac{1}{4} \rho V^3 S_w C_F \quad (2.71)$$

where  $C_F$  is the body-averaged skin friction coefficient defined by integration of the local skin friction coefficient  $C_f$  over the body, that is,

$$C_F = \frac{1}{S_w} \int_{\text{body}} C_f \frac{(\rho V)_{oe}}{\rho V} ds \quad (2.72)$$

Again, the subscript *oe* denotes local boundary-layer outer edge values.

As a result, the body-averaged skin friction coefficient  $C_F$  is seen to be a key parameter in determining both the heating rate and the total heat load for an entry vehicle. As usual, the upstream or approach velocity  $V$  is found as a function of density  $\rho$  from trajectory solutions.

Discussion provided so far relies on the hypothesis that Prandtl number is unity. Nevertheless, a modified Reynolds analogy can be obtained to take into consideration of the fact that Prandtl number is usually not equal to one.

Indeed, for non-unity Prandtl number, comparing the Blasius incompressible flat plate boundary layer solutions for skin friction and heat transfer gives the relationship

$$St = \frac{C_f}{2\sqrt[3]{Pr^2}} \quad (2.73)$$

This result is also found to be applicable with caution for the hypersonic flat plate laminar boundary layer and in region of low-pressure gradient.<sup>15</sup>

Thus, if Reynolds analogy allows estimating the Stanton number through  $C_f$ , the problem is to determine the skin friction coefficient.

Clearly, the boundary-layer flowfield solution must be known to evaluate the wall shear stress and skin friction coefficient. Because the skin friction coefficient was introduced to avoid precisely this difficulty, further approximation is required. To this end, literature provides some results from boundary-layer theory, which,

---

<sup>15</sup>Note that, in regions of high gradient, Reynolds analogy is inappropriate. However, the analogy can be applied even when pressure gradient is nonzero for turbulent flows.

when used with judgment, allows estimation of  $C_f$  for preliminary vehicle design purpose.

Indeed, for low-speed laminar flow over a flat plate, according to Blasius solution, the shear stress reads

$$\tau_w = \left( \mu \frac{\partial u}{\partial y} \right)_{y=0} = 0.332 u_\infty \sqrt{\frac{\rho \mu u_\infty}{x}} \quad (2.74)$$

Therefore, the local friction coefficient is

$$C_f = \frac{\tau_w}{\frac{1}{2} \rho u_\infty^2} = \frac{0.664}{\sqrt{\frac{\rho u_\infty x}{\mu}}} = \frac{0.664}{\sqrt{Re_x}} \quad (2.75)$$

where  $Re_x$  is the Reynolds number referenced to boundary-layer edge conditions and to the x or streamwise coordinate as measured from the leading edge of the plate.

### Explanation Box. The Body-Averaged Skin Friction Coefficient for Laminar Flow on a Flat Plate

Consider a flat plate of unit width and length L in laminar flow conditions. Provide the relationship for the body-averaged skin friction coefficient,  $C_F$ .

The problem is to calculate the integral in the Eq. (2.72). To this end, consider that streamlines wetting the outer edge of the boundary layer obey the steady flow continuity result

$$(\rho V)_{oe} = \rho V \quad (2.76)$$

So, combining Eqs. (2.72), (2.75) and (2.76) and integrating over the flat plate yields the low-speed result

$$\begin{aligned} C_F &= \frac{1}{S_w} \int_{body} C_f \frac{(\rho V)_{oe}}{\rho V} ds = \frac{1}{L} \int_0^L C_f dx \\ &= \frac{1}{L} \int_0^L \frac{0.664}{\sqrt{\frac{\rho V x}{\mu}}} dx = \frac{1}{L} \frac{0.664}{\sqrt{\frac{\rho V}{\mu}}} \int_0^L \frac{dx}{\sqrt{x}} = \frac{1.328}{\sqrt{Re_L}} \end{aligned} \quad (2.77)$$

As a result, Eq. (2.73) becomes

$$St = \frac{C_f}{2 \sqrt[3]{Pr^2}} = \frac{0.332}{\sqrt[3]{Pr^2} \cdot \sqrt{Re_x}} \quad (2.78)$$

On the other hand, a solution proposed for turbulent flow conditions is

$$C_f = \frac{\tau_w}{\frac{1}{2} \rho u_\infty^2} = \frac{0.0594}{(Re_x)^{\frac{1}{5}}} \quad (2.79)$$

Thus,

$$St = \frac{C_f}{2 \sqrt[3]{Pr^2}} = \frac{0.0297}{\sqrt[3]{Pr^2} \cdot \sqrt[5]{Re_x}} \quad (2.80)$$

Finally, it is remarkable that often heat transfer results are correlated as functions of the heat transfer parameter  $\frac{Nu}{\sqrt{Re}}$  since from Eq. (2.57) we get for laminar flow

$$St = \frac{Nu_x}{Re_x \ Pr} = \frac{0.332}{\sqrt[3]{Pr^2} \cdot \sqrt{Re_x}} \quad \rightarrow \quad Nu_x = 0.332 \sqrt[3]{Pr} \sqrt{Re_x} \quad (2.81)$$

and for turbulent flow

$$St = \frac{Nu_x}{Re_x \ Pr} = \frac{0.0297}{\sqrt[3]{Pr^2} \cdot \sqrt[5]{Re_x}} \quad \rightarrow \quad Nu_x = 0.0297 \sqrt[3]{Pr} \sqrt[5]{Re_x^4} \quad (2.82)$$

It is worth noting that flat-plate theory is useful in aerodynamics because most portions of a flight vehicle are of a scale such that the local body radius of curvature dwarfs the boundary-layer thickness. Thus, most of the body appears locally as a flat plate, and good approximate results for skin friction can be obtained by ignoring those portions, small by definition, which do not.

This assumption, however, can be invalid for flight at very high altitude, where the reduced density lowers the Reynolds number and produces a thicker boundary layer.

By concluding, it is remarkable that Eqs. (2.78) and (2.80) can be extended to high-speed, hence compressible, flow through the Eckert's reference temperature approach, as will be discussed in detail in Chap. 3. It is found that, in the worst case (adiabatic wall),  $C_f (Re_x)^{0.5}$  varies from 0.664 at low speed to approximately 0.325 at Mach 20. Compressibility thus has an important but not overwhelming effect on skin friction coefficient and, for entry heating calculations such as presented here, may with some justification be ignored or included in an ad hoc fashion.

In any case, the use of the low-speed value is conservative from an entry heating viewpoint.

 **Explanation Box. Skin Friction Coefficient and Heat Transfer Estimate**

Because of empirical correlations for skin friction coefficient,  $C_f$  have been developed, such as

$$\frac{C_f}{2} = \frac{A}{Re^n}$$

where:

- For *laminar flow*  $A = 0.332$  and  $n = 0.5$ .
- For *turbulent flow*  $A = 0.0296$  and  $n = 0.2$ .

One can produce heat transfer estimates. That is,

$$\dot{q}_w = St\rho_e V_e (H_r - H_w) = \frac{A}{Re^n} \rho_e V_e (H_r - H_w) = \frac{A}{\left(\frac{\rho_e V_e x}{\mu_e}\right)^n} \rho_e V_e (H_r - H_w)$$

Thus,

$$\dot{q}_w = A(\rho_e V_e)^{1-n} \left(\frac{\mu_e}{x}\right)^n (H_r - H_w)$$

#### 2.4.4 Total Entry Heat Load

The total heat load (energy) into the vehicle can be obtained from Eq. (2.71),

$$\frac{dE}{dV} = \frac{dE}{dt} \frac{dt}{dV} = Q \frac{dt}{dV} = 2Q \left(\frac{m}{SC_D}\right) \left(\frac{1}{\rho V^2}\right) = \frac{1}{2} \left(\frac{m}{SC_D}\right) VS_w C_F \quad (2.83)$$

Where, as usual, we have dropped the tangential gravitational force in Eq. (2.1).

Upon integrating from the entry velocity to the final velocity,

$$E = \frac{1}{4} m (V_e^2 - V_f^2) \frac{S_w C_F}{SC_D} \quad (2.84)$$

If, as is usually the case, the final velocity is effectively zero, the total heat load has the particularly simple form

$$\frac{E}{\frac{1}{2} m V_e^2} = \frac{1}{2} \frac{S_w C_F}{SC_D} \quad (2.85)$$

that provides the rationale for the classical blunt-body entry vehicle design. Indeed, the total heat load is minimized when the skin friction drag  $C_F$  is small compared to the total drag  $C_D$ , and the wetted area  $S_w$  is as small as possible in comparison with the reference projected area  $S$ . Both of these conditions are met with an entry vehicle having a rounded or blunt shape. Further, detailed discussion on this design issue can be found in Chap. 3.

Equation (2.85) is valid with any entry profile (ballistic, glide, or skip) and for any vehicle sufficiently *light* that it slows before hitting the ground. This is the same requirement as for a deceleration peak with ballistic entry, and Eq. (2.26) may therefore be used to define a *light* vehicle. A dense vehicle on a steep ballistic trajectory may fail to meet this criterion. If this is the case, the first-order ballistic entry velocity profile given by Eq. (2.22) will be quite accurate and may be substituted in Eq. (2.84) to yield

$$\frac{E}{\frac{1}{2}mV_e^2} = \frac{1}{2} \frac{S_w C_F}{SC_D} \left\{ 1 - \exp \left[ \left( \frac{\rho_s}{\beta \sin \gamma_e} \right) \left( \frac{SC_D}{m} \right) \right] \right\} \quad (2.86)$$

By failing the light vehicle criterion of Eq. (2.26), the exponent has magnitude less than unity, and the expansion  $e^\alpha \cong 1 + \alpha$  may be employed inside the brackets to yield the *heavy body* result

$$\frac{E}{\frac{1}{2}mV_e^2} \cong \frac{1}{2m} \rho_s \frac{S_w C_F}{\beta \sin \gamma_e} \quad (2.87)$$

Finally, Eq. (2.87) shows that a dense ballistic entry vehicle should have a slender profile to minimize the total skin friction and hence the heat load.

#### 2.4.5 Entry Heating Rate

The body-averaged (*avg*) heating rate is also of interest and is found from Eq. (2.71):

$$\dot{q}_{\text{avg}} = \frac{Q}{S_w} = \frac{1}{4} \rho V^3 C_F \quad (2.88)$$

The average heating rate can be found once a trajectory profile giving velocity as a function of atmospheric density (hence altitude) is specified. This can be done as an adjunct to a numerical solution or by substituting the previously obtained first-order results for ballistic, equilibrium glide, and skip trajectories. Using this latter approach, we obtain

$$\dot{q}_{\text{avg}} = \frac{1}{4} \rho C_F V_e^2 \exp \left[ \frac{3}{2} \left( \frac{\rho}{\beta \sin \gamma_e} \right) \left( \frac{SC_D}{m} \right) \right] \quad (2.89)$$

for the ballistic entry heating rate as a function of density. Similarly,

$$\dot{q}_{\text{avg}} = \frac{1}{2} \left( \frac{m}{SC_D} \right) \left( 1 - \frac{V^2}{gr_e} \right) g C_F \frac{V}{(L/D)} \quad (2.90)$$

gives the heating rate for gliding entry vs. velocity. Finally,

$$\dot{q}_{\text{avg}} = \left( \frac{m}{SC_D} \right) \beta V_e^3 \exp \left[ -3 \frac{(\gamma - \gamma_e)}{(L/D)} \right] \frac{(\cos \gamma - \cos \gamma_e)}{2(L/D)} \quad (2.91)$$

is the heating rate for skip entry as a function of flight-path angle.

It is usually of greatest interest to find the value of the maximum body-averaged heating rate, as well as the altitude (or density) and velocity at which this rate occurs. This maximum heating rate will often constrain the entry trajectory. For ballistic entry, the maximum heating rate and critical trajectory conditions are

$$(\dot{q}_{\text{avg}})_{\text{max}} = - \left( \frac{C_F}{6e} \right) \left( \frac{m}{SC_D} \right) \beta V_e^3 \sin \gamma_e \quad (2.92)$$

$$\rho_{\text{crit}} = \left( -\frac{2}{3} \right) \left( \frac{m}{SC_D} \right) \beta \sin \gamma_e \quad (2.93)$$

$$V_{\text{crit}} = \frac{V_e}{\sqrt[3]{e}} \quad (2.94)$$

For equilibrium gliding entry, we find

$$(\dot{q}_{\text{avg}})_{\text{max}} = \sqrt{\frac{g^3 r_e}{27}} \left( \frac{m}{SC_D} \right) \left( \frac{1}{L/D} \right) \quad (2.95)$$

$$\rho_{\text{crit}} = \left( \frac{4}{r_e} \right) \left( \frac{m}{SC_D} \right) \left( \frac{1}{L/D} \right) \quad (2.96)$$

$$V_{\text{crit}} = \sqrt{\frac{gr_e}{3}} \quad (2.97)$$

The corresponding parameters are slightly more difficult to obtain for skip entry.

To obtain explicit algebraic results, it is necessary to assume small  $\gamma_e$ . This assumption is nearly always satisfied, and the results are

$$(\dot{q}_{\text{avg}})_{\text{max}} \cong \frac{\beta}{4} \left( \frac{m}{SC_D} \right) \gamma_e^2 V_e^3 \exp \left[ \frac{3\gamma_e}{L/D} \right] \left( \frac{1}{L/D} \right) \quad (2.98)$$

$$\rho_{\text{crit}} \cong 2\beta \gamma_e \left( \frac{m}{SC_D} \right) \left( \frac{1}{L/D} \right) \quad (2.99)$$

$$V_{\text{crit}} \cong V_e \exp \left[ \frac{\gamma_e}{L/D} \right] \quad (2.100)$$

$$\gamma_{\text{crit}} \cong \frac{-3\gamma_e^2}{L/D} \quad (2.101)$$

We urge caution in the application of the results given here. The heat load calculations of this section implicitly incorporate the approximations in the trajectory solutions for ballistic, gliding, or skip entry. For example, we have seen that the first-order ballistic entry analysis underpredicts the acceleration load for shallow entry angles. Because this result is incorporated in Eqs. (2.84) and (2.89), it is expected that at shallow entry angles the ballistic entry heating rate would be underpredicted and the total heat load overpredicted. This is the case, as shown in Fig. 2.16, which compares the first-order theory with that of Chapman [2].

Moreover, the entry heating analysis is itself approximate, because it assumes laminar boundary-layer heating, invokes the Reynolds analogy to eliminate the Stanton number, ignores radiant energy input, and neglects vibrational and chemical excitation (*real gas effects*) in the gas. These assumptions are quite valid at low speeds, below about 2 km/s, but become progressively less so as typical atmospheric entry speeds are approached. There are some mitigating effects; for example, neglect of radiant heating partially offsets the calorically perfect gas assumption. High-altitude entry flight, with its attendant low Reynolds number, tends to favor laminar flow, particularly for short, blunt vehicles.

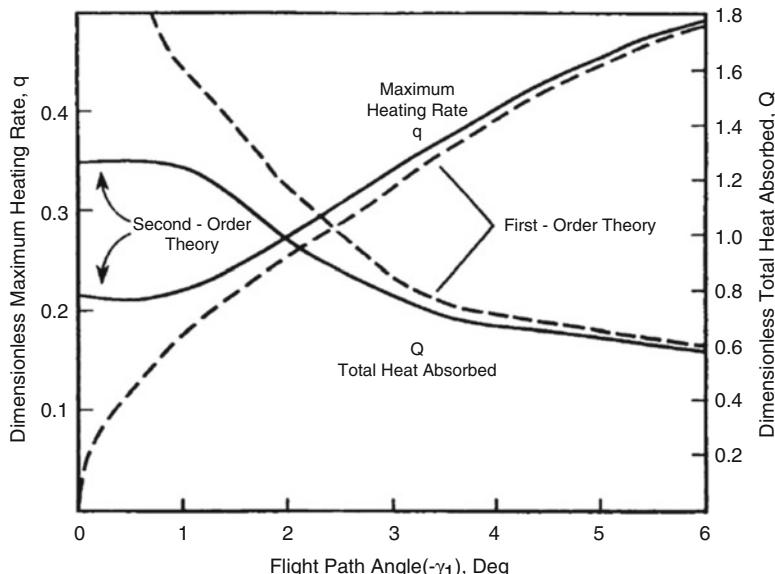


**Fig. 2.16** Comparison of first- and second-order entry heating analysis

For gliding entry vehicles, the situation may be different. While at high altitude, it is likely that the vehicle will encounter laminar flow. As atmospheric density increases, however, it is to be expected that at some point the boundary layer will transition to turbulent flow, with attendant higher drag and, by Reynolds analogy, a higher heating rate. This is obviously a situation to be avoided for as long as possible, leading to the requirement that the wetted surface of a gliding entry vehicle be as smooth and regular as possible, thus avoiding any premature *tripping* of the boundary layer into turbulent flow. We must point out that all too frequently even the most sophisticated calculations yield poor accuracy. Prabhu and Tannehill compared shuttle flight data with theoretical heat transfer results using a state-of-the-art flowfield code together with both equilibrium air and calorically perfect gas models. It was found that, provided a proper value of  $\gamma$  (the ratio of specific heats) is chosen (the authors recommend  $\gamma = 1.2$ ), the calorically perfect gas model does as well as the equilibrium air model. In some cases, substantially better agreement with flight data was obtained with the simpler model!

Other space shuttle flight experience further illustrates the points discussed earlier. For STS missions 1–5, Williams and others show generally excellent agreement between preflight analysis and flight data, particularly in the higher-temperature regions. Heating in the cooler, leeside areas (where the flowfield is typically quite complex) were significantly lower than preflight predictions, even those based on wind-tunnel data. Throckmorton and Zoby attributed this to delayed onset of turbulent flow as compared with subscale wind-tunnel test results.

Subsequent data obtained over the course of over a hundred flights of the space shuttle has revealed some quite complex behavior. The space shuttle typically experiences transition to turbulent boundary-layer flow on the wetted underside at about Mach 8, but has encountered it prior to Mach 11 on approximately 20 % of flights, and in one case (STS-73) as early as Mach 19. Early onset of turbulent transition has been attributed to excessive surface roughness, and in particular to partially dislodged “gap filler” material, placed between the shuttle thermal protection tiles to impede hot gas flow in these interstices. The gap fillers can apparently loosen in flight and intrude into the boundary-layer flow, causing early transition and, in some cases, unexpected damage to the thermal protection system.

Of those flights on which early transition to turbulent flow has been observed, some 60 % have demonstrated asymmetric transition, i.e., one wing goes turbulent, while the other remains laminar, resulting in a significant differential drag and imposing a lateral moment on the vehicle.

This has significant flight-control implications for shuttle as well as for future hypersonic entry vehicle designs. It is necessary to ensure that the combination of reaction control thrusters and aerodynamic surfaces is capable of exerting sufficient control authority, for a sufficient length of time, to overcome the lateral disturbing moment until the other wing also transitions to turbulent flow. It is, of course, also necessary to ensure that the overall heating rate under such adverse conditions remains within the thermal protection system design limits.

Finally, shuttle heat transfer flight experience has varied with time. Scott discusses the effects of wall catalysis on orbiter heat transfer and notes that the heat flux has increased from flight to flight as the shuttle tile properties change with age and use.

Cumulative uncertainties as to model validity argue for due caution in interpreting the results of all heat transfer analysis. We regard entry heating analysis as presented here to be an order-of-magnitude theory, useful in preliminary design but unsuited for detailed work. Even detailed calculations are not generally regarded as accurate to better than 10 %.

#### **2.4.6 Heat Transfer for Chemically Reacting Flows**

In a chemically reacting flow, the chemical composition may change through the boundary layer, from the boundary-layer edge composition to the wall composition since there will be temperature gradients in the boundary layer even for an adiabatic wall. If the gas is in chemical equilibrium, the composition in the boundary layer is determined by local conditions only (i.e., pressure and temperature). The species gradients present give rise to diffusion fluxes of species within the boundary layer. These diffusion fluxes provide an effective transport of mass (and energy) and the local equilibrium relies on a balance of these fluxes. Local equilibrium occurs when the wall temperatures are generally above about 2,000 K in typical entry situations. When the wall temperatures are lower, the reaction rates are slow even compared to the residency time in the boundary layer and the boundary-layer gases are in non-equilibrium. In the limiting case, the boundary-layer gases do not react at all and the boundary-layer edge composition is maintained to the wall.

As a result, Eq. (2.49) applies

$$\dot{q}_w = \left( k \frac{\partial T}{\partial y} \right)_w + \left( \sum \rho Y_i V_i h_i \right)_w = \left( k \frac{\partial T}{\partial y} \right)_w + \left( D_i \rho \sum h_i \frac{\partial Y_i}{\partial y} \right)_w$$

When considering the species diffusion terms in engineering analysis, it is convenient to introduce two other dimensionless groups, the Lewis number

$$Le = \frac{\rho c_p D_i}{k} \quad (2.102)$$

which is the ratio of mass diffusion to thermal diffusion, and the Schmidt number

$$Sc = \frac{\mu}{\rho D_i} \quad (2.103)$$

which is the ratio of viscous to mass diffusion. So, the Lewis number Le is the ratio of the Prandtl number to the Schmidt number

$$Le = \frac{Pr}{Sc} \quad (2.104)$$

### 2.4.7 Film Coefficient Approach

The energy equation in the boundary layer for an incompressible constant property low-speed flow is

$$u \frac{\partial T}{\partial x} + v \frac{\partial T}{\partial y} = \alpha \frac{\partial^2 T}{\partial y^2} \quad (2.105)$$

Solutions are generally correlated in the form of Eq. (2.52) or Eq. (2.60), as discussed above.

For a high-speed chemically reacting flow, if diffusion coefficients are equal and Prandtl and Lewis numbers are in unity, then boundary-layer energy equation becomes

$$\rho u \frac{\partial H}{\partial x} + \rho v \frac{\partial H}{\partial y} = \frac{\partial}{\partial y} \left( \mu \frac{\partial T}{\partial y} \right) \quad (2.106)$$

where  $H$  is the total (sensible + chemical +  $V^2/2$ ) enthalpy.

By analogy to the low-speed case above, then solutions can be correlated in the form

$$\dot{q}_w = St(\rho V)_{oe} (H_e - H_w) \quad (2.107)$$

The heat transfer equation can now be repartitioned according to the enthalpy terms into the frozen chemistry Fourier part and the chemical part:

$$\dot{q}_w = St(\rho V)_{oe} (H_r - H_w)_e + St(\rho V)_{oe} (h_e - H_w)_{\tau_w} \quad (2.108)$$

In the first term, the convective flux is evaluated using the boundary-layer edge composition. In the second term, the chemical flux is evaluated at the wall temperature and is driven by the difference between chemical composition of the edge and wall gases at the wall temperature [see Eq. 2.49]. After partitioning the assumption of unity Lewis number can be relaxed and a mass transfer coefficient  $C_m$  used in the chemical flux term

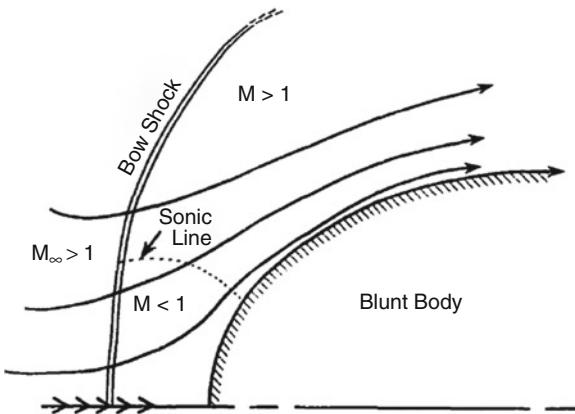
$$\dot{q}_w = St(\rho V)_{oe} (H_r - H_w)_e + C_m (\rho V)_{oe} (h_e - H_w)_{\tau_w} \quad (2.109)$$

If the diffusion coefficients are not approximately equal, i.e., when mixtures of widely different molecular weights are present in the boundary layer, then the direct chemical enthalpy cannot be used and an equivalent enthalpy  $h^*$  using a diffusion coefficient weighted average of mole and mass fraction may be employed

$$\dot{q}_w = St(\rho V)_{oe} (H_r - H_w)_e + C_m (\rho V)_{oe} (h_e^* - H_w^*)_{\tau_w} \quad (2.110)$$

The mass transfer coefficient is related to the heat transfer coefficient by the frequently employed Chilton–Coburn correlation

**Fig. 2.17** Stagnation-point flow



$$\frac{C_m}{St} = Le^\varepsilon \quad (2.111)$$

here  $\varepsilon = 2/3$  is a commonly used value. For dissociating air,  $Pr = 0.71$  and  $Sc = 0.5$ , then  $Le = 1.4$  (see Eq. 2.104) and then  $C_m = 1.26 St$ . In engineering estimates, the Prandtl and Schmidt numbers may be evaluated at a boundary-layer reference condition such as defined by Eckert.

## 2.5 Stagnation-Point Heating

Both the total heat load and the body-averaged heating rate are important in entry analysis, because either may constrain the trajectory. Their relative importance will depend on the entry profile and vehicle parameters, and, as we have mentioned, relief from one is usually obtained by aggravating the other.

Of equal importance is the maximum local heating rate imposed on any part of the entry vehicle, which determines the most severe local thermal protection requirement. With the possible exception of local afterbody hot spots due to turbulent effects and shock-boundary-layer interactions, the body heating rate is maximized at the stagnation point.

Any realistic vehicle design will have a blunt nose or wing/tail leading edges, and this will be a region of stagnation flow, shown schematically in Fig. 2.17 [2].

### Explanation Box. Stagnation-Region Flowfield Properties

The nomenclature for the flow near the stagnation point of a vehicle in a hypersonic stream is illustrated in Fig. 2.18. The flow passes through the normal portion of the shock wave reaching state 2 and then decelerates

(continued)

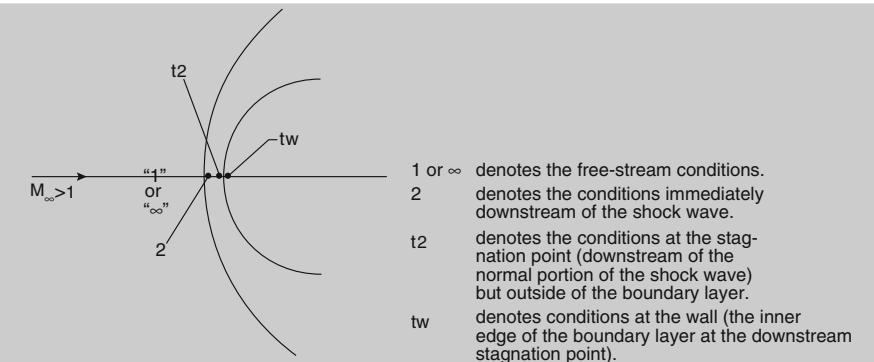


**Fig. 2.18** The nomenclature for the stagnation region

isentropically to state t<sub>2</sub>, which constitutes the outer edge condition for the thermal boundary layer at the stagnation point<sup>16</sup> [3]. This flow state is also indicated by the subscript *oe* or simply by *e* when it is clear from the context that we are talking about of stagnation point conditions.

The static temperature T<sub>2</sub>, the speed of sound a<sub>2</sub>, and the velocity in the shock layer v<sub>2</sub> are less for the equilibrium, real gas flow than for a perfect gas flow. The static pressure computed for air in thermodynamic equilibrium is slightly larger than the perfect gas value. The density is increased considerably, and, as a result, the shock layer thickness is reduced significantly.

At low altitudes, where the free-stream density is sufficiently high, these chemical phenomena tend to reach equilibrium. At higher altitudes, where the free-stream density is relatively low, there are not sufficient collisions for the gas to reach an equilibrium state.

The relations for steady, one-dimensional, inviscid, adiabatic flow in a constant-area stream tube are used to compute the conditions across a normal shock wave:

$$\rho_1 u_1 = \rho_2 u_2 \quad (2.112)$$

$$p_o = p_1 + \rho_1 u_1^2 = p_2 + \rho_2 u_2^2 \quad (2.113)$$

$$H_t = h_1 + \frac{1}{2} u_1^2 = h_2 + \frac{1}{2} u_2^2 \quad (2.114)$$

where H<sub>t</sub> is the total (or stagnation) enthalpy of the flow.

---

<sup>16</sup>Note that the streamline from the shock wave to the stagnation point may be curved for non-axisymmetric flowfields.

(continued)

Assuming that the gas is thermally perfect,

$$p = \rho RT = \rho \frac{R_o}{m_o} T \quad (2.115)$$

also known as an *ideal gas* and that is calorically perfect (i.e., the specific heat is constant)

$$h = c_p T \quad (2.116)$$

If the gas is both thermally perfect and calorically perfect (or, simply, perfect), the ratio of the values of flow properties across the shock wave can be written as a unique function of  $M_1$  and  $\gamma$  (the ratio of specific heats):

$$\frac{p_2}{p_1} = \frac{2\gamma M_1^2 - (\gamma - 1)}{\gamma + 1} \quad (2.117)$$

$$\frac{\rho_2}{\rho_1} = \frac{u_1}{u_2} = \frac{(\gamma + 1) M_1^2}{(\gamma - 1) M_1^2 + 2} \quad (2.118)$$

$$\frac{T_2}{T_1} = \frac{[2\gamma M_1^2 - (\gamma - 1)][(\gamma - 1) M_1^2 + 2]}{(\gamma + 1)^2 M_1^2} \quad (2.119)$$

If one assumes that the flow decelerates isentropically from the conditions at point 2 (immediately downstream of the normal portion of the shock wave) to the stagnation point outside of the thermal boundary layer (point t2),

$$\frac{p_{t2}}{p_1} = \left[ \frac{(\gamma + 1) M_1^2}{2} \right]^{\left( \frac{\gamma}{\gamma-1} \right)} \left[ \frac{(\gamma + 1)}{2\gamma M_1^2 - (\gamma - 1)} \right]^{\left( \frac{1}{\gamma-1} \right)} \quad (2.120)$$

$$\frac{T_{t2}}{T_1} = \frac{T_{t1}}{T_1} = 1 + \frac{(\gamma - 1)}{2} M_1^2 \quad (2.121)$$

Note that, whereas it is generally true that the stagnation enthalpy is constant across a normal shock wave for an adiabatic flow, as can be seen in Eq. (2.114), the stagnation temperature is constant across a normal shock wave only for the adiabatic flow of a perfect gas. See Eq. (2.121).

The reader should note that a gas can be thermally perfect and calorically “imperfect” but not vice versa.

(continued)

In fact,

$$h = u + pv = c_p T \quad (2.122)$$

But

$$pv = RT \rightarrow u + RT = c_p T \rightarrow u = (c_p - R) T = c_v T \quad (2.123)$$

We shall use the term perfect gas to describe a gas which is both thermally and calorically perfect.

Equations (2.112), (2.113), and (2.114) are not restricted to the perfect gas assumption and can be applied to high-temperature hypersonic flow. We can use the US Standard Atmosphere to define the free-stream properties, i.e.,  $p_1$ ,  $\rho_1$ , and  $h_1$ , at any given altitude. Since there are four unknowns in Eqs. (2.112), (2.113), and (2.114), i.e.,  $p_2$ ,  $\rho_2$ ,  $h_2$ , and  $u_2$ , but only three equations, additional relations are needed to obtain a solution such as

$$\begin{aligned} & \rho(p, h) \\ & s(p, h) \\ & T(s, h) \end{aligned} \quad (2.124)$$

The stagnation region behind a strong normal shock is one of particularly intense heating. For example, at an entry speed of Mach 25, the perfect gas shock tables yield  $T_{12}/T_1 = 126$ , where  $T_1$  is the free-stream static temperature and  $T_{12}$  is the stagnation temperature behind the shock. Assuming  $T_1 = 166$  K for the standard atmosphere at 80 km, the total temperature behind the shock<sup>17</sup> is 20,900 K! For comparison, the surface temperature of the Sun is approximately 5,780 K.

The preceding example is interesting and informative regarding attempts to predict individual flowfield properties for high-speed and therefore high-energy flows. A cautionary note should be added, however. The wall heat flux  $\dot{q}_w$  is the parameter of importance in entry vehicle design and is driven by the total enthalpy difference ( $H_{oe} - H_w$ ) between the wall and the outer edge of the boundary layer. The temperature difference is not the relevant parameter, despite what Eq. (2.48) would imply. For a calorically perfect gas, where  $h = c_p T$  applies, no distinction between temperature and enthalpy need be made. In a chemically reacting gas,

---

<sup>17</sup>Such extreme temperatures are of course not attained. The previous calculation assumes the atmosphere to be a calorically perfect gas for which the enthalpy and temperature are related by  $h = c_p T$  where the heat capacity  $c_p$  is a constant, 1,005 J/kgK, for air. In fact, a major fraction of the available thermal energy is used to dissociate and ionize the air molecules, effectively increasing the heat capacity of the gas and lowering the stagnation temperature. For a shuttle entry, the nose cap stagnation region reaches a peak temperature of approximately 1,650 K.

dissociation and ionization will alter the balance between effective heat capacity and temperature and thus significantly affect the flowfield.

As a consequence, in a step-by-step approach, let us investigate first stagnation-point aeroheating for perfect gas and, then, for chemically reacting flow.

### 2.5.1 Stagnation-Point Heat Transfer for Perfect Gas Flow

Our approximate analysis of stagnation heating relies again on Eq. (2.50), which we restate here:

$$\dot{q}_0 = \left( \frac{\text{Nu}_L}{\text{Pr}} \right) \left( \frac{\mu}{L} \right) H_{oe} \left( 1 - \frac{H_w}{H_{oe}} \right)$$

Previously we rearranged this equation to employ the Stanton number instead of the Nusselt number and then used Reynolds' analogy to cast the results in terms of the skin friction coefficient. This was done because skin friction data are more easily obtained and generalized, if only empirically, than are heat transfer data when the complete flowfield solution is not available. However, the boundary-layer flow in the stagnation region shown in Fig. 2.17 is sufficiently well understood that a more direct approach is possible.

In the low-speed stagnation region behind a strong bow shock, incompressible flow theory applies. For such a flow over a rounded nose or wing leading edge, the Nusselt number is found to be

$$\text{Nu}_L = \eta \text{Pr}^{\frac{2}{5}} \sqrt{\frac{K\rho}{\mu}} L \quad (2.125)$$

where  $\eta = 0.763$  for axisymmetric flow, whereas for two-dimensional flow, such as over a wing leading edge,  $\eta = 0.570$ . Further,  $K$  is the stagnation-point velocity gradient in the  $x$ , or streamwise, direction at the edge of the boundary layer

$$K = \left( \frac{dV_{oe}}{dx} \right)_{sp} \quad (2.126)$$

and the subscript  $sp$  or simply  $s$  denotes stagnation-point conditions.

So, the value of  $\eta$  points out that the heat flux in three-dimensional flow conditions is about 30 % larger than that for two-dimensional flow (i.e.,  $0.763/0.570 = 1.33$ ).

The reason for the higher heat flux in the three-dimensional case is in the nature of the flow. Indeed, in two dimensions, the flow can only go in two directions (i.e., up or down), whereas in three dimensions, it can also go sideways (left and right). This causes a thinner boundary layer and thus larger  $(dT/dy)$  in Eq. (2.48). In hypersonic flow, the shock standoff is also reduced.

The stagnation-point velocity gradient  $(dV_{oe}/dx)_{sp}$  is evaluated for high-speed flow by combining the Newtonian wall pressure distribution with the boundary-layer momentum equation and the inviscid flow solution at the stagnation point. This yields

$$K = \left( \frac{dV_{oe}}{dx} \right)_{sp} = \frac{V}{R_N} \sqrt{\frac{2\rho}{\rho_{oe}}} = \frac{1}{R_N} \sqrt{\frac{2(p_{oe} - p_\infty)}{\rho_{oe}}} \quad (2.127)$$

where  $R_n$  is the nose radius of curvature.<sup>18</sup> The term  $(\rho/\rho_{oe})$  is the density ratio for the inviscid flow across a normal shock at upstream Mach number  $M$ :

$$\frac{\rho}{\rho_{oe}} = \frac{(\gamma - 1) M^2 + 2}{(\gamma + 1) M^2} \quad (2.128)$$

This ratio varies from unity at  $M = 1$  to  $(\gamma - 1)/(\gamma + 1)$  at infinite Mach number.

### Explanation Box. The Stagnation-Point Velocity Gradient Evaluation

In order to obtain value of inviscid flow velocity gradient at the stagnation point,  $\left( \frac{du_e}{dx} \right)_{sp}$ , let us use Euler's momentum equation:

$$\left( \frac{dp_e}{dx} \right)_{sp} = - \left( \frac{du_e}{dx} \right)_{sp} \rho_e u_e \cong -\rho_{t2} \left( \frac{du_e}{dx} \right)_{sp} x$$

In fact, the  $x$ -momentum equation reads

$$\rho u \left( \frac{\partial u}{\partial x} \right) + \rho v \left( \frac{\partial v}{\partial y} \right) = -\frac{\partial p}{\partial x} + \frac{\partial}{\partial y} \left( \mu \frac{\partial u}{\partial y} \right) \xrightarrow{\text{Euler}} -\frac{\partial p}{\partial x}$$

Further, the usual thin boundary-layer approximations (from Prandtl's theory) lead to

$$\frac{\partial p}{\partial y} \cong 0$$

That is, the pressure at a point in the boundary layer is equal to the value at the edge of boundary layer,  $p_e$ , which comes from the inviscid flowfield solution.

(continued)

---

<sup>18</sup>This equation provides the well-known result that stagnation point heating varies inversely with the square root of the nose radius, i.e.,  $\dot{q}_0 \propto \frac{1}{\sqrt{R_N}}$ . This does not imply that a flat nose eliminates stagnation point heating; the various approximations employed invalidate the model in this limiting case.

Since the inviscid value is a function of  $x$  only,

$$\frac{\partial p}{\partial x} = \frac{dp_e}{dx} = -\rho_e u_e \frac{du_e}{dx}$$

But the velocity is approximately a linear function of  $x$  (as has been verified through detailed computations and measurements of the stagnation-region flowfield), i.e.,

$$u_e \cong \left( \frac{du_e}{dx} \right)_{sp} x$$

So,

$$\left( \frac{dp_e}{dx} \right)_{sp} = -\rho_e u_e \left( \frac{du_e}{dx} \right)_{sp} \cong -\rho_{t2} \left( \frac{du_e}{dx} \right)_{sp}^2 R_N$$

since in the vicinity of the stagnation point, one can approximate that  $x \cong R_N$ .

Thus, the problem is to calculate the pressure gradient at stagnation point  $(dp_e/dx)_{sp}$ .

#### *Newtonian Stagnation-Point Velocity Gradient*

The pressure gradient at stagnation point can be evaluated by means of the modified Newtonian theory which states that

$$C_{pt2} = \frac{p_{t2} - p_\infty}{\frac{1}{2}\rho_\infty u_\infty^2} = 2\cos^2\phi = \frac{p_e}{\frac{1}{2}\rho_\infty u_\infty^2}$$

So,

$$p_e = \rho_\infty u_\infty^2 \cos^2\phi = (p_{t2} - p_\infty) \cdot \cos^2\phi$$

Thus,

$$\begin{aligned} \frac{dp_e}{dx} &= \frac{d}{dx} [(p_{t2} - p_\infty) \cdot \cos^2\phi] = (p_{t2} - p_\infty) \frac{d(\cos^2\phi)}{dx} \\ &= -2 \cdot (p_{t2} - p_\infty) \cdot \cos\phi \cdot \sin\phi \cdot \frac{d\phi}{dx} \end{aligned}$$

At stagnation point,  $\phi \ll 1$  and then  $\cos\phi \cong 1$  and  $\sin\phi \cong \phi$ .

Further,

$$\phi = \frac{x}{R_N} \rightarrow \frac{d\phi}{dx} = \frac{1}{R_N}$$

(continued)

So,

$$\left( \frac{dp_e}{dx} \right)_{sp} = -\frac{2}{R_N} \cdot (p_{t2} - p_\infty) = -\rho_{t2} \left( \frac{du_e}{dx} \right)_{sp}^2 R_N$$

and, finally,

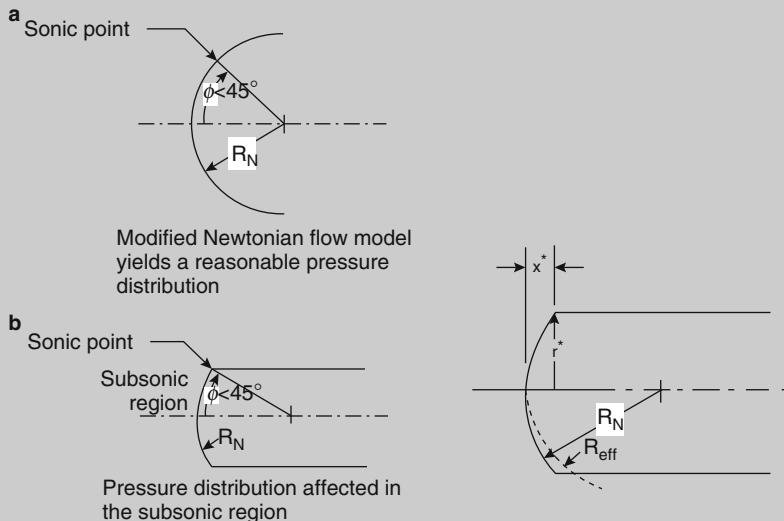
$$\left( \frac{du_e}{dx} \right)_{sp} = \frac{1}{R_N} \cdot \sqrt{\frac{2(p_{t2} - p_\infty)}{\rho_{t2}}}$$

It is worth noting that this relationship applies to modified Newtonian flow over a spherical cap (i.e., axisymmetric flow) or over a cylinder whose axis is perpendicular to the free-stream (i.e., 2-D flow).

#### *Non-Newtonian Stagnation-Point Velocity Gradient*

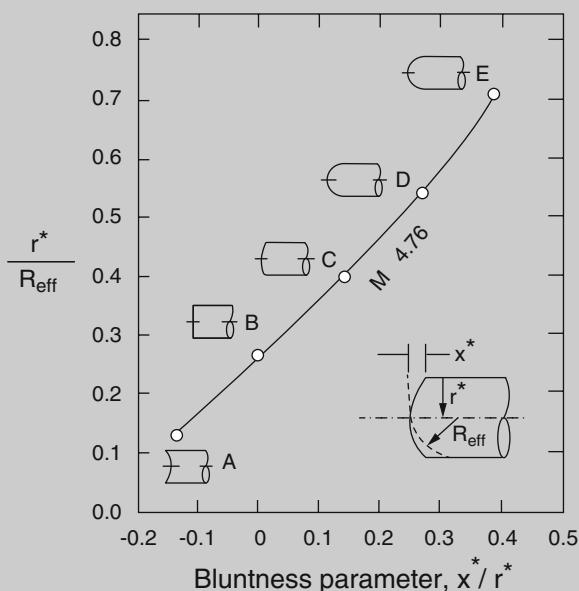
The pressure distribution over a considerable portion of a true hemisphere is reasonably well predicted by the modified Newtonian approximation. However, if the nose is truncated before  $\phi = 45^\circ$ , the sonic point will move to the corner, as shown in the figure. The changes in the inviscid flowfield propagate throughout the subsonic region. As a result, the pressure decreases more rapidly with distance from the stagnation point.

In this case, an effective nose radius must be used [3].



(continued)

**Fig. 2.19** Effective nose radius as a function of the bluntness parameters, using data for  $M_\infty = 4.76$



#### Nomenclature for the velocity gradient correlation

Thus, the resultant pressure gradient (or, equivalently, the velocity gradient) can be calculated by determining the effective radius of a spherical cap,  $R_{\text{eff}}$ .

The correlation for the effective nose radius based on data obtained by Boison and Curtiss for  $M_\infty = 4.76$  is reproduced in Fig. 2.19 [3].

The bow shock wave shape and the stagnation-point velocity gradient are Mach number dependent. However, the values for Mach 4.76 provide a reasonable correlation for hypersonic flow.

#### Evaluation of Apollo Capsule Effective Radius

The Apollo Command Module is an example of a configuration with a truncated spherical nose. Approximate values for the Apollo Command Module are:

$$r^* = 1.956 \text{ m}$$

$$R_N = 4.694 \text{ m}$$

Note that the term approximate is used, since the Apollo Command Module has rounded corners.

Let us first determine the angle of the corner,  $\phi_c$ :

$$\phi_c = \sin^{-1} \frac{r^*}{R_N} = 24.62^\circ$$

(continued)

Thus,

$$\begin{aligned}x^* &= R_N (1 - \cos \phi_c) = 0.09 \cdot R_N \\r^* &= 0.42 \cdot R_N\end{aligned}$$

So that

$$\frac{x^*}{r^*} = 0.21$$

and using Fig. 2.19

$$\frac{r^*}{R_{\text{eff}}} = 0.47$$

Thus,

$$R_{\text{eff}} = 0.88 \cdot R_N = 4.13 \text{ m}$$

As a result, the actual stagnation-point velocity gradient relative to that based on the nose radius  $R_N$  is

$$\frac{\left(\frac{du_e}{dx}\right)_{\text{eff}}}{\left(\frac{du_e}{dx}\right)_{R_N}} = \frac{R_N}{R_{\text{eff}}} = 1.13$$

So, the truncated spherical nose of the Apollo Command Module results in a reduced effective nose radius and, then, in an increased convective heat flux at stagnation point.

Thus, employing Eq. (2.55), Eq. (2.50) now becomes

$$\dot{q}_0 = \left(\frac{\eta}{2}\right) \text{Pr}^{-0.6} \sqrt{(\rho_{oe} \mu_{oe})_{sp}} V^2 \left(1 - \frac{H_w}{H_{oe}}\right) \sqrt{\left(\frac{dV_{oe}}{dx}\right)_{sp}} \quad (2.129)$$

### Explanation Box. Stagnation Region Heat Transfer Estimate

Stagnation-point heat transfer can be obtained if values for  $\rho_e$ ,  $V_e$ ,  $\mu_e$ , and  $H_e$  will be provided.

Further, the flow model used away from the stagnation point assumes that the streamline external to the boundary layer is isentropic. Note that, this is

(continued)

certainly true for any streamline external to the viscous flow region. Although large entropy gradients occur normal to the streamlines (since the flow passes through a curved shock wave), entropy is constant along streamlines in inviscid steady flow.

So,

$$\begin{aligned} p_s &\cong \rho_\infty V_\infty^2 \\ H_s &\cong \frac{V_\infty^2}{2} \\ \rho_s = \frac{p_s}{RT_s} &= \frac{\rho_\infty V_\infty^2}{R \frac{H_s}{c_p}} = \frac{2c_p}{R} \rho_\infty = \frac{2\gamma}{\gamma-1} \rho_\infty \\ \frac{\rho_e}{\rho_s} &= \left( \frac{p_e}{p_s} \right)^{\frac{1}{\gamma}} \rightarrow \rho_e = \rho_s \left( \frac{p_e}{p_s} \right)^{\frac{1}{\gamma}} = \frac{2\gamma}{\gamma-1} \rho_\infty \left( \frac{p_e}{p_s} \right)^{\frac{1}{\gamma}} \\ \frac{h_e}{H_s} &= \left( \frac{p_e}{p_s} \right)^{\frac{\gamma-1}{\gamma}} \end{aligned}$$

and

$$H_s = h_e + \frac{V_e^2}{2} \rightarrow \frac{V_e^2}{2} = H_s - h_e = H_s \left( 1 - \frac{h_e}{H_s} \right) = H_s \left[ 1 - \left( \frac{p_e}{p_s} \right)^{\frac{\gamma-1}{\gamma}} \right]$$

Thus,

$$\begin{aligned} \frac{V_e^2}{2} &= \frac{V_\infty^2}{2} \left[ 1 - \left( \frac{p_e}{p_s} \right)^{\frac{\gamma-1}{\gamma}} \right] \rightarrow \\ \frac{V_e}{V_\infty} &= \sqrt{1 - \left( \frac{p_e}{p_s} \right)^{\frac{\gamma-1}{\gamma}}} \rightarrow V_e = V_\infty \sqrt{1 - \left( \frac{p_e}{p_s} \right)^{\frac{\gamma-1}{\gamma}}} \end{aligned}$$

All properties along the streamline can be related to the pressure ratio and stagnation property values.

For what concerns the viscosity, we can use Sutherland's law in the hypersonic limit:

$$\mu \cong \mu_o \sqrt{T} = \frac{\mu_o}{c_p} \sqrt{h} = C_\mu \sqrt{h}$$

So,

$$\mu_e = C_\mu \sqrt{h_e} = C_\mu \sqrt{H_s \left( \frac{p_e}{p_s} \right)^{\frac{\gamma-1}{\gamma}}} = \frac{C_\mu}{\sqrt{2}} V_\infty \sqrt{\left( \frac{p_e}{p_s} \right)^{\frac{\gamma-1}{\gamma}}}$$

(continued)

We can now insert these values into the heating rate equation and find a relationship for the stagnation-point heat transfer for cold wall conditions (i.e.,  $H_w \cong 0$ ):

$$\begin{aligned}\dot{q}_0 &= A(\rho_e V_e)^{1-n} \left(\frac{\mu_e}{x}\right)^n (H_r - H_w) = A(\rho_e V_e)^{1-n} \left(\frac{\mu_e}{x}\right)^n H_r = \\ &= A \left[ \frac{2\gamma}{\gamma-1} \rho_\infty \left(\frac{p_e}{p_s}\right)^{\frac{1}{\gamma}} V_\infty \sqrt{1 - \left(\frac{p_e}{p_s}\right)^{\frac{\gamma-1}{\gamma}}} \right]^{1-n} \left[ \frac{C_\mu}{\sqrt{2}} \frac{V_\infty}{x} \sqrt{\left(\frac{p_e}{p_s}\right)^{\frac{\gamma-1}{\gamma}}} \right]^n \frac{V_\infty^2}{2} = \\ &= A \left( \frac{2\gamma}{\gamma-1} \right)^{1-n} \left( \frac{C_\mu}{\sqrt{R_N}} \right)^n \frac{1}{2^{\frac{n}{2}+1}} \rho_\infty^{1-n} \left(\frac{p_e}{p_s}\right)^{\frac{1-n}{\gamma} + \frac{\gamma-1}{2\gamma} n} \left[ 1 - \left(\frac{p_e}{p_s}\right)^{\frac{\gamma-1}{\gamma}} \right]^{\frac{1-n}{2}} \left(\frac{R_N}{x}\right)^n V_\infty^3\end{aligned}$$

So that,

$$\dot{q}_0 = K \frac{1}{R_N^n} \rho_\infty^{1-n} V_\infty^3 F(x)$$

Where

$$\begin{aligned}K &= A \left( \frac{2\gamma}{\gamma-1} \right)^{1-n} (C_\mu)^n \frac{1}{2^{\frac{n}{2}+1}} \\ F(x) &= \left( \frac{R_N}{x} \right)^n \left(\frac{p_e}{p_s}\right)^{\frac{1-n}{\gamma} + \frac{\gamma-1}{2\gamma} n} \left[ 1 - \left(\frac{p_e}{p_s}\right)^{\frac{\gamma-1}{\gamma}} \right]^{\frac{1-n}{2}} \\ &= \left( \frac{R_N}{x} \right)^n \left(\frac{p_e}{p_s}\right)^{\frac{2-3n+\gamma n}{2\gamma}} \left[ 1 - \left(\frac{p_e}{p_s}\right)^{\frac{\gamma-1}{\gamma}} \right]^{\frac{1-n}{2}}\end{aligned}$$

As a result,

- for *laminar flow*  $A = 0.332$  and  $n = 0.5$ ; hence,

$$\dot{q}_0 = K \sqrt{\frac{\rho_\infty}{R_N}} V_\infty^3 F(x)$$

- for *turbulent flow*  $A = 0.0296$  and  $n = 0.2$

$$\dot{q}_0 = K \frac{\rho_\infty^{0.8}}{R_N^{0.2}} V_\infty^3 F(x)$$

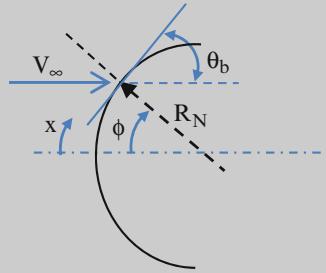
(continued)

So, given the  $F(x)$ , i.e., the pressure distribution, the heat transfer in the stagnation region can now be determined.

As a result, moving away from the stagnation point, the aeroheating of very simple configuration, such as spherical nose and a spherically capped cone, can be evaluated also by means of low order-based approach.

#### *Spherical Nose*

For the circular cross section of a spherical nose, shown in figure results



$$\frac{R_N}{x} = \varphi^{-1}$$

$$\frac{p_e}{p_s} = \frac{p_e}{p_{t2}} = \sin^2 \theta_b + \frac{p_\infty}{p_{t2}} \cos^2 \theta_b \cong \sin^2 \theta_b = \cos^2 \varphi$$

According to the modified Newtonian theory and because of  $\phi + \theta_b = 90^\circ$ , thus,

$$(\dot{q}_0)_{\text{lam}} = K \sqrt{\frac{\rho_\infty}{R_N}} V_\infty^3 F(x)$$

where

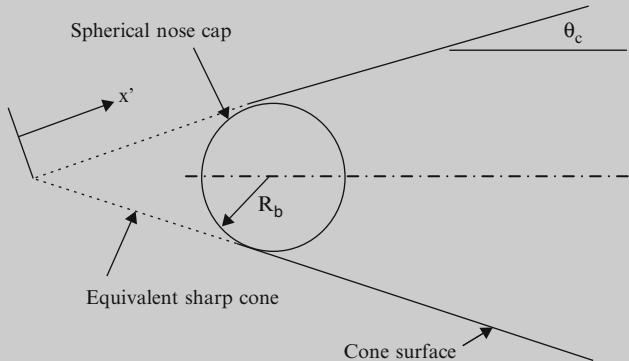
$$\begin{aligned} K &= A \left( \frac{2\gamma}{\gamma-1} \right)^{0.5} \sqrt{C_\mu} \frac{1}{2^{\frac{5}{4}}} \\ F(x) &= \left( \frac{R_N}{x} \right)^{0.5} \left( \frac{p_e}{p_s} \right)^{\frac{\gamma+1}{4\gamma}} \left[ 1 - \left( \frac{p_e}{p_s} \right)^{\frac{\gamma-1}{\gamma}} \right]^{\frac{1}{4}} \\ &= \frac{1}{\sqrt{\varphi}} (\cos \phi)^{\frac{\gamma+1}{2\gamma}} \left[ 1 - (\cos \phi)^{\frac{2(\gamma-1)}{\gamma}} \right]^{\frac{1}{4}} \end{aligned}$$

(continued)

### Spherically Capped Cone

For instance, in Ref. [6] Lees presented a derivation for the variation of the heat transfer around a spherically capped cone for a preliminary useful assessment of the aeroheating for this configuration. The cone at zero angle of attack is a constant pressure surface at high Mach numbers where the shock is attached. As the Mach number increases, very high heat transfer rates are experienced at the sharp tip, and it is difficult to maintain the sharpness due to melting or structural failure. To alleviate this effect, conical bodies for high-speed flight applications are generally capped with a spherical segment, provided that  $\dot{q}_0 \propto \sqrt{\frac{1}{R_b}}$

The flow over a spherically blunted cone will not recover to a constant pressure flow until stations fairly far from the nose are reached, and this modifies the heat transfer distribution from that of the equivalent sharp cone. Lees has considered this problem, as shown in the sketch in figure.



*Schematic diagram of spherically capped cone showing an additional coordinate measuring distance along with the equivalent sharp-nosed cone*

Lees' approach shows that for a blunt cone with nose radius  $R_b$  and semi-aperture vertex angle  $\theta$ , at any point on the cone surface, the ratio  $\frac{\dot{q}_w(\theta)}{\dot{q}_{co}}$  of the wall heat transfer to the stagnation one reads

$$\text{NOSE : } \frac{\dot{q}_w(\theta)}{\dot{q}_{co}} = \frac{2\theta \sin \theta \left(1 - \frac{1}{\gamma_\infty M_\infty^2}\right) \cos^2 \theta + \frac{1}{\gamma_\infty M_\infty^2}}{\sqrt{D(\theta)}} \quad (2.130)$$

$$\text{CONE SKIRT : } \frac{\dot{q}_w(x')}{\dot{q}_{co}} = \frac{A(\theta_c) \frac{x'}{R_b}}{\sqrt{B(\theta_c) + \left(\frac{x}{R_b}\right)^3}} \quad (2.131)$$

(continued)

Equation (2.131) is valid for  $\frac{x'}{R_b} \geq \cot \theta_c$ , where  $x'$  is the curve length measured along with the cone surface of the effective sharp cone (see figure). The distance is related to distance along with the surface of the spherically capped cone by the relation

$$\frac{x'}{R_b} = \cot \theta_c + \left[ \frac{x}{R_b} - \left( \frac{\pi}{2} - \theta_c \right) \right] \quad (2.132)$$

Finally, simplified versions for high Mach number conditions are

$$A(\theta_c) \approx \frac{\sqrt{3}}{2} \left[ \left( 1 - \frac{1}{\gamma_\infty M_\infty^2} \right) \sin^2 \theta_c + \frac{1}{\gamma_\infty M_\infty^2} \right]^{\frac{1}{2}} \sqrt{\frac{\pi}{2} - \theta_c} \quad (2.133)$$

$$B(\theta_c) \approx \frac{3}{16} \frac{D\left(\frac{\pi}{2} - \theta_c\right)}{\left[ \left( 1 - \frac{1}{\gamma_\infty M_\infty^2} \right) \sin^4 \theta_c + \frac{1}{\gamma_\infty M_\infty^2} \right] \theta_c} - \cot^3 \theta_c \quad (2.134)$$

$$D(\theta) \approx \left( 1 - \frac{1}{\gamma_\infty M_\infty^2} \right) \theta^2 - \frac{1}{2} \theta \sin 4\theta + \frac{1}{8} (1 - \cos 4\theta) + \frac{4}{\left( 1 - \frac{1}{\gamma_\infty M_\infty^2} \right)} [\theta^2 - \theta \sin 2\theta + \frac{1}{2} (1 - \cos 2\theta)] \quad (2.135)$$

### Swept Cylinder

A well-known engineering relationship for a swept cylinder, with leading edge radius of  $R_{cyl}$ , is

$$\dot{q}_{0cyl} = 1.29 \times 10^{-4} \sqrt{\frac{\rho_\infty}{R_{cyl}}} (1 - 0.18 \sin^2 \Lambda_{eff}) v_\infty^3 \left( 1 - \frac{h_w}{h_{aw}} \right) \cos \Lambda_{eff} \quad (2.136)$$

where

$$h_{aw} \cong h_\infty + \frac{1}{2} v_\infty^2 (1 - 0.18 \sin^2 \Lambda_{eff})$$

$$\sin \Lambda_{eff} = \sin \Lambda \cos \alpha$$

$$\cos \Lambda_{eff} = \sqrt{1 - \sin^2 \Lambda_{eff}}$$

with  $\Lambda$  as the sweep leading edge angle and  $\Lambda_{eff}$  the effective sweep leading edge.

(continued)

Another relationship, used in the past for the shuttle, is

$$\dot{q}_{\text{0wing-Shuttle}} = \frac{1}{\sqrt{2}} \frac{1}{\sqrt{R_{\text{cyl}}}} \dot{q}_{R_N=1} \cos^{1.2} \Lambda_{\text{eff}} \quad (2.137)$$

known as Gomg's relationship.

Finally, Eq. (2.129) is a perfect gas result and omits the effects of vibrational and chemical excitation.

As a consequence, it is demanding, assessing stagnation-region flowfield properties for both perfect and reacting gas cases.

### 2.5.2 Stagnation-Point Heat Transfer for Chemically Reacting Gas

The landmark analysis of stagnation-point heating including chemically reacting dissociating gas effects was given by Fay and Riddell and later extended by Hoshizaki and by Fay and Kemp to include the effects of ionization. Experimental work in support of these theories includes that of Rose and Stark and Kemp et al. [3, 4, 5].

Fay and Riddell found the stagnation-point heat flux for a non-radiating *binary gas* consisting of atoms (either O or N) and molecules ( $N_2$  or  $O_2$ ) with constant Prandtl and Lewis number and a  $T^{1/2}$  viscosity law to be

$$\begin{aligned} \dot{q}_0 = & \left( \frac{\eta}{2} \right) \text{Pr}^{-0.6} (\rho_{\text{oe}} \mu_{\text{oe}})^{0.4}_{\text{sp}} (\rho_w \mu_w)^{0.1}_{\text{sp}} V^2 \left( 1 - \frac{H_w}{H_{\text{oe}}} \right) \sqrt{\left( \frac{dV_{\text{oe}}}{dx} \right)_{\text{sp}}} \\ & \times \left[ 1 + (\text{Le}^\varepsilon - 1) \frac{h_d}{H_{\text{oe}}} \right] \end{aligned} \quad (2.138)$$

where

$\varepsilon = 0.52$  for equilibrium boundary-layer flow

$\varepsilon = 0.63$  for frozen flow with fully catalytic wall

$\varepsilon = -\infty$  for frozen flow with non-catalytic wall

$h_d = \sum Y_i (\Delta h_f^0)_i$  = average dissociation energy that is the enthalpy of dissociation of the gas mixture

$Y_i$  =  $i$ th species concentration

$\Delta h_f^0$  =  $i$ th species heat of formation

The Fay and Riddell analysis, which agrees quite well with experimental data for typical Earth orbital speeds, modifies Eq. (2.129) by the factor

$$D = \left( \frac{\rho_w \mu_w}{\rho_{oe} \mu_{oe}} \right)_{sp}^{0.1} \left[ 1 + (\text{Le}^\varepsilon - 1) \frac{h_d}{H_{oe}} \right] \quad (2.139)$$

which is due to dissociation.<sup>19</sup> This chemical term, as expected from the partitioning result, gives the exponent of the Lewis number  $\varepsilon$  for the ratio of mass to heat transfer coefficients.

Note the difference between the equilibrium and frozen fully catalytic wall case is quite small since the gas near the wall is composed of a binary mixture of atoms and molecules such that the diffusion flux, given the same wall condition, is nearly equal and thus independent of the kinetics.

When ionization becomes important at high velocity ( $V > 9$  km/s), then the diffusion of electron-ion pairs is greater, leading to reduced Lewis number. The ionization energy must also be taken into account. Overall this leads to an increase in the predicted heat flux.

Importantly in this case, the heat flux for the frozen boundary layer with fully catalytic wall for a diatomic gas is progressively larger than the equilibrium boundary-layer solution with increasing ionization. This is because in the equilibrium case, the mixture is essentially ternary and the large charge-exchange cross section allows a layer of atoms to form which prevent the diffusion of ion-electron pairs toward the wall, and thus their recombination energy is not available at the wall. In the case of the frozen boundary layer with fully catalytic wall, the recombination takes place directly at the wall from ionized to molecular state, and thus the insulating atomic layer is not present.

This effect is not seen in singly ionized atomic gases, for example, Ar or He, where the binary nature of the gas would not lead to significantly different fluxes, but recurs in multiply ionized flows.

Kemp and Riddell show this factor to increase the stagnation heat flux by about 20 % over the calorically perfect gas result for entry from low Earth orbit.<sup>20</sup>

A few comments on the use of Eq. (2.138) are in order.

The equation is evaluated in the forward direction, i.e., the wall temperature is specified and the heat flux computed. If  $\dot{q}_w$  rather than  $T_w$  is known, the wall temperature must be found by iteration.

The free-stream density  $\rho$  and velocity  $V$  are known from the trajectory solution. Specification of altitude fixes, through the standard atmosphere model, free-stream density, pressure, and temperature. Given the wall temperature (which may well be

<sup>19</sup>During atmospheric entry, the passage of the very high kinetic energy free-stream gases through the normal and oblique portions of the strong body shock creates very high temperatures in the shock layer between the bow shock and the body particularly close to the stagnation point. Beyond the stagnation region, the shock layer gases are cooled by expansion processes. These elevated temperatures can result in chemical reaction between the various species in the shock layer as well as ionization and dissociation of polyatomic species.

<sup>20</sup>This quite reasonably tempts the engineer seeking a preliminary result simply to use Eq. (2.138), and then to increase the result by 20 % to obtain a conservative answer.

specified as an upper bound for design), and state relations for the gas comprising the chemically reacting boundary layer, the quantities  $\rho_w$ ,  $\mu_w$ ,  $h_d$ , and  $H_w$  may be computed. The gas properties may be determined from first principles or, with somewhat less effort, found in tables. Reasonably accurate empirical relationships such as Sutherland's viscosity law are also useful.

### Explanation Box. The Heat Flux at the Stagnation Point of a Sphere

Consider a re-entry vehicle with a spherical nose radius,  $R_N$ , of 0.3 m, flying at 7,300 m/s at 70 km altitude. Assume that the wall temperature is 1,400 K and calculate the stagnation-point heat transfer rate supposing the air as

- (A) Perfect gas
- (B) Thermochemical equilibrium gas

From 1976 US Standard atmosphere model, it follows that at  $H = 70$  km free-stream temperature, pressure, density, and sound speed are

$$T_\infty = 219.59 \text{ K}, \quad P_\infty = 5.22 \text{ Pa}, \quad \rho_\infty = 8.28 \times 10^{-5} \text{ kg/m}^3, \quad \text{and} \\ a_\infty = 297.1 \text{ m/s.}$$

Thus,

$$M_\infty = \frac{u_\infty}{a_\infty} = \frac{7,300}{297.1} = 24.57$$

#### Case (A)

In the case of perfect gas,  $h_d = 0$  and the term containing the Lewis number is one. Thus, according to Eq. (2.138), the stagnation-point heat transfer rate becomes

$$\dot{q}_0 = 0.763 \cdot (\text{Pr})^{-0.6} \cdot (\rho_w \mu_w)^{0.1} \cdot (\rho_e \mu_e)_s^{0.4} \cdot (h_e - h_w) \cdot \left( \frac{du_e}{dx} \right)_s^{0.5}$$

So, the problem reduces to evaluate each term in the above equation.

For perfect air, we will assume that the Prandtl number is 0.71 (throughout the flowfield). Further,

$$T_{t2} = T_{t1} = T_\infty \left[ 1 + \frac{(\gamma - 1)}{2} M_\infty^2 \right] = T_\infty (1 + 0.2M_\infty^2) = 26,732.22 \text{ K} \\ \frac{p_{t2}}{p_1} = \left[ \frac{(\gamma + 1) M_1^2}{2} \right]^{\left( \frac{\gamma}{\gamma-1} \right)} \left[ \frac{(\gamma + 1)}{2\gamma M_1^2 - (\gamma - 1)} \right]^{\left( \frac{1}{\gamma-1} \right)} \\ = (1.2 M_1^2)^{3.5} \left( \frac{2.4}{2.8 M_1^2 - 0.4} \right)^{2.5} = 777.74$$

(continued)

Thus,

$$p_{t2} = 777.74 \cdot p_1 = 4,060.58 \text{ Pa}$$

Continuing with the perfect gas relations:

- Stagnation-point density,  $\rho_{t2}$ :

$$\rho_{t2} = \frac{p_{t2}}{R T_{t2}} = \frac{4,060.58}{288.28 \cdot 26,732.22} = 5.26 \times 10^{-4} \frac{\text{kg}}{\text{m}^3}$$

where to evaluate the gas constant for air,  $R$ , it is assumed that  $Y_{\text{N}_2} = 0.79$  and  $Y_{\text{O}_2} = 0.21$ . Thus,

$$R = \frac{R_o}{m_o} = \frac{R_o}{Y_{\text{N}_2} m_{\text{N}_2} + Y_{\text{O}_2} m_{\text{O}_2}} = \frac{8,314.47}{0.79 \cdot 28 + 0.21 \cdot 32} = 288.28 \frac{\text{J}}{\text{Kg K}}$$

where  $m_o$  is the molecular weight of the air in the perfect (or reference) state.

- Stagnation-point viscosity,  $\mu_{t2}$ :

$$\text{According to the Sutherland law } \mu = 1.458 \times 10^{-6} \frac{T_w^{3/2}}{T_w + 110.4}$$

$$\begin{aligned} \mu_{t2} &= 1.458 \times 10^{-6} \frac{T_{t2}^{3/2}}{T_{t2} + 110.4} = 1.458 \times 10^{-6} \frac{(26,732.22)^{1.5}}{26,732.22 + 110.4} \\ &= 2.37 \times 10^{-4} \text{ Pa} \cdot \text{s} \end{aligned}$$

- Density at wall,  $\rho_w$ :

Since the static pressure is constant across a thin boundary layer,  $p_{t2} = p_{w,t}$ . Thus,

(continued)

$$\rho_{w,t} = \frac{p_{t2}}{RT_w} = \frac{4,060.58}{288.28 \cdot 1400} = 1.01 \times 10^{-2} \frac{\text{kg}}{\text{m}^3}$$

– Viscosity at wall,  $\mu_w$ :

$$\begin{aligned}\mu_w &= 1.458 \times 10^{-6} \frac{T_w^{\frac{3}{2}}}{T_w + 110.4} = 1.458 \times 10^{-6} \frac{(1,400)^{1.5}}{1,400 + 110.4} \\ &= 5.06 \times 10^{-5} \text{ Pa} \cdot \text{s}\end{aligned}$$

Then,

$$H_{t2} = c_p T_{t2} = 1,009.10 \cdot 26,732.22 = 26.97 \times 10^6 \frac{\text{J}}{\text{Kg}}$$

$$h_{w,t} = c_p T_w = 1,009.10 \cdot 1,400 = 1.41 \times 10^6 \frac{\text{J}}{\text{Kg}}$$

The velocity gradient is

$$\left( \frac{d u_e}{dx} \right)_{t2} = \frac{1}{R_N} \sqrt{\frac{2(p_{t2} - p_1)}{\rho_{t2}}} = \frac{1}{0.3} \sqrt{\frac{2(4,060.58 - 5.22)}{5.26 \times 10^{-4}}} = 13,089.27 \frac{1}{\text{s}}$$

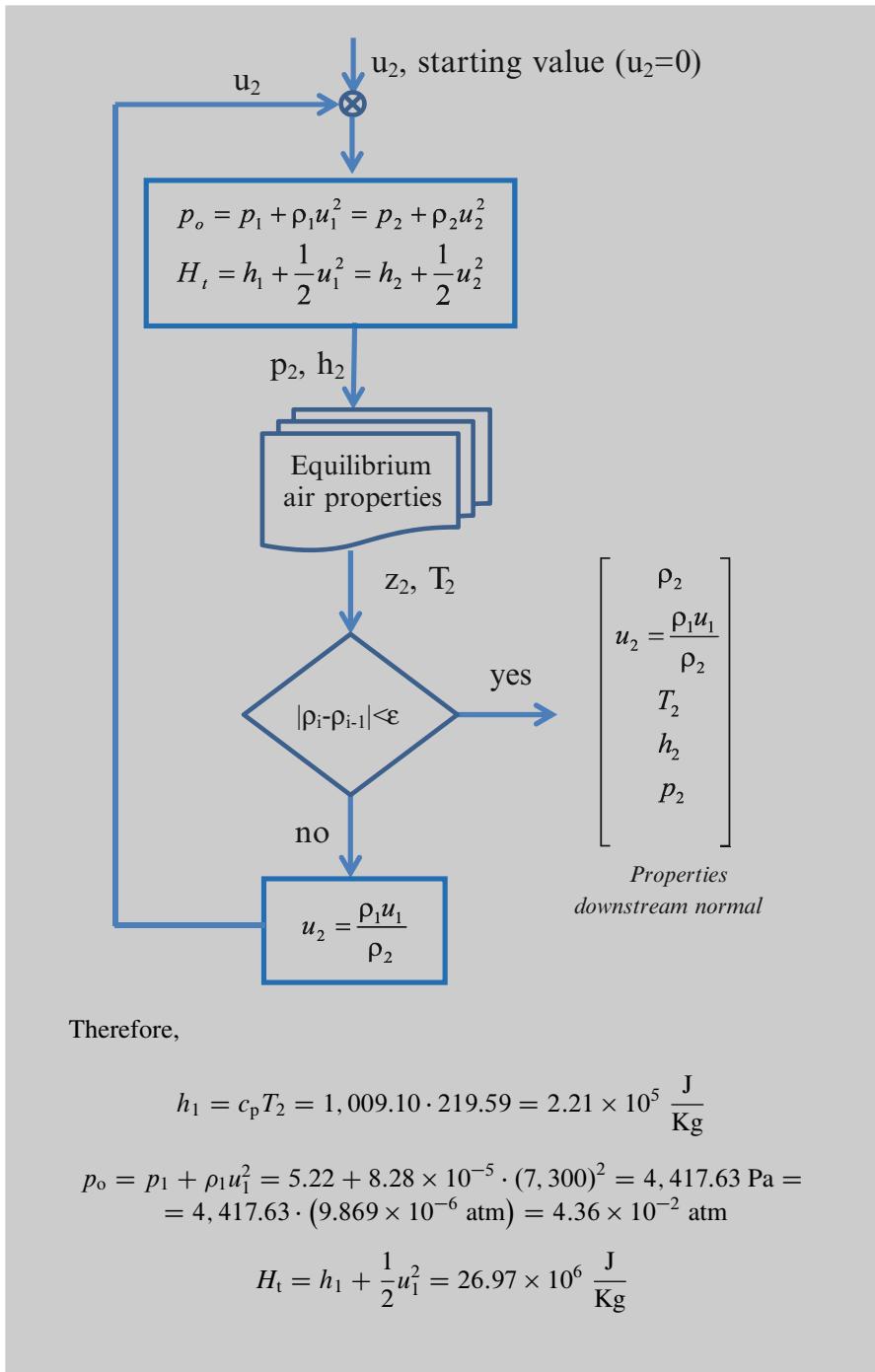
Thus, the stagnation-point heat flux is

$$\dot{q}_0 = 1.11 \frac{\text{MW}}{\text{m}^2}$$

### Case (B)

Let us calculate the flow conditions downstream the local normal shock wave. In this case, as energy is absorbed by the gas molecules entering the shock layer, the conservation laws and the thermophysics dictate certain changes in the forebody flow. Therefore, the heat is transported by conduction and diffusion, according to Eq. (2.49). As a consequence, we will use a recursive approach, according to the following flow chart:

(continued)



(continued)

*Iteration 1:* Assume  $u_2 = 0$  m/s. Thus,

$$p_2 = p_1 + \rho_1 u_1^2 - \rho_2 u_2^2 = p_o - \rho_2 u_2^2 = p_o = 4.36 \times 10^{-2} \text{ atm}$$

$$h_2 = h_1 + \frac{1}{2} u_1^2 - \frac{1}{2} u_2^2 = H_t - \frac{1}{2} u_2^2 = H_t = 26.97 \times 10^6 \frac{\text{J}}{\text{Kg}}$$

Using Fig. 1.17d in Ref. [3]

$$T_2 = 6,057 \text{ K.}$$

$$z_2 = 1.666.$$

Therefore,

$$\rho_2 = \frac{p_2}{z_2 R T_2} = \frac{4,417.63}{1.666 \cdot 288.28 \cdot 6,057} = 1.52 \times 10^{-3} \frac{\text{Kg}}{\text{m}^3}$$

$$u_2 = \frac{\rho_1 u_1}{\rho_2} = \frac{8.28 \times 10^{-5} \cdot 7,300}{1.52 \times 10^{-3}} = 397.66 \frac{\text{m}}{\text{s}}$$

*Iteration 2:* Assume  $u_2 = 397.66$  m/s. Thus,

$$\begin{aligned} p_2 &= p_o - \rho_2 u_2^2 = 4,417.63 - 1.52 \times 10^{-3} \cdot (397.66)^2 = 4,177.27 \text{ Pa} \\ &= 4.12 \times 10^{-2} \text{ atm} \end{aligned}$$

$$h_2 = H_t - \frac{1}{2} u_2^2 = 26.97 \times 10^6 - \frac{1}{2} (397.66)^2 = 26.89 \times 10^6 \frac{\text{J}}{\text{Kg}}$$

Using Fig. 1.17d in Ref. [3]

$$T_2 = 5,950 \text{ K.}$$

$$z_2 = 1.664.$$

Therefore,

$$\rho_2 = \frac{p_2}{z_2 R T_2} = \frac{4,177.27}{1.664 \cdot 288.28 \cdot 5,950} = 1.46 \times 10^{-3} \frac{\text{Kg}}{\text{m}^3}$$

$$u_2 = \frac{\rho_1 u_1}{\rho_2} = \frac{8.28 \times 10^{-5} \cdot 7,300}{1.46 \times 10^{-3}} = 414.01 \frac{\text{m}}{\text{s}}$$

*Iteration 3:* Assume  $u_2 = 414.01$  m/s. Thus,

$$\begin{aligned} p_2 &= p_o - \rho_2 u_2^2 = 4,417.63 - 1.46 \times 10^{-3} \cdot (414.01)^2 = 4,167.38 \text{ Pa} \\ &= 4.11 \times 10^{-2} \text{ atm} \end{aligned}$$

(continued)

$$h_2 = H_t - \frac{1}{2}u_2^2 = 26.97 \times 10^6 - \frac{1}{2}(414.01)^2 = 26.88 \times 10^6 \frac{\text{J}}{\text{kg}}$$

Using Fig. 1.17d in Ref. [3]

$$T_2 = 5,950 \text{ K}$$

$$z_2 = 1.664.$$

The values from successive iterations are unchanged within the accuracy of the chart in Fig. 1.17d in Ref. [3]. Therefore,

$$\rho_2 = \frac{p_2}{z_2 R T_2} = \frac{4,177.27}{1.664 \cdot 288.28 \cdot 5,950} = 1.46 \times 10^{-3} \frac{\text{kg}}{\text{m}^3}$$

To compute the stagnation-point properties, note that the flow decelerates isentropically from the conditions immediately downstream of the normal shock wave, i.e., 2, to the stagnation point, i.e., t2, as defined in Fig. 2.18.

Since t2 is the stagnation point,

$$h_{t2} = H_{t2} = H_t = 26.97 \times 10^6 \frac{\text{J}}{\text{kg}}$$

Using Fig. 1.17d in Ref. [3] and the air properties from iteration 3, the entropy ( $S_2/R$ ) is equal to 54.0.

$$\frac{s_{t2}}{R} = \frac{s_2}{R} = 54.0$$

Following the line of constant entropy from the conditions above to the total enthalpy  $H_{t2}$ , we find that

$$p_{t2} = 4,180.26 \text{ Pa} = 4.12 \times 10^{-2} \text{ atm}$$

$$T_{t2} = 6,037 \text{ K}$$

$$z_{t2} = 1.666$$

(Note that these computations have been made for the equilibrium assumptions, i.e., infinite reaction rates. The parameters will not be applicable to finite-rate nonequilibrium problems.)

We can compare this value of  $z_{t2}$  (1.666) with that provided in Chap. 1 (see Fig. 1.33).

Indeed, for  $p_{t2} = 0.0412 \text{ atm}$  and  $T_{t2} = 6,037 \text{ K}$ ,  $z_{t2} \cong 1.7$ , as we are well into nitrogen dissociation at these conditions. We can now calculate the density:

$$\rho_{t2} = \frac{p_{t2}}{z_{t2} R T_{t2}} = \frac{4,180.26}{1.666 \cdot 288.28 \cdot 6,037} = 1.44 \times 10^{-3} \frac{\text{kg}}{\text{m}^3}$$

(continued)

Using Fig. 2.4 in Ref. [3] and the Sutherland law, the viscosity at stagnation point reads

$$\begin{aligned}\mu_{t2} &= 1.1 \cdot \left[ 1.458 \times 10^{-6} \frac{T_{t2}^{\frac{3}{2}}}{T_{t2} + 110.4} \right] \\ &= 1.1 \cdot \left[ 1.458 \times 10^{-6} \frac{(6,037)^{1.5}}{6,037 + 110.4} \right] = 1.22 \times 10^{-4} \text{ Pa} \cdot \text{s}\end{aligned}$$

To assess density and viscosity at wall, we observe that

$$p_{w,t} = p_{t2} = 4,180.26 \text{ Pa}$$

$$T_w = 1,400 \text{ K}$$

$$z_{w,t} = 1.00$$

The last value ( $z_{w,t}$ ) follows by the fact that at the rather low wall temperature flow, species recombine at wall. Thus,

$$\begin{aligned}\rho_{w,t} &= \frac{p_{t2}}{z_{w,t} R T_w} = \frac{4,180.26}{1.00 \cdot 288.28 \cdot 1,400} = 1.03 \times 10^{-2} \frac{\text{kg}}{\text{m}^3} \\ \mu_w &= 1.458 \times 10^{-6} \frac{T_w^{\frac{3}{2}}}{T_w + 110.4} = 1.458 \times 10^{-6} \frac{(1,400)^{1.5}}{1,400 + 110.4} \\ &= 5.06 \times 10^{-5} \text{ Pa} \cdot \text{s}\end{aligned}$$

The velocity gradient is

$$\left( \frac{d u_e}{dx} \right)_{t2} = \frac{1}{R_N} \sqrt{\frac{2(p_{t2} - p_1)}{\rho_{t2}}} = \frac{1}{0.3} \sqrt{\frac{2(4,180.26 - 5.22)}{1.44 \times 10^{-3}}} = 8,026.81 \frac{1}{\text{s}}$$

Consider the assumption that the term containing the Lewis number is approximately 1. With this assumption and the values of the properties calculated above, the stagnation-point heat transfer rate is

$$\dot{q}_0 = 1.00 \frac{\text{MW}}{\text{m}^2}$$

The external flow properties are much more important than the wall values in determining the heat transfer rate. The uncertainty in the heat transfer is

(continued)

about 40 % of the uncertainty in the external viscosity. The physical reason for the importance of the external viscosity is that the growth of the boundary layer and, hence, the heat transfer to the wall depend mostly upon the external properties.

*Contribution of Le term:*  $\left[ 1 + (\text{Le}^\varepsilon - 1) \frac{h_d}{H_e} \right]$

Fay and Riddell note that the Lewis number does not change appreciably with temperature (below 9,000 K) and, although the exact value is uncertain, it is estimated to be about 1.4.

Further,  $\varepsilon = 0.52$  for equilibrium boundary layer, while when the gas chemistry is not in equilibrium, the convective heat transfer depends on the surface catalyticity, that is, in the case of frozen boundary-layer  $\varepsilon = 0.63$  for fully catalytic wall (FCW) and  $-\infty$  for non-catalytic wall (NCW).

So, the problem is to calculate the dissociation enthalpy,  $h_d$ .

Indeed,

$$h_d = \sum Y_i h_{\text{Ri}} = Y_O \cdot h_{\text{RO}_2} + Y_N \cdot h_{\text{RN}_2}$$

where  $Y_O$  and  $Y_N$  are concentrations of atomic oxygen and nitrogen behind the shock, respectively, while  $h_{\text{RO}_2}$  and  $h_{\text{RN}_2}$  are dissociation enthalpy for oxygen and nitrogen, respectively.

$$h_{\text{RO}_2} = \frac{R_o}{m_{\text{O}_2}} \Theta_{\text{dO}_2} = \frac{8,314.47}{32} \cdot 59,500 = 15.46 \times 10^6 \frac{\text{J}}{\text{Kg}}$$

$$h_{\text{RN}_2} = \frac{R_o}{m_{\text{N}_2}} \Theta_{\text{dN}_2} = \frac{8,314.47}{28} \cdot 113,000 = 33.55 \times 10^6 \frac{\text{J}}{\text{Kg}}$$

where  $\Theta_{\text{dO}_2}$  and  $\Theta_{\text{dN}_2}$  are dissociation temperature for oxygen and nitrogen, respectively.

Species mass fractions in equilibrium flow conditions behind a normal shock at  $M_\infty = 24.57$  and 70 km altitude are:

$$Y_O = 2.09 \times 10^{-1}$$

$$Y_{\text{O}_2} = 9.68 \times 10^{-6}$$

$$Y_N = 4.53 \times 10^{-1}$$

$$Y_{\text{N}_2} = 3.37 \times 10^{-1}$$

$$Y_{\text{NO}} = 1.28 \times 10^{-3}$$

Thus,

$$h_d = 2.09 \times 10^{-1} \cdot 15.46 \times 10^6 + 4.53 \times 10^{-1} \cdot 33.55 \times 10^6$$

$$= 18.43 \times 10^6 \frac{\text{J}}{\text{Kg}}$$

(continued)

and

$$1 + (\text{Le}^\varepsilon - 1) \cdot \frac{h_d}{H_e} = 1 + (1.4^{0.52} - 1) \cdot \frac{18.43 \times 10^6}{26.97 \times 10^6} = 1.13$$

As a result,

$$\dot{q}_0 = 1.13 \frac{\text{MW}}{\text{m}^2}$$

An appreciation for the magnitude of the real gas corrections can be obtained as follows:

$$\text{Equilibrium: } 1 + (\text{Le}^\varepsilon - 1) \cdot \frac{h_d}{H_e} = 1 + (1.4^{0.52} - 1) \cdot 0.5 = 1.095$$

$$\text{Frozen: } 1 + (\text{Le}^\varepsilon - 1) \cdot \frac{h_d}{H_e} = 1 + (1.4^{0.63} - 1) \cdot 0.5 = 1.118$$

A difference of only 2 % (for the most extreme case) between the equilibrium and frozen situations is observed.

Further, from calculations in explanation box, we note that the perfect-air value of the stagnation-point heat transfer rate is close to the equilibrium air value.

Thus, the effects of real gas are minimal.<sup>21</sup>

The implication is that the neglect of real gas effects, although horrifying to a physical gas dynamicist, may be fairly reasonable for preliminary design purposes. This is especially true when chemical equilibrium exists in the boundary-layer flowfield, an approximation that is reasonable in the stagnation region of blunt bodies. Also, the assumption of a nonequilibrium boundary-layer flow with a fully catalytic wall, so that surface equilibrium exists by definition, yields similar results.

### 2.5.3 Engineering Methods and Stagnation-Point Heating Assessment

Although hand-calculator evaluation of Eq. (2.138) is feasible, it is somewhat tedious and therefore to be avoided when possible.

For planetary entry assessments, simple correlations of the heat flux can be developed based on simplifications of the stagnation flow analysis (e.g., Fay and Riddell).

---

<sup>21</sup>One situation where the real gas effects can be appreciable, however, is with the non-catalytic wall (NCW) influence. For recombination heating at the surface, the wall is assumed to be catalytic. If the surface turns out to be NCW, then recombination will not occur on the surface. Thus, a dramatic reduction in heating will result. Shuttle data indicate the possibility of a NCW effect reducing lower surface peak heating by about 40 %.

Indeed, the relative agreement in heat flux estimation for perfect and reacting gas flows suggests that there are some basic parameters that govern the stagnation-point heat transfer rate and that are independent of the air-chemistry model. Therefore, neglecting the Lewis number term, one is able to identify the basic parameters that can be used in correlations for the stagnation-point heat transfer rate:

$$\dot{q}_0 = \eta \cdot (\text{Pr})^{-0.6} \cdot (\rho_w \mu_w)^{0.1} \cdot (\rho_e \mu_e)_s^{0.4} \cdot (h_e - h_w) \cdot \left( \frac{du_e}{dx} \right)_s^{0.5} \quad (2.140)$$

But

$$\rho_{t2} \propto \frac{p_{t2}}{z_{t2} T_{t2}} \quad \rho_{w,t} \propto \frac{p_{t2}}{z_{w,t} T_w}$$

$$\mu_{t2} \propto (T_{t2})^E \quad \mu_{w,t} \propto (T_{w,t})^E$$

where E is an exponent approaching 0.5, according to the Sutherland's law, for high temperature flows and at hypersonic speed

$$(h_e - h_w) \cong h_e \cong \frac{V_\infty^2}{2}$$

Further,

$$\left( \frac{du_e}{dx} \right)_{t2} = \frac{1}{R_N} \sqrt{\frac{2(p_{t2} - p_1)}{\rho_{t2}}} \cong \frac{1}{R_N} \sqrt{\frac{2p_{t2}}{\rho_{t2}}} \cong \frac{1}{R_N} \sqrt{2z_{t2} T_{t2}}$$

being  $(p_{t2} = z_{t2} \rho_{t2} R T_{t2}) \gg p_1$ .

Thus,

$$\begin{aligned} \dot{q}_0 &= \eta \cdot (\text{Pr})^{-0.6} \cdot (\rho_w \mu_w)^{0.1} \cdot (\rho_e \mu_e)_s^{0.4} \cdot (h_e - h_w) \cdot \left( \frac{du_e}{dx} \right)_s^{0.5} = \\ &= \eta \cdot (\text{Pr})^{-0.6} \cdot \left( \frac{p_{t2}}{z_{w,t} T_w} \cdot T_w^E \right)^{0.1} \cdot \left( \frac{p_{t2}}{z_{t2} T_{t2}} \cdot T_{t2}^E \right)^{0.4} \cdot \left( \frac{V_\infty^2}{2} \right) \cdot \left( \frac{1}{R_N} \sqrt{2z_{t2} T_{t2}} \right)^{0.5} = \\ &= \eta \cdot (\text{Pr})^{-0.6} \cdot \left( \frac{p_{t2}}{R_N} \right)^{0.5} \cdot \left[ \frac{T_w^{0.1E} \cdot T_{t2}^{0.4E}}{(z_{w,t} T_w)^{0.1} \cdot (z_{t2} T_{t2})^{0.4}} \right] \cdot \left( \frac{V_\infty^2}{2} \right) \cdot (2z_{t2} T_{t2})^{0.25} = \\ &= \eta \cdot (2)^{0.25} \cdot (\text{Pr})^{-0.6} \cdot \left( \frac{p_{t2}}{R_N} \right)^{0.5} \cdot \left[ \frac{T_w^{0.1E} \cdot T_{t2}^{0.4E}}{(z_{w,t} T_w)^{0.1} \cdot (z_{t2} T_{t2})^{0.15}} \right] \cdot \left( \frac{V_\infty^2}{2} \right) = \\ &= K' \cdot \left( \frac{p_{t2}}{R_N} \right)^{0.5} \cdot \left[ \frac{T_w^{0.1E} \cdot T_{t2}^{0.4E}}{(z_{w,t} T_w)^{0.1} \cdot (z_{t2} T_{t2})^{0.15}} \right] \cdot V_\infty^2 \cong K' \cdot \left( \frac{\rho_\infty}{R_N} \right)^{0.5} \cdot \left[ \frac{T_w^{0.1E} \cdot T_{t2}^{0.4E}}{(z_{w,t} T_w)^{0.1} \cdot (z_{t2} T_{t2})^{0.15}} \right] \cdot V_\infty^3 \end{aligned}$$

being  $p_{t2} \cong \rho_\infty V_\infty^2$

So,

$$\dot{q}_0 = K \cdot \left( \frac{\rho_\infty}{R_N} \right)^{0.5} \cdot V_\infty^3 \quad (2.141)$$

that is the relationship to be found.

In particular, it is worth noting that the heat transfer rate depends only on free-stream parameter and stagnation-point radius,  $R_N$ . This is a very interesting result considering that once the re-entry trajectory is known in the altitude–velocity map, one is able to find straightforward the heat flux expected at the vehicle stagnation point during re-entry.

Several engineering correlations have been proposed:

*Scott et al. relationship:*

$$\dot{q}_0 = 18,300 \cdot \sqrt{\frac{\rho_\infty}{R_N}} \cdot \left( \frac{V_\infty}{10^4} \right)^{3.05} \quad \frac{\text{W}}{\text{cm}^2} \quad (2.142)$$

*Detra et al. relationship:*

$$\dot{q}_0 = \frac{11,030}{\sqrt{R_N}} \cdot \sqrt{\frac{\rho_\infty}{\rho_{SL}}} \cdot \left( \frac{V_\infty}{V_{circ}} \right)^{3.15} \quad \frac{\text{W}}{\text{cm}^2} \quad (2.143)$$

where  $\rho_{SL}$  is the density at sea level,  $1.23 \text{ Kg/m}^3$ , while  $V_{circ}$  is the circular orbit velocity,  $7,950 \text{ m/s}$ .

*Zoby relationship:*

$$\dot{q}_0 = 3.88 \times 10^{-4} \cdot \sqrt{\frac{P_{t2}}{R_N}} \cdot (H_e - H_w) \quad \frac{\text{W}}{\text{m}^2} \quad (2.144)$$

*Anderson relationship:*

$$\dot{q}_0 = 1.83 \times 10^{-4} \cdot \sqrt{\frac{\rho_\infty}{R_N}} \cdot \left( 1 - \frac{H_w}{H_e} \right) \cdot V_\infty^3 \quad \frac{\text{W}}{\text{m}^2} \quad (2.145)$$

It is remarkable that both Zoby and Anderson relationships allow accounting also for the wall enthalpy,  $H_w$ . This may be important when  $H_e$  and  $H_w$  are of the same order of magnitude, for example, in the case of low energy re-entry (e.g., suborbital flight) or when radiation cooling conditions must be accounted for at vehicle wall.

### Explanation Box. The Stagnation-Point Heat Flux for Different Relationships

Consider again a re-entry vehicle with a spherical nose radius,  $R_N$ , of  $0.3 \text{ m}$ , flying at  $7,300 \text{ m/s}$  at  $70 \text{ km}$  altitude. Assume that the wall temperature is  $1,400 \text{ K}$  and calculate the stagnation-point heat transfer rate by using all the relationships shown so far, supposing the air as perfect gas.

(continued)

From 1976 US Standard atmosphere, it follows that at  $H = 70$  km free-stream temperature, pressure, density, and sound speed are

$$T_\infty = 219.59 \text{ K}, \quad P_\infty = 5.22 \text{ Pa}, \quad \rho_\infty = 8.28 \times 10^{-5} \text{ kg/m}^3, \quad \text{and} \\ a_\infty = 297.1 \text{ m/s.}$$

*Fay–Riddell:*

$$\dot{q}_0 = 0.763 \cdot (\text{Pr})^{-0.6} \cdot (\rho_w \mu_w)^{0.1} \cdot (\rho_e \mu_e)_s^{0.4} \cdot (h_e - h_w) \cdot \left( \frac{du_e}{dx} \right)_s^{0.5} \\ = 1.11 \frac{\text{MW}}{\text{m}^2}$$

*Scott et al. relationship:*

$$\dot{q}_0 = 18,300 \cdot \sqrt{\frac{\rho_\infty}{R_N}} \cdot \left( \frac{V_\infty}{10^4} \right)^{3.05} = 1.16 \frac{\text{MW}}{\text{m}^2}$$

*Detra et al. relationship:*

$$\dot{q}_0 = \frac{11,030}{\sqrt{R_N}} \cdot \sqrt{\frac{\rho_\infty}{\rho_{SL}}} \cdot \left( \frac{V_\infty}{V_{circ}} \right)^{3.15} = 1.26 \frac{\text{MW}}{\text{m}^2}$$

*Zoby relationship:*

$$\dot{q}_0 = 3.88 \times 10^{-4} \cdot \sqrt{\frac{P_{t2}}{R_N}} \cdot (H_e - H_w) = 1.15 \frac{\text{MW}}{\text{m}^2}$$

*Anderson relationship:*

$$\dot{q}_0 = 1.83 \times 10^{-4} \cdot \sqrt{\frac{\rho_\infty}{R_N}} \cdot \left( 1 - \frac{H_w}{H_e} \right) \cdot V_\infty^3 = 1.12 \frac{\text{MW}}{\text{m}^2}$$

Note that in this case, the wall enthalpy does not significantly affect the heat flux because of

$$\frac{H_w}{H_e} = 0.05$$

Another general form of the heat transfer rate correlation is

$$\dot{q}_0 = k \rho^a (R_n)^b \left( \frac{V}{10^4} \right)^c \frac{(H_r - H_w)}{(H_r - H_{300})} \quad (2.146)$$

**Table 2.3** Stagnation convective flux correlation constant

	$k (q \text{ in W/cm}^2)$	$a$	$b$	$c$	Range km/s
Venus and Mars	19,513	0.5	-0.5	3.04	0-16
Earth and Titan	20,668	0.5	-0.5	3.15	0-8

**Table 2.4** Stagnation radiative flux correlation constant

	$k (q \text{ in W/cm}^2)$	$a$	$b$	$c$	Range km/s
Venus	7.7e5	0.52	0.48	9.0	~11
Earth	6.54e6	1.6	1.0	8.5	0-8
Mars	3.84	1.16	0.56	21.5	0-7
Titan	8.83e8	1.65	1.0	5.6	4-7

**Table 2.5** Stagnation-point heat flux comparison for entry into CO<sub>2</sub> atmospheres of Mars and Venus

	Marsnet	Pioneer large	ESA Venus
$V_e \text{ m/s}$	5,563	11,660	15,500
$V (q_c \text{ max}) \text{ m/s}$	4,780	9,920	13,560
$q_c \text{ W/cm}^2$ correlation	32	2,794	12,400
$q_c \text{ W/cm}^2$ integral. b.l. code (ibl)	28	2,771	13,600
$q_c \text{ W/cm}^2$ Navier-Stokes	34	2,210 (Moss VSL)	
$q_c \text{ W/cm}^2$ blown		250 (Moss VSL)	184 (ibl)
$V (q_r \text{ max}) \text{ m/s}$	5,305	10,633	13,887
$q_r \text{ W/cm}^2$ correlation (cooled)	0.21	3,635	22,170
$q_r \text{ W/cm}^2$ coupled (cooled)		2,915 (Moss)	

This may be applied to the radiative flux as well as the convective. Tables 2.3 and 2.4 give typical values of the constants with limiting conditions [1].

Other values for these constants are abundant in the literature and cover not just the stagnation region but swept cylinders, laminar and turbulent surfaces, etc. The accuracy of such correlations can be within 5 % of more definitive methods provided sufficient number of ranges is used.

In practice the results of a matrix of boundary layer, full shock layer computations, or coupled radiation solutions (usually 1-D slab) are curve fitted to provide the constants. In this way, the effects of nonequilibrium are taken into account. This may result in altitude- (density) and velocity-dependent values of the constants.

To illustrate the effectiveness of such correlations, it is interesting to look at an example. Table 2.5 shows the convective and radiative fluxes at the stagnation point for entry to Venus and Mars [1].

The velocity at peak convective flux is close to 85 % of the entry velocity as expected. The convective correlation developed for Mars entry agrees well with Navier-Stokes and boundary-layer codes throughout the range but falls below the boundary-layer code at high speed due to the influence of ionization taken into

account in the boundary-layer code transport properties. This is as expected. The increased effect of blowing on the convective fluxes can be seen, such that for the high-speed entry, the convective flux can be ignored and the material ablation is radiation driven.

The radiative fluxes agree reasonably well at 11 km/s where the correlation was developed from 1-D slab equilibrium radiation solutions. The radiative cooling of the flowfield at 14 km/s lowers the radiative flux by a factor of about 3 to the value shown.

Kemp and Riddell used the Fay and Riddell result to correlate stagnation-point heating for entry from Earth orbit as a function of free-stream density and velocity, obtaining

$$\dot{q}_0 = 1.304 \times 10^8 \frac{1}{\sqrt{R_n}} \left( \frac{\rho}{\rho_s} \right)^{\frac{1}{2}} \left( \frac{V}{V_{\text{circ}}} \right)^{3.25} \left( 1 - \frac{H_w}{H_{\text{oe}}} \right) \left( \frac{W}{m^2} \right) \quad (2.147)$$

where the orbital velocity  $V_{\text{circ}} = 7.924$  km/s and surface density  $\rho_s = 1.225$  kg/m<sup>3</sup> were assumed; the correlation is claimed accurate to within 5 %. Note that the cooled wall assumption,  $H_w = 0$ , gives a conservative result.

Finally, a correlation for radiative heat flux is

$$\dot{q}_{0,\text{rad}} = 1,134 R_n \left( \frac{\rho_\infty}{\rho_s} \right)^{1.6} \left( \frac{V_\infty}{10^4} \right)^{8.5} \left( \frac{W}{m^2} \right) \quad (2.148)$$

## 2.6 Free Molecular Heating

Thus far we have discussed only continuum flow results. At high altitudes, however, collisions between molecules are less frequent: the molecular mean free path (i.e., the distance a molecule travels between collisions) can become as large as the scale of the vehicle itself.

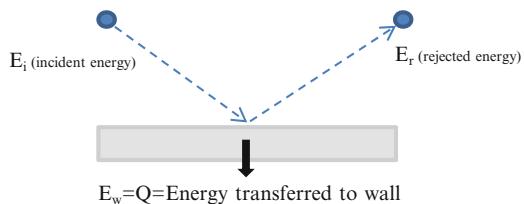
So that, free molecular flow conditions are established and aerodynamic heating in rarefied flow may be important too. For example, free molecular heating (FMH) is relevant during launch vehicle ascent flight and aerobraking. In fact, it is usually FMH constraint that determines the lowest altitude at which the launcher fairing can be jettisoned (e.g., typically around 100 km) and the aeroassisted maneuvers take place.

Indeed, for the case  $\text{Kn} \gg 1$ , let us examine a collision between an air molecule and a surface, as sketched in Fig. 2.20.

The energy balance for the exchange during the collision is given by

$$Q = E_i - E_r \equiv \sigma (E_i - E_w) \quad (2.149)$$

**Fig. 2.20** Collision between air molecules and an ideal surface



where

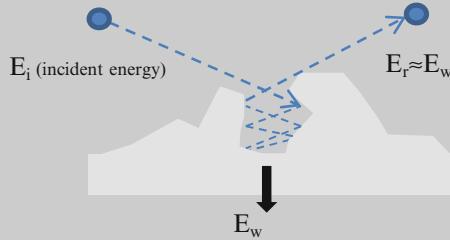
$$\sigma = \frac{E_i - E_r}{E_i - E_w} \quad (2.150)$$

is the thermal accommodation coefficient that accounts for the energy transfer efficiency of the impacting atmosphere particles into the vehicle and can be determined experimentally. This coefficient, as stated by Eq. (2.150), is a function of gas temperature  $T$ , surface temperature  $T_w$ , gas composition, and surface material. So, it is upper bounded by unity, but more commonly values are in the range 0.6–0.8.

So, in rarefied flows, an important factor that directly impacts the surface forces and heating is the nature of the gas–surface interactions. For most low enthalpy flows over technical surfaces, the diffuse scattering model for wall interactions seems quite adequate. However, there are indications that the model of full thermal accommodation and diffuse scattering is not correct at orbital velocities.

An example of the sensitivity of the surface heating and temperature jump was considered in the calculations simulating shuttle entry. For an altitude of 110 km, a calculation was made assuming that half of the particles that interact with the surface do so in a diffuse manner with full thermal accommodation and half interact in a specular manner (elastic collisions) with no thermal accommodation. The net result is a thermal accommodation of 0.5. The results of this calculation were compared with those from the diffuse calculation. The stagnation-point heating is 60 % of that for full accommodation. Similar reductions in heating were evident at other locations downstream of the stagnation point. Altering the gas–surface interaction model produces a substantial change in the state of the gas adjacent to the surface. The impact on the overall temperature adjacent to the surface is to produce a temperature jump that is about 4.5 times that for the diffuse surface with full accommodation. However, the slope of the temperature profiles adjacent to the surface is very similar for both calculations.

 **Explanation Box. Thermal Accommodations Coefficient for a Non-ideal Surface**



With reference to figure, if  
 $E_r \approx E_w$ ,  
then,  $\sigma \approx 1$ .

So, the rate of heat transfer reads

$$\dot{Q} = \sigma (\dot{E}_i - \dot{E}_w) = \sigma (\dot{m} H_s - \dot{m} H_w) = \sigma \rho V A (H_s - H_w) \rightarrow \quad (2.151)$$

$$\dot{q}_w|_{FM} = \sigma \rho V (H_s - H_w) \equiv St \rho V (H_s - H_w)$$

Thus, for  $H_w \cong 0$ , the free molecular heating rate will be of the form

$$\dot{q}_w|_{FM} = \alpha \sigma \rho V^3 \quad (2.152)$$

where  $\alpha$  is an unknown constant and  $\rho$  is the atmospheric density.

As a result, the convective heat flux in free molecular flow can be determined from the kinetic theory of gases or obtained from an experimental correlation of Stanton number ( $St$ ) and thermal accommodation coefficient. For instance, Kemp and Riddell correlated numerous experimental results for stagnation-point heating in the free molecular flow regime, yielding

$$\dot{q}_w|_{FM} = 2.69 \times 10^7 \sigma \left( \frac{\rho}{\rho_s} \right) \left( \frac{V}{V_{circ}} \right)^3 \left( \frac{\text{Btu}}{\text{sft}^2} \right) \quad (2.153)$$

Therefore, with the constants combined, the free molecular stagnation-point heating rate at low Earth orbital speeds becomes<sup>22</sup>

---

<sup>22</sup>Please consider that  $V_{circ} = 7.924 \text{ km/s}$ , Earth surface density  $\rho_s = 1.225 \text{ kg/m}^3$ , and  $(\text{Btu/s/ft}^2) = 11,340 \text{ (W/m}^2\text{)}$ .

$$\dot{q}_0|_{\text{FM}} = \frac{1}{2} \sigma \rho V^3 \left( \frac{\text{W}}{\text{m}^2} \right) \quad (2.154)$$

Finally, in the transitional regime, where  $\text{Kn} \sim 1$ , an ad hoc interpolation for the heat flux may be used as follows:

$$\dot{q}_{0,\text{transitional}} = \frac{\dot{q}_{w,\text{continuum}} + \text{Kn} \dot{q}_{w,\text{FM}}}{1 + \text{Kn}} \quad (2.155)$$

This simple relationship insures that both limits (i.e., continuum and free molecular flow aeroheating) are satisfactorily obtained and permit a continuous calculation of aeroheating throughout the transitional regime.

## 2.7 Entry Corridor

If the entry angle is too shallow, then the entry vehicle may not lose enough energy and the vehicle will pass through the atmosphere and escape to orbit (as in orbital transfer) or escape completely. This critical angle is termed the skipout angle or overshoot boundary. If the vehicle enters too steeply, then large deceleration and peak thermal flux may cause failure. This is called the undershoot boundary. The difference between the two can be thought of as the entry corridor for ballistic vehicles. For a high-energy entry, the undershoot boundary to limit the deceleration (e.g., on a human crew) may be above the overshoot boundary; thus, the entry is not viable with a ballistic vehicle. In this case, some means to raise the overshoot boundary needs to be found. Clearly reducing the velocity by chemical propulsion may make the corridor width real. However, the use of vehicle lift has the same effect since the undershoot boundary may be lowered by employing upward lift and the overshoot boundary raised by employing downward lift (i.e., inverted flight). For the ballistic vehicle, it can be shown that once the flight-path angle changes sign, the vehicle will skip out.

### 2.7.1 Velocity–Flight-Path Angle Map

For ballistic entry, it is common to express the performance envelope in the form of a  $(V_e, \gamma_e)$  map onto which various vehicle design limits can be placed. As an example, we shall look at the map developed for an ESA study of a cometary encounter and sample return vehicle Caesar shown in Fig. 2.21 [1].

The initial concern was to limit entry deceleration to 50 g to avoid sample crushing. The map of deceleration is shown in Fig. 2.22 for the range of return velocities being considered [1].

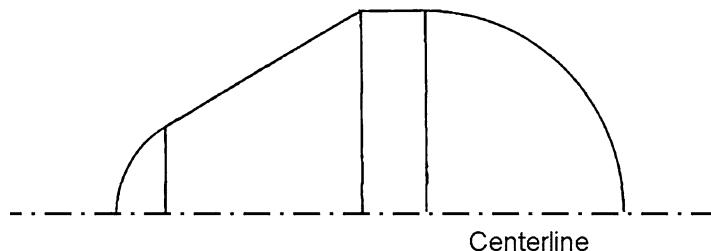


**Fig. 2.21** Caesar Earth return capsule

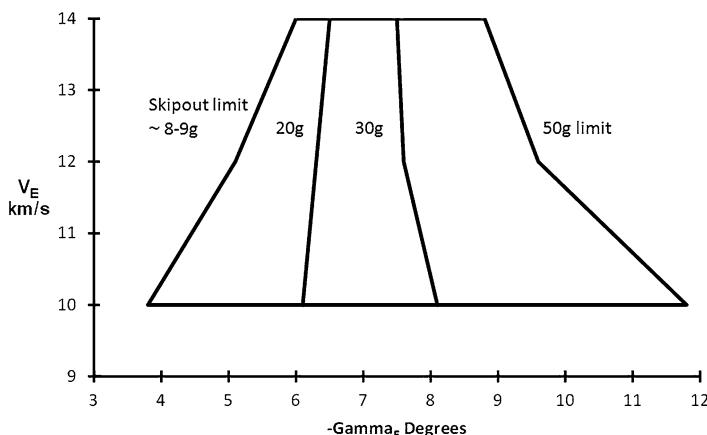


**Fig. 2.22** Initial Caesar ( $V_e$ ,  $\gamma_e$ ) map

The left-hand boundary is the skipout boundary and the right hand the maximum deceleration. The complete map to  $-90^\circ$  is shown in Fig. 2.23 [1]. The entry maximum load was increased during the study to 200 g.

The final design map is shown in Fig. 2.24. The right-hand limit is still the maximum deceleration (now 200 g), but considerations of heat soak into the heat shield and consequent TPS and insulation thickness led to the deletion of the shallow entry angles including skip entries. Thus, the left-hand limit is now a heat soak limit. For a given velocity, the heat soaked into the vehicle surface is dependent primarily on the re-entry time, and thus the shallowest lowest velocities impose this design limit, designated lower left (LL in Fig. 2.24) [1]. As the entry velocity is increased, then the total heat load increases and the maximum occurs for the fastest shallowest entries designated upper left (UL). Finally the maximum heat transfer rate occurs for the fastest steepest entry designated upper right (UR). These are the main aerothermal design cases to be considered for a ballistic entry vehicle and will determine TPS type and mass, as well as primary structural strength.

Shown in Fig. 2.25 is a schematic illustrating the concept of aerobrake entry corridor [1].

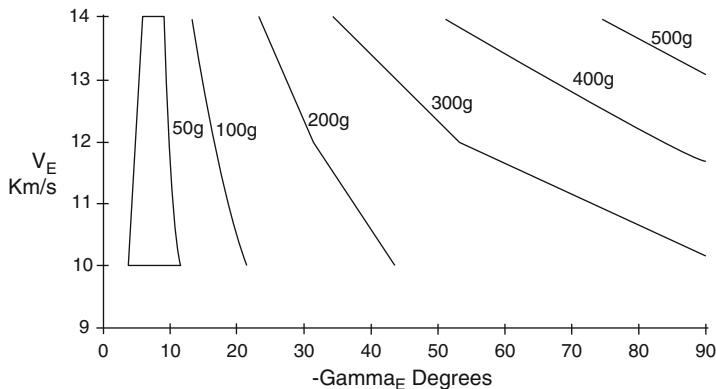


Fig. 2.23 Complete Caesar ( $V_e$ ,  $\gamma_e$ ) map

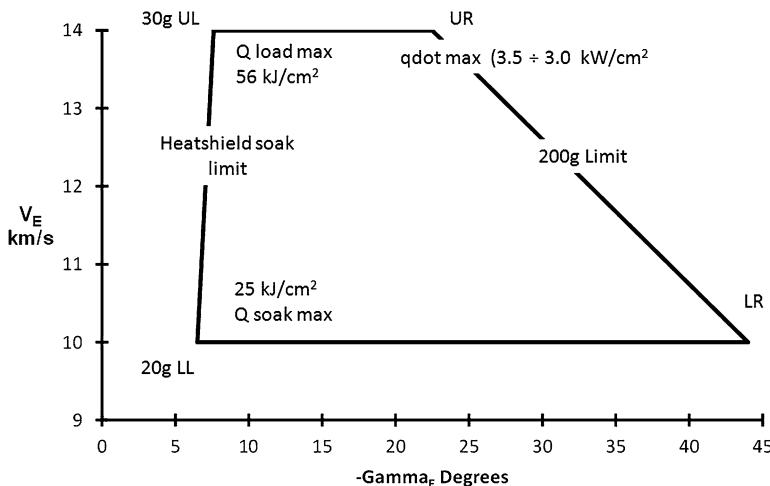
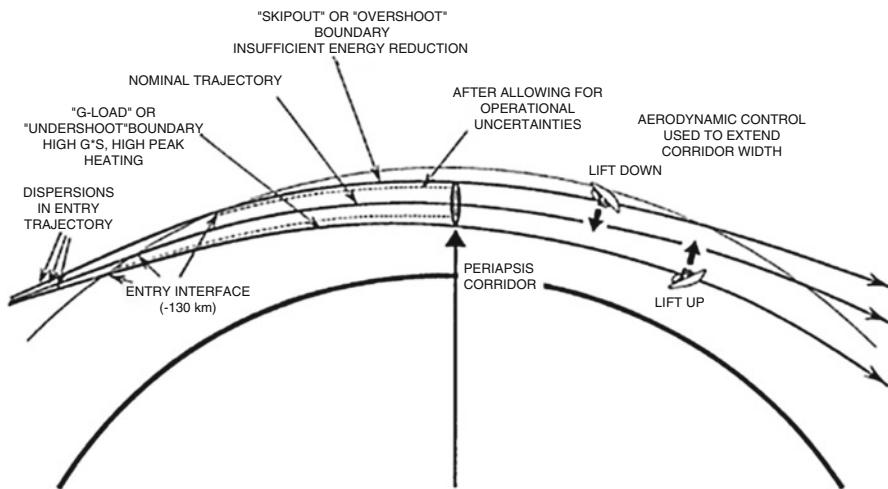


Fig. 2.24 Final Caesar ( $V_e$ ,  $\gamma_e$ ) map

If the vehicle flies outside this corridor, or if its lift is either too small or too large, the vehicle will either crash to the surface or skipout of the desired orbit. As the vehicle L/D is increased, controllability, and hence, corridor width, is increased. Increase in allowable g-load and in allowable maximum temperature also lead to increased allowable corridor width. Increased entry speed, increased capture orbit energy, and uncertainties in atmospheric density, however, reduce corridor width. Perhaps the most important consideration in determining aerothermal environment is the mission itself.



**Fig. 2.25** Aerobraking corridor concept

## References

1. Advisory Group for Aerospace Research and Development (North Atlantic Treaty Organization) (1997) Capsule aerothermodynamics. AGARD-R-808, AGARD, Neuilly sur Seine
2. Griffin MD, French JR (2004) Space vehicle design. American Institute of Aeronautics & Astronautics, Reston, VA
3. Bertin JJ (1994) Hypersonic aerothermodynamics. AIAA education series, American Institute of Aeronautics and Astronautics, Inc., Washington, DC
4. Regan FJ, Anandakrishnan SM (1993) Dynamics of atmospheric re-entry. American Institute of Aeronautics and Astronautics, Washington, DC
5. Anderson JD Jr (1989) Hypersonic high temperature gas dynamics. McGraw-Hill Book Company, New York
6. Lees L (1956) Laminar heat transfer over blunt-nosed bodies at hypersonic flight speeds. J Jet Propuls 26:259–269

# **Chapter 3**

## **Some Preliminary Considerations on Entry Vehicle Design**

### **3.1 Introduction**

The purpose of this chapter is to discuss about design driving parameters and system attributes which allow designing hypersonic entry vehicle configuration. Indeed, all aerodynamic and aerothermodynamic design aspects related to the entry phase of capsule, lifting-body, winged-body, and planetary probe configurations will be covered in detail.

Today, there are a wide variety of vehicles that fly at hypersonic speeds, including vehicles to launch objects into space, vehicles that are designed to cruise through the atmosphere, and vehicles designed to return objects from space. The attributes of a system include performance, safety, cost, operability, reliability, and compatibility with the environment.

The attribute, or attributes, which drive a design, depend on the application. For instance, a military system may place emphasis on performance; a civil transportation system for humans on safety and on reliability; and a system for delivering commercial payloads to space on operability, on reliability, and on cost.

Compatibility with the environment becomes increasingly important to all systems.

To perform its mission, a vehicle must not only exhibit the desired attributes, but its design must satisfy the aerodynamic and aerothermodynamic constraints. Aerodynamic heating restricts the envelope in which the vehicle can operate. It also affects the design of the thermal protection system (TPS) and, hence, the vehicle weight. For example, the body flap deflection of the Shuttle Orbiter was constrained by limits on the thermal seals in the gap. Because lift allows a configuration to decelerate at higher altitudes for a given velocity, it enables reduced heating.

Further, the lift-to-drag ratio not only affects the convective heating, but it also affects the cross-range capability of the vehicle and the ability to reduce the time to

recall a vehicle from orbit. The ability to control the vehicle and to meet the mission requirements is also dependent on the aerodynamic characteristics of the vehicle.

Finally, critical phenomena occurring during the different regimes of flight from the rarefied through the hypersonic, supersonic, transonic and subsonic portions of flight is addressed. The impact of real gas and rarefaction on capsule aerothermodynamics and in particular on forebody and wake flows is also discussed.

### 3.2 Overview of Evolution of Hypersonic Vehicle Configuration

The development of aeronautics and spaceflight, from its practical beginnings with the Wright Brothers' first airplane flew, on December 17, 1903, at Kitty Hawk, and Robert H. Goddard's first liquid-fueled rocket, launch on March 16, 1926, has been driven by one primary urge – *the urge to always fly faster and higher*.

Anyone who has traced advancements in aircraft in the twentieth century has seen exponential growth in both speed and altitude. A look to Fig. 3.1 provides an overview of civil and military aviation evolution [1]. The figure summarized the evolution of aviation for 100 years and, in particular, the evolution of the aerospace when crossing the transonic, supersonic, and hypersonic era. The earliest frontier of speed dealt with supersonic aircrafts traveling at Mach 2–3.

At this particular day and age, the push is to create aircrafts that will travel from Mach 5 to 25 or at hypersonic speed.

One of the important uses of developing vehicles that fly at hypersonic speed is for faster intercontinental travel, for example, being able to potentially fly from New York to Tokyo in less than an hour.

Another important use of developing hypersonic vehicles is to be able to fly and enter into near Earth space without any problems. The key to this initiative becoming successful requires, however, that these hypersonic vehicles demonstrate the use of the airframe-integrated ramjet/scramjet engine technology followed by the development of hypersonic aerodynamic and validation of design tools for air-breathing hypersonic vehicles.

In this framework, it is worth to note that hypersonic aerodynamics is different than the more conventional and experienced regime of supersonic aerodynamics. It can be stated that such differences must exist just by comparing the shapes of hypersonic vehicles with those of more commonplace supersonic aircraft. For example, Fig. 3.2 shows a Lockheed F-104, the first fighter aircraft designed for sustained supersonic flight at Mach 2.

This aircraft embodies principles for good supersonic aerodynamic design; a sharp, needlelike nose and slender fuselage; very thin wings and tail surfaces (3.36 % thickness to chord ratio) with very sharp leading edges (almost sharp enough to pose a hazard during ground handling); and a low-aspect ratio of 2.45 for the straight wing itself, all designed to minimize wave drag at supersonic speeds.

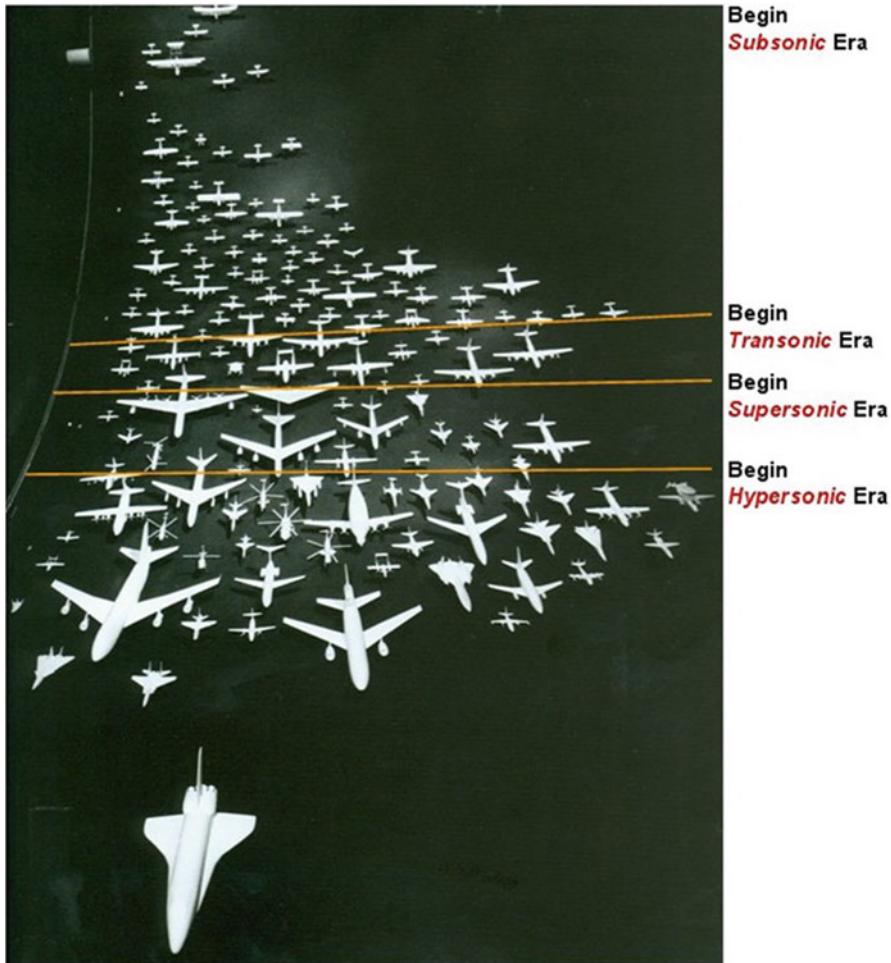


**Fig. 3.1** The evolution of aviation (Springer, 2003)

In order to design a hypersonic airplane for flight at much higher Mach numbers, it is tempting to apply the same design principles – only more so. Indeed, such was the case for an early hypersonic aircraft concept conceived by Robert Carman and Hubert Drake of the NACA (now NASA) in 1953 [2].

One of their hand drawings from an internal NACA memorandum is shown in Fig. 3.3. Here we see an early concept for a hypersonic booster/orbiter combination, where each aircraft has a sharp nose, slender fuselage, and thin, low-aspect-ratio straight wings, the same features that are seen in the F-104 except the aircraft in Fig. 3.3 is designed for Mach 25. However, in 1953 hypersonic aerodynamics was in its infancy.



**Fig. 3.2** The Lockheed F-104 a supersonic airplane designed in the early 1950s

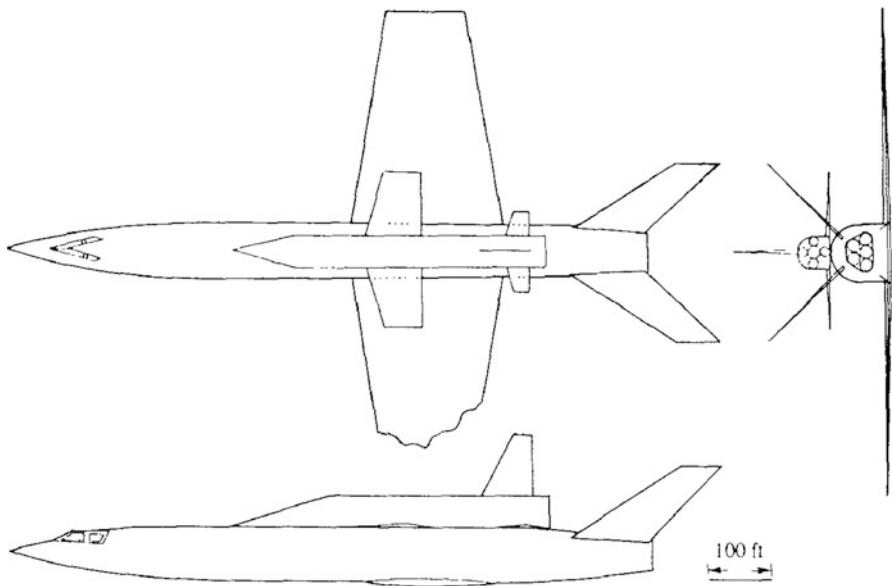


**Fig. 3.3** The Drake Carman hypersonic aircraft/orbiter, proposed in 1953

Comparing Fig. 3.3 with another two hypersonic airplanes designed just 7 years later, the NASA X-15 research airplane (proposed with delta wing) and the X-20 Dynasoar, shown in Fig. 3.4, it can be seen a completely different-looking aircraft, embodying new hypersonic principles which were not fully understood in 1953 [1].

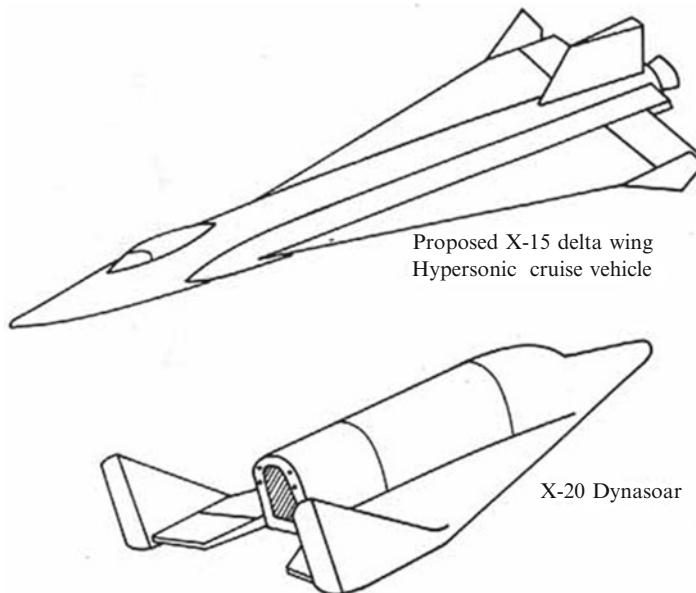


**Fig. 3.4** The NASA X-15 research airplane (*top*) and the Boeing X-20A Dynasoar orbital hypersonic aircraft, 1963 (*bottom*)

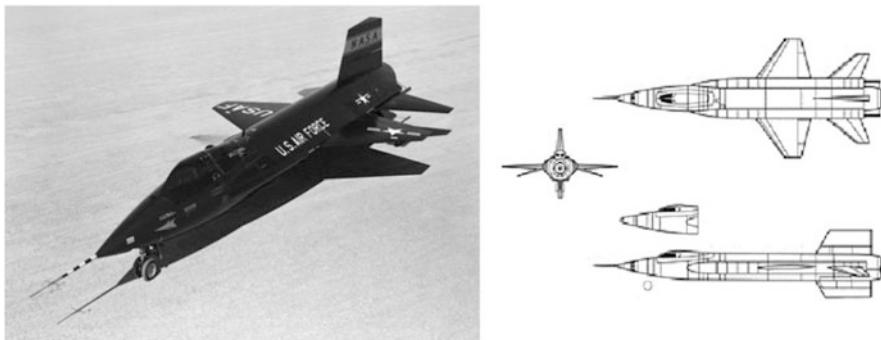


**Fig. 3.5** The X-15 configuration

The X-15, shown in Fig. 3.5, is the only real manned hypersonic airplane flown to date. It was rocket powered and started flight by being dropped from a B-52 carrier, so it was purely a research airplane. The first flight was by Scott Crossfield in June of 1959. The X-15 reached 96 km in July of 1962. An improved version reached a Mach number of 6.7 and an altitude of 31.12 km in October of 1967 with Pete Knight at the controls. The X-15 program flew 199 flights, with the last one being in October of 1968.

Several problems are encountered at hypersonic speeds.

First, the shock waves generated by a body trail back at such a high angle that they may seriously interact with the boundary layers around the body. For the most, these boundary layers are highly turbulent in nature.

Secondly, across the strong shocks, the air undergoes a drastic temperature increase and aerodynamic heating of the body is a major problem. For sustained hypersonic flight most normal metals used in today's airplanes would quickly melt. Therefore, new materials or methods that can withstand the high-temperature effects are required. For example, the temperature of the leading edge of the airplane wing may be reduced by using a high degree of sweepback.

Additionally, to obtain a good lift-to-drag ratio (L/D), a flat plate design wing is mandatory. For example, the X-20 design (shown in Fig. 3.4) utilized a sharply swept delta wing with a blunt, rounded leading edge and a rather thick fuselage with a rounded nose. The fuselage was placed on top of the wing, so that the entire undersurface of the vehicle was flat. The X-20 was intended to be an experimental aircraft for rocket-powered flight at Mach 20. Eclipsed by the Mercury, Gemini, and Apollo manned spaceflight program, the X-20 project was canceled in 1963 without the production of a vehicle. However, the X-20A Dynasoar reflected design features which were uniquely hypersonic and which were later contained in the Space Shuttle.

Starting in the late 1950s, NASA has been involved in designing aircraft that produce more lift than drag and yet resemble spacecraft. They are called lifting bodies and are shown in Fig. 3.6 [1]. As shown, they feature no wings but obtain lift because of their particular body shape.

Figure 3.6 shows four of the shapes being tested to evaluate the handling characteristics and flight qualities of this unusual concept. The M2 vehicle type developed at the NASA Ames Research Center is flat topped with a rounded belly

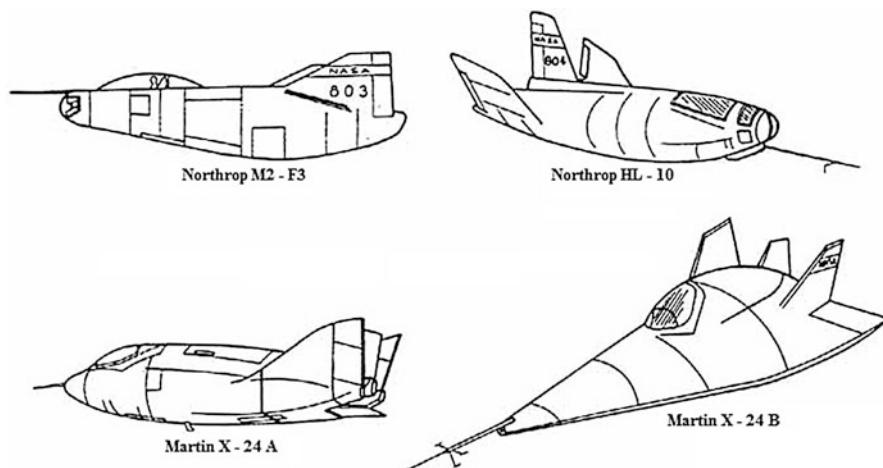


**Fig. 3.6** Lifting bodies research spacecraft

and combines the advantages of stability at hypersonic speeds with high lift-drag ratios at subsonic speeds. The HL-10 lifting body developed by the NASA Langley Research Center is shaped to provide optimum trim at Mach 10, and in contrast to the M2 vehicle, it possesses a rounded top and a flat belly. The Martin Marietta X-24A is very different in shape from the previous two since it is more rounded although it, like the HL-10, has a flat bottom. Rebuilt as the X-24B, it now has a double-delta planform and a more pointed nose.

This difference between supersonic and development hypersonic configurations is dramatically reinforced when we examine Fig. 3.7, which shows the Apollo space vehicle, designed to return humans from the Moon and to enter the Earth's atmosphere at the extreme hypersonic speed of Mach 36.

Here, we see a very blunt body with no wings at all.

After the Apollo era the next developed spacecraft was the Space Shuttle, shown in Fig. 3.8. As one can see, with the Orbiter vehicle design moved a great step ahead to improve astronauts comfort and wellness.

Investigated by NASA to obtain the basic knowledge necessary for design of commercial hypersonic flight in Fig. 3.9, a proposed hypersonic transport (HST) is shown.

By concluding, it is worth to note that to be objective, we have to realize that many considerations besides high-speed aerodynamics go into the design of the vehicles shown from Fig. 3.2, 3.3, 3.4, 3.5, 3.6, 3.7, 3.8, and 3.9. For example, Fig. 3.9 shown the important point to stress here is that hypersonic vehicles are different in respect to supersonic ones, and this is in part due to the different phenomena related to hypersonic aerodynamics not present in supersonic flowfield.



**Fig. 3.7** The Apollo spacecraft



**Fig. 3.8** The Space Shuttle

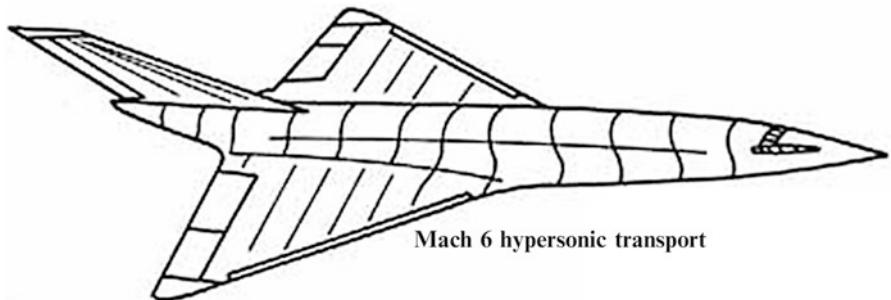


**Fig. 3.9** Proposed hypersonic transport (HST) vehicle

The most frontier will be the development of high challenging aerodynamic configurations propelled by scramjet engine.

### ***3.2.1 Hypersonic Vehicle Powered by Scramjet Engine***

Hypersonic flight, both manned and unmanned, has been successfully achieved, but not yet a commonplace. The era of practical hypersonic flight is still ahead of us, and it poses many exciting challenges to the aerodynamicist. For example, there are contemporary ideas for hypersonic transports, to cruise at Mach 7–12 and to carry people from New York to Tokyo in less than 2 h. Such a modern design concept is illustrated in Fig. 3.10. On an even more ambitious scale, there is the concept of an aerospace plane designed to take off horizontally from a runway, and then to accelerate into orbit around the Earth. It will subsequently carry out a mission in



**Fig. 3.10** A recent concept for a hypersonic transport vehicle

orbit, or within the outer region of the atmosphere, and then reenter the atmosphere at Mach 25, finally landing under power on a conventional runway.

This idea was examined by the U.S. Air Force in the early 1960s, and a combination of air-breathing and rocket propulsion (i.e., combined cycle propulsion) was intended to power the vehicle. Work on the early aerospace plane was canceled in October 1963 due mainly to the design requirements exceeding the state of the art at that time.

This idea was restored in the mid-1980s by both NASA and the Department of Defense, with the X-30 NASP, shown in Fig. 3.11.

These aerospace planes will rely primarily on air-breathing propulsion provided by supersonic combustion ramjet (SCRAMJET) engine. It is important to mention an aspect that distinguishes the hypersonic transport and the aerospace plane concepts from conventional subsonic and supersonic airplane design philosophy. For subsonic and supersonic aircraft, the components which provide lift (wings), propulsion (engines and nacelles), and volume (fuselage) are not strongly coupled with each other. They are separate and distinct components, easily identifiable observing the airplane; moreover, they can be treated as separate aerodynamic bodies with only a moderate interaction when they are combined.

Modern hypersonic aerodynamic design is exactly the opposite. Figure 3.12 is an example of an integrated airframe-propulsion concept for a hypersonic airplane,



**Fig. 3.11** The X-30 NASP vehicle concept

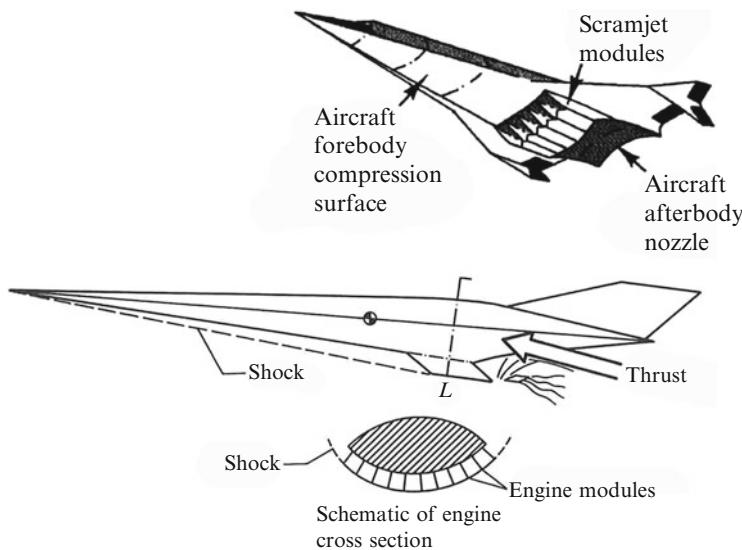


**Fig. 3.12** Hypersonic vehicle with integrated scramjet engine

wherein the entire undersurface of the vehicle is part of the *Scramjet Engine* [3,4]. Initial compression of the air takes place through the bow shock from the nose of the aircraft; further compression and supersonic combustion take place inside a series of modules near the rear of the aircraft. Expansion of the burned gases is partially realized through nozzles in the engine modules, but mainly over the bottom rear surface of the aircraft, which is sculptured to a nozzle-like shape. Hence, the

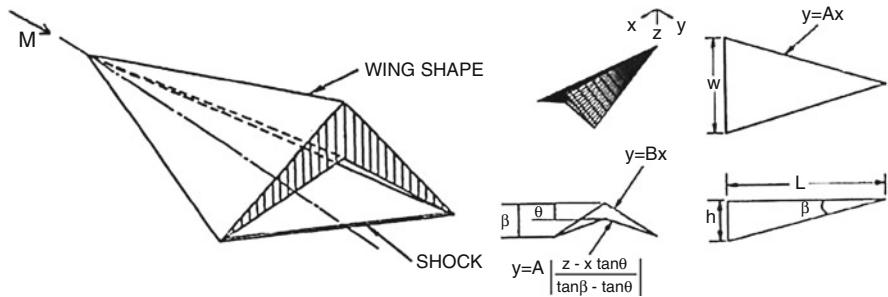


**Fig. 3.13** The caret wing waverider vehicle concept

propulsion mechanism is intimately integrated with the airframe. Moreover, most of the lift is produced by high pressure behind the bow shock wave and exerted on the relatively flat undersurface of the vehicle; the use of conventional wings, in this way, is not necessary for the production of high lift.

The fuel for air-breathing hypersonic airplanes shown in Figs. 3.10, 3.11, and 3.12 will most likely be liquid H<sub>2</sub>, which occupies a large volume. That is why air-breathing vehicles generally feature very long aeroshapes.

All of these considerations combine in a hypersonic vehicle in such a way that the components to generate lift, propulsion, and volume are not separate from each other; rather, they are closely integrated in the same overall lifting shape, in direct contrast to conventional subsonic and supersonic vehicle design.

Within the last 40–50 years, a set of vehicles have been produced in order to achieve the goal of hypersonic air-breathing vehicles as reality, and these vehicles are well known as *waveriders*. A waverider is any hypersonic vehicle that uses its own shock wave (inverse design approach) to improve the overall aerodynamic performance. These vehicles are practical at higher Mach numbers, because the shock wave must remain close to the surface, a quality of hypersonic flow. Various types of waveriders include the caret and conical flow; see Figs. 3.13 and 3.14, respectively [3, 5].

### 3.3 Overview of Entry Vehicle Design Philosophy

The design of an entry vehicle needs to fulfill the demanding requirements of the mission according to mission constraints which usually depend on the state-of-the-art in-space technology. The mission environment may consist of all or some of the following phases:

- Assembly and test
- Transport and integration
- Launch
- Interplanetary cruise, if any

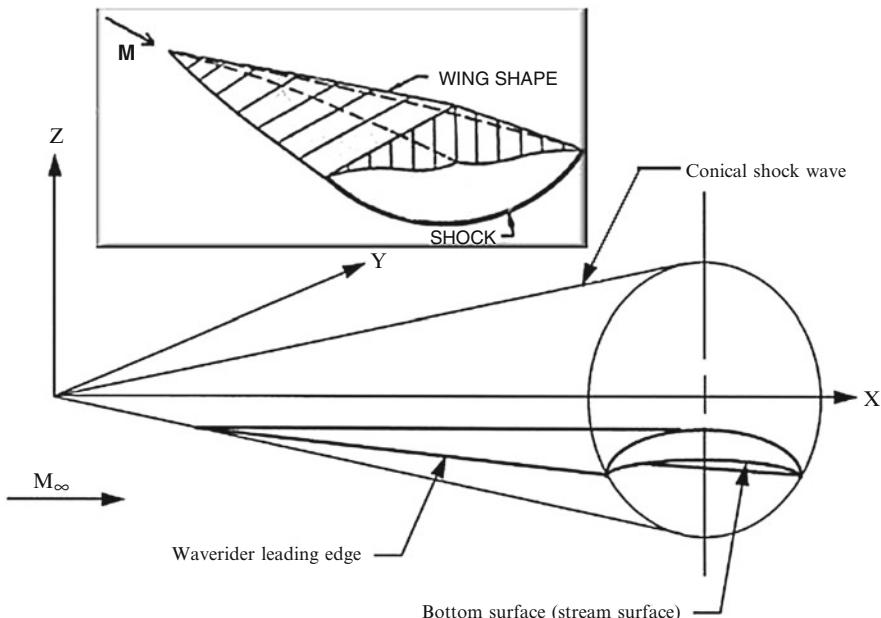


**Fig. 3.14** The conical flow waverider vehicle concept

- Hypersonic entry
- Supersonic/subsonic descent
- Landing/impact
- On-surface performance, if any

The environment effectively imposes engineering constraints on the overall design, and possibly of greatest interest is the hypersonic entry which lasts only a few minutes but can dictate most of the aeroshape configuration and a large proportion of the spacecraft mass budget. As well as the environment the remaining engineering constraints are provided by time scales, both launch opportunity and mission lengths, and most importantly in these times, costs.

The cost driver becomes predominant in tightly budgeted missions and has a great influence on the designs. For instance, in exploration missions, developed so far, the cost driver influence has been subjective at early stages of the projects and has resulted in the adoption of the following philosophy which should allow the maximum confidence in performance at the earliest possible time. This is particularly important at pre-feasibility stage:

- Adoption of ballistic entry where possible (no guidance).
- Simple generic shape to take maximum advantage of existing aerodynamic data and to simplify analysis.
- Interpolation within the existing data where possible rather than extrapolation. This may lead to suboptimal design, but higher confidence.

- Maximum commonality in geometry between missions, such that the confidence in performance is built up and common problems are more likely to be discovered.

Space mission requirements will dictate the generic vehicle configuration. Some of the more obvious major mission drivers are:

- (a) Manned or unmanned
- (b) Reusable or disposable
- (c) Large or small payload
- (d) Atmospheric environment
- (e) GN&C maneuverability (L/D)
- (f) Entry speed range

First is the decision of whether the vehicle is to be manned or just a cargo carrier. Design for manned flight requires stringent constraints on deceleration (g) loads, missions of minimal duration, and, hence, higher speeds, higher factors of safety to assure adequate design tolerance for manned missions, etc. Another major consideration is reusability. Expendable, single use vehicles, such as the Apollo capsules, can be designed with ablative heat shields and will experience a considerably different aerothermal environment than a vehicle that is designed for multiple use and long life cycle, as the Space Shuttle. Such reusable vehicles will have non-ablative, reflective heat shields. Another consideration is vehicle size and associated in-space construction constraints. Small spacecrafts can be launched intact, but large cargo-carrying vehicles will require some in-space construction.

Guidance, navigation, and control (GN&C) considerations will set the L/D requirements for a vehicle.

Vehicles with high L/D will be required when the maximum aeromaneuverability is required. High-drag bluff vehicles with low L/D will be required when maximum deceleration is required such as for direct entry aerobraking or aerocapture maneuvers. Such low L/D configurations are the capsules.

By the very nature of their use, they will generate significant aerothermal loads as they are used to convert the kinetic energy of the capsule into thermal energy in the surrounding medium.

The L/D, in turn, determines the flight angle of incidence which, in turn, determines wake impingement angle.

The vehicle ballistic coefficient determines the maximum heating and dynamic pressure loads, and the heating load sizes the thermal protection system and vehicle size and structure. Direct entry capsules utilizing ballistic entry trajectories require very little GN&C control and hence can be designed to maximize drag characteristics. Aerobraking or aerocapture, on the other hand, will require somewhat more control, and a variety of considerations must be balanced to define an optimal configuration.

So, two types of entry vehicle designs are envisaged, those which are purely ballistic with no means to control the course of the trajectory save changes in

drag and those which have a lifting capability where an on-board control system is required to shape the trajectory.

The decision as to whether a ballistic or lifting entry is chosen rests on a trade-off of general requirements such as:

- Deceleration limits (payload sensitivity, i.e., instruments, humans, or samples)
- Atmospheric uncertainties
- Landing site or targeting and recovery
- Mass and cost limitations
- Lower ballistic coefficient limit

It is possible to make a direct aerobraking entry into all of the atmospheres subject to the above constraints. For Mars, in particular, the ballistic coefficient must be low enough to allow a deceleration to the required descent velocity prior to impact. In practice the minimum achievable ballistic coefficient is about  $20 \text{ kg/m}^2$  due to material and complexity constraints. Thus, for the first entries to Mars, Viking had a modest lifting capability to ensure deceleration to parachute deployment velocity at sufficiently high altitude.<sup>1</sup> For early manned Earth orbital missions, a ballistic entry (Mercury, Vostok, Voshkod) was used since deceleration levels were endurable (8 g) and landing dispersion acceptable for recovery at that time. It should be noted that even Mercury had a control system to initiate spin and maintain zero pitch and yaw to control dispersion and lateral loads. For later missions (Gemini, Apollo) a lifting capsule with roll control was necessary to lower entry deceleration from Lunar return and also provided a means to reduce dispersion and subsequent recovery times due to atmospheric and vehicle performance uncertainties.

Above mission and trade-off requirements will translate into aerothermodynamic requirements during the design process of the vehicle configuration.

As a result, four major classes of hypersonic space vehicles are remarkable:

- Winged re-entry vehicles (RV) such as the Space Shuttle, the Buran and the Hermes
- Hypersonic cruise vehicles (CV) such as the first stage of the Saenger space transportation system
- Ascent and re-entry vehicles (ARV) such as the upper stage Horus of the Saenger system
- Aeroassisted orbit transfer vehicles (AOTV), also known as the aeroassisted space transfer vehicles (ASTV)

Their major aerothermodynamic effects are shown in Fig. 3.15 [6].

The flight aerothermodynamic loads for a spacecraft depend on:

- The atmospheric characteristics such as density and temperature
- The vehicle aerodynamic parameters such as geometry, mass, and aerodynamic coefficients
- The flight conditions such as incidence and speed

---

<sup>1</sup>The Mars atmosphere model had large uncertainties at that time.

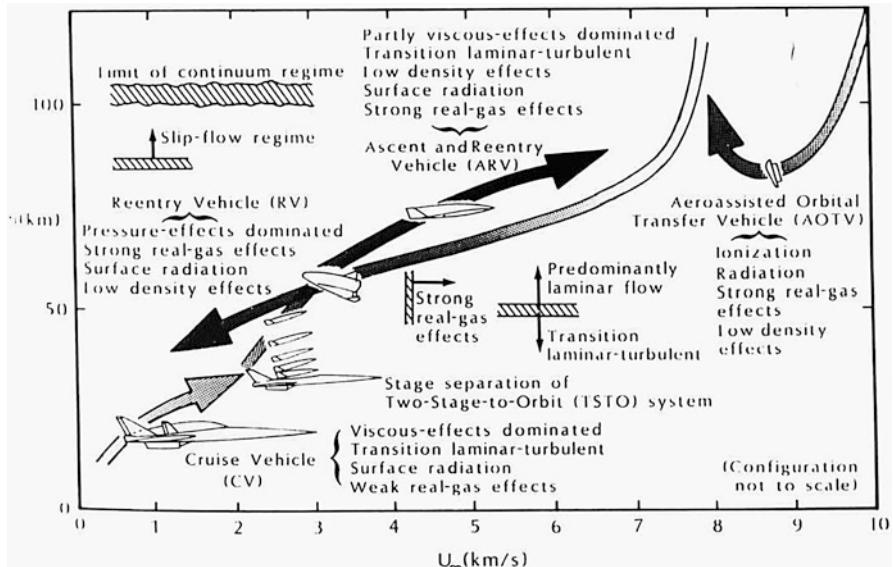


**Fig. 3.15** Four major classes of hypersonic space transport vehicles and major aerothermodynamic effects

Indeed, the most important vehicle parameters (i.e., key entry vehicle parameters) during entry are the:

- Lifting parameter,  $m/C_L S_{\text{ref}}$
- Ballistic coefficient,  $m/C_D S_{\text{ref}}$
- Lift-to-drag ratio,  $L/D$
- Body radius of curvature at the nose, wing and tail leading edges

*The topic of entry vehicle aeroshape design is to achieve suitable combinations of these parameters.*

Some comments on the above key entry vehicle parameters are in order.

The effect of lifting parameter and ballistic coefficient on the vehicle reentry trajectory is shown in Fig. 3.16 on the altitude–velocity map<sup>2</sup> [2]. Thus, vehicles with larger values of  $m/C_L S_{\text{ref}}$  and/or  $m/C_D S_{\text{ref}}$  penetrate deeper into the atmosphere before slowing. The lifting entry curve for  $W/C_L S_{\text{ref}} = 100 \text{ lb}/\text{ft}^2$  pertains approximately to the space shuttle; the curve initiated at escape velocity with  $W/C_D S_{\text{ref}} = 100 \text{ lb}/\text{ft}^2$  pertains approximately to the Apollo entry capsule.

<sup>2</sup>Note that velocity–altitude maps are convenient diagrams to illustrate various aerothermodynamic regimes of supersonic flight, and they will be used as such in some of our subsequent discussion throughout the book.

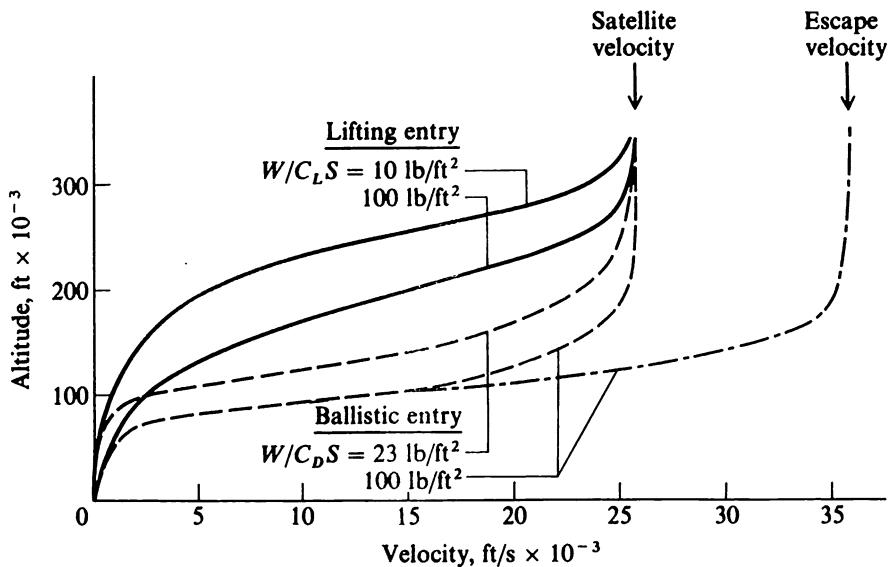


**Fig. 3.16** Atmospheric entry flight paths on a velocity–altitude map

Configurations with rather high aerodynamic efficiency, as opposed to ballistic vehicles where the lift is zero, have the advantage to reduce level of deceleration and to have maneuvering capability<sup>3</sup> and, therefore, enhanced down and cross-range capability; i.e., they can increase the landing region on Earth, as shown in Fig. 3.17 [7].

Note that because hypersonic vehicles have such a broad range of mission/performance/cost criteria and can be subjected to a wide variety of aerothermal environments, there are a wide variety of lift-to-drag (L/D) ratios. Figure 3.18 shows an overview of several vehicle configurations and their corresponding aerodynamic efficiency [7]. This figure points also out that to first-order considerations, the cost of the vehicle and the complexity of the flowfield increase with L/D.

Moreover, the effect of L/D on the stagnation-point heat-transfer rate is shown in Fig. 3.19 [7].

Indeed, lift allows the configuration to decelerate at higher altitudes (see Fig. 3.17, left side). The lower value of the free-stream density at these

<sup>3</sup>It should be noted that with increasing lift-to-drag ratio, one can control also the deceleration forces (see Chap. 2) much better which depending on whether the mission is man rated or not can be a very stringent requirement. Of course, it is worth noting that for manned missions, conservative designs are mandatory. For robotic missions, the low cost–low mass approach requires an accurate design, with small margins and a somewhat higher risk.

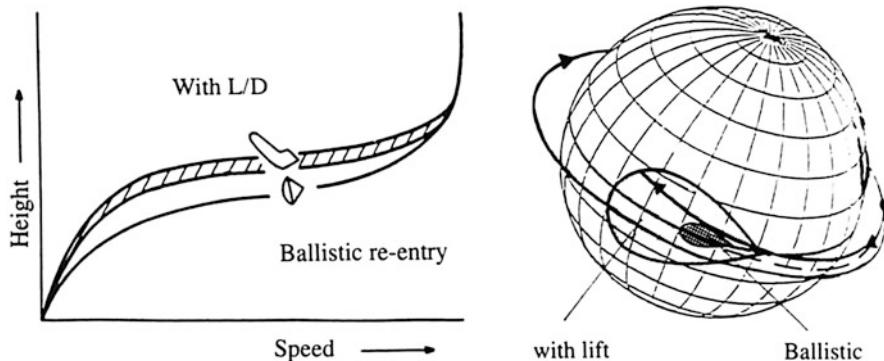


**Fig. 3.17** Influence of L/D for different configurations and landing region on Earth

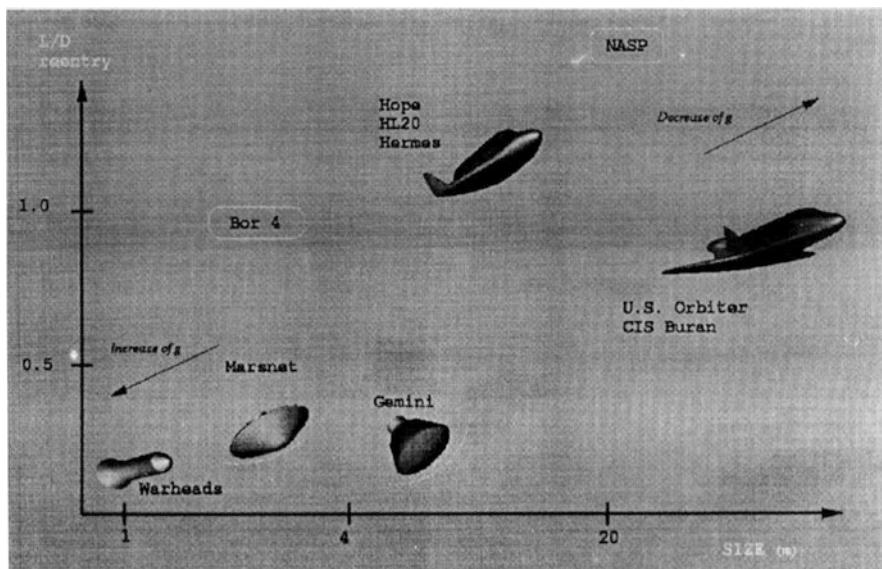


**Fig. 3.18** Overview of several vehicle configurations and their corresponding L/D

altitudes means that the aerodynamic heating will be lower at a given velocity. Note, however, that despite the decrease in heat flux, one can have an increased heat load due to the increase in flight time (see curve with L/D = 1 in Fig. 3.19).

Remember that the integrated heat load reads

$$Q = \int_{t_i}^{t_f} \dot{q} dt$$

**Fig. 3.19** The effect of L/D on the reference heating-rate history

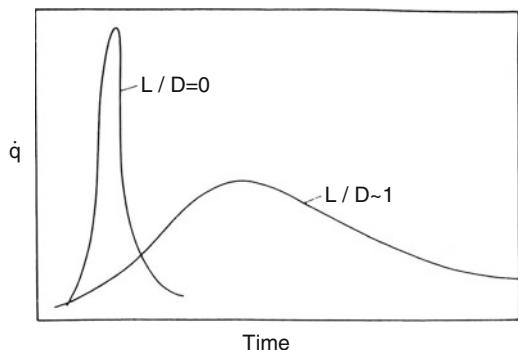
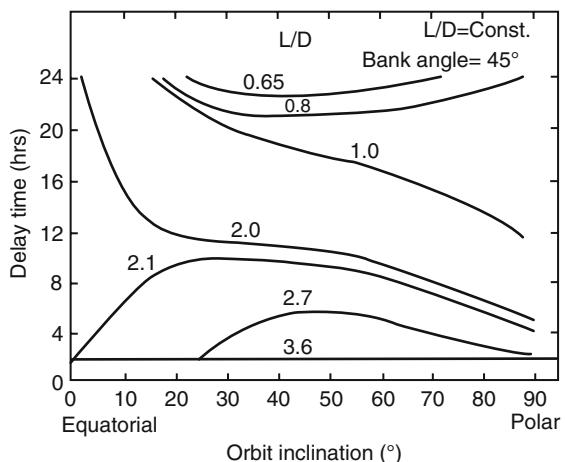


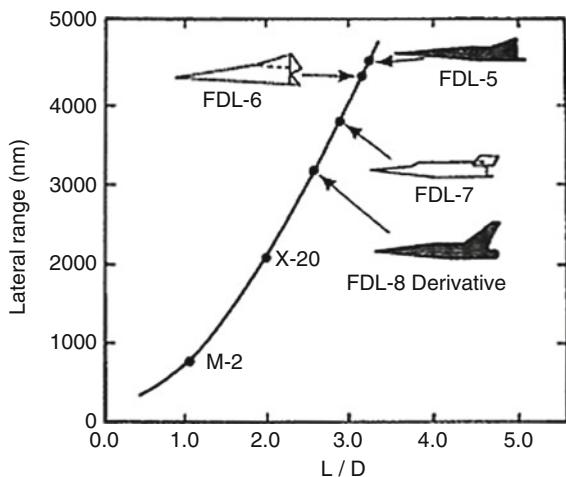
**Fig. 3.20** Maximum time for return to Edwards AFB



The accurate prediction of peak and time-integrated heat fluxes is important for the selection and sizing of the thermal protection system (TPS) material. Further, configurations that achieve relatively high values for L/D may be slender, complex shapes flying at relatively low angle of attack. As a result, the local heating rates for these configurations may be relatively high. Indeed, the simple statement that increased lift reduces aerodynamic heating requires verification for geometries of current interest. A relatively high value for the aerodynamic efficiency provides the capability of arbitrary recall from orbit, as shown in Fig. 3.20, and the capability for high cross range during the re-entry phase of flight [8]. The lateral (or cross) range performance capabilities of several configurations are reproduced in Fig. 3.21 [8]. Similarly, large values for L/D enable efficient orbital plane changes through the combined use of a propulsion system and of aerodynamic forces.

The use both of aerodynamic forces and of a propulsion system to accomplish plane change measurements is generally associated with the need to achieve larger values of the orbital plane change.

**Fig. 3.21** Lateral (or cross) range as a function of L/D for typical configuration designs



Finally, as discussed in detail in Chap. 2, the heat-transfer rate at vehicle stagnation point varies inversely with the square root of local effective radius of curvature.

### 3.3.1 Hypersonic Lift-to-Drag Ratio and Vehicle Ballistic Coefficient

Typical lift-to-drag ratios and ballistic coefficients for a range of representative entry vehicle aerodynamic designs are shown in Fig. 3.22 [7].

As shown, low ballistic coefficient ( $m/C_{DS}$ ) vehicles generally have low L/D. For example, the US manned capsules (sphere segment with offset cg) with L/D from 0.18 to 0.3 (like Mercury, Gemini, and Apollo), raked cones and cones with offset cg from 0.14 to 0.28 (AFE and Viking), had values of ballistic coefficient<sup>4</sup> on the order of 1–100 kg/m<sup>2</sup>.

High L/D (>1) vehicles generally have high-ballistic coefficients such as Shuttle, Buran. Lifting bodies such as Hermes, Bor, and HL10/20 are in between. For example, a quick estimate for the X-38 crew rescue vehicle suggests a value of about 377 kg/m<sup>2</sup>, while the Space Shuttle has a value of nearly 500 kg/m<sup>2</sup>.

Vehicles most often proposed for aerocapture missions are bent biconics and assume the geometric ratios of 2:1 for forward/aft cone angle and aft length over forward length for a maximum L/D of 1–1.5.

<sup>4</sup>Iron meteors have ballistic coefficient of 8,000 d kg/m<sup>2</sup>, and stony meteors have 4,000 d kg/m<sup>2</sup>, where d is the meteor diameter (in m).

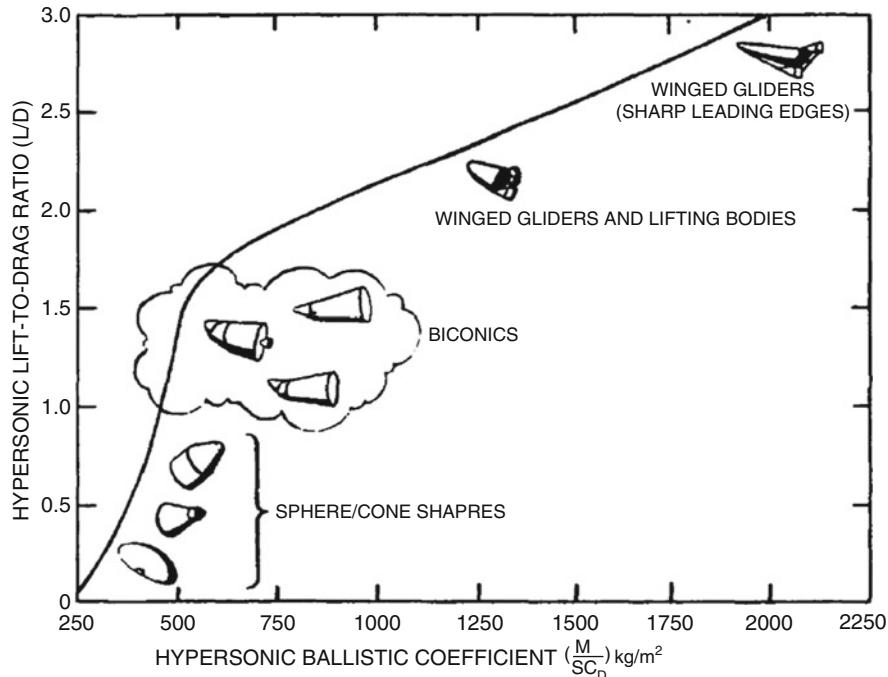


Fig. 3.22 Aerodynamic efficiencies and ballistic coefficients for re-entry configurations

Finally,  $L/D$  greater than 1.5 requires lifting bodies and blended wing/body configurations that have relatively poor volumetric efficiency and higher ballistic coefficients (based on cross-sectional area).

### 3.3.2 **Ballistic Coefficient and Vehicle Volume Factor and Fineness Ratio**

In the framework of preliminary design activities, the vehicle ballistic coefficient for trade-off entry trajectory design can be assessed by means correlation in terms of vehicle's volume factor  $l d^2$  and fineness ratio  $l/d$ , where  $d$  and  $l$  represent the characteristic cross-sectional and longitudinal dimensions (in m) of the spacecraft, respectively.

For instance, a reasonable correlation for the mass (in kg) of a manned spacecraft is given by

$$m \cong 470(d^2 l)^{\frac{2}{3}} \quad (3.1)$$

Then, the ballistic coefficient ( $B_C$ ), measured in  $\text{kg/m}^2$ , is roughly given as a function of vehicle fineness ratio ( $l/d$ ) by

$$B_C \cong \frac{587}{C_D} \left( \frac{l}{d} \right)^{\frac{2}{3}} \quad (3.2)$$

The drag coefficient here is based on the maximum cross-sectional area of the vehicle.

Thus, for capsule-like spacecraft with  $l/d \sim O(1)$  and  $C_D \sim O(1)$ , the ballistic coefficient is around 500 as already indicated for recent and current spacecraft.

### Explanation Box. Vehicle Mass Characteristics and Ballistic Coefficient

The overall mass and major dimensions of 10 manned space vehicles are presented in Table 3.1 along with some other relevant data.

The mass of the space vehicle should scale with the two-thirds power of the volume parameter ( $ld^2$ ) since spacecraft, like aircraft, are essentially pressurized shell structures. Thus, the mass should be proportional to the shell area. Consideration of the published characteristics of 10 space vehicles results in the correlation provided in Eq. (3.1). For instance, comparison between this correlation and the actual data for the space vehicles is shown in Figs. 3.23 and 3.24 for relatively small and large volume factors, respectively.

**Table 3.1** Characteristics of 10 manned space crafts

Name	Crew	Length (m)	Max $d$ (m)	Mass (kg)	Mg/A (kPa)	$B_C$ (kPa)	$(l/d)^{2/3}$
Mercury	1	2.70	1.9	1,300	4.50	2.812	1.264
Gemini	1	3.40	2.3	3,200	7.56	4.723	1.298
Vostok	1	4.30	2.42	4,258	9.08	5.677	1.467
Voshkod	2 or 3	5.00	2.42	4,802	10.24	6.402	1.623
Apollo	3	3.20	3.9	5,900	4.85	3.029	0.876
Soyuz	1–3	7.40	2.7	6,251	10.71	6.695	1.959
Shenzhou	1 or more	8.65	2.8	7,800	12.43	7.768	2.122
Shuttle	6–8	8.82	6.14	24,251	8.04	5.023	1.273
Klipper	6	12.00	3.9	15,000	12.32	7.700	2.116
CEV <sup>a</sup>	4–6	8.83	5	17,170	8.58	5.363	1.461

<sup>a</sup>Note: data estimated from current data

(continued)

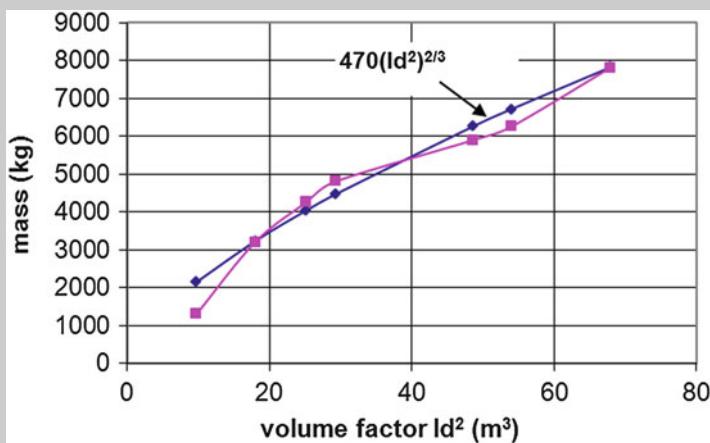


**Fig. 3.23** Spacecraft mass as a function of the volume parameter (Note that the scale for this graph is for relatively small volume factors)

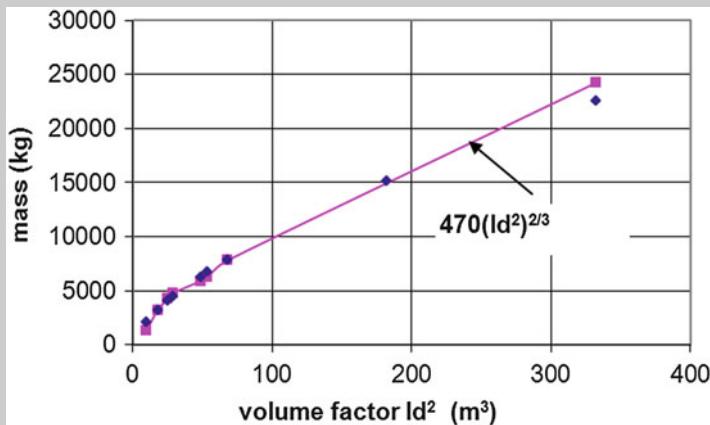


**Fig. 3.24** Spacecraft mass as a function of the volume parameter (Note that the scale for this graph is for relatively large volume factors)

A further correlation was made between the number of crew members and the reduced mass,  $m^{2/3}$ , and this is shown in Fig. 3.25. The correlation is reasonable and the probable range for the mass of the proposed NASA Crew Exploration Vehicle (CEV) is outlined on the figure.

(continued)

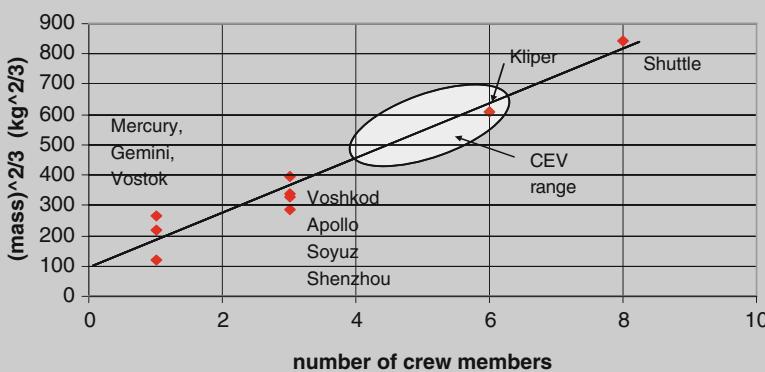


**Fig. 3.25** Correlation between the number of crew members and the reduced mass of a space vehicle

Also shown in Table 3.1 is the ballistic coefficient for each of the vehicles calculated on the basis of the given mass and dimensions and an assumption of an average  $C_{D0} = 1.6$ , estimated from an Apollo-like aeroshape. Then, an estimate of the ballistic coefficient is that provided in Eq. (3.2).

The calculated value for the ballistic coefficient is shown as a function of  $(l/d)^{2/3}$  in Fig. 3.26. The data indicate that Eq. (3.2) is reasonably correct since the data is fit well by the linear function in kPa:

$$B_C \cong 3.6 \left( \frac{l}{d} \right)^{\frac{2}{3}} \quad (3.3)$$

The coefficient is very close to  $587/C_D$ , for  $C_D$  close to the estimated value of 1.6.

The only vehicle that deviates substantially from this correlation is the Apollo spacecraft. This discrepancy may be due to the fact that the length in the Apollo vehicle may be overstated since the afterbody is extended to almost a complete cone whereas most other capsule-like spacecraft have a truncated conical afterbody.

On the other hand, the Space Shuttle, which is more like a space plane, does fit the correlation given.

(continued)

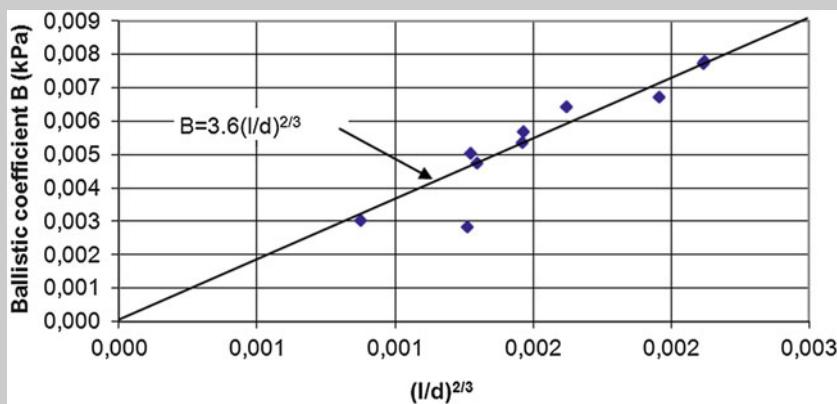


**Fig. 3.26** Correlation between the ballistic coefficient for 10 Spacecraft and the vehicle's fineness ratio  $l/d$

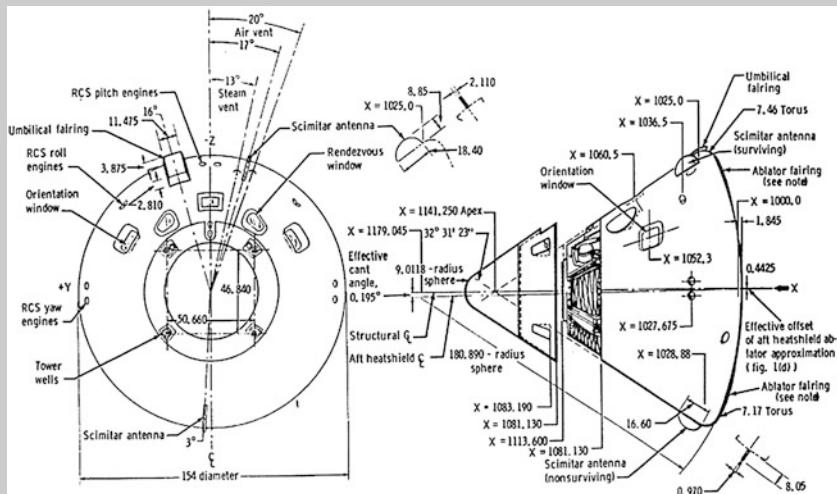


**Fig. 3.27** The Apollo space capsule

Finally, the most celebrated spacecraft capsule is probably the Apollo capsule. A detailed drawing of the capsule is shown in Fig. 3.27.

The other most recognized spacecraft is the Space Shuttle Orbiter which is shown in Fig. 3.28.

(continued)

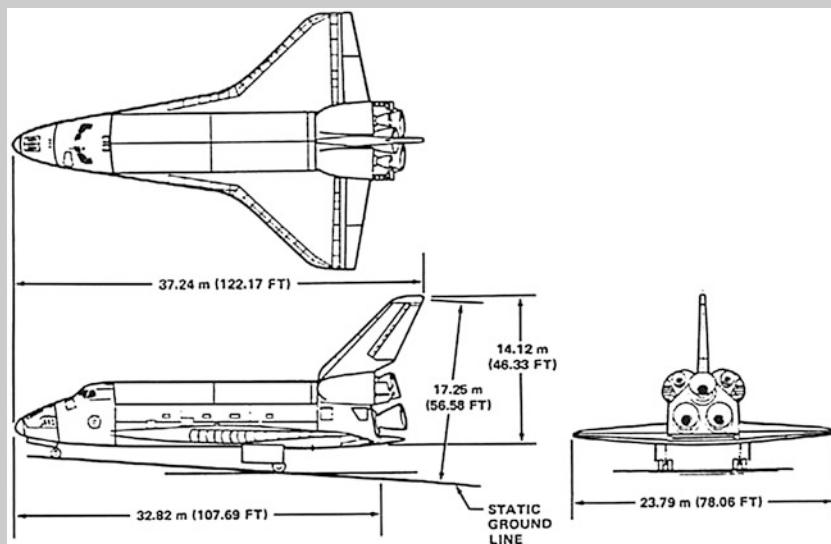


**Fig. 3.28** The Space Shuttle Orbiter

### 3.3.3 Hypersonic Trim Lift-to-Drag Ratio and Vehicle Volumetric Efficiency

The basic physics of atmospheric re-entry are the same now as they were when human spaceflight was young. Figure 3.29 shows the initial factors which must be considered in the configuration and shape of a spacecraft [8].

The figure, which assumes a 7 km/s entry velocity (corresponding to entry from LEO), shows the near linear relationship between volumetric efficiency ( $V^{0.667}/S_w$ ) and the hypersonic trim lift-to-drag (L/D) ratio. The sphere in the upper left hand corner maximizes volume with no L/D while winged vehicles, like the Shuttle, provide significant aerodynamic efficiency at the expense of usable volume. The simple, high-volume spacecraft on the left are also much less expensive to build. Vehicles with lower L/D ratios decelerate more rapidly, which translates into increased g-loading for onboard crew. On the right side of Fig. 3.29, one can see the effect that L/D has on the entry g-load for the different vehicle shapes. Low L/D shapes (such as a sphere) produce large g-loads over a shorter re-entry, while g-loads from high L/D vehicles remain at relatively low levels.

NASA standards show that humans can only withstand high g-loads for short periods of time (10 g are allowable for a maximum of 40 s) but at more moderate

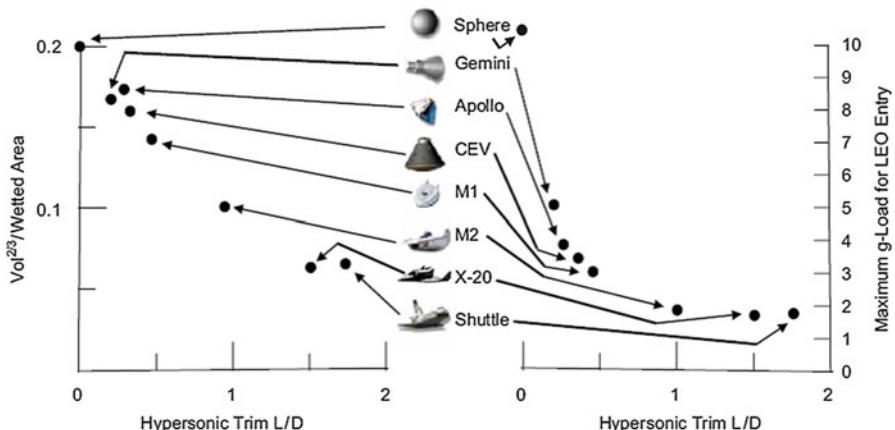


**Fig. 3.29** Effect of lift-to-drag ratio on volume and g-loads

levels human tolerance increases dramatically (7 g can be withstood for 5 min, and 4 g can be withstood indefinitely, even by injured crew). As the figure shows, even modest lift significantly reduces re-entry g-loads, which level out at L/D ratios above 0.5. Of course, cross range for landing accuracy is also a consideration.

The L/D ratio is also a good indicator of the type of re-entry heating a vehicle will encounter. The extreme g-loads resulting from a zero-lift (or ballistic) re-entry are due to the vehicle's rapid descent into the lower, thicker part of the atmosphere. This trajectory causes a high overall heating rate over a relatively short period of time. High L/D vehicles have longer re-entries with lower generalized heating rates, but the same geometry that is used to achieve lift causes higher localized heating at the leading edges. Figure 3.30, an infrared photograph of the Shuttle on re-entry, shows this localized heating vividly [8].

Temperatures across the underside of the orbiter are relatively consistent, but the nose and leading edges are significantly hotter. The net result is that high L/D vehicles generally have higher total heat loads than low L/D vehicles because they must withstand the lower generalized heating rates for a longer period of time. They must also provide a more complex thermal protection system (TPS) to account for the wide variations in localized heating.

Figure 3.31 shows predicted TPS performance at planetary return velocities for various geometry spacecraft. This performance is characterized as a percentage of overall spacecraft mass [8]. Several different estimates are shown for Apollo because the understanding of that design's capabilities improved as flight data became available in the late 1960s. It is clear from the analysis that TPS mass will play a large role in any spacecraft designed to return from Mars.

A capsule shape such as the Apollo CM is a strong competitor for LEO missions but has clear aerothermodynamic advantages for missions beyond LEO. The shape is volumetrically efficient resulting in reduced weight, which for these missions is

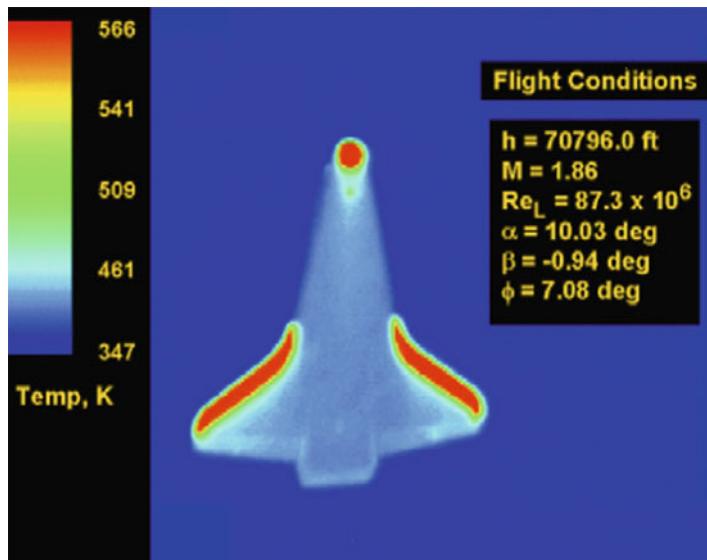


Fig. 3.30 Infrared image of Shuttle on re-entry

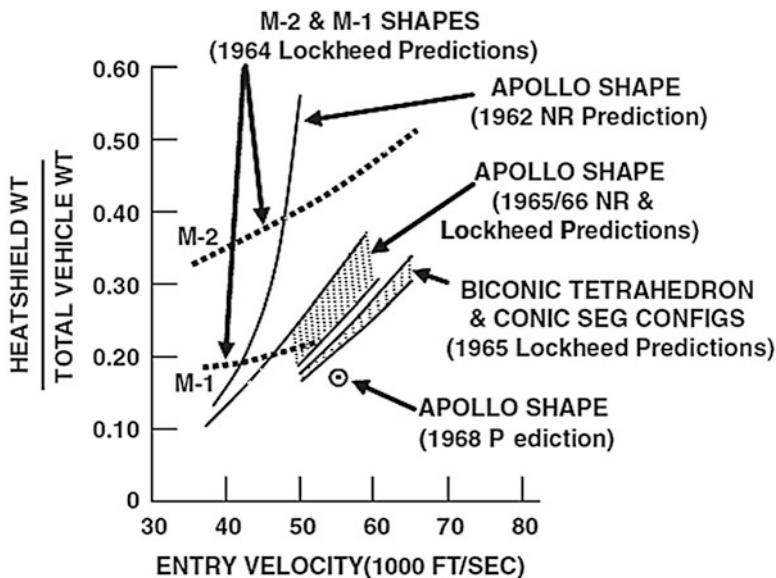


Fig. 3.31 Heat-shield weight predictions

hypercritical. Crew g-loads and localized heating are controlled within manageable limits with a geometry that is simple to analyze and simple to manufacture. Another advantage of this shape is that correct placement of the vehicle's center of gravity results in a craft that is monostable (i.e., there is only one orientation that is

aerodynamically stable). This makes it possible to accomplish a safe ballistic entry from LEO orbits in spite of a complete failure of the primary control system, something which is very difficult to do with a lifting-body configuration.

### 3.4 Spacecraft with High-Pressure Drag Configurations

Allen and Eggers in Ref. [4] noted that the convective heating is minimized by employing shapes with high-pressure drag. Such shapes maximize the amount of heat delivered to the atmosphere and minimize the amount of heat delivered to the body in the deceleration process.

The early manned entry vehicles (e.g., the Mercury, the Gemini, and the Apollo Command Module) and winged vehicles that enter at high angles of attack (e.g., the Space Shuttle Orbiter and the Hermes) are examples of such vehicles.<sup>5</sup>

As well-known, during re-entry, the vehicle and the surrounding air get hot. Therefore, the question is: “*during entry how much of initial spacecraft internal energy goes into the vehicle and how much goes into the surrounding air*”?

To answer this question let us consider a hypersonic vehicle at high altitude and high velocity, hence with large value of potential and kinetic energy. Imagine the vehicle returns to the ground at zero velocity. Hence, the potential and kinetic energy are now both zero. All the energy has been dissipated in the air, and in the vehicle (like heat), because of energy conservation law.

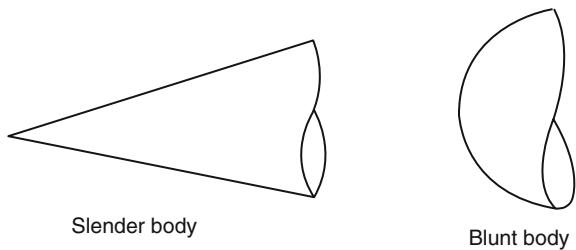
The mechanism for heating the air is in part the temperature increase across the shock wave.

On one hand, if the body is slender with a sharp nose (see Fig. 3.32), the shock wave is weak: hence *less energy will go into heating the air, and more into heating the body*. On the other hand, if the body has a blunt nose the bow shock wave will be strong: hence *more energy will go into heating the air, and less will be available to heat the body* [2].

---

<sup>5</sup>On the other hand, if the vehicle is so heavy or has such a relatively low drag that it is only slightly retarded by aerodynamic drag, irrespective of the magnitude of the drag force, i.e., a high-ballistic coefficient configuration, then the convective heating is minimized by minimizing the total shear force acting on the vehicle. Allen and Eggers define this as *the small cone angle case*. Indeed, the small half-angle cones typical of high-beta ballistic missiles are examples of these configurations. This is the case of hypersonic vehicle powered by an air-breathing propulsion system, such as the National Aero-Space Plane (NASP). Air-breathing hypersonic vehicles must fly at altitudes which are low enough that there is sufficient oxygen, i.e., relatively high density, for the propulsion system to operate effectively. However, the convective heat transfer and the drag increase as the density increases, i.e., as the altitude decreases. Thus, the trajectory of an air-breathing hypersonic vehicle must represent a compromise between the propulsion requirements and the heat-transfer/drag requirements. Since the environments in which these two types of vehicles operate are dramatically different, the designers must evaluate the importance (or lack of importance) of parameters such as boundary-layer transition, chemistry, viscous/inviscid interactions, etc.

**Fig. 3.32** Aerodynamic slender and blunt bodies



Necessity of the use of a blunt body to reach a low aeroheating was already theorized by Allen and Eggers in 1950s. In Ref. [4] they write: “*Blunt shapes appear superior to slender shapes from the standpoint of having lower maximum convective heat-transfer rates, in the region of the nose . . . Generally, the blunt shape with large high pressure drag, would appear to offer considerable promise of minimizing the heat transfer to missiles of the sizes, weights, and speeds of usual interest*”.

They also gave a demonstration of these concepts, as summarized below.

For a re-entry vehicle with a large radius of curvature, the energy balance at surface  $S$  of mass  $m$ , neglecting heat conduction inside the wall, reads:

$$\frac{d}{dt} (c_p m T) = S \dot{q} \quad (3.4)$$

where  $c_p$  is the wall specific heat and  $\dot{q}$  is the convective heat flux. Therefore, it follows that

$$\frac{dT}{dt} = \frac{S}{c_p m} \dot{q} \quad (3.5)$$

This means that the higher the surface-to-mass ratio (e.g., sharp-nosed vehicle), the higher the temperature the vehicle experiences. So, the *bluff body configuration represents the best choice to minimize the aerodynamic heating of hypersonic entry vehicles*.

Moreover, starting with the integrated heat load equation,

$$Q = \frac{1}{4} B_C V_e^2 S C_f \left[ 1 - e^{\left( -\frac{1}{w B_C \sin \gamma_e} \right)} \right] \quad (3.6)$$

It follows that for a *relatively heavy vehicle*, i.e., a vehicle with a value of ballistic coefficient  $B_C \gg 1$ , the term  $1 - e^{\left( -\frac{1}{w B_C \sin \gamma_e} \right)}$  is small compared to one. Therefore, if  $Q$  is expanded in series and only the leading term retained, the Eq. (3.6) becomes

$$Q = \frac{C_f S \rho_s V_e^2}{4 w \sin \gamma_e} \quad (3.7)$$

Thus, the least heat will be transferred when  $C_f S$  is minimum. This is the case, as would be expected if we note that requiring  $B_C >> 1$  is tantamount to requiring the vehicle to be so heavy, of a vehicle that is retarded only slightly by aerodynamic drag in its motion through the atmosphere: so the heat input to the vehicle is simply proportional to the shear force.

On the contrary, for a *relatively light vehicle*, i.e., a vehicle with  $B_C << 1$ , the term  $1 - e^{(-\rho_s \frac{1}{wB_C \sin \gamma_e})}$  is about one, so that Eq. (3.6) becomes

$$Q = \frac{1}{4} B_C V_e^2 C_f S \quad (3.8)$$

In this case the vehicle is already braked in the upper layers of the atmosphere: so *the initial energy is transmitted to the vehicle, instead to the atmosphere*.

About the efficiency of such a conversion, let us remember that for a body falling along with a vertical trajectory, neglecting the weight contribution with respect the aerodynamic forces, it follows that

$$m \frac{dV_\infty}{dt} = -\frac{1}{2} \rho_\infty V_\infty^2 C_D S_{\text{ref}} \quad (3.9)$$

So, neglecting the radiation to and from flow and calling  $\bar{S}t$  the average Stanton number on the body surface, the energy entering the body as heat ( $dQ$ ) in the time  $dt$  is

$$dQ = S_{\text{ref}} \bar{S}t \rho_\infty V_\infty \left[ \frac{V_\infty^2}{2} + c_p T_\infty - T_w \right] dt \quad (3.10)$$

Neglecting the thermal contribution with respect to the kinetic one, and obtaining  $S_{\text{ref}} dt$  from the re-entry equation, it follows that

$$dQ_{\text{reads}} \cong \frac{\bar{S}t}{C_D} m V dV \quad (3.11)$$

which integrated between re-entry velocity  $V_e$  and a generic velocity  $V$ ; it gives the efficiency of the conversion:

$$\eta_q = \frac{\Delta Q}{m \left( \frac{V_e^2 - V^2}{2} \right)} = \frac{\bar{S}t}{C_D} \quad (3.12)$$

Equation (3.12) clearly shows that in order to obtain a low value of  $\eta_q$ , we have to increase  $C_D$ , i.e., the vehicle aerodynamic drag. This means that the most favorable condition to transfer vehicle energy into the atmosphere is attained when re-entry vehicles use bluff body configurations flying at high angle of attack (e.g., high-pressure drag). This was the very important discovery by A.J. Eggers reported in

NACA TN4046 (1953) leading to blunt shaped re-entry bodies. This is true for both noses (fuselage heat shield) and leading edges (wing, etc.).

In particular, it is also possible to try to estimate the value of  $\eta_q$ . To this end let us consider the approaches proposed by Hankey and Ruppe [9].

First, according to Hankey, we get

$$\dot{Q}_B = A \left( k \frac{\partial T}{\partial y} \right)_w = St \rho V A (H_S - H_w) \quad (3.13)$$

where  $A$  is the area,  $k$  the thermal conductivity,  $\rho$  the air density,  $V$  the air velocity,  $H_S$  the flow total enthalpy,  $H_w$  the wall enthalpy, and  $St$  the Stanton number. The thermal energy flow rate of the airstream  $\dot{Q}_A$  is given by

$$\dot{Q}_A = \dot{m} H_S = \rho V A H_S \quad (3.14)$$

So, the ratio of these two heat-transfer rates is

$$\frac{\dot{Q}_B}{\dot{Q}_A} = \frac{St \rho V A (H_S - H_w)}{\rho V A H_S} \cong St \quad (3.15)$$

Further, from Reynolds analogy

$$St = \frac{C_f}{2} \cong 10^{-3} \quad (3.16)$$

Hence,

$$\dot{Q}_B = 10^{-3} \dot{Q}_A \quad (3.17)$$

On the other hand, Ruppe suggests, according to Eq. (2.85), that

$$Q \cong \frac{1}{2} \frac{C_F}{C_D} \frac{S}{A} E \quad (3.18)$$

where typical values are

$$C_F \cong \frac{1}{300} \quad C_D \cong 1 \quad \frac{S}{A} \cong 4 \quad (3.19)$$

So that

$$Q \cong 10^{-2} E \quad (3.20)$$

Both the approaches mean that only a very small percentage of heat goes into the body since most of the energy is absorbed by the atmosphere. This does not mean that there is no heating problem, because a small percentage of a big number still is

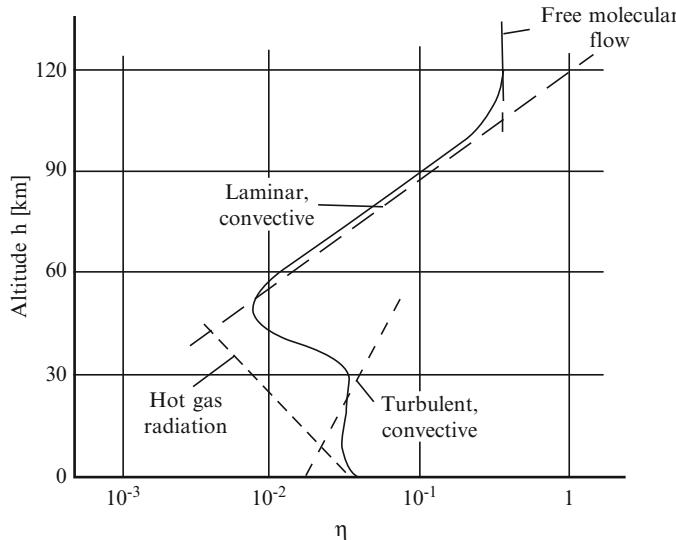


**Fig. 3.33**  $\eta q$  versus altitude

appreciable. But it does show that it is possible to survive the re-entry heating. It is possible to design a thermal protection system from a wide variety of materials and successfully re-enter the atmosphere.

There is *no thermal barrier*, but there is a *thermal obstacle*.

The major problem, however, is not the global amount of heat transfer into the vehicle, but the local hot spot, that exist on the entry vehicle, for example, for shock-shock interaction, laminar-to-turbulent transition, and shock wave-boundary layer interaction, etc..

Finally, it is worth noting that the efficiency of this energy conversion is related to the kind of vehicle configuration and attitude. In particular, Fig. 3.33 shows, for example,  $\eta_q$  as a function of altitude. In fact, among others  $\eta_q$  depends also on vehicle re-entry trajectory [9, 10].

Indeed, since  $C_F \cong C_f \cong \sqrt{\rho_s/\rho}$ , we have

$$Q \cong \frac{E}{\sqrt{\frac{\rho}{\rho_s}}} \quad (3.21)$$

This demands that  $\rho/\rho_s$ , at maximum heat transfer, be as large as possible in order to have  $Q$  as small as possible. Having  $\rho/\rho_s$  as large as possible means, in practice, flying at the minimum altitude of existence of a laminar boundary layer, since a turbulent boundary layer increases  $Q$  by about an order of magnitude. Since use of lift pushes the altitude of maximum heating upward, in the same manner as the altitude of maximum deceleration is moved upward, the usual conclusion is that lift increases the total heat transferred. This is certainly true for the same entry angle of

**Fig. 3.34** Sketch of a high-lift, high-drag configuration

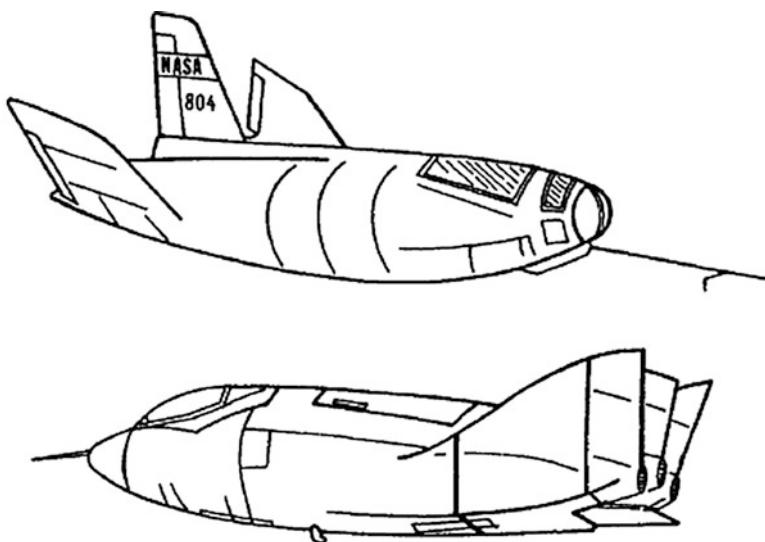
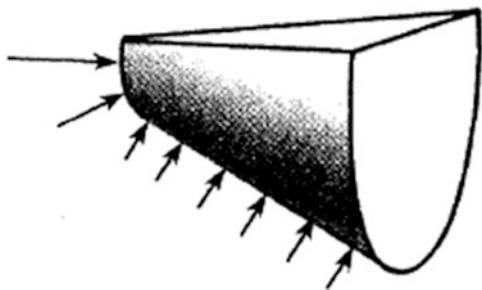


**Fig. 3.35** Examples of blunt, lifting bodies under development in 1960s and 1970s

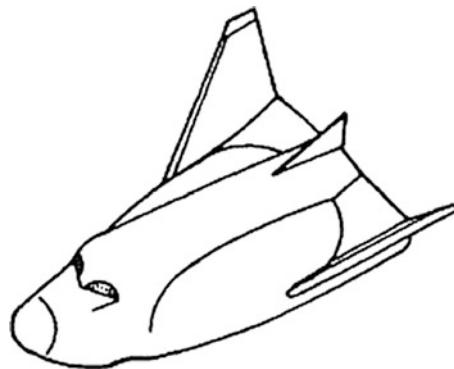
the lifting and non-lifting body, but if we take into account that for a given maximum deceleration the lifting body can enter along a steeper trajectory, then the picture changes, and the lifting body may indeed have typically about 20 % lower heat input, but a higher typically, double maximum input rate.

So, high-pressure drag aeroshapes allow to maximize the amount of heat delivered to the atmosphere. Moreover, with the lift-to-drag requirements satisfied, Eggers concludes, “*We are attracted, therefore, to high-lift, high-drag configurations for sub-satellite applications.*” Eggers suggests flat-top, blunted cones, such as depicted in Fig. 3.34, as satisfying the requirement for a high-lift, high-drag configuration [8].

As indicated by the vehicles depicted in Fig. 3.35, a variety of blunt, lifting bodies were under development in the 1960s and 1970s [8].

One of the candidate designs to satisfy the requirements for an Assured Crew Return Capability (ACRC) from the Space Station Freedom is shown in Fig. 3.36 [8].

**Fig. 3.36** Assured Crew Return Vehicle (ACRV) concept



The concept, developed in part at the Langley Research Center (NASA) from work on the HL-10 and on the X-24 programs of the late 1960s, develops a maximum lift-to-drag ratio of roughly 1.4 for altitudes from about 8 to 80 km. With this lift-to-drag ratio, the vehicle is capable of low g-loadings during re-entry, which is important for medical emergency recovery, and has sufficient cross-range capability to permit increased landing opportunities to specific sites as compared with ballistic shapes (see Fig. 3.20).

Anyway, recalling that in designing space entry vehicles requirements form the foundation of any coherent engineering effort and that there are several concerns and constraints that would require significant analyses, design iterations, testing, and development, it is obvious that configuration trade-off design analysis is mandatory within any space entry vehicle design. An example of summary result of an entry vehicle trade-off study is recognized in Fig. 3.37.

This shape study trade-off accounts for the four major entry vehicle classes, namely, blunt bodies, slender bodies, lifting bodies, and winged bodies. They are compared each other and involved in a competition which considers four figures of merit: aerodynamic efficiency, g-load, heat load, and cross range.

### 3.5 Ballistic Entry Vehicle Design

The primary mission requirement which drives the aeroshell geometry of ballistic entry vehicle is for deceleration at the highest altitude. So, the aerobraking scenario uses a low ballistic coefficient vehicle for a direct entry and aims to lose sufficient energy in the upper atmosphere to achieve the desired velocity and altitude conditions for the later mission phases. For instance, for Huygens this is so that atmosphere experiments can begin at the highest possible altitude (170 km is the target), while for Mars the atmosphere density is so low that maximum deceleration is required to provide sufficient altitude for parachute deployment at some of the chosen higher altitude sites. For Rosetta the requirement is to provide minimum

Vehicle	Lift / Drag Ratio	G load	Heat Load	Cross Range
 Ballistic Capsule	0	High	Low	Low
 Low-Lift Capsule	Low	Moderate	Low	Low
 Biconic Section	Moderate	Low	High	Moderate
 Lifting Body	High	Moderate	Very High	High
 Winged Body	High	Low	Very High	Very High

Fig. 3.37 Entry vehicle trades

mass, at a sufficiently steep entry angle to provide acceptable downrange dispersion for recovery; thus the trade-off is between heat flux and TPS thickness and area.

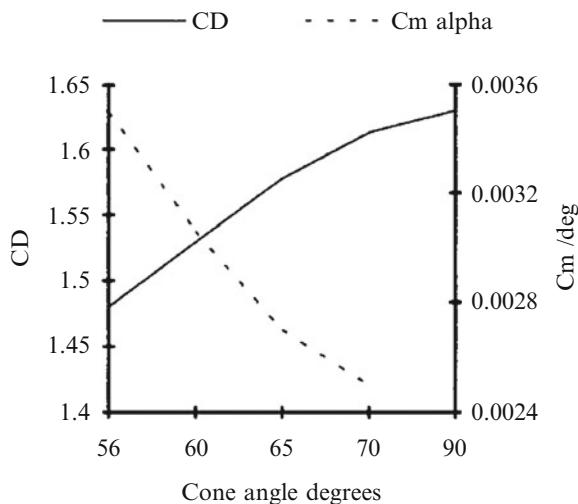
For a ballistic entry no guidance or control is necessary provided that dispersions are acceptable. The aerobraking concept is, therefore, less costly than its aerocapture equivalent but places emphasis on the design of an acceptably low ballistic coefficient stable aeroshell. To achieve a low ballistic coefficient, a large area, high-drag coefficient, low mass vehicle is required, of course. Usually, the mass is critical and the scope for mass reductions below the provisional budget allowable is small. Therefore, the design drivers are for a large area and high-drag coefficient entry vehicles. Large-drag coefficients are achieved usually at the expense of stability, and since the mass and cost budgets cannot provide an onboard stability and control system, the geometric configuration must be sufficiently stable in free flight.

Generally, in the case of exploration missions, the design philosophy is to provide as much as possible a minimum cost solution and the adoption of a simple sphere cone with large half cone angle and sufficient stability can make use of a large amount of existing aerodynamic data and is, therefore, the natural choice.

For sphere-cone configurations, main design parameters are aeroshape:

- Cone angle
- Base diameter

**Fig. 3.38** Typical drag and moment coefficients varying cone angle (Experimental results at Mach 9.5)



- *Nose radius*
- *Corner radius*

Some comments on the above design parameters are in order.

### 3.5.1 Aeroshell Cone Angle

Several studies have covered the range of half cone angles of  $30^\circ$ ,  $45^\circ$ , and between  $56^\circ$  and  $75^\circ$ . For instance, a cone angle of  $70^\circ$  has been used on Viking. It produced a near maximum drag coefficient; further increasing this cone angle has little effect on drag coefficient. Stability of the large-angle cones, however, is lower and therefore to achieve a nominal zero angle of attack through peak heat flux and peak dynamic pressure during entry,  $60^\circ$  was chosen for Huygens. This configuration has an acceptably large drag coefficient (only 4 % less than the  $70^\circ$  cone) but a higher static stability. Low supersonic/transonic dynamic stability is also greatly improved. Figure 3.38, for example, shows experimental pitching moment coefficient about the stagnation point and the drag coefficient for a range of cone angles together with the flat disk limit (i.e.,  $90^\circ$ ) [7].

### 3.5.2 Aeroshell Base Diameter

The aeroshape base diameter represents a key design parameter for a particular class of entry vehicle, namely, deployable decelerators. They allow increasing base diameter during entry, thus providing low ballistic coefficient and, hence, the lowest heat flux.

In the past, the maximum base diameter vehicle is utilized with Mars entry for three landers and for the single Huygens Probe, consistent with the space envelope available on the Spacecraft.

For Rosetta the choice was complicated by the high heat fluxes which required a dense charring ablator. With a heavy heat shield which is the most massive part of the vehicle, increasing the area increases the mass proportionally since the ablator thickness is only marginally reduced. A changeover point in TPS material to a lower density may alleviate the situation. However, even increasing the base diameter to the maximum allowable (3 m) in the space envelope did not produce a lower mass even with a TPS material change. Therefore, given the high-drag shape to give lowest fluxes, the total mass may be minimized by reducing the volume to the minimum required for the payload by reducing the diameter; this of course increases the ballistic coefficient but reduces the total heat load. So, a trade-off design process must be undertaken.

### 3.5.3 *Aeroshell Nose Radius*

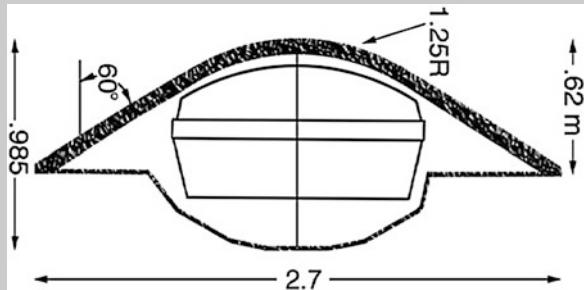
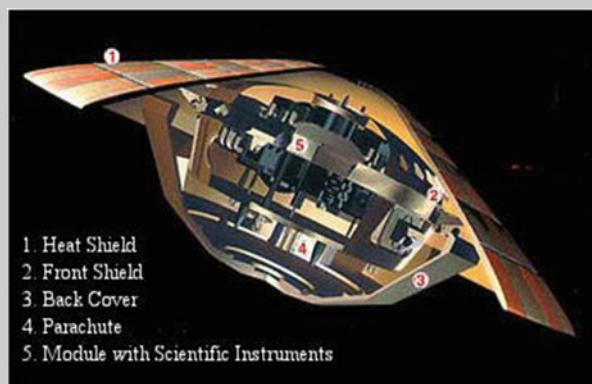
The nose radius is chosen as a near optimum for minimum heat-shield mass, ease of fitment in the spacecraft and launch envelope, for maximum drag coefficient, and for maximum allowable stagnation-point heat flux (both convective and radiative one).

Although the effect of nose radius on drag coefficient is small, a large radius gives a slightly larger drag coefficient and less mass per unit base area.

#### **Explanation Box. Some Design Highlights of Huygens, Marsnet, and Rosetta Spacecrafts**

*Huygens.* For Huygens phase A with a carbon TPS, the decelerator and forward heat shield have adequate thermal margins, and thus the mass is governed by the structural loading and by the thermal insulation requirement. Therefore, the smallest area will give the lowest mass, as the insulation mass is secondary. An instrument cover nose cap had a mass fixed by the ballistic separation requirement and was independent of the nose radius to a first order. Therefore, the largest nose radius consistent with aerodynamic stability and existing data availability (i.e., certainty in aerodynamic coefficients) should provide minimum insulation thickness for a radiative heat-shield concept given the low radiative heating environment (at phase-A configuration). The maximum geometric value was 1.5 m allowing the decelerator to be conical.

(continued)



A beryllium forward TPS was rejected for lack of thermal margin, while a low-density ablative design was also rejected due to excess mass.

The 1.25 m radius chosen was consistent with the limit of bluntness ratio where transonic aerodynamic data is readily available for the probe-less decelerator. This ensures good confidence in the design by using computational methods to interpolate between experimental data rather than relying on extrapolation beyond the available range of data.

*Marsnet.* No optimization came out in the early studies; the initial geometry was chosen as identical to Huygens in order to utilize the same aerodynamics (factored as necessary for atmosphere differences). Reductions in base diameter have been made for Spacecraft envelope fitment purposes with three landers each with reduced mass. However, the maximum nose radius produces the lowest convective coefficient and highest drag, and the nose radius remains large at 1.25 m. Radiative fluxes were found to be negligible with the low entry velocity and relatively low shock layer temperatures. The current ratio of nose radius to base radius is still within

(continued)

the existing aerodynamic databases for bluntness ratio, and, therefore, there is room for optimization in later studies.

*Rosetta.* For Rosetta since the radiative fluxes are significant, the nose radius was optimized for minimum total radiative plus convective heat load. Two distinct designs evolved; *Iteration-1* is a steep entry providing close to the maximum deceleration load allowable for the payload of 100 g. *Iteration-2* is a shallower entry designed to give the payload an easier ride at 45–55 g and is the shallowest entry with acceptable downrange dispersion. The steep entry has a shorter duration heat pulse and even though the heat fluxes are higher this leads to a thinner heat shield. The nose radius is 0.5 m for this case. The shallower entry was preferred by the project team since all structural and payload loadings are the smallest practicable. The nose radius for this case is increased to 1.0 m. Nose radius was chosen to give the combined minimum convective plus radiative heat flux since convective flux is proportional to the inverse square root of nose radius while radiative flux is directly proportional to nose radius. In these selections of nose radius, there is uncertainty in the magnitudes of the fluxes particularly for radiation, due to nonequilibrium effects.

### 3.5.4 Aeroshell Corner Radius

The final geometric feature is a radius to limit heating in the expansion corner region of the decelerator due to local flow acceleration. For Huygens and Marsnet, the provisional carbon–carbon (C–C) and ceramic (C–Sic) decelerators of the entry vehicles had a large thermal margin. However, the corner heating, similar to the nose convective heating, increases as the corner radius decreases.

For a sharp corner the heat transfer is very large value. At angle of attack, the corner heating is further increased, and even the high temperature ability of TPS may be exceeded locally. Introducing a progressively larger corner radius to the rear of the decelerator produces a lowering heat flux at the corner which at zero angle of attack becomes less than the stagnation heating. This is the criteria used and a 5 cm corner radius has been selected representing a corner to base radius ratio of 0.03 for Huygens. Analysis shows that even at large angle of attack ( $20^\circ$ ), the heat flux should be limited to less than twice the zero angle of attack stagnation value.

This increase in heat flux only increases the surface equilibrium temperature by about 20 % and, therefore, is easily within the TPS capability.

A secondary effect of a corner radius is a contribution to hoop stiffness where it is most required, and, therefore, mass penalties should not accrue from this

feature. Introducing a curvier radius reduces the drag coefficient while the center of pressure is moved forward; static stability is increased by the compensating increase in normal force producing an increase in the moment coefficient. The 5 cm corner radius selection for Huygens reduced the drag coefficient by about 2.5 % over a sharp corner. The corner radius should be reduced to the minimum in to allow the maximum drag coefficient. The adoption of an elliptic corner profile may prove to be more efficient but is outside existing databases. The same corner radius is provisionally selected for Marsnet. For Rosetta the situation is similar even with a different TPS, here the TPS is ablating and while the reduction in drag coefficient is important with increasing corner radius, it was judged more important to preserve a nearly constant thickness of forward TPS in order to lessen manufacturing complexity. A smaller radius thicker TPS may be lower in mass however, but shape change and consequent aerodynamic effects would be larger. The corner radius is thus sized to give a total heat flux equal to the stagnation value at zero angle of attack. Radiative flux uncertainties are also taken into account for this computation. The resulting corner radii are larger than for the radiative TPS of Huygens and Marsnet at 8 cm for the *Iteration-2* geometry and 16 cm for the *Iteration-1* geometry.

In conclusions the entry vehicle geometric features are determined by:

- Minimum ballistic coefficient.
- Availability of existing aerodynamic databases.
- High-drag shapes consistent with stability constraints and existing databases. This leads to the choice of large-angle sphere cones.
- Nose radii based on minimum mass, maximum drag. This leads to maximum radius for large margin C-C and C-Sic TPS limited only by bluntness ratios in aerodynamic databases. The minimum heat bad is the criteria for ablators, with equal radiative and convective components.
- Corner radii minimum for maximum drag based on thermo-structural limit for C-C and C-Sic radiator and constant thickness for an ablator.
- Base diameter maximum for minimum ballistic coefficient for maximum altitude missions.
- Deployable decelerators allow low ballistic coefficient but demand for high cost and high complexity.

Other important design issues are:

- *Boundary-Layer Transition*

Boundary-layer transition for all the bluff vehicles developed so far is based on the Viking assessments of a boundary-layer momentum thickness Reynolds number of 140 as being pessimistic. Using this value, Huygens and Marsnet maintain a laminar boundary layer throughout the entry, while on Rosetta the boundary layer becomes turbulent after peak convective flux, such that the total heat load is not greatly affected. This is fortunate for all vehicles since transition uncertainty prior or close to peak heat flux significantly affects the TPS sizing. No attempt was made

to utilize a more sophisticated transition law developed for other vehicles or flow types since extrapolation to this type of vehicle would be dubious considering the small database available.

Anyway, the lack of suitable transition data specific to this class of vehicle leads to pessimistic assumptions.

- *Base Flow*

Base flow effects for ballistic entry vehicles need analysis for two main areas:

- Shear layer impingement on the rear cover can cause local heat flux increases, plus re-attached flow can cause stability problems if the attachment point locks-in with the dynamic motion.
- The base convective heat fluxes determine the rear TPS design and mass.

For Huygens the rear cover is well clear of any impingement and, therefore, only recirculation region heating is of interest. Using a thin C-C decelerator TPS also produces a radiant heat flux to the rear. For Rosetta the rear conical heat shield was designed to be inside the shear layer based on flat base computations and a  $k - \varepsilon$  turbulent model with perfect gas (frozen) flow. The forebody boundary-layer input to the shear layer was included, but the large base radius to boundary-layer thickness means that the boundary-layer state has little effect on the base flow. For Marsnet the rear cover is also expected to be within the shear layer. The base convective fluxes are generally estimated from flight correlations in the early concept stage. Those from Viking being used for Marsnet giving about 4 % of stagnation. For Rosetta with its conical rear TPS, Apollo correlations for the separated regions were used at about 1 % of stagnation, and for Huygens 2 % of stagnation was used as an estimate from other bluff body correlations.

Differing base flow heat flux correlations seem appropriate in differing regions and atmospheres for very bluff vehicles. Anyway, further analysis is still required. Base impingement and reattachment needs to be assessed with Navier-Stokes codes. Accurate predictions of the base convective fluxes are elusive.

- *Catalytic Wall Effects*

Catalytic wall effects are expected when nonequilibrium flows are encountered.

Usually, fully catalytic walls are assumed in the early analysis, but Navier-Stokes solutions show that significant reductions in convective fluxes can occur for non-catalytic TPS surfaces. However, before advantage can be taken of this, the catalytic behavior of the atmosphere gases on the TPS wall must be known with some certainty, especially if the TPS has been exposed to space environments during the interplanetary trip. For example, radiation, debris impact, thruster plume impingement, and thermal cycling may be important effects in assessing heat shield performances.

The reactions for  $O_2$  and  $N_2$  recombination have been studied for some Earth entry TPS, but the data still exhibit large scatter. For Mars the  $CO_2$  recombination is very important to assess.

Similarly for Huygens  $N_2$  and  $CH_X$  recombination appear important.

- *Ablation Effects*

Ablation is significant for entry where heat fluxes are high and dictate the use of a high-density charring ablator such as carbon phenolic. A new technology hot structure hot bond concept is being developed for these type of TPS to reduce the heat-shield mass. Since the shock layer is close to thermochemical equilibrium during the heat pulse, existing chemical equilibrium ablation codes are used to predict the in-depth response. The ablation code also provides the blowing boundary condition for the Navier–Stokes and boundary-layer codes. This is important since the blowing reduces the wall gradients and, therefore, reduces the convective flux. The cool carbon-laden blowing gases can also absorb some of the radiative flux to the wall, the resulting heated boundary-layer gases increasing the convective flux again. Convective and radiation blockage are estimated from engineering correlations in the early stages and later assessed using full Navier–Stokes codes. The effect of blockage can be very large.

Ablator response is fully coupled to the flowfield and thus TPS sizing.

- *Contamination*

TPS contamination can occur when atmospheric gases dissociate to form potential condensates or absorbents. Such is the case for Huygens where carbon is formed from the cracking of CH<sub>4</sub>. Analysis and experiment have shown that the carbon is driven toward the cool wall by diffusion and condenses on the wall. Since the wall temperature is low compared to the carbon sublimation temperature, it is supposed that the carbon is supercooled and gives up its latent heat on touching the surface. A significant build-up of carbon deposits is expected from analysis and experiment for Huygens amounting to 0.3 mg/cm<sup>2</sup>. Other hydrocarbons may be absorbed or formed in the deposit or TPS surface.

Absorbents may outgas during descent, and particulates may shear off if the TPS is present. To date it has not been possible to distinguish between particulate and gaseous material removed, but it has been shown that circumstances could exist where the contaminant removed from the heat shield could enter the instruments if the TPS is present.

### **3.5.5 Blunt Bodies Dynamic Instability**

The dynamic response of a body is strongly coupled to both vehicle design criteria and mission objectives. Thus, accurately quantifying and effectively minimizing the expected oscillation amplitude along the entry trajectory has significant implications on the entire system. Therefore, in the frame of the development phase of a capsule, the body dynamic behavior has to be investigated, as it has strong influence on mission accomplishment and on the design of the descent subsystem (e.g., parachute) and possibly the reaction control system (RCS).

Very blunted shapes, like APOLLO, or planetary entry probes, like Huygens, have been shown to be dynamically unstable, in the sub-, trans-, and even supersonic Mach number range. Indeed, there are several possible causes of dynamic instability:

- *Roll Resonance's.* If the spin frequency becomes equal to the aerodynamic pitch frequency, then a resonant lock-in can occur. This may cause large pitch angle increases and large lateral loads and perhaps failure. Lock-in can occur twice, initially as the pitching frequency increases prior to peak dynamic pressure and passes the spin frequency and then as the pitching frequency decreases after peak dynamic pressure or as the vehicle spin rate increases due to asymmetries. Usually first resonance occurs at high altitude where aerodynamic forces are low, and usually no problem occurs. However, at lower altitude especially if the vehicle has an increasing roll rate due to asymmetry, a problem can occur. The resonant phenomena are entirely avoided if the vehicle spin axis is the major inertial axis. This is the main design goal for all entry vehicles.
- *Pitch Damping.* Instability can occur if there is positive pitch damping. This commonly occurs with bluff vehicles at low supersonic and transonic speeds. Axisymmetric vehicles have this characteristic at zero or small angle of attack, and the bluffer the vehicle the worse the problem. It is therefore avoided by one of three following methods:
  1. Avoid flying through this flight domain. Supersonic parachute deployment is a possibility but can impose additional problems for the parachute design.
  2. Adapt the geometry to a less bluff shape. This is the common route and is a performance trade-off.
  3. Fly at angle of attack where the effect is minimized. A lifting entry requires a guidance system and can increase complexity and costs significantly. This is therefore to be rejected if adequate performance in terms of deceleration/altitude can be achieved with an aerobraking ballistic entry.

Dynamic instability seems to be due to the nature of the flow separation zone, in the case of Apollo, and to the unsteady characteristics of the near-wake recirculating flowfield in the case of planetary probes like Huygens or Viking. Indeed, unsteady flows in separated regions can lock in with the vehicle motion.

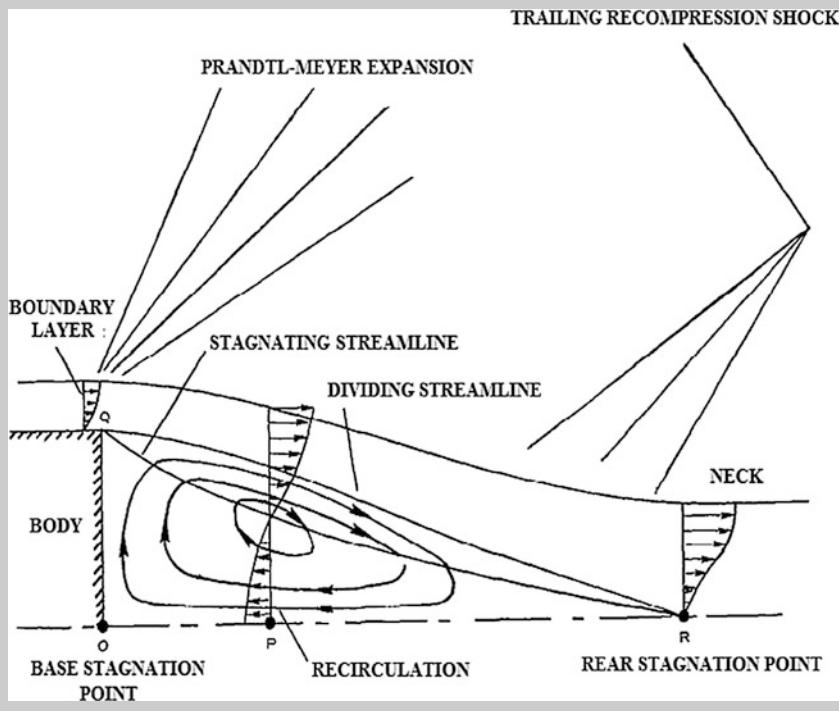
#### **Explanation Box. Dynamics Stability and Blunt Body Wake**

Unsteady pressure forces on the aft body are the primary source of dynamic instability. This problem was not as evident in the early investigations of the dynamic stability of ballistic missile shapes because of the relatively well-behaved convergent flow behind the long, slender bodies being studied. As the focus changed from ballistic missiles to blunt capsule shapes with the rise of the space race, it became clear that an understanding of the aft body flow structure was critical to understanding the dynamic stability phenomenon.

(continued)

In supersonic flow about a blunt body, a bow shock wave leads the nose of the vehicle. Flow downstream of the bow shock stagnates on and accelerates around the forebody. The large turning angle off the shoulder induces the formation of expansion waves and separation of the flow. This creates a low-pressure region behind the body characterized by an unsteady recirculation region in the near wake. Further downstream, the wake flow converges, stagnates, and forms a trailing recompression shock that heats the fluid. The figure graphically depicts these flow features. The core of the wake will be viscous and often partially subsonic while the outer wake is typically inviscid and supersonic. Even in steady flight with zero angle of attack, these factors combine to result in a flow with a time-varying pressure field is a function of axial and radial position relative to the forebody.

When pitch oscillations are added to this scenario, the position of the wake features “lag” behind the motion of the forebody due to the finite convection velocity in the flow. This creates a hysteresis effect on the pitching moment and aft body pressure field, adding further complexity to the wake structure. At present, no experimental or computational methods have accurately and generally captured the time-varying, dynamic wake structure of a blunt body undergoing pitch oscillations. Large uncertainties in the behavior of the aft body wake prevent a clear understanding of dynamic stability phenomena.



Similarly reattachment points can move with the vehicle motion; again resonance can occur. Base flows for the vehicles presented here are of concern, and reattachment is avoided by ensuring that the base aeroshell is within the shear layer up to maximum expected angle of attack. Blowing from ablation is an example where forebody aerodynamics can be affected adversely. The lag in ablation product formation is caused by the heat soak time constant of the material to react and produce pyrolysis gases. This can occur if there is a significant coning motion where the windward meridian is rotating in body coordinates. This is avoided by ensuring a low initial angle of attack and low coning motion.

Finally, forebody acoustic excitation is avoided with a laminar boundary layer, step size minima, and roughness criteria being set.

### 3.5.5.1 Description of the Problem

When entering atmosphere, the incidence evolution of a blunt body behaves like an oscillator response which is submitted to static and dynamic forces and moments, i.e., the aerodynamic ones.

In the case of a statically stable shape, the aerodynamic static torque results in trimming the incidence through a sinusoidal motion.

So, the shape is dynamically stable if the amplitude of the incidence oscillatory motion decreases with decreasing altitude. Incidence is then reaching asymptotically its trim value. A further perturbation of incidence is damped.

At the opposite, if the shape is dynamically unstable, incidence amplitude of the oscillatory motion increases, and incidence diverges.

#### Explanation Box. Dynamics During Entry

Consider a ballistic exploration entry vehicle on a mission to Mars. Usually, it is separated from the carrier module on the direct trajectory approach to the red planet and to preserve its designed attitude for entry is spun slowly at separation. Since the separation can occur several days prior to entry, nutation of the motion is to be avoided, and as such, the principal inertial axis should be arranged to be the spin axis.

Then, the vehicle enters the atmosphere at an angle of attack which is a combination of exoatmospheric coning motion and the inclination of the coning axis to the trajectory velocity vector. The coning motion is caused by the separation tip-off errors from the spacecraft at spin eject time, combined with the mass characteristics of the body, principally the dynamic unbalance.

Note that on entering the atmosphere, it can be arranged that the spin axis is aligned with the velocity vector.

This is chosen for several reasons:

- The vehicle aerodynamics may not be well characterized at rather high degree of incidence.
- Allowance has been included for exoatmospheric coning motion.

(continued)

- Large lateral forces are not desirable.
- Cyclic heat flux variation are not desirable.
- Large pitch angles are not desirable for atmosphere analysis from trajectory data.

However, a small angle of attack is allowable.

During entry as the body experiences atmospheric forces, an aerodynamic moment is generated which acts to decrease the angle of attack if the vehicle is stable. The motion becomes gradually more dominated by the aerodynamic force and less by gyroscopic effects. The entry vehicle begins to respond in a pitching motion. As the aerodynamic stiffness increases, the angle of attack envelope is reduced. This motion is damped by the dynamically induced aerodynamic force generated called the pitch damping force. After peak dynamic pressure the angle of attack envelope would again increase; however, due to the damping of the pitching motion, the angle of attack continues to reduce and becomes asymptotic to the static trim angle of attack.

Blunt cones exhibit a pitching reinforcing (positive) damping force in the transonic to low supersonic regime, and while this does not affect the hypersonic entry phase, it is important to note that the destabilizing coefficients are maximum for the blunter configurations, and the effect must be considered for the supersonic-transonic motion which may include parachute deployment or aeroshell/decelerator jettison sequences. Also of note is that the destabilizing coefficients reduce with increasing angle of attack, such that by 20° incidence the damping coefficients again act to reduce the pitching motion.

Furthermore, structural modes should be well clear of the pitch or spin frequency to prevent any aeroelastic coupling. For the high atmosphere deceleration, low spin rate entries, the frequencies are of order a few Hz, and major structural modes are well above these, for the current designs.

Although not strictly dynamic instabilities, a structure–flowfield coupling can occur, for example, panel flutter. So, aeroelastic analysis is mandatory within capsule design. Further, natural structural modes must be checked against aerodynamic frequencies, e.g., probe pitch and spin frequencies, and base flow pressure oscillations as well.

In this framework, also vehicle asymmetries may affect its dynamics during entry.

Typical vehicle asymmetries are:

(a) *Center of Gravity Lateral Offset*

A center of gravity (cg) lateral offset from the geometric central (spin) axis is normally due to the accuracy of the static balance and leads to both the offset of the principle rotation axis from the geometric centerline and to the generation of a trim angle of attack during atmospheric entry.

(continued)

For very statically stable entry vehicles, the consequences of cg offset on the trajectory are small and any initial angle of attack is quickly damped to the trim angle of attack.

For example, Fig. 3.39 shows that the resultant static trim angle of attack for the Huygens Probe is under  $4^\circ$  for every centimeter lateral cg offset, such that a very small trim should be achievable with a balance within 5 mm.

A much larger maximum cg offset was used in Monte Carlo six degree-of-freedom (6 dof) trajectory stability studies of this vehicle, such that the probe is shown to be statically and dynamically stable during entry.

For Rosetta, sample density<sup>6</sup> and load asymmetry were shown to have a small overall effect on trim.

#### (b) Aeroshell Asymmetry

During manufacture, assembly and flight the aeroshape will gain some degree of distortion resulting in aeroshape asymmetry. This distortion could produce significant trim moments. These again in isolation produce a trim angle of attack which will act the same as a center of gravity offset discussed above. Axial symmetric distortions will have very little effect on the trajectory or entry vehicle (apart from roll moments) and will be well within the predicted accuracy of the ballistic coefficient. Figure 3.39 shows the static trim angle of attack resultant from first harmonic radial distortion of the decelerator on the Huygens Probe [7]. Some results are for Rosetta too.

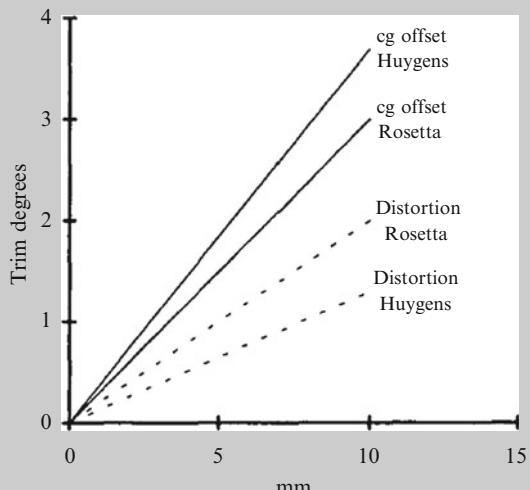


**Fig. 3.39** Static trim from asymmetries

<sup>6</sup>Rosetta landed on the comet 67P/Churyumov–Gerasimenko on November 12, 2014, and initially it was planned to bring to Earth a sample of the comet.

(continued)

The distortion is assumed to be zero at the decelerator/probe joint station and linearly increasing to the maximum at the decelerator rear.

In addition where there is a large amount of surface recession due to ablation, similar asymmetries may occur. For the Rosetta entry vehicle, the effect was estimated by allowing the carbon phenolic char layer to strip from one side of the vehicle only, although in practice this is unlikely with the shear forces predicted. The resultant trim was very small (less than 1°).

### (c) Combined Asymmetries – Spin Rate Limitation

Mass and geometric asymmetries in combination and depending on their angular relationship can produce significant roll torque's which may either spin the entry vehicle up or down (and through zero roll rate). The angular relationship is critical, but for low spin rates, an out of plane (90°) relationship is close to the worst case. Six dof entry simulations with varying asymmetries are used to produce spin rate histories. Figure 3.40 shows contours of spin rate excursions from the spin rate at the start of the entry phase to Mach 1 for a typical Huygens entry [7]. While these will vary with trajectory, this type of figure serves as a design guideline for geometric and mass tolerancing. The heat-shield roll damping due to skin friction has not been included. The effect is likely to be small for these classes of entry but always acts to reduce the spin rate. The choice of an adequately low initial spin rate (initially 60°/s) ensures that the spin rate at the start of the descent phase is in the desired range for Huygens (i.e., the limiting spin up case) and may be a consideration for Rosetta and Mars entry for parachute deployment.

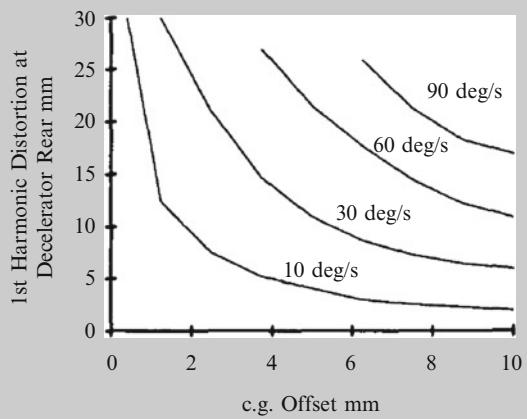


**Fig. 3.40** Change in Huygens Probe Spin to Mach 1

(continued)

Only sufficient spin to ensure low exoatmospheric wobble is necessary. Entry vehicles do not require spin for entry stability, and even spin excursions through zero roll rate do not contribute significantly to ground dispersions when compared with initial trajectory alignment errors and atmosphere density variations.

(d) *Moments of Inertia*

To avoid nutation and consequent tumble during coast, pitching/spin resonance problems during entry, and to relax the tip off error rotation rates budget, the spin or polar moment of inertia  $I_{xx}$  should be larger than the lateral moments of inertia  $I_{yy}$  and  $I_{zz}$ . This should also be observed for the Huygens Probe without decelerator as the Probe pitching frequency is quite low after decelerator jettison, and should the probe spin rate have increased during entry, then a resonance could occur. The possibility of a resonance is removed (and the need for analysis) if  $I_{xx}$  remains greater than  $I_{yy}$  and  $I_{zz}$ . The Huygens Probe, for example, has acceptable inertia ratios of about 1.4:1. Asymmetry of  $I_{yy}$  and  $I_{zz}$  is of little consequence during entry, resulting only in sine squared variation in the spin rate during coning motion. For the missions considered it is desirable to measure roll acceleration to examine the aerodynamic performance, and therefore,  $I_{yy}$  and  $I_{zz}$  should be close. Nonzero products of inertia  $I_{xz}$  and  $I_{xy}$  cause the principal polar axis to be at an inclination to the geometric axis. During exoatmospheric flight, this leads to a coning motion even in the absence of pitch and yaw impulses during spin up and separation from the spacecraft. During the entry phase so long as the entry vehicle spins, then an additional trim angle of attack is induced which is dependent both on the spin rate and the aerodynamic pitching frequency. This effect together with cg offset and trim asymmetries may increase or reduce the roll rate depending again on the phasing. However, the effect is small as when the entry vehicle is close to peak dynamic pressure the aerodynamic pitching frequency is highest and the roll rate low even for large asymmetries. Therefore, products of inertia are only limited by the initial angle of attack generated by the exoatmospheric coning motion. The coning motion angle must be added to the inclination of the coning axis to the trajectory to form the total angle of attack. The practical limit of products of inertia is recommended to be less than 2 % of the difference between the polar and lateral moments of inertia. This may be relaxed considerably once the mission trajectories become inure firmly established in post feasibility stages of the project.

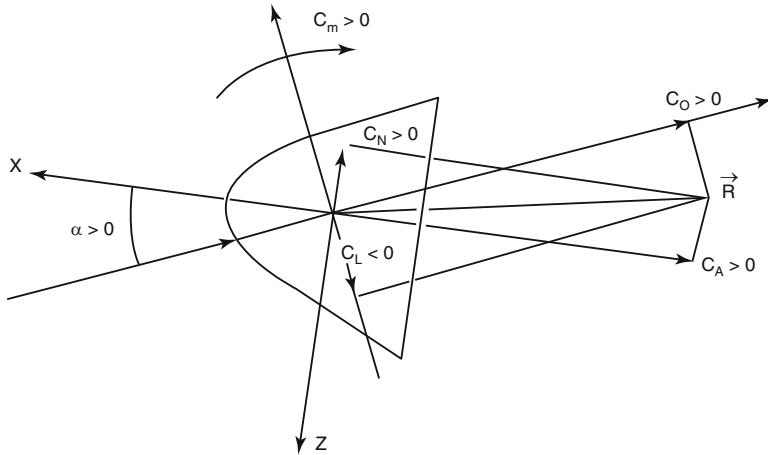


**Fig. 3.41** Aerodynamic forces and moments for an axisymmetric capsule

So, in order to assess vehicle aerodynamic parameters which define stability, let us consider a capsule in free fall, as shown in Fig. 3.41 [7].

As one can see, the aerodynamic efforts are fully described by:

- A force vector  $\vec{R}$ , which is the vectorial resultant of all the aerodynamic forces, which act on the body.
- A torque  $\vec{M}$  given at a certain location, the center of gravity, for example,  $\vec{M}_{cg}$ .

In the body fixed reference frame, we get

$$\vec{R} = \left( -C_A \hat{i} + C_Y \hat{j} - C_N \hat{k} \right) \cdot q_\infty S_{ref} \quad (3.22)$$

$$\vec{M}_{cg} = \left( C_l \hat{i} + C_m \hat{j} + C_n \hat{k} \right) \cdot q_\infty L_{ref} S_{ref} \quad (3.23)$$

where  $q_\infty$  is the upstream dynamic pressure;  $L_{ref}$  and  $S_{ref}$  are the reference length and reference surface, respectively; and  $C_{A,Y,N}$  and  $C_{l,m,n}$  are force and moment coefficient about  $x, y, z$  coordinate axes (see Chap. 1).

Note that in the case of an axisymmetric aeroshape, like Huygens, entry module flying at  $\alpha_0$  angle of attack normal and side force coefficients are equal, that is,

$$C_N (\alpha = \alpha_0, \beta = 0) = C_Y (\alpha = 0, \beta = \alpha_0) \quad (3.24)$$

The same for pitch and yaw moment coefficients:

$$C_m (\alpha = \alpha_0, \beta = 0) = C_n (\alpha = 0, \beta = \alpha_0) \quad (3.25)$$

As a result, vehicle stability depends on pitching moment behavior. Thus, if we get linearity hypothesis, the pitching moment coefficient reads:

$$\begin{aligned} C_m &= \frac{\partial C_m}{\partial \alpha} \cdot \alpha + \frac{\partial C_m}{\partial \left( \frac{\dot{\alpha} L_{ref}}{V_\infty} \right)} \cdot \frac{\dot{\alpha} L_{ref}}{V_\infty} + \frac{\partial C_m}{\partial \left( \frac{q L_{ref}}{V_\infty} \right)} \cdot \frac{q L_{ref}}{V_\infty} \\ &= C_{m\alpha} \cdot \alpha + C_{m\dot{\alpha}^*} \cdot \frac{\dot{\alpha} L_{ref}}{V_\infty} + C_{mq^*} \cdot \frac{q L_{ref}}{V_\infty} \end{aligned} \quad (3.26)$$

Therefore, capsule pitching moment coefficient features a static and a dynamic component. The former pertains to  $C_{m\alpha}$  while the latter to  $C_{m\dot{\alpha}^*}$  and  $C_{mq^*}$  derivatives.

That is why  $C_{m\alpha}$  is namely vehicle static stability parameter while  $(C_{m\dot{\alpha}^*} + C_{mq^*})$  is said vehicle dynamic stability parameter, also known as pitch dumping. Indeed, the shape is statically stable if the aerodynamic torque tends to decrease  $\alpha$ , i.e.,  $C_{m\alpha} < 0$ , because of an incidence increase results in a torque which will oppose to this angular displacement.

On the other hand, it can be demonstrated that the aeroshape is dynamically stable if

$$\xi = C_D - C_{L\alpha} + \left( \frac{L_{ref}^2}{r} \right) \cdot (C_{m\dot{\alpha}^*} + C_{mq^*}) < 0 \quad (3.27)$$

where  $\xi$  namely dynamic stability parameter;  $C_{L\alpha} = \partial C_L / \partial \alpha$  and  $r^2 = I_t/m$  are the transverse radii of gyration being  $I_t$  the inverse inertia and  $m$  the vehicle mass.

#### **Explanation Box. Dynamic Stability and Vehicle Design Considerations**

The most significant vehicle design aspects that affect dynamic stability are the overall geometry and mass properties of the vehicle. Forebody shape, aft body shape, shoulder radius, center of gravity location, and other parameters all influence the dynamic stability characteristics. If a vehicle employs a reaction control system to counteract the dynamic oscillations, this system must be sized and designed to meet the requirements given from an estimated dynamic response. In addition, the heating environment experienced by the body will be altered by the angle of attack history; therefore, the sizing of the thermal protection system of a vehicle must take into account the oscillation amplitudes that are to be experienced during entry.

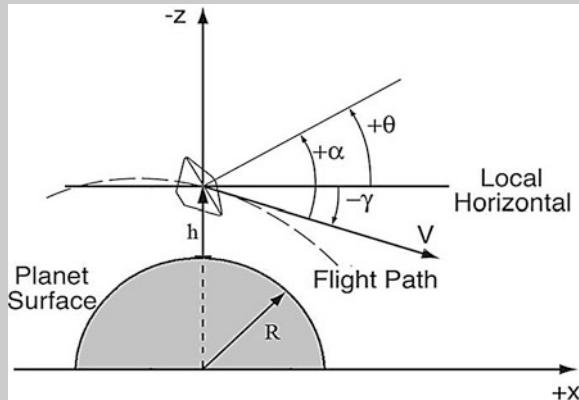
(continued)

As far as mission design considerations are concerned, it is worth noting that to impacting the design of systems and subsystems of the vehicle itself, dynamic stability issues have a critical role in many aspects of the mission design. For any vehicle employing a parachute, it is critical that the oscillation amplitude at the time of parachute deployment be less than approximately  $10^\circ$  to ensure proper inflation.

Entry trajectory design is a significant driver of a vehicle's dynamic response through a dependence on Mach number, Reynolds number, Strouhal number, and dynamic pressure. Additionally, trajectory dispersions, the size of the landing footprint, atmospheric science performed during entry, and on board communication capabilities may be sensitive to angle of attack oscillations.

In this framework, let us consider the equations of motion that describe the dynamic oscillation of a vehicle such that the subsequent discussions on the influence of various parameters in the system are grounded in the context of the governing physics.

The figure describes the coordinate system of the planar formulation of the entry problem. The derivation of the mathematical model describing the dynamic oscillation of a vehicle, presented here, begins with the four planar equations of motion for an entry vehicle that describe rates of change of the altitude, velocity, flight path angle, and pitch angle with respect to time:



(continued)

$$\begin{aligned}
 \frac{dh}{dt} &= \dot{h} = V \sin \gamma \\
 \frac{dV}{dt} &= \dot{V} = -\frac{\rho V^2 C_D S_{\text{ref}}}{2m} - g \sin \gamma \\
 \frac{d\gamma}{dt} &= \dot{\gamma} = \frac{\rho V C_L S_{\text{ref}}}{2m} - \left( \frac{g}{V} - \frac{V}{R} \right) \cos \gamma \\
 \frac{d^2\theta}{dt^2} &= \ddot{\theta} = \frac{\rho V^2 S_{\text{ref}} L_{\text{ref}}}{2I} \left( C_{mq^*} \frac{\dot{\theta} L_{\text{ref}}}{2V} + C_{m\dot{\alpha}^*} \frac{\dot{\alpha} L_{\text{ref}}}{2V} + C_{m\alpha} \alpha \right)
 \end{aligned}$$

Inherent to this description of the motion are several simplifying assumptions:

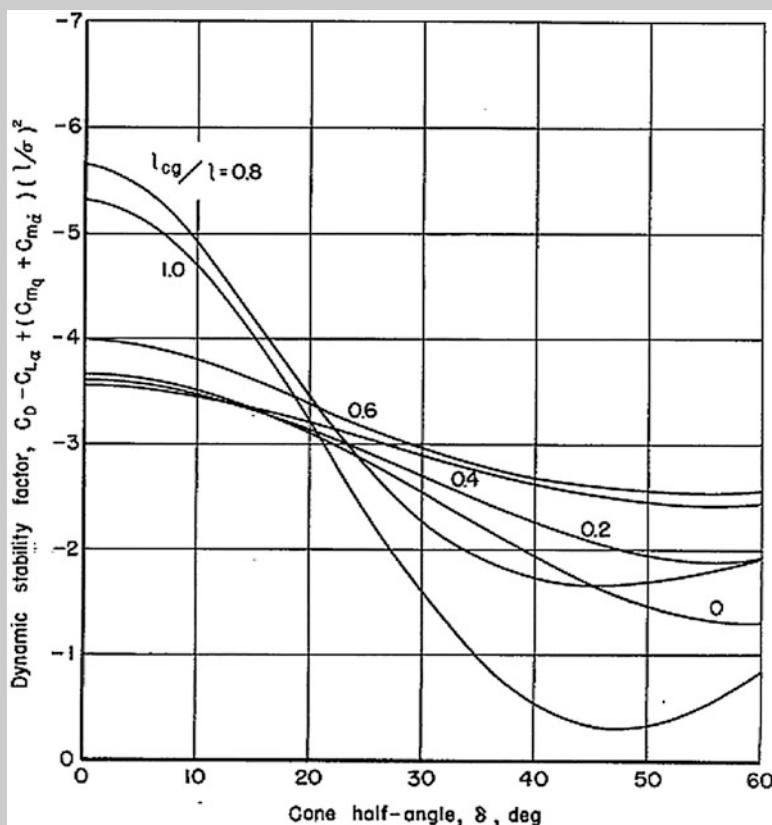
- Motions are restricted to a plane.
- Aerodynamic derivatives are independent of Mach number and vary linearly with  $\alpha$ .
- Small L/D.
- Small angle of attack ( $\alpha < 30^\circ$ ).
- Constant acceleration due to gravity.
- Spherical, nonrotating planet.
- Constant mass vehicle.
- No contribution of atmospheric winds.
- Contributions of the gravitational and centrifugal forces are negligible; the resulting differential description of the angle of attack can be obtained:

$$\begin{aligned}
 \ddot{\alpha} &+ \left( \frac{\rho V S_{\text{ref}}}{2m} \right) C_{L\dot{\alpha}} \dot{\alpha} + \left( \frac{\rho V S_{\text{ref}}}{2m} \right)^2 C_D C_{L\alpha} \alpha \\
 &+ = \frac{\rho V^2 S_{\text{ref}} L_{\text{ref}}}{2I} \left( C_{mq^*} \frac{\dot{\theta} L_{\text{ref}}}{2V} + C_{m\dot{\alpha}^*} \frac{\dot{\alpha} L_{\text{ref}}}{2V} + C_{m\alpha} \alpha \right) \quad (3.28)
 \end{aligned}$$

Often, it is further assumed that the rate of change of angle of attack is much greater than that of the flight path angle and that terms which manifest as small modifications of the frequency of oscillation can be neglected. What remains is a closed form differential equation describing the time evolution of angle of attack for an entry vehicle:

$$\ddot{\alpha} - \left( \frac{\rho V S_{\text{ref}}}{2m} \right) \left[ -C_{L\alpha} + \frac{m L_{\text{ref}}^2}{2I} (C_{mq^*} + C_{m\dot{\alpha}^*}) \right] \dot{\alpha} - \frac{\rho V^2 S_{\text{ref}} L_{\text{ref}}}{2I} C_{m\alpha} \alpha = 0 \quad (3.29)$$

(continued)



In the literature, Eqs. (3.28) and (3.29) above have been manipulated to obtain analytical descriptions of key parameters or special cases which are useful in developing intuition and gaining insight into the expected dynamic response. By using an exponential atmosphere and other assumptions, Allen was able to find an analytical expression for the velocity as function of altitude [4]. By implementing this into the relations above, he then introduced a dynamic stability criterion:

$$\xi = C_D - C_{L\alpha} + \left( \frac{m L_{\text{ref}}^2}{I} \right) \cdot (C_{m\dot{\alpha}*} + C_{mq*}) < 0$$

where  $\xi < 0$  would indicate a dynamically stable configuration. The figure displays this parameter as a function of cone angle and location of the center of gravity for conical missile shapes.

(continued)

It can be seen that at the high cone angles typically used for entry vehicles due to heating concerns, the parameter becomes less negative which indicates the body is less dynamically stable. This criterion is similar to using a negative lift curve slope as an indicator that a vehicle is statically stable. While this parameter is useful for understanding the trends of dynamic stability, the numerous assumptions behind its derivation require that it be used with caution, as a negative  $\xi$  does not guarantee a dynamically stable vehicle. Often, in the literature and throughout this report, the pitch damping sum ( $C_{m\dot{\alpha}^*} + C_{mq^*}$ ) from the dynamic stability parameter is used independently as a measure of dynamic stability, with negative values indicating positive (favorable) damping. This term is effectively a measure of the damping experienced during small oscillation perturbations about a mean angle of attack.

The dynamic instability has consequences at system level and has, therefore, to be taken into account in the design of a vehicle, during its development phase.

Both for planetary probes and manned capsules, the determination of the dynamic derivatives is necessary, in order to, respectively, assess the reliable deployment conditions of the parachute and design the thrusters needed to insure an efficient damping of the vehicle oscillatory motion.

Generally speaking, damping coefficients could be determined either from theoretical, numerical, or experimental means. Nevertheless, both theoretical and numerical approaches are not yet suitable in the case of the large drag shapes, such as large-angle cones or capsules shapes. In fact, the feature of the near-wake flowfield of this kind of shape which is responsible for the dynamic instability is so complex that in practice the wind-tunnel tests are the only viable option to investigate large drag shapes dynamic behavior. However, the experimental investigation is made difficult due to the nature of these capsule dynamic behaviors.

By concluding, in order to avoid dynamic instability during entry, the vehicle should ideally have the following features:

- Geometric axisymmetry.
- Inertial axisymmetry about the geometric symmetry axis (statically and dynamically balanced).
- Spin axis as the major inertial axis.
- Arrange major structural modes away from aerodynamic modes.
- Small initial angle of attack.

## 3.6 Lifting Entry Vehicle Design

In order to generate lift, the vehicle must generate some asymmetry and thus circulation in the flowfield. That is, the pressure and friction forces on the vehicle have a nonzero integrand in a plane normal to the velocity vector.

This may be achieved by flying a symmetric vehicle at angle of attack or by generating an asymmetric vehicle geometry or both.

For the symmetric geometry, the means of maintaining an angle of attack is the offset of the center of gravity. This mechanism was used on Gemini, Apollo, and Viking.

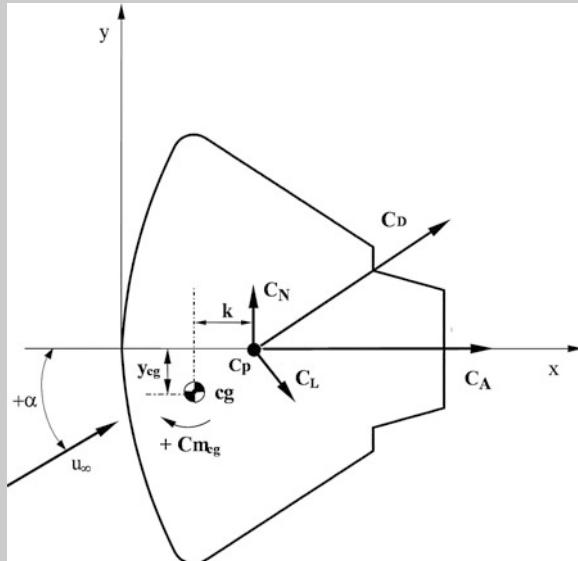
Typical asymmetric geometries are perturbations of the symmetric geometries, for example, a sliced cone such as the AFE or a bent biconic.

In each of these cases, pressure-bearing surfaces are effectively removed from one side of the vehicle, thus inducing a moment which is trimmed out at angle of attack.

Anyway, the most common design solution to achieve a lifting entry is to provide a cg offset to the symmetric vehicle,<sup>7</sup> as discussed in the following explanation box.

#### Explanation Box. Lifting Entry by the Center of Gravity Offset

For a symmetric lifting vehicle, the pitch moment equation about the center of gravity cg is



(continued)

---

<sup>7</sup>A symmetric aeroshape is preferable for the manufacturing point of view, of course.

$$M_{cg} = \frac{1}{2} \rho_\infty V_\infty^2 S_{ref} [C_A y_{cg} - C_N (x_{cp} - x_{cg})] \quad (3.30)$$

where:

$x_{cg}$  is the center of gravity location.

$x_{cp}$  is the center of pressure location.

$y_{cg}$  is the center of gravity offset from the aeroshell centerline.

$C_A$  is the axial force coefficient.

$C_N$  is the normal force coefficient.

Defining  $(x_{cp} - x_{cg})$  as the static stability margin  $k$  and the vehicle in a trimmed condition (i.e.,  $M = 0$ ), then we get

$$C_A y_{cg} = C_N k \quad (3.31)$$

rearranging in terms of aerodynamic efficiency

$$\frac{y_{cg}}{k} = \frac{C_N}{C_A} = \frac{(L/D) \cos \alpha - \sin \alpha}{\cos \alpha - (L/D) \sin \alpha} \quad (3.32)$$

for a typical bluff vehicle, such as an Apollo-like capsule,  $L/D \cong 0.3$  at  $\alpha = 20^\circ$  incidence, and  $k$  is about the vehicle radius  $R_b$  and so  $y_{cg} \cong 7\% R_b$ . The capsule will thus be able to achieve a mass-induced trim at maximum L/D with reasonable tolerance.

On the contrary, for a slender vehicle  $L/D \cong 1.0$  and  $y_{cg} \cong k$  and since  $k$  is about half the base radius  $R_b$ , then mass trim at maximum L/D may be difficult to achieve, and other devices will also have to be used such as body bend or body shaping.

The choice of a lifting entry vehicle configuration is first made on the L/D requirements which are determined by down and cross ranges, entry corridor, and if required aerocapture accuracy (to orbit).

Large cross range, high speed or thin atmosphere (low deceleration), and high accuracy all call for high L/D. Our simple trajectory analysis in Chap. 2 has shown that heating is minimized for low ballistic coefficient which is achieved with a bluff vehicle, and so a small L/D is suitable to provide modest cross-range control for recovery purposes and provide reasonable entry load alleviation while at the same time providing a low heating.

Table 3.2 gives the L/D of some capsule configurations [7].

The slender biconic gives optimal aerocapture to orbit accuracy, while the Shuttle is a compromise vehicle for low-speed handling but presents a maximum radius swept cylindrical lower heat shield during entry at high incidence (i.e., low ballistic coefficient attitude) for minimum heat load. Fat biconics have been considered for

**Table 3.2** Some lifting vehicle characteristics

Capsule	L/D	Geometry
Gemini	0.2	Sphere seg-cyl
Apollo	0.3	Sphere-seg
Viking	0.18	Sphere cone
AFE	0.28	Ellipse/raked cone
“Fat” biconic	0.5	Optimal biconic
Shuttle	1.1	Wing–body
“Slender” biconic’	1.5	Optimal biconic

many planetary entry missions and their medium L/D give good load reduction and good cross range for accurate landing point selection. This type of biconic was also considered for the Rosetta mission at one stage, prior to the trade-off between low L/D and ballistic capsules.

Of interest when considering the lifting capsule is the direction of lift.

For a slender vehicle pitching nose up causes a lift force in the upward direction.

On the contrary, for a bluff vehicle pitching nose up causes a lift force in the downward direction.

The reason for this change is obvious from the lift equation:

$$C_L = C_N \cos \alpha - C_A \sin \alpha \quad (3.33)$$

Indeed, lift changes sign when  $C_A \sin \alpha$  becomes greater than  $C_N \cos \alpha$ .

The bluff capsules have large  $C_A$  and small  $C_N$  and the opposite is the case for slender vehicles.

For newtonian flow over a conic this occurs at a cone angle of  $45^\circ$  where the net lift is zero at all angles of attack. Thus, a  $45^\circ$  sphere cone such as Pioneer, Venus, and Galileo will experience little lateral acceleration but is still stable; thus the internal design may be simplified where very large axial loads are expected.

#### Explanation Box. Blunt Bodies Versus Slender Bodies Entry Load Directions

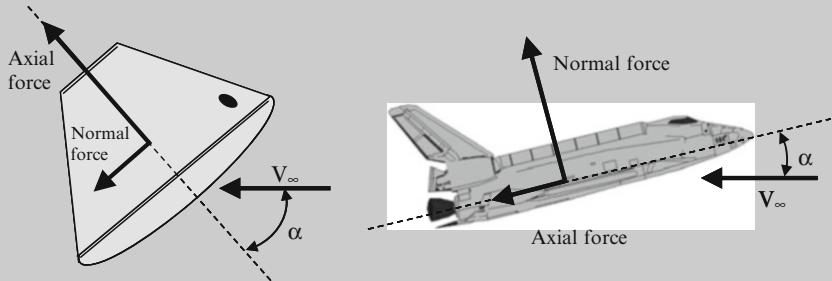
It is important to note that the entry load directions are significantly different between a capsule and a slender body. During entry, the aerodynamic forces on a trimmed blunt body primarily generate axial loads (see figure). As shown, the majority of the deceleration occurs along the axis of the capsule. This is also the same direction that primary loads are generated during ascent when the vehicle is carried by the launcher, during ascent abort, and during landing.

Conversely, slender bodies generate primarily normal aerodynamic loads, so that, on entry, the majority of the acceleration occurs normal to the axis of the slender body (see figure).

(continued)

These loads would be  $90^\circ$  off from the load direction encountered during ascent or ascent abort.

These load directions have implications on the seating orientation of the crew.



For a capsule, the logical crew orientation is with their backs parallel to the heat shield. All primary loads would then be carried through the crews' chest toward their backs (eyeballs in), which is the most tolerable load direction for a human.

For a slender body, the primary load direction changes approximately  $90^\circ$  between launch and entry. Thus, either the crew would have to rotate their orientation in flight or a very benign ascent would have to be designed to allow the crew to take the ascent loads sitting up.

For the low L/D capsule, geometric design features are similar to the ballistic vehicles, since the ballistic vehicles must allow for incidence excursions during entry, and given the aerodynamic efficiency requirement, the ballistic coefficient must still be minimized with little surface area as before. However, as discussed above, the corner radius heating must be considered more carefully as far high incidence the stagnation region can move to the corner making the corner radius the dominant geometric feature for the convective heating, i.e., small radii lead to large convective heating rates because of

$$\dot{q}_0 \propto \frac{1}{\sqrt{R_N}}$$

As far as vehicle stability is concerned, it is worth noting that pitch damping for bluff vehicles is positive transonically at small incidence but changes to negative at incidence. This is an advantage of the lifting vehicle.

Flow attachment to the rear heat shield is also an issue since this increases the wetted area and thus total heat load and may lead to motion-separation coupling.

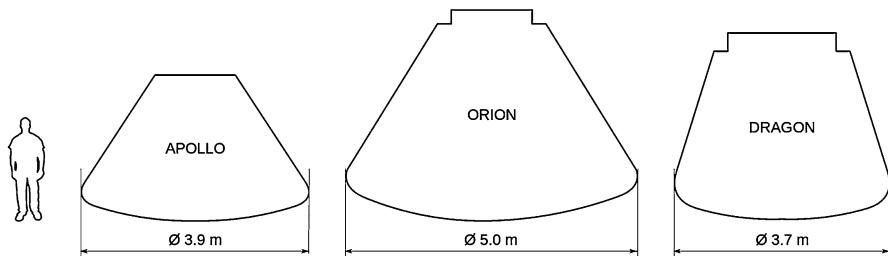


**Fig. 3.42** Apollo-like vehicle under investigation: Orion and Dragon

The decision between asymmetric and symmetric geometries is made initially based on the L/D. For high L/D we will need vehicle asymmetry, and as previously mentioned, the generic design rule for biconics is the 2:1 ratio. Nose radius is then optimized against TPS capability.

For low L/D vehicles we can achieve the required L/D by moving the center of gravity (i.e., cg offset). Thus, the need for asymmetry is removed.

Finally, asymmetry in the rear structure is desirable to alleviate attached flow heating.

### 3.6.1 Example of Design Study for Low Earth Orbit Return

After Shuttle retirement, design studies, currently under investigation, are focusing attention on Apollo-like vehicle as Orion/CEV and Dragon, shown in Fig. 3.42, to ferry crew and supplies to and from the International Space Station (ISS).

The CEV is a spacecraft designed to affordably, reliably, and safely transfer crew from the Earth's surface to destinations beyond. Initially, it will be used to transfer crew and cargo to and from the ISS. By the end of the next decade, it will transfer four astronauts from the Earth's surface, dock with the Earth Departure Stage for the trip to a Lunar Orbit, and then maintain itself autonomously there while the crew explores the surface below. The CEV design utilizes experience and technology from previous programs like Apollo and the Space Shuttle, but combines that with modern materials, manufacturing techniques, and avionics.

Given the short time available for development and the limited funds available, Orion must also be designed to use mature, well-understood technologies wherever practical. Mass, volume, and thermal and functional capabilities must all be balanced to produce a design that is safe and cost-effective to build and operate. Design considerations which are important for LEO spacecraft become increasingly challenging for missions that extend to the Moon or Mars. Orion's design reflects an optimization of these different considerations to produce a versatile yet technically feasible spacecraft.

### ***3.6.2 Example of Design Study for a High-Speed Earth Return from a Comet***

Let us focus attention to lifting capsule which are essentially simple geometries with low to medium L/D.

In the trade-off design of Rosetta sample return mission, two generic lifting capsule types were selected for analysis. These are the Apollo type and a modest 40 raked cone of the type proposed for the US Aeroassisted Orbital Transfer Vehicle (AOTV) and related AOTV flight experiment (AFE). Only a low L/D is required to limit the downrange dispersion to acceptable limits. Trajectory studies identified the desire to increase the corridor width and reduce dispersions by both increasing the L/D and reducing the ballistic coefficient.

As an alternate a higher L/D vehicle such as a biconic has been considered for this mission, as the rear sample loading option and low entry loads made this attractive.

However, this was dropped on the grounds of lack of supporting design data and thus low confidence. Therefore, for this study where aerobraking to ground was the goal, only low L/D capsules were studied. In particular, advantage was taken of extensive US experience with the Apollo program, and more recently with the AOTV flight experiment program, which planned to use a raked cone configuration, the generic type of which has been proposed for planetary entry for many years.

So, for each vehicle configuration, several design issues such as configuration, aerodynamic, and aerothermodynamic are discussed hereinafter.

#### ***3.6.2.1 Apollo Type Capsule***

##### **Configuration**

The Apollo-like capsule is a sphere segment vehicle having a spherical forward heat shield and conical rear heat shield. The large radius forward heat shield gives the lowest convective heating, and was retained at the largest value for maximum axial length of the vehicle when placed nose out in the side mounted position of the spacecraft. This largest nose radius amounts to the same value as the launch fairing radius. For shallow entries the radiative heating is less as a proportion of the total than for steeper entries, and so for the shallowest possible entries, the largest possible nose radius is retained (see aerothermal discussion). The nose radius is thus 2.2 m. A body diameter of 1.85 m is used for consistency with earlier studies with the intention of scaling the final geometry to give the minimum capsule volume and thus mass for the final container design. The capsule geometry was scaled from Apollo to make use of the available databases, thus increasing the confidence in the capsule design with its demonstrated Earth entry capability. In order to accommodate the capsule within the spacecraft envelope either nose in or nose out, the after cone is truncated. These changes have a very small computed effect on the capsule aerodynamic coefficients, allowing direct use of the Apollo aerodynamic database.

## Aerodynamics

### *Continuum Coefficients*

The Apollo continuum aerodynamic coefficients have been taken directly from the Apollo wind-tunnel data. Flight data examination gives an excellent validation of the database.

### *Free Molecular Coefficients*

The free molecular drag coefficients are calculated using the standard method with full specular reflection and equal free-stream and wall temperatures. The free molecular L/D is small due to the relatively large shear forces and for this study can be assumed to be zero.

### *Damping Coefficients*

The damping coefficients are also taken from Apollo wind-tunnel data. The damping coefficients are similar in magnitude to the bluff cone values of the ballistic capsule as might be expected, but with some pitch and yaw reinforcing damping at transonic and subsonic velocities which may be of some concern. However, this was managed adequately by the Apollo GNC.

## Aerothermodynamics

### *Earth Atmosphere Aerothermochemistry*

It is appropriate to mention the aerochemistry environments to be encountered by the Rosetta capsule.

These can be divided into the shock layer and its chemistry and the boundary layer/heat-shield chemistry.

The entry velocities are high enough that in the shock layer, one can expect very high temperatures and appreciable ionization of the gases. The high-altitude (and thus low density) peak-heating due to the shallow entries leads to the chemical and thermodynamic processes not achieving equilibrium in small distances behind any shock. However, this is offset to a certain extent by the relatively large size of the capsule geometries such that gases at the boundary-layer edge are close to equilibrium. Comparison of equilibrium chemistry boundary-layer solutions for convective heating shows acceptable agreement with nonequilibrium flowfield/convective heating results in the stagnation region, and, therefore, for this stage of the study, equilibrium convective heating results were used. The radiant heating is more sensitive to the shock layer property profile and it was necessary to develop a nonequilibrium radiant heat-transfer model. The stagnation heat-transfer rates are large, and a dense charring ablator is necessary for all but the shallowest entries. However, an empirical blockage correction has been computed, which reduce fluxes. The surface temperatures are high and allow the assumption of

surface equilibrium chemistry. However, at the high altitudes at which peak heat transfer occurs, it was recommended that nonequilibrium reaction of the boundary-layer and heat-shield products should be undertaken.

#### *Continuum Convective Heat Transfer*

The laminar convective heat-transfer distribution is based on Apollo data from wind-tunnel tests and flight data. Nine heat-transfer locations were chosen in the body windward–leeward plane for TPS assessment. For the present analysis the stagnation heat transfer was calculated using a correlation based on the theory of Fay and Riddell which is strictly valid only to about 8 km/s. However, to use the results at higher entry velocity, equilibrium air chemistry boundary-layer calculations were undertaken in order to gain confidence in the correlation at velocities up to 17 km/s. The agreement between boundary-layer calculations and the correlations is within about 10 %.

For bluff vehicles the sonic line lies on the corner toroidal regions which are present to reduce the local convective heating with respect to the case of sharp edge corner (see Chap. 4). The acceleration to the sonic line on the decreased radius of curvature increases the velocity gradient close to the stagnation-point equivalent to the effect of reducing the radius of curvature or nose radius and thus increasing the convective heat transfer. The effect increases with incidence as the stagnation-point approaches the toroidal section. The stagnation heat-transfer correlations are thus adjusted for the equivalent stagnation velocity gradient from the usual spherical geometry values, again this agrees well with boundary-layer calculations.

#### *Free Molecular Heat Transfer*

Free molecular heat transfer has been calculated along each trajectory for each capsule using established methods, with thermal accommodation coefficients set to unity and with a cold (300 K) wall temperature. In order to bridge between free molecular and continuum heat transfer in the transitional and slip regimes, a combination of bridging functions has been used (see Chap. 2).

On windward facing surfaces a minimum of either free molecular or continuum heat transfer is taken. On leeward surfaces a Knudsen number-based bridging function is used as with the pressure coefficient. The latter is necessary as free molecular heat transfer to shaded areas is zero for high vehicle speed to molecule speed ratios. Bridging is discontinued in the shaded regions after peak heat transfer for Rosetta. The use of the bridging functions adequately compensates for high continuum heat transfer in the transition and slip regimes, but as with the aerodynamic coefficients, the effect on the total heat transfer is small and so no further refinement of the bridging methodology is justified for this phase of the study.

#### *Boundary-Layer Transition*

Transition to turbulent flow has been predicted using a suitable bluff body correlation to the boundary-layer momentum thickness Reynolds number which is applicable to the attached flow areas. A similar correlation was assumed to apply

in the regions of separated flow. This type of procedure was used successfully on Apollo but based on local flow conditions which are considered less reliable when changing scale or geometries.

#### *Radiant Heat Transfer*

Radiant heating to the Rosetta capsule forms a significant fraction of the total, particularly for the steeper entries, due to the high re-entry velocity (i.e., hyperbolic entry). The radiant heat-transfer distribution was based on that used for Apollo but amended fix differing angles of attack by an engineering correlation.

On the superorbital Apollo test flight (spacecraft 017), the nonequilibrium radiant heating at about 10 km/s was not dominant and equilibrium chemistry theory and flight data agreed well.

#### *Trajectory*

The Apollo type and AFE type trajectories utilized for this study were selected initially as a 20 g peak and a 50 g peak reference; this assumed a 15 km/s entry in the local frame. A minimum flight path angle of  $-1^\circ$  was set to ensure entry and the guidance algorithm maintained this with alternate left-right roll maneuvers.

#### *Mass Characteristics and Stability*

In order to achieve the desired trim, the center of gravity must be offset. The Apollo relative center of gravity position is, therefore, to be used to give the design nominal trim of  $20^\circ$  (i.e., L/D = 0.3). Variations in sample mass and position and ablation asymmetry/mass loss will affect the trim by a few degrees at most, and this is expected to be managed by the GNC system. The static margin is about 1 m for the Apollo type capsule with a center of gravity of 0.5 m aft of the forward heat shield; thus the vehicle is acceptably stable in the continuum regime.

#### *Heat-Shield Considerations*

Maximum heat fluxes for the shallow 20 g entry are small enough on the forward heat shield ( $1,000 \text{ W/cm}^2$ ) to consider a lighter heat-shield material. However, the material choice in this range (Nylon Phenolic) suffers from a low-density char which is stripped under boundary-layer shear forces. Rear cone heat transfer is quite low, and although transition is predicted, a lightweight ablator (ESM) will be adequate in varying thickness at all locations.

Simulations of entries close to the skip out limit at about 9–11 g show heat fluxes less than  $500 \text{ W/cm}^2$  which are in the range of the Apollo ablators and some of the mid-density ESM's. Thus, a very shallow entry could produce a step reduction in heat-shield mass, although the heat soak time is increased requiring greater insulation thickness. It should be noticed that the convective and radiative heat fluxes are nearly equal for the 20 g 15 km/s entry, with convective dominating at shallower angles while at higher entry velocity (for the same g-load) the radiative component begins to dominate, illustrating the choice of the largest possible nose radius (Apollo type capsule) for the shallow entries.

### 3.6.2.2 Raked Cone Capsule

In order to achieve a modest L/D and low ballistic coefficient, a large-angle sphere cone can be utilized. Indeed, for the Viking missions to Mars, this was the geometry chosen (70° cone at 11° incidence and L/D of 0.18) for maximum drag with modest control. During the period leading up to Viking, there was much testing of simple aerodynamic configurations for planetary entry including raked cones. In the early 1980s, attention was focused on planetary missions where aerobraking is used for descent to ground, whereas aerocapture with a large L/D gives most flexibility for capture to orbit. Later attention was turned to aeroassisted orbital transfer to save fuel when returning from high- to low-energy orbits. This effort was refocused on the raked cone for high-drag coefficient and good stability characteristics.

At first glance the requirements seem too dissimilar as the entry energies and mission requirements are quite different. However, closer inspection reveals the similarity in design objectives for the aerodynamic configuration.

These are:

- Low ballistic coefficient
- Low L/D
- Well-understood aerodynamic performance

Although the size and materials will be quite different, the basic geometry serves as a design point from which we may extrapolate if necessary.

#### Configuration

In order to compare performance with the Apollo capsule, the same maximum diameter is chosen which may be scaled to contain the final sample container. The rear heat shield is intended to be in separated flow and an initial 45° dividing streamline is taken as the maximum rear heat-shield envelope at this stage. The cone half angle is 60° with a rake angle of 73° (90° being symmetric). An expansion corner radius of 10 % of the base diameter is used for the AFE vehicle. The nose rather than being spherical is in fact elliptic with a 2:1 major to minor axis ratio. This feature increases the nose radius of curvature over the equivalent sphere and thus reduces the convective heat transfer at zero angle of attack. A slight increase in drag coefficient is also achieved.

#### Aerodynamics

##### *Continuum and Free Molecular Coefficients*

The continuum aerodynamics have been taken from wind-tunnel data for 60° sphere cones and a raked cone and factored by Newtonian ratios to the AFE configuration. Data are also obtained from computations in the literature. Only drag coefficient and L/D were developed for this study.

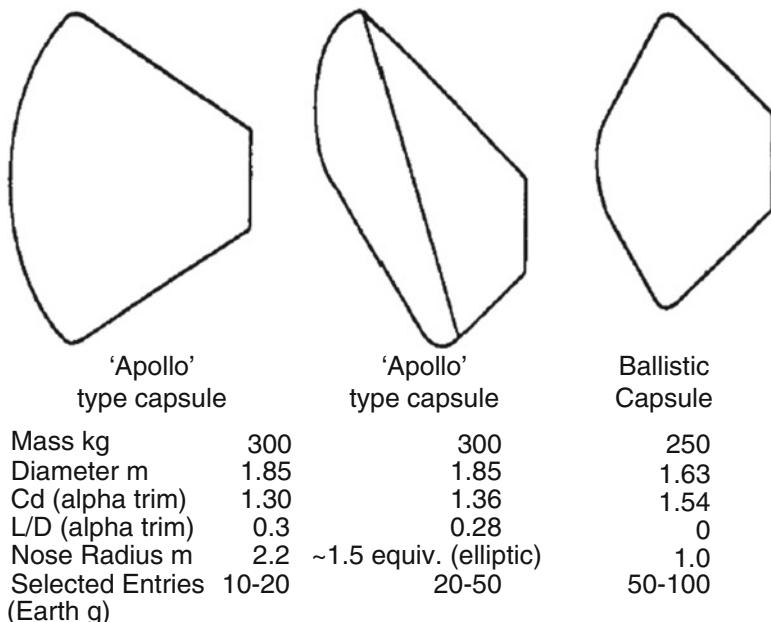


**Fig. 3.43** Comparison of trade-off vehicles

The AFE vehicle is very similar in performance to the Apollo type capsule, but with slightly lower L/D (0.28) at its design angle of attack ( $17^\circ$ ). However, the drag coefficient is higher by about 8 % giving a lower ballistic coefficient for equivalent mass. The comparison of basic characteristics is given in Fig. 3.43, which also shows the guided and ballistic capsules to approximately the same scale [7].

#### *Damping Coefficients*

The damping coefficients have been taken as those for an equivalent sphere cone initially and are thus the same as the ballistic capsule. This is adequate for initial trajectory studies and gives the capsule good damping characteristics in most of the Mach number. These initial damping coefficients are superior to those of the Apollo type capsule.

#### *Aerothermodynamics*

As with the Apollo-like capsule, the reference stagnation heat transfer is based on the results of Fay and Riddell relationship for equilibrium air, corrected for the local curvature effects. The same radiative and distribution correlations have been used as for the Apollo type capsule but applied to the AFE shape. Seven locations were chosen to represent the heat-transfer distribution about the AFE type vehicle for TPS assessment.

### *Trajectory*

The same trajectory entry conditions and control law were used as for the Apollo type capsule.

### *Heat-Shield Considerations*

The AFE vehicle has only slightly higher convective heat flux and lower radiative heat flux than the Apollo vehicle on the forward heat shield. The convective component is dominant at both entry velocities, indicating the desire for a larger nose radius or the use of this type of vehicle at still higher entry velocities or steeper (than 20 g) entries. The rear heat shield is all in separated flow allowing an even thickness of low-density ablator. This is achieved at the expense of reduced capsule volume for the same capsule diameter.

### *Mass Properties and Stability*

For the AFE vehicle a nominal trim angle of attack of 17° is required, but unlike the other capsules considered, the AFE is truly asymmetric in geometry, but the cg position is again located to give the desired trim. The static margin is similar to the Apollo like capsule at 1 m assuming a center of gravity position 0.5 m aft of the forward heat shield. However, the pitching moment coefficients appear larger than for the Apollo type capsule, indicating a greater tolerance to sample mass/position and ablation asymmetries. The AFE type capsule is thus acceptably stable.

#### **3.6.2.3 Guided Capsule Choice**

From aerodynamic point of view, there is little difference in the performance of the two configurations. However, there are advantages and disadvantages to both configurations. The Apollo shape vehicle has the major advantage of having been proven for Earth entry already, and consequently, there is a large volume of aerodynamic and aerothermodynamic data available, which will give a high confidence to the capsule design at an early stage and potentially lead to lower costs. The large forward heat-shield radius is ideal for the shallow entries where the radiative component of the heat transfer is proportionately lower. However, the design of the Apollo rear heat shield does allow attached flow on the windward side at angle of attack, leading to a larger rear heat-shield mass than for a separated flow design. However, this may lead to a lighter capsule if the overall body radius can be reduced.

The AFE design has the potential to achieve similar L/D values given slight modifications to the geometry, i.e., increased rake angle and reduced corner radius, but this would be diverging from the AFE geometry for which there was expected to be much data. Therefore, design confidence will be lower initially and costs potentially higher with a larger test program particularly in the low supersonic, transonic, and subsonic range where no AFE data will be available in any case.

The real choice may well be made on heat-shield mass which forms a large fraction of the total capsule mass. For very shallow entries close to skip out (around 10–15 g), heat-transfer rates are reduced to an extent where a change to a light charring ablator may be considered. For this scenario the largest radius of curvature is required in order to minimize convective heating (radiative heating being proportionately lower for the shallow entries). Therefore, the Apollo style capsule seems attractive at shallow entries less than 20 g. For the steeper guided entries 20 g to about 40 g, the smaller radius of curvature of the AFE vehicle may make it attractive from the heat-shield mass point of view. Additionally a trade-off on increased rear heat-shield mass by allowing flow attachment against reduced body diameter (and thus reduced forward heat-shield mass) is possible. Greater than about 40 g, the ballistic capsule becomes attractive as dispersions reduce.

## 3.7 Maneuvering Systems for Entry Vehicles

Maneuvering systems can be grouped into two main types. Firstly, there are the *bank-to-turn* concepts, which roll the vehicle and use pitch plane-generated lift to provide the maneuvering capability. Such systems require separate roll control and pitch control devices, an example being the single windward flap designs. In these designs, the roll control can be provided by roll thruster, control surfaces, or internal moving mass, and the windward flap itself can be split to generate a roll torque.

The second main type of maneuvering system is the *skid-to-turn* concept, which use full roll, pitch, and yaw control. Examples of this type of system are missiles with cruciform control surfaces. Such systems provide full 6 dof control of the vehicle attitude in flight, but are usually more complex, have aerodynamic heating problems, and may be heavier compared to the bank-to-turn concepts. The maneuvering systems used for capsules and vehicles have all been bank-to-turn.

### 3.7.1 Aerodynamics of the Maneuver

A vehicle will generally be designed to fly at maximum L/D (i.e., at constant angle of attack), and so the roll control system provides the primary control mechanism for entry (e.g., banking maneuvers). To achieve the required static incidence, two moments must come into balance. These are the control moment and the vehicle restoring moment. The former is generated by the control force comprising normal lateral and axial components, all of which act about the vehicle center of gravity. Clearly the relative magnitude of the moments at a given attitude depends on both the magnitude of the forces and the length of moment arm.

### **3.7.2 *Control System Characteristics***

Here some common control systems are described and their limiting characteristics identified.

#### **3.7.2.1 Windward Flap**

The windward flap is conventionally located at the rear of the vehicle, usually on a body slice. It is deployed as a reverse acting mechanism in that it is deployed into the flow to achieve zero trim and retracted to achieve a given trim. By splitting the flap roll moments can be induced, thus combining pitch and roll control. Hinge moments and aerothermal load (especially in the hinge flap cavity) are the main design driver interests here. In the case of aerothermal load, this includes nonequilibrium effects, radiative heating in the cavity, separation and attachment heating (and for an ablator shape change), and snake flow as well.

#### **3.7.2.2 Bent Nose**

The bent nose vehicle achieves its control by inducing vehicle camber. The nose may be bent by conventional hinge which involves a complex joint or by a simpler rotational mechanism.

#### **3.7.2.3 Jet Interaction**

This is the control subsystem well known as reaction control system (RCS). Here a transverse jet is used to provide the control moment. An augmentation of the control moment is afforded by the interaction of the jet and hypersonic shock/boundary layer. The system has the advantage of also being used for exoatmospheric attitude control.

#### **3.7.2.4 Moving Mass**

By moving the center of gravity out of the pitch plane, then a roll torque is induced due to the offset lift. This system of course requires a moving internal mass say along a track near the vehicle maximum diameter and accrues no aerothermodynamic penalty.

## 3.8 Vehicle Stability in Longitudinal and Lateral–Directional Flight

### 3.8.1 Static Stability in Longitudinal Flight

According to Bernard Etkin and Lloyd Duff Reid, “An airplane can continue in steady un-accelerated flight only when the resultant external forces and moments about CG both vanish” [10]. This is the condition of longitudinal balance. “If the pitching moment were not zero, the airplane would experience a rotational acceleration component in the direction of the unbalanced moment”. This situation is depicted in Fig. 3.44.

Traditionally “static margin” has been used as a measure of an air vehicle’s stability. This criterion implies that the center of pressure  $CoP$  lies behind (as measured from the nose) the center of gravity  $CG$ . It should, however, be noted that while this will give stability it will not guarantee steady sustained (or level) flight. The latter requires that there should be a positive angle of attack  $\alpha$ , and that this should be maintained during a steady flight, in order to achieve lift to balance the weight of the vehicle. This condition known as **trim** typically requires the application of a control force through an appropriate fin deflection, creating a positive angle of attack and a shift in  $CoP$  position to a location relative to  $CG$  such that the resultant moment about  $CG$  is zero. If  $CoP$  is above  $CG$  it can be shown that steady sustained flight may be achieved with  $CoP$  behind  $CG$  as shown in Fig. 3.45.

The position of  $CoP$  (defined as the point where total lift and drag forces act) does not remain fixed. In fact, Garnell P. and East DJ, notes that: “It is seen that at subsonic speeds and very low supersonic speeds the  $CoP$  tends to be rather more forward than at higher Mach numbers. Also the changes in  $CoP$  with incidence can be considerable at low speeds; this is mainly due to general rearwards shift in the  $CoP$  of the body with increasing incidence, the  $CoP$  of the control surfaces and wings changing very little” [10].

A plot of the  $CoP$  position as a function of the angle of attack and  $M$ , for a fin controlled vehicle, is given in Fig. 3.46 [11]. The  $CoP$  position, moves aft when angle of attack  $\alpha$  increases, and moves forward when the angle of attack  $\alpha$

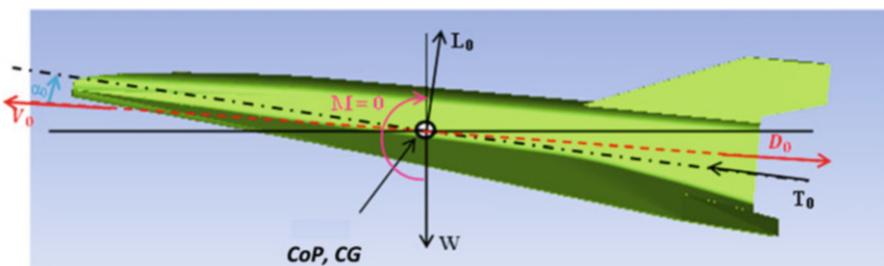


**Fig. 3.44** Aerodynamic forces and moments for steady sustained flight

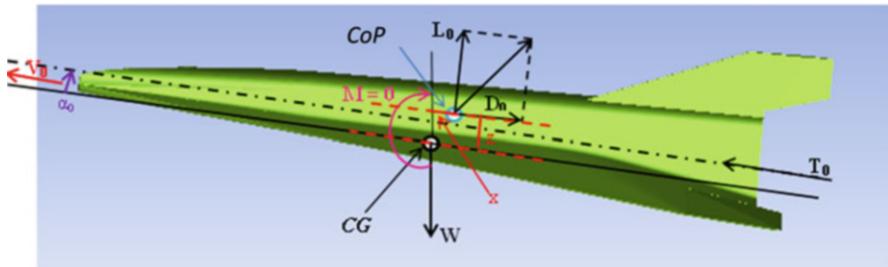


**Fig. 3.45** Aerodynamic forces and moments for steady sustained flight for CoP above CG

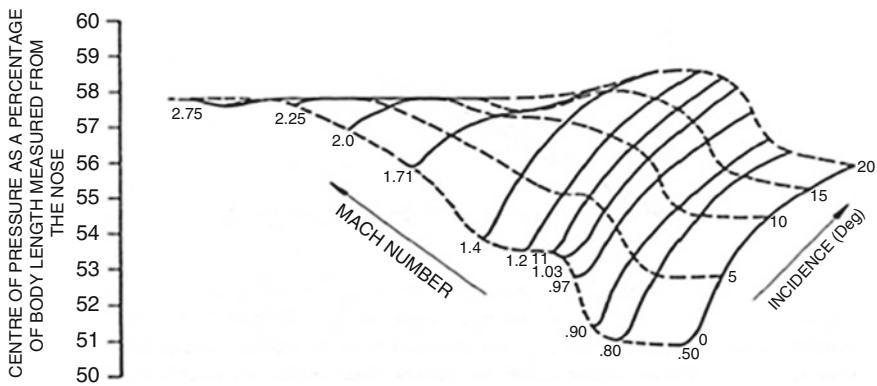


**Fig. 3.46** CoP position variations with angle of attack and Mach number

decreases; in addition, the lift force also increases with increasing  $\alpha$ . This produces a restoring moment that counters the increase in  $\alpha$  and is the very phenomenon that makes stable sustained flight possible. This shift in the *CoP* position as a function of  $\alpha$ , occurs mainly in the subsonic and transonic regimes but is negligible at high supersonic and hypersonic speeds.

Figure 3.47 shows a typical plot for the pitching moment coefficient, about *CG* for a fixed elevator, versus the angle of attack  $\alpha$ ; here [11]:

$$M = C_m q_\infty S_{\text{ref}} L_{\text{ref}} \quad (3.34)$$

Note also, that the lift force is given by

$$L = C_L q_\infty S_{\text{ref}} \quad (3.35)$$

where  $q_\infty = \frac{1}{2} \rho_\infty V_\infty^2$  is the dynamic pressure and the angle of attack is measured w.r.t to the zero-lift line of the vehicle.

For this case if a disturbance causes  $\alpha$  to suddenly increase from its nominal value  $\alpha_0$  then the negative moment (due to aft movement of *CoP* and an increase

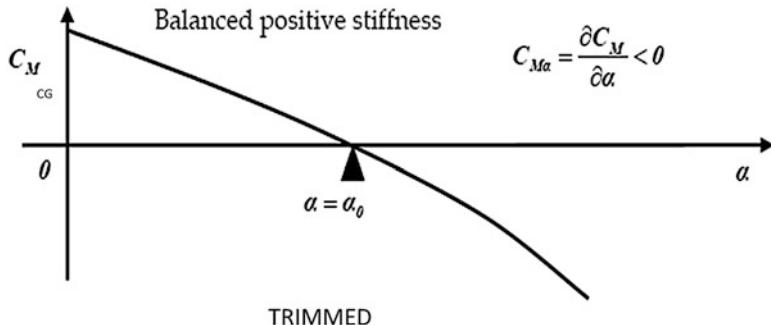


Fig. 3.47 Pitching moment about the vehicle CG. Curve with negative slope

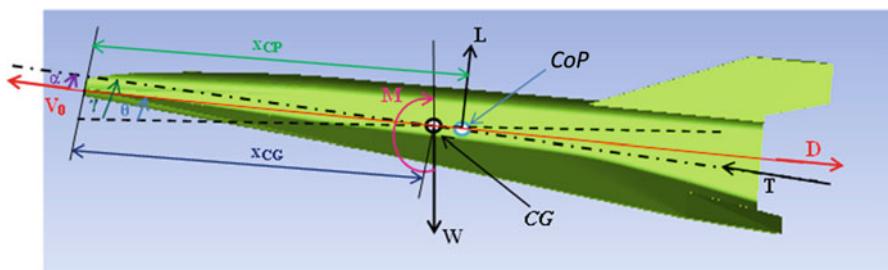


Fig. 3.48 CoP and CG positions and their role in vehicle stability

in  $C_L$ ), acts to restore  $\alpha$  to its nominal value. Similarly a sudden disturbance in the opposite direction induces a positive moment (due to forward movement of  $CoP$  and a decrease in  $C_L$ ) that acts to restore stability. It is assumed that the velocity of the vehicle remains unaltered during these transient disturbances.

Key conditions for stability are:

$$C_m \Big|_{\alpha=\alpha_0} = 0; \quad C_{m\alpha} = \frac{\partial C_m}{\partial \alpha} < 0 \quad (3.36)$$

where  $\alpha = \alpha_0$  defines the equilibrium angle of attack for that steady flight condition. Note, also, that asymptotically stable flight is achieved, following a disturbance, provided there is sufficient aerodynamic damping.

Let us consider, now, the role that the center of pressure plays during the transient behavior of the vehicle. In Fig. 3.48, the positions of  $CoP$  and  $CG$  are shown measured in terms of their respective distances  $x_{CP}$  and  $x_{CG}$  from vehicle's nose. The moment (about CG) equation may be written as (for small  $\alpha$ ):

$$M = M_0 - L(x_{CP} - x_{CG}) \quad (3.37)$$

Or equivalently, in terms of the moment and lift coefficients  $C_m, C_{m_0}, C_L$  respectively, Eq. (3.37) may be written as:

$$C_m = C_{m_0} - \frac{1}{L_{\text{ref}}} C_L (x_{\text{CP}} - x_{\text{CG}}) \quad (3.38)$$

$C_{m_0}$  is the pitching moment independent of  $\alpha$ . For Mach number less than approximately 5,  $C_L = C_{L_\alpha} \alpha$ , thus:

$$C_m = C_{m_0} - \frac{1}{L_{\text{ref}}} C_{L_\alpha} \alpha (x_{\text{CP}} - x_{\text{CG}}) \quad (3.39)$$

For steady flight condition  $\alpha = \alpha_0$ ;  $x_{\text{CP}} = x_{\text{CP}0}$ ;  $C_m = 0$ , that is:

$$C_{m_0} = - \frac{1}{L_{\text{ref}}} C_{L_\alpha} \cdot \alpha_0 (x_{\text{CP}} - x_{\text{CG}}) \quad (3.40)$$

$x_{\text{SM}} = (x_{\text{CP}} - x_{\text{CG}})$  will be referred to as the *static margin*. Partial differentiation of Eq. (3.39) with respect to  $\alpha$ , we get:

$$C_{m_\alpha} = - \frac{1}{L_{\text{ref}}} C_{L_\alpha} \left\{ (x_{\text{CP}} - x_{\text{CG}}) + \alpha \frac{\partial x_{\text{CP}}}{\partial \alpha} \right\} \quad (3.41)$$

Using Eq. (3.36), we get conditions for stability as:

$$C_{m_\alpha} = - \frac{1}{c_{\text{ref}}} C_{L_\alpha} \left\{ (x_{\text{CP}} - x_{\text{CG}}) + \alpha \frac{\partial x_{\text{CP}}}{\partial \alpha} \right\} < 0 \quad (3.42)$$

$$\rightarrow \left\{ (x_{\text{CP}} - x_{\text{CG}}) + \alpha \frac{\partial x_{\text{CP}}}{\partial \alpha} \right\} > 0 \quad (3.43)$$

- (a) Thus if,  $\frac{\partial x_{\text{CP}}}{\partial \alpha} = 0$  (i.e., hypersonic flight), then conditions for stability imply that:  
 $x_{\text{CP}} > x_{\text{CG}}$ , i.e. positive static margin that is CoP must be aft CG for the vehicle to remain stable.
- (b) However, if  $\frac{\partial x_{\text{CP}}}{\partial \alpha} > 0$  (i.e., subsonic or transonic flight or active controlled flight), then conditions for stability imply that  $x_{\text{CP}} > x_{\text{CG}} - \alpha \left| \frac{\partial x_{\text{CP}}}{\partial \alpha} \right|$ . In this case steady and stable flight is achievable with zero or negative static margin.

### 3.8.2 Effect on Stability Due to Shift in CG Position

It was noted that as the Mach number increases the shift in *CoP* due to changes in the angle of attack becomes progressively smaller and is negligible at high

Mach number. Ostapenko, notes that for high supersonic flow: “*The theoretical investigation of the aerodynamic characteristics of circular cones has shown that their centre of pressure does not depend on the angle of attack when the shock wave is attached to the apex of the cone. It was established experimentally for star-shaped bodies that the position of the centre of pressure for such bodies hardly changes in a wide range of Mach numbers and angles of attack*” [11]. In view of this and other published research, it will be assumed that *CoP* position remains constant at hypersonic speeds irrespective of Mach number and angle of incidence.

Let us now consider the case where the *CG* position suddenly moves aft, causing a positive moment to occur and the vehicle angle of attack to increase from its equilibrium value  $\alpha_0$ . At low Mach number the aft movement of *CoP* and increase in  $C_L$  acts to restore vehicle stability about a new equilibrium angle of attack  $\alpha_1$ . However, at high Mach number the aft shift of *CoP* position does not occur and increase in  $C_L$  may not be sufficient to restore stability. In this case the vehicle could become unstable and topple over unless active controls are available. Active control also allows an air vehicle to achieve new trim conditions to counter changes in *CG*.

One obvious way to avoid instability is to design the vehicle with *CG* significantly forward of the *CoP* (large static margin). However, this would make the vehicle sluggish in responding to demands in attitude and flight path changes – a characteristic not very desirable for some applications. Even with large static margin, however, active control will still be required to achieve steady sustained flight.

Unlike subsonic and supersonic vehicles, the stability of hypersonic vehicles (utilizing active control) cannot be assessed purely from static margin alone. In fact, as stated in a study by Johnson DB, Thomas R, and Manor D: “*Static margin has been the standard indicator of longitudinal stability for many years. However, experience with previous air vehicles flown with significant levels of static instability indicated that the conventional static margin is not a valid indicator for these vehicles. In one case, 30 % unstable was flyable, while in another 15 % unstable was completely unacceptable*” [11]. That is, in certain cases, the hypersonic vehicle with active control was stable although the static margin indicated instability.

### 3.8.3 Hypersonic Flight Stability and Control Issues

Hypersonic vehicle aerodynamics and its longitudinal stability and control characteristics have been studied by a number of authors. For example: aerodynamic flow characteristics of a hypersonic glide vehicle ( $M_\infty > 5$ ) was considered by Miele A., [11].

The main characteristics of this flow are that:

- (a) The shock waves originating at the leading edge of the body lie close to the body so that the interaction with the body is strong.
- (b) High temperatures exist in the regions between the shock waves and the body and it may be necessary to consider real gas effects (molecular vibration, dissociation, and ionization) when analyzing the flowfields.

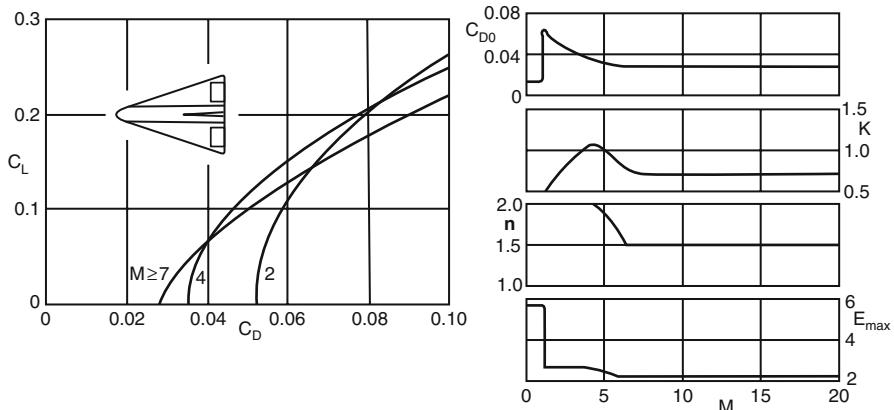


**Fig. 3.49** Aerodynamic characteristics of a hypervelocity glider

- (c) At very high  $M$ , the shock waves may be assumed to be almost identical to the body, at least at the front portion of the body, and the molecules crossing the shock waves conserve the tangential component of the velocity but lose most of the normal component.

In view of the above, a possible design of a glide vehicle operating at high  $M_\infty$  would have to be a compromise between aerodynamic and heat-transfer requirements. For example, the glide vehicle could have lifting surfaces with planar edges and a nose that is blunt.

Aerodynamic lift and drag coefficients:  $C_L$ ,  $C_D$ ; zero lift-drag coefficient  $C_{D0}$ ; aerodynamic efficiency  $E_{MAX} = (C_L/C_D)_{MAX}$ ; the induced drag factor  $K$ , and the exponent  $n$  (as defined in Eq. (3.45) below) are depicted in Fig. 3.49 [11].

As discussed before key differences exist between subsonic/supersonic and hypersonic aerodynamic characteristics. For example, for a supersonic vehicle  $1.2 < M_\infty < 5$ , the lift and drag coefficients are given by Etkin and Reid, [10]

$$C_L = C_{L\alpha} \alpha \quad (3.44)$$

$$C_D = C_{D0} + KC_L^n \quad (3.45)$$

The value of  $n = 2$ , for  $M_\infty < 5$ , and the three constants  $C_{L\alpha}$ ,  $C_{D0}$ ,  $K$  are functions of the configuration, thrust coefficient and Mach number. Whereas for a hypersonic vehicle  $M_\infty > 5$ ,  $n = 3/2$ , we get:

$$C_L = \left( \frac{1}{2} C_{N\alpha} \sin 2\alpha + C_{N\alpha\alpha} \sin \alpha |\sin \alpha| \right) \cos \alpha \quad (3.46)$$

$$C_D = C_{D0} + KC_L^{\frac{3}{2}} \quad (3.47)$$

Here  $C_{N_\alpha} = \left(C_{L_\alpha}\Big|_{\alpha=0}\right)$ ,  $C_{N_{\alpha\alpha}}$  are coefficients (independent of  $\alpha$ ) dependent on  $M$  and configuration. For  $0 < \alpha < 180^\circ$ :

$$C_{L_\alpha} = C_{N_\alpha} (\cos^3 \alpha - 2 \sin^2 \alpha \cos \alpha) + C_{N_{\alpha\alpha}} (2 \sin \alpha \cos^2 \alpha - \sin^3 \alpha) \quad (3.48)$$

For small values of the angle of attack  $\alpha$ , Eqs. (3.46) and (3.48), may be written as:

$$C_L = (C_{N_\alpha} \alpha + C_{N_{\alpha\alpha}} \alpha^2) \quad (3.49)$$

$$C_{L_\alpha} = C_{N_\alpha} (1 - 2\alpha) + C_{N_{\alpha\alpha}} (2\alpha - \alpha^3) \quad (3.50)$$

It is also noteworthy in [12] that the maximum value of the ratio L/D is equal to 5–10 for supersonic vehicles and only about 1–5 for hypersonic vehicles. Also, unlike supersonic vehicles, the lift and drag coefficients remain constant for hypersonic vehicles for  $M_\infty > 6$ .

### Explanation Box. Typical Force and Moment Characteristics of a Hypersonic Vehicle

A numerical example, to demonstrate typical forces and moments characteristics of a hypersonic vehicle is herein recognized [11].

To this end let us consider a hypothetical hypersonic vehicle at a nominal altitude of 53 km, with a trim angle of attack of  $10^\circ$ , and a speed relative to Earth of about 7.4 km/s.

Aerodynamic parameters are:

$$\begin{aligned} C_L &= 1.75 \sin \alpha \cos \alpha |\sin \alpha| \\ C_D &= 0.0625 + 1.69 \sin^2 \alpha |\sin \alpha| \\ C_{L\alpha} &= 3.5 |\sin \alpha| \cos^2 \alpha - 1.75 \sin^2 \alpha |\sin \alpha| \\ C_{D\alpha} &= 5.07 \sin \alpha \cos \alpha |\sin \alpha| \\ C_{mq} &= -0.03 \\ C_{m\alpha} &= -0.055 \\ \alpha_0 &= 10^\circ \\ L_{ref} &= 15.25 \text{ m} \end{aligned}$$

Approximate values in the case of small angle of attack are:

$$\begin{aligned} C_L &= 1.75 \alpha^2 \\ C_D &= 0.0625 + 1.69 \alpha^3 \\ C_{L\alpha} &= 3.5 \alpha - 1.75 \alpha^3 \\ C_{D\alpha} &= 5.07 \alpha^2 \end{aligned}$$

(continued)

From Eq. (3.41) one can evaluate the static margin by setting  $\alpha = \alpha_0 = 10^\circ$  and ignoring the shift in the *CoP* (e.g.,  $\partial x_{\text{cp}} / \partial \alpha = 0$ ), that is:

$$(x_{\text{cp}} - x_{\text{CG}}) = \frac{L_{\text{ref}} C_{m\alpha}}{C_{L\alpha}(\alpha)} = \frac{15.25 \times 0.055}{0.5803} = 1.445 \text{ m}$$

$$C_{m\alpha} = -\frac{C_{L\alpha}(\alpha)}{L_{\text{ref}}} (x_{\text{cp}} - x_{\text{CG}}) = -0.095 C_{L\alpha}(\alpha)$$

From Eq. (3.38), we get for  $\alpha = \alpha_0$ :

$$C_{m0} = \frac{C_L(\alpha)}{L_{\text{ref}}} (x_{\text{cp}} - x_{\text{CG}}) = \frac{0.05197 \times 1.445}{15.25} = 0.00493$$

As result, the pitching moment coefficient of the vehicle is reported in Fig. 3.50 [11].

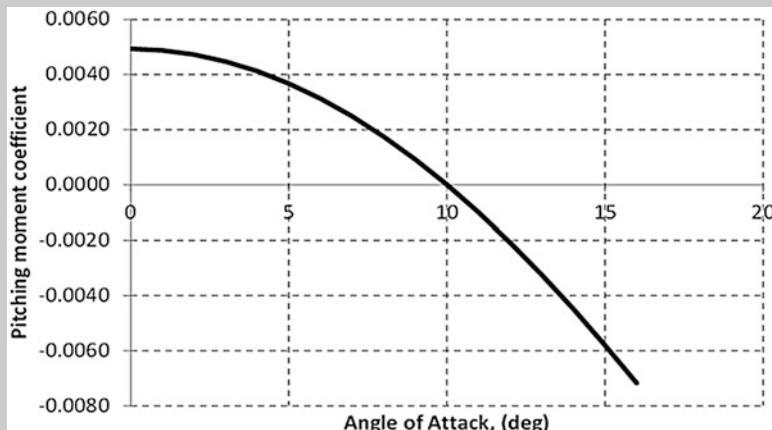


**Fig. 3.50** Pitching moment coefficient of a typical hypersonic vehicle

Several authors have reported that there is significant disparity between the wind-tunnel data (aerodynamic coefficients) and predictions based on this, as compared to the actual flight data. Figure 3.51 shows a plot of the actual (obtained from flight tests) *CoP* position and the predicted values (obtained from ground tests) for the Space Shuttle Orbiter (STS) [2, 12].

Clearly in order to ensure acceptable aerodynamic performance of a hypersonic vehicle, there is a need to have an active control and this has to be robust enough to cater for uncertainties in the predicted and/or computed aerodynamic design parameters.

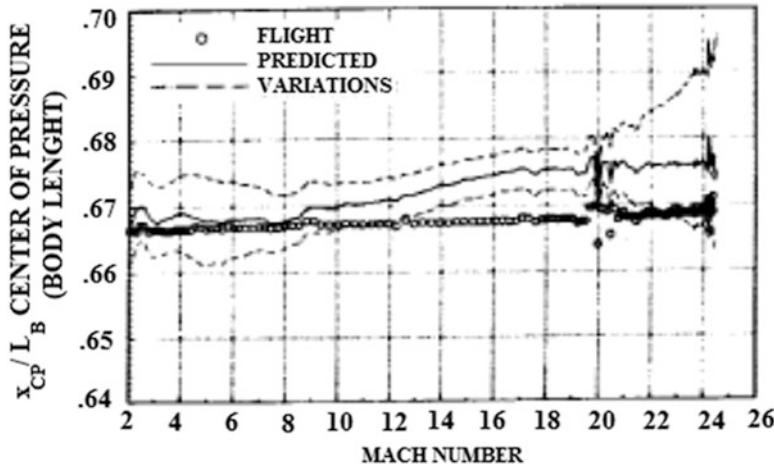


**Fig. 3.51** The STS longitudinal aerodynamic center of pressure location comparison

A control system based on moving the center of gravity (i.e. moving internal weights) still uses lift and drag forces to produce the required control moments. However, it may be difficult to achieve rapid changes in the moments that are needed to give fast enough control response.

The use of this mechanism to achieve stable and steady sustained flight at hypersonic speeds, apart from obvious engineering difficulties may not necessarily achieve the demonstration objective. In fact, various reported studies on stability and control indicate that a hypersonic vehicle tend to be unstable and require active control to achieve desirable transient properties.

### 3.8.4 Static Stability in Lateral-Directional Flight

In the previous sections we have dealt with longitudinal stability, which concerns angular motion about the  $y$ -axis (i.e., pitching motion).

In this section, we briefly examine the stability associated with angular motion about the  $z$ -axis, namely, yawing motion.

Stability in yaw is called directional stability. It applies when:

$$\frac{\partial C_n}{\partial \beta} > 0 \quad (3.51)$$

Indeed, assume the vehicle is suddenly yawed to the left by a disturbance. The vertical tail is now at an angle of sideslip  $\beta$  and experience an aerodynamic force perpendicular to  $V_\infty$ . This force creates a restoring yawing moment about the center of gravity that tends to rotate the vehicle back toward its equilibrium position (e.g., right wing rearward).

Stability in roll is called lateral stability. It refers to stability associated with angular motion about the x-axis, namely, rolling motion.

Lateral stability applies when:

$$\frac{\partial C_l}{\partial \beta} < 0 \quad (3.52)$$

Vehicle vertical tail(s) are usually designed in order to allow spacecraft lateral directional stability.

### 3.8.5 Vertical Tail Design

Tail control is probably the most commonly used form of conventional (subsonic and supersonic) vehicle control in lateral–directional flight. Therefore, tail control sizing represent a fundamental design issue.

To this end sizing rules of thumb also exist, for example, for spatuled-body configuration, which express control surface as percentage of vehicle planform area (see Fig. 3.52):

They are:

*Area of horizontal tail 12–13 % of body planform area*

*Area of vertical tail 8–9 % of body planform area*

Anyway, the parameter governing directional stability, namely, vertical tail volume ratio, ( $V_{VT}$ ), can be considered in designing vehicle vertical tail.

The vertical tail volume ratio is calculated by the following equation (see Fig. 3.53):

$$V_{VT} = \frac{l_{VT} S_{VT}}{b_{ref} S_{ref}} \quad (3.53)$$

where  $b_{ref}$  and  $S_{ref}$  are the vehicle wingspan and planform area, respectively.

The parameter  $l_{VT}$ , [m], is the distance between the mean aerodynamic center (MAC) of the vertical tail and the moment reference center of the vehicle ( $l_V$  in Fig. 3.53).

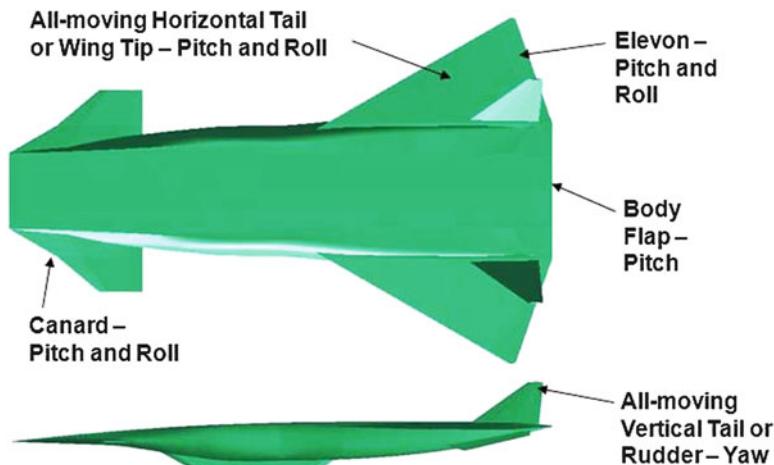
The parameter  $S_{VT}$ , [ $m^2$ ], is the exposed planform area of the vertical tail.

The location of the MAC was estimated as the midchord point of the mean aerodynamic chord of the exposed tail planform.

The mean aerodynamic chord was computed using the following integral evaluated in the reference frame of the vertical tail (see Fig. 3.54):

$$\bar{c} = \frac{1}{S_{VT}} \int_0^{b_V} c^2 dy \quad (3.54)$$

## Aero Control Surface Options



### Control Surface Sizing Rules of Thumb

Area of horizontal tail  $\sim 12\text{--}13\%$  of body planform area

Area of vertical tail  $\sim 8\text{--}9\%$  of body planform area

Elevator tail volume coefficient  $\equiv S_{elev}(X_{ac_e} - X_{CG}) / (\bar{SC}) \approx 0.055$

Rudder tail volume coefficient  $\equiv S_{rudder}(X_{ac_r} - X_{CG}) / (\bar{SC}) \approx 0.015$

**Fig. 3.52** Aero control surface options

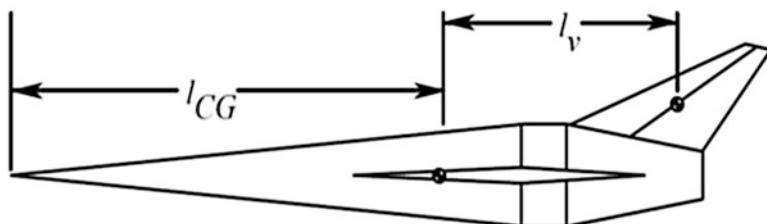


**Fig. 3.53** Model used to address vertical tail volume ratio

### 3.8.6 The Hypersonic Directional Stability Problem

An important design issue for assessing flyability and controllability of a hypersonic vehicle configuration is the hypersonic directional stability problem. In order to introduce this design topic, let us consider that the yawing moment provided by the vehicle tail (VT) is

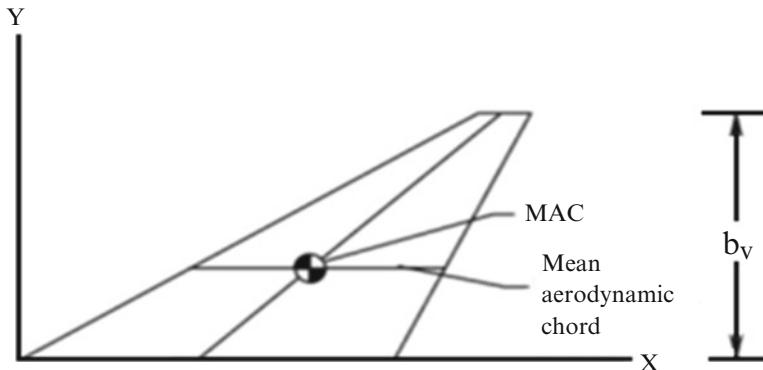


**Fig. 3.54** Reference frame for vertical tail

$$N_{VT} = q_{VT} S_{VT} l_{VT} C_{Y_{VT}} \quad (3.55)$$

On the other hand, the standard definition of the yawing moment coefficient,  $C_n$ , is

$$C_n = \frac{N}{q_{ref} S_{ref} C_{Y_{VT}}} \quad (3.56)$$

As a result, the yawing moment due to the vertical tail can be written as

$$C_{n_{VT}} = \underbrace{\frac{l_{VT} S_{VT}}{b_{ref} S_{ref}}}_{\substack{\text{Vertical tail volume} \\ \text{coefficient, } C_{VT}}} \cdot \underbrace{\frac{q_{VT}}{q_{ref}}}_{\substack{\text{Ratio of dynamic} \\ \text{pressure assume } \approx 1}} \cdot C_{Y_{VT}} \quad (3.57)$$

The nomenclature associated with the problem and the equations is illustrated in Fig. 3.55.

Now, for a high-speed flow, we will assume that the vertical tail is a two-dimensional surface with a constant pressure on each side, so that  $C_{Y_{VT}} = C_{P_{LS}} - C_{P_{US}}$ . Two cases will be considered, one supersonic and the other hypersonic, comparing the results for directional stability at high Mach number using the two-dimensional rule for linearized supersonic flow and Newtonian theory for hypersonic flow, as shown below.

#### *Linear theory*

$$C_p = \frac{2 \theta}{\sqrt{M^2 - 1}}$$

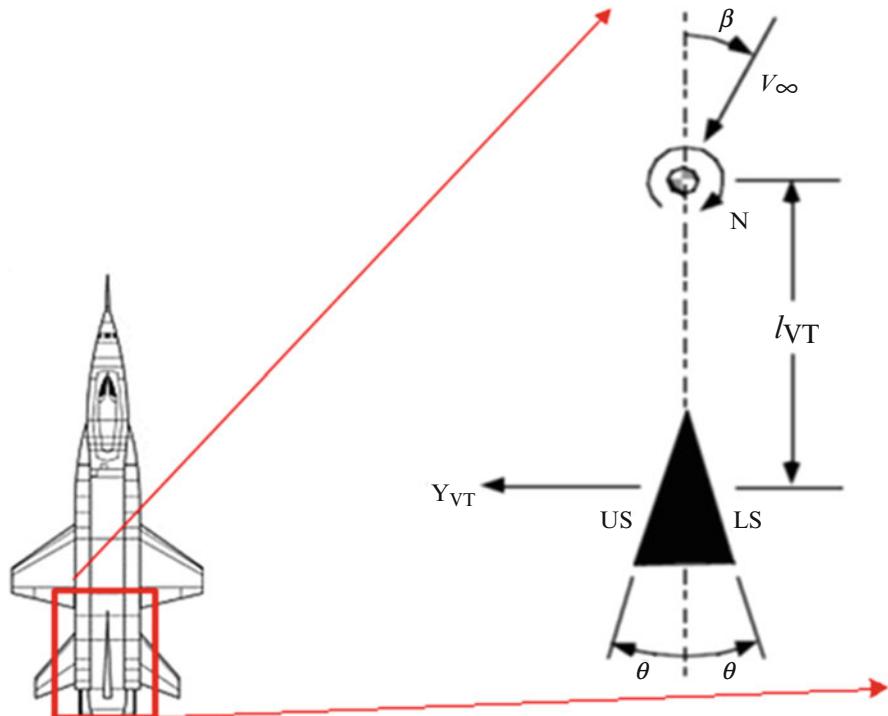


**Fig. 3.55** Sketch defining hypersonic directional stability problem

*Newtonian theory*

$$C_p = 2 \sin^2 \theta$$

Case 1: *Linearized supersonic theory*

$$C_{Y_{VT}} = \Delta C_p = \frac{2(\theta + \beta)}{\sqrt{M^2 - 1}} - \frac{2(\theta - \beta)}{\sqrt{M^2 - 1}} = \frac{4\beta}{\sqrt{M^2 - 1}} \quad (3.58)$$

shows that the  $\theta$ 's cancel. We use this expression to get  $C_{n_\beta}$ :

$$C_{n_{\beta VT}} = C_{VT} \frac{\partial C_{Y_{VT}}}{\partial \beta} = C_{VT} \frac{4}{\sqrt{M^2 - 1}} \quad (3.59)$$

This expression shows that  $C_{n_\beta}$  is positive, but vanishes for hypersonic Mach numbers.



**Fig. 3.56** X-15 configuration with wedge tail

### Case 2: Hypersonic flow – Newtonian theory

This time the expression for the side force is

$$C_{Y_{VT}} = C_{P_{LS}} - C_{P_{US}} = 2 \sin^2(\theta + \beta) - 2 \sin^2(\theta - \beta) \quad (3.60)$$

Using trigonometric functions,

$$C_{Y_{\beta VT}} = 2 \left[ \begin{array}{l} \sin^2 \theta \cos^2 \beta + 2 \cos \theta \sin \beta \sin \theta \cos \beta + \cos^2 \theta \sin^2 \beta \\ - \sin^2 \theta \cos^2 \beta + 2 \cos \theta \sin \beta \sin \theta \cos \beta + \cos^2 \theta \sin^2 \beta \end{array} \right] \quad (3.61)$$

which reduces to

$$C_{Y_{\beta VT}} = 8 \cos \theta \quad \sin \beta \quad \sin \theta \quad \cos \beta \cong 8 \theta \beta \quad (3.62)$$

and

$$C_{Y_{\beta VT}} = 8 V_{VT} \theta \quad (3.63)$$

If  $\theta$  is zero, so is  $C_{n_\beta}$ ! But opening up the wedge angle rapidly increases  $C_{n_\beta}$ . In addition, there is no Mach number dependence. The Case 2 results were verified experimentally, and the wedge vertical tail concept literally saved the X-15 program. This effect is also the reason for flared “skirts” seen on some launch vehicles. The application of this effect is clearly shown in the picture of the X-15, see Fig. 3.56.

### 3.9 An Example of Design for Glide Re-entry Vehicles

The decision to design and to build the Hermes presented the European aerospace community with the opportunity and with the challenge to apply the tools available at the outset of the 1990s to design a new space transportation vehicle.<sup>8</sup> A sketch of a Hermes configuration is presented in Fig. 3.57 [8]. A comparison with the Shuttle Orbiter characteristics (see Fig. 3.28) reveals some major differences and, in particular, the more severe thermal environment which the lower scale of the Hermes will induce. The similar values for the ballistic coefficient and for the hypersonic efficiency imply that the re-entry trajectory will not be substantially different; all other things being equal, the transition to turbulent flow will occur somewhat later on corresponding points of the vehicle, while the heat transfer will be higher, due to the smaller Reynolds number and the smaller radius of curvature of the surfaces. It is necessary, therefore, to round as much as possible both the nose and the leading edges of the wing with corresponding loss on the slenderness of the vehicle.

Hermes was conceived to have the following features:

- Initially, the transportation of six astronauts and 4,500 kg payload into space and after a later reorientation a reduction of the transport capacity to three astronauts and 3,000 kg payload

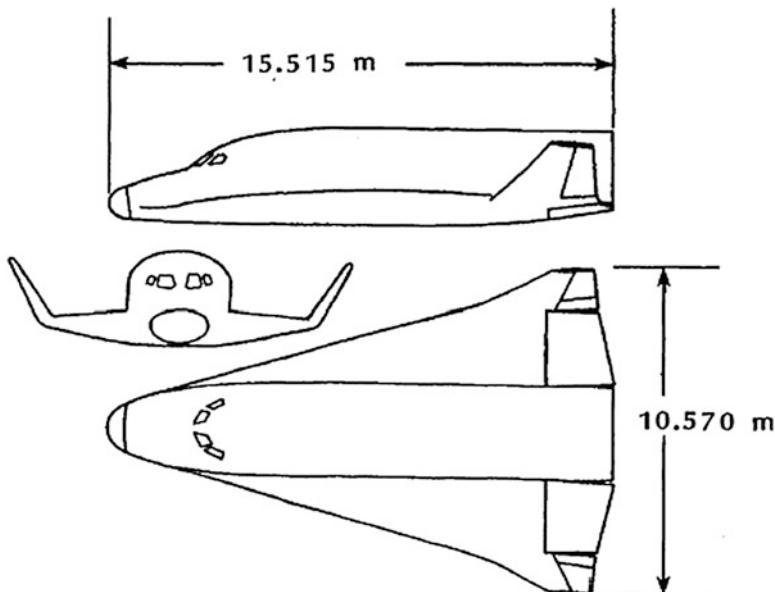


**Fig. 3.57** The configuration of Hermes vehicle concept

---

<sup>8</sup>In 1993 the Hermes project was canceled due to the new political environment (end of the cold war) and budget constraints.

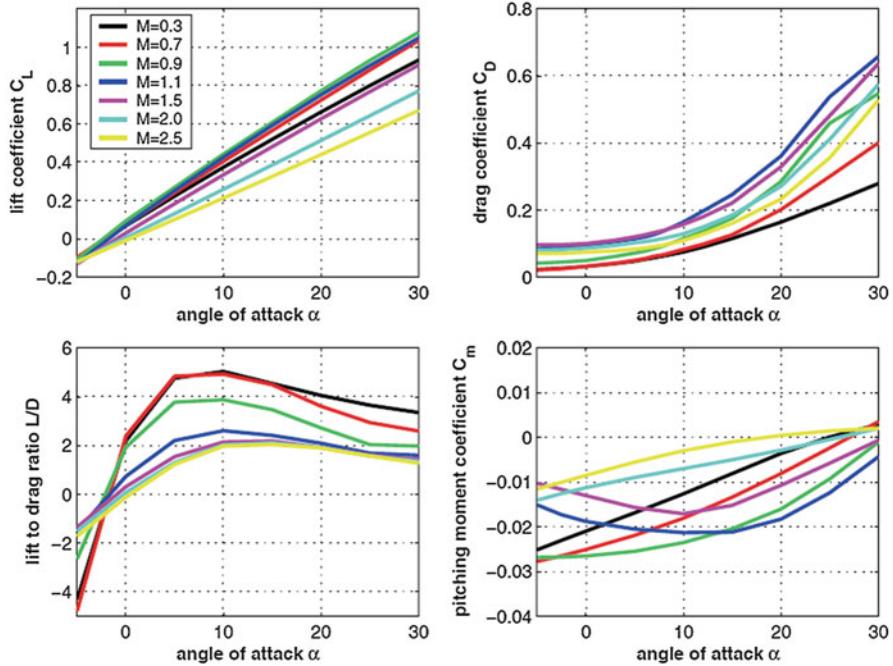


**Fig. 3.58** Aerodynamic data of the Hermes shape 1.0 for the subsonic through low supersonic Mach number regimes, moment reference point  $x_{\text{ref}} = 0.6 L_{\text{ref}}$

- Ascent to near Earth orbit (up to 800 km) on top of the ARIANE V rocket (see Fig. 3.63)
- 30–90 days mission duration
- Total launch mass 21,000 kg
- Full reusability

The concept aerodynamic data from subsonic to hypersonic flight regime are shown in Figs. 3.58 and 3.59, respectively [13]. Such a data were composed with results from wind-tunnel tests, approximate design methods, and numerical simulations. As shown, the lift coefficient  $C_L$  for subsonic Mach numbers shows linear behavior over a large range of angle of attack. The drag coefficient around  $0^\circ$  angle of attack is very small for all Mach numbers, rising with increasing angle of incidence, as expected. The drag coefficient for transonic Mach numbers is largest. Further, the maximum aerodynamic efficiency of about five occurs close to  $10^\circ$  AoA for subsonic Mach numbers and somewhat below 2 in the low supersonic and hypersonic regimes.

The pitching moment data indicate static stability for transonic/low supersonic Mach numbers ( $1.1 \leq M_\infty \leq 1.5$ ) up to  $\alpha \approx 10^\circ$  but no trim point and instability for

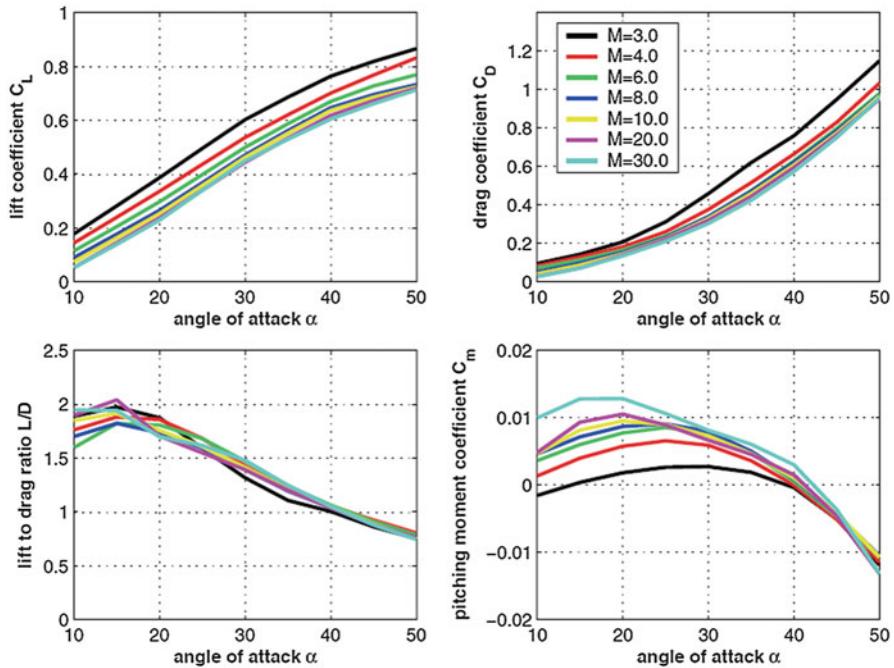


**Fig. 3.59** Aerodynamic data of the HERMES shape 1.0 for the hypersonic Mach number regime, moment reference point  $x_{\text{ref}} = 0.6 L_{\text{ref}}$

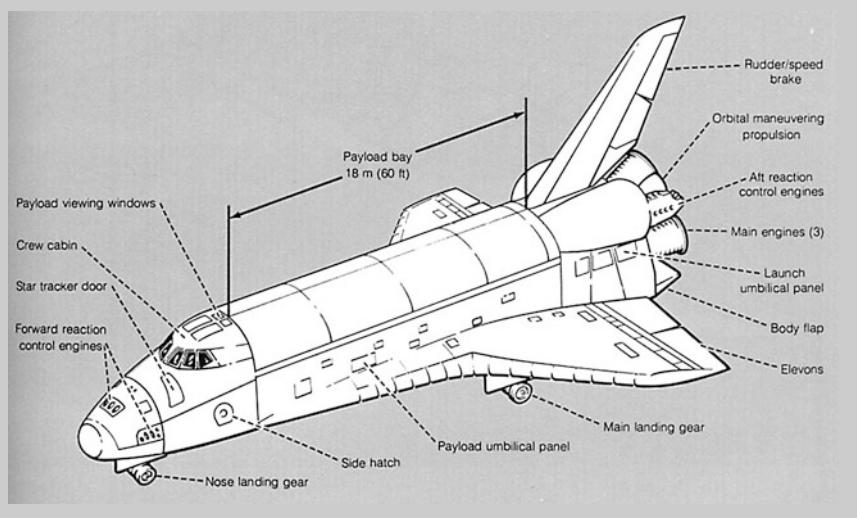
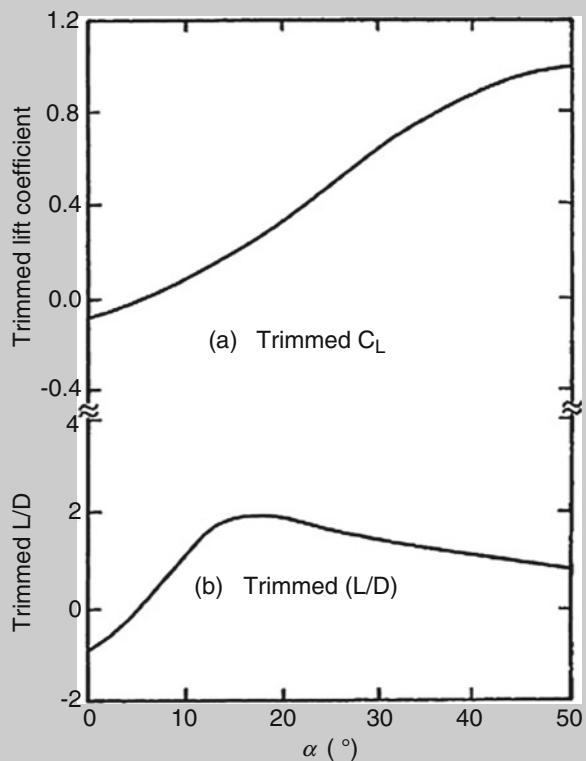
subsonic and low supersonic Mach numbers. For higher supersonic and hypersonic Mach numbers, static stability and trim are observed for  $\alpha \approx 40^\circ$ . Mach number independence of  $C_L$  and  $C_D$  is seen for  $M_\infty > 6$ .

#### Explanation Box. Orbiter Longitudinal Aerodynamic Characteristics at Hypersonic Speed

The pitch plane aerodynamic forces for the Shuttle Orbiter in a hypersonic stream (neglecting viscous interaction effects) are reproduced in Fig. 3.60 [8]. Values of hypersonic lift coefficient and lift-to-drag ratio have been maintained at levels consistent with aeroheating constraints and trajectory requirements. The pitch trim range is sufficiently wide and well centered with respect to the design center of gravity range. The side force necessary for generating cross range was obtained for the Shuttle Orbiter (as it was obtained for the simpler capsule shapes) by rotating the lift vector out of the vertical plane (i.e., bank maneuver).

(continued)

**Fig. 3.60** Orbiter longitudinal aerodynamic for hypersonic regime.  
 $S_{\text{ref}} = 250 \text{ m}^2$ ;  $x_{\text{cg}} = 0.65 L_{\text{ref}}$ ;  $\delta_{\text{bf}} = -11.7^\circ$ ;  
 $\delta_{\text{sb}} = 25^\circ$



(continued)

Thus, although the Orbiter was designed to be a reusable vehicle that lands horizontally, for most of the hypersonic phase of re-entry flight, the Orbiter flies like a spacecraft rather than like an airplane. In fact, as indicated in Fig. 3.22, configurations with relatively high lift-to-drag ratios are generally characterized by highly swept winged configurations possessing low-bluntness ratios and high-fineness ratios like waverider-shaped vehicles. The maximum values of the aerodynamic efficiency for these slender configurations occur at comparatively low angles of attack. Viscous effects, i.e., the skin-friction component of drag, become a significant fraction of the overall drag for such a slender vehicle with very small leading-edge bluntness operating at low angle of attack. As a result, wetted area becomes important. High values of the volumetric efficiency ( $V^{0.667}/S_w$ ) translate into reduced wetted area, which means reduced skin-friction drag. Wetted area is also a first-order indicator of the acreage which must be thermally protected. Consequently, reduced wetted surface area yields higher values for the volumetric efficiency and reduced thermal protection system weight. Carefully designed configurations can achieve values of  $(L/D)_{\max}$  of approximately 6 at hypersonic speeds.

Hermes glides through the earth's atmosphere within the re-entry corridor depicted in Fig. 3.61 [8].

The corridor is bounded by lines representing the maximum load, i.e., the maximum dynamic pressure, the maximum heat-transfer rate, and the maximum altitude at which equilibrium can be maintained between the weight and the aerodynamic forces (i.e., ceiling). During the initial phase of re-entry, the Hermes vehicle is at a relatively high angle of attack, e.g.,  $40^\circ$ , so that it acts as a very blunt body ( $L/D \cong 0.8$ ) with most of the energy heating the air in the shock layer and not the vehicle. For this high-alpha configuration, the flow is dominated by a strong bow shock and a large subsonic region covering the entire windward side of the vehicle followed by a largely separated flow for the leeward side. The angle of attack is reduced, e.g.,  $19^\circ$ , for the latter part of the trajectory, so that Hermes acts as a relatively high L/D glider ( $L/D$  1.5–2 at hypersonic speeds and 2–5 at supersonic speeds). For this lower alpha, the flow around the vehicle is mostly supersonic with the exception of the nose cap.

The fluid mechanic and thermodynamic phenomena encountered by the Hermes during its flight through the Earth's atmosphere are indicated in Fig. 3.62 [8].

Rocket-launched space vehicles (without fairings, see Fig. 3.63), such as the Hermes, experience relatively little aerodynamic heating during launch. The large thrust available during ascent results in passage through the atmosphere in a matter of minutes. Burnout velocity is reached at very high altitudes, where the aerodynamic heating is low.<sup>9</sup>

---

<sup>9</sup>For instance, the time-integrated heating (total heat load) at the Shuttle orbiter nose stagnation point is almost two orders of magnitude less during launch than during atmospheric entry.

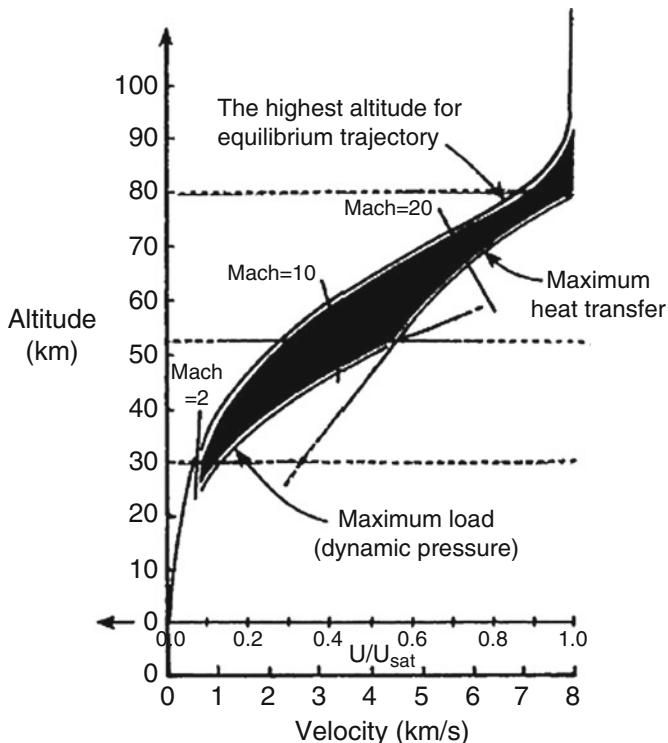


**Fig. 3.61** Re-entry corridor for the Hermes vehicle concept

From the notations in Fig. 3.62, it is evident that the Hermes experiences a variety of dramatically different flow phenomena during re-entry.

Locations of flow and high-temperature real gas phenomena on Hermes aeroshape at hypersonic flight are summarized in Fig. 3.64 [8].

At altitudes in excess of 100 km, one must understand rarefied non-continuum flows. At altitudes in excess of 60–70 km, the aerothermodynamicist must account for nonequilibrium chemistry and surface catalycity. Boundary-layer transition occurs for flight Mach numbers on the order of 10, when the altitude is approximately 50 km.<sup>10</sup> Real gas effects are not a factor for the subsequent flight at lower Mach numbers/lower altitudes. Nevertheless, determining the solution of

---

In contrast, a vehicle using an airbreathing propulsion system must fly a long time in the denser portion of the atmosphere to develop sufficient thrust to accelerate to orbital speed. This extended period of hypervelocity atmospheric flight exposes the vehicle to high local heating rates and large total heating loads.

<sup>10</sup>Note that the determination of the conditions for boundary-layer transition challenges the most experienced designer.

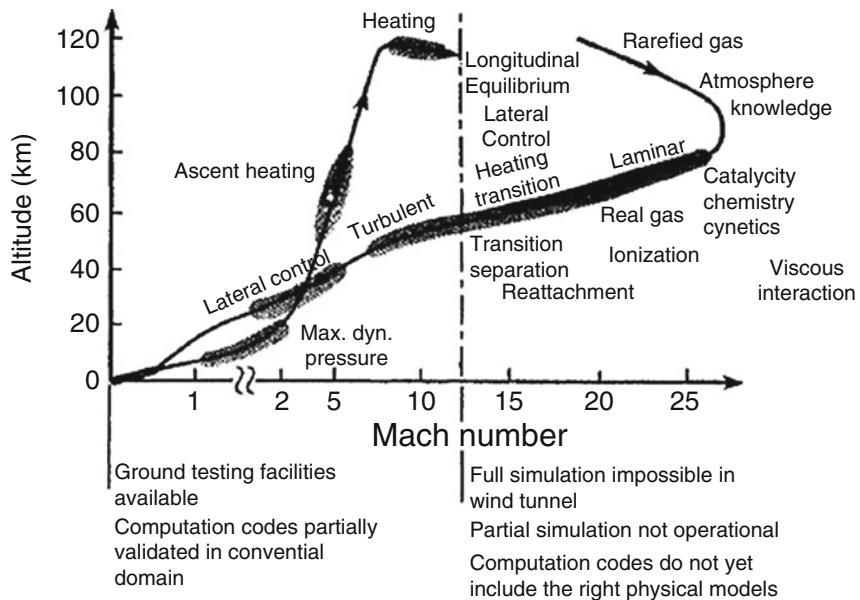


**Fig. 3.62** The aerothermodynamic concerns for the Hermes launch and re-entry trajectories

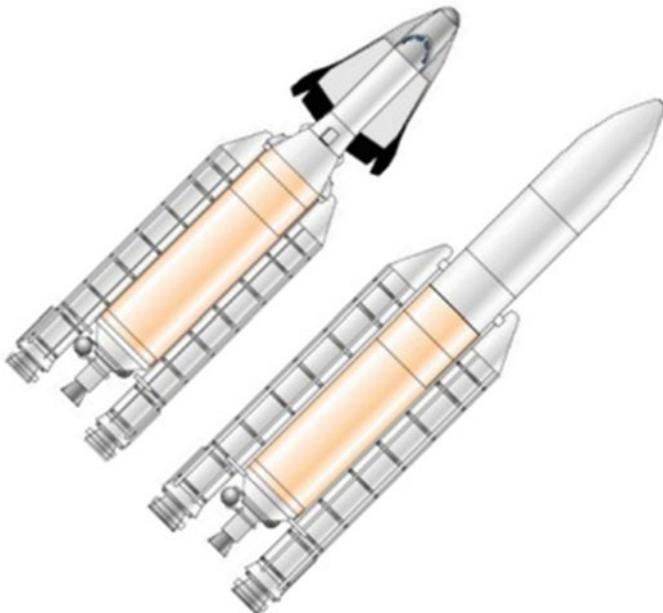


**Fig. 3.63** The Hermes in launch configuration, comparison with Ariane V

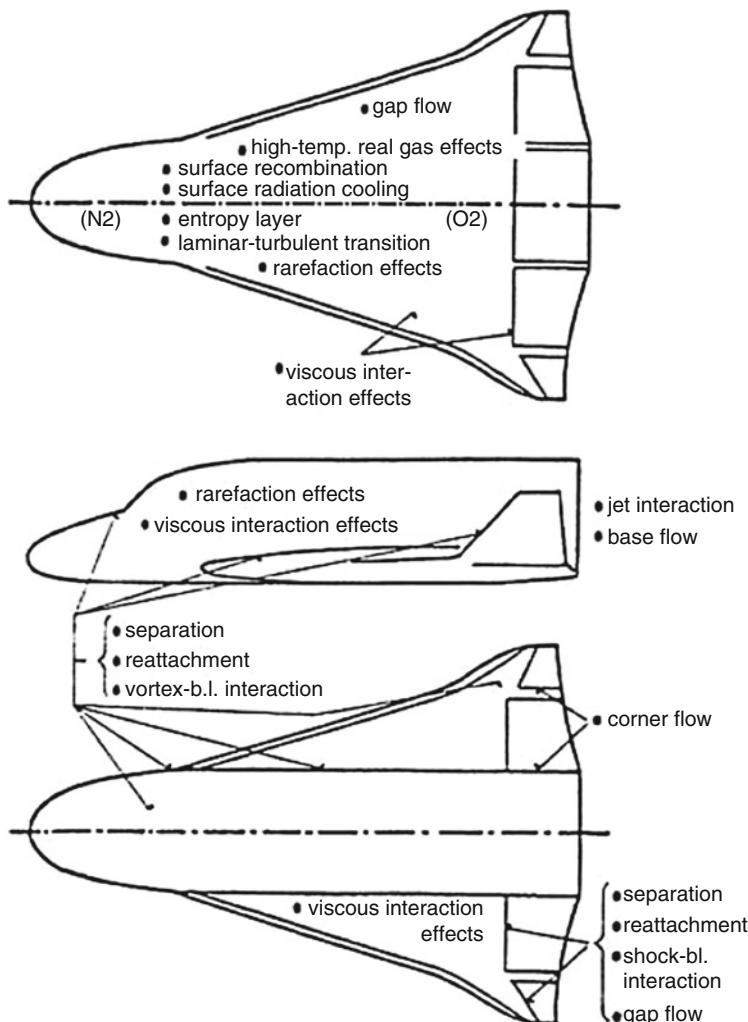


**Fig. 3.64** Locations of flow and high-temperature real gas phenomena on Hermes

the flowfield at these conditions remains a considerable challenge. Problems, such as modeling turbulent boundary layers and viscous/inviscid interactions for the winglets (e.g., corner flows and shock/shock interactions), require considerable understanding on the part of the designer.

The largest part of re-entry trajectory is flown at high angle of attack. The high angle of incidence and the relatively flat windward side of the vehicle (see Fig. 3.57) increase the spacecraft effective bluntness and thus increase further the (wave) drag of the vehicle. The large nose and wing leading-edge radii, and the highly swept

wing, permit effective surface radiation cooling. The very small aspect ratio of such a concept vehicle, as for all hypersonic flight vehicles, causes difficulties in low-speed control, especially during approach and landing. A remedy is to provide a double-delta or strake-delta wing. In the case of Hermes, low-speed handling is improved by the winglets.

Another critical aspect of the spacecraft design is the method by which it will land at the end of space mission. Indeed, landing accuracy and cross range are important considerations for crewed vehicle design. As shown by Figs. 3.20 and 3.21, the crewed vehicle must develop enough aerodynamic efficiency. Increased cross-range capability allows spacecraft to reach a wider number of potential landing sites, and landing accuracy helps ensure a safe landing (and ease of recovery) once a site is chosen. Of course, both nominal and abort case landings must be accommodated too.

While orbital inclination and cross-range capability define the possible landing sites, a number of other technologies dictate exactly how the landing occurs. After the initial re-entry burn is complete, the remainder of the mission can be divided into a descent phase (significant reduction in vertical velocity) and a landing phase (final deceleration and dissipation of the impact forces). How the design challenges of these two phases are answered will further restrict the types of landing sites that can be used.

Vehicles with high L/D configurations (such as winged craft and some lifting bodies) are able to glide or fly into their landing site with very small remaining vertical speed. This provides for a very soft landing, but it limits candidate landing sites to places with large runways and requires either a highly trained pilot or a complex automated landing system. This type of landing occurs with relatively high horizontal speeds at touchdown, so vehicles of this type are required to have wheels (such as those on the Space Shuttle), with the resultant penalties in safety, weight, and complexity.

The importance of a rather high aerodynamic efficiency in landing approach for high-speed vehicle configuration is discussed in the next explanation box.

#### **Explanation Box. Lift-to-Drag Ratio in Landing Approach for High-Speed Vehicles**

The landing approach for high-speed vehicle that typically have limited L/D capability is shown schematically in Fig. 3.65. Here a relatively steep slope is followed by the important flare maneuver.

(continued)

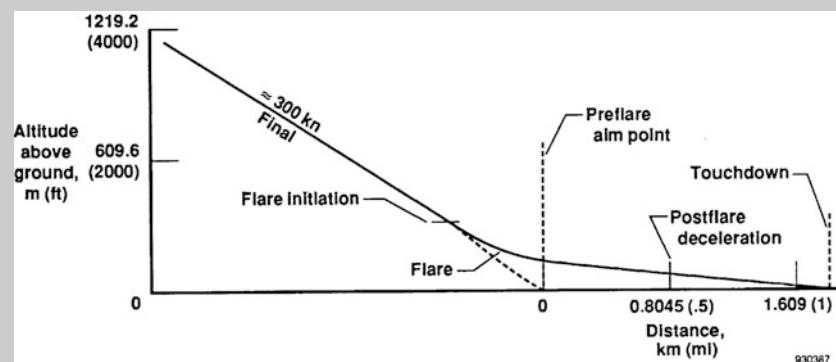


**Fig. 3.65** Landing approach for high-speed vehicles with low L/D



**Fig. 3.66** Three early lifting-body designs at NASA Dryden Research Center. From *left* to *right*, the X-24A, the M2-F3, and the HL-10 (Courtesy of NASA)

Values of  $L/D < 3$  during the flare are considered unacceptable for piloted landing, independent of the vehicle wing loading  $(W/S)_{\text{land}}$ . The  $L/D$  during landing flare is essentially equivalent to  $(L/D)_{\max}$ .

Power-off landings are readily achievable with vehicles whose  $(L/D)_{\max}$  is in the range of 3.5–5. For example, the X-15 and the Space Shuttle Orbiter have  $(W/S)_{\text{land}}$  in the range of 3,800–4,300 Pa and  $(L/D)_{\max}$  in the range of 4.15–4.75.

When we look upon the subsonic aerodynamic performance of lifting-body vehicles, such as those shown in Fig. 3.66, we find a  $(L/D)_{\max}$  which is far below the required value.

(continued)



**Fig. 3.67** X-38 landing with parafoil at Edwards Air Force Base (Courtesy of NASA)

This is the reason why it was foreseen to conduct the final descent and landing of the X-38 vehicle with a steerable parafoil system (see Fig. 3.67).

A comparison of the variation of the aerodynamic efficiency as a function of angle of attack of several bodies ranging from the slender X-15 to the moderate Space Shuttle Orbiter to the bluff HL-10 lifting body is shown in Fig. 3.68.

(continued)

In order to attain the necessary landing L/D of around 4, Fig. 3.68 shows that the lifting-body shape must fly at much larger angles of attack than the more slender bodies. This is illustrated in Fig. 3.69 where the HL-10 is shown landing accompanied by the NASA F-104 chase plane.

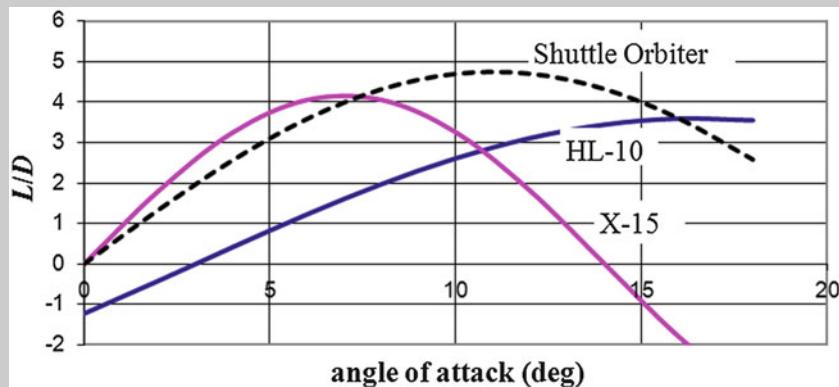


**Fig. 3.68** The variation of  $L/D$  as a function of angle of attack for X-15, Space Shuttle Orbiter, and HL-10 lifting body



**Fig. 3.69** Landing of the HL-10 lifting re-entry body and the F-104 chase plane at NASA Dryden Research Center (Courtesy of NASA)

(continued)

Then, factors in the configuration design which contribute to safe landings are good visibility, good handling qualities, effective speed brakes, and minimal trim changes.

Approach and landing may be considered as quasi-static processes, so the lift is approximately equal to the landing weight.

Further, in order to accommodate surface gusts with adequate margin, 20 % and 30 % increases over the stall speed for landing and approach, respectively, are applied.

So that the landing speed is taken as  $V_{\text{land}} = 1.2 V_s$  and the approach speed as  $V_a = 1.3 V_s$ , where  $V_s$  is the stall speed given by

$$V_s = \sqrt{\frac{(W/S)}{\frac{1}{2} \rho_{\text{s.l.}} \sigma (C_L)_{\max}}} \quad (3.64)$$

In Eq. (3.64)  $\sigma = \rho / \rho_{\text{s.l.}}$  is the ratio of local density to standard sea level density. The stall speed may be considered the minimum usable speed and  $C_{L,\max}$  the maximum usable lift coefficient. Since high-speed aircraft fuselages are generally long, with slenderness ratios  $l/b$  are around 0.5 or less, the true stall angles of attack are never reached in landing because of the danger of tail strikes and other controllability issues. For example, the maximum usable angle of attack for the X-15 is about 13°.

The range of limitations found on angle of attack of the X-15 is shown in Fig. 3.70, and these are representative of most high-speed vehicles.

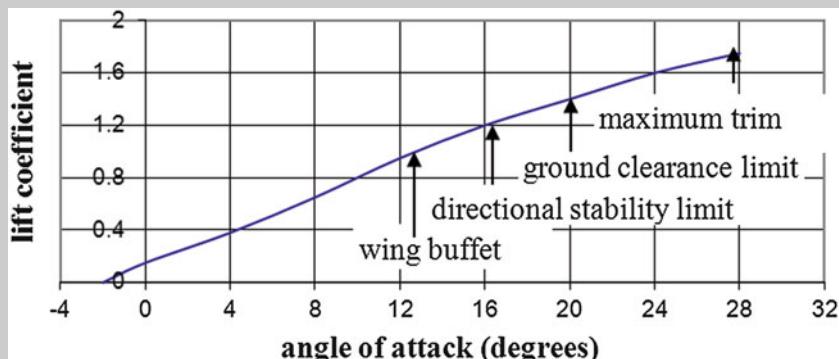


**Fig. 3.70** Lift coefficient of the X-15 as a function of angle of attack (Shown on the figure are the limiting operational factors)

(continued)

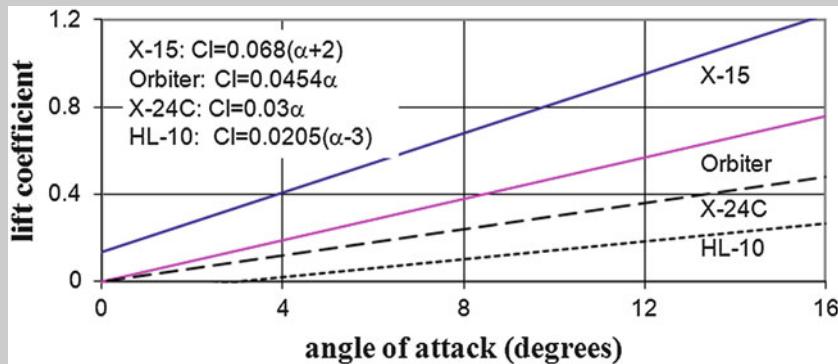


**Fig. 3.71** Nominal lift curves as a function of angle of attack for several hypersonic vehicles

Nominal lift curves for several hypersonic vehicles are shown in Fig. 3.71.

Moreover, the equivalent airspeed, which is generally used since it is effectively the indicated airspeed monitored by the pilot, is given by

$$V_E = V \sqrt{\sigma} \quad (3.65)$$

Then, the equivalent speed at stall, in knots, is

$$V_{E,s} = 17.17 \sqrt{\frac{(W/S)}{C_{L,max}}} \quad (3.66)$$

The nominal landing speed, in knots, is

$$V_{E,land} = 1.2 V_{E,s} = 20.60 \sqrt{\frac{(W/S)_{land}}{C_{L,max}}} \quad (3.67)$$

Likewise, the nominal approach speed, in knots, is

$$V_{E,a} = 1.3 V_{E,s} = 22.32 \sqrt{\frac{(W/S)_{land}}{C_{L,max}}} \quad (3.68)$$

The approach speeds for some high-speed aircraft are shown in Fig. 3.72.

(continued)

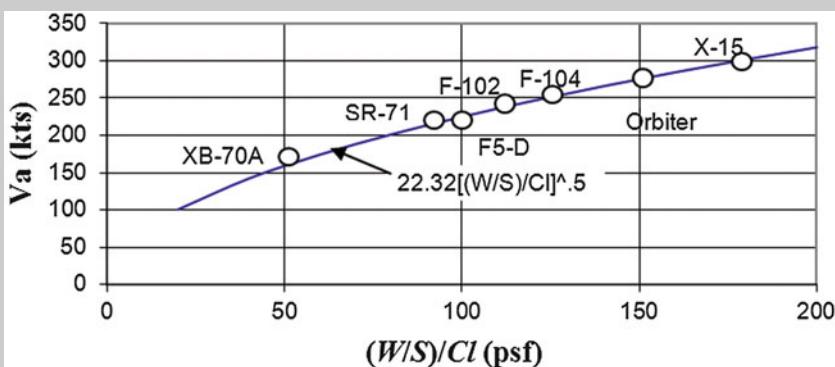


Fig. 3.72 Approach speeds for several high-speed aircraft

Note that  $1 \text{ psf} = 47.88026 \text{ Pa}$

Finally, the comments relating to ground testing and to computational codes, which are presented along the abscissa of Fig. 3.62, indicate that ground-testing facilities are available up to Mach 12.5. Above this Mach number, full simulation is not possible in the wind tunnel.

Of course, these comments should be considered qualitative, subject to changes in technology and in application. They depend on the state-of-art in-space technology.

### 3.10 Spatuled-Body Configuration

This paragraph provides an overview on a highly innovative hypersonic vehicle, namely, waverider. It represents, by aerodynamic point of view, a step beyond toward the future.

In order to understand why, let us consider that a basic feature of all in-flight hypersonic vehicles is the creation of relatively strong shock waves emanating from their leading edges. Associated with the flowfields behind these shock waves are severe aerothermodynamics, propulsion system integration, and aeroelastic design problems. This feature is characteristic of both ballistic and lifting vehicles, so in either case the relationship between shock wave shape and vehicle aeroshape is of fundamental importance to effective vehicle design.

In this framework, after a thorough review of flight vehicle performance over a range of Mach numbers, Kuchemann established an L/D barrier and the associated aircraft configurations that perform best with this barrier:

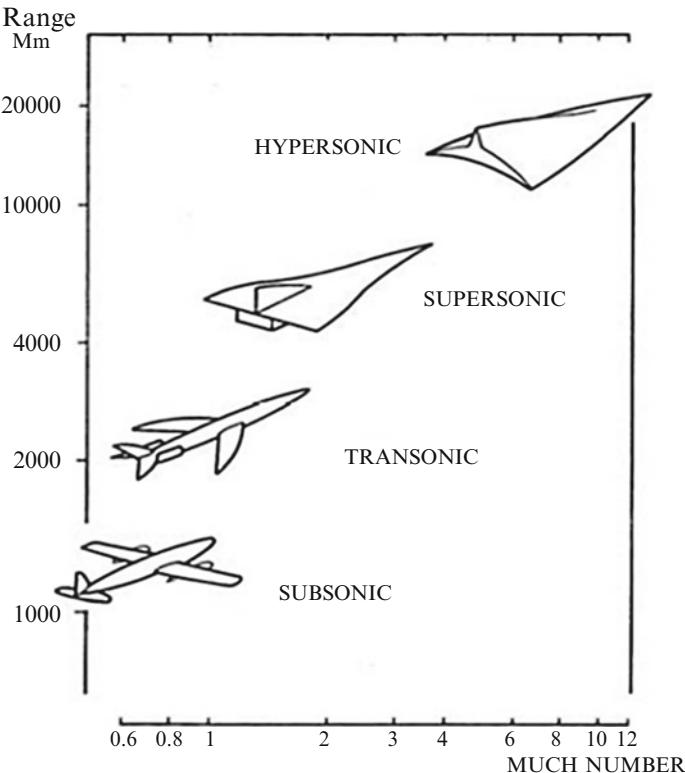


**Fig. 3.73** Influence of flight Mach number and performance on aircraft shape

$$\left(\frac{L}{D}\right)_{\max} = \frac{4(M_\infty + 3)}{M_\infty} \quad (3.69)$$

where  $L$  is the aerodynamic lift force,  $D$  is the aerodynamic drag force, and  $M_\infty$  is the Mach number.

Kuchemann demonstrated in Fig. 3.73 that at high Mach numbers in order to maximize aircraft performance, blended body configurations with tightly integrated forebodies, propulsion, and nozzle afterbodies are favored [14].

Later, Bowcutt showed not only that waverider configurations supported the Kuchemann findings but that viscous optimized waverider configurations can potentially outperform the blended body aircraft configurations and thus break the “L/D barrier” Kuchemann established. Bowcutt’s findings were later supported by others as demonstrated in the illustration depicted in Fig. 3.74 [2].

As shown, it is noticeable to see that the white dots trimmed in block fall under the solid line Kuchemann curve that’s due to strong viscous effects (which leads to high skin-friction drag) and strong shock wave (which leads to high wave drag) that they suffer when flying at those high speeds.

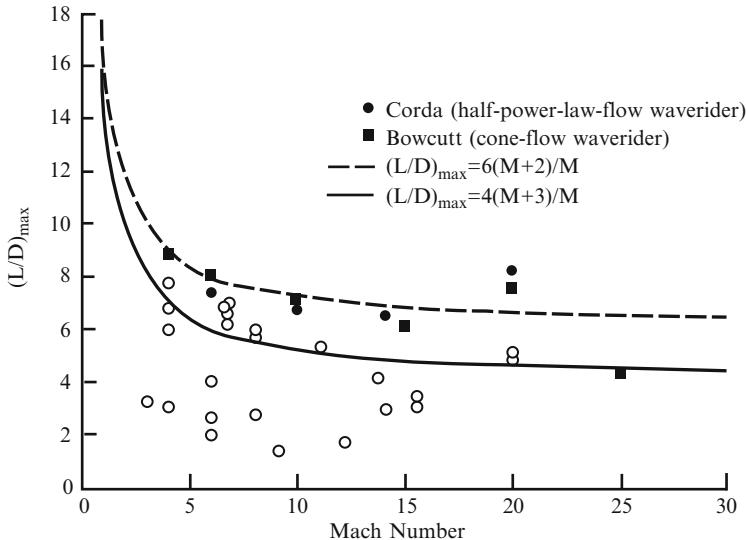


Fig. 3.74 The Kuchemann “L/D barrier” and waverider performance

Moreover, the goal of using also the curve:

$$\left(\frac{L}{D}\right)_{\max} = \frac{6(M_\infty + 2)}{M_\infty} \quad (3.70)$$

dashed line in the Fig. 3.74, is to create a vehicle that demonstrates an aerodynamic performance within the two curves (both the solid and dotted curves) or exceed what is being shown. Note that the theory states that the dashed curve cannot be exceeded unless there's no engine in the vehicle.

The lesson learned in the past is that hypersonic sizing approach is very different from subsonic and supersonic aircraft. In fact, as shown in Fig. 3.75, the maximum L/D of a design tends to decrease as the Mach number increases. However, a class of vehicles referred to as *waveriders* has shown the potential to break the L/D barrier and therefore can offer performance advantages as compared to conventional designs when applied to hypersonic mission profiles. Indeed, at high Mach numbers, high L/D ratios are very difficult to achieve because of high skin-friction wave drag.

Kuchemann analyzed this trend and formulated the general empirical relationship:

$$\left(\frac{L}{D}\right)_{\max} = \frac{4(M_\infty + 3)}{M_\infty} \quad (3.71)$$

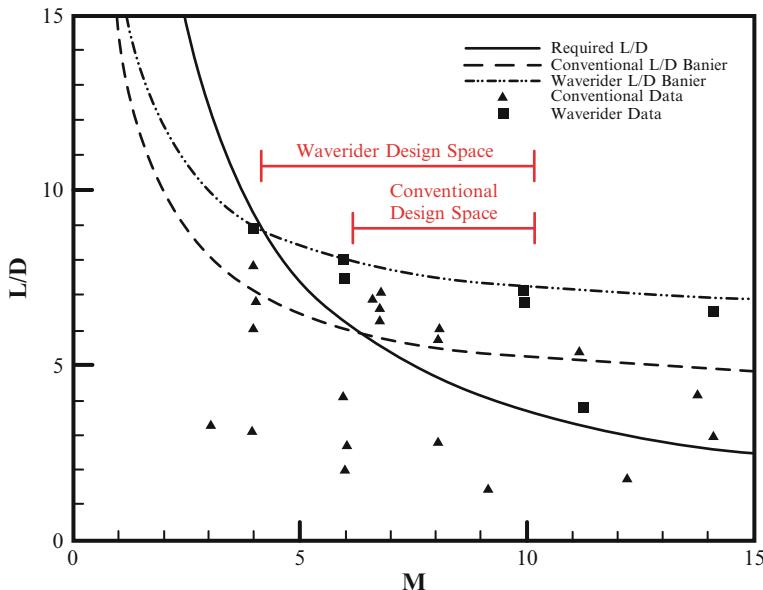


Fig. 3.75 L/D vs. Mach number

A waverider is a supersonic or hypersonic configuration that exhibits the characteristic of an attached shock wave along its entire leading edge.

This attached shock wave limits leakage of the high-pressure lower-surface flow into the upper-surface region, thus allowing the potential of a high L/D relative to conventional designs. Waveriders are typically created using an *inverse design process* in which the supersonic or hypersonic flowfield around a simple object is used as the generating flowfield for the design. The streamlines behind the shock wave are traced to create the lower surface of the waverider (such that the waverider will be able to recreate the same shock wave shape from its own leading edge); the upper-surface configuration is arbitrary and is commonly created as a surface parallel to the free-stream direction. An example of a waverider designed from a wedge generating flowfield is shown in Fig. 3.76.

Waveriders were initially proposed by Nonweiler as a solution to the large stagnation heating rates experienced by ballistic re-entry vehicles; a waverider would theoretically provide a higher L/D and allow for lower-heating lifting re-entry trajectories [5]. His proposals for waveriders focused on “caret” designs (named because their base shape resembles the typographical “^” symbol) designed using two-dimensional wedge flowfields; an example of a caret waverider is shown in Fig. 3.77 [5].

Although initial interest in waveriders was substantial, several problems were present, including low volumetric efficiency of the caret waverider designs, possible degradation of performance at off-design conditions, and issues regarding the realistic implementation of sharp leading edges. Later investigations indicated that the

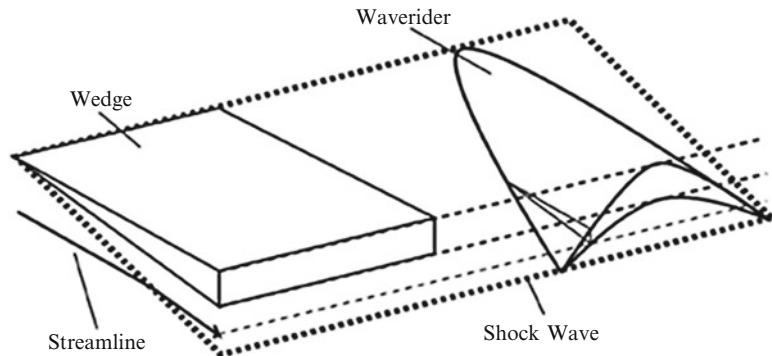


**Fig. 3.76** Waverider generation from a two-dimensional wedge in supersonic/hypersonic flow

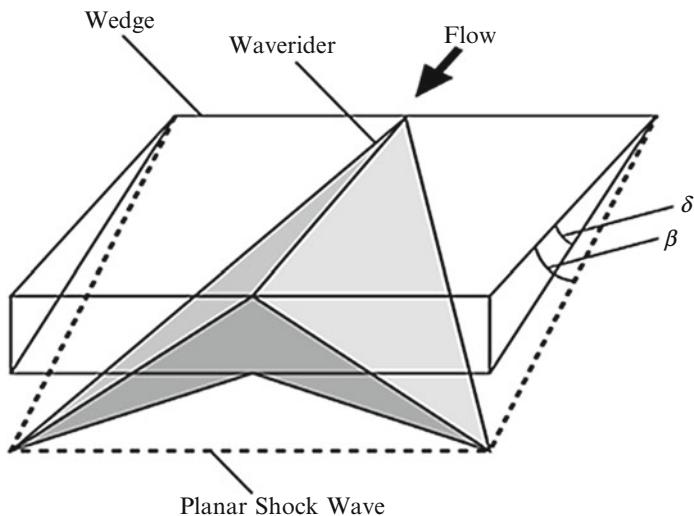


**Fig. 3.77** Caret waverider designed from two-dimensional wedge in supersonic/hypersonic flow

initially predicted high L/D properties were not maintained by real configurations (primarily due to viscous effects), and the concept was relatively ignored for several decades.

In the late 1980s and early 1990s, interest in waveriders again proliferated, due to several new designs and analysis techniques that overcame some of the original disadvantages. The development of viscous-optimized waveriders reaffirmed the high L/D characteristics of the design by including viscous analyses into the design and optimization process, and both numerical and experimental investigations led to further verification of these properties. Finally, investigation into the performance of waveriders has led to the conclusion that the high L/D properties can be maintained at moderate off-design conditions (e.g., angle of attack, Mach number, blunt leading edges).

New design methods, such as the use of conical generating flowfields, allowed the design of configurations that included other favorable characteristics (e.g., higher volumetric efficiency) from the standpoint of mission integration.

In recent years, the *osculating cone method* has seen increased popularity as a means to obtain the generating flowfield for waverider design – this method is advantageous in that relatively arbitrary three-dimensional shock wave shapes can be generated using analytical flow solution methodologies (i.e., an analytical cone flow solution is applied in osculating planes rather than axisymmetric planes). Finally, three-dimensional marching methods have been used to allow the use of generating flowfields with variable shock wave strength and shock curvature in the flow direction (i.e., a fully three-dimensional shock wave – osculating cone methods, on the other hand, still rely on a single cone solution scaled to each osculating plane).

### ***3.10.1 An Introduction to Waverider Configuration Design: The Inverse Design Method***

Waveriders are typically characterized by a wedge-like configuration, consisting of a high-pressure lower-surface and a low-pressure upper surface. In order to meet the requirements of an attached leading-edge shock wave, waveriders are frequently created using the *inverse design method*. In this technique, the generating flowfield (i.e., the flowfield that will define the shape of the waverider) is first specified; the generating flowfield is simply the supersonic or hypersonic flow past a body (typically wedge or cone bodies are used). Next, the shape of the waverider in a given generating flowfield is described by its lower-surface base curve (LBC). The lower surface of the waverider is created by starting from the LBC and tracing the streamlines in the generating flowfield upstream until the shock wave is intersected (this indicates the leading edge of the waverider) [14, 15].

Finally, the shape of the upper surface of the waverider is arbitrary; typically this surface is created by tracing from the leading edge to the base plane in the free-stream direction. This creates an “idealized waverider,” which is simply a waverider with its upper-surface parallel to the free-stream. These ideas are summarized in Fig. 3.78.

### ***3.10.2 Osculating Cone Waveriders***

The osculating cone method is a third technique that has seen increased use recently; it basically combines the best features of both wedge and cone-generating flowfields. This method is essentially a “strip method” in which a cone flow solution is scaled locally over strips (i.e., osculating planes) of a specified shock profile curve (SPC) to create a non-axisymmetric three-dimensional shock wave (see Fig. 3.79) for a comparison of how waveriders can be created from both

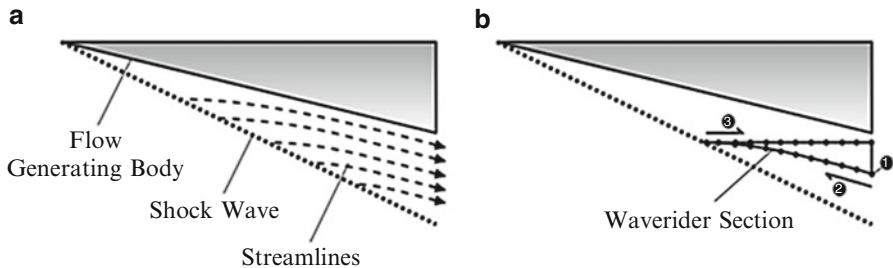


**Fig. 3.78** Waverider creation from a generating flowfield (e.g., axisymmetric cone flow). (1) Define LBC in generating flowfield base plane. (2) Trace streamlines to form lower surface. (3) Trace in free-stream direction from leading edge to create upper surface. (a) Generating flowfield. (b) Idealized waverider design

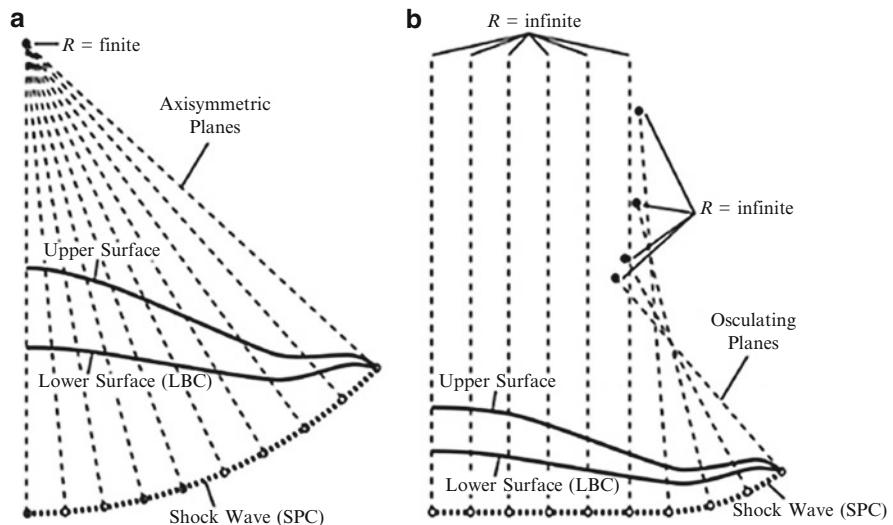
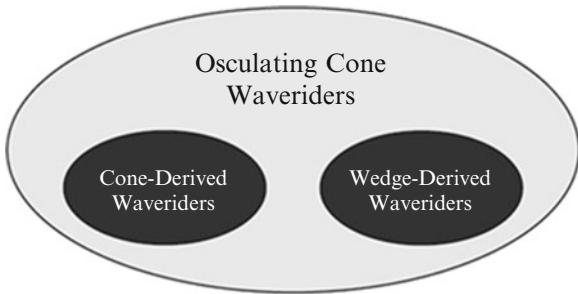


**Fig. 3.79** Axisymmetric cone and osculating cone flowfields (half-symmetric diagrams of base plane). (a) Axisymmetric cone flowfield. (b) Osculating cone flowfield

axisymmetric cone and osculating cone flowfields) [16–18]. The curvature of the shock wave determines the local cone radius and axis position (since the cone solution is applied in a plane normal to the shock curvature). A curvature of zero implies that the cone is infinitely large; in this case the flow conditions correspond to the region immediately after the cone shock wave – equivalent to the flow behind a two-dimensional oblique shock wave. Because only a single cone flow solution is required, the computational cost is minimal. These properties (i.e., ability to create both wedge and cone flow regions based on scaling the size of the osculating plane) indicate that the osculating cone method encompasses both wedge and cone-derived waveriders, as shown in Fig. 3.80.

**Fig. 3.80** Relationship between waveriders derived from osculating cone, axisymmetric cone, and wedge flowfields



The osculating cone method is a strip method, and therefore it makes the assumption of no cross-flow perpendicular to each osculating plane (i.e., this is a requirement due to the application of an axisymmetric cone flow solution to each osculating plane). This assumption is valid assuming that there is no pressure gradient in the azimuthal direction (i.e., between neighboring osculating planes); however this is not always the case due to the scaling of the cone flow solution for each osculating plane.

### 3.10.3 Wedge and Cone-Derived Waveriders

The simplest generating flowfield to use in waverider design is that of the supersonic or hypersonic flow past a two-dimensional wedge. If the shock wave angle  $\beta$  is specified, the flow turning angle  $\theta$  can be calculated using the analytical relations for an oblique shock wave:

$$\theta = \tan^{-1} \left[ 2 \cot \beta \frac{M_\infty^2 \sin^2 \beta - 1}{M_\infty^2 (\gamma + \cos 2\beta) + 1} \right] \quad (3.72)$$

where  $M_\infty$  is the free-stream Mach number before the shock wave and  $\gamma$  is the ratio of specific heats. The flow properties behind the shock wave (e.g., pressure, temperature, density) can be calculated by applying the normal shock relations to the normal components of the oblique shock wave.

Another common generating flowfield used to create waveriders is that of a cone in supersonic or hypersonic flow (see Fig. 3.81), which can be expressed analytically by the Taylor–MacColl equation (in spherical coordinates) [19]:

$$\left( 1 - \frac{v^2}{a^2} \right) \frac{d^2 u}{d\theta^2} + \cot \theta \frac{du}{d\theta} + \left( 2 - \frac{v^2}{a^2} \right) u = 0 \quad (3.73)$$

$$v = \frac{du}{d\theta}$$

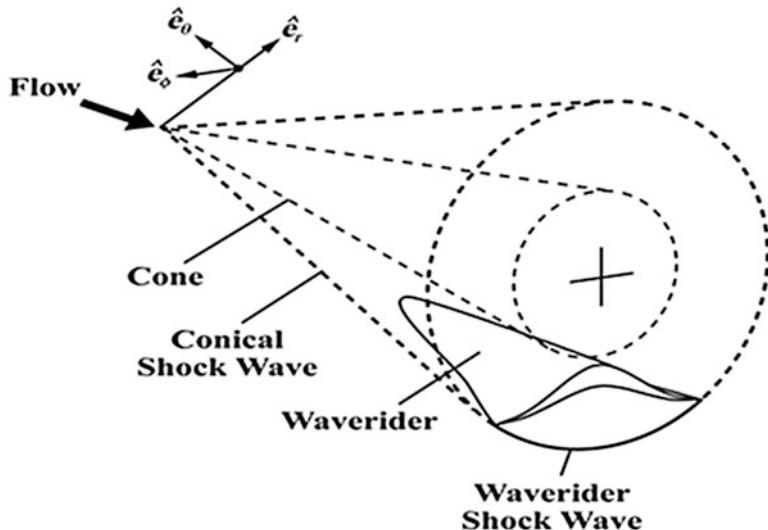


**Fig. 3.81** Spherical coordinate system used to generate waveriders from cone flowfields

where  $u$  and  $v$  are the flow velocities in the  $r$  and  $\theta$  directions, respectively, and  $a$  is the local speed of sound. Numerical integration of Eq. (3.73) is possible if adequate boundary conditions are supplied. A straightforward method is to supply the flow properties at the specified shock angle  $\beta$  and then to integrate Eq. (3.73) until the surface-normal velocity  $v$  is zero – this defines the surface of the cone.

The local speed of sound can be obtained by using the relation:

$$h_t = \text{constant} = \frac{a^2}{\gamma - 1} + \frac{u^2 + v^2}{2} \quad (3.74)$$

where  $h_t$  is the total enthalpy and is calculated initially from free-stream conditions.

When using wedge and cone flowfields to create waveriders, it can be noted that both types of generating flowfields tend to produce waveriders with specific characteristics. In particular, wedge-derived waveriders have the advantage of a two-dimensional lower-surface flowfield (due to the two-dimensionality of analytical wedge flow), which is advantageous for integration of a high-speed propulsion system. However, the planar nature of the shock wave requires a large anhedral angle and typically results in a relatively low-volume vehicle. Cone-derived waveriders, on the other hand, tend to have more of their volume concentrated near the vehicle center, which can increase the usable volume available to an aerospace configuration. Unfortunately, however, the axisymmetric cone flowfield implies that cone-derived waveriders will have a three-dimensional lower-surface flowfield, which is less desirable from an engine-integration standpoint [20].

### 3.11 Vehicle Aerodynamic Heating and Skin Temperature

Vehicle aeroheating (i.e., heat flux at wall) discussed so far focused attention only to flow temperature gradient at wall, being the *driving force* of heat-transfer rate. But, no attempt was done to what about the temperature related boundary condition to consider at vehicle solid wall. Thus, let us consider the energy balance for the vehicle's skin element shown in Fig. 3.82 [8].

Let us neglect conduction through the (end) surfaces perpendicular to the exposed surface.

This one-dimensional assumption implies that the changes in the flowfield and in the wall temperature in directions tangent to the vehicle surface are relatively small. Since the heat flux is one dimensional (in the negative  $y$ -direction), the flux per unit area can be used.

For the element at the surface of the thermal protection system (TPS),

$$\dot{q}_{\text{conv}} = \dot{q}_{\text{stored}} + \dot{q}_{\text{cond}} + \dot{q}_{\text{rad}} \quad (3.75)$$

where the incident convective heat flux is (see Chap. 2)

$$\dot{q}_{\text{conv}} = h_c \cdot (T_r - T_w) \quad (3.76)$$

where  $T_r$  is the recovery or adiabatic wall temperature.

The rate at which energy is stored in the element is

$$\dot{q}_{\text{stored}} = \rho_w c_w \Delta \frac{dT_w}{dt} \quad (3.77)$$

This storage term is zero for steady-state calculations (of course). The rate at which energy is conducted through the backface of the element is

$$\dot{q}_{\text{cond}} = k_w \frac{dT_w}{dy} \quad (3.78)$$

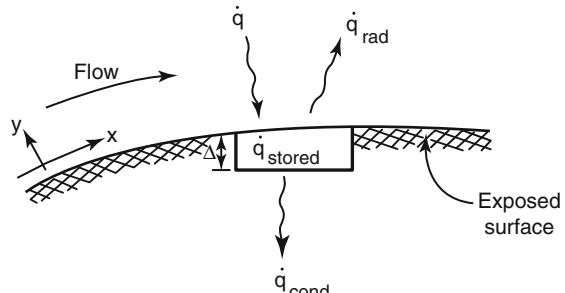


**Fig. 3.82** Energy balance for a surface element of the thermal protection system (TPS)

The rate at which energy is radiated from the exposed surface is

$$\dot{q}_{\text{rad}} = \sigma \varepsilon T_w^4 \quad (3.79)$$

where  $\sigma$  is the Stefan–Boltzmann constant ( $5.67 \times 10^{-8} \frac{W}{m^2 K^4}$ ) and  $\varepsilon$  is the surface emissivity ( $0 < \varepsilon < 1$ ). Therefore, energy equation at wall reads:

$$\dot{q}_{\text{conv}} = h_c \cdot (T_r - T_w) = \rho_w c_w \Delta \frac{dT_w}{dt} + k_w \frac{dT_w}{dy} + \sigma \varepsilon T_w^4 \quad (3.80)$$

Three types of thermal boundary conditions apply at the wall. Assume that the energy stored in the element is negligible ( $\dot{q}_{\text{stored}} \cong 0$ ).

*The wall temperature is prescribed.*

With  $T_w$  given, the incident convective heat flux,  $\dot{q}_{\text{conv}}$ , and the rate at which heat is radiated from the surface,  $\dot{q}_{\text{rad}}$ , are fixed. One can then use Eq. (3.80) to determine the rate at which heat is conducted through the backface of the element into the adjacent material:

$$k_w \frac{dT_w}{dy} = h \cdot (T_r - T_w) - \sigma \varepsilon T_w^4 \quad (3.81)$$

*The wall is assumed to be adiabatic, i.e.,  $\dot{q}_{\text{cond}} = 0$ .*

If  $\dot{q}_{\text{rad}}$  is significant, the wall temperature is determined from the energy flux balance:

$$T_w = \sqrt[4]{\frac{\dot{q}_{\text{conv}}}{\sigma \varepsilon}} \quad (3.82)$$

If  $\dot{q}_{\text{rad}}$  is negligible, the energy balance requires that

$$T_r = T_w \quad (3.83)$$

i.e., the wall temperature is equal to the recovery temperature (which is, therefore, also known as the adiabatic wall temperature). Note that for perfect gas,

$$\frac{T_r}{T_{\text{te}}} = r + \frac{1-r}{1 + \frac{\gamma-1}{2} M_e^2} \quad (3.84)$$

*The incident convective heat flux is prescribed,  $\bar{q}_{\text{conv}}$*

As a result, the wall temperature is determined from the energy-flux balance:

$$k_w \frac{dT_w}{dy} + \sigma \varepsilon T_w^4 + \bar{q}_{\text{conv}} = 0 \quad (3.85)$$

Thus, at supersonic speeds ( $M_\infty \cong 3$ ), the surface temperature is essentially the adiabatic wall temperature, as stated by Eq. (3.84).

At hypersonic speeds ( $M_\infty \cong 7$ ), however, the external surface temperatures generally will be  $0.3 \div 0.5$  of the adiabatic wall temperatures as a result of considerable radiative cooling and internal heat transfer. In particular, for hypersonic flight, the thermal design of the vehicle heat shield and the material selection depends on the convective heating rate. For instance, the convective peak heating determines the thermal protection material (TPM), while the integrated heat load suggests the TPS thickness.

Instrumentation placed on the Shuttle Orbiter provided valuable aerothermodynamic data during the re-entry phases of the first five flights of the Space Transportation System (STS), i.e., the Space Shuttle. Thermocouples, located approximately 0.38 mm beneath the surface coating of the tiles, provided temperature histories from which heating-rate histories were inferred. The incident convective heat flux was assumed to be equal to

$$\dot{q} = f \cdot \sigma \varepsilon T_w^4 \quad (3.86)$$

with  $f = 1.06$  as obtained using an inverse thermal math model to account for conduction into the tile and for the fact that the thermocouple was not on the external surface.

### Explanation Box. The Surface Temperature at the Stagnation Point of the Shuttle Orbiter

Let us determine the surface temperature at the stagnation point of the Shuttle Orbiter at the following conditions:

- (a)  $V_\infty = 7.20$  km/s,  $H_\infty = 75$  km altitude and  $\alpha = 40.0^\circ$  angle of attack (AoA).
- (b)  $V_\infty = 2.96$  km/s,  $H_\infty = 48$  km, and  $\alpha = 34.8^\circ$ .

Consider that the effective nose radius for the Shuttle Orbiter is 0.7196 m (although the effective nose radius for computing the stagnation-region flowfield would be a function of the AoA).

Let us use the energy balance represented by Eq. (3.80) to determine the surface temperature. Neglecting the energy stored in the element and incorporating the heat conducted out of the element into a factor such as was done in Eq. (3.86), the right-hand side of the equation becomes

$$\dot{q} \cong \sigma T_w^4$$

(continued)

Note that the product of the factor times the surface emissivity has been assumed equal to unity, which is a reasonable approximation for a surface whose emissivity is near unity.

For the stagnation-point heat-transfer rate, we will use Anderson relationship to account for a finite wall temperature.

Thus,

$$\begin{aligned}\dot{q}_0 &= 1.83 \times 10^{-4} \cdot \sqrt{\frac{\rho_\infty}{R_N}} \cdot \left(1 - \frac{H_w}{H_e}\right) \cdot V_\infty^3 \\ &= \sigma T_w^4 \quad \rightarrow \quad \sigma T_w^4 - 1.83 \times 10^{-4} \cdot \sqrt{\frac{\rho_\infty}{R_N}} \cdot \left(1 - \frac{H_w}{H_e}\right) \cdot V_\infty^3 = 0\end{aligned}$$

which must be solved for  $T_w$ .

Case (a)

Free-stream conditions at 75 km altitude are

$T_\infty = 208.40 \text{ K}$ ,  $P_\infty = 2.39 \text{ Pa}$ ,  $\rho_\infty = 3.99 \times 10^{-5} \text{ kg/m}^3$ , and  $a_\infty = 289.4 \text{ m/s}$ .

Thus,

$$M_\infty = \frac{V_\infty}{a_\infty} = \frac{7,200.0}{289.4} = 24.88$$

To calculate the factor  $\left(1 - \frac{H_w}{H_e}\right)$ , let us introduce the approximations:

$$H_e \cong \frac{1}{2} V_\infty^2 = 25.92 \times 10^6 \frac{\text{J}}{\text{kg}}$$

$$p_{t2} \cong \rho_\infty V_\infty^2 = 2,069.53 \text{ Pa} = 0.0204 \text{ atm}$$

The energy balance for these conditions is

$$9.58 \times 10^{12} \left(1 - \frac{H_w}{H_e}\right) = T_w^4$$

For the first iteration, neglect the correction for the wall enthalpy and solve for  $T_w$ .

$$T_w = 1,759 \text{ K}$$

(continued)

With  $T_w = 1,759$  K and  $p_{t2} = 0.02$  atm,

$$\frac{H_w}{H_e} = 0.076$$

Having obtained a value of  $H_w = 0.076 H_e$ , for the second iteration, we will use  $(1 - H_w/H_e) = 0.92$  and solve for  $T_w$ .

$$T_w = 1,723 \text{ K}$$

which is only slightly different than the value ( $T_w = 1,759$  K) obtained in the first iteration. For this value of  $T_w$ , the value of the wall enthalpy term is 0.92 (as assumed) and the iterative process is complete.

Case (b)

Free-stream conditions at 48 km altitude are  $\rho_\infty = 1.317 \times 10^{-3}$  kg/m<sup>3</sup> and  $a_\infty = 329.8$  m/s.

Thus,

$$M_\infty = \frac{V_\infty}{a_\infty} = \frac{2,960.0}{329.8} = 8.97$$

Using the approximations for the stagnation conditions downstream of the normal-shock wave,

$$H_e \cong \frac{1}{2} V_\infty^2 = 4.38 \times 10^6 \frac{\text{J}}{\text{Kg}}$$

$$p_{t2} \cong \rho_\infty V_\infty^2 = 11,539.02 \text{ Pa} = 0.1139 \text{ atm}$$

The energy balance for these conditions is

$$3.35 \times 10^{12} \left( 1 - \frac{H_w}{H_e} \right) = T_w^4$$

For the first iteration, neglect the correction for wall enthalpy. Thus,  $T_w \cong 1,352$  K. With  $T_w = 1,352$  K and  $P_{t2} = 0.1139$  atm,  $H_w/H_e = 0.356$ .

For the second iteration, assume  $(1 - H_w/H_e) = (1 - 0.3) = 0.70$ .

As a result,  $T_w = 1,237$  K. With  $T_w = 1,237$  K and  $p_{t2} = 0.1139$  atm,  $H_w/H_e = 0.305$ , which is very close to the value assumed at the start of the iteration. Thus, we have obtained the wall temperature.

Note that  $(1 - H_w/H_e)$  is 0.92 for the conditions of part (a) and is 0.70 for the conditions of part (b).

### 3.11.1 Convective Heat Transfer and the Eckert's Reference Temperature Method

Solutions of the boundary layer, subject to the appropriate boundary conditions, will provide the temperature, the velocity, and the gas-component distributions adjacent to the surface from which one can determine the convective heat-transfer rate and the skin friction.

Techniques of various rigor can be used to generate distributions for the convective heat transfer and for the skin friction.

As discussed so far, these techniques include relatively simple correlations, analytical solutions based on similarity transformations, boundary-layer solutions as part of a two-layer flowfield model, and the viscous region of a single-layer flowfield model.

Regardless of which technique is used, one must model the physical phenomena characteristic of the boundary layer in its various states: laminar, transitional, or fully turbulent.

In the 1950s and early 1960s, there were numerous attempts to develop correlations which would approximate the results from numerical solutions of the boundary layer. One of the most recognized of these correlations is the Eckert reference temperature (or reference enthalpy) approach.

In this approach, the heat-transfer rates are calculated using the relations developed for incompressible flows with the temperature-related parameters evaluated at Eckert's reference temperature,  $T^*$ :

$$T^* = \frac{1}{2} (T_e + T_w) + 0.22r (T_{te} - T_e) \quad (3.87)$$

where  $T_e$  is the temperature at edge of boundary layer,  $T_w$  is the wall temperature, and  $T_{te}$  is the total temperature at edge of boundary layer.

For the reference enthalpy method,

$$h^* = \frac{1}{2} (h_e + h_w) + 0.22 (h_r - h_e) \quad (3.88)$$

To calculate the corresponding skin friction, Reynolds analogy is used to relate the skin friction to the convective heat-transfer rate (see Chap. 2).

The Eckert reference-enthalpy technique was used in the calculation of the heating environment for the design of the Space Shuttle Orbiter. For example, Fig. 3.83 shows that aft of the 20 % body length station ( $x/L = 0.2$ ), Eckert's flat plate reference enthalpy method allowed to predict the laminar flow heating [8]. Streamline divergence and cross-flow effects were taken into account by calibration factors which represent the ratio of wind-tunnel data to the theoretical calculations. Scaling to flight was accomplished by applying the calibration factors to the theoretical calculations adjusted for real-gas conditions.

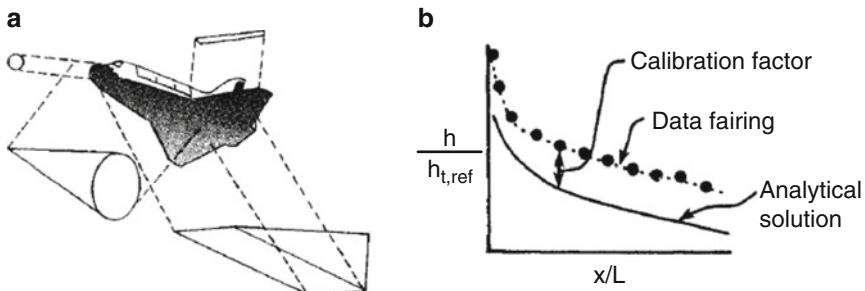


**Fig. 3.83** Design methodology for the windward (lower) surface of the Orbiter. **(a)** Representative flow models. **(b)** Fuselage lower centerline

Indeed, for the windward (or lower) surface of the Orbiter, the empirical correlations complemented by analytical techniques were developed as follows. As shown in Fig. 3.83a, the Orbiter (or, in general, a typical winged re-entry vehicle) can be divided into a combination of simple shapes, i.e., spheres for the nose, swept cylinders for the wing/tail leading edges, cones for the forebody fuselage, flat plates for the lower side of the aft fuselage, and wedges for the wing windside, for which analytical solutions are available. For example, the wing leading edge was represented by a swept cylinder in order to obtain estimates for the leading-edge heating rates (outside of the shock/shock interaction region).

The heating to the windward fuselage was calculated using the standard Eckert reference enthalpy flat plate solutions, designated *Analytical solution* in Fig. 3.83b. Because the flow over the simple shape is only a crude approximation of the actual flow, there are significant differences in edge flow properties and in streamline patterns, which produce significant differences between the theoretical heat transfer and that measured in the wind tunnel on the Orbiter model. Adjustments, designated *Calibration factor* in Fig. 3.83b, were used to take into account such variations as streamline divergence and flow running lengths. When the analytical solutions for the simple geometric shapes are multiplied by position-dependent calibration factors, one can match the wind-tunnel measurements, designated data fairing in Fig. 3.83b.

These calibration factors, developed both for laminar and for turbulent boundary layers, were held constant in extrapolations to flight conditions. For the upper (or leeward) surface, the wind-tunnel data were nondimensionalized as the ratio of the local heat-transfer coefficient divided by a reference, stagnation-point heat transfer, i.e.,  $(h/h_{t,\text{ref}})_{\text{wt}}$ .

Using correlations of this dimensionless heat-transfer ratio as a function of angle of attack, of angle of sideslip (yaw), of the free-stream Mach number, and of the free-stream Reynolds number, the wind-tunnel data were applied directly to flight.

The uncertainties inherent in extrapolating wind-tunnel heat-transfer data to flight conditions, including wind-tunnel data scatter, scaling to flight, uncertainty

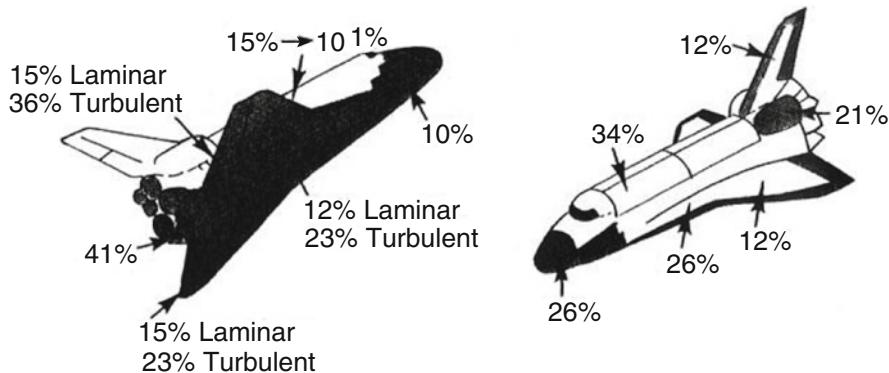


**Fig. 3.84** Uncertainties in preflight heating estimates for the Shuttle Orbiter based on empirical correlations complemented by analytical solutions

in local flow properties, and extrapolating data from regions where multiple shock waves interact with the boundary layer, force the introduction of conservatism into the estimates of the heating environment prior to the first flight. Estimates of the heating uncertainties are reproduced in Fig. 3.84 [8].

The magnitude of these uncertainties may seem large, but the determination of the heat-transfer rates represents a severe challenge both to the experimentalist and to the analyst.

#### Explanation Box. The Eckert's Reference Temperature Method and Cone Aeroheating

Figure 3.83a illustrates that the Shuttle forebody was represented by a sharp cone. So, let us calculate the heat transfer along a sharp cone ( $\delta_c = 15^\circ$ ) exposed to a wind tunnel's hypersonic stream of air where  $M_\infty = 10.6$ ,  $P_{t1} = 8.27 \text{ MPa}$ , and  $T_t = 1,100 \text{ K}$ . Assume that the air behaves as a perfect gas ( $Pr = 0.71$ ) and  $T_w = 310 \text{ K}$ .

First calculate the free-stream static properties in the test section.

For  $M_\infty = 10.6$ ,

*Static pressure*

$$\frac{p_{t1}}{p_1} = \left(1 + \frac{\gamma - 1}{2} M_1^2\right)^{\frac{\gamma}{\gamma-1}} = \left[1 + 0.2 \cdot (10.6)^2\right]^{3.5}$$

$$= 62650.61 \quad \rightarrow \quad p_1 = \frac{8.27 \times 10^6}{62,650.61} = 132.02 \text{ Pa}$$

(continued)

*Static temperature*

$$\begin{aligned}\frac{T_{t1}}{T_1} &= \left(1 + \frac{\gamma - 1}{2} M_1^2\right) = 1 + 0.2 \cdot (10.6)^2 \\ &= 23.47 \quad \rightarrow \quad T_1 = \frac{1,100}{23.47} = 46.87 \text{ K}\end{aligned}$$

*Density*

$$\rho_1 = \frac{p_1}{RT_1} = \frac{132.02}{288.28 \cdot 46.87} = 9.77 \times 10^{-3} \frac{\text{Kg}}{\text{m}^3}$$

The heat-transfer reads:

$$\dot{q}_w = St \rho_e u_e (H_r - H_w) = St \rho_e u_e c_p (T_r - T_w)$$

and exploiting the Eckert's method

$$\dot{q}_w = \rho^* u_e c_p (T_r - T_w) St$$

where  $\rho^*$  depends on Eckert's reference temperature, i.e.,  $\rho^* = \rho^*(T^*)$ .

So, let us determine  $\rho^*$ ,  $u_e$ ,  $T_r$  and  $St$ :

$$\rho^* = \frac{p_e}{R T^*}$$

where

$$T^* = \frac{1}{2} (T_e + T_w) + 0.22r (T_{te} - T_e)$$

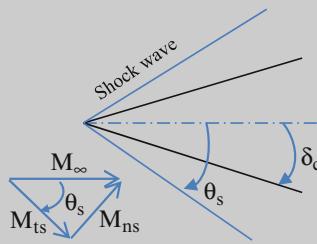
and

$$\frac{T_{te}}{T_e} = 1 + \frac{\gamma - 1}{2} M_e^2$$

From tangent cone method one is able to estimate the Mach number and pressure coefficient expected at the edge of boundary layer,  $M_e$  and  $C_{pe}$ , respectively.

(continued)

Thus,



$$M_{ns} = \frac{M_{\infty} \sin \delta_c}{(1 - \varepsilon) \cos (\theta_s - \delta_c)}$$

and

$$M_e = M_{ts} = \sqrt{M_{\infty}^2 - M_{ns}^2}$$

But for rapid calculation a relationship for  $M_{ns}$  as function of  $M_{\infty} \sin \delta_c$  only<sup>11</sup> that satisfy the following requirements:

1. The effect of shock detachment is neglected;
2. At  $M_{\infty} \sin \delta_c = 0 \rightarrow M_{ns} = 1$ ;
3. The solution asymptotically approaches  $M = \infty$  line;
4. Have the correct slope,  $\frac{dM_{ns}}{d(M_{\infty} \sin \delta_c)}$  at  $M_{\infty} \sin \delta_c = 0$ .

is:

$$M_{ns} = \frac{\gamma + 1}{2} M_{\infty} \sin \delta_c + e^{-2(\frac{\gamma+1}{\gamma+3}) M_{\infty} \sin \delta_c}$$

The pressure coefficient may now be determined by the following relationship

$$C_p = 2 \sin^2 \delta_c \left[ 1 - \frac{(\gamma - 1) M_{ns}^2 + 2}{4(\gamma + 1) M_{ns}^2} \right]^{-1}$$

Thus,  $M_e = 5.85$  and  $C_{pe} = 0.143$ :

---

<sup>11</sup>In this way one avoids to evaluate the shock angle  $\theta_s$ .

(continued)

$$\frac{T_{te}}{T_e} = 1 + \frac{\gamma - 1}{2} M_e^2 = 1 + 0.2(5.85)^2 = 7.84$$

$$\rightarrow T_e = 0.127 \cdot T_{te} = 0.127 \cdot 1,100 = 140.23 \text{ K}$$

The recovery factor,  $r$ , is

$$\text{for laminar flow } r = \sqrt{\text{Pr}} = \sqrt{0.71} = 0.843$$

$$\text{for turbulent flow } r = \sqrt[3]{\text{Pr}} = \sqrt[3]{0.71} = 0.892$$

Therefore,

$$T^* = \frac{1}{2} (T_e + T_w) + 0.22r (T_{te} - T_e) =$$

$$= \frac{1}{2} \cdot (140.23 + 310) + 0.22 \cdot 0.843 \cdot (1,100 - 140.23) = 403.11 \text{ K}$$

Let us calculate  $p_e$ :

$$C_{pe} = \frac{p_e - p_\infty}{q_\infty} \rightarrow p_e = p_\infty + C_{pe} q_\infty \rightarrow \frac{p_e}{p_\infty} = 1 + \frac{q_\infty}{p_\infty} C_{pe}$$

$$= 1 + \frac{\gamma M_\infty^2}{2} C_{pe}$$

So,

$$p_e = p_\infty \left( 1 + \frac{\gamma M_\infty^2}{2} C_{pe} \right) = 132.02 \cdot \left[ 1 + \frac{1.4 \cdot (10.6)^2}{2} \cdot 0.143 \right]$$

$$= 1,616.88 \text{ Pa}$$

Thus,

$$\rho^* = \frac{p_e}{R T^*} = \frac{1,616.88}{288.28 \cdot 403.11} = 1.39 \times 10^{-2} \frac{\text{Kg}}{\text{m}^3}$$

The velocity at the edge of boundary layer reads:

$$u_e = M_e \cdot \sqrt{\gamma R T_e} = 5.85 \cdot \sqrt{1.4 \cdot 288.28 \cdot 140.23} = 1,391.71 \frac{\text{m}}{\text{s}}$$

Using Sutherland's equation to calculate the viscosity and thermal conductivity,

(continued)

$$\begin{aligned}\mu^* &= 1.458 \times 10^{-6} \frac{(T^*)^{\frac{3}{2}}}{T^* + 110.4} = 1.458 \times 10^{-6} \frac{(403.11)^{1.5}}{403.11 + 110.4} \\ &= 2.29 \times 10^{-5} \text{ Pa} \cdot \text{s} \\ k^* &= 1.993 \times 10^{-3} \frac{(T^*)^{\frac{3}{2}}}{T^* + 112} = 1.993 \times 10^{-3} \frac{(403.11)^{1.5}}{403.11 + 112} \\ &= 3.13 \times 10^{-2} \frac{\text{W}}{\text{mK}}\end{aligned}$$

The Stanton number,  $St$ , is evaluated according to the modified Reynolds analogy:

$$St = \frac{0.332}{(\Pr^*)^{\frac{2}{3}} \cdot (Re_x^*)^{\frac{1}{2}}}$$

where

$$\begin{aligned}\Pr^* &= \frac{\mu^* c_p}{k^*} = \frac{2.29 \times 10^{-5} \cdot 1,009.10}{3.13 \times 10^{-2}} = 0.74 \\ Re_x^* &= \frac{\rho^* u_e x}{\mu^*} = \frac{1.39 \times 10^{-2} \cdot 1,391.71 \cdot x}{2.29 \times 10^{-5}} = 8.45 \times 10^5 x\end{aligned}$$

Thus,

$$St = \frac{0.332}{(0.74)^{0.667} \cdot (8.45 \times 10^5 \cdot x)^{0.5}} = \frac{4.41 \times 10^{-4}}{\sqrt{x}}$$

Finally, the recovery temperature reads:

$$T_r = T_e + r(T_{te} - T_e) = 140.23 + 0.843 \cdot (1,100 - 140.23) = 949.32 \text{ K}$$

Thus,

$$\begin{aligned}\dot{q}_w &= \rho^* u_e c_p (T_r - T_w) St \\ &= 1.39 \times 10^{-2} \cdot 1391.71 \cdot 1009.10 \cdot (949.32 - 310) \cdot \frac{4.92 \times 10^{-4}}{\sqrt{x}} = \\ &= \frac{6.14}{\sqrt{x}} \left[ \frac{\text{kW}}{\text{m}^2} \right]\end{aligned}$$

where  $x$  is the distance from the apex along a conical generator.

### 3.11.2 The Eckert's Reference Temperature Method and Flat Plate Aeroheating

Figure 3.83a illustrates that the Shuttle (or in general any lifting vehicle) lower surface can be approximated as a flat plate at the angle of attack,  $\alpha$ .

So, let us calculate the heat transfer along a flat plate exposed to a hypersonic stream of air with incidence  $\alpha$  (of course, in the case of a wedge, this angle is the sum of the angle of incidence and the wedge semi-aperture angle).

From Reynolds analogy, discussed in Chap. 2, it follows that the heat-transfer rate reads:

$$\dot{q}_w = A(\rho_e u_e)^{1-n} \left( \frac{\mu_e}{x} \right)^n (H_r - H_w) \quad (3.89)$$

So, by evaluating all properties at an enthalpy of  $h^*$ , we get

$$\dot{q}_w = A(\rho^* u_e)^{1-n} \left( \frac{\mu^*}{x} \right)^n (H_r - H_w) \quad (3.90)$$

where

$$\begin{aligned} \rho^* &= \frac{c_p p_e}{R h^*} \\ \mu^* &= C_\mu \sqrt{h^*} \\ p_e &\cong \rho_\infty V_\infty^2 \sin^2 \alpha \\ \frac{u_e}{V_\infty} &\cong \cos \alpha \end{aligned}$$

Thus,

$$\begin{aligned} \frac{\dot{q}_w(\alpha)}{\dot{q}_{\text{ref}}} &= \left( \frac{\rho^* u_e}{\rho_{\text{ref}}^* u_{\text{ref}}} \right)^{1-n} \left( \frac{h^*}{h_{\text{ref}}} \right)^{\frac{n}{2}} = \left( \frac{p}{p_{\text{ref}}} \right)^{1-n} \left( \frac{h^*}{h_{\text{ref}}} \right)^{\frac{3(n-1)}{2}} \left( \frac{u_e}{u_{\text{ref}}} \right)^{1-n} \\ &= (\sin^2 \alpha \cos \alpha)^{1-n} \end{aligned} \quad (3.91)$$

since

$$\left( \frac{h^*}{h_{\text{ref}}} \right)^{\frac{3(n-1)}{2}} \approx 1$$

This relationship is inserted into the heating equation to produce the lower-surface heating relationship:

$$\dot{q}_{w,\text{flat plate}} = \frac{K}{x^n} \left( \frac{V_\infty}{1,000} \right)^3 \left( 1 - \frac{H_w}{H_s} \right) (\rho_\infty \sin^2 \alpha \cos \alpha)^{1-n} \left[ \frac{\text{kW}}{\text{m}^2} \right] \quad (3.92)$$

where  $n = 0.5$  and  $K = 137.214$  for laminar flow and  $n = 0.2$  and  $K = 4,7854.8$  for turbulent flow

### 3.11.3 Thermal Protection Techniques

The design and analysis of an entry vehicle and flight profile to meet the thermal protection requirement is a multidiscipline task involving aerodynamics chemistry, flight mechanics, structural analysis, and materials science. Three basic approaches to entry vehicle thermal control have evolved: *heat sinking, radiative cooling, and ablative shielding*.

The heat sink technique, as the name implies, uses a large mass of material with a high melting point and high heat capacity to absorb the entry heat load.

The initial Mercury spacecraft design utilized this approach, employing a beryllium blunt body heat shield. This design was used on the unmanned tests and on the first manned Mercury-Redstone suborbital flights. However, the increased system weight for protection against the order-of-magnitude higher orbital entry heat load forced the use of an ablative shield on the subsequent orbital missions. The second manned suborbital mission tested the ablative heat shield. This weight penalty is a typical and important limitation of the heat sink approach to entry thermal control.

The principle of radiative cooling is to allow the outer skin of the vehicle to become, literally, red hot due to the convectively transferred heat from the flowfield around the vehicle. Blackbody radiation, primarily in the infrared portion of the spectrum, then transports energy from the vehicle to the surrounding atmosphere. Convective heating to the vehicle is proportional to the temperature difference between the fluid and the wall (see Eq. 3.76), whereas the energy radiated away is in proportion to the difference in the fourth powers of the fluid and wall temperatures (see Eq. 3.79). The net result is that thermal equilibrium can be reached at a relatively modest skin temperature provided that the rate of heating is kept low enough to maintain near-equilibrium conditions.

Radiative cooling obviously requires excellent insulation between the intensely hot outer shell and the internal vehicle payload and structure. This is exactly the purpose of the shuttle tiles, the main element of the shuttle thermal protection system. Essentially a porous matrix of silica (quartz) fibers, these tiles have such low thermal conductivity that they can literally be held in the hand on one side and heated with a blowtorch on the other.

As stated, radiative cooling relies on equilibrium, or near equilibrium, between the entry vehicle and its surroundings to shed the absorbed heat load. This is most easily achieved in a lengthy, high-altitude gliding entry where the instantaneous heating rate is minimized as the speed is slowly reduced. The vehicle aerodynamic design (ballistic coefficient and L/D), the entry flight trajectory, and the heat shield material selection are intimately related when radiative cooling is used. This complicates the design problem. However, significant mass savings are possible when a system-level approach is taken.

A potential problem with an insulated, radiatively cooled vehicle having a lengthy flight time is that ultimately some heat will soak through to the underlying structure. Coolant fluid may thus need to be circulated through the vehicle so that this energy can be radiated away to a portion of the surroundings, such as the aft region, which is cooler. This can occur even if the flight time is sufficiently short that in-flight cooling is not required. Such is the case with the shuttle, which must be connected to cooling lines from ground support equipment if postflight damage to the aluminum structure is to be prevented.

Although heat sinking is best suited to a brief, high-drag entry and radiative cooling is more appropriate for a gliding trajectory, ablative cooling offers considerably more flexibility in the flight profile definition. Ablative cooling is also typically the least massive approach to entry heat protection. These advantages accrue at the expense of vehicle (or at least heat shield) reusability, which is a pronounced benefit of the other techniques.

Ablative cooling occurs when the heat shield material, commonly a fiber glass resin matrix, sublimes under the entry heat load. When the sublimed material is swept away in the flowfield, the vehicle is cooled. This process can produce well over 107 J/kg of effective energy removal. Ablative cooling has been the method of choice for most entry vehicles, including the manned Mercury, Gemini, and Apollo vehicles.

## 3.12 A Look to the Computational Fluid Dynamics Effort During Design

So far entry vehicle aeroshape has been generally defined by simple laws and can be accomplished with relatively simple tool set which is adequate in the very early project stages.

This may be designated the *level one* analysis, using:

- 3 dof and/or 6 dof trajectory codes with planetary atmosphere models
- Newtonian aerodynamic code to quickly assess vehicle aerodynamic performance and/or interpolate existing aerodynamic databases
- Free molecular aerodynamic code and suitable empirical bridging functions for lift, drag, and pitching moment coefficients
- Correlations for convective and radiative heat fluxes
- Heat-shield sizing algorithms

However, in all but the trajectory codes, detailed knowledge is required to develop or confirm the basis of the engineering-based solutions. For example, for an exploration vehicle, it is very important the determination of accurate aerodynamic coefficients<sup>12</sup>, while stability is always a consideration whatever the mission. Hence, vehicle aerodynamic performance (both free molecular and continuum aerodynamic coefficients with a suitable bridging function<sup>13</sup>) and planetary atmosphere constants (e.g., planetary radius, atmosphere scale height, and surface level density) allow assessing the descent flight path.

Once entry trajectory is available, vehicle aerothermal environment can be estimated, thus assessing the aerodynamic and aerothermal flight regimes through which the vehicle will pass. This will also give the engineer a clear perception of where in the entry particular analysis methods should be used. Hence, the heat flux distribution and history determine the choice of TPS and geometric ratios, and so on.

This level one analysis, however, is not enough to guarantee the mission accomplishment. Indeed, design analysis should consolidate the classical regimes and should investigate the thermal and chemical regimes in more detail.<sup>14</sup> To carry out this investigation, a chemically reacting shock layer simulation is most useful, and since the whole entry parameters space needs to be investigated, the method should be fast. In this respect a loosely coupled suite consisting of an Euler code with frozen or equilibrium chemistry assumptions may be employed. Hence, boundary-layer edge conditions are taken as a post process of the Euler solutions for convective heat flux analysis using usually an integral code. Radiation calculations are also performed from the shock layer results as a post process. The radiation source terms can also be fed back to the Euler solution, as can boundary-layer thickness. However, for regime scoping studies, an uncoupled procedure is usually sufficient. Wall conditions can be accommodated in the boundary-layer solution in a simple manner, blowing is accommodated with a correlation within the integral boundary-layer code, while for the frozen boundary-layer solution, a catalytic wall can be introduced by substituting the wall enthalpy for equilibrium wall enthalpy at the same temperature.

Usually, parametric investigations using these methods are carried out to varying degrees in the early design stages of a space mission. In general, the results are acceptably accurate excepting radiation in highly nonequilibrium flow at present. Such a suite also allows rapid comparison of the sensitivity of differing thermochemical mechanisms and allows rapid construction of a viable set prior to more complex computations. These *level two* results can be used to calibrate the engineering correlations in the level one analysis. The level two codes are, therefore:

---

<sup>12</sup>For instance, this design issue is fundamental for an exploration vehicle since the atmosphere composition is generally determined from the vehicle performance.

<sup>13</sup>A simple Knudsen based bridge is most common for lift, drag, and pitching moment coefficients.

<sup>14</sup>Most commonly thermochemical regimes are classified in terms of the Damkohler number, Da.

1. Fast inviscid shock layer solution
2. Loosely coupled chemistry solution
3. Boundary-layer codes
4. Uncoupled or loosely coupled slab radiative solution
5. Charring material ablation code

Once the thermochemical data has been assembled and tested with the level two codes, and the results validated as far as practicable, a more sophisticated analysis again must be carried out to verify the simpler results in areas beyond the validation (here verification is defined as being correct numerical implementation of the physics and chemistry, while validation is the comparison of the models with the real world). For continuum regimes this verification is by a full or thin layer thermochemical nonequilibrium Navier–Stokes solution. Due to the lack of other suitable methodologies, the Navier–Stokes codes are used well into the transitional regime, and account can be taken of slip effects.

Direct Simulation Monte Carlo method should be used to confirm bridging functions between continuum and free molecular flow conditions.

So, the *level three* codes are:

1. Thermochemical nonequilibrium Navier–Stokes simulations for laminar, transitional, and turbulent flow conditions
2. Direct simulation Monte Carlo with suitable chemistry and radiation models
3. Full 2-D nonequilibrium radiation code

The level three codes are used sparingly in the early stages due to the costs involved but must be used in development phases to confirm design viability, while experiments provide validation data for these codes.

Further, these codes are often the only way to investigate the entry phenomena where no flight data are available and ground tests are impractical.

In conclusion, this three-level design approach is time and cost efficient for vehicle design studies. However, level one codes are readily available but require careful calibration.

Level two codes have been widely developed in the past and are still very useful.

Level three codes can simulate many situations, but the required level of expertise and time needed for use must not be underestimated.

### 3.12.1 Flow Physics

In the framework of the three-level design approach, flow physics plays a fundamental role in assessing the aerothermal environment expected by the entry vehicle.

Flow physics depends, of course, on the considered atmosphere, provided that major differences exist between the atmospheres of celestial bodies in our Solar System.

The atmospheric composition of Earth is fairly well known.

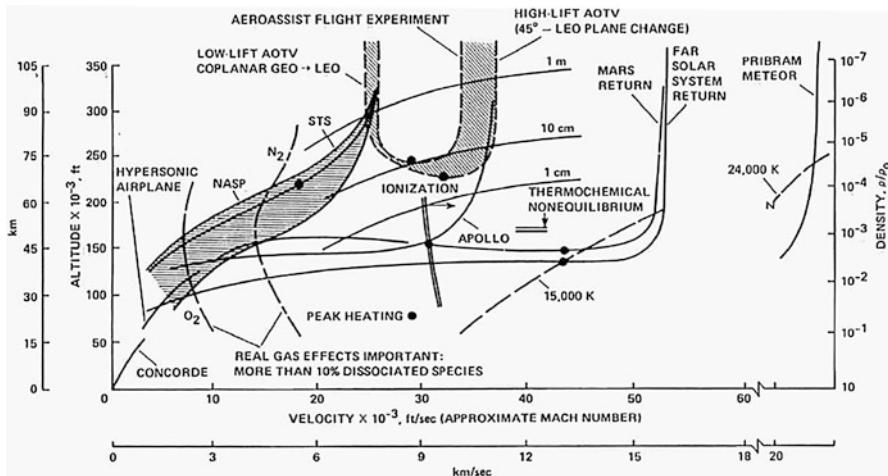


Fig. 3.85 Comparison of vehicle flight regimes in Earth's atmosphere

The atmosphere of Mars, which consists primarily of Carbon dioxide at a relatively low barometric pressure, is also fairly well defined, although there are observed seasonal variations. Carbon dioxide is a triatomic gas and exhibits substantially different radiative characteristics than observed in air. Also, the Martian atmosphere is subject to major dust storms that can significantly affect the aerothermal environment about a vehicle.

The atmospheres of the major planets are comprised primarily of Helium and Hydrogen which are not strong radiators.

Considering only Earth entry missions, a variety of flight environments can be identified. Indeed, Fig. 3.85 provides typical flight regimes experienced by several re-entry vehicles [8].

For example, the direct entry Apollo trajectory is seen to pass rapidly through the high-altitude regime where ionization effects may be important. The spacecraft experiences the bulk of its deceleration and, hence, aerothermal heating in the lower atmosphere (about 45 km altitude) where the flow is continuum and radiation from the bow shock layer is in equilibrium.

A reusable aeroassisted space transfer vehicle (ASTV), undergoing an aeropass maneuver, has its trajectory in the upper atmosphere where the gas is less dense and nonequilibrium processes, including radiation, are important.

A vehicle returning from Mars, or the far Solar System, on the other hand, flies a significant part of its trajectory in the lower altitude (about 50–65 km) where the shock layer gas, while in equilibrium, is highly ionized. Peak heating is expected to occur in this regime as the high kinetic energy of the vehicle (i.e., super-orbital entry) is being converted to thermal energy.

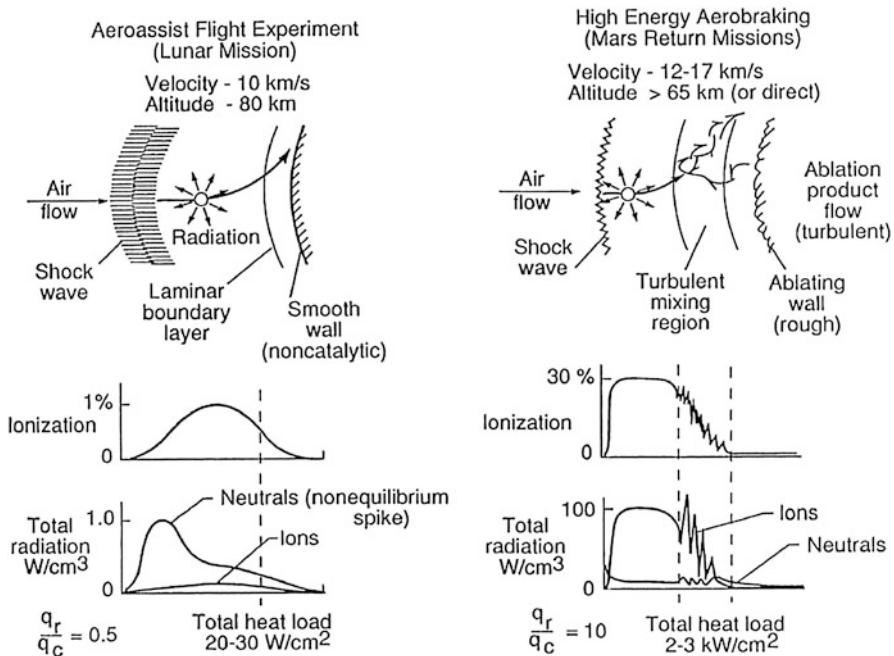


Fig. 3.86 Comparison of low-energy and high-energy re-entry shock layer flow physics

A schematic which illustrates the difference in shock layer physics between an ASTV cislunar mission and a Mars return mission is shown in Fig. 3.86 [7].

Here, a typical ASTV entry speed of a lunar mission is about 10 km/s at an altitude of 80 km.

The gas is heated as it passes through the bow shock, and at that altitude, the density is low enough that the shock layer is essentially in thermochemical nonequilibrium and the boundary layer is laminar. Ionization levels will be small, (<1 %) and the radiation from the shock heated gas cap will be nonequilibrium and will provide a heat flux to the surface comparable to the convective heat load.

On the other hand, a capsule on return from Mars will be characterized by a speed greater than 12 km/s at an altitude of about 65 km. Here, the gas behind the bow shock will be essentially in equilibrium as will the gas cap radiation. Further, at the high kinetic energy associated with the higher speed entry, there will be substantial levels of ionization (up to 30 %). Radiative heating will be quite high and will dominate the total heating to the spacecraft. Therefore, ablative heat shields will be required to accommodate the high radiative heat loads and will, in turn, create a highly turbulent flow near a rough ablating surface. The ablation products will affect the gas composition near the capsule surface and in the wake.

A table has been assembled, Table 3.3, which, in a qualitative sense, characterized some of the important capsule aerobraking parameters and essential flow physics for typical cislunar and Mars missions [7]. Included is a recently considered ASTV flight experiment, AFE (Aeroassist Flight Experiment), direct entry lunar return, unmanned Mars return (reusable), manned Mars return (expendable capsule), unmanned Mars aerocapture, and manned Mars aerocapture.

Listed aerobraking parameters and flow features include entry speed, altitude at maximum deceleration which corresponds closely with peak heating, stagnation pressure, convective and radiative peak heating, required TPS, shock layer ionization level, fraction of shock layer thickness in nonequilibrium state, and boundary-layer character. Also identified are important physical issues such as radiation/ablation interaction, wall catalysis, and boundary-layer transition. It can be seen from this table that the gamut of physical phenomena associated with capsule aerothermodynamics is quite large and that the only viable means to reduce analysis requirements and optimize designs using the most refined CFD tools is to consider problems on a mission basis.

As discussed early, the character of a real gas is described by the internal degrees of freedom and state of constituent molecules: nitrogen and oxygen for air. The internal energy states, rotation, vibration, and electronic, of the molecules are excited, and, in the limit, the molecular bonds are exceeded and the gas dissociated into atomic and, possibly, ionic constituents.

The process of energy transfer causing excitation, dissociation, and recombination is a rate process controlled by particle collisions.<sup>15</sup>

Binary, two-body, collisions are sufficient to cause internal excitation, dissociation, and ionization, while three-body collisions are required to recombine the particles into molecular constituents.

Each of the definitive states of a real gas, equilibrium, frozen, reacting, can be applied to a gas undergoing compression and heating, such as the gas flowing through a strong shock ahead of a bluff body, or to an expanding and cooling gas, such as a gas flowing away from a stagnation region of a bluff body or a gas expanding into a base region. In the first case the gas will be thermally excited and dissociate and ionize; in the second, the atomic constituents will recombine and internal energy states will relax to lower energy levels. A real gas implies the existence of any, or all, of the above states. This includes the possibility that a real gas can look identical to a perfect gas or a chemically frozen gas.

---

<sup>15</sup>That is why at high altitude, the flowfield is in thermochemical nonequilibrium flow conditions.

**Table 3.3** Aerobraking parameters for space exploration missions

Mission	AFFE	Lunar return	Mars return reusable	Mars return capsule	Mars entry unmanned	Mars entry manned
Entry speed (km/s)	10	11	13	14	6–8	7–9
Deceleration altitude (km)	75	75	66	65	40	40
Stagnation pressure (atm)	0.03	0.05	0.20	0.30	0.1–0.15	0.1–0.2
Peak heating (Conv/Rad) (w/cm <sup>2</sup> )	40/7	50/30	150/500	500/900	100/10	100/10 (L/D = 1) 30/50 (L/D = .3)
Thermal protection system	Reflective	Reflective or ablating	Ablating	Ablating	Reflective or ablating	Reflective or ablating
% ionization	0.5–1	5–10	15	25	0–1	0–2
Nonequilibrium standoff %	0.4	0.2	0.2	0.1	Large	Large
Boundary-layer character	Laminar	Laminar	Turbulent	Lam/turb	Turbulent	Turbulent
<i>Important physics</i>						
Radiation/ablation interaction	None	Small	Large	Large	Small	Small
Wall catalysis	Yes	Yes	No	No	Yes	Yes
Boundary-layer transition	No	No	Yes	Yes	Yes	Yes

 **Explanation Box. Real Gas Flow Physics for Blunt Body Capsules**

Real gas flow physics for capsule re-entry vehicles influences forebody, lee, and base flowfield past the vehicle. For instance, real gas thermochemical nonequilibrium processes are important in the determination of aerodynamic heating: both convective (including wall catalytic effects) and radiative heating. In this framework, let us consider the hypervelocity flow over a bluff body typical of an atmospheric entry vehicle or an aerospace transfer vehicle.

Let us qualitatively discuss aspects of a hypersonic flowfield over a bluff body with attention to which particular physical effects must be included in a CFD analysis. This will also indicate what type of numerical modeling will be adequate in each region of the flowfield.

*Forebody Flowfield*

A bluff forebody flowfield, illustrated schematically in Fig. 3.87, is dominated by the presence of a strong bow shock wave and the consequent heating and chemical reaction of the gas [7].

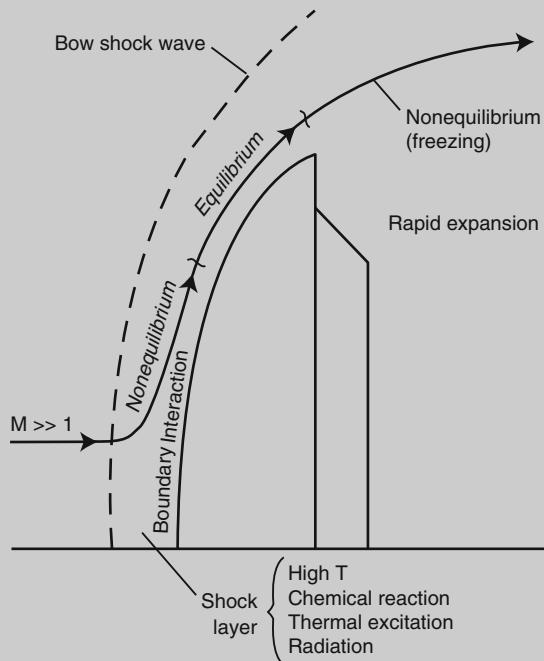


**Fig. 3.87** Schematic of hypervelocity bluff forebody flowfield

(continued)

At high-altitude hypersonic flight conditions, the thermal excitation and chemical reaction of the gas occur slowly enough that a significant portion of the flowfield is in a state of thermochemical nonequilibrium.

A second important effect is the presence of the thick boundary layer along the forebody surface.

In this region there are large thermal and chemical species gradients due to the interaction of the gas with the vehicle wall. Also at high altitudes the shock wave and the boundary layer may become so thick that they merge.<sup>16</sup>

In this case the entire shock layer is dominated by viscous effects.

A gas is in thermal nonequilibrium if, for a given density and internal energy, it is in a thermodynamic state where the internal energy modes cannot be characterized by a unique temperature<sup>17</sup>, while it is in chemical nonequilibrium if its chemical state does not satisfy chemical equilibrium conditions.

Thermal nonequilibrium influences the rates at which certain chemical reactions proceed. Translational temperature behind the shock is increased, but vibrational and electronic temperatures are decreased. This implies that the onset of ionization is enhanced because of the dependence of ionization reactions (other than electron impact) on the translational temperature, whereas dissociation is diminished because of the dependence of dissociation reactions on the vibrational temperature.

The combination of high thermal energy and ionization overshoot causes enhancement of radiation, i.e., nonequilibrium processes can also effect the heat-transfer distribution. This phenomenon known as nonequilibrium radiation enhancement tends to maintain the radiative heat fluxes to the heat-shield surface at a nearly constant value. This is believed to be caused by a region of high temperature and high concentration of excited atoms and molecules that is created during the process of thermal and chemical relaxation behind the shock wave. This nonequilibrium enhancement phenomenon tends to be offset by two phenomena known as collision limiting and truncation.

---

<sup>16</sup>At hypersonic speed, the boundary-layer thickness  $\delta$  depends on Mach and Reynolds numbers:  $\delta/x \cong (M_\infty^2 / \sqrt{Re_\infty})$ . At the high altitudes the Reynolds number is relatively small (typically on the order of 10 based on free-stream conditions and nose radius), while the Mach number is rather high.

<sup>17</sup>Indeed, as flow species may translate, rotate, vibrate, and ionize in accurate physical model flow, internal energy modes are characterized by three temperatures:  $T$ ,  $T_v$ , and  $T_e$ . The first one pertains to roto-translational mode,  $T_v$  to vibrational mode and, finally,  $T_e$  to electronic mode. However, two temperature models ( $T$ ,  $T_v$ ) are widely used. The effect of  $T$  and  $T_v$  on chemical kinetics is accounted for by means of  $\bar{T} = \sqrt{TT_v}$  in the Arrhenius reaction rate temperature.

(continued)

As was asserted above, a portion of the forebody flowfield is in thermochemical nonequilibrium. This can be seen by considering the trajectory of a control volume of air (see streamline in Fig. 3.87) that enters the shock layer. The translational modes of this volume of gas are heated strongly as it passes through the bow shock wave. The translational modes transfer their energy to the other internal energy modes of the molecules through intermolecular collisions. Also chemical reactions of the gas species occur such as dissociation and ionization. These processes require a series of intermolecular collisions for equilibrium to be reached. Thus, as the volume element of gas is convected through the shock layer, these energy exchanges and chemical reactions occur at a finite rate until, at some point on the streamline, equilibrium is achieved. Therefore, there will be significant thermochemical nonequilibrium near the bow shock wave and equilibrium will be approached at large distance along the fluid element's path line (see Fig. 3.87).

The rate at which equilibration is realized is dependent on the free-stream density and speed, or altitude and Mach number.

A parameter that quantifies the degree of chemical nonequilibrium for a particular condition is the Damkohler number, the ratio of the fluid time scale to the chemical time scale; a similar parameter may be derived for the relaxation of energy modes.

The second important effect in the forebody region is the interaction of the wall with the thermally excited and reacted gas in the boundary layer. Indeed, the heat-shield wall can interact chemically with the flowfield due to catalytic effects that promote the recombination of reacted species at the wall.

Finally, at high altitudes, the usual assumption of perfect thermal accommodation and no slip at the wall breaks down. Therefore, for some conditions, temperature and velocity slip effects must also be included.

#### *Afterbody Flowfield*

The flow about an afterbody, illustrated in Fig. 3.88, is dominated by two phenomena: the presence of the rapid expansion as the highly compressed gas flows around the shoulder of the vehicle and the related initiation of separation of the gas near the vehicle corner [7]. These two effects require specific modeling approaches and capabilities.

(continued)

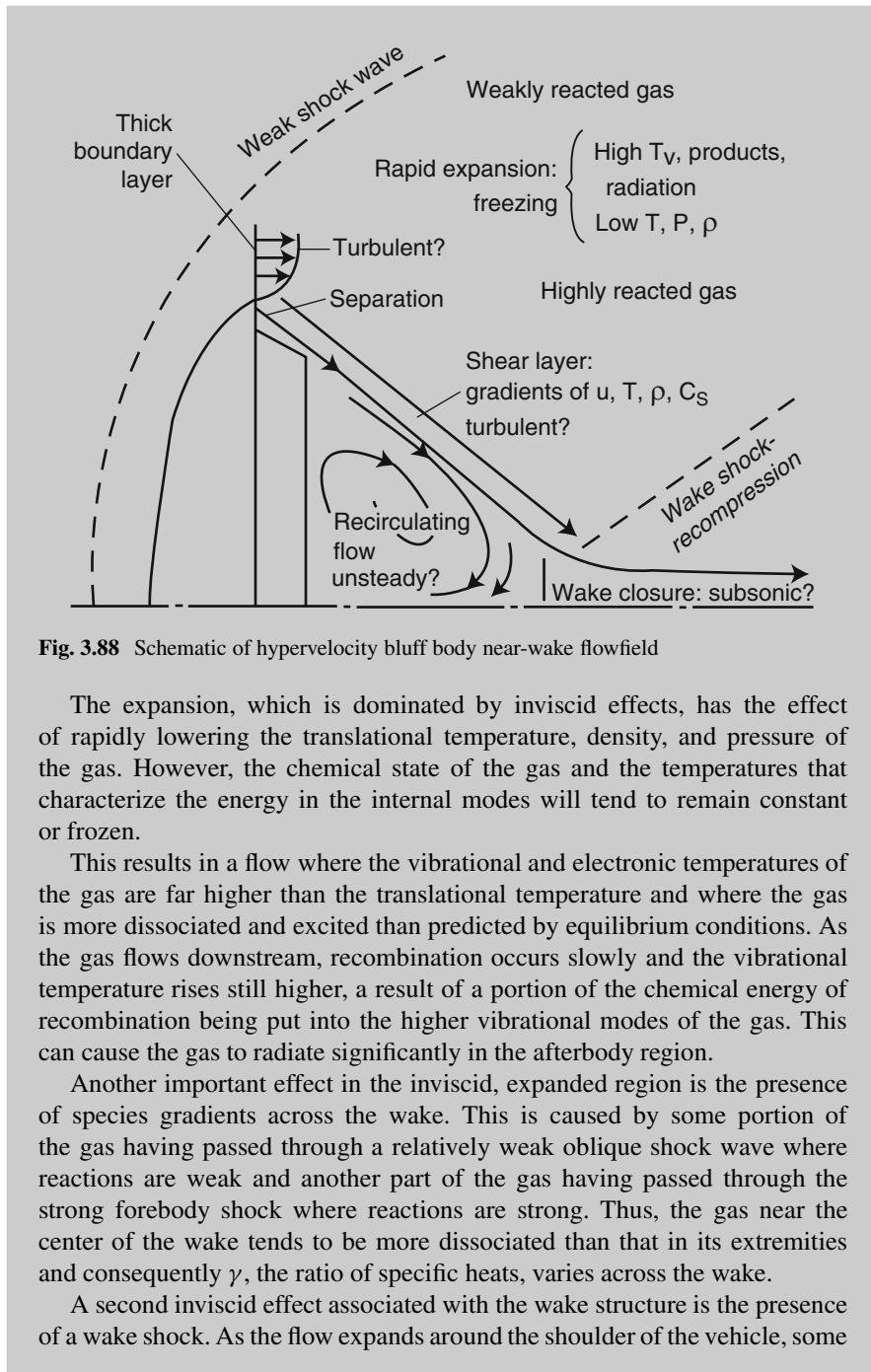


**Fig. 3.88** Schematic of hypervelocity bluff body near-wake flowfield

The expansion, which is dominated by inviscid effects, has the effect of rapidly lowering the translational temperature, density, and pressure of the gas. However, the chemical state of the gas and the temperatures that characterize the energy in the internal modes will tend to remain constant or frozen.

This results in a flow where the vibrational and electronic temperatures of the gas are far higher than the translational temperature and where the gas is more dissociated and excited than predicted by equilibrium conditions. As the gas flows downstream, recombination occurs slowly and the vibrational temperature rises still higher, a result of a portion of the chemical energy of recombination being put into the higher vibrational modes of the gas. This can cause the gas to radiate significantly in the afterbody region.

Another important effect in the inviscid, expanded region is the presence of species gradients across the wake. This is caused by some portion of the gas having passed through a relatively weak oblique shock wave where reactions are weak and another part of the gas having passed through the strong forebody shock where reactions are strong. Thus, the gas near the center of the wake tends to be more dissociated than that in its extremities and consequently  $\gamma$ , the ratio of specific heats, varies across the wake.

A second inviscid effect associated with the wake structure is the presence of a wake shock. As the flow expands around the shoulder of the vehicle, some

(continued)

of it is directed toward the centerline of the body. However, this supersonic flow must change direction and a reflecting shock and an oblique shock wave is formed. The gas becomes compressed in this region, yet the vibrational and electronic temperatures remain high due to freezing, and the gas may radiate significantly.

The location of the separation on the back face of the bluff body is affected by the state of the boundary layer on the shoulder, the Reynolds number, whether the flow is turbulent or laminar, the ratio of specific heats, and the body geometry.

For many cases of interest, particularly at high altitude, the flow can remain attached over a significant portion of the vehicle's afterbody. The location of separation influences the dimension of the recirculation zone and the strength of the shear layer that forms between the recirculating gas and the external, rapidly expanding, supersonic flow. The recirculation zone entrains gas that was in the forebody boundary layer which was cooled during expansion into the base region, but remains highly dissociated. This recirculation zone will be unsteady, the magnitude of which depends on how the shear layer behaves and the feedback between the body motion and the state of the gas in the separated region.

The modeling of the free shear layer must account for large gradients of velocity, temperature, density, and species concentration across it and for the possibility that the flow may be turbulent and unsteady. The numerical treatment of the problem is particularly difficult because of these effects and also due to the uncertain location of this structure. Thus, the presence of thermochemical nonequilibrium, large gradients in thermodynamic quantities and chemical state, and a large separated region stretches computational fluid dynamics beyond its current capabilities.

As a result, in order to treat all possible mission scenarios, CFD tools must be developed that account for flow regimes that range from free molecular through transitional to continuum. Turbulent flows, including transitional flows and flows with massive wall turbulence, can be encountered, as well as unsteady phenomena. Real gas phenomena will encompass thermal and chemical equilibrium and nonequilibrium processes and ionization. Aerodynamic heating will be due both to convective and radiative (equilibrium and nonequilibrium) processes, and material responses will include catalycity, gas/surface accommodation, ablation, and transpiration. Complex flow features, such as shock/shock, shock/surface, vortex, and shear layer interactions, may also be encountered.

As far as discussion on experimentation is concerned, it is worth noting that in a real gas flow, the model scale is a primary parameter. The possibility exists to

generate a spectrum of *real gas* test conditions at a single geometrically similar test point. These flows can vary from frozen to equilibrium flow.

In the limit of chemically frozen flow, there is little value to *real gas* experimentation on the nose region; if the flow is frozen at the stagnation point, it will remain frozen as it expands about the blunt nose and over the afterbody where it may equilibrate. Nose region information for such a flow will be identical to perfect gas wind-tunnel results and can be predicted reliably within the limits of our knowledge of thermodynamic and transport properties.

Afterbody data, however, may be of somewhat greater interest, particularly data describing flow over secondary surfaces which may induce further chemical activity.

Similarly for chemical equilibrium flow, *real gas* experiments are not required. In this case, the extrapolation from a perfect gas to a real gas is straightforward, involving appropriate thermodynamic and transport properties for the reacting gas species.

Between the two limits, in the region of reacting gas flows, is the greatest uncertainty and the greatest need for test data. Facilities required for CFD validation of high enthalpy flows, and for developing and verifying phenomenological models, are devices capable of generating a reacting gas flow over configurations of interest and must have sufficient diagnostics to describe the character and behavior of the flow.

Ground facilities which, although they have serious limitations in simulating full scale flight conditions, are capable of examining selected aspects are expected to be vital to success in the full-scale flights. Theoretical analyses of the real gas phenomena, based on quantum and statistical mechanics, require experimental verification in order to assure that the analyses correctly account for all vital phenomena.

The ground test facilities offer the advantage of observations, such as optical flow visualization, which are impractical in actual flight. For these reasons impulse tunnels, which include shock tubes, shock-tube wind tunnels (shock tunnels), and hotshot wind tunnels (hotshot tunnels), ballistic ranges, and arc-jet wind tunnels, have been built and operated since the 1960s. The experiments made therein have been effective in verifying to a first order the results of some of the theoretical works. But neither analysis nor test has approached the level of maturity achieved by those for the lower flight speed ranges.

### 3.13 Aerothermal Regimes and Vehicle Design

Now that we have an understanding of the atmosphere and the physical and chemical processes in the shock layer, it is possible to distinguish different aerothermal regimes the vehicle usually faces during an atmospheric entry. They are flow regimes and thermochemical flow regimes. In the former case we consider low-density flow effects on the flowfield past the vehicle, while in the latter case the ones promoted by thermochemical processes due to the high enthalpy flow conditions.

From vehicle design point of view, it is obvious that in order to develop and apply CFD prediction methodology for vehicle aerothermodynamics, it is necessary to have some a priori knowledge of the expected flow environment. This will permit the proper choice of the most appropriate form of the conservation equations to be solved and the proper choice of phenomenological models and gas properties necessary to capture the critical flow environment features.

So, a brief physical description of these regimes is given in the order in which they will be encountered by an entry vehicle, followed by the boundary definition in terms of the related nondimensional characteristic number.

### **3.13.1 Flow Regimes**

Low-density flow effects can be classified in:

#### *Free Molecular Flow Regime*

At extreme altitudes, where the gas is very rarefied, the flow has to be described using kinetic theory. This region is known as the free molecular regime, and as the vehicle descends, it enters the near free molecular regime. Here, the molecules reach the body surface after only a few collisions with surface reflected molecules, and in the free molecular regime, the molecules are assumed to reach the surface without colliding with any reflected molecules since they are so widely spaced.<sup>18</sup> As the vehicle descends further, it encounters a region of transition from the near free molecular to the continuum, and engineering results can be obtained using bridging schemes between the two regimes.

#### *Merged Layer Regime*

As the vehicle descends further, the flow begins to exhibit continuum characteristics but is still influenced by rarefied gas effects. Within the merged layer regime, a boundary can be identified that divides the free stream and the shock layer, but within the shock layer, the shock wave and boundary layer are not distinguishable. The no-slip condition which is assumed to hold for continuum flows does not hold at these high altitudes. Specifically, at low densities the flow velocity at the surface takes on a finite value, and also the gas temperature at the surface differs from the actual surface temperature. The shock wave cannot be described as a discontinuity and the shock layer must now be treated as fully viscous, and conventional boundary-layer analysis is no longer applicable.

---

<sup>18</sup>At the surface of the vehicle, the gas–surface interactions are very important as they significantly influence the aerodynamic forces and heating that the vehicle experiences. Evidence of this is the rather spectacular change in aerodynamic and heating coefficients that occur in the transitional regime.

### *Slip Flow*

As the density increases, (i.e., altitude decreases), the shock wave thins to a point where it can now be treated as a discontinuity in the flowfield and, as the density increases further, is no longer merged with the boundary layer. The boundary layer remains very thick and hence results in stronger viscous interaction. As the altitude decreases, the discontinuity in temperature and velocity at the wall reduces. Eventually, these effects disappear altogether, and the non-slip condition can be assumed to hold.

### *Continuum Flow Regime*

The assumption of a continuum flowfield requires that the mean free path be very much smaller than the smallest characteristic length of the flowfield (i.e., the boundary-layer thickness). So that sufficient molecular collisions occur to establish continuum conditions within this region at every instance. Viscous effects can now be confined to the boundary layer. In such environments, where the density is high, several assumptions can be made about the flowfield around a bluff body. Due to the entropy increase across the shock, there are strong entropy gradients in the nose region where shock curvature is greatest. The boundary layer grows inside the entropy layer and is affected by it, since it is also a region of strong vorticity.

At the high Mach numbers associated with the high-altitude end of the continuum regime, viscous dissipation within the boundary layer causes an increase in temperature within the boundary layer, which in turn causes the boundary layer to thicken. This can exert a major displacement effect on the inviscid flow outside the boundary layer, and the resulting changes in the inviscid flow effect the boundary-layer growth. Since the flow behind the near-normal portion of the bow shock is subsonic, the viscous interaction will be strongest away from the stagnation region where the flow has accelerated to supersonic velocities.

The high temperature in the boundary layer due to viscous dissipation and in the shock layer due to the shock wave will mean high heat-transfer rates to the surface.

Generally, convective heating dominates, but if the temperature is sufficiently high, the thermal radiation emitted by the gas itself, radiative heating, can be significant.

As the altitude decreases, viscous dissipation effects are reduced, and the boundary layer thins. At high Reynolds numbers/low Mach numbers, where the boundary layer is very thin, the shock layer is essentially inviscid, and viscous interaction is weak.

#### **3.13.1.1 Flowfield Boundary Definitions**

The various flowfield regimes can be characterized in terms of the Knudsen number, defined as

$$\text{Kn} = \frac{\lambda}{d} \propto \frac{M_\infty}{Re_d} \quad (3.93)$$

where  $\lambda$  is the molecular mean free path and  $d$  is a characteristic dimension (e.g., body length or diameter). In this form, the Knudsen number is applied to low Reynolds number flows (typically  $Re_d < 10^2$ ).

When  $d$  is set to the boundary-layer thickness  $\delta$ ,

$$Kn = \frac{\lambda}{\delta} \propto \frac{M_\infty}{\sqrt{Re_d}} \quad (3.94)$$

and in this form the Knudsen number is applied to higher Reynolds number flows (typically  $Re_d > 10^2$ ).

### Explanation Box. The Knudsen Number in Terms of Reynolds and Mach Numbers

The  $Kn$  can be expressed in terms of Mach and Reynolds numbers. Indeed, the equilibrium mean free path for a simple hard sphere gas is given as

$$\lambda = \frac{1}{\sqrt{2\pi d^2 n}} = \frac{16}{5} \sqrt{\frac{m}{2\pi k T}} \frac{\mu}{\rho} \quad (3.95)$$

Since the most probable molecular thermal speed  $C'_m$  is given as

$$C'_m = \sqrt{\frac{2kT}{m}} \quad (3.96)$$

and related to the speed of sound as

$$C'_m = a \sqrt{\frac{2}{\gamma}} \quad (3.97)$$

then Eq. (3.95) can be written as

$$\lambda = \frac{16}{5} \sqrt{\frac{\gamma}{2\pi \rho a}} \frac{\mu}{\rho} \quad (3.98)$$

with the  $Kn$  given as

$$Kn = 1.276 \sqrt{\gamma} \frac{M_\infty}{Re_\infty} \quad (3.99)$$

If one uses the boundary-layer thickness,  $\delta$ , as a characteristic length, then  $Kn \cong \frac{M_\infty}{\sqrt{Re_\infty}}$  since  $\frac{\delta}{L} \cong \frac{1}{\sqrt{Re_\infty}}$ .

Using these definitions, the boundaries of the various regimes can be specified, albeit somewhat arbitrarily,<sup>19</sup> as

<i>Free molecule</i>		$\frac{M_\infty}{Re_d} > 10$
<i>Transitional</i>	<i>Near free molecule</i>	$1 < \frac{M_\infty}{Re_d} < 10$
	<i>Merged layer</i>	$\frac{M_\infty}{Re_d} < 1$ to $\frac{M_\infty}{\sqrt{Re_d}} > 10^{-1}$
<i>Slip flow</i>		$10^{-2} < \frac{M_\infty}{\sqrt{Re_d}} < 10^{-1}$
<i>Continuum flow</i>		$\frac{M_\infty}{\sqrt{Re_d}} < 10^{-2}$

As an example, Fig. 3.89 shows the boundaries on the velocity–altitude map for the Rosetta Earth return mission [7]. Here, the Knudsen number considers the boundary-layer thickness. The definition of the classical regimes is based on this value for the Kn of the entry vehicle, and it can be seen that the entry takes place between  $10^{-1}$  and  $10^{-2}$  (i.e., slip flow, vorticity interaction effects being negligible on the forward heat shield and only important at the expansion corner). Here we may still use continuum techniques where the effects of boundary-layer thickness are accounted for (i.e., Navier–Stokes solutions) and evaluation of the wall conditions undertaken. In practice, however, the heat-transfer rates are overpredicted using no slip, and the slip condition becomes another empirical factor.

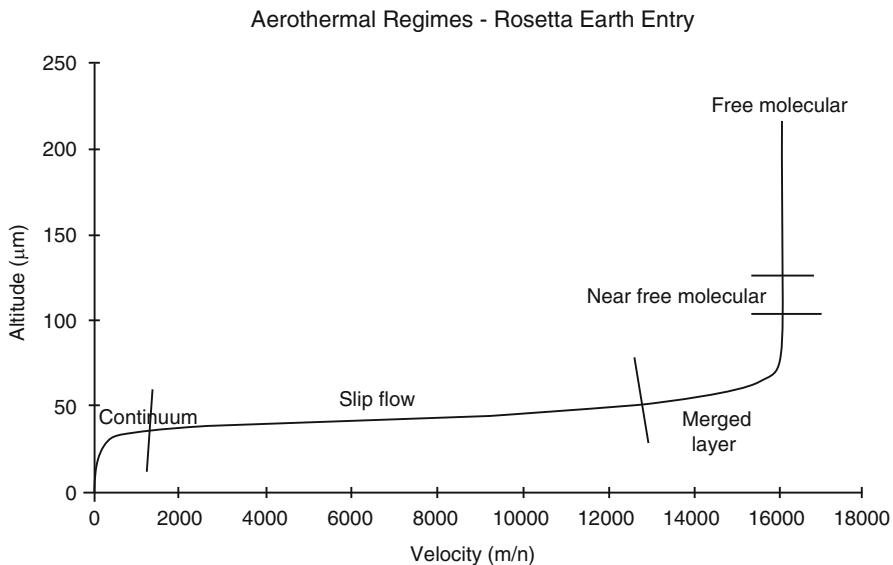


Fig. 3.89 Rosetta aerodynamic regimes

<sup>19</sup>The value of  $Kn$  that provides an indication of the boundary between continuum and transitional flows is approximate at best and differs appreciably depending on which of the two approaches is used for defining  $Kn$  (overall or local).

Clearly entry vehicles have geometric features of largely different sizes, the base radius to corner radius for example, and the definition of regimes need to be treated with caution since continuum flowfields may exhibit rarefied flow effects in particular regions, the corner or vehicle leading edges, for instance. The regimes are a broad guideline therefore.

Furthermore, expansion of the forebody flow into the wake extends to lower altitudes, the conditions for which rarefaction effects are important in establishing the near-wake closure and the level of heating experienced on vehicle afterbody or payload. This is particularly true of aeroassisted space transfer vehicles (ASTV) where determination of wake closure is a critical issue for aerobrakes because the low lift-to-drag ratio aeroshell designs impose constraints on payload configuration/spaceship design. The issue is that the payload should fit into the wake in such a manner as to avoid the shear layer impingement to minimize heating.

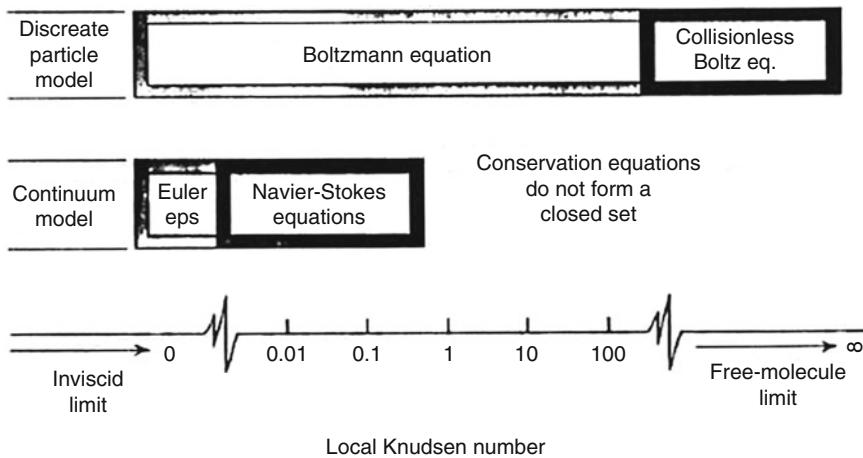
From computational point of view, note that low-density flows present unique difficulties for numerical simulations since the model equations used to describe continuum flows (i.e., Navier–Stokes) become deficient as the flow becomes more rarefied. In fact, in this case the particulate or molecular structure of the gas must be recognized. So, the mathematical model of such flows is the Boltzmann equation which presents overwhelming difficulties to computational methods for realistic flows. Consequently, the mathematical models that are readily applicable to both continuum and free molecular (collisionless) flows experience serious limitations when applied to transitional flows. Fortunately, direct simulation methods have evolved over the past 35 years that readily lend themselves to the description of rarefied flows. These developments have generally been concerned with the direct simulation Monte Carlo (DSMC) method.<sup>20</sup> It takes advantage of the discrete structure of the gas and provides a direct physical simulation as opposed to a numerical solution of a set of model equations. This is accomplished by developing phenomenological models of the relevant physical events, as translational, thermal, chemical, and radiative nonequilibrium effects.

Figure 3.90 presents the  $Kn$  limits for the mathematical models at both the microscopic and macroscopic levels [8, 7].

As shown in figure, the limitation of the macroscopic or continuum description as expressed by the Navier–Stokes equations arises from the fact that the conservation equations do not form a determinate set unless the shear stress and heat flux can be expressed in terms of lower order macroscopic quantities. Expressions for the transport terms in the Navier–Stokes equations fail when gradients of the macroscopic variables become so steep that their length scale is of the same order as the average distance traveled by molecules between collisions, or mean free paths.

---

<sup>20</sup>The DSMC method is a technique for the computer modeling of a real gas by thousands to millions of simulated molecules. When the flow loses its continuum nature, it appears to a first approximation as a stream of independent particles. The velocity components and position coordinates of these molecules are concurrently followed through representative collisions and boundary interactions in simulated physical space. The DSMC method of Bird along with many variants is the most used method today for simulating rarefied flows in an engineering context.



**Fig. 3.90** The Knudsen number limits on the mathematical models

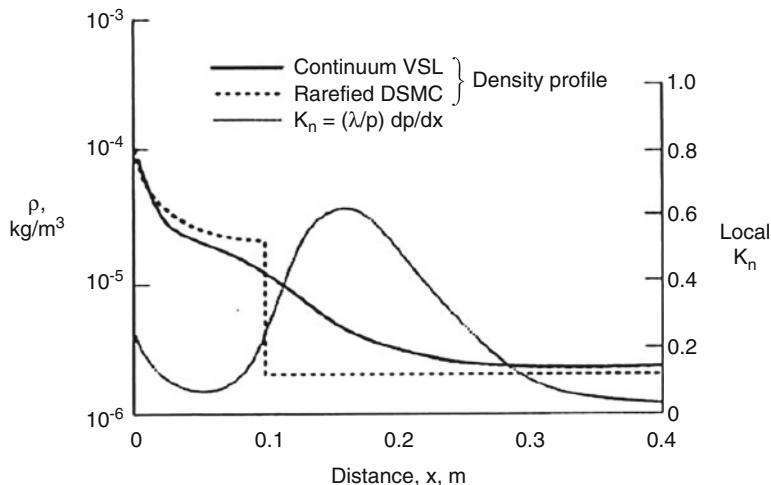


**Fig. 3.91** Density distribution along the stagnation streamline of the re-entering. Shuttle Orbiter at 93 km altitude

As an example, results shown in Fig. 3.91 demonstrate the importance of the transport properties in the shock layer and the conditions adjacent to the surface along the stagnation streamline for the Shuttle Orbiter at 93 km altitude [7]. The overall Kn based on a Shuttle effective nose radius of 1.296 m is 0.028.

Figure 3.91 compares the density profile calculated with the viscous shock layer (VSL) method with that calculated by the DSMC method. Evident is the inadequacy of the continuum assumption to describe the overall flowfield for this case.

The shock thickness is greater than the standoff distance and the shock wave structure merges with that of the thermal boundary layer. At the same time, the surface pressure and heat-transfer rates given by the continuum method are in good agreement with those from the DSMC method.

Also shown in Fig. 3.91 is the variation of the local Kn based on density scale length. The behavior of the local Kn parameter within the shock is no surprise because it is well known that continuum methods cannot be applied to the structure of strong shock waves. The local Kn near the surface is rather large, being an order of magnitude larger than the overall Kn and larger than the limiting value for the validity of the continuum transport equations. The surface temperature is approximately 1,043 K while the gas temperature adjacent to the surface is approximately 1,400 K. The fractional temperature jump is of the same order as the local Kn.

For what concerns applications where rarefied flowfield analysis is extremely important, the aerodynamic and aerothermodynamic design of aeroassist missions for capsules and spacecraft is remarkable.<sup>21</sup> Indeed, almost any mission that involves changes in orbital altitude and/or inclination in the vicinity of an atmospheric-bearing planet is a candidate for aeroassist.<sup>22</sup> Possible aeroassisted space missions are:

1. Synergetic plane change
2. Planetary mission applications
3. Orbital transfer vehicle applications

Figures 3.92, 3.93 and 3.94 illustrate several possible planetary missions and orbital transfer vehicle (OTV) maneuvers [7]. Indeed, Fig. 3.92 includes OTV maneuvers between high Earth orbit (HEO) and low Earth orbit (LEO) as well as lunar return missions [7].

An illustration of multipass aerobraking mission is illustrated in Fig. 3.93, while Fig. 3.94 shows an example of planetary aerocapture [7].

Note that aeroassisted OTV vehicles have a much enhanced payload delivery capability compared to all propulsive ones.

---

<sup>21</sup>The central design issues are nonequilibrium heating and the nature of the wake closure at perigee conditions of transfer orbits. Aerobraking is carried out at such high altitudes that highly rarefied flow conditions are encountered, of course.

<sup>22</sup>Aeroassisted vehicles are able to perform maneuvers by exploiting planet atmosphere, thus saving fuel.

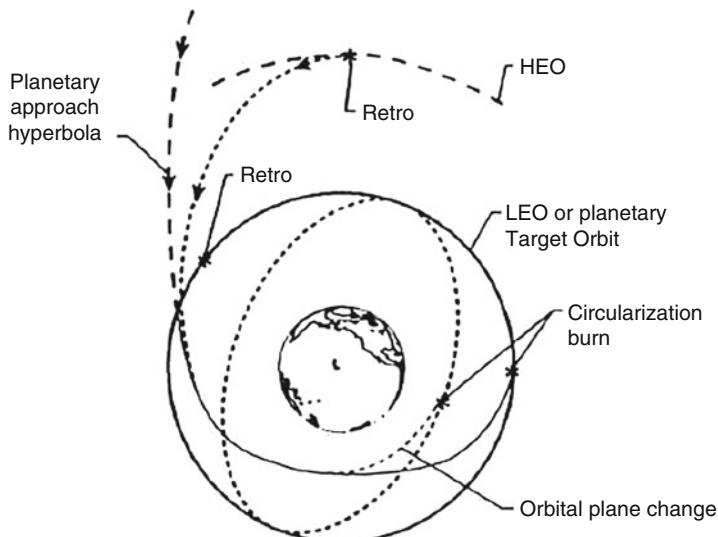


**Fig. 3.92** Aeroassisted maneuvers for synergetic plane change and planetary aerocapture missions

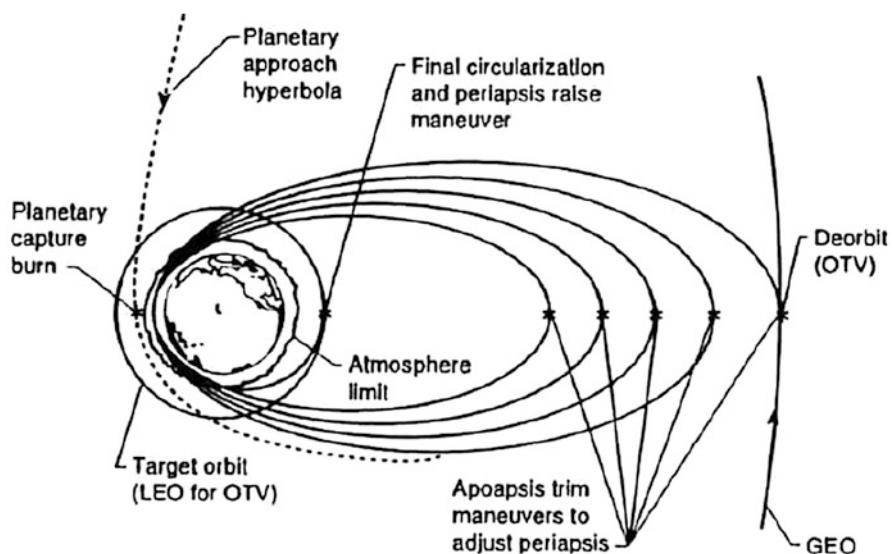


**Fig. 3.93** Multipass aeroassisted maneuvers for planetary aerobraking and orbital transfer vehicle mission

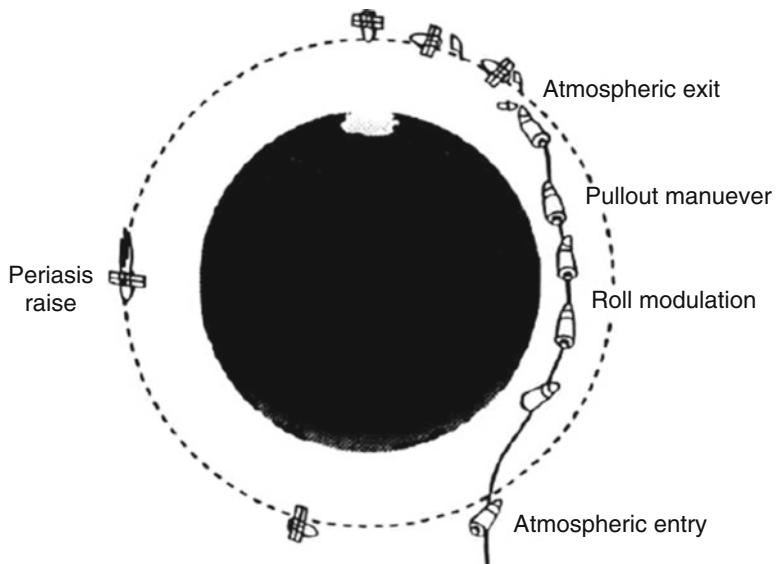


**Fig. 3.94** Planetary aerocapture maneuver

#### Explanation Box. Orbital Transfer by Aerocapture

Usually, orbital transfer techniques use chemical propulsion to insert spacecraft into a highly elliptic orbit and then use a small apoapsis burn to lower periapsis into the atmosphere. Indeed, on arrival at a planetary destination, the spacecraft may be required to maneuver into an orbit in order to make scientific measurements, drop probes, or relay information. In all missions to date, this has been carried out using chemical propulsion systems in a periapsis retro-burn to slow the spacecraft down to orbital velocity. This may be followed by minor orbital transfer maneuvers again using chemical propulsion. However, to lower energy orbits, atmospheric braking, such as that shown in Fig. 3.93, represents a formidable alternative solution, provided that the transport of the required propulsion system and more importantly the propellant is a mass expensive solution [7]. For example, in 1990, the spacecraft Magellan used the atmosphere of Venus to circularize its orbit due to a lack of onboard fuel. This was achieved in 840 passes losing only 1.5 m/s per pass. Magellan was not designed for this purpose but has demonstrated the feasibility of such maneuvers to save fuel.

Also, the Mars Global Surveyor spacecraft inserted into an elliptical capture orbit at Mars and then used multipass aerobraking to achieve a nearly circular, polar mapping orbit with a 2 h period.

(continued)

Furthermore, the low velocity decrement on each pass makes the navigation and control of such maneuvers relatively straightforward since errors can be corrected in successive passes. Such maneuvers require only vehicle drag (i.e., a ballistic vehicle) since orbit is assured and a deep entry is avoided in any case.

For a high-margin over propulsive systems and short time scale of operations and indeed for hyperbolic arrival, the single pass orbital transfer or aerocapture may save propulsive mass up to twice the payload in orbit.

However, the disadvantages of orbital transfer by aerobraking are the long time required for multiple passes, and of course an orbital velocity must already have been achieved.

Note that aerocapture is achievable with low L/D provided the entry corridor is large enough. In general a large (compared to capsules) L/D is required to achieve an aerocapture to orbit with large super-orbital arrival velocity. Since all the excess energy is taken out in one pass, this requires precise control during the atmospheric pass and a higher level of technology compared to direct aerobraking or orbital lowering. For example, the Aeroassist Flight Experiment (AFE) was a vehicle design to explore the single pass orbital transfer or low performance aerocapture and had a lifting capability to control the energy lost.

The vehicle uses its lifting capability to maintain a constant drag in the continuum flow regime until the desired velocity is reached. The vehicle then pulls up above the atmosphere and at apoapsis uses a small chemical propulsion burn to raise periapsis above the atmosphere. Alternatively the vehicle may remain in the atmosphere and decelerate to descent speed.

Apollo's Lunar return was an aerocapture to ground from 11 km/s and achieved this with  $L/D \cong 0.3$  and within 12 g deceleration.

Aerocapture to Earth of high-speed comet or planetary return capsules has also been studied at speeds up to 17 km/s and is also possible with modest 0.3 L/D.

The modulation of the lift is achieved by either pitch control or by rolling a fixed L/D vehicle (i.e., banking maneuvers). The latter method simplifies vehicle design but requires greater attitude changes because bank reversals must be used to equalize the effects of the out of plane lift on the cross range. The rationale for following a constant drag profile as opposed to a position, velocity, or entry angle profile (i.e., a constant flight path angle also assures entry) is because onboard accelerometers can easily measure drag directly whereas estimates of position require more sophisticated techniques and integrations which may compound errors. Also variations in the atmosphere can be accounted for directly.

Aerocapture to orbit applies to almost all atmospheres but performance advantages diminish for planets with masses larger than Uranus due to the

(continued)

large TPS mass requirements. However, this could be overcome to a certain extent at least for Saturn by using an atmosphere bearing moon such as Titan to perform the capture to Saturn orbit.

Three factors determine the aerocapture aerodynamic shape and performance characteristics:

- Volumetric efficiency
- Accuracy
- Vehicle mass

The accuracy requirement essentially sets the L/D. During the initial entry the vehicle must have sufficient L/D for control to keep the drag constant and avoid under or overshoot, either of which would be disastrous. L/D defines the width of the corridor, and increasing L/D widens the corridor to a certain extent. Aerocapture accuracy increases with increasing L/D until it reaches a maximum at about 1.5.

Planetary aerocapture (see Fig. 3.94) is an aeroassist mission where the velocity decrement is achieved in a single deep atmospheric pass<sup>23</sup> to transfer the vehicle from its hyperbolic approach trajectory to a target orbit about the planet [7].

Consequently, the critical loads occur in the continuum flow regime. The most frequently used aeroassist maneuver is where the capsule or probe is aerobraked by direct atmospheric entry. Examples of aerobraked missions are the Apollo entry capsule, the Galileo Probe for entry into Jupiter's atmosphere, and the Mars Pathfinder mission. Again, as for single pass aerocapture, the primary aerodynamic loads and heating occurs under continuum conditions. Consequently, rarefaction effects are of paramount importance when the aeroassist maneuver is designed to produce the desired drag decrement at high altitudes to avoid excessive aerodynamic heating. For aeroassist missions where the deceleration occurs much deeper into the atmosphere, rarefaction plays a secondary role on capsule performance but would be critical in defining and interpreting experiments conducted during the transitional portion of entry.

In the framework of rarefaction effects, the appraisal of vehicle aerodynamic and aerothermodynamic performance in the early phase of re-entry trajectory is significant. As an example in the next explanation box, Orbiter aerodynamics and aerothermodynamics in transitional flow conditions are discussed.

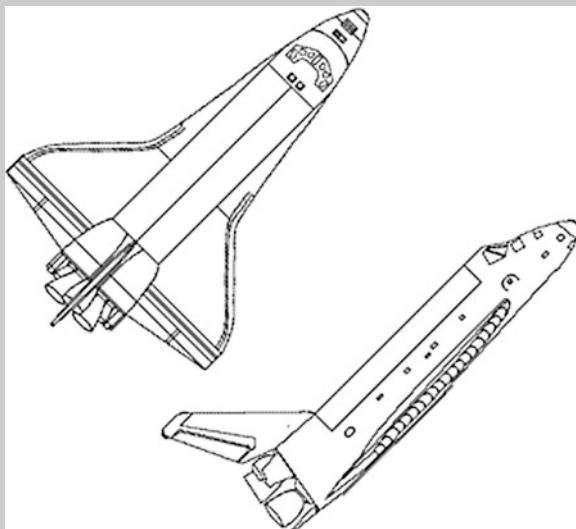
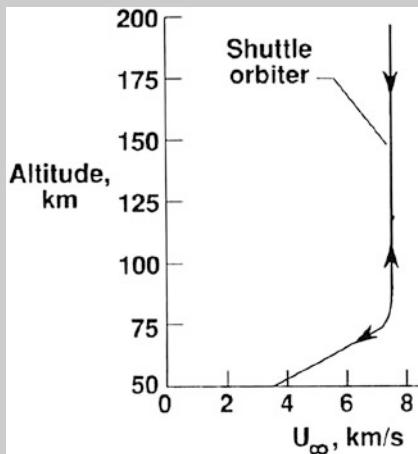
---

<sup>23</sup>For single pass aerocapture, the atmospheric penetration is normally deep in order to deplete the excess velocity.

**Explanation Box. Orbiter Aerodynamics and Aerothermodynamics in Transitional Flow Conditions**

Figure 3.95 illustrates the altitude and velocity conditions that are the focus of these applications [7]. Details of the flowfield structure and surface conditions as calculated with the DSMC method are presented and comparisons are made when possible between the DSMC results and that obtained using Navier–Stokes (NS) and viscous shock layer (VSL) methods. Computations are made for five nominal altitudes ranging from 170 to 100 km.

**Fig. 3.95** Entry trajectories



(continued)

The variable hard sphere (VHS) intermolecular collision model is used while accounting for internal energy transfer and chemistry among colliding molecules. The gas–surface interactions are modeled as diffuse with complete thermal accommodation.<sup>24</sup> Micro-g accelerometers have been used to measure the axial and normal forces during entry in the altitude range of 160–60 km. The ratio of these two forces is of special interest in that it is independent of dynamic pressure. When the computed and flight results are compared, good agreement is observed over the entire range of the calculations.

Figure 3.96 presents these data in terms of the aerodynamic efficiency as a function of altitude [7].

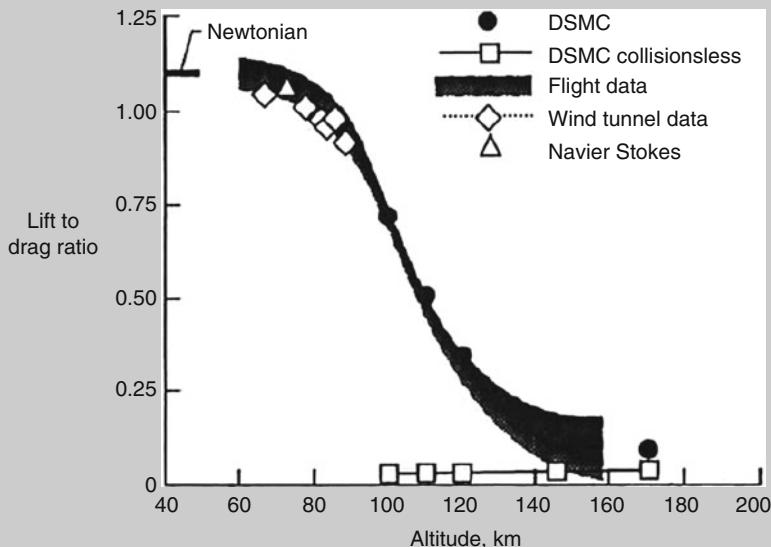


**Fig. 3.96** Orbiter lift-to-drag ratio in transitional flow conditions

<sup>24</sup>The flow is hypersonic. This implies that any pressure forces produced by random thermal motion are small in comparison to those due to the directed motion of the spacecraft through the upper atmosphere. Nevertheless, random thermal motion is important, as in the exact, nonelastic nature of the interaction of the gas molecules with the body surface. A more accurate treatment results from the assumption that atmospheric molecules striking the spacecraft are in Maxwellian equilibrium, having both random and directed velocity components. Some of the molecules that strike the surface are assumed to be re-emitted inelastically, with a Maxwellian distribution characteristic of the wall temperature  $T_w$ . This model results in a pressure force on the wall of:  $p = 2p_i - \sigma_n(p_i - p_w)$  where  $p_i$  is the pressure due to incident molecular flux,  $p_w$  is the pressure due to wall re-emissions,  $\sigma_n$  is the normal momentum accommodation coefficient with Maxwellian distributions assumed, and  $p_i$  and  $p_w$  may be computed and the net pressure force obtained. A similar analysis yields the shear force and introduces a dependence on the tangential momentum accommodation coefficient  $\sigma_t$ .

(continued)

The L/D ratio can be derived from the normal and axial forces since the incidence angle  $\alpha$  is known:

$$\frac{L}{D} = \frac{(F_N/F_A) - \tan \alpha}{1 + (F_N/F_A)} \quad (3.100)$$

The band of flight data shown in Fig. 3.96 corresponds to a series of Shuttle flights occurring under varying atmospheric conditions. Agreement between computed and flight data is good. The modified Newtonian limit, corresponding to a hypersonic inviscid flow, is shown to be  $L/D = 1.1$ , which is very close to the value of  $L/D = 1.06$  computed using a Navier–Stokes code. Also shown in Fig. 3.96 are the results obtained with the DSMC code run in a collisionless mode [7].

Flowfield structure analysis in the range 150–92 km altitude, where the free-stream Knudsen number range was 23–0.03, is also performed. In this case an “equivalent axisymmetric body” concept was used to model the windward centerline of the Shuttle, at a given angle of attack, with an appropriate axisymmetric body at zero angle of attack. The axisymmetric body was a hyperboloid with a nose radius of approximately 1.36 m and asymptotic body half angle of approximately  $42.5^\circ$ . The DSMC calculations accounted for translational, rotational, vibrational, and chemical nonequilibrium effects for a 5-species reacting air model. Even for the lowest altitude case considered, the DSMC results show that the shock wave is merged with the shock layer and that the shock thickness is of the same order as the shock layer.

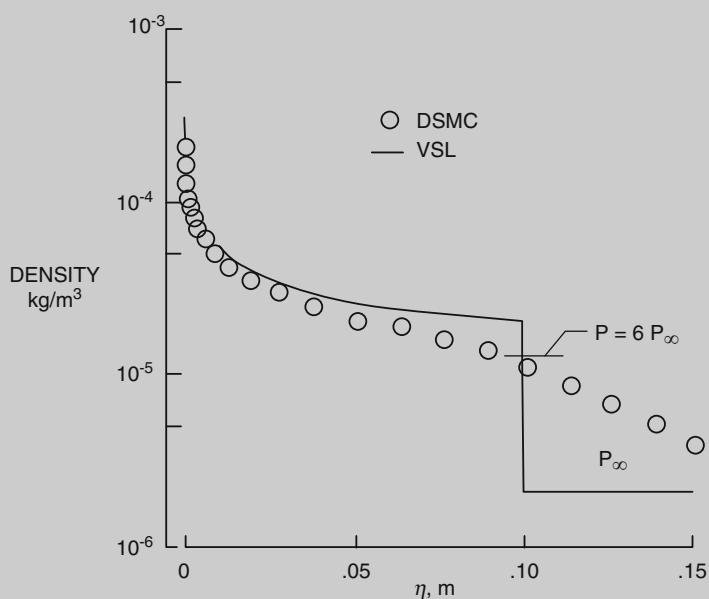
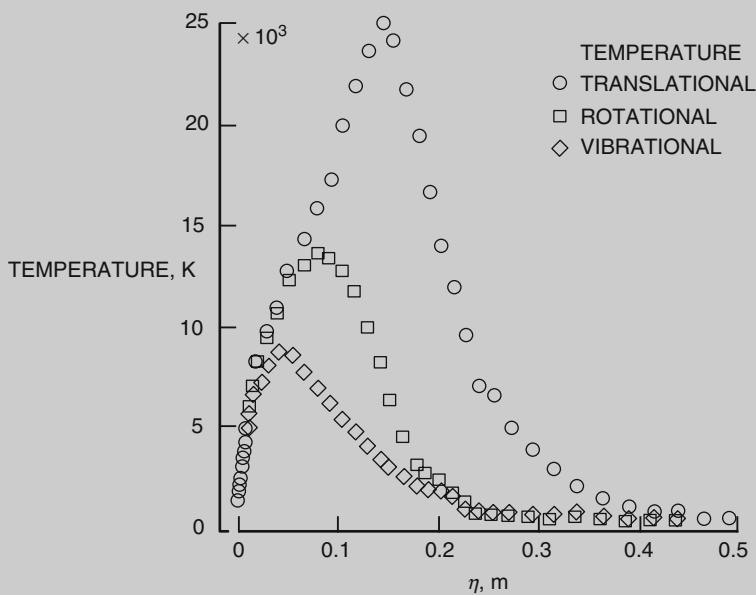
Figure 3.97 through Fig. 3.99 show details of the calculated flowfield structure and provide a comparison of the DSMC and continuum results as obtained with a VSL analysis, along the stagnation streamline of Shuttle Orbiter at 92.3 km altitude [7]. For instance, Fig. 3.97 shows the extent of thermal nonequilibrium as computed by DSMC [7].

As one can see, the temperature begins to rise appreciably at a distance of about 0.4 m from the body, while the VSL calculation, using a discontinuous shock, has a total shock layer thickness of 0.1 m, as shown in Fig. 3.98 [7].

---

The accommodation coefficients  $\sigma_n$  and  $\sigma_t$  characterize the type of interaction the gas particles make with the surface. The equation  $\sigma_n = \sigma_t = 0$  implies specular reflection, as in Newtonian flow, whereas  $\sigma_n = \sigma_t = 1$  implies diffuse reflection, i.e., total accommodation (“sticking”) of the particles to the surface followed by subsequent Maxwellian re-emission at the wall temperature.

(continued)



(continued)

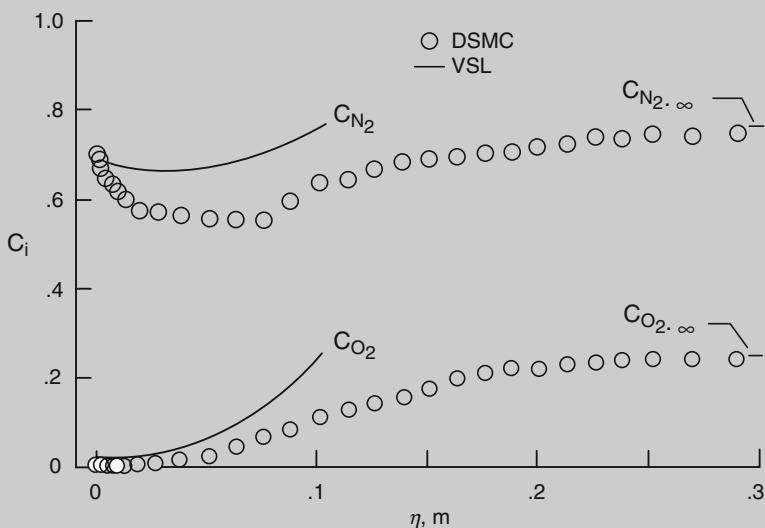


**Fig. 3.99** Comparison of species mass fraction profiles for  $O_2$  and  $N_2$  along with stagnation streamline of Orbiter at 92.3 km

When the individual temperature components are examined for the DSMC solution (see Fig. 3.97), the rotational and vibrational temperatures are seen to lag far behind the translational temperatures since they depend on molecule collision rate. The differences between the translational and internal temperature modes increase with altitude, since the collision rate decreases [7].

The chemical composition profiles along the stagnation streamline resulting from the DSMC and VSL solutions are presented in Fig. 3.99 for  $O_2$  and  $N_2$  [7].

The profile resulting from the two solutions has the same general shape. However, the DSMC results show a significant influence of the thick shock wave on the chemical composition within the shock layer. A significant number of chemical reactions occur in the shock wave, producing atomic mass fraction in excess of 20 % at the shock location, as given by the continuum solution. By including slip boundary conditions in the VSL solution, the chemical composition profile would compare more favorably with the DSMC results within the shock layer.

The effect of increasing the altitude is to create a more rarefied situation in which the shock layer and shock wave merge (see Figs. 3.100 and 3.101) [7].

(continued)

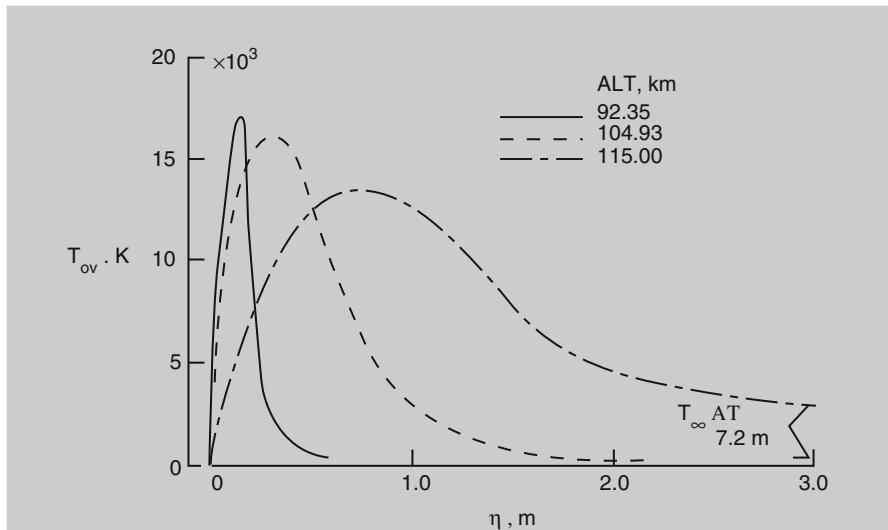


**Fig. 3.100** Effect of rarefaction on flowfield structure (stagnation streamline for Orbiter). Overall kinetic temperature

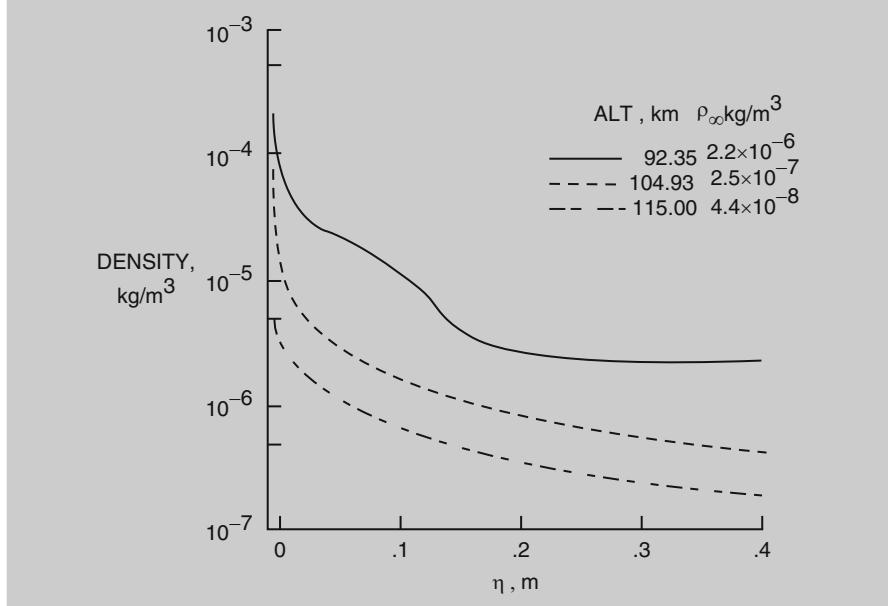


**Fig. 3.101** Effect of rarefaction on flowfield structure (stagnation streamline for Orbiter). Density profiles

(continued)

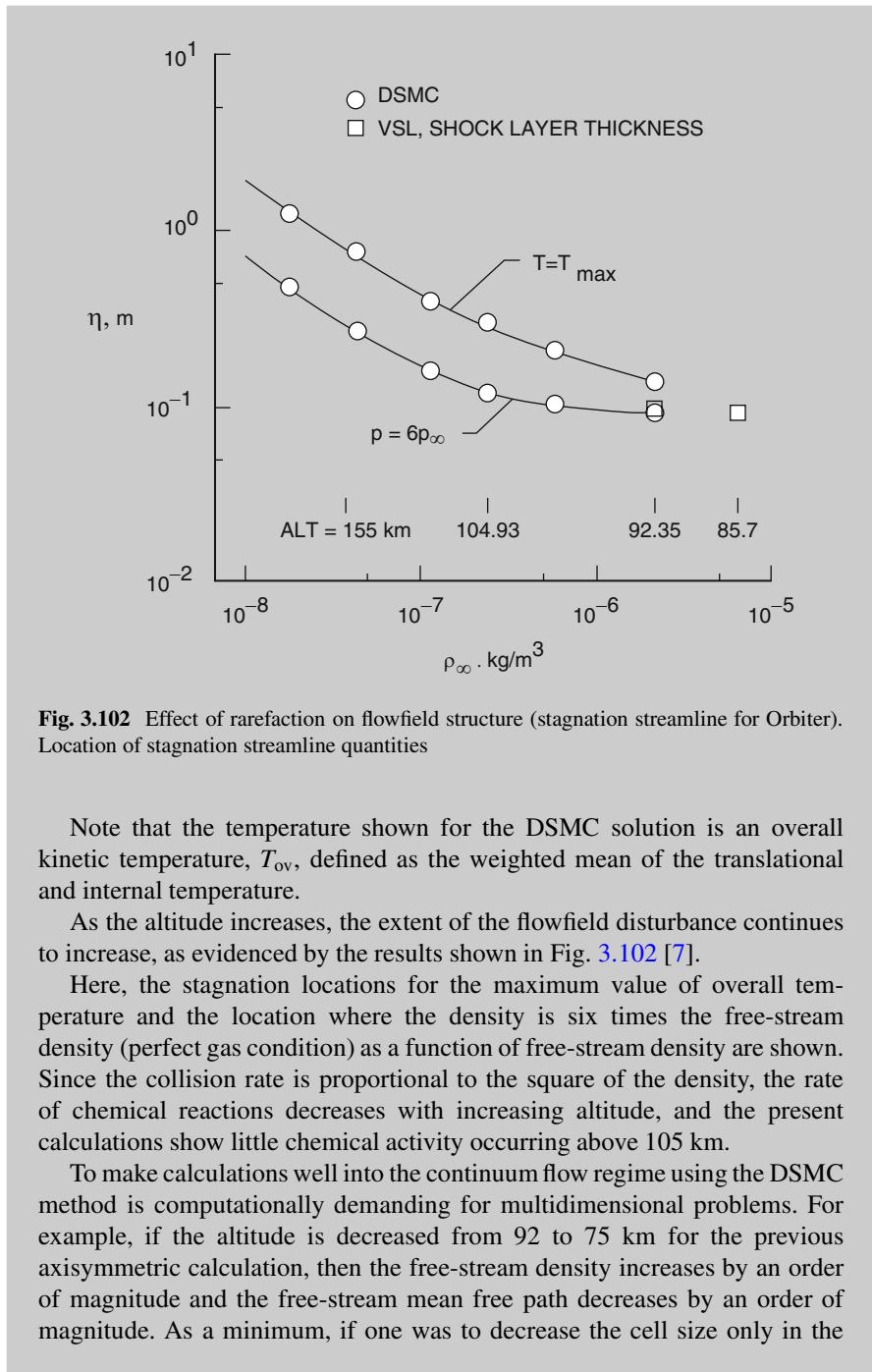


**Fig. 3.102** Effect of rarefaction on flowfield structure (stagnation streamline for Orbiter). Location of stagnation streamline quantities

Note that the temperature shown for the DSMC solution is an overall kinetic temperature,  $T_{ov}$ , defined as the weighted mean of the translational and internal temperature.

As the altitude increases, the extent of the flowfield disturbance continues to increase, as evidenced by the results shown in Fig. 3.102 [7].

Here, the stagnation locations for the maximum value of overall temperature and the location where the density is six times the free-stream density (perfect gas condition) as a function of free-stream density are shown. Since the collision rate is proportional to the square of the density, the rate of chemical reactions decreases with increasing altitude, and the present calculations show little chemical activity occurring above 105 km.

To make calculations well into the continuum flow regime using the DSMC method is computationally demanding for multidimensional problems. For example, if the altitude is decreased from 92 to 75 km for the previous axisymmetric calculation, then the free-stream density increases by an order of magnitude and the free-stream mean free path decreases by an order of magnitude. As a minimum, if one was to decrease the cell size only in the

(continued)

direction normal to the body to maintain a cell thickness that is less than the local mean free path, then the number of computational cells would have to be increased by an order of magnitude (the number of particles in the simulation would also increase by an order of magnitude) and the time step reduced by an order of magnitude. At the higher density condition, the collision frequency increases. This results in increased computing time since the time required to calculate the collisions appropriate for a time step is more demanding than the time to move the particles. The combined effects of an increase in the number of particles, a decrease in the time step, and an increase in the collision frequency would increase the time requirement more than two orders of magnitude and the storage requirements by an order of magnitude.

As far as aerodynamic heating is concerned, Fig. 3.103 compares DSMC and VSL results for stagnation surface heat-transfer coefficient for several Shuttle entry conditions. As shown, DSMC and VSL calculations showed good agreement each other [7].

Both solutions were also in good agreement with the Orbiter flight-measured value. However, as the altitude increased, the VSL results, without slip boundary conditions, began to depart rapidly from the DSMC results for  $\lambda_{\infty}/R_N$  values greater than 0.03. Results of continuum calculation using the NS equations for the stagnation streamline are also compared with the DSMC data for altitudes of 92–115 km. The NS and VSL results presented are for altitudes as low as 74.98 km. The NS results agree better with DSMC values for more rarefied conditions than the VSL results. When the NS calculations

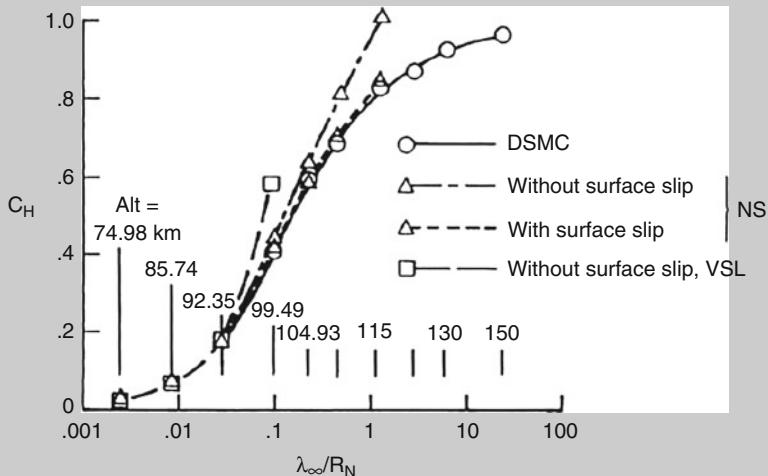


Fig. 3.103 Comparison of calculated heat-transfer coefficient for Shuttle entry condition

(continued)

are made with surface slip boundary conditions, the agreement with the DSMC values is substantially improved, and the agreement is good for the range of conditions for which the comparisons are made. Even though all three numerical methods are in good agreement with respect to stagnation-point heat transfer at an altitude of 92 km, there are substantial differences in the flowfield structure as previously discussed and these differences increase with increasing rarefaction.

### 3.13.2 Thermochemical Flow Regimes

As highlighted before, the parameter which characterizes the thermochemical regimes is the Damkohler number, Da. This number can be applied to internal degrees of freedom of the molecules (i.e., thermal nonequilibrium) or to chemical reactions in the fluids (i.e., chemical nonequilibrium).

The Damkohler number is the ratio of the characteristic time of particles passing a region of the flow  $t_u$  to the relaxation time  $\tau$  in question, where the flow time is usually the ratio of the characteristic dimension  $L$  (e.g., the shock standoff distance) and the velocity  $u$ :

$$\text{Da} = \frac{L}{u\tau} \quad (3.101)$$

For chemical reaction we compute the Damkohler number as

$$\text{Da} = \frac{Ln_k}{u\omega_k} \quad (3.102)$$

and for thermal relaxation we can define the Damkohler as

$$\text{Da} = \frac{L}{u\tau_v} \quad (3.103)$$

The chemical and thermal regimes may be loosely defined as follows:

- $\text{Da} = 0 \rightarrow$  chemically frozen
- $10^{-3} < \text{Da} < 10^3 \rightarrow$  nonequilibrium flow
- $\text{Da} = \infty \rightarrow$  chemical equilibrium

At very high altitudes where the densities are very small or at low speeds where temperatures are low, reaction rates are slow compared to the hydrodynamics time scales ( $\text{Da} \ll d$ ). This enables the frozen flow assumption to be used and solutions are restricted to those which model the flow of a multicomponent fluid

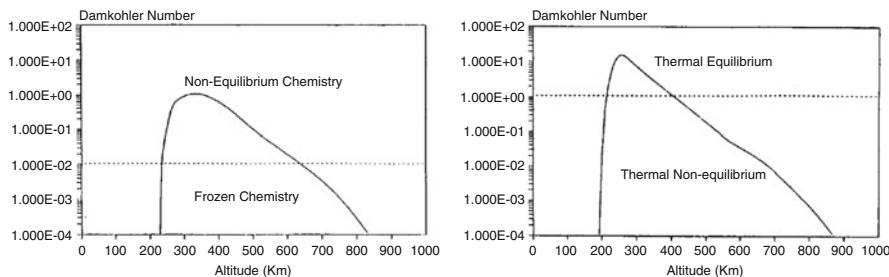


**Fig. 3.104** Huygens chemical and thermal Damkohler

as a continuum (or a free molecular) problem utilizing an appropriate equation of state and real (i.e., temperature dependent) thermodynamic data.

Note that the Damkohler number can be applied equally well to thermodynamic relaxation (vibration, rotation, etc.) as to chemical processes and particular reactions. For example, a particular reaction may be so fast that it can be replaced by an equilibrium reaction.<sup>25</sup> Or the reaction may be so slow that it can be excluded from the mechanism [7].

At low altitudes the densities are high and the flow is likely to be characterized by fast chemical reaction whose time scale is short when compared with that of the fluid velocity ( $Da > l$ ). In this regime the assumption of equilibrium chemistry in the shock layer is more appropriate. In the midrange density regime, the assumption of either frozen or equilibrium flow, while accurate in some portions of the shock layer, would lead to over (frozen) or under (equilibrium) prediction of temperature in other areas. In reality between these two regimes, the density is such that the flow cannot be accurately characterized as being either frozen or as being in chemical equilibrium. It is in this flight region that nonequilibrium chemical kinetics must be considered [7].

Examples of the variation of chemical and thermal Damkohler with altitude are shown in Fig. 3.104 for the Huygens entry trajectory [7].

Note that for the formulation employed at one tenth of the distance along the stagnation streamline, the regime boundaries were found to be best fitted by lowering the critical values by  $10^3$ .

Approximate chemical and thermal boundaries are shown for the Titan entry in Fig. 3.105, thus assessing the chemical and thermal regimes [7].

Since methane dissociates very quickly, the thermal regimes are also based on the relaxation of diatomic nitrogen.

Finally, for nonequilibrium processes involving two-body molecular collision, an interesting and important scaling can be obtained for nonequilibrium flowfields. This scaling is called *binary scaling parameter*. Indeed, consider two different flows with the same temperature  $T_\infty$ , and velocity  $V_\infty$ , but with differing values of density

<sup>25</sup>For example, the dissociation of methane in the Titan atmosphere.

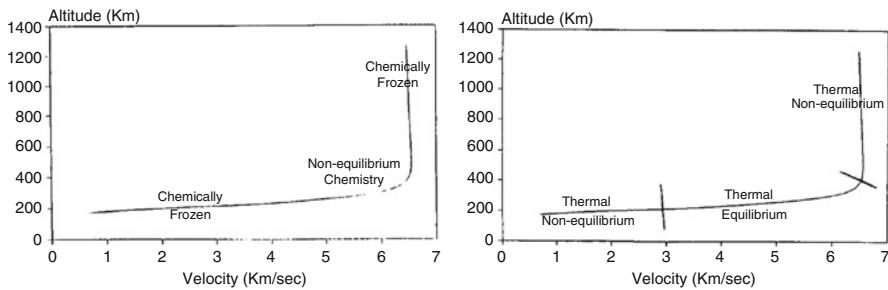


**Fig. 3.105** Huygens chemical and thermal regimes

$\rho_\infty$ , and  $d$  (characteristic length, the nose radius, say). Plots of mass fraction against distance inside the shock will be the same for the two flows if the product  $\rho_\infty d$  is the same between the two flows. This product,  $\rho_\infty d$ , is known as the binary scaling parameter and is used for matching wind-tunnel conditions to flight conditions.

## References

1. Hallion RP (1983) The path to the space shuttle: the evolution of lifting reentry technology. AFFTC historical monograph. Air Force Flight Test Center, Edwards Air Force Base, California
2. Anderson JD Jr (1989) Hypersonic high temperature gas dynamics. McGraw-Hill Book Company, New York
3. Lobbia MA (2004) A framework for the design and optimization of waverider-derived hypersonic transport configurations. University of Tokyo, Tokyo
4. Julian Allen H, Eggers AJ Jr (1958) A study of the motion and aerodynamic heating of ballistic missiles entering the earth's atmosphere at high supersonic speeds, NACA report 1381. U.S. Government Printing Office, Washington, DC
5. Nonweiler TRF (1959) Aerodynamic problems of manned space vehicles. J R Aeronaut Soc 63:521–528
6. Bertin JJ, Cummings RM (2003) Fifty years of hypersonics: where we've been, where we're going. Prog Aerosp Sci 39:511–536
7. Advisory Group for Aerospace Research and Development (North Atlantic Treaty Organization) (1997) Capsule aerothermodynamics, AGARD-R-808. AGARD, Neuilly sur Seine
8. Bertin JJ (1994) Hypersonic aerothermodynamics, AIAA education series. American Institute of Aeronautics and Astronautics, Washington, DC
9. Regan FJ, Anandakrishnan SM (1993) Dynamics of atmospheric re-entry. American Institute of Aeronautics and Astronautics, Washington, DC
10. Etkin B, Reid LD (1996) Dynamics of flight: stability and control. Wiley, New York
11. Chavez FR, Schmidt DK (1994) Analytical aeropropulsive/aeroelastic hypersonic-vehicle model with dynamic analysis. J Guid Control Dyn 17(6):1308–1319
12. Iliff KW, Shafer MF (1993) Space shuttle hypersonic aerodynamic and aerothermodynamic flight research and the comparison to ground test results. NASA technical memorandum 449, Washington, DC
13. Hirschel E, Weiland C (2009) Selected aerothermodynamic design problems of hypersonic flight vehicles. AIAA/Springer, Reston/Berlin/London

14. Strohmeyer D, Eggers T, Haupt M (1998) Waverider aerodynamics and preliminary design for two-stage-to-orbit missions. Part 1. *J Spacecr Rocket* 35(4):450–458
15. Bowcutt KG, Anderson JD Jr, Capriotti D (1987) Viscous optimized hypersonic waveriders. AIAA 25th Aerospace Sciences Meeting, 12–15 January 1987. Reno, Nevada AIAA paper 87-0272, Washington, DC
16. Zucrow MJ, Hoffman JD (1976) Gas dynamic. Wiley, New York
17. Talay TA (1975) Introduction to the aerodynamics of flight, NASA SP-367. Scientific and Technical Information Office National Aeronautics and Space Administration, Washington, DC
18. Lewis MJ, McRonald AD (1992) Design of hypersonic waveriders for aeroassisted interplanetary trajectories. *J Spacecr Rocket* 29(5):653–660
19. Heinze W, Bardenhagen A (1998) Waverider aerodynamics and preliminary design for two-stage-to-orbit missions. Part 2. *J Spacecr Rocket* 35(4):459–466
20. Dornheim MA (2004) A breath of fast air. *Aviation Week & Space Technology*, April 5

# Chapter 4

## Analysis of an Apollo-Shaped Crew Return Vehicle

### 4.1 Introduction

Accurate numerical simulations are mandatory for a proper design of re-entry vehicles since, e.g., real gas thermodynamics, transport properties variations, and finite rate chemical reactions (i.e., real gas effects) influence vehicle aerothermodynamics, aerodynamics, as well as their heat shield design [1–3]. For example, real gas effects, in the past, have been responsible for the inadequate prediction of body flap efficiency on the US Space Shuttle Orbiter. Indeed, real gas thermodynamics, transport properties, and finite rate chemistry have a pronounced effect on shock and Mach wave's positions and shapes, emitted radiation, heterogeneous chemical reactions at vehicle walls, and aerodynamic drag, thus affecting in turn the re-entry trajectory of the vehicle.

As a consequence, flow physics greatly influence the vehicle re-entry performances as well as those of the vehicle heat shield. The risk involved, due to an inadequate knowledge of real gas effects, is that integrity and performance of the re-entry spacecraft may be severely compromised due to wrong design choices as, for example, additional weight for the thermal protection system (TPS).

In this work, an Apollo-shaped capsule concept was explored as a possible Crew Return Vehicle (CRV) of the ISS, and/or as LEO mission support vehicle as, for example, for Hubble space telescope servicing, as done by National Aeronautics and Space Administration (NASA) with the Crew Exploration Vehicle (CEV), considering also the renewed interest of manned exploration mission to Moon.

This configuration, in fact, represents the most natural and viable option being the Apollo vehicle the only manned spacecraft returned from the Moon [4]. Moreover, in 1998, European Space Agency (ESA) successful launched the Atmospheric Re-entry Demonstrator (ARD) which was also an Apollo-like capsule. The ARD

program was conducted primarily to validate existing and future ground-based experimental and numerical aerothermodynamics models [5].

In this way, the CRV development can take advantage of the huge amount of knowledge, both experimental and flight data, obtained with Apollo and ARD programs.

This blunt-body configuration, chosen for the CRV, follows also from the constrain that for high specific energy re-entries as those coming back from the Earth satellite (say about 60 MJ/kg), a lower stagnation-point heating rate is the most important vehicle design parameter rather than the high cross range and low g-load capabilities experienced by a winged lifting configuration. Indeed, a design solution like Space Shuttle is still unrealistic because it would demand a large mass for the heat shield, which has to withstand to very high heating rates on the vehicle leading edges as well as to manage high overall integrated heat load due to the long duration of lifting return trajectories compared to the ballistic ones.

In this framework, a detailed and extensive numerical simulation of the flowfield past the CRV carried out at different flight conditions along with the re-entry trajectory plays an important role within the space vehicle design [6, 7]. Indeed, CFD simulations lead to great benefits as, for example, vehicle with enhanced aerodynamics or provision of much more accurate vehicle aerodynamic and aerothermodynamic databases for reliable flight missions and allow to significantly reduce the number of in-flight and plasma wind tunnel (PWT) experimental test campaigns, as well as to account for real gas flow features which are difficult to reproduce in ground test facilities [8]. For example, CFD allows to investigate the effects of the sonic line position shift, due to changes of the gas-specific heat ratio ( $\gamma$ ) as well as of the heat shield surface catalyticity on the vehicle aeroheating. Indeed, the sonic line analysis is a key parameter of spacecraft design process since the vehicle static aerodynamic instability markedly depends on changing of the sonic line shape and location [9]. Then, the TPS could promote, at the vehicle surface, the recombination of the flow dissociated chemical species produced behind the strong bow shock [10]. These recombination reactions, through the releasing of heat of formation of the molecular species leaving the heat shield surface, increase the overall heat flux at the vehicle walls. Such augmented heat flux can be up to twice the value experienced by a non-catalytic wall [11, 12].

In this framework, a LEO re-entry scenario characterized by a ballistic and a lifting re-entry trajectory has been computed to supply realistic flight conditions to the vehicle flowfield calculations, as, for example, free-stream conditions of the trajectory peak heating.

To accomplish work goal, two levels of numerical simulations are adopted.

The first one refers to engineering analyses of loading environment and the second one to CFD detailed analyses.

Within engineering-based analyses, the modified Newtonian (MN) theory is widely used, due to the fast computations and to the reliable results. In fact, despite the simplicity of the MN method, it provides quite accurate vehicle aerodynamic

predictions especially considering that real gas effects can be evaluated by means of the relationship between density ratio ( $\varepsilon$ ) and the specific heat ratio ( $\gamma$ ).

CFD simulations are carried out with perfect gas (PG) and reacting gas (RG) models for the air. Indeed, upon the CRV re-entry, loading scenario is assessed; axisymmetric and three-dimensional thermochemical nonequilibrium Euler and Navier-Stokes computations are performed by using several reaction mechanisms and chemical kinetics. Different wall boundary conditions (e.g., non-catalytic NC, partially catalytic PC, and fully catalytic FC) accounting for both cold wall and radiative surface cooling are also considered to underline the effect of the heat shield catalytic on the aerodynamic heating.

As secondary objective, since the heat shield development program concerning performance of ablative TPS in moderate aeroheating environment is not sufficiently mature, this work aims to provide a preliminary assessment of the capabilities of a capsule forebody thermal shield built of shuttle-like TPS tiles to withstand to a re-entry from LEO.

Therefore, the effects of complexity of some state-of-the-art chemical models, kinetics of reactions, vibrational relaxation, and wall reaction mechanism on vehicle aerothermodynamics and aerodynamics, and on some flowfield features, on the CRV are highlighted.

The present work confirms that dissociated gas may increase much more the heat load that the vehicle thermal shield has to withstand during descent, due to the heterogeneous catalysis phenomena that may take place at the vehicle surface. It also confirms that high-temperature transport phenomena influence the vehicle flowfield and, in turn, the vehicle aerodynamics and aerothermodynamics, but it also stress that, with an acceptable loss of results accuracy, we do not need to use models of so high complexity, thus saving much computing time.

Thus, the numerical rebuilding of the flowfield about ELECTRE probe in plasma wind tunnel (PWT) is performed.

Indeed, high accuracy in modeling coupling of flow and chemistry may result only in a poor increase of accuracy of numerical results, despite the high modeling efforts and the increased computational cost. CFD analyses are still time consuming and expensive. So, one must balance the theoretical and computer time effort needed to use a more general and sophisticated model against the expected accuracy of the numerical results. Then, the question arises to which extent number of reactions, coefficients, reaction mechanism, etc., influence the flow.

To answer this question, a step-by-step numerical investigation has been carried out. Indeed, several simulations have been performed to examine the influence of the chemical reactions, its mechanisms and kinetics, and thermal nonequilibrium on aerodynamic and aeroheating of CRV.

Finally, the reliability of the numerical analyses, however, strongly requires accurate wind tunnel (WT) and flight data to be used for code validation, before the CFD code can serve for predicting flow phenomena.

## 4.2 Overview of Flow and Chemistry Coupling Within LEO Re-entry Scenario

As discussed in Chap. 1, one of the problems facing the design of atmospheric re-entry vehicle is the phenomenon of “real gas behavior”, which may become very relevant and challenging. In fact, flight measurements, collected during re-entry, have demonstrated that real gas effects can significantly influence both aerodynamics (e.g., the vehicle stability) and aerothermal loads of hypervelocity vehicles. On the other hand, trajectory calculation for atmospheric re-entry involves determination of vehicle aerodynamics and aerothermodynamics. Therefore, accurate modeling of flow physics, in particular flow chemistry, is mandatory within numerical computations of re-entry vehicle design.

In this chapter, we stress this point with an application to the proposed CRV.

When flow velocity is low (say up to about 3 km/s or temperature up to about 2,000 K), energy is absorbed only into particles vibration and rotation degrees of freedom (dof).

But as velocity increases enough (e.g., high free-stream enthalpy), chemical effects come in, since the bow shock is strong enough to suddenly elevate the temperature of the surrounding air, especially around the nose where the shock is more intense. Thermal energy of the gas becomes comparable with the energy associated with a whole range of gas-phase chemical processes such as the excitation of molecular modes of vibration, the dissociation of oxygen and nitrogen into their atomic forms, the formation of other chemical species through recombination reactions, and the ionization of both molecular and atomic species. Hence, the microscopic structure of the mixture species, affecting the ways in which energy may be redistributed (e.g., number of active degrees of freedom of the species), influences the specific heat ratio ( $\gamma$ ), the chemical reaction rates, and the transport properties. These quantities, in turn, affect the dynamics of the flow and the character of shock and expansion waves (i.e., pressure, temperature, and velocity distributions), the chemical energy diffused to the surface (i.e., the chemical contribution to the heat flux at the wall), and the boundary-layer structure (i.e., the heat flux and shear stress).

As a consequence, the flowfield chemical composition around the re-entry vehicle, during descent, varies spatially and temporally, and because shock layer molecules continuously exchange its energy between the translational and internal dof, the air results in a mixture of several reacting and vibrating species in thermal and/or chemical nonequilibrium. Of course this scenario emphasizes depending on the kind of re-entry (i.e., orbital or super-orbital one). Therefore, the accurate numerical simulation of re-entry flows can be very challenging, depending on the more or less correct and accurate modeling of the thermochemical processes, as will be discussed hereinafter.

For example, the multispecies reacting gas must account for two temperatures  $T$  and  $T_v$ :  $T$  characterizes the translational and rotational modes and  $T_v$  the vibrational modes.

Further, “real gas effects” play a relevant role in the thermodynamics of the flow around the vehicle because thermodynamic equilibrium is not established instantaneously in the moving gas, but requires a finite time known as *relaxation time*. Departure from thermodynamic equilibrium can have significant effects on shock wave structure, thus affecting the flowfield around the vehicle.

In fact, flow chemical dissociation that takes place in the shock layer results in a large density ratio  $\varepsilon$  across the strong bow shock (compared with a flow of the same gas where no dissociation occurs) that, in turn, markedly influences both the shock shape and standoff distance as prescribed by continuity equation for a 1-D stream tube.

On the other hand, the surface pressures are affected by a change in shock density ratio, because the level of pressure at the stagnation point (e.g.,  $C_{p\max}$ ) is changed:

$$C_{p\max} = C_{p,t2} = \frac{P_{t2} - P_\infty}{q_\infty} = \left( \frac{P_{t2}}{P_\infty} - 1 \right) \frac{2}{\gamma M_\infty^2} \cong 2 - \varepsilon \quad (4.1)$$

where the density ratio across the bow shock wave,  $\varepsilon = \rho_1/\rho_2$ , in the hypersonic limit reads

$$\lim_{M_\infty \rightarrow \infty} \frac{\rho_1}{\rho_2} = \lim_{M_\infty \rightarrow \infty} \frac{2 + (\gamma - 1) M_\infty^2}{(\gamma + 1) M_\infty^2} = \frac{\gamma - 1}{\gamma + 1} \quad (4.2)$$

Moreover, the nondimensional distribution of surface pressure relative to stagnation-point pressure is changed as highlighted by Fig. 4.1 and numerical results collected hereinafter. Therefore, under conditions where dissociation exists, the aerodynamics of capsules depends primarily on shock density ratio since the change of aerodynamic characteristics is the result of change in surface pressure acting on the vehicle.

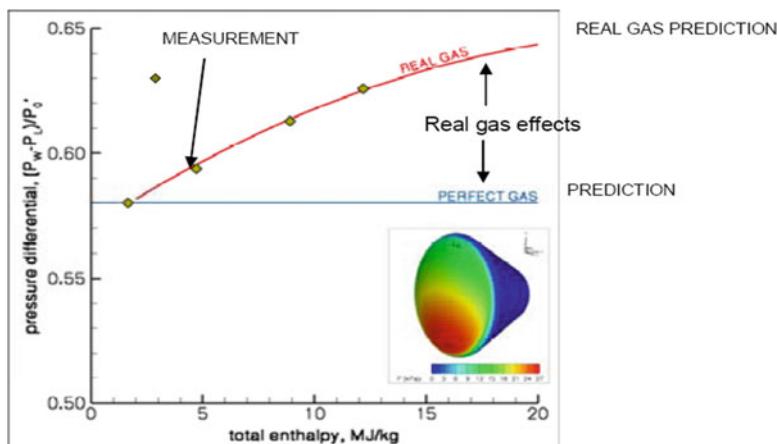


**Fig. 4.1** Pressure differential

Also, the sonic line position shifts because of the change in  $\gamma$ . Therefore, as static aerodynamic instability is associated with changing sonic line location, high-temperature effects result in modifying vehicle hypersonic aerodynamics and aerothermodynamics by means of a very abrupt change in the trim angle of attack of the capsule.

Body stability is a critical requirement for re-entry vehicle, because static instability could lead to catastrophic failure if the thermal shield is not protecting the vehicle anymore. This is the explanation of the relation that exists between pitching moment coefficient ( $C_{MY}$ ) and sonic line location. For instance, the change of  $C_{MY}$  is associated to the motion of the sonic line location on vehicle leeside. In particular, the number of both chemical species and reactions to consider as relevant depend on the vehicle trajectory. For example, numerical computation of a flowfield involving ionized species, as for super-orbital re-entries, demands at least 11 chemical species ( $N_2, O_2, N, O, NO, N_2^+, O_2^+, N^+, O^+, NO^+$ , and  $e^-$ ) with 20 reactions, whereas for lower velocity re-entries, 5 non-ionized species ( $N_2, O_2, N, O, NO$ ) and 17 reactions are sufficient. Simulation problems may arise because the coupling of flow and chemistry leads to a stiff problem due to differences in reaction rate characteristic times; dissociation rate coefficients can differ by orders of magnitude, and since reaction rates are very difficult to be measured, different values may exist for the same coefficient. Therefore, the appropriate set of reactions, to be used in a given application, represents a very relevant choice.

Such a choice is still more relevant because, in general, increasing model complexity does not equal to increasing accuracy of numerical results, despite the higher computational cost needed for increased reaction set. Moreover, when one increases the number of chemical reactions, numerical results can be much influenced by the effect of the uncertainty in input data, such as species transport coefficients and relaxation times for thermal and chemical nonequilibrium. So, it could be important to simplify the reaction mechanisms, by reducing as much as possible the number of chemical reactions, without loss in accuracy but greatly reducing computing time. Among the most simple reaction mechanisms, currently in use, there is the set of three reactions, named Zeldovich process, summarized hereinafter.

The reactions considered above, taking place only in the gas phase, are termed homogeneous chemical reactions. They differ from the heterogeneous reactions that, instead, occur near the vehicle wall involving gas and solid species. Heterogeneous reactions describe recombination of flowfield atomic species that were formed by gas dissociated through the bow shock. They can be catalyzed by the thermal protection material (TPM) and, being exothermic, contribute to the aeroheating of the vehicle. Thus, the TPM, promoting or preventing species recombination at wall, depending on its catalyticity, plays an important role in the aerodynamic heating, as explained in the next paragraph.

### 4.3 Heat Shield Surface Catalyticity Effects

Real gas effects influence not only aerodynamic but also vehicle aeroheating: dissociated gas may increase much more the heat load that the vehicle thermal shield has to withstand during descent, due to the heterogeneous catalysis phenomena that may take place at the vehicle surface. For instance, the thermal protection material (TPM) may promote the chemical recombination, at wall, of atomic species produced during the flow dissociation processes, taking place when the gas passes through the strong bow shock wave ahead of the re-entry vehicle. These recombination reactions, by means of the heat of formation of the molecular species that leave the heat shield surface, increase the overall heat flux up to about two times or more with respect to a non-catalytic wall. These phenomena depend both on re-entry energy and vehicle configuration. If a blunt-body vehicle design is adopted, careful attention to the catalytic heat transfer has to be paid, especially when the vehicle re-enters at high angle of attack (AoA). In this case, in fact, due to the high free-stream enthalpy, a strong detached shock wave takes place ahead of re-entry vehicle, thus causing molecular dissociation. Therefore, the airflow results into a plasma which impinges on the vehicle wall.

As the dissociated atoms reach the body wall, a lot of them recombine in molecules either in the boundary layer or at the vehicle surface, where they dump their energy of recombination. This process depends on the vehicle surface temperature and on the chemical flow conditions, providing an additional contribution to the heat transfer, due to species diffusion, that is typically of the same order of magnitude as the Fourier contribution.

For instance, neglecting the heat conduction into the vehicle wall and radiation from the gas, the energy balance at a radiation cooled vehicle surface reads [see Eq. (3.80) and Eq. (2.49)]:

$$\begin{aligned} \dot{q}_w = \sigma \varepsilon T_w^4 &= k_{tr} \left( \frac{\partial T}{\partial y} \right)_w + \sum_{i=1}^{N_v} k_{v,i} \left( \frac{\partial T_{v,i}}{\partial y} \right)_w \\ &+ \rho \sum_{i=1}^{N_s} \left( \int_{T_0}^T C_{Pi} dT + \Delta h_{fi}^o \right) D_i \left( \frac{\partial Y_i}{\partial y} \right)_w \end{aligned} \quad (4.3)$$

The first and the second terms, on the right side, are the conductive heat flux from fluid to the wall, due to the temperature gradient (both the translational and vibrational one); the third one is the diffusion term due to the species gradient. This contribution depends strongly on the surface catalytic properties of TPS. In fact, as the chemical nonequilibrium flow enters the boundary layer (reacting boundary layer), the vehicle surface may act as third body promoting heterogeneous reactions that take place at the wall.

So the TPM may be involved in the surface recombination which becomes the main factor of the aerodynamic heat transfer, especially when gas-phase recombination in the boundary layer is frozen and the wall absorbs the entire energy released by surface reactions (i.e., fully catalytic wall with frozen boundary layer).

Therefore, the catalytic effects of vehicle surface could result in very substantial differences in heat transfer that must be accounted for a reliable vehicle TPS design: the spacecraft TPS should be a poor catalyst.

Thus, in order to protect the CRV from this intense heat, the catalytic properties of the candidate heat shield TPMs must be carefully known. For instance, close to wall, the effect of TPM on the recombination rates of heterogeneous reactions is accounted for by the catalytic efficiency coefficients  $\gamma_i$ . The recombination coefficient  $\gamma_i$  is the combination of the probability that atoms of the species  $i$  will recombine as they collide on the surface ( $\gamma'_i$ ) and the fraction of dissociation energy released effectively to the surface ( $\beta$ ), known as accommodation coefficient of the TPM surface:

$$\gamma_i = \gamma'_i \beta \quad (4.4)$$

$\gamma'_i$  refers to the ratio of the number of atoms impinging on body surface which recombines in molecules to the overall number of atoms striking on the surface.

$$\gamma'_i = \frac{\dot{m}_{i,\text{recomb}}}{\dot{m}_{i,\text{all}}} \quad (4.5)$$

So that, when  $\gamma'_i = 1$ , all atoms that impact the surface recombine and leave it as molecules. In this case, the wall refers as *fully catalytic* one. On the other side, when  $\gamma'_i = 0$ , no recombination occurs and the TPM is said *non-catalytic*.

These above two cases (NC and FC wall) are extreme ones which are not encountered practically. Real TPS materials (like C/SiC) have, in fact, a *finite catalyticicity* and then  $\gamma'_i$  takes a value between 0 and 1.

Silicate and ceramics are fair approximations to non-catalytic surfaces while metals and metal oxides are highly catalytic. For example, values of  $\gamma_i$  are of the order  $<0.01$  on ceramic surfaces, while on metallic, metallic oxide or graphitic surfaces values might be expected to be  $>0.1$  and are normally assumed to be fully catalytic; that is, equilibrium exists at the surface.

Values of  $\gamma_i$  for nitrogen recombination on metals can be of the order of 0.1–0.2, and metal impurities are thought to be the primary cause of surface reactivity.

Regarding to  $\beta$ , experimental observations suggest that numerical modeling needs to take into account for an incomplete energy release at the surface when atoms combine on a surface:

$$\beta = \frac{\dot{q}_{\text{recomb}}}{\dot{m}_{i,\text{recomb}} \cdot h_{Di}} \quad (4.6)$$

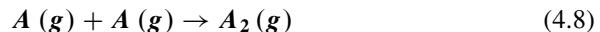
stating that the energy release due to the combined atoms differs from the total available dissociation energy of the atoms. However, for real space vehicle TPMs, very little is known about this coefficient and, for the sake of simplicity, full accommodation condition, i.e.,  $\beta = 1$ , is generally accepted (conservative condition). Therefore, it follows that

$$\gamma_i = \gamma'_i \quad (4.7)$$

This is the case when the residence time for recombined molecules is long enough to complete the transfer of all the chemical energies created by surface recombination to the chemical surface heating of the vehicle wall. One argument of Park to support this assumption is that the energy cannot be released in the boundary layer since it meets an adverse temperature gradient and hence enters the wall, although Scott shows some evidence that glassy material might have incomplete energy accommodation ( $\beta < 1$  or *partial accommodation*).

From the application point of view, several wall catalysis models exist that describe the catalytic efficiency coefficients, when the wall behaves as partially catalytic one.

One first way to construct a model of  $\gamma_i$  is the *one-step global mechanisms*:



with the reaction rate given by the catalytic reaction rate constant,  $K_w$ .

This results in a significant improvement of the model since elementary reaction rates depend on the temperature only. Therefore, generally,  $\gamma_i$  is independent on pressure and density as most recombination reactions are first order, but depends on surface temperature ( $T_w$ ):

$$\gamma_i = \gamma_i(T_w) \quad (4.9)$$

and is characteristic of the recombining gaseous species and of the TPM surface involved.

Equation (4.9) is essentially available only at the elevated temperatures experienced in hypersonic flight and for a small number of reactions, e.g., nitrogen/oxygen recombination, either by fitting experimental data or by some physical model.

The available data suggest an Arrhenius-type expression which leads to an analogy with gas-phase reactions and an energy barrier or activation energy which must be overcome by atoms colliding with the surface:

$$\gamma_i = P_i \exp\left(-\frac{E_i}{kT_w}\right) \quad (4.10)$$

where  $P_i$  is a spherical factor accounting for directional effects,  $E_i$  is the activation energy,  $k$  is the Boltzmann constant, and  $T_w$  is the wall temperature.

This has been done by Scott, Stewart, Kolodziej, Rakich, Lanfranco, Zoby, and Gupta for different TPMs starting from different ground experiments in arc-jets and shuttle flight data rebuilding.

In Ref. [7], Stewart and Kolodziej, for example, provided the following values for single species O and N recombination on reaction cured glass (RCG) coating for the shuttle high-temperature reusable surface insulation (HRSI) tiles:

$$\gamma_O = 40 \exp\left(-\frac{11,440}{T_w}\right) \quad \text{for } 1,435 \text{ K} < T_w < 1,580 \text{ K} \quad (4.11)$$

$$\gamma_O = 39 \times 10^{-9} \exp\left(\frac{21,410}{T_w}\right) \quad \text{for } 1,580 \text{ K} < T_w < 1,845 \text{ K} \quad (4.12)$$

$$\gamma_N = 6.1 \times 10^{-2} \ exp\left(-\frac{2,480}{T_w}\right) \quad \text{for } 1,410 \text{ K} < T_w < 1,640 \text{ K} \quad (4.13)$$

$$\gamma_N = 6.1 \times 10^{-2} \ exp\left(\frac{5,090}{T_w}\right) \quad \text{for } 1,640 \text{ K} < T_w < 1,905 \text{ K} \quad (4.14)$$

while at high temperature ( $T_w > 1,500$  K) for C/C-SiC

$$\gamma_O = 39 \times 10^{-9} \ exp\left(\frac{21,410}{T_w}\right) \quad (4.15)$$

$$\gamma_N = 6.2 \times 10^{-6} \ exp\left(\frac{12,100}{T_w}\right) \quad (4.16)$$

One shortcut with such models is that usually activation energies cannot really be considered as unique over the considered wide range of temperatures. Moreover, such a relation obtained by empirical fitting is limited to conditions very similar to that of the fit process and extrapolation is a risky procedure. As an example, no maximum can be inferred from the above formula for  $\gamma_i$ , whereas experimental data do exhibit such a maximum. For high temperatures, these models are limited to a constant maximum value.

Further, TPM catalytic data are also provided by means of the reaction rate  $K_w$  of the first-order reactions that occur in the homogeneous gaseous phase.

The results of the laboratory and flight experiments on the Space Shuttle tile heat shield can be approximated by the dependences (curve-fit relations):

$$K_{wi} = 53 \ exp\left(\frac{-1,875}{T}\right) \quad 500 \text{ K} < T_w < 900 \text{ K} \quad (4.17)$$

$$K_{wi} = 660 \ exp\left(\frac{-8,017}{T}\right) \quad 900 \text{ K} < T_w < 1,670 \text{ K} \quad (4.18)$$

The catalytic reaction rate constant,  $K_w$ , is related to the recombination probability  $\gamma_i$  by means of the Hertz-Knudsen relationship:

$$K_{wi} = \gamma_i \left( \frac{R_0 T_w}{2\pi M_A} \right)^{0.5} \quad (4.19)$$

where  $M_A$  is the atomic mass of  $i$  and  $R_0$  the universal gas constant.

Measurements on the US Space Shuttle surface insulation lead to values of the catalyzed reaction rate constants for atomic oxygen and nitrogen of about 1 m/s. It is worth noting that the experimental values of  $\gamma_i$  and  $\beta$  are characterized by

heavy scatter since they depend on the conditions under which they were obtained. Therefore, in general, the use of effective coefficients does not make it possible to correctly describe the heat transfer over the entire surface and along with the entire vehicle re-entry trajectory. However, catalytic effects result in very substantial differences in heat transfer that must be taken into account for a reliable vehicle TPS design.

## 4.4 The Apollo-Like CRV Concept and the LEO Re-entry Flight Scenario

In the light of Space Shuttle retirement, the capsule technology is still the safest and cheapest way to get into orbit and return back to Earth, especially in the case of high energy re-entry as those for manned space exploration missions to Moon and Mars. Therefore, in this chapter, a low-lift capsule design concept, close to the NASA Orion Crew Exploration Vehicle (CEV), was further investigated, as Crew Return Vehicle (CRV) for the International Space Station (ISS) support servicing.

### 4.4.1 *Vehicle Concept Overview*

The re-entry system is an Apollo-style capsule measuring about 5 m in diameter, with a nose radius of 6.05 m, a sidewall angle of  $33^\circ$ , and an overall height of 3.8 m. The offset center of gravity (cg) is located at  $x/D = 0.26$  and  $y/D = -0.0353$  (Fig. 4.42).

This vehicle concept represents a scaled-up version of the ARD capsule, which is a flying test bed successfully experimented by ESA, in October 1998, on the top of the Ariane 503 launcher, to obtain accurate flight data for comparison with results from experimental and numerical tools used for space vehicle design through all phases of flight [5]. So, the ARD was oversized to accommodate up to six crew members for the ISS (see Figs. 4.3 and 4.4). In particular, the capsule diameter was chosen to allow for the CRV/Ariane 5 integration, since the ESA launcher features a diameter of about 5.4 m.

As preliminary TPS design approach, the capsule heat shield has been supposed to be made of shuttle-like tiles. This design assumption is suggested since the LEO servicing is in more need of the immediate mission scenario, and lack of maturity in new ablative material kind exists. Therefore, let us assume that the capsule forebody thermal shield is built of high reusable surface insulator (HRSI) tiles, for the hemispherical part, and of reinforced carbon–carbon (RCC) tiles, for the corner side, where are expected more challenging heat flux conditions.

HRSI tiles cover the bottom of the US Shuttle Orbiter and provide protection against temperature up to about 1,530 K. They have a black ceramic coating (RCG)

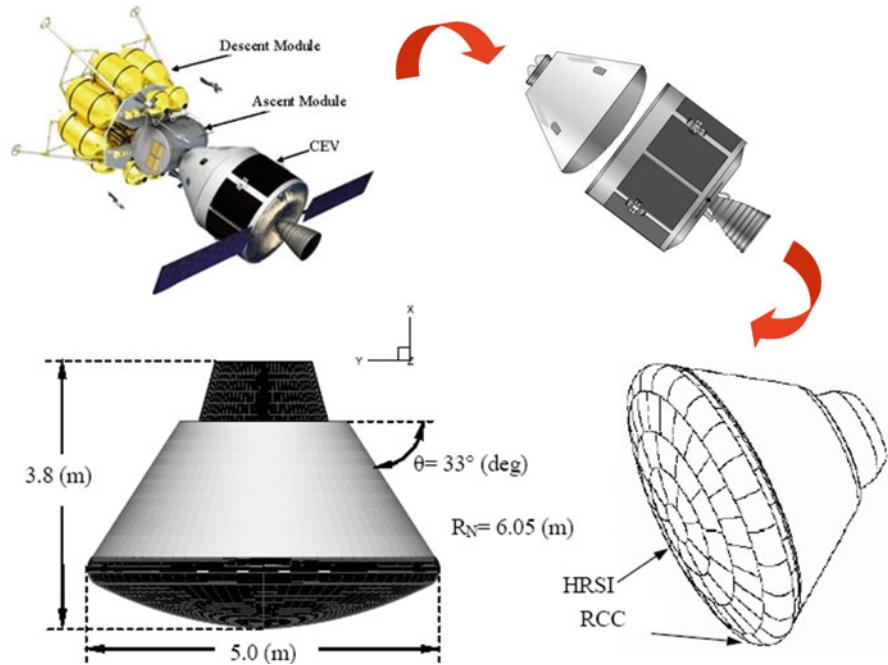


Fig. 4.2 Vehicle configuration with quotes and thermal shield layout



Fig. 4.3 ARD with Ariane V



**Fig. 4.4** CRV internal layout

that is a powdered tetrasilicide and borosilicate glass, which helps them to radiate heat during re-entry ( $\varepsilon = 0.85$ ).

RCC tiles cover nose and wing leading edges of Orbiter, which are the highest temperature areas of the shuttle. RCC is a composite material consisting of carbon fiber reinforcement in a matrix of graphite, often with a silicon carbide coating to prevent oxidation. The operating range of RCC is from 120 K to about 1,920 K.

#### 4.4.2 Description of Design Approach and Used Tools

The CRV vehicle has a number of extreme loading flight conditions for which analyses are required. It must return from orbit, fly trimmed throughout hypersonic and supersonic regimes until landing is gained, and withstand severe aeroheating. CRV aerodynamics (AEDB) and aerothermodynamics (ATDB) design relies on both engineering-level and numerical-based analysis. Indeed, the CRV re-entry scenario, together with the associated loading conditions, is assessed by means of ENTRY code (see Fig. 4.5); then, increasing the order of accuracy, ENTRY outputs are considered as realistic flight conditions to be supplied as input for more reliable vehicle flowfield analysis carried out by means of CFD simulations. In particular, CRV aerodynamics, needed for flight mechanics analyses, is provided as a function of Mach number, Reynolds number, Kundsen number, and angle of attack (AoA), according to the “space-based” design approach (SBDA).

On the other hand, CRV aerothermodynamics, needed for TPS sizing activities, is evaluated at a number of selected points along with the re-entry trajectory of the vehicle, as prescribed by the “trajectory-based” design approach (TBDA).

As suggested by Fig. 4.6, the first design approach (i.e., SBDA) dictates the generation of a complete data set as function of a number of independent parameters (i.e.,  $M_\infty$ ,  $Re_\infty$ ,  $\alpha$ ,  $\beta$ ); the second one (i.e., TBDA) consists in performing the aerothermal computations at a finite number of “critical” points on the given

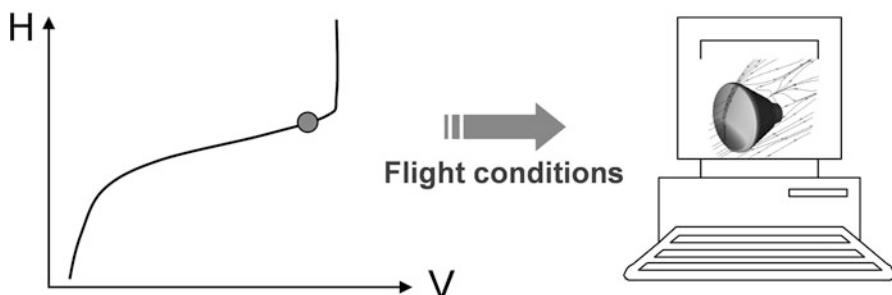
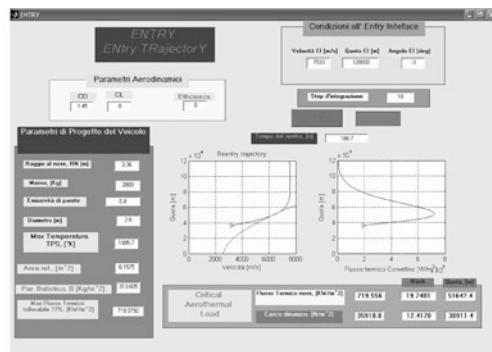


**Fig. 4.5** ENTRY code and CFD simulation

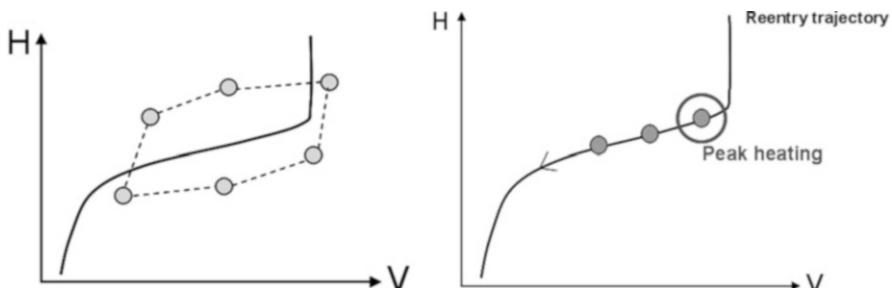


**Fig. 4.6** Space-based and trajectory-base design approaches

nominal design trajectory. In both cases, by using an engineering-based design tool, one can rapidly develop both AEDB and ATDB databases as a function of the free-stream parameters in a matter of hours.

The AEDB development plan centers on the philosophy of using engineering-based analyses as the primary database development tool while using CFD investigations as a database validation tool, as a complementary tool where appropriate, and as a primary database development tool where simplified analysis is inappropriate.

In particular, the appraisal of CRV aerodynamic characteristics has been performed with engineering-level code SIM, CFD codes, and the DSMC code DS2V, described in the following paragraphs.

#### 4.4.2.1 Engineering-Based Design Tool

From engineering point of view, several reliable correlation formulae exist to support design estimations.

A lot of them have been collected by the authors in ENTRY code in order to define the re-entry flight scenario of a proposed vehicle. ENTRY synthesizes the state of art of engineering analysis with careful attention to provide realistic re-entry flight conditions to be supplied as input to the CFD calculations, to simulate the flowfield around the vehicle, and hence to design its heat shield.

Engineering-based aerodynamic and aerothermodynamic analyses have been extensively performed by using a 3-D panel methods code, namely SIM (surface impact method). This tool at high supersonic and hypersonic speeds is able to accomplish the aerodynamic and aerothermodynamic analyses of a complex re-entry vehicle configuration by using simplified approaches as local surface inclination methods and approximate boundary-layer methods, respectively. Surface impact methods (SIM), typical of hypersonics, are Newtonian, modified Newtonian, tangent-cone and tangent-wedge theories.

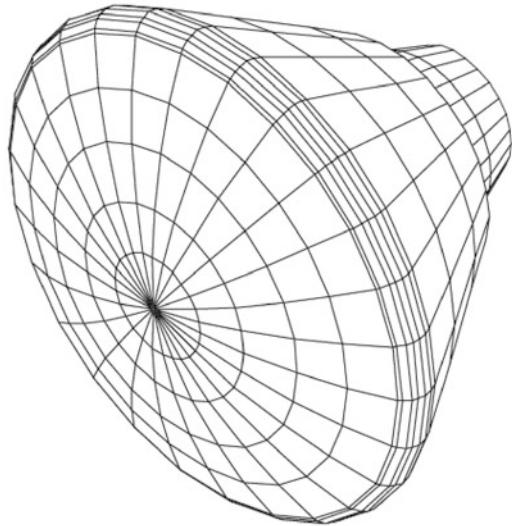
The heat flux calculations have been performed using both SIM code and simplified engineering relationships. This in order to confirm and integrate the tool results (heat loads) at the most critical parts of the vehicle (e.g., vehicle stagnation-point and shoulder leading edges).

The SIM engineering code performs the aero-thermal analysis of the vehicle configurations based on the surface streamlines. The streamlines are generated starting from the inviscid surface velocities generated previously by the code, in the aerodynamic analysis phase. The aeroheating analysis is performed along each streamline by using a simple one-dimensional boundary-layer method.

The generic vehicle component may be modeled as either a flat plate or a leading edge by selecting the appropriate boundary-layer model. In Fig. 4.7 a typical mesh surface of CRV that has been used for engineering-level computations is shown.

Moreover, ENTRY enables also rapid performance estimations within trade studies, such as for example evaluation of TPS requirements for evolving mission profiles. For example, ENTRY quickly finds the heating rate profile as well as the corresponding heat load, by only providing the geometry of the OML (outer mold line) of the processing capsule vehicle, as will be shown hereinafter.

The trajectory heating profile is also computed. ENTRY performs stagnation-point heating calculation by using alternatively Zoby, Scott, or Tauber equations in the case of perfect gas and Fay–Riddell relationship for chemically reacting flow. The latter yields

**Fig. 4.7** CRV panel mesh

$$\dot{q}_{\text{co}} = 0.57 \left( \frac{4}{3} \right)^k \text{Pr}^{-0.6} (\rho_w \mu_w)^{0.1} (\rho_e \mu_e)_s^{0.4} \left[ 1 + (Le^\phi - 1) \left( \frac{h_d}{h_e} \right) \right] (h_e - h_w) \left( \frac{du_e}{dx} \right)_s^{0.5} \quad (4.20)$$

where the index  $k$  is equal to 0 for two-dimensional flow and  $k$  is equal to 1 for axisymmetric flow, while the free-stream density  $\rho$  and velocity  $u$  are known from the re-entry trajectory solution. The wall enthalpy refers to radiative equilibrium conditions at a constant emissivity  $\varepsilon$  of 0.8. The exponent  $\phi$  of Lewis number is 0.52 for the equilibrium boundary layer, 0.63 for the frozen case over a FCW, and  $-\infty$  for frozen flow with NCW.

The term  $h_d$  is the chemical heat of formation of each of the species times the atomic mass fraction ( $Y_i$ ) in the boundary-layer edge flow:

$$h_d = \sum_i Y_i (\Delta h_f^o)_i \quad (4.21)$$

$h_d$  represents the chemical energy stored by the molecular dissociation behind the shock, i.e., when the TPM is FC,  $h_d$  is released by atomic recombination at the surface.

The stagnation-point velocity gradient ( $du_e/dx$ )<sub>s</sub> reads

$$\left( \frac{du_e}{dx} \right)_s = \frac{1}{(R_N)_{\text{eff}}} \sqrt{\frac{2(p_e - p_\infty)}{\rho_e}} \quad (4.22)$$

It utilizes an effective nose radius ( $R_N$ )<sub>eff</sub> as a function of the forebody bluntness parameter of the vehicle because the CRV features a truncated spherical nose. In Ref. [10] can be found (see also Chap. 2) that

$$(R_N)_{\text{eff}} = 0.877 R_N \quad (4.23)$$

Note that when the capsule flies at AoA, this effective nose radius was expected to decrease, suggesting that the engineering estimations result in nonconservative evaluations and CFD simulations must be considered.

The edge condition, denoted by subscript “e” refers to air in local thermodynamic and chemical equilibrium behind a normal shock wave. In effect in all likelihood, the gas behind the shock is in a nonequilibrium state, but the approximation of chemical equilibrium boundary layer is reasonable in the stagnation region. In any case, fully catalytic heating values are fairly insensitive to the exact edge conditions (catalytic recombination helps to proceed toward equilibrium faster, but does not change equilibrium states (temperature, density) and composition of a gas).

In the calculation of the heat transfer rates, the wall enthalpy is set to the value corresponding to the radiation equilibrium temperature at the previous time step.

Results for finite catalytic case lie between the results of the two limiting case of FCW and NCW and can be determined by using an approach like Goulard’s. Assuming that the total heat of recombination for the atoms reacting at the wall be transferred to the heat shield surface, this yields

$$\dot{q}_{\text{co}} = \dot{q}_c + \dot{q}_{\text{cat}} = \dot{q}_c + \eta \dot{q}_D \quad (4.24)$$

where  $\dot{q}_c$  is the conduction component of heat transfer (i.e., with  $\phi = -\infty$  in Eq. 4.20) and  $\dot{q}_{\text{cat}}$  the diffusion one, where

$$\dot{q}_D = 0.57 \left( \frac{4}{3} \right)^k \text{Pr}^{-0.6} \text{Le}^{0.63} \left( \frac{\rho_w \mu_w}{\rho_e \mu_e} \right)^{0.1} (\rho_e \mu_e)^{0.5} \left( \frac{h_e - h_w}{h_e} \right) h_d \left( \frac{du_e}{dx} \right)_s^{0.5} \quad (4.25)$$

The factor  $\eta$  accounts for the recombination rate of atoms diffusing to the heat shield wall and reads

$$\eta = \frac{1}{1 + \frac{S}{K_w}} \quad (4.26)$$

where the boundary-layer diffusion rate, S, is

$$S = 0.763 \frac{\text{Pr}^{-0.6} \text{Le}^{0.63}}{\rho_w} \left( \frac{\rho_w \mu_w}{\rho_e \mu_e} \right)^{0.1} (\rho_e \mu_e)^{0.5} \left( \frac{du_e}{dx} \right)_s^{0.5} \quad (4.27)$$

and  $K_w$  is the catalytic reaction rate constant.

The computational procedure performed by ENTRY in these cases starts from the equilibrium flow conditions behind the normal shock wave evaluated by means of NASA code, namely, CEA (Chemical Equilibrium with Applications). Hence, the total pressure  $P_{t2}$  is determined by isentropically compressing the gas until  $h_2 = h_{t2}$ . From the total properties  $P_{t2}$ ,  $h_{t2}$ , and the wall temperature  $T_w$ , the parameters  $\rho_e$ ,  $\mu_e$ ,  $\rho_w$ ,  $\mu_w$ , and  $h_w$  for Eqs. (4.20) and (4.24) are finally determined and used for calculating  $\dot{q}_{co}$  and  $T_w$  at radiative equilibrium conditions.

#### 4.4.2.2 CFD-Based Design Tool

CFD analyses of the CRV vehicle are performed with both the H3NS in-house code developed at CIRA and the FLUENT commercial code.

H3NS solves the flowfield governing equations, including chemical and vibrational nonequilibrium, with a finite volume approach; a flux-difference splitting upwind scheme is used for the convective terms, with a second-order ENO-like reconstruction of cell interface values. The viscous fluxes are calculated by central differencing, i.e., computing the gradients of flow variables at cell interfaces by means of Gauss theorem. Time integration is performed by employing an Euler Forward scheme coupled with a point implicit treatment of the species and vibration energies source terms. Both sequential and parallel versions of the code are currently available. Computational analyses of the CRV flowfields are also performed by means of several user-defined functions (UDF) developed by the authors, which incorporate as core solver the FLUENT code. With such UDF, FLUENT can manage, e.g., vibrational relaxation, many catalyticity models, radiative equilibrium at the wall and other boundary conditions, etc.

#### 4.4.2.3 Direct Simulation Monte Carlo Method

When rarefaction effects become important and the continuum hypothesis no longer holds, CFD Navier–Stokes simulation fail and a molecular approach such as the Direct Simulation Monte Carlo (DSMC) method is necessary. It considers the gas as made up of discrete molecules that are represented by millions of simulated molecules; it relies on formulae from the kinetic theory of gases. The Direct Simulation Monte Carlo (DSMC) software used in this chapter is the DS2V code of Bird which is briefly described in the following. The DSMC method considers the gas as made up of discrete particles that are represented by millions of simulated molecules; it relies on formulas from the kinetic theory of gases. Movement and evolution of each molecule in the simulated physical space is produced by collisions with other molecules and with the body under study, in both cases exchanging momentum and energy. Excitation of rotational and vibrational degrees of freedom and chemical reactions (if any) can be also taken into account. The computational domain, including the test body, is divided in cells; these are used only for sampling

the macroscopic properties and for selecting the colliding molecules. Movement of each molecule from a cell to another one is the product of the velocity (i.e., the resultant of the convective and thermal velocities) and a time step. Macroscopic thermo-fluid-dynamic quantities of the flowfield (density, temperature, pressure, and so on) are computed in each cell as an average over the molecules. DS2V uses transient subcelles in which a transient background grid is built on a single cell and the collision routine, based on nearest-neighbor collisions, is applied. The resolution of the transient grid depends on the number of simulated molecules, and, approximately, one simulated molecule corresponds to one subcell.

DS2V provides in output, during the run, the ratio of the local mean separation between collision partners to the local mean free path. This parameter is indicative of the quality of a run; it should be less than unity everywhere in the computational domain. Bird suggests the value of 0.2 as a limit value.

The present applications rely on the fully accommodated Maxwell gas–surface interactions.

DSMC simulation, however, is very time consuming; thus, performing a very high number of simulations within a phase A design is not allowable. Therefore, some bridging formulae have been tested for quick computations of CRV high-altitude aerodynamics appraisal.

## 4.5 Mathematical Formulation and Numerical Solution

The physical-mathematical modeling describing a flowfield around an hypersonic vehicle deals with balance equations for a multispecies chemically reacting gas mixture supplemented with an appropriate set of chemical reactions (i.e., the reaction mechanism) and with equations modeling species vibrations relaxation (i.e., thermal nonequilibrium).

### 4.5.1 Flowfield Governing Equations

The mathematical formulation describing the flowfield around a hypervelocity vehicle deals with balance equations for mass, momentum, total energy, and individual species. The full set of equations for a laminar viscous compressible continuum flow in thermal and chemical nonequilibrium, assuming the air to be a mixture of  $N_s$  perfect gases (mixture species) and  $N_v$  vibrating species, can be written in the integral conservation form as follows:

$$\frac{\partial}{\partial t} \int_V \vec{W} \, dV + \int_S (\vec{F}_{\text{inv}} + \vec{F}_{\text{vis}}) \cdot \vec{n} \, dS + \frac{\Gamma}{r} \int_V (\vec{A}_{\text{inv}}^* + \vec{A}_{\text{vis}}^*) \, dV = \int_V \vec{\Omega} \, dV \quad (4.28)$$

where  $\vec{W} = [\rho, \rho u, \rho v, \rho w, e_t, \rho_1, \dots, \rho_{Ns-1}, \rho e_{v1}, \dots, \rho e_{vN_v}]^T$  is the unknown state vector of the conserved quantities, in which  $\rho$  is the fluid density;  $\rho u$ ,  $\rho v$ , and  $\rho w$  are the momentum densities;  $e_t$  is the total internal energy per unit mass; and  $\rho_i$  and  $e_{vi}$  are, respectively, the density and the vibrational energy of the  $i$ th species, while  $\rho e_{vi}$  accounts for vibrational energy conservation.  $\vec{F}$  is the flux vector (splitted into an inviscid and a viscous part).

The vector  $\vec{F}$  expression is well known, and therefore, it is not written here for simplicity.  $\vec{A}^*$  is the axisymmetric terms matrix (splitted into an inviscid and a viscous part), and  $\Gamma$  is equal to 1 for axisymmetric flows and 0 for 2-D and 3-D flows.  $\vec{\Omega} = [0, 0, 0, 0, 0, \Omega_1, \dots, \Omega_{Ns-1}, \Omega_{v1}, \dots, \Omega_{vN_v}]^T$  is the source terms vector. It defines the mass and energy exchange among the species as a result of the chemical reaction rate and the energy transfer due to the internal energy excitation processes. Hence,  $\vec{\Omega}$  models the nonequilibrium reactions of the gas.

Finally,  $V$  is the arbitrary control volume cell,  $S$  is its closed boundary control surface, and  $\vec{n}$  is the outward normal unit vector.

Equation (4.28) can be written in differential form as follows:

*Continuity:*

$$\frac{\partial \rho}{\partial t} + \vec{\nabla} \cdot (\rho \vec{V}) = 0 \quad (4.29)$$

*Momentum:*

$$\frac{\partial (\rho \vec{V})}{\partial t} + \vec{\nabla} \cdot (\rho \vec{V} \vec{V}) + \vec{\nabla} p = 2 \vec{\nabla} \cdot [\mu (\vec{\nabla} \vec{V})_o^s] \quad (4.30)$$

where

$$(\vec{\nabla} \vec{V})_o^s = \frac{1}{2} \left[ (\vec{\nabla} \vec{V}) + (\vec{\nabla} \vec{V})^T \right] - \frac{1}{3} (\vec{\nabla} \cdot \vec{V}) \vec{U} \quad (4.31)$$

*Energy:*

$$\begin{aligned} \frac{\partial (\rho e_t)}{\partial t} + \vec{\nabla} \cdot [(\rho e_t + p) \vec{V}] &= \vec{\nabla} \cdot \left[ \lambda \nabla T + 2\mu (\vec{\nabla} \vec{V})_o^s \cdot \vec{V} + \sum_i h_i \vec{J}_i \right] \\ &\quad - \sum_i h_i \dot{\omega}_i - \sum_j \dot{e}_{vj} \end{aligned} \quad (4.32)$$

where

$$\dot{e}_{vj} = (e_{vj}^{eq} - e_{vj}) \tau_{vj} \quad (4.33)$$

*Species:*

$$\frac{\partial(\rho Y_i)}{\partial t} + \vec{\nabla} \cdot (\rho \vec{V} Y_i) + \vec{\nabla} \cdot \vec{J}_i = \dot{\omega}_i \quad (4.34)$$

where

$$\dot{\omega}_i = m_i \sum_k \dot{\omega}_{ik} \quad (4.35)$$

*Vibrational energy:*

$$\frac{\partial(\rho e_{vj})}{\partial t} + \vec{\nabla} \cdot (\rho \vec{V} e_{vj}) = \dot{e}_{vj} \quad (4.36)$$

In these equations,  $\vec{V}$  is the velocity vector;  $Y_i$  is the mass fraction of the  $i$ th species and  $\dot{\omega}_i$  is the rate of change of  $\rho_i$  due to chemical reactions;  $J_i$  is the diffusive flux of  $i$ th species, which arises due to concentration gradients;  $m_i$  and  $h_i$  are, respectively, the molecular weight and enthalpy of  $i$ th species;  $p$  is the pressure;  $\underline{U}$  is the unit tensor;  $\mu$  is the viscosity; and  $\lambda$  is the thermal conductivity.

For each species, the perfect gas model applies and the Dalton's law is applicable:

$$p = \sum_i p_i \quad (4.37)$$

where  $p_i$  is the partial pressure of the  $i$ th species of the mixture.

As a consequence, the following relation for density holds:

$$\rho = \frac{p}{R_0 T \sum_i Y_i / m_i} \quad (4.38)$$

where  $R_0 = 8,314.5 \text{ JKmol}^{-1} \text{ K}^{-1}$  is the universal gas constant.

The internal energy of the mixture is defined as

$$e = \sum_i (Y_i e_i) \quad (4.39)$$

where  $e_i$ , internal energy of the single component gas, is the sum of the energies representing the different degrees of freedom of the molecules. Finally, the enthalpy is

$$h = \sum_i (Y_i h_i) \quad (4.40)$$

where the specific enthalpy for each species can be calculated as

$$h_i = e_i + R_i T \quad (4.41)$$

where  $R_i$  is the gas constant.

Computation of the diffusive fluxes requires knowledge of the transport coefficient.

#### 4.5.1.1 Transport Properties

For pure species, the following expressions are derived from kinetic theory of gases:

*Viscosity:*

$$\mu_i = \frac{2.6693 \times 10^{-6} \sqrt{m_i T}}{\sigma_i^2 \Omega_{\mu i}} \quad (4.42)$$

*Thermal conductivity:*

$$\lambda_i = \frac{15}{4} \left( \frac{\mu_i R_0}{m_i} \right) \left( \frac{4}{15} \frac{c_{pi} m_i}{R_0} + \frac{1}{3} \right) \quad (4.43)$$

*Mass diffusivity:*

$$D_{ij} = \frac{0.0188 \times T^{\frac{3}{2}} \sqrt{(m_i + m_j) / m_i m_j}}{p \sigma_{ij}^2 \Omega_{Dij}} \quad (4.44)$$

For what concern, instead, the global transport properties of the gas mixture, semiempirical rules may be applied, such as Wilke's mixing rule for viscosity  $\mu$  and thermal conductivity  $\lambda$ :

$$a = \frac{\sum_i \chi_i a_i}{\sum_j \chi_j \left\{ \frac{1}{\sqrt{8}} \left( 1 + \frac{m_i}{m_j} \right)^{-\frac{1}{2}} \left[ 1 + \left( \frac{a_i}{a_j} \right)^{\frac{1}{2}} \left( \frac{m_i}{m_j} \right)^{\frac{1}{4}} \right]^2 \right\}} \quad a = \mu, \lambda \quad (4.45)$$

where  $\chi_i$  is the mole fraction of specie  $i$  and  $a_i$  (equal to  $\mu_i$  or  $\lambda_i$ ) is obtained by kinetic theory of gases.

For the diffusion coefficient of the species  $i$  in the reacting mixture, the multicomponent diffusion coefficient is applied:

$$D_i = \frac{(1 - \chi_i)}{\sum_j \frac{\chi_i}{D_{i,j}}} \quad (4.46)$$

with  $D_{ij}$  evaluated by kinetic theory.

Finally, vibrational relaxation is modeled using a Landau–Teller formulation, where relaxation times are obtained from Millikan and White, assuming simple harmonic oscillators.

#### 4.5.1.2 Chemical Species and Reaction Mechanism

The chemically active species of much relevance in dissociated air are N<sub>2</sub>, O<sub>2</sub>, N, O, and NO. These species can be supplemented with ionized ones as flow energy becomes higher and higher. Therefore, within a LEO re-entry scenario (no flowfield ionization occurs), the gas is approximated as a finite rate chemistry mixture of the above species. The elementary reaction mechanism, governing the species in high-temperature air, deals with three dissociation reactions and two exchange reactions, as reported in Tables 4.1 and 4.2; there M, namely, reacting partner or third body,

**Table 4.1** Reaction rate parameters by Dunn and Kang model

No.	Reaction	$A_{f,r}$ (m <sup>3</sup> /kg mole s)	$\beta_{f,r}$	$E_{a,f,r}$ (J/kg mole)	Third body efficiency
1.	O <sub>2</sub> + M = 2O + M	$3.60 \times 10^{15}$	-1.0	$4.938 \times 10^8$	O <sub>2</sub> = 9, N <sub>2</sub> = 2, O = 25, N = NO = 1
2.	N <sub>2</sub> + M = 2N + M	$1.92 \times 10^{14}$	-0.5	$9.404 \times 10^8$	O <sub>2</sub> = 1, N <sub>2</sub> = 2.5, O = N = NO = 1
3.	N <sub>2</sub> + N = 3N	$4.15 \times 10^{19}$	-1.5	$9.404 \times 10^8$	—
4.	NO + M = N + O + M	$3.97 \times 10^{17}$	-1.5	$6.286 \times 10^8$	O <sub>2</sub> = N <sub>2</sub> = 1, O = N = NO = 20
5.	NO + O = O <sub>2</sub> + N	$3.18 \times 10^6$	1.0	$1.638 \times 10^8$	—
6.	N <sub>2</sub> + O = NO + N	$6.75 \times 10^{10}$	0.0	$3.118 \times 10^8$	—

**Table 4.2** Reaction rate parameters by Park model

No.	Reaction	$A_{f,r}$ (m <sup>3</sup> /kg mole s)	$\beta_{f,r}$	$E_{a,f,r}$ (J/kg mole)	Third body efficiency
1.	O <sub>2</sub> + M = 2O + M	$1.00 \times 10^{19}$	-1.5	$4.947 \times 10^8$	O <sub>2</sub> = N <sub>2</sub> = NO = 0.2, O = N = 1
2.	N <sub>2</sub> + M = 2N + M	$3.00 \times 10^{19}$	-1.6	$9.412 \times 10^8$	O <sub>2</sub> = N <sub>2</sub> = NO = 0.233, O = N = 1
3.	NO + M = N + O + M	$1.10 \times 10^{14}$	0.0	$6.277 \times 10^8$	O <sub>2</sub> = N <sub>2</sub> = 0.05, O = N = NO = 1
4.	NO + O = O <sub>2</sub> + N	$2.40 \times 10^6$	1.0	$1.598 \times 10^8$	—
5.	N <sub>2</sub> + O = NO + N	$1.80 \times 10^{11}$	0.0	$3.193 \times 10^8$	—

can be any of the five reacting species, thus providing or removing collision energy. Efficiencies of the third body are also reported in Tables 4.1 and 4.2, since they are employed in computations to increase CPU time efficiency. Hence, the reaction mechanism results in a system of 17 chemical reactions, with 17 forward and backward reactions rate coefficients

Chemical reactions proceed with forward ( $f$ ) reaction rates,  $k_{f,r}$  ( $r = 1 \dots 17$ ), which appear in the source terms ( $\dot{\omega}_i$ ) of the species transport equation (Eq. (4.34)). Those rates are expressed in the Arrhenius form as

$$k_{f,r} = k_{f,r}(\bar{T}) = k_f(T^a T_v^b) = A_{f,r} \bar{T}^{\beta_{f,r}} \exp\left(-\frac{E_{a_{f,r}}}{R_o \bar{T}}\right) \quad (4.47)$$

with the constant provided in Tables 4.1 and 4.2.

Dunn–Kang model uses only one temperature to describe all the energy modes ( $\bar{T} = T$ , thermal equilibrium), whereas Park model assumes that the temperature  $\bar{T}$  can be  $T$ ,  $T_v$ , or  $T^a T_v^b$  (namely, rate controlling temperature) depending on the reaction; as well known, Park's two-temperature model, accounting for both  $T$  and  $T_v$ , provides more accurate results. In fact, Park uses  $T$  to describe translational and rotational energy modes and  $T_v$  for vibrational and electron-translational modes [13–15].

As shown in Tables 4.1 and 4.2, considerable discrepancies among the reaction rate coefficients are introduced into the chemical model by experimental uncertainties in the determination of the chemical kinetics constants. Since the experimental determination of these constants are differing in the literature by nearly two orders of magnitude, it became essential to choose the reaction rate coefficients which have a significant influence on the chemical composition of the gas. For example, the nitrogen exchange and dissociation reaction are dominant for the gas composition at about 75 km altitude. While nearly to 50 km altitude the reactions are closer to the equilibrium state, the dissociation reactions of nitrogen and oxygen dominate the gas composition.

Among the simpler sets of homogeneous reactions, it is standard to use the following set of only three chemical reactions, known as Zeldovich process:



It considers only oxygen dissociation, due to collisions with molecular nitrogen, and two exchange reactions. This model can be explained considering that the gas is so hot that the oxygen dissociates nearly completely, while the nitrogen does not dissociate completely and is not as fast as the oxygen. Finally, exchange reactions are important because they determine the speed of nitrogen dissociation.

### 4.5.1.3 Boundary Conditions

The properties of a surface are represented by the emissivity ( $\varepsilon$ ) and by the wall chemical activity (i.e.,  $\gamma_i$  or  $K_{wi}$ ). As atoms produced by dissociation reactions strike the surface, the catalytic property of a wall is implemented by means of a production term (i.e.,  $\dot{\omega}_{wi} \neq 0$ ) for the boundary condition of the boundary-layer problem to solve. Indeed, steady-state mass atomic conservation at the wall leads that the production of  $i$ th species due to the catalytic recombination rate must be balanced by the rate of diffusion to the surface:

$$(\dot{\omega}_a)_w = -(\rho_a v_a)_w \quad (4.49)$$

The source term  $\dot{\omega}_a$  is given by Goulard's relationship:

$$\dot{\omega}_a = K_{wa} (\rho_w Y_{iw})^p \quad (4.50)$$

where  $p$  is the reaction order and  $K_{wa}$  is the catalytic reaction rate.

The diffusive flux  $\rho_a v_a$  is expressed by means of Fick's law:

$$\rho_a v_a = -\rho D_a \frac{\partial Y_a}{\partial y} \quad (4.51)$$

So that

$$(\dot{\omega}_a)_w = K_{wa} (\rho_w Y_{iw})^p = \left( \rho D_a \frac{\partial Y_a}{\partial y} \right)_w \quad (4.52)$$

When the TPM does not promote any particular reaction, the TPS surface refers as NCW (i.e.,  $K_{wi} = 0$  and  $\gamma_i = 0$ ); the wall is considered to be absolutely indifferent to kinetics, and there is no species depletion or production at the wall (i.e.,  $\dot{\omega}_{wi} = 0$ ).

On the contrary, if the TPM can activate any reactions at its surface, it is called FCW (i.e.,  $K_{wi} = \infty$  and  $\gamma_i = 1$ ), that is, complete recombination, because the flow tends toward chemical equilibrium at the wall.

The molecular species concentrations at the wall have to be set equal to their equilibrium concentrations according to the local temperature and pressure. For wall temperatures below 2,000 K (cold walls), this corresponds to the free-stream composition.

Between these two limit cases (i.e.,  $0 < \gamma_i < 1$ ), the vehicle surface is considered as PCW, and the heat fluxes to the vehicle can greatly differ depending on the value of  $\gamma_i$ . Furthermore, when a low conductive TPS protects the vehicle (as modern fiber ceramic material with high emissivity), the radiative equilibrium boundary condition holds at vehicle surface (i.e., the heat flux transported through conductive and diffusive mechanisms toward the wall is fully reradiated into atmosphere). Therefore, during numerical simulations, the wall temperature is calculated by the

Stephan–Boltzman law and is updated explicitly at each stream wise station by means of a Newton–Raphson approach that usually achieves convergence within a number of iterations.

### 4.5.2 Numerical Technique

The governing equations, together with the proper boundary conditions, are discretized using a cell centered finite volume formulation on a structured multiblock grid. For the single mesh cell, the discretized equation reads:

$$\frac{d\vec{W}_c}{dt} + \frac{1}{V_c} \sum_{f=1}^6 \left( \vec{F}_{cinv} + \vec{F}_{cvvis} \right)_f \cdot \vec{n} + \frac{\Gamma}{r} \left( \vec{A}_{cinv}^* + \vec{A}_{cvvis}^* \right) = \vec{H}_c \quad (4.53)$$

where  $f$  is the index of the cell face, while  $c$  refers to the single cell of the computational domain.

The inviscid fluxes at cell interfaces are calculated by using a flux-difference splitting (FDS) Riemann solver, since upwind methods are particularly suitable for high-speed flows. However, second-order accuracy is not automatically reached; for this reason, a second-order ENO (Essentially Non Oscillatory) technique for the reconstruction of cell interface values is employed. The viscous fluxes are calculated by central differencing, i.e., computing the gradients of flow variables at cell interfaces by means of Gauss theorem. The method is second-order accurate in space. Time integration is performed by employing both an explicit single-stage (Euler forward) algorithm and an explicit five-stage Runge–Kutta scheme, coupled with an implicit evaluation of the chemical and vibrational source terms, under the hypothesis of time marching approach to reach the steady solution for the flow. Multigrid techniques are used to accelerate convergence.

### 4.5.3 The Computational Grid Domain

CFD computations have been carried out on a multiblock structured grid (shown in Fig. 4.8) since accurate computations of the gradients appearing in the field equations require structured grids. The grid used consists of 50 cells in the body-normal direction, 40 cells circumferentially, and 150 in stream wise direction. All the computational grid domains are tailored for free-stream conditions at the selected trajectory points. Therefore, for each case, new grid has been created to properly accommodate for the detached bow shock location. The baseline grid topology for this work consists of 32 grid blocks for an overall number of about 750.000 cells (half body only, since no sideslip velocity has been accounted for) and is constructed to permit local refinement of the shoulder and the wake core regions while maintaining point matching at every block interface.

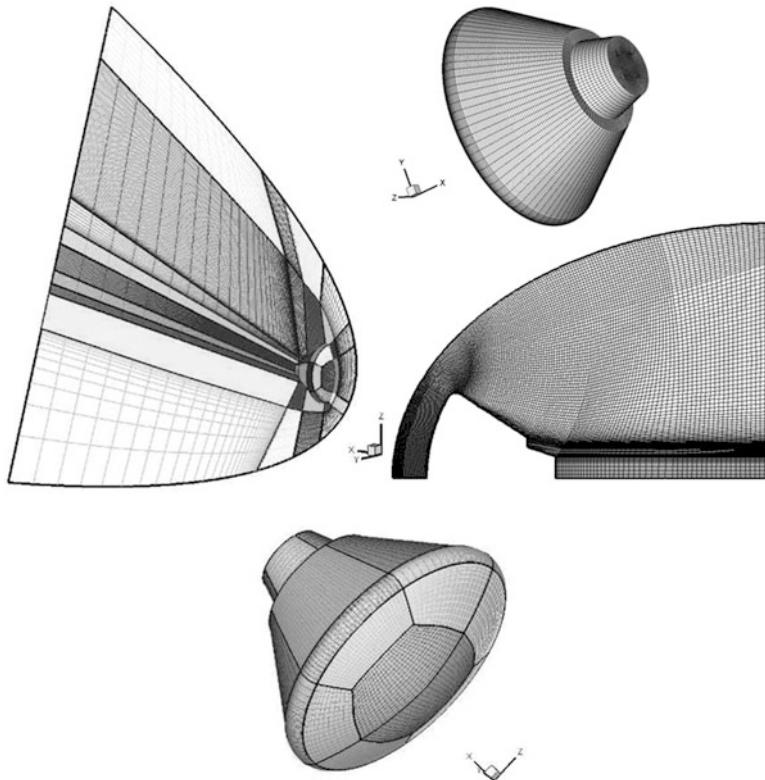


**Fig. 4.8** Multiblock computational grids. 3-D and 2-D axisymmetric mesh domains

The mesh was initially generated algebraically and then adapted as the solution evolved (i.e., solution adaptive approach), aligning the grid with the bow shock and clustering points in the boundary layer. This reduces spurious oscillations in the stagnation area one often gets for hypersonic flow especially for large blunt-body flowfield computations. A close-up view of 2-D axisymmetric and 3-D mesh on vehicle surface can be seen in Fig. 4.8.

The distribution of surface grid points was dictated by the level of resolution desired in various areas of vehicle such as stagnation region and base fillet, according to the computational scopes. For example, the distribution of grid points in the wall-normal direction is driven by a prespecified value of cell Reynolds number:

$$\text{Re}_{\text{cell}} = \frac{\rho_w a_w \tau_w}{\mu_w} \quad (4.54)$$

at the wall, as a constraint, where  $\rho_w$ ,  $a_w$ , and  $\mu_w$  are the density, sonic velocity, and viscosity evaluated at the surface of the vehicle. A cell Reynolds number of 10 was found to be able to determine a grid spacing ( $\tau_w$ ) for a reliable laminar

heating predictions. Further, the number of grid points in the shoulder region is large enough to capture the rapid expansion that the flow experienced locally and, then, to accurately predict flow separation and angle of the resulting shear layer. There are also sufficient points in the separated flow region to resolve the vortical structure at the beginning of the wake flow.

Finally, several boundary conditions can be applied for the viscous computations, including different catalycity models and the possibility to assign at the wall a fixed temperature or a radiative equilibrium condition.

## 4.6 Model Validation

The key to perform reliable flow simulations is the aerothermodynamic validation of the theoretical models, describing the high-temperature effects in hypersonic gas flow, by using wind tunnel and free flight experimental data.

To this aim, the tests of ELECTRE model in PWT were considered as benchmark evaluations. Therefore, some experimental activities performed in wind tunnel with this standard test article were duplicated numerically through CFD evaluations. Experimental and numerical comparison of results concerning the hypersonic flow around the test model was reported.

### 4.6.1 Test Article Geometry and Computational Domain

ELECTRE test article (see Fig. 4.9) consists of a blunt conical body with total length of 0.4 m, semiaperture cone angle of  $4.6^\circ$ , and hemispherical nose with radius of 0.035 m. It was tested in flight and in wind tunnel, becoming a standard reference model to study nonequilibrium hypersonic flow past blunt-body configurations. The

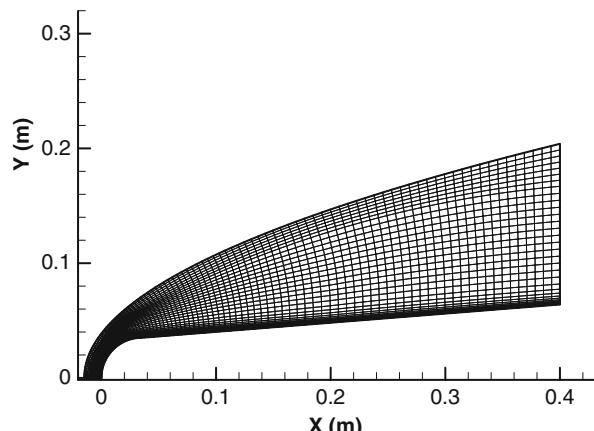


**Fig. 4.9** ELECTRE test article geometry and axisymmetric mesh domain ( $60 \times 120$  cells)

**Table 4.3** Reference calibration point conditions of the HEG nozzle

$T_\infty$ (K)	$P_\infty$ (Pa)	$\rho_\infty$ (kg/m <sup>3</sup> )	$V_\infty$ (m/s)	$M_\infty$ (—)	$Re_\infty/m$ (1/m)	$Y_O$ (—)	$Y_N$ (—)	$Y_{NO}$ (—)	$Y_{O_2}$ (—)
790	430	$1,640 \times 10^{-6}$	5,919	9.7	$270 \times 10^3$	0.179	$1.0 \times 10^{-6}$	$3.3 \times 10^{-2}$	$3.6 \times 10^{-2}$

computational domain employed for CFD analyses is shown in Fig. 4.9. It consists of  $60 \times 120$  cells with a minimum normal wall spacing of  $10^{-5}$  m, as a sensitivity of the computed solutions with respect to the grid has shown to be necessary to obtain a sufficient resolution of the important flow features.

This mesh have been selected by means of several accuracy tests performed starting from a coarse mesh of  $50 \times 70$  cells and also taking into account for comparisons between CFD and engineering results, as provided by ENTRY.

#### 4.6.2 Test Conditions and Engineering Analysis

Test conditions are summarized in Table 4.3. They correspond to operating conditions of the HEG wind tunnel located at DLR Gottingen. In correspondence of these test conditions, two different test cases were run considering alternatively the specimen wall as NC, and FC for N and O species.

As early assessment of work, several engineering evaluations have been accomplished by means of ENTRY.

Pressure coefficient and convective heat transfer distributions on the test article wall were provided. ENTRY quickly evaluates the pressure distribution by using the surface impact method, typical of hypersonics:

$$C_p = C_{p12} \cos^2 \theta \quad (4.55)$$

where  $C_{p12}$  is the stagnation-point pressure coefficient that depends on the flow theory one considers, while  $\theta$  represents the angle between free-stream direction and radius vector from center of curvature of nose.

If Newtonian flow theory holds,  $C_{p12}$  is equal to 2, while in the case of modified Newtonian theory, it follows that  $C_{p12}$  reads:

$$C_{p12} = \left( \frac{p_{12}}{p_\infty} - 1 \right) \frac{2}{\gamma M_\infty^2} \quad (4.56)$$

Regarding to the aeroheating, ENTRY evaluates the convective heat transfer around both hemispherical nose and spherically capped cone, according to the Lees theory (see Chap. 2). Lees approach shows that at high Mach number conditions, for a blunt cone with nose radius  $R_N$  and semiaperture vertex angle of  $\theta_c$ , at any point on the cone surface, the ratio of heat transfer  $\dot{q}_w(s')$  to the stagnation value  $\dot{q}_{co}$  reads:

$$\text{Nose} \quad \frac{\dot{q}_w(\theta)}{\dot{q}_{co}} = \frac{2\theta \sin \theta \cos^2 \theta}{\sqrt{D(\theta)}} \quad (4.57)$$

$$\text{Cone skirt} \quad \frac{\dot{q}_w(s')}{\dot{q}_{co}} = A(\theta_c) \frac{s'}{R_N} \left[ B(\theta_c) + \left( \frac{s'}{R_N} \right)^3 \right]^{-\frac{1}{2}} \quad (4.58)$$

Equation (4.58) is valid for  $s'/R_N \geq \cot \theta_c$ , where  $s'$  is the curve length measured along the cone surface of the effective sharp-nosed cone and

$$\begin{aligned} A(\theta_c) &\approx \frac{\sqrt{3}}{2} \sin \theta_c \sqrt{\frac{\pi}{2} - \theta_c} \\ B(\theta_c) &\approx \frac{3}{16} \frac{1}{\sin^4 \theta_c} \left[ \frac{D(\theta)}{\theta} \right]_{\theta=\frac{\pi}{2}-\theta_c} - \cot^3 \theta_c \\ D(\theta) &\approx \theta^2 - \frac{1}{2}\theta \sin 4\theta + \frac{1}{8}(1 - \cos 4\theta) \end{aligned} \quad (4.59)$$

### 4.6.3 CFD Results

CFD aerothermodynamic computations have been performed with different wall catalytic boundary conditions for the test article. The computations refer to fully laminar nonequilibrium flow conditions with model temperature fixed to  $T_w = 300$  K. The flowfield past the test bed is shown in Fig. 4.10, where the Mach

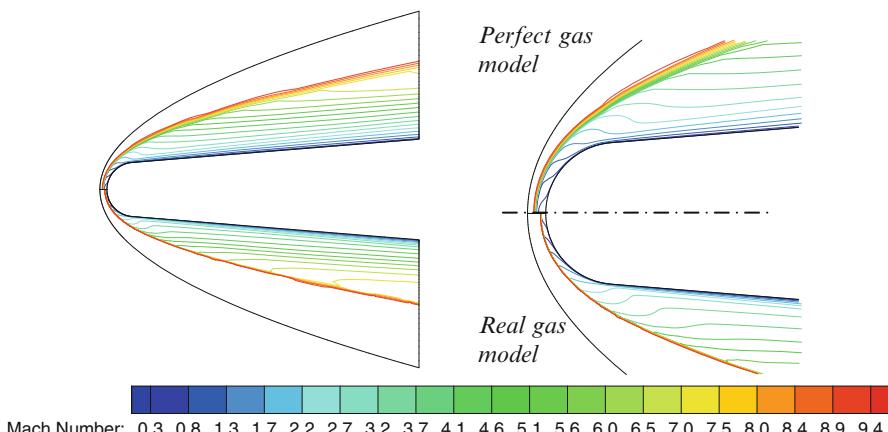


**Fig. 4.10** Mach number contours field. Comparison between perfect gas (up) and real gas model. Detail on the nose region of test bed (right)

number contour field is plotted, comparing the results obtained in the case of perfect gas and real gas model.

As one can see, the flowfield in the case of real gas model markedly differs from the perfect gas one, since the shock envelopes more closely the test bed than in the perfect gas case, as confirmed by pressure and temperature distributions along the stagnation line reported in Figs. 4.11 and 4.12, respectively. In these figures are reported some comparisons for pressure and temperature distribution along the stagnation line, in the case of perfect gas and real reacting gas, the last one for both cases of NCW and FCW.

In particular, the dashed curve on the left of Fig. 4.12 highlights that the stagnation shock layer is in nonequilibrium condition up to boundary layer, while, on the right, the temperature profile along with the stagnation line for both NCW

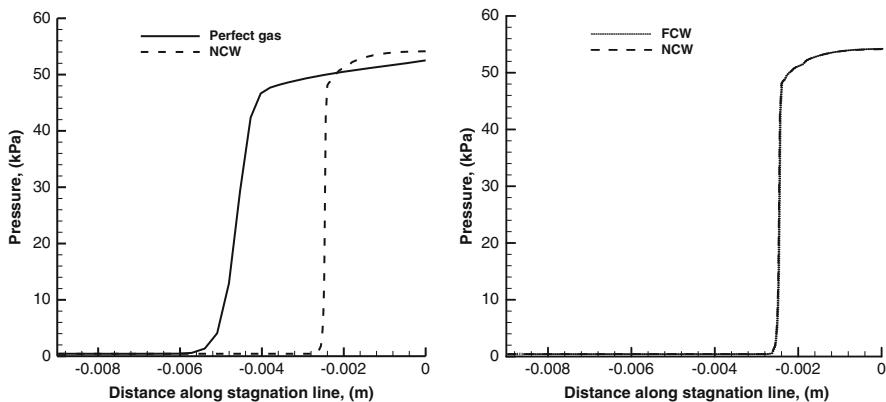


**Fig. 4.11** Pressure distribution along the stagnation line. Comparison between perfect gas and reacting (i.e., NCW) gas case

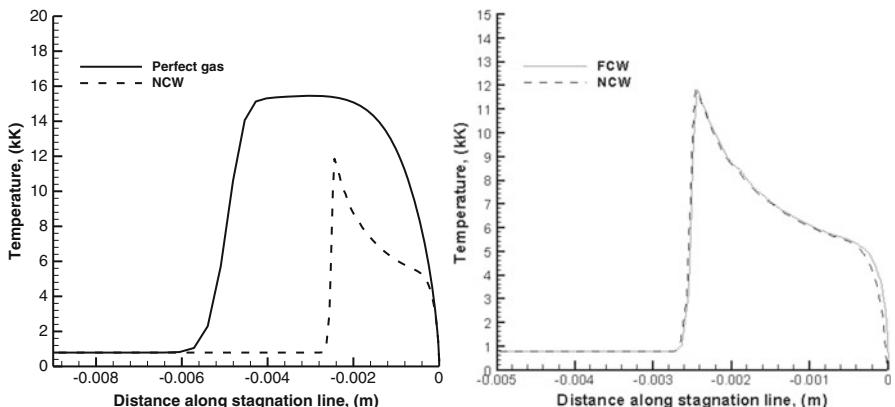


**Fig. 4.12** Temperature distribution along the stagnation line. Comparison between perfect gas and reacting (i.e., NCW and FCW) gas case

(dashed line) and FCW (dotted line) is essentially the same up to boundary layer, where in the case of FCW feature a large gradient at wall ( $\partial T / \partial y$ )<sub>w</sub>, as expected.

Pressure coefficient and wall heat flux distributions for different wall catalytic conditions are reported in Figs. 4.13 and 4.14, respectively. In both figures, CFD results were compared with engineering and available experimental results of HEG test campaign (i.e., shot157, shot159, shot164).

Regarding the pressure coefficient comparison, the numerical, experimental, and engineering results show a good agreement in the first part of the test specimen, giving differences only at the end of the model. In particular, Fig. 4.13 highlights that no differences exist between NC and FC wall boundary condition, as expected. The comparison with the ENTRY results shows a good agreement with the modified Newtonian theory, where the  $C_{p12}$  has been evaluated using the inflow-specific heat and Mach number as provided by CFD analyses.

As shown, the pressure on the probe nose decreases with curve length from the stagnation point, becoming constant on the conical skirt, as predicted by ENTRY

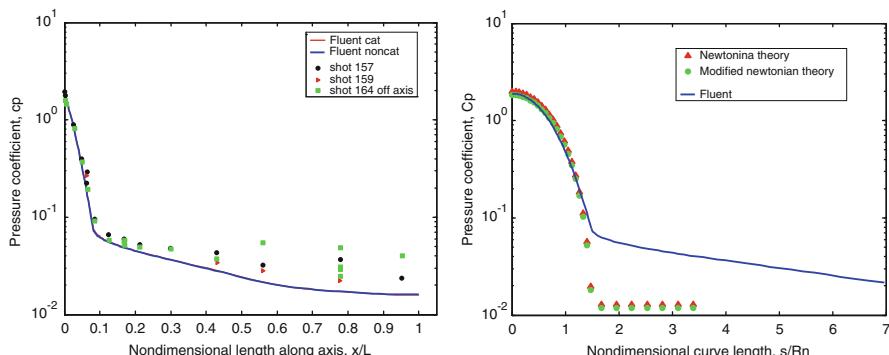


**Fig. 4.13** Pressure coefficient ( $C_p$ ). Comparison between numerical, engineering, and experimental data. Detail on the nose probe (right)

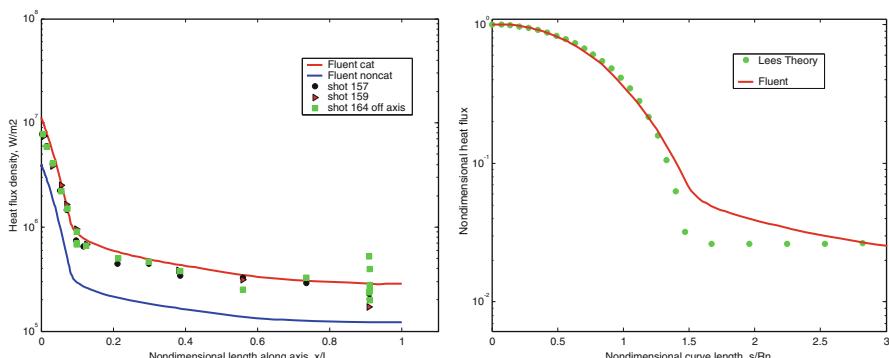


**Fig. 4.14** Heat flux comparison between numerical, engineering, and experimental data. Detail on the probe nose (right)

( $\theta = \theta_c = \text{const}$ ). However, as highlighted by CFD, locally the modified Newtonian theory losses in accuracy because, in reality, the surface pressure depends on many factors such as the interaction of compression and expansion waves which originate from body curvature, reflection from the bow shock, and slip lines due to the rotationality introduced by the curved bow shock wave. In particular, as one can see, as the cone is very slender, the surface pressure in the expanding flow decreases so slowly that the asymptotic (sharp cone) value is not reached, resulting in an underexpanded flow.

The experimental heat flux distribution compares rather well with the numerical FC solution on the nose of the test article, whereas on the rear part of cone, there is a mismatch between experimental data and CFD results, as already seen in the case of pressure coefficient (see Fig. 4.13).

Both these mismatches could be probably caused by flowfield perturbations due to the support of the experimental model that is located at the end of the test bed.

At the end, as one can see on the right side of Fig. 4.14, CFD results compare very good with Lees theory.

## 4.7 CRV Design Analysis

### 4.7.1 Re-entry Flight Scenario

The CRV re-entry analysis from ISS orbit has been performed by using the ENTRY code. It is capable to run descent trajectories with three degrees of freedom (3-dof), using the US Standard Atmosphere (1976) and a non-rotating oblate Earth model, when the vehicle aerodynamic database and its ballistic coefficient are available. To this aim, the ENTRY code quickly finds the Newtonian aerodynamic database of the re-entry vehicle after its outer mold line (OML) is provided. ENTRY evaluates thermal environment, deceleration environment, cross range and down range performances, re-entry corridor, and real gas effects, experienced by the space vehicle along the descent trajectory. ENTRY is able to provide a number of entry trajectories for various entry velocities, entry angle couples ( $v_E$ ,  $\gamma_E$ ), and trim angle of attach profiles for trade-off design analysis.

In the framework of a feasibility study, a vehicle gross weight of about 9 t was assumed. For this value of vehicle mass, starting from the atmospheric entry interface ( $h_E = 120$  km) with  $v_E = 8$  km/s inertial, and  $\gamma_E = -2^\circ$ , ENTRY provides the re-entry trajectories reported in the altitude-velocity plane of Fig. 4.15.

In this figure are also reported the iso-Mach and iso-Reynolds curves, which characterize the aerodynamics and aerothermodynamics of CRV with respect to the re-entry flight scenario. The red curve is a ballistic re-entry trajectory and represents the worst case by convective heat flux point of view. Along with the blue and green curves, the capsule is flying trimmed at an AoA of about  $20^\circ$  and  $28^\circ$  (respectively), during the critical heating regime, thus employing aerodynamic lift to sustain the descent flight path (i.e., lifting returns).

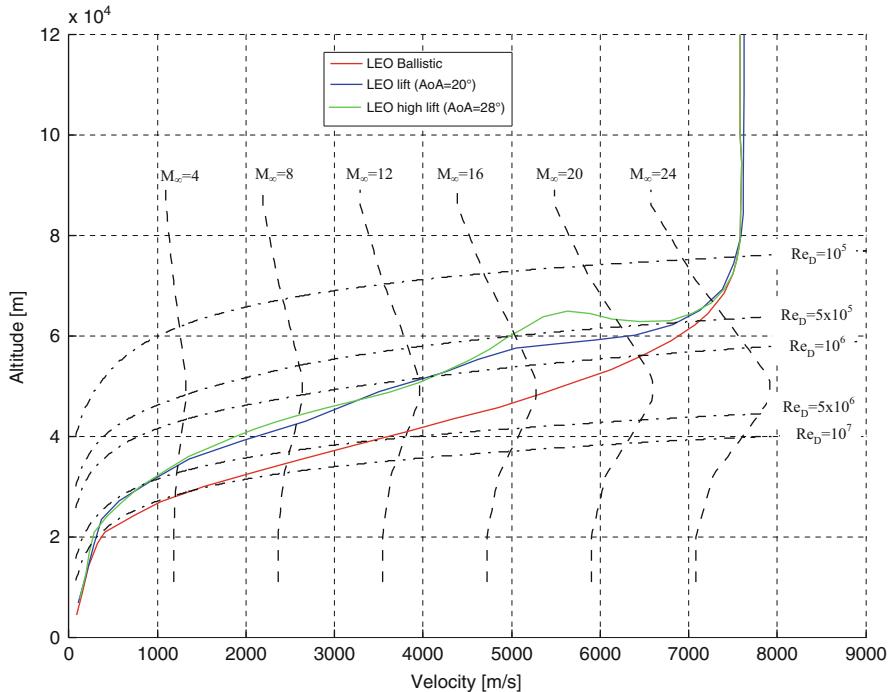
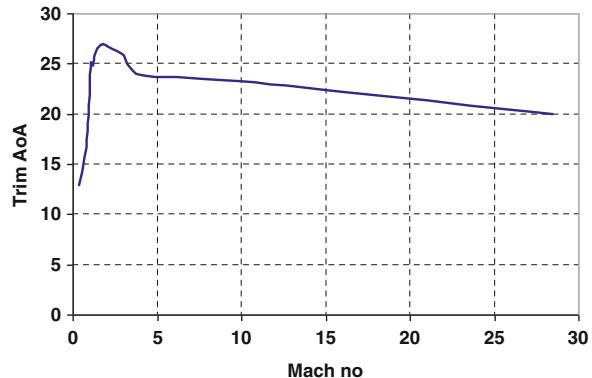


**Fig. 4.15** Re-entry flight scenario, starting from LEO orbit

**Fig. 4.16** Trim angle of attack versus Mach number



In Fig. 4.16, a typical profile of the trim angle of attack is provided [8].

Then, the capsule, moving from a very rarefied atmosphere (at entry interface) to a denser one, shifts from the free molecular flow (FMF) regime, where individual molecular collisions are important, to the transitional one, where slip effects are important, and then to the continuum regime, as represented in Fig. 4.17 in the Mach–Reynolds plane.

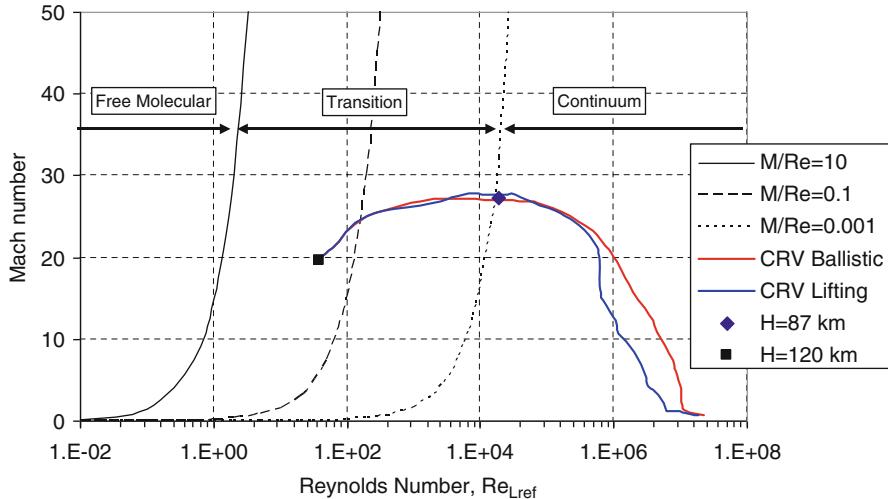


**Fig. 4.17** CRV re-entry trajectory in the M-Re map with constant Knudsen numbers

The red and blue curves represent the ballistic and lifting ( $\text{AoA} = 20^\circ$ ) re-entry trajectories, respectively.

As shown in Fig. 4.17, the region for  $10^{-3} < \text{Kn}_{\infty L_{\text{ref}}} < 10$  is the rarefied transition region, according to Bird classification, where  $L_{\text{ref}}$  is the characteristic length of the body (e.g., the capsule diameter).

These re-entry trajectories result in an aerothermodynamic loading environment that must be accurately predicted for a reliable vehicle design. Indeed, the aeroheating environments generated for both trajectory cases were intended to bound the TPS thermal requirements of CRV capsule.

#### 4.7.2 Appraisal of the Aeroheating Loading Environment

When the spacecraft reaches the atmosphere on the final leg of orbital phase, the aeroheating environment becomes the biggest concern in order to keep safe the spacecraft and its crew members. It consists of the time history, throughout the trajectory, of the convective heating due to the friction between the vehicle and the atmosphere and of the surface pressure acting on vehicle configuration.

By flying, the work done by aerodynamic drag in braking the capsule heats the vehicle surface with severity that depends on the re-entry vehicle configuration and, hence, on the initial conditions of the descent trajectory kind (i.e., ballistic or lift sustained). Therefore, based on the re-entry, flight profile followed the aeroheating environment that the capsule has to withstand during the atmospheric descent.

Due to relatively low entry velocities, no radiation heat flux drives and only convective heat flux applies.

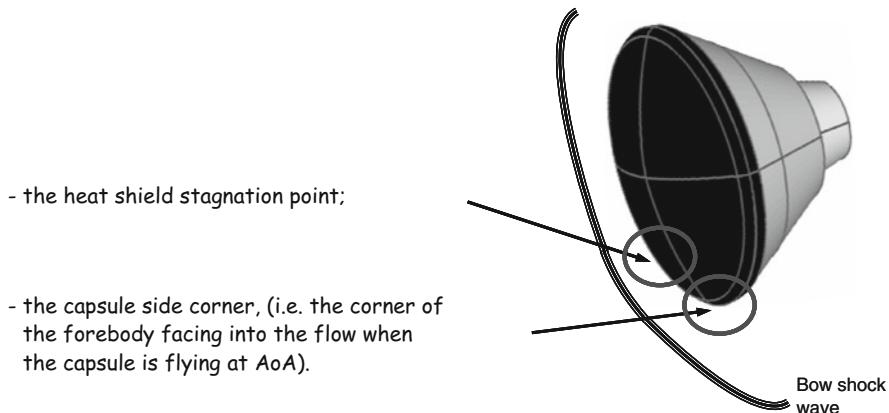


**Fig. 4.18** Aerothermal critical regions expected onto CRV heat shield

By aeroheating point of view, two critical regions onto the vehicle heat shield are expected. They are the heat shield stagnation point (capsule flying at  $\text{AoA} = 0^\circ$ ) and the capsule side corner (capsule flying at  $\text{AoA} \neq 0^\circ$ ), as shown in Fig. 4.18 [16–18].

At engineering level, only stagnation region was considered, and the aeroheating analysis of capsule corner was left to the more accurate CFD analyses, provided hereinafter.

As discussed above, from engineering point of view, several reliable correlation formulae exist to support aerothermodynamic design estimations, as, for example, Scott and Fay–Riddell relationships.

The aerothermal loading corresponding to the flight scenario proposed for the CRV is summarized in Figs. 4.19 and 4.20, where the plots of the stagnation-point heating rate as a function of the altitude are shown in the case of lifting ( $\text{AoA} = 20^\circ$ ) and ballistic descent, respectively.

All heat flux densities were provided versus NC, PC, and FC wall boundary conditions, with an emissivity equal to 0.85 to compute the radiation equilibrium wall temperature.

Figure 4.19 shows that, when the CRV performs the lifting re-entry, a peak heating ( $\text{ph}$ ) of about  $372 \text{ kW/m}^2$  occurs at  $H_{\text{ph}} = 62.3 \text{ km}$  and  $M_{\text{ph}} = 21.8$  conditions, if the heat shield wall is supposed as FC. When the TPM is NC a value of  $245 \text{ kW/m}^2$  is foreseen; if the PCW condition is considered, the values of  $275 \text{ kW/m}^2$  is obtained at capsule stagnation point.

On the other hand, for the reference ballistic trajectory, ENTRY evaluates a peak heating of about  $430 \text{ kW/m}^2$  attained at  $H_{\text{ph}} = 57.0 \text{ km}$  and  $M_{\text{ph}} = 19$  flight conditions, in the case of FCW. The peak heating reads  $280 \text{ kW/m}^2$  when the wall is NC, while in the case of PCW the value of  $325 \text{ kW/m}^2$  is obtained at the capsule stagnation point.

When the heating rate profile is known, the capsule heat shield can be designed. The aeroheating environment dictates, in fact, the type and size of the thermal

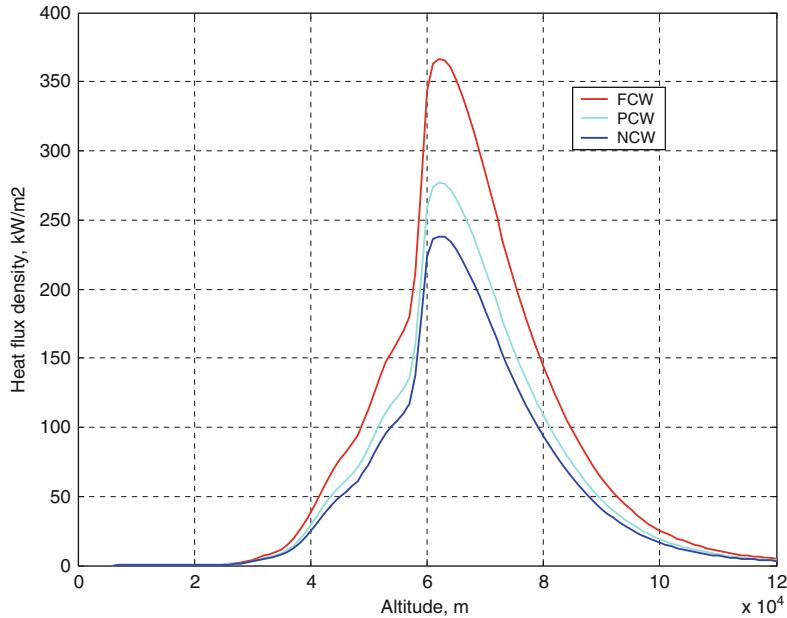


Fig. 4.19 Vehicle aeroheating environment for the lifting re-entry

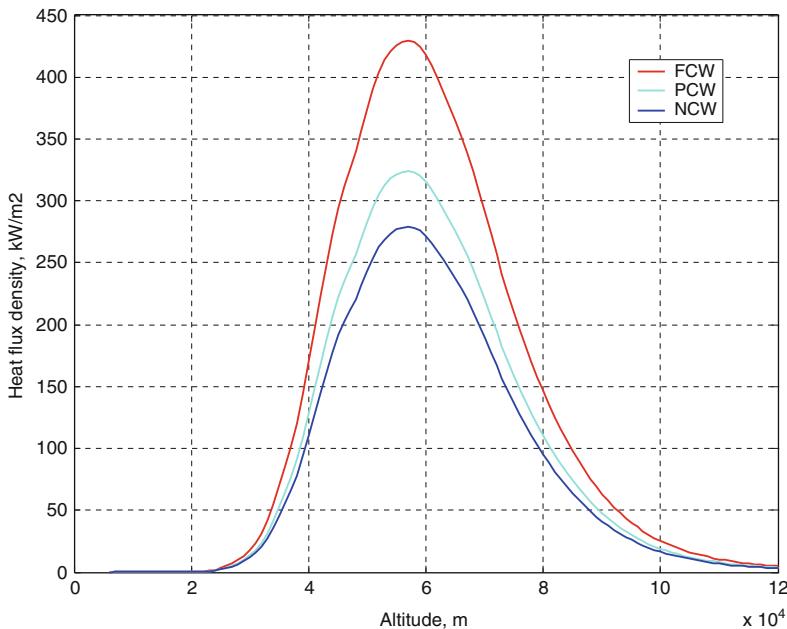


Fig. 4.20 Vehicle aeroheating environment for the ballistic re-entry

protection system (TPS) to be used. Peak heat rate generally determines the range of possible TPM, while the integrated heat load determines the thickness and hence the mass of the heat shield.

Heat flux time histories of both figures, however, are not enough exhaustive for designing CRV heat shield. Indeed, CFD design analyses are mandatory. Therefore, the problem to which flow physical-mathematical model to consider arises. In fact, depending on the altitude and Mach number, low density and thermochemical nonequilibrium effects should be expected because thermal excitation and chemical reaction of the gas occur slowly enough (i.e., finite rate chemistry).

So that the Knudsen (Kn) and Damkohler (Da) nondimensional numbers must be evaluated:

$$\text{Kn}_{\infty L_{\text{ref}}} = \frac{\lambda}{L_{\text{ref}}} = \frac{\text{molecular mean free path}}{\text{reference lenght}} \quad (4.60)$$

$$\text{Da} = \frac{t_c}{t_r} = \frac{\text{characteristic flow time}}{\text{characteristic relaxation time}} \quad (4.61)$$

where the relaxation time refers both to chemical reaction and to internal degrees of freedom of the flow molecules.

When  $t_c \ll t_r$  ( $\text{Da} \ll 1$ ), the flow is chemically frozen since the reacting mixture has not enough time to relax. If  $t_c \cong t_r$  ( $\text{Da} \cong 1$ ), the flow evolves in thermochemical nonequilibrium condition.

Finally, when  $t_c >> t_r$ , we have a near-equilibrium flow because the reacting mixture evolves nearly completely during the time  $t_c$ .

ENTRY, of course, does not foresee the thermochemical state of the overall flowfield about the vehicle. For example, in order to determine the global chemical state of flow, it is needed to compare each other the characteristic time scale of the chemical reactions and that of the local flow, and because the reaction mechanism can be complex (up to 11 reactions), identifying the correct chemical time scale to compare is not trivial. In fact, complex evaluation such as those of computational singular perturbation (CSP) method has to be taken into account.

So for the sake of simplicity, ENTRY considers only oxygen and nitrogen dissociation and the vibrational relaxation of nitrogen along with the stagnation streamline:

$$\begin{aligned} (\text{Da})_{\text{O}_2} &= \frac{t_c}{t_{\text{D},\text{O}_2}} = \frac{C_{\text{O}_2} k_{\text{f},\text{O}_2}(T_2)}{V_2} \Delta \\ (\text{Da})_{\text{N}_2} &= \frac{t_c}{t_{\text{D},\text{N}_2}} = \frac{C_{\text{N}_2} k_{\text{f},\text{N}_2}(T_2)}{V_2} \Delta \\ (\text{Da})_{\text{v},\text{N}_2} &= \frac{t_c}{t_{\text{v},\text{N}_2}} = \frac{\Delta}{V_2 \cdot t_{\text{v},\text{N}_2}} \end{aligned} \quad (4.62)$$

where  $\Delta$  is the stand-off distance and  $V_2$  is the flow velocity behind the bow shock. In Fig. 4.21, the plot of the Kn versus the stagnation-point heating rate is shown,

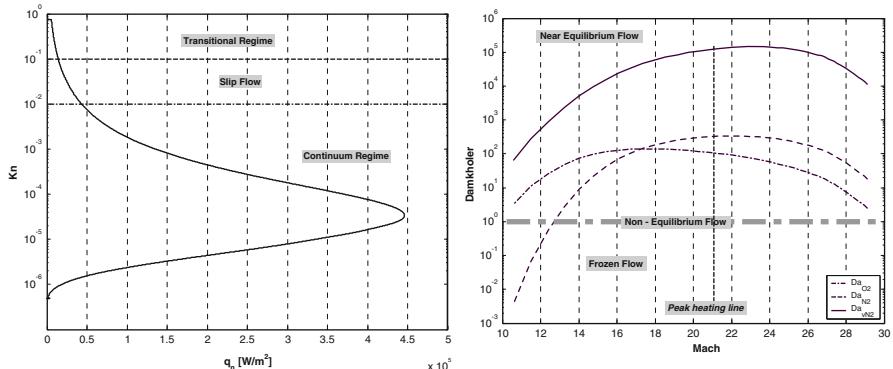


**Fig. 4.21** The vehicle aeroheating environment

while, on the right side, the Da for oxygen ( $O_2$ ) and nitrogen ( $N_2$ ) versus Mach number plot, where the peak heating conditions are also highlighted.

As shown, the peak heating in the case of ballistic trajectory is expected to lie in continuum thermochemical equilibrium flow conditions.

Further, to take an idea of real gas effects that the capsule will experience during descent, Fig. 4.22 shows the re-entry trajectory superimposed on the fields of vibrational excitation, dissociation, and ionization of flow species and on the flow regimes of chemical and thermal nonequilibrium at CRV stagnation point, as expected by applying the binary scaling principle at the stagnation region air chemistry for a 0.3 m radius sphere.

Figure 4.22 confirms that the peak heating occurs in the domain A of thermochemical equilibrium, but very close to the range B of thermal equilibrium and chemical nonequilibrium flow conditions, where the oxygen dissociation is over and that of nitrogen takes place. Ionization can be neglected due to the low entry velocity of the spacecraft returning from LEO mission.

Figure 4.22 also suggests that the flow mixture is expected to be made of seven species  $N_2, O_2, N, O, NO, NO^+,$  and  $e^-$  (i.e., region III). But for sake of simplicity, CFD simulation of the flowfield past the CRV will be made considering five species only (e.g., region II).

### 4.7.3 CRV Computational Flowfield Analysis

The numerical scheme is used to compute the flowfield around the CRV, thus providing at different free-stream conditions interesting high-temperature effects on the flow structure surrounding the vehicle. In fact, real gas thermodynamics, transport properties, and finite rate chemistry have a pronounced effect on shock and Mach wave positions and shapes, emitted radiation, heterogeneous chemical

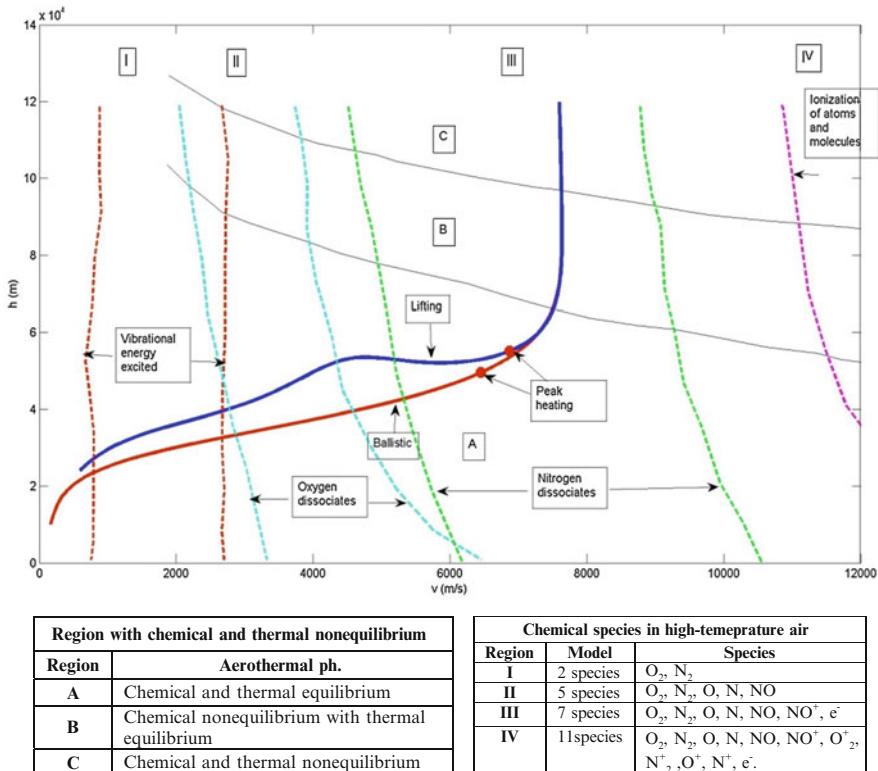


Fig. 4.22 The stagnation-point flow regimes and thermochemical phenomena of re-entry

reactions at vehicle walls, and aerodynamic drag, thus affecting the re-entry flight of the vehicle.

Note that, although Fig. 4.22 provides some insight into the trends which should be expected, a detailed CFD aerothermodynamic analysis is mandatory to establish the thermochemical state of flow and then to provide deep knowledge of the flowfield surrounding the descent capsule, especially at the most critical flight conditions (e.g., trajectory peak heating).

With this in mind, CRV flowfield numerical computations are performed in a step-by-step approach: simulations started with perfect gas model; hence, chemistry comes in by considering first the flow in equilibrium conditions and then in nonequilibrium one. In the latter case, the effects of both reaction mechanism and chemical kinetics are considered, as, for example, by means of Zeldovich reaction mechanism and Dunn-Kang and Park kinetic models. Finally, thermal nonequilibrium and wall catalyticicity are accounted, thus providing a complete overview of high-temperature effects on CRV flowfield.

In particular, both 2-D axisymmetric and fully 3-D CFD solutions are computed, at the trajectories free-stream conditions listed in Table 4.4.

**Table 4.4** Free-stream conditions of CFD computations

Altitude (km)	Mach (-)	Pressure (Pa)	Temperature (k)	AoA (°)
50	10	79.78	270.65	0
57	19	32.78	255.27	10
57	19	32.78	255.27	17.5
57	19	32.78	255.27	20
57	19	32.78	255.27	21
57	19	32.78	255.27	28
57	16	32.78	255.27	28
57	12	32.78	255.27	28

Six AoAs have been considered (i.e., 0°, 10°, 17.5°, 20°, 21°, and 28°). Concerning reacting computations, the farfield is assumed composed of 79 % of diatomic nitrogen ( $N_2$ ) and 21 % of oxygen ( $O_2$ ).

All the simulations have been performed assuming the condition of steady laminar flow. It is worth noting that the capsule TPS design is out of scope of this work. In fact, vehicle thermal shield design dictates vehicle aeroheating assessment for turbulent equilibrium flow conditions as a conservative assumption.

Note that the assumption of steady-state laminar flow is justified considering that experimental results showed that for re-entry orientations of 140–170°, windward surface flow is entirely laminar for  $Re_{\infty D} \leq 1.5 \times 10^6$  over the Mach number range 1.6–4. Moreover, at the Arnold Engineering Development Center (AEDC) wind tunnel for  $M_{\infty} = 10$  conditions, the data indicated laminar behavior at  $Re_{\infty D} = 78.7 \times 10^6$ , the beginning of leeside transition at about  $Re_{\infty D} = 146 \times 10^6$ , and fully developed turbulent flow over at least part of the leeside for  $Re_{\infty D} = 239.4 \times 10^6$ . Therefore, the flow on the CRV heat shield at peak heating conditions of both lifting and ballistic trajectories is expected to be laminar since the highest  $Re_{\infty D}$  is close to  $0.89 \times 10^6$ , while the lowest Mach is 20.2. Note that the Mach number at the edge of the boundary layer has a strong influence on the stability of the laminar boundary layer: the higher the Mach number, the higher the transition Reynolds number.

Anyway, the extremely high laminar heating levels occurring early in the entries at higher altitudes and velocities are expected to exceed the turbulent levels which are likely to occur after the peak heating condition for non-ablating surfaces. Furthermore, for an Apollo-like configuration at AoA, turbulence is expected to occur first over the “leeward” side of the front face of the heat shield, near the “cooler” corner. The likelihood of transition, particularly during the high heating phase of the entry, is reduced due to the short running lengths associated with the CRV. This study assumed that the laminar heating levels at the hot corner would exceed the turbulent levels at the cooler corner. Thus, aeroheating analysis for the laminar hot corner was assumed to be sufficient. Unknown, however, is the impact of ablation on transition to turbulent flow, and this issue was not considered in this limited trade study.

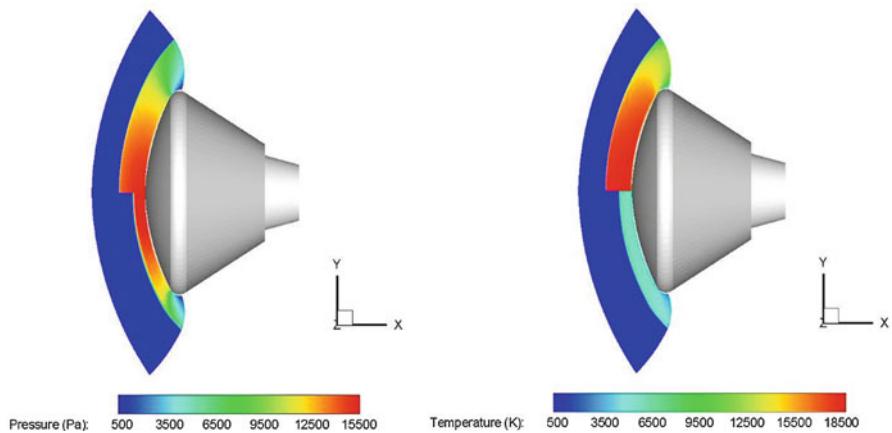


**Fig. 4.23** Contours of static pressure and temperature for  $\text{AoA} = 0^\circ$ ,  $M_\infty = 19$ , and  $H = 57 \text{ km}$ . Comparison among perfect gas and nonequilibrium computation

In particular, capsule aeroheating analysis refers to only forebody heat shield where no vortex systems were expected. Therefore, the conservative assumption of steady laminar flow at capsule peak heating conditions is justified.

#### 4.7.3.1 Axisymmetric Computations

A number of 2-D axisymmetric computations have been carried out to investigate the flowfield past the CRV at the peak heating flight conditions of the ballistic trajectory of Fig. 4.15. A general overview of the flowfield past the vehicle is shown in Fig. 4.23, where contours of pressure and translational temperature in the forebody flowfield are plotted, respectively. These contours refer to  $M_\infty = 19$ ,  $H = 57 \text{ km}$ , and  $\text{AoA} = 0^\circ$ , and compare results in the case of perfect gas (up) and nonequilibrium flow (down).

Fig. 4.24 show the comparison of nondimensional temperature profile among perfect gas (PG), equilibrium gas (EG), chemical nonequilibrium gas with NCW, and chemical nonequilibrium gas with FCW, evaluated along with the stagnation line. As a result, Fig. 4.23 and Fig. 4.24 also show that the shock layer becomes thinner because high-temperature phenomena absorb heat, thus decreasing the effective specific heat ratio  $\gamma$ .

As clearly shown, the temperature is large enough to cause the complete oxygen dissociation in the shock layer while nitrogen partially dissociates. Moreover, differences can be found on temperature peak, on standoff distance, and also on the equilibration trend for translational temperature. In particular, in the case of chemical nonequilibrium computation, the temperature profile on the stagnation line exhibits a sharp discontinuity at the shock wave and a large overshooting value due to the finite rate dissociation of molecules. Hence, the temperature profile highlights

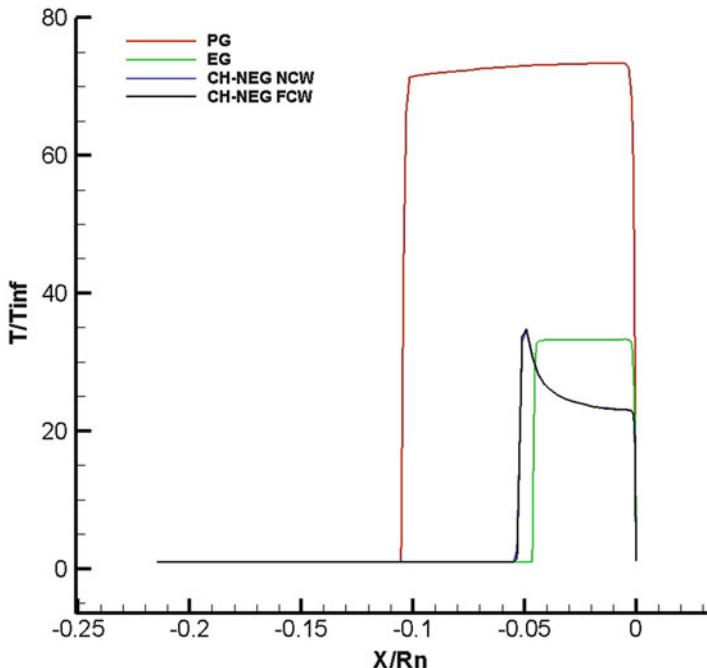


**Fig. 4.24** Comparison of static temperature for  $\text{AoA} = 0^\circ$ ,  $M_\infty = 19$ , and  $H = 57$  km, along stagnation line

that the flow reacting mixture evolves in the shock layer and then in the boundary layer according to finite rate chemistry.

As a result, the gas compressibility changes, which leads to changes in the shapes of shock waves around the vehicle. In particular, as green curve highlights, this phenomenon occurs more prominently in the equilibrium flow than in a nonequilibrium one, as expected.

If we account for the influence of chemical kinetics, in Fig. 4.25 the comparison of nondimensional temperature profiles between results for Dunn–Kang and Park models has been provided.

As shown, chemical kinetics slightly changes both standoff distance and the peak temperature. Differences are also in the shape of temperature profiles in the shock layer, considering that, for Dunn–Kang model, the flow equilibrates before reaching boundary layer (e.g.,  $\frac{\partial T}{\partial x} = 0$ ). The effect of vibrational relaxation can be appreciated in Fig. 4.26, where comparison between translational temperature distributions, along the stagnation line, is reported for Park kinetics. Results remark only slight differences between the case of thermal equilibrium and nonequilibrium computation. When vibrational equilibrium holds (green curve), there is no incubation time for vibration to relax, as highlighted by temperature rise of the curve.

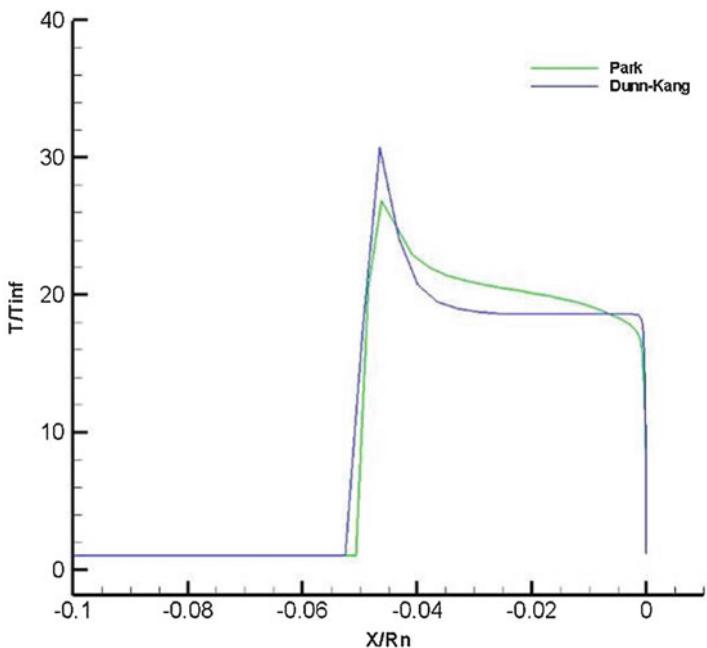


**Fig. 4.25** Comparison of translational temperature along the stagnation line for different chemical models

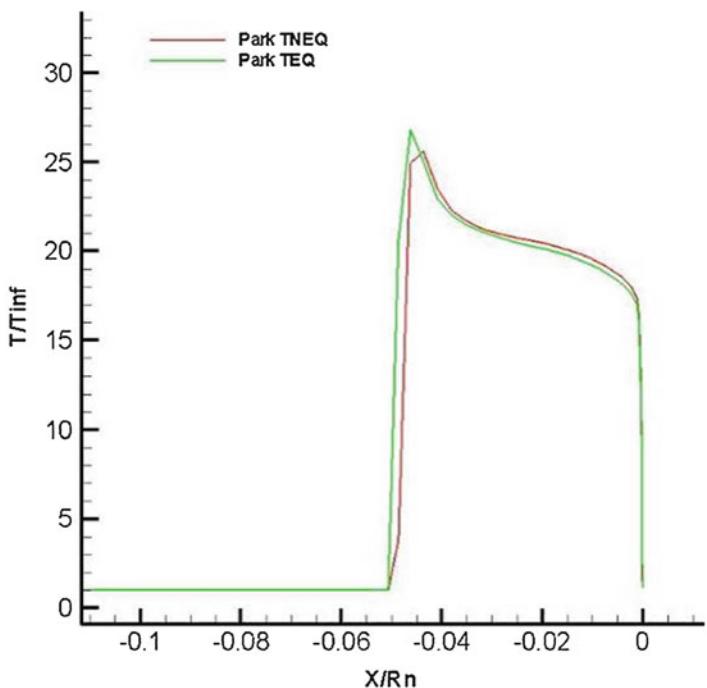


**Fig. 4.26** Translational temperature along the stagnation line. Comparison between thermal equilibrium and nonequilibrium conditions. Park kinetics

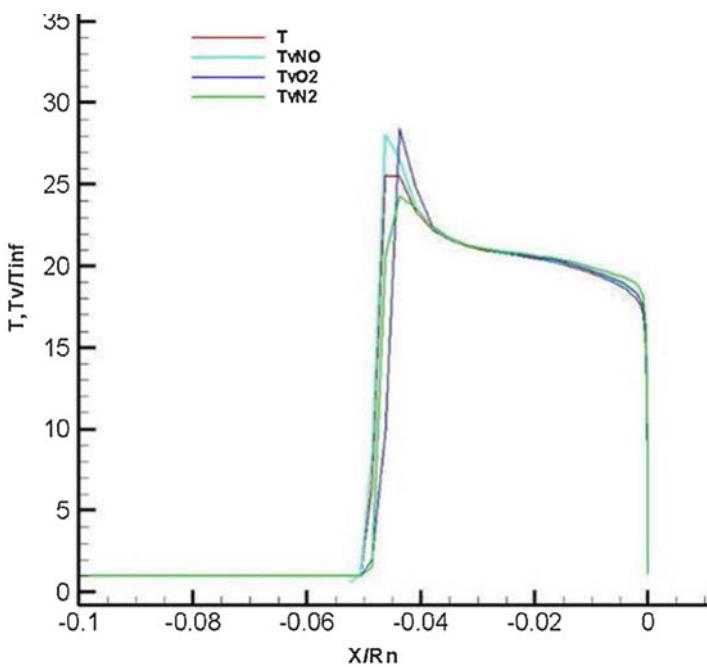


**Fig. 4.27** Comparison of translational and vibrational temperatures for  $\text{AoA} = 0^\circ$ ,  $M_\infty = 19$ , and  $H = 57$  km, along stagnation line for NCW

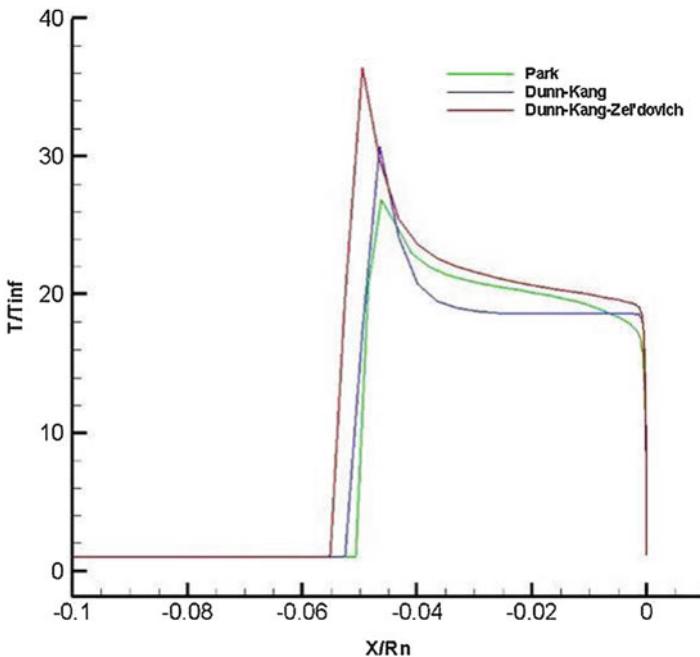


**Fig. 4.28** Translational and vibrational temperatures for  $\text{AoA} = 0^\circ$ ,  $M_\infty = 19$ , and  $H = 57$  km. Comparison along stagnation line for complete reaction system and Zeldovich model

Therefore, we can conclude that at the peak heating of the ballistic trajectory, the flowfield past the CRV is characterized by quite thermal equilibrium conditions (remember that capsule features a large forebody radius,  $R_N = 6.05$  m). Hence, chemistry is active just behind the shock and energy goes only in chemistry, thus yielding lower translational temperature in the shock layer. In fact, even if the exact functional dependence is unknown, it is agreed that a reaction mechanism depending only on  $T$  overpredicts the amount of dissociation [19].

Thermal equilibrium conditions are also confirmed by results summarized in Fig. 4.27, where comparison of translational and vibrational nondimensional temperatures is reported. As we can see, the temperature profiles are almost overlapped except across the shock, with the vibrational temperature of molecular nitrogen that slightly lags behind the others. Note that  $T_v$  increases much more slowly since it is density dependent: the energy transfer takes a certain number of collisions to proceed. In particular,  $O_2$ ,  $NO$ , and  $N_2$  quickly equilibrate. For what concerns the effects of reaction mechanism, Fig. 4.28 reports the same evaluations as in Fig. 4.25, but in the case of Zeldovich reaction mechanism. As shown, by numerical results, the Zeldovich reaction mechanism overestimates both temperature peak and standoff distance. In particular, the temperature profile of complete reaction mechanism (blue curve) shows that flowfield in the shock layer tends toward equilibrium faster than Park and Zeldovich results.

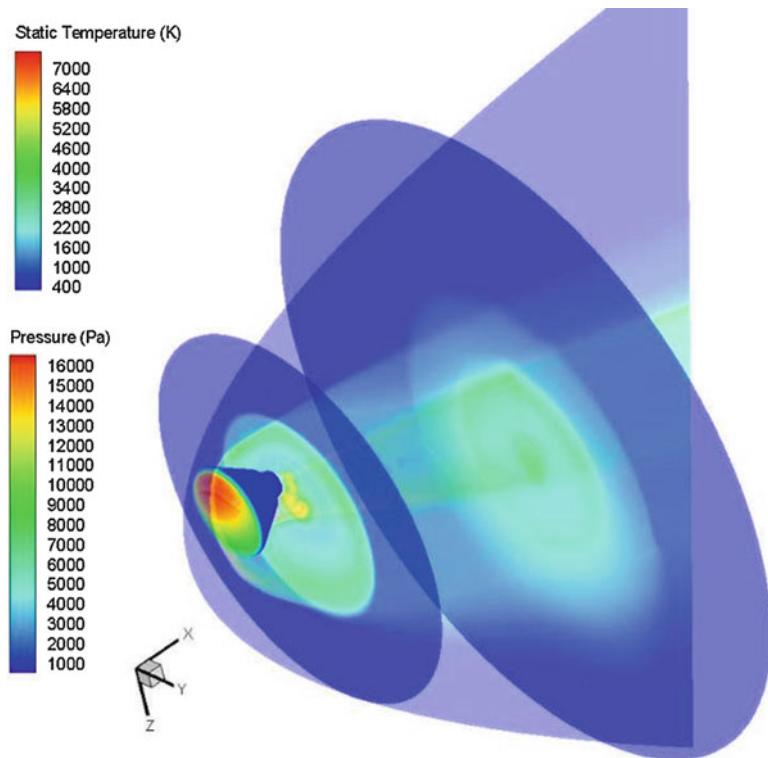
#### 4.7.3.2 Three-Dimensional Computations

In the framework of 3-D computations, four AoAs have been considered (i.e.,  $10^\circ$ ,  $17.5^\circ$ ,  $21^\circ$ ,  $28^\circ$ ). Present CFD results are summarized from Figs. 4.29, 4.30, 4.31, 4.32, 4.33, 4.34, 4.35, 4.36, 4.37, 4.38, 4.39, 4.40, and 4.41, where contour fields of several flowfield features are plotted. For example, Fig. 4.29 shows the static temperature contours on capsule symmetry plane and two flowfield cross sections together with the static pressure contours on capsule surface at  $M_\infty = 19$  and  $\alpha = 21^\circ$ , considering the flow as a reacting gas mixture. Note also that CRV is presented in pitch down configuration since for blunt-body vehicle pitching nose up causes a lift force in the downwards direction, as discussed in Chap. 3. See also CRV aerodynamic analysis.

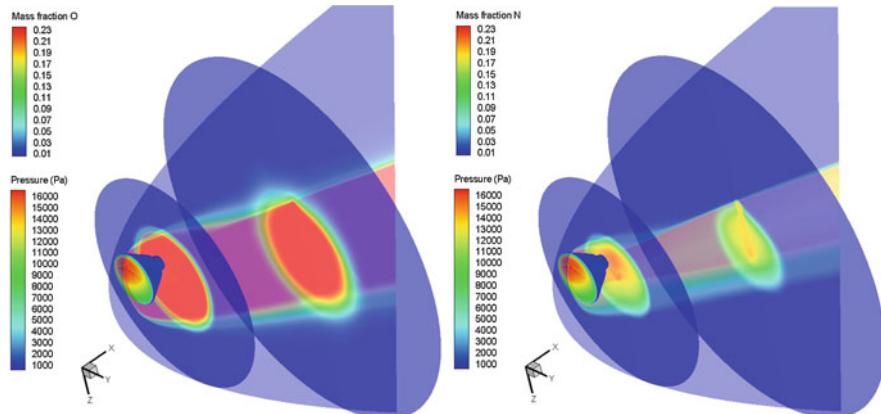
As shown, the CRV bow shock structure around the descent vehicle can be appreciated as well.

Figure 4.30 reports the flowfield contours of oxygen (O) and nitrogen (N) mass fraction (on the right side) for  $M_\infty = 19$ ,  $H = 57$  km, and  $AoA = 21^\circ$ . As expected, the oxygen is fully dissociated.

A close-up view of species field in the plane of the flow velocity vector can be seen in Fig. 4.31, where the mass fraction comparison between atomic (up) and molecular (down) species was reported for the FCW, in the case of ballistic return.



**Fig. 4.29** The static temperature field on CRV symmetry plane and two cross sections at  $M_\infty = 19$ ,  $H = 57$  km, and  $\alpha = 21^\circ$ . Static pressure contour on capsule forebody. Reacting gas computation



**Fig. 4.30** Flowfield contours of oxygen and nitrogen (right) mass fraction for  $M_\infty = 19$ ,  $H = 57$  km, and  $\alpha = 21^\circ$  on CRV symmetry plane and two cross sections. Static pressure contour on capsule forebody

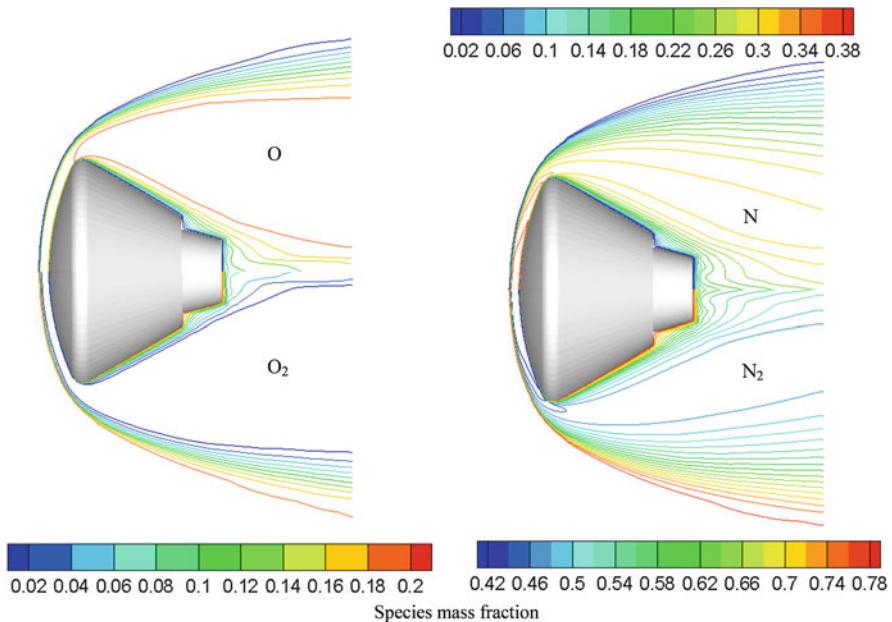


**Fig. 4.31** Mass fraction comparison between atomic (*up*) and molecular (*down*) species in the plane of the flow velocity vector, for FCW. Ballistic re-entry case

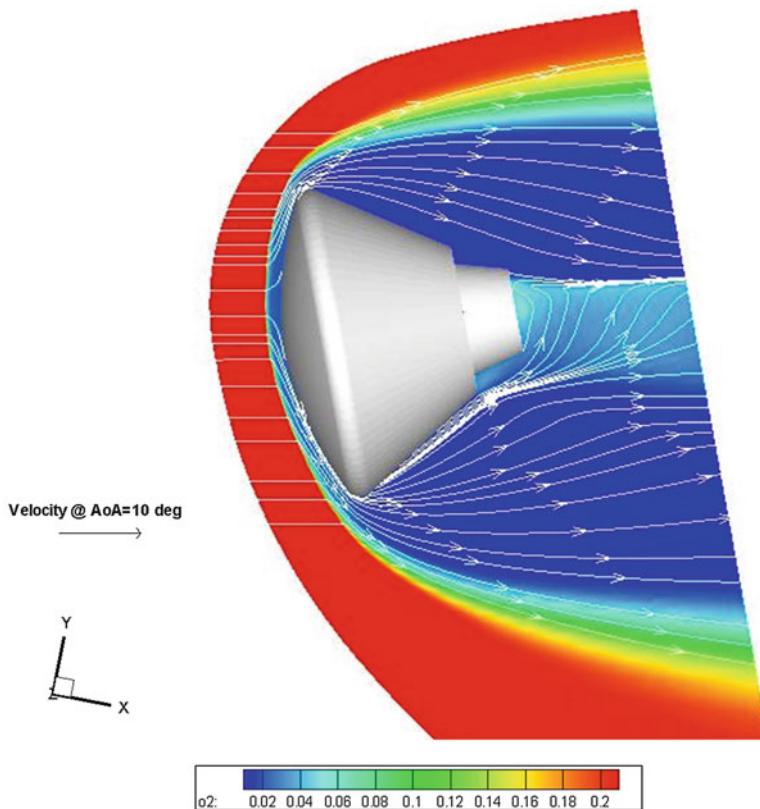
The oxygen ( $O_2$ ) mass fraction distribution with streamtraces on the CRV pitch plane for  $M_\infty = 19$ ,  $H = 57$  km, and  $AoA = 10^\circ$  is reported in Fig. 4.32. As shown, also in this case the oxygen is fully dissociated, as expected.

Figure 4.33 shows Mach number flowfield contours and streamtraces around CRV flying at  $AoA = 21^\circ$ ,  $M_\infty = 19$  at an altitude of 57 km.

The pressure flowfield contours (Pa) when the CRV is flying at  $M_\infty = 19$ , and  $H = 57$  km is recognized in Figs. 4.34 and 4.35, where streamtraces are also reported. Looking at Figs. 4.33, 4.34, and 4.35, it follows that when the CRV is flying at  $AoA$  at the forward capsule corner, the flow is highly compressed. Then, at the shoulder, the flow turns and expands rapidly. The boundary layer detaches, forming a free shear layer that separates the inner recirculating region behind the base flow. Hence, as highlighted by streamtraces, the wake flow evolves in a highly asymmetric way with the separation bubble confined to the leeward side of the spacecraft.

The effect of  $AoA$  on the pressure distribution (Pa) on CRV forebody can be appreciated in Fig. 4.35, thus highlighting the characteristic of high pressure drag atmospheric decelerators of such kind of re-entry configurations.

Finally, Figs. 4.36 and 4.37 report 3-D flowfield streamtraces, colored by static temperature, past the CRV. As one can see, the recirculation in the CRV leeside can be well appreciated, thus giving also a three-dimensional representation of the vortex flow structure shown in the pitch plane of the Fig. 4.34.



**Fig. 4.32** Contours of oxygen mass fraction with streamtraces for  $\text{AoA} = 10^\circ$ ,  $M_\infty = 19$ , and  $H = 57 \text{ km}$

Concerning capsule static stability, the transition in sonic line location is shown in Figs. 4.38, 4.39, 4.40, and 4.41 for different AoAs and Mach numbers. Figure 4.38 reports sonic line location for four cases, involving two different Mach numbers (i.e., 10, 19) and all the AoAs considered in the CFD computations (i.e.,  $\text{AoA} = 0^\circ, 10^\circ, 21^\circ, 28^\circ$ ).

As one can see, both sonic line location and shape around the capsule markedly depend on free-stream Mach number, altitude, and AoA, thus highlighting that capsule attitude conditions are highly influenced during descent flight. In order to appreciate the effect of finite rate chemistry, the sonic line comparison between PG and RG computations both for  $M_\infty = 16$  and  $M_\infty = 19$  is summarized in Fig. 4.39, respectively. In this figure the effect of different chemical kinetics on sonic line location is addressed as well.

In both cases, it is highlighted that for the PG solution, the flowfield around almost all the CRV is entirely subsonic with consequent high pressure distribution. Therefore, as sonic line shifts, due to the chemical reactions, the flow goes entirely

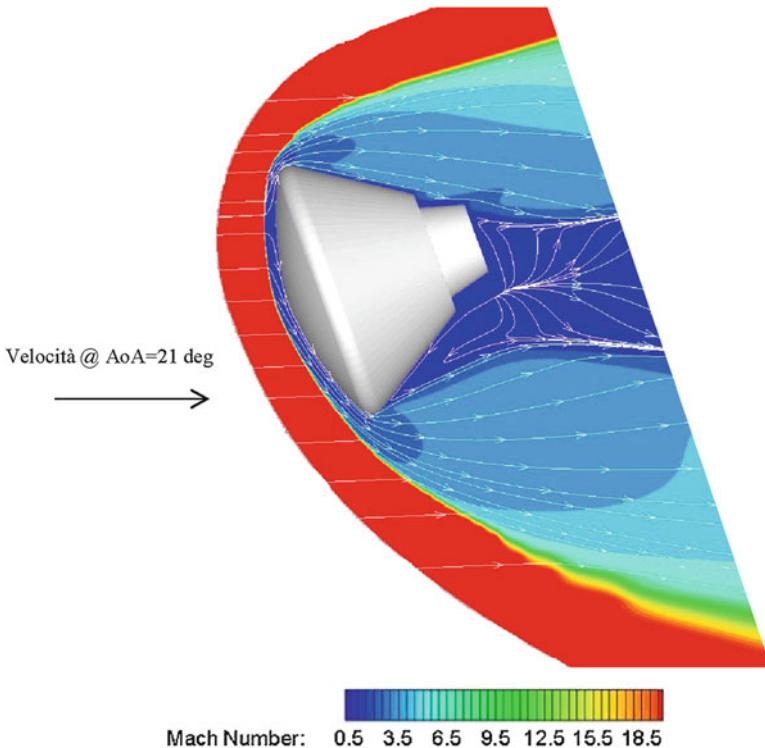
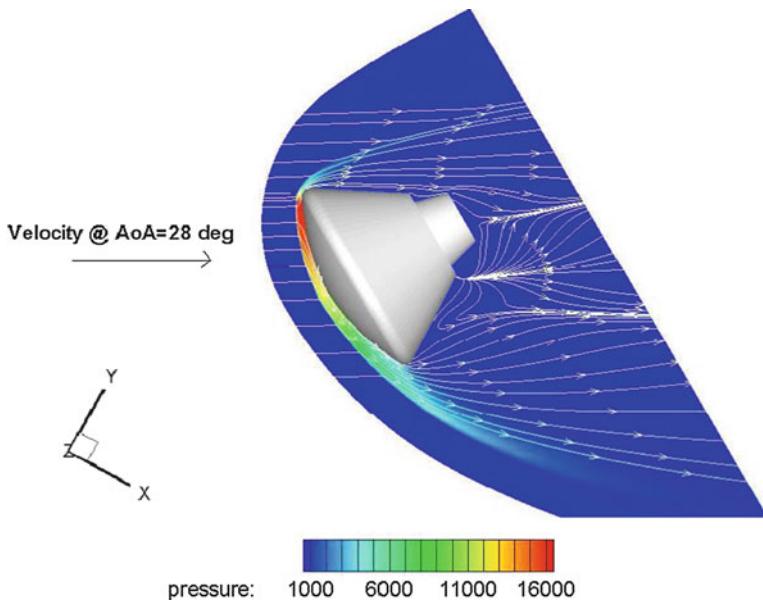


**Fig. 4.33** Mach number contours and streamtraces for  $\text{AoA} = 21^\circ$ ,  $M_\infty = 19$ , and  $H = 57 \text{ km}$

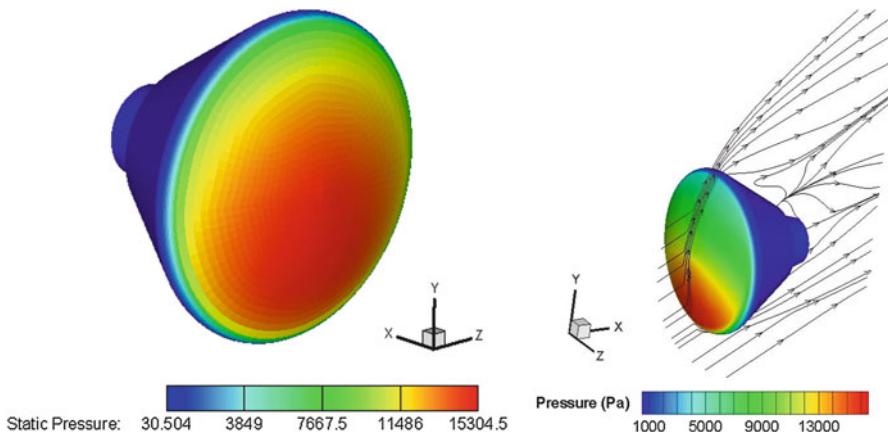
supersonic and the pressure decreases, thus confirming that pitching moment and, then, trim AoAs are affected by high-temperature real gas effects. It is worth noting that in order to attain a static stable trim, the slope of  $C_{Mz}$  must be negative when in trim (i.e.,  $C_{M\alpha} = \frac{\partial C_{Mz}}{\partial \alpha} < 0$ ). In particular, differences between green and blue lines on the capsule afterbody underline that at  $M_\infty = 19$  the pitching moment coefficient estimation is affected by the chemical kinetics, while no differences are expected when capsule is flying at  $M_\infty = 16$  (see Fig. 4.39).

Figure 4.40 shows the sonic line for the CRV for different Mach number (i.e.,  $M_\infty = 12$ , 16, and 19) at the same AoA (i.e.,  $28^\circ$ ), thus appreciating the effect of Mach number. The sonic line at  $M_\infty = 12$  highlights that, in this case, a lesser contribution to the pitching moment coefficient is expected for the capsule forebody. Therefore, the sonic line shift results in a pitching moment and trim AoA shift, and, depending on capsule cg location, region of vehicle static instability can be expected during re-entry.

Finally, as far as the effect of reaction mechanism is concerned, using the Zeldovich model, the sonic line at  $M_\infty = 19$  compares to that of complete reaction mechanism, as summarized in Fig. 4.41. As a result, the sonic line as computed for Zeldovich model differs only slightly from that of the complete reaction mechanism.



**Fig. 4.34** Pressure flowfield contours (Pa) and streamtraces for  $\text{AoA} = 28^\circ$ ,  $M_\infty = 19$ , and  $H = 57 \text{ km}$ . Reacting gas computation



**Fig. 4.35** Contours of pressure distribution (Pa) on capsule surface at  $\text{AoA} = 10^\circ$  (left) and at  $\text{AoA} = 28^\circ$  (right) with streamtraces for  $M_\infty = 19$  and  $H = 57 \text{ km}$ . Reacting gas computations

## 4.8 CRV Aerodynamic Analysis

The evaluations of the preliminary aerodynamic performance of CRV have been provided in the following. Lift ( $C_L$ ), drag ( $C_D$ ), and pitching moment ( $C_{M_y}$ ) coefficients are of primary interest for an axisymmetric capsule. Therefore, the

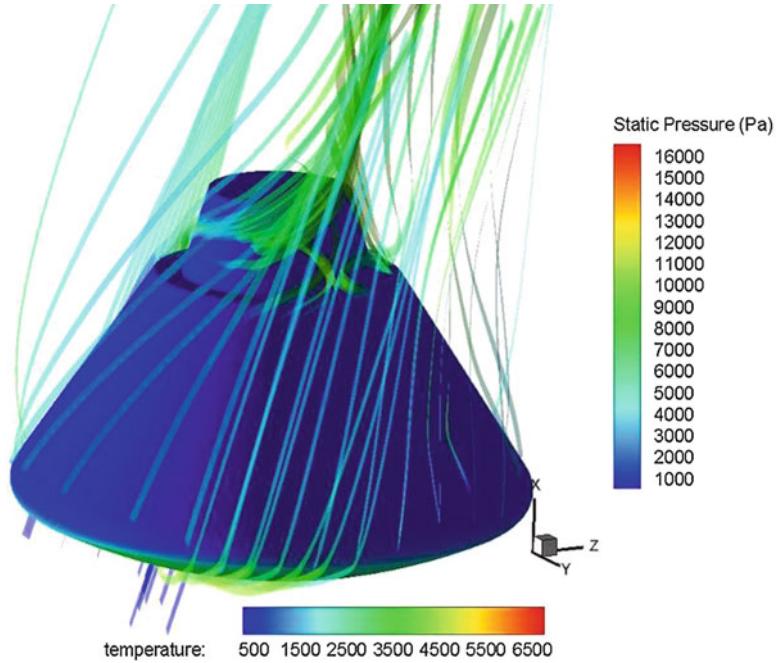


**Fig. 4.36** Pressure contours (Pa) and streamtraces for AoA = 28°,  $M_\infty = 19$ , and  $H = 57$  km. Reacting gas computation

spacecraft aerodynamic analysis is shown in terms of those parameters, which are calculated according to Eqs. (4.63) and (4.64), respectively:

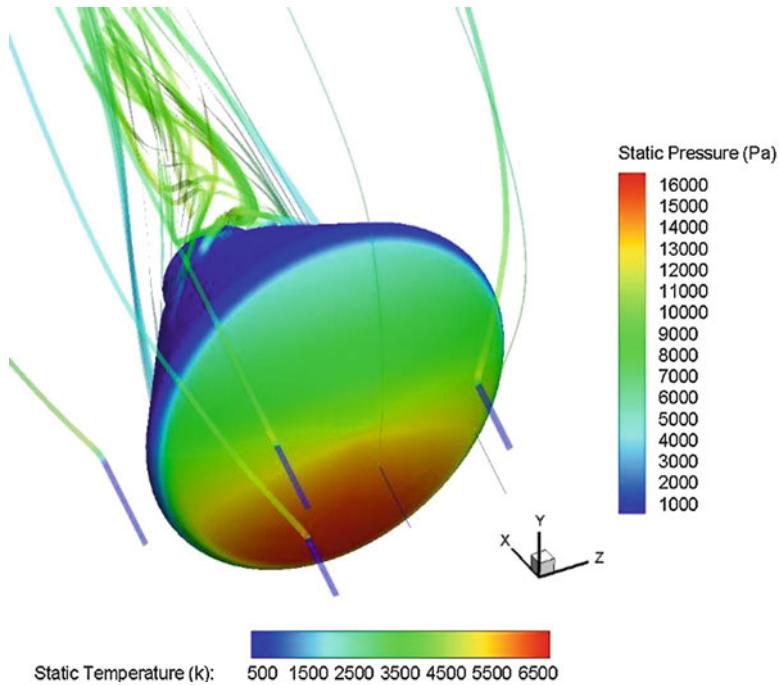
$$C_i = \frac{F_i}{\frac{1}{2} \rho_\infty v_\infty^2 S_{\text{ref}}} \quad i = L, D \quad (4.63)$$

$$C_{M_j} = \frac{M_j}{\frac{1}{2} \rho_\infty v_\infty^2 L_{\text{ref}} S_{\text{ref}}} \quad j = Y \quad (4.64)$$

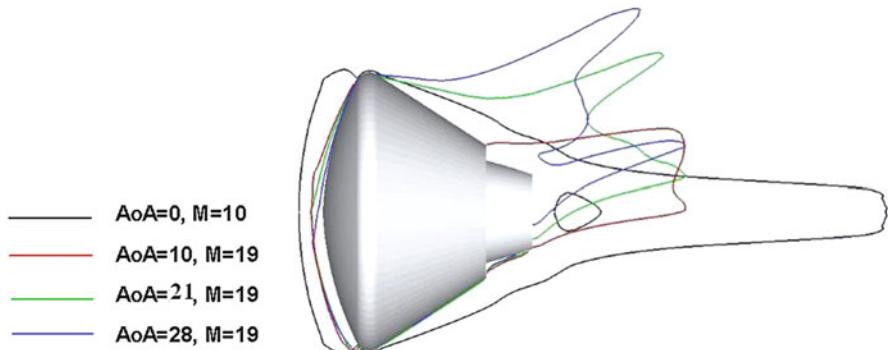
The reference parameters that have been chosen in order to make aerodynamic forces and moment nondimensional coefficients are the longitudinal reference length ( $L_{\text{ref}} = D = 2R_b$ ), equal to the capsule diameter (e.g., 5.0 m), and the reference area ( $S_{\text{ref}} = \pi R_b^2 = 19.6 \text{ m}^2$ ), equal to the maximum cross-section area of the CRV. Pole coordinates for the pitching moment calculation are (0,0,0) m (i.e., vehicle nose) and vehicle CoG ( $x/D = 0.26$ ,  $y/D = 0.0353$ ,  $z/D = 0$ ).

Based on re-entry flight scenario summarized in Fig. 4.15, the CRV aerodynamic data set (AEDB) has been generated for the following ranges:

1.  $3 < M < 24$  [3, 4, 8, 12, 16, 20, 24].



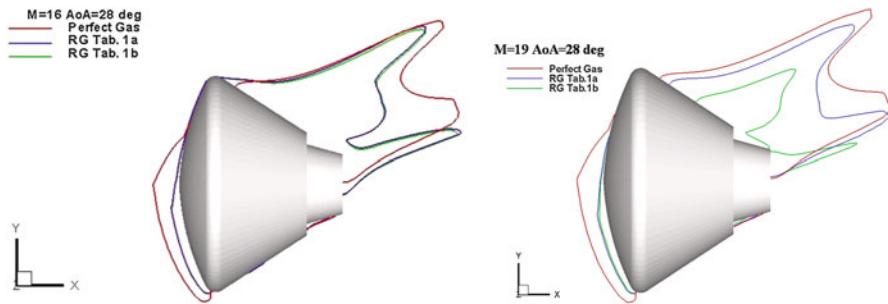
**Fig. 4.37** Pressure contours (Pa) and streamtraces for  $\text{AoA} = 28^\circ$ ,  $M_\infty = 19$ , and  $H = 57 \text{ km}$ . Reacting gas computation



**Fig. 4.38** Sonic line location in the capsule pitch plane for different AoAs (i.e.,  $0^\circ$ ,  $10^\circ$ ,  $21^\circ$ , and  $28^\circ$ ) and Mach numbers (i.e., 10 and 19). Reacting gas computations

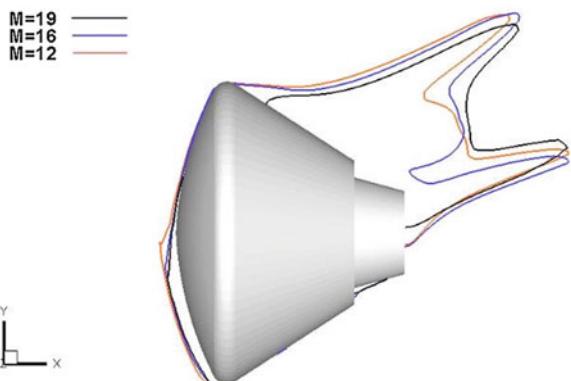
2.  $130^\circ < \alpha < 180^\circ$  [130, 135, 140, 143, 145, 147, 150, 155, 160, 165, 170, 175, 180].
3.  $10^5 < Re < 10^7$   $[0.1, 0.5, 1, 5, 10] \times 10^6$ .
4.  $\beta = 0^\circ$ .

No lateral directional analysis has been taken into account in this work.

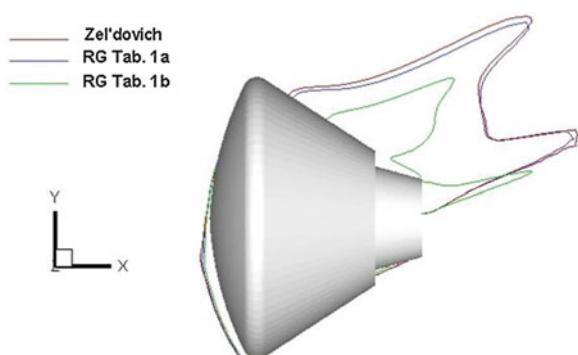


**Fig. 4.39** Sonic line location in the capsule pitch plane at  $\text{AoA} = 28^\circ$  (i.e.,  $152^\circ$ ). Comparison between PG and RG computations for  $M_\infty = 16$  (left side) and  $M_\infty = 19$  (right side) at  $H_\infty = 57 \text{ km}$ . RG Tab. 1a refers to Dunn–Kang model, while Tab. 1b to park’s kinetics

**Fig. 4.40** Sonic line location in the capsule pitch plane at  $\text{AoA} = 28^\circ$  (i.e.,  $152^\circ$ ) and  $H_\infty = 57 \text{ km}$ . Comparison among Mach number equal to 12, 16, and 19. Reacting gas computations



**Fig. 4.41** Sonic line location in the CRV pitch plane at  $\text{AoA} = 28^\circ$ ,  $M_\infty = 19$  and  $H_\infty = 57 \text{ km}$ . Results for Zeldovich reaction mechanism. RG Tab. 1a refers to Dunn–Kang model, while Tab. 1b to park’s kinetics



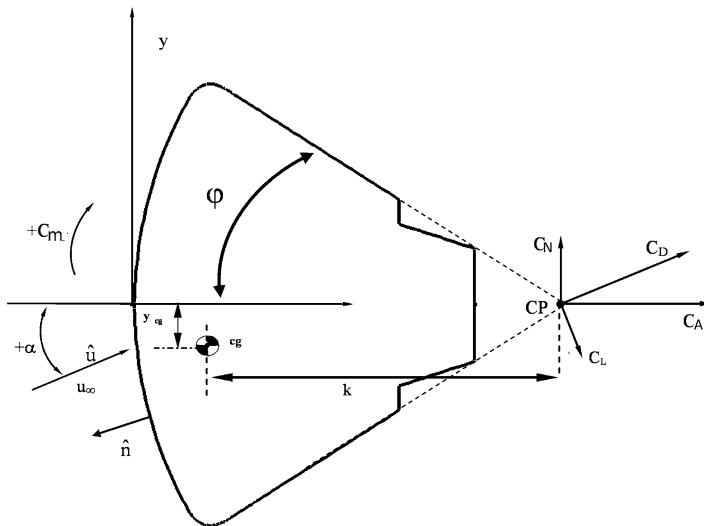


**Fig. 4.42** Capsule OML used for surface impact method aerodynamics

#### 4.8.1 Engineering Assessment of CRV Aerodynamics

Upon re-entry the capsule falls very deep in the Earth's atmosphere, traveling at hypersonic velocities for the majority of the time of flight. In those conditions, the forces are dominated by pressure effects, with viscous and other effects, as base drag, representing only about ten per cent of the total. Therefore, as early assessment of the CRV aerodynamics, several engineering evaluations can be accomplished. Indeed, the flow may be approximated as inviscid, and the surface inclination methods as modified Newtonian theory (MN) can be used. With this in mind, let us consider Fig. 4.42 where the outer mold line (OML) of the CRV is shown.

Assuming that the free-stream particles impact only on the frontal area of the body and cannot curl around it, MN theory states that the pressure coefficient ( $C_p$ ) reads:

$$C_p = C_{p12}(\hat{u} \cdot \hat{n})^2 \quad (4.65)$$

where  $C_{p12}$  is the stagnation-point pressure coefficient,  $\hat{u}$  the velocity unit vector, and  $\hat{n}$  the wall outboard normal, while the surfaces in the shadow of the vehicle can be neglected (i.e.,  $C_p = 0$ ). So that when real gas effects are taken into account, Eq. (4.1) suggests that the pressure coefficient becomes

$$C_p = (2 - \varepsilon)(\hat{u} \cdot \hat{n})^2 \quad (4.66)$$

By integrating Eq. (4.66) over the whole vehicle surface, one is able to evaluate aerodynamic forces acting on the vehicle, both for zero-lift and AoA cases, as recognized in the following paragraphs.

#### 4.8.1.1 CRV Zero-Lift Aerodynamics

When  $\alpha = 0^\circ$ , the pressure coefficient reads:

$$C_p = (2 - \varepsilon) (\hat{u} \cdot \hat{n})^2 = (2 - \varepsilon) \sin^2 \theta = (2 - \varepsilon) \cos^2 \varphi \quad (4.67)$$

where  $\theta$  is the local slope body angle and  $\varphi$  is the body polar angle (see explanation box). Therefore, the CRV zero-lift drag coefficient is given by

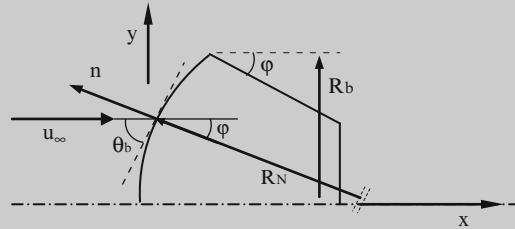
$$C_{D0} = \frac{(2 - \varepsilon)}{2} (1 + \cos^2 \varphi) \quad (4.68)$$

where  $\varphi = \sin^{-1} \left( \frac{R_b}{R_N} \right)$  is also the capsule frustum angle (i.e.,  $33^\circ$ ) and  $\varepsilon = \left( \frac{\rho_1}{\rho_2} \right)$  is the density ratio across the bow shock at the stagnation point.

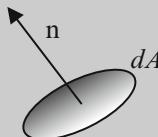


#### Explanation Box. Zero Lift Drag Coefficient of an Apollo-Like Capsule

The derivation of Eq. (4.68) is herein outlined:



The force  $d\vec{F}$  acting on the CRV forebody region of area  $dA$  (see below) is given by



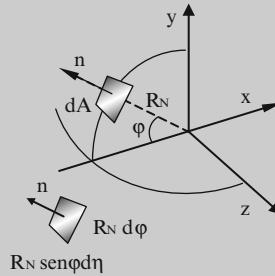
$$d\vec{F} = -(p - p_\infty) dA \hat{n} = -q_\infty C_p dA \hat{n}$$

(continued)

Hence, the drag  $dD$  acting on  $dA$  reads:

$$\begin{aligned} dD &= d\vec{F} \cdot \hat{u}_\infty = -C_p q_\infty dA \left( -\cos \varphi \hat{i} + \sin \varphi \hat{j} \right) \cdot \hat{i} \\ &= C_p q_\infty \cos \varphi dA = C_{pt2} q_\infty \cos^3 \varphi dA \end{aligned}$$

Therefore, the drag force  $D$  acting on the CRV is given by



$$\begin{aligned} D &= \iint_{\text{forebody}} dD = C_{pt2} q_\infty \iint_{fs} \cos^3 \varphi dA = 2 C_{pt2} q_\infty \\ &\times \int_0^\pi \left( R_N^2 \int_0^\varphi \cos^3 \delta \sin \delta d\delta \right) d\eta \\ &= 2\pi R_N^2 C_{pt2} q_\infty \int_0^\varphi \cos^3 \delta \sin \delta d\delta = -2\pi R_N^2 C_{pt2} q_\infty \int_0^\varphi \cos^3 \delta d \cos \delta \\ &= \frac{1}{2}\pi R_N^2 C_{pt2} q_\infty \cos^4 \delta \Big|_0^\varphi = \frac{1}{2}\pi R_N^2 C_{pt2} q_\infty (1 - \cos^4 \varphi) \\ &= \frac{1}{2}\pi R_N^2 C_{pt2} q_\infty (1 - \cos^2 \varphi) (1 + \cos^2 \varphi) = \frac{q_\infty C_{pt2}}{2} S_{ref} (1 + \cos^2 \varphi) \end{aligned}$$

because of  $dA = R_N^2 \sin \varphi d\varphi d\eta$ ,  $R_b = R_N \sin \varphi$  and  $S_{ref} = \pi R_b^2$ .

$$\text{Therefore, } C_D = \frac{D}{q_\infty S_{ref}} = \frac{1}{2} C_{pt2} (1 + \cos^2 \varphi) = \frac{(2-\varepsilon)}{2} (1 + \cos^2 \varphi).$$

#### 4.8.1.2 CRV AoA Aerodynamics

As well known, lift is generated if the axis of symmetry of capsule is misaligned with respect to the velocity vector (i.e., AoA  $\neq 0^\circ$ ). This asymmetry trim condition is produced by displacing the CoG from capsule axis. In particular, a statically stable

trim attitude with CRV heat shield forward is produced by placing the vehicle CoG close to capsule blunt face (see Fig. 4.42).

When capsule is flying at an AoA,  $\alpha$ , the pressure coefficient on vehicle's wall facing flow, reads:

$$C_p = (2 - \varepsilon) (\hat{u} \cdot \hat{n})^2 = (2 - \varepsilon) (\cos \alpha \cos \varphi + \sin \alpha \sin \varphi)^2 \quad (4.69)$$

So, when  $\alpha < \varphi$  (i.e., the sidewall surface is shadowed), the axial and normal force coefficients follow as respectively

$$C_A = \frac{(2 - \varepsilon)}{2} \left[ \cos^2 \alpha (1 + \cos^2 \varphi) + \frac{1}{2} \sin^2 \alpha \sin^2 \varphi \right] \quad (4.70)$$

$$C_N = \frac{(2 - \varepsilon)}{2} \cos \alpha \sin \alpha \sin^2 \varphi \quad (4.71)$$

Therefore, the lift, drag and lift to drag ratio of the CRV for a range of angles of attack are

$$\frac{C_L}{C_D} = \frac{C_N \cos \alpha - C_A \sin \alpha}{C_N \sin \alpha + C_A \cos \alpha} \quad (4.72)$$

Further, by imposing the pitch moment balance about the vehicle CG, we have

$$C_{mcg} = \frac{1}{c} (y_{cg} C_A - k C_N) \quad (4.73)$$

where  $c = L_{ref}$  is the normalizing length of pitching moment and  $k$  is the static stability margin of the vehicle that is expected to be influenced by the real gas effects, thus affecting trim angle and in turn the own CRV flight profile due to the lower aerodynamic efficiency of spacecraft (see Fig. 4.42).

As a results, for very high Mach numbers (say larger than five), surface impact method (SIM) states that the aerodynamic characteristic of a spacecraft does not depend on the vehicle velocity but rather on the  $\alpha$  and the geometric angle of the body shape  $\varphi$ .

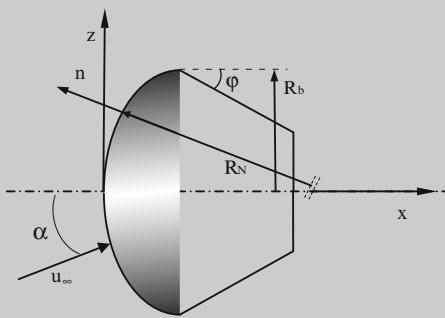
In particular, note that  $C_L$  expression in Eq. (4.72) states that for blunt-body vehicle, pitching nose up causes a lift force in the downwards direction, i.e.,  $L/D < 0$ , because they have large  $C_A$  and small  $C_N$ .



#### Explanation Box. Axial Coefficient of an Apollo-Like Capsule

The derivation of Eq. (4.70) is herein outlined:

(continued)



The axial force  $dX$  acting on the CRV forebody region of area  $dA$  is given by

$$dX = d\vec{F} \cdot \hat{i} = q_\infty C_p \cos \phi dA$$

Note that

$$\begin{aligned}\hat{u}_\infty &= \cos \alpha \hat{i} + \sin \alpha \hat{k} \\ \hat{n} &= -\cos \phi \hat{i} + \sin \phi \hat{k}\end{aligned}$$

So that

$$\begin{aligned}C_p &= C_{p12}(\hat{u} \cdot \hat{n})^2 = C_{p12}(\cos \alpha \cos \phi + \sin \alpha \sin \phi)^2 = \\ &= (2 - \varepsilon)(\cos \alpha \cos \phi + \sin \alpha \sin \phi)^2\end{aligned}$$

Therefore, the axial force  $X$  acting on the CRV is given by

$$\begin{aligned}X &= \iint_{\text{forebody}} dX = C_{p12} q_\infty \iint_{\text{fs}} \cos \phi (\cos \alpha \cos \phi + \sin \alpha \sin \phi)^2 dA = \\ &= 2 C_{p12} q_\infty \int_0^\pi \left( R_N^2 \int_0^\varphi \cos \delta (\cos \alpha \cos \delta + \sin \alpha \sin \delta)^2 \sin \delta d\delta \right) d\eta = \\ &= 2\pi R_N^2 C_{p12} q_\infty \int_0^\pi (\cos \alpha \cos \delta + \sin \alpha \sin \delta)^2 \cos \delta \sin \delta d\delta = \\ &= \frac{1}{2} \pi R_N^2 C_{p12} q_\infty [\cos^2 \alpha (1 - \cos^4 \phi) + \frac{1}{2} \sin^2 \alpha \sin^4 \phi] = \\ &= \frac{q_\infty C_{p12}}{2} S_{\text{ref}} [\cos^2 \alpha (1 + \cos^2 \phi) + \frac{1}{2} \sin^2 \alpha \sin^2 \phi]\end{aligned}$$

because of  $dA = R_N^2 \sin \phi d\phi d\eta$ ,  $R_b = R_N \sin \phi$  and  $S_{\text{ref}} = \pi R_b^2$ .

(continued)

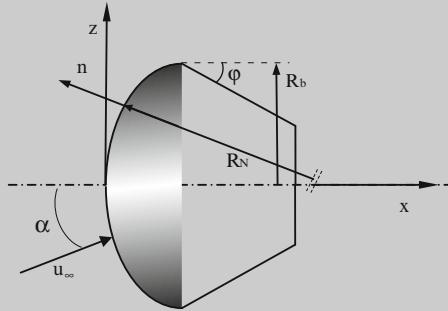
Therefore,

$$\begin{aligned} C_A &= \frac{X}{q_\infty S_{\text{ref}}} = \frac{C_{\text{pt2}}}{2} \left[ \cos^2 \alpha (1 + \cos^2 \varphi) + \frac{1}{2} \sin^2 \alpha \sin^2 \varphi \right] \\ &= \frac{(2 - \varepsilon)}{2} \left[ \cos^2 \alpha (1 + \cos^2 \varphi) + \frac{1}{2} \sin^2 \alpha \sin^2 \varphi \right]. \end{aligned}$$



### Explanation Box. Normal Coefficient of an Apollo-Like Capsule

The derivation of Eq. (4.71) is herein outlined:



The normal force  $dN$  acting on the CRV forebody region of area  $dA$  is given by

$$dN = d\vec{F} \cdot \hat{k} = q_\infty C_p \sin \varphi dA$$

Note that

$$\begin{aligned} \hat{u}_\infty &= \cos \alpha \hat{i} + \sin \alpha \hat{k} \\ \hat{n} &= \begin{cases} -\cos \varphi \hat{i} + \sin \varphi \hat{k} & \text{2nd quad.} \\ -\cos \varphi \hat{i} - \sin \varphi \hat{k} & \text{3rd quad.} \end{cases} \end{aligned}$$

So that

$$\begin{aligned} C_p &= C_{\text{pt2}} (\hat{u} \cdot \hat{n})^2 = C_{\text{pt2}} (\cos \alpha \cos \varphi + \sin \alpha \sin \varphi)^2 = \\ &= (2 - \varepsilon) (\cos \alpha \cos \varphi + \sin \alpha \sin \varphi)^2 \end{aligned}$$

(continued)

Therefore, the normal force N acting on the CRV is given by

$$\begin{aligned}
 N &= \iint_{\text{forebody}} dN = C_{\text{pt2}} q_\infty \iint_{fs} \text{sen}\varphi (\cos\alpha \cos\varphi + \text{sen}\alpha \text{sen}\varphi)^2 dA = \\
 &= 2 C_{\text{pt2}} q_\infty \int_0^\pi \left( R_N^2 \int_0^\varphi (\cos\alpha \cos\delta + \text{sen}\alpha \text{sen}\delta)^2 \text{sen}^2\delta d\delta \right) d\eta = \\
 &= \pi R_N^2 C_{\text{pt2}} q_\infty \int_0^\varphi (\cos\alpha \cos\delta + \text{sen}\alpha \text{sen}\delta)^2 \text{sen}^2\delta d\delta - \pi R_N^2 C_{\text{pt2}} q_\infty \\
 &\quad \times \int_0^\varphi (-\cos\alpha \cos\delta + \text{sen}\alpha \text{sen}\delta)^2 \text{sen}^2\delta d\delta = \\
 &= \pi R_N^2 C_{\text{pt2}} q_\infty \left( 4 \cos\alpha \text{sen}\alpha \int_0^\varphi \text{sen}^3\delta \cos\delta d\delta \right) \\
 &= \pi R_N^2 C_{\text{pt2}} q_\infty \left( 4 \cos\alpha \text{sen}\alpha \int_0^\varphi \text{sen}^3\delta d\delta \text{sen}\delta \right) = \\
 &= \pi R_N^2 C_{\text{pt2}} q_\infty \cos\alpha \text{sen}\alpha \text{sen}^4\varphi = \frac{q_\infty C_{\text{pt2}}}{2} S_{\text{ref}} \cos\alpha \text{sen}\alpha \text{sen}^2\varphi
 \end{aligned}$$

because of  $dA = R_N^2 \text{sen}\varphi d\varphi d\eta$ ,  $R_b = R_N \text{sen}\varphi$  and  $S_{\text{ref}} = \pi R_b^2$ .

Therefore,

$$C_N = \frac{N}{q_\infty S_{\text{ref}}} = \frac{C_{\text{pt2}}}{2} \cos\alpha \text{sen}\alpha \text{sen}^2\varphi = \frac{(2-\varepsilon)}{2} \cos\alpha \text{sen}\alpha \text{sen}^2\varphi.$$

As further expression to compute drag and lift coefficient, we have the following relationships:

$$C_D = C_{\text{Do}} + 12 (1 - C_{\text{Do}}) \sin^2 \frac{\alpha}{2} - 6 (6 - 5C_{\text{Do}}) \sin^4 \frac{\alpha}{2} + 4 (6 - 5C_{\text{Do}}) \sin^6 \frac{\alpha}{2} \quad (4.74)$$

$$C_L = \left[ 2 (1 - C_{\text{Do}}) - \left( 3 - \frac{5}{2} C_{\text{Do}} \right) \sin^2 \alpha \right] \sin \alpha \quad (4.75)$$

Moreover, by imposing the pitch moment balance about the vehicle heat shield nose we have:

$$C_{m_{\text{nose}}} = -\frac{x_{\text{cp}}}{L_{\text{ref}}} C_N = -\frac{(2-\varepsilon)}{2L_{\text{ref}}} x_{\text{cp}} \cos\alpha \sin\alpha \sin^2\varphi \quad (4.76)$$

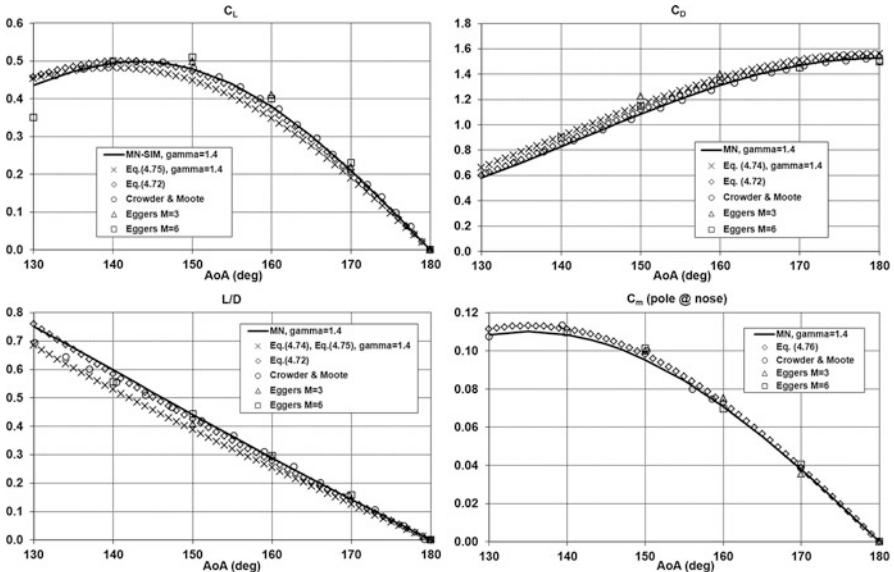


**Fig. 4.43** Lift, drag, L/D ratio, and pitching moment coefficients versus AoA  $\alpha$ . Comparison among theoretical, numerical, and experimental data

where  $x_{cp}$  is the abscissa of the vehicle center-of-pressure (cp) that is influenced, as well known, by the real gas effects.

The curves of lift, drag, aerodynamic efficiency and of pitching moment coefficients for  $130^\circ \leq \alpha \leq 180^\circ$  (note that AoA is measured from capsule apex, as done in the past for Apollo command module) are shown in Fig. 4.43.

In particular, the capsules' thermal shield nose is assumed as pole for moment calculation (i.e., 0,0,0).

Figure 4.43 collects CRV aerodynamic coefficients as evaluated by SIM with panel method and modified Newtonian Theory (MN). Some experimental results (i.e., Crowder and Moote) and numerical data (i.e., Eggers) are also reported in order to highlight accuracy of results [20]. As one can see, theoretical, experimental, and numerical data compare very well, thus confirming that engineering-based estimations represent a reliable design tool in order to assess preliminary aerodynamics of capsule.

#### 4.8.1.3 Pressure Distribution on the Pitch Plane Forward Heat Shield

The pressure distribution ( $p_w$ ) on the capsule pitch plane forward thermal shield (see Fig. 4.48) can be evaluated considering that Eq. (4.67) can be rearranged to give

$$\frac{p_w}{p_{t2}} = \sin^2\theta + \frac{p_\infty}{p_{t2}} \cos^2\theta = \cos^2\varphi + \frac{p_\infty}{p_{t2}} \sin^2\varphi \quad (4.77)$$

where, assuming that all of the air particles at the edge of the boundary layer have essentially the same entropy, the ratio  $p_\infty/p_{t2}$  can be evaluated by means of an isentropic expansion:

$$\frac{p_\infty}{p_{t2}} = \frac{2 \left[ 2 \left( 2\gamma - \frac{\gamma-1}{M_\infty^2} \right) \right]^{\frac{1}{\gamma-1}}}{M_\infty^2 (\gamma + 1)^{\frac{\gamma+1}{\gamma-1}}} \quad (4.78)$$

#### 4.8.2 Numerical Assessment of CRV Aerodynamics

CRV aerodynamics evaluated in the present CFD effort analysis is summarized in Table 4.5, while the curves of lift, drag, aerodynamic efficiency, and pitching moment coefficients for  $\alpha$  ranging from  $150^\circ$  to  $180^\circ$  are shown in Figs. 4.44, 4.45, 4.46, and 4.47, where results of engineering analysis, obtained for different specific heat ratio ( $\gamma$ ), and experimental data provided in Ref. [20], are also reported.

As shown in Table 4.5, CFD results involve both Dunn–Kang and Park chemical kinetic models in order to appreciate the effect of finite rate chemistry on CRV aerodynamics. Indeed, results summarized in Table 4.5 highlight that, from aerodynamic point of view, there are not very significant differences when using Dunn–Kang or Park chemical kinetic models.

**Table 4.5** Numerical CRV aerodynamics

Mach	Flow model	AoA	$C_D$	$C_L$	L/D	$C_m$ (pole at nose)
10	PG <sup>a</sup>	180	1.4760	0.0000	0.0000	0.0000
	RG <sup>a</sup> (Table 4.1)		1.5300	0.0000	0.0000	0.0000
12	RG (Table 4.1)	152	1.1814	0.4664	0.3948	0.1064
16	PG	152	1.0965	0.4339	0.3957	0.0964
	RG (Table 4.1)		1.1392	0.4479	0.3932	0.1067
	RG (Table 4.2)		1.1389	0.4480	0.3934	0.1066
19	PG	170	1.4300	0.2104	0.1471	0.0341
	RG (Table 4.1)		1.5000	0.2143	0.1429	0.0424
19	PG	159	1.2400	0.3750	0.3024	0.0733
	RG (Table 4.1)		162.5	1.3800	0.3437	0.2491
19	PG	152	1.0940	0.4328	0.3956	0.0956
	RG (Table 4.1)		1.1315	0.4456	0.3938	0.1060
	RG (Table 4.2)		1.1386	0.4541	0.3988	0.1008

<sup>a</sup>PG perfect gas, RG reacting gas

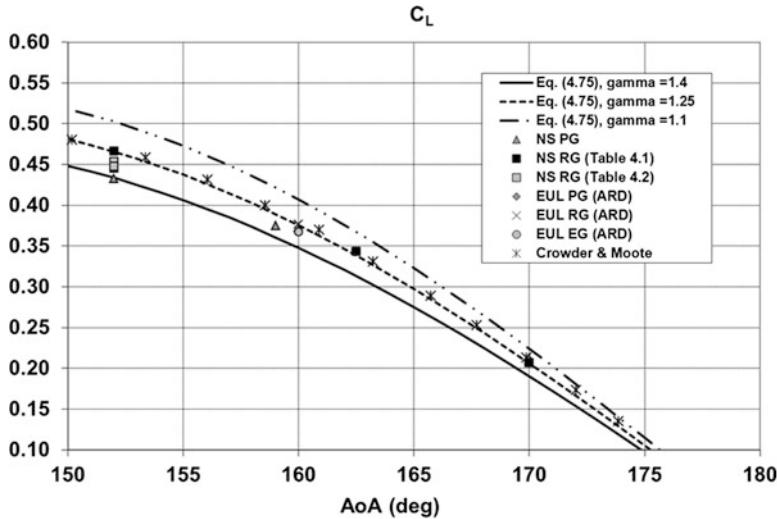


Fig. 4.44 Lift coefficient

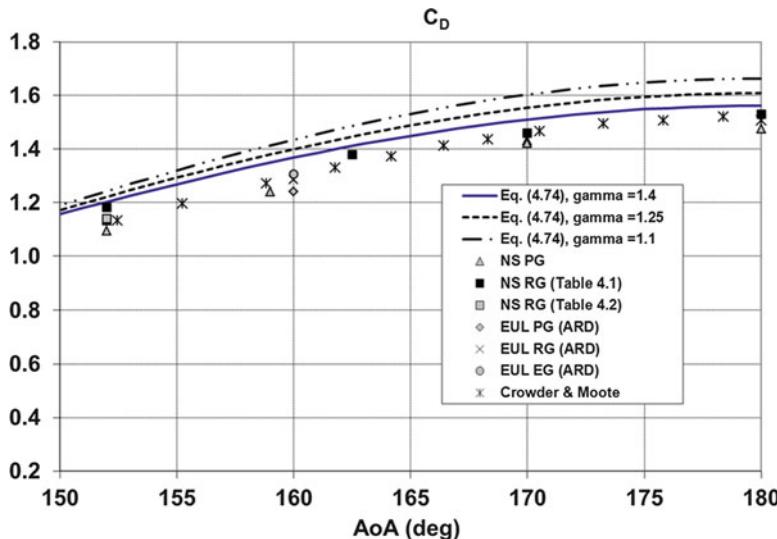


Fig. 4.45 Drag coefficient

Moreover, result comparisons reported in Figs. 4.44, 4.45, 4.46, and 4.47 show that, despite the simplicity of the surface impact method (i.e., MN), this engineering-based method provides relatively accurate prediction of CRV aerodynamic efficiency. However, the displacement from MN theory solution is in the

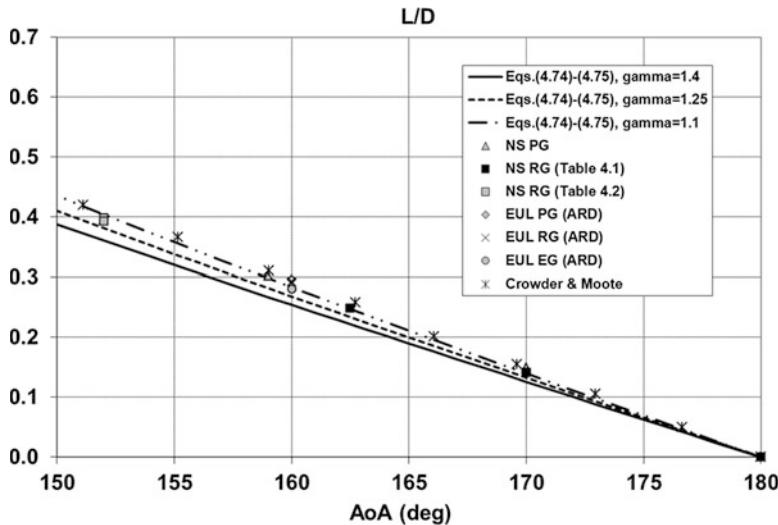


Fig. 4.46 Aerodynamic efficiency

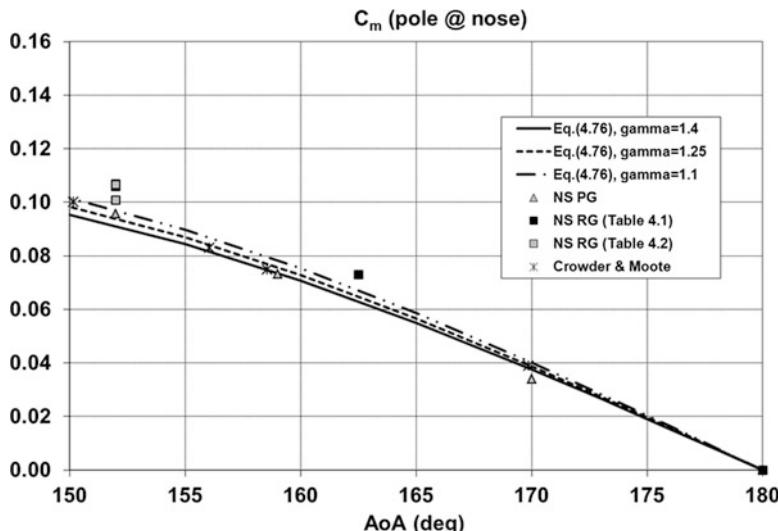
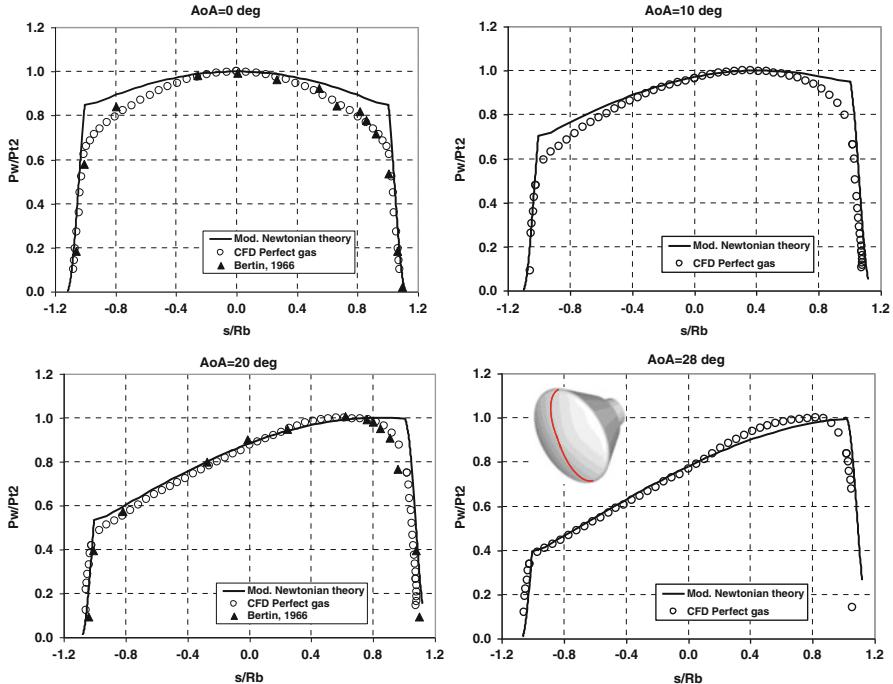


Fig. 4.47 Pitching moment coefficient

range of 10 % for the lift and drag coefficients, whereas is of 20 % for the pitching moment, thus confirming the strong effect of the real gas behavior on the capsule trim conditions.

The next set of comparisons between engineering, experimental, and CFD results are reported in Fig. 4.48. This figure displays the pressure ratio  $p_w/p_{t2}$  comparison,



**Fig. 4.48** Pressure distribution in the capsule pitch plane for four AoAs (i.e., 0, 10, 20, 28°). Comparison among MN, present CFD results, and wind tunnel data

on the capsule pitch plane forward thermal shield, between MN theory, present CFD computations and wind tunnel (WT) experimental data provided in Ref. [20], for four AoAs (i.e., 0°, 10°, 20°, and 28°).

Experimental data refer to a test performed in the Tunnel C at Arnold Engineering and Development Centre (AEDC) at free-stream Mach number of 10.18, Reynolds number  $R_{\infty D}$  of  $1.1 \times 10^6$ , and AoA = 0° and 20°. As one can see, numerical, experimental, and theoretical data compare rather well for all the AoAs. Note that the differences existing between numerical and modified Newtonian pressures, close to the capsule corner (i.e.,  $s/R_b = 0.965$ ), are due to the fact that capsule forebody is a truncated spherical cap.

This means that the stream wise velocity gradients must be relatively large (i.e., above the value needed for a full hemisphere) in order to produce sonic flow at capsule corner. As a consequence, an increasing of local heat flux is also expected.

As far as chemical kinetics effect is concerned, Fig. 4.49 shows for lift and drag coefficients the comparison among MN and CFD results for PG and RG computations at  $M_\infty = 16$  and  $M_\infty = 19$ . The same comparison for pitching moment coefficient is reported in Fig. 4.50.

Figure 4.49 confirms that for both Mach numbers, MN results represent a reliable estimation provided that they are confined between MN and PG estimations.

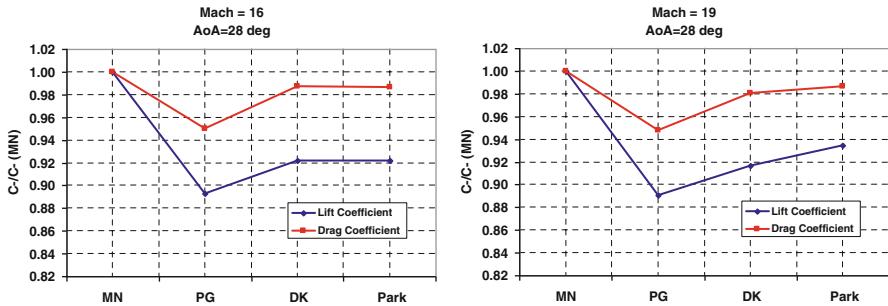


**Fig. 4.49** Effect of chemical reactions at  $\text{AoA} = 28^\circ$  for  $M_\infty = 16$  and  $M_\infty = 19$ . Comparison among MN, PG, Dunn–Kang, and Park computations

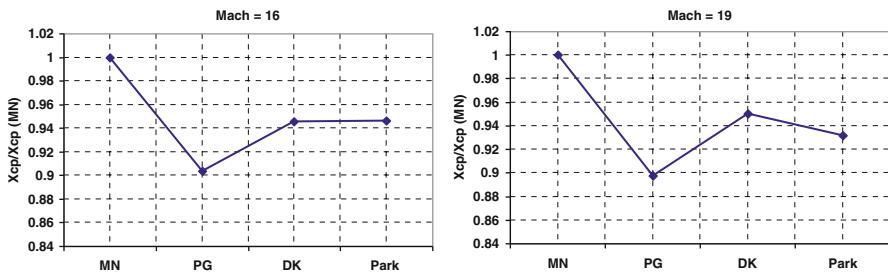


**Fig. 4.50** Effect of chemical reactions on  $x_{\text{cp}}$  at  $\text{AoA} = 28^\circ$  for  $M_\infty = 16$  and  $M_\infty = 19$ . Comparison among MN, PG, Dunn–Kang, and Park computations

Moreover, the left side of figure highlights that at  $M_\infty = 16$  no differences are expected for aerodynamic force coefficients passing from Dunn–Kang to Park kinetics.

On the contrary at  $M_\infty = 19$ , both lift and drag coefficients increase ranging from PG through DK and Park kinetics. Differences of about 2 % and 5 % are observed concerning the value of  $C_L$  and  $C_m$ , respectively. These conclusions are confirmed by Fig. 4.50 where is recognized the abscissa of CRV center of pressure ( $x_{\text{cp}}$ ) nondimensionalized with respect to the MN estimation.

$C_p$  increases at the stagnation region and decreases over the remaining CRV surface, thus leading to a forward (toward nose) shift of center-of-pressure, or equivalently, positive (nose up) pitching moment, as the flow  $\gamma$  decreases.

In particular, Fig. 4.50 (left) shows that at  $M_\infty = 16$ , the value  $x_{\text{cp}}$  in the case of PG solution decreases of about 10 % with respect to the MN estimation. However, at this value of Mach, there is no difference between the values provided by both chemical models. The right side, instead, shows that at  $M_\infty = 19$ , even if the value of  $x_{\text{cp}}$  in the case of PG solution decreases again of about 10 % with respect to the MN estimation, the two chemical models provide values that differ each other of about 2 %. Note that the latter difference may be dangerous if neglected when designing vehicle thermal shield.

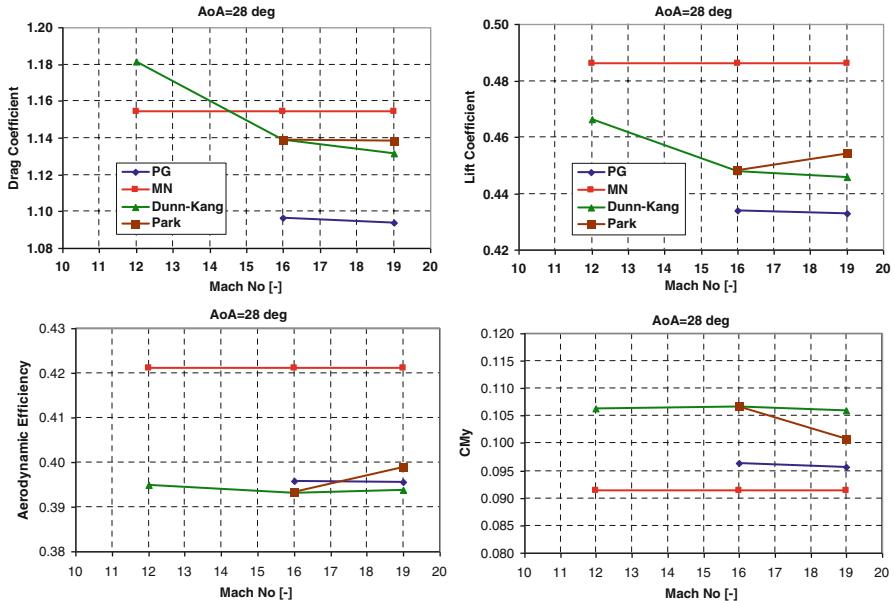


**Fig. 4.51** Effect of chemical kinetics on capsule aerodynamics at  $\text{AoA} = 28^\circ$  vs. Mach number. Comparison among MN, PG, Dunn–Kang, and Park computations

Finally, the Mach number effect on the capsule aerodynamics can be recognized in Fig. 4.51.

It can be observed that for a fixed value of AoA (i.e.,  $152^\circ$ ), assuming the Dunn–Kang chemical model, an increase in the Mach number causes a slight reduction of  $C_L$  and  $C_D$ , while their ratio and the values of  $C_{M\gamma}$  remain practically constant. On the contrary, for Park kinetics passing from  $M_\infty = 16$  to  $M_\infty = 19$   $C_L$  increases,  $C_D$  does not change, while  $C_m$  decreases.

Finally, Fig. 4.52 shows the effects of reaction mechanism on CRV aerodynamics when the capsule is flying at  $\text{AoA} = 28^\circ$ ,  $M_\infty = 19$ , and  $H = 57$  km.

This figure highlights, in a step-by-step approach, the effect of each reaction mechanism. As one can see, results for Zeldovich model compares globally well with those of the complete reaction mechanism, i.e., 17 reactions.

#### 4.8.2.1 CRV High-Altitude Aerodynamics

As far as high-altitude CRV aerodynamics is concerned, it is worth noting that upon the re-entry vehicle started its descent leg, the atmospheric density is low enough such that the continuum assumption breaks down and one must begin to consider the general macroscopic mass, force, and energy transfer problem at the vehicle surface. The viscous flow no-slip assumptions (zero velocity at the wall and gas temperature

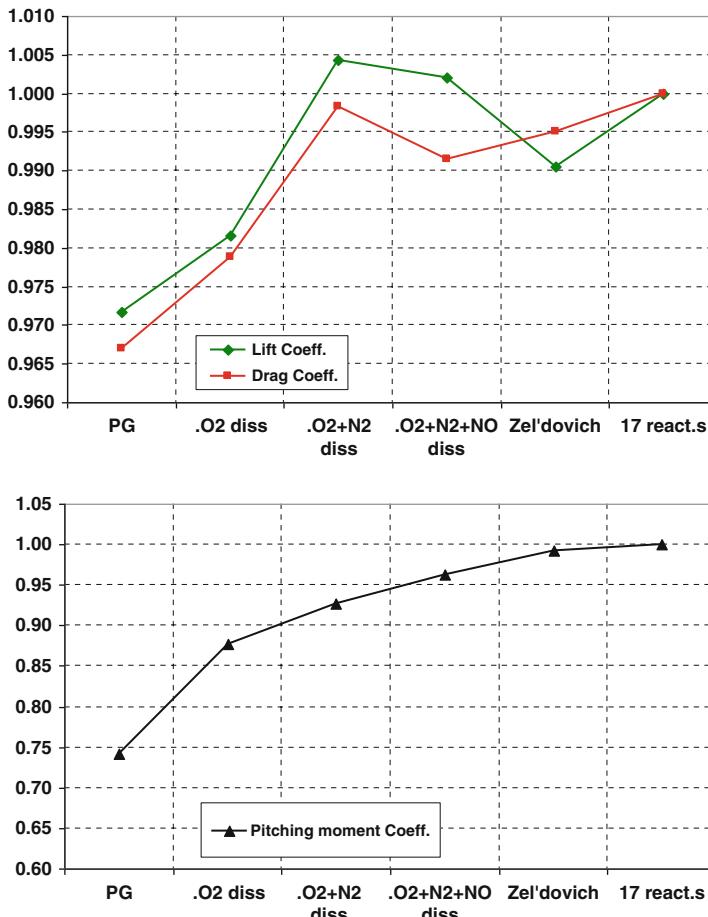


**Fig. 4.52** Effects of reaction mechanism on CRV aerodynamics at  $\text{AoA} = 28^\circ$ ,  $M_\infty = 19$ , and  $H_\infty = 57 \text{ km}$

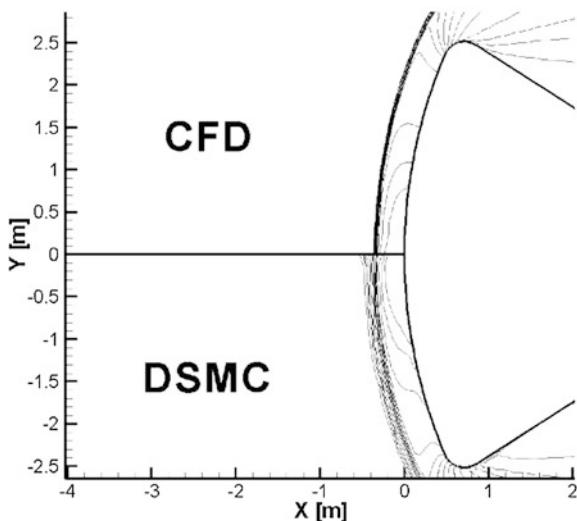
equals the wall temperature) begin to fail. In fact, they have to be replaced by slip effects, in which a velocity and temperature jump at the wall must be assumed. Further, Navier–Stokes model fails as well and the DSMC method must be used for the flowfield analysis.

Indeed, the aerodynamic characteristics of the CRV are determined by individual, scattered molecular impacts, and must be analyzed on the basis of kinetic theory. For example, at 200 km altitude, the CRV is in free molecular (FM) flow. In fact, the Knudsen number is about  $\text{Kn}_{\infty,\text{Lref}} = 70$ . Thus, CRV aerodynamics assessment for the altitude ranging from entry interface (e.g., 120 km) to about 90 km has been provided by means of axisymmetric DSMC computations, summarized in Table 4.6.

**Table 4.6** Free-stream conditions of DSMC simulations

Altitude (km)	$T_\infty$	$\text{Kn}_\infty$	$M_\infty$	Chemical model
85	181	0.0019	28.12	Park
105	211	0.06	25.5	Park
105	211	0.06	25.5	Dunn and Kang
115	304	0.32	20.01	Park
125	433	1.0	16.67	Park

**Fig. 4.53** Pressure isolines; comparison between CFD and DSMC at 85 km altitude



For each altitude, the free-stream velocity of 7,600 m/s has been taken into account and the wall has been considered cold ( $T_w = 300 \text{ K}$ ). Free-stream thermodynamic parameters were provided by the US Standard Atmosphere 1976. Air was considered made up of five chemical species ( $\text{O}_2$ ,  $\text{N}_2$ ,  $\text{O}$ ,  $\text{N}$ , and  $\text{NO}$ ).

Figure 4.53 shows the pressure isolines comparison between CFD and DSMC results at 85 km altitude, while Fig. 4.54 exhibits the pressure profiles along with the stagnation line evaluated by means of DSMC and CFD with slip and no-slip flow boundary conditions.

As a result, the shock wave thickness computed by the particle code is larger with respect to the Navier–Stokes with and without slip conditions; this value, generally expressed as a multiple of the upstream mean free path, is well predicted by DSMC code for all the analyzed cases.

The CFD aerodynamic drag coefficients, evaluated by means of present DSMC simulations, have been reported and compared in Fig. 4.55, with those assessed through a quick engineering estimation provided by a bridging relationship between FM flow results and continuum that reads:

$$C_D \text{ Transitional} = C_D \text{ Continuum} + (C_D \text{ FM} - C_D \text{ Continuum}) \cdot \bar{C}_D \quad (4.79)$$

**Fig. 4.54** Pressure profiles along with the stagnation line. Comparison among CFD slip, CFD no-slip condition, and DSMC at 85 km altitude

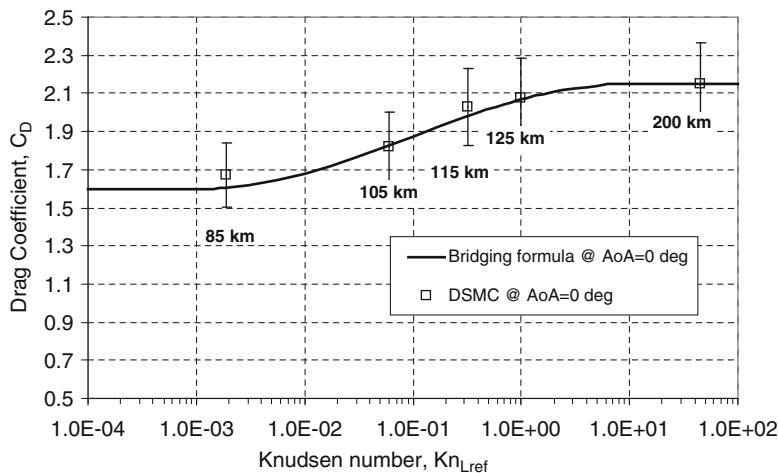
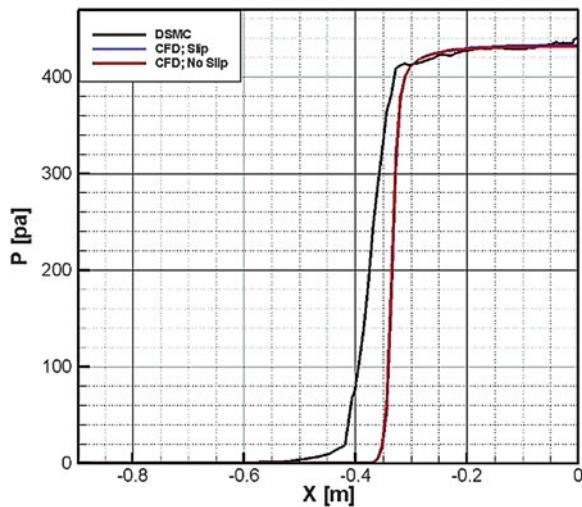


**Fig. 4.55** Drag coefficient vs. Knudsen number for AoA = 0°

where the normalized coefficient  $\bar{C}_i$  uses Knudsen number as the independent parameter:

$$\bar{C}_D = \frac{C_D - C_{D\text{Continuum}}}{C_{D\text{FM}} - C_{D\text{Continuum}}} = F(Kn_\infty) = \text{sen}^2 \left[ \frac{\pi}{8} (3 + \log_{10} Kn_\infty) \right] \quad (4.80)$$

$10^{-3} < Kn_\infty < 10$  and  $C_{D\text{Continuum}}$  and  $C_{D\text{FM}}$  are the aerodynamic drag coefficient in continuum and FM flow regimes, respectively.

The effect of rarefaction on the aerodynamic drag is clearly shown considering that  $C_D$  at AoA = 0° increases of about 24 % passing from 85 to 125 km, whereas the drag at  $H = 200$  km is 25 % higher than the one at 85 km.

## 4.9 CRV Aerothermodynamic Features

The CRV aeroheating analysis relies on several Navier–Stokes computations performed assuming chemically reacting gas model and the vehicle heat shield surface as NC, PC, and FC wall. The computations refer to fully laminar nonequilibrium flow conditions with capsule surface temperature fixed at 300 K (cold wall condition) or in radiative equilibrium (radiative cooling) condition. Note that, due to relatively low entry velocities (e.g., no radiation heat flux applies), only convective heat flux is taken into account; moreover, no heat shield ablation and recession were assumed for simplicity.

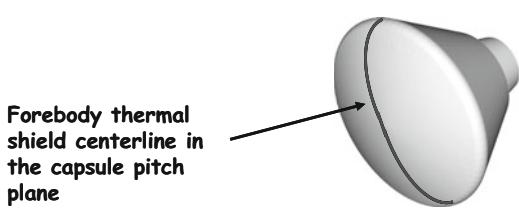
### 4.9.1 CRV Zero-Lift Aerothermodynamics

In order to illustrate the high-temperature real gas effects on CRV zero-lift aeroheating wall, heat flux comparison on the spacecraft forebody centerline (see Fig. 4.56) will be provided at the peak heating conditions of the ballistic trajectory for  $\alpha = 0^\circ$ .

For example, Fig. 4.57 compares the heat flux evaluated for PG, EG, and chemical nonequilibrium gas computation; for this latter case, the results for NCW and FCW are also reported. All these heat flux profiles are calculated for cold wall conditions.

As one can see, the higher wall heat flux is attained in the case of chemical equilibrium condition, and it is closer to the heat flux for PG simulation. This can be explained considering that, as the CRV wall is supposed cold, the chemical equilibrium leads to the recombination of dissociated atoms. When the boundary layer (BL) is in chemical nonequilibrium, CFD simulations confirm that the higher heat flux is attained for FCW. As shown, this value is lower than that for EG, but is very large compared with the case of NCW, as expected. Therefore, we can conclude that if the gas in the boundary layer is in equilibrium (e.g., fast recombination), then a surface catalyst will not have any effect on the formation of molecules. In this

**Fig. 4.56** CRV forebody centerline



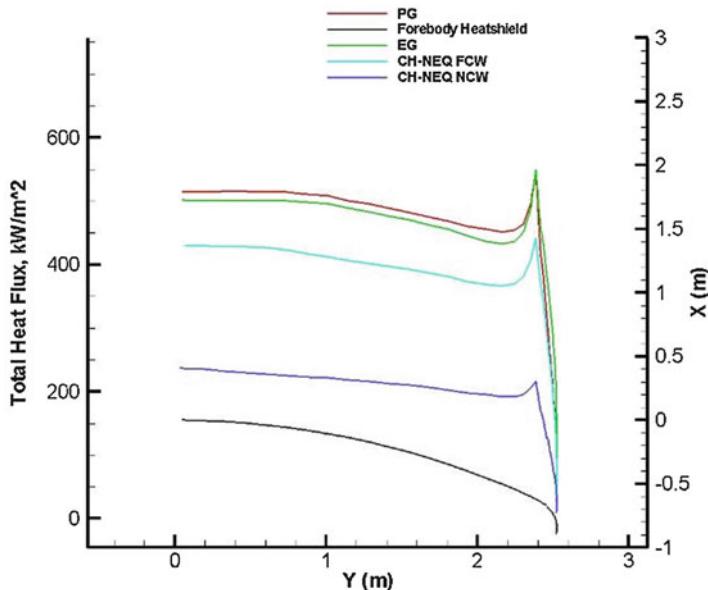


**Fig. 4.57** High-temperature air effect on capsule forebody total heat flux at AoA = 0°,  $M_\infty = 19$ , and  $H_\infty = 57$  km.  $T_w = 300$  K half body

case, in fact, atoms recombine and liberate their energy of dissociation to the gas in the BL yet. This added heat tends to increase the heat flux to the surface via thermal conduction, thus concluding that the recombination of atoms is more important than in the case of a FCW. For this reason, we regard the equilibrium condition as the reference condition in much of the state-of-the-art TPS design activities, together with the assumption of turbulent flow conditions.

In particular, Fig. 4.58 shows comparisons of the convective heat flux, along with the forebody centerline, between the cases of FC and NC cold wall, highlighting both the convective and diffusive components of heat flux in order to appreciate the effect of the chemical species diffusion toward the wall (see Eq. 4.3).

Note that the bold continuous line is the capsule forebody centerline so that x and y coordinates help the reader to localize the heat flux profile on the spacecraft OML. As shown, the ratio  $(\dot{q}_{FC}/\dot{q}_{NC})_w$  of heating for FC over that for NC is equal to about 1.5, and it is expected to decrease when the wall temperature increases, but in any case, it will be higher than the case of adiabatic radiative equilibrium wall.

As far as effect of chemical kinetics is concerned, Fig. 4.59 shows that for FCW boundary condition, a large part of  $\dot{q}_c$  is due to the energy released by the recombination of atoms at the wall so that the influence of chemical kinetics in this case is small.

On the contrary, differences in the heat flux profile for NCW underline that chemical kinetics plays a role when assessing vehicle aerodynamic heating. Therefore, we can conclude that the chemical kinetics are negligible for a catalytic wall and may

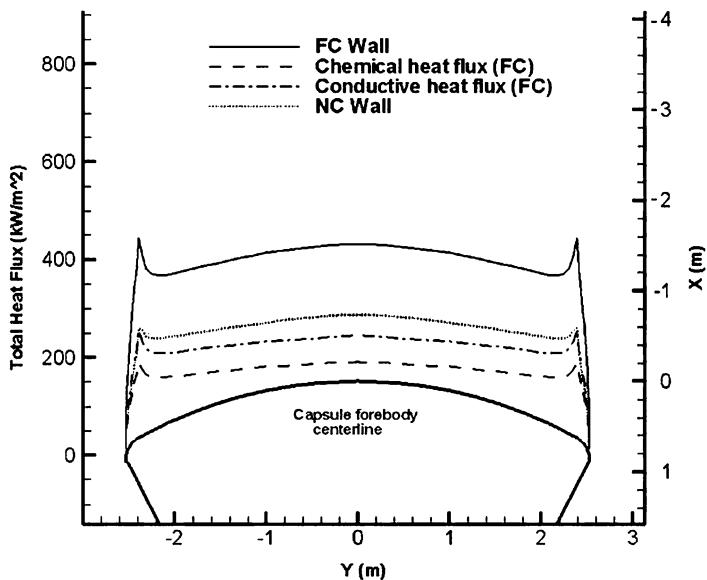


**Fig. 4.58** Heat flux on the CRV forebody centerline for  $\alpha = 0^\circ$ ,  $M_\infty = 19$ ,  $H = 57$  km,  $T_w = 300$  K. Full forebody

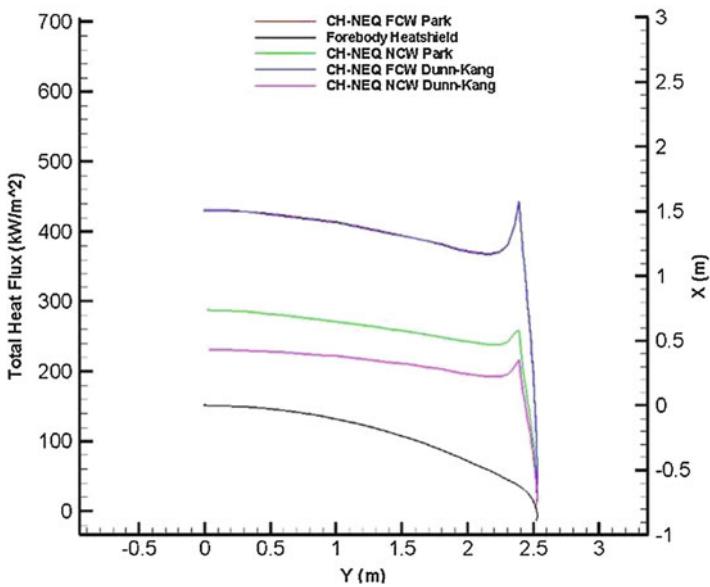


**Fig. 4.59** Effect of chemical kinetics on CRV forebody total heat flux at  $\text{AoA} = 0^\circ$ ,  $M_\infty = 19$ , and  $H_\infty = 57$  km for  $T_w = 300$  K

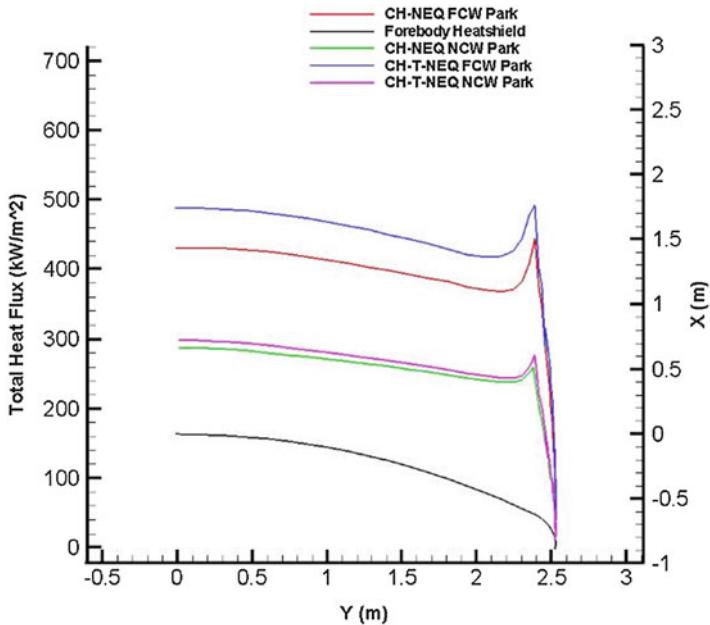


**Fig. 4.60** Effect of vibrational relaxation on CRV forebody heat flux at  $\text{AoA} = 0^\circ$ ,  $M_\infty = 19$ , and  $H_\infty = 57 \text{ km}$  for  $T_w = 300 \text{ K}$  half body

be significant in the non-catalytic case. Of course, the latter conclusion is expected depending on free-stream conditions. Indeed, at high altitude the shock layer has not dissociated because the shock layer is tenuous since pressure and density are low. Therefore, the number of particle collisions is low enough so that the chemical reactions are not much activated (e.g., the flow is nearly frozen): there is not much energy involved in dissociation. Most of the energy is in translational modes. As flying altitude decreases, the density suddenly increases and the chemical reactions are activated. At very low altitude, the shock layer is so dense that the boundary layer is close to equilibrium and the atoms recombine in the boundary layer before they have a chance to strike the wall. Hence, the BL is heated and there is more potential for heat transfer by conduction (i.e., reactions rate comeback to have a little effect).

Finally, Fig. 4.60 displays the effect of vibrational relaxation on the wall heat flux. As one can see, the heat flux profile in the case of FCW depends on vibrational relaxation more than in the case of NCW boundary condition.

#### 4.9.2 CRV AoA Aerothermodynamics

In order to illustrate the magnitude of the effects of catalytic activity on CRV Aerothermodynamics when the capsule is flying at nonzero AoA, Fig. 4.61 shows

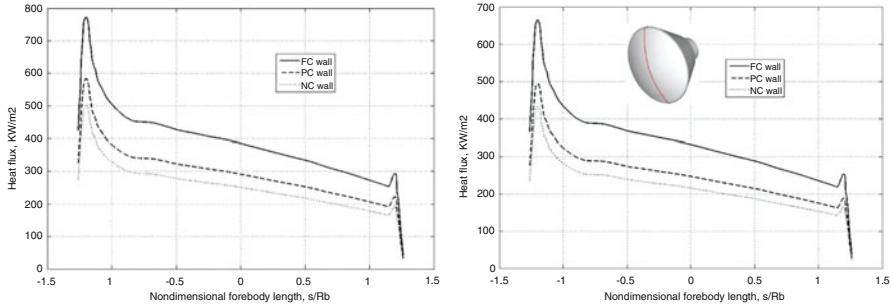


**Fig. 4.61** Heat flux on the forebody capsule centerline for ballistic (*left*) and lifting (*right*) trajectory. CRV trimmed at  $\alpha = 20^\circ$  with radiative cooled wall. Comparison among the cases FC, PC, NC wall

the comparison of the heat flux along with the forebody centerline at surface radiative cooling conditions ( $\varepsilon = 0.85$ ), among the cases of FC, PC, and NC wall, at the peak heating conditions of both ballistic and lifting re-entries. It is worth nothing that to take in to account for altitude effect on CRV aeroheating, we have supposed that the ballistic entry is performed at the same angle of attack as the guided case (i.e.,  $\alpha = 20^\circ$ ). Moreover, no heat shield ablation and recession were assumed for simplicity. As one can see, the peak heating does not occur at the stagnation point, which is on the spherical cap, but on the capsule toroidal surface where large changes in the flow gradients along the surface occur (see Fig. 4.18). In particular, the overheating caused by the catalytic action is potentially very large compared with the case of NCW: the largest difference occurs at the sphere-cone junction (corner fillet). The heat flux attained in correspondence of the hotter capsule corner ranges from about 500 to 800  $\text{Kw/m}^2$  in the case of ballistic re-entry, while when the capsule performs a lifting return, the heating range refers to about  $400 \div 700 \text{ Kw/m}^2$ .

Therefore, the corner radius is the dominant geometric feature for the convective heating (instead of heat shield radius of curvature,  $R_N$ ), and it is confirmed that significant reduction in convective heat flux occurs if the thermal shield is made of a non-catalytic TPM.

In reality, TPS tiles are generally coated with far less catalytic layer as RCG (reaction cured glass); the heating rates should be referred to PCW boundary conditions. In this case, the radiative equilibrium temperature comparison between ballistic and lifting return can be seen in Fig. 4.62. This figure confirms that the ballistic re-entry represents a more challenging trajectory from the aeroheating point of view. Figure 4.62 also shows that the temperature distribution expected on the CRV forebody is not compatible with a reusable thermal shield made of HRSI. Therefore, in the light of the results of Fig. 4.62, another TPM must be considered.

Figure 4.63 displays the surface distribution of both static pressure and radiative cooling temperature over the CRV front shield in the case of NCW (left side) and FCW (right side). As it is clearly evident, the catalytic behavior of the heat

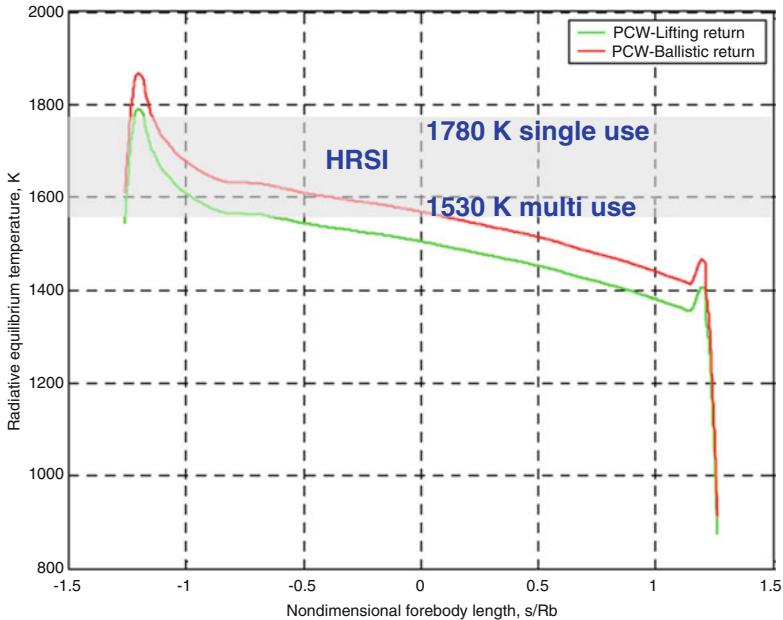


**Fig. 4.62** Radiative equilibrium temperature at CRV forebody centerline. Ballistic (red) and lifting (green) return for PCW thermal shield

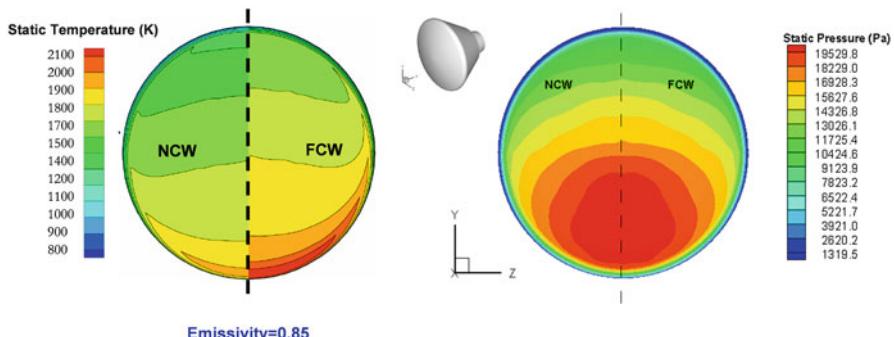


**Fig. 4.63** Surface distribution of static pressure and radiative cooling temperature over CRV forebody heat shield for both NCW (left side) and FCW (right side). Ballistic return

shield material does not affect the surface distribution. Also a peak pressure of about 20 kPa occurs at the stagnation point, while the temperature distribution, as highlighted before, depends significantly on the thermal shield catalyticity.

Finally, Fig. 4.64 shows the skin friction distribution both on the capsule leeside and windsides with static pressure contours. As one can see, surface streamlines highlight the complexity of the flow structure that takes place on CRV at 20° AoA

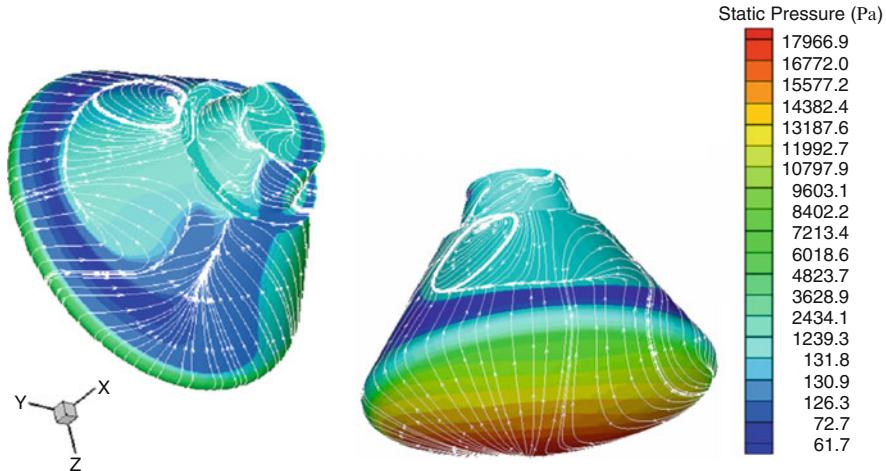


**Fig. 4.64** Pressure distribution and vehicle surface flow patterns.  $M_\infty = 19$ ,  $\text{AoA} = 20^\circ$ ,  $H = 57 \text{ km}$ , reacting gas computation

as, for example, the separation bubble at the vehicle afterbody. As shown, the flow remains attached on the windward side of the conical afterbody, while separation occurs near the maximum diameter point on the CRV shoulder. It should be noted that the knowledge of this point is relevant for the CRV afterbody aeroheating assessment.

### 4.9.3 CRV High-Altitude Aerothermodynamics

As far as CRV high-altitude aeroheating is concerned, Fig. 4.65 shows the heat flux computed by DSMC when the CRV is flying at 105 km altitude, considering both Park and Dunn–Kang chemical kinetics for NCW boundary conditions. For the particle simulations, Park model exhibits a higher heat flux and is confirmed by Fig. 4.66 in which the temperature profiles along the stagnation line for the two used chemical models is reported.

In fact, the temperature of the particles hitting the wall computed by Park model is higher and, as a consequence, also the energy. Note that in the NCW case the global heat flux at wall is calculated by DSMC tool as difference between incident energy and reflected one without chemical contribution. The reflected energy is a function of the imposed wall temperature (equal for both cases) since the fully accommodated Maxwell gas–surface interactions hypothesis is taken into account; then the temperature of the hitting particles causes the higher incident energy for the Park model case and therefore for the global heat flux too.

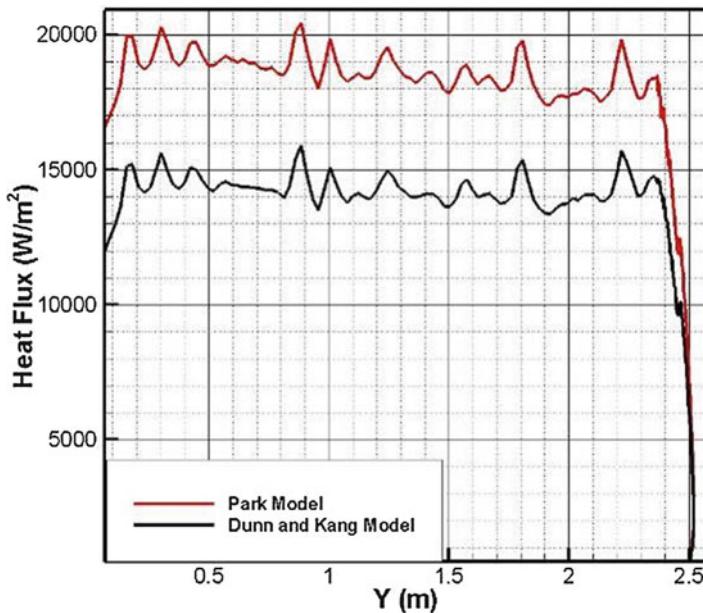


Fig. 4.65 DSMC Heat flux distribution at 105 km altitudes

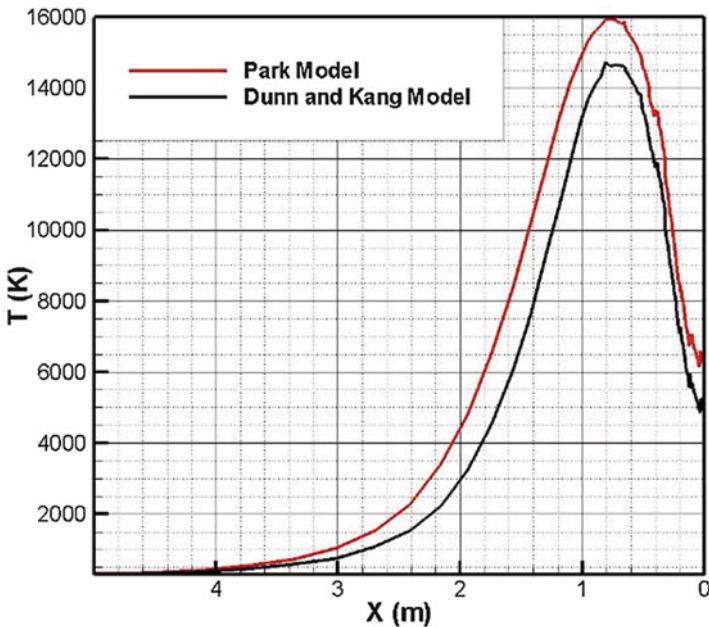


Fig. 4.66 DSMC temperature profiles along with the stagnation line; at 105 km altitudes

**Table 4.7** ONERA S4 exit conditions

$P_0$ (bar)	85	25
$T_0$ (k)	1151	1,108
$Re_D$	967,237.3	319,208
$M$	9.92	9.72
$P$ (Pa)	211.3	71.17
$T$ (k)	55.7	55.7
$T_{wall}$ (k)	300	300
Xeg/D	0.26	0.26
Yeg/D	0.0353	0.0353
AoA ( $^\circ$ )	-20	-20

Ref. [21]

## 4.10 Reliability of Numerical Study

In order to assess the reliability of present CFD analyses, a numerical rebuilding of both available experiment test campaigns and flight data has been performed. In particular, for what concerns pressure distribution and aerodynamic coefficient, a numerical rebuilding of ONERA S4 WT test, reported in Ref. [21], and of flight data of ARD experimental flying test bed has been performed.

Finally, for the aeroheating, a number of tests performed in Tunnel C of AEDC have been numerically rebuilt. The S4 tests campaign provided pressure profiles on the forebody centerline of the ARD capsule to assess vehicle aerodynamics. Test reservoir conditions considered are  $P_0 = 25$  bar and  $T_0 = 1,108$  K. These values correspond to free-stream conditions of  $M_\infty = 9.72$ ,  $P_\infty = 71.17$  Pa,  $T_\infty = 55.70$  K, and  $\alpha = 20^\circ$ , as summarized in Table 4.7.

They refer to S4 exit conditions for two different Reynolds number, at a Mach number of about 10. Pitching moment versus AoA is also provided.

Recalling that experimental tests were performed with a flow total temperature of about 1,100 K, the CFD simulations are carried out with perfect gas model only [22, 23]. Results of present computations are summarized and compared with experimental data hereinafter. For example, the flowfield past the CRV is shown in Fig. 4.67, where the Mach number contour field is plotted and compared with a Schlieren image captured in the S4 facility [21].

As shown, good agreement is obtained for bow shock stand-off and curvature; this is an important prerequisite for the validation of a CFD code against experimental data [24, 25].

Further, Fig. 4.68 compares experimentally obtained oil flow patterns with our numerically predicted wall-shear stress. The separated zone on the back side is rather well captured.

As far as pressure field analysis is concerned, several comparisons for the pressure coefficient ( $C_p$ ) are provided among present numerical results and numerical and flight data available for Apollo and ARD capsules [5, 19, 21].

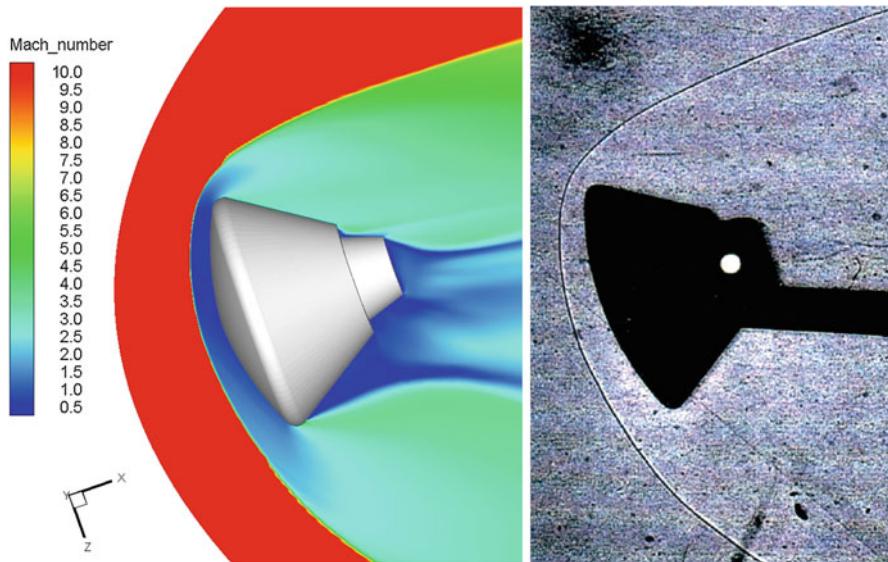


**Fig. 4.67** Mach number computed contours and comparison with the ARD Schlieren photograph taken in the ONERA S4 WT for  $M_\infty = 10$  and  $\alpha = 20^\circ$  ( $P_0 = 25$  bar)

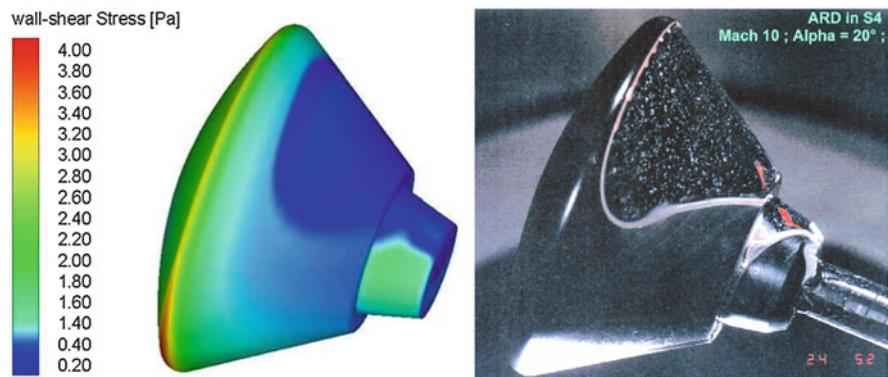


**Fig. 4.68** Wall shear stress. Comparison with ARD oil flow patterns in the ONERA S4 WT

For example, Fig. 4.69 shows pressure coefficient comparisons among present computation, experimental data, and numerical results provided by Walpot in Ref. [21]. In the same figure, it is also shown comparison for the aerodynamic pitching moment coefficient. As one can see, from Figs. 4.67, 4.68, and 4.69, experimental and numerical data compare rather well.

For what concerns capsule aeroheating, Fig. 4.70 shows the comparison of the heat flux at the capsule forebody centerline among present results and heating rates measured in Tunnel C, for a nominal free-stream Mach number of 10 and for free-stream Reynolds number, based on the model body diameter, of  $1.2 \times 10^6$  [19].

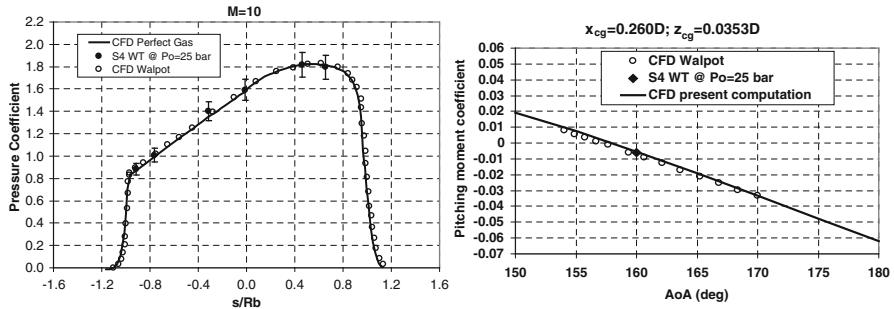
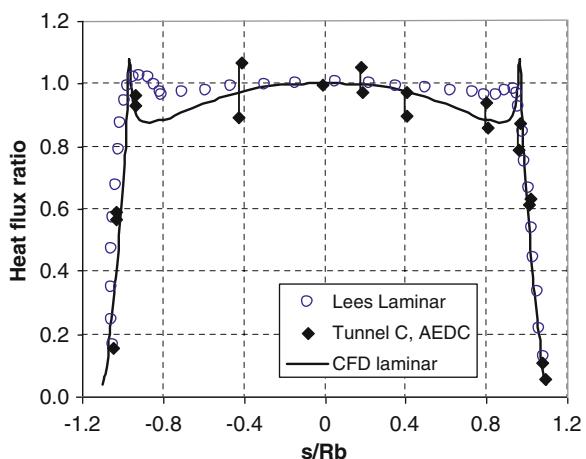


**Fig. 4.69** Pressure coefficient on forebody centerline (left) and pitching moment coefficient (right). Comparison among present computations and data provided in Ref. [21]

**Fig. 4.70** Heat flux distribution on the forebody centerline. Comparison among present, WT, and Lees data [19]



Note that in Fig. 4.70 Lees theoretical estimations are also reported as reference. Figure 4.71 provides present CFD results and flight data comparisons at the ARD trajectory point at Mach 10 and  $\alpha = 20^\circ$  [5]. As shown, numerical reconstruction refers to PG and nonequilibrium computations, whereas the error bars associated to flight data account for uncertainties of preflight aerodynamic database (drag coefficients), measurements, and atmospheric pressure dispersion [5].

Real gas effects are clearly displayed on the stagnation region [26–28]. Figure 4.72 compares CFD results and ARD flight data sampled at the trajectory point at Mach number 15 [5]: the magnitude of real gas effects is increased at this flight condition compared to Mach 10 one. Real gas effects, however, are maximized at Mach number of 24, a case displayed in Fig. 4.73 [29–32]. Therefore, Figs. 4.71, 4.72, and 4.73 suggest that CFD results compare rather well with flight data both for PG and RG computations. Note that RG CFD results refer to both nonequilibrium and equilibrium conditions in order to assess also the effect of flow chemical conditions.

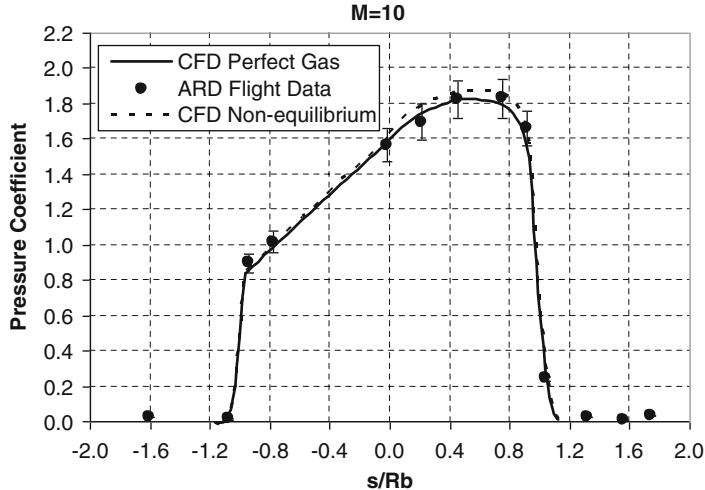


**Fig. 4.71** Pressure coefficient distribution on the CRV forebody centerline at  $M_\infty = 10$ . Comparison between present CFD results and ARD flight data [5]

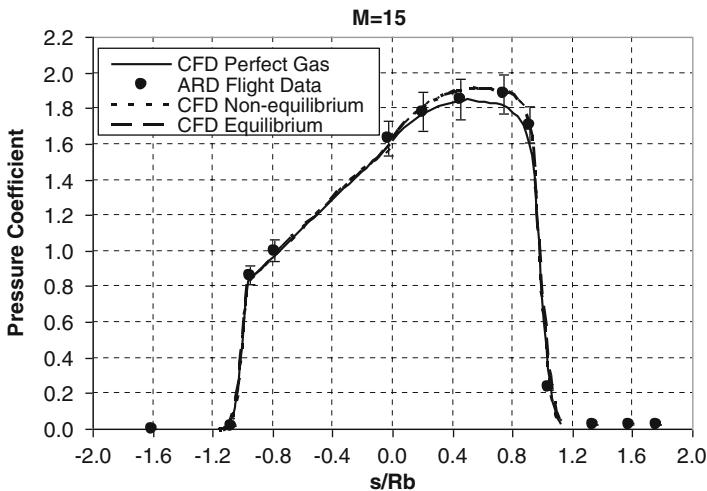


**Fig. 4.72** Pressure coefficient distribution on the CRV forebody centerline at  $M_\infty = 15$ . Comparison between CFD and ARD flight data [5]

In particular, as shown in Fig. 4.74, where  $C_p$  profiles at various Mach numbers are provided, numerical computations are able to describe the differences between RG and PG, which increase with the altitude along the ARD re-entry trajectory. Indeed, the main impact on the pressure coefficient is localized at the stagnation-point region and on the windward and leeward expansion zones [33, 34]. The stagnation point shifts in the direction of the windward side and the stagnation

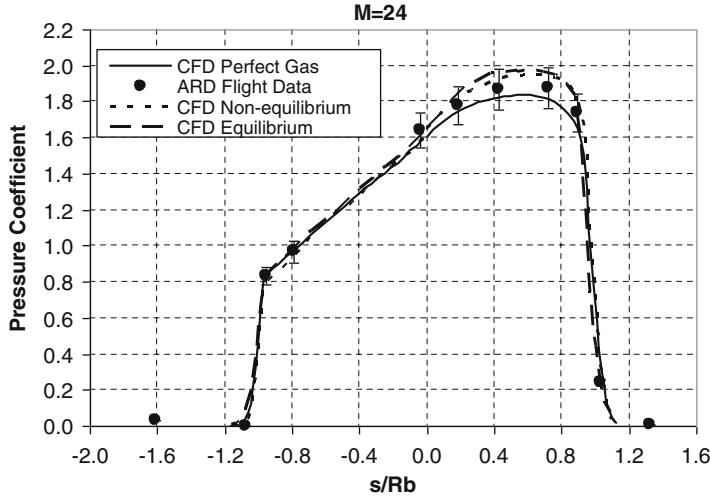


**Fig. 4.73** Pressure coefficient distribution on the CRV forebody centerline at  $M_\infty = 24$ . Comparison between CFD and ARD flight data [5]

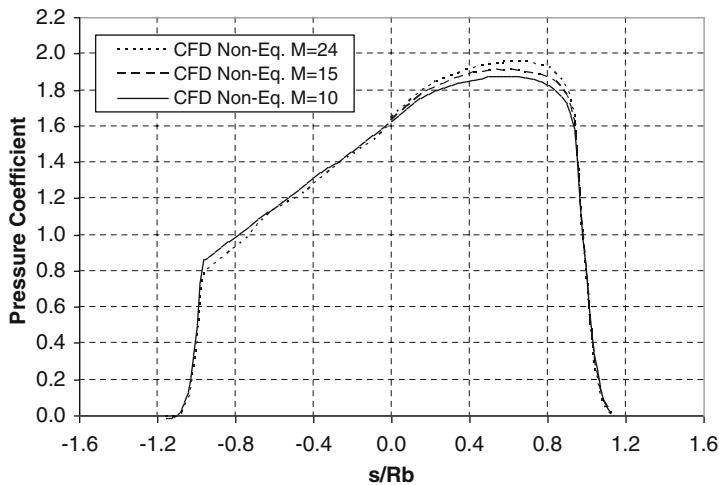


**Fig. 4.74** Pressure coefficient distribution on the CRV forebody centerline at  $M_\infty = 10, 15$ , and 24

pressure increases with the Mach number. The  $C_p$  level of the leeward shoulder (tore) decreases with the Mach number, whereas on the windward tore is stronger when the Mach increases [35, 36]. To further verify the reliability of CRV aerodynamics, Figs. 4.75 and 4.76 compare the present numerical results with ARD aerodynamics flight data reconstruction [5].

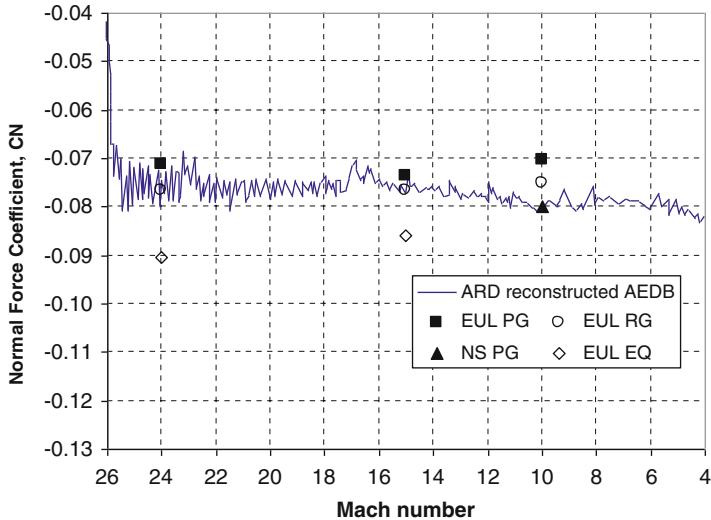


**Fig. 4.75** Normal force coefficient. Comparison between present CFD and ARD reconstructed data [5]

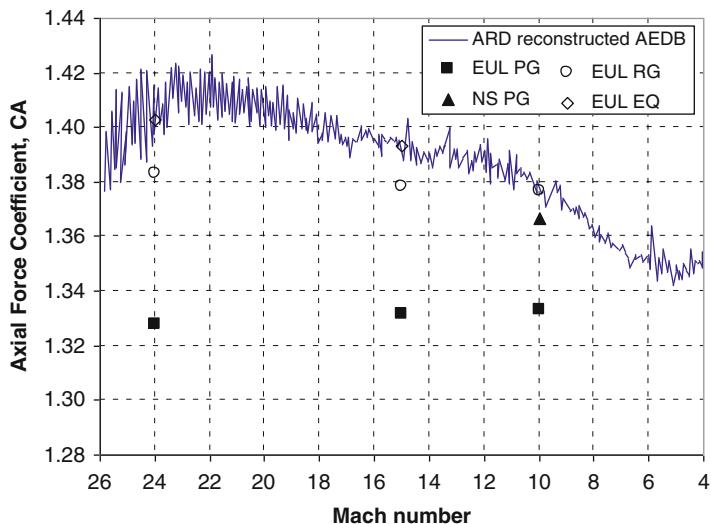


**Fig. 4.76** Axial force coefficient. Comparison between present CFD and ARD reconstructed data [5]

As shown, the trend of both axial force ( $C_A$ ) and normal force ( $C_N$ ) coefficients is coherent with the experimental data. In particular, with reference to the axial force coefficient, the CFD PG values do not match the reconstructed values, which are closer to the CFD RG values, thus suggesting a relevance of real gas effect in flight.

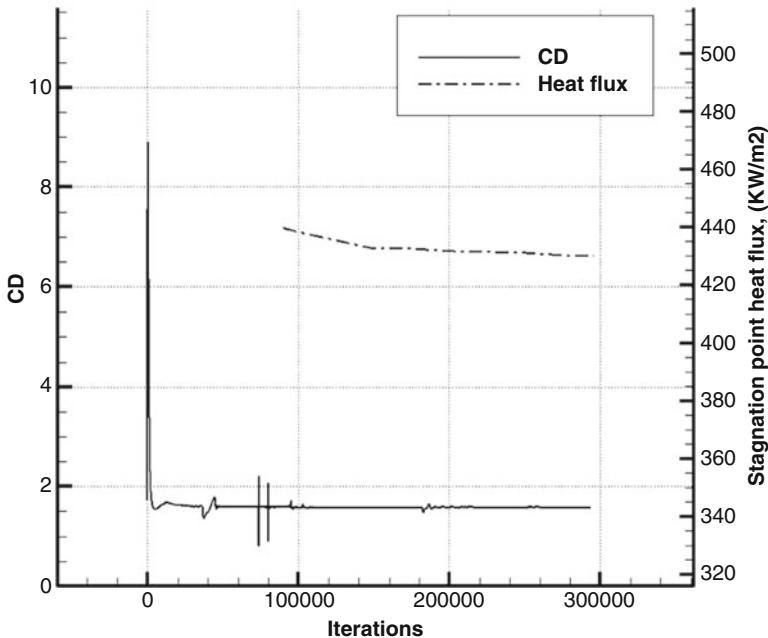


**Fig. 4.77** The convergence history of drag coefficient and stagnation-point heat flux for  $M_\infty = 19$ ,  $H = 57$  [km], and  $\alpha = 0^\circ$  CFD computation

On the other hand, for the normal force coefficient, discrepancy between present CFD results and flight data seems low. Moreover, the CFD results/flight data matching for  $C_N$  seems to be the best when a nonequilibrium assumption is considered, while for  $C_A$  matching, the best is for the equilibrium assumption. This can be explained recalling that  $C_N$  is more sensitive to the pressure flowfield, on the rear conical part of the capsule, than the  $C_A$ ; that part of the vehicle is quite difficult to compute, and the comparison with flight results in terms of pressure field is not so good, so that present CFD results for  $C_N$  cannot be considered as fully realistic [5].

All CFD results, provided in the chapter, refer to both converged and grid independent computations, as described hereinafter. In order to assess numerical solution convergence, equation residuals and aerodynamic coefficients (i.e.,  $C_L$ ,  $C_D$ , and  $C_{My}$ ) as well as the stagnation-point heat flux have been monitored during iterations. Solution convergence is assumed when equation residuals drop more than three orders of magnitude and both the aerodynamic coefficients and the stagnation-point heat flux plots are flat for enough iterations [35].

As an example, the convergence histories of drag coefficient and of stagnation-point heat flux in the case of  $M_\infty = 19$ ,  $H = 57$  km, and  $\alpha = 0^\circ$  are reported in Fig. 4.77. As one can see, numerical computation is stopped and assumed converged at about 300,000 iterations, since the plotted curves look flat.

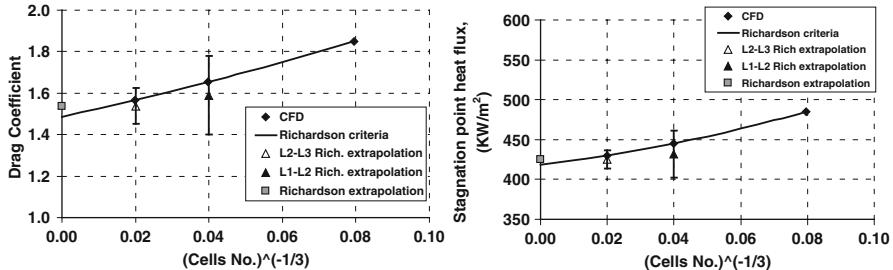


**Fig. 4.78** Grid Sensitivity Analysis: drag coefficient and stagnation-point heat flux for  $M_\infty = 19$ ,  $H = 57$  km, and  $\alpha = 0^\circ$

As far as grid convergence analysis is concerned, mesh sensitivity analyses have been carried out on three levels of the structured multiblock grid ( $L_1$ ,  $L_2$ ,  $L_3$ ), and the Richardson extrapolation criteria have been applied. The medium grid ( $L_2$ ) is obtained by halving the size of cells of the coarse ( $L_1$ ) grid, so the number of cells of  $L_2$  is 8 times larger than the number of cells of  $L_1$ . Similarly, the finer grid ( $L_3$ ) is obtained halving the size of cells of the medium grid, so its number of cells is 64 times larger than the number of cells of  $L_1$ .

As a numerical strategy, the single computation is started on the coarsest grid level, and then, when a satisfying level of accuracy has been reached, the solution is successively interpolated on finer ones and restarted. Hundreds of thousands of iterations have been necessary to reach solution convergence, both in terms of steady-state solution and grid independence of results. If the solution is in the asymptotic range of convergence, it is possible, by means of the Richardson extrapolation criteria, to estimate the value of a global ( $C_L$ ,  $C_D$ , ...) or a local (pressure, heat flux) solution functional  $f$  at virtually zero cell dimension ( $\bar{h} = 0$ ), i.e., at an infinite number of cells. This value can be obtained by interpolating the variable  $f$  versus the inverse of the cubic root of the number of cells (representative of a mean value of the cell dimension,  $\bar{h}$ ). For example, Fig. 4.78 shows the grid sensitivity analysis for both the drag coefficient  $C_D$  and the stagnation-point heat flux for the CFD computation at  $M_\infty = 19$ ,  $H = 57$  km, and  $\alpha = 0^\circ$ .

The values reported are the  $L_1$ ,  $L_2$ ,  $L_3$  and the Richardson extrapolated ones both for  $L_1 - L_2$  and  $L_2 - L_3$  grid spacing that, in the hypothesis of a spatial second-order scheme and a grid level ratio equal to 2, can be obtained by means the following formula:

$$f(\bar{h} = 0) \cong \frac{4}{3} \cdot f_{L_{i+1}} - \frac{1}{3} \cdot f_{L_i} \quad (4.81)$$

To take into account for the uncertainty levels due to the grid dependence of the variable, both Richardson extrapolated values show the Grid Convergence Index (GCI) as an error bar.

The GCI on the fine grid ( $L_3$ ) is defined as

$$GCI_{L3} = \frac{F_s}{(r^p - 1)} \left| \frac{f_{L3} - f_{L2}}{f_{L2}} \right| \quad (4.82)$$

where  $F_s$  is a safety factor (1.25 for three or more grid levels),  $r$  is the ratio between the grid spacing of two grid levels ( $r = 2$ ), and  $p$  is the (effective) order of the spatial discretization (not equal to that of theoretical consideration) that can be obtained with the following formula:

$$p = \ln \left( \frac{f_{L1} - f_{L2}}{f_{L2} - f_{L3}} \right) \cdot \frac{1}{\ln(r)} \quad (4.83)$$

For a better comprehension, the error bars are located at level three and two, of grid spacing, respectively. It is interesting to note as the  $L_2 - L_3$  error bar is fully contained within the  $L_1 - L_2$  one. In addition, as a good convergence factor, we can note as the  $L_1 - L_2$  extrapolated value is contained within the  $L_2 - L_3$  error bar [16]. Finally, note also as the  $L_1 - L_2$  Richardson extrapolation is a good estimation of the Level 3 CFD computation.

As a conclusion of this grid convergence analysis, it is worth noting that, as a general rule for such complex geometry, the maximum number of cells used was chosen in accordance with an acceptable convergence CPU time estimation.

## References

1. Balakrishnan A, Davy WC, Lombard CK (1985) Real-gas flowfields about three-dimensional configurations. *J Spacecr Rocket* 22(1):46–53
2. Park C, Yoont S (1992) Calculation of real-gas effects on blunt-body trim angles. *AIAA J* 30(4):999–1007
3. Hassan B, Candler GV, Olynick D (1993) Thermo-chemical nonequilibrium effects on the aerothermodynamics of aerobraking vehicles. *J Spacecr Rocket* 30(6):647–655
4. Putnam ZR, Braun RD, Rohrschneider RR, Dec JA (2005) Entry system options for human return from the Moon and Mars. In: AIAA atmospheric flight mechanics conference, paper AIAA-2005-5915, San Francisco, CA, USA
5. Tran Ph, Paulat JC, Boukhobza P (2007) Re-entry flight experiments lessons learned – the atmospheric reentry demonstrator ARD. In: Flight experiments for hypersonic vehicle development. Educational Notes RTO-EN-AVT-130, Paper 10. Neuilly-sur-Seine, France: RTO, pp 10–1 – 10–46. Available from: <http://www.rto.nato.int/abstracts.asp>
6. Mitcheltree RA, Gnoffo PA (1991) Thermochemical nonequilibrium issues for earth re-entry of Mars mission vehicles. *J Spacecr Rocket* 28(5):552–559
7. Riabov VV (2002) Simulation techniques in hypersonic aerodynamics. In: Proceedings of the 23rd ICAS congress, 8–13 September 2002, paper ICAS 2002 no. 181, Toronto, Canada
8. Anderson JD (1989) Hypersonic and high temperature gas dynamics. McGraw-Hill Book Company, New York
9. Wood WA (1997) Hypersonic pitching-moment shift for stardust re-entry capsule forebody, NASA/TM-206266. National Aeronautics and Space Administration, Langley Research Center, Hampton

10. Bertin JJ (1994) Hypersonic aerothermodynamics, AIAA education series. American Institute of Aeronautics and Astronautics, Washington, DC
11. Fay JA, Riddell FR (1958) Theory of stagnation point heat transfer in dissociated air. *J Aeronaut Sci* 2(25):73–85
12. Anderson LA (1973) Effects of surface catalytic activity on stagnation heat transfer rates. *AIAA J* 11(5):649–656
13. AGARD Report 808. Capsule aerothermodynamics. 1997 Advisory Group for Aerospace Research and Development (North Atlantic Treaty Organization), Neuilly sur Seine
14. Ranuzzi G, Borreca S (2006) CLAE project. H3NS: code development verification and validation, CIRA-CF-06-1017. Capua, Italy
15. Gnoffo PA, Gupta RN, Shinn J (1989) Conservation equations and physical models for hypersonic air flows in thermal and chemical nonequilibrium, NASA TP 2867. National Aeronautics and Space Administration, Office of Management, Scientific and Technical Information Division, Washington, DC
16. Roncioni P et al (2006) An extrapolation-to-flight methodology for wind tunnel measurements applied to the PRORA-USV FTB1 vehicle. In: Proceedings of the international astronautical congress, 2–6 October 2006, paper IAC-06-D2.3.09, Valencia, Spain
17. AGARD-LS-42-Vol.1. Aerodynamic problems of hypersonic vehicles. 1972 Advisory Group for Aerospace Research and Development (North Atlantic Treaty Organization), Neuilly sur Seine
18. Prabhu DK (2004) System design constraints-trajectory aerothermal environments. In: Critical technologies for hypersonic vehicle development, RTO AVT/VKI lecture series, 10–14 May 2004, Rhode-St-Genèse, Belgium
19. Bertin JJ (1966) The effect of protuberances, cavities, and angle of attack on the wind-tunnel pressures and heat-transfer distribution for the Apollo command module, NASA TM X-1243, NASA, USA
20. Crowder RS, Moote JD (1969) Apollo entry aerodynamics. *J Spacecr Rocket* 6(3):302–307
21. Walpot L (2002) Numerical analysis of the ARD capsule in S4 wind tunnel. In: Proceedings of the 4th European symposium aerothermodynamics for space applications, 15–18 Oct 2001, ESA SP-487, Capua, Italy
22. Gupta RN, Yos JM, Thompson RA, Lee KP (1990) A review of reaction rates and thermodynamic and transport properties for an 11-species air model for chemical and thermal nonequilibrium calculations to 30,000 K, NASA/RP-1232, NASA, USA
23. Park C, Lee, S-H (1993) Validation of multi-temperature nozzle flow code Noznt. In: Proceedings of the 28th AIAA thermophysics conferences, 6–9 July 1993, paper AIAA-93-2862, Orlando, FL, USA
24. Roe PL (1986) Characteristic based schemes for the Euler equations. *Annu Rev Fluid Mech* 18:337–365
25. Viviani A, Pezzella G, Cinquegrana D (2006) Aerothermodynamic analysis of an Apollo-like re-entry vehicle. In: Proceedings of the 14th AIAA/AHI space planes and hypersonic systems and technologies conferences, 6–9 November 2006, paper AIAA-2006-8082, Canberra, Australia
26. Prabhu DK (2004) System design constraints-trajectory aerothermal environments. In: Critical technologies for hypersonic vehicle development, RTO AVT/VKI lecture series, 10–14 May 1659 2004, Rhode-St-Genèse, Belgium,
27. Olynick D (1998) Trajectory-based thermal protection system sizing for an X-33 winged vehicle concept. *J Spacecr Rocket* 35(3):249–257
28. Pezzella G et al (2007) Hypersonic aerothermal environment preliminary definition of the CIRA FTB-X re-entry vehicle. In: Proceedings of the west–east high speed flow field conferences, 19–22 November 2007, Moscow, Russia
29. Rasmussen ML (1994) Hypersonic flow. Wiley, New York
30. Viviani A, Pezzella G (2007) Catalytic effects on non-equilibrium aerothermodynamics of a re-entry vehicle. In: Proceedings of the 45th AIAA aerospace sciences meeting and exhibit, 8–11 January 2007, paper AIAA-2007-1211, Reno, NE, USA

31. Viviani A, Pezzella G (2007) Influence of surface catalyticity on re-entry aerothermodynamics and heat shield. In: Proceedings of the 39th AIAA thermophysics conference, 25–28 June 2007, paper AIAA-2007-4047, Miami, FL, USA
32. Sarma GSR (1995) Aerothermochemistry for hypersonic technology, VKI Lecture series 1995–04. Von Karman Institute for Fluid Dynamics, Rhode Saint Genèse
33. Scott CD (1987) The effects of thermochemistry, nonequilibrium, and surface catalysis in the design of hypersonic vehicles. 1th joint Europe-US short course on hypersonic. GAMNI-SMAI, Paris, France, 7–11 December
34. Inger GR (1966) Nonequilibrium hypersonic stagnation flow with arbitrary surface catalyicity including low Reynolds number effects. *Int J Heat Mass Transf* 9:755–772
35. Viviani A, Pezzella G, Borrelli S (2008) Effect of finite rate chemical models on the aerothermodynamics of re-entry capsules. In: Proceedings of the 15th AIAA space planes and hypersonic systems and technologies conferences, 28 April – 1 May 2008, paper AIAA-2008-2668, Dayton, OH, USA
36. Olynick DP, Hassan HA (1993) New two-temperature dissociation model for reacting flows. *J Thermophys Heat Transf* 7(4):687–696

# Chapter 5

## Lifting-Body Vehicles

### 5.1 Introduction

This research effort deals with the development of a six-degrees-of-freedom Aerodynamic Database (AEDB) of the Intermediate Experimental Vehicle (IXV) by integrating all the heritage data available from computational fluid dynamics (CFD) as well as wind tunnel tests (WTT) campaigns.

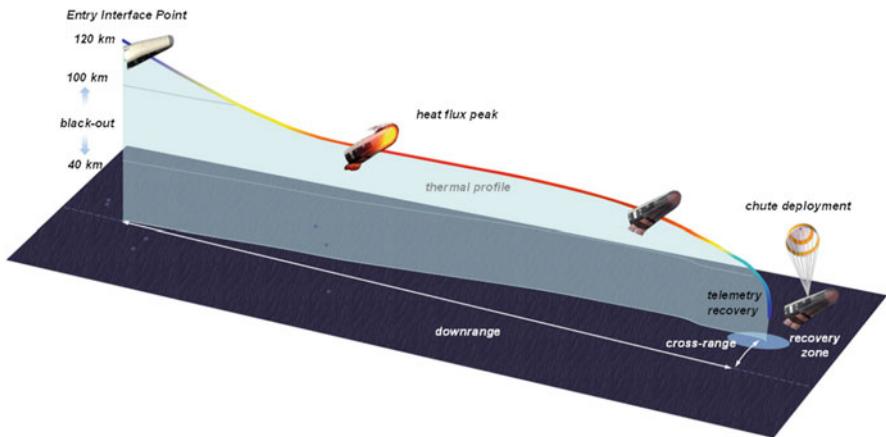
The IXV program, developed by the European Space Agency (ESA) in the framework of the Future Launchers Preparatory Programme (FLPP), aims to demonstrate European capabilities in hypersonic unpowered maneuvering re-entry flight of a lifting configuration [1]. The vehicle is also intended to serve as a test bed for in-flight qualification of vehicle subsystems and systems and to provide another source of data on fundamental hypersonic aerothermodynamic phenomena for validation of tools, databases, and design processes [2]. These goals led to the decision to develop a lifting-body concept with a simple aeroshape that could fly a representative reusable launch vehicle (RLV) trajectory to the maximum extent possible, to be launched by means of the Vega rocket, and which could be recovered at the end of the flight with a parachute landing.

Figure 5.1 illustrates the IXV entry, the recovery of the vehicle being done after a final descent phase under chutes [3].

IXV will be also used to demonstrate maneuverability in the upper atmosphere; to test advanced thermo-structure concepts, such as body flaps made of ceramic matrix composite (CMC); and to investigate the flowfield features during re-entry in order to validate European numerical (e.g., CFD) and experimental prediction capabilities (e.g., WTT).

The IXV configuration is reported in Fig. 5.2 [4].

The aerodynamic analysis, carried out for the whole flight domain, relies on engineering-based design, CFD, and WTT data generated during the project phases, from rarefied flow conditions to hypersonic continuum flow up to reach subsonic



**Fig. 5.1** The IXV re-entry

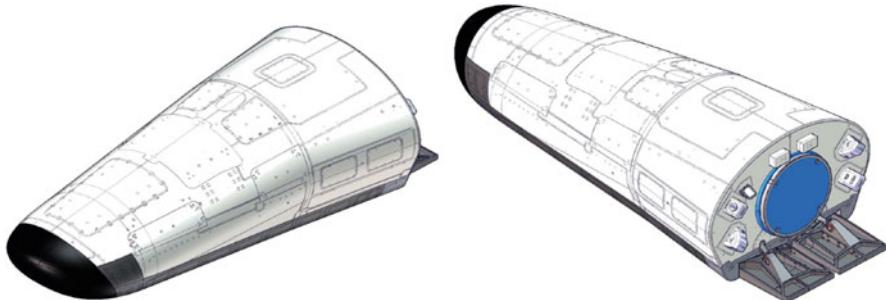


**Fig. 5.2** IXV configuration

speeds. Therefore, the vehicle aerodynamic database covers the range of Mach number, angle of attack (AoA)  $\alpha$ , angle of sideslip (AoS)  $\beta$ , and control surface deflections ( $\delta$ ) foreseen for the vehicle nominal re-entry. Bridging formulation for lift, drag, and pitching moment coefficient in order to take into account for rarefaction effects is included as well.

These databasing activities are developed in the light of buildup approach. Therefore, all aerodynamic data are provided in a format which will allow a buildup from a basic configuration by means of contributing elements to each force or moment component such as the effect of sideslip, of aerodynamic control surface effectiveness, etc. In order to facilitate the buildup procedure, for each force and moment coefficients, equations are provided in which all the pertinent contributions for obtaining the total coefficient for any selected flight conditions appear. To this aim, all the available aerodynamic data are gathered in order to explicit the functional dependencies from each aerodynamic model addend through polynomial expressions obtained in a least squares sense. These polynomials are a function of

the primary variable that drives the phenomenon, whereas secondary dependencies are introduced directly into its unknown coefficients which are determined by means of best-fitting algorithms.

Finally, results provided in the chapter show that the AEDB, thanks to the polynomial formulation, is able to provide, in a continuum fashion, vehicle aerodynamic performances in points of the IXV re-entry scenario where neither WTT nor CFD data exist.

## 5.2 Historical Background

One of the main targets for new-generation launchers is the reusable launch vehicle able to perform an atmospheric glided re-entry.

The in-flight experimentation of a gliding re-entry spacecraft is seen as a critical key technology for future space applications. In this frame, CNES decided to initiate the study for a re-entry experimental vehicle starting from white sheet, dubbed Pre-X and mainly focused on thermal protections, aerothermodynamics, and guidance to secure the second generation of re-entry X vehicles [5].

During the preliminary analysis, and even during the pre-development, there were large evolutions of chosen technical solutions, not only due to technical issues. Nevertheless, the technical aspects were the main constraints. For instance, one clearly identified objective consisted in the attitude control performed by body flaps and reaction thrusters overall the re-entry hypersonic flight, with functional and experimental objectives.

Past experience of winged and lifting-body re-entry demonstration has been focused on some particular vehicles such as the US X-15 and X-38, the Russian BORs, and the Japanese HYFLEX.

The Space Shuttle Program took advantage of numerous experimental lifting vehicles, such as ASSET, X-15, X-23A, and X-24 (see Fig. 5.3) [5].

An important experience in the hypersonic flight domain has been gained with X-15 in terms of thermal metallic protection, terminal area energy management (TAEM), and non-propelled landing for a vehicle with a poor L/D ratio. With ASSET and PRIME orbital and suborbital re-entry flights, flight control system (FCS) and reaction control system (RCS) efficiency, thermal protection system (metallic), aerothermodynamic measurements, flight worthiness, and guid-

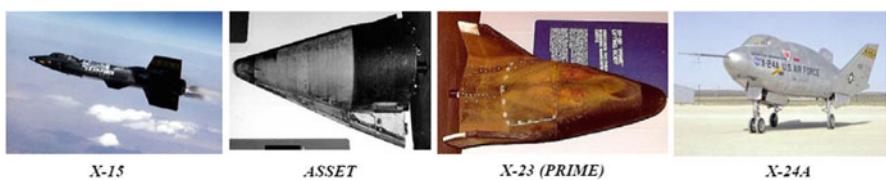


**Fig. 5.3** US experimental lifting vehicles

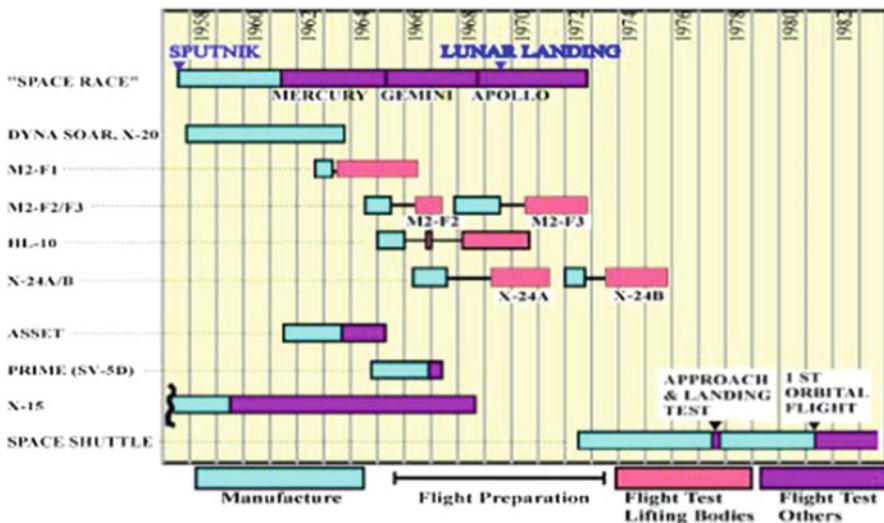


**Fig. 5.4** US experimental programs between 1957 and 1982

**Fig. 5.5** X-38 re-entry vehicle



ance accuracy have been explored. With X-24 (USAF), landing training vehicles with poor aerodynamic characteristics and transonic controllability have been investigated. A scaled model of the space shuttle has never been flown. The main US space programs concerning re-entry are depicted in Fig. 5.4 in the time frame 1967–1982 [5].

More recently, the X-38 (see Fig. 5.5) has constituted a lifting-body vehicle whose shape is very close to the X-23 experimental vehicle (see Fig. 5.3), and it was supposed to be a scaled model of the crew rescue vehicle to the International Space Station (ISS) [5]. ESA has been associated to this NASA program, which actually stopped in 2002. The X-38 permitted to gain experience in the frame of



**Fig. 5.6** BOR-4 (left) and BOR-5 (right) experimental flying test beds

nose and body flap technology in Europe as well as in the field of aerodynamic characterization at high speeds shapes design, guidance, navigation and control (GNC), and TPS architecture. A space flight has never been performed, but the vehicle performed transonic and subsonic flights.

Russian in-flight experimentation is mainly based on two experimental vehicles developed in the frame of the Buran program. Those are BOR-4 (flown between 1982 and 1984 up to Mach 25) and BOR-5 (flown between 1983 and 1988, up to Mach 18), shown in Fig. 5.6 [5].

The Russian strategy was to split the re-entry demonstration in two missions (consequently two vehicles) in order to avoid the management of the compromise between aerothermodynamics problems and aerodynamic ones, due to the scale effect of the demonstrator.

As a result of that logic, BOR-4 (see Fig. 5.6) was dedicated to orbital re-entry with a shape representative at scale 1 of the Buran nose/windward curvature [5].

The BOR-5 (see Fig. 5.6) was a subscale of Buran dedicated to aerodynamic efficiency, flight worthiness, and GNC [5]. These two vehicles were only a little part of a bigger program to get to wing–body orbital and re-entry flight. The BOR vehicles, from BOR-1 to BOR-5, were part of the SPIRAL program.

In Japan, an important fleet of experimental vehicles has been developed to support the development of the HOPE-X program. The HYFLEX (see Fig. 5.7, left side) and HSFD have been developed in this frame, but the high hypersonic domain has never been explored with a controlled glider [5]. France and Germany cooperated in the frame of the HSFD and HYFLEX vehicles for what concerns flight guidance, aerodynamics, and postflight analysis. The flight envelope target of the Japanese program is depicted in Fig. 5.7, right side [5].

In Europe, the Hermes<sup>1</sup> (Fig. 5.8, left side) program has been the first concrete development to conceive a reusable vehicle with a Shuttle/Buran-like technology [5]. Even though this program was cancelled, it permitted the development in Europe of know-hows, technologies, computer codes, and test means. Typically, the high enthalpy wind tunnels, the reusable TPS, and the algorithms for guided re-entry are some examples of the Hermes heritage.

---

<sup>1</sup>The aerodynamic characterization of Hermes is summarized in Chap. 3.

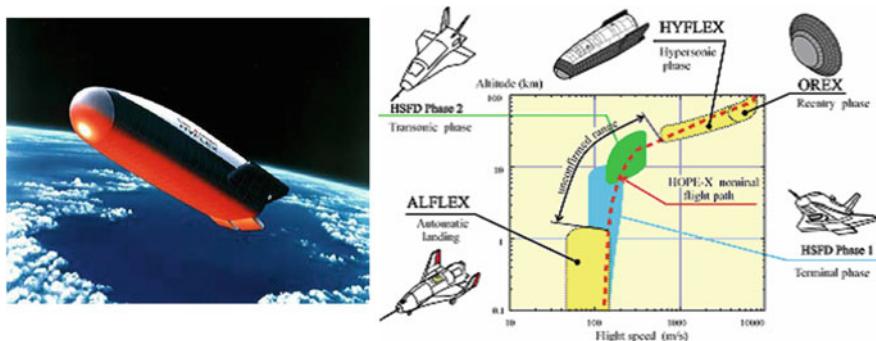


**Fig. 5.7** The hypersonic glider HYFLEX (*left*) and target envelope of Japanese in-flight demonstration (*right*)

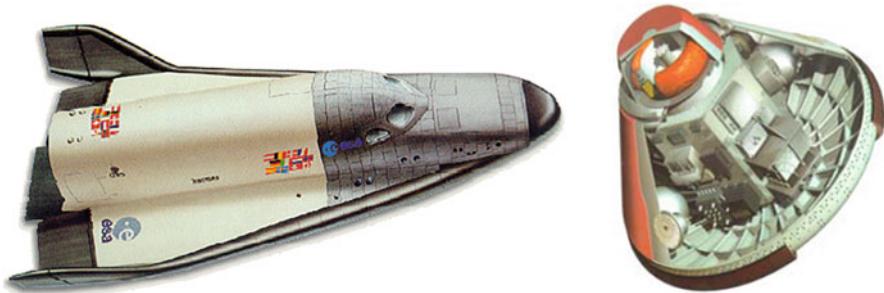


**Fig. 5.8** The Hermes space plane (*left*) and the ARD re-entry capsule (*right*)

After Hermes, the civil re-entry studies had been continued by other ESA, ESA/NASA, and national programs such as FESTIP, X-38, FLTP, ANGEL, PHOENICS, and ARD. These programs permitted to continue developing the key technologies for re-entry.

The first main concrete European experience in the field of re-entry is the ARD capsule (Fig. 5.8, right side), which had the same shape as the Apollo capsule with a similar descent system but was uninhabited. ARD was conceived to demonstrate the European ability to master the manned re-entry missions, performing a high precision impact. In addition, it permitted important experiences concerning aerothermodynamics (ATD), TPS samplings, GNC, blackout management, and RCS attitude control. In particular, the short time available for this program and the low budget permitted to go to flight by using “on-the-shelf” equipment derived from the launch vehicle Ariane 5. The system recovery and telemetry has been tested as well.

The ARD flew with Ariane 503, the last qualification flight of Ariane 5, and demonstrated the capability of Europe to master the automatic re-entry of a capsule with an ablative heat shield. Even if the flight occurred in 1998, the ARD development was achieved in 1996.

After the cancellation of the FLTP ESA program (Future Launchers Technology Program) in 2001, it appeared that there was no more European program to sustain and develop competences in the field of atmospheric re-entry. Then, considering this domain as a key competence to be preserved, CNES proposed the ANGEL dossier in which a logic for new-generation launch vehicles was proposed. One important slice of the program was dedicated to demonstration of the technologies necessary to achieve sufficient maturity to be used on the new systems. The demonstrators were divided into two categories: the ground-based and in-flight demonstrators.

In-flight experimentation related to re-entry was designed to test as close as possible some generic techniques/technologies related to a reusable space system vehicle re-entering the Earth atmosphere. In particular, the idea was to design experimental vehicles, i.e., vehicles which are not completely representative of an actual re-entry vehicle but have some of their invariant characteristics (center of gravity location, ballistic coefficient, L/D ratio, etc.).

They can be considered more as flying test beds with technical and technological objectives relatively independent on the shape and size or whose effects can be corrected or found by compromises. This kind of vehicles is less expensive but permits conception, design, and manufacturing experience as part of the experimentation. This class of vehicles is quite different from what is called demonstrator, which is fully representative of a clearly identified concept but scaled down.

The ANGEL-proposed logic was based on two European experimental vehicles [5].

- The first-generation dubbed Pre-X corresponds to vehicles simple and cheap, giving rapidly in-flight experimentation results in order to validate and calibrate tools, facilities, design, and technological solutions. They were conceived to prepare and secure the following step.
- The second-generation dubbed Pre-X corresponded to the experimental vehicles able to perform the full demonstration and mastering on the entire flight domain. The ARD flew with Ariane 503, with some reusable TPS material samples which have been tested during this flight, as well as ATD prediction codes. The Pre-X experimental lifting body was conceived in order to make a step forward after ARD, keeping on gaining experience on automatic re-entry in a twofold objective:
  - Demonstrate the ability of Europe to master lifting-body low Earth orbital re-entry from a system point of view.
  - Create a project of common interest in Europe to demonstrate some launcher future technology, focusing on reusable TPS architectures (including nose and body flaps), aerodynamics and ATD experiences, and GNC.

As well as Space Shuttle took advantage of the Apollo and X vehicles experience of the previous years, the starting point for Pre-X consisted in using at the maximum the experience and materials commercial off-the-shelf (COTS) coming from ARD, with the additional advantage of limiting the development effort. Typically, the GNC used on ARD has been fully reemployed for Pre-X in terms of logic, algorithm,

and equipment. The most important modification concerned the attitude control, performed by means of RCS and elevons. A lot of avionics components were intended to be retrieved from the Ariane 5, ARD, and Vega launch vehicles in order to save development money and add reliability. This permitted to concentrate more founding on in-flight experimentation [5].

At the same time, Pre-X was something between ARD and Hermes. In order to optimize inner volume, it has been preferred to have a lifting-body concept more than a winged one. However, this took to degraded performances in lateral stability and control.

The experience gained during the Hermes and X-38 programs has been used in order to be transferred to Pre-X. The industrial organization was based on a European team, including cooperation with Russia and Japan. These partners permitted to get the heritage of previous experiences in the field of re-entry experimental vehicles such as BORs and HYFLEX [5].

In the frame of a CNES/DLR agreement, this project has been led by ASTRIUM SAS as the prime contractor, including Dassault Aviation, SPS, ONERA, German agency DLR and companies, MTA, ASTRIUM GmbH, and, mainly for phase B, Spanish (CASA) and Belgian companies (SONACA, SABCA, ALCATEL-ETCA). Additionally, the project benefited of cooperation with Russia (TSNIIMASH as prime contractor, MOLNYIA, LII Gromov, NIPS, KOSMOTRAS, TsAGI) and Japan (JAXA) [5].

The project was initiated in December 2000 with the following CNES requirements:

- Test reusable TPS at system level in future RLV representative environment.
- Characterize relevant ATD phenomena in future RLV representative environment.
- Demonstrate the European capability to conceive and flight a re-entry vehicle end to end.
- To perform the flight experiment within the domain Mach 25–Mach 5 and then recover the vehicle under parachute
- To implement flight measurement (if possible, innovative measurements) in order to check their reliability and also that the flight measurement is relevant for the ATD and TPS postflight analysis
- Use COTS as far as possible.
- Study 2 classes of vehicles:
  - Medium class for 60 M€ excluding the launcher cost
  - Small class for 30 M€ excluding the launcher cost
- To fly after a 4-year development

Then a 2-month phase 0 study was launched at EADS (ASTRIUM): Pre-X was born.

During phase 0 and early phase A, constraints appeared and numerous trade-offs were initiated, but some of them not concluded satisfactory. In the mean time,

fortunately soon, some main drivers and rules were identified and applied as far as possible. All these points are summarized hereafter [5].

The phase 0 conclusion led to selection of the “medium class” Pre-X because the “light” one was not an enough representative in terms of ATD and TPS.

The initial configuration of Pre-X was as follows:

- V-like shape but with needed improvement in lateral dynamic stability performance, center of mass position management, etc.
- Shape design compliant with the constraint of the launcher fairing volume.
- New technology with a TRL at least 5 at the end of phase B.
- RCS control but option between movable mass + fixed body flap and active body flap.
- Use a Rockot (most affordable launcher expected at the 2004 launch time).
- Mission based on an orbital flight and Pre-X deorbiting.
- Recovery in Atlantic Ocean.

As far as Pre-X shape design is concerned, it is worth to note that at the beginning of the project (phase 0), a trade-off between two families of vehicles has been carried out with respect to high-level specifications, which can be summarized by four objectives: ATD, in-flight measurement, TPS, and GNC. The trade-off was reduced to two families of vehicles, of light or medium size, mainly due to limited budget of the project. The size is imposed by the available volume under the fairing of the candidate launcher (Vega, DNIIEPR). The iteration process of the definition of the geometry of these vehicles is initiated by classical biconic shape. Then consider the following:

- External dimension imposed by allocated volume under launcher fairing.
- Internal volume required for equipments, instrumentations, and assembly integration and test (AIT).
- Drag coefficient, for ballistic coefficient definition.
- L/D, for cross range.
- Nose radius for heat flux level.
- Longitudinal trim.
- Center of mass location.
- Longitudinal and lateral stabilities capability, the geometric iteration process has been undertaken. At this preliminary level analysis, the aerodynamic characterization of the vehicle shape was undertaken by both the engineering method (modified Newton) and Euler computations. Heat fluxes were computed with stagnation and empirical formula. For the trim and stability analysis, the uncertainties on Newton results were too high and lead to use only Euler results.

Besides the geometry, a key parameter of the vehicle design is the center of mass location resulting from the global layout of the vehicle. This was foreseen to be between 58 and 59 % from nose. The layout and architecture of the vehicle were driven also by the center of mass position. Other variables to consider were the inner volume, aerodynamics, and mass budget.

The most important criteria for the vehicle choice have been:

- *ATD*: A demonstrator must encounter flight conditions compatible with the physics of these phenomena; then extrapolation to a reference vehicle must be feasible either from aerodynamic or from ATD point of view. The capacity of having a realistic flap environment of an RLV flap is also interesting. For this objective, the larger vehicle is in better agreement than the light one.
- *In-flight experiment*: The capability of having on-board classical and/or innovative measurements is easier for a larger vehicle.
- *TPS*: The possibility of having an RLV like TPS avoiding any ablation can be feasible on a medium vehicle.
- *GNC*: The trade-off is also rather clear. If the guidance and control is a demonstration objective, the combined RCS and elevons control is more interesting than an RCS alone. A gliding vehicle (higher L/D) is more convenient for this objective.

The medium-size vehicle seemed more interesting with respect to the trade-off criteria but has limitations in terms of similarity with respect to the phenomena encountered on a full-scale reference vehicle. The shape was defined for a medium or light size, presented in Fig. 5.9 [5].

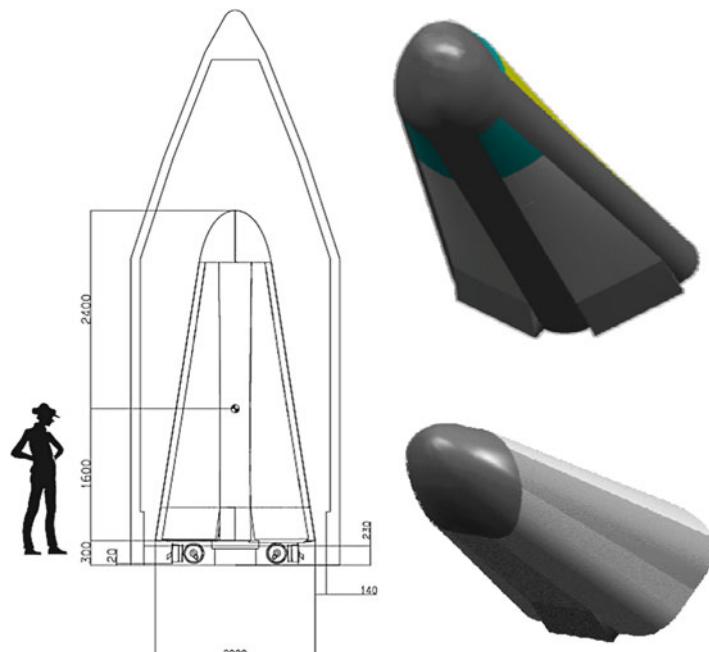


**Fig. 5.9** Example of the Pre-X vehicle under the Rockot fairing (*left*) – Pre-X medium and light vehicle (*right*)

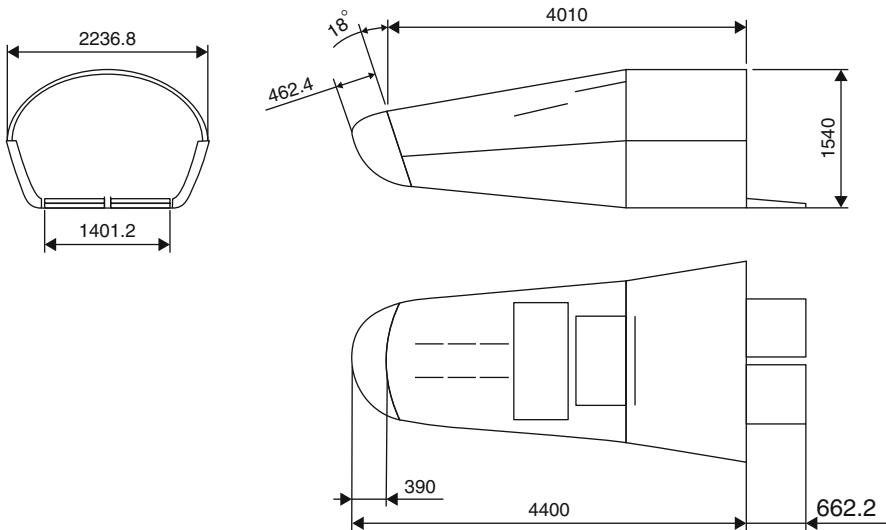


**Fig. 5.10** Pre-X phase B geometry (mm)

Once this first loop was achieved, the medium demonstrator was preferred to the light one. But, due to nonrespect of the criteria in terms of longitudinal static margin and lateral trim, a reorientation of the shape of the Pre-X vehicle has been performed. The initial V shape of the vehicle was withdrawn, and some camber of the windward side was introduced, which has the consequence to increase the L/D coefficient. Besides, in order to increase flap efficiency, the flaps were positioned standing out of the base in cantilever position. Finally, in order to fulfill the lateral decoupling criteria between flap differential control and side slip flow, the hinge axes of the elevons were rotated inside the windward plane in order to slightly face each other (i.e., tilted hinge line). A sketch of the phase B geometry vehicle is shown in Fig. 5.10 [5].

This aeroshape was the result of multidisciplinary trades-off analysis, as common during preliminary design phases.

The main important options involved in the trade-off were the following:

- Which launch vehicle (LV) to employ to perform the mission. This choice has a non negligible impact on the vehicle itself and on cost. At the beginning of the program, Rockot and DNEPR have been selected mainly for cost reasons. In particular, DNEPR was selected since offering more robustness for the Pre-X design (environment, operations and mostly fairing volume). Indeed, it was possible to upscale the Pre-X shape in order to recover more margins for center of mass position management. A baseline LV and a backup have been always considered. During the phase B and up to preliminary design review (PDR), the baseline LV was Vega and the backup DNEPR.
- Which trajectory to perform: orbital with desorbitation or suborbital. The suborbital option has been selected since it is considered to have less impact

on the Pre-X vehicle design but needed a precise trajectory strategy associated to the LV. This choice was also dictated by the fact that landing in the Pacific Ocean was preferred to the Atlantic option for safety reason. In this case, the suborbital scenario was less demanding.

- How to retrieve the vehicle: by landing or splashdown. Finally, splashdown has been selected, requiring less precision on the GNC system and being safer than landing. However, it is more difficult to guarantee the TPS integrity.
- Descent phase.

The last design issue is extremely challenging. In fact, one important trade-off concerned a shape definition compatible with the mission requirements. As previously said, the main experimentation had to be performed for Mach numbers higher than 5, then the mission success was dependent on data and vehicle recovery. Hence, the vehicle has been essentially designed to accomplish the experimentation objectives up to Mach 5, resulting in a non-optimized vehicle for lower Mach number.

A specific shape requirement file has been written in order to better define shape design specifications. This file concerned mostly flight stability and flight qualities with specific constraint due to inner volume for experimentation, nose equivalent diameter for heat flux similarity, etc.

Different vehicle shapes have been proposed before converging on the final phase A/B shape, which has been retained by the FLPP project for the IXV vehicle. This was one of the main Pre-X trade-offs [5].

Even if the actual Pre-X mission is occurring for Mach numbers greater than 5, the mission success depends strongly on the recovery phase after the experimentation phase. It is possible either to recover the vehicle by means of controlled flight up to landing or by opening a parachute as soon as possible. In addition, the vehicle can be recovered either on ground or on sea. This latter option has the advantage to have less constraints from the safety point of view, and this was the result of a specific trade-off.

But one more important trade-off concerned the descent phase up to splashdown. From the vehicle requirement, it is apparent that the main domain of investigation concerning aerodynamics and ATD is the hypersonic range. The vehicle has been designed in order to have good flying qualities and ATD similarity with full-scale spacecraft from Mach 25 to 5. However, the vehicle performance for Mach numbers below 5 is important to take the vehicle in safe conditions up to parachute opening. In particular, this phase can be very critical because of parachute reliability in conjunction with the Pre-X system and the need to transmit the measurements recorded during blackout to the ground system. Hence, the mission success, in terms of vehicle and data recovery, is strictly tight to this phase.

The transonic region can be passed in two ways:

- Supersonic scenario: A drogue chute opens at about Mach 1.5; then the main parachute is opened once suitable conditions are reached.
- Subsonic scenario: A main chute opens at a descent velocity of about 65 m/s and takes the vehicle to a descent velocity of about 9 m/s.

For this reason, tests and computations on Fluid Dynamics codes have been performed up to Mach 0.8 and an aerodynamic database (AEDB) computed for the Mach range from 25 to 0.81.

The transonic flight study has been performed between Mach 2 and 0.8 or 0.6. An active control system is necessary to cross the transonic flight regime with an “ad hoc” algorithm. The results show a compatibility with the A5 OBC having a 7 Hz bandwidth limit. In the flight regime between Mach 2 and 1, the control is essentially performed by means of elevons. Below Mach 1, the RCS are necessary to guarantee the lateral control, and the ailerons give just a small contribution.

The conclusion of the study is that Pre-X can pass the transonic regime by means of controlled symmetric flight but the overall impacts on the Pre-X budgets (mass, power, etc.) and the TPS behavior as well have not been yet fully analyzed. Therefore, it has been chosen to set the supersonic scenario as a reference during phase B. From the parachute standpoint, this is more general to treat the descent phase.

For what concerns the vehicle architecture, three examples can be given:

- The windward and sides protected with shingles. This particular TPS system had been developed in the frame of the Hermes program, and the choice to employ it in Pre-X was straightforward: demonstrate the capability to fly a system with this TPS architecture and skills (first time in the world). A parallel program has been run in order to improve the technology readiness level (TRL) of such a device and investigate its performance to be assembled on a re-entry vehicle.
- The avionics architecture has been designed to be simple and cheap. It was based only on COTS and Simplex.
- The experimentation architecture was one of the main drivers of the vehicle design. In particular, the main experiments, namely, the TPS architecture/samples and the ATD, were the driving factors for the vehicles’ mission and design.

The time of occurrences of the experiences has also been clearly identified, as shown in Fig. 5.11 [5]. About 700 measurements have been identified.

The nose assembly baseline during phase B is an adiabatic one, essentially based on the X-38 concept (Fig. 5.12) [5]. During phase B, the trade-off between the adiabatic and radiating concept has been performed and the adiabatic concept retained. The radiation box smoothes hot spots by temperature surface homogenization, but AIT is more complex and TRL lower than the adiabatic nose solution (X-38 like). The passive/active oxidation transition law (from SPS) compared with pressure and adiabatic temperature of phase B gives no active oxidation (even with 100 % catalytic surface) for both concepts.

The body flaps are active and independent (see Fig. 5.13). The technology employed is strongly inspired of that implemented on X-38. From the hardware point of view, the body flaps are composed of two half pieces joined together [5]. The actuation structure is mounted by means of ceramic matrix composite (CMC) bolts to the flap main body. For the elevons, the proposed advanced CMC bearing layout is based on the X-38 bearing development experience and improvements

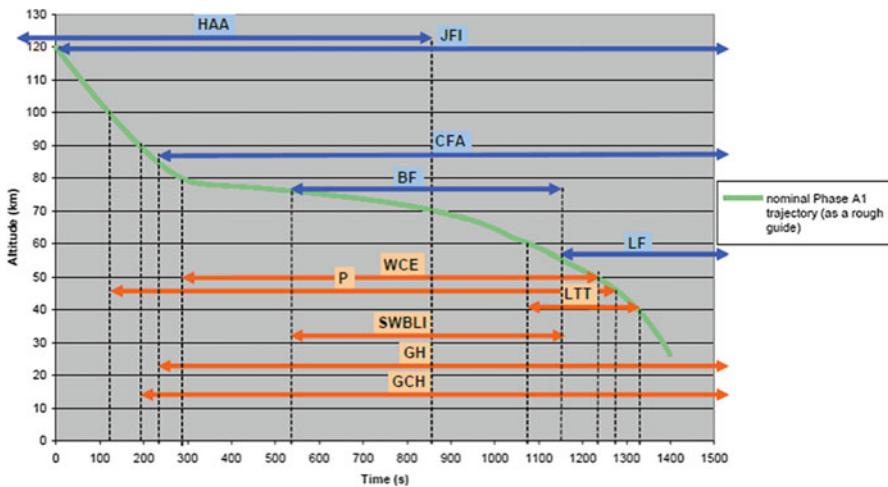


**Fig. 5.11** Time interval of occurrence for ATD experiences on Pre-X

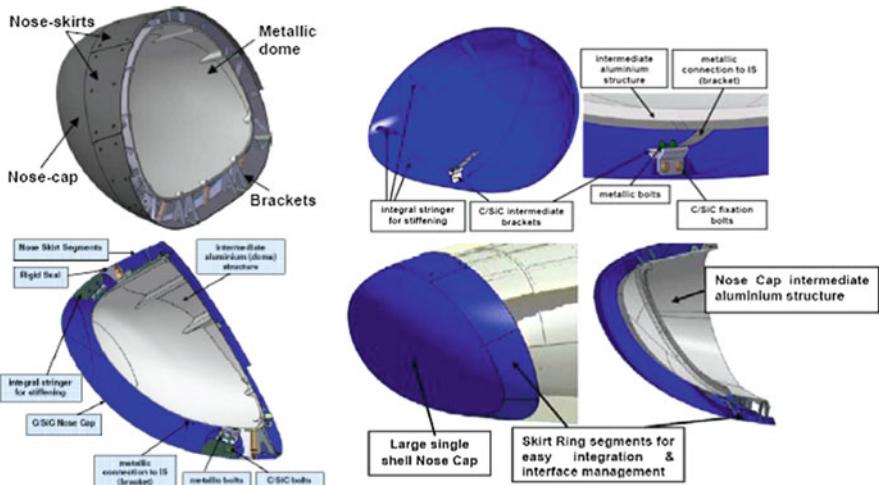


**Fig. 5.12** Adiabatic nose assembly

implemented with regard to higher lifetime and reliability and a reduced cost approach. This type of bearing especially allows a high flexibility for integration and provides a high radial load-carrying capacity.

Finally, Pre-X is the re-entry experimental hypersonic glider that ESA has retained in its selection for the best IXV of the FLPP program. This is the necessary step for risk mitigation of future re-entry space planes or lifting bodies. The main goal of the program is to demonstrate that Europe has the technology to master gliding re-entry of a reusable vehicle controlled by movable surfaces and jets.

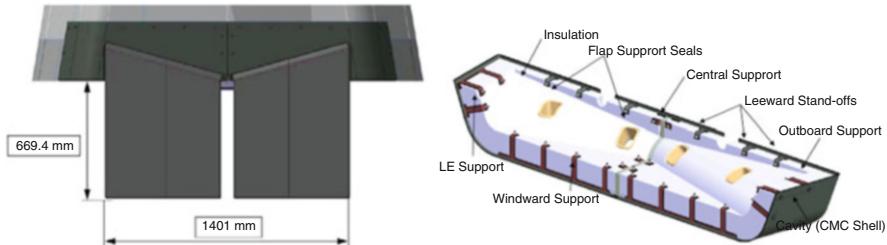


**Fig. 5.13** Body flap main dimensions (*left*) – hinge TPS design (*right*)

### 5.3 IXV Trade-Off Objectives and Logic

As mentioned above, the first step of the consolidation study consisted in assessing and performing a trade-off between all potential IXV candidates, with the objectives to:

- Recommend one concept out of all IXV potential candidates, which results from a trade-off analysis on technical but also programmatic and project-related aspects, and which design will be consolidated (step 2) to better meet the IXV specific set of requirements.
- Identify interesting design features in the concepts screened, with the intention to further enhance the IXV design by integrating and implementing them during the design consolidation loop.

The logic adopted to perform the trade-off consisted of the following sequential steps:

1. Identify preliminary experimentation objectives for the IXV and elaborate a corresponding preliminary set of high-level requirements.
2. Derive from these requirements a set of selection criteria and assessment parameters.
3. Elaborate a trade-off methodology.
4. Collect all the candidate input data needed to perform their assessment and run the trade-off analysis.
5. Perform the assessment of each concept identified, and recommend one of them as being the most appropriate one according to the set of selection criteria and to be further design consolidated.
6. Derive, from the optimized in-flight experimentation road map and from the associated needs toward the IXV, a set of consolidated high-level requirements for the IXV.
7. Identify all the open issues and all the discrepancies of the recommended concept design with respect to these consolidated IXV high-level requirements.
8. Define, based on these discrepancies, corrective actions and design improvement tracks to be implemented in the IXV design consolidation loop (step 2).

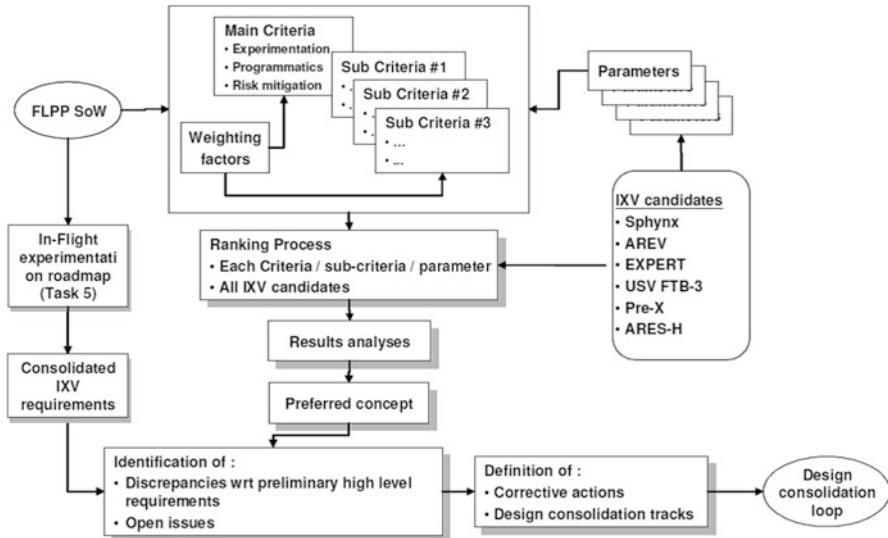


**Fig. 5.14** Trade-off methodology

**Table 5.1** Candidates list

IXV candidate concepts	Customer	Prime
Sphynx	ESA	ALS
AREV	ESA	ALS
EXPERT	ESA	ALS
USV (FTB-3)	CIRA	CIRA
Pre-X	CNES	EADS ST
ARES-H	EADS ST	EADS ST

The methodology implemented to identify the most appropriate concept to be used for the design consolidation loop and become the IXV was based on a ranking of the candidate concepts, resulting from an assessment of each concept according to a set of selection criteria. This methodology is depicted in Fig. 5.14 [6].

The complete set of concepts considered in the present study is summarized in Table 5.1, and the following sections give a synthetic overview of the project status, the current system designs, and the inputs used for the trade-off [6].

The Sphynx is a project initiated by ESA after the CRV/X-38 program shutdown decided by NASA. Beginning 2002, a CTRV study has been started with the dual goal to provide a recommended and optimal strategy meeting on one hand the SLI crew delivery and return needs and on the other hand the ISS crew rescue ones. The Sphynx concept has then been studied by an international industrial team led by ALS as the prime contractor and involving Dutch Space and Deimos companies at subcontractor level. The goal was to support the CTRV study initiative, by deepening and possibly adapting the Sphynx concept to a CTRV option derived from

the X-38 concept. The Sphynx study ended in November 2003 after a feasibility consolidation study had been performed at system level.

The concept and its system design approach are based on the following principles:

- Derive the Sphynx aeroshape from the X-38 one (downscaling factor), in order to take benefit from the extensive aerodynamic and heating characteristics that have already been measured and documented through wind tunnel testing.
- Make also extensive use of available equipment and technology already developed in the frame of the European X-38 activities (including advanced hot structures and TPS technologies).

The Sphynx aeroshape has been downscaled from the X-38 V201 one with a 1:3 scale factor. The upper rudders are fixed but the lower body flaps still movable. The mission analysis is based on Rockot launch from Plesetsk, a 200 km circular orbit, and a recovery on ground in Woomera. A launch with Vega from Kourou could be an interesting alternative scenario.

The vehicle design is depicted in Fig. 5.15 [6].

The AREV study is an assessment study initiated in 2004 by ESA and conducted by an industrial consortium led by ALS. The bottom line of the AREV study is to complement the experimentation/demonstration objectives of intermediate re-entry experimental vehicles, like the IXV proposed in the FLPP in-flight experimentation road map, but being in addition shape representative of target operational vehicles. Thus, the AREV study (see Fig. 5.16) takes into consideration experimental vehicle requirements, including but not only restricted to those currently expressed for the IXV, with a potential expansion to shape representativity if technologically feasible and economically advantageous, as part of an end-to-end demonstration logic [6]. The AREV study has traded three vehicle configurations according to experimental re-entry vehicle objectives outlined for human space transportation (considered as applicable) and for launchers (considered only for assessment):

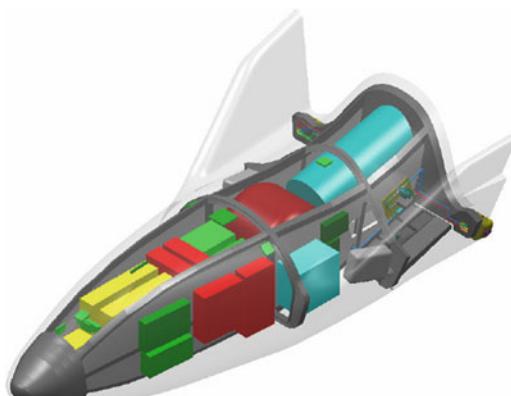


**Fig. 5.15** The Sphynx concept

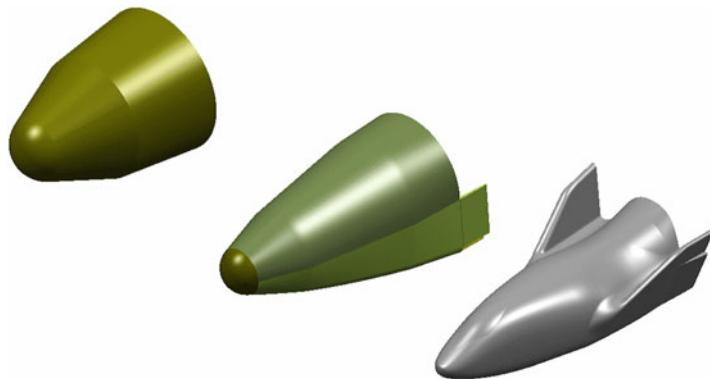


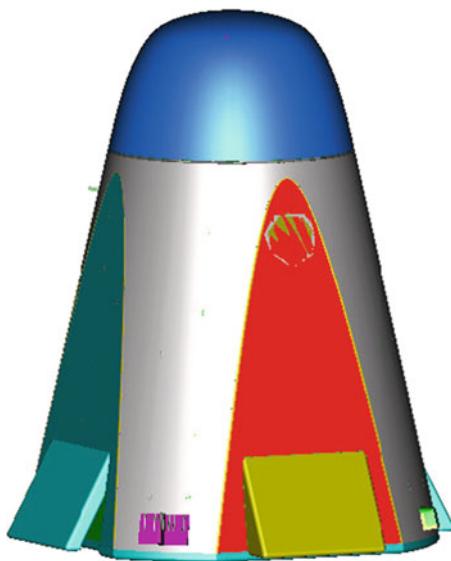
**Fig. 5.16** AREV concepts (biconic, slender lifting body, Sphynx-like)

- Blunt biconic, which is derived from a re-entry space capsule concept, studied in the frame of CTV/CRV past ESA studies
- Lifting body Sphynx-like, which is based on a 20 % upscaled version of the Sphynx aeroshape (see above)
- Lifting slender body, to complement and address all potential shape configurations

The EXPERT program has been built on the need for improving the aerothermodynamic predictions and design tools, regarding the CFD computations and WT tests on one side but also the ground-to-flight extrapolation methodologies on the other side. The EXPERT vehicle has been conceived precisely to address these shortcomings by obtaining an aerothermodynamic flight database, allowing addressing the specific phenomena and validating the tools. Therefore, the primary objective of EXPERT is to provide a test bed for the validation of aerothermodynamics models, codes, and ground test facilities in a representative flight environment, to improve the understanding of issues related to analysis, testing, and extrapolation to flight.

In this sense, the EXPERT concept is rather designed for ATD experimentation than for TPS or system design improvement. Various candidate shapes were analyzed and traded off. The retained solution consists of a low-cost re-entry capsule with conical shape and blunt nose, launched by the low-cost Russian submarine-based Volna suborbital launcher (which employs the R-29R missile). EXPERT is designed for suborbital flights with a re-entry velocity range, which may vary from 5 to 7 km/s. The foreseen landing site is the Russian military base in the Kamchatka peninsula. At least three recurring flights (with dedicated flight units) are envisaged for different re-entry conditions. The EXPERT program has reached a PDR maturity, with the definition of the experiment interface and the elaboration of the technical and programmatic data package for phase C/D, operations, and postflight analyses [6] (Fig. 5.17).

**Fig. 5.17** The EXPERT concept



The Unmanned Space Vehicle (USV) Program is a CIRA initiative with the main objective to provide a technological focus for the research activities in the field of aerospace [6].

The USV Program is structured in two parallel main activities:

- One devoted to develop technologies oriented to medium- to long-term needs
- One devoted to design and realize flight test beds (originally 3 vehicles: FTB-1, FTB-2, FTB-3)

The system design activities were originally foreseeing three different vehicles, which would demonstrate and validate, in real flight conditions, the results achieved in the development of the identified strategic technologies. These three vehicles were designed to achieve four specific missions: DTFT (Dropped Transonic Flight Test), SRT (Suborbital Re-entry Test), HFT (Hypersonic Flight Test), and ORT (Orbital Re-entry Test).

Among this set of vehicles and missions, the ones that best match the IXV objectives are the FTB-3 and the ORT mission. Therefore, the FTB-3 has been taken into account as an interesting candidate in the trade-off analysis conducted to select the most appropriate concept for the IXV consolidation and on the basis of the inputs data provided by CIRA for this purpose. However, the whole USV Program has been recently reshaped, so that the FTB-2 and FTB-3 vehicles have been merged in one single vehicle: the FTB-X (see Chap. 6). This vehicle and its mission objectives and requirements are currently under reconfiguration and consolidation (Fig. 5.18).

With the perspective to enhance the European experience and capabilities in the atmospheric re-entry domain, the CNES French Space Agency has engaged in 2001 the feasibility study of a gliding hypersonic re-entry vehicle, named Pre-X. At this

**Fig. 5.18** The USV FTB-3 concept



**Fig. 5.19** The ARES-H (Atmospheric Re-entry Experimental Spaceplane-Hypersonic) concept



moment in time, the study is completing phase A ending with a SRR by end of 2005, before completing phase B until PDR by end of 2006. The Pre-X study is led by EADS Space Transportation as the prime contractor, with the support of an industrial team that will be enlarged for the phase B.

The Pre-X main objectives are twofold. The first objective is to test reusable TPS which are currently available in Europe and which could be used for an RLV. The second objective is to gather aerothermodynamics (ATD) data in the hypersonic regime and to improve the process of in-flight measuring the right output at the right time.

The ARES concept (see Fig. 5.19) has been elaborated by EADS ST on its own; thanks to an internal R&D effort [6]. It resulted from a global assessment and trade-off analysis conducted in the late 1990s, between two major in-flight experimentation/demonstration options on the way to a next-generation launcher: the first option was to fly a set of vehicles with different features and missions,

with at least one vehicle dedicated to aerodynamics representativity and the other to aeroheating purpose; the second option was to fly one vehicle and then accept some compromises at vehicle level or/and mission with, for instance, designing a TPS with locally some material recession accepted.

The main outcome of the evaluation performed is that it is more suitable to follow the first option and get a set of two vehicles:

1. One dedicated to the hypersonic re-entry down to subsonic regime with mission parameters and vehicle design such that a fair compromise between aerodynamic and aeroheating loads is reached: ARES-H vehicle dedicated to the hypersonic part of the flight envelope (H for hypersonic)
2. One designed to experiment low speed range down to automatic, horizontal landing on a conventional runway with completing the terminal area energy management (TAEM) leg of the mission: ARES-S vehicle dedicated to the supersonic/subsonic part (S for supersonic/subsonic) and being partially covered by the Phoenix concept

So, with this abovementioned macro-goal, the ARES-H objectives were to:

- Master the gliding re-entry of a generic two stage to orbit (TSTO) orbiter under relevant re-entry conditions (e.g., representative shape, mass, and centering) and from the entry interface down to landing conditions. In particular:
  - Aerodynamic and aerothermic issues and flight control techniques
- Get on hand some TPS assemblies for postflight analysis and expertise.

The ARES-H concept has been especially elaborated from 1998 to 2002, to reach a pre-phase A design maturity level [6].

The assessment criteria have been defined on the basis of preliminary experimentation objectives and requirements that have been consolidated through a concurrent in-flight experimentation road map optimization (see later section).

On the basis of these preliminary requirements, the down-selection criteria have been structured in three main classes:

1. Technological/system experimentation
2. Programmatic
3. Risk mitigation

The technological/system experimentation criteria include all the technical criteria that are related to the experimentation objectives assigned to the IXV. It has been split into four subcategories, according to the four topics addressed by the preliminary experimentation objectives of the IXV. Among them, the priority has been given to the TPS and hot structures and to the system, which are considered as the top level experimentation objectives of the IXV.

The programmatic criteria (see Fig. 5.20) are derived from constraints that are necessary to fulfill in order to be compliant with the overall FLPP road map [6]. It concerns mainly the launch date, the development duration and cost, the minimum TRL at start, and the European autonomy and cooperation. The risk mitigation

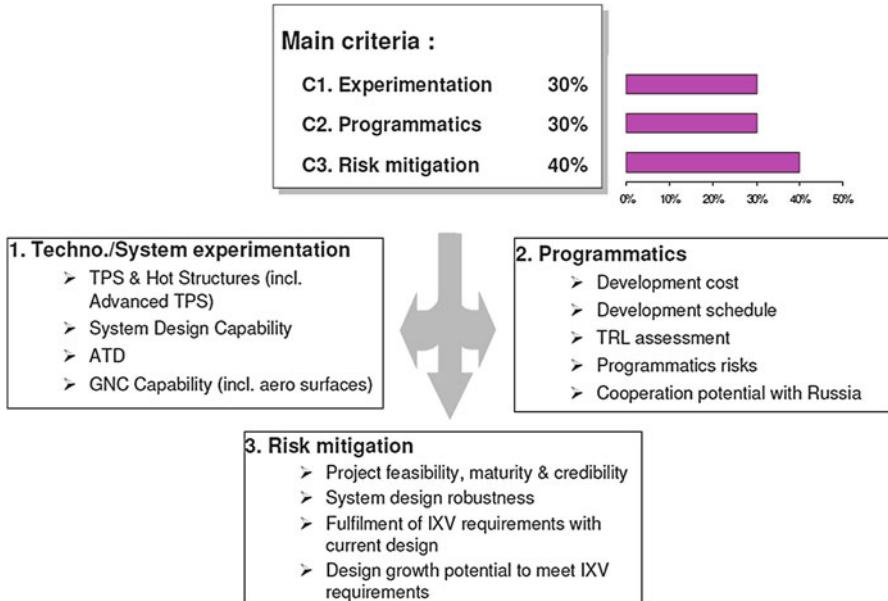


**Fig. 5.20** Trade-off criteria concept

criteria reflect the degree of attractiveness of one concept in terms of risk mitigation for the IXV project itself. Risk mitigation is the bottom line of the IXV concept to secure the way forward to the next generation of experimental re-entry vehicle and to the NGL on programmatic aspects. Moreover, the design of the selected concept being dedicated to be consolidated, the robustness of the concepts, and more generally the evolution potential of their design are considered a lot more important than the way they fulfill the criteria with their current design status.

As far as trade-off results and recommendations are concerned, the main result of this basic assessment is that the final global ranking well reflects the concepts classification, in terms of aerodynamic shape configuration [6]. As shown in Fig. 5.21, from the lowest to the highest ranking, the three concept classes are [6]:

### 5.3.1 The Capsule Class

This class includes the EXPERT and the AREV biconic configurations. The strong advantages of these concepts, exhibiting much simpler design features than the concepts of the other classes, lie in the very attractive programmatic features. On the other hand, these concepts are much appropriate and best optimized toward the ATD experimentation. Their relevance for the other experimentation objectives defined for the IXV is quite low, especially regarding the TPS experimentation and

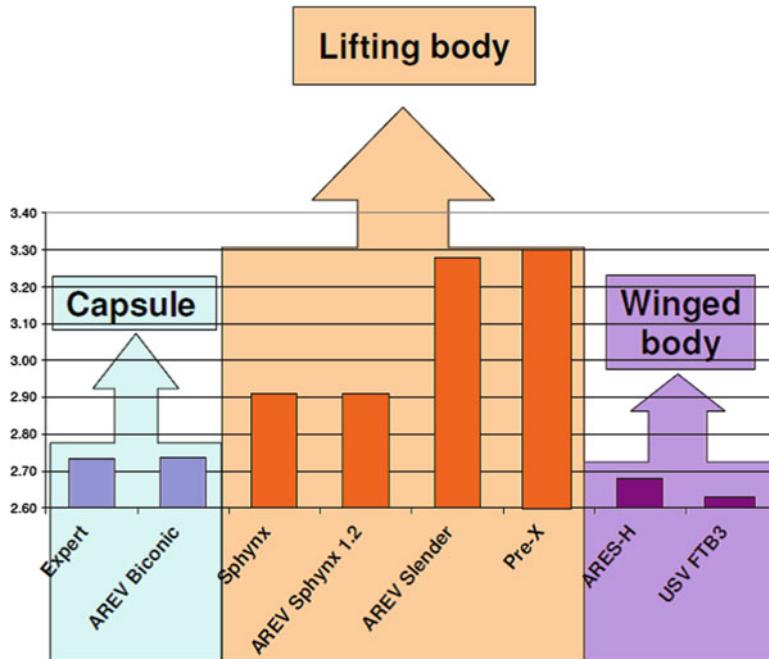


**Fig. 5.21** Trade-off results

the opportunity to enhance and gain experience in Europe on the system design for preparing the next-generation experimental vehicles. Furthermore, they offer a very low growth potential in terms of design evolution capability, since their shape design is highly constrained by the ballistic nature of the mission, and also in terms of flight envelope coverage, since their gliding capability is quite low.

### 5.3.2 *The Wing–Body Class*

The wing–body class includes the ARES-H and the USV FTB-3 concepts. They are in a way opposite to the capsule concepts, since they offer very interesting features for the experimentation purpose regarding all objectives, but they are not relevant with respect to the programmatic criteria. Their development appears costly and long for the IXV needs. The USV FTB-3 concept is lower ranked compared to the ARES-H one mainly due to a lower maturity achieved in the design process of the concept. The FTB-3 concept has not gone through a complete system design loop, as the ARES-H did.

### 5.3.3 *The Lifting-Body Class*

The lifting-body class, which is ranked first compared to the two other classes, includes the Sphynx, AREV Sphynx-like, AREV slender body, and Pre-X concepts. Regarding this lifting-body class, two subclasses could be identified:

- The Sphynx-derived shape (with fins/winglets)

This subclass includes the Sphynx concept itself and the AREV Sphynx1.2 one, which is a scaled version of the original one. These concepts are slightly lower ranked than the slender ones, mainly because of the aeroshape completely derived from the X-38 one. This has two main consequences that lower the attractiveness of such concepts for the IXV. First, the experience gained on system design is very limited for the design process of an aerodynamic shape, which is obviously a key element of the overall design process of an operational re-entry vehicle. Second, the design growth potential of such concepts is slightly lower than the slender body ones, since the aerodynamic performances are frozen by the aeroshape which can only be upscaled or downscaled.

- The slender body shape

The slender body subclass, which includes the AREV slender and Pre-X concept, resulted the most promising category according to the IXV preliminary requirements [6].

A sensitivity analysis has been performed to assess in which extent the results and conclusion of the IXV trade-off can be affected by the subjectivity inherent to any grading exercise. The major outcome of this analysis is that the main conclusion of the overall trade-off is not changed: the lifting/slender body class is the best option to be down-selected. Therefore, the main conclusion of the trade-off performed is that the lifting/slender body concept class is recommended as baseline starting point for the design consolidation loop to follow.

## 5.4 IXV Vehicle Description and Configuration Rationale

The IXV concept is a lifting-body configuration which features a compact body with rounded edge fuselage cross section, a delta planform shape, a rounded nose, a flat windward side, and two splitted body flap. The overall full-scale vehicle dimensions are length (without flap), 4.40 m; width, 2.22 m; and height (with non deflected flaps) 1.54 m.

The vehicle configuration is characterized by a lift-to-drag ratio (L/D) of  $\sim 0.7$  in hypersonic regime to achieve aerodynamically high cross range and by the center of gravity (CoG) positioned at a distance from the nose to guarantee the capability of trimmed flight over a wide range of angles of attack, in compliance with the system requirement to fly at high AoA and compatibly with the thermal constraints and the usage of both conventional and advanced thermal protection systems.

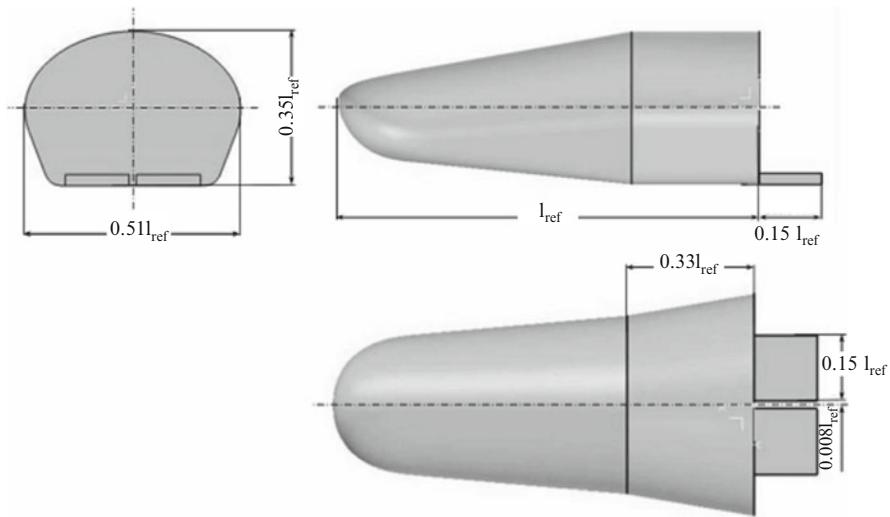


**Fig. 5.22** IXV shape and size in nondimensional form with respect to  $l_{\text{ref}} = 4.4 \text{ m}$

Geometry of the shape of IXV and the size of the flaps are shown in nondimensional form in Fig. 5.22 [4].

The fuselage was designed to be longitudinally tapered, in order to improve aerodynamics and lateral–directional stability, and with a cross section large enough to accommodate all the vehicle subsystems such as, for example, the propellant tanks of reaction control system (RCS) which have to support the requirement of mission duration. This has a large impact on vehicle performance. In fact, from the aerodynamic point of view, the lift and the aerodynamic efficiency are mainly determined by the fuselage fineness, flat-bottomed surface and planform and cross-section shapes.

The forebody is characterized by a double-curvature blunted nose geometry with smooth streamlined surfaces on the upper and lower side of the fuselage and by the nose drop-down configuration, typical of hypersonic vehicles.

Finally, the flaps can be deflected independently thus working as elevators or ailerons (e.g., pitch and roll control). In fact, as shown in Fig. 5.23, the flap features a tilted hinge line to provide, together with vehicle trim, a slight lateral control as well [4].

The IXV configuration rationale follows by the need to get similarity with full-scale vehicles [5]. Indeed, one of the objectives of an experimental vehicle is to provide a flying test bed capable of capturing ATD phenomena with suitable similarity laws. Some of these phenomena are impossible to reproduce by on-ground facilities because of the peculiarity of the environment for an orbital re-entry [7].

The main similarity parameters used in the frame of ATD are the following (see Table 5.2):

- Mach number,  $M$ , which gives the flow compressibility
- Reynolds number,  $Re$ , which gives the ratio between the inertial and viscous forces

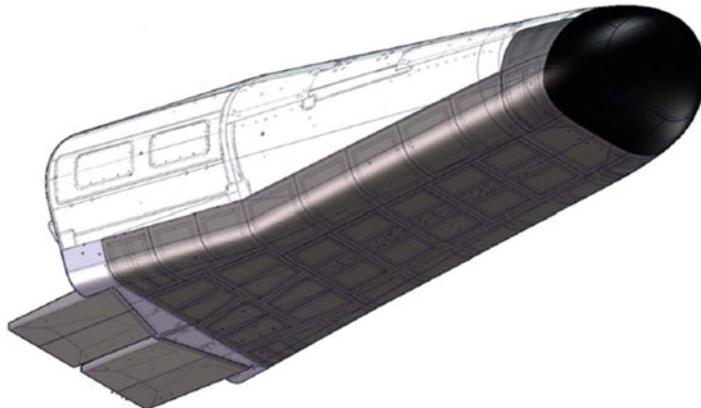


**Fig. 5.23** IXV splitted body flap with tilted hinge line

**Table 5.2** Similarity parameters

Similarity parameter	Characteristic dimension $L$	Physical phenomena	Relevant similarity
Reynolds number $Re = \frac{\rho V L}{\mu}$	Body length	Viscous effects on flaps (SWBLI)	Major
	Nose radius	Viscous effects on nose/forebody (transition on windward side)	Major
Dissociation parameter (Binary mixture) $\rho L$	Body length	Real gas effects (body flap)	Minor
	Nose radius	Real gas effects behind front shock (stagnation region) – catalycity	Major
Heat flux $\Phi_{Nose} = C \cdot \sqrt{\rho} \cdot \frac{V^3}{R_{Nose}}$	Body length		Not relevant
	Nose radius	Nose heat flux	Major

- Dissociation parameter,  $\rho L$ , which is tight to the gas dissociation and hence to real gas effects
- Heat flux per unit area at nose stagnation point  $\Phi$

The similarity parameters in Table 5.2 must be evaluated with respect to the geometric variables such as  $\lambda = L_{x\text{-vehicle}}/L_{\text{ref-vehicle}}$ , where  $L_{x\text{-vehicle}}$  is a characteristic length of the experimental vehicle and  $L_{\text{ref-vehicle}}$  is the correspondent characteristic length of the full-scale vehicle [5]. Together with the geometrical factors, a trajectory factor can be defined as the ratio of the density of a reference full-scale vehicle and that of the scaled model:

$$K = \frac{\rho_{\text{ref-vehicle}}}{\rho_{x\text{-vehicle}}} \quad (5.1)$$

Supposing that the full-scale and experimental vehicle have the same velocity, similarities are respected when  $\lambda/K = 1$  for aerodynamics and  $(\lambda \cdot K)^{0.5} = 1$  for

**Table 5.3** Similarity conditions versus  $\lambda$ , Z

For X or RLV similarity: IXV should fly		
In case	Aerodynamics	Heat flux
$\lambda < 1$	Lower Z	Higher Z
$\lambda > 1$	Higher Z	Lower Z

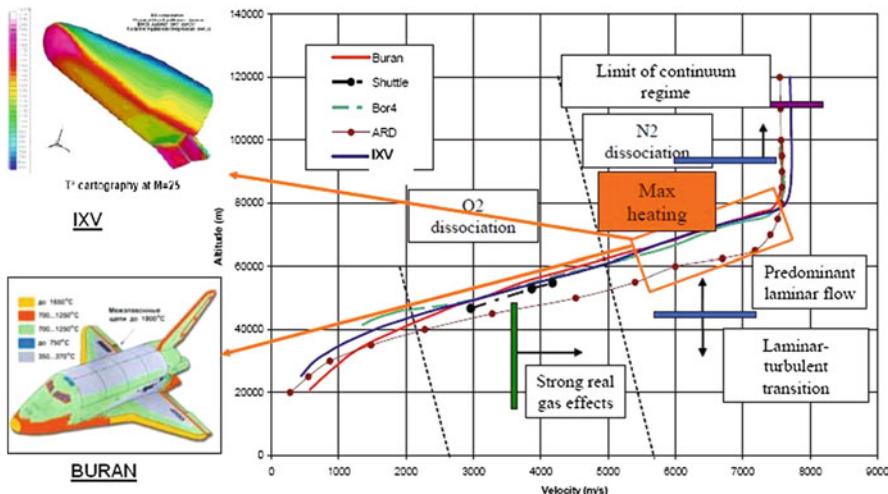


**Fig. 5.24** IXV re-entry trajectory in comparison with other vehicles

thermal flux. Table 5.3 gives the similarity conditions for aerodynamics and heat flux for flight of the experimental vehicle at the same velocity but at different altitudes with respect to a reference vehicle, as a function of  $\lambda$  [5].

The IXV design has been focused on the heat flux and ATD phenomena more than aerodynamics. A typical profile of altitude versus velocity for a class of re-entry vehicles is illustrated in Fig. 5.24 and shows the similarity of IXV with Buran, BOR-4, and Shuttle for the re-entry profile [5].

## 5.5 IXV Top Level Drivers

IXV is an experimental vehicle whose main goals are recalled hereafter:

- The demonstration of flight capabilities of new European technologies, such as innovative reusable TPS (e.g., shingles), and the mastering of vehicle flight worthiness and controllability using both aerodynamic flap and RCS control.
- The demonstration for Europe to conduct an end-to-end development, of a new re-entry vehicle.
- A prototype philosophy. The IXV is a one-shot experimental vehicle, without recurrent use. In other words, it is not mandatory to design the IXV for multiple uses in flight.

- IXV as an experiment in itself. Mastering the experiment system is a key element of the project as, let us recall, the main objective is to get the relevant in-flight results and measurement: all this in order to be able to refine the design margins and to calibrate necessary tools (as CFD or WT facilities) that are necessary for ground design and therefore for future re-entry vehicle development. The development will still have to manage a compromise between the experiment and the vehicle functional aspects.
- Protoflight model approach to be followed. It will impact strongly the qualification and integration logic.

The project has to be conducted in a large European frame. Therefore, mastering the lot of subsystems I/F between several companies will be a key element of the development.

Since its beginning, the IXV was conceived as a technology platform that, building on a series of technology investments and achievements (e.g., ESA TRP, GSTP, Hermes, MSTP, FESTIP, X-38, FLPP, and national programs), would perform the step forward with respect to the ARD and the EXPERT demonstrations, by increasing its in-flight maneuverability to verify the technology performance against a wider re-entry corridor [8]. As indicated in its name, the IXV is designed to be the “intermediate” element of a technology-effective and cost-efficient European road map for in-flight verification of technology performance necessary to prepare future ambitious operational system developments with limited risks for Europe [9].

Once in LEO orbit, after the Vega’s fairing jettisoning (see Fig. 5.25), the vehicle will perform a separation maneuver and with the assist of AVUM (Attitude

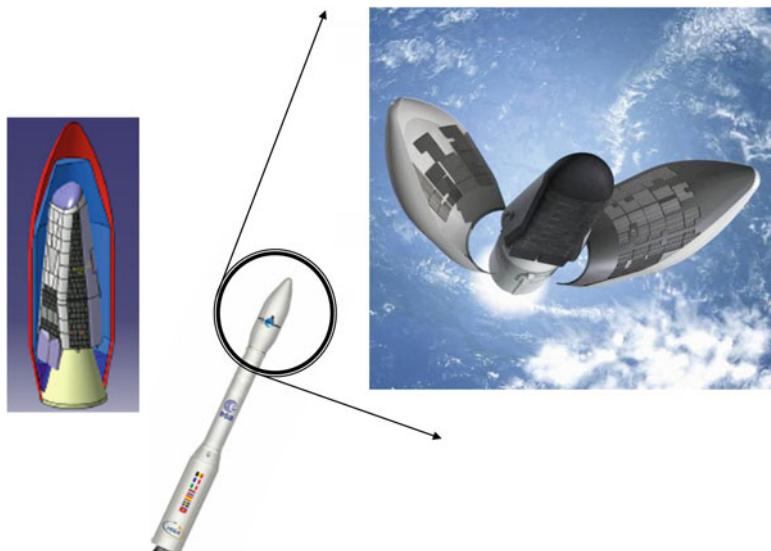


**Fig. 5.25** IXV accommodation into the Vega fairing

and Vernier Upper Module) service module will start the re-entry phase, during which it will fly trimmed and will maneuver in a hypersonic flight, accordingly to the experimental requirements, up to supersonic, and transonic regimes, until the landing parachute will be deployed.

## 5.6 IXV Project Background

Since 2000, the number of experimental vehicles for re-entry technologies under studies in Europe, including France, Germany, Italy, and ESA, underlined the strategic need for Europe to gain relevant in-flight experience on enabling re-entry systems and technologies, to consolidate its position, and to play ambitious roles in future international cooperation in the area of space transportation [9]. In 2004, the ESA Future Launchers Preparatory Programme (FLPP) was conceived by the ESA Member States to provide the European programmatic frame to develop, among other technological challenges, the IXV re-entry system as a technology platform to verify in-flight the performance of critical re-entry technologies when integrated at the system level. In 2005, a thorough industrial trade-off was performed among all ESA and national existing concepts, and the concept down-selected for the IXV was a lifting re-entry body, to be launched and injected on a re-entry path by the ESA Vega Launcher and to be able to perform a set of dedicated maneuvers prior to land for postflight inspection and analysis [10].

Therefore, in 2007, the successful IXV System Requirements Review (SRR) has frozen the key aspects of the IXV mission and system, focusing on the consolidation of the European know-how for controlled Earth re-entry from low Earth orbit (LEO), integrating at system level key re-entry technologies for the in-flight verification of their performance in representative flight environment [9]. On the basis of today's status of the IXV industrial activities, about to conclude the project phase B upon successful completion of the system preliminary design review by end 2008, several aspects are recognized to contribute to the advancement and consolidation of the European know-how for future re-entry missions. Among the most important ones there are [9]:

- Mission and system aspects, since the IXV constitutes the technological step ahead after the ARD capsule, developed and flown in the 1990s. With respect to classical capsules, the IXV configuration exhibits higher L–D ratio, higher cross-range and down-range, and significant roll-control authority for alleviating deceleration loads and addressing maneuverability and controllability to increase spaceflight safety and comfort.
- Design standard aspects, since the current ECSS (European Cooperation for Space Standardization) standards, which are the basis for ESA applications, are tailored for satellite applications. At the start of the IXV project, a dedicated tailoring of the available ECSS was performed, where a critical tailoring of the specific technical and product assurance standards was made. In case of missing

reference guidelines for critical areas, dedicated working groups were created with the involvement of experts from industries, research institutes, and agencies across Europe.

- Design tools validation aspects, since the current lack of precise knowledge of some phenomena occurring during re-entry (e.g., aerothermodynamics) induces the need of extra margins into the design, with the objective to improve design performance. Flying back from an Earth entry velocity equal to approximately 7.5 km/s (typically of re-entry from LEO), the IXV mission ensures occurrence of all key real gas effects and enables to validate the extensive aerodynamic and aerothermodynamics aspects, including computational fluid dynamics (CFD) and wind tunnel tests data.
- Assembly, integration, and verification aspects, for the complexity induced by re-entry-specific technologies (e.g., TPS) and/or by existing technologies in new environments (e.g., GNC). The IXV assembly, integration, and verification experience, including methods, rules, and procedures, will provide know-how relevant to any future space transportation system for LEO re-entry applications.
- Operational aspects, for the handling of radio frequency, telemetry, communication blackout, stations visibility with links to ESA and non-ESA fixed and mobile ground stations, and recovery operations. The IXV operations experience, including established methods, rules, and procedures, will provide know-how relevant to any future space transportation system for LEO re-entry applications.
- Safety and reliability aspects, due to the current uncertainties with respect to safety policy for nondestructive re-entry applications in Europe, necessary to ensure sensitive flight and ground safety requirements during the re-entry, descent, and landing phases. The IXV experience will prepare a commonly recognized European methodology to safety data submission to launching authorities, necessary for future re-entry applications.
- Guidance navigation and control aspects, since the guidance algorithms inherited by the ARD, the use of the inertial measurement unit coupled with GPS for navigation, and the use of combined flaps and reaction control systems, make the IXV addressing all complex GNC issues related to the hypersonic phase of a re-entry from LEO.
- Thermal protection aspects, due to the complexity introduced by the severe thermomechanical environment into critical design issues as thermal expansions at interfaces, junctions, seals, gaps, steps, and singularities. The in-flight verification of several thermal protection materials performance and design solutions will provide know-how relevant to any future space transportation system for LEO re-entry applications.
- Additional TRL aspects, stemming from the utilization of technologies commonly adopted as off-the-shelf (e.g., avionics system components) in launchers or spacecraft developments but necessitating further qualification in representative environment for re-entry applications. The IXV mission will provide the opportunity to increase the technology readiness levels of such components up to 8 and 9, with relevance to future space transportation systems developments for LEO re-entry applications.

In synthesis, the IXV project objectives tackle a large part of the basic European needs for re-entry from LEO, consolidating the experience and know-how necessary for the development of any future European re-entry system [9].

## 5.7 IXV Mission Requirements and Description

The IXV is designed to fulfill a set of high-level requirements and objectives that have been iteratively discussed and jointly defined by the agency and industry.

The IXV mission will use a Vega launcher flight to be injected on an equatorial trajectory, specifically selected and tuned to ensure re-entering through the atmosphere with environmental conditions fully representative of return missions from LEO.

The IXV mission focuses on the following objectives [9]:

- Mission/system aspects, step ahead from ARD
- Specific technology verification (ATD, GNC, TPS)
- Generic technology readiness levels
- Design standards tailoring
- Design tools validation
- Operations and safety

The main technical and programmatic constraints that define the project are [10]:

- Perform the atmospheric re-entry with a lifting configuration controlled by combined thrusters and aerodynamic surfaces.
- Perform verification and experimentation of a well-defined set of critical re-entry technologies and disciplines (e.g., aerodynamics, aerothermodynamics, thermal protections, hot structures, guidance, navigation, and control).
- Concentrate the verification and experimentation in the hypersonic and high supersonic flight domains.
- Perform landing and recovery of the vehicle at sea and in an “intact” state to allow postflight inspection and analysis.
- Utilize the ESA Vega as the baseline launcher to perform an end-to-end (ETE) European mission at limited cost.
- Implement a strict system design-to-cost approach with protoflight model development philosophy.
- Ensure a stringent system development and qualification plan targeting a launch date within the year 2012.

As far as the design trajectory is concerned, it has the goal to satisfy a wide set of requirements to ensure:

- The precise re-entry flight profile to provide the environment compatible with the experimentation purposes (e.g., heat flux, heat load, g-load, dynamic pressure)

- The minimization of the IXV flight over densely inhabited regions.
- The compatibility with the Vega launcher performance from Kourou spaceport, and its stages fall-out.

The resulting nominal ETE trajectory is shown in Fig. 5.26, where the maximum altitude is set at  $\sim 475$  km in the ballistic arc [9]. It provides a velocity at the entry gate equal to about 7,450 m/s and a flight path angle of  $-1.6^\circ$ , fully representative of a re-entry from low Earth orbit (LEO) missions. The entry gate conventionally defines the beginning of the re-entry phase, and it is located at 120 km altitude.

The fulfilment of the assigned main trajectory requirements is recalled in Table 5.4 below [9].

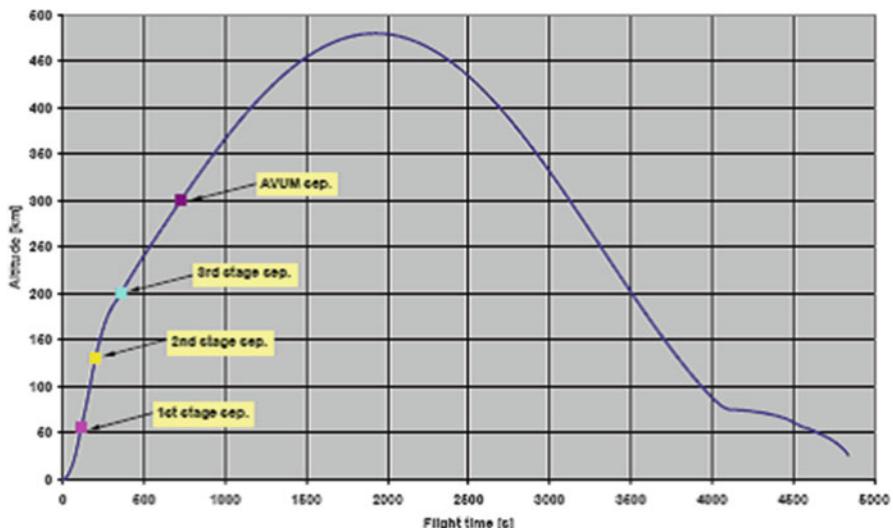
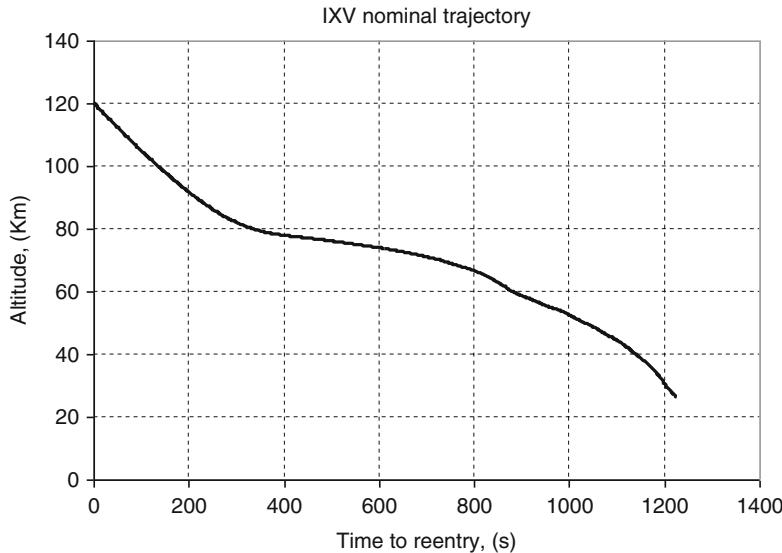


Fig. 5.26 Nominal ETE trajectory foreseen for the IXV

Table 5.4 Reference trajectory parameters

Sizing trajectory for:	Trajectory parameters			
	Heat flux ( $\text{kW/m}^2$ )	Heat load ( $\text{MJ/m}^2$ )	G load	Dyn. Pr. (kPa)
Heat flux peak (<482)	468.4	258.1	2.15 g	4.77
Heat load (<280)	456.4	259.5	2.09 g	4.51
G-load peak (<4)	436.8	248.7	2.30 g	5.23
Dyn. Pr. peak (<6)	457.6	238.3	2.20 g	5.85



**Fig. 5.27** IXV nominal re-entry trajectory in the altitude–time map

Finally, Fig. 5.27 shows the nominal re-entry trajectory in the altitude–time map. As far as technical requirements are concerned, we have:

### 5.7.1 Mission

- The IXV mission shall allow validation of TPS&HS assemblies and components performance in RLV representative environment, including RLV nominal (for representative re-entry time exposure), and if possible abort mission scenarios (for representative excess of thermal loading).
- The IXV mission shall be based on the utilization of the ESA/Vega launcher for the IXV injection into orbit and the ESA/Vega launcher upper stage for the IXV deorbiting.
- The IXV mission shall be based on an IXV ground landing scenario, minimizing the landing impact to preserve and allow for the TPS&HS recovery in intact status.

### 5.7.2 System

- The IXV system shall take into account all the major drivers of its constituents since the very early design definition phase, e.g., by foreseeing the allocation of reasonable mass, volume, and power budgets for passenger experiments though not yet defined.

- The IXV system shall perform the necessary measurements to allow postflight vehicle model identification to validate the IXV vehicle mathematical models of dynamics.
- The IXV vehicle shall be based on a slender lifting-body outer shape with active aerodynamic control surfaces.
- The IXV passenger experiments, not yet defined, shall be relevant for TPS&HS technologies investigation and design tool improvements, e.g., validation of CFD and WTT results.

### ***5.7.3 TPS and Hot Structures***

- The IXV TPS&HS shall be based on ceramic, metallic, and FEI-family assemblies including insulations, attachments, junctions, and seals (static and dynamic).
  - The IXV TPS&HS ceramic assemblies shall experience highly loaded windward environments, such as in nose region, in leading edges, and in aerodynamic control surfaces.
  - The IXV TPS&HS metallic assemblies shall experience mildly loaded windward environments, as well as leeward and/or base/aft environments.
  - The IXV TPS&HS FEI-family assemblies shall experience adequate leeward and/or base/aft environments.
- The IXV TPS&HS shall be based on both ceramic and metallic attachment systems, including metallic-to-ceramic junctions.
- The IXV TPS&HS shall preserve its recovery in intact status after the landing impact, to allow postflight inspection, to guarantee assemblies' dismount ability, and to evaluate assemblies' and components' residual performance for reusability issues through ground testing.

### ***5.7.4 Dependability***

The IXV mission success criteria shall be:

- To recover exploitable flight data, ensuring proper postflight analysis, with a probability higher than 95 % (excluding launcher reliability)
- To recover tested hardware in an intact/exploitable state with a probability higher than 90 % (excluding launcher reliability)
- To fulfill the experimental objectives for the vehicle and passenger experiments
- Complementary requirements

### **5.7.5 ATD**

The IXV mission shall allow collection of in-flight data in representative environment relevant for the investigation and the design tools validation regarding the following ATD phenomena:

- Real gas effects
- Shock wave–boundary layer interaction
- Shock–shock interaction
- Laminar-to-turbulent transition
- Transitional separation
- Turbulent heating
- Cavity heating
- Materials catalytic behavior
- Materials oxidation effects
- Control surface efficiency
- RCS efficiency

### **5.7.6 Innovative Materials and Concepts for TPS&HS**

The IXV mission shall allow a minimum set of innovative materials and concepts or TPS&HS in-flight experimentation, including:

- Ceramic based
- Metallic based

### **5.7.7 HMS**

The IXV mission shall allow a minimum set of HMS sensors and techniques in-flight experimentation, including:

- GNC subsystem related
- TPS&HS subsystem related
- Cold structures subsystem related

### **5.7.8 GNC**

The IXV mission shall allow a minimum set of GNC technologies in-flight experimentation, including:

- Onboard software and hardware related
- Off-board software and hardware related

## 5.8 WTT and CFD Data Comparisons with IXV Nominal Trajectory

The vehicle AEDB generates as output the aerodynamic coefficients of IXV in terms of flight conditions ( $M$ ,  $Re$ , altitude) and vehicle attitude (i.e.,  $\alpha$ ,  $\beta$ ,  $\delta_e$ ,  $\delta_a$ ).

The aerodynamic analysis, based on engineering-based analysis, CFD, and WTT, is carried out for the whole flight domain from rarefied flow conditions down to subsonic regime. The reference Mach number range is from  $M_\infty = 25$  down to  $M_\infty = 0.8$ . Therefore, the AEDB covers the range of Mach numbers, angles of attack, sideslip, and control surface deflections foreseen for the IXV nominal re-entry scenario.

These databasing activities rely on several wind tunnel (WT) and CFD data. Wind tunnel tests data refer to several test campaigns carried out in different European facilities, while CFD computations have been performed strictly by partners actually involved in technical assistance activities for ESA.

All data are provided in a format which will allow a buildup from a basic configuration by means of contributing elements to each force or moment component such as aerodynamic control surface effectiveness, etc. They are presented in a manner which treats each force and moment separately, and equations are provided to facilitate the buildup procedure which also accounts for the effects of rarefied atmosphere. Then, a bridging formulation for lift, drag, and pitching moment coefficients in order to take into account for rarefaction effects is included as well. In particular, experimental data for the hypersonic regime refer to test campaigns performed in S4ma and H2K wind tunnels, whereas for the supersonic, transonic, and subsonic regimes, experiments are carried out in DNW-SST and FOI T1500 wind tunnels. Test flow conditions are recognized in Table 5.5 for each wind tunnel [7].

Some CFD data performed by ESTEC and CIRA are recognized in terms of free-stream conditions in Tables 5.6 and 5.7, respectively [7]. The different models and flow conditions considered in the numerical computations have been provided as well (see column “notes”).

As a result, by superimposing all WTT and CFD free-stream conditions over the IXV nominal trajectory, both Figs. 5.28 and 5.29 can be provided [7].

As one can see, all data sources enable to address the Mach–Reynolds full duplication along descent since WTT and CFD matrices were defined in order to provide good coverage of the foreseen flight domain and to exploit the synergy between experimental and computational activities. Indeed, H2K and S4Ma WT sizes and conditions enable to fully duplicate the Reynolds number at Mach 6, 8.7, and 10. This means also that extrapolation to flight activities of experimental aerodynamic data can be avoided, except for the high Mach number results provided

**Table 5.5** Free-stream conditions of WT tests

S4ma				H2K			
Test ID	Notes	Reynolds	Mach	Test ID	Notes	Reynolds	Mach
[ - ]	[ - ]	[ - ]	[ - ]	[ - ]	[ - ]	[ - ]	[ - ]
548	S4ma	9.18E+05	9.857	24 to 53	H2K	1.12E+06	6
559	S4ma	7.30E+05	9.825	58 to 76	H2K	7.80E+05	8.7
581	S4ma	5.76E+05	9.777				

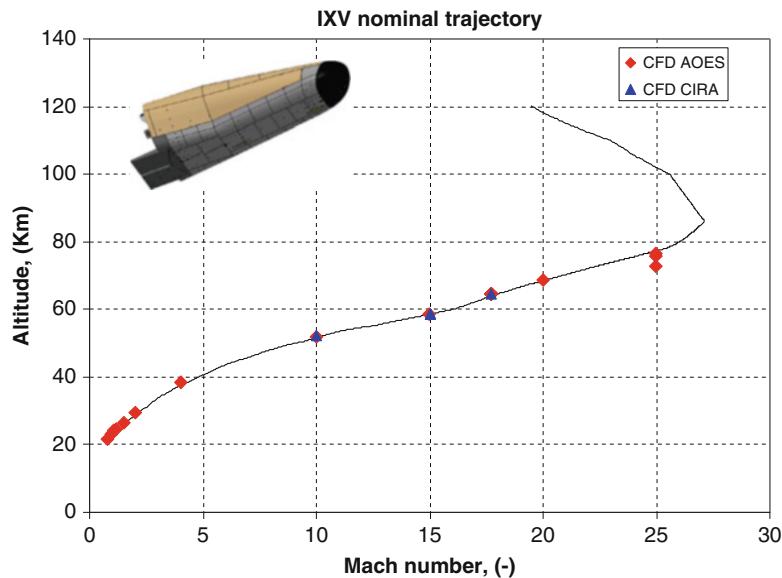
SST				FOI T1500			
Test ID	Notes	Reynolds	Mach	Test ID	Notes	Reynolds	Mach
[ - ]	[ - ]	[ - ]	[ - ]	[ - ]	[ - ]	[ - ]	[ - ]
	SST	5.50E+06	1.47		FOIT1500	5.50E+06	0.8
	SST	6.10E+06	2.01		FOIT1501	5.00E+06	0.95
	SST	1.10E+07	3.02		FOIT1502	4.20E+06	1.2
	SST	1.51E+07	3.94		FOIT1503	3.90E+06	1.4

**Table 5.6** Free-stream conditions of ESTEC CFD simulations

AOES							
# Sim (-)	Test ID (-)	Notes (-)	Mach (-)	Altitude (km)	Reynolds (-)	Knudsen (-)	
1	1	PG”TURB”SST”	0.8	21.74	5.007E + 06	2.391E-07	
2	11	PG”TURB”SST”	1.0	23.33	4.634E + 06	3.061E-07	
3	21	PG”TURB”SST”	1.1	24.11	4.614E + 06	3.500E-07	
4	33	PG”TURB”SST”	1.2	24.82	4.567E + 06	3.913E-07	
5	43	PG”TURB”SST”	1.5	26.32	4.526E + 06	5.014E-07	
6	53	PG”TURB”BL”	2	29.60	3.540E + 06	8.436E-07	
7	59	PG”TURB”BL”	4	38.31	1.802E + 06	3.314E-06	
8	65	NEQ”TURB”BL”	10	52.06	6.826E + 05	2.184E-05	
9	80	NEQ”TURB”BL”	15	58.57	4.832E + 05	4.621E-05	
10	95	NEQ”TURB”BL”	17.7	64.70	2.684E + 05	9.832E-05	
11	106	NEQ”TURB”BL-CMP”	17.7	64.70	2.684E + 05	9.832E-05	
12	107	NEQ”TURB”SST-CMP”	17.7	64.70	2.684E + 05	9.832E-05	
13	108	NEQ”TURB”K-EPS”	17.7	64.70	2.684E + 05	9.830E-05	
14	109	NEQ”TURB”K-EPS-CMP”	17.7	64.70	2.684E + 05	9.830E-05	
15	110	NEQ”TURB”K-EPS”	17.7	64.70	2.684E + 05	9.832E-05	
16	111	NEQ”TURB”SST”	17.7	64.70	2.684E + 05	9.832E-05	
17	114	EQ”TURB”BL”	17.7	64.70	2.684E + 05	9.833E-05	
18	117	PG”TURB”BL”	17.7	64.70	2.684E + 05	9.847E-05	
19	125	NEQ-LAM	20	68.66	1.808E + 05	1.649E-04	
20	140	NEQ-LAM	25	75.73	8.330E + 04	4.475E-04	
21	145	NEQ-LAM	25	76.52	7.385E + 04	5.039E-04	
22	147	NEQ-LAM	25	72.78	1.260E + 05	2.953E-04	

**Table 5.7** Free-stream conditions of CIRA CFD simulations

CIRA						
# Sim (-)	Test ID (-)	Notes (-)	Mach (-)	Altitude (km)	Reynolds (-)	Knudsen (-)
1	FL02	EQ-TURB K-EPS	10	52.1	6.79E + 05	
2	WT1	PG-LAM	14			
3	WT5	PG-TRANS	14			
4	WT7	PG-TURB	14			
5	FL01	EQ-TRANS K-EPS	15	58.7	4.86E + 05	
6	2	EQ-TURB K-EPS	15	58.7	4.86E + 05	
7	10	NEQ-TRANS K-EPS	15	58.7	4.86E + 05	
8	5	EQ-TRANS K-EPS	17.7	64.6	2.68E + 05	

**Fig. 5.28** Nominal trajectory and AEDB (CFD) source data. Mach–altitude duplication

by the DNW-SST. Note that the Reynolds number that could be realized for the IXV model in the SST exceeds that in free flight due to the higher air density in this WT, because the SST exit is at ambient pressure.

This parameter is difficult to satisfy with a scaled model and has led to development of pressurized and cryogenic wind tunnels in which the viscosity of the working fluid can be greatly changed to compensate for the reduced scale of the model.

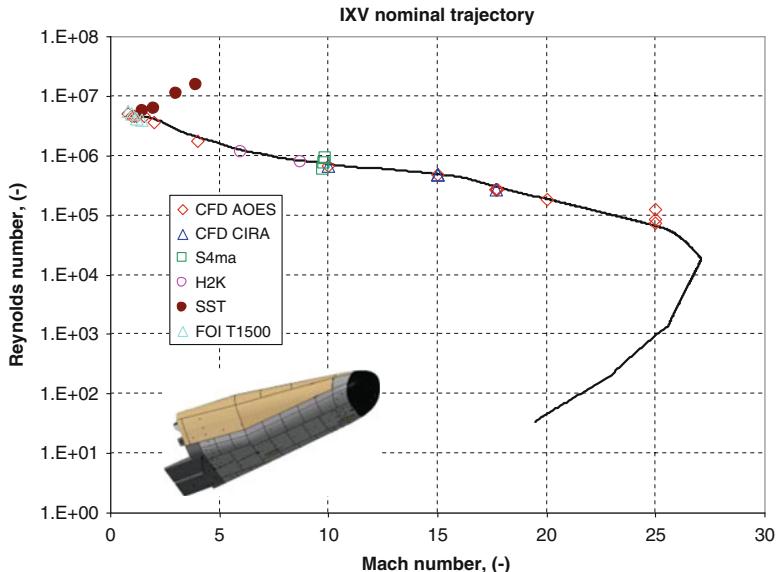


**Fig. 5.29** Nominal trajectory and AEDB (CFD, WTT) source data. Mach–Reynolds duplication

## 5.9 Results of WTT Campaigns

The validation of the IXV-AEDB requires reference experimental data in order to properly address both the nominal aerodynamic coefficients value and the related uncertainties band.

Indeed, a reliable data (CFD or WTT) must be ever accompanied by accuracy in measure. That is why margin policy is extremely important within design process.

Generally speaking, one of the main features of the system loop process is to take suitable margins (which are reduced during the study), perform trade-off, and compromise. Margins are directly tight to cost. The challenge consists in designing a system capable to perform all these functions with sufficient margins, safety, and limited cost.

The margin policy applies to all the vehicle designs (trajectories, GNC, avionics, thermomechanics, vehicle design, etc.) and constitutes the driver for subsystems design. The margins cover essentially the following:

- Uncertainties
- Dispersions
- Clearance

Which are supposed to lower during the program evolution (phases A, B, C, D, etc.). A scheme of this evolution is given in Fig. 5.30 [5].

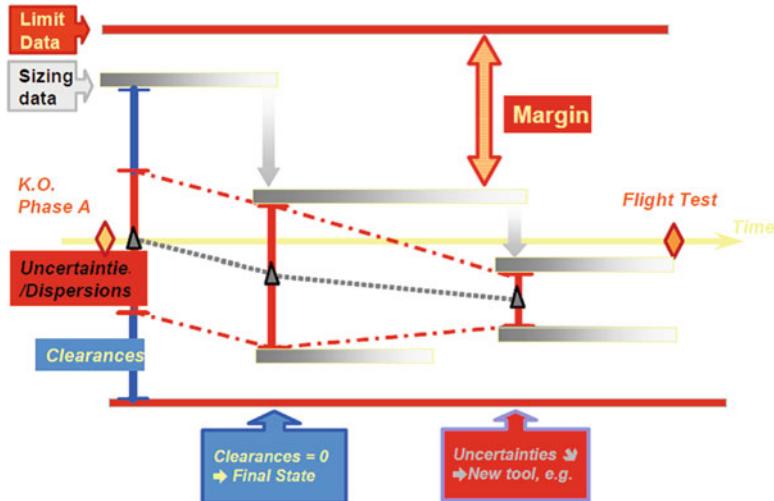


**Fig. 5.30** Margin policy scheme

The way the margin policy is applied is really an important matter of the system design. In particular, for experimental vehicles, the margin should be usually reduced in order to be capable of catching the physical phenomena that need to be investigated. This is more a research or prototype approach than an industrial design. The Pre-X (and ARD) experiences have taught that margins must be kept under reasonable values during all development in order to avoid the design of a too robust operative vehicle more than an experimental one [5].

A typical example is given by the heat flux (and maximum temperatures) calculations all over the vehicle and, in particular, on body flaps. Sufficient margin has to be kept in order to assure vehicle integrity, but always allowing sufficient deflection for experimental purposes and actual attitude control by this device [5]. In cold hypersonic regime (low or no real gas effects), it is possible to gather reliable ground data from H2K and S4ma WTs.

### 5.9.1 ONERA S4ma Test Highlights

The ONERA S4ma cold hypersonic WTT results contribute to the construction of the AEDB (aerodynamic database) by measurements of aerodynamic force and moment coefficients for various longitudinal and lateral configurations and flaps with different settings. Additionally, local pressure measurements and flowfield visualizations have been performed. The runs have been performed on a 1/13.75<sup>th</sup> scale model ( $L_{ref} = 0.320 \text{ m}$ ) [11].

Thirty runs (including the repeatability and visualization runs) have been performed in the following test conditions:

- Mach number: 10
- Reservoir pressure: 25, 35, and 45 bars corresponding to Reynolds number ( $L_{ref} = 0.32$  m) of  $5 \times 10^5$ ,  $7 \times 10^5$  (flight Reynolds number), and  $9 \times 10^5$ , respectively;
- Angle of attack sweep:  $30^\circ$ – $57^\circ$  and  $57^\circ$ – $30^\circ$
- Sideslip angle sweep:  $-10^\circ$  to  $+10^\circ$
- Flap deflection range:  $-10^\circ$  to  $15^\circ$
- Forced transition via a tripping device with 4 rows of cylindrical wires spaced from each other by 1 mm and placed close to the nose part and the first ramp part junction region perpendicular with regard to the main flow.

Example of S4ma results are displayed on Fig. 5.31, where the pitching moment coefficient versus  $\alpha$  is reported at different flap settings (i.e.,  $\delta_e = -10^\circ$ ,  $-5^\circ$ ,  $0^\circ$ ,  $5^\circ$ ,  $10^\circ$ , and  $15^\circ$ ) [11].

As shown, experimental results highlight, concerning the efficiency of elevon, nonlinear evolution of  $C_m$  with AoA above  $45^\circ$  and for large elevon deflection (e.g.,  $\delta_e > 10^\circ$ ).

With the S4ma test campaign, excellent repeatability has been achieved on all aerodynamic components [11]. No hysteresis has been observed during the AoA or sideslip sweep up followed by a sweep down. Excellent flow and aeroshape symmetry have been achieved.

A slight offset on yawing moment has been observed to occur along the campaign. Transition tripping results in  $C_m$  increases with elevons deflection making the vehicle to be more pitch down which might be consistent with an elevons efficiency

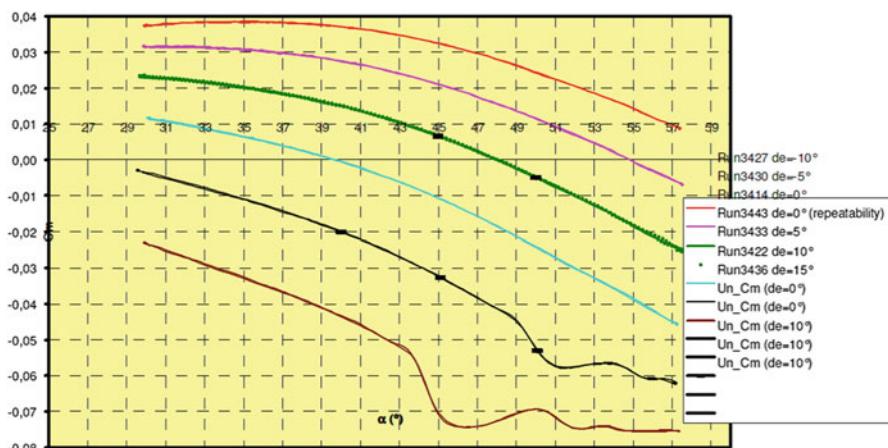


**Fig. 5.31** Pitching moment coefficient versus AoA at  $M_\infty = 10$  in S4ma WT

increase because of a turbulent boundary layer. Additional investigations are needed with a denser pressure instrumentation in the elevons zone and more accurate oil flow visualizations.

### 5.9.2 DLR H2K Test Highlights

The DLR H2K cold hypersonic WTT results contribute to identification of Mach effects on aerodynamic characteristics with respect to ONERA S4ma Mach 10. Additionally, local pressure measurements and flowfield visualizations have been performed [11].

The runs have been performed on a 1/17.6<sup>th</sup> scale model ( $L_{ref} = 0.250$  m). Thirty runs (including the repeatability and visualization runs) have been performed in the following conditions:

- Mach number: 6 and 8.7
- Reservoir pressure: 4 and 16 bars corresponding to the flight Reynolds number ( $1.12 \times 10^6$  and  $0.78 \times 10^6$ , respectively)
- Angle of attack sweep:  $30^\circ$ – $55^\circ$  and  $55^\circ$ – $30^\circ$
- Sideslip angle:  $-8^\circ$  to  $+8^\circ$
- Flap deflection range:  $-10^\circ$  to  $15^\circ$
- Forced transition via a tripping device with two strips of carborundum grains of 0.18 and 0.4 mm

Figure 5.32 shows an example of some H2K results obtained at Mach 6 by means of a schlieren visualization [11]. As one can see, the bow shock that takes place ahead of vehicle at  $M_\infty = 6$ ,  $\alpha = 45^\circ$ , and  $\delta_e = 10$  is clearly shown, as well as the SSI and the SWIBLI phenomena in the flap region.

Very good-quality data were obtained, providing with expected Mach number effects in cold conditions that are still currently under analyses.



**Fig. 5.32** H2K Schlieren visualization at  $M = 6$

### 5.9.3 DNW-SST Test Highlights

The SST is a wind tunnel of the blow down type; see the layout in Fig. 5.33 [12].

A 5 MW compressor fills the 600 m<sup>3</sup> storage vessel (1) with air up to 4,000 kPa pressure in about 45 min [12]. The capacity of the vessel enables effective run times between 20 and 50 s duration depending on the selected Mach number and the total pressure  $P_0$  [12]. Heat regenerators (2) stabilize the air temperature inside the vessel. During a run, the main valve (3) and the pressure regulator valve (4) allow the stored air to reach the settling chamber (6), which is equipped with several mesh screens to reduce the turbulence level and to promote the uniformity of the flow [12]. The pressure regulator valve keeps the total pressure in the settling chamber during a run at a constant level, which is preselected by the tunnel operator. The air escapes from the settling chamber through nozzle (7) and reaches the test section (8), where the model is located. The adaptation of the tunnel to a selected Mach number consists of the adjustment of the height of the rectangular shaped nozzle and test section and of the accommodation of the contour and the inclination of the upper and lower wall of the wind tunnel between the nozzle and the test section. Downstream of the test section the tunnel is composed of a variable diffuser with a movable upper and lower wall (9), used from Mach 3 upward, a fixed diffuser (10) and the silencer and exhaust (11).

The trim of the model was expected at an AoA as high as 55–60°. The support mechanism of the SST allows a continuous change of the incidence angle from –6° to +15°. A pneumatically operated shifter system can add a stepwise increase of 20°. The application of a dedicated mounting plate, sting adapters, and a 33° cranked sting resulted in the setup as presented in Fig. 5.34 [12].

The model was mounted on the balance with a tilting angle of +5° in order to limit the interaction between the sting and the base flowfield. For  $M_\infty \leq 2$ , an AoA range from 30° to 70° was reached. At higher Mach, the mounting angle of the internal balance inside the IXV model had to be reduced from 5° to 0° in order to avoid balance overloads. As a result, for  $M_\infty > 2$ , an AoA range from 25° to

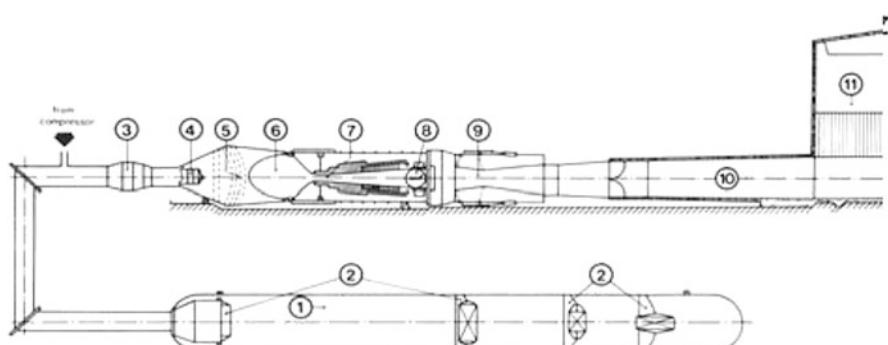


**Fig. 5.33** Schematic layout of wind tunnel SST

**Fig. 5.34** FLPP IXV in scale 1/21 on 33° cranked sting in the SST

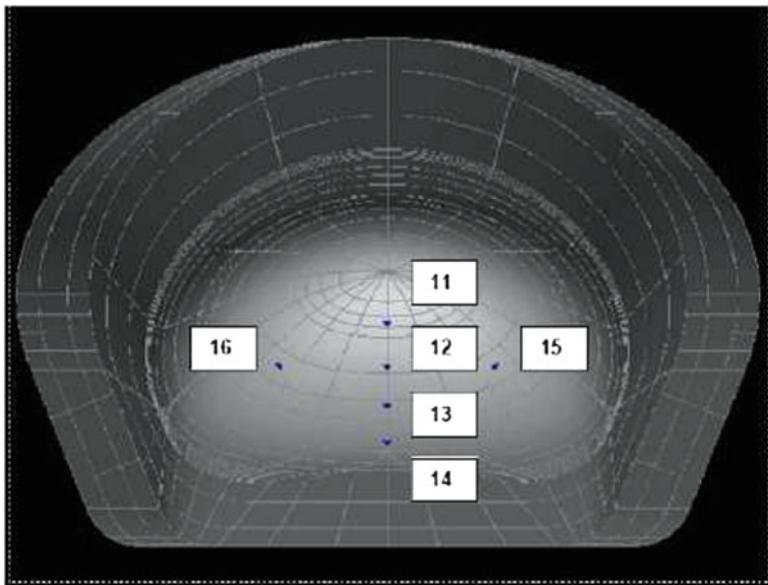


**Fig. 5.35** Location of pressure taps belonging to the FADS on the IXV nose cone

65° was measured. An internal six-component balance, FOI I-682, and a 16-port 200 kPa pressure module were mounted inside the IXV model. Six pressure taps are positioned in the nose cone area and stem from the Flush Air Data System (FADS) of the IXV; see Fig. 5.35 [12].

Eight other taps are distributed over the model; see Fig. 5.36 [12].

A resolver in the model support measured the angle of incidence of the model; a correction for the deflection of balance and sting based on the measured balance loads was applied.

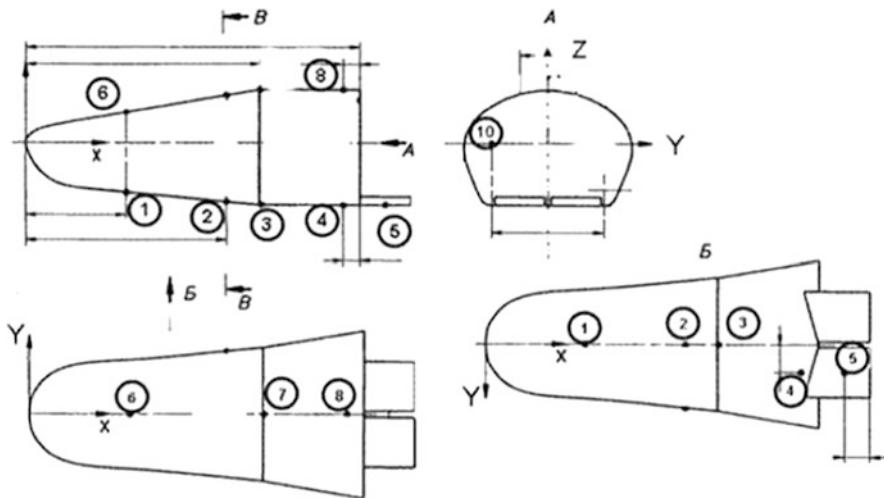


**Fig. 5.36** Distribution of remaining pressure taps over the IXV surface

**Table 5.8** Test conditions in SST and flight conditions of IXV

SST conditions							Flight conditions	
Mach	$P_0$ (kPa)	$P$ (kPa)	$T_0$ (K)	$V$ (m/s)	$Q$ (kPa)	$Re$ ( $\times 10^6$ )	$Re$ ( $\times 10^6$ )	
1.45	165	48	282	410	71	5.5		
1.99	224	29	289	507	81	6.1	3.5	
2.99	649	18	283	605	112	11.0		
3.91	1,481	11	294	667	117	15.1	1.6	

Runs were conducted by performing continuous alpha sweeps at constant Mach numbers:  $M_\infty = 1.45$ ,  $M_\infty = 1.99$ ,  $M_\infty = 2.99$ , and  $M_\infty = 3.91$ .

Table 5.8 contains the test conditions in the wind tunnel and the free flight conditions [12].

Several flap settings with corresponding elevator ( $\delta_e$ ) and aileron ( $\delta_a$ ) were investigated; the tested flow conditions are listed in Table 5.9 [12].

The pitch moment behavior in Fig. 5.37 indicates the efficiency of the elevator at  $M_\infty = 1.99$  [12].

As shown, IXV in clean configuration (i.e.,  $\delta_e = \delta_a = 0$ ) features a natural trim point at alpha 44°.

The curves for roll and yaw moment at  $M_\infty = 1.45$  and for different flap settings (i.e., aileron efficiency for roll and yaw moments) are reported in Figs. 5.38 and 5.39, respectively [12].

A comparison of the lines for  $\delta_a = 0^\circ$ ,  $5^\circ$ , and  $10^\circ$  shows a nonlinear yaw moment performance. The aileron deflection also affects the elevator efficiency, as Fig. 5.40 exhibits [12].

**Table 5.9** Performed test matrix on IXV in SST

Serie	Remark	de (dg)	da (dg)	deL (dg)	deR (dg)	$\alpha$ (dg)	$\beta$ (dg)	Run ( $M = 1.45$ )	Run ( $M = 1.99$ )	Run ( $M = 2.99$ )	Run ( $M = 3.91$ )
5		-10	0	-10	-10	AoA	0	10	22		57
1		-5	0	-5	-5	AoA	0	8	23		
2	Longi	0	0	0	0	AoA	0	7/66	24		56
3		5	0	5	5	AoA	0	9	25		
4		10	0	10	10	AoA	0	11	26		58
2	Lateral	0	0	0	0	AoA	-5	32	31	34	
2	Lateral	0	0	0	0	AoA	-2		37	74	
2	Lateral	0	0	0	0	AoA	2		38		
14	Lateral	-5	5	-10	0	AoA	0		40		
13	Alleron	-2.5	2.5	-5	0	AoA	0		39		
8		0	-5	5	-5	AoA	0	20			
7		0	5	-5	5	AoA	0	16	28		61
10		0	10	-10	10	AoA	0	19/67	30/47		65
16		2.5	-2.5	5	0	AoA	0	14		60	
11		2.5	2.5	0	5	AoA	0	13		59	
17		5	-10	15	-5	AoA	0	54			
9		5	-5	10	0	AoA	0	21			
6		5	5	0	10	AoA	0	15	27	53	63
15		5	10	-5	15	AoA	0	50	49	64	
4	visu	10	0	10	10	50	0	42			

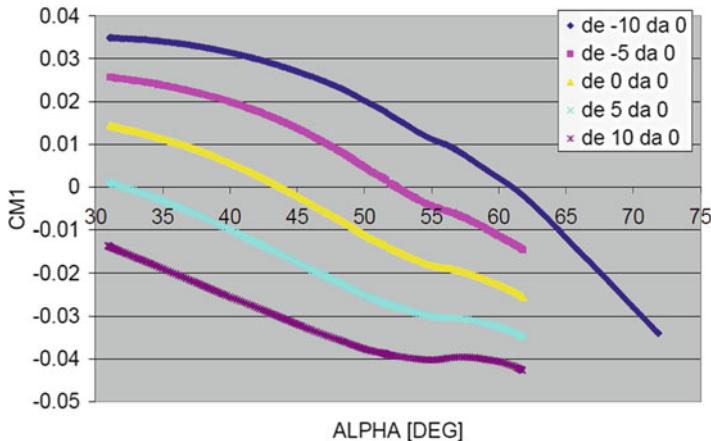


Fig. 5.37 Elevator efficiency of IXV at  $M_\infty = 1.99$

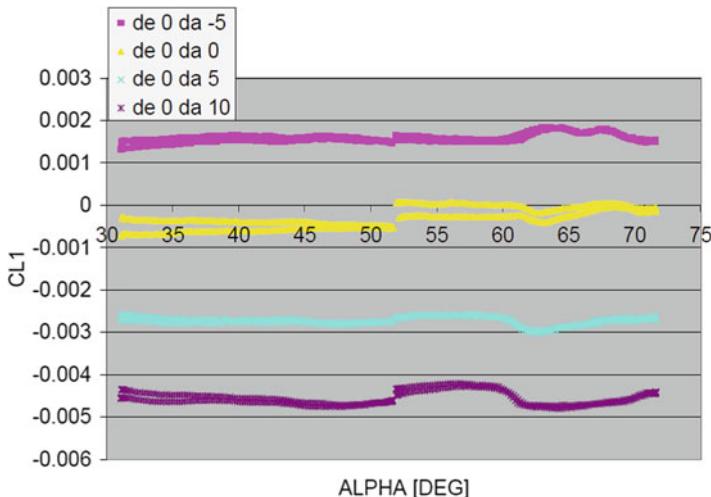
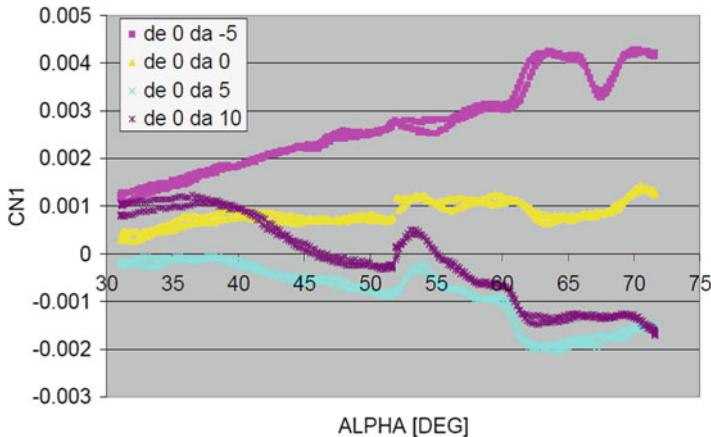


Fig. 5.38 Aileron efficiency in roll at  $\text{Ma} = 1.45$

The drag properties of IXV are visualized in Fig. 5.41 as a function of  $M$  and Re numbers [12].

The sidewalls of the test section are equipped with optical windows. Schlieren pictures were recorded during all runs to document the shock patterns and flow separation.

Figure 5.42 shows an example of schlieren pictures at  $M_\infty = 1.99$  and at  $\alpha = 60^\circ$  [12].



**Fig. 5.39** Aileron efficiency in yaw at  $M_\infty = 1.45$

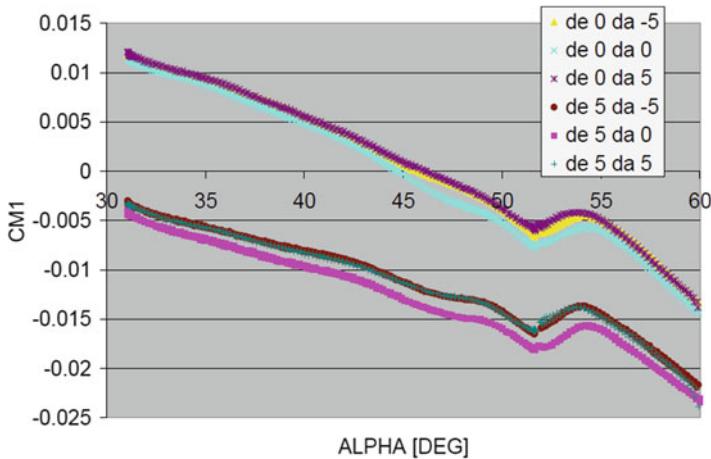


**Fig. 5.40** Aileron effect on pitch moment at  $M_\infty = 1.45$

### 5.9.4 FOI T1500 Test Highlights

The wind tunnel test campaign was conducted in the FOI/FFA T1500 injection-driven closed circuit tunnel; see Fig. 5.43 [13].

The tunnel is driven with high-pressure air from a storage and from the tunnel the air is exhausted to the atmosphere. The test section of the T1500 tunnel is 1.5 m in cross section, and it is 4.0 m long [13]. The walls are slotted and there are four slots in each of the four walls. A controlled amount of air is sucked out through the slots into the plenum surrounding the test section. At Mach numbers less than 1.0, Mach number control is carried out by the downstream choke and at higher Mach numbers

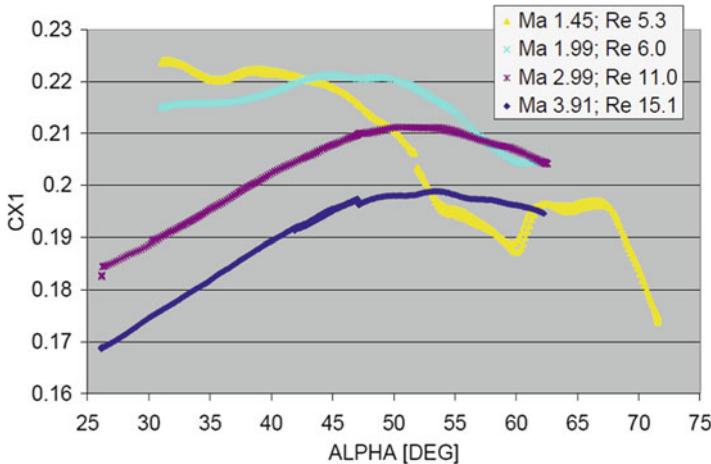


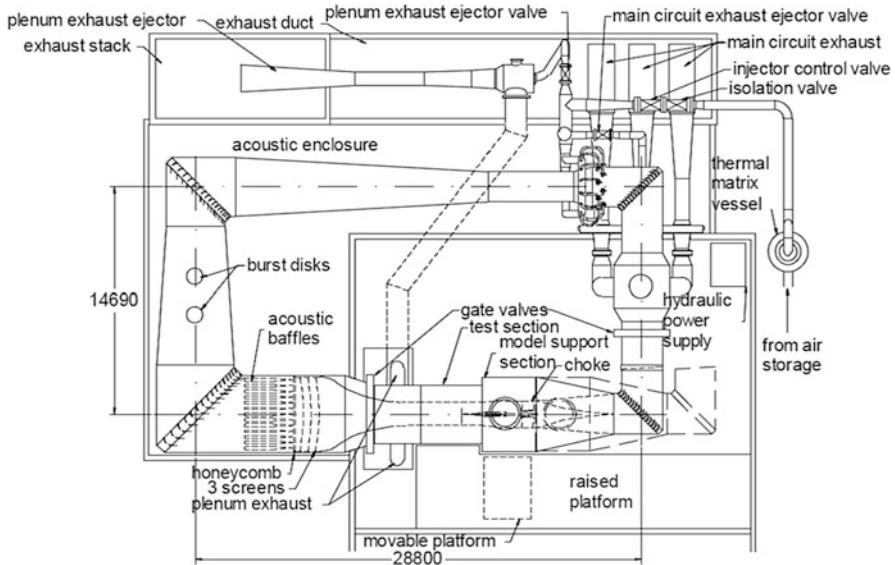
Fig. 5.41 Drag of IXV dependent of  $M$  and  $Re$



Fig. 5.42 Schlieren picture of IXV in the SST at  $M_{\infty} = 1.99$  and  $60^\circ$  AoA

by plenum suction. The regular contraction is used at Mach numbers up to 1.20, but at  $M = 1.40$ , this contraction is changed to a contraction with a built-in nozzle. The slotted walls are retained, and because the model is positioned downstream of the test rhombus, the Mach number can be controlled within a narrow range by plenum suction. Downstream of the test section is the model support section. In the center of the tunnel, there is a vertical strut on which there is a sting pod mounted.

A photo of the model in the wind tunnel is shown in Fig. 5.44 [13].



**Fig. 5.43** Plan view of the FOI T1500 wind tunnel

**Fig. 5.44** Model A installed in the test section for tests in the high angle of attack range



A roll drive is mounted to the front face of the sting pod. In the roll drive, a  $32^\circ$  bent sting is mounted. In the front end of the bent sting, another sting is mounted. In the angle of attack range  $23^\circ < \alpha < 56^\circ$ , it is a straight sting. The model as installed in the tunnel for this AoA range is shown in Fig. 5.45a [13].

In the higher AoA range,  $56^\circ < \alpha < 90^\circ$ , the straight sting is replaced by a  $33^\circ$  bent sting.

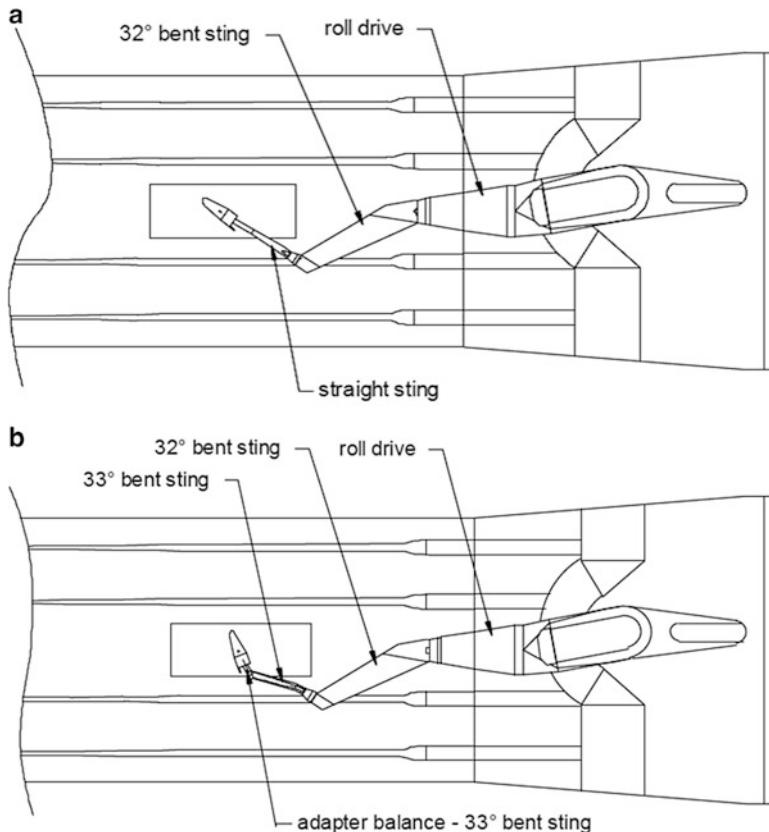


**Fig. 5.45** Model support setup for testing in the low angle of attack range (a)  $23^\circ < \alpha < 56^\circ$ ; (b)  $56^\circ < \alpha < 90^\circ$

There is also a short adapter between this sting and the balance, and the setup in the wind tunnel is shown in Fig. 5.45b [13].

The model tested in T1500 is one of several models of the FLPP IXV and is called Model A. Its shape is representative of the IXV 2.2 geometry, and the scale of this model is 1:21. This is a small model compared to the T1500 test section size, but the scale was chosen with respect to the high angles of attack ( $90^\circ$ ) in combination with low supersonic Mach numbers the model was going to be tested at. This was the smallest size that still would permit the installation of a 16-port PSI pressure module together with a 6-component balance. The model blockage in wind tunnel T1500 at an angle of attack of  $90^\circ$  is 0.82 %. The reference area for the model is the projected area in the horizontal plane except the flaps. In the blockage figure above, the blockage of the flaps has been included.

The body of the model is made in two parts, an upper and a lower half. There is a balance adapter mounted in the lower body half. The balance centerline is tilted

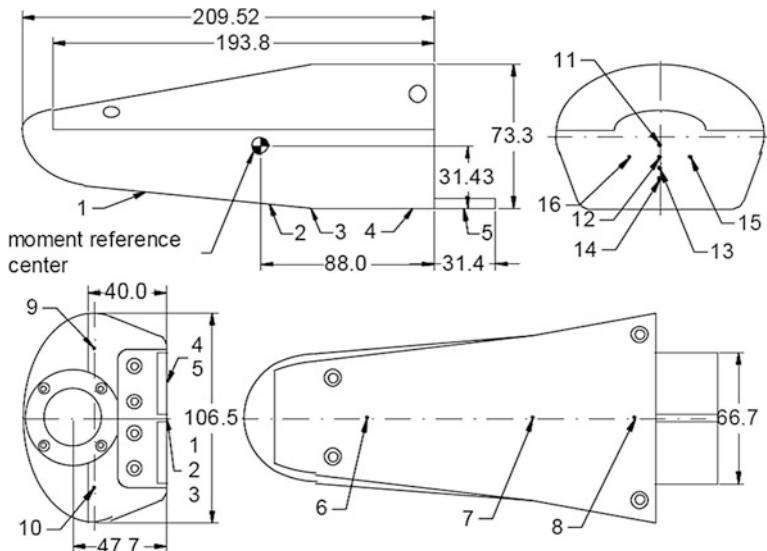


**Fig. 5.46** A 3-plan view of the FLPP IXV model A with pressure tap positions

$5^\circ$  from the model centerline. This made it easier to design a bent sting to reach  $90^\circ$  and should also reduce the sting interference on the flaps. The actual tilt angle was later measured to  $4.93^\circ$ .

Two rectangular flaps are mounted to the base of the model. Their lower surfaces are flush with the lower surface of the body. There is one flap for each flap angle.

A three-plan view of the model is shown in Fig. 5.46 [13].

Except for the first run, the model was equipped with transition trips for all runs. These consisted of carborundum grits in 4-mm-wide bands glued to the model. The grit size was  $60 \mu\text{m}$ . The transition trips were positioned in a ring around the nose and along two longitudinal lines at the outskirts of the lower surface flat surface [13].

The model is equipped with 16 surface pressure taps for measuring static pressure. Six of these are located in the nose to serve as a base for a Flush Air Data System (FADS). Figure 5.46 shows the pressure tap numbering and their positions.

In the planning stages, two 25 mm balances with different load ranges were candidates for this wind tunnel test. After a few initial runs, it became obvious that the complete wind tunnel campaign had to be run with the stronger balance due to high axial loads caused mainly by the  $5^\circ$  tilt between the model and balance axes.

For measurement of the 16 static pressures on the model surface, a PSI pressure module, ESP-16 TL, was used. The measurement range for this module is 30 psid. Installation in the model was quite difficult due to limited space, and the tubes on the module had to be bent down. One corner also had to be rounded off and the module housing had to be electrically isolated from the model. This is shown on the photo in Fig. 5.47 [13].



**Fig. 5.47** The PSI pressure module with bent tubes and a rounded corner installed in the model

**Table 5.10** Reynolds number and corresponding stagnation pressure in T1500 for different Mach numbers

$M$	0.80	0.95	1.20	1.40
$\text{Re} \times 10^{-6}$	5.55	4.99	4.10	3.80
$P_0$ (kPa)	184	154	121	114

In addition to the PSI pressure module, there is a separate pressure transducer measuring the balance cavity pressure. This transducer is of the absolute type and mounted in the sting pod and connected to the balance cavity with a plastic tube.

By choosing the right stagnation pressure, the tests were possible to perform at full-scale Reynolds number although the model is quite small; see Table 5.10 [13].

The tests were run at four Mach numbers with different elevator and aileron settings, also in combination. The full test matrix is shown in Table 5.11 [13].

One example of the longitudinal characteristics (i.e., pitching moment coefficient) at  $M_\infty = 0.95$  with zero aileron flap setting is shown in Fig. 5.48 [13].

As shown, the vehicle is unstable at  $\alpha < 31^\circ$ . With zero elevator setting (i.e., clean configuration), the trim angle of attack is  $57^\circ$ . Generally, the effect of different elevator settings is reduced with increasing AoA and is almost nonexistent at  $\alpha \approx 85^\circ$ .

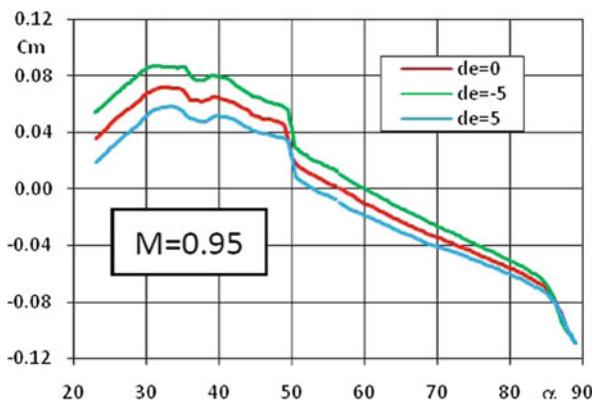
The effect of an angle of sideslip at changing angle of attack has been investigated, and the results for yawing (CLN) and rolling (CLL) moments are shown for  $M_\infty = 0.80$  in Fig. 5.49 [13].

The sideslip angle was  $\pm 5^\circ$ , but not all combinations of Mach number, angle of sideslip, and angle of attack range were tested. The results show anyway that the vehicle is stable in yaw at angles of attack above  $54^\circ$ . The rolling moment is almost independent of angle of attack, and its direction is to reduce the angle of sideslip [13]. The effect of different aileron settings on yawing and rolling moments with zero elevator setting is shown in Fig. 5.50 for  $M_\infty = 1.20$  [13].

The different aileron settings influence the yawing moment in the whole angle of attack range tested although it is quite small at the lowest angles. With an overlaid elevator setting of  $+5^\circ$ , the aileron effect increases at all Mach numbers (not shown). The rolling moment caused by different aileron settings is almost independent of the angle of attack.

**Table 5.11** Test matrix

Remark	de	da	$\alpha$	$\beta$	$M$				No. of runs
					0.80	0.95	1.20	1.40	
TN	10	0	$\rightarrow$	0					B 1
TD	10	0	$\rightarrow$	0					B 1
Longitudinal	-5	0	$\rightarrow$	0	A	A + D	A + B	B	6
	0	0	$\rightarrow$	0	A + B	A + B	A + B + C	B	8
	5	0	$\rightarrow$	0	A	A + B	A + B	B	6
Lateral sideslip	0	0	$\rightarrow$	5	A + B	A	A + B	B	6
	0	0	$\rightarrow$	-5	A			B	2
	0	0	70	$\rightarrow$	E + F				2
Lateral aileron	5	5	$\rightarrow$	0	A		A + B	B	4
	0	5	$\rightarrow$	0	A + B	A	A + B	B	6
	0	-5	$\rightarrow$	0	A + B	A	A + B	B	6
	5	-5	$\rightarrow$	0	A		A + B	B	4
	-5	-5	$\rightarrow$	0	A		A + B	B	4
	-5	5	$\rightarrow$	0	A		A + B		3
Oil flow	5	0	50	0				B	1
Total number of runs									60
TN = natural transition					TD = forced transition				
$\alpha$ or $\beta$ range					$\alpha$ or $\beta$ range				
A	56°–90°			D	23°–56°–23°				
B	23°–56°			E	-12°–12°				
C	56°–90°–56°			F	12°–12°				

**Fig. 5.48** Longitudinal characteristics at  $M = 0.95$  with different elevator settings.  $\delta_a = 0^\circ$ 

Results from the surface static pressure measurements and the four FADS pressures on the nose symmetry line are shown in Fig. 5.51 for just one Mach number [13]. These curves are quite smooth also at the transition from low to high angle of attack ranges. Results at the other Mach numbers tested are similar. When

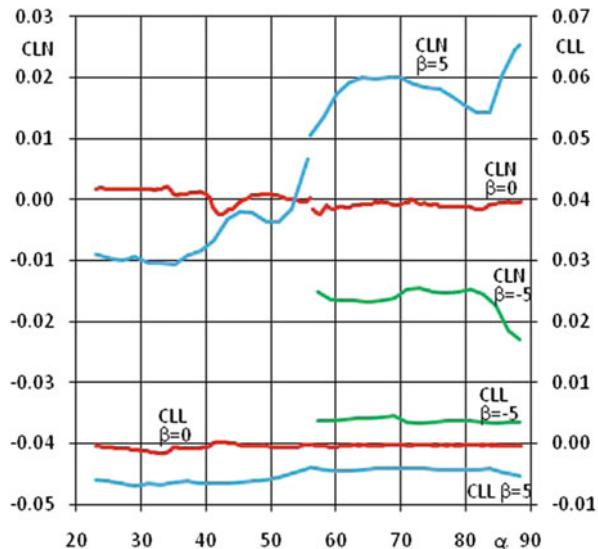


**Fig. 5.49** Lateral behavior due to an angle of sideslip at  $M_{\infty} = 0.80$ .  $\delta_e = \delta_a = 0$

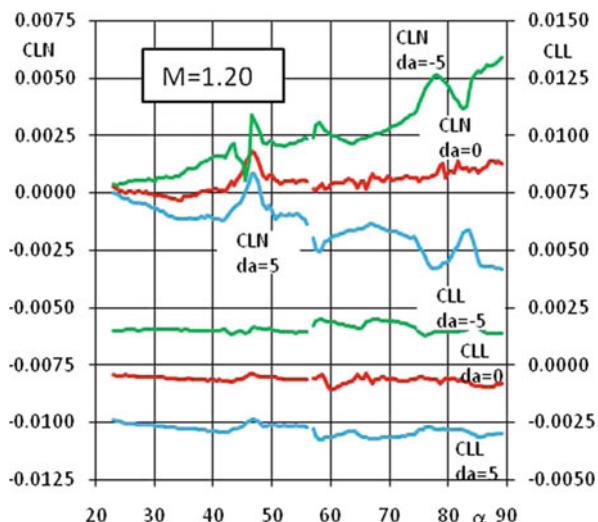


**Fig. 5.50** Effect of different aileron settings on lateral coefficients.  $M_{\infty} = 1.20$ .  $\delta_e = 0$

the angle of sideslip is varied, a similar linear dependence from the side-mounted FADS pressure ports is recorded.

Results from the leeside pressure ports 6 and 7 are shown in Fig. 5.52 [13].

These curves are not as smooth as the FADS pressures. Above  $=60^\circ$ , the curves become smoother, indicating completely separated flow.

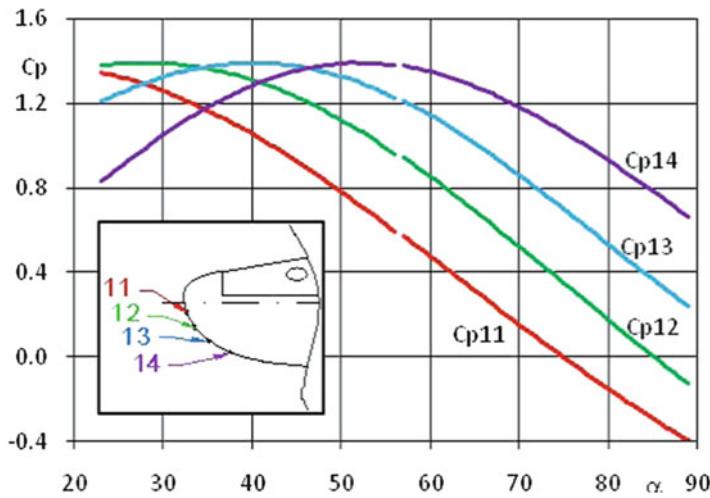


**Fig. 5.51** Symmetrical FADS pressure changes with angle of attack.  $M_\infty = 1.20$

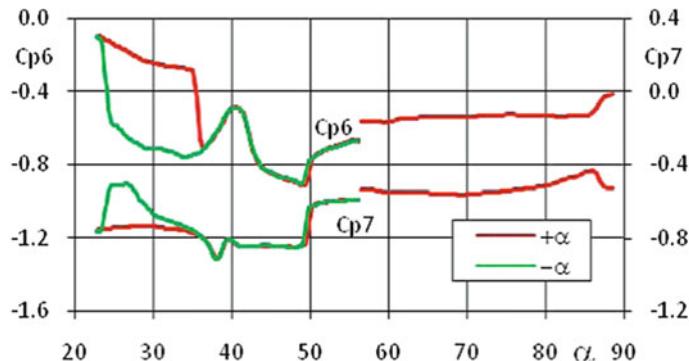


**Fig. 5.52** Hysteresis on two leeside static surface pressures.  $M_\infty = 0.95$

The flow below  $\alpha = 37^\circ$  is hysteresis dependant which is evident from the figure where plots from both increasing and decreasing angle of attack are shown.

There was one oil flow visualization run performed where one photo from this run is shown in Fig. 5.53 [13].

The run conditions were  $\alpha = 50^\circ$  and  $M_\infty = 1.40$ . A separation line is possible to see on the photo from the side.

Schlieren pictures were video recorded throughout the whole wind tunnel test. Only a few frames are shown here. Indeed, in Fig. 5.54, there are two consecutive photos from an angle of attack sweep run at  $M_\infty = 0.95$  [13]. At  $\alpha \approx 50^\circ$ , the schlieren pictures spaced  $0.16^\circ$  in angle of attack unveil a sudden change in the flowfield.

**Fig. 5.53** Oil flow visualization photo.  
 $M_\infty = 1.40$ ,  $\alpha = 50^\circ$

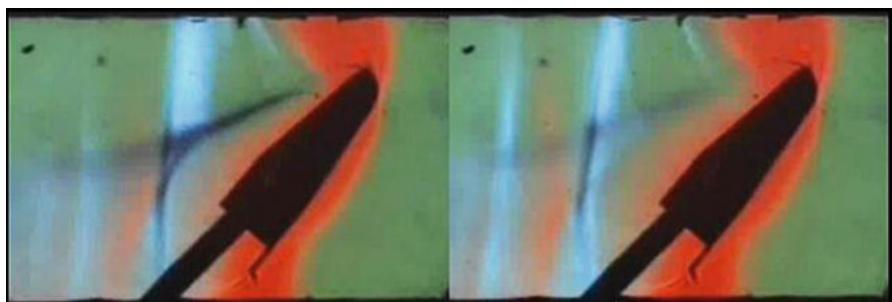


**Fig. 5.54** Schlieren photos from two consecutive frames.  $M_\infty = 0.95$ ,  $\alpha \approx 50^\circ$

Looking at the force and moment measurements, Fig. 5.48, there is almost a step change in pitching moment at the same AoA. There is also a corresponding loss of lift.

### 5.9.5 IXV and HEG Wind Tunnel

In order to correctly model the chemical relaxation occurring behind the bow shock of a re-entry vehicle, the flight binary scaling parameter must be reproduced in ground-based testing.

Further, for high enthalpy testing, an additional driving parameter which must be reproduced is the flow velocity. For example, the operating conditions of HEG are discussed in Fig. 5.55 in terms of the binary scaling parameter  $\rho L$  and the flow velocity  $u$  [14]. Here,  $L$  represents the length of the considered configurations. In addition to the HEG operating conditions, the most important fluid mechanical and chemical processes occurring during re-entry of a spacecraft in the Earth's

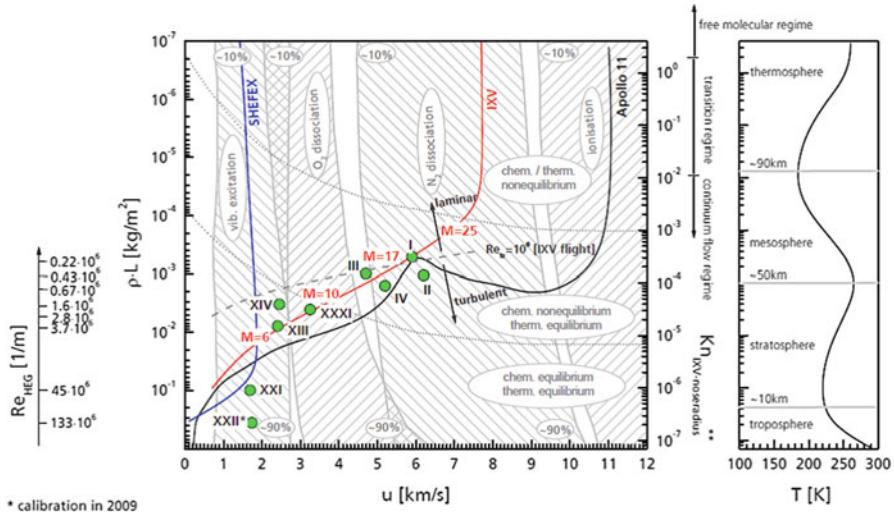


**Fig. 5.55** HEG operating conditions in terms of the binary scaling parameter  $\rho L$  and the flow velocity  $u$

atmosphere are also depicted in Fig. 5.55 [14]. Further, as reference, the flight trajectories of a lifting-body re-entry from low Earth orbit (IXV), a ballistic superorbital re-entry (Apollo 11), and a hypersonic flight experiment (SHEFEX) are provided as well.

An indication of the corresponding flight altitudes is given in the right diagram of Fig. 5.55 showing the temperature variation of the Earth's atmosphere. The transitions between regimes of different physical and chemical properties here reported depend on the chosen reference length and vary when different configurations are considered. Further, the boundaries shown have only symbolic character. In reality, no clear-cut dividing lines between the different regimes exist. The Knudsen number given in Fig. 5.55 shows that the HEG operating conditions are located in the continuum flow regime. The high energy content of re-entry flows leads to strong heating of the air in the vicinity of a spacecraft.

Depending on the temperature level behind the shock wave (i.e., the flight velocity), the vibrational degrees of freedom of the air molecules are excited, and dissociation reactions of oxygen and nitrogen molecules may occur. Further, ionization of the air constituents occurs. The high-temperature effects described here are enabled by energy transfer from the translational energy stored in the random motion of the air particles, which is increased by the gas heating, to other forms of energy. Because this energy transfer is realized by air particle collisions, it requires a certain time period to develop. The time required to reach an equilibrium condition is, e.g., defined by the local temperature and density. Therefore, depending on the ratio of the relaxation time to a characteristic timescale of the flow, the chemical and thermal relaxation processes can be either in nonequilibrium or in equilibrium.

Further, along a re-entry trajectory, the Reynolds number varies over several orders of magnitude. In high altitude flight, the wall boundary layer of a re-entry vehicle is initially laminar. After exceeding a critical Reynolds number (shown exemplarily for the IXV configuration in Fig. 5.55), the transition from a laminar to a turbulent boundary layer takes place [14]. This process is linked with an increase of the skin friction and the wall heat flux.

## 5.10 Results of CFD Analysis

As far as numerical results are concerned, a number of CFD computations will be shown hereinafter. Those simulations, carried out also to focus on several flowfield features evaluation, as, for example, conjugate heat transfer analysis of the body flaps and radiation heating in the hinge cavity, provided also further aerodynamic data gathered in the vehicle aerodynamic database development [15].

In this framework, two trajectory points have been considered for the analysis of the flowfield past the aeroshape 2.3. Those flight conditions refer to two Mach numbers, namely, 10 and 25, as summarized in the test matrix in Table 5.12, where vehicle attitude, boundary layer state, and wall catalyticity conditions are also reported [15].

In the present CFD analysis, only continuum regime with the air modeled as a mixture of five perfect gases species, N<sub>2</sub>, O<sub>2</sub>, NO, N, and O, and three vibrating species, N<sub>2</sub>, O<sub>2</sub>, NO, was analyzed. The far-field is assumed made of 79 % of diatomic nitrogen (N<sub>2</sub>) and 21 % of oxygen (O<sub>2</sub>).

Flowfield simulations have been performed by means of steady-state Navier-Stokes computations assuming chemically reacting gas model and considering alternatively the heat shield surface as non-catalytic (NC) and fully catalytic (FC) wall at radiative equilibrium temperature conditions (surface emissivity,  $\varepsilon = 0.8$ ). Simulations at  $M_\infty = 10$  have been performed assuming the condition of fully laminar flow and natural transition (i.e., transition at vehicle hinge line, Trans. HL), whereas at  $M_\infty = 25$ , only laminar flow conditions are considered.

CFD computations have been carried out on hybrid grids, similar to those shown in Fig. 5.56, made of about  $5 \times 10^6$  cells (half body) [15].

**Table 5.12** CFD test matrix

$M_\infty$ (-)	$H_\infty$ (km)	$\alpha$ ( $^\circ$ )	$\beta$ ( $^\circ$ )	$\delta_a$ ( $^\circ$ )	$\delta_e$ ( $^\circ$ )	$Re_{L_{ref\infty}}$ (-)	BL state	Catalysis
10	52.1	45	0	0	10	Flight	Laminar	NCW
10	52.1	45	0	0	10	Flight	Laminar	FCW
10	52.1	45	0	0	10	Flight	Turbulent	FCW
10	52.1	45	0	0	10	Flight	Tran. HL	FCW
25	76.5	45	0	0	10	Flight	Laminar	NCW
25	76.5	45	0	0	10	Flight	Laminar	FCW

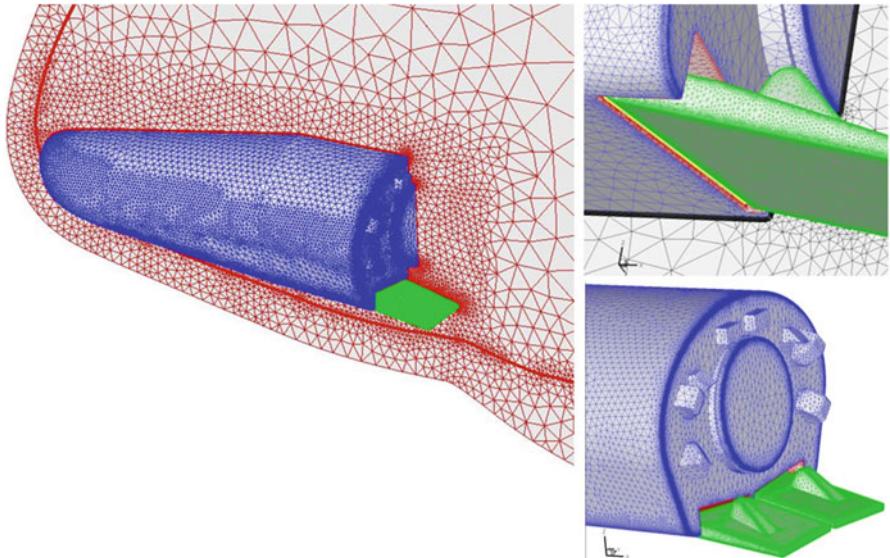


**Fig. 5.56** Example of one of the considered CFD hybrid grid

It is worth to note that grids are hybrid because they are unstructured but feature also prisms in order to capture as much as possible boundary layer at wall and shock structure at each considered flight conditions. First cell in the boundary layer is  $10^{-6}$  m height.

For instance, Fig. 5.56 shows mesh on vehicle surface and symmetry plane where is shown the boundary layer at wall and the shock fitting made of prisms. Hence, Fig. 5.57 shows a bottom view of flap assembly [15].

The right flap cavity is clearly recognized in Fig. 5.58, where the seal is also shown [15].

Finally, the convergence of each CFD simulation has been reached by means of a pseudo-transient procedure. The simulation is stopped when the global aerodynamic coefficient does not vary any more.

CFD result comparisons have been performed considering both contour field and selected vehicle sections as those reported in Fig. 5.59 [15].

Numerical results highlight a very complex flowfield that takes place past the vehicle both at Mach 10 and 25, such as strong bow shock, shock–shock interaction, shock wave–boundary layer interaction, base flow, and huge flow expansions. This makes the numerical simulations very stiff, especially for the initial start-up phase. As a consequence, each numerical computation has been afforded with simplified numerical settings, and, at the end of this start-up phase, the far-field and wall boundary conditions of Table 5.12 have been applied [15]. As an example of the results of the Navier–Stokes simulations, some interesting flowfield features are reported for both  $M_\infty = 10$  and  $M_\infty = 25$  trajectory point conditions.

**Fig. 5.57** Mesh on vehicle surface. Bottom view of flap assembly

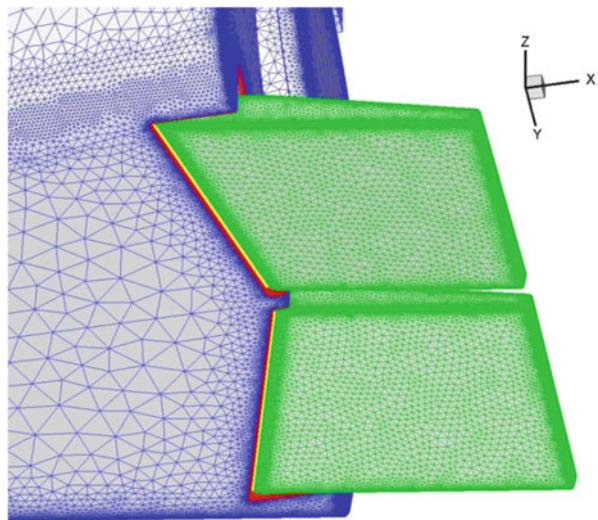
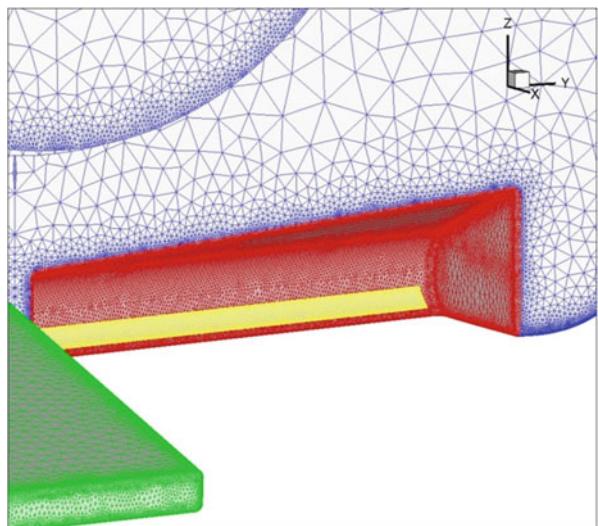


**Fig. 5.58** Mesh on vehicle surface. Rear view with flap cavity



For example, Fig. 5.60 shows the Mach number field on the IXV symmetry plane and pressure distribution on vehicle surface at  $M_\infty = 10$ ; while in Fig. 5.61, for the same flight conditions, the radiative cooling temperature on vehicle surface and pressure contours on symmetry plane are reported [15].

Backward views for the flowfield features of Figs. 5.60 and 5.61 are reported in Figs. 5.62 and 5.63, respectively [15].

Figure 5.64 shows 3-D flow streamlines on the concept backside. Pressure distribution is provided on vehicle surface [15].

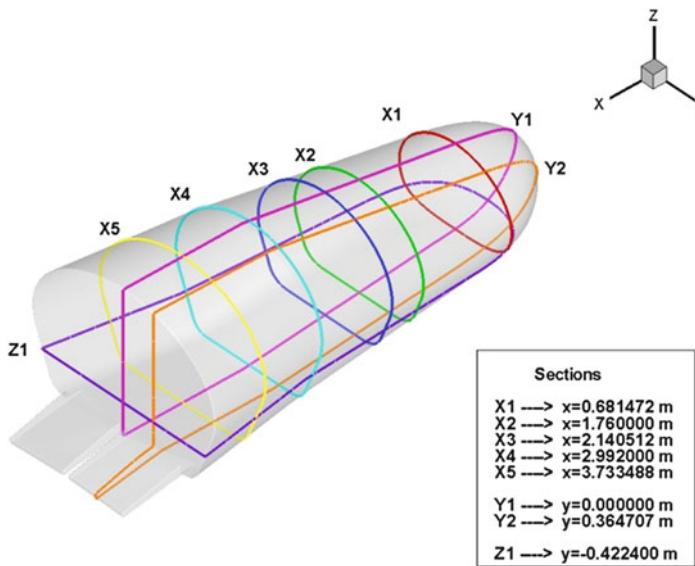


Fig. 5.59 IXV slices for results comparison

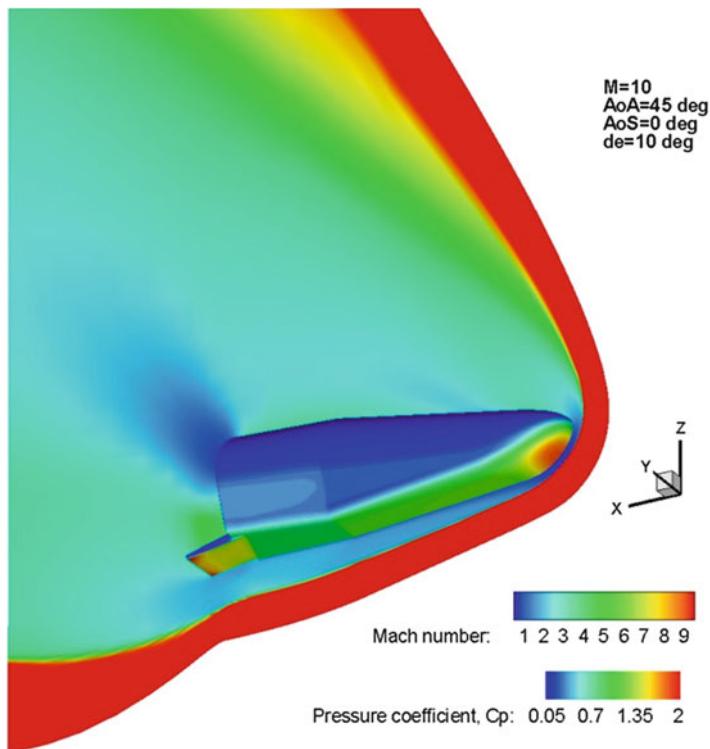
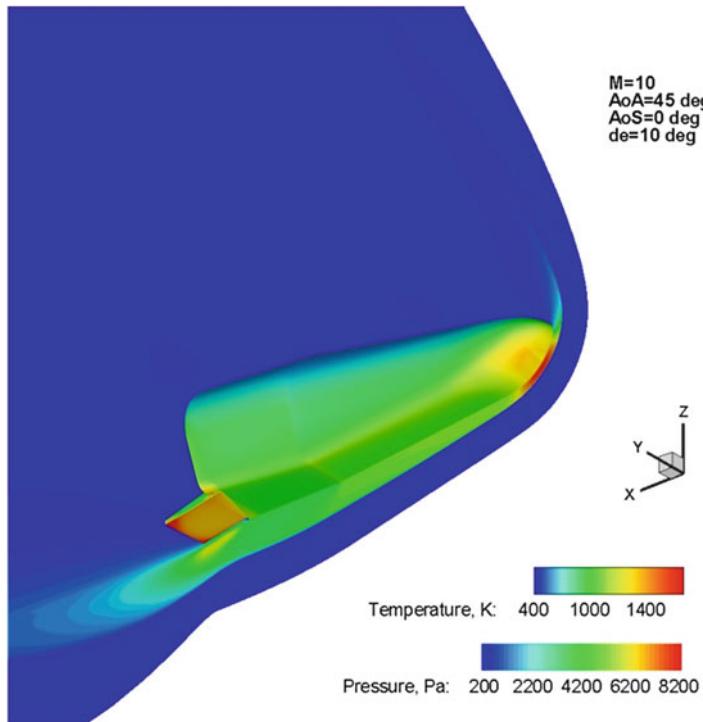


Fig. 5.60 Mach contours on IXV symmetry plane and  $C_p$  on the vehicle surface at  $M_\infty = 10$



**Fig. 5.61** Pressure contours on IXV symmetry plane and surface radiative cooling temperature at  $M_{\infty} = 10$

Both figures highlight streamtraces which start from the hot shock layer flow at the IXV belly side evolve toward the base flow passing through the hinge cavity. This hot flow, namely, snake flow, contributes together with radiative heat flux coming from the hot flap surface, to cavity heating.

The aeroheating expected in the flap region is a great deal for the vehicle design. For instance, Fig. 5.65 points out the static temperature's contours on vehicle windside with skin friction distribution at flap assembly for  $M_{\infty} = 10$  and laminar flow with FC wall [15].

As one can see, the maximum temperature of about 1,750 K is expected at the outboard edge of the flap cavity. Those heat flux and temperature peaks, however, are overestimated with reference to real conditions as during the computations the heat conduction inside the cavity body was neglected.

Anyway, those overshoots can be explained considering contours result provided in Fig. 5.66. This figure shows the flowfield that takes place in the cross plane at  $x = 4.3$  m from vehicle nose.

As shown in Fig. 5.66, the flow coming from the vehicle belly side (IXV is flying at  $45^\circ$  AoA) impinges on the outboard side edge of the flap cavity which is characterized by a very small leading edge radius (see Fig. 5.65). On the other

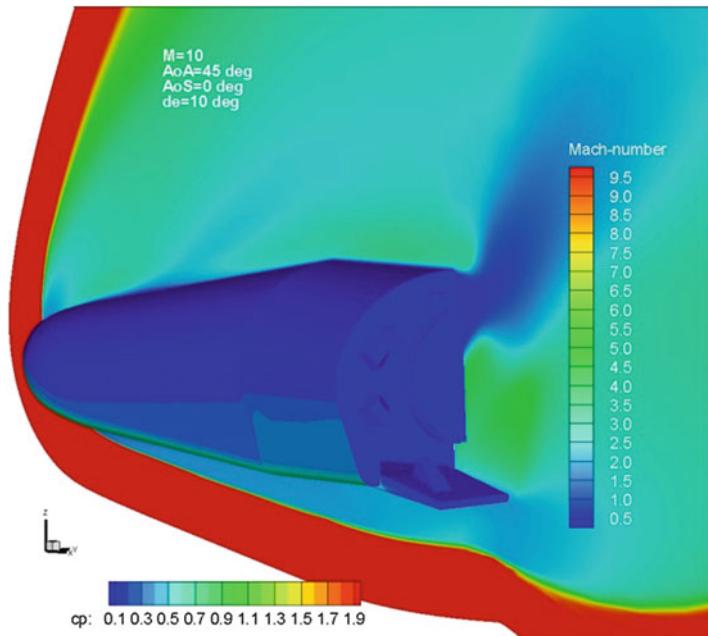


Fig. 5.62  $C_p$  on IXV and Mach contours on pitch plane at  $M_\infty = 10$

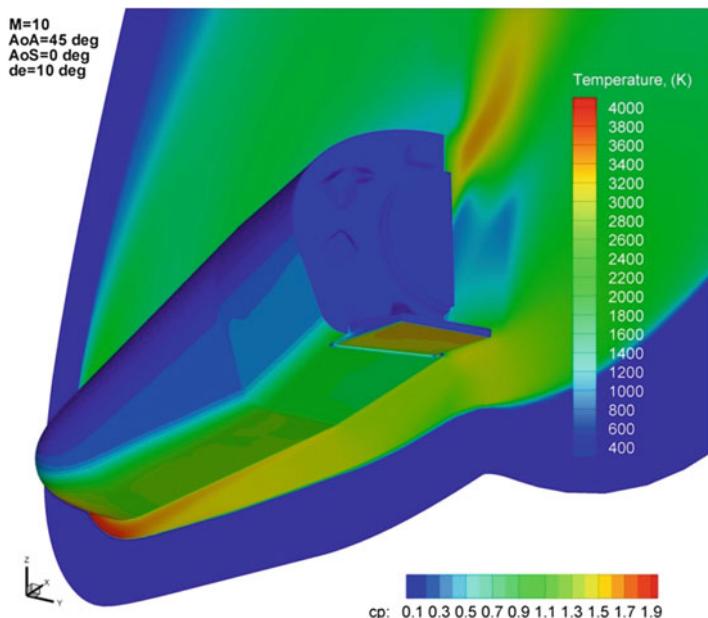
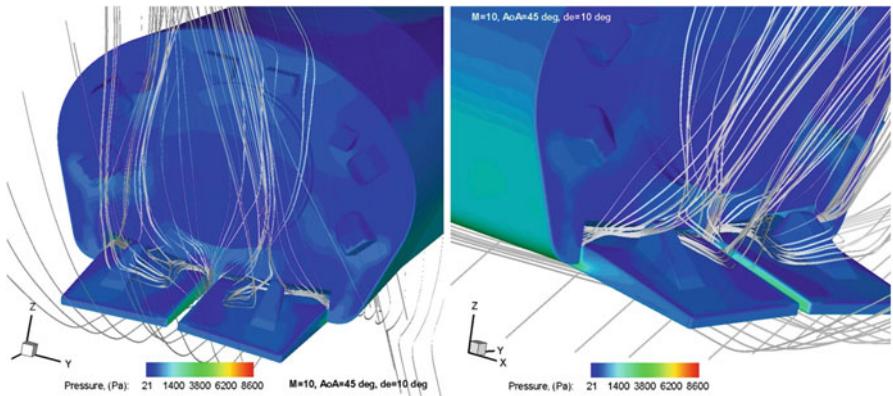
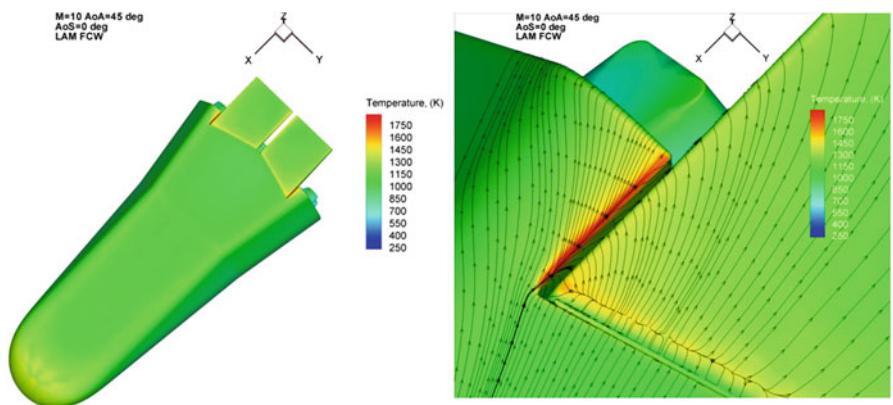


Fig. 5.63  $C_p$  on IXV and temperature contours on pitch plane at  $M_\infty = 10$



**Fig. 5.64** Streamlines on IXV backside and pressure contours on vehicle surface at  $M_{\infty} = 10$



**Fig. 5.65** Temperature's surface contours at  $M_{\infty} = 10$ , laminar flow with FCW. Skin friction on flap and fuselage

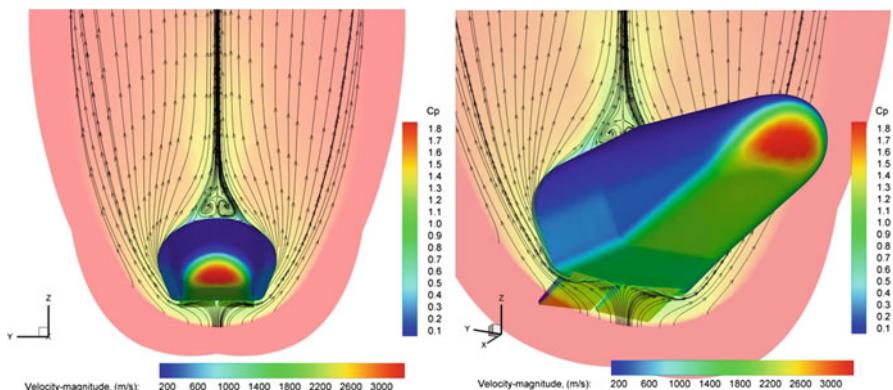


**Fig. 5.66** Contours of velocity magnitude on the cross section at  $x = 4.3$  m.  $M_{\infty} = 10$  laminar flow with FCW. Streamtraces on cross flow

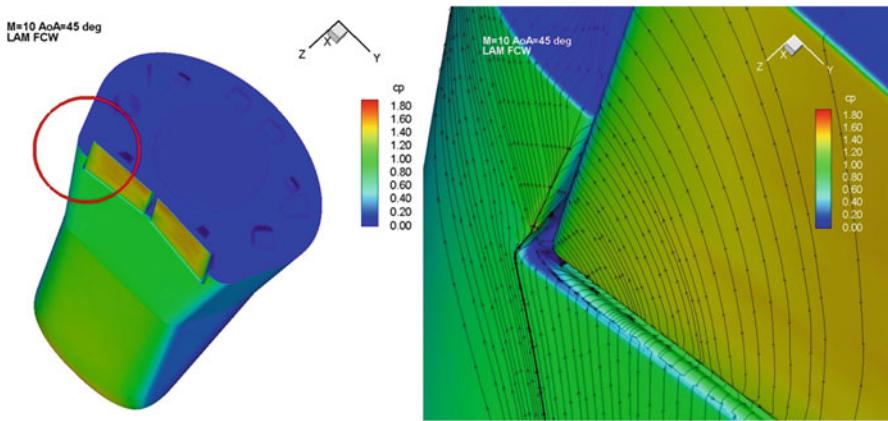


**Fig. 5.67** Pressure coefficient's surface contours at  $M_\infty = 10$ , laminar flow with FCW. Skin friction on flap and fuselage

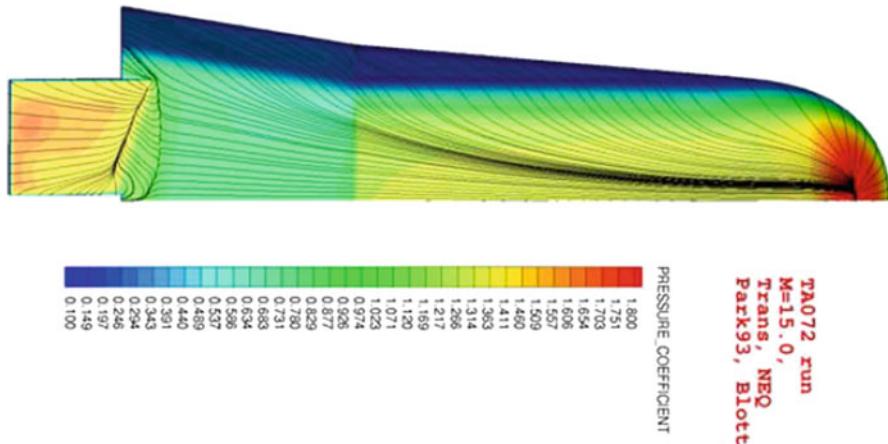


**Fig. 5.68** Pressure coefficient's surface contours at  $M_\infty = 10$ , transitional nonequilibrium flow with FCW. Skin friction on flap and fuselage

hand, Fig. 5.66 confirms that, locally, there is a strong flow spillage from the flap to the cavity (diverging flow pattern). Therefore, the flow turns determining in this region a very thin boundary layer. This is further enforced also by a remarkable flow expansion that occurs along with the borders of the cavity, as shown in Fig. 5.67.

Moreover, comparing Figs. 5.67 and 5.68, it is interesting to note that present CFD numerical effort highlights that the separation bubble pattern, predicted in the past with computations performed considering a cantilever flap (see Fig. 5.68), completely changes when flap cavity is accounted for (e.g., gap flow).

For instance, Figs. 5.65 and 5.67 point out that a short bubble is recognizable in the front part of flap (see Fig. 5.65), where the hot spot arises at the attachment line<sup>2</sup>, while a separation takes place in front of seal (see Fig. 5.67).

Moreover, it is worth to note that the flow through the hinge-line gap, called bleed flow, can influence flap effectiveness because it may affect flow momentum [16, 17].

The comparison among numerical results for fully turbulent (FT), transitional (TRANS), and fully laminar (FL) CFD computations performed at  $M_\infty = 10$  in the case of FCW is recognized from Figs. 5.69, 5.70, 5.71, 5.72, 5.73, 5.74, and 5.75 at different vehicle sections (see Fig. 5.59).

For instance, pressure coefficient distributions at three vehicle sections, namely, X1, Y1 (vehicle centerline), and Y2 (to focus attention on the flowfield feature distribution on the IXV flap), are reported from Figs. 5.69, 5.70, and 5.71.

Wall heat flux distributions at X1, X5, Y1, and Y2 are summarized from Figs. 5.72, 5.73, 5.74, and 5.75 [15].

Results concerning pressure coefficient underline that only slight differences arise passing from laminar to turbulent flow conditions.

On the other hand, result comparison reported from Figs. 5.72, 5.73, 5.74, and 5.75 highlights that higher aerodynamic heating is expected at vehicle windside in the case of turbulent boundary layer [15].

Roughly, a ratio of 3–4 is estimated between turbulent and laminar flow assumption.

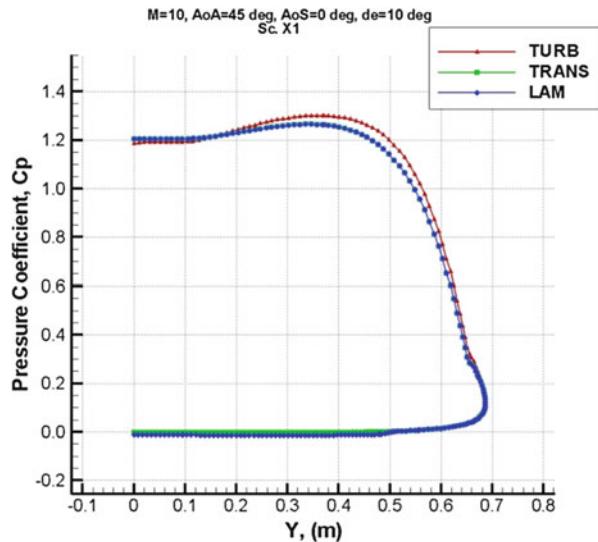


**Fig. 5.69** Pressure coefficient  $C_p$  at Sec-X1. Results comparison among FT, FL, and TRANS computations at  $M_\infty = 10$

<sup>2</sup>At the attachment line, due to the diverging flow pattern, the boundary layer is thinner than that in the vicinity.

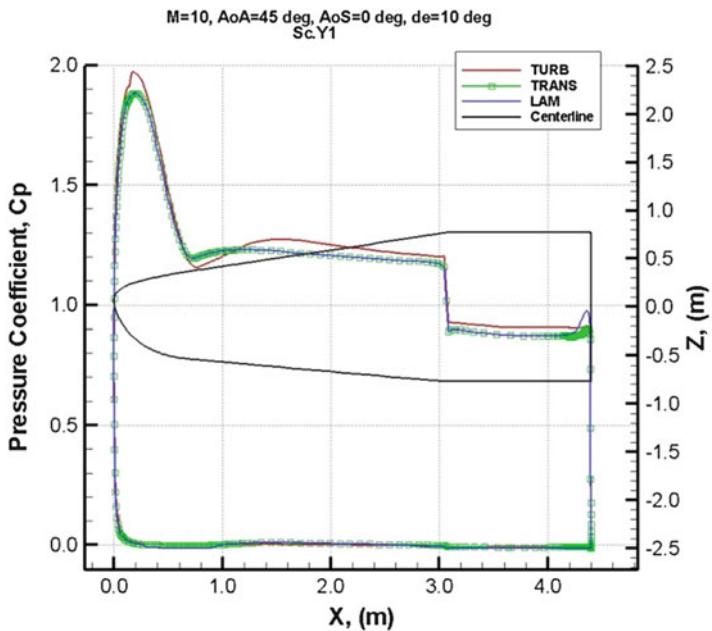


**Fig. 5.70** Pressure coefficient,  $C_p$  at Sec-Y1. Results comparison among FT, FL, and TRANS computations at  $M_\infty = 10$

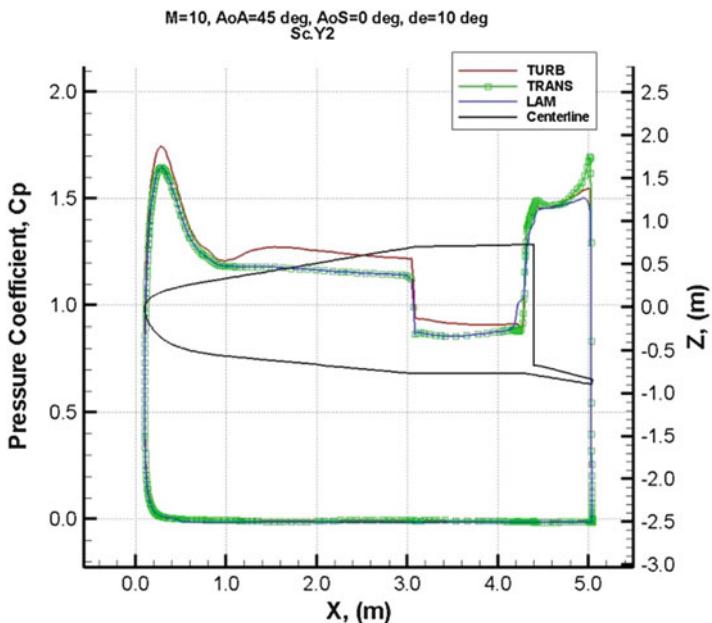


**Fig. 5.71** Pressure coefficient,  $C_p$  at Sec-Y2. Results comparison among FT, FL, and TRANS computations at  $M_\infty = 10$

**Fig. 5.72** Wall heat flux at Sec-X1. Results comparison among FT, FL, and TRANS computations at  $M_\infty = 10$

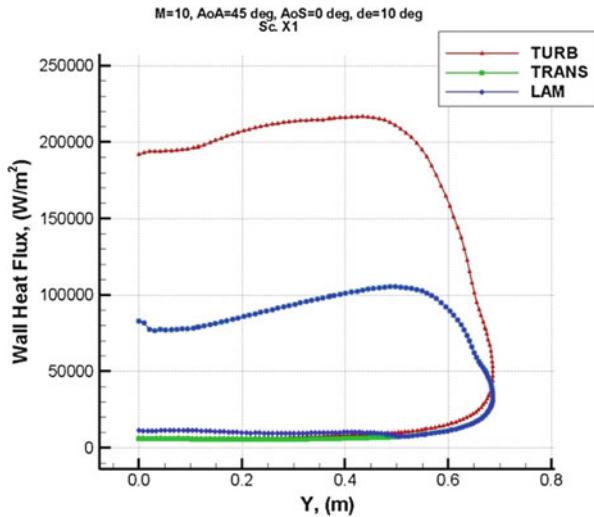
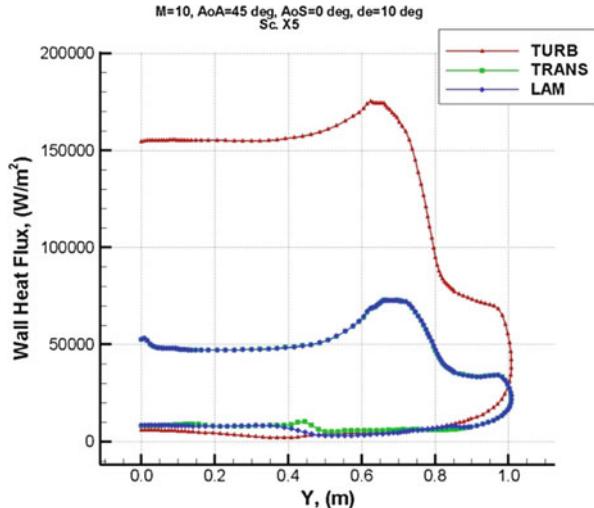


**Fig. 5.73** Wall heat flux at Sec-X5. Results comparison among FT, FL, and TRANS computations at  $M_\infty = 10$



Note that heat flux differences from laminar to transitional flow conditions exist only on the vehicle flap because CFD simulations consider transition front at concept hinge line.

As shown in Fig. 5.75, the transitional heat flux is equal to about  $150 \text{ kW/m}^2$  roughly constant along with the flap, up to reaching nearly  $250 \text{ kW/m}^2$  at the trailing edge of the aerodynamic control surface at  $\delta_e = 10^\circ$  [15].

For  $M_\infty = 25$  flight conditions, Fig. 5.76 shows Mach number contours on four vehicle cross sections, namely, X2, X4, X5 (see Fig. 5.59), and  $X = 5 \text{ m}$  and pressure distribution on the IXV surface. The strong bow shock is clearly evident looking at the flowfield features reported on those cutting slices.

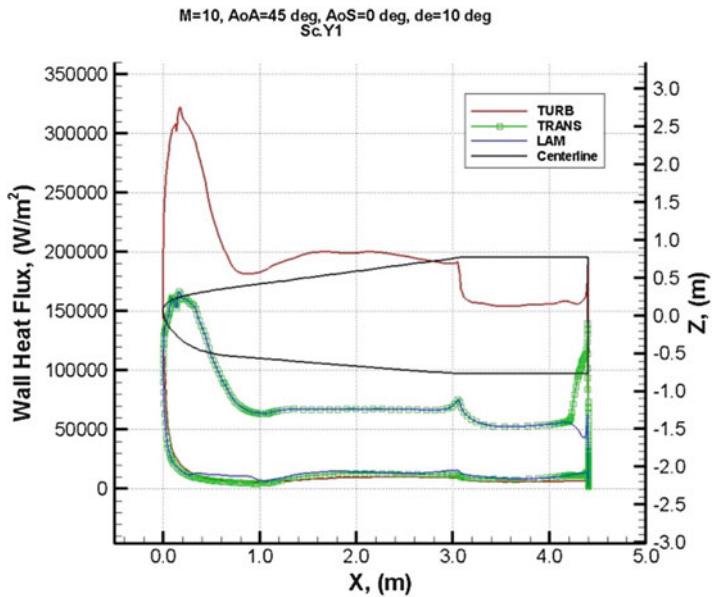


**Fig. 5.74** Wall heat flux at Sec-Y1. Results comparison among FT, FL, and TRANS computations at  $M_\infty = 10$

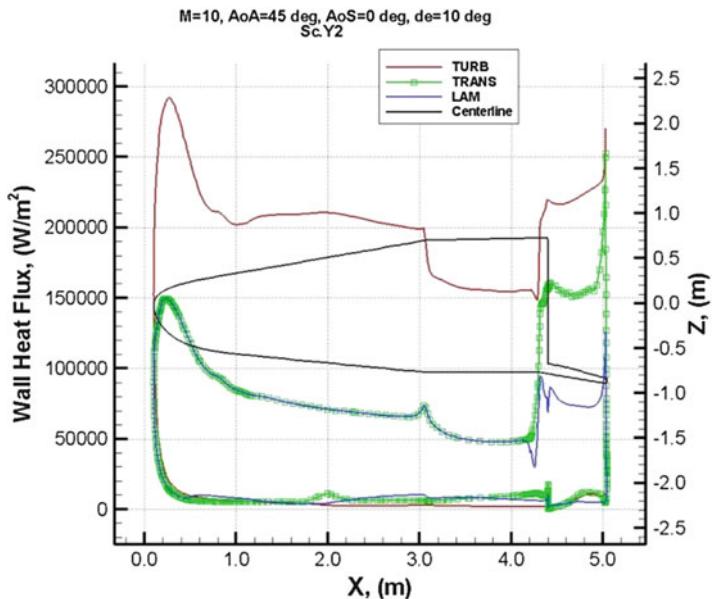


**Fig. 5.75** Wall heat flux at Sec-Y2. Results comparison among FT, FL, and TRANS computations at  $M_\infty = 10$

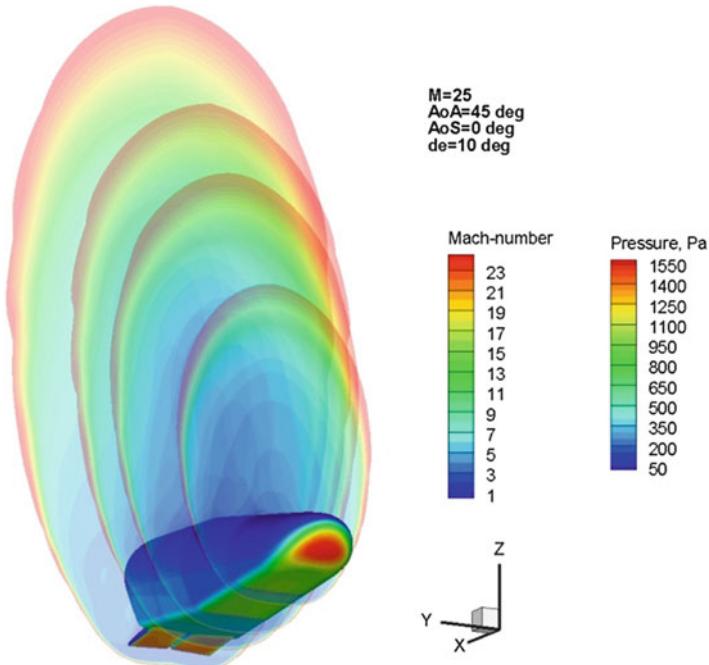


**Fig. 5.76** Mach contours on Sections X2, X4, and X5 and at  $X = 5$  m and pressure contours on the vehicle surface at  $M_\infty = 25$

The temperature contour field past the vehicle is reported in Fig. 5.77 [15]. Flow streamtraces are also included in order to highlight the flowfield structure in the vehicle symmetry plane.

The complexity of the cross flow that takes place past the vehicle at  $M_\infty = 25$ ,  $\alpha = 45^\circ$ , and  $\delta_e = 10^\circ$  can be appreciated in Fig. 5.78 where Mach number contours with streamtraces are reported on the section X5 [15].

Streamlines are also shown in both Figs. 5.79 and 5.80 in order to appreciate the flowfield structure surrounding the vehicle, especially in the base flow of the experimental vehicle (see Fig. 5.80) [15].

As far as results comparison between FCW and NCW boundary conditions at  $M_\infty = 25$  is concerned, Figs. 5.81, 5.82, 5.83, 5.84, 5.85, 5.86, 5.87, 5.88, 5.89, and 5.90 show surface distributions of pressure coefficient, wall heat flux, and radiative cooling temperature, as well as profiles evaluated along with the vehicle sections of Fig. 5.59 [15].

Results comparisons for pressure coefficient are shown in Figs. 5.81, 5.82, 5.83, 5.84, and 5.85 [15].

As expected, catalytic wall boundary conditions do not influence pressure distribution on vehicle concept.

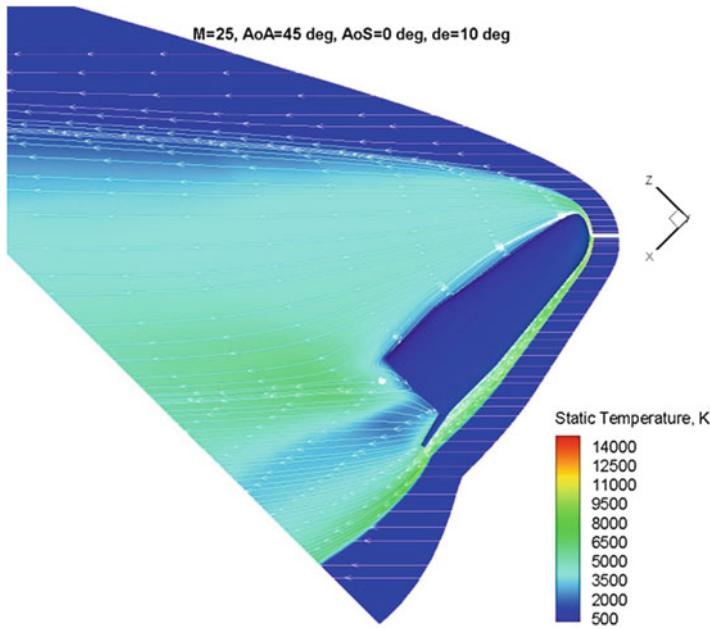


**Fig. 5.77** Temperature contours on IXV symmetry plane and  $C_p$  on the vehicle surface at  $M_\infty = 25$

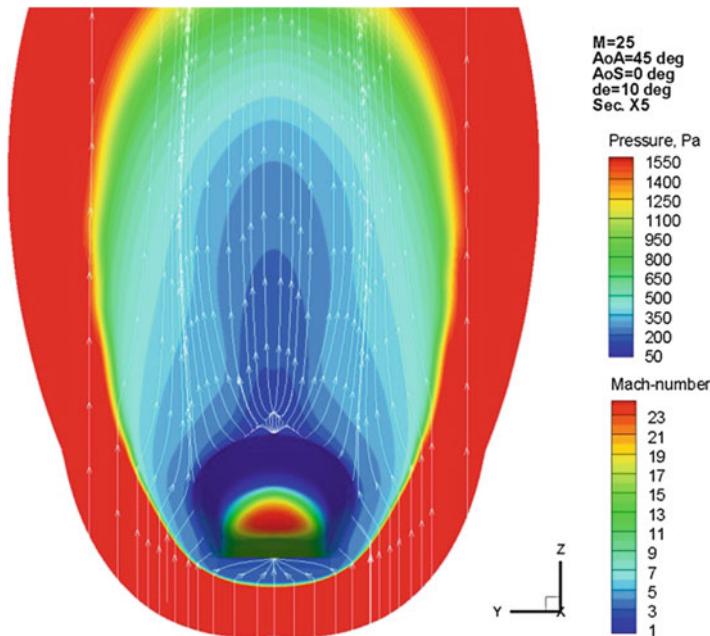


**Fig. 5.78** Mach contours on Section X5 with cross flow streamtraces and pressure contours on the vehicle surface at  $M_\infty = 25$

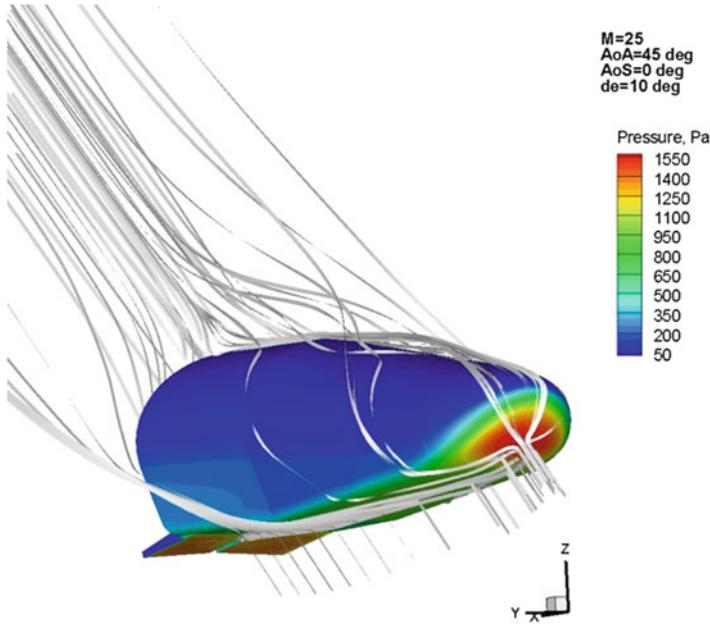


**Fig. 5.79** Pressure contours on the vehicle surface with streamtraces at  $M_{\infty} = 25$ . Front view

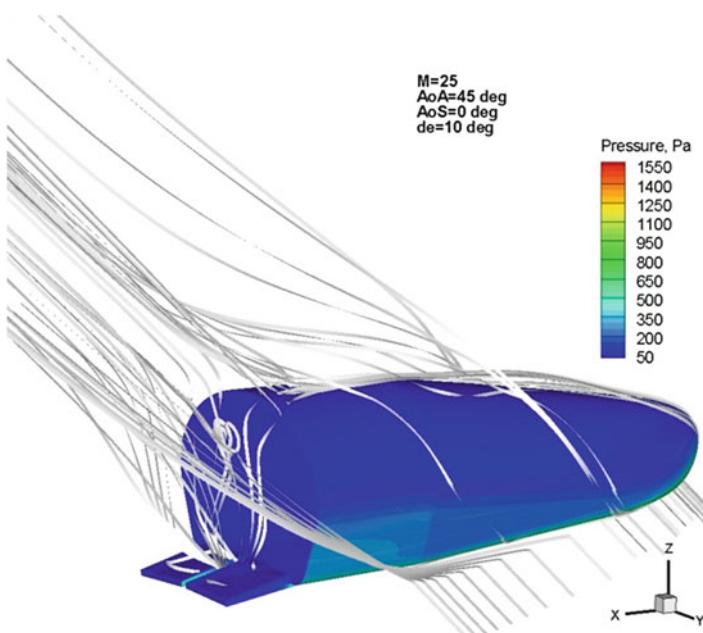
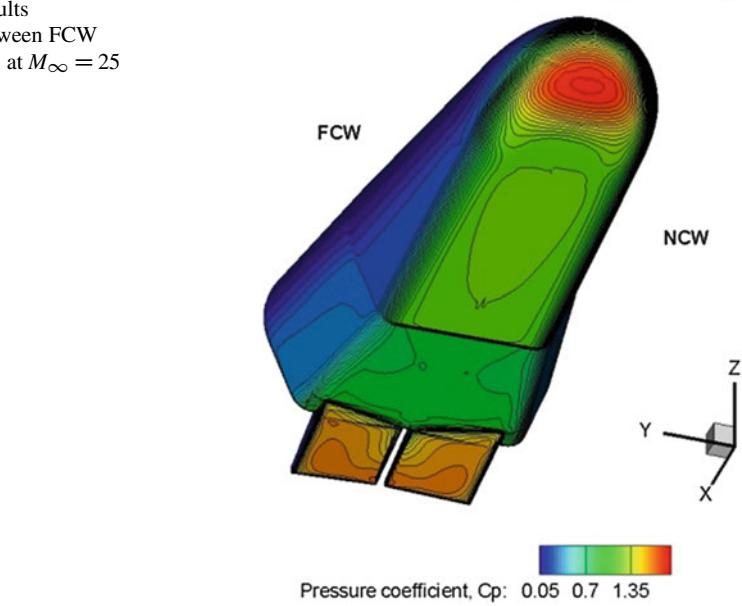


**Fig. 5.80** Pressure contours on the vehicle surface with streamtraces at  $M_{\infty} = 25$ . Side view

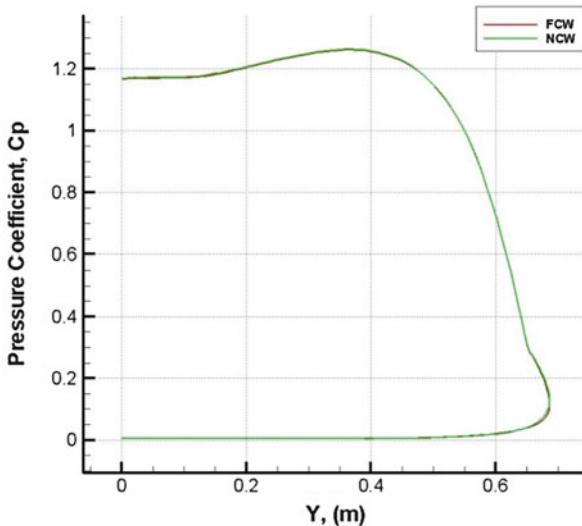
**Fig. 5.81** Pressure coefficient. Results comparison between FCW (left) and NCW, at  $M_\infty = 25$

$M=25$ , AoA=45 deg, AoS=0 deg, de=10 deg

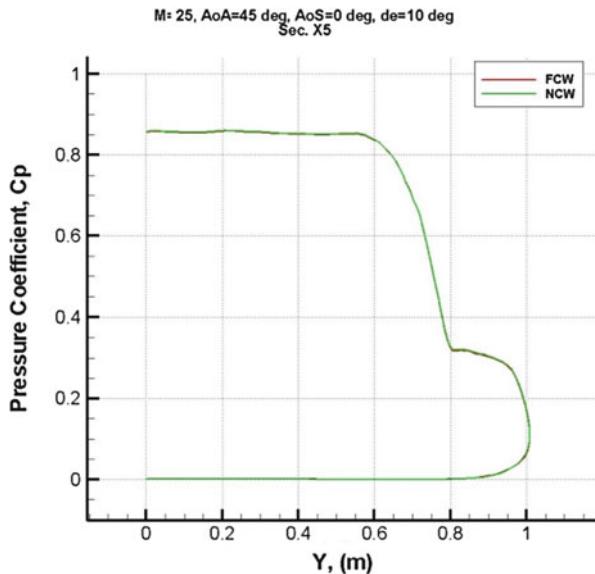


Pressure coefficient,  $C_p$ : 0.05 0.7 1.35

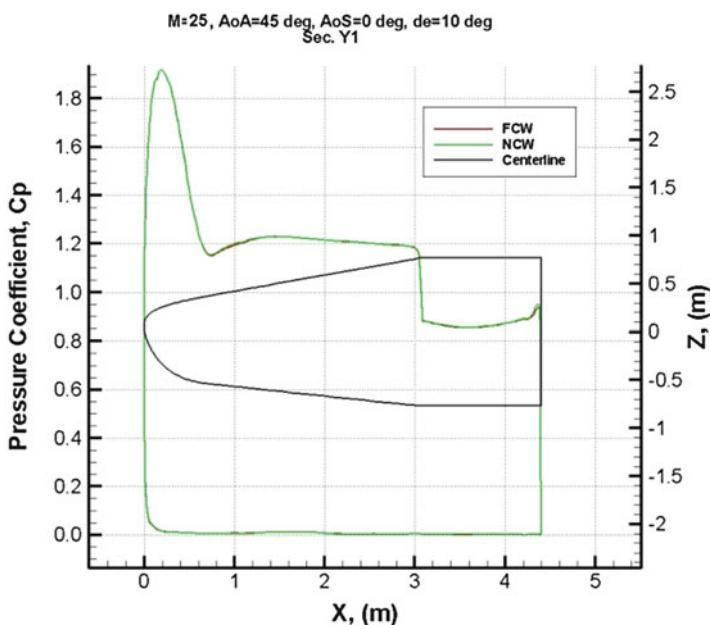
$M=25$ , AoA=45 deg, AoS=0 deg, de=10 deg  
Sec. X1



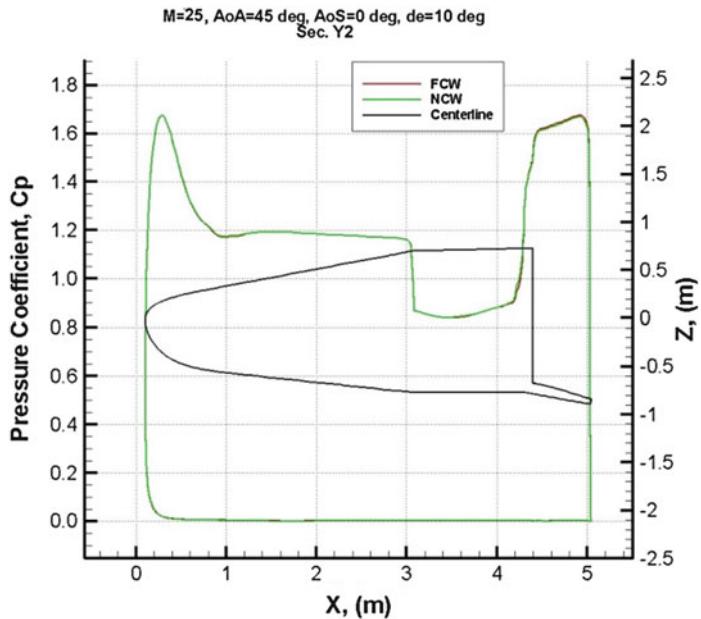
**Fig. 5.82** Pressure coefficient at Sec-X1. Results comparison between FCW and NCW at  $M_\infty = 25$



**Fig. 5.83** Pressure coefficient at Sec-X5. Results comparison between FCW and NCW at  $M_{\infty} = 25$



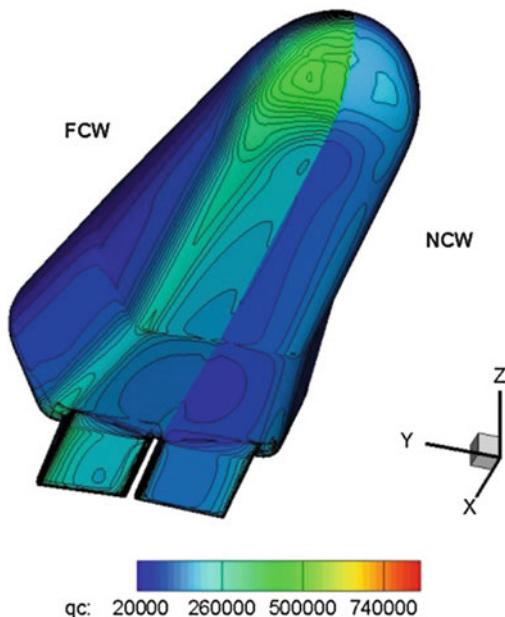
**Fig. 5.84** Pressure coefficient at Sec-Y1. Results comparison between NCW and FCW at  $M_{\infty} = 25$



**Fig. 5.85** Pressure coefficient at Sec-Y2. Results comparison between NCW and FCW at  $M_{\infty} = 25$

**Fig. 5.86** Wall heat flux.  
Results comparison between  
FCW (*left*) and NCW at  
 $M_{\infty} = 25$

**M=25, AoA=45 deg, AoS=0 deg, de=10 deg**



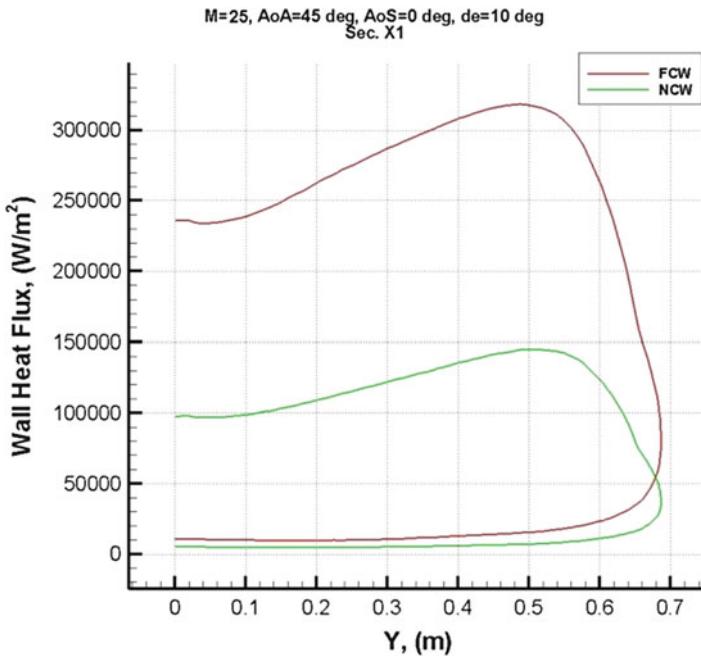


**Fig. 5.87** Wall heat flux at Sec-X1. Results comparison between FCW and NCW at  $M_\infty = 25$

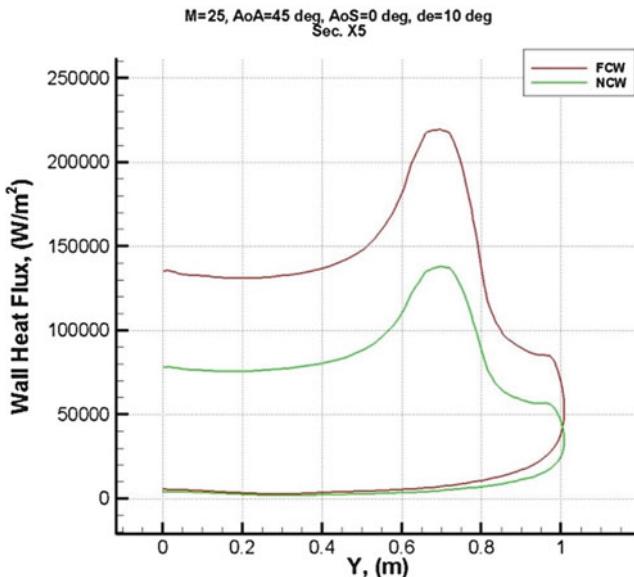


**Fig. 5.88** Wall heat flux at Sec-X5. Results comparison between FCW and NCW at  $M_\infty = 25$

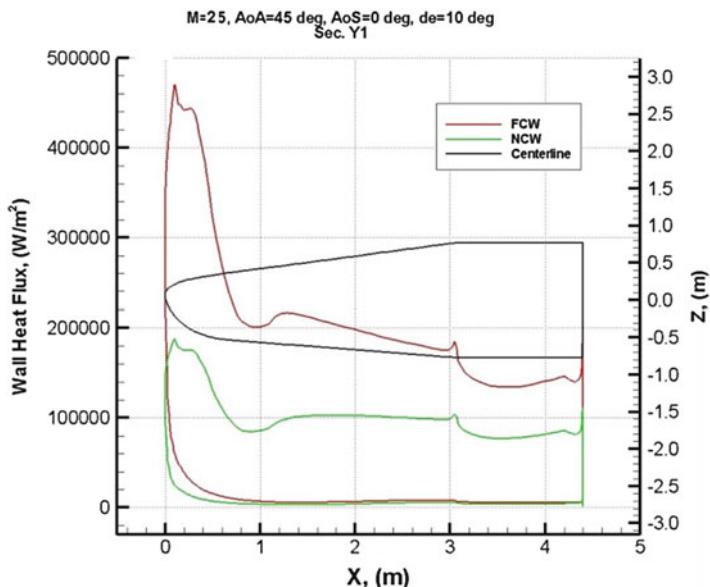


**Fig. 5.89** Wall heat flux at Sec-Y1. Results comparison between FCW and NCW at  $M_\infty = 25$

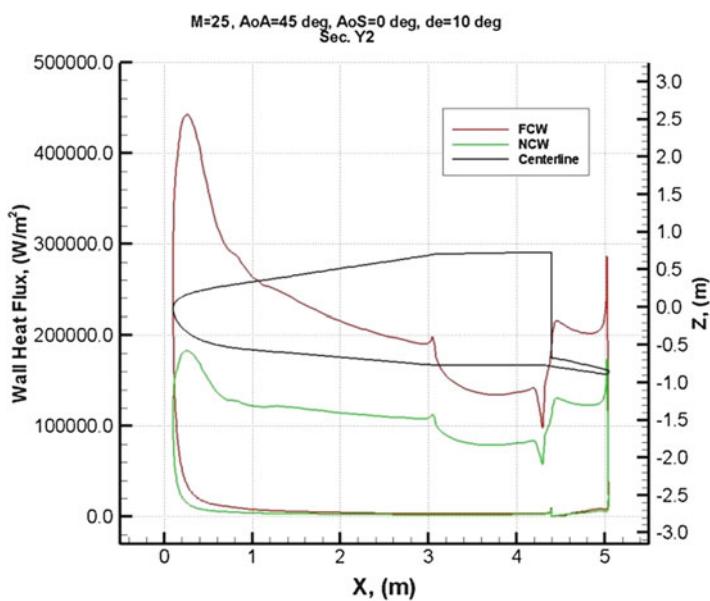


**Fig. 5.90** Wall heat flux at Sec-Y2. Results comparison between FCW and NCW at  $M_\infty = 25$

To illustrate the magnitude of the effects of catalytic activity on vehicle aeroheating, Fig. 5.86 shows the comparison of the convective heat flux distribution over the vehicle surface, between the cases of an FCW and NCW in the case of radiative cooled wall (i.e.,  $T_w = \sqrt[4]{\frac{q}{\sigma\varepsilon}}$ ).

As one can see, the overheating caused by the catalytic action is potentially very large compared with the case of NCW (see also results comparison shown in Figs. 5.87, 5.88, 5.89, and 5.90) [15].

In particular, numerical results, in this case, underline that great differences arise on the vehicle forebody, where heat flux for FCW increases about 250 %. This value decreases, moving away from IXV nose [15, 18].

## 5.11 Aerodynamic Analysis

The aerodynamic analysis is shown in terms of lift ( $C_L$ ), drag ( $C_D$ ), side ( $C_Y$ ), rolling moment ( $C_I$ ), pitching moment ( $C_m$ ), and yawing moment ( $C_n$ ) coefficients, which are calculated according to the following equations:

$$C_i = \frac{F_i}{\frac{1}{2}\rho_\infty V_\infty^2 S_{ref}} \quad i = L, D, Y \quad (5.2)$$

$$C_I = \frac{M_x}{\frac{1}{2}\rho_\infty V_\infty^2 l_{ref} S_{ref}} \quad (5.3)$$

$$C_m = \frac{M_y}{\frac{1}{2}\rho_\infty V_\infty^2 l_{ref} S_{ref}} \quad (5.4)$$

$$C_n = \frac{M_z}{\frac{1}{2}\rho_\infty V_\infty^2 l_{ref} S_{ref}} \quad (5.5)$$

### 5.11.1 General Inputs for Aerodynamic Data Set Generation

The following reference parameters have been considered according to all the available aerodynamic data:  $l_{ref} = 4.40$  m (i.e., body length – longitudinal reference length),  $S_{ref} = 7.26$  m<sup>2</sup> (i.e., projected area in the horizontal plane except the flaps – reference area), and pole coordinates are (2.552, 0, -0.110) m (CoG location) [4].

The following ranges have been analyzed to generate the longitudinal aerodynamic data sets:  $0.8 \leq M_\infty \leq 25$ ,  $0^\circ \leq \alpha \leq 70^\circ$  for  $M_\infty < 2$ ,  $0^\circ \leq \alpha \leq 55^\circ$  for  $M_\infty \geq 2$ , and  $-10^\circ \leq \delta \leq 20^\circ$  (flap deflection).

### 5.11.2 Reference Coordinate System and Aerodynamic Sign Conventions

In Fig. 5.91, the adopted reference frame with aerodynamic coefficients conventions is shown. The reference system for the aerodynamic data is a body-fixed axis system, compliant with the ISO 1151 standard [4, 7, 15].

The reference coordinate system to assess CoG position is shown in Fig. 5.92 [4]. The  $x$ -axis points from nose to base and the origin is where the  $x$ -axis is intersecting the surface of the nose tip. The  $x$ -axis is parallel to the top and bottom meridian in the section near to the base of the configuration and passing through the midpoint of the vertical height of the base area (as indicated in Fig. 5.22). The  $z$ -axis is in the plane of symmetry, perpendicular to  $x$ -axis and pointing upward toward the vehicle leeside. The  $y$ -axis completes the right-handed system (pointing port side). Therefore, the axis system for aerodynamic coefficients are rotated by  $180^\circ$  about  $y$ -axis and the origin shifted to the CoG.

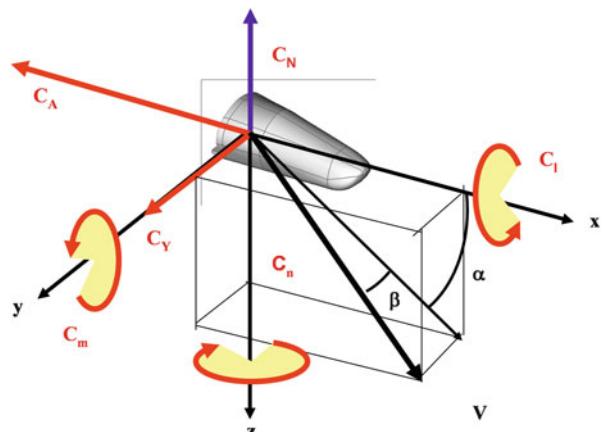


**Fig. 5.91** Reference frame and aerodynamic coefficients convention

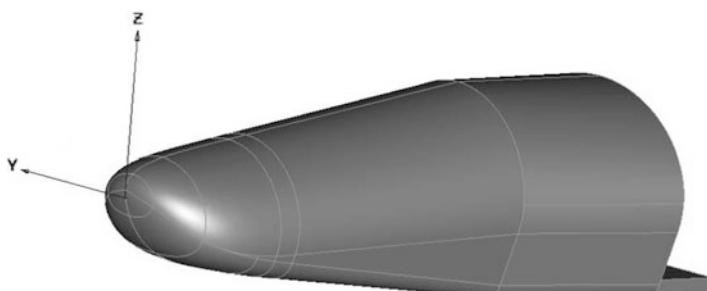
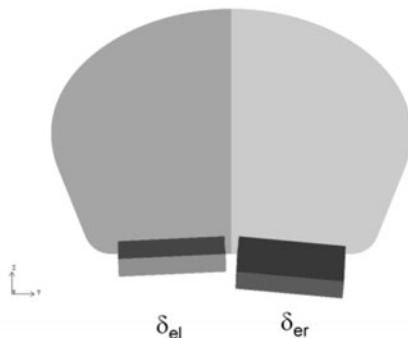


**Fig. 5.92** Reference coordinate system

**Fig. 5.93** Aerodynamic control surface deflections with forces and hinge moments signs



$$\delta_e = (\delta_{er} + \delta_{el})/2$$

$$\delta_a = (\delta_{er} - \delta_{el})/2$$

Positive deflection of	Aero Forces and Moments
Elevon, $\delta_e$	$+C_L + C_D - C_m$
Right, $\delta_{er}$	$+C_Y - C_l - C_n$
Left, $\delta_{el}$	$-C_Y + C_l + C_n$

The definition of elevator and aileron deflection is recognized in Fig. 5.93, where are also reported signs of aerodynamic force and moment coefficients corresponding to positive flap deflections. Note that flap deflection angle is positive when trailing edge down [19].

### 5.11.3 IXV Aerodynamic Model and Database Development

The independent variables recognized as those affecting the IXV aerodynamic state are

$$\{M, Re, \alpha, \beta, \delta_{el}, \delta_{er}, p, q, r, \dot{\alpha}\} \quad (5.6)$$

The couple  $(M, Re)^3$  identifies the aerodynamic environment, while the angle of attack ( $\alpha$ ) and of sideslip ( $\beta$ ) completely describes the flowfield direction. Elevator deflections (i.e.,  $\delta_{el}$  and  $\delta_{er}$ ) describing the state of vehicle aerodynamic control

---

<sup>3</sup>Note that the couple  $(M, Re)$  is able to define also rarefied flow regime conditions since the Knudsen number is proportional to the Mach-to-Reynolds ratio.

surfaces are also considered as input variables. Moreover, also the components of the angular velocity in the body reference frame ( $p$ ,  $q$ , and  $r$ ) together with the time derivative of the angle of attack ( $\dot{\alpha}$ ) are considered as input parameters [19]. However, all the source data available, on which the IXV AEDB formulation is based on, rely on the trajectory-based approach, as clearly shown in both Figs. 5.28 and 5.29 [2]. Therefore, the functional structure of the IXV aerodynamic model (AM) does not consider the Reynolds number effect. So, only the following independent variables are concerned:

$$\{ M, \alpha, \beta, \delta_{el}, \delta_{er}, p, q, r, \dot{\alpha} \} \quad (5.7)$$

It is worth noting that left and right deflections of the splitted body flap are considered independently, provided that they are used both for longitudinal and lateral control.

In particular, as typically done in a classical approach, dependence from  $\dot{\beta}$  is neglected, and each aerodynamic coefficient can be derived by supposing that each contribution to the single global coefficient is treated independently from the others [2, 18].

This means, from an operational point of view, that each aerodynamic coefficient can be described by a linear summation over a certain number of incremental contributions [2, 20]. Each contribution is based on a small number of parameters, as recognized herein.

Further, as done in the past for the US Orbiter, X-33 and X-34 vehicles, the IXV AM development relies on the following assumptions: no RCS effects are considered; only rigid body aerodynamic coefficients are evaluated, i.e., no aeroelastic deformations are accounted for; no Reynolds and Knudsen numbers effects on aerodynamic control surfaces are assumed; no effects of protrusions, gaps, and roughness are here considered; no side slip effects on aerodynamic control surfaces are assumed; mutual aerodynamic interference between control surfaces is considered only for lateral–directional force and moments coefficients; no Knudsen number effects on side force and aerodynamic moment coefficients are assumed (except for pitching moment coefficient) [2, 20, 21].

### **5.11.4 Formulation of the Aerodynamic Database**

The aerodynamic characteristics pertaining to the longitudinal and lateral degrees of freedom of IXV are presented as full-scale rigid force and moment coefficients. They are presented in a form which will allow a buildup to any desired vehicle attitude, flap deflections, and/or flight condition by incremental addition to the basic coefficient [20].

Each aerodynamic coefficient has been considered separately by the appropriate equation in which appear all the pertinent contributions for obtaining the total

coefficient for any selected flight condition. Each element of the equation is defined and referenced.

For instance, assuming that the vehicle is operating at a combined AoA and AoS, the generic aerodynamic coefficient  $C_i$  reads:

$$\begin{aligned} C_i(M, \alpha, \beta, \delta_{er}, \delta_{el}, \dot{\alpha}, p, q, r) = & C_{i,b} + \Delta C_{i,\beta} + \Delta C_{i,\delta_e} + \Delta C_{i,\delta_a} + \Delta C_{i,\dot{\alpha}} \\ & + \Delta C_{i,p} + \Delta C_{i,q} + \Delta C_{i,r} \end{aligned} \quad (5.8)$$

where  $C_{i,b}$  is the baseline contribution to the global coefficient  $C_i$  at a particular Mach number and angle of attack  $\alpha$ , zero sideslip, zero control surface deflections (i.e., in clean configuration), and with no dynamic effects ( $\dot{\alpha}, p, q, r$ ).

$$\Delta C_{i,\beta} = C_i(M, \alpha, \beta) - C_i(M, \alpha) \quad (5.9)$$

is the incremental coefficient due to the sideslip angle ( $\beta$ ) in clean configuration; as shown, to get the incremental coefficient due only to  $\beta$ , we have to subtract the incremental due to  $\alpha$ , as shown by the second term on the right-hand side of the equation.

$$\Delta C_{i,\delta_e} = C_i(M, \alpha, \delta_e) - C_i(M, \alpha) \quad (5.10)$$

is the incremental effect due to elevator (i.e.,  $\delta_{er} = \delta_{el}$ ) deflection at zero sideslip;  $\Delta C_{i,\delta_a} = C_i(M, \alpha, \delta_a)$  represents the incremental coefficient due to aileron (asymmetric) deflections at zero sideslip. For lift, drag, and pitching moment coefficients:

$$\Delta C_{i,\delta_a} = \frac{1}{2} (\Delta C_{i,\delta_e=\delta_{er}} + \Delta C_{i,\delta_e=\delta_{el}}) - \Delta C_{i,\delta_e} \quad (5.11)$$

Note that this equation follows by the hypothesis that the longitudinal effects of each elevator is independent. Here, the elevator data is used twice, once assuming  $\delta_e = \delta_{er}$ , to obtain  $\Delta C_{i,\delta_e=\delta_{er}}$  and then assuming  $\delta_e = \delta_{el}$  to determine  $\Delta C_{i,\delta_e=\delta_{el}}$ . As a check when aileron deflection is zero (i.e.,  $\delta_{el} = \delta_{er}$ ),  $\Delta C_{i,\delta_a} = 0$ , as expected.

$$\Delta C_{i,\dot{\alpha}} = C_{i,\bar{\alpha}}(M, \alpha) \frac{\dot{\alpha} l_{ref}}{2V_\infty} = C_{i,\bar{\alpha}} \bar{\dot{\alpha}} \quad (5.12)$$

$$\Delta C_{i,j} = C_{i,\bar{j}}(M, \alpha, \text{CoG}) \frac{j l_{ref}}{2V_\infty} = C_{i,\bar{j}} \bar{j} \quad j = p, q, r \quad (5.13)$$

represent the effects of the time derivative of the AoA and of the vehicle angular velocity, where

$$\bar{\dot{\alpha}} = \frac{\dot{\alpha} L_{\text{ref}}}{2V_\infty} \quad (5.14)$$

and

$$\bar{j} = \frac{j L_{\text{ref}}}{2V_\infty} \quad j = p, q, r \quad (5.15)$$

As shown, a linear behavior has been assumed.

Then, as an example, the total lift coefficient is given by

$$C_{L,\text{total}} = C_{L,b}(M, \alpha) + \Delta C_{L,b,\beta}(M, \alpha, \beta) + \Delta C_{L,\delta_e}(M, \alpha, \delta_e) + \Delta C_{L,\delta_a}(M, \alpha, \delta_a) + C_{L,\bar{\dot{\alpha}}}(M, \alpha) \bar{\dot{\alpha}} + C_{L,\bar{q}}(M, \alpha, \text{CoG}) \bar{q} \quad (5.16)$$

where  $C_{L,\text{total}}$  is the total coefficient of the vehicle for a given flight condition as expressed by the flight Mach number  $M$ , AoA  $\alpha$ , sideslip  $\beta$ , and right and left elevator deflection, respectively.

The parameter  $C_{L,b}(M, \alpha)$  is the baseline lift coefficient. It takes into account also for rarefaction effects through bridging relationship.

$$\Delta C_{L,\delta_e}(M, \alpha, \delta_e) = C_L(M, \alpha, \delta_e) - C_L(M, \alpha) \quad (5.17)$$

represents incremental lift coefficient due to elevators deflection with respect to the baseline

$$\Delta C_{i,\delta_a}(M, \alpha, \delta_a) = \frac{1}{2} (\Delta C_{L,\delta_e=\delta_{er}} + \Delta C_{L,\delta_e=\delta_{el}}) - \Delta C_{L,\delta_e} \quad (5.18)$$

The incremental lift coefficient due to baseline in sideslip is given by:

$$\Delta C_{L,b,\beta} = C_L(M, \alpha, \beta) - C_L(M, \alpha) \quad (5.19)$$

$C_{L,\bar{\dot{\alpha}}}$  is the change in lift force coefficient with rate of change of AoA,  $\bar{\dot{\alpha}}$ , whereas  $C_{L,\bar{q}}$  accounts for change in lift force coefficient with pitch rate,  $\bar{q}$ . Both those contributions are evaluated on engineering-based approach only [20].

In a similar fashion, we assume that the drag and pitching moment coefficients are given by

$$C_{D,\text{total}} = C_{D,b}(M, \alpha) + \Delta C_{D,b,\beta}(M, \alpha, \beta) + \Delta C_{D,\delta_e}(M, \alpha, \delta_e) + \Delta C_{D,\delta_a}(M, \alpha, \delta_a) \quad (5.20)$$

The change in drag force coefficient due to dynamic effects is assumed to be negligible for the total drag coefficient.

$$\begin{aligned} C_{m,\text{total}} = & C_{m,b}(M, \alpha) + \Delta C_{mb,\beta}(M, \alpha, \beta) + \Delta C_{m,\delta_e}(M, \alpha, \delta_e) + \Delta C_{m,\delta_a}(M, \alpha, \delta_a) \\ & + C_{m,\bar{\alpha}}(M, \alpha) \bar{\alpha} + C_{m,\bar{q}}(M, \alpha) \bar{q} \end{aligned} \quad (5.21)$$

$C_{m,\bar{\alpha}}$  is the change in pitching moment coefficient due to rate of change of AoA,  $\bar{\alpha}$ , whereas  $C_{m,\bar{q}}$  accounts for change in pitching moment coefficient due to pitch rate,  $\bar{q}$ .

The side force coefficient is assumed to be given by

$$\begin{aligned} C_{Y\text{total}} = & C_{Y,b}(M, \alpha) + \Delta C_{Yb,\beta}(M, \alpha, \beta) + \Delta C_{Y,\delta_a}(M, \alpha, \delta_a) \\ & + C_{Y,\bar{p}}(M, \alpha, \text{CoG}) \bar{p} + C_{Y,\bar{r}}(M, \alpha, \text{CoG}) \bar{r} = C_{Y,b}(M, \alpha, \beta) \\ & + \Delta C_{Y,\delta_a}(M, \alpha, \delta_a) + C_{Y,\bar{p}}(M, \alpha, \text{CoG}) \bar{p} + C_{Y,\bar{r}}(M, \alpha, \text{CoG}) \bar{r} \end{aligned} \quad (5.22)$$

since the vehicle configuration is symmetric (i.e.,  $C_{Y,b}(M, \alpha) = 0$ ) and

$$\Delta C_{Y,b,\beta} = C_{Y,b}(M, \alpha, \beta) - C_{Y,b}(M, \alpha) = C_{Y,b}(M, \alpha, \beta) \quad (5.23)$$

$$\Delta C_{Y,\delta_a}(M, \alpha, \delta_a) = \eta_{lr} \Delta C_{Y,\delta_{er}} + \eta_{rl} \Delta C_{Y,\delta_{el}} \quad (5.24)$$

where

$$\Delta C_{Y,\delta_{er}} = C_Y(M, \alpha, \delta_{er}, \delta_{el}) = 0 \quad (5.25)$$

and

$$\Delta C_{Y,\delta_{el}} = C_Y(M, \alpha, \delta_{er} = 0, \delta_{el}) = -C_Y(M, \alpha, \delta_{er} = \delta_{el}, 0) \quad (5.26)$$

while the couple  $(\eta_{lr}, \eta_{rl})$  represents, according to the sixth assumption, the mutual effect of the left aileron on the right one (i.e.,  $\eta_{lr}$ ) and the mutual effect of the right aileron on the left one (i.e.,  $\eta_{rl}$ ), respectively.

Proceeding in a similar way, the rolling and yawing moment coefficients are assumed to be given by

$$\begin{aligned} C_{l,\text{total}} = & C_{l,b}(M, \alpha, \beta) + \Delta C_{l,\delta_a}(M, \alpha, \delta_a) + C_{l,\bar{p}}(M, \alpha, \text{CoG}) \bar{p} \\ & + C_{l,\bar{r}}(M, \alpha, \text{CoG}) \bar{r} \end{aligned} \quad (5.27)$$

where

$$\Delta C_{l,\delta_a}(M, \alpha, \delta_a) = \eta_{lr} \Delta C_{l,\delta_{er}} + \eta_{rl} \Delta C_{l,\delta_{el}} \quad (5.28)$$

$$\begin{aligned} C_{n,\text{total}} = & C_{n,b}(M, \alpha, \beta) + \Delta C_{n,\delta_a}(M, \alpha, \delta_a) \\ & + C_{n,\bar{p}}(M, \alpha, \text{CoG}) \bar{p} + C_{n,\bar{r}}(M, \alpha, \text{CoG}) \bar{r} \end{aligned} \quad (5.29)$$

where

$$\Delta C_{n,\delta_a}(M, \alpha, \delta_a) = \eta_{lr} \Delta C_{n,\delta_{er}} + \eta_{rl} \Delta C_{n,\delta_{el}} \quad (5.30)$$

Moreover, no dependency from Reynolds number is assumed for the elevator contribution. Indeed, even though this effect exists, it is small and difficult to be modeled. Then, it has been considered as part of the aerodynamic coefficients uncertainty.

### 5.11.5 Aerodynamic Database Development

Each aerodynamic coefficient has been considered separately by the appropriate equation in which all contributions needed to obtain the total coefficient for any selected flight condition appear. To this aim, all the available aerodynamic data are gathered in order to explicit the functional dependencies of each AM addend through polynomial expressions obtained via the least squares method.

These polynomials are function of the primary variable that drives the phenomenon, whereas secondary dependencies are introduced directly into its unknown coefficients which are determined by means of best-fitting algorithms. For example, the baseline contribution of the generic aerodynamic coefficient is

$$C_{i,b}(M, \alpha) = \sum_{j=1}^n a_j(M, \alpha_r) \alpha^{j-1} \quad (5.31)$$

So, the polynomial variable is the AoA ( $\alpha$ ) and the coefficients are function of Mach number,  $M$ . In particular, for  $M_\infty < 1.2$ , there is also a dependence from  $\alpha_r$  that corresponds to the range of considered AoA. This second dependence is introduced in order to consider the AoA effect present only at this Mach range, as will be explained hereinafter. Therefore, it follows that the aerodynamic database evaluates the polynomial and its coefficients once the state of vehicle (e.g., flight conditions and attitude) is provided. Then, suitable interpolation has to be adopted in order to obtain coefficients for Mach numbers not included in the AEDB set.

Finally, the IXV AEDB relies on three segments: the free-molecule flow, the transitional flow regime, and the continuum flow (subsonic up to hypersonic flow).

Results of each segment are described hereinafter.

### 5.11.6 Free Molecular and Transitional Flow Regimes

Once IXV vehicle started its descent, the atmospheric density is low enough such that the continuum assumption breaks down and one must begin to consider the

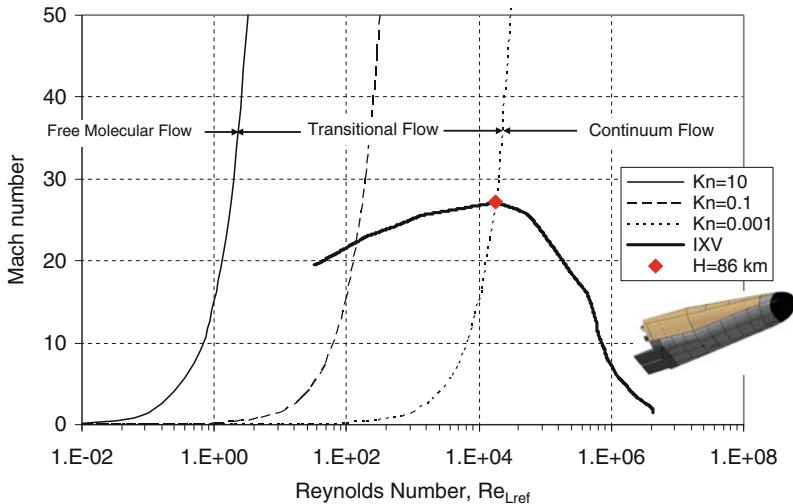


**Fig. 5.94** IXV re-entry trajectory in the Ma–Re map with constant Knudsen numbers

general microscopic mass, force, and energy transfer problem at the vehicle surface [21]. In this regime, two distinctions can be made. They are the re-entry through the upper part of the high atmosphere and that through the lower part of the Earth's high atmosphere. In the former, the free molecular regime is completely established. Indeed, when the air density becomes rarefied enough, the molecular mean free path ( $\lambda$ ) can become as large as the scale of the body itself. This condition is known as free molecular flow (FMF) regime, and the aerodynamic characteristics of the vehicle are determined by individual, scattered molecular impacts and must be analyzed on the basis of kinetic theory [22]. Therefore, the IXV concept, moving from a very rarefied atmosphere (at entry interface) to a denser atmosphere, shifts from the FMF regime, where individual molecular collisions are important, to the transition one, where slip effects are important, and then to the continuum regime, as represented in Fig. 5.94.

As shown in Fig. 5.94, the region for  $10^{-3} < Kn_{\infty l_{ref}} = \frac{\lambda}{l_{ref}} = 1.25 \sqrt{\lambda} \frac{M_\infty}{Re_{\infty l_{ref}}} < 10$  is the rarefied-flow transition region, according to the Bird classification [22]. Therefore, at 200 km altitude, IXV is in FMF (in fact,  $Kn_{\infty l_{ref}} = 70$ ), while for altitude ranging from entry interface (e.g., 120 km) to about 86 km, it is in transitional flow conditions.

Finally, below about 86 km altitude, continuum flow conditions are established.

When rarefaction effects become important and the continuum hypothesis no longer holds, CFD Navier–Stokes simulation fails and a molecular approach such as the Direct Simulation Monte Carlo (DSMC) method is necessary.

It considers the gas made up of discrete molecules that are represented by millions of simulated molecules; it relies on formulae from the kinetic theory

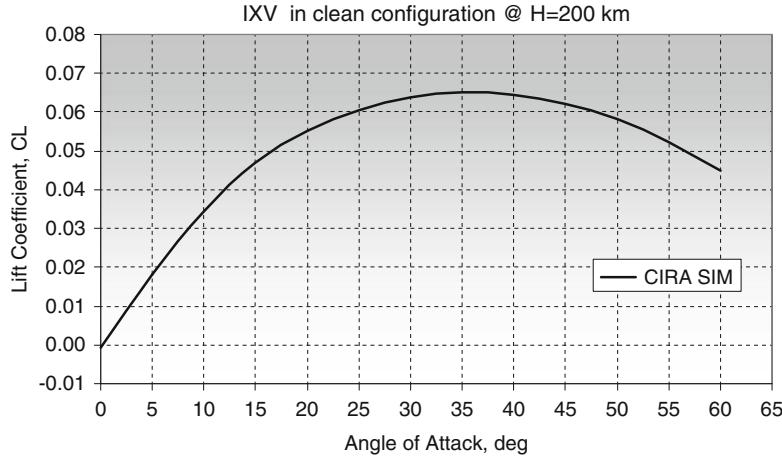


**Fig. 5.95** Lift coefficient versus AoA at  $H = 200$  km altitude

of gases. DSMC simulation, however, is very time consuming. Therefore, some bridging formulae have been tested for quick computations of the IXV transitional flow aerodynamics.

A very simple relationship to bridge the transitional flow regime from continuum regime to FMF is given as

$$C_{i\text{Transitional}} = C_{i\text{Continuum}} + (C_{i\text{FM}} - C_{i\text{Continuum}}) \cdot \bar{C}_i \quad (5.32)$$

where the normalized coefficient  $\bar{C}_i$  uses Knudsen number as the independent parameter:

$$\bar{C}_i = \frac{C_i - C_{i\text{Continuum}}}{C_{i\text{FM}} - C_{i\text{Continuum}}} = F(\text{Kn}_\infty) = \sin^2 \left[ \frac{\pi}{8} (3 + \log_{10} \text{Kn}_\infty) \right] \quad (5.33)$$

where  $10^{-3} < \text{Kn}_\infty < 10$  and  $C_{i\text{Continuum}}$  and  $C_{i\text{FM}}$  are the aerodynamic coefficient in continuum and FMF regimes, respectively. This formula has been used in the past for the US Orbiter aerodynamics assessment [23].

The results for  $C_L$ ,  $C_D$ , and  $C_m$  in FMF are summarized in Figs. 5.95, 5.96, and 5.97 for IXV in symmetric flight at  $H = 200$  km altitude [4].

The aerodynamic analysis was carried out on the vehicle in clean configuration and at the free stream velocity of about 7,500 m/s, constant with altitude. In all computations, the wall temperature was set equal to 300 K, and the aerodynamic forces were evaluated on the assumption of a Maxwell fully accommodate model [4]. Free stream thermodynamic parameters were provided by the US Standard Atmosphere 1976.

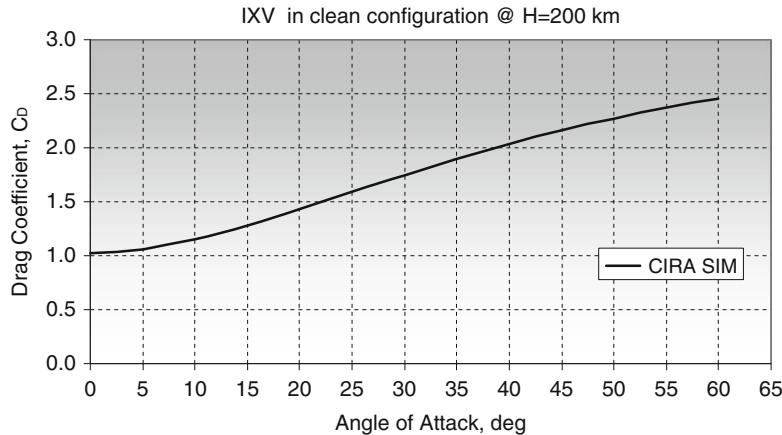


Fig. 5.96 Drag coefficient versus AoA at  $H = 200$  km altitude

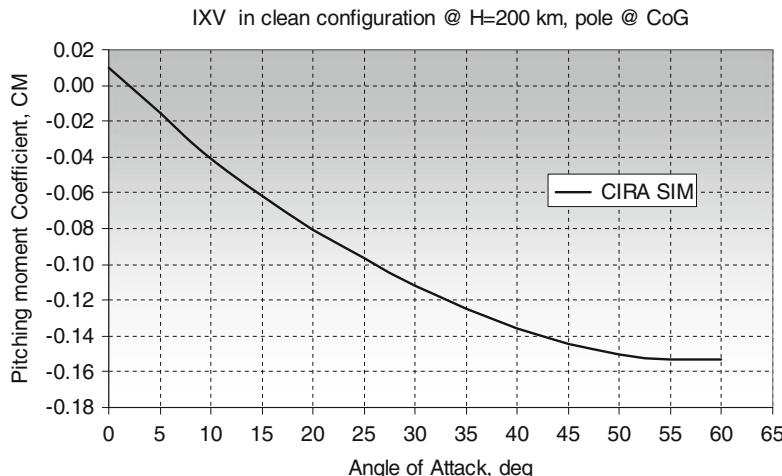
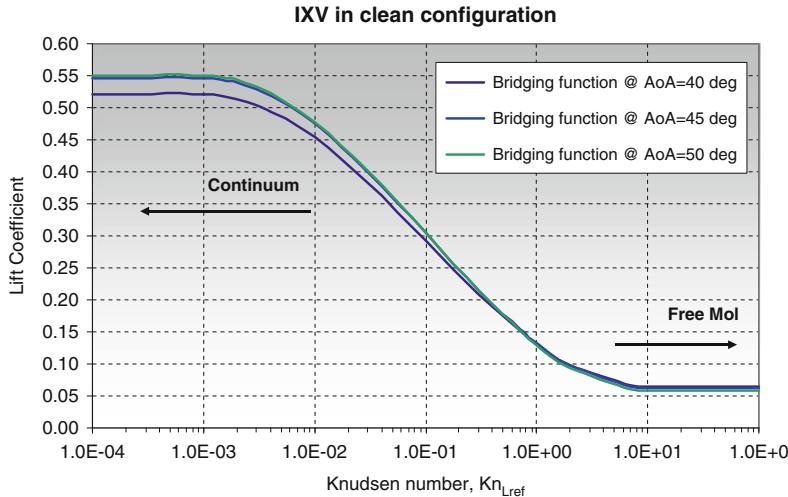


Fig. 5.97 Pitching moment coefficient versus AoA at  $H = 200$  km altitude

As far as transitional regime is concerned, the plots of the lift, drag, and pitching moment coefficients of IXV vehicle versus the Knudsen number are reported in Figs. 5.98, 5.99, and 5.100 [4].

As shown, at very high altitude, when the Reynolds number decreases and rarefaction effects are present, there is a strong increase of the drag coefficient and a consequent reduction of the maximum aerodynamic efficiency. In particular, in the Fig. 5.98, unlike drag and pitching moment coefficient (Figs. 5.99 and 5.100), the shifting of the lift curves corresponding to AoA 40, 45, and 50° is not gradual.



**Fig. 5.98** Lift coefficient versus Knudsen number for  $\text{AoA} = 40^\circ, 45^\circ$ , and  $50^\circ$

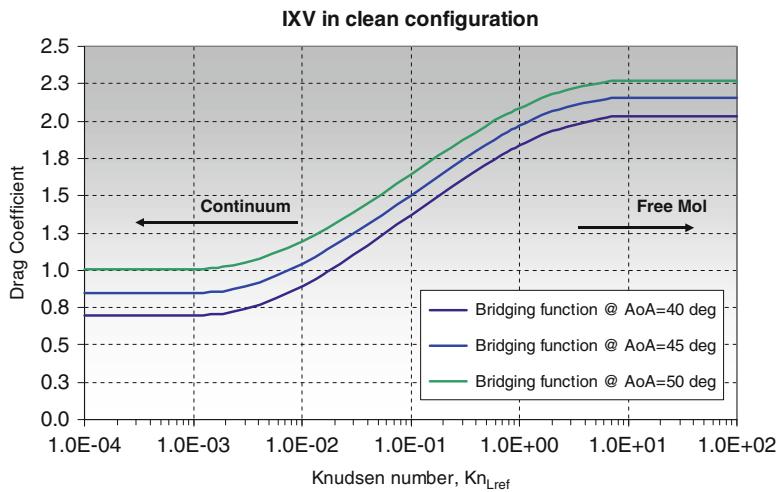


**Fig. 5.99** Drag coefficient versus Knudsen number for  $\text{AoA} = 40^\circ, 45^\circ$ , and  $50^\circ$

As shown in this figure, in the continuum regime, there is an abrupt shift of lift curve from  $40$  to  $45^\circ$  AoA, while the lift curve at  $45^\circ$  is close to that of  $50^\circ$  AoA. This non-monotonic behavior can be explained considering the behavior of  $C_L$  in continuum hypersonic flow conditions. For example, Fig. 5.104 highlights that the lift slope at  $M_\infty = 10$  is non-monotonic unlike  $C_D$  and  $C_m$  (see Figs. 5.105 and 5.106, respectively).

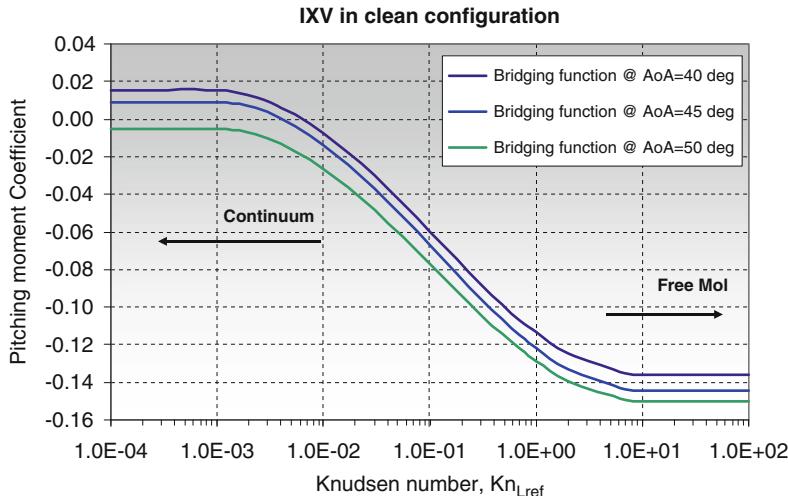


**Fig. 5.100** Pitching moment coefficient versus Knudsen number for AoA = 40°, 45°, and 50°

### 5.11.7 Continuum Flow Regime

As far as the baseline contribution is concerned, due to the symmetry of the IXV shape with respect to the vehicle pitch plane, this contribution will appear only on the longitudinal aerodynamic actions (e.g., lift, drag, and pitching moment coefficients).

#### 5.11.7.1 Lift Coefficient, $C_{L,b}$

From the analysis of different data sources, it comes out that the best choice to fit data is a fifth-order polynomial for  $M$ , while for  $M_\infty > 1.2$ , third-order polynomial is to be used. Therefore, the analytical expression for the lift coefficient reads:

$$C_{L,b}(M, \alpha) = \sum_{i=1}^6 a_i(M, \alpha_r) \alpha^{i-1} \quad M_\infty \leq 1.2 \quad (5.34)$$

$$C_{L,b}(M, \alpha) = \sum_{i=1}^4 b_i(M) \alpha^{i-1} \quad M_\infty > 1.2$$

where polynomial coefficients are collected in the following Tables 5.13 and 5.14 [4].

**Table 5.13** Polynomial coefficients for  $C_L$  for  $0.8 \leq M_\infty \leq 1.2$ 

Longitudinal clean configuration						
Mach no.	Lift coefficient 1st AoA range					
	a6	a5	a4	a3	a2	a1
0.80	-1.863E-08	3.114E-06	-2.321E-04	9.106E-03	-1.572E-01	1.284E + 00
0.95	1.846E-07	-2.837E-05	1.612E-03	-4.160E-02	4.985E-01	-1.853E + 00
1.20	-3.786E-09	1.076E-06	-1.133E-04	4.659E-03	-4784E-02	2.060E-01
Lift Coefficient 2nd AoA range						
Mach no.	a6	a5	a4	a3	a2	a1
0.80	-5.343E-08	1.909E-05	-2.718E-03	1.927E-01	-6.813E + 00	9.684E + 01
0.95	-5.627E-08	2.007E-05	-2.845E-03	2.002E-01	-7.002E + 00	9.819E + 01
1.20	-1.696E-07	6.489E-05	-9.873E-03	7.463E-01	-2.804E + 01	4.199E + 02

**Table 5.14** Polynomial coefficients for  $C_L$  for  $1.2 < M_\infty \leq 25$ 

Longitudinal clean configuration				
Mach no.	Lift coefficient			
	b4	b3	b2	b1
1.40	4.125E-06	-1.261E-03	8.641E-02	-9.021E-01
1.47	4.064E-06	-1.261E-03	8.634E-02	-9.192E-01
1.52	3.992E-06	-1.238E-03	8.482E-02	-9.030E-01
2.00	-2.900E-06	-1.454E-04	3.113E-02	-1.676E-01
4.00	-3.562E-02	4.286E-05	2.033E-02	-1.198E-01
6.00	-6.059E-06	3.059E-04	1.233E-02	-4.671E-02
8.70	-5.414E-06	2.640E-04	1.266E-02	-6.512E-02
10.00	-4.381E-06	1.285E-04	1.909E-02	-1.714E-01
15.00	-4.350E-06	1.276E-04	1.895E-02	-1.702E-01
17.70	-4.364E-06	1.279E-04	1.901E-02	-1.707E-01
20.00	-4.376E-06	1.283E-04	1.906E-02	-1.712E-01
25.00	-4.337E-06	1.272E-04	1.889E-02	-1.697E-01

### 5.11.7.2 Drag Coefficient, $C_{D,b}$

From the analysis of different data sources, it comes out that the best choice to fit data is a fifth-order polynomial for  $M$ , while for  $M_\infty > 1.2$ , third-order polynomial is to be used. Therefore, the analytical expression for the drag coefficient reads:

$$C_{D,b}(M, \alpha) = \sum_{i=1}^6 c_i(M, \alpha_f) \alpha^{i-1} \quad M_\infty \leq 1.2 \quad (5.35)$$

$$C_{D,b}(M, \alpha) = \sum_{i=1}^4 d_i(M) \alpha^{i-1} \quad M_\infty > 1.2$$

where polynomial coefficients are collected in the following Tables 5.15 and 5.16 [4].

**Table 5.15** Polynomial coefficients for  $C_D$  for  $0.8 \leq M_\infty \leq 1.2$ 

Longitudinal clean configuration

Mach no.	Drag coefficient 1st AoA range					
	c6	c5	c4	c3	c2	c1
0.80	-7.372E-08	1.287E-05	-8.921E-04	3.100E-02	-5.198E-01	3.572E + 00
0.95	1.802E-07	-3.185E-05	2.155E-03	-6.928E-02	1.079E + 00	-6.286E + 00
1.20	3.381E-09	-4.016E-07	-9.892E-06	2.543E-03	-6.447E-02	7.797E-01
Drag coefficient 2nd AoA range						
Mach no.	c6	c5	c4	c3	c2	c1
0.80	5.747E-09	-1.292E-06	6.855E-05	3.402E-03	-3.945E-01	9.793E + 00
0.95	9.080E-09	-2.085E-06	1.255E-04	3.239E-03	-5.204E-01	1.346E + 01
1.20	-2.087E-07	7.701E-05	-1.133E-02	8.303E-01	-3.031E + 01	4.420E + 02

**Table 5.16** Polynomial coefficients for  $C_D$  for  $1.2 < M_\infty \leq 25$ 

Longitudinal clean configuration

Mach no.	Drag coefficient			
	d4	d3	d2	d1
1.40	-8.796E-06	9.073E-04	-3.091E-04	6.252E-02
1.47	-9.094E-06	9.358E-04	-1.351E-03	6.488E-02
1.52	-9.374E-06	9.646E-04	-1.393E-03	6.687E-02
2.00	-1.199E-05	1.514E-03	-3.476E-02	5.571E-01
4.00	-8.528E-06	1.173E-03	-2.647E-02	4.078E-01
6.00	-4.923E-06	7.579E-04	-9.568E-03	1.897E-01
8.70	-8.075E-06	1.108E-03	-2.279E-02	3.289E-01
10.00	-7.386E-06	1.052E-03	-2.112E-02	3.118E-01
15.00	-7.611E-06	1.084E-03	-2.176E-02	3.213E-01
17.70	-7.493E-06	1.067E-03	-2.143E-02	3.164E-01
20.00	-7.561E-06	1.077E-03	-2.162E-02	3.192E-01
25.00	-7.757E-06	1.104E-03	-2.218E-02	3.275E-01

### 5.11.7.3 Pitching Moment Coefficient, $C_{m,b}$

Fourth-order polynomial was chosen to fit drag coefficient data as expressed by the following equations:

$$C_{m,b}(M, \alpha) = \sum_{i=1}^5 e_i(M, \alpha_r) \alpha^{i-1} \quad M_\infty \leq 1.2 \quad (5.36)$$

$$C_{m,b}(M, \alpha) = \sum_{i=1}^5 f_i(M) \alpha^{i-1} \quad M_\infty > 1.2$$

where polynomial coefficients are collected in the following Tables 5.17 and 5.18 [4].

**Table 5.17** Polynomial coefficients for  $C_m$  for  $0.8 \leq M_\infty \leq 1.2$ 

Longitudinal clean configuration					
Mach no.	Pitching moment coefficient 1st AoA range				
	e5	e4	e3	e2	e1
0.80	-4.318E-07	5.838E-05	-2.856E-03	6.151E-02	-4.624E-01
0.95	3.632E-07	-4.568E-05	1.889E-03	-2.692E-02	1.113E-01
1.20	-1.579E-07	2.353E-05	-1.269E-03	2.878E-02	-2.090E-01
Pitching moment coefficient 2nd AoA range					
Mach no.	e5	e4	e3	e2	e1
0.80	-2.273E-07	6.245E-05	-6.360E-03	2.814E-01	-4.522E + 00
0.95	-1.622E-07	4.140E-05	-3.892E-03	1.570E-01	-2.261E + 00
1.20	5.297E-07	-1.589E-04	1.769E-02	-8.682E-01	1.587E + 01

**Table 5.18** Polynomial coefficients for  $C_m$  for  $1.2 < M_\infty \leq 25$ 

Longitudinal clean configuration					
Mach no.	Pitching moment coefficient				
	f5	f4	f3	f2	f1
1.40	2.069E-08	-4.964E-06	3.802E-04	-1.222E-02	1.530E-01
1.47	-8.976E-09	6.550E-07	4.429E-06	-1.900E-03	5.455E-02
1.52	-8.976E-09	6.550E-07	4.429E-06	-1.900E-03	5.455E-02
2.00	1.996E-08	-2.131E-06	3.227E-05	1.147E-03	-6.948E-03
4.00	6.139E-08	-9.870E-06	5.315E-04	-1.214E-02	1.242E-01
6.00	-5.285E-09	-4.277E-09	2.283E-06	-1.223E-04	2.900E-02
8.70	-1.823E-09	-1.107E-06	1.081E-04	-3.925E-03	7.196E-02
10.00	3.948E-08	-6.515E-06	3.411E-04	-7.501E-03	8.498E-02
15.00	3.937E-08	-6.534E-06	3.420E-04	-7.576E-03	8.513E-02
17.70	3.922E-08	-6.546E-06	3.430E-04	-7.582E-03	8.491E-02
20.00	3.907E-08	-6.557E-06	3.439E-04	-7.583E-03	8.486E-02
25.00	3.902E-08	-6.584E-06	3.449E-04	-7.589E-03	8.291E-02

Some results of the AEDB tool are hereinafter provided. All the available data (both CFD and WTT) are also reported in the figures in order to underline the accuracy of AEDB results.

One example of the longitudinal characteristics with zero aileron flap setting is shown in Figs. 5.101, 5.102, and 5.103, where lift, drag, and pitching moment coefficients are shown for  $M_\infty = 0.8$  [7, 15]. In this case, aside from experimental data provided by FOI T1500, some CFD results from ESTEC (AOES) database are available [4].

These longitudinal characteristics in clean configuration underline that the evolution of aerodynamic coefficient of IXV requires a quite complex polynomial to describe all the AoA range. To avoid such complex formula which could introduce too many unphysical oscillations, it was preferred to split the polynomial in two different expressions. In particular, it was decided to split at  $\alpha = 56^\circ$  as in this point

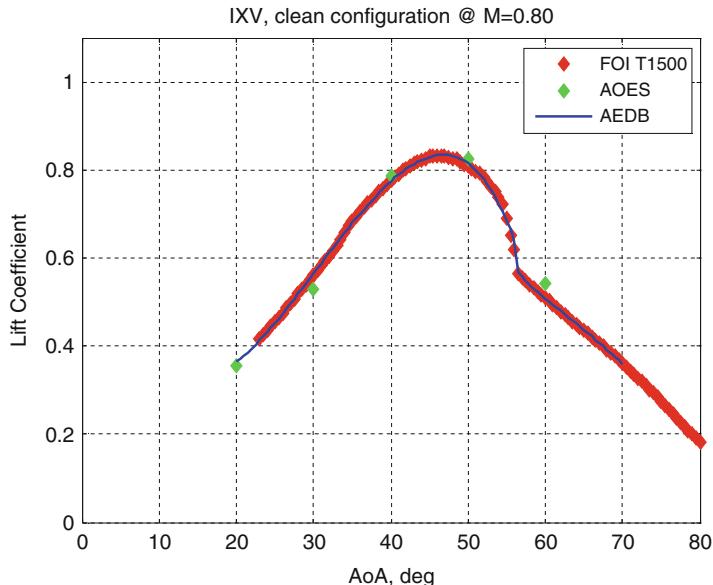


Fig. 5.101 Lift coefficient in clean configuration at  $M_\infty = 0.80$

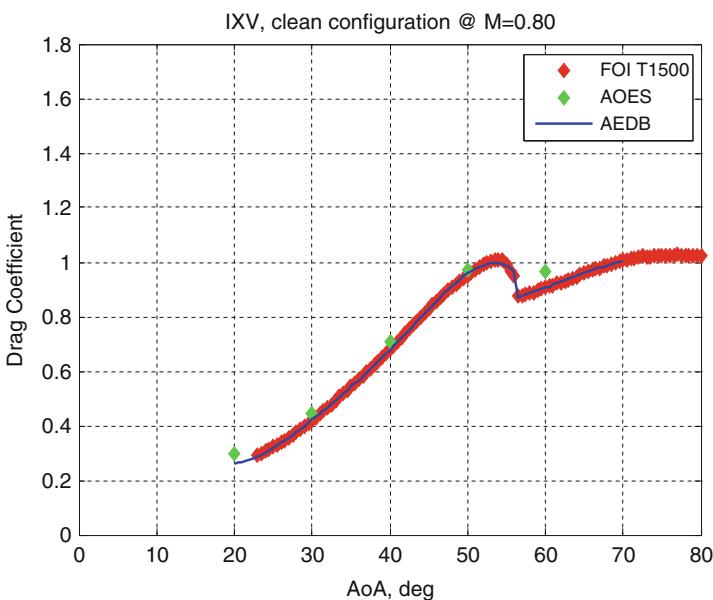


Fig. 5.102 Drag coefficient in clean configuration at  $M_\infty = 0.80$

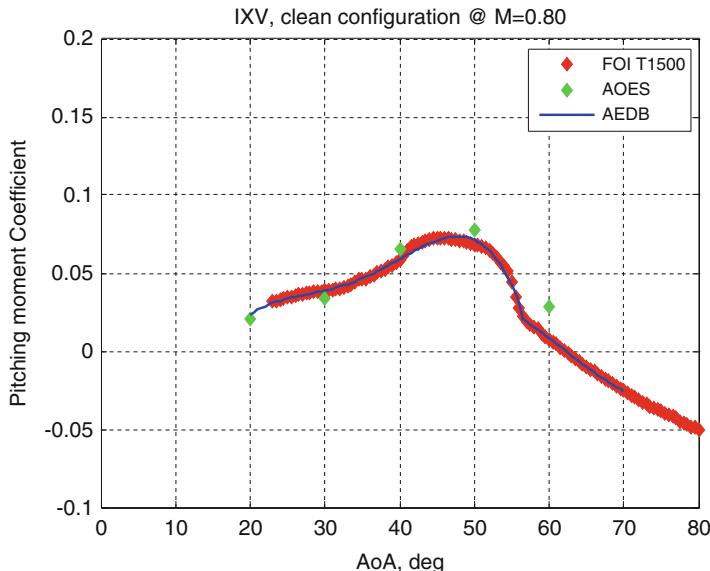


Fig. 5.103 Pitching moment coefficient in clean configuration at  $M_\infty = 0.80$

is evident the change in slope of the aerodynamic characteristics. Further, it is worth to note that at  $M_\infty = 0.8$ , the vehicle is unstable (e.g.,  $C_{m\alpha} > 0$ ) at  $\alpha < 44^\circ$ , and the trim AoA ( $\alpha_{trim}$ ) is about  $62^\circ$ . Such behavior was identified as a result of the partial or complete flowfield separation occurring at the leeward side for those AoAs as this part of the vehicle is rounded (no triggering of the flowfield separation). In particular, large deviation between CFD and WTT data at  $\alpha = 60^\circ$  highlights that numerical computation does not assess the flowfield separation that takes place at vehicle leeside at this flow incidence. Therefore, wind tunnel investigations have shown that range of transonic speeds is the most complex. For instance, around trim angles of attack, low-frequency fluctuations occur at transonic speeds, depending on fluctuations of a separation zone on leeward side of IXV vehicle.

Aerodynamic results for  $M_\infty = 10$  are summarized in Figs. 5.104, 5.105, and 5.106 [4, 7, 15].

As one can see, the lift force coefficient increases nearly linearly with increasing AoA but with a change of the gradient at about  $\alpha = 45^\circ$ . The drag force coefficient increases nearly linearly with increasing AoA, while the pitching moment coefficient  $C_m$  decreases nearly linearly with increasing  $\alpha$  up to about  $42^\circ$ .

Anyway, the trend of the pitching moment  $C_m$  highlights that the vehicle is statically stable in longitudinal flight (i.e.,  $C_{m\alpha} < 0$ ) with the given CoG, and it is characterized by a natural trim point at about  $45^\circ$ . Moreover, being the  $C_m$  positive for  $\alpha \leq \alpha_{trim}$ , it can be trimmed with positive flap deflections at  $\alpha < 45^\circ$ .

As far as concept aerodynamics at  $\alpha = 45^\circ$  and in clean configuration is concerned, Figs. 5.107, 5.108, and 5.109 report lift, drag, and pitching moment

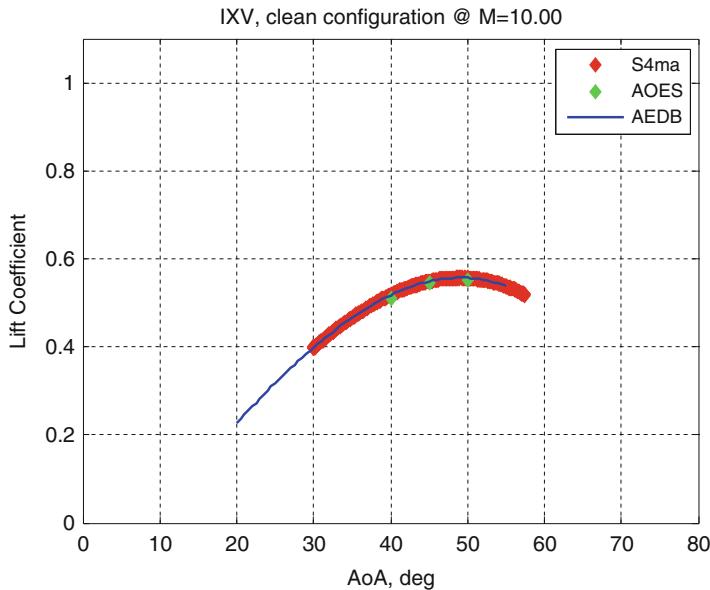


Fig. 5.104 Lift coefficient in clean configuration at  $M_\infty = 10$

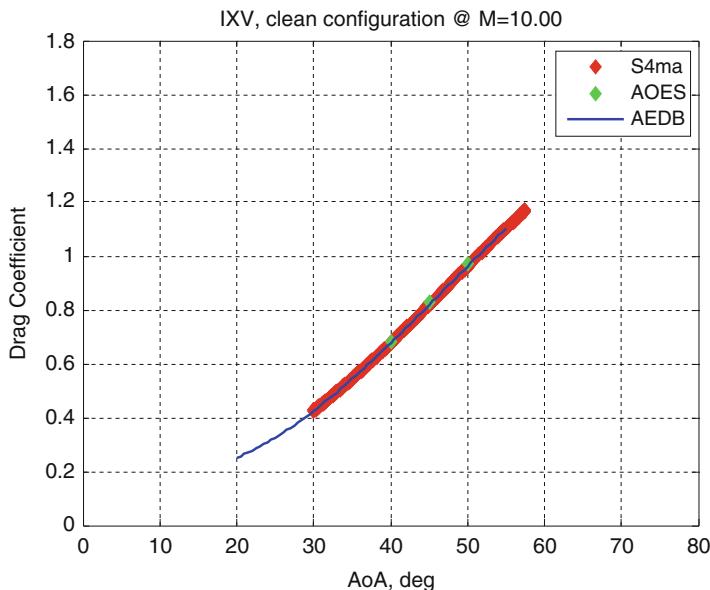


Fig. 5.105 Drag coefficient in clean configuration at  $M_\infty = 10$

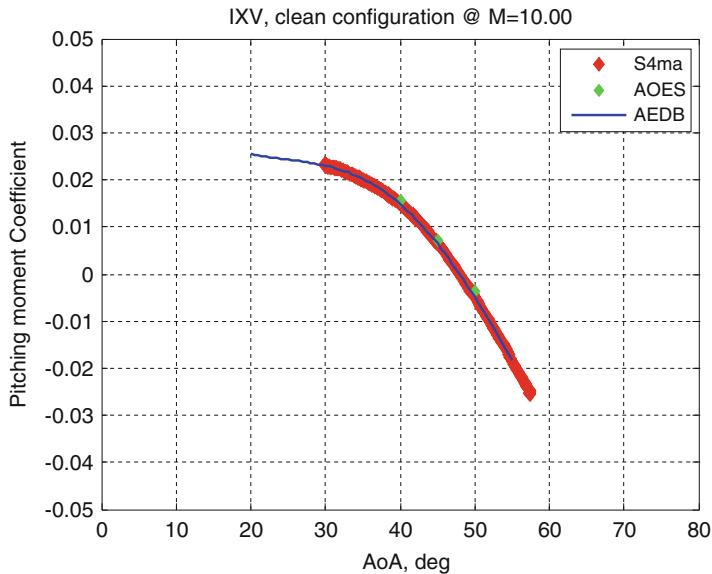


Fig. 5.106 Pitching moment coefficient in clean configuration at  $M_{\infty} = 10$

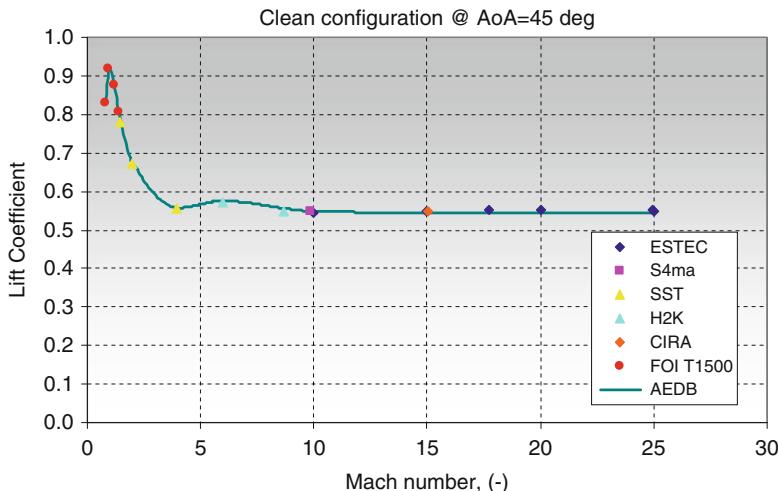
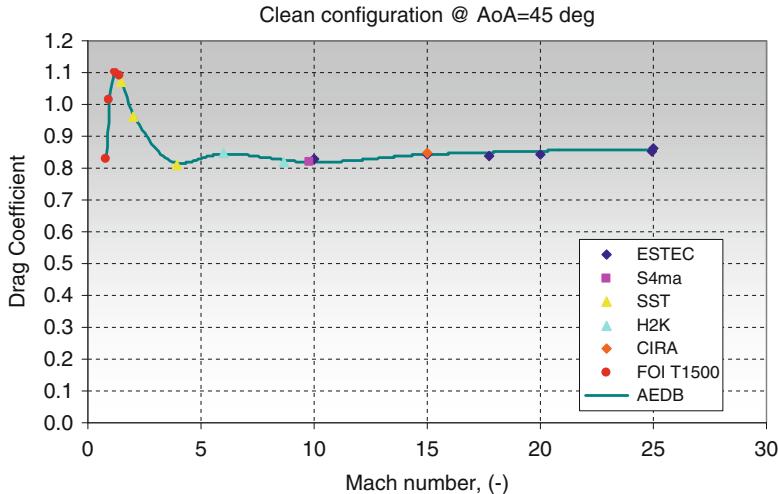
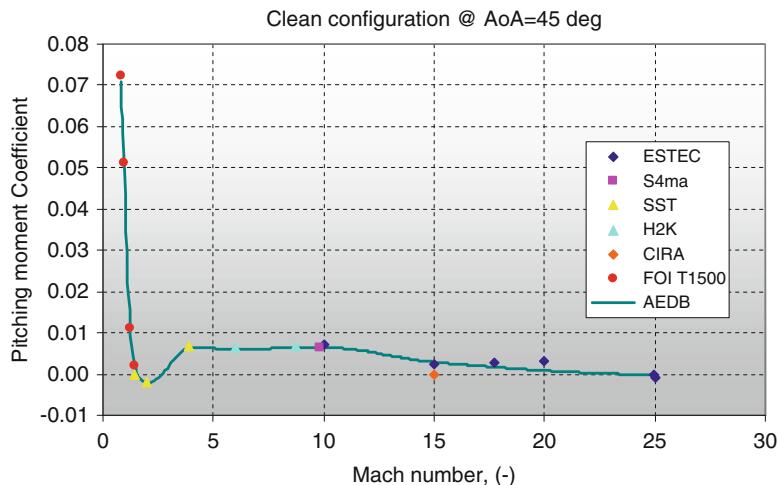


Fig. 5.107 Lift coefficient versus Mach in clean configuration at  $\alpha = 45^\circ$

coefficients versus the whole Mach number range [4, 7, 15]. All the available data (both CFD and WTT) are also shown in order to underline the accuracy of AEDB results. As shown, all the AEDB data provided so far compare rather well with both experimental and numerical data.



**Fig. 5.108** Drag coefficient versus Mach in clean configuration at  $\alpha = 45^\circ$



**Fig. 5.109** Pitching moment coefficient versus Mach in clean configuration at  $\alpha = 45^\circ$

### 5.11.8 Elevator Effectiveness on Longitudinal Coefficients

In order to characterize the elevator effectiveness first of all, starting from the available source data, it is needed to extract the delta coefficients  $\Delta C_{i,\delta_e} = C_i(M, \alpha, \delta_{er}, \delta_{el}) - C_i(M, \alpha)$  by subtracting to the value of the coefficient at  $\delta_{er} = \delta_{el} \neq 0$ , the corresponding ones in clean configuration. Once those sets

of data are ready, it is possible to generate best-fit polynomials for lift, drag, and pitching moment contributions as hereinafter reported:

$$\Delta C_{L,\delta_e}(M, \alpha, \delta_e) = \sum_{i=1}^4 g_i(M, \alpha) \delta_e^{i-1} \quad (5.37)$$

$$\Delta C_{D,\delta_e}(M, \alpha, \delta_e) = \sum_{i=1}^5 h_i(M, \alpha) \delta_e^{i-1} \quad (5.38)$$

$$\Delta C_{m,\delta_e}(M, \alpha, \delta_e) = \sum_{i=1}^6 l_i(M, \alpha) \delta_e^{i-1} \quad (5.39)$$

One of the remarkable results to highlight of IXV longitudinal aerodynamic characteristics is the pitching moment behavior versus the AoA that exhibits the vehicle concept at high Mach number. As an example, results for  $M_\infty = 10$  are shown in Fig. 5.110 [4].

Looking at the figure, it is clear that for  $\delta_e$  ranging from  $-10$  to  $15^\circ$ , most significant change for the  $C_m(\alpha)$  function is detected. In fact,  $C_m(\alpha)$  is monotonic at the flap deflection  $\delta_e < 10^\circ$  and displays nearly constant shift with respect to a basis curve  $C_m(\alpha)$  (flaps deflections  $\delta_e = 0^\circ$ ). But already at  $\delta_e = 7.5^\circ$ , the break point and the range of no monotonic behavior appear on the curve  $C_m(\alpha)$ .

Finally, when the vehicle is flying at  $M_\infty = 10$ , to trim IXV vehicle in pitch at  $\alpha = 45^\circ$  requires only a slight flap deflection (about  $2.5^\circ$ ). If IXV is flying at  $M_\infty = 10$  and  $\alpha = 40^\circ$ , a flap deflection of  $5^\circ$  is needed to trim the vehicle, whereas

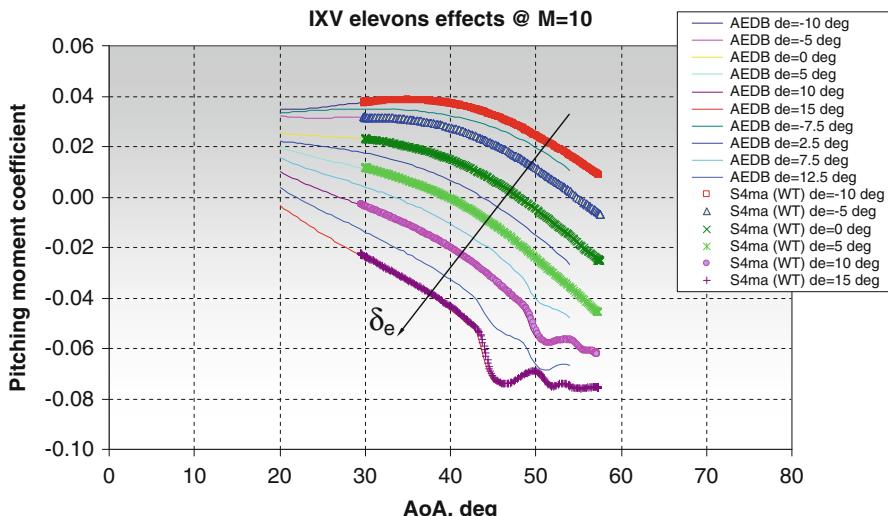


**Fig. 5.110**  $C_m$  at  $M_\infty = 10$  and for  $-10 \leq \delta_e \leq 15^\circ$

for  $\alpha = 50^\circ$ , vehicle trimming demands negative flap deflection. Therefore, also in the case of  $\delta_e$  effect assessment, the reliability of the AEDB tool in terms of consistency and trends is verified.

Further, important critical phenomena occur in the flap region as the shock wave–boundary layer interaction (SWBLI) and the shock wave–shock wave interaction (SWSWI), thus resulting in a loss of flap control efficiency, as highlighted by curves oscillations in Fig. 5.110.

In fact, an atmospheric re-entry vehicle such the IXV is designed primarily for hypersonic speeds. As a consequence, the vehicle embodies principles for good hypersonic design as a very rounded and thick body to decrease heat loads that allow for a lighter structural design. The thick fuselage and rounded leading edges, however, create strong shocks, which interact with boundary layers and often induce flow separation.

Such flow is complex and very sensitive to actual flight conditions (e.g., Reynolds number). Moreover, oil film surface streamline visualizations corresponding to those cases show that a unified separation zone is formed in front of flaps. As a result, looking at Figs. 5.111, 5.112, 5.113, 5.114, 5.115, 5.116, and 5.117, most significant change for the  $C_m(\alpha)$  function is detected [4, 7, 15]. In fact,  $C_m(\alpha)$  is monotonic at the flap deflection  $\delta_e < 10^\circ$  and displays nearly constant shift with respect to a basis curve  $C_m(\alpha)$  (flaps deflections  $\delta_e = 0^\circ$ ). But already at  $\delta_e = 10^\circ$ , the break point and the range of no monotonic behavior appears on the curve  $C_m(\alpha)$ . This behavior depends on the flowfield that takes place on the belly side of IXV, as highlighted by tests campaigns in both H2K and S4ma WTs.

For instance, flow topology around deflected flaps (e.g.,  $\delta_e = 15^\circ$ , ) changes from pure supersonic to transonic and subsonic with increasing angles of attack, as shown in Fig. 5.111. At angles of attack from  $\alpha \approx 42^\circ$  to  $\alpha \approx 57^\circ$  (see Fig. 5.111 – case B, case C, and case D), a complex system of shock and expansion waves is formed; above these angles of attack range subsonic flow occurred in the aft part of windward surface of IXV vehicle. Therefore, as local Mach number decreases with  $\alpha$  increases, the oblique shock situation tends to disappear with respect to a detached shock situation.

In agreement with the behavior of the shock structure near the flaps, the aerodynamic coefficients change with the AoA equal to or higher than  $45^\circ$ , as shown in Fig. 5.112. The angle of the shock starting at the hinge line of the flaps is much bigger at  $45^\circ$  AoA than at  $30^\circ$  AoA. Also, the images at  $50$  and  $55^\circ$  AoA show that there is a strong interaction of the shocks in the flap region for high AoAs. Further, Fig. 5.113 highlights as the  $C_m$  behavior strongly depends on free-stream conditions (e.g., Mach and Reynolds numbers) as well as on vehicle attitude (e.g., AoA).

As it has been said, at the body flaps, the laminar to turbulent transition (LTT), SWBLI, and SWSWI can be observed for certain angles of attack, flow conditions, and flap deflections. As an example, some CFD results are presented in Fig. 5.114 for  $M_\infty = 17$  and  $25$  in laminar flow hypothesis [5]. As one can see, the separation region increases for lower Mach number and higher Reynolds number, thus affecting the flap efficiency and the total pitching moment  $C_m$  as well.

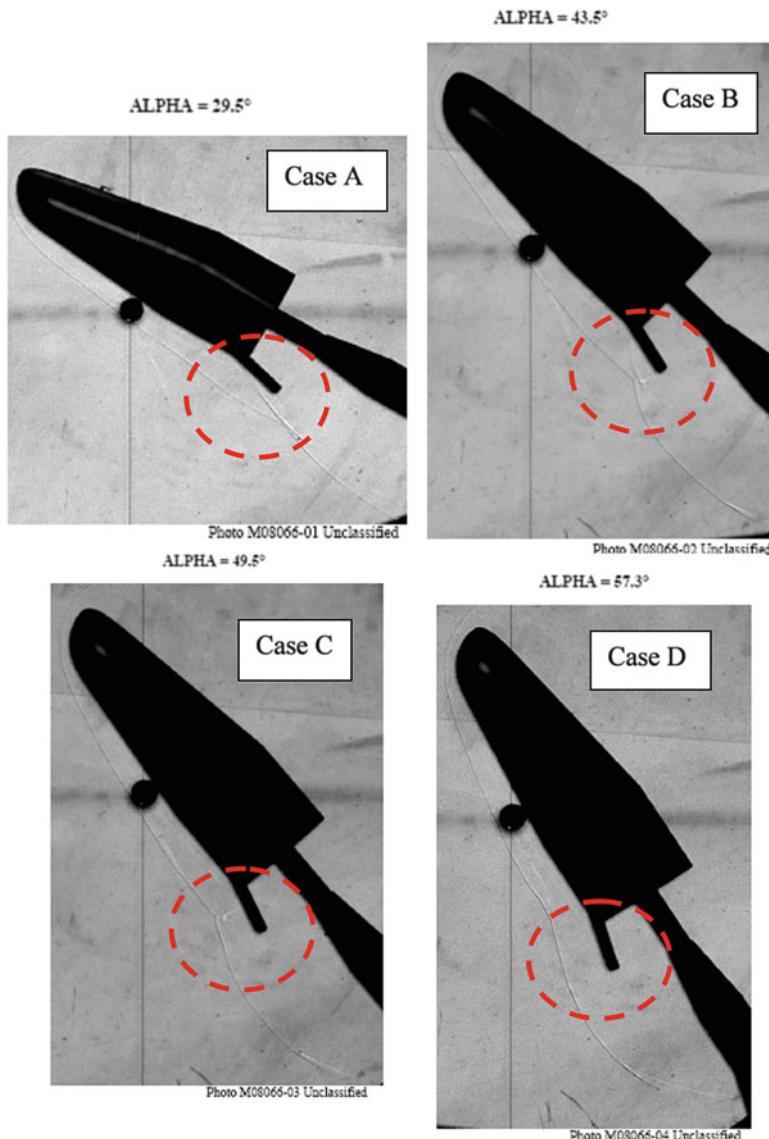


**Fig. 5.111** The flow pattern variations versus the AoA at  $\delta_e = 15^\circ$ . Test in S4ma WT

As further confirmation, Fig. 5.115 shows the pressure coefficient distribution and the skin friction lines on the IXV vehicle windsides for the  $M_\infty = 15.0$  transitional, equilibrium flow modeling, and radiative equilibrium wall case ( $\varepsilon = 0.80$ ). The pattern of lines on the flat part of fuselage can be observed (where the pressure is nearly constant) as well as the separation bubble around the body flap hinge line, with clearly predicted separation and reattachment lines.

IXV @  $M=10.00$ ,  $\beta=0$  deg,  $\delta_e=15$  deg and  $\delta_a=0$  deg ( $\delta_{er}=15$  deg,  $\delta_{el}=15$  deg)

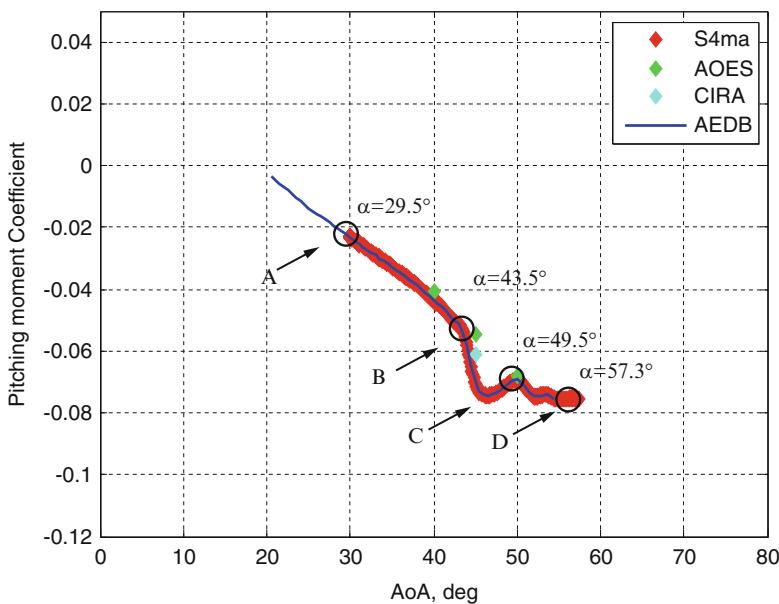


**Fig. 5.112** The pitching moment coefficient variations versus the AoA at  $\delta_e = 15^\circ$

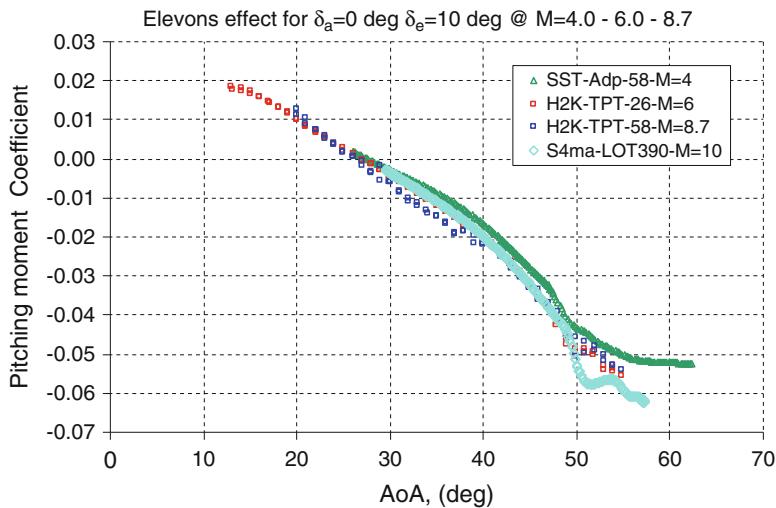


**Fig. 5.113** Effect of elevons for  $M_\infty = 4, 6$  and  $8.7$  at  $\delta_e = 10^\circ$

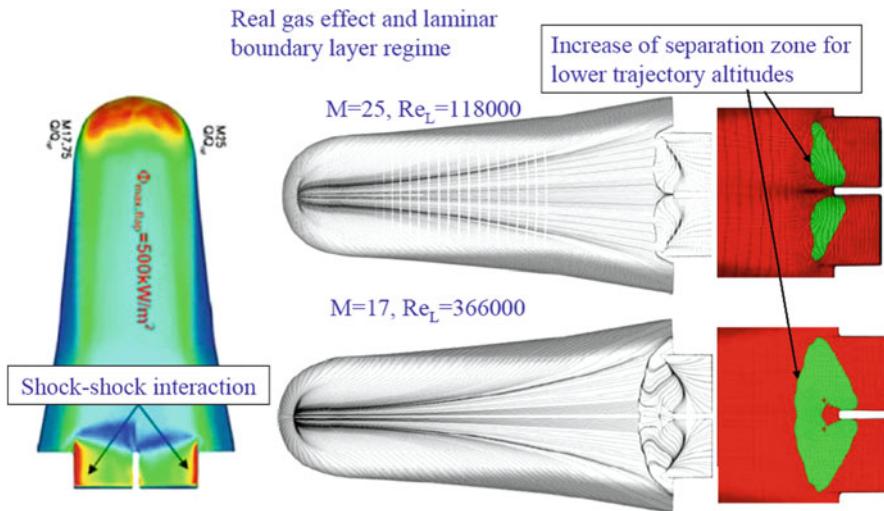


**Fig. 5.114** Separation zone and shock–shock interaction at different Mach and Reynolds number

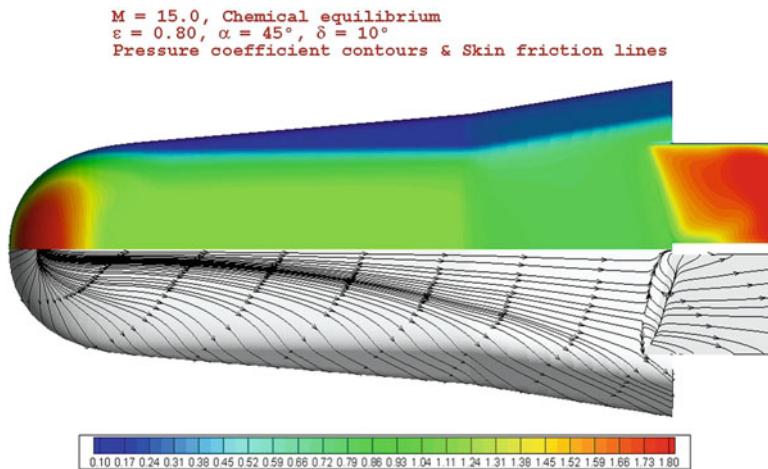


**Fig. 5.115** Windside skin friction lines and pressure coefficient distribution for  $M_\infty = 15.0$ ,  $\alpha = 45^\circ$ , transitional, equilibrium, and radiative wall ( $\varepsilon = 0.80$ ) case

The analysis of the predicted skin friction lines reported in Fig. 5.116 for the windside shows as the increase of Mach number (from 15.0 to 17.7) causes a reduction of the extent of three-dimensional recirculation around the body flap hinge line due mainly to a delay in separation (separation line moves toward the hinge line; see Fig. 5.116) and a consequent reduction of flow spillage between the two body flaps.

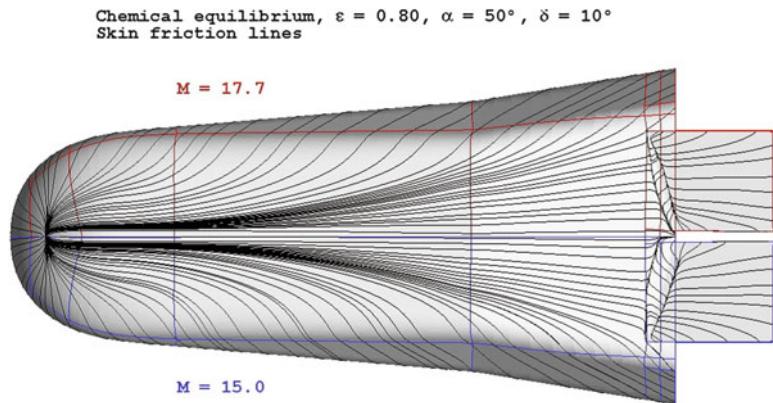


**Fig. 5.116** Chemical equilibrium and radiative wall ( $\varepsilon = 0.80$ ).  $M_\infty = 15.0$  vs.  $M_\infty = 17.7$  comparison. Windside skin friction lines

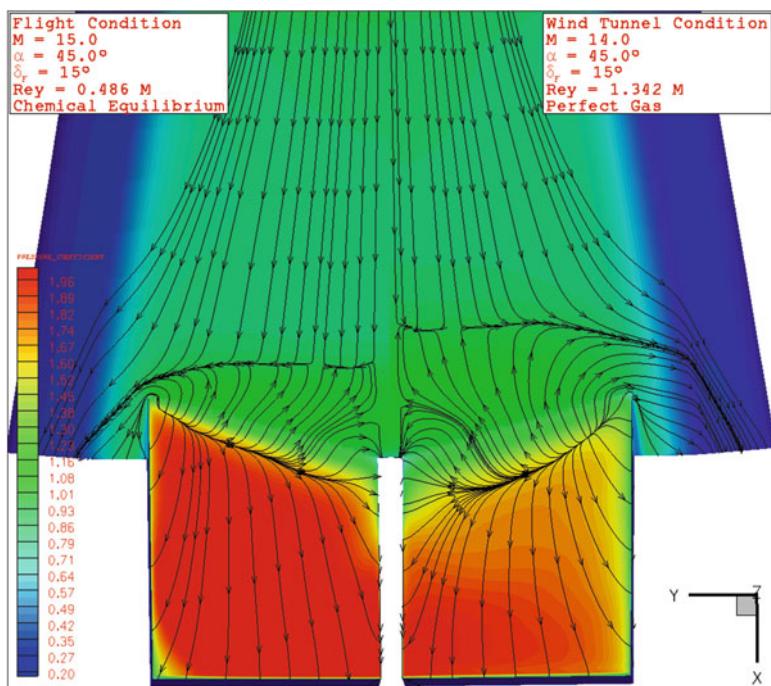


**Fig. 5.117** Comparison of skin friction lines. Numerical simulations of flight (left) and wind tunnel (right) conditions

Finally, in Fig. 5.117, a significant comparison between one simulation in flight condition ( $M_\infty = 15$ ,  $\text{Re}_{\infty,L} = 4.86 \times 10^5$ ) and one simulation in wind tunnel condition ( $M_\infty = 14$ ,  $\text{Re}_{\infty,L} = 1.34 \times 10^6$ ) is reported in terms of skin friction lines pattern around the flap.

For both simulations  $\alpha = 45^\circ$ ,  $\beta = 0^\circ$  and  $\delta_{\text{flap}} = 15^\circ$ , while laminar to turbulent transition has been imposed at flap hinge line. As shown, the reproducibility of flight conditions seems to be qualitatively good, both in terms of flow features and surface properties as a similar separation bubble can be observed. The larger pattern of wind tunnel case suggests, however, a combined effect, on the transitional shock wave–boundary layer interaction, of ideal gas hypothesis (with respect to the equilibrium gas assumption in flight) and greater Reynolds number.

### 5.11.9 Sideslip Angle Effects on Longitudinal and Lateral–Directional Actions

The contribution to longitudinal coefficient due to nonzero sideslip relies on the axisymmetries in pressure distribution caused by the presence of  $\beta$  angle. Only a small contribution to the aerodynamics forces acting on the longitudinal plane are observed. The contribution is obtained by subtracting the baseline curves to the same-order fitting polynomials used for nonzero  $\beta$  cases:

$$\Delta C_{L,b,\beta}(M, \alpha, \beta) = \sum_{i=1}^N m_i(M, \beta) \alpha^{i-1} - C_{L,b}(M, \alpha) \quad \begin{cases} N = 6, \text{ if } M_\infty < 2 \\ N = 4, \text{ if } M_\infty \geq 2 \end{cases} \quad (5.40)$$

$$\Delta C_{D,b,\beta}(M, \alpha, \beta) = \sum_{i=1}^N n_i(M, \beta) \alpha^{i-1} - C_{D,b}(M, \alpha) \quad \begin{cases} N = 6, \text{ if } M_\infty < 2 \\ N = 4, \text{ if } M_\infty \geq 2 \end{cases} \quad (5.41)$$

$$\Delta C_{m,b,\beta}(M, \alpha, \beta) = \sum_{i=1}^5 p_i(M, \beta) \alpha^{i-1} - C_{m,b}(M, \alpha) \quad (5.42)$$

Obviously, being zero, the lateral–directional actions in clean configuration at  $\beta=0^\circ$ , the delta contribution assumes the same form of the baseline terms for longitudinal coefficients. Fourth- and third-order polynomials were chosen to fit side force, rolling and yawing moment coefficients data, as expressed by the following equations:

$$\Delta C_{Y,b,\beta}(M, \alpha, \beta) = \sum_{i=1}^4 q_i(M, \alpha) \beta^{i-1} - C_{Y,b}(M, \alpha) = \sum_{i=1}^4 q_i(M, \alpha) \beta^{i-1} \quad (5.43)$$

$$\Delta C_{l,b,\beta}(M, \alpha, \beta) = \sum_{i=1}^3 r_i(M, \alpha) \beta^{i-1} - C_{l,b}(M, \alpha) = \sum_{i=1}^3 r_i(M, \alpha) \beta^{i-1} \quad (5.44)$$

$$\Delta C_{n,b,\beta}(M, \alpha, \beta) = \sum_{i=1}^4 s_i(M, \alpha) \beta^{i-1} - C_{n,b}(M, \alpha) = \sum_{i=1}^4 s_i(M, \alpha) \beta^{i-1} \quad (5.45)$$

where the coefficients depend upon Mach and from the AoA  $\alpha$ . As an example, Figs. 5.118, 5.119, and 5.120 show the side force, rolling moment and yawing moment coefficients for  $M_\infty = 10$  and for  $\beta = -5^\circ$  and  $5^\circ$  [4, 7].

As shown, the AEDB compares rather well with experimental results obtained in the ONERA S4ma wind tunnel.

Finally, note that all the asymmetries with respect to  $\beta = 0^\circ$  are due to the available data in the WT repository provided that the AEDB tool is anchored on those data.

### 5.11.10 Ailerons Effect on Lateral–Directional Actions

The expressions for side force, roll and yaw moment contributions, together with the order of the fitting polynomials, read:

$$\Delta C_{Y,\delta_{ej}}(M, \alpha, \delta_{ej})|_{j=l,r} = \sum_{i=1}^N t_i(M, \alpha) (\delta_{ej})^{i-1} \Big|_{j=l,r} \quad \begin{cases} N = 5, \text{ if } M_\infty \leq 1.47 \\ N = 4, \text{ if } M_\infty > 1.47 \end{cases} \quad (5.46)$$

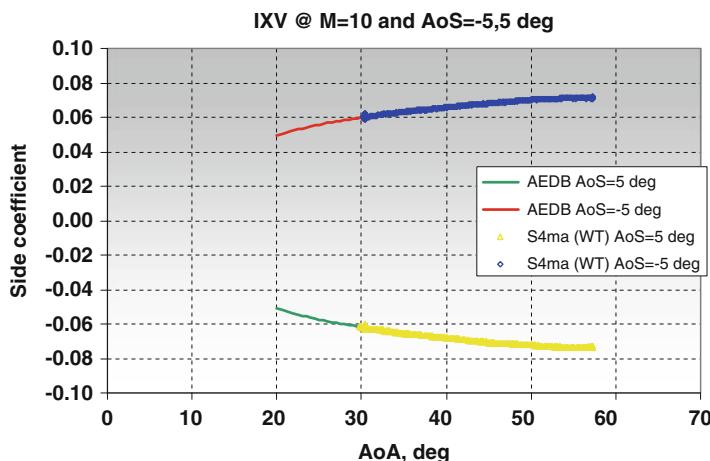
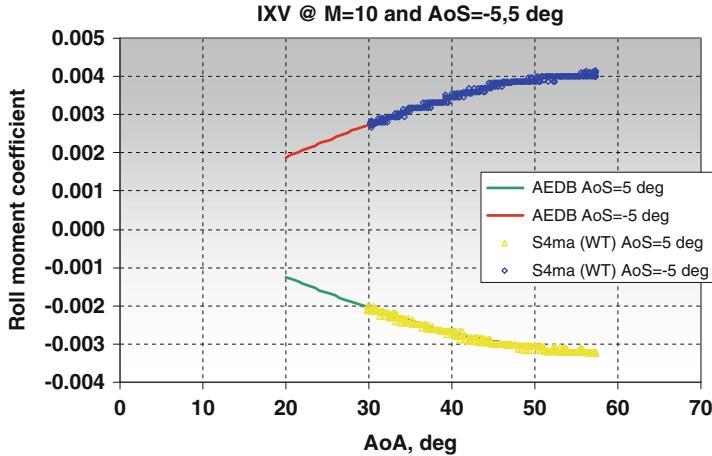
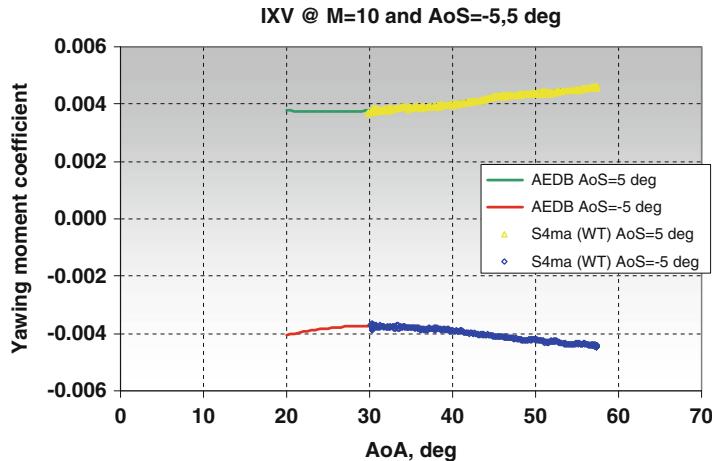


Fig. 5.118  $C_Y$  at  $M_\infty = 10$  and for  $\beta = -5^\circ$  and  $5^\circ$



**Fig. 5.119**  $C_l$  at  $M_\infty = 10$  and for  $\beta = -5^\circ$  and  $5^\circ$



**Fig. 5.120**  $C_n$  at  $M_\infty = 10$  and for  $\beta = -5^\circ$  and  $5^\circ$

$$\Delta C_{l,\delta_{ej}}(M, \alpha, \delta_{ej})|_{j=l,r} = \sum_{i=1}^N u_i(M, \alpha) (\delta_{ej})^{i-1} \Big|_{j=l,r} \quad \begin{cases} N = 5, & \text{if } M_\infty \leq 1.47 \\ N = 4, & \text{if } M_\infty > 1.47 \end{cases} \quad (5.47)$$

$$\Delta C_{n,\delta_{ej}}(M, \alpha, \delta_{ej})|_{j=l,r} = \sum_{i=1}^N v_i(M, \alpha) (\delta_{ej})^{i-1} \Big|_{j=l,r} \quad \begin{cases} N = 6, & \text{if } M_\infty \leq 1.47 \\ N = 4, & \text{if } M_\infty > 1.47 \end{cases} \quad (5.48)$$

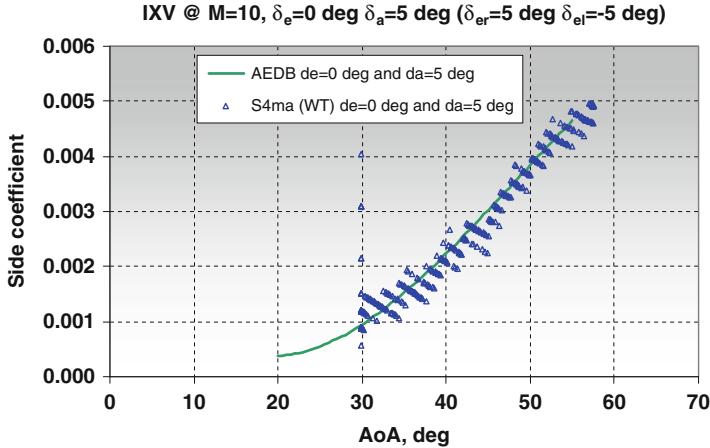


**Fig. 5.121**  $C_Y$  at  $M_\infty = 10$  and for  $\delta_{er} = 5$  and  $\delta_{el} = -5^\circ$

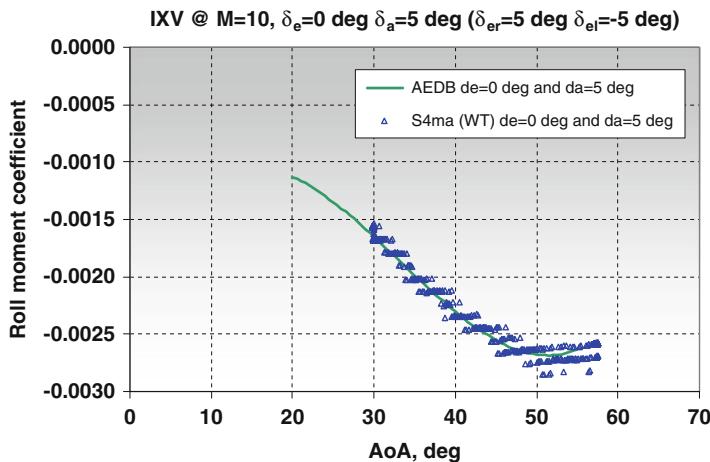


**Fig. 5.122**  $C_l$  at  $M_\infty = 10$  and for  $\delta_{er} = 5$  and  $\delta_{el} = -5^\circ$

Note that each flap features a tilted hinge line (see Fig. 5.23), thus providing vehicle trim and a slight lateral control as well. The reliability of the AEDB tool can be appreciated in Figs. 5.121, 5.122, and 5.123 where, for example, the comparison between AEDB and experimental results at  $M_\infty = 10$  and for  $\delta_{er} = 5^\circ$  and  $\delta_{el} = -5^\circ$  is reported [4],[7].

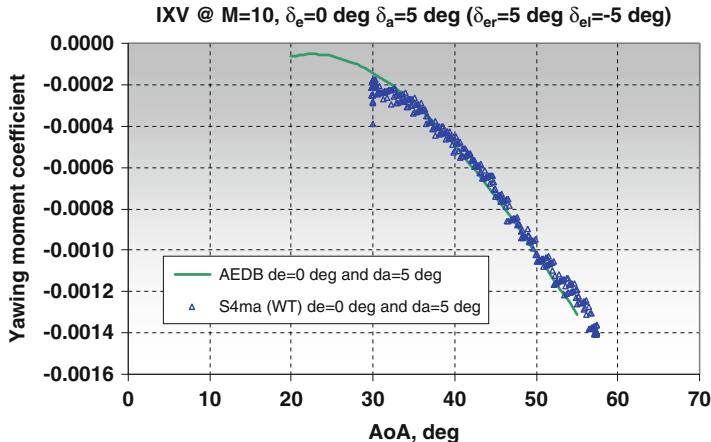


**Fig. 5.123**  $C_n$  at  $M_\infty = 10$  and for  $\delta_{er} = 5$  and  $\delta_{el} = -5^\circ$

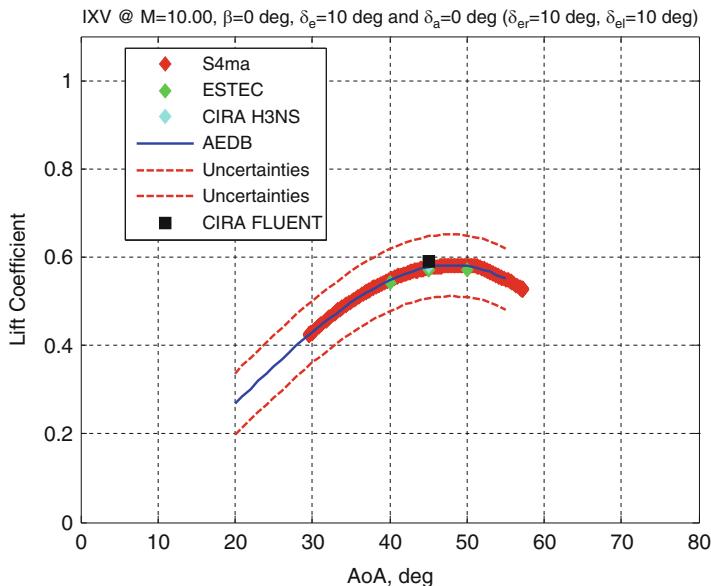


**Fig. 5.124** Lift coefficient with uncertainties limit at  $M_\infty = 10$  and  $\delta_e = 10^\circ$

### 5.11.11 Aerodynamic Database Accuracy

The assessment of AEDB accuracy has been also addressed in databasing activities. For instance, Figs. 5.124, 5.125, and 5.126 show the profiles of lift, drag, and pitching moment coefficients bounded by uncertainty limits at  $M_\infty = 10$  and  $\delta_e = 10^\circ$  [4, 7].

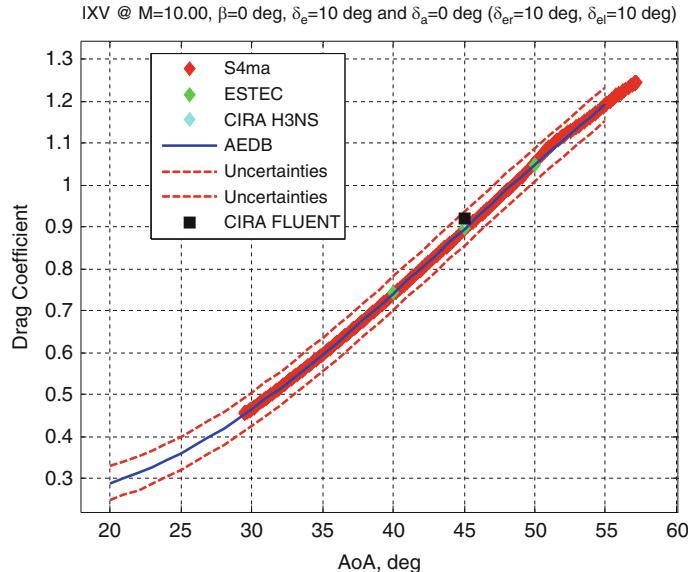


Fig. 5.125 Drag coefficient with uncertainties limit at  $M_\infty = 10$  and  $\delta_e = 10^\circ$

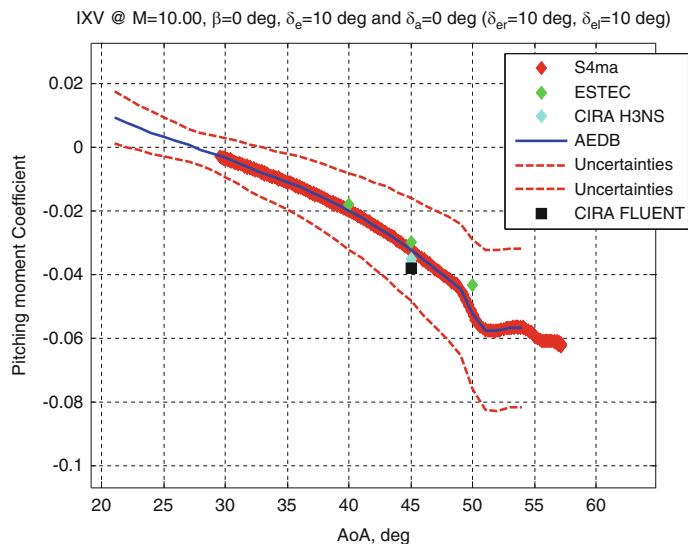
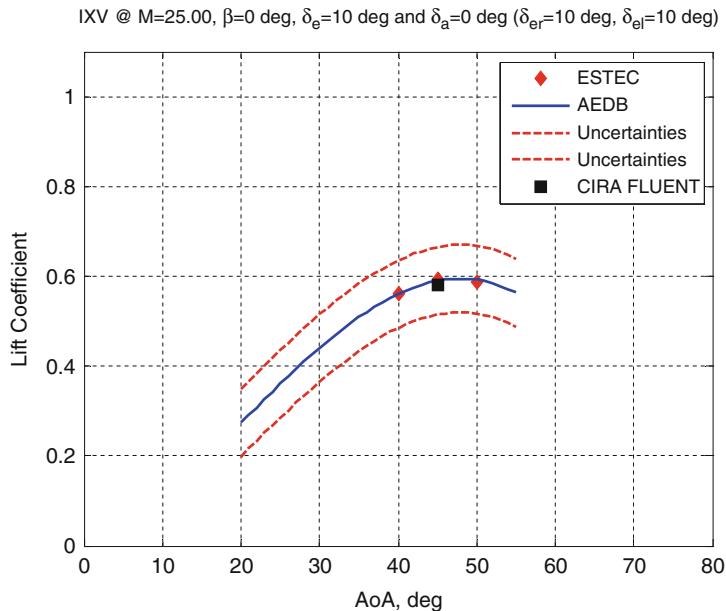


Fig. 5.126 Pitching moment coefficient with uncertainties limit at  $M_\infty = 10$  and  $\delta_e = 10^\circ$

It is worth to note that these limits are the result of the reconstruction of error chains evaluated for each test campaign.

By concluding, Figs. 5.127, 5.128, and 5.129 show lift, drag, and pitching moment coefficients and the corresponding uncertainties for  $M_\infty = 25$  and  $\delta_e = 10^\circ$  [4, 7, 15].



**Fig. 5.127** Lift coefficient with uncertainties limit at  $M_\infty = 25$  and  $\delta_e = 10^\circ$

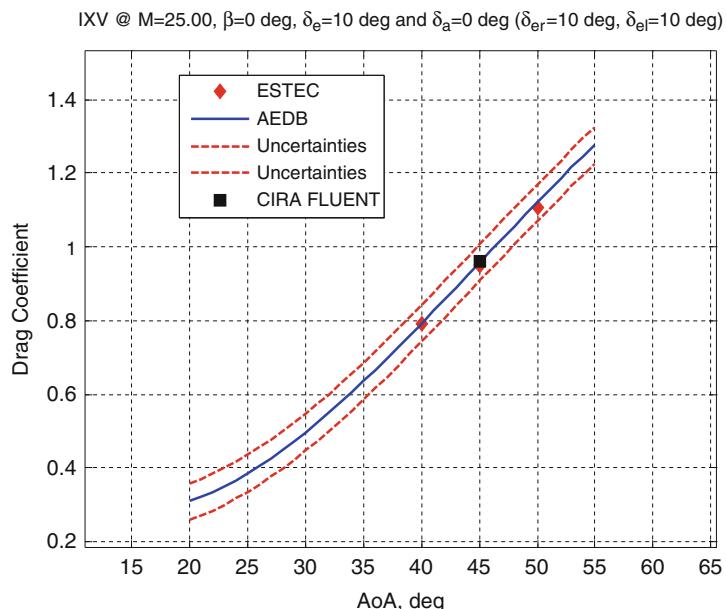


**Fig. 5.128** Drag coefficient with uncertainties limit at  $M_\infty = 25$  and  $\delta_e = 10^\circ$

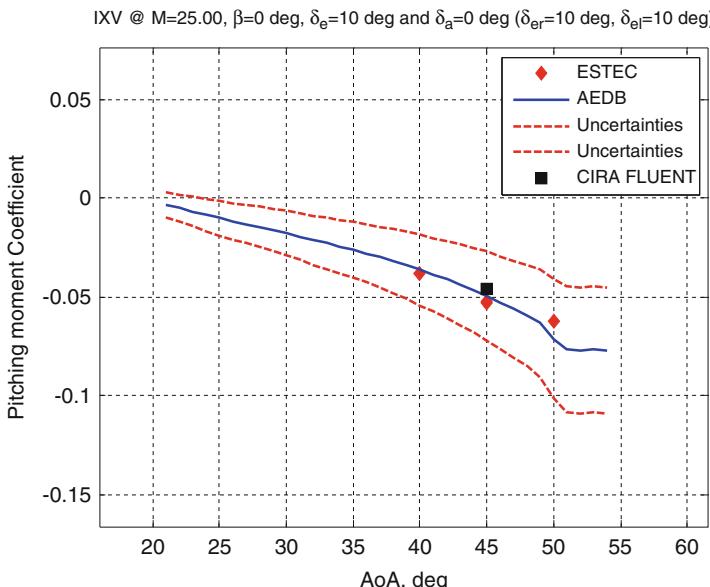


**Fig. 5.129** Pitching moment coefficient with uncertainties limit at  $M_\infty = 25$  and  $\delta_e = 10^\circ$

## References

1. Tumino G, Angelino E, Leleu F, Angelini R, Plotard P, Sommer J (2008) The IXV project. The ESA re-entry system and technologies demonstrator paving the way to European autonomous space transportation and exploration endeavours. In: IAC-08-D2.6.01, Glasgow, Scotland, 29 September–3 October 2008
2. Prabhu DK (2004) System design constraints-trajectory aerothermal environments. In: RTO AVT/VKI lecture series in critical technologies for hypersonic vehicle development, 10–14 May 2004
3. Vernis P, Gelly G (2008) From ARD to IXV: ten years of GNC studies on atmospheric entry. Paper presented at the 2nd International ARA Days, Arcachon, 21–23 October 2008
4. Pezzella G, Marino G, Rufolo G (2014) Aerodynamic database development of the ESA intermediate experimental vehicle. *Acta Astronaut* 94(1):57–72. ISSN (0094–5765). doi:[10.1016/j.actaastro.2013.07.019](https://doi.org/10.1016/j.actaastro.2013.07.019)
5. Baiocco P, Plotard P, Guedron S, Moulin J (2008) Historical background and lessons learnt of the Pre-X atmospheric experimental re-entry vehicle. In: 2nd international ARA days “10 years after ARD”, Arcachon, France, 21–23 October 2008
6. Gérard Y, Tumino G (2005) FLPP re-entry in-flight experimentation: the intermediate experimental vehicle (IXV) technical and programmatic objectives, IAC-05-D2.P.04
7. Pezzella G, Marini M, Rufolo G (2011) Aerodynamic characterization of the ESA intermediate experimental vehicle. In: 17th AIAA international space planes and hypersonic systems and technologies conference, San Francisco, CA, 11–14 April 2011. AIAA 2011–2232, USA
8. Hirshel EH (2009) Selected aerothermodynamic design problems of hypersonic flight vehicles. Springer, Berlin/London. ISBN 978-3-540-89973-0
9. Gérard Y, Tumino G (2006) FLPP re-entry in-flight experimentation: current status of the 1859 intermediate experimental vehicle (IXV). In: Proceedings of the 57th International Astronautical Congress (IAC 2006) Valencia, Spain from 2–6 October 2006. Paper IAC-06-D2.6.5

10. Cosson E, Giusto S, Del Vecchio A, Mancuso S (2008) Overview of the in-flight experiments and measurements on the IXV experimental vehicle, ESA SP-659. The 6th European Symposium on Aerothermodynamics for Space Vehicles, 3–6 November 2008, Versailles, France
11. Tran P, Dormieux M, Fontaine J, Gulhan A, Tribot JP, Binetti P, Walloschek T (2008) FLPP IXV re-entry vehicle, hypersonic aerodynamics characterization, ESA SP-659. Paper presented at the 6th European symposium on aerothermodynamics for space vehicles, Versailles, 3–6 November 2008
12. Kapteijn C, Maseland H, Chiarelli C, Mareschi V, Tribot J-P, Binetti P, Walloscheck T (2008) FLPP IXV re-entry vehicle, supersonic characterization based on DNW SST wind tunnel tests and CFD. Paper presented at the 6th European Symposium on Aerothermodynamics for Space Vehicles, 3–6 November 2008, Versailles, France
13. Torngren L, Chiarelli C, Mareschi V, Tribot J-P, Binetti P, Walloschek T (2008) FLPP IXV re-entry vehicle, transonic characterization based on FOI T1500 wind tunnel tests and CFD". Paper presented at the 6th European Symposium on Aerothermodynamics for Space Vehicles, 3–6 November 2008, Versailles, France
14. Hannemann K, Schramm JM, Karl S (2008) Recent extensions to the high enthalpy shock tunnel GÖTTINGEN (HEG). In: 2nd international ARA days "10 years after ARD", Arcachon, France, 21–23 October 2008
15. Pezzella G, Rufolo G, Marino G (2012) Aerodynamic performance analysis of the IXV vehicle. In: 63rd international astronautical congress, IAC-2012, Naples, Italy, 1–5 October 2012. IAC-12-D2.6.3.p1
16. Hirshel EH (2005) Basics of aerothermodynamics. Springer, Berlin/New York. ISBN 3-540-22132-8
17. Anderson J (1994) Hypersonic aerothermodynamics. American Institute of Aeronautics and Astronautics, Inc., Washington, DC. ISBN 1-56347-036-5
18. Pezzella G, Battista F, Schettino A, Marini M, De Matteis P (2007) Hypersonic aerothermal environment preliminary definition of the CIRA FTB-X re-entry vehicle. In: West-east high speed flow field conference, Moscow, Russia, 19–22 November 2007
19. Rufolo G, Roncioni P, Marini M, Votta R, Palazzo S (2006) Experimental and numerical aerodynamic data integration and aerodatabase development for the PRORA-USV-FTB\_1 reusable vehicle. In: AIAA-2006-8031, 14th AIAA/AHI space planes and hypersonic systems and technologies conference, Canberra, Australia, 6–9 November 2006
20. Pamadi BN, Brauckmann GJ, Ruth MJ, Fuhrmann HD (2001) Aerodynamic characteristics, database development, and flight simulation of the X-34 vehicle. *J Spacecr Rocket* 38(3):334–344. ISSN 0022-4650. doi:[10.2514/2.3706](https://doi.org/10.2514/2.3706)
21. Pezzella G, Marini M, Roncioni P, Kauffmann J, Tomatis C (2009) Preliminary design of vertical takeoff hopper concept of future launchers preparatory program. *J Spacecr Rocket* 46(4):788–799. ISSN 0022-4650. doi:[10.2514/1.39193](https://doi.org/10.2514/1.39193)
22. Bird GA (1994) Molecular gas dynamics and the direct simulation of gas flows. Oxford Science, Oxford
23. Blanchard RC, Larman KT, Moats CD (1994) Rarefied-flow shuttle aerodynamics flight model. *J Spacecr Rocket* 31(4):550–556. doi:[10.2514/3.26477](https://doi.org/10.2514/3.26477)

# **Chapter 6**

## **Winged Re-entry Vehicles**

### **6.1 Introduction**

This chapter deals with the aerodynamic and aerothermodynamic performance analysis of reusable and unmanned vehicles conceived as flying laboratories to perform experimental flights returning from low Earth orbit (LEO). Therefore, each vehicle concept belongs to the class of orbital re-entry vehicle (ORV), e.g., re-entry energy of the order of 25 MJ/kg. Indeed, concepts under investigation in the present research effort are flying test beds (FTB) that will re-enter Earth's atmosphere, thus allowing to perform a number of experiments on critical re-entry technologies. For example, the primary objective is to test various in-flight thermal protection system (TPS) technologies and hot structures as potential candidates for the next-generation re-entry vehicles in representative flight conditions. The secondary objectives are to provide system design experiences for such re-entry vehicles, to address controlled gliding re-entry, and to validate know-how related to in-flight measurement techniques. Besides these objectives, the concepts are also aiming at providing aerodynamic and aerothermodynamic flight data to correlate with ground test (e.g., the CIRA Plasma Wind Tunnel "Scirocco") results, thus providing new insights into the understanding of complex aerothermodynamic phenomena occurring in flight and improving prediction methodologies (i.e., computational fluid dynamics, CFD) and extrapolation to flight capabilities. So far Europe has undertaken the development of three very different FTBs, namely, ARD (atmospheric re-entry demonstrator), Expert (European Experimental Re-entry Test Bed), and IXV (Intermediate Experimental Vehicle).

Based on past experience in experimental vehicles, a progressive flight demonstration approach is preferable to limit the risks, to allow progressive investment efforts, and to assure that more challenging developments benefit from results and findings obtained through a step-by-step approach.

**Fig. 6.1** The ARD capsule

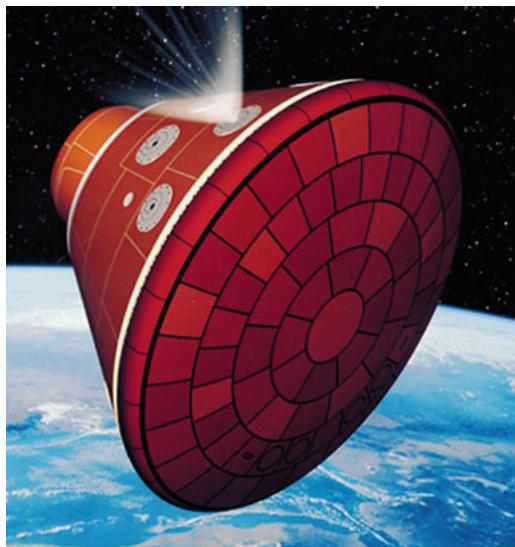
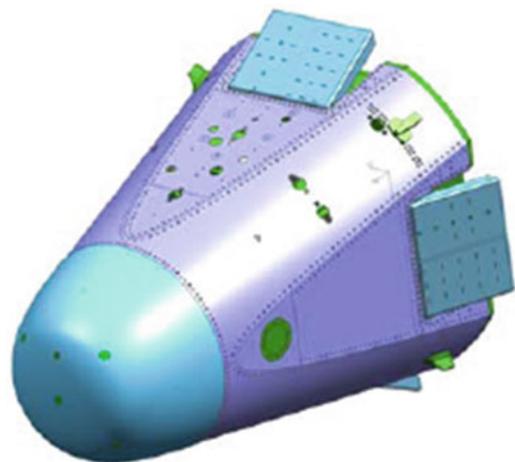


**Fig. 6.2** The EXPERT capsule  
(Courtesy of ESA)



ARD, shown in Fig. 6.1, was a scaled-down version of an Apollo capsule. It was launched by ARIANE 5 V503 on October 21, 1998 [1]. After a fully successful suborbital and re-entry flight, it was recovered in the Pacific Ocean [2]. ARD allowed Europe to assess the aerodynamics of such kind of capsule that still represents a very attractive design solution for what concerns manned high-energy re-entry (e.g., return from Mars/Moon missions).

Expert, not yet flown, is shown in Fig. 6.2. It a small sphere-cone FTB designed to perform several in-flight experiments, such as advanced thermal protection system (TPS), wall catalyticity, flow transition assessment, etc [3].

**Fig. 6.3** The IXV (Courtesy of ESA)



Finally, the Intermediate Experimental Vehicle, which is still under development by the European Space Agency (ESA), is shown in Fig. 6.3. It is a rather blunt FTB which features a lifting-body configuration [4]. It undertaken re-entry flight conditions, on February the 11th 2015, at the end of a suborbital flight, characterized by an energy level very close to that of an orbital re-entry (e.g., 25 MJ/kg) [5].

IXV will allow addressing several in-flight experiments like GN&C of a flapped lifting-body aeroshape, TPS catalyticity, etc. The aerodynamic and aerothermodynamic characterization of IXV can be found in Chap. 5.

As shown, FTB developed so far belong to the class of capsule and lifting-body vehicles only. Therefore, in a framework of a step-by-step approach with increasing level of complexity, only wing–body configurations have to be explored, as discussed in the present research effort.

Generally speaking, a reusable ORV operates at different flight regimes from subsonic to hypersonic speeds. A typical mission profile includes:

- *Ascent phase*, where the spacecraft is attached to a launch vehicle and placed at an orbit altitude
- *Orbit phase*, where the vehicle orbits in space till completion of desired mission
- *Descent phase*, where the ORV re-enters in the atmosphere and lands like a conventional airplane for subsequent reuse

During the descent up to the landing phase, the spacecraft encounters several flowfield regimes (i.e., rarefied, transitional, and continuum flow) and speed flow (i.e., hypersonic, supersonic, transonic, and subsonic flow). Therefore, the choice of vehicle aeroshape and its aerodynamic characterization at different flight conditions is fundamental for safe return and successful mission accomplishment.

Usually, the vehicle configuration is continuously adapted throughout the design phase by means of a trade-off study (e.g., multidisciplinary design optimization, MDO) involving several competing concepts according to the satisfaction of mission requirements and design constraints. For example, the vehicle concept will have to be carried to low Earth orbit with a small launcher and re-enter the atmosphere

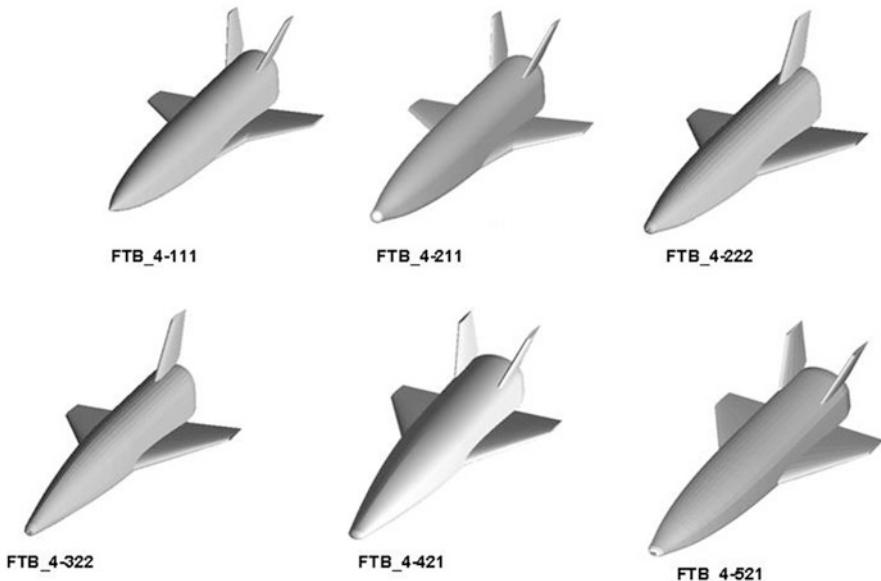


**Fig. 6.4** FTB trade-off configurations

allowing performing a number of experiments on critical re-entry technologies, being able to perform a descent flight from hypersonic regime down to landing. In Fig. 6.4 some of the most promising wing–body configurations, considered within trade-off analyses, are reported.

As shown, such configurations differ in terms of several vehicles' features as, for example, planform shape, cross section, nose camber, wing swept angle, and vertical empennages. Of course the winning configuration from the aerothermal point of view is the one showing, at the same time, the best aerodynamic and aerothermodynamic performances.

Right now the most promising vehicle configurations, resulted from trade-off design analyses, are shown from Figs. 6.5, 6.6, 6.7, and 6.8.

Side views of concept configuration are provided in Fig. 6.5, where ranging from up to down the rather blunt, sharp, and spatuled body configurations are reported.

Figure 6.6 shows the rather sharp vehicle configuration, namely, ORV-WSB. In this figure the concept also docked with the service module with deployed solar panels (e.g., orbital stationing phase) [6, 7].

The rather blunt configuration, named ORV-WBB, is provided in Fig. 6.7 [7].

Finally, Fig. 6.8 displays a spatuled body (SB) configuration, namely, ORV-SB [7].

This kind of vehicle configuration is most attractive considering that it represents the only viable way to accomplish and optimize the integration of scramjet propulsion with the vehicle aerodynamic configuration (see Fig. 6.9, where the ORV-SB

**Fig. 6.5** Rather blunt (*up*), sharp (*middle*), and spatuled body configurations

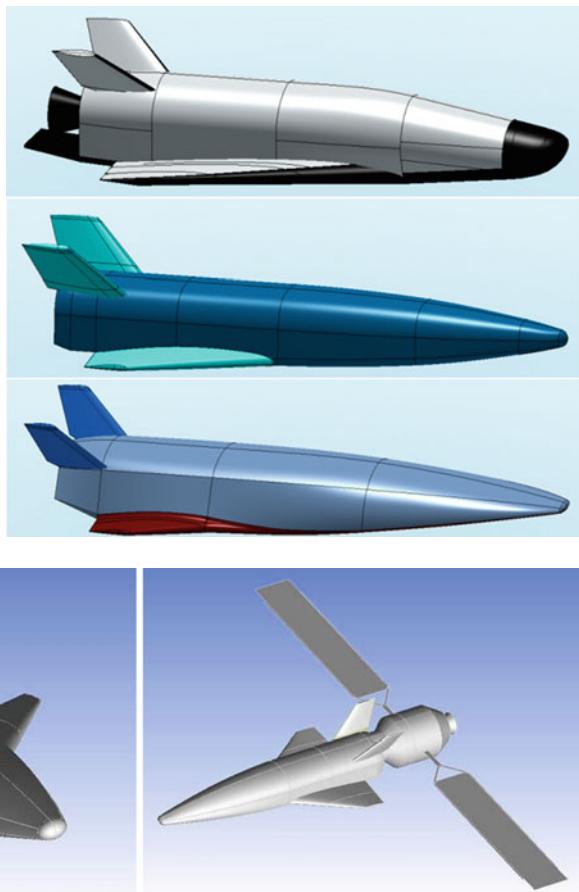
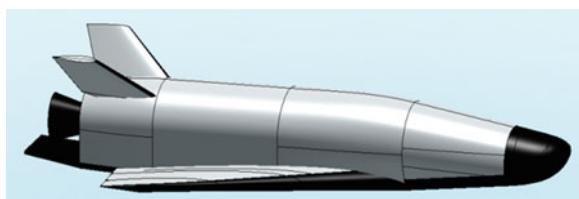


**Fig. 6.6** Rather sharp vehicle configuration and the service module with solar panels

**Fig. 6.7** Rather blunt vehicle configuration



features a scramjet engine on the belly side), thus evolving toward waverider aeroshape [8].

Indeed, since the beginning of aviation, the trend in aircraft design has been toward greater speed. The next frontier of speed envelope is travel at hypersonic speeds. One of the most practical and efficient approaches to travel at these high speeds is known as the waverider. Figure 6.10 shows that concerning

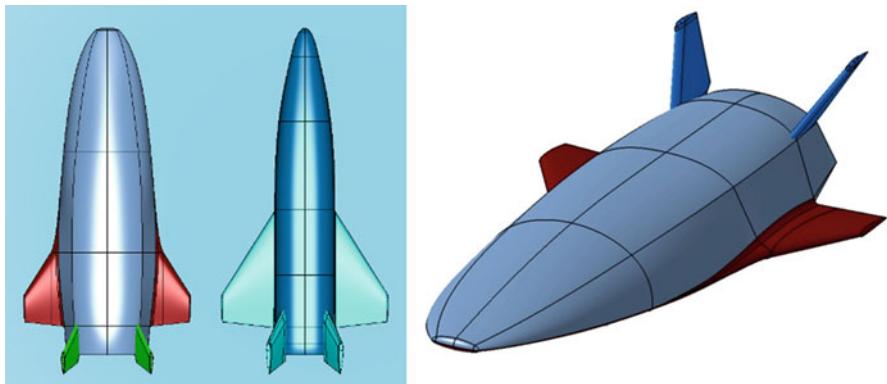


**Fig. 6.8** The spatular body configuration

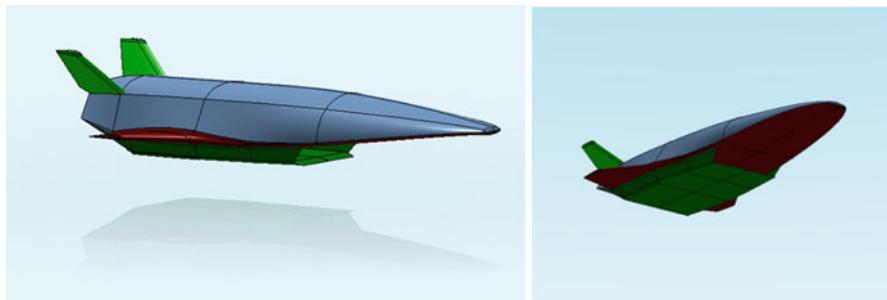


**Fig. 6.9** The spatular body configuration with scramjet

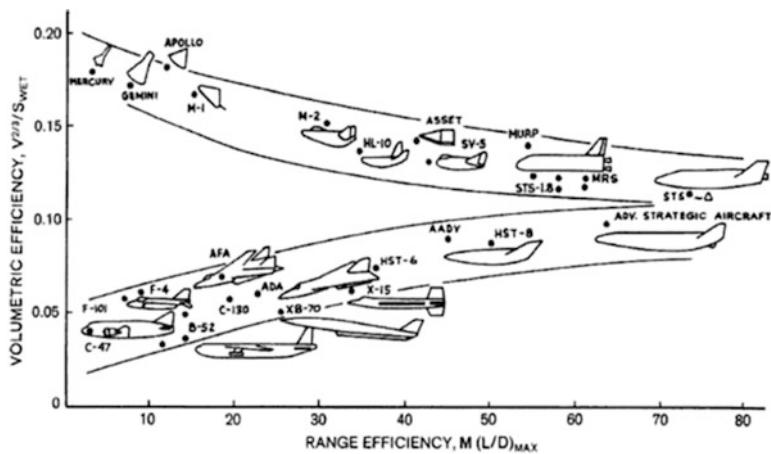


**Fig. 6.10** Space and atmospheric vehicle development coverage.  $M$  = Mach number

high-performance flight vehicle architecture converges with the technology of air-breathing configuration. Such a configuration demands high aerodynamic efficiency [8].

For instance, the infinitely thin flat plate represents the most efficient hypersonic lifting surface. The lift-to-drag ratio of the flat plate is the highest that can be achieved at hypersonic speeds. However, the flat plate is obviously not practical, especially since it cannot contain any volume for payload, engines, fuel, etc. Therefore, a more realistic configuration design converges to spatular vehicle architecture.

The characteristics of this design are: very small frontal area and highly streamlined shape to minimize total surface area; very little wing area, but the fuselage is often shaped to generate additional lift; and propulsion assembly highly integrated into the vehicle.

Anyway, all ORV concepts belong to the wing–body vehicle class. Such configurations, however, differ in terms of nose camber, planform shape, cross section, wing swept angle, and vertical empennages.

Differences in concept aeroshape can be clearly appreciated in Fig. 6.11, where each configuration is over imposed on each other.

These aeroshapes are conceived in such a way to allow the ORV concept to re-enter the Earth atmosphere exhibiting an aerodynamic efficiency (L/D) in excess with respect to the Space Shuttle vehicle, which show a maximum L/D ratio of about 1. ORV shall fly a re-entry trajectory with long-endurance leg in the higher sensible atmosphere, using “low” (with respect to the Shuttle guidance approach) and modulated angle of attack (AoA) guidance.

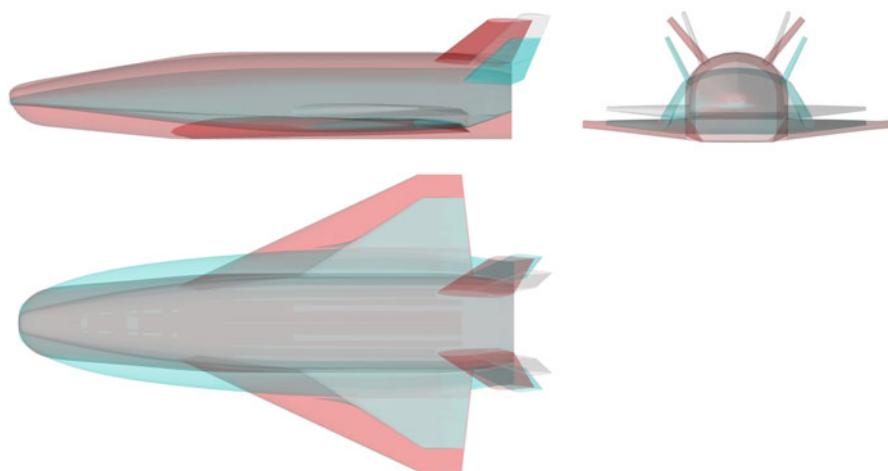


**Fig. 6.11** ORV aeroshapes comparison

This shall assure a number of benefits, such as:

- To overcome the critical heat flux region in a quasi-thermal equilibrium condition that shall assure that internal structure temperature may remain under the peak temperature that a steep re-entry can produce
- To expose small vehicle parts to the higher heat flux, to protect with an advanced TPS such as ultra-high-temperature ceramics (UHTC), but leave the most vehicle surface to lower heat flux, so to allow the use of simpler material, that is in terms of cost and weight.

In this framework, this research effort provides a review analysis of aerodynamic performances of these ORVs from hypersonic down to subsonic regime. Both low-order methods (i.e., hypersonic panel methods) and CFD design analysis have been considered to assess vehicle aerodynamic characteristics, compliant with a phase A design level.

At this early design stage, low-order methods are extensively used, while CFD simulations are performed only to address the reliability of low-order method design results and to investigate on complex flowfield phenomena not predictable with simplified tools [9–11].

Indeed, both perfect gas and thermochemical nonequilibrium CFD simulations are performed at several points of the flight scenario in the range between Mach 0.3 to Mach 25. In the reacting gas computation, the air is modeled as a mixture of five species (i.e., O<sub>2</sub>, N<sub>2</sub>, NO, N, and O).

An analysis of the longitudinal and lateral-directional stability has been also provided for one concept, together with some of the main interesting features of the flowfield past the vehicles at different Mach numbers as those where real gas effects occur. In fact, it is well known that the pitching moment can be highly modified by high-temperature real gas effects, thus affecting the vehicle's stability behavior and trimming conditions [12].

## 6.2 Vehicles Description

Vehicle concepts feature a compact wing–body configuration equipped with a rounded edge delta-like fuselage cross section, a delta wing, and V-tail. The vehicle architecture shows a blended wing–body interface and a flat bottomed surface to increase its overall hypersonic performance. The fuselage was designed to be longitudinally tapered, in order to improve aerodynamics and lateral–directional stability, with a cross section large enough to accommodate all the vehicle subsystems, for example, the propellant tanks of the reaction control system (RCS) to cope with the requirement of long mission duration.

The fuselage's cross section has a large impact on vehicle performance. In fact, from the aerodynamic point of view, the lift and the aerodynamic efficiency are mainly determined by the fuselage fineness and by the shape of the vehicle cross section [13].

The forebody is characterized by rather simple cone–sphere geometry with smooth streamlined surfaces on the upper and lower side of fuselage and by the nose drop-down configuration, typical of winged hypersonic vehicles.

The nose camber is low enough to reduce elevon size in order to provide desired trim range and to improve internal packaging. The wing size and location were defined on the basis of trade-off studies so to improve vehicle aerodynamics and to provide static stability and controllability during flight [9, 11, 14].

Finally, the wing is swept back to assure best performance with respect to supersonic drag and aerodynamic heating. A properly designed strake could be added in the future, depending on the confirmation of a specific landing requirement. A wing dihedral angle of  $5^\circ$  is also provided to enhance vehicle lateral–directional stability.

The wing also features a high length-to-width ratio to minimize drag, and a section shape that is maintained from root to wing tip; and a nearly flat bottomed surface to efficiently dissipate aeroheating. Vertical tails sweep angle is  $45^\circ$ .

Control power for vehicle is provided by two wing-mounted elevon surfaces (which must serve as ailerons and elevators) and rudder surface. Used symmetrically, the elevons are the primary controls for the pitch axis, i.e., pitch control. Roll control is obtained through asymmetrical usage of these elevons. Rudders help to provide the directional control, i.e., sideslip stability.

During entry, when the vehicle is flying at high angles of attack, rudders should be augmented by RCS. For example, Fig. 6.12 shows the ORV-WSB concept with RCS pods on base. The arrows indicate the thrust provided by each pod. Therefore, opportunely combining the thrust vectors, one is able to control vehicle pitch, roll, and yaw.

Then, the vehicle may be provided by a body flap located at the trailing edge of the fuselage in order to augment pitch control and to shield the nozzle of propulsion subsystem (see ORV-WBB in Fig. 6.7). Indeed, trim capability to relieve elevon

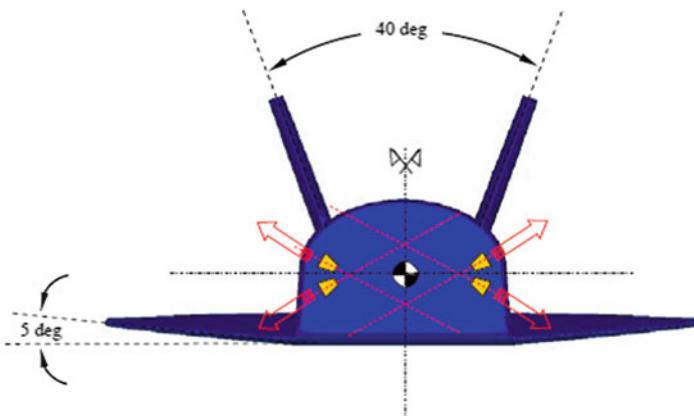


**Fig. 6.12** ORV-WSB dihedral angles with RCS pods on base

loads is obtained by body flap deflection. A surface behind the vehicle CoG balances the nose-up pitching moment typical of such kind of configuration at hypersonic speeds.

Finally, the aerodynamic control surfaces are designed to be large enough to provide stability without sacrificing too much lift.

### 6.3 Flight Scenario and Flow Regime Assessment

ORV aims to perform a complete re-entry flight from LEO at 200 km. The return trajectory is based on strategy, alternative from the guidance point of view. The vehicle will be held as long as possible in the highest sensible atmosphere layers, compatibly with the descent thermal constraints. An improved gliding re-entry and a high maneuvering capability, as compared to the reference re-entry of the Space Shuttle, characterized by moderate angle of attacks (up to 20°) and a longer flight duration are developed. This also allows for more extended in-flight testing capabilities in high-energy hypersonic flight conditions. In the framework of the Flight Mechanics trade-off analyses, several re-entry trajectories have been computed, thus defining a vehicle flight envelope needed to address vehicle aerodynamic. For example, Figs. 6.13 and 6.14 show a number of re-entry trajectories evaluated supposing that the vehicle heat flux constraint ranges between 1.1 and 2 MW/m<sup>2</sup>, while the dynamic pressure limit is equal to 12 kPa. The Mach–Reynolds numbers grid in the altitude–velocity map of Fig. 6.14 is also reported in order to characterize vehicle aerodynamics, according to the space-based design approach [15].

It is possible to note that the re-entry time reaching value close to about 5,000 s is larger than the one of a conventional re-entry as, for example, that of the Space Shuttle. Note that for each trajectory shown in Fig. 6.13, the guidance technique is the same, but the AoA profiles are different (see Fig. 6.13 right side). Typically, the more common approach to the definition of the guidance strategy makes use of a predefined AoA profile, characterized by high values for the most critical re-entry phase, during which the heat flux is critical for the vehicle safety. Instead, the

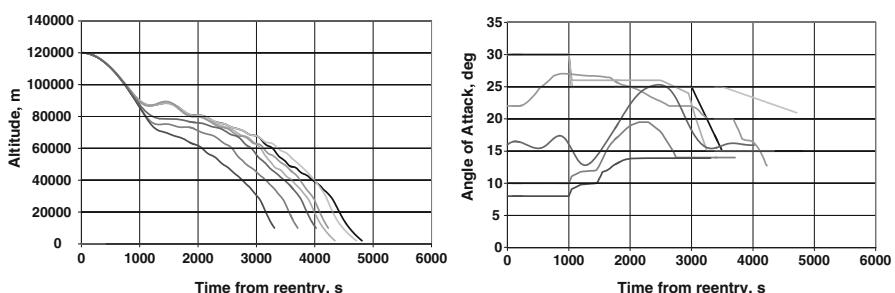


**Fig. 6.13** Time history of ORV flight envelope and AoA profiles

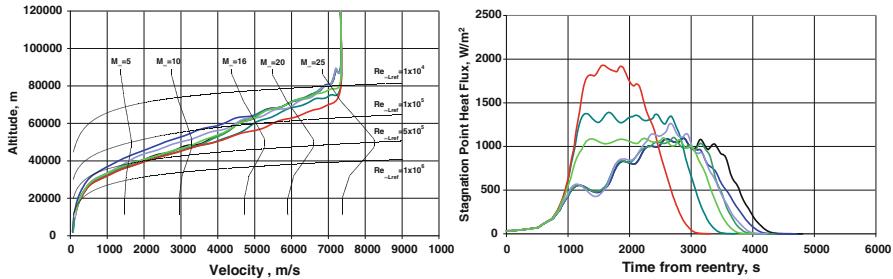


**Fig. 6.14** The ORV flight envelope in the velocity–altitude map and time history of stagnation-point heat flux profiles

bank angle control is usually applied in such a way that the flight path can follow a predefined drag versus velocity profile and realize the required cross-range.

An alternative approach has been adopted here, in order to be compliant with the specific ORV project requirement. The strategy we would experiment in the orbital re-entry mission of the FTB is to modulate the AoA profile during critical entry phases. The angle of attack will be taken as close as possible to the one corresponding to the maximum efficiency (at least in the “dense” atmosphere range), compatibly with the maximum heat flux the vehicle (TPS and cold structure) could sustain.

This kind of AoA guidance profile should allow benefiting of a number of factors, such as to have greater vehicle maneuverability along the trajectory and as to expose a smaller part of the vehicle to the higher heat flux, then allowing a thermal protection system mass reduction and increasing the mission safety level. For instance, the optimized long-endurance trajectories are characterized (for a relevant part of the trajectory) by a quasi-steady thermal equilibrium condition near the maximum admissible heat flux value at the stagnation point (see Fig. 6.14 right side), thus taking advantage of radiative cooling.

As far as flight regimes assessment is concerned, it is worth noting that along with the atmospheric re-entry trajectory, going from upper to lower altitude, the vehicle experiences three main flow regimes. They are the *hypersonic-supersonic regime*, concerning the upper part of descent trajectory; the *transonic regime*; and the *subsonic regime*, regarding the flight within lower atmospheric layers.

Moreover, within the hypersonic speed flow, three main and heavily overlapping regimes apply. They are the *rarefied-transitional regime*, on the one hand, and the *viscous interaction regime* and the *real gas regime*, on the other hand, which lie in the continuum flow regime.

As a consequence, the knowledge of that part of vehicle re-entry trajectory, where each one of all these flight regimes is established, is extremely important in order to address vehicle performances. For example, it is well known that real gas and viscous effects play a significant role in the vehicle aerodynamics (e.g., drag rise and trim conditions) and aerothermodynamics.

This also means that vehicle design demands different flow model, ranging from perfect gas to reacting gas mixture, and flowfield solution approach, ranging from Direct Simulation Monte Carlo (DSMC) to Navier–Stokes with and without slip flow conditions to provide a valuable description of key flow phenomena affecting vehicle aerodynamic and aerothermodynamic characteristics.

### 6.3.1 Rarefied-Transitional Regimes

Once the concept vehicle started its descent, the atmospheric density is low enough such that the continuum assumption breaks down, and one must begin to consider the general microscopic mass, force, and energy transfer problem at the vehicle surface since individual molecular collisions are important.

In this regime, two distinctions can be made. They are the re-entry through the upper part of the atmosphere and that through the lower part of the high atmosphere. In the former the free molecular regime (FMR) is completely established, while in the latter the transitional flow regime (TFR) applies. Of course, the limit between these two flow conditions depends on altitude and vehicle dimensions. For instance, the similarity parameter that governs these different flow regimes is the Knudsen number, defined as (rarefaction parameter)

$$\text{Kn}_{\infty L_{\text{ref}}} = \frac{\lambda}{L_{\text{ref}}} = 1.25\sqrt{\gamma} \frac{M_{\infty}}{Re_{\infty L_{\text{ref}}}} \quad (6.1)$$

where  $\lambda$  is the molecular mean free path,  $L_{\text{ref}}$  is the characteristic length of the body, and  $\gamma$  is the specific heat ratio. Indeed, when the air density becomes rarefied enough, the molecular mean free path ( $\lambda$ ) can become as large as the scale of the body itself. This condition is indeed known as free molecular flow (FMF) regime. In this condition, the aerodynamic characteristics of the vehicle are determined by individual, scattered molecular impacts and must be analyzed on the basis of kinetic theory. So that, several particle simulations, e.g., DSMC analyses, are mandatory. FM flow conditions result in an abrupt loss of vehicle aerodynamic efficiency due to a suddenly increase of drag and lift drop. Falling further in the atmosphere (i.e., higher  $\lambda$ ), the TFR is established. DSMC approach is still valid but demands high computational effort to account for the increasing number of molecules to simulate. Fortunately, in this flow conditions, the slip conditions and temperature jump can be introduced in the continuum approach (i.e., Navier–Stokes approximation) to take into account for the rarefaction effects.

The rarefied and transitional regimes for ORV concepts are recognized in Fig. 6.15.

In this figure the ORV re-entry trajectory is reported in the Mach–Reynolds numbers map together with iso-Knudsen curves which bound the different flow regimes, according to the Bird regime classification [16, 17]. As one can see, the region for  $10^{-3} < \text{Kn}_{\infty} < 10$  is the transitional flow region. Therefore, above about 200 km altitude ORV is in FMF (in fact,  $\text{Kn}_{\infty L_{\text{ref}}} \approx 70$ ), while ranging from entry

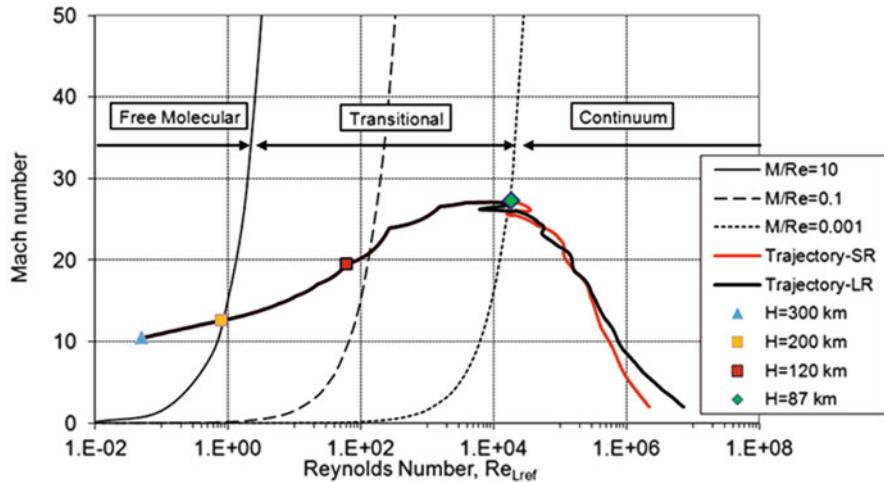


**Fig. 6.15** ORV re-entry scenario in the Mach–Reynolds map with iso-Knudsen curves

interface (e.g., 120 km, red square in Fig. 6.15) to about 87 km (green rhombus in Fig. 6.15), the vehicle is flying in the transitional flow regime. Finally, after that continuum flow conditions are, then, established.

### 6.3.2 Viscous Interaction Regime

It is the flow regime where, due to low Reynolds number and high Mach number effects, the boundary layer and the shock layer merge into a viscous shock layer enveloping the vehicle concept. This result in a loss of ORV aerodynamic performance provided that vehicle drag, in this regime, is expected to rise up, thus lowering spacecraft aerodynamic efficiency.

Generally speaking, the viscous interaction regime is defined by the hypersonic viscous interaction parameter (VIP) that reads:

$$\bar{V}'_{\infty} = M_{\infty} \sqrt{\frac{C'_{\infty}}{Re_{\infty L_{ref}}}} \quad (6.2)$$

where

$$C'_{\infty} \propto f \left( \frac{T'}{T_{\infty}} \right) \quad (6.3)$$

and

$$\frac{T'}{T_{\infty}} = 0.468 + 0.532 \frac{T_w}{T_{\infty}} + 0.195 \frac{\gamma - 1}{2} M_{\infty}^2 \quad (6.4)$$

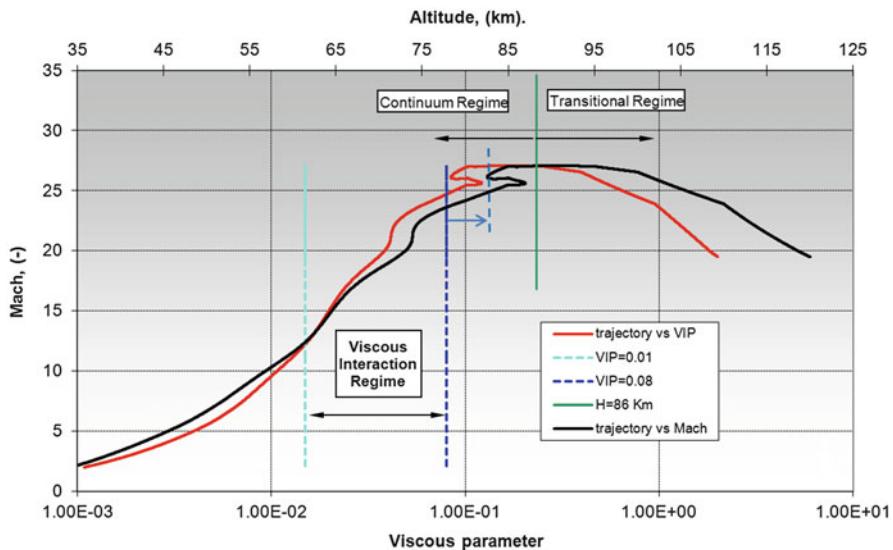


**Fig. 6.16** ORV re-entry trajectory in the Mach/altitude-viscous parameter map

By using reference enthalpy concepts, to account for compressibility effects, an estimation of the viscous interaction regime for the ORV can be found in the Fig. 6.16. In this figure the vehicle re-entry trajectory both by means of altitude vs. Mach curve and Mach vs. viscous interaction parameter (VIP) curve is reported. As shown, two boundaries are also reported in the figure according to the criterion chosen in the past to address the viscous interaction regime (VIR) for the Space Shuttle. Therefore, very roughly one can conclude that for the ORV the VIR ranges from about 60 to 83 km that is close to the boundary of 86 km highlighted for the beginning of the transitional flow regime.

### 6.3.3 Real Gas Regime

The equilibrium/nonequilibrium real gas regime is characterized by relatively high density and still high velocity flow conditions.

For instance, the highest thermal environment is encountered, and many chemical reactions occur. Therefore, the modeling of such phenomena requires enforcing the Navier–Stokes equations with several data such as chemical equilibrium constants as well as reaction rates for the reaction mechanism involving all the species which compose the gas mixture at the specified flight conditions.

In this framework, the current ORV nominal re-entry trajectory is illustrated in Fig. 6.17, in the altitude–velocity map, where the real gas phenomena occurring during re-entry and relevant for the vehicle AEDB/ATDB are reported.

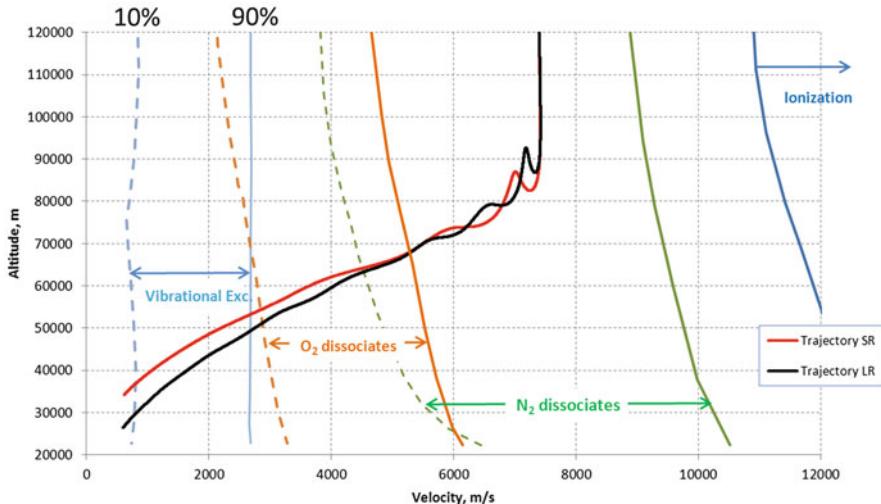


**Fig. 6.17** ORV re-entry scenario in the altitude–velocity plane with real gas map

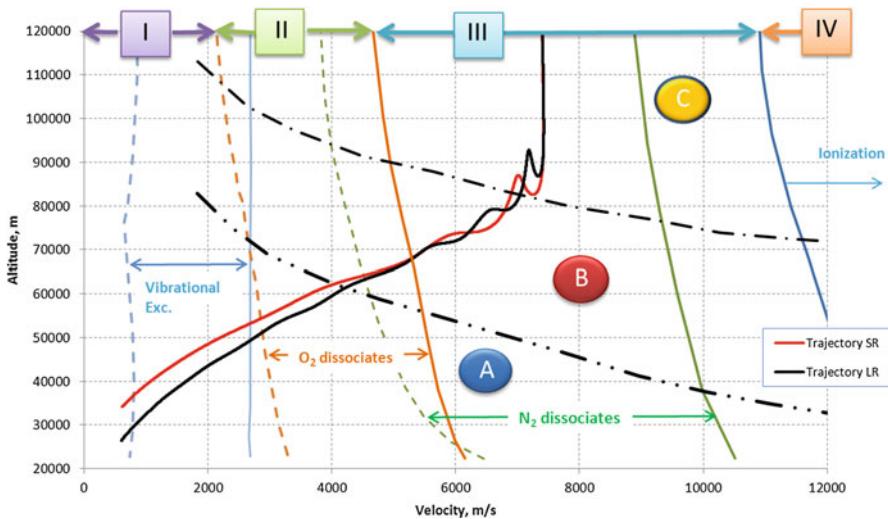
For instance, Fig. 6.17 highlights that when the ORV is flying at 6 km/s at about 70 km altitude, oxygen is completely dissociated because we are at velocity larger than that corresponding to the O<sub>2</sub> dissociated domain. On the other hand, nitrogen begins to dissociate because we are near the green dashed line which represents the N<sub>2</sub> 10 % dissociation boundary. Indeed, the high-energy content of re-entry flows leads to strong heating of the air in the vicinity of vehicle concept. Depending on the temperature level behind the bow shock wave (i.e., the flight velocity), the vibrational degrees of freedom of the air molecules are excited, and dissociation reactions of oxygen and nitrogen molecules may occur.

Anyway, the high-temperature real gas effects described here are enabled by energy transfer from the translational energy stored in the random motion of the air particles, which is increased by the gas heating, to other forms of energy. Because this energy transfer is realized by air particle collisions, it requires a certain time period to develop.

The time required to reach an equilibrium condition is defined by the local temperature and density. Therefore, depending on the ratio of the relaxation time to a characteristic timescale of the flow, the chemical and thermal relaxation processes can be in nonequilibrium, in equilibrium, or in frozen flow, thus influencing the vehicle aerodynamic and aerothermodynamic performances as, for example, pitching trim and heat flux conditions along with the re-entry flight.

For instance, the similarity parameter that governs the thermochemical regimes is the Damkohler (Da) number, defined as

$$\text{Da} = \frac{t_c}{t_r} = \frac{\text{characteristic flow time}}{\text{characteristic relaxation time}} \quad (6.5)$$



Region with chemical and thermal nonequilibrium	
Region	Aero thermal ph.
A	Chemical and thermal equilibrium
B	Chemical nonequilibrium with thermal equilibrium
C	Chemical and thermal nonequilibrium

Chemical species in high-temperature air		
Region	Model	Species
I	2 species	O <sub>2</sub> , N <sub>2</sub>
II	5 species	O <sub>2</sub> , N <sub>2</sub> , O, N, NO
III	7 species	O <sub>2</sub> , N <sub>2</sub> , O, N, NO, NO <sup>+</sup> , e <sup>-</sup>
IV	11 species	O <sub>2</sub> , N <sub>2</sub> , O, N, NO, NO <sup>+</sup> , O <sup>2+</sup> , N <sub>2</sub> <sup>+</sup> , O <sup>+</sup> , N <sup>+</sup> , e <sup>-</sup>

**Fig. 6.18** Re-entry scenario in the altitude–velocity plane with the stagnation-point flow regimes and thermochemical phenomena

where the relaxation time refers both to chemical reaction and to internal degrees of freedom of the flow molecules [17–19].

Figure 6.17 also suggests that there will be an increasing number of species occurring in the different domains along with the descent trajectory. Therefore, accurate CFD simulations, in the vehicle design analysis, must rely on a flow thermochemical model opportunely tuned on the base of trajectory point to simulate. In fact, due to the continual exchange of energy between the transitional and internal degrees of freedom of the flow molecules, the air results in a mixture in thermal and/or chemical nonequilibrium in the different domains of the altitude–velocity map, as recognized in Fig. 6.18.

This figure provides several insights into the trends which should be expected in the flight stagnation region air chemistry of the ORV forebody. For instance, Fig. 6.18 shows three different regions with chemical and thermal nonequilibrium, namely, A, B, and C. Region A deals with chemical and thermal equilibrium. Region B deals with chemical nonequilibrium and thermal equilibrium. Finally, C reports the region of chemical and thermal nonequilibrium.

So that, looking at this chart, one can rapidly assess the thermochemical model to most likely consider in the high-fidelity CFD simulation once free-stream conditions are known.

### 6.3.4 Laminar-to-Turbulent Transition

During descent re-entry, vehicles experience transition from fully laminar to fully turbulent flow conditions; in the latter case both aerodynamic drag and aeroheating increase must be accounted for in vehicle design. For example, heat flux at vehicle wall may increase up to 4–5 times that expected in laminar flow conditions. Therefore, the assessment of flight conditions (e.g., altitude, Mach, and attitude) at which takes place laminar-to-turbulent transition represents a critical design issue. Indeed, boundary-layer transition is usually based on local flow conditions such as local Mach and Reynolds numbers.

For example, an empirical correlation for hypersonic transition that has found some use is the transition criterion based on the parameter  $Re_\theta/M_e$  [20–22].

$$\frac{Re_\theta}{M_e} = 100 \quad (6.6)$$

Here,  $Re_\theta$  is the momentum thickness Reynolds number and  $M_e$  the boundary-layer edge Mach number. This criterion was used for the preliminary design of the space shuttle. Practically, through experimental investigations, designers try to correlate the value assumed by the parameter  $Re_\theta/M_e$  in correspondence of the transition front detected in wind tunnel (Fig. 6.20).

Applying this process to X-33 experimental test campaign yielded values between 250 and 325 so that an average value of  $Re_\theta/M_e = 285$  was chosen for this vehicle (see Fig. 6.19 and Fig. 6.20).

A relationship for transition at a body point was derived by interpolation of the LATCH database to locate the altitudes where transition occurs for all combinations of velocity and angle of attack. Figure 6.21 shows this relationship using the X-33 criterion ( $Re_\theta/M_e = 250$ ) and a point at  $x/L = 0.8$  on the windward centerline. The result is a nearly planar surface in three-dimensional trajectory space that separates laminar flow above from turbulent flow below. In practice, this function can be used to identify regions of transition by plotting a trajectory in this space and locating the point where the path intersects the surface as shown in the figure.

However, because the assessment of the local flow condition demands accurate CFD computations which are, of course, not compliant with a phase A design level, a transition method based on free-stream Reynolds ( $Re_\infty$ ) and Mach ( $M_\infty$ ) numbers has been adopted.

For example, Fig. 6.22 reports the transitional Reynolds limit evaluated by means of the following transition criterion:

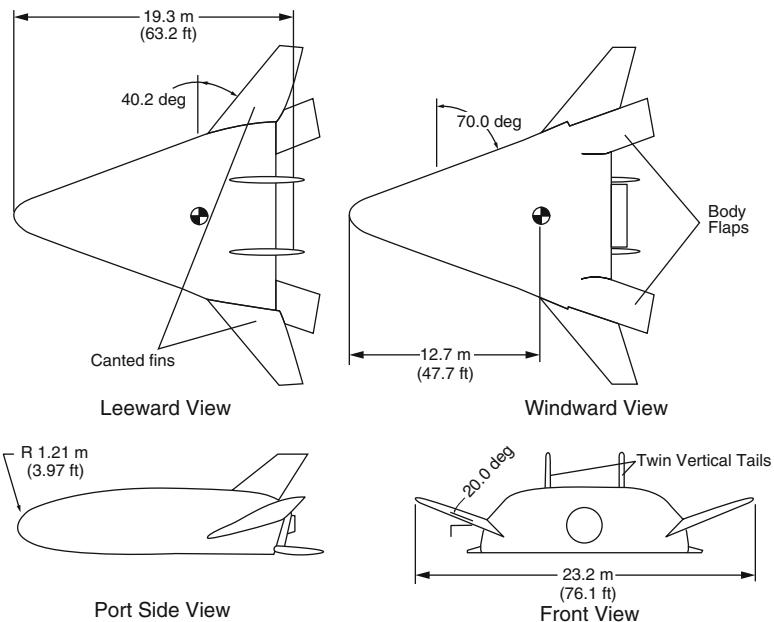


**Fig. 6.19** Primary geometric features of the Lockheed-Martin X-33 vehicle

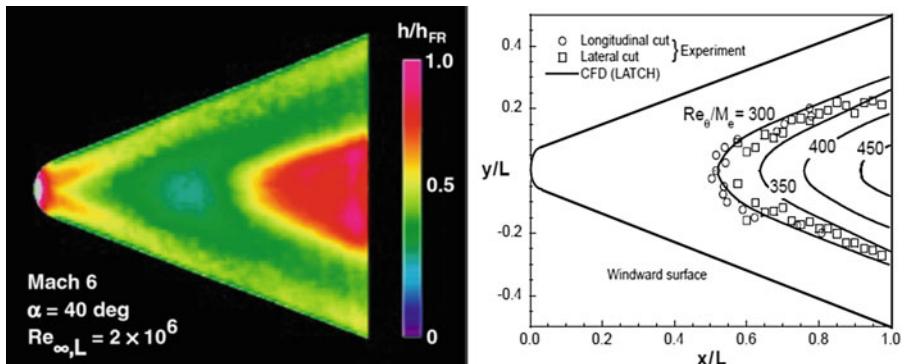


**Fig. 6.20** Correlation of boundary-layer transition on “smooth” X-33 forebody

$$\log Re_{\infty} > [\log Re_T + C_m(M_{\infty})] \quad \text{turbulent flow} \quad (6.7)$$

where  $Re_T$  and  $C_m$  depend on the type of flow, flying AoA, leading edge sweep angle, and leading edge nose bluntness. As shown, transition criterion highlights that below about 46 km altitude, turbulent flow conditions are expected.

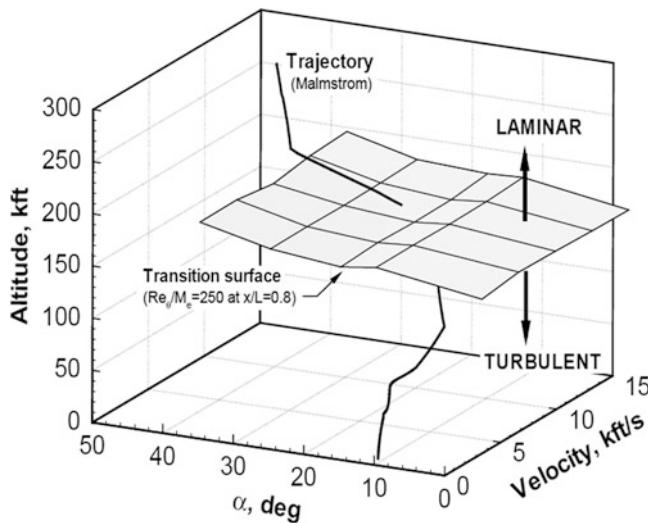


**Fig. 6.21** Transition criterion in trajectory space

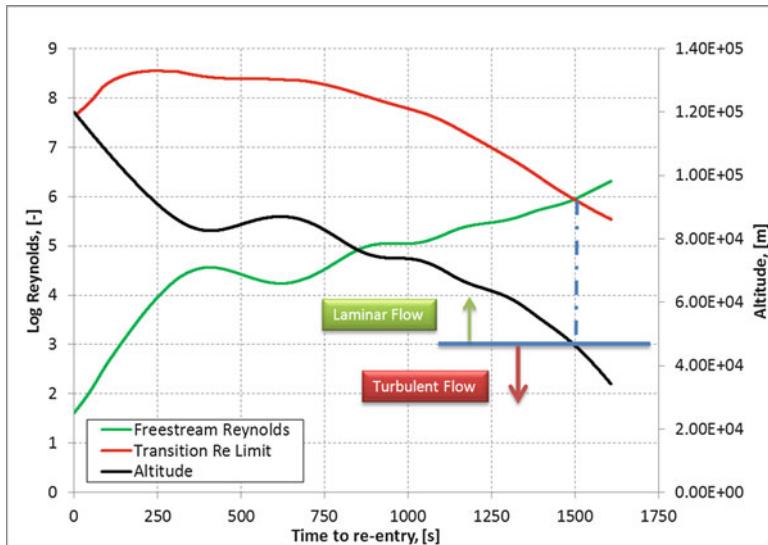


**Fig. 6.22** Assessment of laminar-to-turbulent transition

## 6.4 Design Approach and Used Tools

A summary review of the aerodynamic database (AEDB) of vehicle concepts is herein performed. These evaluations are aimed only to carry out a preliminary AEDB for such configurations, compliant with a phase A design level [14–16]. The

activities' goal is to provide aerodynamic characteristics for Flight Mechanics and thermal shield design analyses. In fact, it must be verified that vehicle, after deorbit maneuver, is able to stay within the load constraints (e.g., entry corridor) flying trimmed during descent up to conventional runway landing. The AEDB has been provided as a function of Mach number, angle of attack, sideslip angle, aerodynamic control surface deflections, and Reynolds number, according to the space-based design approach [15]. This design approach dictates the generation of a complete data set as function of a number of independent parameters (i.e.,  $M_\infty$ ,  $Re_\infty$ ,  $\alpha$ ,  $\beta$ ) as schematized in Fig. 6.23.

An accurate aerodynamic analysis of all these flight conditions, however, is very complex and time consuming and is not compatible with a phase A design study, in which fast predicting methods are mandatory. In the preliminary design phases, the evaluation of the vehicle AEDB is mainly accomplished by means of engineering tools and a limited number of more reliable CFD computations (continuum regime only), according to the work flow shown in Fig. 6.24 [16–18].

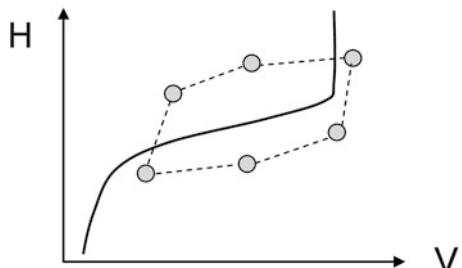


**Fig. 6.23** Space-based design approach in the altitude–velocity map

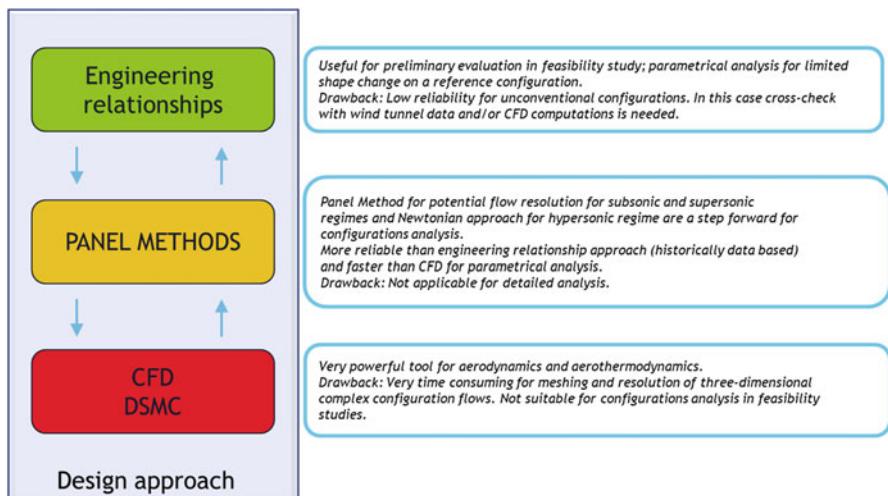


**Fig. 6.24** Tools and methods of present design approach

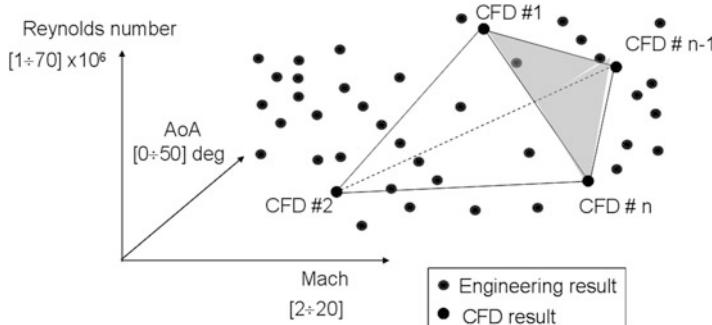


**Fig. 6.25** Hypothetical CFD anchoring mesh in Reynolds–Mach–AoA space

Indeed, CFD computations are performed in order to verify the attained accuracy and to focus on some critical design aspects not predictable with simplified tools. This overall process is referred to as “anchoring” of the engineering-level methods. The anchoring process permits a few, select, CFD solutions to be used beyond the specific flight conditions at which they were original run.

Moreover, the anchoring process allows for the cost-effective use of high-fidelity, and computationally expensive, CFD solutions, early in the design process when the vehicle trajectories are often in a constant state of change [17, 18]. The CFD anchoring “space” is defined by a small number of CFD solutions in Reynolds–Mach–AoA space as shown in Fig. 6.25.

Note that CFD analysis is nevertheless essential in preliminary design studies, keeping in mind the limited capability of engineering-based approach to model complex flow interaction phenomena and aerodynamic interferences, as shock–shock and shock-wave–boundary-layer interactions.

Experience shows that an aerodynamic configuration which seems to be promising as evaluated by simplified methods is not always a feasible solution after performing more detailed calculations. But every layout deemed as infeasible by the preliminary aerodynamic examination has no reasonable chance of realization. Therefore, the approach implemented in the engineering-based approach is fully justified as it is much easier and more rapid to operate, and hence the assessment of rearrangements can be done extremely fast.

So, ORV aerodynamics in free molecular flow conditions has been provided with low-order methods; in the transitional flow regime (the one bridging the continuum and the free molecular regimes) the bridging relationships approach was applied, and, finally, in the continuum flow regime, vehicle aerodynamic appraisal is accomplished with both low-order and CFD methods.

Anyway, all aerodynamic data are provided in a format which will allow a buildup from a basic configuration by means of contributing elements to each force or moment component such as control surface effectiveness, sideslip effect, etc. Data are presented in a manner which treats each force and moment separately to facilitate the buildup procedure.

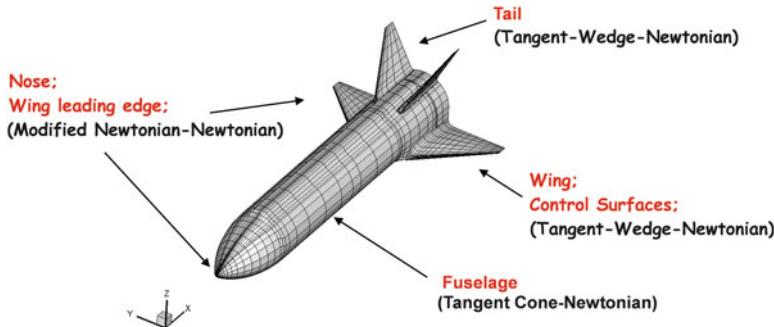


**Fig. 6.26** Design methodology. Representative flow models for hypersonic panel method code

In the framework of low-order methods codes vehicle aerodynamics has been addressed by means of HPM code, while CFD analysis for sub-transonic and hypersonic speed, both Euler and Navier–Stokes, has been carried out with commercial code FLUENT.

The HPM code is a 3-D Supersonic–Hypersonic Panel Method code, developed at CIRA, that computes the aerodynamic characteristics of complex arbitrary three-dimensional shapes by using surface inclination methods (SIM), typical of Newtonian aerodynamics, including control surface deflections and pitch dynamic derivatives [12, 14, 19].

Within HPM simulations, the surface is approximated by a system of planar panels, the lowest level of geometry used in the analysis being a quadrilateral element.

In Fig. 6.26 it is shown a typical surface mesh to be provided to HPM for design analysis.

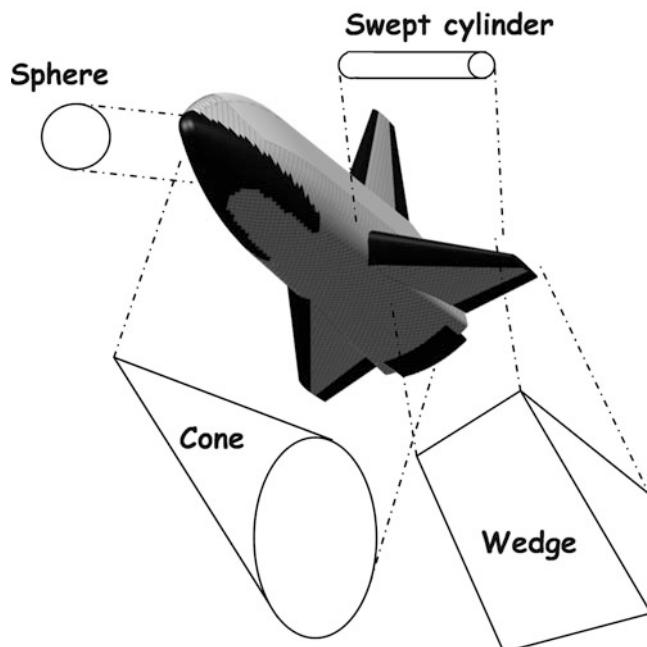
As one can see, the mesh differs with reference to finer ones, typically considered within CFD analysis. In this case, in fact, only surface inclination variations are accounted for by HPM analysis (e.g., Newtonian aerodynamics), so flat surfaces have a coarse mesh; while in presence of curvature, a more dense mesh is done. Therefore, surface mesh generation is a dedicated activity for the HPM design analysis.

As shown in the figure, the pressure acting on each panel is evaluated by user-specified compression–expansion and approximate boundary-layer methods. The methods to be used in calculating the pressure in impact and shadow regions of vehicle may be specified independently and can be selected by the user; several methods are available as reported in the following Table 6.1. More information about these theories can be found in Ref. [19].

These simplified methods apply considering that, as shown in Fig. 6.27, the generic vehicle configuration can be divided into a combination of simple shapes, i.e., cones, cylinders, flat plates, spheres, and wedges, for which analytical solutions are available. For example, the wing leading edge was represented by a swept

**Table 6.1** Available methods for inviscid analysis

Impact flow	Shadow flow
Modified Newtonian	Newtonian
Modified Newtonian–Prandtl–Meyer	Modified Newtonian–Prandtl–Meyer
Tangent wedge	Prandtl–Meyer empirical
Tangent wedge empirical	OSU blunt-body empirical
Tangent cone empirical	Van Dyke unified method
OSU blunt body	High Mach no. base pressure
Van Dyke unified method	Shock expansion method
Blunt-body skin friction	Input pressure coefficient
Shock expansion method	Free molecular flow
Free molecular flow	
Input pressure coefficient	
Hankey flat surface empirical	
Delta wing empirical	
Dahlem–Buck empirical	
Blast wave	
Modified tangent code	

**Fig. 6.27** Design methodology. Representative geometric models

cylinder in order to obtain estimates for the leading edge heating rates (outside of the shock–shock interaction region).

It is worth to note that this design approach is a viable option especially within vehicle aeroheating analysis.

In the usual hypersonic vehicle applications, Prandtl–Meyer expansion flow theory and tangent cone–wedge methods are widely applied, together with the modified Newtonian method. Note that the flow separation is not accounted for; hence, the obtained results are not reliable for cases where significant flow separations exist (i.e., the wing stall is not predicted).

The different parts of the vehicle (fuselage, wing, and vertical tail) are analyzed separately, and global vehicle aerodynamic coefficients are obtained by appropriate summation of the different component contributions, following a typical “buildup” approach, according to Fig. 6.26.

As far as the base drag is concerned, the following simple formula is used:

$$\Delta C_{D\text{base}} = -C_{P\text{base}} \frac{S_{\text{base}}}{S_{\text{ref}}} \quad (6.8)$$

where

$$C_{P\text{base}} \cong -\frac{1}{M_{\infty}^2} \quad (6.9)$$

in hypersonic conditions and  $S_{\text{base}}$  and  $S_{\text{ref}}$  are the base and reference vehicle’s surfaces, respectively [23].

In order to predict viscous contribution to aerodynamic forces and moments, the shear force is determined on each vehicle panel. The skin friction is estimated basing on the assumption of a laminar or turbulent flat plate as

$$\Delta C_{D,\text{friction}} = C_f \frac{S_{\text{wet}}}{S_{\text{ref}}} \quad (6.10)$$

where  $C_f$  is the skin friction coefficient,  $S_{\text{wet}}$  is the panel wetted area, and  $S_{\text{ref}}$  is the reference vehicle’s surfaces. Reference temperature and reference enthalpy methods are available for both laminar and turbulent flows. The viscous calculation is performed along streamlines, and the results are then interpolated to the panel centroids. The streamlines are traced on the configuration described by quadrilateral elements by using the Newtonian steepest descent method, which uses only the element inclination angle relative to the velocity vector to determine the streamline trace. The only information required to generate streamlines are quadrilateral description of the geometry and the flight attitude of the vehicle.

The HPM code is also able to perform detailed viscous analysis on 3-D configurations [24].

The viscous analysis needs the streamline evaluation on the vehicle’s surface since it is performed along each streamline using a simple one-dimensional boundary-layer method, and the results are then interpolated at each element centroid.

To do this, the generic vehicle component is modeled as either a flat plate or a leading edge by selecting the appropriate boundary-layer model. The flat plate boundary-layer model includes both laminar and turbulent methods as well as the cone correction. It sets the Mangler factor ( $M_f$ ) which transforms the solution of the two-dimensional boundary layer to the axially symmetric case. The two available laminar skin friction and aeroheating correlations in the plate laminar method option are the Eckert and the  $\rho-\mu$  methods. Both are based on the classic Blasius flat plate boundary-layer solution corrected with the reference enthalpy compressibility factors. If plate turbulent method option is chosen, four turbulent methods are available: the Schultz–Grunow, the  $\rho-\mu$ , the Spalding–Chi, and the White one.

In particular, for both laminar and turbulent flows, the reference temperature ( $T_{\text{ref}}$ ), based on Eckert's method, reads

$$T_{\text{ref}} = 0.5 (T_e + T_w) + 0.11 r (\gamma - 1) M_e^2 T_e \quad (6.11)$$

where the recovery factor,  $r$ , is calculated as the square root of the Prandtl number for laminar flows and the cube root of the Prandtl number for turbulent flows. The Prandtl number is evaluated at the reference temperature.

For laminar flows, the skin friction coefficient and Stanton number are calculated as

$$\begin{aligned} C_f &= 0.664 / \sqrt{Re/M_f} T_e / T_{\text{ref}} \\ S_t &= 0.5 C_f \text{Pr}^{-2/3} \end{aligned} \quad (6.12)$$

For turbulent flows, the relations for skin friction and Stanton number are

$$\begin{aligned} C_f &= 0.37 / [\log_{10} (Re/M_f)]^{2.584} T_e / T_{\text{ref}} \\ S_t &= 0.5 C_f \text{Pr}^{-2/3} \end{aligned} \quad (6.13)$$

In the above relations,  $M_f$  is the Mangler factor. For laminar flows,  $M_f$  is equal to 3 and for turbulent flows it is set to 2. The enthalpy-based film coefficient, recovery enthalpy, and convective heating are defined as

$$\begin{aligned} C_H &= \rho_{\text{ref}} U_e \text{St} \\ H_{\text{rec}} &= H_e + 0.5 r U_e^2 \\ \dot{q}_{\text{conv}} &= C_H (H_{\text{rec}} - H_w) \end{aligned} \quad (6.14)$$

In the above relations,  $H_e$  is the edge static enthalpy,  $H_{\text{rec}}$  is the recovery enthalpy,  $U_e$  the edge velocity, and  $H_w$  is the wall enthalpy.

$H_w$  can be evaluated both at cold and radiative cooling wall boundary conditions. In the latter case, a Newton–Raphson technique is considered to assess wall temperature, provided that the energy radiated from the surface must equal the sum of the convective and incident shock-radiative heating:

$$\dot{q}_{\text{convective}} + \dot{q}_{\text{radiative}} = \sigma \varepsilon T_{\text{wall}}^4 \quad (6.15)$$

Indeed, since the convective heating depends on the final wall temperature, this nonlinear relationship must be solved iteratively at each panel centroid.

With the leading edge boundary-layer model, the vehicle nose and leading edge may be modeled as either a sphere, a cylinder, or a swept cylinder.

For instance, the stagnation-point convective heat transfer for spherical and unswept cylinder leading edges, according to Fay and Riddell work, reads

$$\dot{q}_{co} = 0.57 \left( \frac{4}{3} \right)^k \text{Pr}^{-0.6} (\rho_w \mu_w)^{0.1} (\rho_e \mu e)_s^{0.4} \left[ 1 + (\text{Le}^\phi - 1) \left( \frac{h_d}{h_e} \right) \right] (h_e - h_w) \left( \frac{du_e}{dx} \right)_s^{0.5}$$

where the index  $k = 0$  for two-dimensional flow and  $k = 1$  for axisymmetric flow.

Here the subscripts  $w$ ,  $e$ , and  $s$  denote conditions at the wall, the external flow, and the stagnation point, while  $\phi = 0.52$  for equilibrium boundary layer and  $\phi = 0.63$  for frozen boundary layer and fully catalytic wall (FCW).

The term in square brackets represents the effects of equilibrium chemical reactions occurring in the stagnation region and:

$$\begin{aligned} \text{Pr} &= \frac{\mu c_p}{k} \\ \text{Le} &= \frac{\rho D_{12} c_p}{k} \\ h_D &= \sum_{i=1}^n c_i \Delta h_{f,i} \end{aligned}$$

The Prandtl number  $Pr$  and the Lewis number  $Le$  are similarity parameters like the Reynolds number and measure the relative importance of friction to heat conduction and of species diffusion (mixing) to conduction, respectively. The gas considered is air which, for the purposes of mixing, can be considered to be a binary mixture, that is, a mixture made up of two species: atoms ( $O$  or  $N$ ) and molecules ( $O_2$  and  $N_2$ ). The quantity  $D_{12}$  is the binary diffusion coefficient that measures the ability of species 1 to mix with species 2. The quantities  $c_i$  and  $\Delta h_{f,i}$  are the molar concentrations of the individual species present ( $O$ ,  $O_2$ ,  $N$ , and  $N_2$ ) and the chemical heat of formation of each of the species, respectively.

The Lewis number for air-like mixtures is close to unity,  $Le \cong 1.4$ , so that the quantity  $(\text{Le}^{0.52} - 1) \cong 0.19$ , and the contribution of the chemical reaction term can often be safely neglected in preliminary studies.

The velocity gradient along the  $x$ -axis, that is, along the body surface, at the stagnation point may be found to be given by

$$\frac{du_e}{dx} = \frac{1}{R_n} \sqrt{\frac{2(p_e - p_\infty)}{\rho_e}}$$

Then, the methods used for spherical and unswept cylinder leading edges include Lee's method for laminar flow and the Detra-Hidalgo method for turbulent flow to provide heat flux distribution around the leading edge.

As far as the influence of leading edge sweep angle is concerned, the analysis uses Lee's method with the addition of the sweep angle effect ( $K_{\text{sweep}}$ ) that, according to the swept cylinder method, reads

$$\frac{\dot{q}_\Lambda}{\dot{q}(\Lambda = 0)} = K_{\text{sweep}} \quad (6.16)$$

where  $K_{\text{sweep}}$ , according to Cato–Johnson, is

$$K_{\text{sweep}} = \cos^{1.25}(\Lambda) + 0.05 \sin(\Lambda) \quad (6.17)$$

while for Beckwith–Gallagher reads

$$K_{\text{sweep}} = 1 + \Lambda^2 (-1.875 + 1.097 \Lambda) \quad (6.18)$$

where  $\Lambda$  is the leading edge sweep angle.

The CFD code FLUENT solves the full Reynolds Averaged Navier–Stokes (RANS) equations in a finite volume approach, with a cell-centered formulation on a multi-zone block-structured grid. In the present research effort, the thermal and chemical nonequilibrium flowfield governing equations are integrated in a density-based approach with an upwind flux difference splitting (FDS) second-order upwind numerical scheme for the spatial reconstruction of the convective terms, while for the diffusive fluxes a cell-centered scheme is applied. In some computations, however, flux vector was computed by using a flux vector splitting scheme, namely, Advection Upstream Splitting Method (AUSM). It provides exact resolution of contact and shock discontinuities, and it is less susceptible to Carbuncle phenomena.

Implicit solver formulation was considered in the computations of this work. Indeed, due to broader stability characteristics of the implicit formulation, a converged steady-state solution can be obtained much faster using the implicit formulation rather than the explicit one.

Global transport properties of the gas mixture relied on semiempirical rules such as Wilke's mixing rule for viscosity and thermal conductivity. The viscosity and thermal conductivity of  $i$ th species was obtained by kinetic theory of gases. For the diffusion coefficient of the  $i$ th species in the mixture, the multicomponent diffusion coefficient was applied, where species mass diffusivity is evaluated by kinetic theory. Flowfield chemical reactions proceed with forward rates that are expressed in the Arrhenius form, and reaction rate parameters are due to Park [25]. In particular, a number of in-house modifications (i.e., user-defined functions, UDF) for the thermal nonequilibrium were considered since vibrational nonequilibrium conditions are not basic code features. In the UFD vibrational relaxation is modeled using a Landau–Teller formulation, where relaxation times are obtained from Millikan and White, assuming simple harmonic oscillators [25–27].

Finally, the  $k$ - $\omega$  SST model has been considered to account for turbulence effects, and only steady-state computations are carried out so far.

## 6.5 Aerodynamic Characterization

Usually the vehicle aerodynamic characterization is provided in terms of force and moment coefficients and control surfaces effectiveness. Force coefficients are lift ( $C_L$ ), drag ( $C_D$ ), and side ( $C_Y$ ), while moments refer to rolling ( $C_l = C_{Mx}$ ), pitching ( $C_m = C_{My}$ ), and yawing ( $C_n = C_{Mz}$ ) coefficients, according to the following equations:

$$\begin{aligned} C_l &= C_{Mx} = \frac{M_x}{\frac{1}{2}\rho_\infty v_\infty^2 b_{ref} S_{ref}} \\ C_i &= \frac{F_i}{\frac{1}{2}\rho_\infty v_\infty^2 S_{ref}} \quad i = L, D, Y \quad C_m = C_{My} = \frac{M_y}{\frac{1}{2}\rho_\infty v_\infty^2 L_{ref} S_{ref}} \\ C_n &= C_{Mz} = \frac{M_z}{\frac{1}{2}\rho_\infty v_\infty^2 b_{ref} S_{ref}} \end{aligned}$$

where  $S_{ref}$  is the reference surface (usually the vehicle planform area),  $L_{ref}$  the longitudinal reference length (usually the fuselage length, L), and  $b_{ref}$  the lateral-directional reference length (usually the wingspan).

### 6.5.1 ORV Aerodynamic Reference Parameters

For the ORV concept, the geometric reference parameters (see Fig. 6.28) that have been chosen in order to make aerodynamic forces (i.e.,  $F_L$ ,  $F_D$ , and  $F_Y$ ) and moments (i.e.,  $M_x$ ,  $M_y$ , and  $M_z$ ) nondimensional coefficients are  $L_{ref} = 1.6$  m (mean aerodynamic chord),  $b_{ref} = 3.6$  m (wing span), and  $S_{ref} = 5.80$  m<sup>2</sup> (wing area), and pole coordinates are ( $x_{CoG}/L, 0, 0$ ) m.

### 6.5.2 Reference Coordinate System and Aerodynamic Sign Conventions

In Fig. 6.30 the adopted reference frames with aerodynamic coefficients conventions are shown. The subscript  $b$  indicates the body reference frame (BRF), and  $s$  refers to stability reference frame (SRF), while  $w$  indicates the wind reference frame (WRF). The origin of both reference systems is in the center of gravity (CoG) of the vehicle. The pole for the calculation of the moment coefficients is assumed in the CoG; the positive  $x$ -axis for the ORV body axis system is shown parallel to the fuselage reference line (FRL). The aerodynamic reference axis systems are sets of conventional, right-hand, orthogonal axes with the  $x$ - and  $z$ -axes in the plane of symmetry and with the positive  $x$ -axis directed out of the nose (in the body axis system) or pointing into the component of the wind (in the stability axis system) which lies in the plane of symmetry [19, 24] (Fig. 6.29).

**Fig. 6.28** Aerodynamic reference parameters

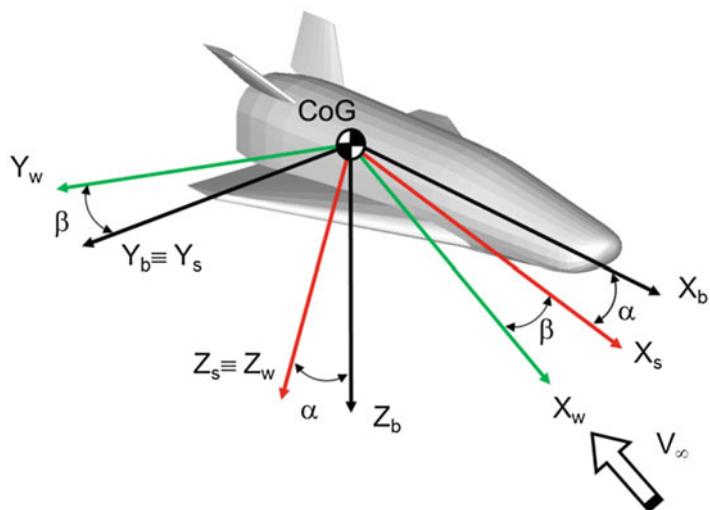
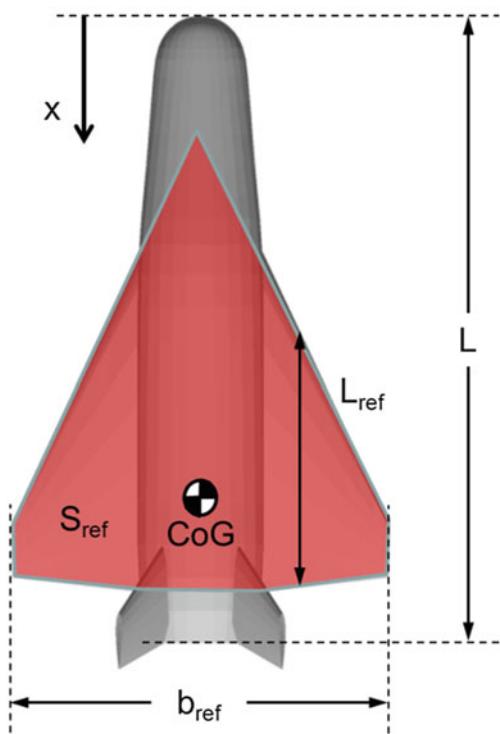


**Fig. 6.29** Aerodynamic reference frames

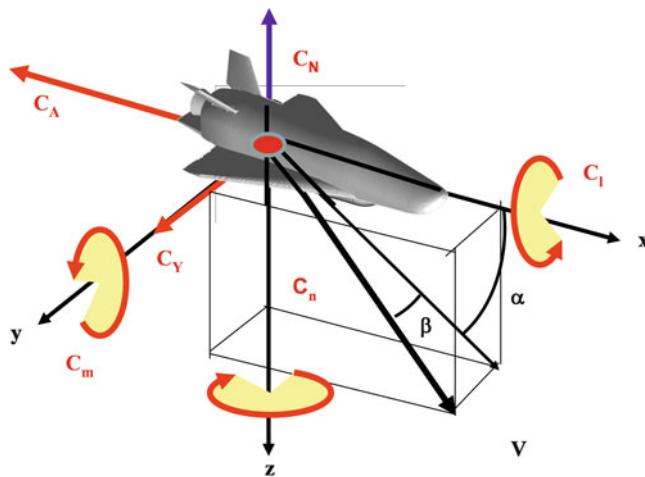


**Fig. 6.30** Body reference frame and aerodynamic sign conventions

The reference system for the aerodynamic data is a body-fixed axis system, compliant with the ISO 1151 standard. It is displayed in Fig. 6.30.

Therefore, normal force ( $C_N$ ), axial force ( $C_A$ ), and side force ( $C_Y$ ) coefficients and rolling moment ( $C_l$ ), pitching moment ( $C_m$ ), and yawing moment ( $C_n$ ) coefficients refer to the BRF, while lift force ( $C_L$ ) and drag force ( $C_D$ ) coefficients are provided in the WRF.

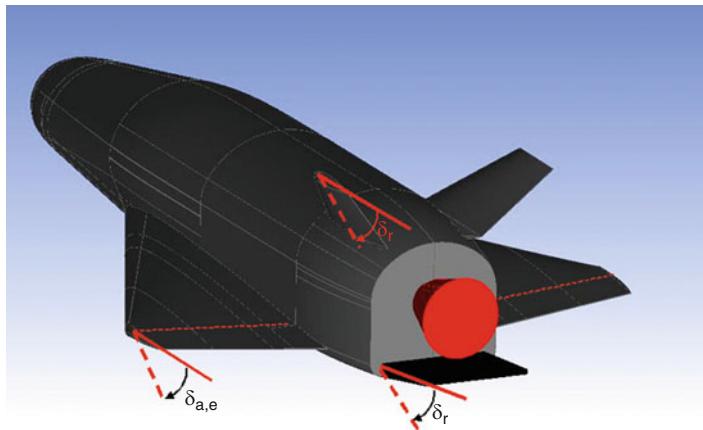
The aerodynamic sign convention (see Fig. 6.30 where directions are positive as shown) for forces, moments, and velocity is detailed in Chap. 1.

ORV aerodynamic control surface deflections, forces, and hinge moments are summarized and illustrated in Fig. 6.31. In general, control surface deflection angles are measured in a plane perpendicular to the control surface hinge axis. An exception is the rudder control surface deflections which are measured in a plane parallel to the fuselage reference plane.

### 6.5.3 Inputs for ORV Aerodynamic Database Generation

Based on the re-entry flight scenario recognized in Figs. 6.13 and 6.14, the aerodynamic data set has been generated for the flight envelope bounded by the following ranges:

- $0.3 \leq M_\infty \leq 1.7$  [0.3, 0.5, 0.7, 0.9, 1.1, 1.3, 1.5, 1.7]
- $Re_{\infty/m} = 1 \times 10^7 \text{ m}^{-1}$
- $0^\circ \leq \alpha \leq 20^\circ$  [0, 2, 4, 6, 8, 10, 12, 14, 16, 18, 20]



Positive deflection of	Aero Forces and Moments
Rudder, $\delta_r$	$+C_Y - C_n$
Elevon, $\delta_e$	$-C_m$
Right, $\delta_{e,R}$	$-C_l$
Left, $\delta_{e,L}$	$+C_l$
Body-flap, $\delta_{bf}$	$-C_m$

**Fig. 6.31** ORV aerodynamic control surface deflections effect on ORV aerodynamics

- $-8^\circ \leq \beta \leq 8^\circ$        $[-8, -4, -2, 0, 2, 4, 8]$
- $-30^\circ \leq \delta \leq 30^\circ$        $[-30, -20, -10, 10, 20, 30]$  for aileron, elevon, and rudder

for the subsonic to supersonic flow conditions, while for the remaining part of the re-entry trajectory the ranges are

- $2 \leq M_\infty \leq 25$        $[2, 3, 4, 6, 8, 12, 16, 20, 25]$
- $2 \times 10^4 \text{ m}^{-1} \leq Re_{\infty/m} \leq 2 \times 10^6 \text{ m}^{-1}$        $[2 \times 10^4, 10^5, 5 \times 10^5, 2 \times 10^6]$
- $0^\circ \leq \alpha \leq 50^\circ$        $[0, 2, 5, 7, 10, 12, 14, 15, 17, 20, 22, 25, 27, 30, 35, 40, 45, 50]$
- $-4^\circ \leq \beta \leq 4^\circ$        $[-4, -2, 0, 2, 4]$
- $-30^\circ \leq \delta \leq 30^\circ$        $[-30, -20, -10, 10, 20, 30]$  for aileron, elevon, and rudder

It must be noted that the range of Reynolds number was chosen in such a way to cover a wide part of the re-entry, based on a preliminary re-entry trajectory, as shown in Fig. 6.32.

In this figure the ORV preliminary reference flight envelope is reported, together with the iso-Mach and iso-Reynolds curves, in the altitude–velocity map.

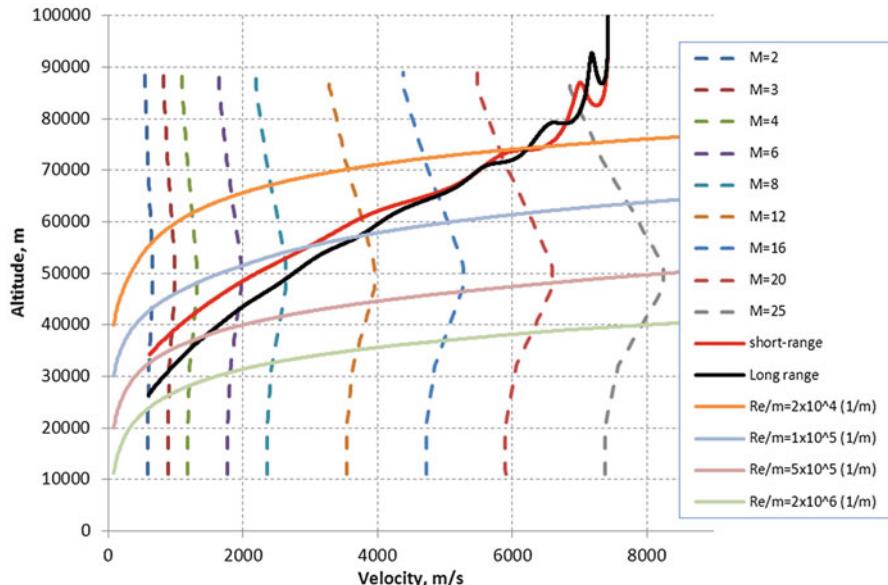


**Fig. 6.32** ORV re-entry scenario in the altitude–velocity map with iso-Mach and Reynolds curves

#### 6.5.4 ORV Aerodynamic Model

This section contains the ORV aerodynamic model (AM) needed for the development of the vehicle aerodynamic database to be used for Flight Mechanics analysis, subsystem design and analyses, as well as for flight control analysis.

An important aspect of developing an aerodynamic database is the formulation of an aerodynamic model. For example, the accuracy of the database depends on the degree to which the AM represents the physics of the problem. Therefore, it is important that all the aerodynamic and control variables that may have influence on the given aerodynamic coefficient must be included in the aerodynamic model.

To this end, a number of hypotheses have been assumed in developing the ORV AM. Indeed, the independent variables that have been recognized as influent on the ORV aerodynamic state are

$$\{M, Re, \alpha, \beta, \delta_e, \delta_a, \delta_r, q, \dot{\alpha}\}$$

The couple  $(M, Re)$ <sup>1</sup> identifies the aerodynamic environment, while the remaining variables completely describe the flow field direction. Therefore, the functional structure of the AM of ORV is based on these independent variables.

---

<sup>1</sup>Note that the couple  $(M, Re)$  is able to define also rarefied flow regime conditions since the Knudsen number is proportional to the Mach–Reynolds ratio.

Note, however, that the AEDB under developing at this time of project phase does not consider the contribution of dynamic effects considering that low-order methods, widely used in this framework, are unable to address this contribution.

Further, as done in the past for the US Orbiter and X-34 vehicles, the ORV AM development relies on the following assumptions:

1. No RCS effects are considered.
2. Only rigid body aerodynamic coefficients are evaluated, i.e., no aeroelastic deformations are accounted for.
3. No Reynolds and Knudsen numbers effects on aerodynamic control surfaces are assumed.
4. No sideslip effects on aerodynamic control surfaces are assumed, except for rudder efficiency.
5. No effects of protrusions, gaps, and roughness are here considered.
6. No Knudsen numbers effects on side force and aerodynamic moment coefficients are assumed (except for pitching moment coefficient).
7. No mutual aerodynamic interference between various control surfaces is considered.

Finally, it is worth to note that, as typically done in a classical approach, each aerodynamic coefficient can be derived by supposing that each contribution to the single global coefficient is treated independently from the others. This means, from an operational point of view, that each aerodynamic coefficient is described by a linear summation over certain number of incremental contributions (i.e., build-up approach). Each contribution is based on a small number of parameters, as recognized herein.

### ***6.5.5 Formulation of the Aerodynamic Database***

The aerodynamic characteristics pertaining to the longitudinal (i.e.,  $C_L$ ,  $C_D$ , and  $C_m$ ) and lateral ( $C_Y$ ,  $C_l$ , and  $C_n$ ) degrees of freedom are presented as full-scale rigid force and moment coefficients. They are presented in a form which will allow a build-up to any desired configuration and/or flight condition by incremental addition to the basic coefficient.

Each aerodynamic coefficient has been considered separately by the appropriate equation in which appear all the pertinent contributions for obtaining the total coefficient for any selected flight condition.

Indeed, following the formulation used for the Space Shuttle assuming that the vehicle is operating at a combined AoA ( $\alpha$ ) and AoS ( $\beta$ ), the total lift coefficient is given by

$$\begin{aligned} C_{L,\text{total}} = & C_{L,b}(\alpha, M, Re) + \Delta C_{L,\delta_e} + \Delta C_{L,\delta_a} + \Delta C_{L,\delta_{bf}} + \Delta C_{L,\delta_r} + \Delta C_{L,b,\beta} \\ & + \Delta C_{L,\delta_r,\beta} + C_{L,\bar{\alpha}} \frac{\dot{\alpha} c_{\text{ref}}}{2V_\infty} + C_{L,\bar{\beta}} \frac{q c_{\text{ref}}}{2V_\infty} \end{aligned} \quad (6.19)$$

where  $C_{L,\text{total}}$  is the total lift coefficient of the vehicle for a given flight condition as expressed by the flight Mach number  $M$ , AoA  $\alpha$ , sideslip  $\beta$ , elevon deflection  $\delta_e$ , ailerons deflections  $\delta_a$ , body flap deflections  $\delta_{bf}$ , and rudder deflection  $\delta_r$ .

The parameter  $C_{L,b}(\alpha, M, Re)$  is baseline lift coefficient in zero sideslip and zero control surface deflections (i.e., in clean configuration). It takes into account also for rarefaction effects through bridging relationship. The parameter  $\Delta C_{L,\delta_e}$  represents incremental lift coefficient due to symmetric elevon deflections above the baseline and is given by

$$\Delta C_{L,\delta_e} = C_L(\alpha, M, \delta_e) - C_{L,b}(\alpha, M) \quad (6.20)$$

The parameter  $\Delta C_{L,\delta_a}$  represents the incremental lift coefficient due to aileron (asymmetric elevons) deflections above the baseline and can be evaluated using the data on symmetric elevons as follows:

$$\Delta C_{L,\delta_a} = \left( \frac{\Delta C_{L,\delta_e=\delta_{e,L}} + \Delta C_{L,\delta_e=\delta_{e,R}}}{2} \right) - \Delta C_{L,\delta_e} \quad (6.21)$$

Here, we use the elevon data twice, once assuming  $\delta_e = \delta_{e,L}$ , to obtain  $\Delta C_{L,\delta_e=\delta_{e,L}}$  and then assuming  $\delta_e = \delta_{e,R}$ , to determine  $\Delta C_{L,\delta_e=\delta_{e,R}}$ . As a check, when aileron deflection is zero, i.e.,  $\delta_e = \delta_{e,L} = \delta_{e,R}$ , the value of  $\Delta C_{L,\delta_a}$  vanishes as expected.

The parameter  $\Delta C_{L,\delta_{bf}}$  represents incremental lift coefficient due to body flap deflections above the baseline and is given by

$$\Delta C_{L,\delta_{bf}} = C_L(\alpha, M, \delta_{bf}) - C_{L,b}(\alpha, M) \quad (6.22)$$

The incremental lift coefficient  $\Delta C_{L,\delta_r}$  due to rudder is defined as follows:

$$\Delta C_{L,\delta_r} = C_L(\alpha, M, \delta_r) - C_{L,b}(\alpha, M) \cong 0 \quad (6.23)$$

The incremental lift coefficients due to baseline and rudder in sideslip are given by

$$\Delta C_{L,b,\beta} = C_L(\alpha, \beta, M) - C_L(\alpha, M) \quad (6.24)$$

$$\Delta C_{L,\delta_r,\beta} = [C_L(\alpha, \beta, M, \delta_r) - C_L(\alpha, \beta, M)] - \Delta C_{L,\delta_r} \quad (6.25)$$

Note that the first term in square brackets on the right-hand side of the last equation gives the combined incremental coefficient due to rudder at an AoA and sideslip over the baseline at the same values of AoA and AoS. To get the incremental coefficient due only to sideslip  $\beta$ , we have to subtract the incremental due to AoA as shown by second term on the right-hand side of equation.

All above contributions represent aerodynamic cross-coupling effects, and they have been found to be significant, especially at higher values of AoA.

Finally,  $C_{L,\bar{\alpha}}$  is the change in lift force coefficient with rate of change of AoA,  $\bar{\alpha}$  (per radian), whereas  $C_{L,\bar{q}}$  accounts for change in lift force coefficient with pitch rate,  $\bar{q}$  (per radian). However, both those contributions are assumed zero [16].

In a similar fashion, we assume that the drag and pitching moment coefficients are given by

$$\begin{aligned} C_{D,\text{total}} &= C_{D,b}(\alpha, M, Re) + \Delta C_{D,\delta_e} + \Delta C_{D,\delta_a} + \Delta C_{D,\delta_{bf}} + \Delta C_{D,\delta_r} \\ &\quad + \Delta C_{D,b,\beta} + \Delta C_{D,\delta_r,\beta} \end{aligned} \quad (6.26)$$

$$\begin{aligned} C_{m,\text{total}} &= C_{m,b}(\alpha, M, Re) + \Delta C_{m,\delta_e} + \Delta C_{m,\delta_a} + \Delta C_{m,\delta_{bf}} + \Delta C_{m,\delta_r} \\ &\quad + \Delta C_{m,b,\beta} + \Delta C_{m,\delta_r,\beta} + C_{m,\bar{\alpha}} \frac{\dot{\alpha} c_{\text{ref}}}{2V_\infty} + C_{m,\bar{q}} \frac{qc_{\text{ref}}}{2V_\infty} \end{aligned} \quad (6.27)$$

The change in pitching moment coefficient due to rudder deflection,  $\Delta C_{m,\delta_r}$ , is assumed zero.

The side force coefficient is assumed to be given by

$$\begin{aligned} C_{Y,\text{total}} &= C_{Y,b}(\alpha, M) + \Delta C_{Y,\delta_a} + \Delta C_{Y,\delta_r} + \Delta C_{Y,b,\beta} + \Delta C_{Y,\delta_r,\beta} \\ &= \Delta C_{Y,\delta_a} + \Delta C_{Y,\delta_r} + \Delta C_{Y,b,\beta} + \Delta C_{Y,\delta_r,\beta} \end{aligned} \quad (6.28)$$

since the vehicle configuration is symmetric, i.e.,  $C_{Y,b}(\alpha, M) = 0$ . Further,

$$\Delta C_{Y,b,\beta} = C_{Y,b}(\alpha, \beta, M) - C_{Y,b}(\alpha, M) = C_{Y,b}(\alpha, \beta, M) \quad (6.29)$$

Similarly,

$$\begin{aligned} \Delta C_{Y,\delta_a} &= C_Y(\alpha, M, \delta_a) \\ \Delta C_{Y,\delta_r} &= C_Y(\alpha, M, \delta_r) \end{aligned} \quad (6.30)$$

Then,

$$C_{Y,\text{total}} = C_{Y,b}(\alpha, \beta, M) + C_Y(\alpha, M, \delta_a) + C_Y(\alpha, M, \delta_r) + \Delta C_{Y,\delta_r,\beta} \quad (6.31)$$

where the incremental side force coefficient due to rudder is sideslip is defined as

$$\Delta C_{Y,\delta_r,\beta} = [C_Y(\alpha, \beta, M, \delta_r) - C_{Y,b}(\alpha, \beta, M)] - \Delta C_{Y,\delta_r} \quad (6.32)$$

Proceeding in a similar way, the rolling and yawing moment coefficients are assumed to be given by

$$C_{l,\text{total}} = C_{l,b}(\alpha, \beta, M) + C_{l,\delta_a}(\alpha, M, \delta_a) + C_{l,\delta_r}(\alpha, M, \delta_r) + \Delta C_{l,\delta_r,\beta} \quad (6.33)$$

$$C_{n,\text{total}} = C_{n,\text{b}}(\alpha, \beta, M) + C_{n,\delta_z}(\alpha, M, \delta_a) + C_{n,\delta_z}(\alpha, M, \delta_r) + \Delta C_{n,\delta_r, \beta} \quad (6.34)$$

Therefore, it is assumed that the sideslip has effect only on the baseline and when the rudder is deflected, but it has no effect when elevons, body flap, or ailerons are deflected.

Moreover, as stated in assumption No. 3, no dependency on Reynolds number is assumed for the elevon contribution. Indeed, even though this effect exists, it is small and difficult to be modeled. Then, it has been considered as part of the aerodynamic coefficients uncertainty.

### 6.5.6 Process of Development of the Aerodynamic Database

The above formulation of the AM for the free flight provides a framework for building the ORV aerodynamic database (AEDB). It consists of aerodynamic data tables in the form of total and incremental coefficients. They are provided in a convenient form so that the user can evaluate each of the terms appearing in the free flight aerodynamic models and then sum all the terms to get the desired aerodynamic coefficient.

In particular, the ORV AEDB relies on the following segments:

- The free molecular flow conditions
- The transitional flow conditions
- The continuum flow conditions:
  - Hypersonic flow
  - Supersonic flow
  - Transonic flow
  - Subsonic flow

according to Fig. 6.33, that can be considered as guidelines in using vehicle AEDB.

In this figure the ORV reference flight scenario in the altitude–Mach map together with the altitude limits which clearly bound each different flow regimes is provided.

Finally, it is worth to note that in the transitional flow conditions, a very simple relationship to bridge the FMF regime to continuum flow (see Fig. 6.33) is given as

$$C_{i,\text{Transitional}} = C_{i,\text{Continuum}} + (C_{i,\text{FM}} - C_{i,\text{Continuum}}) \cdot \bar{C}_i \quad (6.35)$$

where the normalized coefficient  $\bar{C}_i$  uses Knudsen number as the independent parameter:

$$\bar{C}_i = \frac{C_i - C_{i,\text{Continuum}}}{C_{i,\text{FM}} - C_{i,\text{Continuum}}} = F(\text{Kn}_\infty) = \sin^2 \left[ \frac{\pi}{8} (3 + \log_{10} \text{Kn}_\infty) \right] \quad (6.36)$$

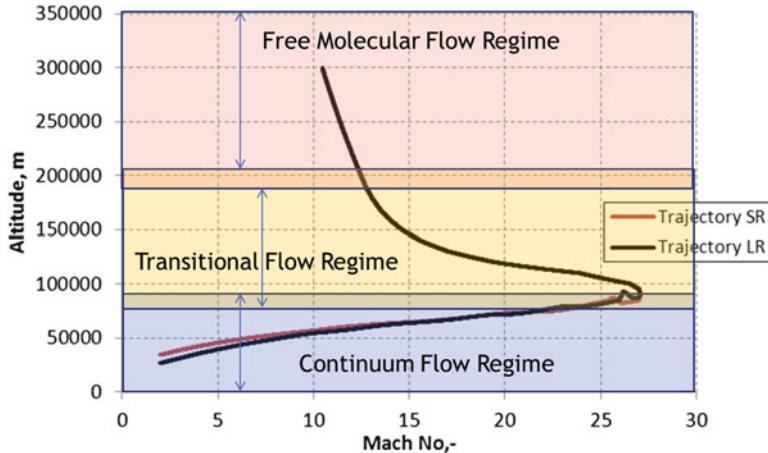


**Fig. 6.33** ORV flow regime in the altitude–Mach map

where  $10^{-3} < Kn_{\infty} < 10$  and  $C_{i\text{Continuum}}$  and  $C_{i\text{FM}}$  are the aerodynamic coefficient in continuum and FMF regimes, respectively. This formula has been used in the past for the US Orbiter aerodynamics assessment [17, 18, 26, 28].

The results of each segment are described in detail in the next paragraphs.

## 6.6 Low-Order Methods Aerodynamic Results

Simplified aerodynamic analysis for supersonic and hypersonic speeds was accomplished on panel mesh close to those shown in Fig. 6.34.

### 6.6.1 HPM Results for Rarefied and Transitional Flow Conditions

As shown in Figs. 6.15 and 6.33, ORV above 200 km altitude experiences FMF conditions.

This means that the several particle simulations, e.g., Direct Simulation Monte Carlo (DSMC), should be performed to address vehicle aerodynamics. At an early design stage, however, only low-order analyses, as those obtained from SIM computations, can be carried out. Indeed, the aerodynamic analysis was performed on the vehicle in clean configuration and, at the free-stream velocity of 7,330 m/s, considered constant with altitude. In all computations the wall temperature was set equal to 300 K (i.e., body temperature ratio equal to 0.351), and the aerodynamic forces were evaluated on the assumption of a Maxwell fully accommodate model.

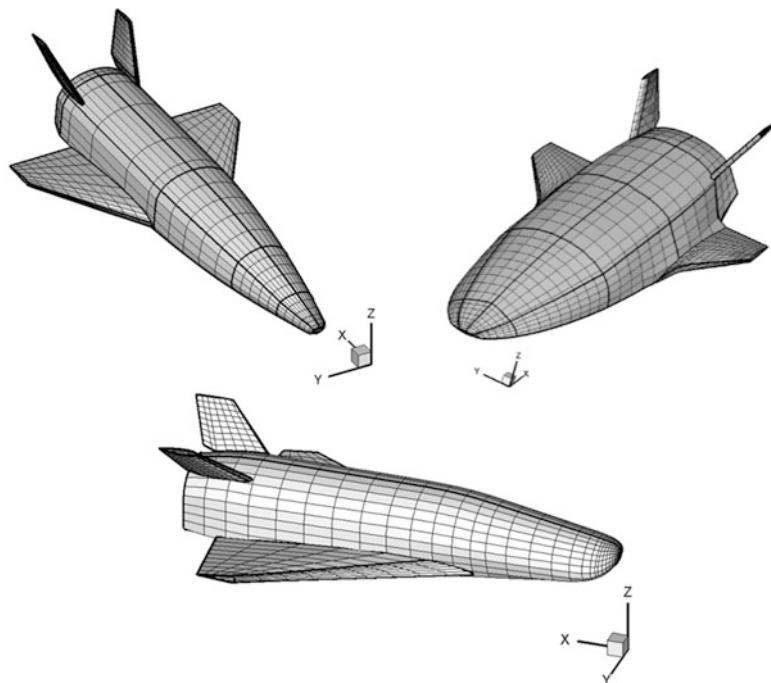


**Fig. 6.34** Examples of the ORV panel mesh

Free-stream thermodynamic parameters were provided by the US Standard Atmosphere 1976.

An example of ORV aerodynamics in FMF conditions is given in Figs. 6.35, 6.36, and 6.37.

As shown, above figures highlight that FMF conditions result in an abrupt loss of vehicle aerodynamic efficiency due to the both suddenly increase of drag and lift drop.

As far as transitional flow aerodynamics is concerned, Figs. 6.15 and 6.33 highlight that ORV flies in that flow regime from about 200 to 87 km altitude. Lift, drag, and pitching moment coefficients versus the Knudsen ( $\text{Kn}_{L\text{ref}\infty}$ ) number are reported from Figs. 6.38, 6.39, 6.40, 6.41, and 6.42 for different AoAs, namely, 10°, 20°, 30°, and 40°.

The behavior of lift coefficient at 10° and 20° and at 30° and 40° is shown in Figs. 6.38 and 6.39, respectively [9, 29–31].

The variation of drag and pitching moment coefficient of ORV-WBB at 30° and 40° AoA, along with the Knudsen number, is reported in Figs. 6.40 and 6.41, respectively.

As one can see, the classical *S-shape* of bridging formulation is clearly recognized ranging from continuum to free molecular flow conditions. Further, note that

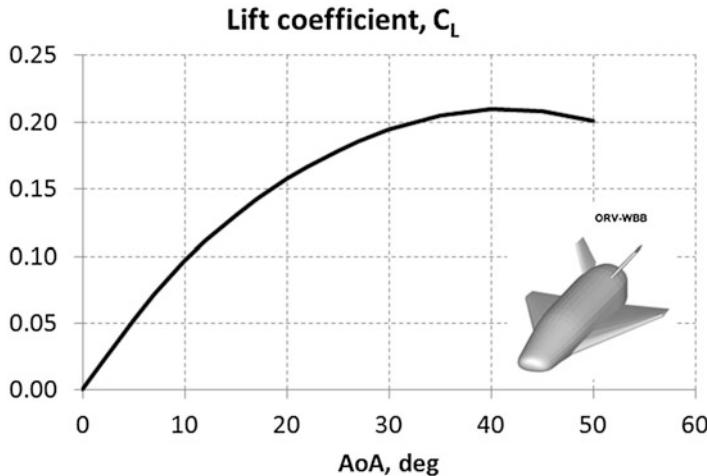


Fig. 6.35 ORV-WBB lift coefficient vs. AoA in FMF

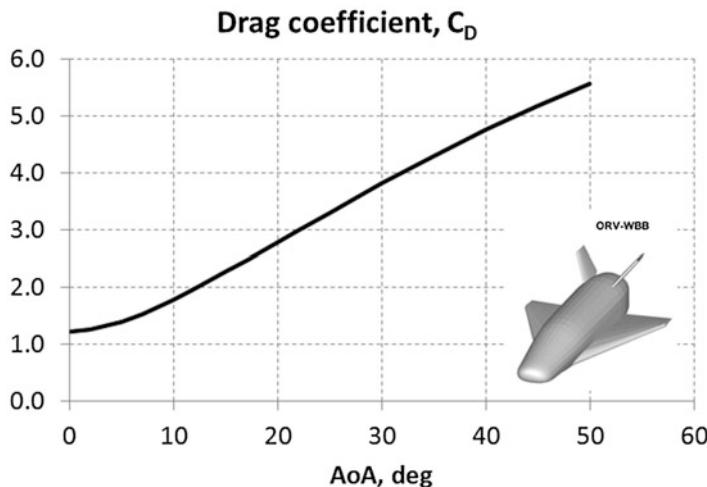
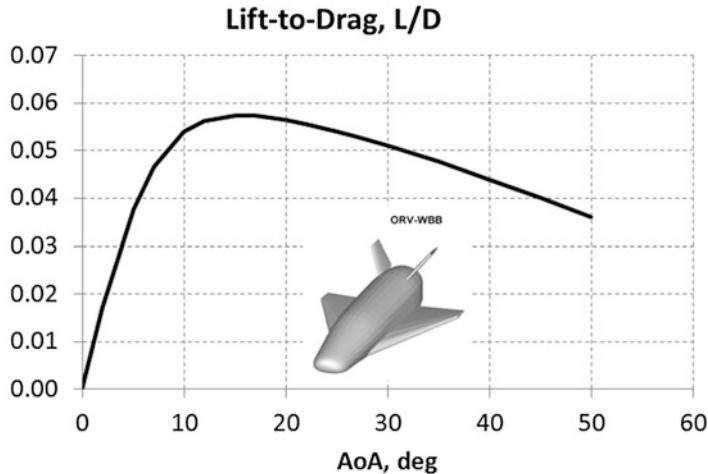


Fig. 6.36 ORV-WBB drag coefficient vs. AoA in FMF

in each figure, the variation of the altitude versus  $K_n$  is also provided to help the reader in understanding at which flight conditions the aerodynamic results must be associated.

The effect of rarefaction on the aerodynamic lift results in an abrupt loss of  $C_L$ . For example, Fig. 6.39 suggests that at  $\text{AoA} = 40^\circ$   $C_L$  decreases of about 90 % ranging from 80 to 200 km. The same consideration applies for  $C_m$  (see Fig. 6.41). In this case  $C_m$  ranges from 0.4 to about -0.6 passing from 80 to 200 km altitude. As far as aerodynamic drag is concerned, Fig. 6.40 shows that



**Fig. 6.37** ORV-WBB aerodynamic efficiency vs. AoA in FMF

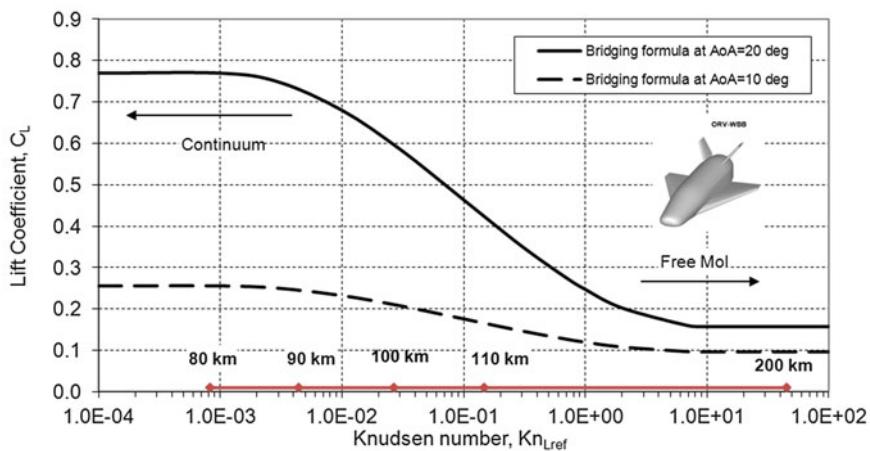


**Fig. 6.38** Lift coefficient vs. Knudsen number for ORV-WBB at  $AoA = 10^\circ$  and  $20^\circ$

$C_D$  at  $AoA = 30^\circ$  increases of about 200 % passing from 90 to 110 km, whereas the drag at  $H = 200$  km is 320 % higher than the one at 90 km. As a consequence, the strong reduction of the aerodynamic efficiency due to rarefaction effects is very clear in Fig. 6.42 [10, 11, 32].

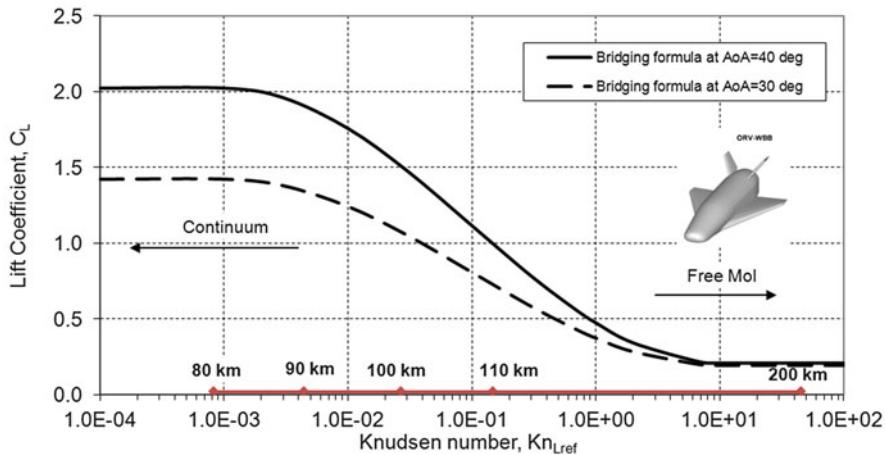


Fig. 6.39 Lift coefficient vs. Knudsen number for ORV-WBB at  $\text{AoA} = 30^\circ$  and  $40^\circ$

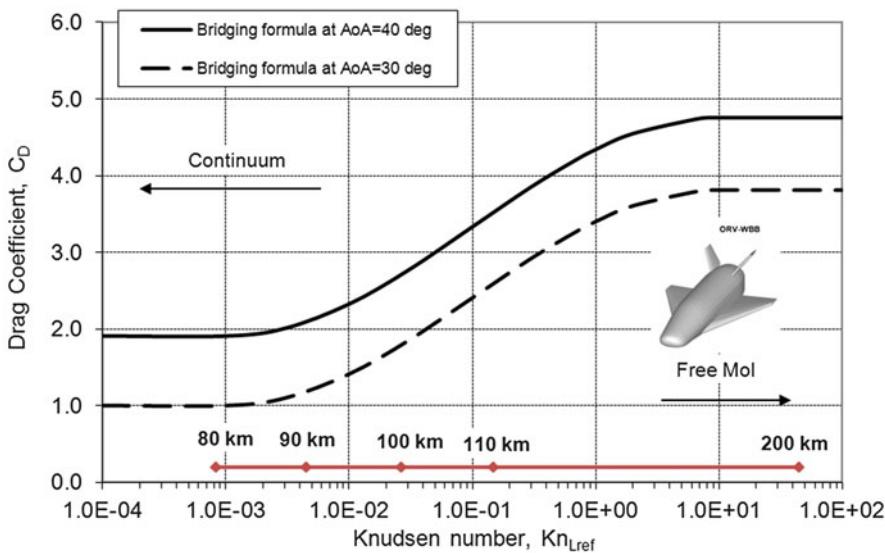
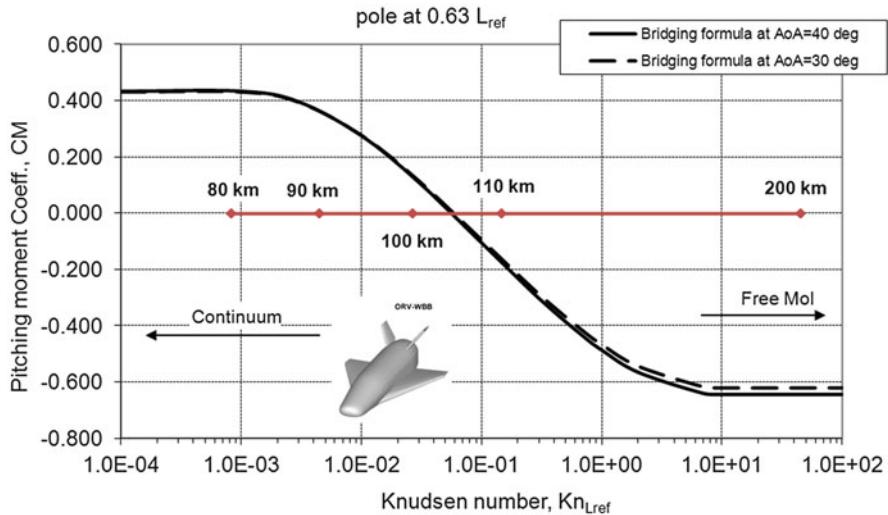


Fig. 6.40 Drag coefficient vs. Knudsen number for ORV-WBB at  $\text{AoA} = 30^\circ$  and  $40^\circ$

### 6.6.2 HPM Results for Continuum Flow Condition

HPM results refer to both clean and flapped configuration, as hereinafter summarized.

Trade-off design analyses highlighted that the best surface inclination methods (see Table 6.1) to consider in assessing vehicle aerodynamic performance in continuum flow conditions are tangent cone and tangent wedge empirical methods



**Fig. 6.41** Pitching moment coefficient vs. Knudsen number for ORV-WBB at  $\text{AoA} = 30^\circ$  and  $40^\circ$

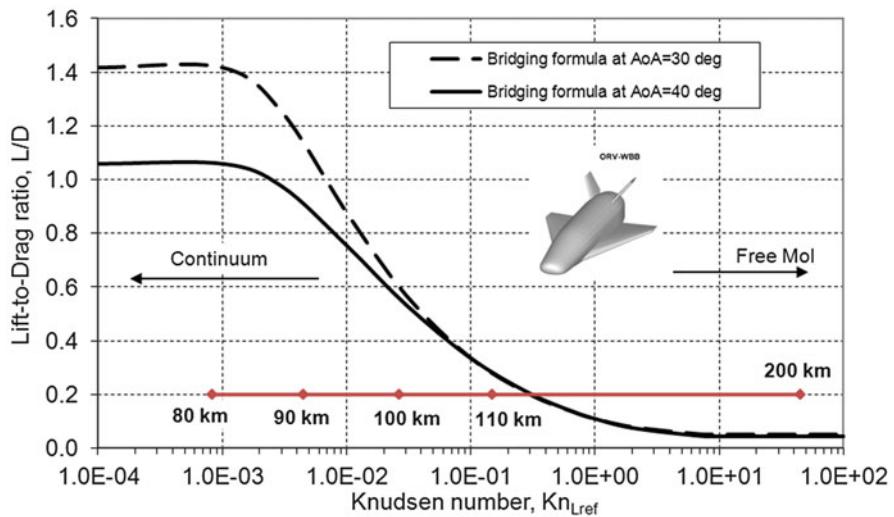


**Fig. 6.42** ORV-WBB aerodynamic efficiency vs. Knudsen number for  $\text{AoA} = 30^\circ$  and  $40^\circ$

for fuselage<sup>2</sup> and wing belly side, respectively. Modified Newtonian–Prandtl–Meyer at leading edges is considered while Newtonian method (i.e.,  $C_p = 0$ ) at vehicle leeside [26, 27].

<sup>2</sup>At fuselage windsides of ORV-SB tangent wedge empirical is applied.

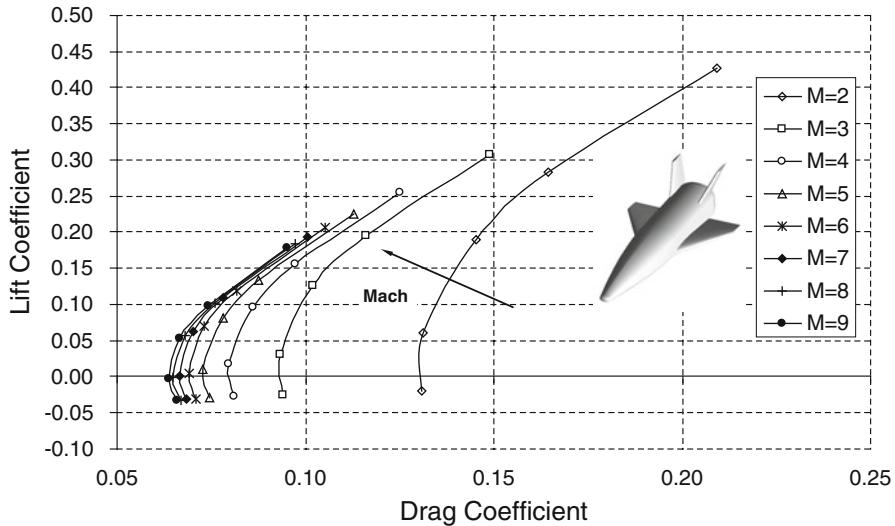


Fig. 6.43 ORV-WSB aerodynamic polars for  $2 \leq M_{\infty} \leq 9$

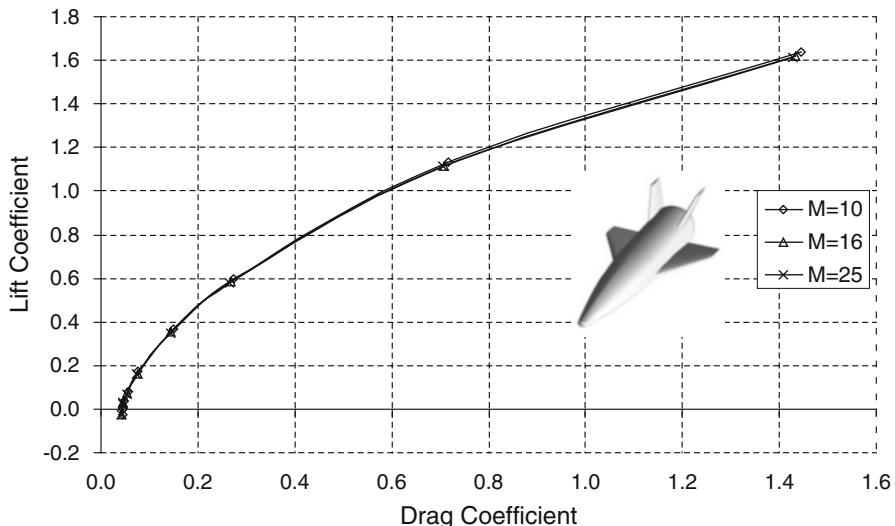


Fig. 6.44 ORV-WSB aerodynamic polars for  $M_{\infty} = 10, 16$ , and  $25$

Some of main results obtained for the ORV-WSB in clean configuration aerodynamic (i.e., no aerodynamic surface deflected) are shown from Figs. 6.43, 6.44, 6.45, 6.46, 6.47, 6.48, 6.49, 6.50, 6.51, 6.52, 6.53, 6.54, 6.55, and 6.56.

Figures 6.43 and 6.44 show the aerodynamic polars while Figs. 6.45 and 6.46 the pitching moment coefficients for Mach ranging from 2 to 25 and  $\alpha$  from  $0^{\circ}$  to  $40^{\circ}$ . As shown, ORV-WSB drag and lift decrease as Mach number increases

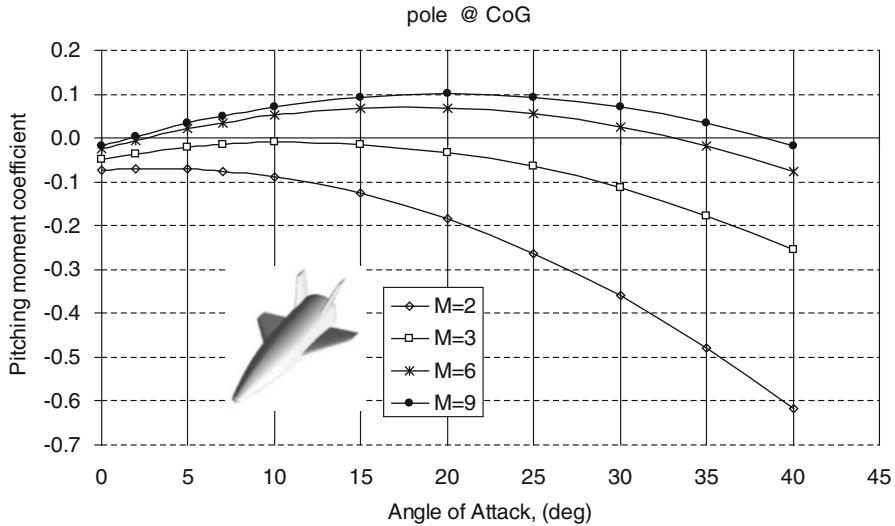


Fig. 6.45 ORV-WSB pitching moment coefficient for  $M_{\infty} = 2, 3, 6$ , and 25

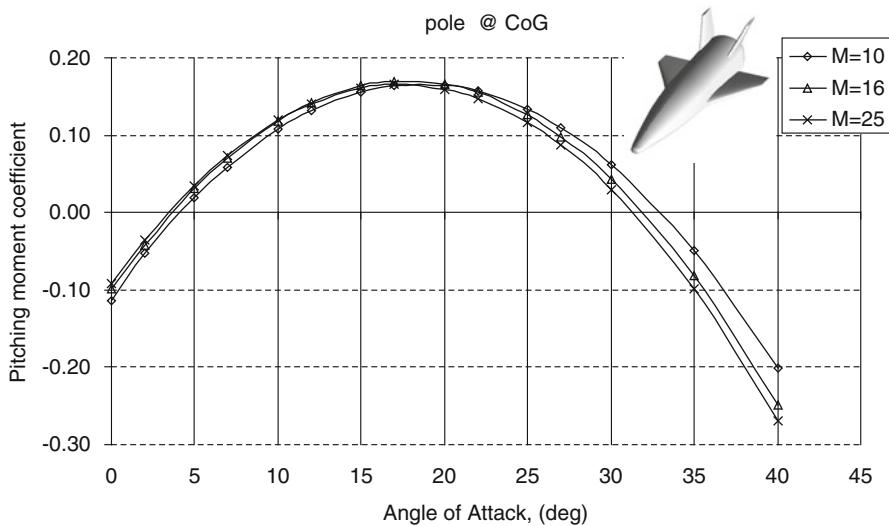


Fig. 6.46 ORV-WSB pitching moment coefficient for  $M_{\infty} = 10, 16$ , and 25

up to reach a value that does not change even if Mach still rises, according to the Oswatich principle (i.e., independence of aerodynamic coefficients to  $M_{\infty}$ ) starting already from  $M_{\infty} = 10$  [12, 14]. Figure 6.45 also shows that the configuration is statically stable (i.e.,  $C_{ma} < 0$ ) for  $\alpha$  higher than 20° in hypersonic conditions [14]. In particular, the concept in clean configuration features a natural trim point

(i.e.,  $C_m = 0$ ) at about  $33\text{--}38^\circ$  for AoA for  $M_\infty = 6$  and 9, respectively. At higher Mach number trim AoA ranges from about  $31^\circ$  to  $33^\circ$  (see Fig. 6.46). Moreover, the pitching moment behavior highlights that ORV-WSB can be trimmed through flap positive deflection (i.e., downward) only at hypersonic speed. At  $M_\infty = 2$  and  $M_\infty = 3$  pitching moment derivative is negative for  $\alpha$  larger than  $5^\circ$  and  $15^\circ$ , respectively.

### Explanation Box. An Example of Aerodynamic Trade-Off

As an example of the aerodynamic trade-off design results, Figs. 6.47 and 6.48 show the aerodynamic polars ( $\alpha = 0^\circ, 2^\circ, 5^\circ, 7^\circ$ , and  $10^\circ$ ) and the pitching moment coefficients of all the competing FTB configurations of Fig. 6.4 for  $M_\infty = 6$  and  $M_\infty = 7$ , respectively.

Note that the ORV-WSB concept, during trade-off analysis, has been named with the code string FTB\_4-521. This code allows distinguishing each configuration. The first four digits indicate the program (i.e., FTB\_4, which stands for fourth series of flying test bed), while the first, second, and third digits of the remaining string refer to fuselage, wing, and tail, respectively. So that, the configurations FTB\_4-211 and FTB\_4-222 feature the same fuselage but different wing and tail (see Fig. 6.4).

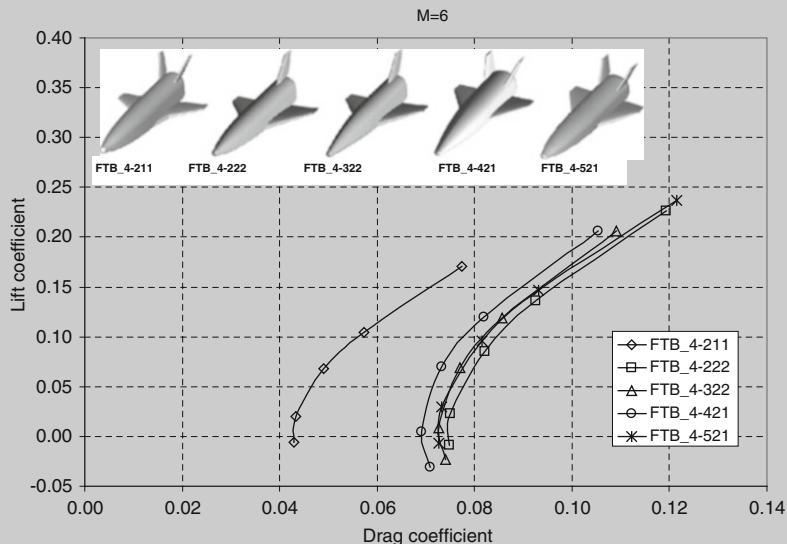


**Fig. 6.47** FTB\_4 aerodynamic polars at  $M_\infty = 6$

(continued)

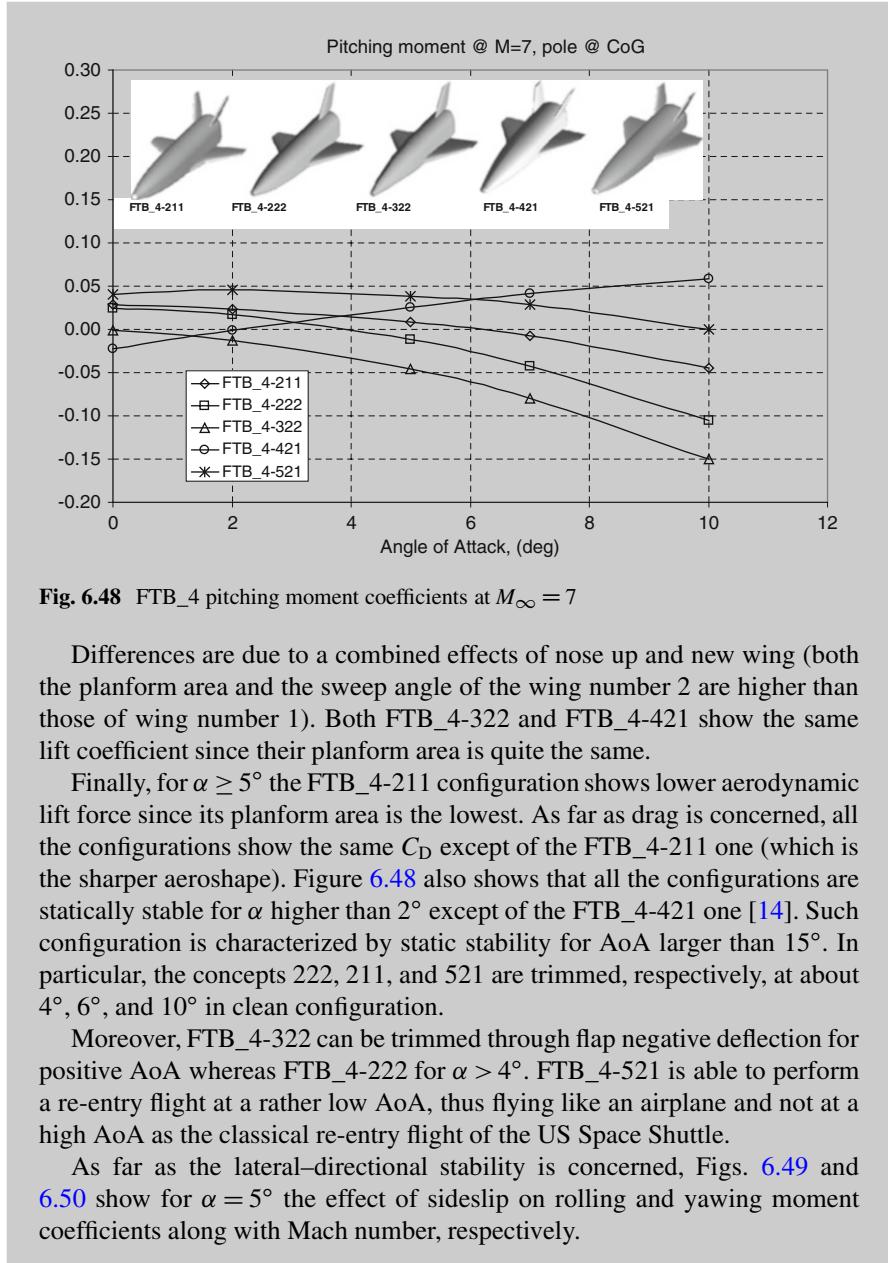


**Fig. 6.48** FTB\_4 pitching moment coefficients at  $M_{\infty} = 7$

Differences are due to a combined effects of nose up and new wing (both the planform area and the sweep angle of the wing number 2 are higher than those of wing number 1). Both FTB\_4-322 and FTB\_4-421 show the same lift coefficient since their planform area is quite the same.

Finally, for  $\alpha \geq 5^\circ$  the FTB\_4-211 configuration shows lower aerodynamic lift force since its planform area is the lowest. As far as drag is concerned, all the configurations show the same  $C_D$  except of the FTB\_4-211 one (which is the sharper aeroshape). Figure 6.48 also shows that all the configurations are statically stable for  $\alpha$  higher than  $2^\circ$  except of the FTB\_4-421 one [14]. Such configuration is characterized by static stability for AoA larger than  $15^\circ$ . In particular, the concepts 222, 211, and 521 are trimmed, respectively, at about  $4^\circ$ ,  $6^\circ$ , and  $10^\circ$  in clean configuration.

Moreover, FTB\_4-322 can be trimmed through flap negative deflection for positive AoA whereas FTB\_4-222 for  $\alpha > 4^\circ$ . FTB\_4-521 is able to perform a re-entry flight at a rather low AoA, thus flying like an airplane and not at a high AoA as the classical re-entry flight of the US Space Shuttle.

As far as the lateral-directional stability is concerned, Figs. 6.49 and 6.50 show for  $\alpha = 5^\circ$  the effect of sideslip on rolling and yawing moment coefficients along with Mach number, respectively.

(continued)

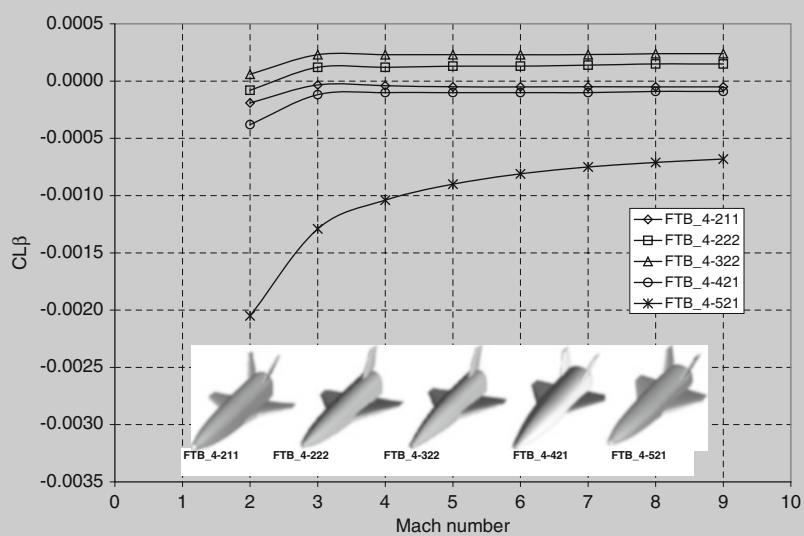


**Fig. 6.49** FTB\_4 effect of sideslip on rolling moment coefficients along with Mach at  $\alpha = 5^\circ$

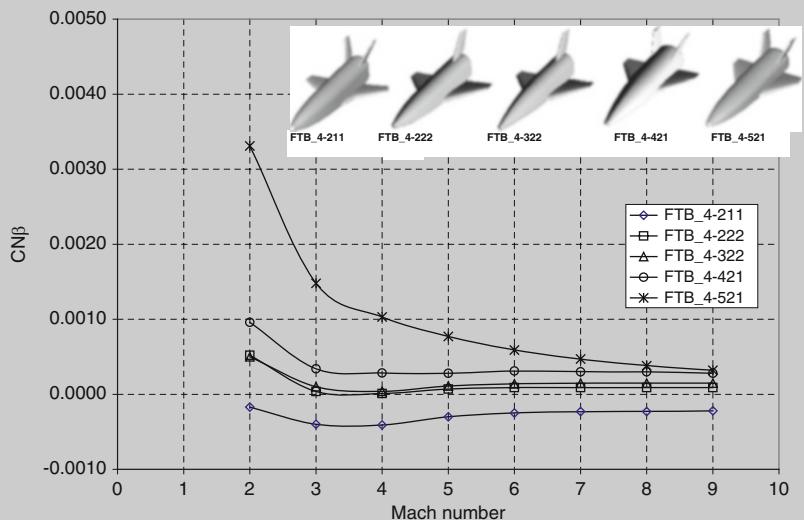


**Fig. 6.50** FTB\_4 effect of sideslip on yawing moment coefficients along with Mach at  $\alpha = 5^\circ$

(continued)

As shown, the FTB\_4-421 configuration is statically stable in lateral-directional flight.

Recall that the safe flight of an airplane depends on the static directional stability (the weather vane effect) and on the dihedral effect (roll due to yaw). For directional stability,  $C_{n\beta} > 0$ . For dihedral effect,  $C_{l\beta} < 0$ . The effect of the wing flaps on vehicle aerodynamic coefficients as a function of aileron deflection and AoA is shown in Figs. 6.51 and 6.52 for Mach number equal to 6,7 and  $\alpha = 5^\circ$ . For all the cases, the magnitude of the increments increases with AoA, with a quite linear trend. In particular, in Fig. 6.51, it can be seen that, at  $M_\infty = 7$ , for both the FTB\_4-211 and FTB\_4-521 configurations, the wing flap deflection needed to trim the vehicle is equal to about  $10^\circ$ , whereas at  $M_\infty = 6$  the latter concept can be trimmed at a lower flap deflection (say about  $7^\circ$ ).

For low deflections, Fig. 6.52 highlights that the aerodynamic efficiency slightly increases. However, it must be stressed that this result is a consequence of the  $C_m$  trend that depends also on the final real position of the CoG. The current design is made to realize small positive values of  $C_m$  in the flight conditions of interest, but the trim and stability analysis should also guarantee a sufficient margin in order to avoid negative values of  $C_{my}$ .

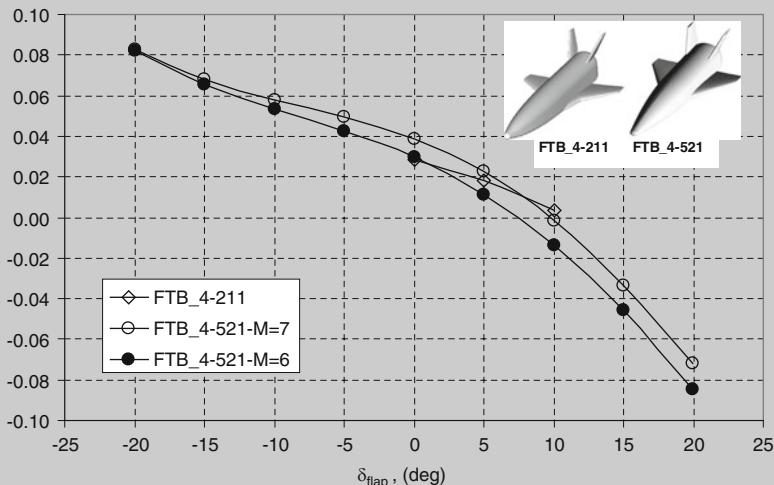


**Fig. 6.51** Effect of wing flap deflection on  $C_m$  at  $M_\infty = 6, 7$  and  $\alpha = 5^\circ$ . Pole at CoG

(continued)

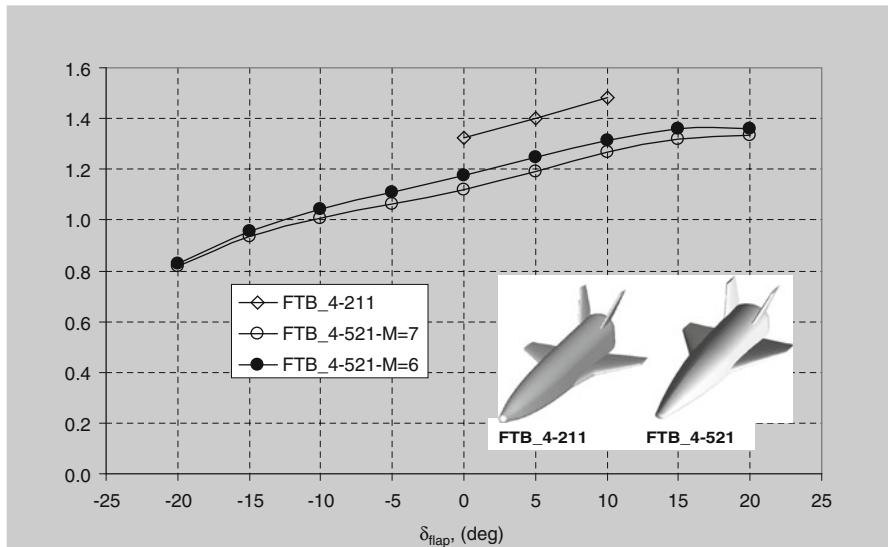


Fig. 6.52 Effect of wing flap deflection on L/D at  $M_\infty = 6, 7$  and  $\alpha = 5^\circ$

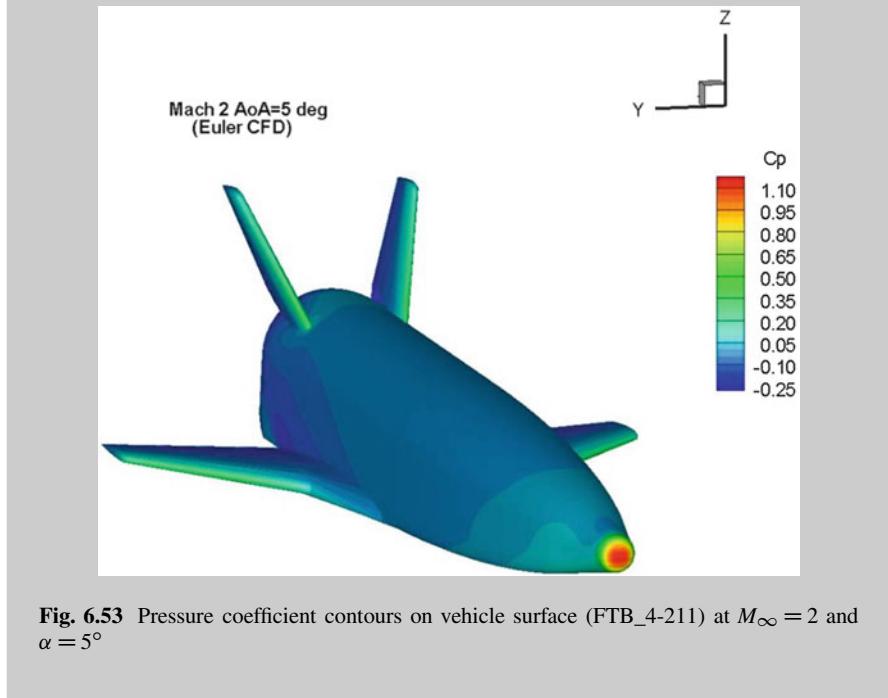
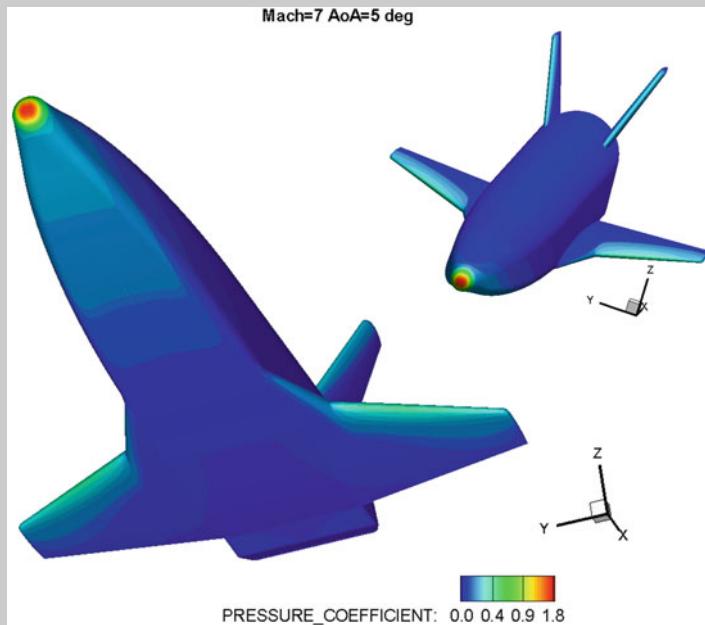


Fig. 6.53 Pressure coefficient contours on vehicle surface (FTB\_4-211) at  $M_\infty = 2$  and  $\alpha = 5^\circ$

(continued)

Finally, in Figs. 6.53 and 6.54 the pressure coefficient ( $C_p$ ) contours on the FTB\_4-211 vehicle surface are shown, flying at  $\alpha = 5^\circ$  at  $M_\infty = 2$  and  $M_\infty = 7$ , respectively.



**Fig. 6.54** Pressure coefficient contours on vehicle surface (FTB\_4-211) at  $M_\infty = 7$  and  $\alpha = 5^\circ$

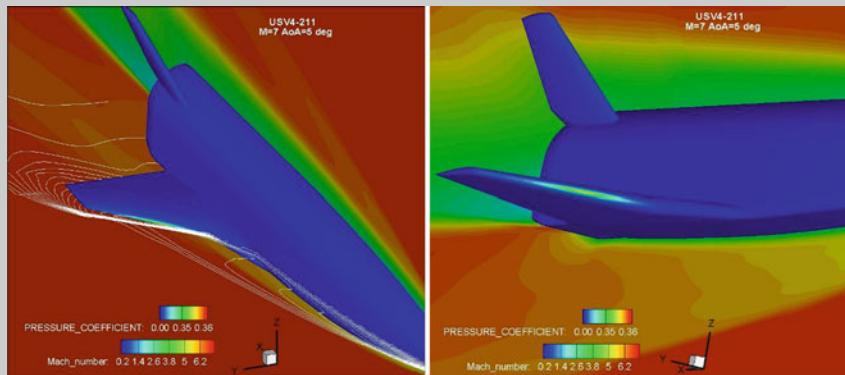


**Fig. 6.55** Contours of pressure coefficient over FTB\_4-211 surface. Mach number contours on vehicle symmetry plane and wing plane

(continued)

Another design issue accounted in the trade-off analysis is the shock–shock interaction (SSI) phenomenon, detected by means of CFD simulations. For example, the SSI that takes place on the FTB\_4-211 at  $M_\infty = 7$  and  $\alpha = 5^\circ$  can be seen in Fig. 6.55, where contour plots of pressure coefficient on vehicle surface and of Mach number on the FTB\_4-211 symmetry plane are shown. Indeed, Fig. 6.55 left side points out the bow shock cut in the wing plane where it is clearly recognized the interaction with bow and wing shocks. This interaction results in pressure and heat flux overshoots, where the SSI impinges the wing leading edge, as clearly shown in the right side of Fig. 6.55. Therefore, for a reliable wing aeroheating estimation, Navier–Stokes computations are mandatory as FTB\_4 design matures.

As far as the lateral–directional stability is concerned, Fig. 6.56 shows for  $\alpha = 5^\circ$  the effect of sideslip on rolling ( $C_l$ ) and yawing moment ( $C_n$ ) coefficients along with Mach number.

As shown, the configuration is statically stable in lateral–directional flight at  $\alpha = 5^\circ$ . Note that the body flap can obviously offer advantages also on both longitudinal and lateral–directional stability by providing margins on CoG location. In fact, the body flap, located on the rear lower portion of the aft fuselage, allows to pitch trim the vehicle, while elevons provide concept roll control. The lift-to-

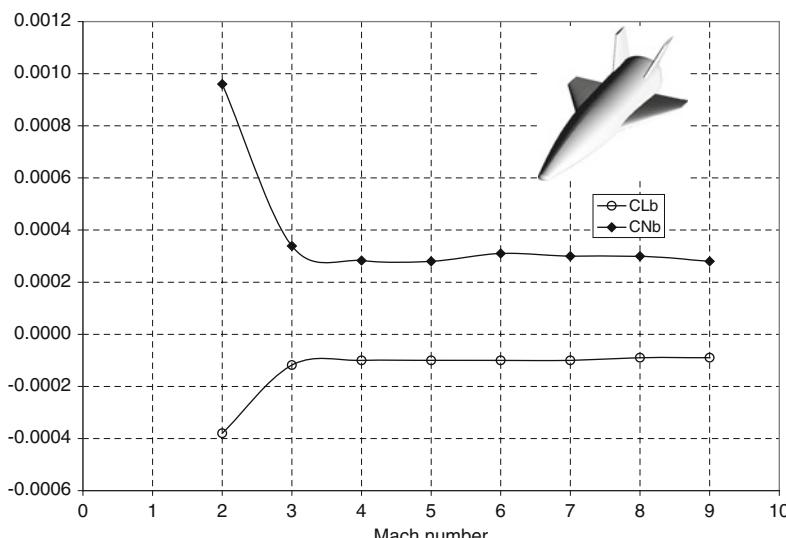
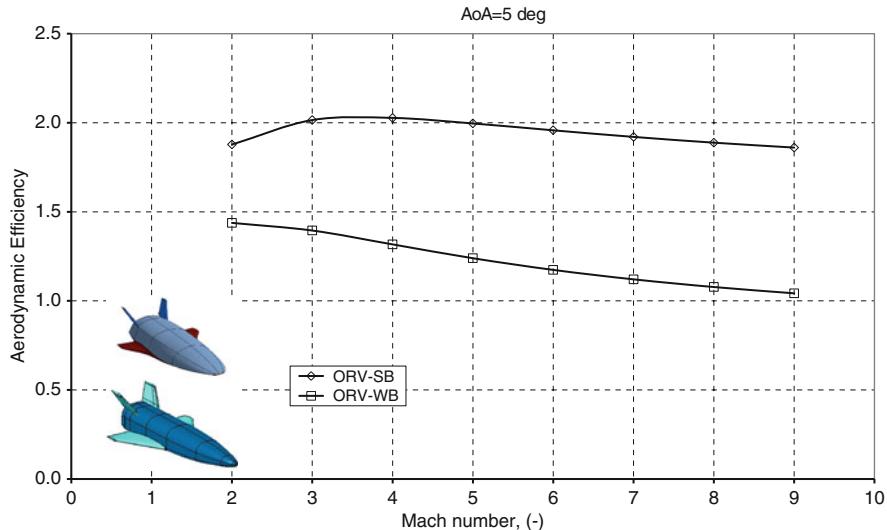


Fig. 6.56 ORV-WSB sideslip derivatives of  $C_l$  and  $C_n$  up to  $M_\infty = 9$ , at  $\alpha = 5^\circ$



**Fig. 6.57** L/D versus Mach at  $\alpha = 5^\circ$ . Comparison between ORV-WSB and ORV-SB concepts

drag ratio of ORV-WSB and ORV-SB concepts is recognized in Fig. 6.57 for Mach number ranging from 2 to 9 at  $\alpha = 5^\circ$ .

As one can see, the ORV-SB concept features an enhanced aerodynamic efficiency due to its highly streamlined aeroshape compared with ORV-WSB one, as expected.

Finally, lift, drag, aerodynamic efficiency, and pitching moment comparison at  $M_\infty = 10$  among ORV-WSB, ORV-WBB, and ORV-SB concepts can be recognized from Figs. 6.58, 6.59, 6.60, and 6.61.

Figure 6.58 shows the comparison of aerodynamic lift coefficient of each concept [1, 2, 33].

As one can see, ORV-SB and ORV-WBB feature the same lift slope that is larger than that of the ORV-WSB concept.

The comparison of aerodynamic drag is provided in Fig. 6.59. In this case, and in that of lift, discussed above, differences in aerodynamic performance at rather low AoA are dictated by difference in fuselage forebody slopes and cross-sectional area (see Fig. 6.11). Indeed, the larger the vehicle's cross section, the greater the drag coefficient.

On the other hand, at high AoA, differences in aerodynamic coefficients are due to different planform shapes which characterize each concept (see Fig. 6.11). The ORV-WSB is the lower planform surface concept.

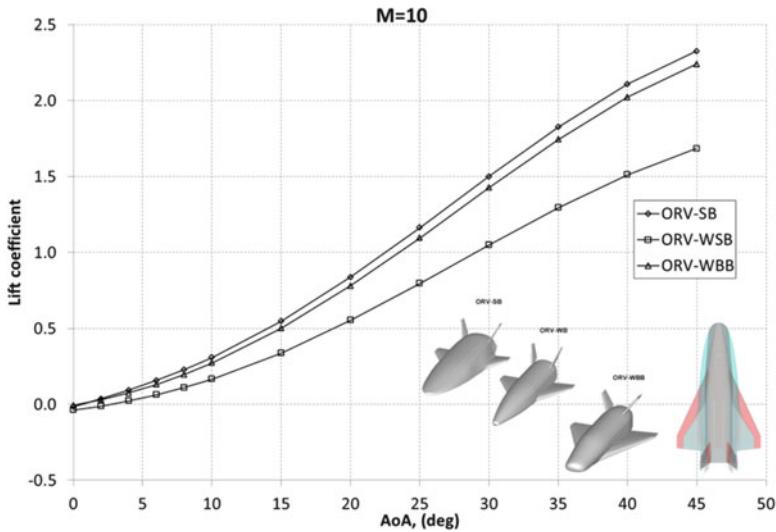


Fig. 6.58 Lift coefficients at Mach 10. Comparison among concept performances

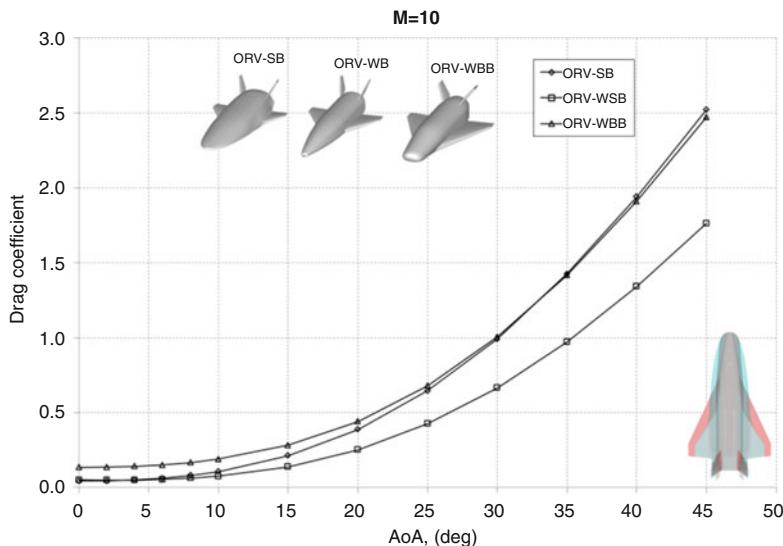


Fig. 6.59 Drag coefficients at Mach 10. Comparison among concept performances

Anyway, the slope<sup>3</sup> of lift and drag coefficients is close, respectively, to  $\sin^2\alpha \cos\alpha$  and  $\sin^3\alpha$ , as stated by impact flow theory [1, 5].

<sup>3</sup>The fact that aerodynamic coefficients are nonlinear functions of angle of attack is a typical feature of hypersonic flow regime.

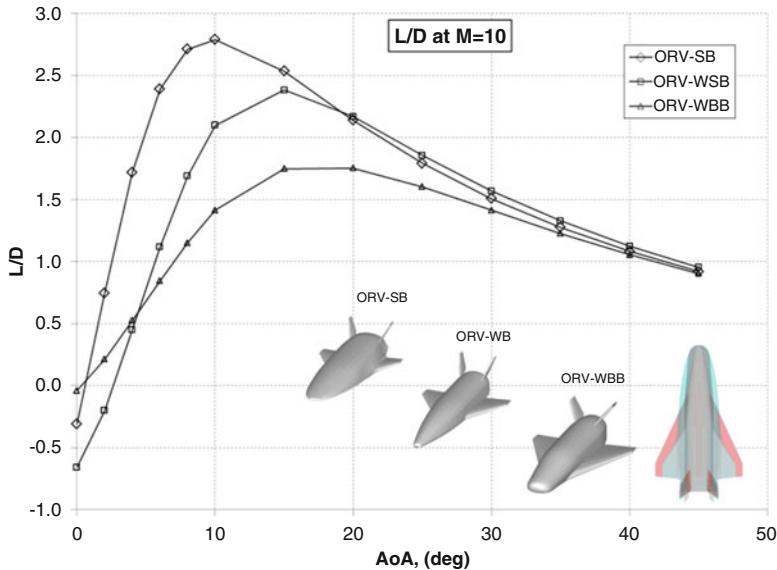


Fig. 6.60 Lift-to-drag ratio at Mach 10. Comparison among concept performances

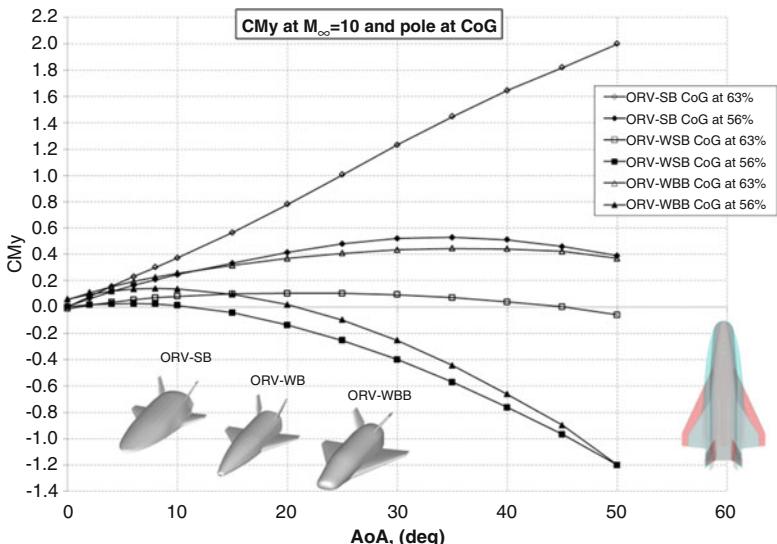


Fig. 6.61 Effect of CoG position on  $C_m$  at Mach 10. Comparison among concept performances

Differences in aeroshape discussed above result in different L/D profiles versus AoA, of course (Fig. 6.60). For instance, L/D suddenly increases with  $\alpha$  in the case of streamlined configuration, while  $(L/D)_{\max}$  decreases as vehicle bluntness increases (the larger the vehicle bluntness, the lower the peak aerodynamic efficiency).

It is worth to note that this high ( $L/D$ ) slope of very streamlined aeroshape is extremely important for scramjet propelled vehicle considering that such kind of spacecraft must fly at small AoA in order to assure proper air flow conditions at scramjet intake and minimize aerodynamic drag.

Furthermore, the lift-to-drag ratio is one of the most important features of vehicle aerodynamic performances. In fact, it has a direct impact on range and cross-range capabilities of the re-entry vehicle that has to reach its nominal landing site at the end of space mission by unpowered flight.

In particular, the ORV-SB concept features the best lift-to-drag ratio up to about  $\alpha = 20^\circ$ .

The  $(L/D)_{\max}$  of the ORV-SB is equal to about 2.8 and is attained at  $\alpha = 10^\circ$  AoA.

On the other hand, the maximum aerodynamic efficiency of ORV-WB and ORV-WBB is reached nearly to  $\alpha = 15^\circ$  and is equal to about 2.4 and 1.5, respectively.

For AoA larger than  $20^\circ$ , differences in aerodynamic efficiency decrease as  $\alpha$  increases, and they vanish for  $\alpha > 35^\circ$ . As a result, in the framework of re-entry at high angle of attack, namely,  $35\text{--}40^\circ$  (e.g., close to that of US Orbiter), differences in aeroshape do not significantly affect the descent flight. In fact, as said before, at hypersonic speed and at high AoA, vehicle aerodynamic is dictated essentially by its planform shape.

As far as pitching moment is concerned, the effect of CoG position (with respect to the fuselage length) on the  $C_m$  for each vehicle concept is summarized in Fig. 6.61.

As shown, when the CoG is at 63 % of fuselage length, the ORV-SB features a strong static instability in longitudinal flight highlighting that the center of pressure is well ahead of the CoG (i.e., negative static margin); the ORV-WBB is statically stable in pitch for  $\alpha > 40^\circ$  and can be trimmed by positive flap deflections, while the ORV-WSB is statically stable in pitch for  $\alpha > 30^\circ$  and shows also a natural trim point at about  $45^\circ$  AoA.

On the contrary for CoG at 56 %, the ORV-SB concept becomes statically stable in longitudinal flight for  $\alpha > 35^\circ$  and trim AoA can be attained by positive flap deflections; the other two concepts (WSB and WBB) are statically stable in pitch for  $\alpha > 5^\circ$  and feature a natural trim point at  $10^\circ$  and  $20^\circ$  AoA, respectively. In particular, they can be trimmed at high AoA by means of negative (i.e., trailing edge up) flap deflections [1, 4, 5, 34].

Note that in statically stable and trimmed flight, the attitude of the vehicle is aligned in such a way that the total external moment acting on the vehicle is zero. This means that after a disturbance, the vehicle tends always to move back toward the trimmed state.

Anyway, pitching moment behavior versus AoA points out that vehicle subsystems arrangement (i.e., CoG position) must be carefully addressed. Indeed, in order to have a statically stable and trimmable vehicle concept, the CoG has to be carefully chosen with reference to the vehicle shape.

## 6.7 CFD-Based Aerodynamic Results

For what concerns numerical flowfield computations, on the base of the flight envelope of Fig. 6.13, a number of flight conditions have been chosen to perform some CFD computations in steady-state conditions, according to the space-based design approach.

Numerical results aim to anchor engineering analyses in order to increase their accuracy and to focus on some critical design aspects not predictable by using simplified tools as, for example, shock–shock interaction (SSI) and shock-wave–boundary-layer interaction (SWIBLI) phenomena and real gas effects as well [12]. Indeed, SSI phenomenon determines pressure, and heat flux overshoots on leading edges of both wing and tail to account for in TPS design, while SWIBLI influences control surfaces effectiveness. The CFD test matrix is summarized in Table 6.2.

Note that each cell identifies a CFD run (i.e., check point).

It is worth noting that at  $M_\infty = 8, 10, 16$ , and  $20$ , nonequilibrium CFD computations are also carried out. Real gas effects can be important because, during atmospheric re-entry, dissociation process takes place in the shock layer, which can have an influence on the aerodynamic coefficients. Real gas effects are expected to influence stability and control derivatives of vehicle, in particular its pitching moment, as highlighted by the first shuttle re-entry (STS-1) where an unexpected higher nose-up pitching moment required a body flap deflection twice than that predicted by the preflight analyses to trim the Orbiter [12, 14].

Further, real gas effects cause a shock that lies closer to the vehicle with respect to the position that would characterize a perfect gas case (i.e., thin shock layer)

**Table 6.2** CFD test matrix

Mach	CFD test matrix							AoS @ AoA=5°		
	0	5	10	20	30	40	45	2	4	8
2	X	X	X	X				X		
3	X	X	X	X				X	X	X
4		X						X		
5	X	X	X	X				X		
6	X	X	X					X		
7	X	X	X					X		
8		X	X							
8		X	X							
10			X	X	X					
16			X	X	X					
20			X	X	X	X				
20			X	X	X	X				
25					X		X			
X	Perfect Gas									
X	Reacting Gas									

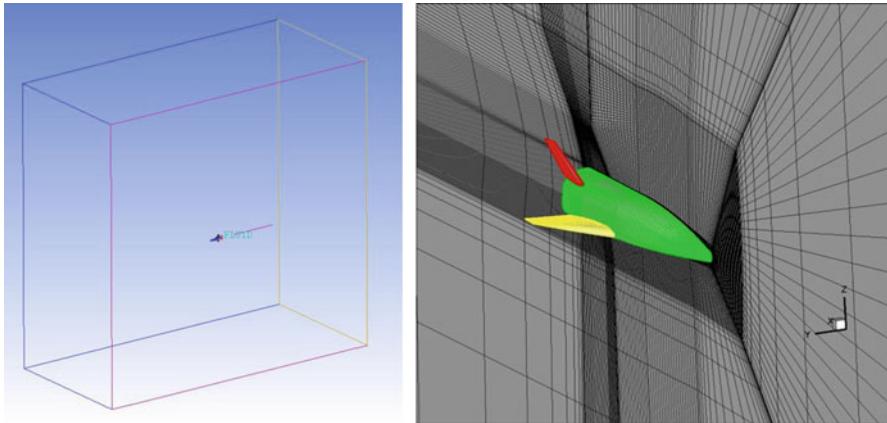


**Fig. 6.62** Sub-transonic computational domain. Mesh on symmetry plane and ORV-WSB surface

[12, 14]. This means that strong SSI phenomenon arises. These effects obviously occur only at high Mach numbers [12–14].

Also, numerical nonequilibrium investigations allow assessing good characterization of the wall catalyticicity in order to reduce the design margins, avoiding the need to apply the too conservative hypothesis of fully catalytic wall, usually used.

CFD simulations also help in finding the effect of laminar-to-turbulent transition to account for in vehicle TPS design. It is well known that it can cause strong dangerous overheating on the vehicle skin. Numerical CFD computations have been carried out on both a multiblock structured and hybrid unstructured grid similar to those shown in Figs. 6.62 and 6.63. Figure 6.62 shows the sub-transonic computational domain considered to address ORV-WSB aerodynamic at sub-transonic speed.

As one can see, the external boundary of the half-body grid has been built as a Cartesian block, and farfield surfaces are located at about ten body lengths far from the body (upstream and downstream) to ensure that the flow at the boundary is close to free stream. Indeed, the farther we are from the vehicle, the less effect it has on the flow and so more accurate is the farfield boundary condition.

Close-up views of 3-D sup-hypersonic mesh on both vehicle surface and symmetry plane can be seen in Fig. 6.63 in the case of ORV-WSB (left) and ORV-WBB (right side).

Of course, for all the computational domains, made of about  $6 \times 10^6$  cells (half body), the distribution of surface grid points is dictated by the level of resolution desired in various areas of vehicles, such as stagnation region, according to the computational scopes. Grid refinement in strong gradient regions of flowfield is addressed by means of solution adaptive approach.

The coordinate  $y^+$  of the first cell adjacent to the surface is about 1.

As far as numerical results are concerned, it is worth to note that they refer to both converged and grid independent computations [6, 7, 16, 20]. Indeed,

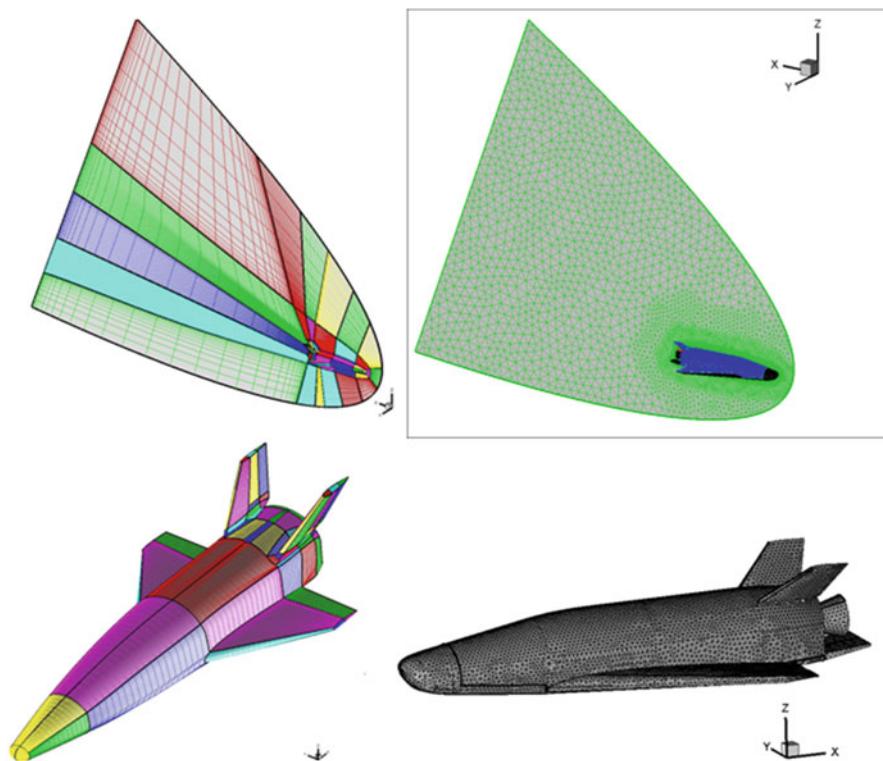


**Fig. 6.63** Sup-hypersonic computational domain. Mesh on symmetry plane and vehicle surface

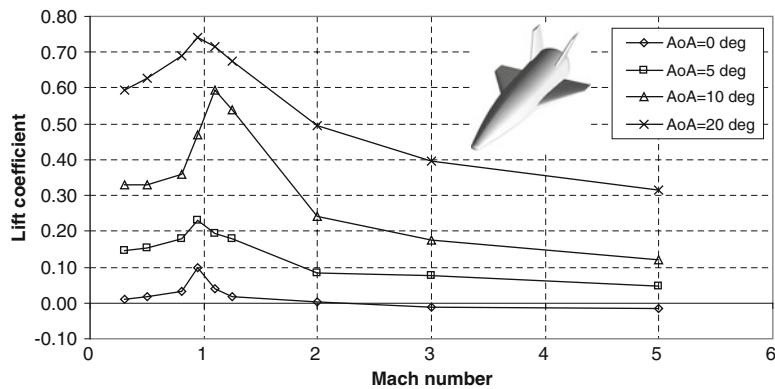


**Fig. 6.64** Lift coefficient versus Mach number for different AoA. ORV-WSB concept

Figs. 6.64 and 6.65 summarize the ORV-WSB aerodynamics at  $Reynolds = 10^6$ , for Mach ranging from 0.3 to 5 and for  $\alpha = 0^\circ, 5^\circ, 10^\circ$ , and  $20^\circ$ . As shown, lift and drag coefficients rise in the transonic region where the presence of the shock wave

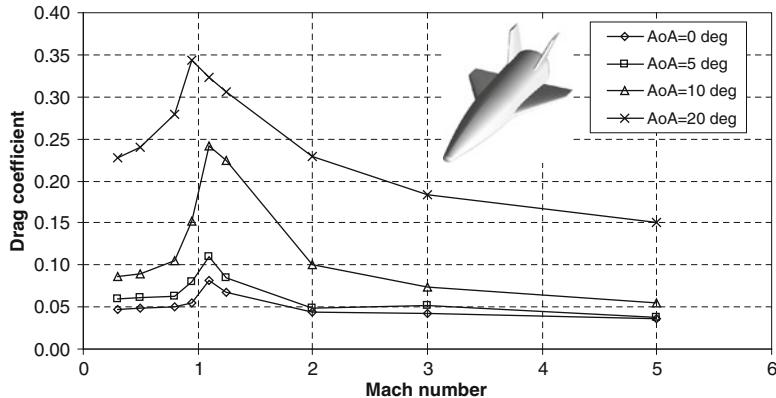


Fig. 6.65 Drag coefficient versus Mach number for different AoA. ORV-WSB concept

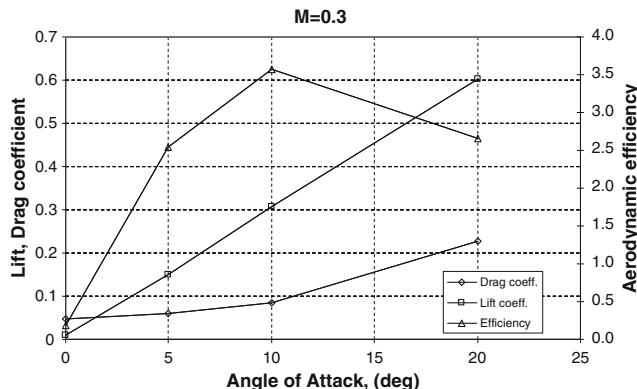
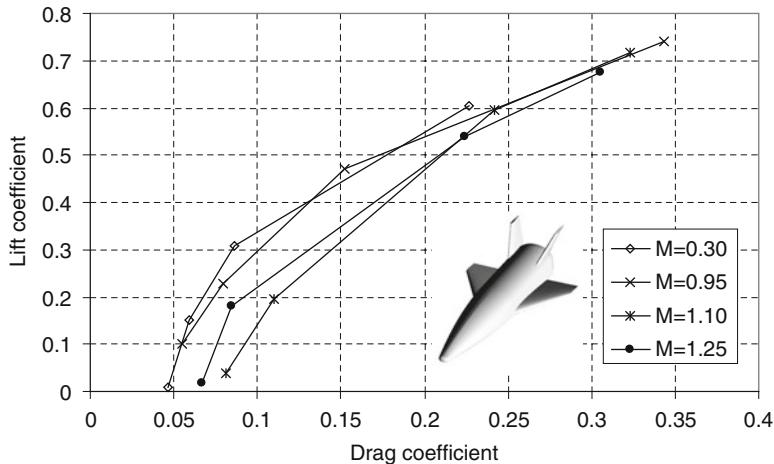


Fig. 6.66  $C_L$ ,  $C_D$  and L/D versus AoA for  $M_\infty = 0.3$ . ORV-WSB concept

produces a large increase of the aerodynamic forces on the vehicle, e.g., increase of wave drag and base drag that in this region reach their maximum values, as expected. On the contrary, when Mach number increases, aerodynamic coefficients tend to reach a limit value, according to the Mach number independence principle (i.e., Oswatich principle).

In particular, this behavior is similar for all the considered AoA, and the strong dependence of the drag on the AoA is essentially due to the large increases of the induced drag with  $\alpha$ .

In Fig. 6.66, on the same chart, the aerodynamic lift, drag, and L/D versus  $\alpha$  at  $M_\infty = 0.3$  are reported. Aerodynamic results at this flight conditions are extremely important considering that  $M_\infty = 0.3$  represents the nominal landing condition at the end of the unpowered re-entry flight. Indeed, Fig. 6.66 shows that the lift coefficient at  $M_\infty = 0.3$  steadily increases from  $\alpha = 0^\circ$  to  $20^\circ$  indicating that the vehicle does not stall up to  $20^\circ$  at this Mach number conditions. Hence, the drag



**Fig. 6.67** Drag polars for Mach ranging from 0.3 to 1.25 and for  $\alpha = 0^\circ, 5^\circ, 10^\circ$ , and  $20^\circ$ . ORV-WSB concept

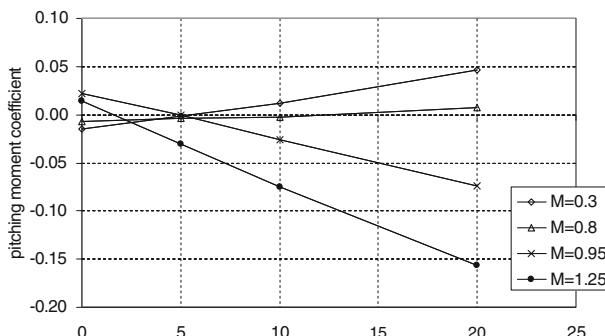


**Fig. 6.68**  $C_m$  vs.  $\alpha$  at different Mach numbers. ORV-WSB concept

coefficient at zero AoA is about 0.047, and it continues to rise as AoA increases, which is expected, up to reach about 0.22 at  $\alpha = 20^\circ$ . The maximum L/D close to 3.5 is attained at  $\alpha = 10^\circ$ . Of course, extra lift can be provided by means of positive flap deflections, thus providing also statically stable trim conditions at landing AoA.

In Fig. 6.67 vehicle polars for Mach number ranging from 0.3 to 1.25 and for  $\alpha = 0^\circ, 5^\circ, 10^\circ$ , and  $20^\circ$  are also reported, thus pointing out ORV-WSB aerodynamics in sub-transonic flow conditions [6–8].

The variation of the pitching moment coefficient of ORV-WSB versus  $\alpha$  is presented in Fig. 6.68.

As shown, at low subsonic speed (Mach 0.3 and 0.8), the ORV-WSB vehicle is statically unstable in longitudinal flight (i.e.,  $C_{m\alpha} > 0$ ) with the given CoG for all the considered AoA.

Concept's stability changes for Mach larger than 0.95. This means that at these flight conditions, a perturbation which produces an increased angle of attack causes a nose-down (negative) pitching moment, which decreases the AoA, restoring the vehicle to its original position. In particular,  $C_m$  in the sub-transonic regime follows a fairly linear trend.

Further, the AoA at which the moment coefficient about the center of gravity equaled zero (i.e., trim condition) is approximately 5° for  $M_\infty = 0.30$  and  $M_\infty = 0.95$ , 12° at  $M_\infty = 0.80$ , and  $\alpha = 2^\circ$  for  $M_\infty = 1.25$  [9–11].

In order to well understand vehicle subsonic aerodynamic performances, Figs. 6.69, 6.70, and 6.71 show the pressure coefficient contours maps over the ORV-WSB surface for all the analyzed AoA at  $M_\infty = 0.3$ .

As shown, on the leading edge, we see a stagnation point where the velocity of the flow is nearly zero. The fluid accelerates on the upper surface (i.e., leeside) as highlighted by the negative value of  $C_p$  (i.e., pressure less than atmosphere one).

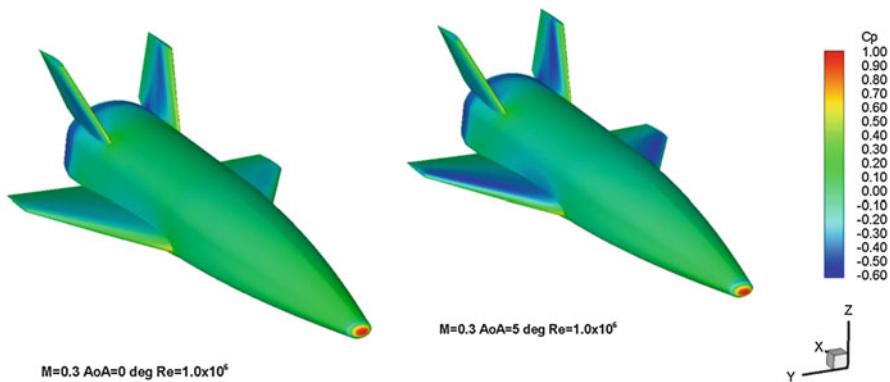


**Fig. 6.69** Pressure coefficient at  $M_\infty = 0.3$  and for  $\alpha = 0^\circ$  and  $5^\circ$ . ORV-WSB concept

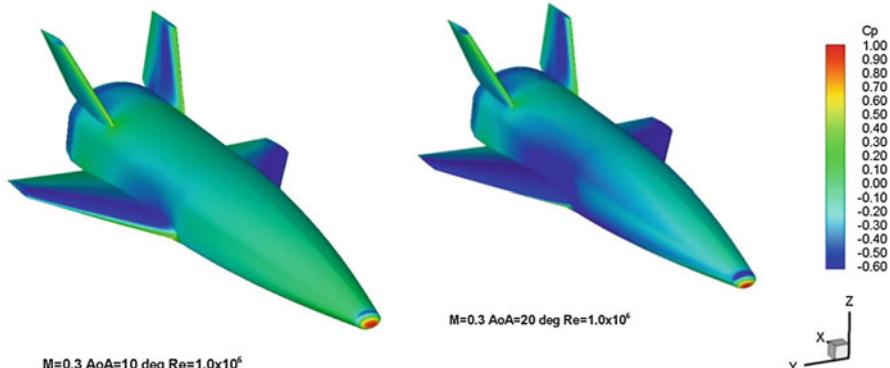


**Fig. 6.70** Pressure coefficient at  $M_\infty = 0.3$  and for  $\alpha = 10^\circ$  and  $20^\circ$ . ORV-WSB concept

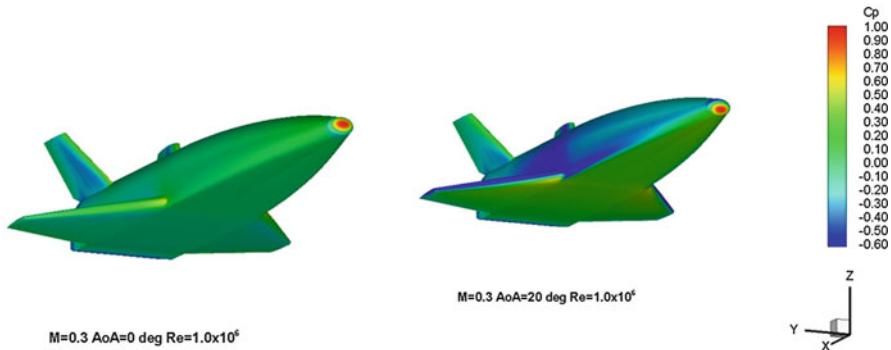


**Fig. 6.71** Pressure coefficient at  $M_\infty = 0.3$  and for  $\alpha = 0^\circ$  and  $20^\circ$ . ORV-WSB concept

On the contrary, at the trailing edge the flow on the upper surface decelerates and converges with the flow on the lower surface (i.e., windside) according to the Bernoulli equation (i.e., whenever there is high velocity vectors, we have low pressures, and *vice versa*).

With the pressure distributions as sketched above, the effect on the vehicle upper surface is the larger, and there is a resultant upward force on the spacecraft, that is the lift [12–14].

In particular, the pressure reduction on the upper surface increases both in intensity and extent at high incidence (see Figs. 6.70 and 6.71), while the stagnation point moves progressively further back on the lower surface, and the increased pressure on the lower surface covers a greater proportion of the surface, as shown in Fig. 6.71.

Therefore, the following conclusions may be drawn: at low incidence the lift is generated by the difference between the pressure reductions on the upper and lower surfaces; at higher incidences the lift is partly due to pressure reduction on the upper surface and partly due to pressure increase on the lower surface. Figure 6.72 shows the effect of AoA on the flowfield streamlines on the vehicle symmetry plane at  $M_\infty = 0.3$  and for  $\alpha$  ranging from  $0^\circ$  to  $20^\circ$  AoA.

Streamtraces are displayed in order to highlight the flowfield structure surrounding the vehicle, especially the complexity of the wake flow. As one sees, a rather strong base expansion together with a vortex feature can be appreciated as well. Indeed, for all the AoA in the wake flow is clearly visible the pattern of two swirling vortices, close to that of Von Karman ones, which characterize the unsteady<sup>4</sup> downstream separation of flow over the bluff bodies (in this case the blunt base).

<sup>4</sup>When large flow separation arises at vehicle base, for example, at high angle of incidence, large oscillation of global aerodynamic loads can be observed. In this case unsteady CFD analyses are mandatory to address vehicle aerodynamic performances. A nondimensional frequency of Strouhal ( $St = f \frac{L}{V}$ ) number must be chosen as a target value for the simulation time step. Indeed, it represents the shedding frequency of a circular cylinder which is almost constant over a wide

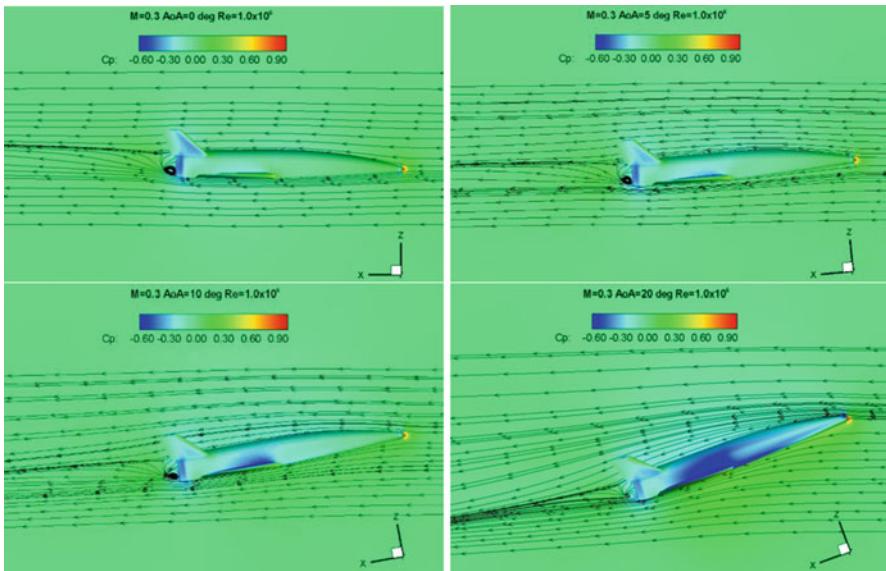


**Fig. 6.72** Pressure field past ORV-WB with streamtraces on the vehicle symmetry plane at  $M_{\infty} = 0.3$  and for  $\alpha = 0^\circ, 5^\circ, 10^\circ$ , and  $20^\circ$

This determines an increase in drag (i.e., pressure drag). It is worth to note that space vehicles need drag to decelerate as much as possible during the atmospheric descent in order to lose their great amount of internal energy (kinetic plus potential) to safe land. Therefore, space vehicles typically have a truncated afterbody (or blunt base), which resulted in base drag being a significant component of the total vehicle drag [35]. Anyway, the blunt base of re-entry vehicle is also needed to allocate the nozzles of the rocket motor (like the Space Shuttle Orbiter) for the boost needed in the ascent phase and the de-boost necessary to start the deorbiting maneuver before the atmospheric re-entry flight (see nozzle at the base of ORV-WBB in Fig. 6.7).

In Fig. 6.73 an example of the 3-D flowfield streamtraces, predicted by CFD computations, is reported for the ORV-WSB. It is possible to note the formation of the leading edge vortex, typical of delta-wing configuration, and its interaction with the wingtip vortex.

Note that leading edge vortex lift is an important source of vehicle lift. The pressure on the upper surface of the wing is lower than that of the surrounding atmosphere, while the pressure on the windside is greater than that on the leeside. Thus, over the upper surface, air will tend to flow inward toward the root from the

---

range of Reynolds number. Hence, the corresponding nondimensional period  $T$  if divided by a number  $N$  of time steps provides the nondimensional time step of  $\Delta t = T/N$ .

A number of time steps, corresponding to a total number of convective time units ( $CTU = t_{\text{inf}}/L_{\text{ref}}$ ), referred to the vehicle reference length, may be needed to obtain the averaged flow field along with the global loads.

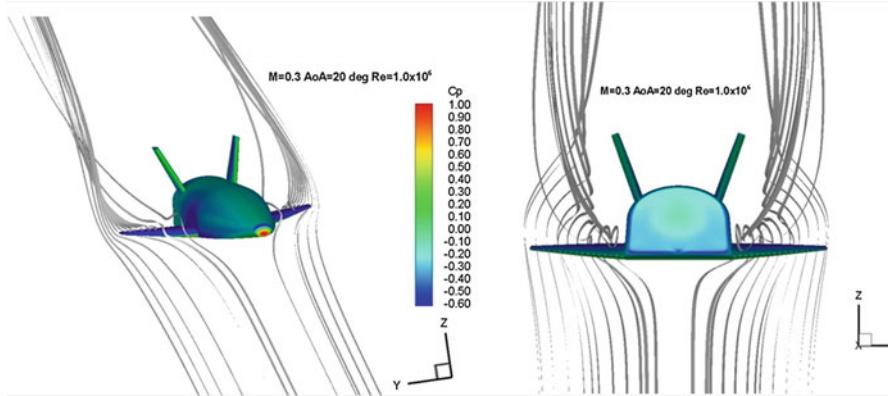


**Fig. 6.73**  $C_p$  on ORV-WSB surface with flowfield streamtraces at  $\alpha = 20^\circ$  and  $M_\infty = 0.3$ .

tips, being replaced by air that was originally outboard of the tips. Similarly, on the undersurface air will either tend to flow inward to a lesser extent or may tend to flow outward. Where these two streams combine at the trailing edge, the difference in spanwise velocity will cause the air to roll up into a number of small streamwise vortices, distributed along the whole span. These small vortices roll up into two large vortices just inboard of the wingtips.

Further, in the following figures, some of main interesting hypervelocity flowfield features obtained for the ORV-WSB concept are shown. For example, the Mach number and flow species fields for  $M_\infty = 10$  and 20 at  $\text{AoA} = 10^\circ, 30^\circ$ , and  $40^\circ$  are reported from Figs. 6.74, 6.75, 6.76, 6.77, and 6.78. Looking at contour fields on the vehicle symmetry plane, one can appreciate the rather strong bow shock that occurs ahead of the vehicle concept during descent at these flight conditions, especially at higher AoA. Indeed, Figs. 6.74 and 6.75 show the Mach number field past the rather sharp wing–body vehicle for  $M_\infty = 10$  and for  $10^\circ$  and  $30^\circ$  AoA, respectively [14, 16, 36].

Figure 6.76 shows the blow-up of the flow field past the vehicle for both free-stream conditions. Streamtraces are also displayed.

As shown, even if the CFD computations are carried out in the case of perfect gas flow, the bow shock is very close to the vehicle due to its streamlined configuration.

The effect of AoA on flowfield past ORV-WSB flying at  $M_\infty = 10$  can be appreciated as well. Figure 6.77 displays the blow-up of the flowfield surrounding the rather sharp wing–body vehicle for  $M_\infty = 20$  and  $\alpha = 40^\circ$ . In this figure the Mach number and the static temperature contours field both on the vehicle symmetry plane and concept outer surface are provided.

Streamtraces are also displayed in order to highlight the flowfield structure surrounding the vehicle, especially the complexity of the wake flow.

As one can see, the flow stagnates downstream, thus increasing the local temperature distribution, and a strong base expansion together with a vortex feature can be appreciated as well at  $\alpha = 40^\circ$ .

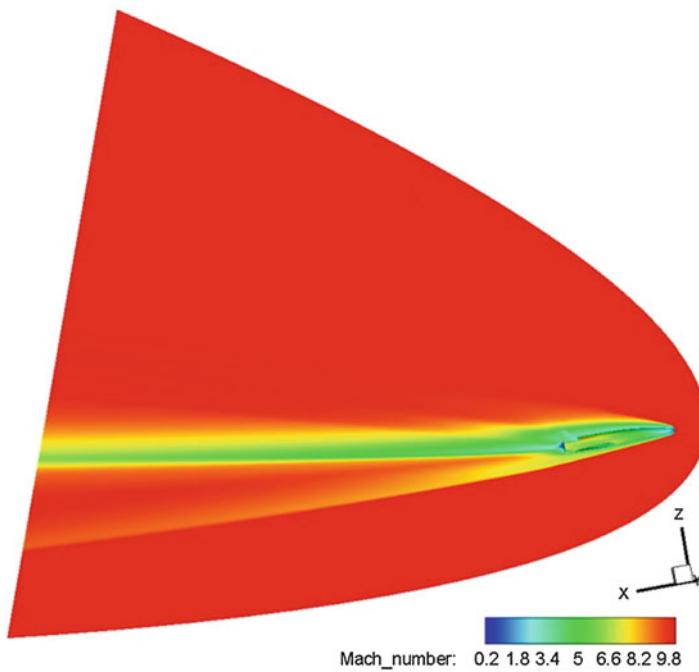


**Fig. 6.74** Mach contours on symmetry plane and ORV-WSB surface at  $M_\infty = 10$  and  $\alpha = 10^\circ$

In this case, air was considered made up of five chemical species ( $O_2$ ,  $N_2$ ,  $O$ ,  $N$ , and  $NO$ ) and in thermochemical nonequilibrium conditions.

The corresponding oxygen ( $O$ ) and nitrogen oxide ( $NO$ ) mass fractions contour fields are shown in Fig. 6.78.

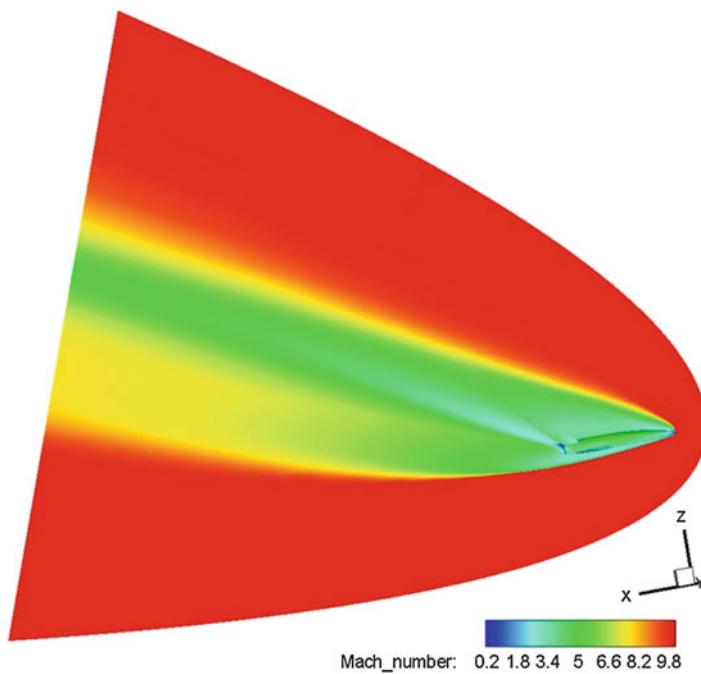
As far as AoS effect is concerned, Fig. 6.79 shows the Mach number contours on a fuselage cross plane and those of the static pressure on the vehicle surface at  $M_\infty = 6$ ,  $\alpha = 5^\circ$  and  $\beta = 2^\circ$ .

Figure 6.80 shows the same flowfield features as Fig. 6.79 but for  $M_\infty = 3$ ,  $\alpha = 5^\circ$  and  $\beta = 4^\circ$  and  $8^\circ$ . A different line of sight for  $M_\infty = 3$ ,  $\alpha = 5^\circ$ , and  $\beta = 8^\circ$  is provided in Fig. 6.81.

The effect of sideslip angle on flowfield features is clearly shown on the nonsymmetrical distribution of contour fields. This determines apart from lift, drag, and pitching moment the presence of lateral-directional aerodynamic force and moment acting on the vehicle concept.

Finally, Figs. 6.82 and 6.83 provide the pressure spike due to the SSI that takes place on the ORV-WSB at  $M_\infty = 6$ ,  $M_\infty = 7$  and  $\alpha = 5^\circ$ , respectively. Of course, the point of wing leading edge where this interaction impinges depends on the free-stream conditions.

Figure 6.82 shows the contour plot of pressure coefficient on vehicle surface, whereas Fig. 6.83 displays also the Mach number on the wing plane. It is clearly



**Fig. 6.75** Mach contours on symmetry plane and ORV-WSB surface at  $M_\infty = 10$  and  $\alpha = 30^\circ$

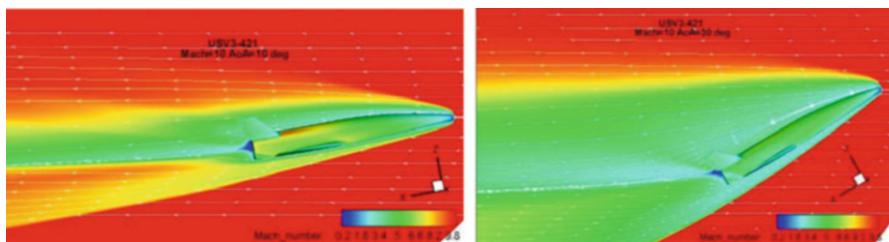


**Fig. 6.76** Mach number contours on symmetry plane and vehicle surface at  $M_\infty = 10$  and  $\alpha = 10^\circ$  and  $30^\circ$

shown the pressure overshoot where SSI impinges the wing leading edge as well as the trace of bow shock on the wing plane (see Fig. 6.83).

Numerical flowfield results for the ORV-WBB concept are provided in Figs. 6.84 and 6.85 for  $M_\infty = 25$  and  $\alpha = 30^\circ$ .

In particular, Fig. 6.84 highlights the Mach number and the  $N_2$  mass fraction contour fields on the vehicle symmetry plane and  $C_p$  on the concept outer surface.

Side and bottom views of the surface distribution of  $C_p$  at these flight conditions are summarized in Fig. 6.85. Here three flowfield cross sections are also reported to get an idea of the three-dimensional bow shock that envelopes the ORV-WBB at these flight conditions.

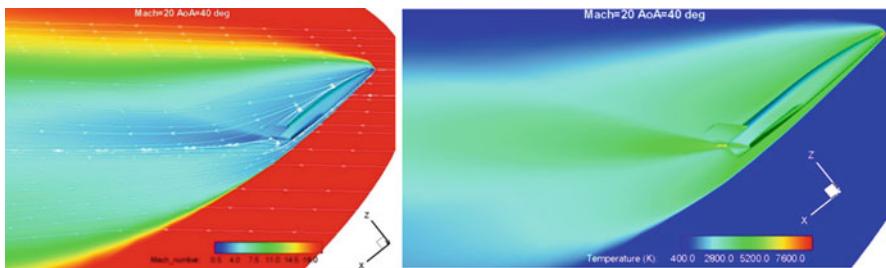


**Fig. 6.77** Nonequilibrium CFD computation at  $H_{\infty} = 70$  km,  $M_{\infty} = 20$ , and  $\alpha = 40^\circ$ . Mach and temperature contour fields. ORV-WSB

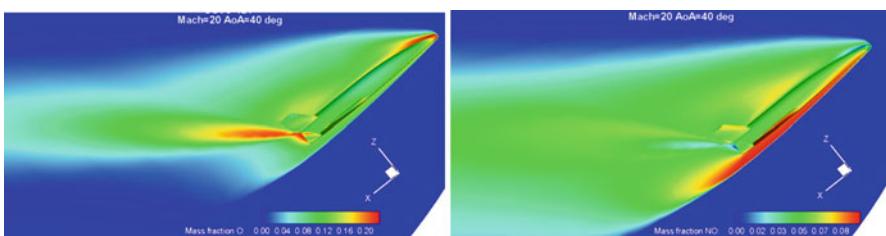


**Fig. 6.78** O and NO mass fractions. CFD computation at  $H_{\infty} = 70$  km,  $M_{\infty} = 20$ , and  $\alpha = 40^\circ$ . ORV-WSB concept

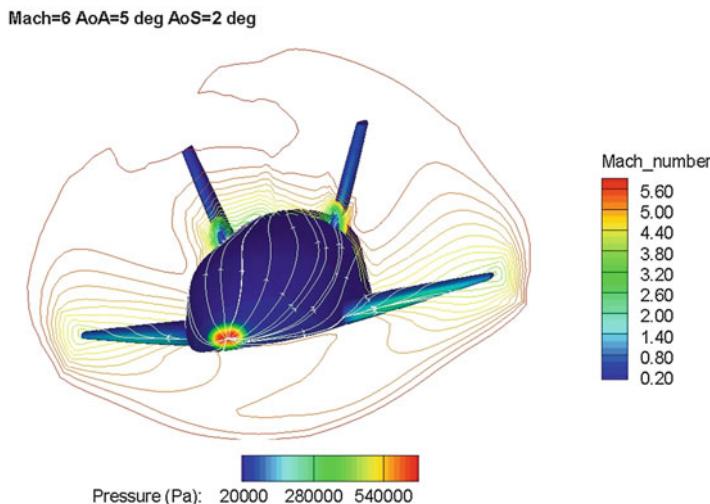


**Fig. 6.79** Mach contours on a fuselage cross plane and pressure contours on vehicle surface at  $M_{\infty} = 6$ ,  $\alpha = 5^\circ$ , and  $\beta = 2^\circ$ . Euler computation for ORV-WSB concept

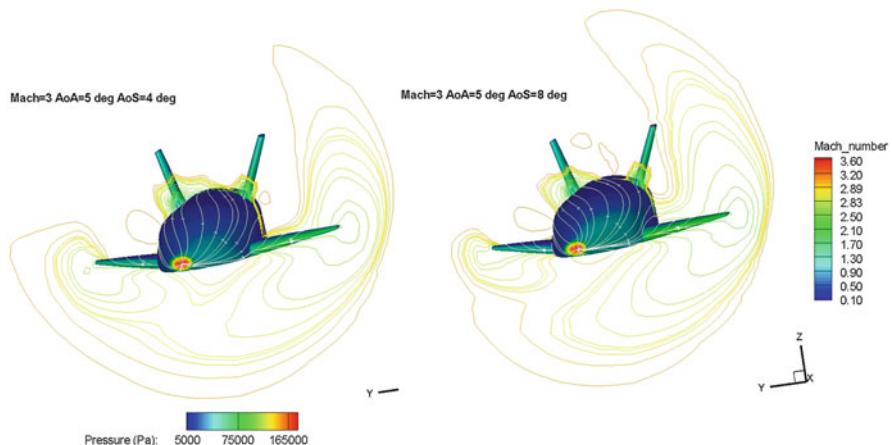


**Fig. 6.80** Mach contours on a fuselage cross plane and pressure contours on vehicle surface at  $M_\infty = 3$ ,  $\alpha = 5^\circ$ , and  $\beta = 4$  and  $8^\circ$ . Euler computation for ORV-WSB concept

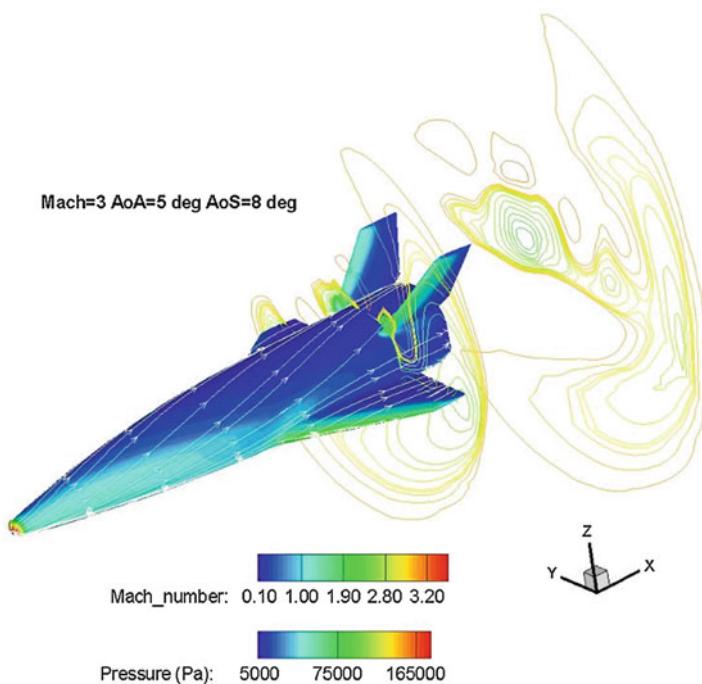


**Fig. 6.81** Mach contours on two fuselage cross planes and pressure contours on vehicle surface at  $M_\infty = 3$ ,  $\alpha = 5^\circ$ , and  $\beta = 8^\circ$ . Euler computation for ORV-WSB concept

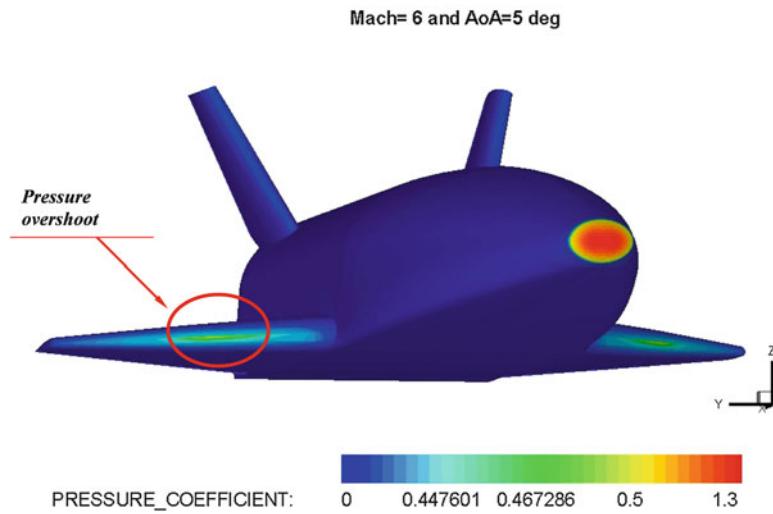


Fig. 6.82 Pressure coefficient distribution on ORV-WSB surface at  $M_{\infty} = 6$  and  $\alpha = 5^\circ$

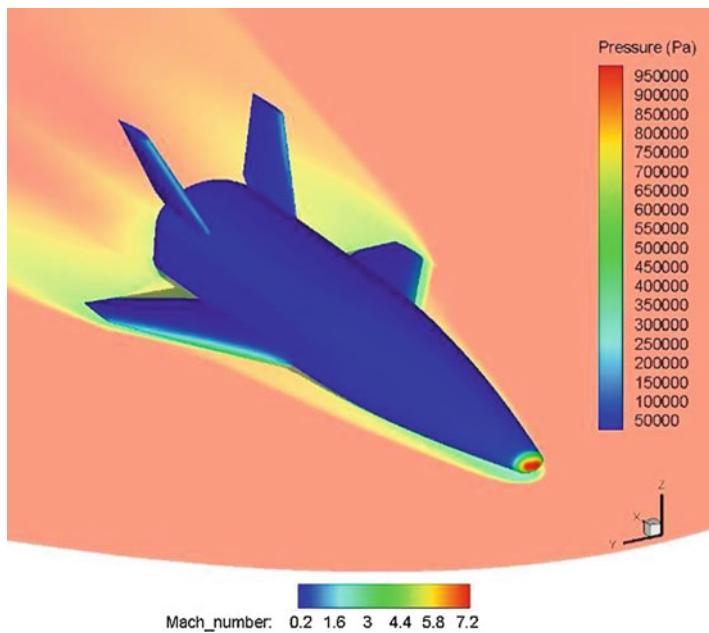
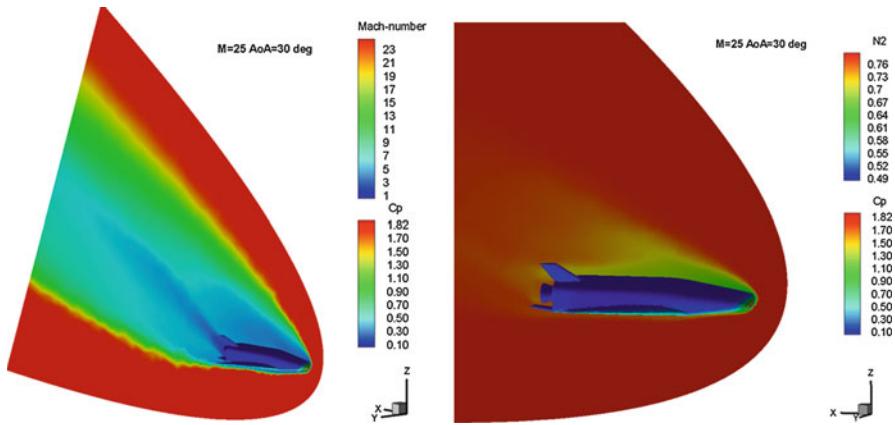
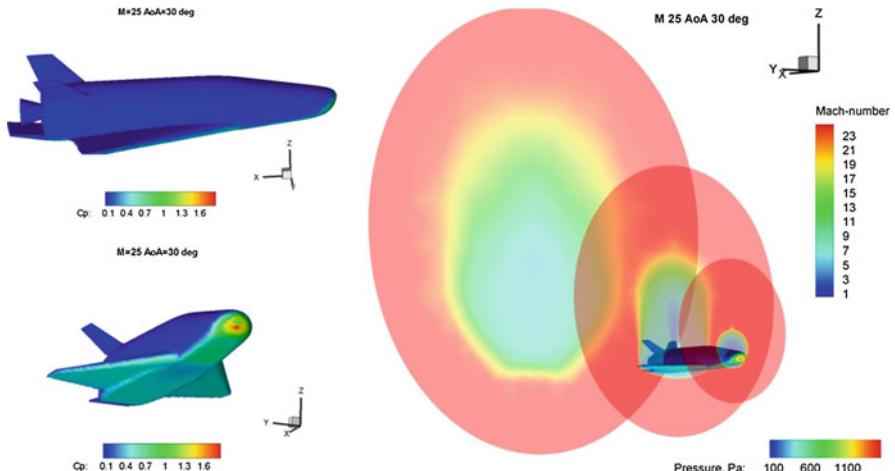


Fig. 6.83 Pressure and Mach number distributions on ORV-WSB surface and wing plane at  $M_{\infty} = 7$  and  $\alpha = 5^\circ$



**Fig. 6.84** Mach (left) and  $N_2$  (right) contours on symmetry plane and  $C_p$  on vehicle surface at  $M_\infty = 25$  and  $\alpha = 30^\circ$ . ORV-WBB concept



**Fig. 6.85**  $C_p$  on vehicle surface at  $M_\infty = 25$  and  $\alpha = 30^\circ$ . ORV-WBB concept

For what concerns the flowfield past the ORV-SB concept, Fig. 6.86 shows the Mach number contour field on vehicle symmetry plane and pressure distribution on concept surface at  $M_\infty = 25$  and  $\alpha = 30^\circ$ . Streamlines are also provided.

Three-dimensional streamtraces at these flight conditions together with a cross-flow section colored by Mach number are provided in Fig. 6.87. Also in this case, a very narrow shock layer is expected for this concept [37].

As far as aerodynamic results comparison between numerical and engineering analysis are concerned, several results in the case of  $M_\infty = 10, 20$  and for  $0 < \alpha < 40^\circ$  are provided in Figs. 6.88 and 6.89 for the ORV-WSB concept.

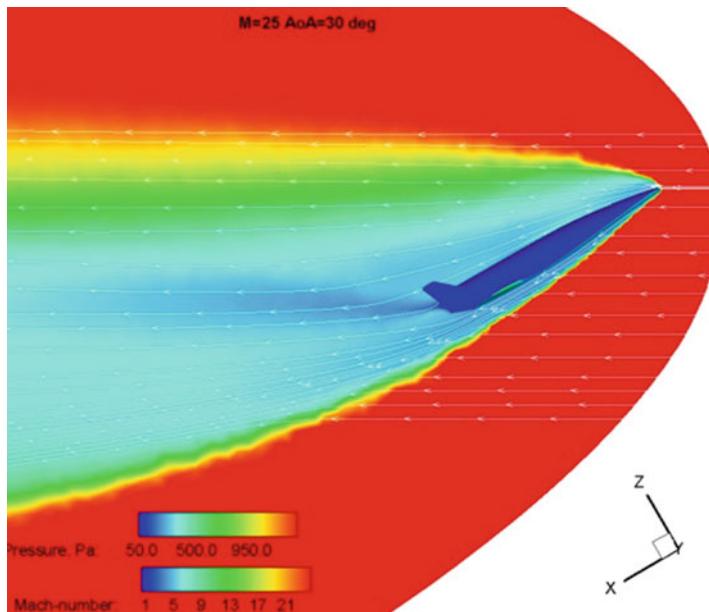


Fig. 6.86  $C_p$  on ORV-SB surface at  $M_\infty = 25$  and  $\alpha = 30^\circ$

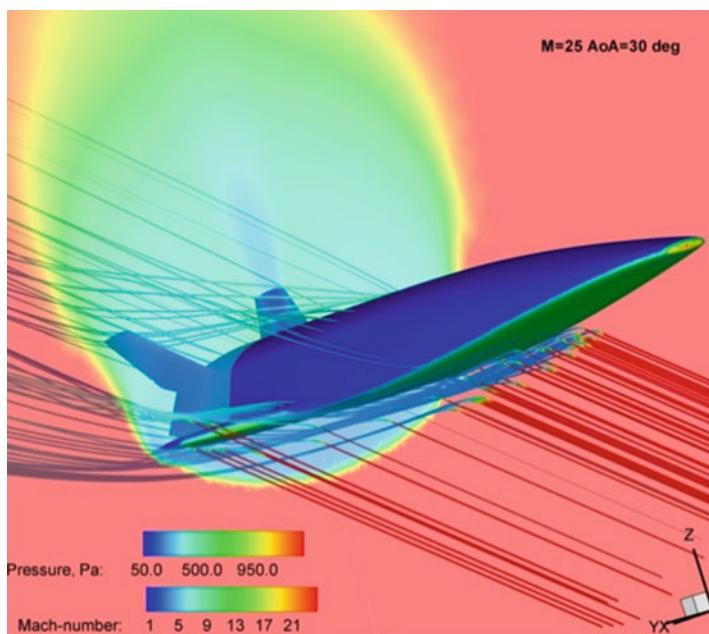
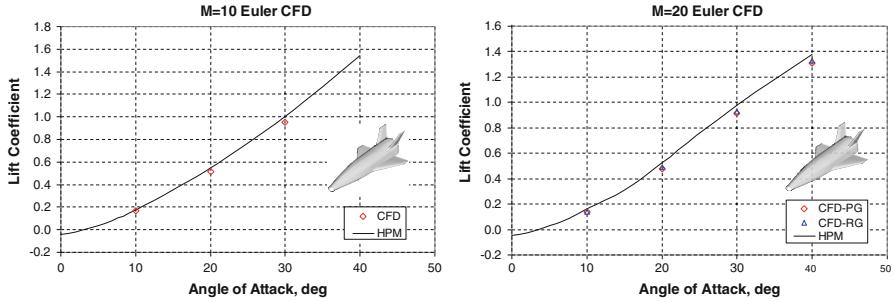
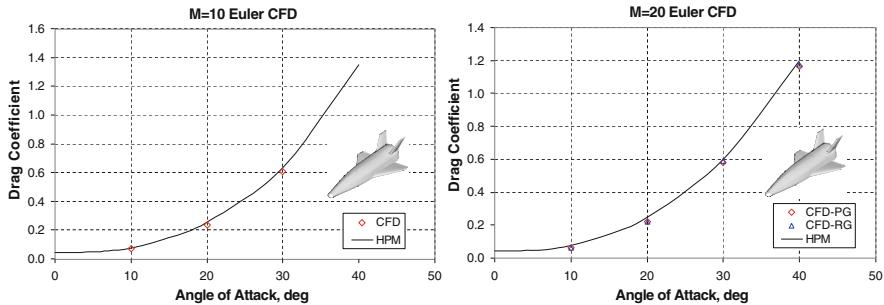


Fig. 6.87  $C_p$  on ORV-SB surface at  $M_\infty = 25$  and  $\alpha = 30^\circ$  with 3-D streamtraces and flowfield cross section colored by Mach number



**Fig. 6.88**  $C_L$  vs.  $\alpha$ . HPM and CFD results comparison at  $M_\infty = 10$  and 20. ORV-WSB concept



**Fig. 6.89**  $C_D$  vs.  $\alpha$ . HPM and CFD results comparison at  $M_\infty = 10$  and 20. ORV-WSB concept

As shown, results comparison confirms that engineering-based (i.e., HPM) and numerical data fit each other very well. Moreover, differences between real gas and frozen gas coefficients, collected also in Table 6.3 for  $M_\infty = 20$  and  $10 < \alpha < 40^\circ$ , suggest that high-temperature gas effects are negligible for lift and drag, whereas a significant effect on vehicle pitching moment is expected along the re-entry trajectory varying from 8 to 50 %.

Finally, numerical and engineering-based aerodynamic results comparison for ORV-WBB and ORV-SB are summarized in Figs. 6.90 and 6.91, respectively [17, 19, 22, 25].

For instance, Fig. 6.90 compares aerodynamic results for axial force coefficient ( $C_A$ ) and pitching moment coefficient ( $C_m$ ) at  $M_\infty = 25$  and  $\alpha = 30^\circ$ , while Fig. 6.91 provides results comparison for normal force coefficient ( $C_N$ ) at  $M_\infty = 10$  and  $\alpha = 30^\circ$  and for axial force coefficient ( $C_A$ ) at  $M_\infty = 25$  and  $\alpha = 30^\circ$  and  $45^\circ$ . As shown, also in those cases it is confirmed that HPM provides reliable results in the framework of a phase A design level.

**Table 6.3** Real gas effects  
on ORV-WSB aerodynamics

	AoA	PG	RG	Err %
<b>C<sub>L</sub></b>				
10	0.14	0.14	-1.15	
20	0.49	0.48	1.37	
30	0.93	0.91	1.97	
40	1.33	1.31	1.46	
<b>C<sub>D</sub></b>				
10	0.06	0.06	3.80	
20	0.22	0.22	2.00	
30	0.59	0.58	1.72	
40	1.18	1.16	0.94	
<b>C<sub>M</sub></b>				
10	0.036	0.043	-17.01	
20	0.086	0.094	-7.98	
30	0.082	0.096	-14.55	
40	0.025	0.048	-47.82	

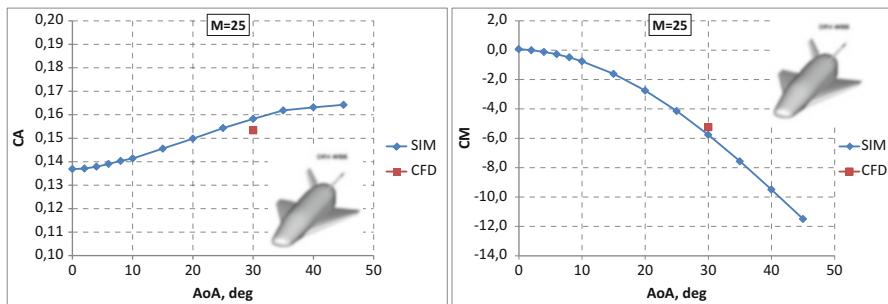


**Fig. 6.90**  $C_A$  and  $C_m$  at  $M_\infty = 25$  and  $\alpha = 30^\circ$ . ORV-WBB concept. CFD and HPM comparison

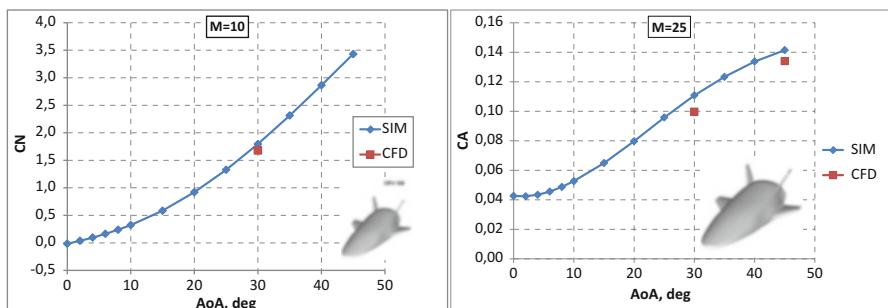


**Fig. 6.91**  $C_A$  and  $C_N$  at  $M_\infty = 25$  and  $\alpha = 30^\circ$ . ORV-SB concept. CFD and HPM comparison

## 6.8 Aerodynamic and Aerothermodynamic Appraisal of the FTB-X Vehicle Concept

The eXperimental Flying Test Bed (FTB-X) vehicle concept, shown in Fig. 6.92, provides further example of design activities where several tools are involved to assess vehicle performance.

For instance, hypersonic panel method (e.g., Newtonian theory), computational fluid dynamics (CFD), and the molecular approach such as the Direct Simulation Monte Carlo (DSMC) are considered to address vehicle aerodynamic and, especially, aerothermodynamic.

### 6.8.1 Vehicle Configuration

FTB-X is a wing-body configuration equipped with a delta wing and one vertical tail. The three-view drawing of the vehicle is shown in Fig. 6.93.

The overall vehicle dimensions are summarized as follows:

- Total length (tail included): 5.68 m
- Total height (tail included): 1.62 m
- Fuselage length: 5.31 m
- Maximum fuselage width: 0.90 m
- Maximum fuselage height: 0.90 m
- Wingspan: 2.14 m
- Wing area:  $3.05 \text{ m}^2$
- Nose radius ( $R_N$ ): 0.10 m
- Wing leading edge radius ( $R_{WN}$ ): 0.04 m

The fineness ratio of the fuselage is about 6, while the wing aspect ratio is 0.9.

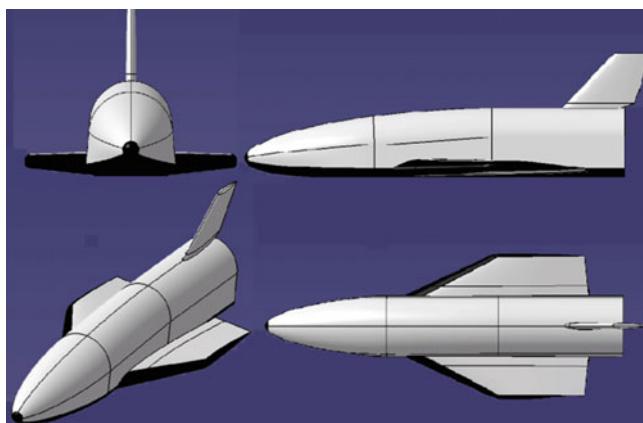


**Fig. 6.92** The FTB-X three views

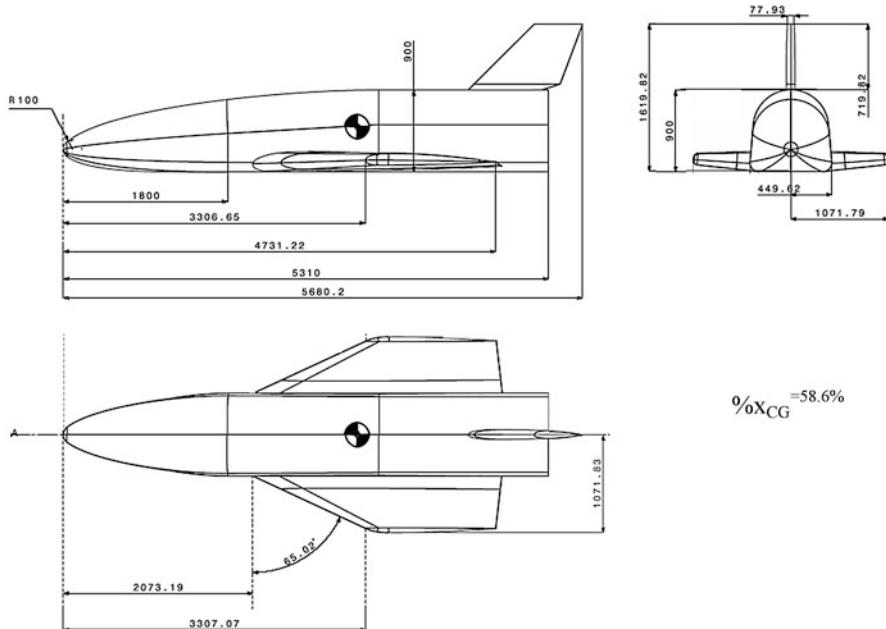


**Fig. 6.93** Three-view drawings of FTB-X configuration

Such a configuration is the result of mission and system requirements satisfactions, of course. Indeed, among system requirements that directly impact on the vehicle design, there are:

- The FTB-X capability to manage long duration re-entries with well-improved aerodynamics and maneuverability characteristics
- The use of the small launcher VEGA (see Fig. 6.94)

This means that the vehicle aeroshape must be characterized by a rather high aerodynamic efficiency. Therefore, FTB-X must be designed in such a way to exhibit small nose and wing leading edge radii and fly at moderate angle of attack (AoA). This, in turn, results in a vehicle configuration able to achieve high cross-range (due to the high L/D) and that must be able to be trimmed over a wide range of angles of attack.

Moreover, high L/D means long time re-entry that, in turn, results in high thermal load to be accommodated by vehicle thermal shield. Hence, high re-entry time demands large use of RCS, i.e., large tanks. The latter consideration determines, in this case, large vehicle cross section.

On the other hand, the requirement to be launched by VEGA has a strong impact on vehicle dimensions, provided that the vehicle must be accommodated in the fairing of launcher. This limits the overall dimensions of the vehicle as wingspan and fin height as well as the location of vehicle center of gravity (CoG) [38].

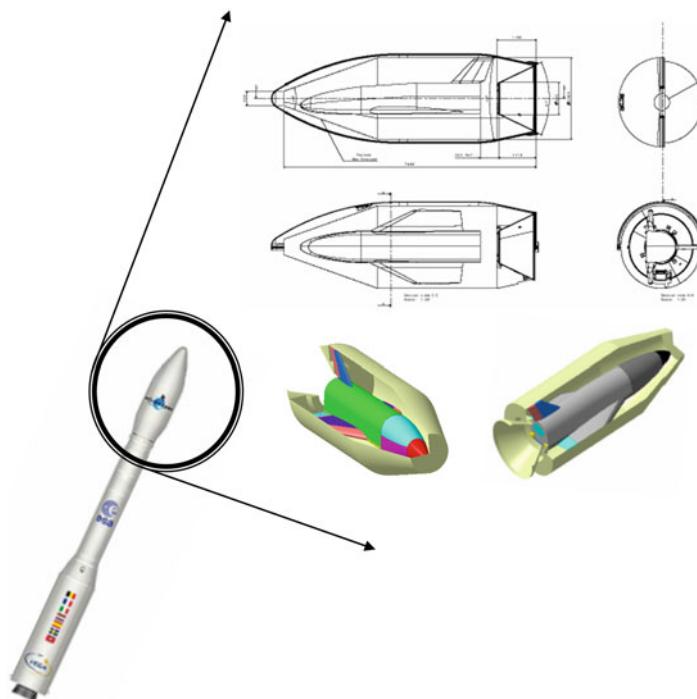


**Fig. 6.94** The FTB-X three views and its accommodation within VEGA fairings

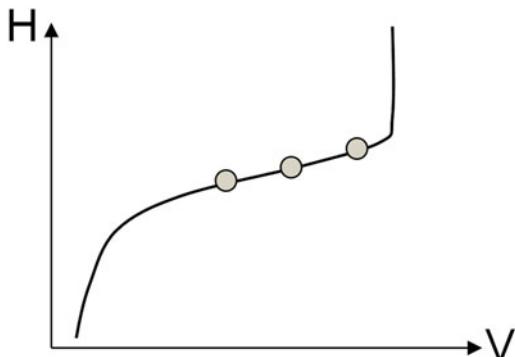
The wing size and location were defined on the basis of trade-off studies so to improve vehicle aerodynamics and to provide static stability and controllability during flight. Indeed, the wing was located forward in order to keep the aerodynamic center of pressure (CoP) close to the CoG, whose current position is at 58.6 % of fuselage length. Further, moving the wing forward increases the  $C_m$ , thus allowing to pitch trim the vehicle with positive deflections of control surfaces, for an improved vehicle stability and controllability for major parts of the flight envelope.

The vertical tail sweep angle is 45°. Note that the requirement to fly at moderate AoA along the re-entry implies that the tail is expected to be slightly more effective unlike a classical re-entry (e.g., Orbiter-like, where at high AoA the vertical fin is shielded from the flow, thus providing no control).

### 6.8.2 Analysis Method and Used Tools

The appraisal of FTB-X aerodynamic and aerothermodynamic characteristics has been performed with engineering-level code HPM, the CFD code H3NS, and the DSMC codes of Bird, namely, DS2V and DS3V.

**Fig. 6.95** Trajectory-based design approach in the altitude–velocity map



Of course, design analyses are performed essentially with simplified tools, while CFD and DSMC computations have been used to anchor engineering estimations, thus providing the errors estimations of the more simplified design approach, according to a phase A design level. The reliability of HPM estimations within free molecular flow (FMF) regime conditions is also highlighted by results provided hereinafter. Then, some bridging formulae, proposed in the past for the US Space Shuttle, have been tested for quick computations of FTB-X high altitude aerodynamics appraisal. The aerodynamic design approach is that discussed previously in paragraph 6.4. That is vehicle aerodynamic appraisal according to the space-based design approach (see Fig. 6.23).

On the contrary, concept aerothermodynamic, discussed hereinafter, relies on the trajectory-based design approach, summarized in Fig. 6.95.

This design approach dictates the generation of a complete aerothermodynamic database by performing the aero thermal computations at a finite number of critical points sampled along with the vehicle design trajectory (see Fig. 6.95). Therefore, the surface heat flux distributions on vehicle configuration have been provided as a function of Mach number, AoA, and altitude (no active aerodynamic control surface deflections).

The capability of HPM to assess also vehicle aerodynamic heating has been discussed in paragraph 6.4. Here, aerodynamic and aerothermodynamic results carried out by DSMC are provided. Indeed, when rarefaction effects become important and the continuum hypothesis no longer holds, CFD Navier–Stokes simulation fail, and a molecular approach such as the DSMC method is necessary. It considers the gas as made up of discrete molecules that are represented by millions of simulated molecules; it relies on formulae from the kinetic theory of gases.

Movement and evolution of each molecule in the simulated physical space is produced by collisions with other molecules and with the body under study, in both cases exchanging momentum and energy. Excitation of rotational and vibrational degrees of freedom and chemical reactions (if any) can be also taken into account.

The computational domain, including the test body, is divided in cells; these are used only for sampling the macroscopic properties and for selecting the colliding

molecules. Movement of each molecule from a cell to another one is the product of the velocity (i.e., the resultant of the convective and thermal velocities) and a time step.

Macroscopic thermofluid dynamic quantities of the flowfield (density, temperature, pressure, and so on) are computed in each cell as an average over the molecules.

DSMC codes use transient subcells in which a transient background grid is built on a single cell and the collision routine, based on nearest-neighbor collisions, is applied. The resolution of the transient grid depends on the number of simulated molecules, and, approximately, one simulated molecule corresponds to one subcell. They provide in output, during the run, the ratio of the local mean separation between collision partners to the local mean free path ( $mcs/\lambda$ ). This parameter is indicative of the quality of a run; it should be less than unity everywhere in the computational domain. Bird suggests the value of 0.2 as a limit value.

The present applications rely on the fully accommodated Maxwell gas–surface interactions.

### **6.8.3 Vehicle Aerodynamic Appraisal**

FTB-X aerodynamic performances are provided in FMF, transitional flow, and in continuum flow conditions. The reference parameters considered assessing vehicle aerodynamic force and moments coefficients are:

$L_{ref} = 2.30$  m (wing mean aerodynamic chord – longitudinal reference length)

$c_{ref} = 2.06$  m (wingspan – lateral–directional reference length)

$S_{ref} = 3.05$  m<sup>2</sup> (area of the exposed part of the wing)

Pole coordinates are (3.113, 0, 0) m (preliminary CoG location)

Of course, consideration about aerodynamic characterization, reference frames, aerodynamic model, and process of development of the aerodynamic database, previously discussed for the ORV in paragraph 6.5, is still valid. Anyway, Fig. 6.96 refreshes aerodynamic sign conventions, currently adopted in assessing vehicle aerodynamics.

### **6.8.4 FTB-X Aerodynamics in Rarefied and Transitional Flow Conditions**

FTB-X aerodynamics assessment for the altitude ranging from entry interface (i.e., 120 km) to about 90 km is provided by means of DSMC computations and bridging formulations for lift, drag, and pitching moment coefficients. For instance, results of several particle simulations (i.e., DSMC) are summarized from Tables 6.4, 6.5, and 6.6, where aerodynamic moment coefficients are evaluated with  $L_{ref} = 5.31$  m

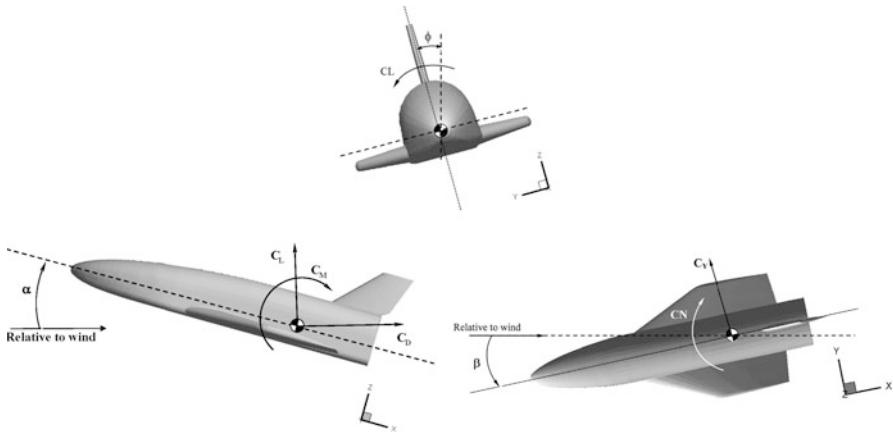


**Fig. 6.96** Aerodynamic sign convention

**Table 6.4** FTB-X aerodynamics in symmetric flight; FMF at  $H = 200$  km. DSMC computations

$H = 200$  km free molecular flow

$\alpha [^\circ]$	$C_L$	$C_D$	L/D	$C_m$
0	-0.0100	0.8806	-0.0113	0.0262
10	0.0589	1.1995	0.0491	-0.1600
20	0.1047	1.8343	0.0571	-0.4535
30	0.1329	2.5116	0.0529	-0.8529
40	0.1447	3.1500	0.0459	-1.3185

(i.e., fuselage length).<sup>5</sup> The aerodynamic analysis was carried out on the vehicle in clean configuration, and at the free-stream velocity of 7,330 m/s, constant with altitude. In all computations the wall temperature is set equal to 300 K, and the aerodynamic forces and moments are evaluated on the assumption of a Maxwell fully accommodate model. Free-stream thermodynamic parameters are provided by the US Standard Atmosphere 1976. Air is considered made up of five chemical species ( $O_2$ ,  $N_2$ ,  $O$ ,  $N$ , and  $NO$ ).

The values of the FTB-X aerodynamic coefficients in symmetric flight (i.e.,  $\beta = 0^\circ$ ) at 200 km altitude (i.e.,  $Kn_{ref} \cong 50$ ) and as function of the AoA are reported in Table 6.4 [14].

Table 6.5 summarizes concept aerodynamic coefficients ranging from 90 to 110 km altitude, in symmetric flight [14].

All the aerodynamic coefficients summarized above in both Table 6.4 and Table 6.5 are also shown in Figs. 6.97 and 6.98 [25, 35, 20].

<sup>5</sup>To account for different reference length in evaluating pitching moment coefficient, one can observe that  $L'_{ref} C'_m = L''_{ref} C''_m$ .

**Table 6.5** FTB-X aerodynamics in symmetric flight. DSMC computations

<b>h [Km]</b>	<b><math>\alpha [^\circ]</math></b>	<b>0</b>	<b>10</b>	<b>20</b>	<b>30</b>	<b>40</b>
110	$C_L$	-0.0332	0.1643	0.3397	0.5131	0.6430
100	$C_L$	-0.0333	0.1585	0.4023	0.6806	0.9255
95	$C_L$	-0.0300	0.1449	0.4138	0.7400	1.0139
90	$C_L$	-0.0280	0.1426	0.4353	0.7933	1.0832
<b>h [Km]</b>	<b><math>\alpha [^\circ]</math></b>	<b>0</b>	<b>10</b>	<b>20</b>	<b>30</b>	<b>40</b>
110	$C_D$	0.7264	0.8923	1.3352	1.9327	2.5691
100	$C_D$	0.5587	0.6449	0.9176	1.3967	1.9666
95	$C_D$	0.4142	0.4835	0.7447	1.1775	1.7484
90	$C_D$	0.3025	0.3649	0.6032	1.0229	1.5898
<b>h [Km]</b>	<b><math>\alpha [^\circ]</math></b>	<b>0</b>	<b>10</b>	<b>20</b>	<b>30</b>	<b>40</b>
110	L/D	-0.0457	0.1842	0.2544	0.2655	0.2503
100	L/D	-0.0595	0.2458	0.4385	0.4873	0.4706
95	L/D	-0.0725	0.2997	0.5556	0.6285	0.5799
90	L/D	-0.0926	0.3908	0.7217	0.7756	0.6814
<b>h [Km]</b>	<b><math>\alpha [^\circ]</math></b>	<b>0</b>	<b>10</b>	<b>20</b>	<b>30</b>	<b>40</b>
110	$C_m$	0.0332	-0.1846	-0.4659	-0.8526	-1.2958
100	$C_m$	0.0256	-0.1481	-0.3956	-0.7533	-1.1623
95	$C_m$	0.0202	-0.1229	-0.3679	-0.7192	-1.1183
90	$C_m$	0.0169	-0.1114	-0.3546	-0.7025	-1.0901

 $L_{ref} = 5.31 \text{ m}$ 

Pole @ nose

**Table 6.6** FTB-X aerodynamics in sideslip flight at  $\alpha = 30^\circ$  and  $\beta = 15^\circ$ . DSMC computations

<b>h [Km]</b>	<b><math>\alpha [^\circ]</math></b>	<b><math>\beta [^\circ]</math></b>	<b><math>C_L</math></b>	<b><math>C_D</math></b>	<b><math>C_Z</math></b>	<b>L/D</b>
110	30	15	0.4762	1.9398	0.4952	0.2455
100	30	15	0.6452	1.4156	0.3621	0.4558
95	30	15	0.6927	1.1729	0.3075	0.5906
90	30	15	0.7313	1.0201	0.2734	0.7168
<b>h [Km]</b>	<b><math>\alpha [^\circ]</math></b>	<b><math>\beta [^\circ]</math></b>	<b><math>C_l</math></b>	<b><math>C_m</math></b>	<b><math>C_n</math></b>	
110	30	15	-0.0069	-0.8249	0.2804	
100	30	15	-0.0171	-0.7358	0.1940	
95	30	15	-0.0182	-0.6868	0.1594	
90	30	15	-0.0171	-0.6632	0.1373	

 $L_{ref} = 5.31 \text{ m}$ 

Pole @ nose

The effect of rarefaction on the aerodynamic lift is clearly shown in Fig. 6.97. For example, at  $\alpha = 30^\circ$   $C_L$  decreases to about 65 % ranging from 90 to 110 km, whereas at  $H = 200$  km the lift coefficient is equal to about 16 % of its value at 90 km.

As far as aerodynamic drag is concerned, Fig. 6.97 shows that  $C_D$  at  $\alpha = 30^\circ$  increases of about 100 % passing from 90 to 110 km, whereas the drag at  $H = 200$  km is 250 % higher than the one at 90 km. As a consequence, the strong

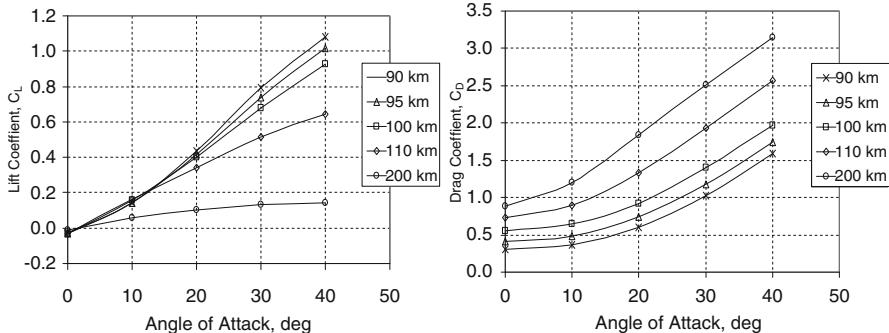


Fig. 6.97 Lift and drag coefficients vs. AoA and altitude. DSMC computations

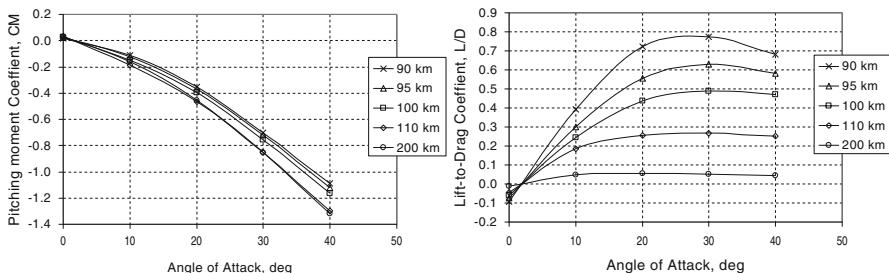


Fig. 6.98 Pitching moment coefficient and lift-to-drag ratio vs. AoA and altitude. DSMC computations

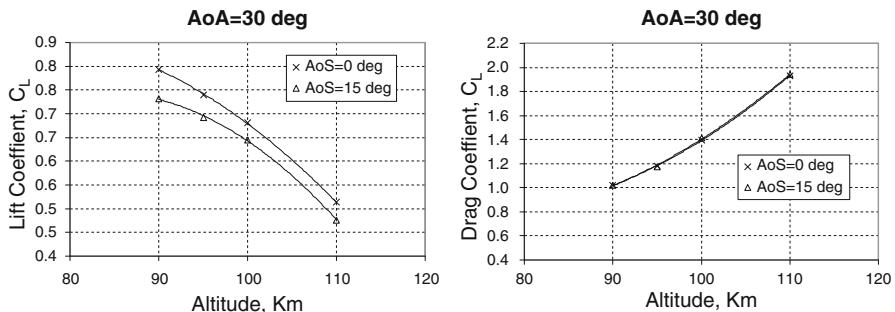
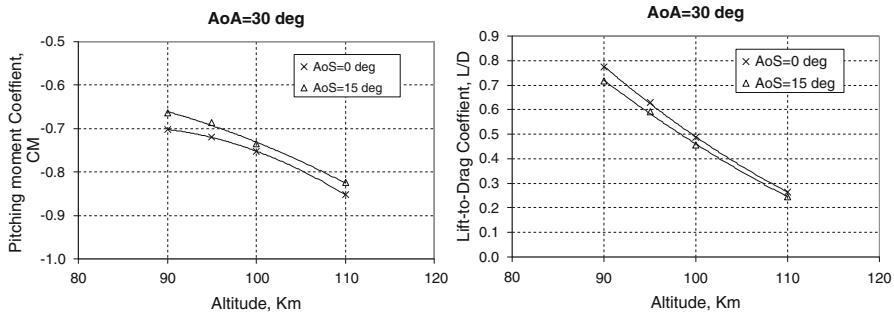


Fig. 6.99 Effect of AoS on lift and drag coefficients at  $\text{AoA} = 30^\circ$ . DSMC computations

reduction of the aerodynamic efficiency due to rarefaction effects is very clear in Fig. 6.98, where the pitching moment vs AoA is also reported.

Sideslip effects in transitional flow aerodynamics when  $\alpha = 30^\circ$ ,  $\beta = 15^\circ$ , and for the altitude range 90–110 km are summarized in Table 6.6 and in Figs. 6.99 and 6.100.



**Fig. 6.100** Effect of AoS on  $C_m$  and lift-to-drag ratio at  $AoA = 30^\circ$ . DSMC computations

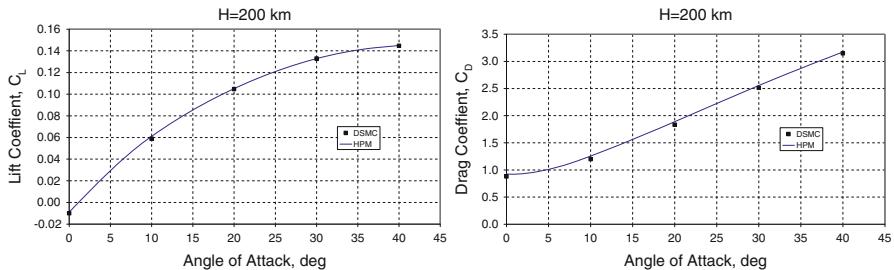


**Fig. 6.101** Lift and drag coefficients vs. AoA at  $H = 200$  km. Comparison between HPM and DSMC

As expected, the effects of sideslip flow are detrimental for the aerodynamic performances of FTB-X in the transitional regime: the lift reduces and both drag and pitching moment increase.

These aerodynamic coefficients have been evaluated by means of expensive and time-consuming DSMC simulations. However, the FTB-X aerodynamics in FMF conditions can be assessed also by means of quick engineering estimations as those obtained from HPM computations, as summarized in Figs. 6.101 and 6.102. In these figures HPM and DSMC results comparison can be also assessed in order to address accuracy of panel method aerodynamics in free molecular flow conditions.

Moreover, above results suggest that the vehicle aerodynamics in the transitional regime can be useful shown through bridging formulation between FMF results and continuum ones.

For example, the plots of the lift and drag and pitching moment coefficients of vehicle concept versus the Knudsen number are reported in Figs. 6.103, 6.104, and 6.105, respectively.

A deep analysis of aerodynamic coefficients at high altitudes is shown in Ref [13] and [14], where also some bridging formulae have been used to correlate the results in continuum and rarefied regime.

**Fig. 6.102** Pitching moment coefficient ( $L_{ref} = MAC$ ) vs. AoA at  $H = 200$  km.  
 Comparison between HPM and DSMC. Error Bar of 10 %

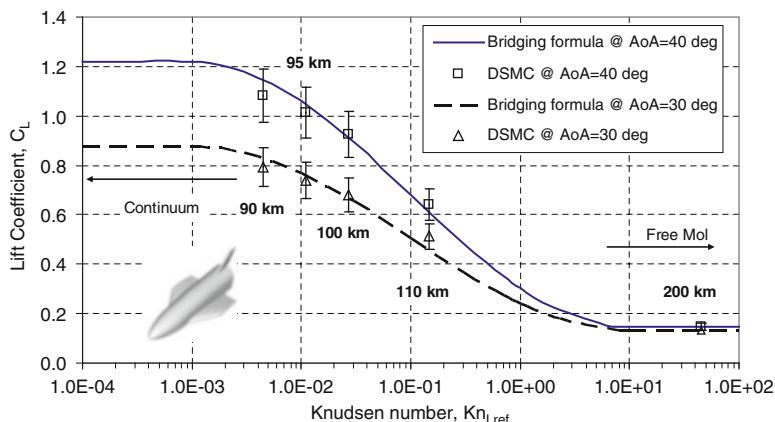
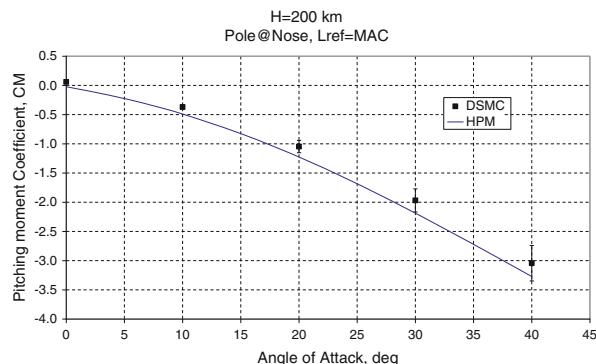


**Fig. 6.103** Lift coefficients vs. Knudsen number for AoA = 30° and 40°

### 6.8.5 FTB-X Aerodynamics in Continuum Flow Conditions

Continuum flow aerodynamics is extensively assessed by means of panel method design analysis carried out on surface meshes close to that shown in Fig. 6.106. Here, the mesh with deflected elevons and body flap is provided.

Main results obtained for the appraisal of FTB-X clean configuration aerodynamic are shown from Figs. 6.107, 6.108, 6.109, 6.110, 6.111, 6.112, 6.113, 6.114, and 6.115. For instance, Figs. 6.107 and 6.108 show FTB-X lift, drag, and aerodynamic efficiency at  $Re/m = 10^5 \text{ m}^{-1}$  and  $Re/m = 5 \times 10^5 \text{ m}^{-1}$ , respectively. In each figure the behavior of  $C_L$ ,  $C_D$ , and  $(L/D)$  is provided versus AoA and Mach number. In the latter case, however, neither viscous interaction nor real gas effects are considered, provided that panel method aerodynamic is not able to account for these complex flowfield phenomena. Anyway aerodynamic results highlight that the Oswatitch principle is satisfied already starting from Mach = 7 in both cases.

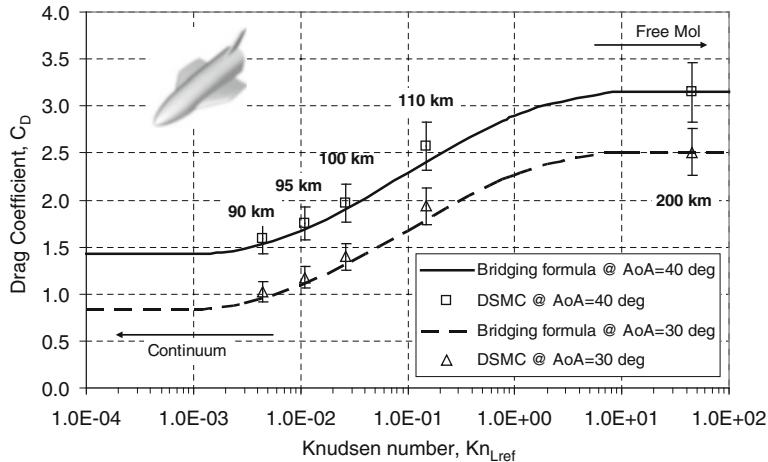


**Fig. 6.104** Drag coefficient vs. Knudsen number for  $\text{AoA} = 30^\circ$  and  $40^\circ$

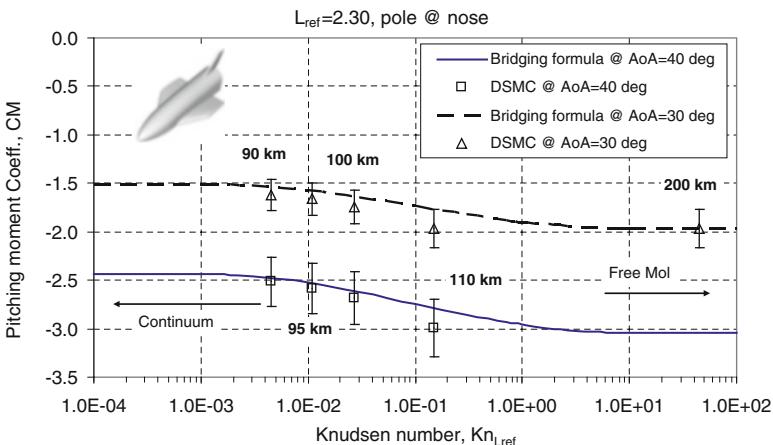


**Fig. 6.105** Pitching moment coefficient vs. Knudsen number for  $\text{AoA} = 30^\circ$  and  $40^\circ$

Comparing results provided in Figs. 6.107 and 6.108, one can observe that the viscous effect on the aerodynamic efficiency is not negligible. For instance, the effect of Reynolds number on the concept aerodynamic efficiency at  $M_\infty = 8$  is provided in Fig. 6.109.

On the right side of the figure instead, the effect of Mach number at a fixed Reynolds ( $Re/m = 2 \times 10^6 \text{ 1/m}$ ) on the lift to drag is shown. These diagrams confirm also the fulfillment of the high aerodynamic efficiency requirement necessary for a long-endurance hypersonic flight.

It must be stressed, however, that especially for what concerns the assessment of viscous effects, more detailed CFD computations are mandatory.

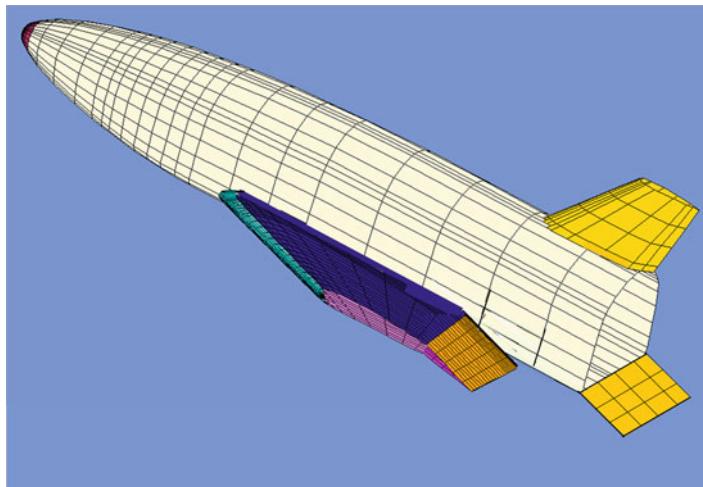


**Fig. 6.106** Example of surface mesh used for engineering analysis of FTB-X aerodynamics

The trend of the pitching moment  $C_m$  versus AoA and Mach number can be seen in Fig. 6.110 for  $Re/m = 10^5 \text{ m}^{-1}$ . Therefore, the vehicle, with the given CoG, is statically stable in longitudinal flight for AoA higher than  $15^\circ$ , and being the  $C_m$  positive for higher Mach numbers, it can be trimmed with wing and/or body flaps positive deflection angles (see Fig. 6.31).

To highlight the effect of AoA on the clean configuration aerodynamics, in Fig. 6.111 the static pressure distribution over the wetted vehicle surface for three AoA (i.e.,  $13^\circ$ ,  $20^\circ$ , and  $25^\circ$ ) is shown.

As shown, ranging from  $13^\circ$  to  $25^\circ$  AoA, the static pressure increases, thus leading to an enhanced aerodynamic performance (note that in this case tail pressure distribution is not shown for simplicity).

As far as lateral-directional performances are concerned, from Figs. 6.112, 6.113, 6.114, and 6.115, there are plots of roll and yaw moment coefficients for different Mach numbers and for clean configuration at  $\alpha = 10^\circ$  and  $25^\circ$  and for  $Re/m = 5 \times 10^5 \text{ m}^{-1}$ .

As expected, the vehicle is statically unstable in lateral-directional flight.

In any case it is known that for a Space Shuttle-type vehicle, at high Mach number, to obtain a positive  $C_{n\beta}$  is almost impossible unless a very high dihedral angle is used for the wing (i.e., X-38). So, another important aspect that should be verified is the possibility to stabilize the vehicle through RCS for a large part of the trajectory (as done with Shuttle up to  $M_\infty = 3$ ).

In order to provide data for the trim and stability analysis, a preliminary hypothesis is made for the control surfaces, i.e., wing ailerons, rudder, and body flap. They are shown in Fig. 6.116.

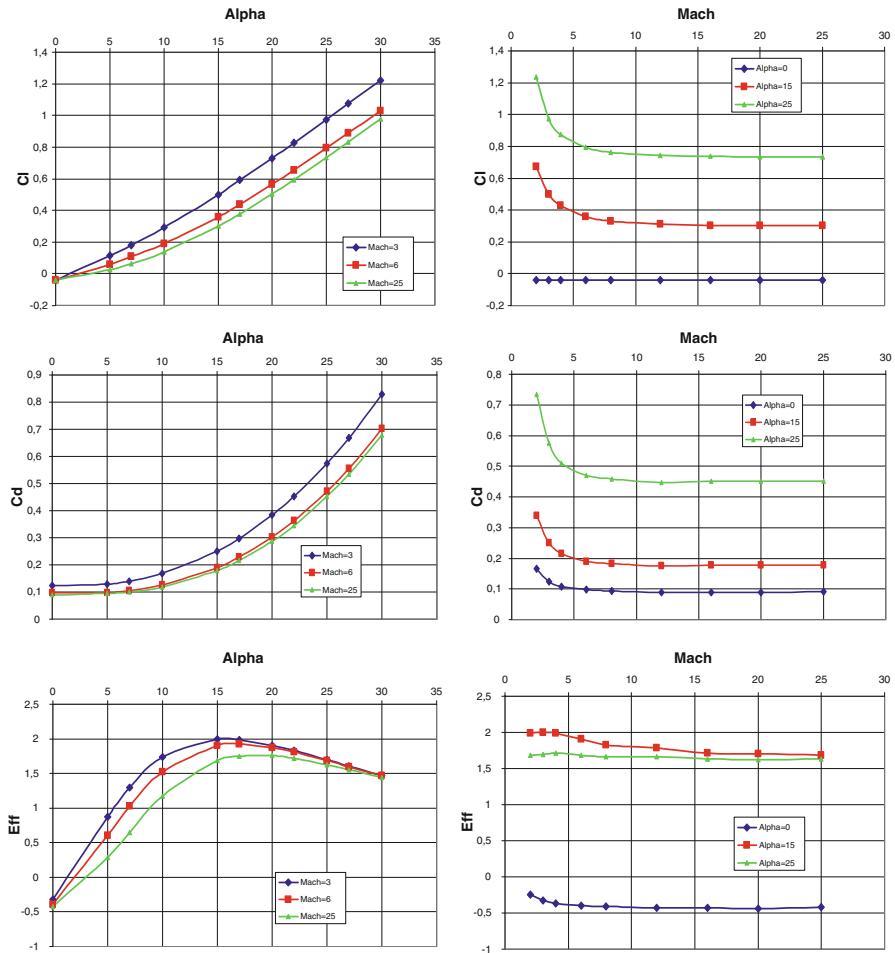


**Fig. 6.107** Lift, drag, and aerodynamic efficiency.  $Re/m = 10^5 \text{ m}^{-1}$

The wing control surface is characterized by the chord equal to  $1/3$  of that of the wing tip. The rudder chord is equal to about  $1/2$  the one of tail tip, while at root the rudder chord is equal to about  $1/3$  of the total chord.

Finally, the body flap is located at the end of the rear part of fuselage floor. As preliminary sizing hypothesis, a body flap of  $0.30 \text{ m}$  long was considered.<sup>6</sup>

<sup>6</sup>It is worth noting, however, that the contribution of control surfaces to vehicle aerodynamics has been computed only with panel method. Indeed, the effects of the flow separation due to the shock-wave-boundary-layer interaction (SWBLI) phenomenon cannot be taken into account by HPM code; it is known that these phenomena cause a loss of surface efficiency, but reliable estimation

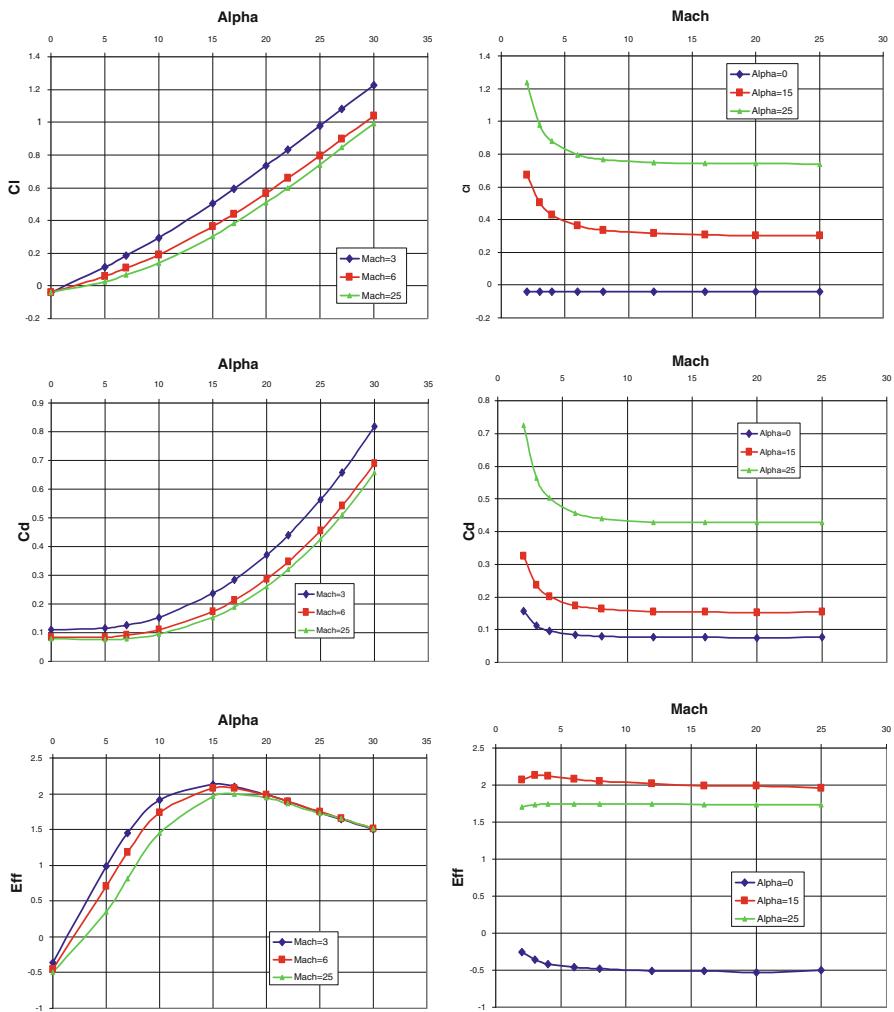


Fig. 6.108 Lift, drag, and aerodynamic efficiency.  $Re/m = 5 \times 10^5 \text{ m}^{-1}$

The effect of the wing flaps on vehicle aerodynamic coefficients as a function of elevon deflection and AoA is shown in Figs. 6.117 and 6.118 for two Mach numbers (6 and 25) and two AoAs ( $15^\circ$  and  $25^\circ$ ).

Figure 6.117 shows the effect of elevon deflection on global  $C_L$  and  $C_D$  of the vehicle flying at  $Re/m = 5 \times 10^5 \text{ m}^{-1}$ , at  $M_\infty = 6$  and 25, and with  $\alpha = 15^\circ$  and  $25^\circ$ . The same effect but for  $C_m$  and L/D is summarized in Fig. 6.118.

---

of control surfaces effectiveness and control authority for stability and trim is possible only with a more detailed CFD analysis and WTT campaigns.

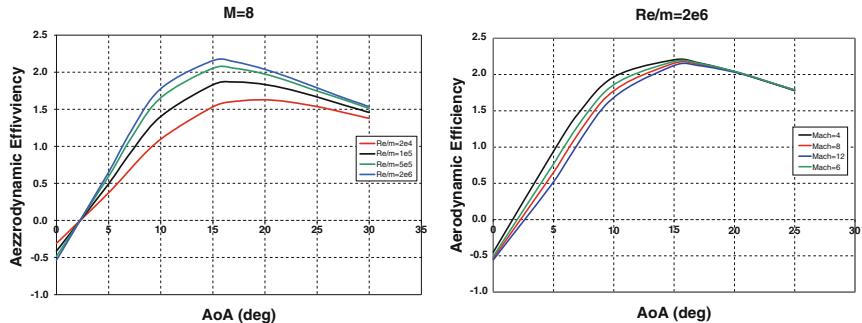


**Fig. 6.109** Aerodynamic efficiency (Eff) for  $M_\infty = 8$  for different  $Re/m$  (left side). On the right Eff for  $Re/m = 2 \times 10^6$  1/m for different Mach number

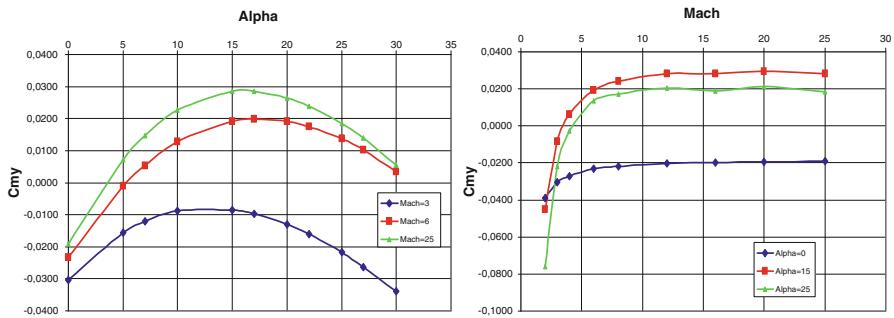


**Fig. 6.110** Pitching moment coefficient.  $Re/m = 10^5$  m<sup>-1</sup>

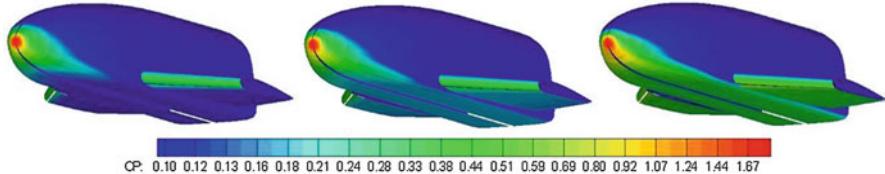


**Fig. 6.111** FTB-X. Pressure coefficient contours on vehicle surface. Comparison among  $\alpha = 13^\circ$ ,  $20^\circ$ , and  $25^\circ$

As shown, both lift and drag increase with  $\delta$  in a nonlinear fashion. As a result, L/D decreases as  $\delta$  increases. Then, the effect of elevon deflections on vehicle pitching moment is significant. Indeed, from Fig. 6.118, it can be seen that the elevon deflection to trim the vehicle is very low, smaller than  $10^\circ$  for both Mach 6 and 25. At  $M_\infty = 6$  the trim deflection angle of elevons passes from about  $7^\circ$  to  $4^\circ$  for  $\alpha$  ranging from  $15^\circ$  to  $25^\circ$  AoA. At higher Mach number,  $\delta_e$  varies from about  $10^\circ$  to  $5^\circ$  for  $\alpha$  ranging from  $15^\circ$  to  $25^\circ$  AoA. For these low deflections, the loss of aerodynamic efficiency is very small. However, it must be stressed that this result is a consequence of the  $C_m$  trend that depends also on the final real position

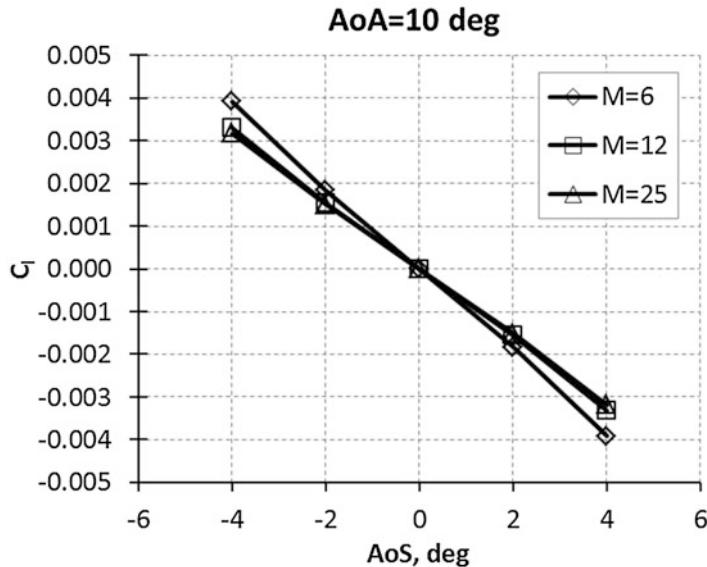


**Fig. 6.112** Roll moment coefficient for  $M_\infty = 6, 12$ , and  $25$  at  $\text{AoA} = 10^\circ$  and  $Re/m = 5 \times 10^5 \text{ m}^{-1}$

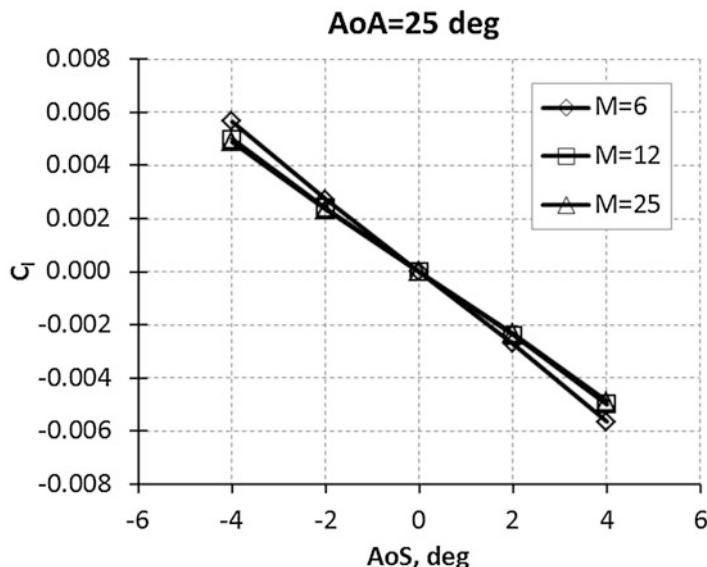


**Fig. 6.113** Roll moment coefficient for  $M_\infty = 6, 12$ , and  $25$  at  $\text{AoA} = 25^\circ$  and  $Re/m = 5 \times 10^5 \text{ m}^{-1}$

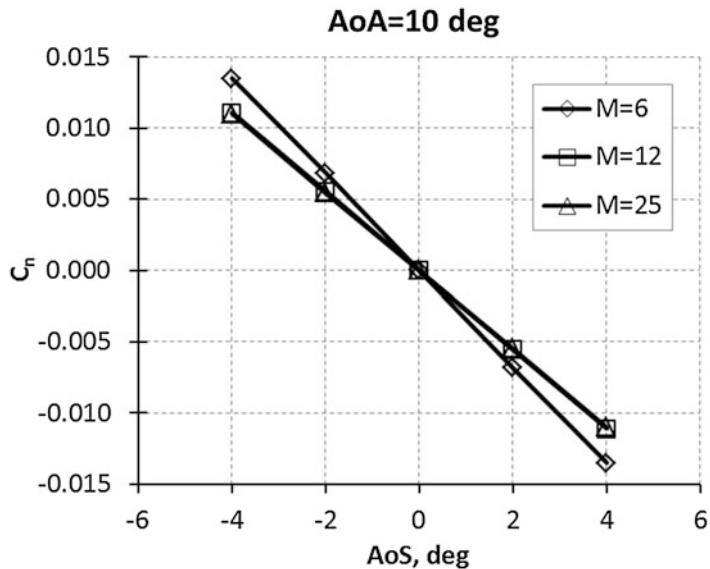


**Fig. 6.114** Yaw moment coefficient for  $M_\infty = 6^\circ$ ,  $12^\circ$ , and  $25^\circ$  at  $\text{AoA} = 10^\circ$  and  $Re/m = 5 \times 10^5 \text{ m}^{-1}$

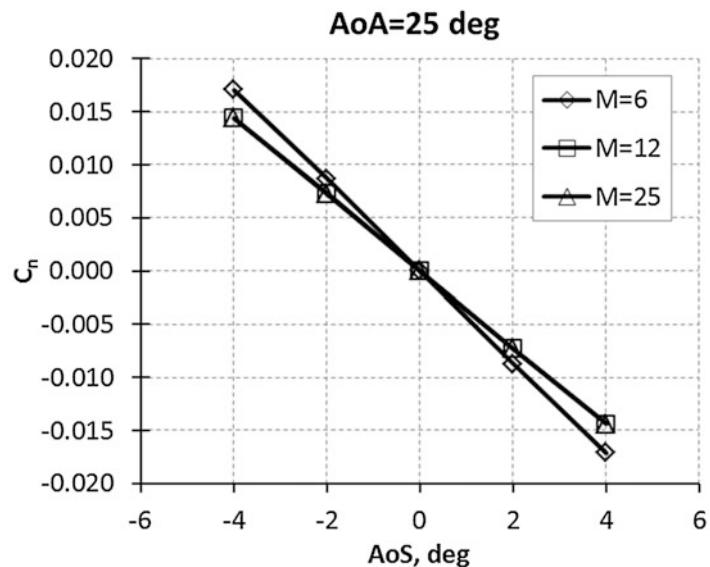


**Fig. 6.115** Yaw moment coefficient for  $M_\infty = 6$ , 12, and 25 at  $\text{AoA} = 25^\circ$  and  $Re/m = 5 \times 10^5 \text{ m}^{-1}$

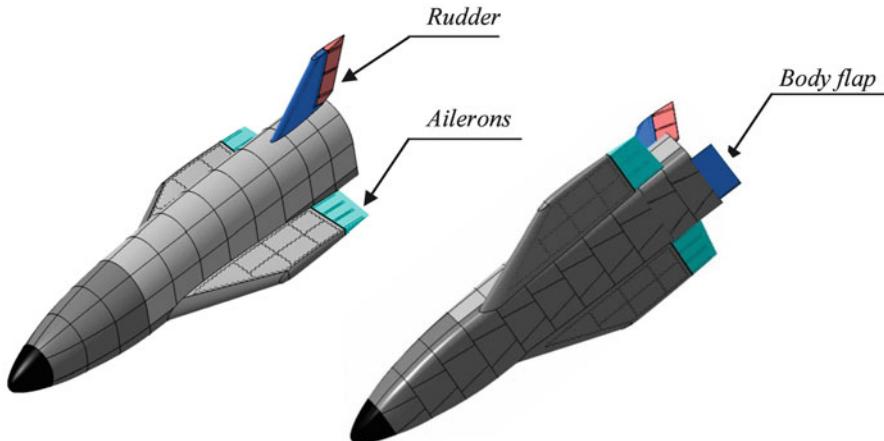


**Fig. 6.116** FTB-X aerodynamic control surfaces

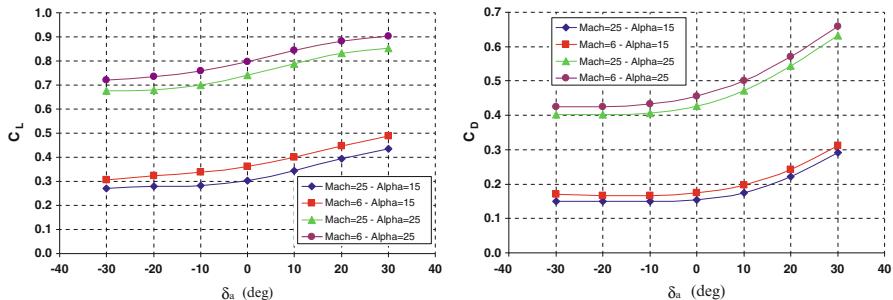


**Fig. 6.117** Effect of elevon deflection on global  $C_L$  and  $C_D$  at  $Re/m = 5 \times 10^5 \text{ m}^{-1}$

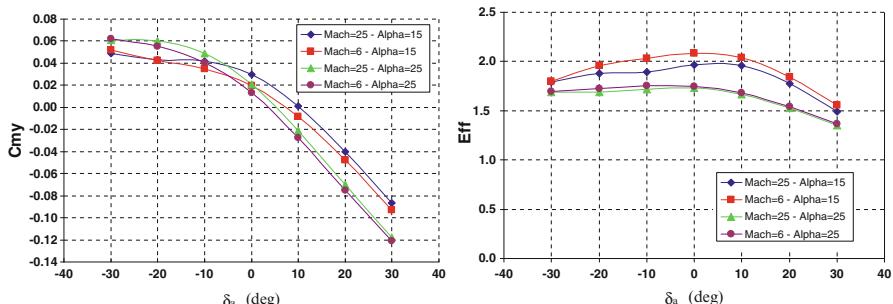


**Fig. 6.118** Effect of elevon deflection on global  $C_m$  and  $L/D$  at  $Re/m = 5 \times 10^5 \text{ m}^{-1}$

of the CoG. The current design is made to realize small positive values of  $C_m$  in the flight conditions of interest, but the trim and stability analysis should also guarantee a sufficient margin in order to avoid negative values of  $C_m$ .

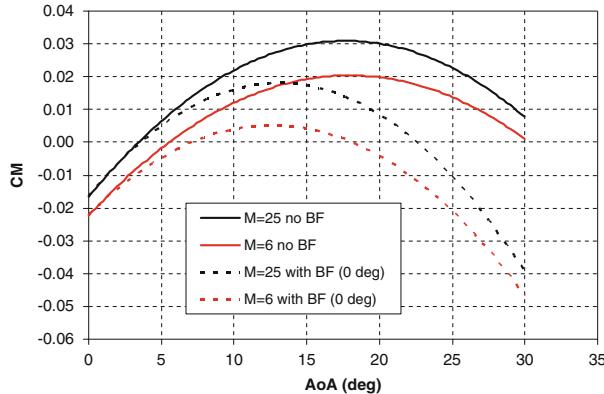


**Fig. 6.119** Pitching moment coefficient vs. AoA. Effect of a not deflected body flap

Anyway, it is worth to note that even if the first data seem to confirm that the wing control surfaces could be sufficient to trim the vehicle, the use of a body flap is advisable in order to have a wider margin in the maneuverability and in the final choice of the CoG position.

As far as the contribution of the body flap is concerned, in Fig. 6.119 the effect of a not deflected body flap on the pitching moment of FTB-X is shown. Here the slope of  $C_m$  for Mach 6 and 25 without and with body flap (not deflected) is provided.

As one can see, even if the pitch control surface is not deflected, it modifies the slope of the  $C_m$  curves. As a result, the longitudinal static stability of the FTB-X concept is improved for the AoAs higher than  $15^\circ$ . Moreover, the pitch trim of FTB-X can be provided at lower deflection angle of elevons, as suggested by Fig. 6.119. In particular, this figure points out that the vehicle with body flap (not deflected) features a natural trim point at about  $22^\circ$  AoA at  $M_\infty = 25$ . At lower Mach number natural, trim is achieved close to  $16^\circ$  AoA.

The effect of the body flap on vehicle aerodynamic coefficients as a function of surface deflection and AoA is shown in Figs. 6.120 and 6.121 for two Mach numbers (6 and 25) and for  $\alpha = 15^\circ$  and  $25^\circ$ .

As shown, body flap deflections ranging from about  $-10^\circ$  to  $10^\circ$  allow to pitch trim the vehicle from  $M_\infty = 25$  to 6 and for  $15 \leq \alpha \leq 25^\circ$  AoA.

For what concerns the effect of the rudder deflection on FTB-X aerodynamics, Figs. 6.122, 6.123, 6.124, and 6.125 point out the behavior of yawing and rolling moment coefficients plotted versus AoS, at two Mach numbers, namely,  $M_\infty = 6$  and 25, at  $\alpha = 25^\circ$ , and for all possible rudder deflections (i.e., from  $-30^\circ$  to  $30^\circ$ ).

As shown, the rudder effectiveness depends on Mach number conditions and is able to null yawing moments at several angle of sideslip. For example, at  $M_\infty = 6$  a rudder deflection of  $-20^\circ$  nulls the yawing moment coefficient at about  $-1.5^\circ$  angle of sideslip and for  $\alpha = 25^\circ$ . On the other hand, at  $M_\infty = 25$ ,  $\delta_r = 30^\circ$  provides  $C_n = 0$  at nearly  $\beta = -3^\circ$  for  $\alpha = 25^\circ$ .

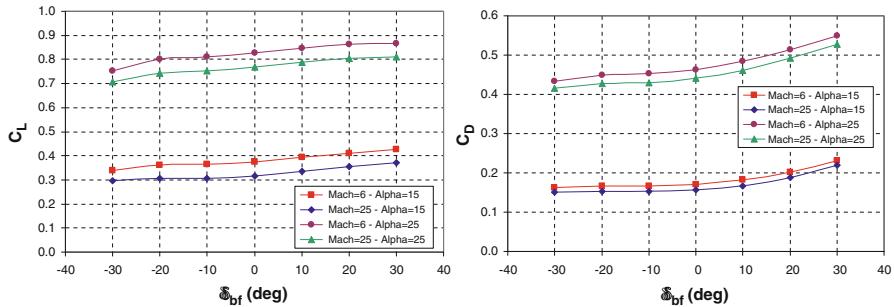


Fig. 6.120 Effect of body flap deflection on global  $C_L$  and  $C_D$  at  $Re/m = 5 \times 10^5 \text{ m}^{-1}$

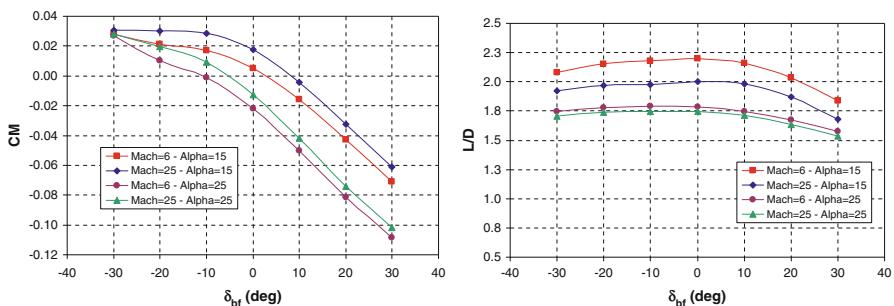


Fig. 6.121 Effect of body flap deflection on global  $C_m$  and  $L/D$  at  $Re/m = 5 \times 10^5 \text{ m}^{-1}$

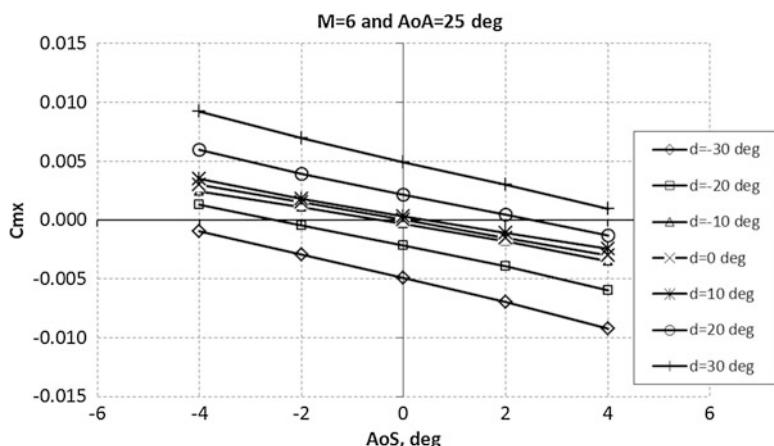
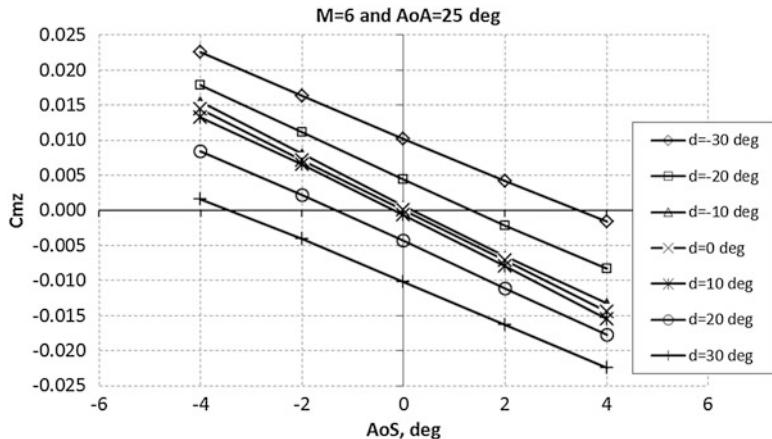
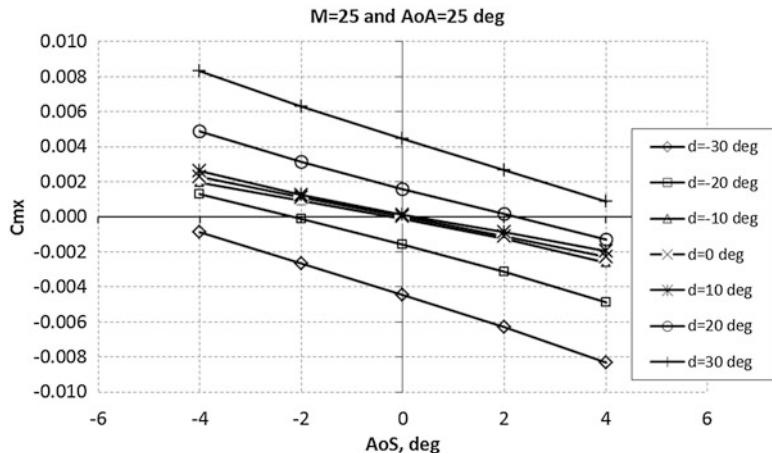


Fig. 6.122 Effect of rudder deflection on  $C_l$  at  $M_\infty = 6$  and  $\text{AoA} = 25^\circ$



**Fig. 6.123** Effect of rudder deflection on  $C_n$  at  $M_\infty = 6$  and  $\text{AoA} = 25^\circ$



**Fig. 6.124** Effect of rudder deflection on  $C_l$  at  $M_\infty = 25$  and  $\text{AoA} = 25^\circ$

Finally, CFD-based concept aerodynamic design relies on the results of several CFD computations, according to the test matrix in Table 6.7.

As shown in table, at  $M_\infty = 20$  nonequilibrium CFD computations are also performed in order to account for the effect of real gas flow conditions.

CFD computations have been carried out on a multiblock structured grid similar to that shown in Fig. 6.126. The grid has consisted of 110 blocks for an overall number of about  $3 \times 10^6$  cells (half body). It is tailored for the free-stream conditions of the design check points, summarized in Table 6.7.

An example of CFD design result is shown in Fig. 6.127, where a three-dimensional view of the flowfield past the vehicle concept is provided. In this figure the Mach number contours are reported on the vehicle surface while the static

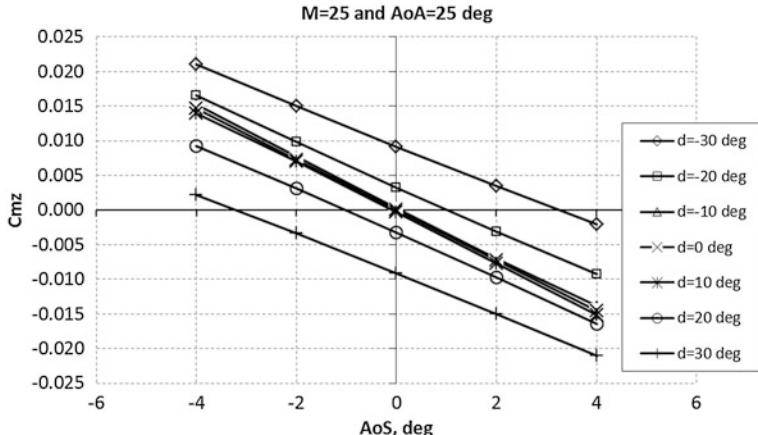


**Fig. 6.125** Effect of rudder deflection on  $C_n$  at  $M_\infty = 25$  and  $\text{AoA} = 25^\circ$

**Table 6.7** Euler CFD test matrix for FTB-X

AoA [°]	Mach [-]			
	10	16	20 (perfect gas)	20 (Real gas)
0				
5				
10				
15				
20				
25				
30				
35				
40				

temperature field is recognized on two cross sections, thus highlighting the shape that takes the bow shock at different streamwise stations. 3-D streamlines can be appreciated as well.

The CFD contribution to FTB-X aerodynamic database is summarized in Table 6.8.

As far as reliability of engineering AEDB is concerned, in the following several comparisons between numerical (CFD) and engineering (HPM) results are provided. They allow assessing the error margins of engineering-based design analyses. In fact, since aerodynamic analyses are based on empirical correlations and approximate theories, it is important to calibrate them against the more accurate CFD results. For instance, in Figs. 6.128 and 6.129 vehicle surface pressure contours and the Mach number contours field, obtained by means of an inviscid CFD simulation at  $M_\infty = 20$  and  $\alpha = 10^\circ$ , are compared to those provided by HPM (see Fig. 6.128).

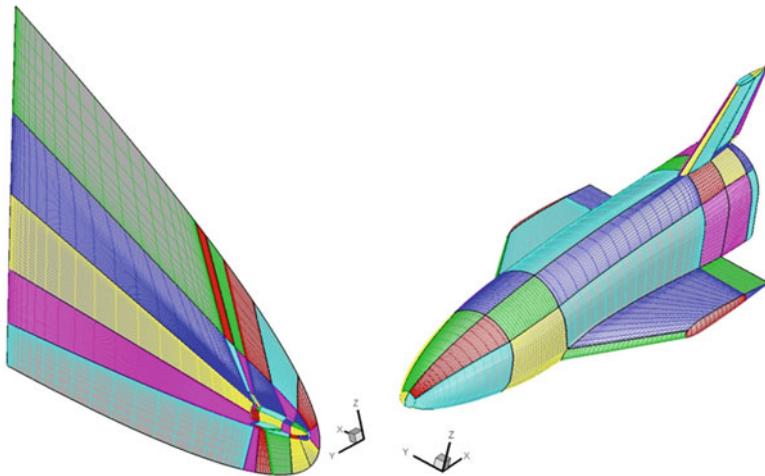


**Fig. 6.126** Multiblock CFD domain. Mesh on symmetry plane and vehicle surface

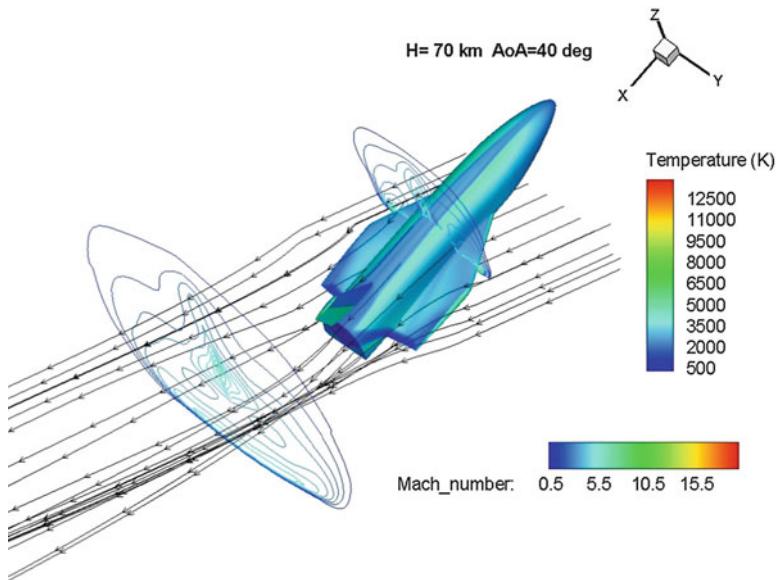


**Fig. 6.127** Nonequilibrium CFD Euler computation at  $H = 70 \text{ km}$ ,  $M_\infty = 20$ , and  $\text{AoA} = 40^\circ$

It can be seen that pressure distributions are very similar, except for the wing leading edge where HPM is not able to determine the pressure spike due to the SSI, of course. The Mach number field on vehicle symmetry plane can be also noted in Fig. 6.128.

**Table 6.8** CFD contribution to FTB-X aerodynamic database assessment

		Euler perfect gas				Euler nonequilibrium gas			
		USV-X-392-FW50				USV-X-392-FW50			
Mach	AoA	L <sub>ref</sub> = 2.30		L <sub>ref</sub> = 2.30		Mach		Mach	
		(0,0,0)	(-3,113,0,0)	(0,0,0)	(-3,113,0,0)	(0,0,0)	(0,0,0)	(0,0,0)	(-3,113,0,0)
	Nose	C <sub>m</sub>	C <sub>m</sub>	C <sub>m</sub>	C <sub>m</sub>	Nose	C <sub>m</sub>	Nose	C <sub>m</sub>
	CoG					CoG		CoG	
AoA	C <sub>L</sub>	C <sub>D</sub>	C <sub>m</sub>	AoA	C <sub>L</sub>	C <sub>D</sub>	C <sub>m</sub>	C <sub>m</sub>	C <sub>m</sub>
10	0.1491	0.0768	-0.2116	0.0052	10	0.1252	0.0669	-0.1728	0.0098
20	0.5115	0.2385	-0.7606	0.0003	20	0.4857	0.2254	-0.7177	0.0044
30	0.9627	0.6154	-1.5669	-0.0221	30	0.9275	0.5915	-1.5029	-0.0155
40					40	1.3170	1.1721	-2.4347	-0.0495
Mach	16								
AoA	C <sub>L</sub>	C <sub>D</sub>	C <sub>m</sub>						
10	0.1286	0.0686	-0.1790						
20	0.4897	0.2284	-0.7260						
30	0.9442	0.6029	-1.5351						
40									
Mach	20								
AoA	C <sub>L</sub>	C <sub>D</sub>	C <sub>m</sub>						
10	0.1235	0.0670	-0.1710						
20	0.4844	0.2260	-0.7176						
30	0.9397	0.5999	-1.5274						
40	1.3378	1.1908	-2.4800						

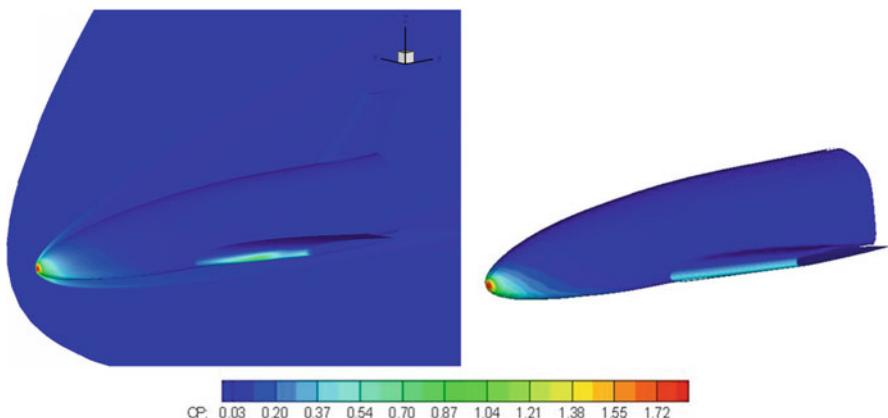


**Fig. 6.128** Pressure coefficient at  $M_\infty = 20$  and  $\text{AoA} = 10^\circ$ . Comparison between CFD (left) and HPM (right)

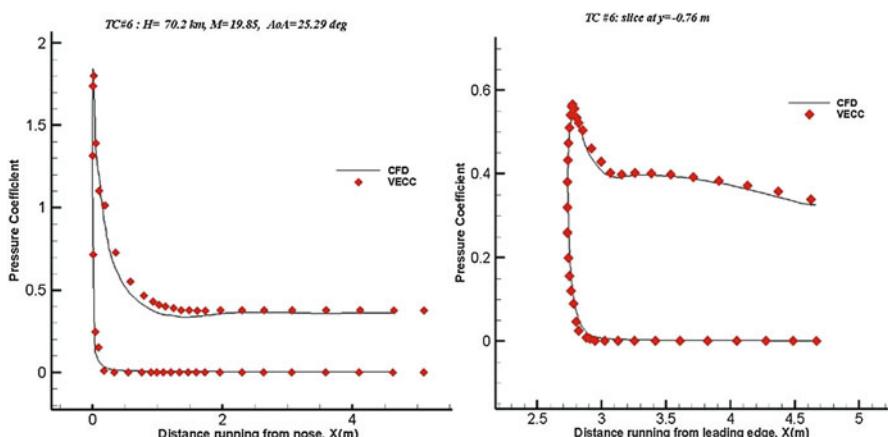


**Fig. 6.129** Pressure coefficient comparison between CFD and HPM at  $M_\infty = 20$ ,  $\alpha = 25^\circ$ , and 70 km altitude, for fuselage centerline (left) and wing section at  $y = 0.76$  m

Further, the pressure coefficient  $C_p$  evaluated at vehicle centerline for  $M_\infty = 20$ ,  $\alpha = 25^\circ$ , and 70 km altitude is compared between engineering and CFD computations in Fig. 6.129.

From the previous Figs. 6.128 and 6.129, it can be seen that the engineering-based results are in good agreement with CFD solutions.

As far as aerodynamic results comparisons are concerned, lift, drag, and pitching moment coefficient comparisons in the case of  $M_\infty = 10$  and  $M_\infty = 20$  for  $10^\circ < \alpha < 30^\circ$  are provided from Figs. 6.130, 6.131, and 6.132.

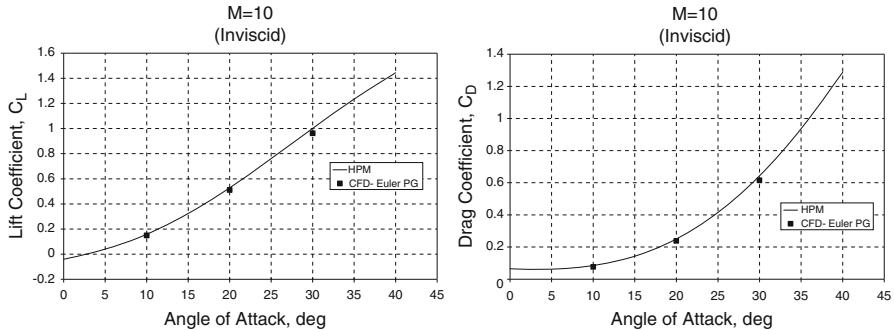


Fig. 6.130 Lift and drag coefficients vs. AoA. Comparison between HPM and CFD at  $M_\infty = 10$

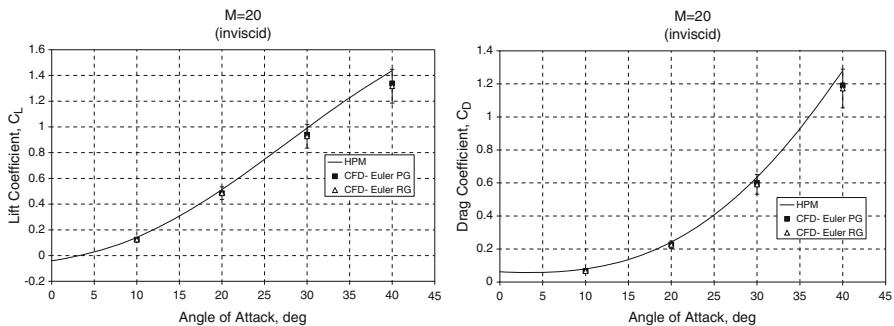


Fig. 6.131 Lift and drag coefficients vs. AoA. Comparison between HPM and CFD (both perfect gas and nonequilibrium gas) at  $M_\infty = 20$ . Error bar of 10 %

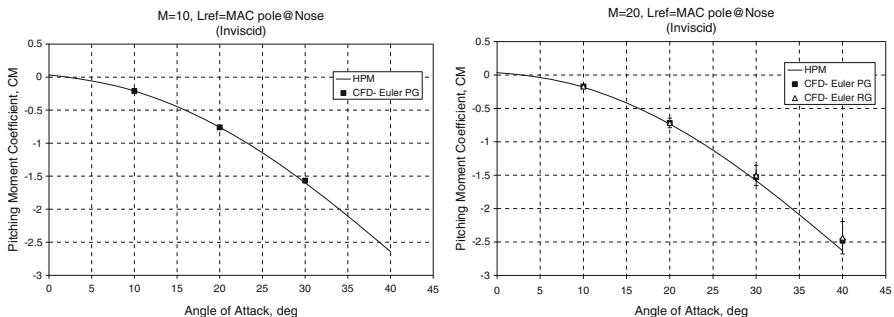


Fig. 6.132 Pitching moment coeff. vs. AoA. Comparison between HPM and CFD (both perfect gas and nonequilibrium gas) at  $M_\infty = 10$  and 20. Error bar of 10 %

**Table 6.9** Real gas effects on FTB-X aerodynamics at  $M_\infty = 20$

Mach = 20			
AoA	PG	RG	Err %
$C_L$			
10	0.1235	0.1252	1.3
20	0.4844	0.4857	0.3
30	0.9397	0.9275	-1.3
40	1.3378	1.3170	-1.6
$C_D$			
10	0.0670	0.0669	-0.1
20	0.2260	0.2254	-0.3
30	0.5999	0.5915	-1.4
40	1.1908	1.1721	-1.6
$C_m$			
10	-0.1710	-0.1728	1.0
20	-0.7176	-0.7177	0.0
30	-1.5274	-1.5029	-1.6
40	-2.4800	-2.4347	-1.9

Pole @ nose

$L_{ref} = MAC$

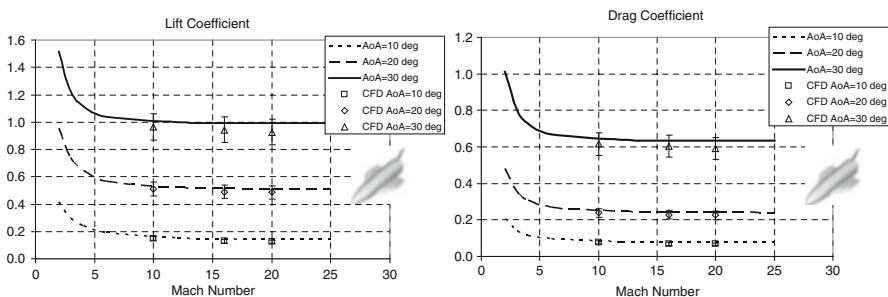


**Fig. 6.133** Lift and drag coefficients vs. Mach. Error bar of 10 %. Comparison between HPM and CFD Euler at  $\text{AoA} = 10^\circ, 20^\circ, \text{ and } 30^\circ$

From the previous CFD and HPM comparisons, it results that the engineering-based results are in good agreement with more reliable CFD solutions. Indeed, overall available results confirm that the difference between CFD and HPM aerodynamic coefficients is smaller than 10 % at least for the flight conditions of comparisons. Moreover, the available numerical data seem also to confirm that the differences between the real gas and frozen gas coefficients are very small (see Table 6.9), even if a significant effect on vehicle pitching moment may be expected along with the re-entry trajectory.

Finally, Fig. 6.133 shows the comparisons of lift and drag coefficients as functions of Mach number between HPM and CFD results for  $\text{AoA} = 10^\circ, 20^\circ, \text{ and } 30^\circ$ .

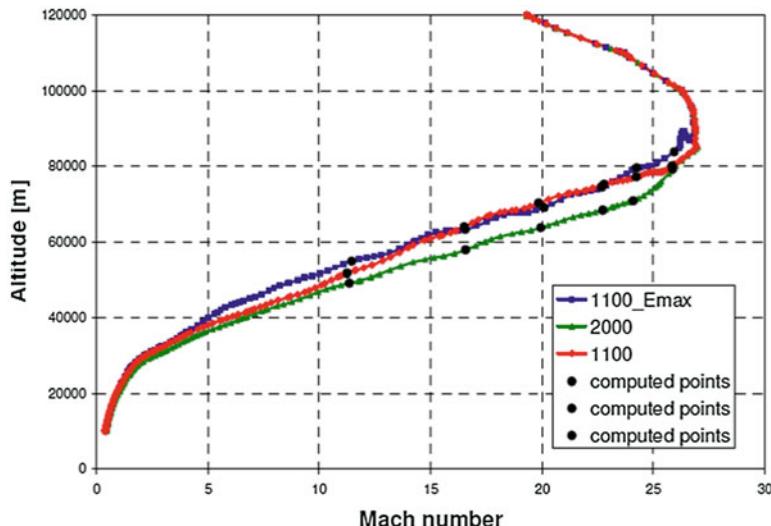


**Fig. 6.134** Reference trajectories

As one can see, the comparisons are very good both for  $C_L$  and  $C_D$ . In the next phases of FTB-X design, however, further analyses are recommended to be performed on specific topics as, for example, real gas effects and laminar-to-turbulent transition in order to increase the reliability of the vehicle database and reduce the design margins.

### 6.8.6 Vehicle Aerothermal Environment

The appraisal of vehicle aero thermal environment, i.e., the envelope of thermomechanical loads (e.g., pressure, shear stress, heat flux, and integrated heat load) the vehicle has to withstand during re-entry, is fundamental to determine the loads for the TPS design. Among others, there is the critical issue of the small radius of the nose and of the wing leading edge that are currently, respectively, 10 cm and 4 cm due to the need to guarantee a high aerodynamic efficiency. In this framework, the reference trajectories shown in Fig. 6.134 are taken into account. The main hypotheses made to calculate these trajectories are the following:

1. *1100\_Emax*: maximum heat flux on the nose stagnation point equal to 1,100 kW/m<sup>2</sup>, maximized efficiency
2. *1100*: maximum heat flux on the nose stagnation point equal to 1100 kW/m<sup>2</sup>, minimized angle of attack
3. *2000*: stagnation heat flux on the nose point of 2,000 kW/m<sup>2</sup>, minimized angle of attack

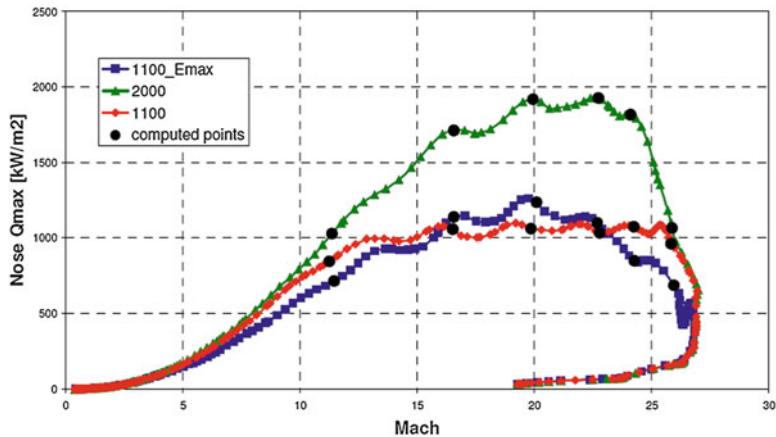


Fig. 6.135 Nose stagnation-point heat flux profiles

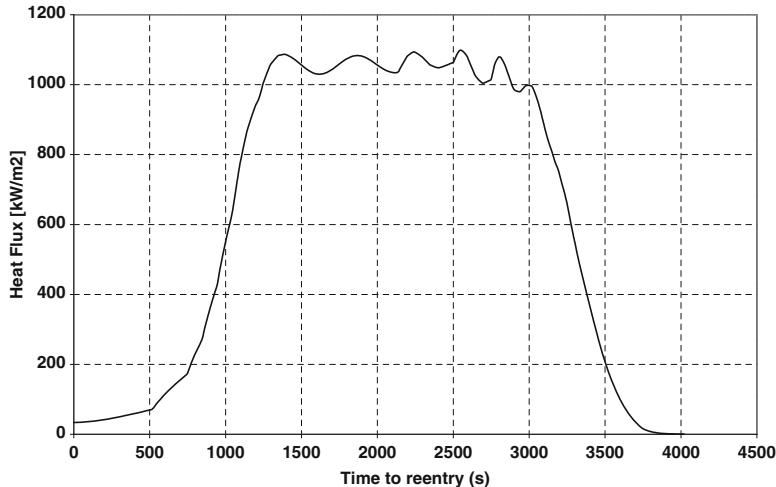


Fig. 6.136 Preliminary reference FTB-X aerothermal flight scenario with regard to stagnation point

In the same figure also the six design points sampled along with the re-entry trajectory are reported, according to the trajectory-based design approach.

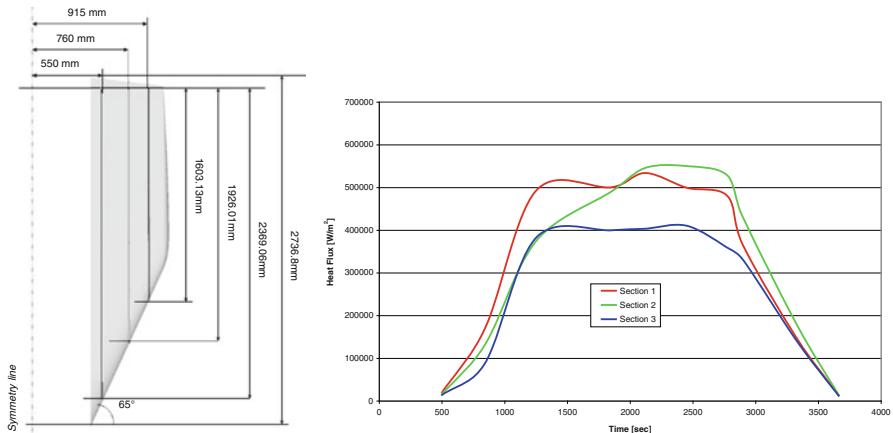
The corresponding heat flux profiles for the fuselage stagnation point are provided in Fig. 6.135.

On the other hand, the time history of the heat flux over the stagnation point of the nose can be found in Fig. 6.136.

The rationale used to choose such a design points is clear: they are selected in such a way to reconstruct the entire history of the heat flux along the trajectories.

**Table 6.10** CFD check points

Check point No.	Time to re-entry (s)	Altitude (m)	Mach No. (-)	Heat Flux ( $\text{kW/m}^2$ )	AoA ( $^\circ$ )
3	1,220.20	80,079.18	25.84	961.50	12.94
4	1,800.00	77,146.22	24.24	1,074.20	19.24
5	2,119.17	75,208.34	22.79	1,034.38	23.70
6	2,492.99	70,241.79	19.85	1,062.48	25.29
7	2,773.56	63,981.31	16.51	1,058.19	22.74
8	2,900.00	60,427.10	14.71	846.08	20.18

**Fig. 6.137** Preliminary reference FTB-X aerothermal flight scenario with regard to wing leading edge

As a result, the heating pulse the vehicle has to withstand is captured. These check points and the corresponding free-stream conditions are summarized in Table 6.10.

As far as wing leading edge aeroheating is concerned, in Fig. 6.137 the heat fluxes along the trajectory are shown over the wing with respect to three meaningful sections as defined in the figure. As one can see, the aeroheating at wing leading edge results in a less severe environment with respect to stagnation point, mainly thanks to the effect of wing swept.

Note, however, that because of the long mission requirement, the above re-entry aerothermal scenario resulted in a very high time integrated heat load  $Q$  that reads

$$Q_{\text{sp}}(t) = \int_{t_E}^t \dot{q}_{\text{sp}}(\tau) d\tau$$

It must be underlined that, while the peak of heat flux drives the selection of the nose geometry, given a TPS material type, the integrated heat load determines the

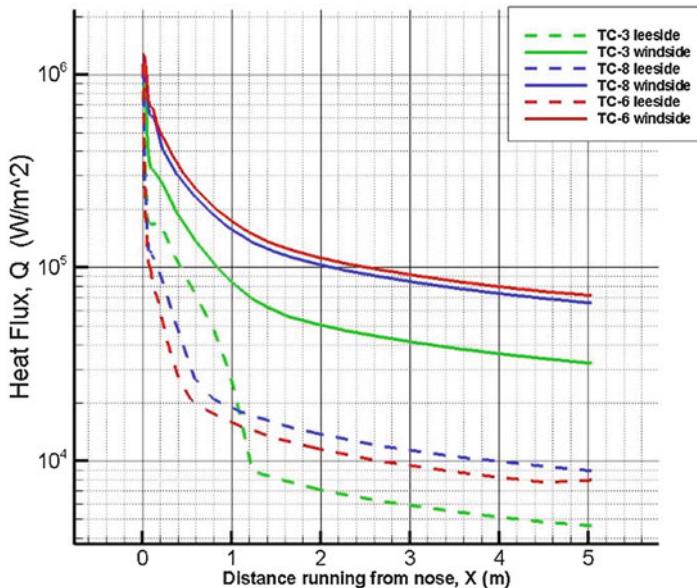


**Fig. 6.138** Heat flux distribution on the fuselage centerline. Effect of AoA

thickness of the TPS. Therefore, the points to be selected on the trajectory for CFD analysis should be chosen also to replicate the area under the heat pulse, which markedly drives the vehicle thermal shield design.

For the TPS sizing, the heat fluxes are shown for different Mach numbers only along with the centerline for the flowfield conditions of several check points, namely TC-3, TC-8, and TC-6, summarized in Fig. 6.138.

As one can see, the stagnation-point heat flux is close to the trajectory aero-heating constraint and is quite insensitive to these changes in AoA of test case conditions. This is not unexpected as the surface radius of curvature is nearly constant in the vicinity of the nose tip.

Along the fuselage, however, there is an AoA influence on the surface heat flux both on windside (continuous line) and leeside (dashed line).

When AoA is the smallest (TC-3), areas on the upper surface of the vehicle are more exposed to the flow environment than for the other TC conditions and typical RLV ( $\text{AoA} \cong 40^\circ$ ), thus reaching higher heat flux distribution (green dashed line), at least in the forward part, due to the drop-down nose configuration.

Moreover, ranging from TC-8 to TC-6, small differences are present, as expected, both on vehicle belly side and leeside.

It must be underlined that, also for the trajectories 1100 and 1100\_Emax, the stagnation point heat flux resulting from both HPM and CFD computations is often higher than the limit of  $1,100 \text{ kW/m}^2$ ; in particular, from the CFD computations, the heat flux reaches also a value of  $1,400 \text{ kW/m}^2$  if the wall is simulated as a fully catalytic body.

Furthermore, such very high values of heat flux are limited to a very small zone of approximately 2 cm, and therefore it can be expected that a possible overheating can be avoided due to the heat sink effect of the nose.

Nevertheless, the results of such detailed analysis shall be taken into account in the prosecution of the project.

Finally, it must be underlined that the results presented in the following section refer only to the 1,100 trajectory, since the 2,000 trajectory resulted too critical for the standard TPS materials currently taken into account.

The employment of alternative hot structure concepts made of innovative ceramic composites in place of traditional TPS for structural parts subjected to high thermal fluxes could be taken in consideration in order to enhance the mission performance. Sharp nose cap and leading edge hot structures made of massive ultra-high-temperature ceramics (UHTC), i.e., advanced ZrB<sub>2</sub>–SiC dense ceramic blends capable to withstand temperatures higher than 2,000 K, are envisaged.

#### *Further ongoing analyses*

In this preliminary analysis some important topics have been neglected:

- Laminar-to-turbulent transition
- Shock impinging over the wing
- Rarefaction effects
- Real gas effects

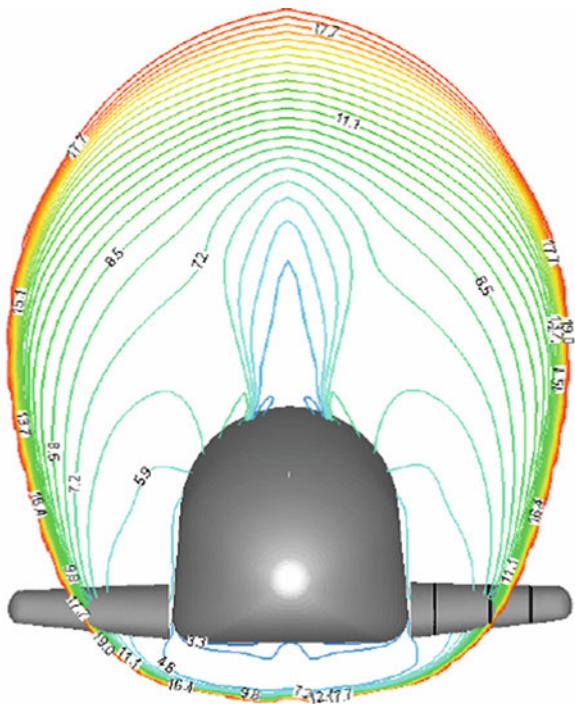
Hereinafter some highlights are given for each of these topics; a more detailed analysis will be made in the prosecution of the activity.

##### **6.8.6.1 Laminar-to-Turbulent Transition**

It is well known that, when the flow regime becomes turbulent, the wall heat fluxes increase significantly, up to 2–3 times with respect to the laminar case. In general it is therefore important to take into account this effect. On the other hand, the FTB-X, according to the project requirements, will be characterized by a very “high” trajectory with respect, for example, to the one of the Space Shuttle Orbiter, due to the high aerodynamic efficiency. This means that the Reynolds number will be quite low for a large part of the trajectory; for example, for trajectory 1,100, the Reynolds number based on the vehicle length is lower than 1 million up to Mach 11. Therefore, it can be expected that the transition will occur at a Mach number sufficiently low and that the related overheating should be less critical.

Nevertheless, a premature transition is always possible due to wall discontinuities, shock-wave–boundary-layer interactions, and other unpredictable reasons. Therefore, a detailed analysis of the problem is needed and will be performed in the next phase of the activity, including specifically designed experimental tests that can assess the risk of premature transition and will help the definition of proper design margins.

**Fig. 6.139** Example of shock impinging over the wing



### 6.8.6.2 Wing–Fuselage Interaction

Another important problem that was not yet taken into account in the TPS design, but is currently under investigation, is the local overheating that occurs over the wing leading edge in the region where the shock generated by the fuselage impinges over the wing itself. An example is shown in Fig. 6.139. A preliminary analysis has shown that the heat flux, over the FTB-X wing, can be also doubled with respect to the case without shock impinging. This pick is obviously local, limited to the section of the impinging, that moves toward the tip, along the trajectory, due to the decrease of the Mach number. Moreover, the interested section obviously depends on the angle of attack. However, this is a problem that must be very carefully taken into account, also considering that in the current baseline the radius of the wing leading edge is very small (4 cm) (Fig. 6.139).

### 6.8.6.3 Rarefaction Effects

Due to the peculiarity of the FTB-X mission, the rarefaction effects are particularly important to be taken into account both on the aerodynamic coefficients and on the heat loads estimation. For instance, in order to get an idea of aeroheating in rarefied

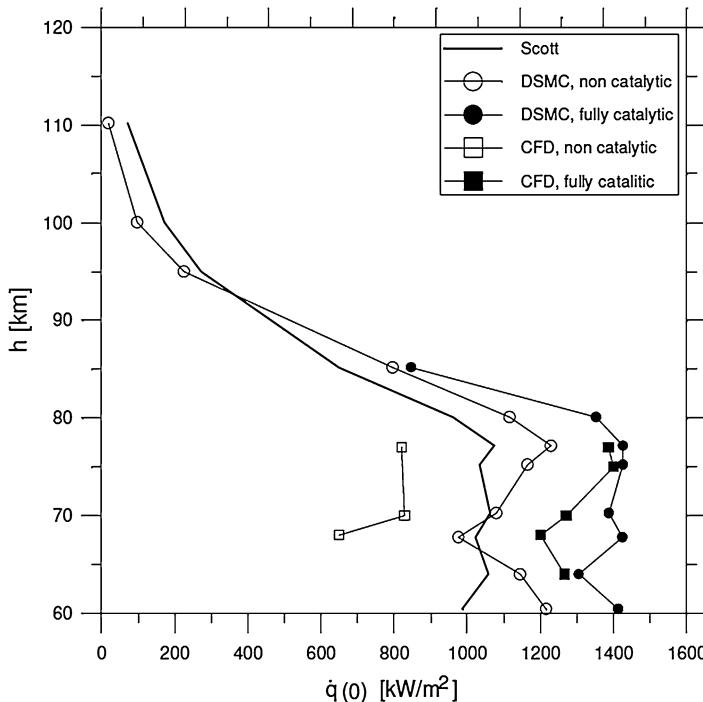


**Fig. 6.140** Heat flux at the stagnation point of the FTB-X nose

flow conditions, Fig. 6.140 shows the profiles of the heat flux at the nose stagnation point versus altitude from DSMC and CFD for fully catalytic and non-catalytic wall.

These results are compared with the heat flux predicted by the Scott formula, already used in the trade-off design of FTB-X. The profiles of  $\dot{q}(0)$  from DSMC and CFD in fully catalytic wall conditions are similar; both computations agree in stating the maximum value of stagnation-point heat flux since high altitudes ( $h \cong 80$  km). The fact that DSMC and CFD codes give comparable results, even though based on different approaches, is due to the fully catalytic wall condition that “forces” the solution on the wall. The Scott formula instead underestimates the results from DSMC and CFD; the maximum value of  $\dot{q}(0)$ , predicted by Scott, is about 1,100 kW/m<sup>2</sup>, while for the DSMC and CFD codes the maximum value is about 1,400 kW/m<sup>2</sup>.

When the wall is non-catalytic, strong discrepancies appear between DSMC and CFD. In this case DSMC gives results comparable with those from the Scott formula, while CFD calculations underestimate these ones. At  $h \cong 80$  km,  $\dot{q}(0)$  from DSMC is about 1,230 kW/m<sup>2</sup> and from CFD is about 821 kW/m<sup>2</sup>. CFD, in non-catalytic wall condition, shows its limits in simulating rarefied flows, because of the failure of phenomenological models, such as the Fourier and the Fick laws.

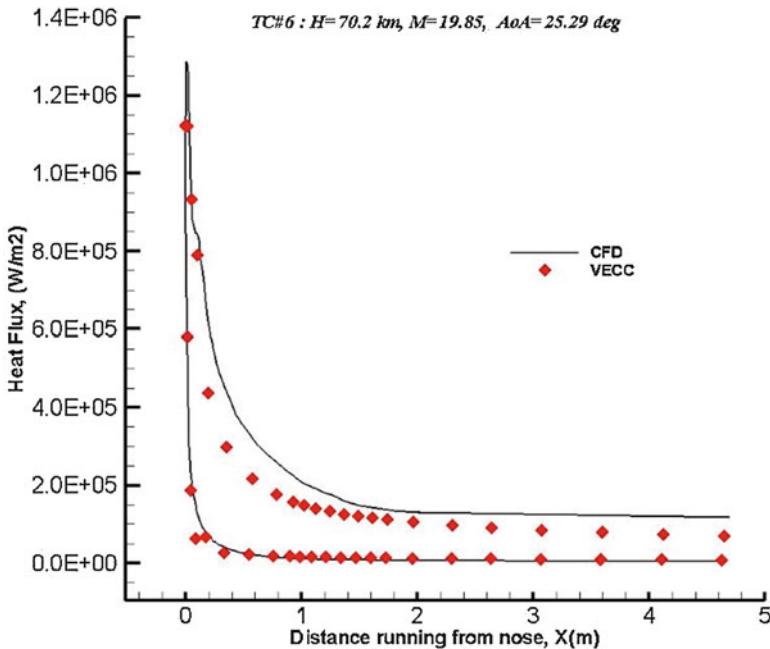


Fig. 6.141 Heat flux comparison between CFD and HPM at TC#6, for fuselage centerline

As a conclusion, also in a trade-off design of TPS, an accurate methodology is needed in the prediction of the heat flux. In fact, depending on the catalytic behavior of the wall, the Scott formula could significantly underestimate the heat flux. Therefore, it is important, on one side, to have good characterization of the wall catalicity also in rarefied conditions and, on the other side, to evaluate the heat flux by means of appropriate methods like DSMC.

Finally, several comparisons were performed between HPM and CFD results; hereinafter only a comparison over the fuselage is shown, while more details concerning the heat loads over the wing can be found in Ref. [10], where attention is focused also on the interaction that occurs in the region of the wing leading edge on which impinges the vehicle bow shock.

As an example, in Fig. 6.141 the heat flux on the vehicle centerline is plotted as a function of the distance from the nose for the TC-6 flowfield conditions.

It can be seen that HPM solution compares well with respect to the CFD one. However, the comparison is not so good in the regions where 3-D flowfield effects exist. This means that a proper margin should be adopted in this phase; therefore a 30 % margin is conceived for the next TPS analysis, with respect to the HPM data. It must be also considered that all these analyses have been performed in the hypothesis of laminar flow; this hypothesis should be quite realistic in a large part of the trajectory, since it is characterized by low Reynolds numbers up to quite low Mach numbers, and in particular in the range where the maximum heat loads occur; however, the effect of possible premature transition induced by wall discontinuities should be taken into account in the future.

Note that the CFD heat flux markedly differs from that evaluated with engineering methods, only at windside at about  $x \leq 1$  m due to the downstream effects of nose blunting that originate a combining effect of the entropy layer and AoA. Therefore, the comparisons show the effect of local entropy values, thus highlighting, in addition, the fact that the HPM code considers that the shock layer is rotational only [17]. Indeed, the bow shock produced by the blunted nose facing the flow at AoA generates entropy gradients in the inviscid shock layer, thus resulting in inviscid velocity gradient normal to the FTB-X surface that the panel method code does not take into account for (e.g., the entropy layer) [15, 18].

Further details on aeroheating trade studies can be found in ref. [5, 10].

#### 6.8.6.4 Design of the TPS

Before describing the results of the thermal design, it is worth to give an overview of the structural concept that was proposed for the FTB-X.

#### 6.8.6.5 Structural Concept

Basically, the structural architecture (see Fig. 6.142) is composed by ten bulkheads connected by six longerons (“T” and “H” section) for each of the nine subdivisions of the external shell (the only exception is between the first the second bulkheads in

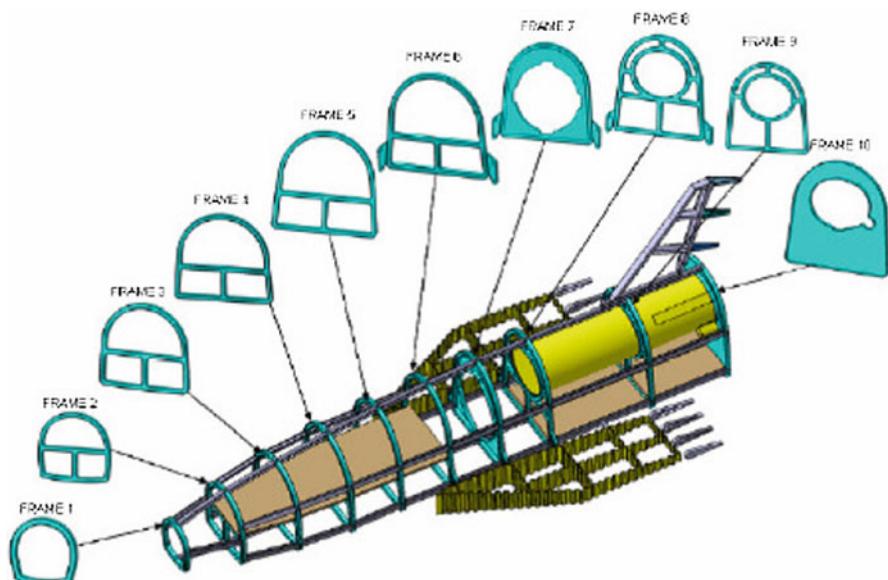


Fig. 6.142 Structural concept

the nose area, where the longerons are only four). The bulkheads are constituted by machined titanium plates that allow the accommodation of the parachute canister and the propellant tank.

Waffle architecture has been chosen for the rear bulkhead, providing a stiff interface for the parachute canister mounting flange and for the attachments to the launch adapter. The wings are conceived as hot structures in order to minimize the mass and to enhance the technological valence of the vehicle itself.

The wing internal skeleton will comply with the thermal-induced deformations of the leading edge as well as the ones of the leeward and windward skin, all of them being made with dissimilar materials, with highly different values of the thermal expansion coefficient; hence there will be the necessity of a hard skeleton able to maintain the structural integrity of the wings in all conditions but flexible enough to be compatible with the deformations of its various parts without losing the wings aerodynamic efficiency.

These performances are pursued with spars and ribs realized as wrinkled sheets, characterized by high bending stiffness but low longitudinal stiffness. The maximum internal temperature of the wing will be limited to 400 °C.

This limitation is not due to structural reasons (the materials used could exceed such limits) but for functional reasons (feasibility of an affordable aileron command chain). Within the abovementioned limit, the Ti alloy could be a valid candidate for the wrinkle, although the PM1000 was considered into the mass budget for sake of structural safety, hence to provide the structure with some margin in front of possible non-nominal events such as the loss of a small portion of the TPS function; this approach is considered applicable to an experimental vehicle such as the USV, for which the mission envelope will be affected by serious contingencies. The wings are linked to the fuselage through a system of rods (so far considered in PM1000, but a Ni-based MMC is envisaged as an attractive potential substitute) enabling the transportation of fuselage and wings disassembled and then an easy reassembly on the launch site facilities. The aileron is an integral C/SiC structure with embedded C/SiC stiffening. The selected solution is the best option both for the mass saving and for the thermal efficiency. Due to the high thermal conductivity of the C/SiC, the aileron hinge bearings hosted into the wings will be in ceramic; their life will have to be checked in front of the missions to be performed by the USV, considering a possible bearing re-furbishing after a given number of missions. The baseline wing leading edge is made of UHTC, but the wing will be able to host the fluidic distribution lines in case an actively cooled leading edge is chosen.

The aeroshell has been kept only as a support for the TPS panel in the leeward area where flexible protective insulation blankets are present.

### 6.8.6.6 Thermal Design

The energy management accomplishes two main functions:

- To protect the Kevlar primary structure from the severe aerothermal fluxes experienced especially during the re-entry phase

- To ensure that the internal environment is maintained within the temperature limits suitable for the operative conditions of the avionics equipment, of the actuators, and of the RCS tank

### Internal Thermal Control System

The vehicle internal environment has to ensure a temperature range compatible with the avionics operative requirements. Heat transfer can affect avionics temperature according to the following couplings:

- Radiative heat transfer between the Kevlar structure and the internal equipment. The radiative coupling depends on the distance between the Kevlar structure and the equipment and on the thermal level of the Kevlar structure, maintained below 200 °C by TPS during all the mission phases.
- Conductive heat transfer through the equipment supporting structure.

In order to assess the operative temperature range of the internal equipment during both re-entry and post-landing phases, dedicated analysis cases will have to be run in future program activities, when a complete mathematical model will be available.

These analyses will allow verifying the need of additional thermal capacitors, in particular for those equipment, as the beacon, whose temperature has to be controlled for the entire mission, up to the end of post-landing phase, or that have, as the batteries, a more stringent temperature requirement (40 °C).

### External Thermal Protection System

The thermal isolation from the convective re-entry aero thermal heat fluxes is achieved by means of different thermal protection system (TPS) materials distributed through the entire FTB-X surface on the base of two driving criteria:

- To sustain the surface equilibrium temperature derived from the aero thermal heating, as the friction effect between the hypersonic flow and the TPS aerodynamic surface. Also chemical reactions, depending on the wall catalicity, contribute to the heating exchange between the external boundary layer and the TPS surface. The highest temperatures are expected in correspondence of the leading edges and of the windward area.
- To provide the adequate stiffness against the dynamic pressure to maintain the aerodynamic shape.

All the aerodynamic surface of FTB-X is protected with different insulating materials, whose characteristics were selected firstly to withstand the temperature peak occurring during the re-entry reference trajectory. The TPS material selected was then sized by evaluating the total heat load incident on its surface during the re-entry phase.

The aerothermal heat load determines an increase of the Kevlar substructure temperature with a rate that is inversely proportional to the TPS thermal capacity. The TPS thickness is determined in order not to exceed the Kevlar maximum temperature of 200 °C.

This thickness, evaluated on the base of the total heat load incident on TPS sizing points, is maintained constant along the length of the vehicle. This is a conservative assumption that maintains the Kevlar structure close to the requirement of 200 °C max in correspondence of the sizing point and colder for all the stations aft the sizing point.

The nose is protected by means of ceramic material (C/SiC). In addition, ceramic material is present in all zones where high-temperature levels are foreseen: windward part of the vehicle and leeward zone close to the nose area and flap. In all these zones the thermal insulation is assured, in the internal part, by thermal blankets of high-temperature insulation (HTI) and internal flexible insulation (IFI), glued on the internal side of the ceramic panels.

Leeward fuselage zone and rear part of the vehicle are covered by flexible external insulation (FEI) blankets with maximum allowable temperature of about 1,000 °C.

In detail:

- The TPS nose area, for a length of 450 mm, consists of a C/SiC monolithic cap.
- Three circumferential series of C/SiC panels are foreseen in the leeward area, for a length of 1,350 mm; maximum panel dimension is of 500 × 500 mm. The panels are fixed by means of brackets to the structural frames that are in correspondence of the interface between two adjacent panels; ceramic thermal isolators are foreseen to limit the heat exchange.
- Trapezoidal C/SiC panels are foreseen in the windward area; in this zone, due to the high aerothermal heat fluxes, the panel layout was studied in such a way that the interfaces between panels are not in correspondence of the flow lines and so to avoid possible hot plasma inclusion during re-entry phase.

The panels are fixed by means of brackets to the structural frames in the forward area and to the longerons in the aft area.

In all these zones, the monolithic nose cap and the C/SiC panels are load carrying, and the fuselage is no longer required.

A Kevlar fuselage is foreseen only in leeward aft part: the blankets of FEI 1000 are glued to it. The blankets are in correspondence of the fuselage panels, and their size is the same of the corresponding fuselage panel to which they are attached to. The FEI blankets are characterized by being lightweight, robust, and easy to apply, inspect, and substitute in case of maintenance. The drawback is represented by the fact that their external surface is porous and wavy and then of poor aerodynamic quality. This characteristic could negatively affect the results of payloads experiment placed on FEI surface.

A metallic TPS (PM1000) could replace the FEI 1000 in the leeward zone, offering a smooth surface. In the PM1000 zone, the thermal insulation is ensured by the presence of IFI. In this case, the presence of the fuselage would be no longer

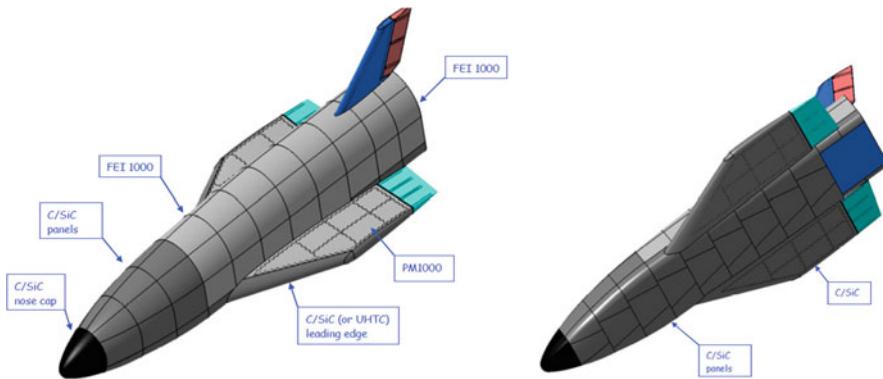


**Fig. 6.143** TPS layout

needed, being PM1000 panels the load-carrying structure. The disadvantage in this case would be represented by a significant increase in mass.

Wings and rudder are hot structures with leading edges (and wing lower side) in C/SiC and the remaining part in PM1000. The proposed TPS distribution along the FTB-X vehicle is shown in Fig. 6.143.

#### TPS Sizing Results

The TPS sizing is obtained by using an overall mathematical model representing the entire vehicle, with the complete internal avionics architecture. The heat fluxes used as input are those reported in Fig. 6.138 for the 1,100 trajectory. However, also the 1100\_Emax and the 2,000 trajectories have been taken into account: the first one has similar characteristics with respect to the 1,100, and therefore the same TPS layout and a similar thickness distribution can be assumed. The second one resulted instead in too large TPS thicknesses, if standard materials have to be used. The purpose of the TPS sizing is to maintain the Kevlar structure temperature below the maximum value of 200 °C and to control the avionics equipment below their maximum allowed temperature values (40 °C for the batteries and 60 °C for the other equipment). Due to the considerable duration of the re-entry phase, resulting in a very high total integrated heat load entering the vehicle, the possibility of an internal air cooling at the moment of the parachute opening, with beneficial effects on the equipment temperature (in particular for those, beacon MMU and batteries, whose temperature has to be controlled for the entire post-landing phase duration), was considered. The TPS thicknesses are in any case maintained below the maximum overall value (60 mm) allocated in the CATIA model. The Table 6.11 shows the thickness resulting from the thermal analyses.

**Table 6.11** TPS thickness

FTB_X-3.9.2 TPS thickness		
Zone	Material	Thickness [mm]
Nose	C/SiC	6
Windward	HTT	20
	I FI	40
	C/SiC	3
Leeward forward	HTI	20
	I FI	35
	C/SiC	3
Leeward	HTI	20
	I FI	35
	FEI 1000	40
Body flap	C/SiC	3
Rear	HTI	20
	I FI	20
	FEI 1000	15
Leeward wing	PM1000	2
Windward wing	C/SiC	3

### 6.8.7 FTB-X Re-entry Flight Mechanics Performance and Effects of Air Rarefaction

Analyses have been also carried out to assess how much relevant could be neglecting the rarefaction effects, which FTB-X experiences in the highest atmosphere layers, in the reference trajectory computation. This design aspect demands particular attention considering that the FTB-X must be able to fly along with “long-endurance” trajectories that are flight paths in which the vehicle must exchange a non-negligible part of its potential plus kinetic energy in higher atmosphere layers. Therefore, re-entry trajectory assessment may be highly affected if the Flight Mechanics (FM) computations refer to an AEDB which accounts for the rarefaction effects (RE). In this framework a typical re-entry trajectory has been first used to assess rarefaction effects, in which the vehicle is supposed to enter the Earth atmosphere at an altitude of 120 km, with a flight path angle of 1.1° pointing down to Earth and a velocity of 7,420 m/s. Because the approach we used in defining a reference re-entry path relies on the numerical solution of a constrained optimization problem, we defined the root mean square (RMS) value of the difference between the altitude, velocity, and AoA profiles, computed through the optimization procedure, with and without taking into account for RE, as a figure of merit to highlight the relevance that those effects have on the re-entry trajectory.

Altitude and velocity profiles are, in fact, the parameters normally used in the guidance system design, directly or indirectly through the use of derived parameters, while the AoA is the command used to guide the vehicle on the design flight path. Thus, we considered that those RMS values can conveniently be used to assess

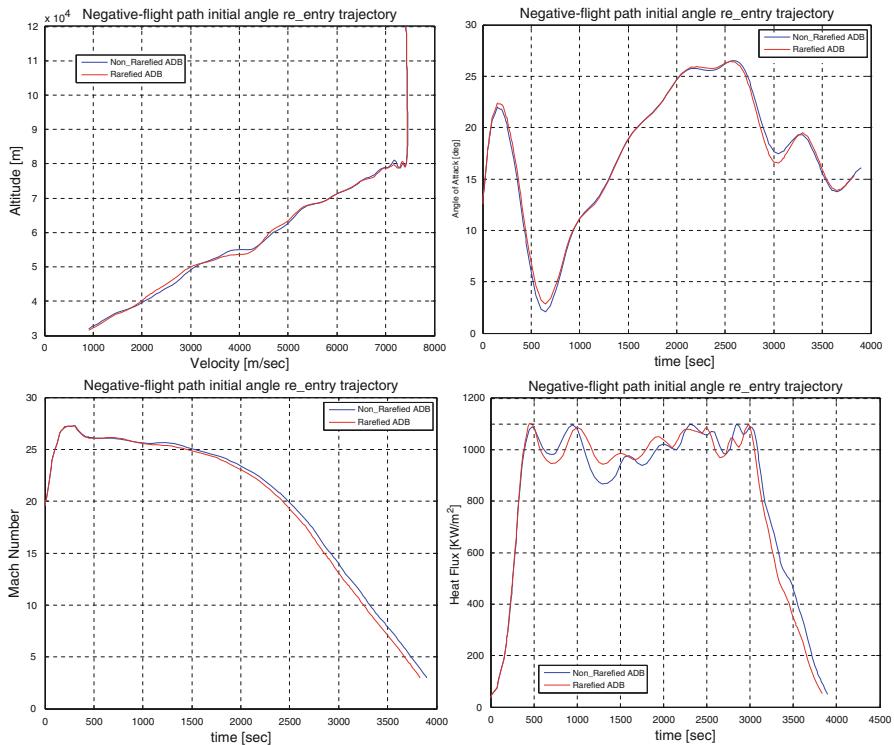


Fig. 6.144 “Deep” re-entry paths. Rarefaction effects on USV-X re-entry trajectory

Table 6.12 Rarefaction Effects on “deep” re-entry trajectory

	RMS	Mean	%
Alt <sub>r</sub> -Alt <sub>nr</sub> [m]	1,190	70,000	1.7
Vel <sub>r</sub> -Vel <sub>nr</sub> [m/s]	148	5,350	2.8
AoA <sub>r</sub> -AoA <sub>nr</sub> [ $^\circ$ ]	0.44	17.6	2.5

the relevance of the rarefied atmosphere effects. In Figure 6.144 the comparison between the trajectories obtained optimizing the re-entry path taking into account or neglecting, respectively, the effect of a rarefied atmosphere on the vehicle aerodynamics is drawn.

The trajectories are both optimized in the presence of normal load factor, dynamic pressure, and heat flux constraints, the latter being the most relevant in the paths computation. The two trajectories look very close in the figure, and the selected RMS parameters take the values in Table 6.12.

As further assessment of RE on concept re-entry performance, a “worse” kind of path has been considered, in which the initial re-entry velocity vector is supposed to be tangent to the 120 km altitude circular orbit, that is, the initial flight path is assumed to be zero and the return to Earth is obtained slowing down the vehicle

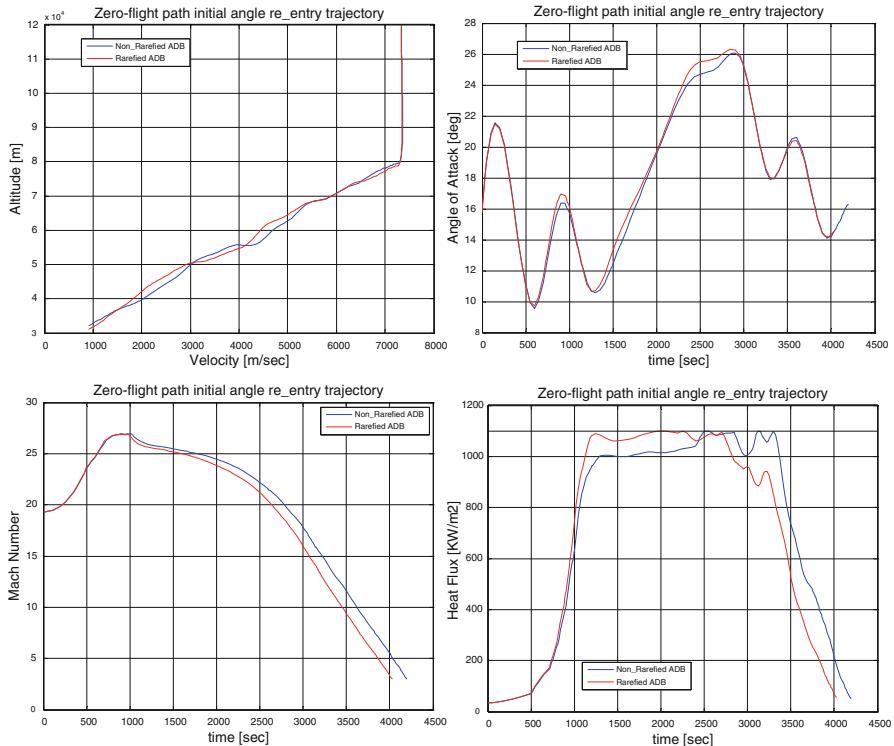


**Fig. 6.145** “Shallow” re-entry paths. Rarefaction effects on USV-X re-entry trajectory

**Table 6.13** Rarefaction Effects on “shallow” re-entry trajectory

	RMS	Mean	%
Alt <sub>r</sub> -Alt <sub>nr</sub> [m]	2,480	70,940	3.5
Vel <sub>r</sub> -Vel <sub>nr</sub> [m/s]	356	5,200	6.8
AoA <sub>r</sub> -AoA <sub>nr</sub> [ $^\circ$ ]	0.4	17.6	2.3

from its orbital velocity. This kind of re-entry path, in fact, will stand longer than previous examined path in high atmosphere, thus being stronger affected by the RE. Results are collected in Fig. 6.145, whereas the corresponding RMS values are summarized in Table 6.13.

As expected, the RMS values are worse respect to the “deep” trajectory results.

Anyway, it seems that for the FTB-X re-entry path computation, the rarefaction effects on the re-entry flight performance can be neglected.

Finally, it is worth noting that, for what concerns the transitional regime, the heat flux profiles provided in Figs. 6.144 and 6.145, being computed with engineering-based relationship, must be confirmed by more reliable DSMC simulations since higher heat flux may be expected in this flight regime [13].

## 6.9 Aerodynamic Data Uncertainties

Many sources of uncertainty exist that can be applied to a model used to simulate a vehicle's flight. The first is the uncertainty in the vehicle aerodynamic model. Indeed, even if the vehicle aerodynamic data is available, i.e., lift, drag, side, and moment coefficients along with aerodynamic points and wetted surface areas, the aerodynamic model accuracy is limited by the accuracy of wind-tunnel tests on various scale models across several wind tunnels and of CFD simulations on various models across several flight regimes. As a consequence, after the vehicle's flight, the aerodynamic uncertainties can usually be bounded by analyzing the collected in-flight data. Therefore, the uncertainties are based on comparisons between historical flight measurements and preflight predictions of other similar aircraft configurations. In most cases, the preflight predictions were based on wind-tunnel data, although some prediction code data were used. These uncertainties provide the basis for "stress" testing of candidate USV-X guidance, navigation, and control systems.

For statistical error analysis where uncertainties need to be combined, tolerances and variations can be treated as three-sigma ( $3\sigma$ ) errors normally distributed about the mean.

### 6.9.1 Formulation of the Aerodynamic Database Uncertainty

Generally speaking, the uncertainties may be considered as a combination of "tolerances" (e.g., dispersion from the estimation means: computation codes, wind tunnels) and of "variations" (e.g., flight transposition error). So, the breakdown of contributors to these uncertainties may be as follows.

#### 6.9.1.1 Tolerances

CFD	WTT
<ul style="list-style-type: none"><li>• Meshing inaccuracy</li><li>• Solving method (Euler, Navier- Stokes, ...)</li><li>• Computation code</li><li>• Inaccuracy due to convergence</li><li>• Models (turbulence, real gas, chemistry...)</li></ul>	<ul style="list-style-type: none"><li>• Model inaccuracy</li><li>• Flow similitude (Reynolds ...)</li><li>• Mounting effect (sting ...)</li></ul>

All these contributions induce CFD to CFD dispersions as well as WTT to WTT and WTT to CFD dispersions. It is out of question to quantify separately each contribution. The way of estimating the tolerances is based on the assessment of deviations between CFD or WTT results, WTT repeatability tests, etc. In other

words, the tolerance assessments are obtained from the analysis of the available data resulting from the various prediction means.

### 6.9.1.2 Variations

- **Representativeness of the prediction means (models, flow characteristics ...)**
- **Realization of the vehicle (consistency with the theoretical shape, aeroelastic distortion ...)**

The variation cannot result from the observation of result dispersions. We have here to assess what could be the deviation from the flight. It can only result either from experience or from some rationale about physical phenomena well known to be difficult to predict, such as real gas effect in hypersonics.

### 6.9.1.3 Formulation of Uncertainty

Basing on the above considerations and expertise, as well, the considered uncertainties for the AEDB are additive, and they are modeled through the following relations:

$$\Delta C_{D,unc} = \Delta C_{D,b,unc}(M)$$

$$\Delta C_{Y,unc} = \Delta C_{Y,\beta,unc}(M) \cdot \beta + \Delta C_{Y,\delta_a,unc}(M) \cdot \delta_a + \Delta C_{Y,\delta_r,unc}(M) \cdot \delta_r$$

$$\Delta C_{L,unc} = \Delta C_{L,b,unc}(M)$$

$$\Delta C_{l,unc} = \Delta C_{l,\beta,unc}(M) \cdot \beta + \Delta C_{l,\delta_a,unc\%}(M) + \Delta C_{l,\delta_r,unc}(M) \cdot \delta_r$$

$$\Delta C_{m,unc} = \Delta C_{m,b,unc}(M) + \Delta C_{m,\delta_{bf},unc\%}(M) + \Delta C_{m,\delta_e,unc\%}(M)$$

$$\Delta C_{n,unc} = \Delta C_{n,\beta,unc}(M) \cdot \beta + \Delta C_{n,\delta_a,unc}(M) \cdot \delta_a + \Delta C_{n,\delta_r,unc\%}(M)$$

All the uncertain contributions are dependent on Mach number. It is worthy to note that in the above-listed relations, three different kinds of contribution are considered:

Baseline uncertainty: it is an additive uncertainty ( $\Delta C_{D,b,unc}$ ,  $\Delta C_{L,b,unc}$ ,  $\Delta C_{m,b,unc}$ ).

Derivative uncertainty: it should be multiplied for the related independent variable in order to compute the uncertain contribution ( $\Delta C_{Y,\beta,unc}$ ,  $\Delta C_{Y,\delta_a,unc}$ ,  $\Delta C_{Y,\delta_r,unc}$ ,  $\Delta C_{l,\beta,unc}$ ,  $\Delta C_{l,\delta_r,unc}$ ,  $\Delta C_{n,\beta,unc}$ ,  $\Delta C_{n,\delta_a,unc}$ ).

Percentage uncertainty: it expresses an additive uncertainty that should be computed as percentage of the correspondent nominal term ( $\Delta C_{l,\delta_a,unc\%}$ ,  $\Delta C_{m,\delta_{bf},unc\%}$ ,  $\Delta C_{n,\delta_r,unc\%}$ );  $\Delta C_{m,\delta_e,unc\%}$  also belongs to this group, but it is equal to 80 % of the nominal  $\Delta C_{m,\delta_{bf}}$ .

The total aerodynamic coefficients, when uncertainties are considered, are given by

$$C_{i,\text{total}} = C_{i,\text{nominal}} + \Delta C_{i,\text{unc}} \quad i = D, Y, L, l, m, n$$

Therefore, the vehicle aerodynamic characteristics, reported so far, embody the mean values (adjusted for flight conditions), while uncertainties represent deviations from those means and describe the scattering of observations about the mean. The tolerance, or lower uncertainty bounds, represents a measure of the experimental data scatter adjusted for flight conditions (essentially support-free and scale effect) about the mean values of the data sections.

Tolerances are intended for the use in operational subsystem design and may be referred to as design-to or operational uncertainties. Variations, or upper uncertainty bounds, represent the uncertainties associated with wind-tunnel-derived experimental data and full-scale vehicle flight measurements and may be referred to as preorbital flight test uncertainties.

These uncertainties provide the basis for “stress” testing of candidate vehicle guidance, navigation, and control systems.

Thus, each  $\Delta C_{i,\text{unc}}$  contribution must be provided for the whole re-entry flight. To this end, the impact of WTT, CFD, and flight data to vehicle aerodynamic uncertainties is discussed hereinafter.

### **6.9.2 Aerodynamic Database Uncertainty and WTT Measurements**

Laboratory (wind tunnel) or experimental data are always accompanied by measurement precision errors. Therefore, it becomes important to assign some parameters such as a limit of error to represent the precision of experimental data measurement. The error of a measurement is the observed value minus the true value, where the true value is unknown. Errors can be classified as either accidental or systematic.

Accidental errors are those which in a large number of measurements will be negative as often as positive and will, therefore, affect a mean value only slightly.

Systematic errors, arising from the same cause, will affect the mean in the same sense (either positive or negative) and, rather than balance one another, will result in a definite bias to a mean. Examples of systematic errors would be model support effects, wind-tunnel wall effects, blockage, etc.

When all systematic errors have been eliminated (insofar as possible), it is possible to consider the sample of individual repeated measurements of a quantity



Fig. 6.146 Knowledge Management Space

with the objective of securing the best estimate of the true value and assessing the degree of reproducibility which has been obtained. The best estimate of the unknown true value is the mean value of all the measurements. Therefore, the contribution of WTT measurements to vehicle aerodynamic database uncertainties relies on the accuracy of the measurement devices available at the WT facility.

### 6.9.3 Aerodynamic Database Uncertainties and CFD Data

Usually, CFD data repository features numerical simulations performed with different codes and models. Therefore, numerical results are affected by limitations in modeling and calculation according to the Knowledge Management Space shown in Fig. 6.146.

When undertaking a numerical CFD simulation, the researcher is faced with known unknowns, i.e., phenomena of which she/he is aware but cannot quantify, and unknown unknowns, i.e., phenomena which have not yet been identified as important to the design.

For example, this consideration applies to the flow modeling choice within the CFD simulation of the selected flight condition.

### 6.9.4 Aerodynamic Database Uncertainties and Flight Data

When no flight data exist to support an aerodynamic uncertainty model, assessment data available in literature for space vehicles of the same class are considered, for example, those shown in Fig. 6.147 and the US Space Shuttle one (see Fig. 6.148) [39]. Therefore, the uncertainties are based on comparisons between historical flight measurements and preflight predictions of other similar aircraft configurations. In

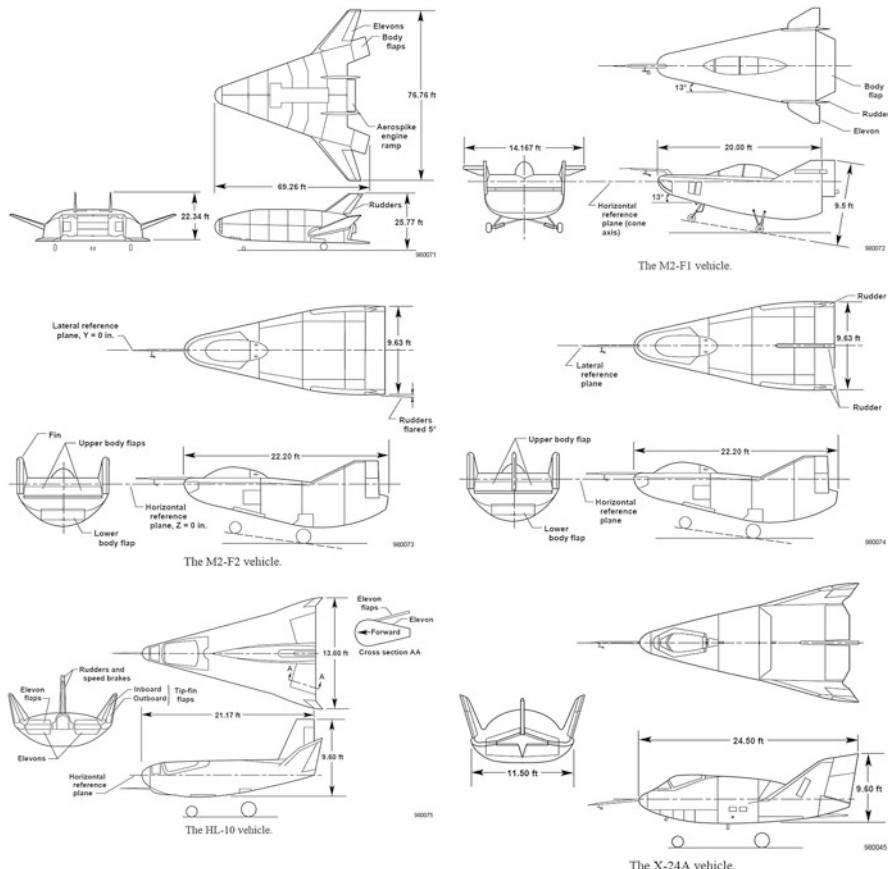
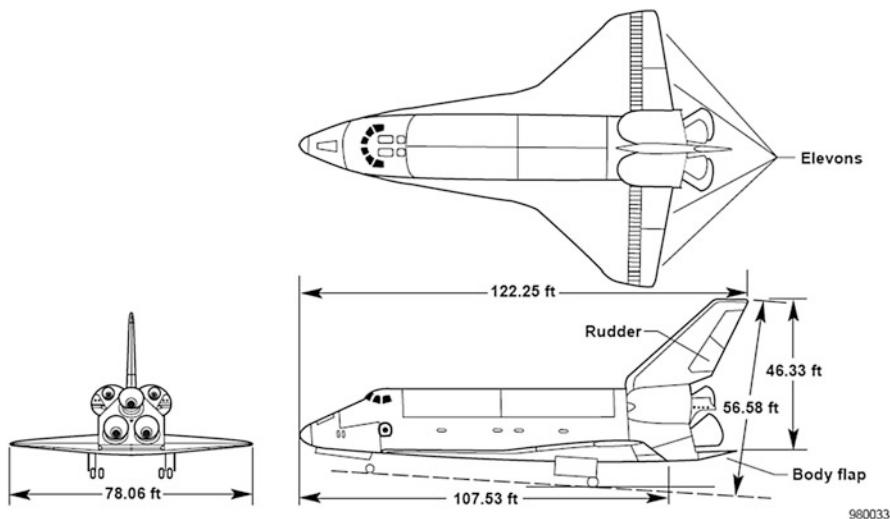


Fig. 6.147 Lifting-body research vehicles

most cases, the preflight predictions were based on wind-tunnel data, although some prediction code data were used.

This design choice has been suggested also by the fact that one of the most detailed analyses into aerodynamic uncertainty modeling was completed for the US Space Shuttle Orbiter program. The Orbiter aerodynamic uncertainty model consisted of two parts.

The first part was based on the wind-tunnel-to-wind-tunnel and model-to-model variations gathered during the 27,000-h wind-tunnel test program that was used to derive the aerodynamic model. These deviations, termed “tolerances,” were considered to be the minimum errors that should be expected. The control laws would need to be able to handle these errors with little or no effect on the vehicle stability or guidance. The second part of the uncertainty model was based on the differences between the historical flight test measurements and the preflight



**Fig. 6.148** The Space Shuttle Orbiter

predictions found for many similar (in configuration or mission) vehicles. By combining as many similar vehicles as possible, a pseudo “worst-case” aerodynamic prediction error bound was estimated for each of the important aerodynamic coefficients.

These worst-case aerodynamic uncertainties were termed “variations.”

### 6.9.5 *Orbiter and X-33 Aerodynamic Uncertainties*

The Orbiter aerodynamic database has been derived from an enormous wind-tunnel test program. In terms of wind-tunnel testing, the Orbiter has perhaps the best preflight wind-tunnel prediction that can be expected so far. Because the Orbiter aerodynamic database was developed from such an extensive ground test program, its uncertainty levels would, in general, be smaller than those expected for the ORV concept.

The Orbiter and X-33 uncertainties are documented as a function of Mach number and are valid to a maximum  $10^\circ$  AoA deviation from the nominal schedule.

The recommended Orbiter and X-33 lift and drag coefficient uncertainties are shown in Figs. 6.149 and 6.150, respectively [39]. In these figures, flight data of some of the research vehicle shown in Fig. 6.147 are also reported.

For a variety of reasons (model sting, Reynolds number, real gas, and tunnel blockage effects), total aerodynamic drag is susceptible to errors during wind-tunnel testing. This susceptibility is evident in the flight-to-prediction comparisons for the Orbiter. The drag coefficient prediction is incorrect by as much as 100 counts to

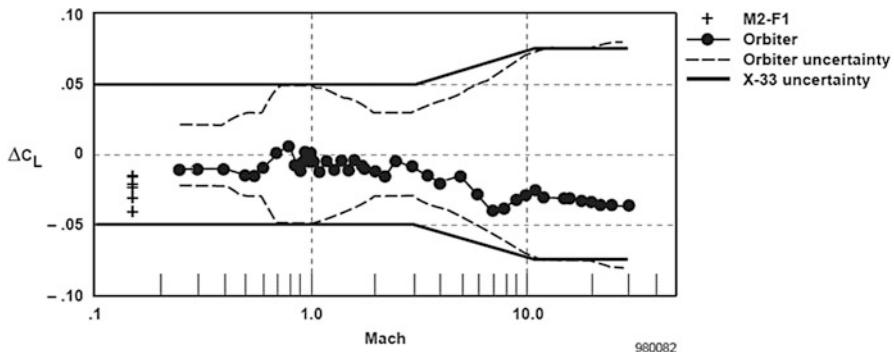


**Fig. 6.149** Lift uncertainty for Orbiter and X-33 vehicles

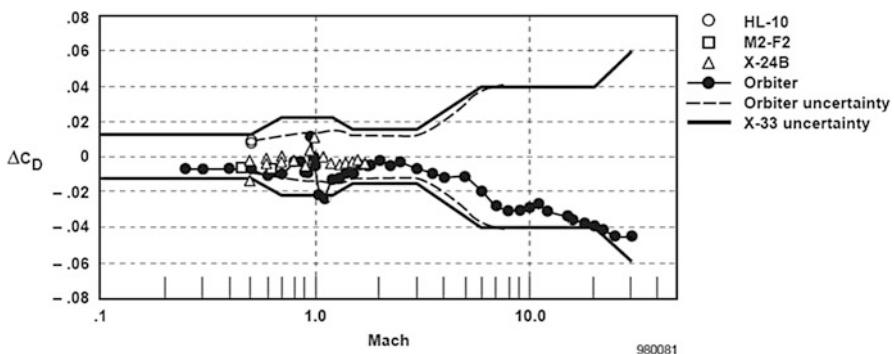


**Fig. 6.150** Drag uncertainty for Orbiter and X-33 vehicles

–200 counts in transonic regime. At subsonic and low supersonic Mach numbers, the Orbiter AoA is less than 15°. At Mach numbers greater than 5, the drag error increases. Explanations for the increasing drag uncertainty include increasing errors in the induced drag at increasing AoA and difficulties in reproducing the hypersonic Reynolds number and real gas environments in a wind tunnel.

Figure 6.151 shows the pitching moment prediction errors for the Orbiter and X-33 concepts [39].

Like drag, pitching moment is also susceptible to wind-tunnel measurement errors. The Orbiter had large pitching moment errors at hypersonic speeds caused by real gas effects in addition to the typical variations seen both in subsonic and transonic regime. These real gas effects are reasonably well-understood phenomena that can be estimated through modern CFD codes.

The recommended Orbiter and X-33 body flap effectiveness coefficient uncertainty is shown in Fig. 6.152 [39]. For lack of a better method at the current time, the shape of the body flap effectiveness uncertainty is also used for the elevon control uncertainty. Because the elevons are located outside the base area separated flowfield, a reduction in the uncertainty seems warranted.

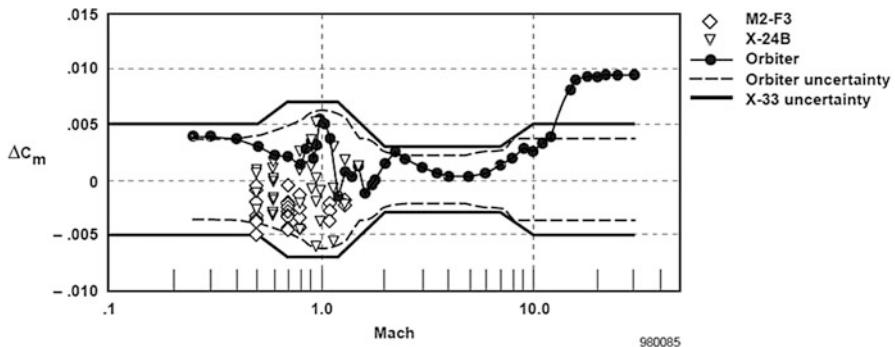


**Fig. 6.151** Pitching moment uncertainty for Orbiter and X-33 vehicles

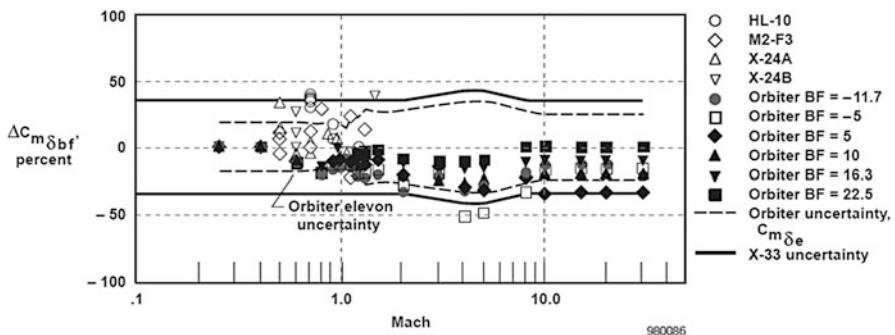


**Fig. 6.152** Body flap pitching moment uncertainty for Orbiter and X-33 vehicles

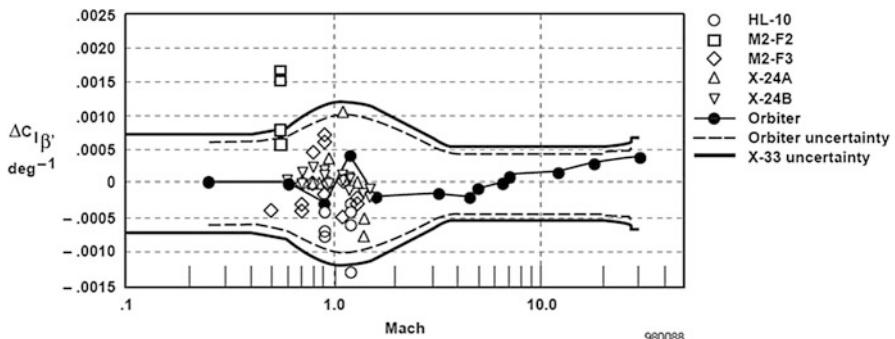


**Fig. 6.153** Rolling moment due to sideslip uncertainty for Orbiter and X-33 vehicles

The lateral-directional derivative uncertainties are discussed hereinafter. The uncertainty model is composed of effects caused by sideslip and control deflection.

The Orbiter and X-33 sideslip derivative uncertainties are summarized from Figs. 6.153, 6.154, and 6.155 [39].

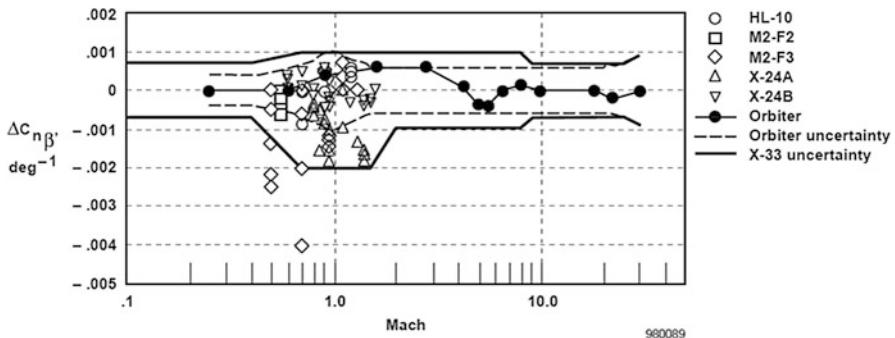


**Fig. 6.154** Yawing moment due to sideslip uncertainty for Orbiter and X-33 vehicles

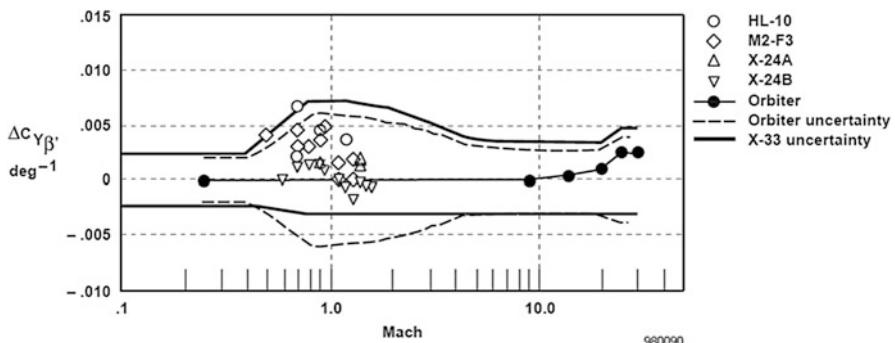


**Fig. 6.155** Side force due to sideslip uncertainty for Orbiter and X-33 vehicles

Figure 6.153 shows the derivative errors for rolling moment due to sideslip,  $\Delta C_{l\beta}$ .

Figures 6.154 and 6.155 show the directional stability,  $\Delta C_{n\beta}$ , and the derivative errors for the side force due to sideslip,  $\Delta C_{Y\beta}$ , respectively.

The Orbiter and X-33 aileron derivative uncertainties are summarized from Figs. 6.156, 6.157, and 6.158 [39]. Figure 6.156 shows the roll control power increments,  $\Delta C_{L\delta_a}$ .

The increments of yawing moment due to aileron,  $\Delta C_{n\delta_a}$ , are shown in Fig. 6.157. Figure 6.158 shows increments of the side force due to aileron,  $\Delta C_{Y\delta_a}$ .

### 6.9.6 FTB-X Aerodynamic Uncertainty Model

USV-X aerodynamic coefficients, given so far, are intended as mean values (adjusted for flight conditions) of vehicle aerodynamic characteristics.

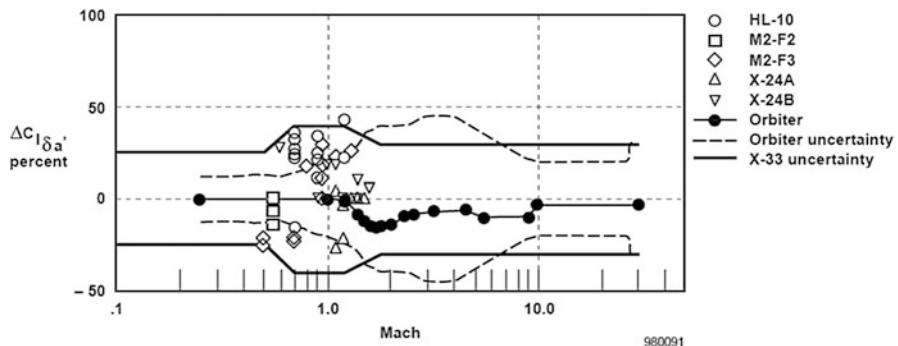


**Fig. 6.156** Rolling moment due to aileron uncertainty for Orbiter and X-33 vehicles

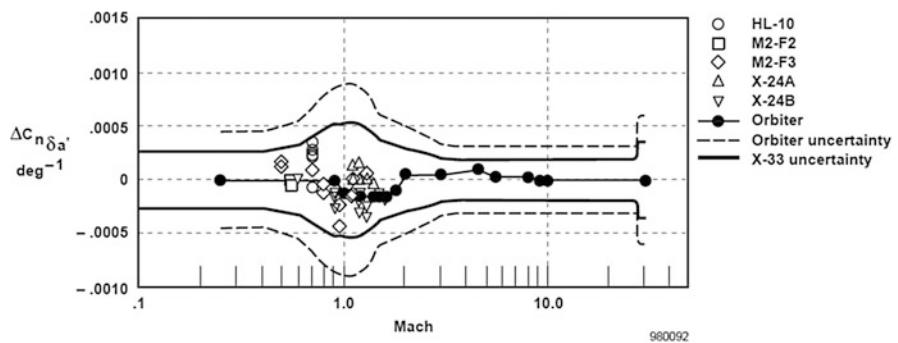


**Fig. 6.157** Yawing moment due to aileron uncertainty for Orbiter and X-33 vehicles

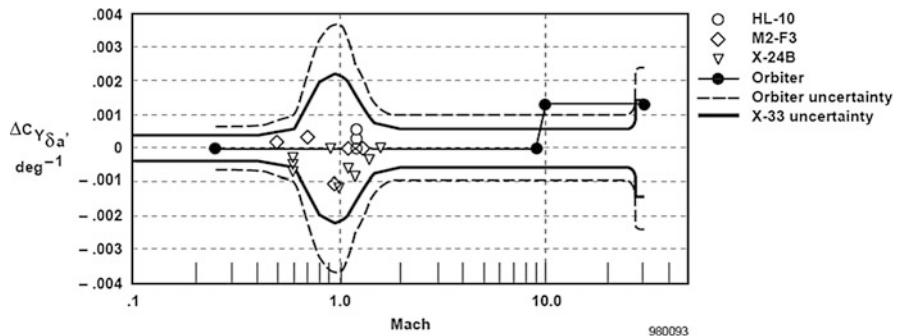


**Fig. 6.158** Side force due to aileron uncertainty for Orbiter and X-33 vehicles

Uncertainties, described in this section, represent deviations from those means and describe the scattering of observations about the mean. The tolerance, or lower uncertainty bounds, represents a measure of the experimental data scatter adjusted for flight conditions (essentially support-free and scale effect) about the mean values of the data sections.

Tolerances are intended for use in operational subsystem design and may be referred to as *design-to or operational* uncertainties. Variations, or upper uncertainty bounds, represent the uncertainties associated with wind-tunnel-derived experimental data and full-scale vehicle flight measurements and may be referred to as preorbital flight test uncertainties.

As said before, the development of an appropriate uncertainty model for the FTB-X aerodynamics began with a review of the historical flight test documentation of similar vehicle configurations. By comparing the flight test-measured aerodynamics to wind-tunnel measurements or engineering code estimates of other similar vehicles, a database of actual prediction errors was generated. This database was used as a guide in determining an appropriate uncertainty magnitude for each of the important aerodynamic parameters as a function of flight condition. Therefore, the US Orbiter was selected for its largely similar OML and mission profile and its excellent flight-to-preflight prediction documentation.

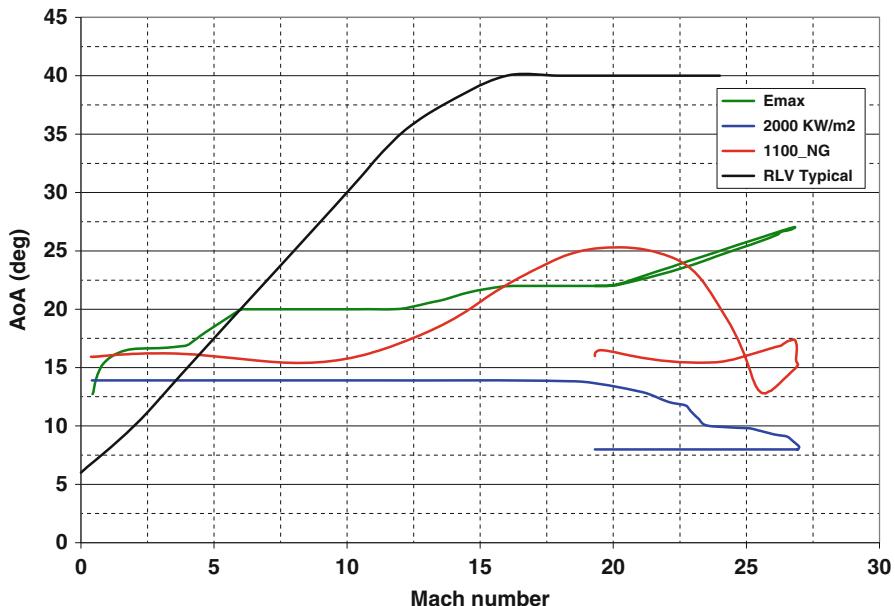
Note that FTB-X uses the mean aerodynamic chord as the reference length to normalize the pitching moment coefficient as the Orbiter aerodynamic model. Therefore, a correct comparison to the Orbiter pitching moment coefficients is ensured. The Orbiter uncertainties are documented as a function of Mach number. The Orbiter uncertainty database is valid to a maximum 10° AoA deviation from the nominal schedule.

Figure 6.159 shows a comparison between the Orbiter and some FTB-X nominal trajectories. As one can see, during the re-entry the FTB-X AoA is lower than the Orbiter one for a given Mach number. Assuming that the uncertainties generally increase with increasing AoA, using the re-entry schedule uncertainties during other phases of the flight should be a conservative approach.

The coefficient uncertainty data described in the previous sections were combined and plotted as functions of Mach number for each of the coefficients and derivatives. When plotted, a judgment on the maximum expected uncertainties in the predicted parameters was made. Where data were sparse, the Orbiter uncertainty was used to help in defining the shape of the FTB-X aerodynamic uncertainty. An explanation of the development of each coefficient uncertainty is given herein. The aerodynamic uncertainties generated in this work do not attempt to account for structural flexibility.

$$\text{(Method 1) uncertainty (percent)} = \frac{(\text{flight} - \text{prediction})}{\text{prediction}} \times 100$$

The percentage data format was used for the  $C_{l\delta a}$ ,  $C_{n\delta a}$ ,  $C_{m\delta bf}$ ,  $C_{m\delta e}$ , and  $C_{mq}$  derivatives. Parameters that had small magnitudes or changed signs somewhere in the flight envelope were not good candidates for presenting the uncertainties in a



**Fig. 6.159** Comparison of FTB-X (Emax, 2,000 kW/m<sup>2</sup>, 1100\_NG) and Space Shuttle Orbiter (RLV Typical) re-entry trajectories

percentage format. As a result, many of the aerodynamic parameters are presented as an increment from the prediction.

$$\text{(Method 2) uncertainty (increment)} = \text{flight} - \text{prediction}$$

This method was done for the  $C_L$ ,  $C_D$ ,  $C_m$ , and L/D coefficients and the  $C_{Y\beta}$ ,  $C_{l\beta}$ ,  $C_{n\beta}$ ,  $C_{Y\delta_a}$ ,  $C_{n\delta_a}$ ,  $C_{Y\delta_r}$ , and  $C_{l\delta_r}$  derivatives.

In general, the rotary derivatives had a larger amount of variation than the rest of the parameters, making it difficult to select a flight-estimated value that would summarize the data. The data points from each individual maneuver (rather than a fairing of the data) were compared to the preflight estimation. As a result, additional scatter in uncertainty data would be expected. Originally, the damping derivative uncertainty data were collected in incremental format as shown in Method 2.

Now that the aerodynamic uncertainty models have been generated, some method for applying the aerodynamic errors in a logical way must be developed. Several types of testing have to use the aerodynamic uncertainty models. These test methods include, for example, Monte Carlo simulations of the complete mission and linear analysis of the flight control laws from each of the flight phases of the vehicle under development. This type of testing ensures that adequate margins (control, thermal, structural, and so forth) exist throughout the envelope. In order to implement the aerodynamic uncertainty model into a Monte Carlo simulation,

the distribution of the uncertainties must be defined. For different flight programs, the aerodynamic uncertainties were assumed to be normally distributed with the uncertainty magnitudes defined in this paragraph equivalent to a 3- $\sigma$  value.

## References

1. The Atmospheric Reentry Demonstrator. ESA Bullettin. BR-138 October 1998
2. Tran P, Paulat JC, Boukhobza P. Re-entry flight experiments lessons learned – The Atmospheric Reentry Demonstrator ARD. RTO-EN-AVT-130
3. Schettino A, Votta R, Roncioni P, Di Clemente M, Gerritsma M, Chiarelli C, Ferrarella D. Aerodynamic and aerothermodynamic data base of expert capsule. In: Proceedings of the west-east high speed flow field conference; 19–22 November 2007, Moscow, Russia
4. Pezzella G, Marino G, Rufolo G (2014) Aerodynamic database development of the ESA intermediate experimental vehicle. *Acta Astronaut* 94(1):57–72. doi:[10.1016/j.actaastro.2013.07.019](https://doi.org/10.1016/j.actaastro.2013.07.019), ISSN (0094-5765)
5. Paris S, Charbonnier D, Tran D (2011) Experimental and numerical investigation of aerothermal characteristics of the IXV hypersonic vehicle. Paper presented at the 7th European symposium on aerothermodynamics for space vehicles. Brugge, 9–12 May 2011
6. Viviani A, Pezzella G (2012) Aerodynamic performance analysis of an unmanned re-entry vehicle from hypersonic down to subsonic regime. In: Proceedings of the 63rd international astronautical congress, Naples, Italy. IAC-12-D2.3.4. 2012
7. Viviani A, Pezzella G (2013) Aerodynamic performance analysis of three different vehicle concepts at hypersonic speed. In: Proceedings of the XXII conference of Italian Association of Aeronautics and Astronautics, 9–12 September 2013, Naples, Italy, Paper 74
8. “Aerodynamic Problems of Hypersonic Vehicles”, AGARD lecture series no. 42; AGARD-LS-42, vol.1
9. Schettino A, Pezzella G et al (2006) Mission trade-off analysis of the Italian USV Reentry Flying Test Bed. In: Proceedings of the 14th AIAA-AHI space planes and hypersonic systems and technologies conference, 6–9 November 2006, Canberra, Australia, paper AIAA-2006-8017
10. Schettino A, Pezzella G et al (2006) Aero-thermal trade-off analysis of the Italian USV Reentry Flying Test Bed. In: Proceedings of the 14th AIAA-AHI space planes and hypersonic systems and technologies conference; 6–9 November 2006, Canberra, Australia, paper AIAA-2006-8114
11. Pezzella G, Battista F, Schettino A et al (2007) Hypersonic aerothermal environment preliminary definition of the CIRA FTB-X reentry vehicle. In: Proceedings of the west-east high speed flow field conference, 19–22 November 2007, Moscow, Russia
12. Anderson JD (1989) Hypersonic and high temperature gas dynamics. McGraw-Hill Book Company, New York
13. Pezzella G, Marini M, Roncioni P, Kauffmann J, Tomatis C (2009) Preliminary design of vertical takeoff Hopper concept of future launchers preparatory program. *J Spacecr Rocket* 46(4):788–799. doi:[10.2514/1.39193](https://doi.org/10.2514/1.39193), ISSN 0022-4650
14. Bertin JJ (1994) Hypersonic aerothermodynamics, AIAA education series. American Institute of Aeronautics and Astronautics, Washington, DC
15. Prabhu DK (2004) System design constraints – trajectory aerothermal environments. In: RTO AVT/VKI lecture series in critical technologies for hypersonic vehicle development, 10–14 May 2004
16. Pezzella G, Gardi R, Guidotti G, Richiello C (2011) Aerodynamic and aerothermodynamic trade-off analysis of the Italian USV2 Flying Test Bed in the framework of an Hypersonic Flight Test. In: Proceeding of the 3rd international ARA days. 2–4 May 2011. Arcachon, France, AA-1-2011-54

17. Kinney DJ (2004) Aero-thermodynamics for conceptual design. In: Proceedings of the 42nd AIAA Aerospace sciences meeting and exhibit, Reno, NV, USA, 5–8 January 2004, AIAA-2004-31
18. Kinney DJ (2006) Aerodynamic shape optimization of hypersonic vehicles. In: Proceedings of the 44th AIAA Aerospace sciences meeting and exhibit, Reno, NV, USA, 9–12 January 2006, AIAA-2006-239
19. Bonner E, Clever W, Dunn K (1991) Aerodynamic preliminary analysis system II Part I- theory, NASA Contractor Report 182076. April 1991
20. Pezzella G (2011) Aerodynamic and aerothermodynamic trade-off analysis of a small hypersonic flying test bed. *Acta Astronaut* 69(3–4):209–222. doi:[10.1016/j.actaastro.2011.03.004](https://doi.org/10.1016/j.actaastro.2011.03.004), ISSN (0094-5765)
21. Pezzella G (2012) Aerodynamic and aerothermodynamic design of future launchers preparatory program concepts. *Aerospace Sci Technol* 23(1):233–249. <http://dx.doi.org/10.1016/j.ast.2011.07.011>
22. Pezzella G (2013) Hypersonic aerothermal environment assessment of the CIRA FTB-X reentry vehicle. *Aerospace Sci Technol* 25(1):190–202. <http://dx.doi.org/10.1016/j.ast.2012.01.007>
23. Moore FG, Hymer T, Wilcox F (1994) Base drag prediction on missile configurations. *J Spacecr Rocket* 31(5):759–765
24. Pezzella G (2011) Aerodynamic and aerothermodynamic trade-off analysis of a small hypersonic Flying Test Bed. *Acta Astronaut*. 69(3–4):209–222. doi:[10.1016/j.actaastro.2011.03.004](https://doi.org/10.1016/j.actaastro.2011.03.004), ISSN (0094-5765)
25. Park C (1993) Review of chemical kinetic problems of future NASA missions: earth entries. *J Thermophys Heat Transf* 7(3):385–398
26. Maughmer M, Ozoroski L, Straussfogel D, Long L (1993) Validation of engineering methods for predicting hypersonic vehicle control forces and moments. *AIAA J Guid Control Dyn* 160(4):762–769
27. Moore M, Williams J (1989) Aerodynamic prediction rationale for analyses of hypersonic configurations. In: Proceedings of the 27th Aerospace sciences meeting, Reno, NV, USA, 9–12 January 1989, AIAA-89-0525
28. Burns K et al (1995) “Viscous effects on complex configurations” software User’s Manual WL-TR-95-3060, McDonnell Douglas Aerospace, August 1995
29. Gomg L, Ko WL, Quinn RD (1984) Thermal response of space shuttle wing during re-entry heating, NASA TM 85907, June 1984
30. Battista F, Rufolo G, Di Clemente M (2007) Aerothermal environment definition for a reusable experimental re-Entry vehicle wing. In : AIAA-2007-4048, 39th AIAA Thermophysics Conference, Miami, FL, 25–28 June 2007
31. Di Clemente M et al. Numerical prediction of aerothermodynamic effects on a re-entry vehicle body flap configuration, paper IAC-06-D2.6.08
32. Zuppardi G, Costagliola F, Rega A, Schettino A, Votta R (2006) Evaluation of rarefaction effects on a winged, hypersonic re-entry vehicle. In: Proceedings of the 14th AIAA/AHI international space planes and hypersonic systems and technologies conference, Canberra, AU, AIAA-2006-8032, November 2006
33. Balnchard CR, Larman KT, Moats C (1994) Rarefied-flow shuttle aerodynamics flight model. *J Spacecr Rocket* 31(4):550–556
34. Schettino A, Votta R, Roncionni P, Di Clemente M, Gerritsma M, Chiarelli C, Ferrarella D (2007) Aerodynamic and aerothermodynamic data base of expert capsule. In: Proceedings of the west-east high speed flow field conference, 19–22 November 2007, Moscow, Russia
35. Pezzella G, Filippone E, Serpico M (2009) Re-entry aerodynamics and aerothermodynamics analyses of the Flying Test Bed USV-X in the framework of a High Lift Return. In: Proceeding of 16th AIAA/DLR/DGLR international space planes and hypersonic systems and technologies conference, AIAA 2009-7425
36. Prabhu DK (2004) System design constraints – Trajectory aerothermal environments. In: RTO AVT/VKI lecture series in critical technologies for hypersonic vehicle development, 10–14 May 2004

37. Viviani A, Pezzella G (2010) Computational flowfield analysis over a blunt-body reentry vehicle. *J Spacecr Rocket* 47(2):258–270. doi:[10.2514/1.40876](https://doi.org/10.2514/1.40876), ISSN 0022-4650
38. Vega User's Manual Iss. 3/Rev.0, Mar. 2006
39. Cobleigh BR (1998) Development of the X-33 aerodynamic uncertainty model. NASA/TP-1998-206549 April 1998. NASA

# Chapter 7

## Analysis of Sample Return Capsules

### 7.1 Introduction

Sample return mission aims for selecting, collecting, and, finally, returning extraterrestrial samples to Earth to perform their analysis.

The capability to send vehicles into space with the aim of collecting samples from planets (i.e., Mars) and other celestial bodies, for example, from comets, represents an important step toward space exploration activities and a more accurate knowledge of the Earth and universe [1, 2]. In this context, the design of a sample return vehicle (SRV) demands to solve strong technological design issues such as the good understanding of the loading environment encountered by the spacecraft during the Earth re-entry at super-orbital speed. In order to make affordable sample return missions in the coming decade, Europe has planned to design several high-speed re-entry missions, crucial for planetary exploration (see Fig. 7.1) [3].

In this framework, this chapter performs an overview on the design method approach which can be used to address the design of a generic sample return capsule (SRC). Generally speaking, the design process demands of satisfying some set of requirements, usually in some optimal manner. To attain this optimal solution, or at least to satisfy as many as possible the imposed requirements, usually requires trade-offs between individual elements or systems. To mediate these trade-offs requires an engineering familiarity and literacy, if not outright talent, with all of the systems and engineering disciplines involved. Spacecraft represents particularly broad challenges, in that a wide range of disciplines is involved – communications, power, thermal control, propulsion, and so on. Arguably, planetary probes are even broader, in that all the usual spacecraft disciplines are involved, plus several aspects related to delivery to and operation in planetary environments,

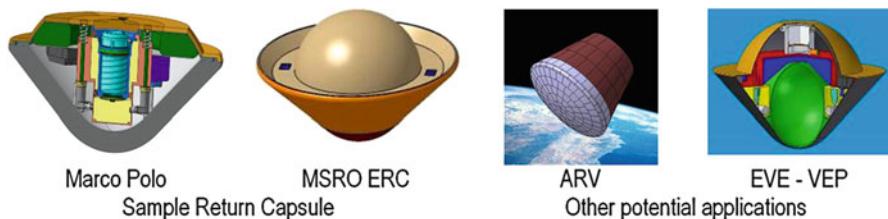


**Fig. 7.1** Future European atmospheric entry missions with high-speed entry

such as aerothermodynamics, soil mechanics, and so on. It is crucial that the requirements be articulated in a manner that adequately captures the intent of the “customer”.

Anyway, once mission requirements and constraints are established, the SRC design analysis starts taking into account for design results, available both from literature and previous missions, throughout similarity and scaling processes. A formidable example of a challenging design issue for SRV comes considering that, during the re-entry, when the capsule flies in the Earth’s atmosphere, a strong bow shock detaches ahead of the vehicle. It is subjected to a wide range of pressure, heat transfer, and shear stresses. Several features specific of hypersonic regime appear, such as thin shock layer, entropy layer, viscous interaction, etc. [4–7]. Among those phenomena, one could remark the high-temperature effects, also known as real gas effects, since they appear as one of the critical points in the design phase of the vehicle mission [6, 7]. Indeed, across the shock, a large amount of kinetic energy is converted into thermal energy. This energy leads to high temperature of the gas mixture in the shock layer where dissociation and ionization take place. It results into a plasma flow which impinges on the vehicle wall. To sustain this important heat transfer, the spacecraft must be equipped with suitable thermal protection system (TPS), as those made of ablative material needed to accommodate very high-energy re-entry. Ablative heat shield is essential for the success of the re-entry maneuver, but their design is complex due to the nature of the heat transfer involving aerothermodynamic phenomena such as mass blowing of the heat shield species into the boundary layer and their interaction with dissociated air [8–10]. In this framework, the capability to address computational flowfield analysis past a capsule returning at super-orbital speed is fundamental [11, 12]. In fact, these extraterrestrial samples have to be returned to Earth, and very high-speed re-entry trajectories must be performed by the space vehicles, according to Celestial Mechanics laws. Therefore, the design of an Earth entry SRV requires strong technological bases and has to rely on a good understanding of the loading environment encountered during the super-orbital Earth re-entry. A high-speed Earth entry vehicle has the following characteristics: entry velocity higher or equal to 11.7 km/s (compared to 7.5 km/s for the US Space Shuttle), very high heat fluxes (more than  $10 \text{ MW/m}^2$ ), and heat loads (in the range of  $200 \text{ MJ/m}^2$ ), where the radiative part is rather important. Indeed, the extreme environment in which the SRV must fly is recognized in Fig. 7.2, where the

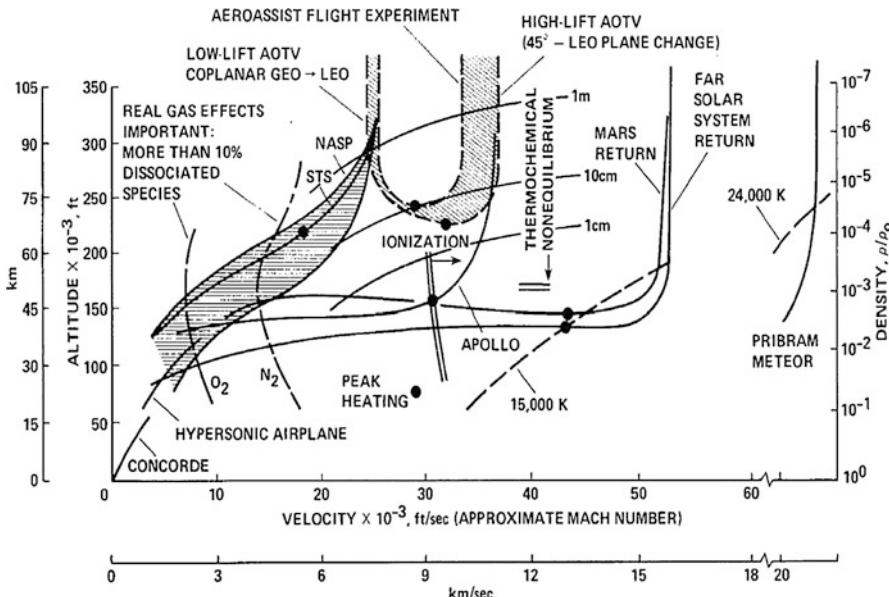


**Fig. 7.2** Comparison of thermochemical nonequilibrium flight regimes in the Earth's atmosphere

range of velocities of interest together with thermochemical nonequilibrium flight regimes in Earth's atmosphere are also indicated [4].

In this framework, the chapter provides an overview of the research activities carried out with the aim to assess the effects of aeroshape modification, flowfield radiation, and surface mass blowing on the SRV aerodynamics and aerothermodynamics. To this end, an SRV capsule configuration has been selected, and a re-entry trajectory has been computed to address research analysis. In the first design task, namely, assessment of aeroshape modification, twelve CFD simulations are performed. They refer to two-dimensional (2-D) Navier–Stokes (NS) computations in thermochemical nonequilibrium at given points along the re-entry trajectory, namely, point M. This task foresees six simulations on non-ablated aeroshape and six on ablated aeroshape, thus assessing the effect of aeroshape modification due to the heat shield ablation.

In the second design task, named assessment of flowfield radiation, twelve 2-D Navier–Stokes computations in thermochemical nonequilibrium at given points along the re-entry trajectory, namely, point R, are performed to evaluate plasma radiation effect through the European Space Agency (ESA) code PARADE.

Finally, in the last design task, namely, assessment of mass blowing, eight CFD simulations are planned. They refer to 2-D Navier–Stokes computations in thermochemical nonequilibrium performed on non-ablated shape considering blowing species due to heat shield ablation. So the objective of this task is to assess the effect of blowing species on the flowfield past the re-entry vehicle.

## 7.2 Design Process for Sample Return Spacecrafts

The analytical, computational, and experimental methods described in this chapter can be used to address the design of a generic sample return vehicle (SRV).

Usually, the design process demands different stages which may require several iterations to obtain an optimization of the SRV design. For instance, a typical scheme that synthesizes the design process of an SRV is shown in Fig. 7.3.

Once mission requirements and constraints are established, the SRV design analysis starts taking into account for design results available both from the literature and previous missions, throughout similarity and scaling processes. This phase is most important considering that it represents the initial condition from which the SRV design evolves and matures. For example, the design starts basing on initial assumptions as SRV configuration, mass, stability considerations during entry, descent, and loading environment. Hence, the ballistic parameter is estimated from size, weight, and drag coefficient early evaluated. This value of ballistic coefficient is used to calculate atmospheric trajectories and perform parametric analysis of SRV re-entry flight and so on.

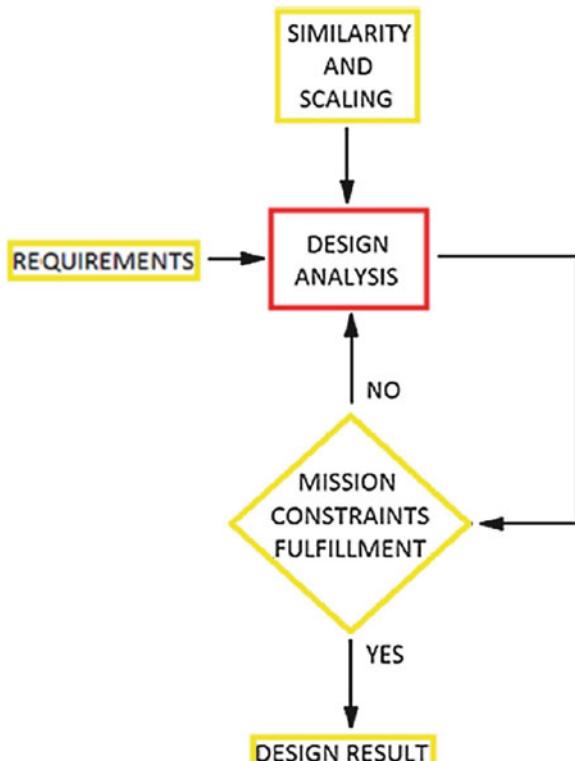


**Fig. 7.3** Typical design process scheme

### 7.2.1 Requirements and Constraints

In the framework of the design of any space mission, both requirements and constraints must be considered. Example of constraints for SRV are the curve limits of the re-entry corridor such as re-entry velocity fixed to about 12 km/s for an altitude of 200 Km, maximal deceleration below 100 g, maximum heat flux below 15 MW/m<sup>2</sup>, and total heat load below 300–350 MJ/m<sup>2</sup>.

Hence, once the heat flux has been estimated, one can calculate the stagnation pressure, thus evaluating approximate TPS layout and thickness. Typical requirement limits are landing, maximal carrying capacity with minimal total volume, stability during entry, descent and landing, maximal heat flux, maximum heat load, maximum g-load, impact velocity, and maximum TPS ratio.

On the other hand, typical constraints are initial entry velocity into the Earth is (given by a mission analysis and it is equal to) 12.3 km/s for an altitude of 120 km; the landing on Earth shall be performed with a fully passive entry (i.e., no parachute) for the SRV. The latter constraint represents one of the main considerations in entry vehicle design: i.e., if a parachute system should be included. The advantages of parachute recovery are: entry vehicle tracking at high altitude is easier; the probe or canister has a lower ground impact velocity; and recovery operations are easier (the probe is easier to find). Disadvantages may include slight increase in mass, increased mechanical complexity with the separation of the probe from the aft-cover and parachute, and slight decrease in static stability margin. A small parachute may be able to decelerate the entry vehicle adequately. Even though impact-area drift may increase significantly, ground radar should be able to track the probe and parachute to ensure efficient recovery operations.

### 7.2.2 Similarity and Scaling

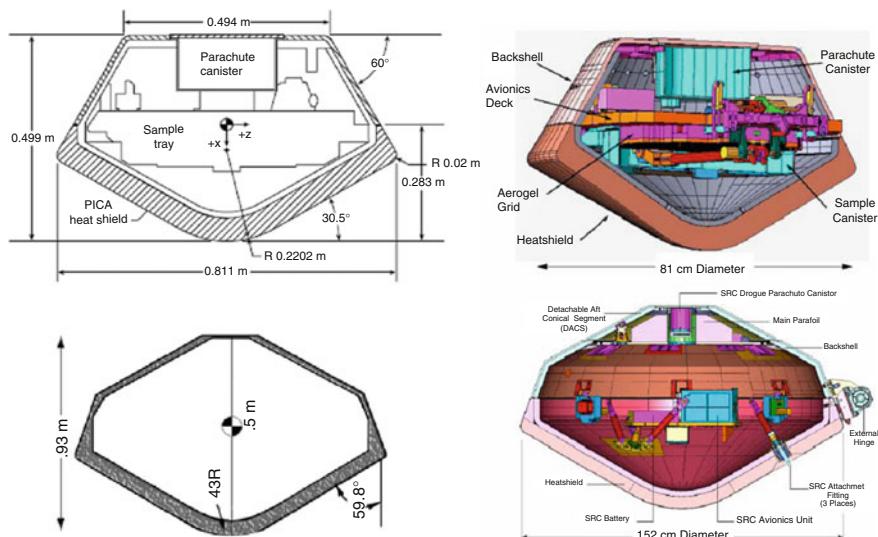
Generally speaking, a preliminary design of any space mission is obtained comparing the requirements of this mission with the requirements of previous ones. Therefore, it is useful to individuate missions which have similar characteristics to our and use them to obtain a work line (e.g., similarity). Obviously, some data (capsule size, re-entry velocity, etc.) will be different to ours, so we can adapt these to our mission through a scaling process. In Table 7.1, some examples of the entry capsules which can be taken as a guideline are summarized.

Examples of SRC configurations are summarized in Figs. 7.4, 7.5, and 7.6.

Figure 7.4 shows an overview of both the internal and external layout of Stardust and Genesis sample return capsules. An overview of the main mission parameters such as trajectory, vehicle geometry, aerothermal environment, and TPS for both Stardust and Genesis SRV can be recognized in Tables 7.2 and 7.3, respectively. It is worth to note that the SRV layout is an extremely important design issue. For instance, it determines the position of the vehicle center of gravity (CoG). In

**Table 7.1** Overview of some fundamental SRV parameters

	Stardust	Genesis	Hayabusa	Marco Polo
$R_{\text{nose}} \text{ m/cone angle}^{\circ}$	0.23/60	0.43/60	0.202/45	0.41/45
$V_{\text{entry}} \text{ km/s}$	12.6	11	11.3	11.8
$\gamma_{\text{entry}}^{\circ}$	-8.2	-8	-13.8	-12
M kg	45.8	210	16.3	76
Ballistic coeff. kg/m <sup>2</sup>	60	80	113.5	70
Area m <sup>2</sup>	0.56	1.78	0.128	0.95
$\dot{Q}_{\text{max}} \text{ MW/m}^2$	13	7	15	11
$\int_0^{(\text{end})} \dot{Q} dt \text{ MJ/m}^2$	360	166	320	210
TPS material/mass frac.	PICA-15/22 %	C-C/18 %	C phenol/43 %	PICA?/38 %

**Fig. 7.4** Stardust (up) and Genesis (down) sample return capsules

fact, if a non-spherical entry shell is used, the CoG of the configuration must lie adequately below the aeroshell's center of pressure (CoP), which in turn moves the spacecraft and its dense components (batteries, mechanisms, sensors and cables etc.) closer to the leading face of the entry shell.

If the offset between the CoG and CoP (i.e., spacecraft static margin) is made too small, then the spacecraft may be unstable to disturbances and make large pitching movements, exposing non-shielded parts to the energetic airflow. As an example, a spacecraft's transition from supersonic to subsonic speed causes changes in the wake flow which in turn can be coupled to the craft, destabilizing it. Some entry spacecraft, such as that of the Genesis sample return mission, are designed to deploy small drogue parachutes at supersonic speeds to provide extra stability through the transonic region.

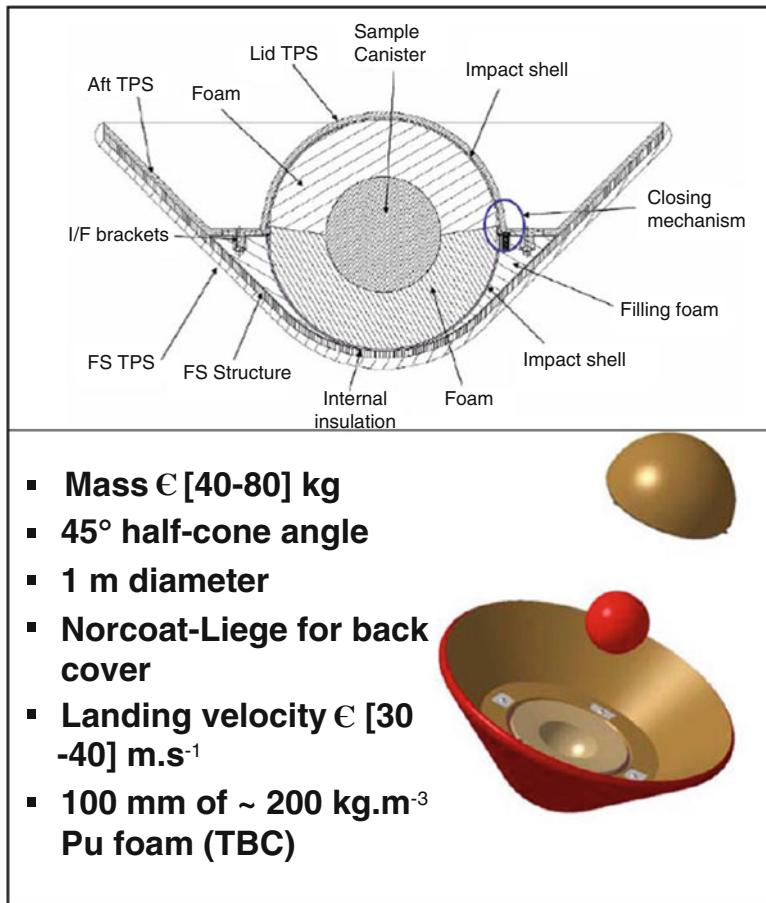


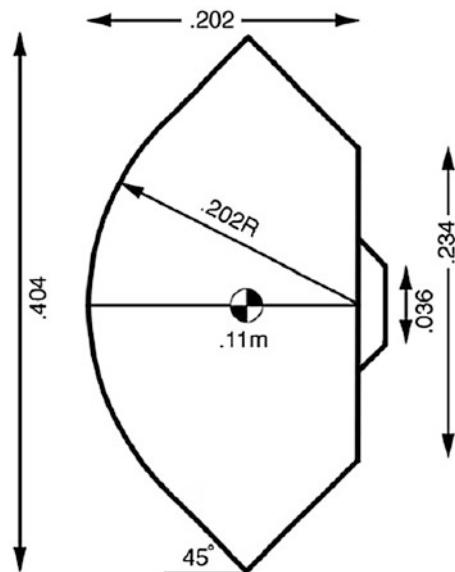
**Fig. 7.5** Example of SRV study results

Figures 7.5, 7.6, and 7.7 highlight examples of SRV design study results. Figure 7.5 shows a typical SRV configuration under investigation in Europe so far. Such a configuration relies on a spherocone aeroshell with a 45° half cone angle, a 1.1-m-diameter front shield, and a smaller back cover.

Figure 7.6 showed the configuration of the Hayabusa SRC, whose main mission parameters are summarized in Table 7.4.

As far as Flight Mechanics is concerned, Fig. 7.7 shows a typical re-entry corridor of an SRV reported in the flight path angle (FPA) ballistic coefficient map. Of course, the green surface represents the flyable conditions during descent. This re-entry envelope refers to an atmospheric velocity of 11.8 km/s, at  $-12^\circ$  FPA, landing load on the sample of 80 g, peak heat flux of  $15 \text{ MW/m}^2$ , heat load of  $220 \text{ MJ/m}^2$ , and entry duration of 484 s.

**Fig. 7.6** Hayabusa sample return capsule



The lower boundary of the re-entry corridor in the hypersonic phase of descent is the heat flux limit (both convective and radiative). Indeed, at high entry speeds, the temperature increase in the shock wave around the capsule may be sufficiently intense for radiative heating from the hot plasma flow to be equivalent to the convective heating rate. For Earth entry, this occurs at speeds above 10 km/s for bluff bodies, as shown in Fig. 7.8.

In particular, Fig. 7.8 shows radiative and convective heating rates compared for two spheres of different radii entering the Earth's atmosphere. Note that the same equivalence in the heating processes occurs at higher speeds for objects with smaller radii, but for such spacecraft, the temperatures in the shock would be far higher, potentially compromising the temperature limits of the TPS.

A possible internal and external TPS layout is shown in Fig. 7.9.

In this example, the TPS layout refers to PICA-like ( $260 \text{ kg/m}^3$ ) front heat shield, Norcoat-Liege rear TPS, 45° half cone angle, 1.1 m base diameter, 200 mm reticulated vitreous carbon (RVC) foam, and 76 kg capsule.

Figure 7.10 together with Fig. 7.11 summarized the thermal protection systems for several space missions. As we can see, there are two regression curves that can be used for the TPS preliminary design.

In fact, once stagnation pressure and peak heat flux are known, Fig. 7.10 suggests what kind of TPS must be used, while Fig. 7.11 gives an idea of TPS mass fraction once the total heat load is known. Examples of SRV thermal design adopted for the Marco Polo mission is reported in Fig. 7.12 [3]. As shown, the TPS layout of the Marco Polo SRV is made of Saffil, RVC, and CFRP (carbon-fiber-reinforced polymer).

Some TPS materials and related properties are summarized in Table 7.5.

**Table 7.2** Overview of the Stardust main parameters

Trajectory	Geometry	Aero/thermal	TPS
Entry angle	Shape	Trim LD (specify trim $\alpha$ )	Material designation
Inertial entry velocity	Nose radius	Blunt-nosed 60° half cone angle 0.23 m initial	PICA-15
Relative entry velocity	Base area (ablated)	Ballistic coeff. (ablated) 0.52 m <sup>2</sup> , 0.50 m <sup>2</sup>	Thickness 60.0 kg/m <sup>2</sup> 60.4 kg/m <sup>2</sup>
Velocity at peak heating	Vehicle mass	Stagnation heating rate Integrated heat load 45.8 kg	5.82 cm Ablating? 1,200 W/cm <sup>2</sup> 36,000 J/cm <sup>2</sup>
Control method	TPS mass fraction, inc. insul.	Radiative heat flux	Ejected? Resin mat., matrix mat.
Center of gravity, $X_{CG/D}$	Payload mass	PH stag. pressure	Resin dens., matrix density 109 kg/m <sup>3</sup> 160 kg/m <sup>3</sup> Total material density 250 kg/m <sup>3</sup> approx.

**Table 7.3** Overview of the Genesis main parameters

Trajectory	Geometry			Aero/thermal		TPS
<i>Entry angle</i>	$-8^\circ$	<i>Shape</i>	59.81° blunt cone	<i>Trim L/D (specify trim <math>\alpha</math>)</i>	0	<i>Material designation</i>
<i>Inertial entry velocity</i>	11.0 km/s	<i>Nose radius</i>	.43 m	<i>Ballistic coeff.</i>	80 kg/m <sup>2</sup>	<i>Thickness</i>
<i>Relative entry velocity</i>	10.8 km/s	<i>Base area</i>	1.78 m <sup>2</sup>	<i>Stagnation heating rate</i>	700 W/cm <sup>2</sup>	<i>Ablating?</i> <i>Ejected?</i>
<i>Velocity at peak heating</i>	9.2 km/s	<i>Vehicle mass</i>	210 kg	<i>Integrated heat load</i>	16,600 J/cm <sup>2</sup>	<i>Resin mat.</i> <i>Matrix mat.</i>
<i>Control method</i>	Spin-stabilized aero-ballistic	<i>TPS mass fraction, inc. insul.</i>	18 %	<i>Radiative heat flux</i>	30 W/cm <sup>2</sup>	<i>Resin dens., matrix density</i>
<i>Center of gravity, <math>X_{CG/D}</math></i>	.33	<i>Payload mass</i>		<i>PH stag. pressure</i>		<i>Total material density</i>

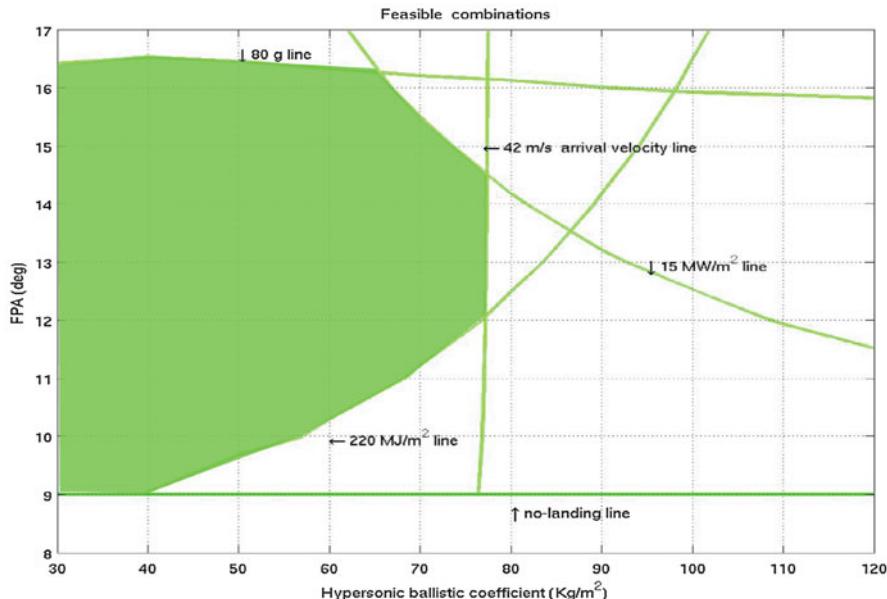


**Fig. 7.7** Example of SRV study results: re-entry corridor

As far as capsule mass budget is concerned, Tables 7.6 and 7.7 summarized the examples of the impact of each capsule subsystem on the overall vehicle mass. In particular, Table 7.6 refers to Mars Sample Return Study while Table 7.7 to the Mercury Sample Return Mission Study.

### 7.2.3 Overview of SRV Design Analysis

Within each design loop of Fig. 7.3, several sciences are involved, from structural mechanism to electronics to Fluid Dynamics, etc. As a consequence, the SRV is a result of a multidisciplinary design optimization (MDO) [5, 10, 11].

The design process evolves through “trade-off” analysis. For example, requirements and constraints have impact on the design in terms of trade-off analysis that accounts for:

- Heat flux
- Heat input (Integrated heat load)
- Drag
- Stability
- Landing accuracy
- Landing conditions
- Accommodation into launcher fairing

- Vehicle mass
- Entry angle
- Entry velocity, etc.

But what we have to underline here is that to return Mars samples to Earth, very high-speed re-entry trajectories must be performed by the space vehicles. As a consequence, the aerodynamic and aerothermodynamic design of an Earth entry sample return vehicle requires strong technological bases and has to rely on a good understanding of the loading environment encountered during the superorbital Earth re-entry. Therefore, a detailed description of the flowfield past the re-entry vehicle is mandatory to address the impact of several design issues [8, 9]. For instance, CFD analysis is necessary for the determination of convective and radiative heat fluxes, and these fluxes have a direct impact on the selection of the material for the TPS [11]. For instance, thermal radiation is generated by emissions from each of the excited species in the shock layer. Thus, at the body surface, heat flux is calculated by summing all the emission and absorption activity from the shock layer gases in view, and this may include absorption and reemission activity in any ablation products and indeed from the wall itself.

This will allow also a more accurate determination of the TPS thickness distribution. Then, detailed knowledge of the flowfield past the re-entering vehicle allows the designer to evaluate SRV aerodynamic performances as well as static and dynamic stability to improve Flight Mechanics analysis and so on.

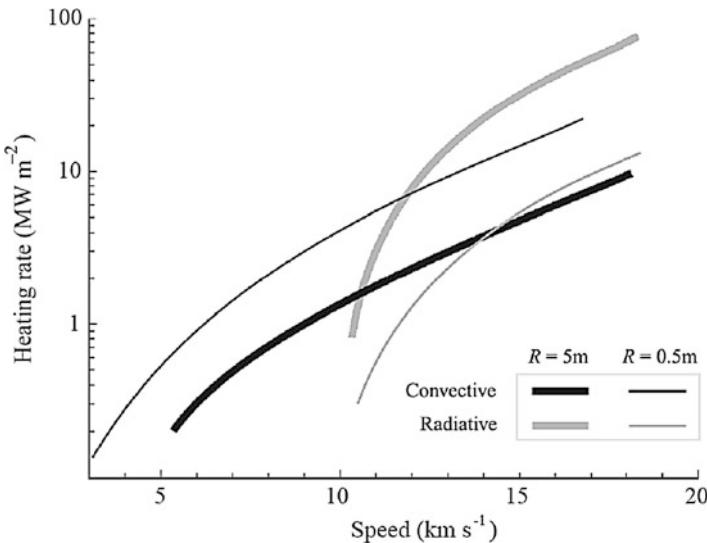
Example of a design analysis can be found in Fig. 7.13 where it shows the contour field of CO species, blowing from the heat shield made of carbon phenolic material, past a sphere-cone aeroshell (close to that shown in Fig. 7.5) flying at 55.11 km altitude and  $M_\infty = 31.87$ . Note that CO is one of the main ablation products (for carbon-based materials), and it lowers significantly the SRV wall enthalpy [11–13].

Figure 7.13 also highlights that TPS ablation demands particular care within flowfield CFD analysis because it may influence SRV aerothermal performance considering that heat shield roughness promotes turbulence transition; TPS ablation determines convective and radiative aeroheating blockage because ablation reduces the surface gradients of temperature and that of various species' mass fractions, causing a decrease of convective and diffusive heat fluxes; heat shield ablation influences the flowfield past the SRV by means of introduction of new species in the boundary layer, which in turn may increase flowfield ionization [14, 17].

Further example of design analysis is shown in Fig. 7.14 where the influence of ablation on flowfield and shock standoff distance for a high-speed Earth entry is recognized. In particular, the top figure represents nonequilibrium predictions with ablation. The bottom figure shows nonequilibrium without ablation. This comparison puts in evidence the influence of ablation on the results of nonequilibrium simulations since the temperature predicted in the ablative case is lower than in the non-ablative one. Moreover, the shock wave is closer to the capsule in the ablative simulation. Therefore, ablation has a large influence on the nonequilibrium results. As a consequence, this process has to be carefully studied when designing the SRV thermal protection shield.

**Table 7.4** Overview of the Hayabusa main parameters

Trajectory	Geometry			Aero/thermal	TPS
<i>Entry angle</i>	$-13.8^\circ$	<i>Shape</i>	$45^\circ$ sphere-cone	<i>Trim L/D (specify trim a)</i>	0
<i>Inertial entry velocity</i>	11.7 km/s	<i>Nose radius</i>	.202 m	<i>Ballistic coeff.</i>	113.5 kg/m <sup>2</sup>
<i>Relative entry velocity</i>	11.3 km/s	<i>Base area</i>	.128 m <sup>2</sup>	<i>Stagnation heating rate</i>	1,500 W/cm <sup>2</sup>
<i>Velocity at peak heating</i>	10.2 km/s	<i>Vehicle mass</i>	16.27 kg	<i>Integrated heat load</i>	32,000 J/cm <sup>2</sup>
<i>Control method</i>	None	<i>TPS mass fraction, inc. insul.</i>	43 %	<i>Radiative heat flux</i>	300 W/cm <sup>2</sup>
<i>Center of gravity XCG/D</i>	0.28	<i>Payload mass</i>	1.04 kg	<i>PH stag. pressure</i>	0.61 atm
				<i>Total material density</i>	1,400 kg/m <sup>3</sup>



**Fig. 7.8** Radiative and convective heating rate limits for Earth entry

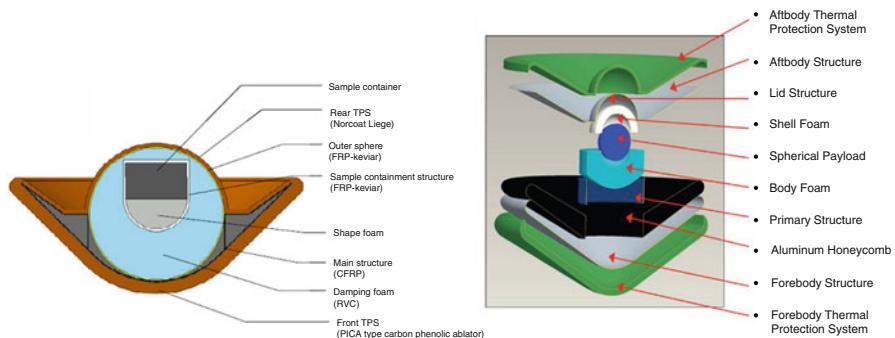


**Fig. 7.9** Example of SRV study results: TPS layout

Generally speaking, the ablation products in the boundary layer mainly consist of  $H_2$ ,  $C_2H$ ,  $C_2H_2$ ,  $CO$ ,  $C$ , and  $H$ . For example, the mass fraction fields of  $H_2$ ,  $H$ ,  $CO$ , and  $C$  that take place in the shock layer in front of a 1.1-m-diameter spherically blunted  $45^\circ$  half-angle forebody (i.e., close to that shown in Fig. 7.9) flying at at 71.86 km altitude and  $M_\infty = 41.54$  are reported in Figs. 7.15 and 7.16, respectively.

Finally, it is worth noting that the determination of the ablation products distribution within the shock layer is extremely important since species such as  $C_2$ ,  $C_3$ , and also  $CO$  have strong radiative properties. In particular,  $C_2$  and  $C_3$  possess absorption properties while  $CO$  is a strong radiator [13–16].

Further, the formation of small amounts of  $CN$  induces a more severe heat flux distribution because of a major nonequilibrium radiation contribution (i.e.,

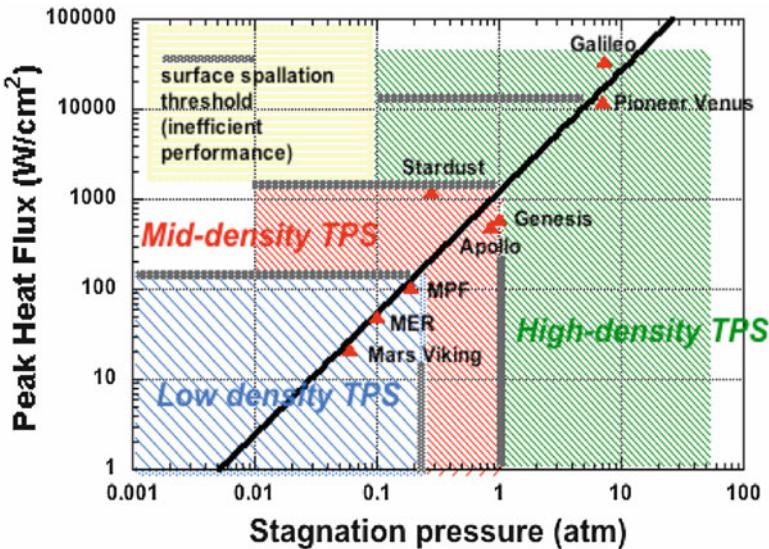


Fig. 7.10 Mission environments for ablative TPS applications

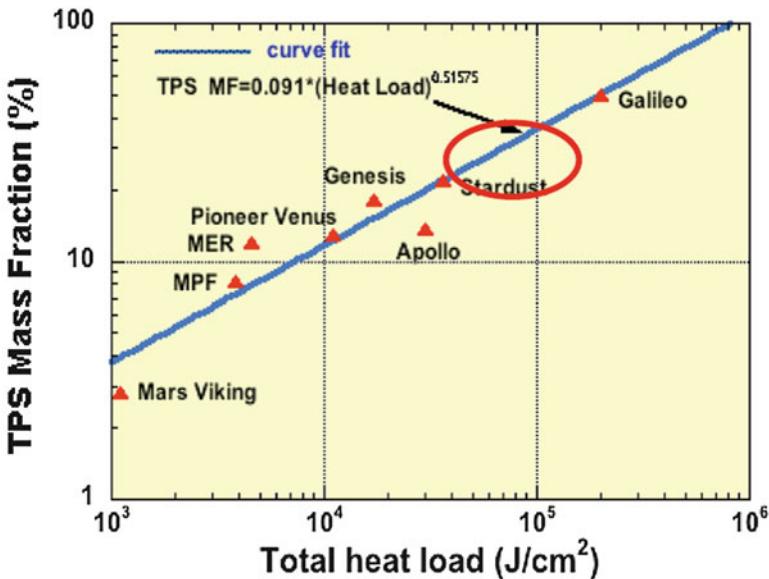
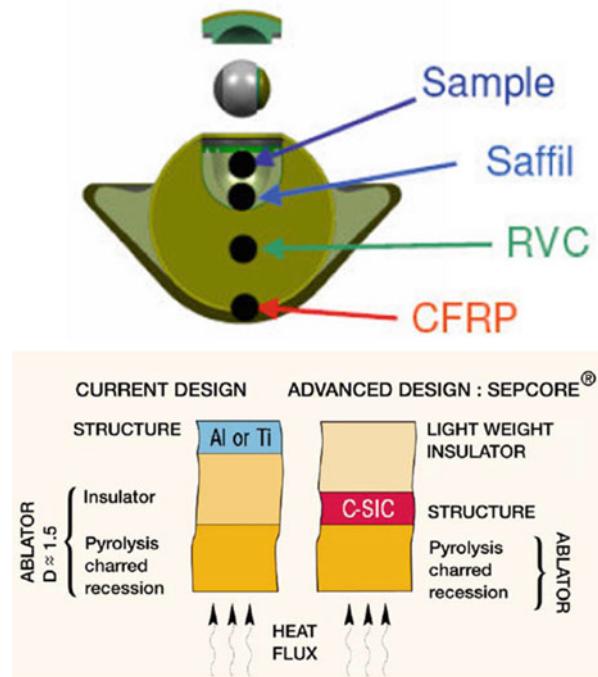


Fig. 7.11 TPS mass fraction for ablative heat shield missions

CN molecule is a highly emissive product). This radiation is highly dependent on the CN electronic temperature and on the degree of ionization of the flow. Indeed, another important issue in designing SRV capsule is the coupling of plasma radiative effects and the CFD computation. For example, Fig. 7.17 presents, on the left, the

**Fig. 7.12** Internal and external (*lower side*) layout of Marco Polo TPS



**Table 7.5** Properties of some TPS materials

Material	Density, kg/m <sup>3</sup>	Thermal conductivity <sup>a</sup> , W/m-K	Emissivity <sup>a</sup>	Melt temp., K
AVCOAT 5026 (virgin)	529	0.242	0.67	1,920
AVCOAT 5026 (char)	264	—	0.49	—
Carbon phenolic (Acusil I)	480	0.112	0.95	2,000
Reinforced carbon–carbon (RCC)	1,580	5.05 (normal), 7.88 (parallel)	0.54 to 0.9	2,030 <sup>b</sup>
Teflon	2,190	0.251	—	—
Shuttle tile (LI-900)	144	0.047	0.88	1,755 <sup>b</sup>
Beryllium	1,840	170	—	810 <sup>b</sup>
Oak	610	0.146	—	—

<sup>a</sup>Thermal conductivity and emissivity are functions of temperature

<sup>b</sup>Single-use temperature limit

front shield shock layer temperature field and, on the right, temperature profiles along with the stagnation line of the Huygens probe with and without radiation coupling effects. As shown, a reduction of the standoff distance can be observed as well as a faster decrease of the temperature for the coupled computations due to the energy removal from the flowfield by radiation phenomenon [17, 18].

**Table 7.6** Examples of mass budget for SRV

Element	Mass (Kg)
Heat shield	11.19
Afterbody TPS	1.96
Primary structure	4.71
Secondary structures	2.96
Canisters (2)	7.20
Receptacles	1.36
Energy absorbing mat.	2.52
Beacons (2)	0.60
Mechanisms	1.90
Sensors and cables	0.20
Miscellaneous	1.14
<b>Launch total</b>	<b>28.53</b>
<b>Entry total</b>	<b>35.73</b>
<b>Launch total (+25 %)</b>	<b>35.66</b>
<b>Entry total (+25 %)</b>	<b>42.86</b>

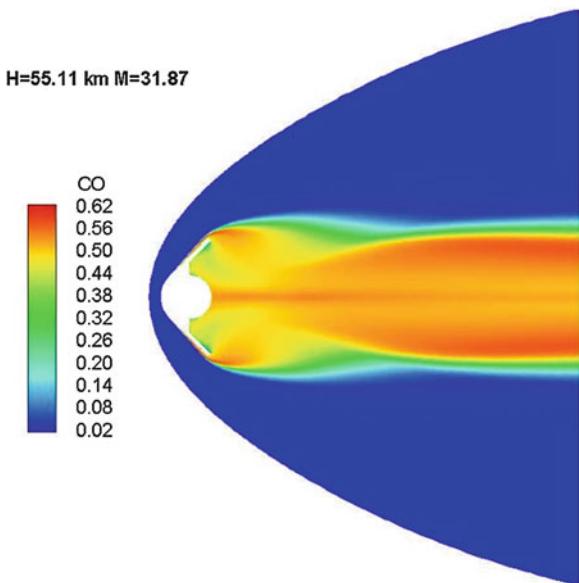
**Table 7.7** Examples of mass budget for SRV

Subsystem	Basic, kg	Equipment margin		Nominal, kg	System margin		Total, kg
		%	kg		%	kg	
Thermal protection	2.1	20.0	0.4	2.5			
Stabilizer	1.2	20.0	0.2	1.4			
Parachute system	2.6	20.0	0.5	3.1			
Shock absorber	0.4	20.0	0.1	0.5			
Control unit	1.7	20.0	0.3	2.0			
Recovery equipment	1.1	20.0	0.2	1.3			
Power supply system	0.5	20.0	0.1	0.6			
Samples container	2.5	20.0	0.5	3.0			
Cabling	0.5	20.0	0.1	0.6			
Structure	1.3	20.0	0.3	1.6			
<b>Total mass</b>	<b>13.9</b>		<b>2.8</b>	<b>16.7</b>		<b>20.0</b>	<b>20.0</b>

Some relevant mission examples are given below.

- *High-speed Earth return representative of a Mars, lunar, or cometary mission at 13–16 km/s with a mix of equilibrium and nonequilibrium chemistry with carbon surface ablation and phenolic resin pyrolysis gas products injection into the boundary layer.* Radiation is significant for these entries and can be equal to the convective flux. Data are available from Apollo 4 and Fire 1 and 2 missions at 11 km/s. Apollo had an ablative TPS with special provision for radiometry and calorimetry with radiative fluxes about 30 % of the total. PAET and the recent UV precursor flights at between 3 and 5 km/s provide detailed radiometry for code phenomenology validation, for selected Earth atmosphere shock layer species.

**Fig. 7.13** CO mass fraction distribution at 55.11 km altitude and  $M_{\infty} = 31.87$



- *Venus entry.* The atmosphere of Venus is very similar in composition to Mars with a high proportion of carbon dioxide, but entry speeds are much higher at 11–12 km/s and the atmosphere is very dense. At this speed, there is a considerable radiation from the shock layer and an ablative heat shield is necessary. Carbon phenolic TPS has been used on Pioneer, but an alternative such as silica phenolic is attractive especially if its reflectivity is taken into account. Many Venera crafts have successfully entered the Venus atmosphere.
- *Jupiter entry at over 40 km/s or Saturn/Uranus entry at 25–30 km/s.* Much analysis has been carried out for the Jupiter Galileo mission with its carbon phenolic TPS, and if data is available after the entry, some post test analysis will undoubtedly be undertaken. The hydrogen/helium atmosphere and high ablation rates (30–50 % of vehicle mass is TPS) provide challenging radiation-dominated cases, of which only a Jupiter mission is underway at present.
- *Titan entry.* At modest entry velocity of 6 km/s, the Huygens probe will encounter a high radiative heat flux due to the unique atmosphere of Titan. The low proportion of methane in a thin nitrogen atmosphere produces a nonequilibrium radiation environment where radiative and convective fluxes are approximately equal. Current efforts of the project team to estimate this environment are of interest. The ablative TPS is low-density quartz phenolic.
- *Mars entry.* Currently, radiative fluxes are considered negligible for direct Mars entry at about 6 km/s. At higher entry velocities, i.e., should higher-energy trajectories be used, radiation may become important. Nevertheless, any Mars entry mission will need to confirm that the radiative environment is low,

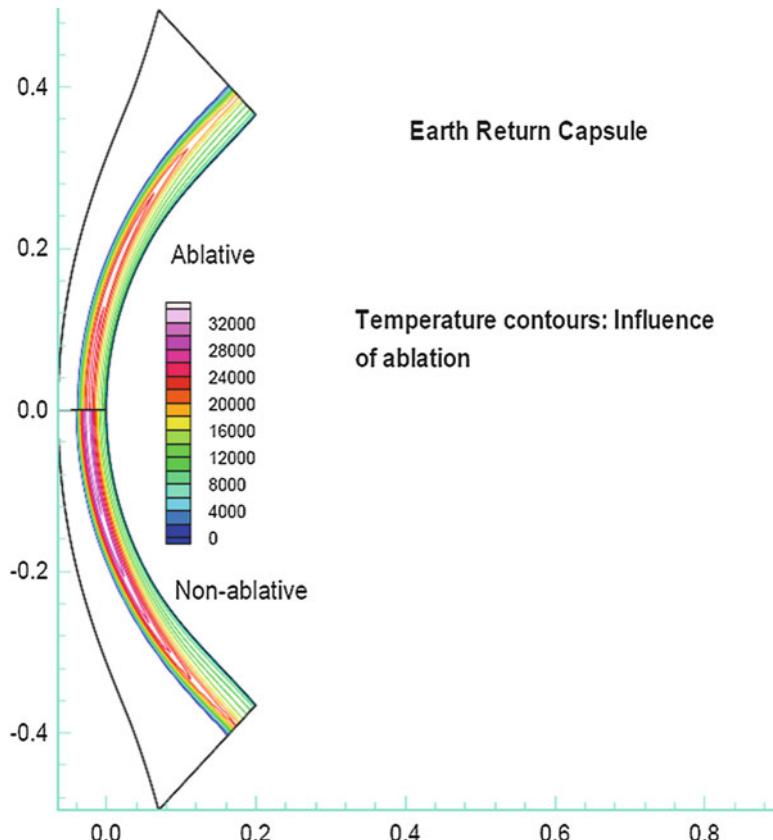


**Fig. 7.14** Static temperature contours (K). Influence of ablation

in particular with ablation products from low-density ablators reacting with the atmosphere to enhance the number density of radiating species or the effect of catalytic surfaces.

The importance of radiation has been illustrated above, but where does it come from? Some of the basic phenomena are summarized below.

#### 7.2.4 Shock Layer Condition

At high entry velocities, the temperatures behind the bow shock wave may reach very high values with the free-stream chemical species becoming dissociated and in some cases highly ionized. The high shock layer temperatures lead to significant radiation from the hot shock layer gases. For the flowfields considered in entry problems, the radiation is mainly due to electronic transitions and is thus visible or UV.

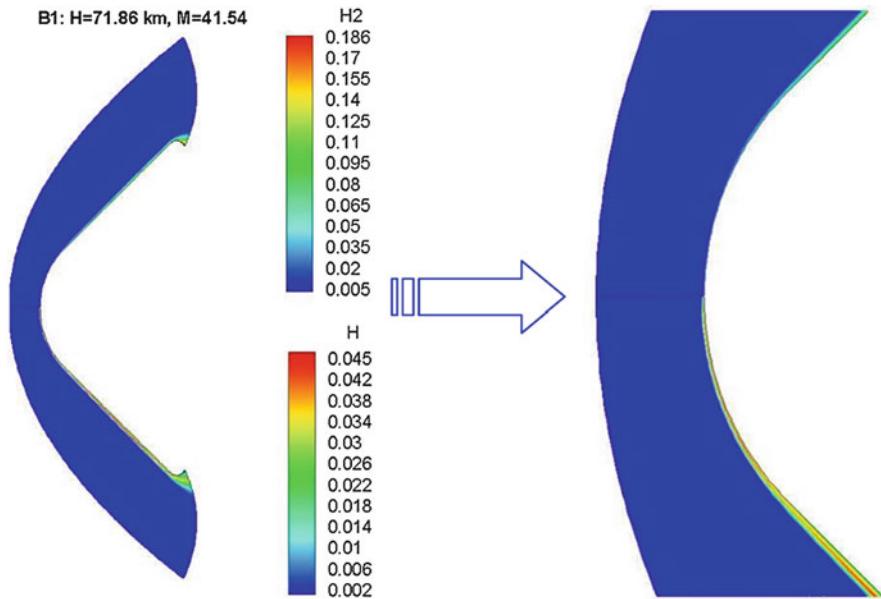


Fig. 7.15 H<sub>2</sub> and H mass fractions at  $H_{\infty} = 71.86$  km and  $M_{\infty} = 41.54$

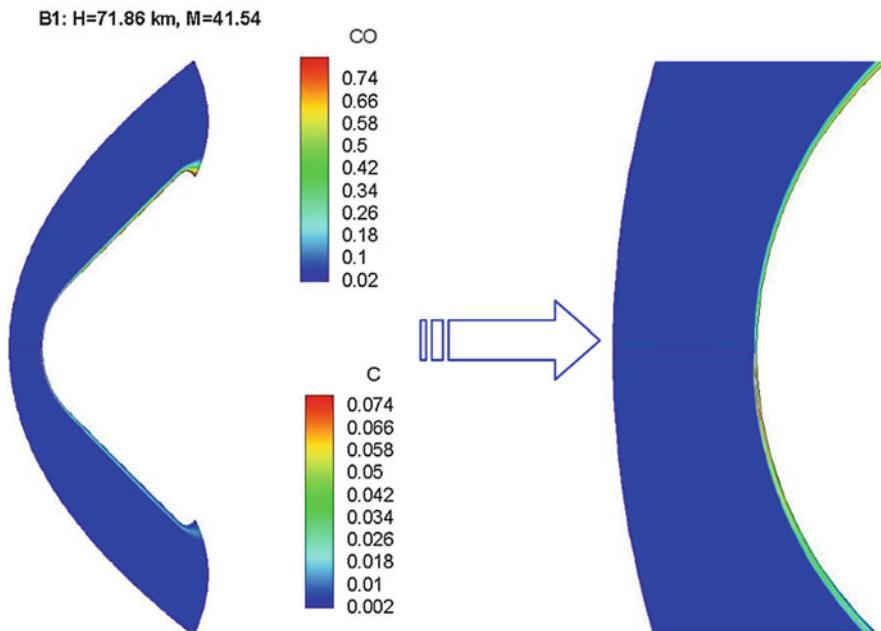
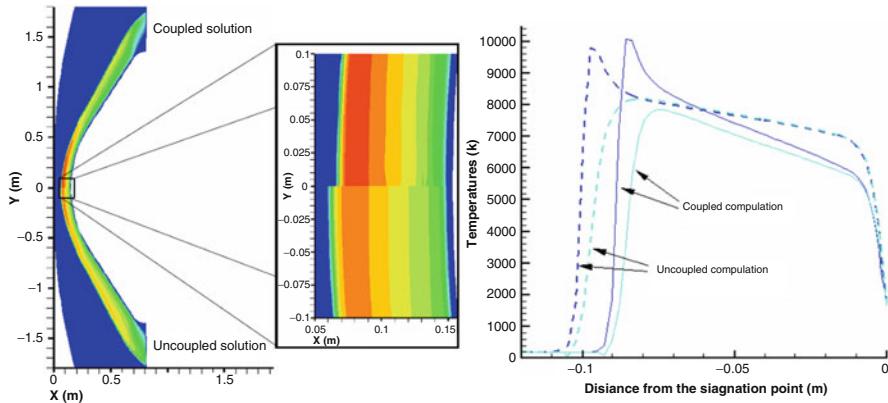


Fig. 7.16 CO and C mass fractions at  $H_{\infty} = 71.86$  km and  $M_{\infty} = 41.54$



**Fig. 7.17** Temperature contours: influence of radiation

For typical low ballistic coefficient entries, significant nonequilibrium may exist in regions of the shock layer both in thermodynamic (i.e., species internal energy distribution between rotational, vibrational, and electronic modes or states and the translational mode) and chemical processes. The thermal nonequilibrium is commonly expressed as different temperatures for each mode, the internal modes lagging the translational by differing degrees. Chemical nonequilibrium in the entry environment of the forebody means that dissociation reactions are delayed, and the mole fractions of molecular species and molecular intermediates is higher after the shock than in the equilibrium case. This leads to the nonequilibrium overshoot phenomena.

The radiated energy travels in all directions through the flowfield, either by being absorbed by the shock layer gases or continuing until it leaves the vicinity of the vehicle or reaches the surface of the vehicle. Radiation that travels upstream of the bow shock leads to heating of the shock precursor region with corresponding increase in free-stream enthalpy. Of more significance in general is the radiation that falls on the vehicle surface, or radiative heat flux. In some entry scenarios, the radiative heat flux is the dominant mechanism (e.g., for Jovian entry where entry velocities are 40 km/s) with the convective contribution becoming insignificant. The forebody flowfield of such vehicles is further complicated by the fact that the only viable material choice for thermal protection systems is a charring ablator type. Pyrolysis gases and subliming or reacting surface species therefore become significant features of the vehicle boundary layer. In general, these products will have a beneficial effect in the reduction of radiative heat flux since they act to absorb incident radiation. The flux is thus reduced by radiation blockage.

On the other hand, the absorption of radiation will increase the temperature of the boundary-layer gases with a possible associated increase in convective heat flux. The simulation may be further complicated when ablation products or interaction of these with free-stream species gives rise to species which themselves are particularly strong radiators. An example of this is the formation of CN in the boundary layer of carbon heat shields in high enthalpy air flows.

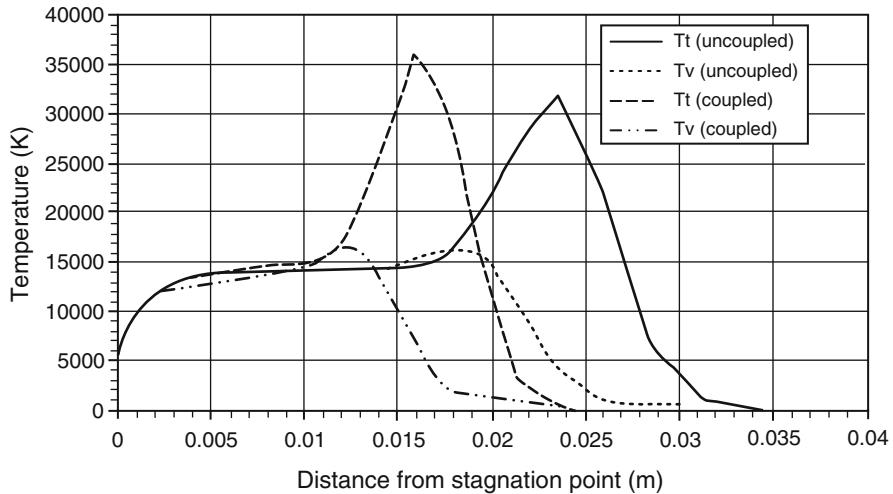


Fig. 7.18 Stagnation streamline temperatures with and without radiation coupling

To give an idea of the sensitivity of the radiative fluxes, the intensity of radiative emission is strongly dependent on the shock layer gas pressure and thickness (i.e., nose geometry). In existing engineering correlations for both convective and radiative heat flux, vehicle velocity, nose radius, and free-stream density are usually independent variables for a given atmosphere. The velocity exponent is typically in the range 5–16 for radiative fluxes, whereas for convective flux, correlations of the velocity exponent are typically 3.

The Rosetta entry vehicle provides a good example to illustrate these phenomena. The effects of coupling the radiative transport to the flowfield are shown in Figs. 7.18 and 7.19 showing stagnation streamline temperature profiles and surface heat fluxes, respectively [19, 20].

The flow of ablation products into the boundary layer provides a boundary condition for the solution of the boundary-layer equations whereby a mass flux normal to the wall is present.

For a single perfect gas, it is obvious that a component of velocity normal to the wall will decrease the asymptotic gradient of the tangential velocity such that the shear stress at the wall will be decreased:

$$\tau_w = \left( \mu \frac{\partial V}{\partial y} \right)_w \quad (7.1)$$

Also we may expect from Reynolds analogy that the heat flux will also be decreased (Fig. 7.19).

In an ablation or transpiration-cooled system, the injected gases are most likely to be of different chemical composition to the boundary-layer gases. Diffusion and mixing will take place, chemical reactions will occur, and energy will be transferred. Thus, the process will be complex.

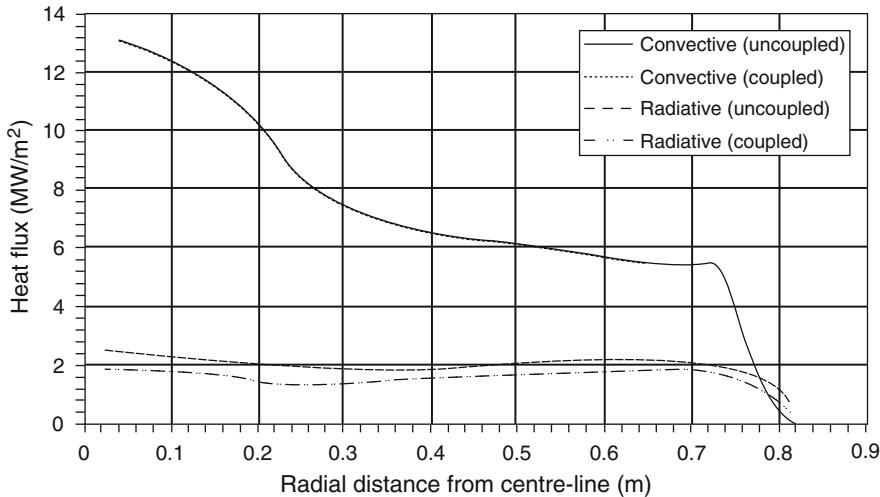


**Fig. 7.19** Surface heat fluxes, with and without radiation coupling

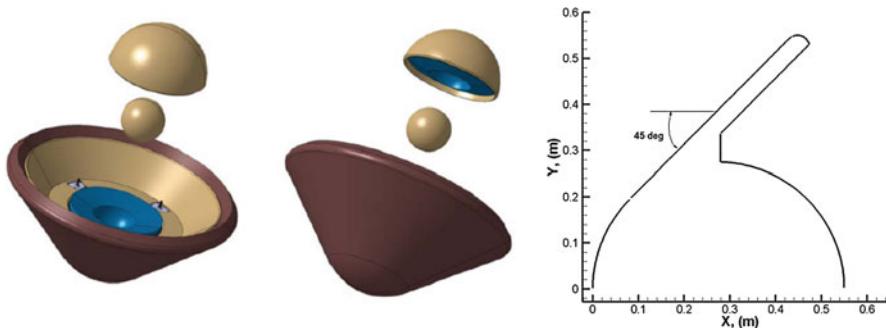


**Fig. 7.20** Capsule geometry with quotes

### 7.3 Spacecraft Reference Configuration and Re-entry Flight Scenario

Trade-off design analysis among hypersonic drag (heating), subsonic drag (impact velocity), and subsonic stability (available crush stroke) suggests to consider, for example, a spherocone capsule aeroshape with a 45° half cone angle, a 1.1-m-diameter front shield, a nose radius equal to 0.275 m, a shoulder radius of curvature equal to 0.0275 m, and a smaller back cover (see Fig. 7.20) [14]. The spacecraft, including margins, is estimated to weigh about 50 kg with the center of gravity (CoG) at 26.9 % from the nose relatively to the SRV diameter.

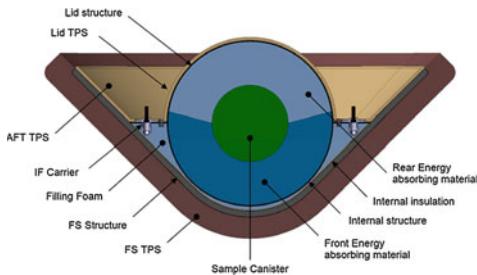


**Fig. 7.21** SRV layout

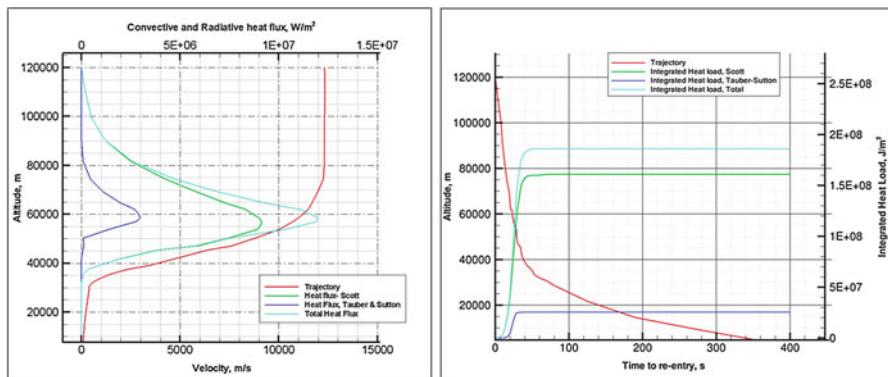


**Fig. 7.22** Re-entry trajectory in the altitude–velocity map and aerothermal loading conditions

The layout and design of the capsule (see Fig. 7.21) assure a safe return of the sample canister, relying on a fully passive concept. The stability requirement of such a shape ( $\text{CoG} < 26.5\%$ ) is the main critical parameter in this SRV design.

The flight design scenario of the SRV concept is shown in Fig. 7.22. It refers to an Earth descent characterized by  $-12.5^\circ$  of flight path angle (FPA), 12.3 km/s of entry velocity ( $V_e$ ) at 120 km altitude, and, therefore, by a rather high heat flux peak. The evolutions of heat fluxes (convective and radiative part) with the corresponding integrated heat load are also presented in Fig. 7.22.

In the preliminary design, the convective and radiative heat fluxes were estimated by using analytical engineering correlations such as Scott relationship for convective heat flux and Tauber–Sutton for the radiative heat flux evaluation [9, 16]. All the preliminary estimations provided in Fig. 7.22 are extremely important for designing the capsule. Indeed, the descent trajectory provides initial conditions for CFD solutions, while the aeroheating environment dictates the type and size of the TPS to be used. Peak heat rate generally determines the range of possible thermal protection material (TPM), while the integrated heat load determines the thickness and hence the mass of the capsule heat shield.

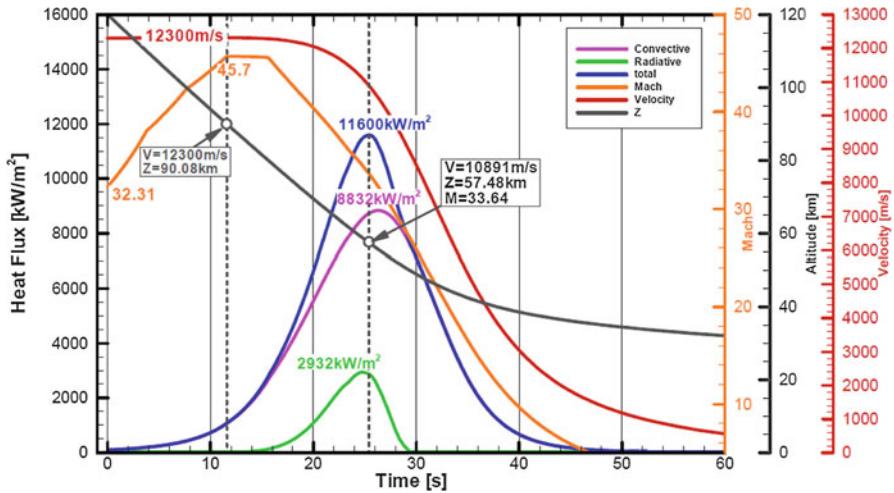


Fig. 7.23 Heat flux, Mach, altitude, velocity vs. time

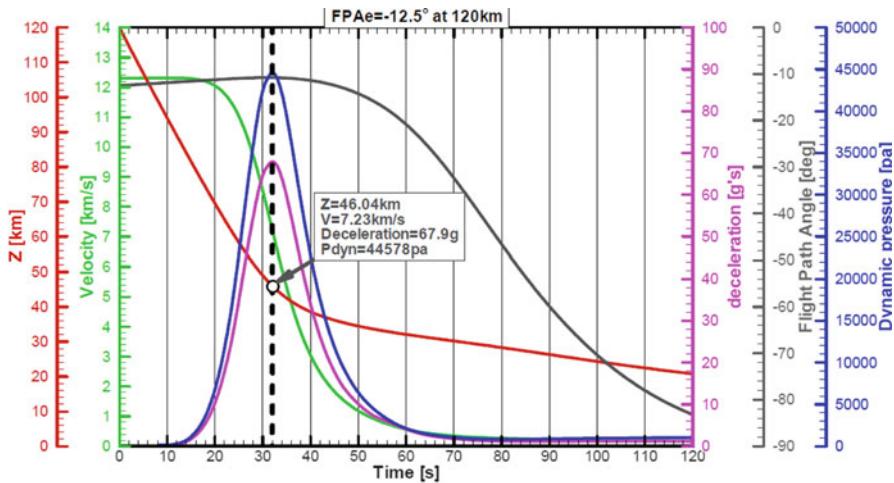


Fig. 7.24 Deceleration, dynamic pressure, altitude, velocity, and FPA vs. time

The time histories of heat fluxes (convective and radiative parts), Mach number, altitude, and velocity are presented in Fig. 7.23.

The evolutions of deceleration, dynamic pressure, altitude, velocity, and FPA vs. time are presented in Fig. 7.24. As shown, the peak dynamic pressure is equal to about 44,578 Pa, while the maximal aerodynamic deceleration is less than 70 g.

The materials chosen for the heat shield (see Fig. 7.21) is the ASTERM (a low-density carbon phenolic material) for the front shield and the Norcoat-Liège (a cork-based material) for the back shield [15]. The ASTERM and the

Norcoat-Liège were shown well adapted to the aerothermal and mechanical stress of the mission. The maximum TPS thickness needed is sized with 1-D calculation on the more thermally severe conditions with regard to a maximum allowable criterion of 150 °C for the bonding material. To simplify the design and to tend toward a more robust configuration, the thickness on both the front shield and the back shield was considered constant. This leads to the following thickness: front-shield (FS TPS) 56 mm and back-shield (AFT TPS) 8 mm [15].

## 7.4 Aerodynamic and Aerothermodynamic Performance Analysis

The appraisal of the aerodynamic and aerothermodynamic characteristics of the SRV concept is performed.

These evaluations are aimed to address the aerothermal loads the vehicle has to withstand during re-entry at super-orbital speed. To this aim, a number of extreme loading flight conditions have been focused along with the sizing flight trajectory, according to the trajectory-based design approach [6]. The heat flux distributions, both convective and radiative, are also addressed for each chosen trajectory design point. Indeed, planetary entries, and particularly sample return missions, are often characterized by strong radiation and ablation effects. For example, one of the most challenging topics of SRV design is to evaluate the blocking effect induced by the blowing of pyrolysis gases on the heat flux and on the shock layer. Therefore, computations are performed in order to account for both radiation and ablation effects on SRV aerothermal performances. However, it is worth noting that due to the prohibitive computational effort, no fully coupled computations of heat shield ablation and flow plasma radiation were undertaken in this work.

In the present analysis, only continuum regime (between Mach 3 and Mach 41.54) with the air modeled as a mixture of several gases (including also those coming from heat shield ablation) has been analyzed.

In particular, the appraisal of the vehicle aerodynamic and aerothermodynamic was performed by means of both engineering-based tools and Navier–Stokes CFD computations in thermochemical nonequilibrium and both in laminar and turbulent flow conditions. Then, results of CFD simulations are provided to PARADE code for the estimation of the radiative heat fluxes the capsule has to withstand during the super-orbital re-entry flight [17].

Engineering-based aerodynamic analyses were extensively performed by using a 3-D panel method code, namely, HPM (hypersonic panel method) [6, 12]. This tool at high supersonic and hypersonic speeds is able to accomplish the aerodynamic and aerothermodynamic analyses of a complex re-entry vehicle configuration by using simplified approaches such as local surface inclination methods and approximate boundary-layer methods, thus avoiding the time consuming and complex grid generation phase and the computation processes of a CFD analysis.

The numerical tool used to carry out the CFD analyses is the CIRA code H3NS/CAST [7, 12] and the commercial code FLUENT. CAST solves the flowfield governing equations, including chemical and vibrational nonequilibrium, with a finite volume approach. The fluid is treated as a mixture of perfect gases, and the energy exchange between vibrational and translational modes (TV) is modeled with the classical Landau–Teller nonequilibrium equation, with average relaxation times taken from the Millikan–White theory modified by Park. As far as the transport coefficients are concerned, the viscosity of the single species is evaluated by a fit of collision integrals calculated by Yun and Mason; the thermal conductivity is calculated by means of the Eucken law; the viscosity and thermal conductivity of the gas mixture are then calculated by using the semiempirical Wilke formulas. The diffusion of the multicomponent gas is computed through a sum rule of the binary diffusivities of each couple of species (from the tabulated collision integrals of Yun and Mason).

Transport coefficients, in the hypothesis of an ideal gas, are derived from Sutherland law, suitably modified to take into account for low temperature conditions. With respect to the numerical formulation, conservation equations, in integral form, are discretized with a finite volume, cell-centered technique. Convective fluxes are computed with a flux difference splitting (FDS) upwind scheme. Second-order formulation is obtained by means of an ENO-like reconstruction of cell interface values. Viscous flux is computed with a classical centered scheme, i.e., computing the gradients of flow variables at cell interfaces by means of Gauss theorem.

Integration in time is performed by employing an explicit multistage Runge–Kutta algorithm coupled with an implicit evaluation of the species and vibration energies source terms. Also a parallel version of the code is currently available.

The governing equations describing a flowfield around a hypervelocity vehicle deal with balance equations for a multi-species chemically reacting gas mixture.

#### 7.4.1 Flowfield Governing Equations

The mathematical model is made up of equations for mass conservation, momentum balance, total energy (less vibrational one) conservation, individual species balance, and vibrational energy conservation. The full set of equations for a viscous compressible continuum flow in thermal and chemical nonequilibrium, assuming the air to be a mixture of  $N_s$  perfect gases (mixture species) and  $N_v$  vibrating species, can be written in the integral conservation form as follows:

$$\frac{\partial}{\partial t} \int_V \vec{W} \, dV + \int_S (\vec{F}_{\text{inv}} + \vec{F}_{\text{vis}}) \cdot \vec{n} \, dS + \frac{\Gamma}{r} \int_V (\vec{A}_{\text{inv}}^* + \vec{A}_{\text{vis}}^*) \, dV = \int_V \vec{\Omega} \, dV \quad (7.2)$$

where  $\vec{W} = [\rho, \rho u, \rho v, \rho w, e_t, \rho_1, \dots, \rho_{N_s-1}, \rho e_{v1}, \dots, \rho e_{vN_v}]^T$  is the unknown state vector of the conserved quantities, in which  $\rho$  is the fluid density;  $\rho u$ ,  $\rho v$ , and

$\rho w$  are the momentum densities;  $e_t$  is the total internal energy per unit mass;  $\rho_i$  and  $e_{vi}$  are, respectively, the density and the vibrational energy of the  $i$ th species, while  $\rho e_{vi}$  takes into account for vibrational energy conservation; and  $\vec{F}$  is the flux vector (splitted into an inviscid and a viscous part). The vector  $\vec{F}$  expression is well known in literature, and therefore, it is not written here for simplicity.  $\vec{A}^*$  is the axisymmetric terms matrix (splitted into an inviscid and a viscous part), and  $\Gamma$  is equal to 1 for axisymmetric flows and 0 for 2-D and 3-D flows.  $\vec{\Omega} = [0, 0, 0, 0, 0, \Omega_1, \dots, \Omega_{Ns-1}, \Omega_{v1}, \dots, \Omega_{vN_v}]^T$  is the source terms vector that defines the mass and energy exchange among the species as a result of the chemical reaction rate and the energy transfer due to the internal energy excitation processes. Hence,  $\vec{\Omega}$  models the nonequilibrium reactions.

Finally,  $V$  is the arbitrary control volume cell,  $S$  is its closed boundary control surface, and  $\vec{n}$  is the outward normal unit vector. Equation (7.1) can be written in differential form as follows:

### Continuity

$$\frac{\partial \rho}{\partial t} + \vec{\nabla} \cdot (\rho \vec{V}) = 0 \quad (7.3)$$

### Momentum

$$\frac{\partial (\rho \vec{V})}{\partial t} + \vec{\nabla} \cdot (\rho \vec{V} \vec{V}) + \vec{\nabla} p = 2 \vec{\nabla} \cdot [\mu (\vec{\nabla} \vec{V})_o^s] \quad (7.4)$$

where

$$(\vec{\nabla} \vec{V})_o^s = \frac{1}{2} \left[ (\vec{\nabla} \vec{V}) + (\vec{\nabla} \vec{V})^T \right] - \frac{1}{3} (\vec{\nabla} \cdot \vec{V}) \underline{\underline{U}} \quad (7.5)$$

### Energy

$$\begin{aligned} \frac{\partial (\rho e_t)}{\partial t} + \vec{\nabla} \cdot [(\rho e_t + p) \vec{V}] \\ = \vec{\nabla} \cdot \left[ \lambda \nabla T + 2\mu (\vec{\nabla} \vec{V})_o^s \cdot \vec{V} + \sum_i h_i \vec{J}_i \right] - \sum_i h_i \dot{\omega}_i - \sum_j \dot{e}_{vj} \end{aligned} \quad (7.6)$$

where

$$\dot{e}_{vj} = (e_{vj}^{eq} - e_{vj}) / \tau_i \quad (7.7)$$

### *Species*

$$\frac{\partial(\rho Y_i)}{\partial t} + \vec{\nabla} \cdot (\rho \vec{V} Y_i) + \vec{\nabla} \cdot \vec{J}_i = \dot{\omega}_i \quad (7.8)$$

where

$$\dot{\omega}_i = m_i \sum_k \dot{\omega}_{ik} \quad (7.9)$$

### *Vibrational Energy*

$$\frac{\partial(\rho e_{vj})}{\partial t} + \vec{\nabla} \cdot (\rho \vec{V} e_{vj}) = \dot{e}_{vj} \quad (7.10)$$

In these equations,  $\vec{V}$  is the velocity vector;  $Y_i$  is the mass fraction of the  $i$ th species;  $\dot{\omega}_i$  is the rate of change of  $\rho_i$  due to chemical reactions;  $J_i$  is the diffusive flux of  $i$ th species, which arises due to concentration gradients;  $m_i$  and  $h_i$  are, respectively, the molecular weight and enthalpy of  $i$ th species;  $p$  is the pressure,  $\underline{U}$  is the unit tensor;  $\mu$  is the viscosity; and  $\lambda$  is the thermal conductivity.

For each species, the perfect gas model applies and Dalton's law is used:

$$p = \sum_i p_i \quad (7.11)$$

where  $p_i$  is the partial pressure of the  $i$ th species of the mixture.

As a consequence, the following relation for density holds:

$$\rho = \frac{p}{R_0 T \sum_i Y_i / m_i} \quad (7.12)$$

where  $R_0 = 8,314.5 \text{ JKmol}^{-1} \text{ K}^{-1}$  is the universal gas constant.

The internal energy of the mixture is defined as

$$e = \sum_i (Y_i e_i) \quad (7.13)$$

where  $e_i$ , internal energy of the single-component gas, is the sum of the energies representing the different degrees of freedom of the molecules. Finally, the specific enthalpy for each species can be calculated as

$$h_i = e_i + R_i T \quad (7.14)$$

where  $R_i$  is the gas constant.

As far as plasma radiation modeling is concerned, it is worth noting that the flow radiative heat flux at the SRV wall has been computed through the code PARADE, starting from the results of the fluid dynamic computations (in terms of gas composition and temperature) [17].

This code is able to compute flowfield emission and absorption, between the shock layer and the surface of the probe. The spectral emission and absorption are determined as a function of transition level (from upper level to lower level) and emitting population of this level. The population can be derived from the quasi-steady-state (QSS) method or by a Boltzmann method in order to take into account for the nonequilibrium or equilibrium regime, respectively. The radiative computations have been performed with the Boltzmann assumption for the determination of the population of the excited molecular states. Indeed, due to the very high temperatures reached in the shock layer caused by the strong bow shock in front of the capsule, the gas not only dissociates and ionizes but can also emit radiated energy which travels across the entire flowfield interacting with the gas itself. At the entry velocity foreseen for the capsule, this contribution, that is, generally very low with respect to other “energies” in the flowfield, cannot be neglected because it can cause an additional source of heat load at the wall to be taken into account [7]. From a general point of view, the flowfield and the radiative field are coupled: the radiated energy travels across the flowfield, interacts with the fluid dynamic field which changes its configuration and causes the change of the radiated energy, and so on. From a mathematical point of view, this interaction is represented by a source term in the classical Navier–Stoke equation for energy conservation which represents the quantity of radiated energy traveling across the flowfield.

In the present case, however, we consider a simplified, non-coupled, approach: it assumes that the energy emitted mainly just behind the shock region travels toward the wall, being in part absorbed by the gas in the shock layer, without changing its structure, and arrives at the wall increasing the total heat flux. Different results presented in the literature provided that this uncoupled approach is conservative if applied to the radiative heat flux estimation at the wall [7]. In order to compute the contribution to the wall due to the radiative processes in the field, it is necessary, therefore, to know the radiative properties in the gas which have been computed through PARADE starting from the results of the Fluid Dynamics computations (in terms of gas composition and temperature).

The *radiative heat transfer equation* (RTE) has been solved using the one-dimensional tangent slab approximation (i.e., radiation properties are assumed to vary only in the direction normal to the wall) [17].

The intensity of radiation at a given wavelength  $\lambda$  satisfied the equation of radiative transfer:

$$\frac{\partial I_\lambda}{\partial s} = j_\lambda - k_\lambda I_\lambda \quad (7.15)$$

where  $j_\lambda$  and  $k_\lambda$  are, respectively, the emission and absorption coefficients, computed through PARADE [17]. These coefficients are integrated along with straight lines toward the wall according to the above equation to compute  $I_\lambda$ .

Radiative heat flux at a given wavelength  $\lambda$  is then obtained through integration of  $I_\lambda$  over the solid angle, whereas the total radiative heat flux is obtained through integration over the spectrum of interest. In particular, a spectral region between 100 and 40,000 nm using 50,000 spectral grid locations has been considered in the calculations.

### 7.4.2 Loading Scenario and Air Mixture Composition

SRV aerothermal analyses refer to CFD simulations performed at several discrete points of the flight scenario summarized in Fig. 7.25 [14], and the results are used to address vehicle AEDB and ATDB.

Furthermore, in order to get an idea of real gas effects that the capsule will experience during descent, Figure 7.25 shows the re-entry trajectory superimposed on the fields (from 10 to 90 %) of vibrational excitation (VE), oxygen and nitrogen dissociation (OD and ND), and ionization (I) of flow species [6, 10].

The assessment of aeroshape modification on both aerodynamic and aerothermodynamic is determined by means of twelve 2-D axisymmetric NS simulations in thermochemical nonequilibrium carried out at six given points (i.e., points M) along the re-entry path. These trajectory points have been selected thanks to the examination of the recession level occurring at the stagnation point during descent, as summarized in Fig. 7.26.

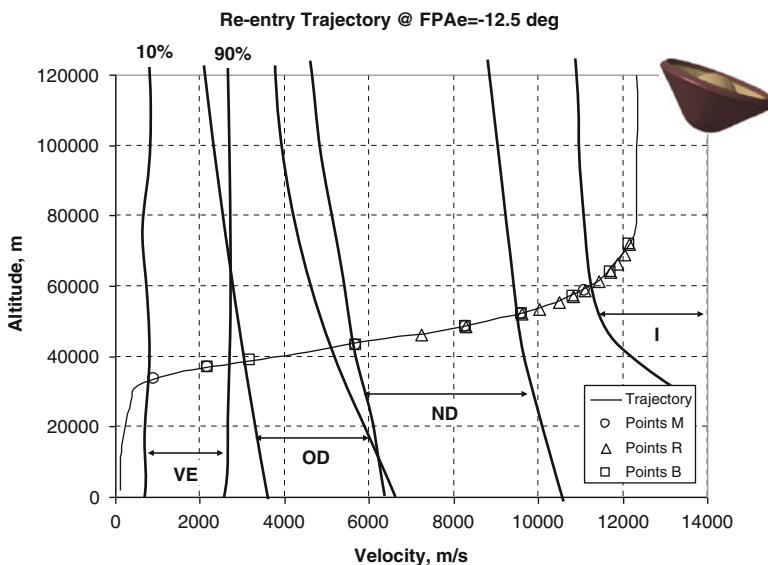


**Fig. 7.25** Re-entry trajectory in the altitude–velocity map with CFD design point

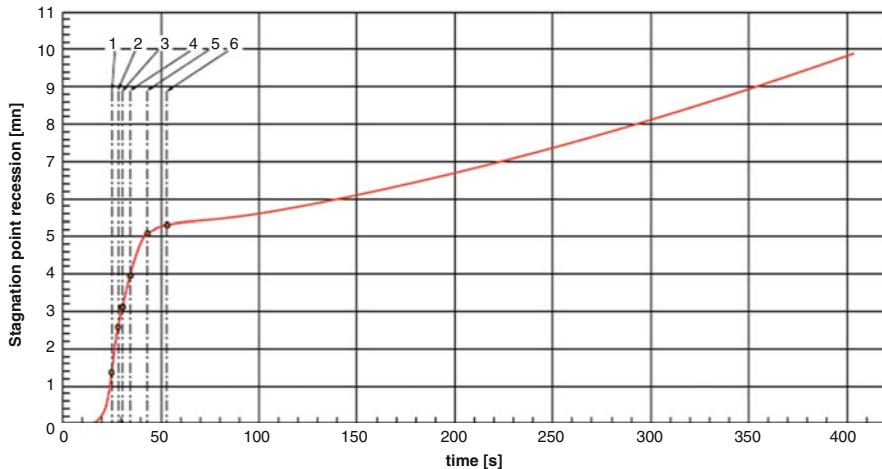


Fig. 7.26 Stagnation-point recession level vs. trajectory time and the 6 points M

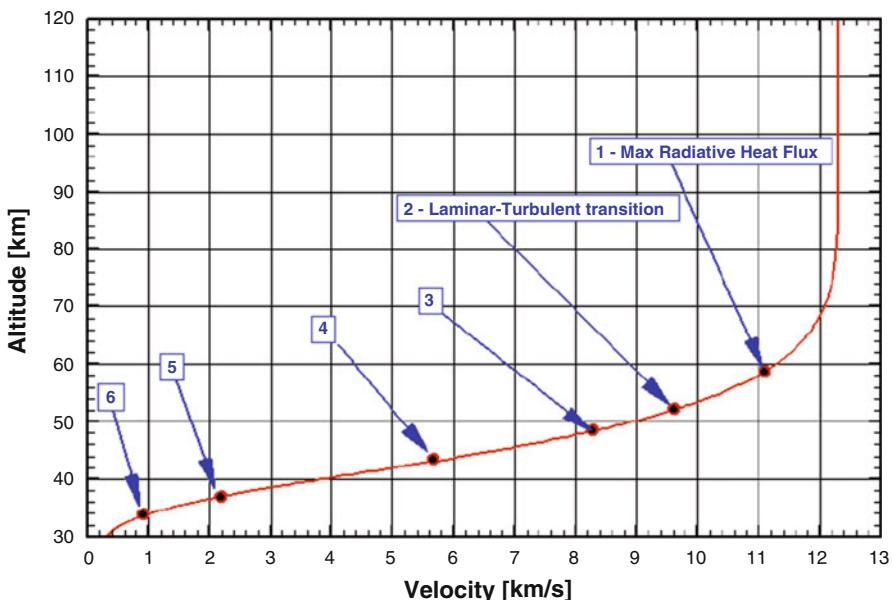
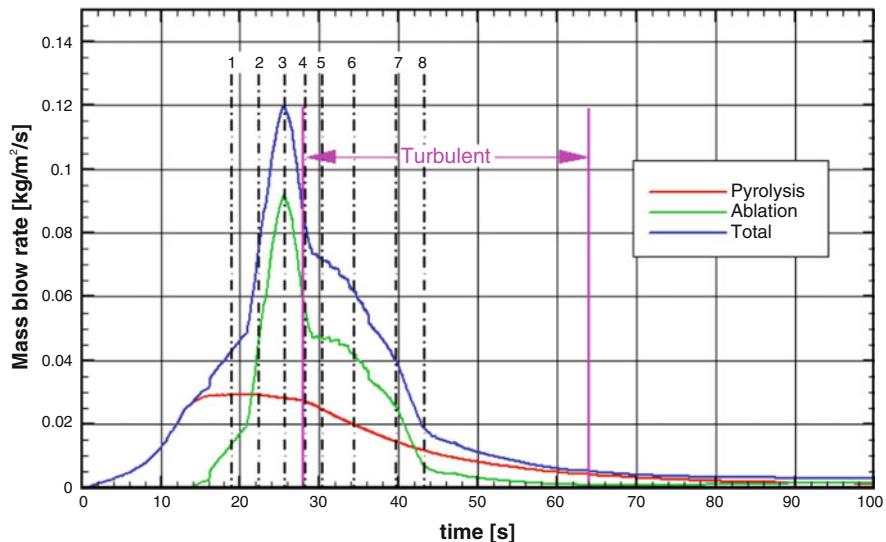


Fig. 7.27 The points M in the altitude–velocity map – aeroshape modification assessment

As one sees, the six points M have been chosen according to the increase of recession level. Moreover, the recession increases rapidly during the first 50 s of the trajectory but still remains half (about 5.5 mm) compared with the final recession level of 10 mm. Points M are plotted in the altitude–velocity map, as presented in Fig. 7.27, while the free-stream conditions are summarized in Table 7.8

**Table 7.8** Free-stream conditions of points M (yellow, laminar regime; pink, turbulent regime)

Points	Time [s]	Altitude [km]	$V_\infty$ [m/s]	$p_\infty$ [pa]	$\rho_\infty$ [kg/m <sup>3</sup> ]	$T_\infty$ [K]	Mach	Recession level - stagnation point [mm]
M1&M1a	24.8	58.73	11099	26.49	$3.5732 \times 10^{-4}$	258.26	34.45	1.3
M2&M2a	28.2	52.05	9604	61.84	$7.9596 \times 10^{-4}$	270.65	29.12	2.6
M3&M3a	30.4	48.36	8280	97.84	$1.2594 \times 10^{-3}$	270.65	25.11	3.2
M4&M4a	34.4	43.14	5681	189.53	$2.5491 \times 10^{-3}$	259.02	17.61	4.0
M5&M5a	43.2	36.93	2181	437.43	$6.3007 \times 10^{-3}$	241.86	7.00	5.1
M6&M6a	53.2	33.62	922	701.11	$1.0497 \times 10^{-2}$	232.69	3.02	5.3

**Fig. 7.28** Mass blow rate vs. time (ablation and pyrolysis contribution)

The eight trajectory points (i.e., points B) for the assessment of heat shield ablation effects are selected by the examination of mass blow rate vs. time, reported in Fig. 7.28. As shown, the major part of these points is around the maximum value of total mass blow rate.

Points B are plotted in the altitude–velocity map in Fig. 7.29, while free-stream conditions are summarized in Table 7.9.

Finally, design points (i.e., points R) considered in assessing SRV aerodynamic and aerothermodynamic performance within the plasma radiation effects are depicted in Fig. 7.30.

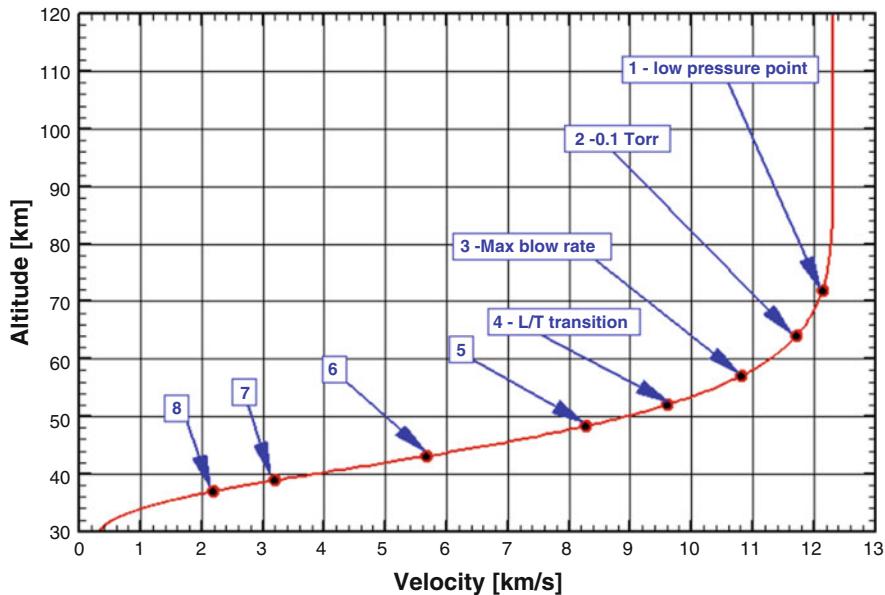


**Fig. 7.29** The eight selected points plotted in the altitude–velocity diagram – blowing assessment

**Table 7.9** Free-stream conditions of points B yellow: laminar regime, pink: turbulent regime

Points	Time [s]	Altitude [km]	$V_\infty$ [m/s]	$p_\infty$ [pa]	$\rho_\infty$ [kg/m <sup>3</sup> ]	$T_\infty$ [K]	Mach	Stagnation point mass blow [kg/m <sup>2</sup> /s]
B1	19.0	71.86	12138	4.14	$6.7859 \times 10^{-5}$	212.41	41.54	0.043
B2	22.4	63.98	11711	13.19	$1.8886 \times 10^{-4}$	243.29	37.45	0.076
B3	25.6	57.07	10816	32.84	$4.3738 \times 10^{-4}$	261.52	33.07	0.120
B4	28.2	52.05	9604	61.84	$7.9596 \times 10^{-4}$	270.65	29.12	0.083
B5	30.4	48.36	8280	97.84	$1.2594 \times 10^{-3}$	270.65	25.11	0.071
B6	34.4	43.14	5681	189.53	$2.5491 \times 10^{-3}$	259.02	17.61	0.062
B7	39.6	38.85	3184	335.8	$4.7331 \times 10^{-3}$	247.16	10.10	0.040
B8	43.2	36.93	2181	437.43	$6.3007 \times 10^{-3}$	241.86	7.00	0.019

Points R have been selected following the evolution of the convective, radiative, and, therefore, total heat flux, as shown in Fig. 7.31. Free-stream conditions are summarized in Table 7.10

The atmosphere composition is considered which is made of  $Y_{N_2} = 0.75548$ ;  $Y_{O_2} = 0.23161$ ; and  $Y_{Ar} = 0.01291$ . Therefore, the specific gas constant for air is  $R_{air} = R_0/M = 287.182 \text{ J/Kg/K}$ . The model proposed for the air mixture is composed of 13 species: molecules, N<sub>2</sub>, O<sub>2</sub>, and NO; atoms, N, O, and Ar; and ions, N<sub>2</sub><sup>+</sup>, O<sub>2</sub><sup>+</sup>, NO<sup>+</sup>, N<sup>+</sup>, O<sup>+</sup>, Ar<sup>+</sup>, and e<sup>-</sup>; while to account for heat shield blowing mass, the air mixture consists of 32 species—molecules, N<sub>2</sub>, O<sub>2</sub>, NO, C<sub>2</sub>, H<sub>2</sub>, C<sub>3</sub>,

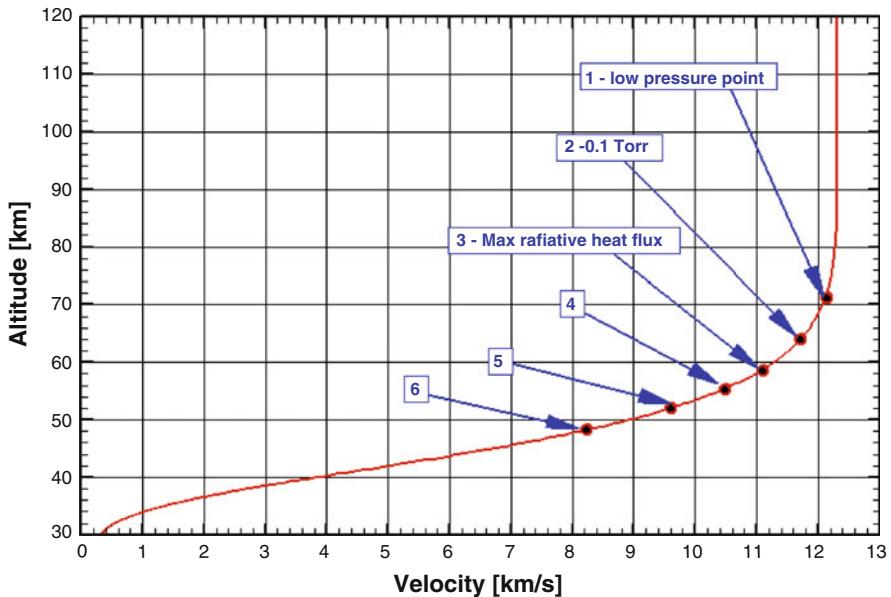


Fig. 7.30 The 6 selected points plotted in the altitude–velocity map – plasma radiation effect

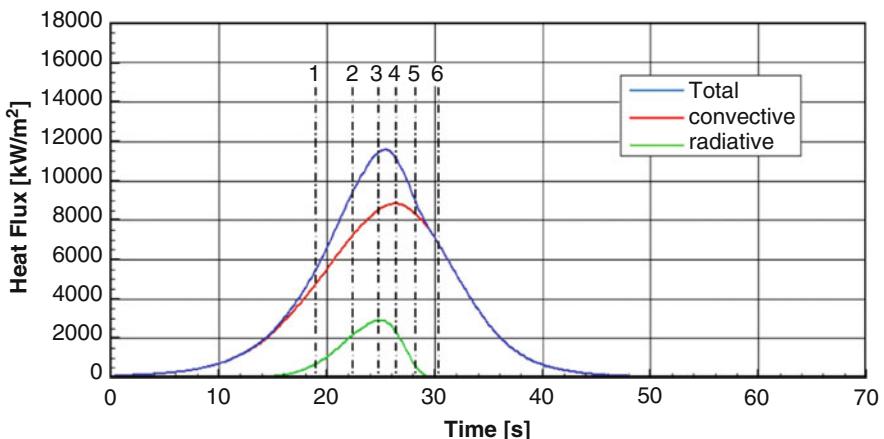


Fig. 7.31 Heat flux evolution vs. trajectory time – plasma radiation effect

$\text{C}_2\text{H}_2$ ,  $\text{C}_2\text{H}$ ,  $\text{CO}_2$ ,  $\text{H}_2\text{O}$ ,  $\text{CN}$ ,  $\text{CH}$ ,  $\text{NH}$ ,  $\text{HCN}$ ,  $\text{OH}$ , and  $\text{CO}$ ; atoms,  $\text{N}$ ,  $\text{O}$ ,  $\text{Ar}$ ,  $\text{C}$ , and  $\text{H}$ ; and ions,  $\text{N}_2^+$ ,  $\text{O}_2^+$ ,  $\text{NO}^+$ ,  $\text{N}^+$ ,  $\text{O}^+$ ,  $\text{CN}^+$ ,  $\text{CO}^+$ ,  $\text{C}^+$ ,  $\text{H}^+$ ,  $\text{Ar}^+$ , and  $\text{e}^-$ . The chemical model is based on Park [18]. It is composed, when mass blowing is off, of 13 species and 22 chemical reactions that account also for third-body efficiency.

The reaction mechanism is summarized in Table 7.11.

**Table 7.10** Free-stream conditions of points R

Points	Time [s]	Altitude [km]	$V_\infty$ [m/s]	$P_\infty$ [Pa]	$\rho_\infty$ [kg/m <sup>3</sup> ]	$T_\infty$ [K]	Mach	Total heat flux [MW/m <sup>2</sup> ]
R1&R1c	19.0	71.86	12138	4.14	$6.7859 \times 10^{-5}$	212.41	41.54	5.5
R2&R2c	22.4	63.98	11711	13.19	$1.8886 \times 10^{-4}$	243.29	37.45	9.5
R3&R3C	24.8	58.73	11099	26.49	$3.5732 \times 10^{-4}$	258.26	34.45	11.5
R4&R4C	26.4	55.46	10490	40.33	$5.3082 \times 10^{-4}$	264.69	32.16	11.1
R5&R5C	28.2	52.05	9604	61.84	$7.9596 \times 10^{-3}$	270.65	29.12	8.98
R68.R6C	30.4	48.36	8280	97.84	$1.2594 \times 10^{-3}$	270.65	25.11	6.77

When heat shield species diffuse in the shock layer, the chemical model is composed of 67 chemical reactions which feature also the effect of collisional partner. For what concerns the thermal nonequilibrium model, it is worth to note that a three-temperature model is recommended: ( $T$ ,  $T_v$ ,  $T_e$ ) [8, 11],  $T$  for translational and rotational mode for heavy species,  $T_v$  for vibrational modes, and  $T_e$  for translational mode of free electron.

In the present CFD computations, however, only a two-temperature model ( $T$  and  $T_{\text{vib}}$  for each molecule of reacting mixture, i.e.,  $T_{v\text{N}_2}$ ,  $T_{v\text{O}_2}$ ,  $T_{v\text{NO}}$ ,  $T_{v\text{N}_2^+}$ ,  $T_{v\text{O}_2^+}$ ,  $T_{v\text{NO}^+}$ ) has been considered.

Vibrational relaxation is modeled using a Landau–Teller formulation, where relaxation times are obtained from Millikan–White with the high-temperature correction from Park [8].

Finally, flight regime assessment was made in order to be sure that all trajectory design points lie within the continuum flow regime to be able to use CFD analysis, as discussed in the next paragraph.

#### 7.4.3 Flight Regime Overview and Flow Simulation Modeling

Once the SRV vehicle started its descent, the atmospheric density is low enough that the molecular mean free path ( $\delta$ ) can become as large as the scale of the body itself. As a consequence, the continuum assumption does not apply.

This condition is known as free molecular flow (FMF) regime, and the aerodynamic and aerothermodynamic characteristics of the capsule are determined by individual, scattered molecular impacts and must be analyzed on the basis of kinetic theory. Therefore, the SRV concept, moving from a very rarefied atmosphere (at entry interface) to a denser atmosphere, shifts from the FMF regime, where individual molecular collisions are important, to the transitional one, where slip effects are important, and then to the continuum regime, as represented in Fig. 7.32.

**Table 7.11** Reaction mechanism and chemical kinetics model for air only

		$k_f = AT^n(-Ta/T)$			
Reaction Id		$K_f$ (cm <sup>3</sup> /mole/s)	$n$	$Ta$ [k]	Tr (control temperature) [K]
<i>Dissociation reactions</i>					
R1,1	$N_2 + \text{Molecules} \leftrightarrow N + N + \text{Molecules}$	$7.00 \cdot 10^{21}$	-1.60	113,200	$T^{0.5} T_v^{0.5}$
R1,2	$N_2 + \text{Atoms} \leftrightarrow N + N + \text{Atoms}$	$3.00 \cdot 10^{22}$	-1.60	113,200	$T^{0.5} T_v^{0.5}$
R1,3	$N_2 + e^- \leftrightarrow N + N + e^-$	$3.00 \cdot 10^{24}$	-1.60	113,200	$T^{0.5} T_v^{0.5}$
R2,1	$O_2 + \text{Molecules} \leftrightarrow O + O + \text{Molecules}$	$2.00 \cdot 10^{21}$	-1.50	59,500	$T^{0.5} T_v^{0.5}$
R2,2	$O_2 + \text{Atoms} \leftrightarrow O + O + \text{Atoms}$	$1.00 \cdot 10^{22}$	-1.50	59,500	$T^{0.5} T_v^{0.5}$
R3,1	$NO + \text{Molecules} \leftrightarrow O + N + \text{Molecules}$	$9.64 \cdot 10^{14}$	0	74,700	$T^{0.5} T_v^{0.5}$
R3,2	$NO + N_2 \leftrightarrow O + N + N_2$	$1.45 \cdot 10^{15}$	0	74,700	$T^{0.5} T_v^{0.5}$
R3,3	$NO + \text{Atoms} \leftrightarrow O + N + \text{Atoms}$	$9.64 \cdot 10^{14}$	0	74,700	$T^{0.5} T_v^{0.5}$
<i>Exchange reactions: neutrals</i>					
R4	$NO + O \leftrightarrow O_2 + N$	$8.40 \cdot 10^{12}$	0	19,400	$T$
R5	$N_2 + O \leftrightarrow NO + N$	$6.40 \cdot 10^{17}$	-1.00	38,400	$T$
<i>Associative ionization reactions</i>					
R6	$N + N \leftrightarrow N_2^+ + e^-$	$2.00 \cdot 10^{13}$	0	67,500	$T$
R7	$O + O \leftrightarrow O_2^+ + e^-$	$1.10 \cdot 10^{13}$	0	80,600	$T$
R8	$N + O \leftrightarrow NO^+ + e^-$	$5.30 \cdot 10^{12}$	0	31,900	$T$
<i>Electron impact ionization reactions</i>					
R9	$N + e^- \leftrightarrow N^+ + e^- + e^-$	$2.50 \cdot 10^{34}$	-3.82	168,200	$T^{0.5} T_v^{0.5}$
R10	$O + e^- \leftrightarrow O^+ + e^- + e^-$	$3.90 \cdot 10^{33}$	-3.78	158,500	$T^{0.5} T_v^{0.5}$
R11	$Ar + e^- \leftrightarrow O^+ + e^- + e^-$	$2.50 \cdot 10^{34}$	-3.82	181,700	$T^{0.5} T_v^{0.5}$
<i>Exchange reactions: ions</i>					
R12	$NO^+ + O_2 \leftrightarrow O_2^+ + NO$	$2.40 \cdot 10^{13}$	0.41	32,600	$T$
R13	$O_2^+ + N_2 \leftrightarrow N_2^+ + O_2$	$9.90 \cdot 10^{12}$	0	40,700	$T$
R14	$O_2^+ + N \leftrightarrow N^+ + O_2$	$8.70 \cdot 10^{13}$	0.14	28,600	$T$
R15	$O_2^+ + O \leftrightarrow O^+ + O_2$	$4.00 \cdot 10^{12}$	-0.09	18,000	$T$
R16	$N^+ + N_2 \leftrightarrow N_2^+ + N$	$1.00 \cdot 10^{12}$	0.50	12,200	$T$
R17	$O^+ + N_2 \leftrightarrow N_2^+ + O$	$9.10 \cdot 10^{11}$	0.36	22,800	$T$
R18	$O^+ + N_2 \leftrightarrow N_2^+ + O$	$1.40 \cdot 10^5$	1.90	15,300	$T$
R19	$NO^+ + N \leftrightarrow N_2^+ + O$	$7.20 \cdot 10^{13}$	0	35,500	$T$
R20	$NO^+ + N \leftrightarrow O^+ + N_2$	$3.40 \cdot 10^{13}$	-1.08	12,800	$T$
R21	$NO^+ + O \leftrightarrow O_2^+ + N$	$7.20 \cdot 10^{12}$	0.29	48,600	$T$
R22	$NO^+ + O \leftrightarrow N^+ + O_2$	$1.00 \cdot 10^{12}$	0.50	77,200	$T$

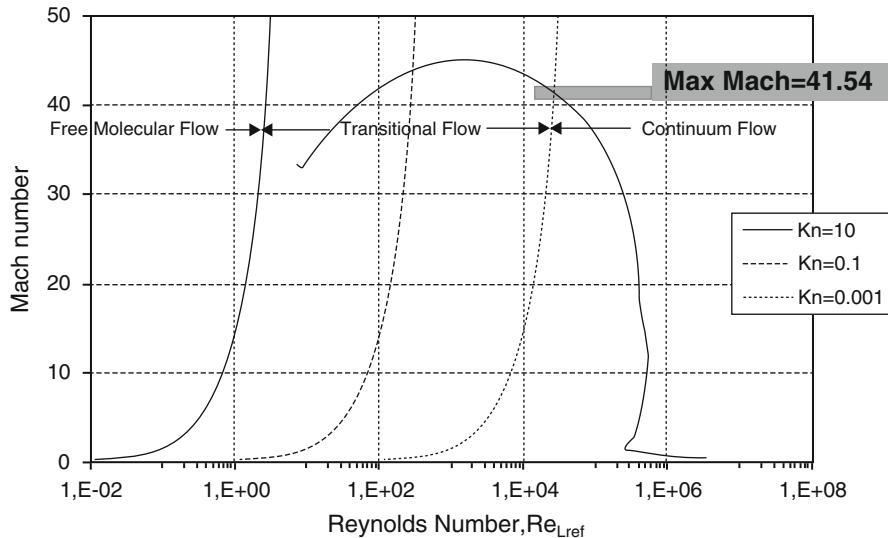


**Fig. 7.32** SRV re-entry trajectory in the Ma–Re map with constant Knudsen numbers

For instance, the similarity parameter that governs these different flow regimes is the Knudsen number (rarefaction parameter):

$$\text{Kn}_{\infty L_{\text{ref}}} = \frac{\delta}{L_{\text{ref}}} = 1.25 \sqrt{\gamma} \frac{M_{\infty}}{Re_{\infty L_{\text{ref}}}} \quad (7.16)$$

where  $L_{\text{ref}}$  (i.e., 1.1 m – capsule diameter) is the characteristic length of the body. As shown in Fig. 7.32, the maximum Mach number (i.e.,  $M_{\infty} = 41.54$ ) evaluated by the SRV Flight Mechanics analysis lies in the continuum flow regime. Therefore, all CFD computations have been performed with Navier–Stokes approximation without slip conditions at the wall.

As far as laminar-to-turbulent flow transition is concerned, CFD computations are carried out in turbulent flow conditions for points below 51.9 km altitude, according to the ARD postflight data criterion [12].

$$Re_{\infty,D} = \left( \frac{\rho_{\infty} u_{\infty} D}{\mu_{\infty}} \right) \geq 5.0 \times 10^5 \quad (7.17)$$

This criterion, however, represents only the first viable option considering that the effect of higher Mach number of the SRV trajectory compared to that of ARD and the mass blowing effect, as well, should influence departure from laminar boundary-layer flow conditions at lower altitude. Furthermore, transition can be triggered by roughness due to ablation and/or gaps and steps of heat shield.

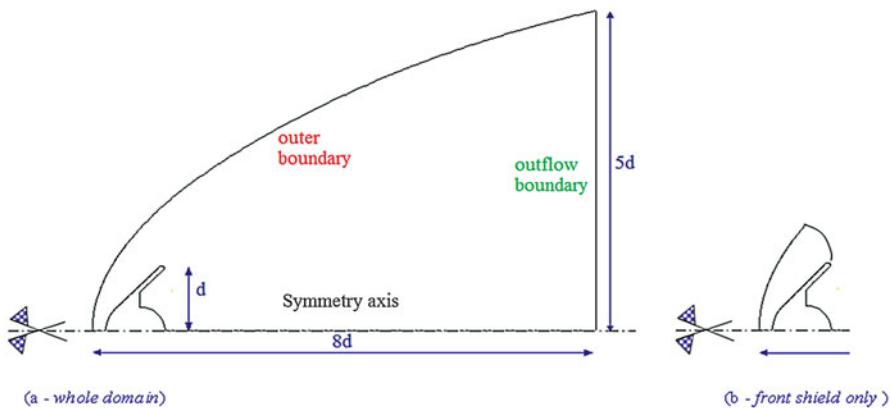


**Fig. 7.33** CFD computational domains: both whole domain **(a)** and front shield only **(b)**

#### 7.4.4 Computational Domains, Boundary Conditions, and Solution Convergence

CFD computations have been carried out on multiblock structured grids. In particular, two kinds of computational domain, similar to those shown in Fig. 7.34, have been considered.

As shown, 3-D and 2-D axisymmetric computational domains for both whole and front shield domains have been considered. The effective dimensions of the outflow boundary, axis, and outer boundary are modified in each simulation in order to obtain a grid compliant to the flowfield conditions to simulate. They are estimated by engineering-based methods. For example, the standoff distance has been estimated by means of Seiff and Probstein relationships (see Chap. 1) [8].

This means that all grids are tailored for the free-stream conditions of each trajectory points to simulate (Fig. 7.33).

The strategy adopted was to build the volume mesh be large enough to accommodate the free-stream Mach number, while the distribution of grid points in the wall-normal direction is driven by free-stream Reynolds number. Hence, the distribution of surface grid points was dictated by the level of resolution desired in various areas of vehicle such as stagnation region and base fillet, according to the computational scopes. For example, wake flows are sensitive to the details of volume grid construction, and it is important that the grid be aligned to anticipate flow features. Furthermore, the grid has sufficient points in the shoulder region to capture the rapid expansion and accurately predict the flow separation point and the angle of the resulting shear layer. There are also enough points in the separated flow region to resolve the vortical structure at the beginning of the wake flowfield. Three-dimensional computations are carried out on a mesh domain made of 48 blocks with about 800,000 cells. The generic 2-D for whole domain grid consisted of about 30 blocks for an overall number of about 72,000 cells (half body). The grid (front shield

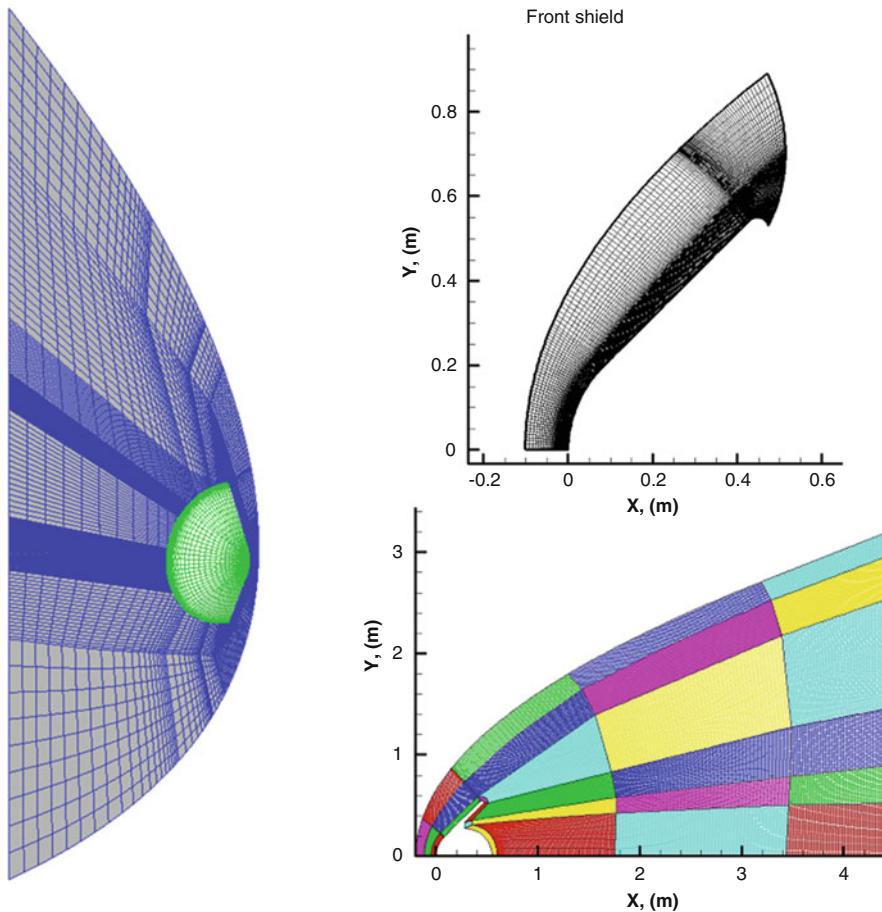


**Fig. 7.34** CFD multiblock computational domains

case) is composed of  $124 \times 160$  cells (longitudinal  $x$  normal to the wall direction) and assures fully spatially converged results. A local refinement has been done in the shock region in front of the capsule to better resolve the steep gradients, aligning the grid with the bow shock and clustering points into the boundary layer. This reduced the spurious oscillations in the stagnation area that are often observed in hypersonic flows, especially for large bluff-body flowfield computations. The minimum spacing at the wall is equal to  $10^{-6}$  m to accurately predict heat transfer at the vehicle surface. When the flow is in turbulent conditions, the values of the viscous coordinate  $y^+$  are less than 1;  $y^+$  is defined as

$$y^+ = \frac{\eta\rho}{\mu} \sqrt{\frac{\tau_w}{\rho}} \quad (7.18)$$

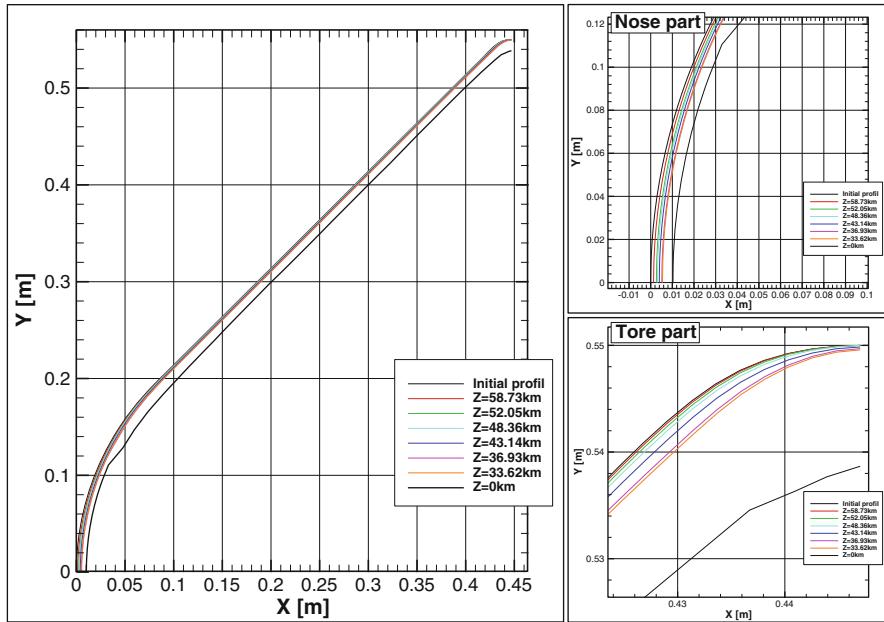


**Fig. 7.35** SRV aeroshape modification due to TPS ablation

where the quantities  $\eta$  and  $\tau_w$  are the surface normal distance and the shear stress, respectively.

Closeup views of 3-D and 2-D axisymmetric meshes (for both whole and front shield domains) can be seen in Fig. 7.34. Grid refinement in strong gradient regions of flowfield was made through a solution adaptive approach. As shown, grids for whole computational domain take advantage of the o-gird domain decomposition technique around the capsule in order to have meshes block wrapping the SRV and with direction outgoing from the body wall, necessary for boundary-layer stretching.

The SRV aeroshape to consider in mesh generations for numerical simulations regarding aeroshape modification effect is summarized in Fig. 7.35.

As shown, there are slight aeroshape modifications compared with the initial profile for the selected trajectory points. The most important aeroshape change occurs in the nose and tore parts (the cone angle does not change). Therefore, only limited impact on aerodynamic coefficients and on heat fluxes is expected.

As far as wall boundary conditions are concerned, all simulations without heat shield ablation (i.e., points M and R) are performed with a wall temperature of  $T_w = 1,000$  K (i.e., isothermal wall) and a fully catalytic wall (FCW) assumption, i.e., chemical equilibrium at the wall. For instance, as atoms produced by flow dissociation strike the surface, the catalytic property of the wall is implemented by means of a production term (i.e.,  $\dot{\omega}_{wi} \neq 0$ ) for the boundary condition of the boundary-layer problem to solve. Indeed, steady-state mass atomic conservation at

the wall states that the production of  $i$ th species due to the catalytic recombination rate must be balanced by the rate of diffusion to the surface:

$$(\dot{\omega}_a)_w = K_{wa} (\rho_w Y_{iw})^\delta = \left( \rho D_a \frac{\partial Y_a}{\partial y} \right)_w \quad (7.19)$$

where  $\delta$  is the reaction order. When the TPS surface if FCW (i.e., activates all the recombination reactions at wall)  $K_{wa} = \infty$ . This means a complete recombination because the flow tends toward chemical equilibrium at the wall. In this case, the molecular species concentrations at the wall have to be set equal to their equilibrium concentrations according to the local temperature and pressure. For wall temperatures below 2,000 K (i.e., cold walls), this corresponds to the free-stream composition.

When heat shield mass diffuses in the shock layer (i.e., points B), numerical simulations are carried out considering a prescribed mass fraction profile at the wall for each blowing species. The ablation model for ASTERM is based on thermochemical equilibrium oxidation of carbon as a function of surface temperature, pressure, and pyrolysis gas mass flow which exercise a blocking effect on heating flux. Therefore, the heat shield recession to consider at each CFD computation was provided by means of suitable boundary conditions to consider at the capsule wall, as shown in Fig. 7.36.

As one can see, wall temperature, mass blow rate, and composition of injected products are variable along the capsule centerline and re-entry trajectories. Indeed, for the charring ablators such as a carbon phenolic material, the reaction at the surface itself is divided into oxidation-dominant regime below 3,000 K of surface temperature and sublimation-dominant regime for higher temperature. In the latter regime, the surface recession rate increases rapidly with temperature rise, and a massive flow of ablation product must be taken into consideration in addition to pyrolysis gassing.

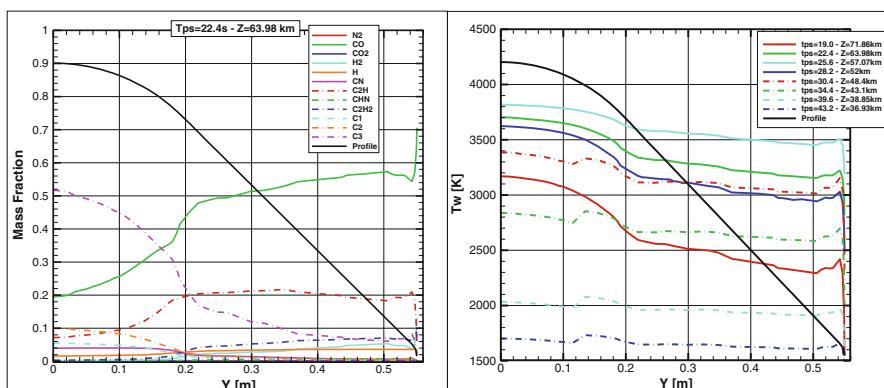


**Fig. 7.36** Mass fraction profiles at  $H_\infty = 63.98$  km altitude and temperature profile at different altitudes

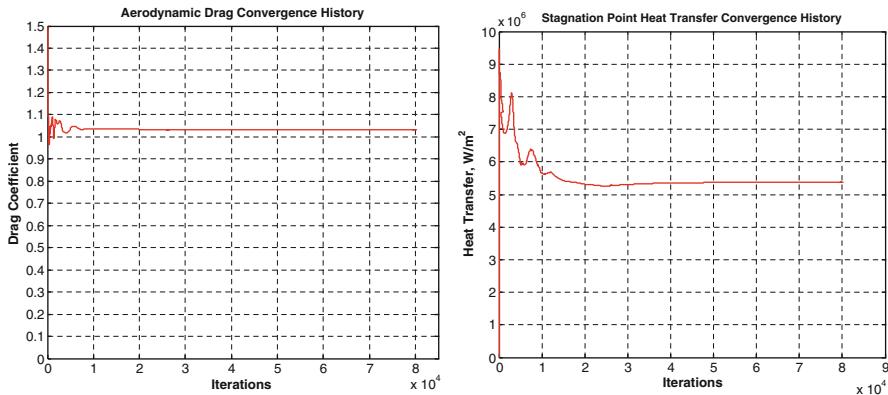


**Fig. 7.37** Drag coefficient and stagnation-point heat flux vs. iterations for R8 2-D axisymmetric simulation

All CFD results refer to both converged and grid independent computations. In order to assess numerical solution convergence, equation residuals and aerodynamic coefficient (i.e.,  $C_D$ ) as well as the stagnation-point heat flux have been monitored during iterations. Solution convergence is assumed when equation residuals drop more than three orders of magnitude and both the aerodynamic coefficient and the stagnation-point heat flux plots are flat for enough CFD iterations. For example, Fig. 7.37 shows the aerodynamic drag and stagnation-point heat flux convergence histories for the R8 point 2-D axisymmetric simulation.

Mesh sensitivity analyses have been carried out on the three levels of the structured multiblock grid ( $L_1, L_2, L_3$ ), and the Richardson extrapolation criteria have been applied [19].

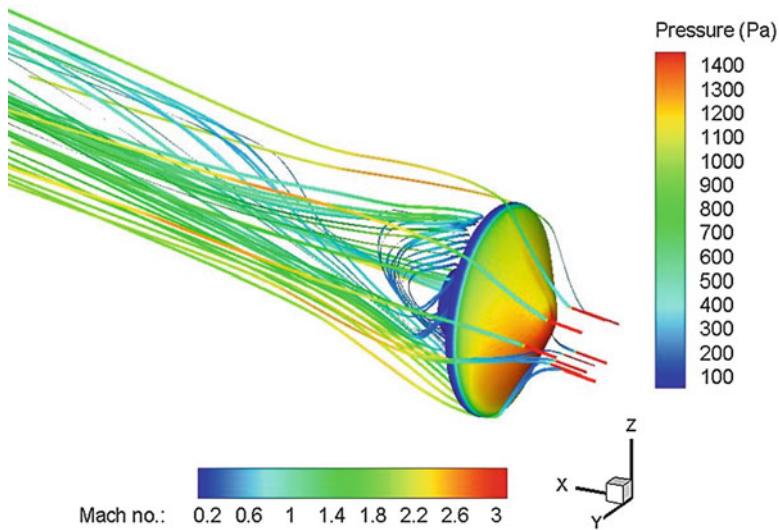
## 7.5 Numerical Results

Example of 3-D numerical analysis can be found in Figs. 7.38 and 7.39. Three-dimensional streamtraces, colored by Mach number, past the capsule at  $M_\infty = 3$  and  $\alpha = 10^\circ$  and pressure distribution on the spacecraft front shield can be found in Fig. 7.38.

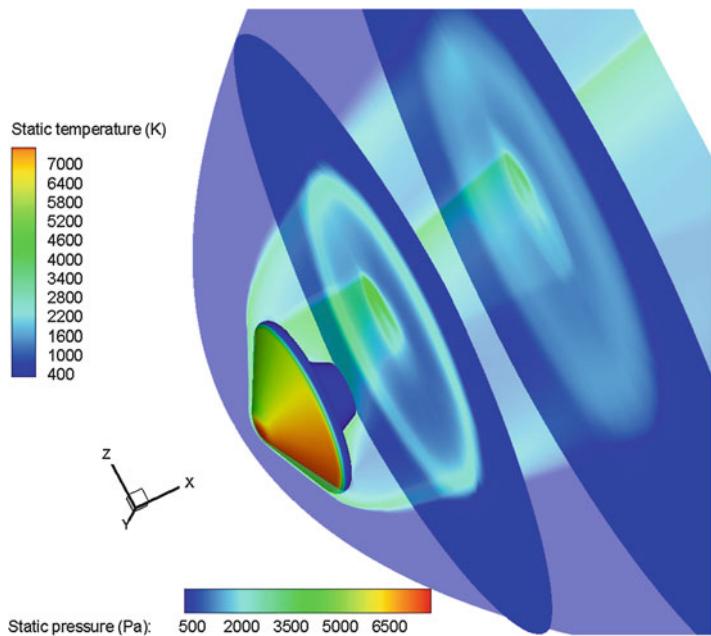
This figure provides very interesting flowfield features as the flow expansion at the capsule shoulder and the complexity of the base flow.

Figure 7.39 reports on the flowfield predicted around the SRV at  $M_\infty = 22.07$  and  $10^\circ$  AoA. In particular, the figure shows the temperature contours provided on the capsule pitch plane and two flowfield cross sections.

The pressure distribution over the SRV forebody is also provided. As shown, the maximum flowfield temperature is close to about 7,000 K since, due to the high Mach number, thermochemical processes occur behind the bow shock as



**Fig. 7.38** 3-D streamtraces past SRV, colored by Mach, and pressure field on heat shield at  $M_\infty = 3$  and  $\alpha = 10^\circ$



**Fig. 7.39** Static temperature field on SRV pitch plane and on two cross sections at  $M_\infty = 22.07$  and  $\alpha = 10^\circ$

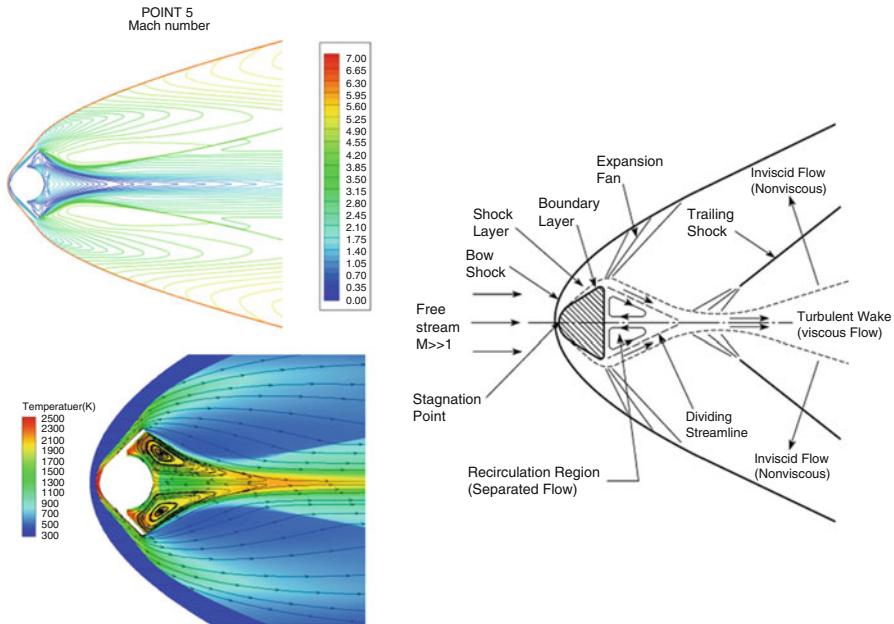


**Fig. 7.40** Mach number and static temperature contours at M5 design point. Characteristics of hypersonic flow around a blunt body (*right side*)

species' vibrational excitation and dissociation, as discussed hereinafter. As shown in Fig. 7.39, at hypersonic speed, the flowfield is dominated by a strong bow shock and is characterized by all the typical hypersonic flowfield features such as shock waves very close to the body surface (i.e., thin shock layer), thick boundary layers, high temperatures, and aerodynamic coefficients that can be nonlinear functions of angle of attack, etc. [6–8, 11].

Example of 2-D flowfield analysis can be found in Fig. 7.40, where Mach number and static temperature contours are provided at M5 design point.

Figure 7.40 also shows, on the right side, the characteristics of hypersonic flow around a blunt body, provided by literature as a reference [12]. As one can see, present CFD result is characterized by all the typical hypersonic flowfield features. As one sees, numerical results in the figure highlight a strong bow shock in front of the capsule well resolved by the adopted spatial discretization. This strong shock wave causes a sonic region at stagnation point.

Indeed, the flow crossing the bow shock suddenly decelerates thus increasing the pressure and temperature in the shock layer close to the stagnation region. The high angle of cone after the rounded stagnation region (equal to 45°) causes the curvature of the shock wave and, therefore, the presence of an entropy layer that affects the results at the wall.

A smooth conical flow along the SRV conical part and a strong flow expansion at the shoulder can be also found.

Streamlines are also shown in Fig. 7.40 in order to appreciate the flowfield structure surrounding the SRV capsule, especially the complexity of the wake flow. A strong base expansion together with a vortex feature can be appreciated as well.

In particular, at the rearward facing the base of the SRV, the flow separates and creates a region of recirculating flow bounded by dividing streamlines. In fact, it is clearly shown that the shear layer that starting from the SRV shoulder separates the recirculating zone and converges on the capsule axis, undergoing normal shock at the neck of this flow to redirect in the direction of the farfield. Hence, from neck flow, it develops an oblique trailing shock wave, ultimately forming a viscous core or inner wake. Fluid in the inviscid wake crosses the trailing shock, increasing pressure, temperature, and density thereby, and in continuing downstream, this outer wake merges with the inner wake.

The Mach number and the static temperature fields past the SRV at M4 design point are shown in Fig. 7.41. It highlights a very strong shock wave in front of a re-entering SRV. As a consequence, the air crossing the bow shock is suddenly heated thus reaching a temperature of the order of 8,000 K.

Illustrated in Fig. 7.41 is also the presence of a rapid expansion as the highly compressed gas flows around the shoulder of the vehicle. This expansion, dominated by inviscid effects, determines the rapid lowering of the gas translational temperature, density, and pressure, while the flow chemical state and temperatures, which characterize the energy in the internal modes, tend to remain frozen and the gas is still dissociated and excited (see Fig. 7.42, where contours of vibrational temperature for O<sub>2</sub> and N<sub>2</sub> at this design point are provided). This aspect is important by capsule aeroheating point of view.

In fact, as the gas flows downstream, because recombination occurs slowly, the vibrational temperature rises still higher with the consequence that the gas can radiate significantly in the afterbody region.

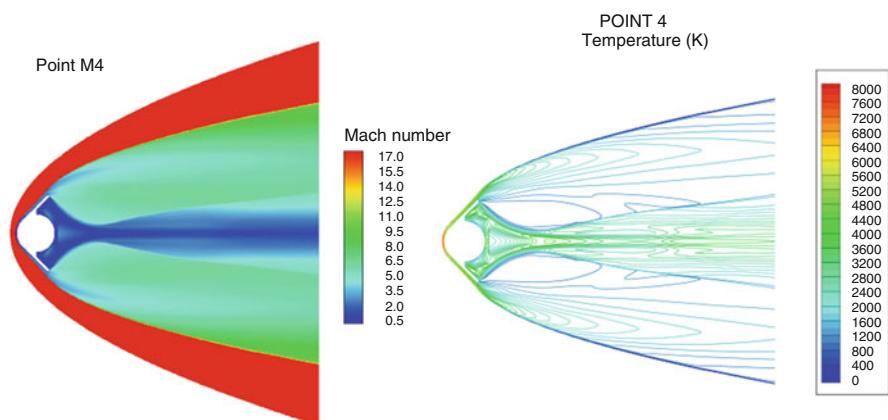


**Fig. 7.41** Mach number and static temperature [K] contours at M4 design point

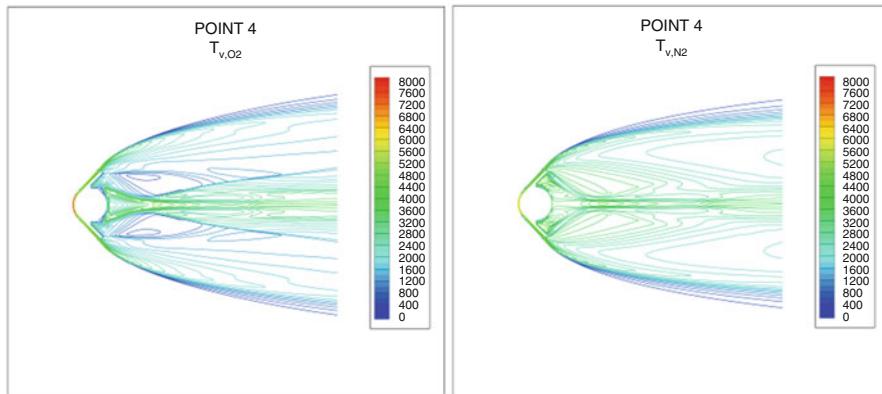
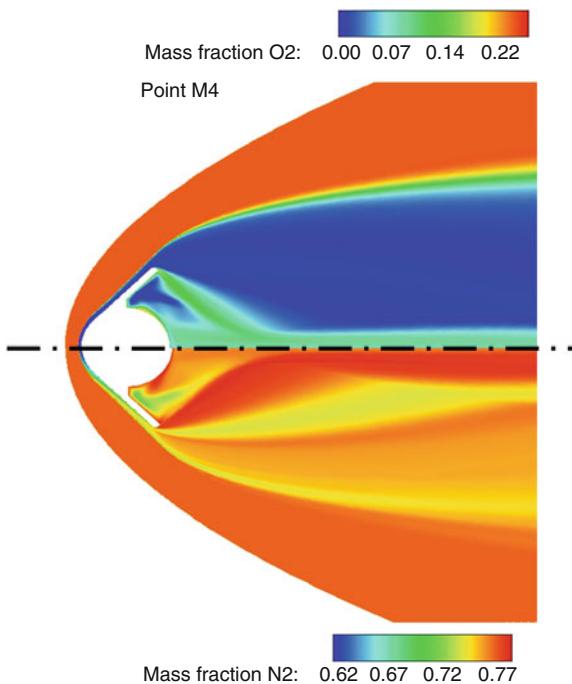


**Fig. 7.42**  $O_2$  and  $N_2$  vibrational temperatures at M4 design point

**Fig. 7.43** Species mass fractions contour field at M4 design point



The  $O_2$  and  $N_2$  mass fractions contours past the SRV at M4 TP are shown in Fig. 7.43 (e.g., axisymmetric 2-D computations, whole domain).

At this flight conditions, the free-stream Mach number is equal to 17.61. Therefore, the air crossing the bow shock is suddenly heated and converted in a reacting mixture. As one can see, at these flight conditions, the oxygen completely dissociates while nitrogen starts to dissociate.

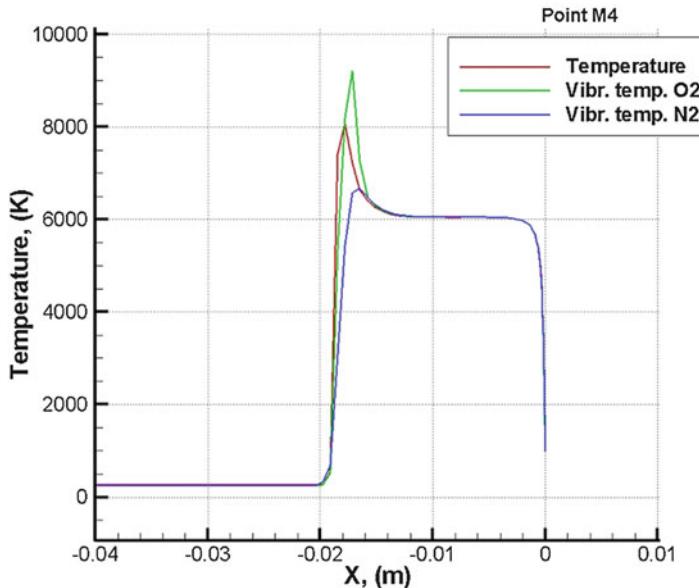


**Fig. 7.44** Temperature profiles along with SRV stagnation line at M4 design point

A comparison among translational and vibrational temperatures is reported in Fig. 7.44 for the CFD design point M4.

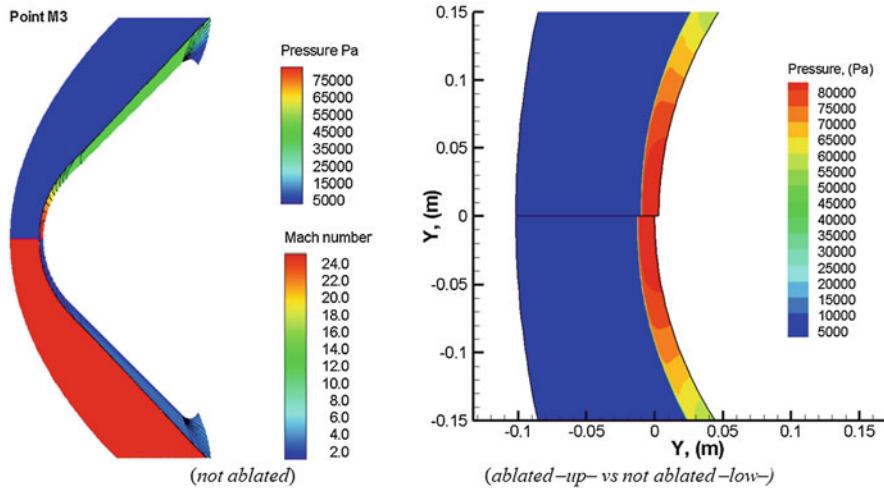
As shown, the vibrational temperature profiles show that the thermal nonequilibrium region extends only close to the shock region. In fact, even if  $T_v$  increases much more slowly since it is density dependent, the two temperatures ( $T$ ,  $T_v$ ) are nearly equilibrated throughout the shock layer.

Pressure and Mach number contours at M3 design point are shown in Fig. 7.45, where the comparisons between ablated and not ablated aeroshape at M3 design point are reported. As shown, the shock layer is very narrow, as expected, and no differences apply between not ablated and ablated aeroshape, as also suggested by Fig. 7.46.

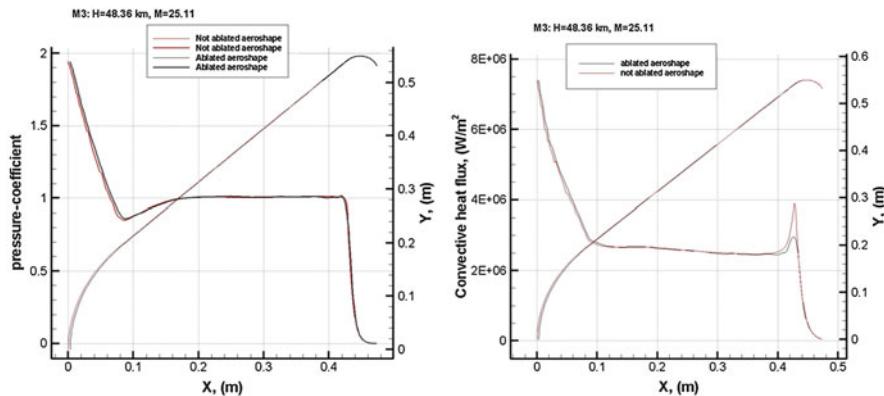
Figure 7.46 shows that centerline profiles of  $C_p$  and convective heat flux do not change significantly passing from not ablated to ablated aeroshape. Indeed, at the nose and along with the SRV conical part, the heat flux profile is quite the same for both aeroshapes. Difference arises only at the shoulder where the heat flux decreases in the case of ablated heat shield (larger local radius of curvature of the shoulder).

Figure 7.47 shows the static pressure and Mach number front shield fields at M1 flight conditions.

As shown, a very strong shock wave is generated in front the capsule due to the very high Mach number (i.e.,  $M_\infty = 34.45$ ). Indeed, as the capsule enters into the Earth's atmosphere directly from the hyperbolic Earth return trajectory, the atmospheric entry speed of SRV is over 12 km/s.



**Fig. 7.45** Pressure and Mach number contours at M3 design point. Comparison between ablated and not ablated aeroshape



**Fig. 7.46**  $C_p$  and heat flux comparison between ablated and not ablated aeroshape at M3 design point without mass blowing effects

As a consequence, a large contribution to vehicle aeroheating comes from the radiative heating of the plasma flow within the shock layer. This can be taken into account for the SRV TPS design. Such a strong shock causes molecules of the atmosphere to be dissociated and ionized, and consequently, the gas in the shock layer consists of molecules, atoms, ions, and electrons. Pressure and temperature (i.e., translational and vibrational ones) distributions along with the capsule's stagnation line when the SRV is flying at M1 trajectory point are given in Figs. 7.48 and 7.49, respectively.

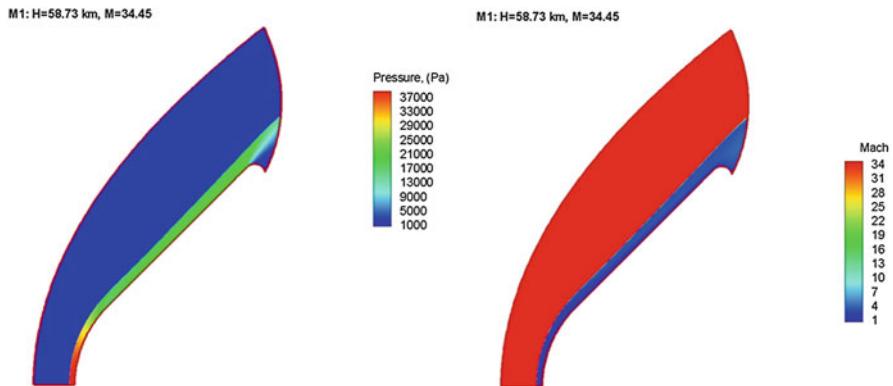


**Fig. 7.47** Static pressure and Mach flowfields past SRV at M1 design point

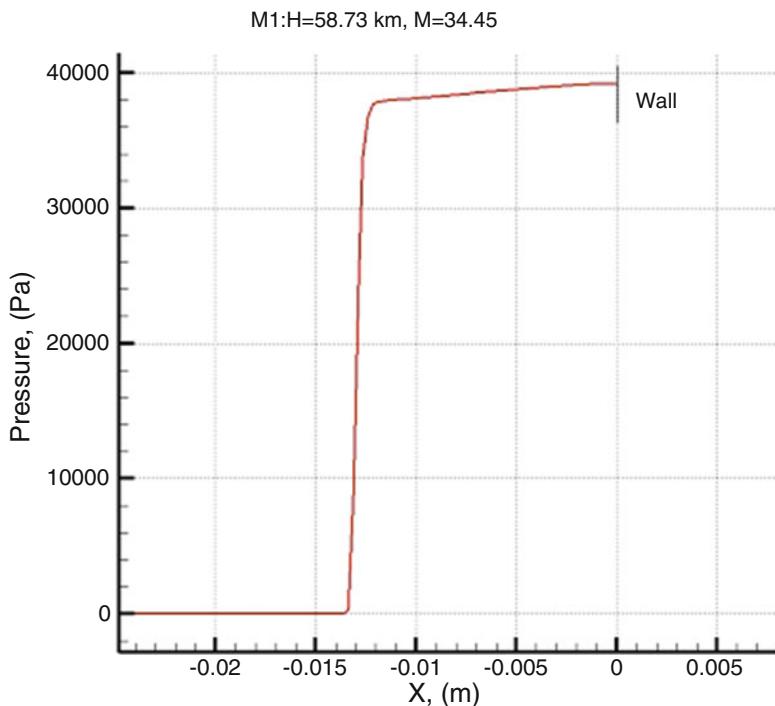


**Fig. 7.48** Static pressure along with the stagnation line at M1 design point

As one can see, pressure suddenly increases as flow crosses the bow shock passing from 26.49 Pa, at free-stream conditions, to about 40 kPa, at the SRV stagnation point. On the other hand, the temperature behind the bow shock is very high thus causing complete oxygen and nitrogen dissociation inside the shock layer,

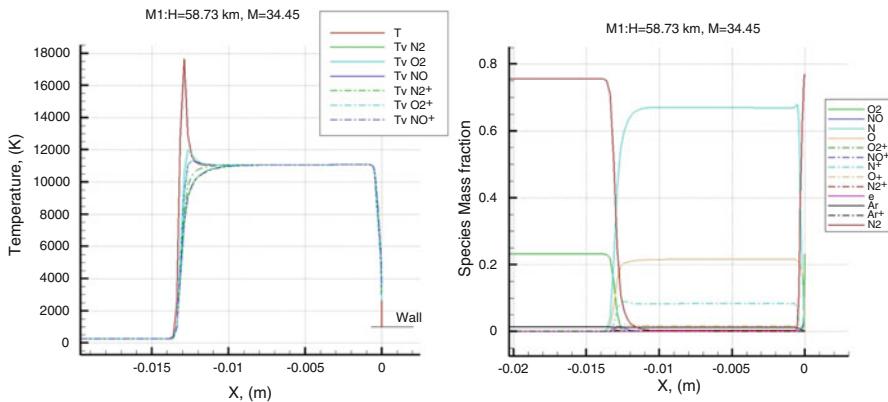


**Fig. 7.49** Temperature and species mass fraction along with the stagnation line at M1 design point

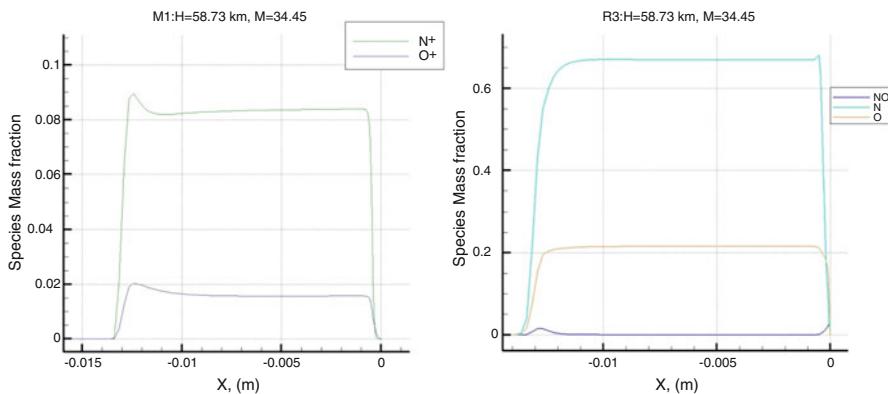


**Fig. 7.50** Species mass fractions along with the stagnation line at M1/R3 design point

as shown in the right side of Fig. 7.49. Here, the distributions of the mass fraction of the neutral and ionized species along with the stagnation line are reported. This figure points out that  $N_2$  and  $O_2$  molecules dissociate rapidly, and successively, the generation of  $NO$  molecule, the atomic nitrogen and oxygen, and the ionization of the molecules such as  $N_2$ ,  $O_2$ , and  $NO$  occur in the thermal nonequilibrium region. In general, the level of each formed species reaches a state of near chemical equilibrium for a large portion of the shock layer. Then, at the edge of the boundary layer, the levels of the species start to change rapidly again as the temperature falls and the density rises through the boundary layer:  $N$  and  $O$  recombine to their molecular forms resulting in an increase in the levels of  $N_2$  and  $O_2$  and a fall in the levels of  $N$  and  $O$ . The reason for this is that the ionized species recombine with the electrons to form neutral species of  $N$ ,  $O$ ,  $N_2$  and  $O_2$ , and  $NO$ , as shown in Fig. 7.50.

In particular, Figs. 7.49 and 7.50 illustrate also that a large portion of the shock layer is in thermochemical equilibrium (i.e., the temperature profiles are quite flat until the boundary layer is reached) and only near the shock and in the boundary layer there is a departure from this state: the nonequilibrium region is just downstream the bow shock wave, and the size is of the order of the shock-wave thickness. In fact, even if  $T_v$  increases much more slowly since it is density dependent, the two temperatures ( $T, T_v$ ) are nearly equilibrated throughout the shock layer.

Moreover, the temperature trends exhibit a sharp discontinuity at the shock wave with a rapid decrease behind the bow shock due to finite rate chemical reactions. For instance, the translational–rotational temperature,  $T$ , reaches the maximum value at about  $x = 14$  mm, while the vibrational–electronic temperature,  $T_v$ , is still much lower than  $T$ .  $T_v$  begins to be equilibrated around  $x = 10$  mm and continues to be equilibrated until the surface. On the contrary, the thermal nonequilibrium is observed at the region adjacent to the equilibrium one, i.e., from  $x = 14$  mm to 10 mm. The equilibrated temperature amounts up to about 11,000 K. Concerning the ionic species, there are substantial levels of  $O^+$  and  $N^+$ , while the mass fractions of  $N_2^+$ ,  $O_2^+$  and  $NO^+$  are very low. In fact, crossing the shock,  $O_2$  is rapidly and highly dissociated to form  $O$  and  $O^+$ .  $N_2$  is dissociated to form  $N$  and  $NO$  by recombination with  $O$ , but a small fraction of  $NO$  is created. A large part of the atomic nitrogen produced by the dissociation of  $N_2$  is ionized in  $N^+$ . Figure 7.50 shows that the mass fractions of  $N^+$  and  $O^+$  amount up to around 0.085 and 0.015, respectively. Note that the ionization process is very important considering that it has a non-negligible impact on radiative heat flux at high-velocity flight conditions.

The prediction of the forebody pressure distribution at each R design point is shown in Fig. 7.51, where the translational temperature along with the capsule stagnation streamline is also reported (right side).

This figure (left side) illustrates that pressure distributions (and thus aerodynamic forces) are affected by the sonic character of the shock layer. When supersonic, the

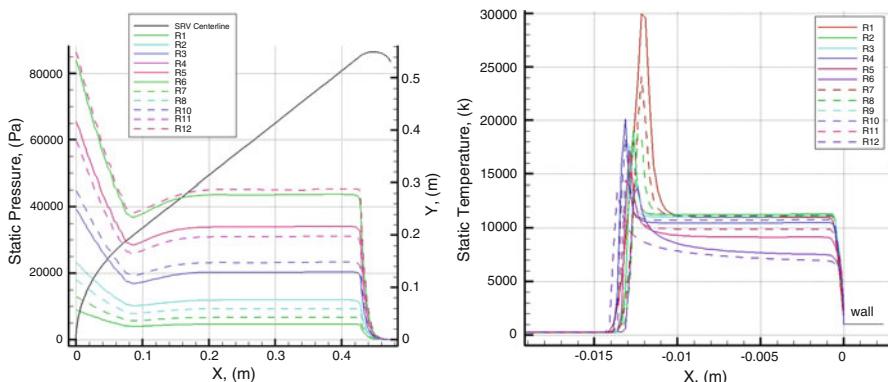


**Fig. 7.51** Pressure and temperature results comparison for R1 to R12 design points

pressure distributions on the conical flank are flat, which is characteristic of conical flow; when the entire forebody shock layer is subsonic, the elliptic nature of that flow results in higher, more rounded distributions.

Moreover, the effect of local entropy values is also clearly shown. Indeed, the entropy layer swallowing, due to the curvature of the bow shock, decreases pressure at the sphere-cone junction. After that pressure increases up to reach quite a constant value at the conical skirt.

Figure 7.51 (right side) points out also that the temperature profiles feature a sharp discontinuity at the bow shock wave with a rapid decrease behind the shock due to finite rate dissociation of the molecules (i.e., finite rate chemistry). Further, a large portion of the shock layer is in thermochemical equilibrium, and only near the shock there is a departure from this state. In particular, the nonequilibrium region is just downstream the bow shock wave. Therefore, the shock layer changes along the descent flight due to real gas phenomena, as expected. Note that the maximum temperature of 30,000 K is attained just downstream the bow shock that takes place when the SRV is flying at  $M_\infty = 41.54$  at 71.86 km altitude (i.e., point R1). In fact, at this trajectory point, the capsule features the maximum internal energy (i.e., kinetic plus potential). This huge mechanical energy converts into thermal energy when flow crosses the bow shock.

As far as SRV aeroheating (without accounting for heat shield ablation) is concerned, heat flux distributions at capsule front shield centerline for flight conditions ranging from R1 to R6 are shown in Fig. 7.52.

Results refer to convective and radiative heat fluxes at the wall. The latter one has been computed with PARADE with the density, the molar fractions, and the two temperatures (translational and vibrational) of all the R design points coming from CFD simulations. As shown, Fig. 7.52 highlights that the maximum radiative heat flux is equal to about 6 MW/m<sup>2</sup> and is reached at the R3/M1 flight conditions (i.e.,  $H_\infty = 58.73$  km altitude and  $M_\infty = 34.45$ ). The convective peak heating reaches 8.5 MW/m<sup>2</sup>, and it is attained at R5/M2 design points (i.e.,  $H_\infty = 52.05$  km altitude and  $M_\infty = 29.12$ ). Anyway, the maximum total heat flux is equal to about 12.5 MW/m<sup>2</sup>, and it arises when the SRV is flying at  $H_\infty = 58.73$  km altitude and  $M_\infty = 34.45$  (i.e., R3/M1 design points). Therefore, plasma radiation is an additional contribution to surface aeroheating that must be taken into account in designing the SRV thermal protection system. In particular, the generic convective heat flux profile in Fig. 7.52 highlights that after the peak at the stagnation point, the heat flux decreases along with the surface as the boundary layer develops up to an inflection point that corresponds to the end of the spherical shape of the capsule. Hence, it continues to decrease along with the conical part with a different shape, and then, it increases near the shoulder due to the local small radius of curvature and to the expansion that causes a reduction of the boundary-layer thickness.

Radiative heat flux profiles for the remaining R7 to R12 cases are quite the same as those of R1 to R6 reported in Fig. 7.52 and, therefore, are not reported for brevity.

The skin friction coefficient ( $C_f$ ) over the SRV centerline is summarized in Fig. 7.53 for several TPs. As shown, the peak of  $C_f$  is confirmed at the shoulder where the boundary layer is extremely thin due to flow rotation around it.

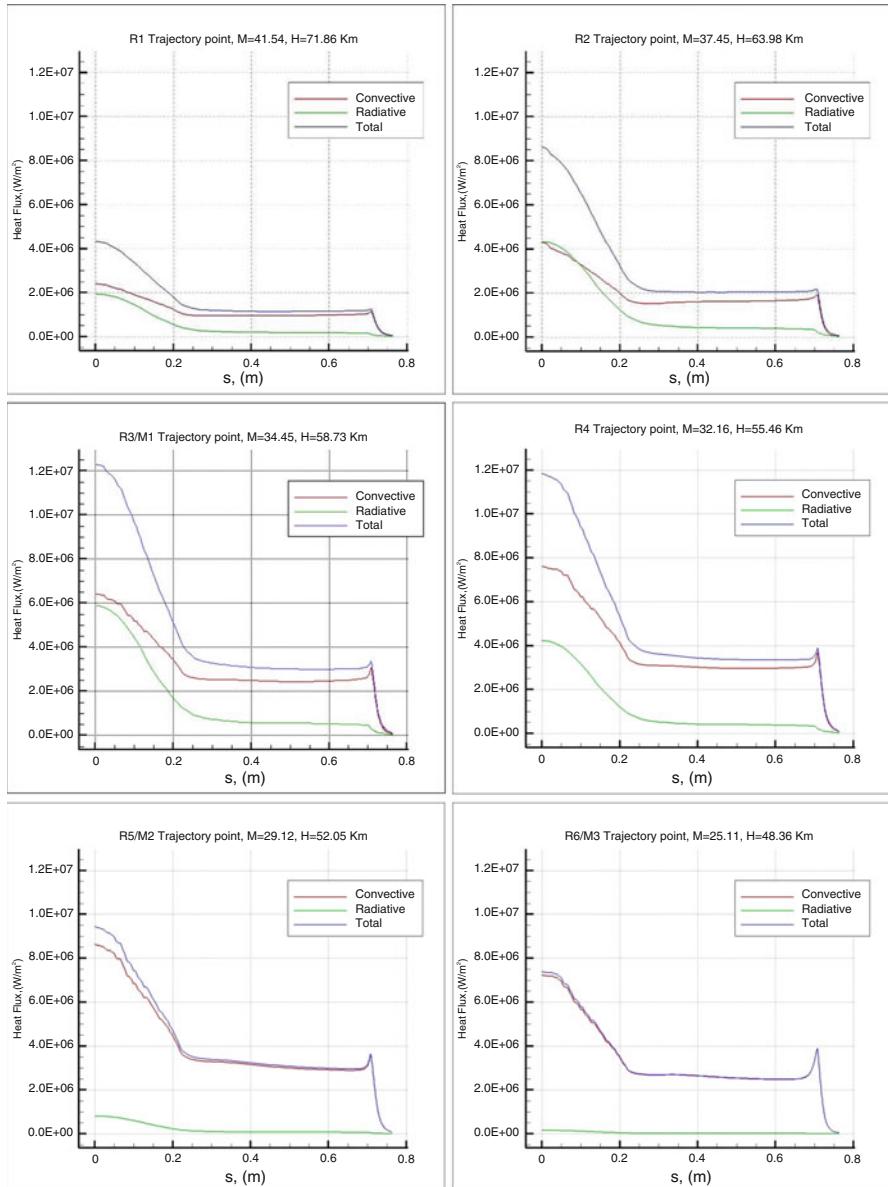


**Fig. 7.52** Convective and radiative heat fluxes comparison for R1–R6 design points

The discussion of the flowfield features given previously for the non-ablating case is largely appropriate also for the flowfield analysis with mass blowing. This task deals with eight NS in 2-D axisymmetric configuration and aims to address the impact of the flowfield contamination by TPM chemical species coming from

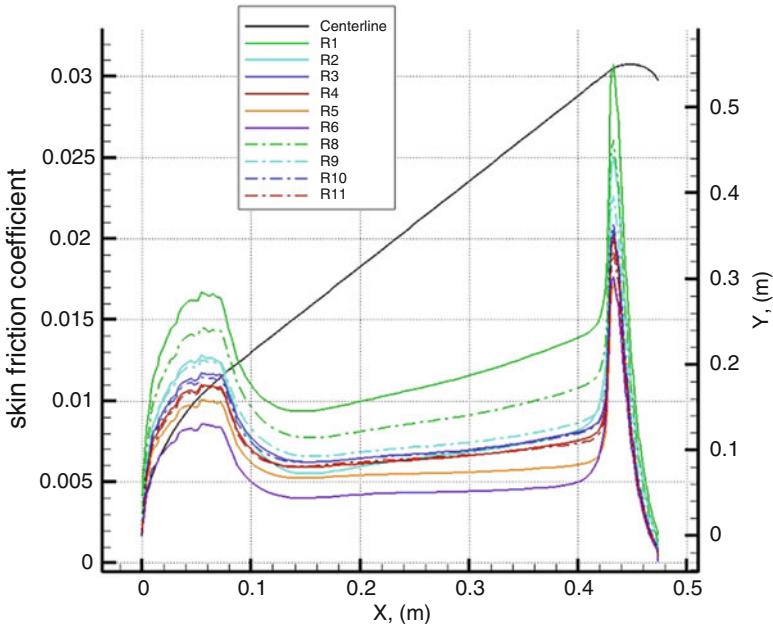


**Fig. 7.53** Skin friction coefficient for several R trajectory points

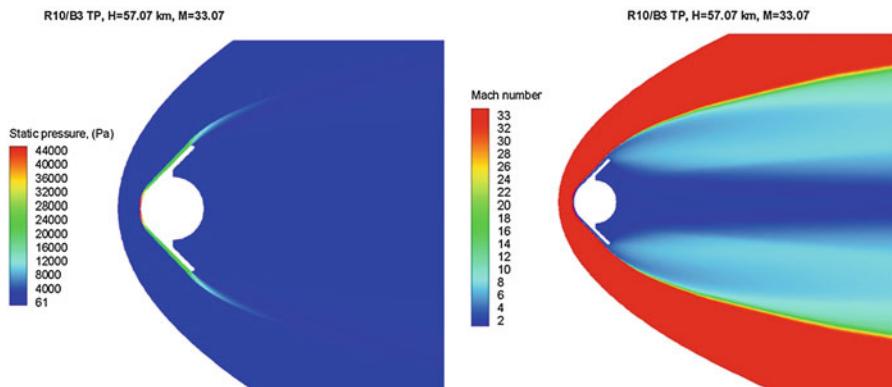


**Fig. 7.54** Mach number and static pressure contours field at R10/B3 TP

the heat shield recession on capsule aerothermal performances. The gas model to consider is air (32 species) in thermochemical nonequilibrium conditions. For example, the Mach number and static pressure fields past the SRV front shield at R10/B3 design point (i.e.,  $H_\infty = 57.07$  km altitude and  $M_\infty = 33.07$  at which occurs the maximum stagnation-point total mass blow rate) are recognized in Fig. 7.54.

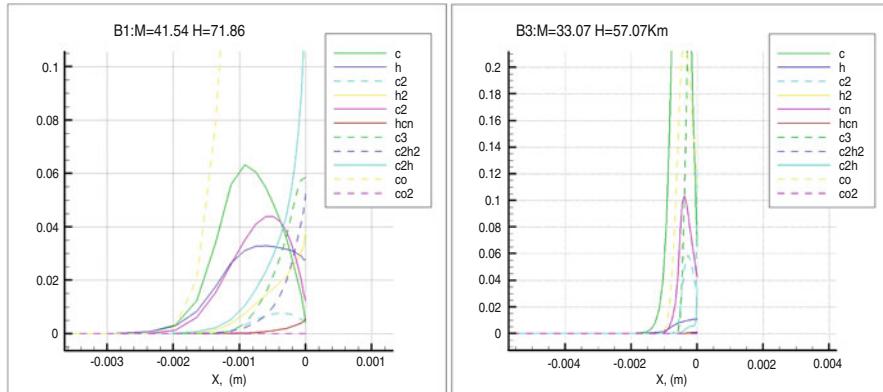


**Fig. 7.55** Ablation products on the stagnation streamline at R1/B1 and R10/B3 TP

The boundary layer, however, is significantly different with respect to the non-ablating cases [19]. Indeed, the species produced by blowing along the stagnation streamline at R1/B1 and R10/B3 design points are plotted in Fig. 7.55.

The level of all air species falls as the wall is approached, and the presence of the blown gases becomes more dominant. Moreover, it is evident from the profiles that some of the ablation products are undergoing chemical change, and it is interesting to note that although most of the ablation products are restricted to the boundary layer, there is a significant level of some of these products, specifically C, at positions slightly beyond the edge of the boundary layer. The ablation products in the boundary layer mainly consist of H<sub>2</sub>, C<sub>2</sub>H, C<sub>2</sub>H<sub>2</sub>, CO, C, and H [19]. In particular, the level of C<sub>3</sub> falls rapidly as the distance from the body increases, because it dissociates to form C<sub>2</sub> and C and also indirectly leads to the formation of CN and HCN. However, the rise in the level of C in the boundary layer is mainly attributable to the dissociation of CO. The relatively slow rate at which the level of H falls with increasing distance from the wall suggests that either H<sub>2</sub> or alternatively some of the hydrocarbons present are dissociating [19].

Figures 7.56 and 7.57 highlight C<sub>2</sub> and C<sub>3</sub> and C and CO mass fractions field past the SRV, respectively.

Note that the determination of the distribution of the products of the ablation process within the shock layer is very important since species such as C<sub>2</sub>, C<sub>3</sub>, and also CO have strong radiative properties. In particular, C<sub>2</sub> and C<sub>3</sub> possess absorption properties while CO is a strong radiator.

Finally, the comparison of the convective heat flux at SRV centerline for all B trajectory points is shown in Fig. 7.58.

As one can see, heat shield ablation mitigates the convective heat fluxes the capsule has to withstand during descent, as expected. For instance, the maximum convective heat flux lowers from 8.5 MW/m<sup>2</sup> to 4 MW/m<sup>2</sup> when ablation is turned on in the numerical CFD computations. Heat shield ablation reduces the surface gradients of the temperature and that of various species mass fractions, thus causing

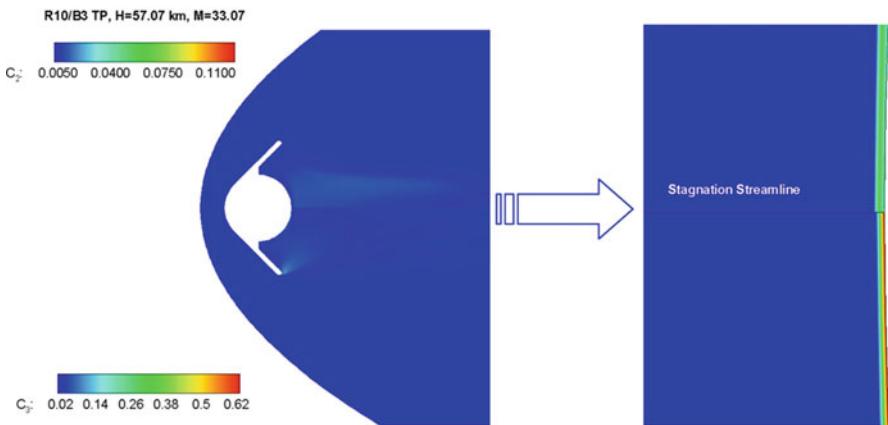


**Fig. 7.56**  $C_2$  and  $C_3$  mass fractions at R10/B3 design point

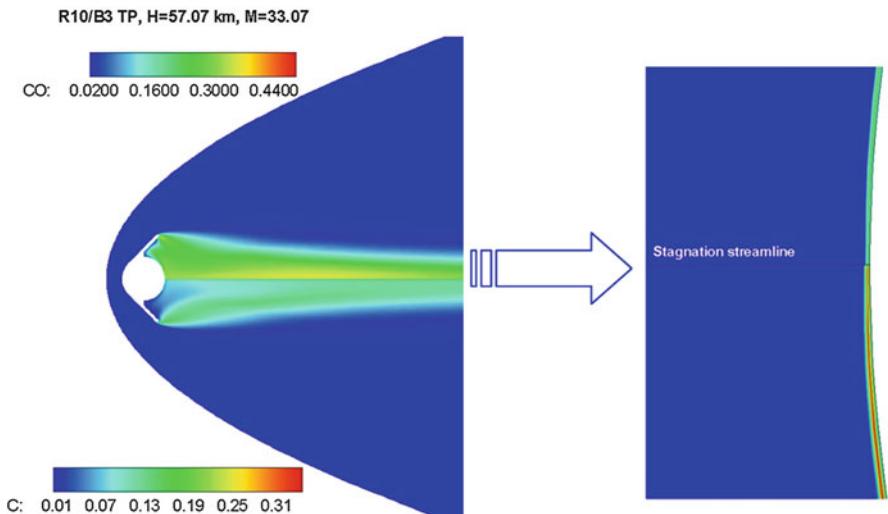


**Fig. 7.57** C and CO mass fractions at R10/B3 design point

a decrease of convective and diffusive heat fluxes [14]. Furthermore, CO, one of the main ablation products (for carbon-based materials), lowers significantly the wall enthalpy.

On the other hand, flowfield contamination by chemical species coming from heat shield recession is expected to provide a blocking effect also on radiative heat flux and increase ionization (design issues not addressed in the present research effort).

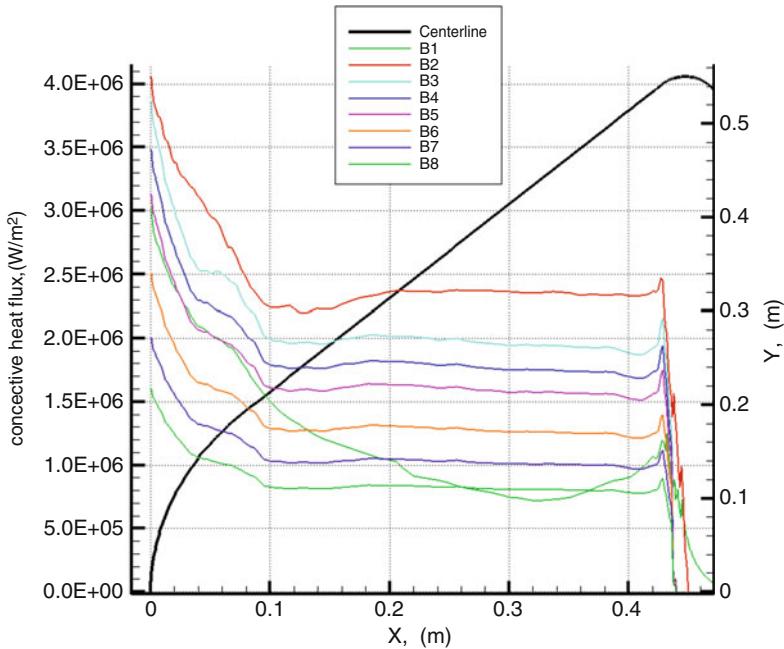


**Fig. 7.58** Convective heat flux at SRV centerline for all B TPs

## 7.6 SRV Aerodynamics

As far as capsule aerodynamics is concerned, a summary review of SRV lift ( $C_L$ ), drag ( $C_D$ ), and pitching moment ( $C_m$ ) coefficients (only drag in CFD analysis) is recognized both for engineering-based and CFD-based approaches, respectively.

Aerodynamic coefficients are calculated considering  $S_{\text{ref}} = 0.95 \text{ m}^2$  (i.e., maximum SRV cross-sectional area),  $L_{\text{ref}} = 1.1 \text{ m}$  (i.e., maximum SRV diameter), and pole at center of gravity, according to the following equations:

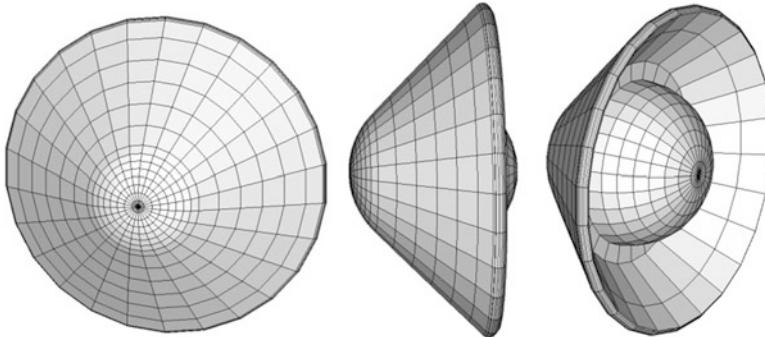
$$C_L = \frac{L}{\frac{1}{2}\rho_\infty v_\infty^2 S_{\text{ref}}}$$

$$C_D = \frac{D}{\frac{1}{2}\rho_\infty v_\infty^2 S_{\text{ref}}}$$

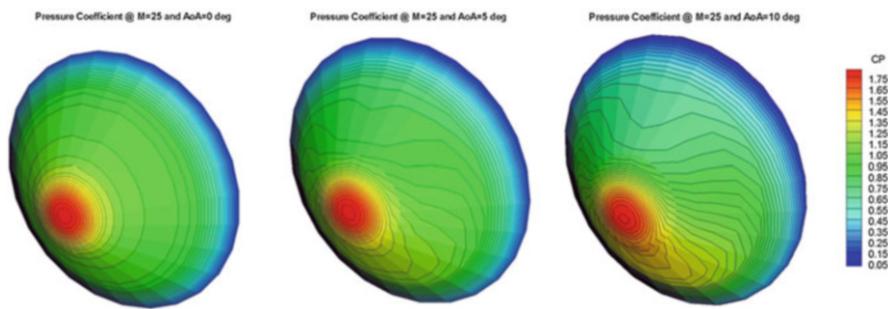
$$C_m = \frac{M_y}{\frac{1}{2}\rho_\infty v_\infty^2 L_{\text{ref}} S_{\text{ref}}}$$

Figure 7.59 shows a typical mesh surface of SRV that has been used for the engineering-level computations.

Analysis has been performed also in FMF conditions.



**Fig. 7.59** SRV panel mesh



**Fig. 7.60** Pressure coefficient at  $M_{\infty} = 25$  and  $\text{AoA} = 0, 5^\circ$ , and  $10^\circ$

### 7.6.1 Engineering-Based Aerodynamic Results of SRV

Analysis has been performed on the whole Mach number profile of re-entry up to  $M_{\infty} = 3$ .

In continuum flow conditions, SRV aerodynamic relies on Prandtl–Meyer expansion flow and modified Newtonian theories [10]. As an example of engineering-level results, the static pressure distributions over the wetted vehicle surface for  $M_{\infty} = 25$  and for three different angles of attack, namely, 0, 5, and  $10^\circ$ , are summarized in Fig. 7.60.

As shown, the surface pressure distribution on the capsule windsides changes as the AoA increases. At the same time, flow expansion on the capsule leeside determines locally lower-pressure contours.

The lift, drag, and pitching moment coefficients for AoA ranging from 0 to  $180^\circ$ , in free molecular (at  $M_{\infty} = 10.3$ ) and hypersonic continuum (at  $M_{\infty} = 25$ ) flow conditions, are summarized in Figs. 7.61 and 7.62, respectively. As one can see, capsule aerodynamic features a nonlinear behavior, typical of high-speed flow regime. In particular, lift coefficient nulls at zero degree AoA, as expected being

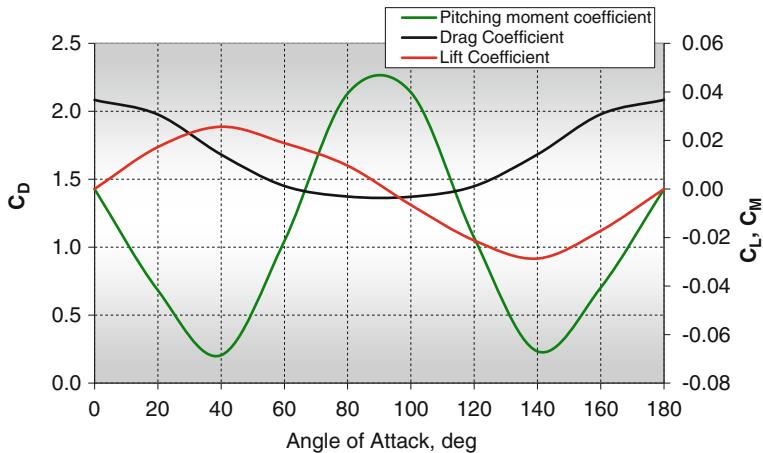


**Fig. 7.61** Lift, drag, and pitching moment coefficients of SRV at  $M_\infty = 10.3$  and  $H_\infty = 200$  km (FMF)

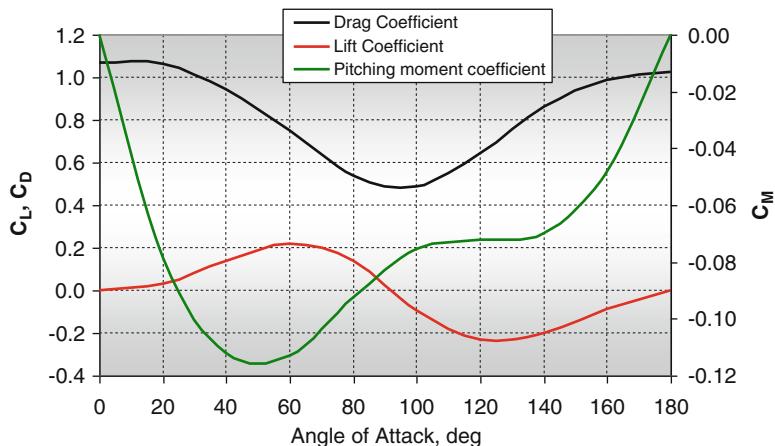


**Fig. 7.62** Lift, drag, and pitching moment coefficients of SRV at  $M_\infty = 25$

SRV a symmetric aeroshape. In rarefied flow regime, it is essentially negligible for  $0 < \alpha < 180^\circ$ , while in continuum flow,  $C_L$  reaches 0.2 at  $\alpha = 60^\circ$ . Therefore, a lifting re-entry can be envisaged for this kind of mission, in contrast with classical ballistic flight, provided that the aeroshape can fly at AoA in static stability condition.

On the other hand, the maximum drag coefficient in both regimes is of order one, and it is attained at  $\alpha = 0$  and  $180^\circ$ . Of course, the latter AoA does not work considering the TPS layout and capsule static instability at this angle.

Trim analysis of SRV in free molecular flow highlights that the capsule features four trim angles of attack (i.e., where the pitching moment at the center of gravity

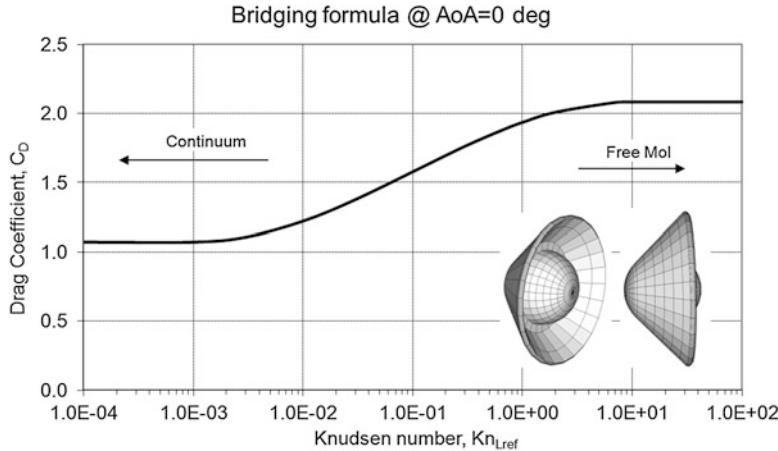


**Fig. 7.63** Drag coefficient of SRV in transitional flow conditions

is equal to zero; see green curve in Fig. 7.61), namely,  $\alpha = 0, 65, 112$ , and  $180^\circ$ . However, the sign of  $C_{m\alpha}$  points out that only  $\alpha = 0$  and  $112^\circ$  are static stability pitch trim AoA.

As illustrated in Fig. 7.62, the chosen aeroshape in continuum hypersonic flow has two trim angles of attack (i.e.,  $C_m = 0$  at  $\text{AoA} = 0^\circ$  and  $180^\circ$ ). But for the  $180^\circ$  AoA, the slope of the pitching coefficient ( $C_{m\alpha}$ ) is positive, and consequently, the aeroshape has only one single static stable position for  $\text{AoA} = 0^\circ$ . This trim AoA ensures that the probe will not flip over and depart from the expected re-entry in hypersonic regime.

SRV drag profile in transitional flow conditions is summarized in Fig. 7.63.

As one can see, the drag profile vs. Knudsen features the classical expected S-shape and, ranging from rarefied to continuum flow conditions, points out that  $C_D$  passes from about 2 to 1.

Results provided for aerodynamic drag in continuum flow agree with the analytical results available for blunt cone at hypersonic speed. Indeed, for a blunt cone with a semivertex angle  $\theta_c$ , nose radius  $R_N$ , and base radius  $R_B$ , the drag coefficient reads [2] (see Chap. 1):

$$C_D = 2\sin^2\theta_c + \left(\frac{R_N}{R_B}\right)^2 \cos^4\theta_c \quad (7.20)$$

The drag coefficient  $C_D$  is shown as a function of bluntness ratio  $R_N/R_B$  and cone-section semivertex angle  $\theta_c$  in Fig. 7.64.

In the present case, the nose-to-base radius ratio is equal to 0.5. Therefore, analytical and engineering-based results compare quite good each other.

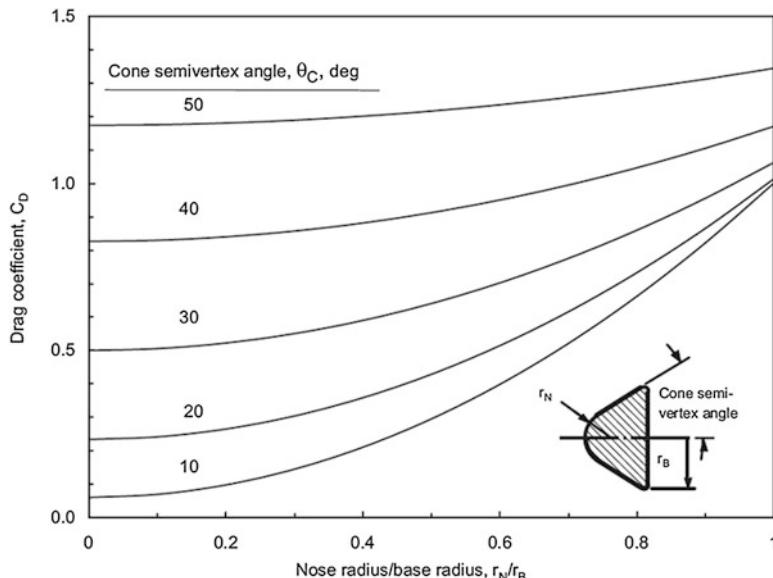


Fig. 7.64 Hypersonic drag coefficient for sphere-cones

### 7.6.2 CFD-Based Aerodynamics of SRV

Capsule drag coefficients have been evaluated for all performed CFD computations, starting from the value of pressure and shear stress at the spacecraft wall.

Comparison among present CFD results and literature data for  $C_D$  in continuum flow conditions is shown in Fig. 7.65 [5].

It presents an approximation of the drag coefficient across the Mach range for the 45-degree half-angle shape. The hypersonic value, 1.07, was computed at Mach 31.8 and 21.5 using the Langley Aerothermodynamic Upwind Relaxation Algorithm (LAURA) [5].

The subsonic value, 0.65, comes from tests conducted in the Langley 20 ft Vertical Spin Tunnel. The supersonic and transonic values are from Brooks and Nichols wind tunnel data on a similar geometry [5].

For the purposes of this feasibility study, the important data are the hypersonic value, which affects the heat pulse, and the subsonic value that determines the impact velocity [5]. The drag coefficients of the present evaluation compare rather well with literature data, especially at very high Mach number flow conditions (i.e., wave drag). Below Mach 7, forebody-only CFD will not accurately predict the aerodynamics.

The calculations must include the afterbody and wake. Therefore, differences are recognized at rather low Mach number. In these cases, the effect of base drag could

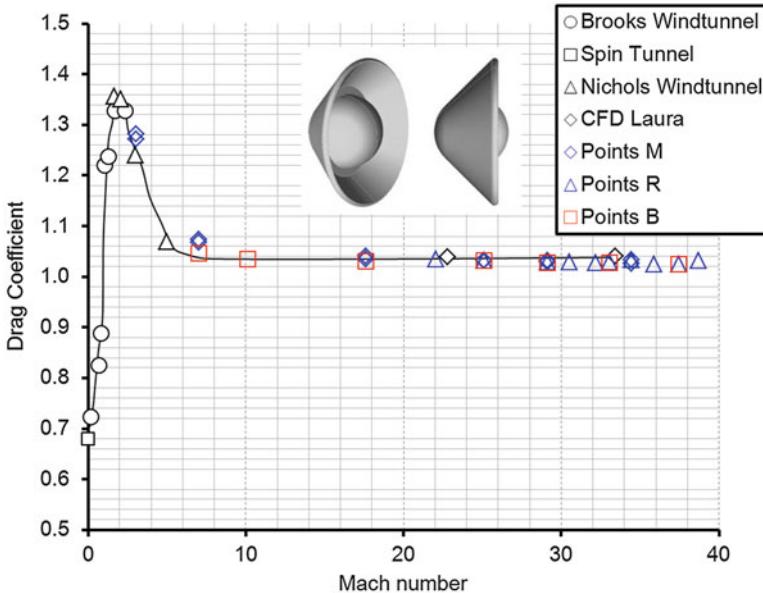


**Fig. 7.65** Drag coefficient of SRV vs. Mach. Comparison between present and literature results

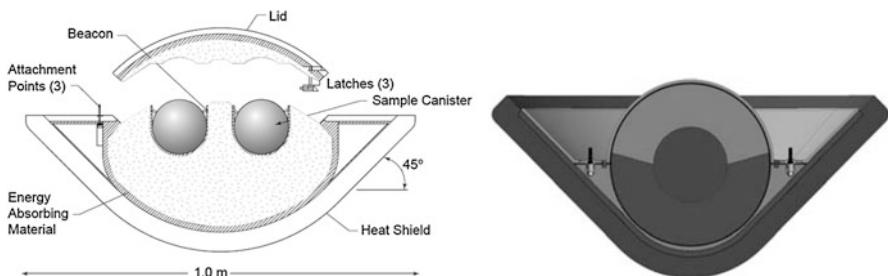


**Fig. 7.66** SRV configuration comparison

come from the differences between the back shell configurations between SRV and the capsule considered in the literature data shown in Fig. 7.66 [5].

## References

1. Preliminary Planning for an International Mars Sample Return Mission Report of the International Mars Architecture for the Return of Samples (iMARS) Working Group June 1, 2008
2. Notes on Earth Atmospheric Entry for Mars Sample Return Missions. NASA/TP-2006-213486. 2006

3. Adler M (2011) Marco Polo-R near earth asteroid sample return mission. In: 8th international planetary probe workshop, 6–10 June 2011, Portsmouth, VA, USA
4. Howe J (1989) Hypervelocity atmospheric flight: real gas flow fields, NASA TM 101055
5. Mitcheltree RA, Kellas S, Dorsey JT, Desai PN, Martin CJ (1998) A passive earth-entry capsule for Mars sample return. In: 51st international astronautics federation congress, Rio de Janeiro, IAF-00-Q.3.04
6. Viviani A, Pezzella G. Computational flowfield analysis of a planetary entry vehicle. In: Numerical simulations – examples and applications in computational fluid dynamics. Published by In-Tech, Kirchengasse 43/3, A-1070 Vienna, Austria. Hosti 80b, 51000 Rijeka, Croatia. ISBN: 978-953-307-153-4
7. Viviani A, Pezzella G (2010) Computational flowfield analysis over a blunt-body reentry vehicle. *J Spacecr Rocket* 47(2):258–270. doi:[10.2514/1.40876](https://doi.org/10.2514/1.40876), ISSN 0022-4650
8. Bertin J (1994) Hypersonic aerothermodynamics, AIAA educational series. American Institute of Aeronautics and Astronautics, Washington, DC
9. Scott CD, Ried RC, Maraia RJ, Li CP, Derry SM (1985) An AOTV aeroheating and thermal protection study. In: Nelson HF (ed) Thermal design of aeroassisted orbital transfer vehicles, vol 96 of Progress in Astronautics and Aeronautics, AIAA, New York, pp 198–229
10. Viviani A, Pezzella G, Golia C (2010) Effects of thermochemical modelling and surface catalyticity on an earth re-entry vehicle. In: Proceedings of the Institution of Mechanical Engineers, Part G. *J Aerosp Eng* 225(5). doi:[10.1177/2041302510392875](https://doi.org/10.1177/2041302510392875), ISSN: 0954–4100 (Print) 2041–3025 (Online). Sage Publications, pp 1–18
11. Anderson J (1989) Hypersonic and high temperature gas dynamics. McGraw-Hill Book Company, New York
12. Viviani A, Pezzella G (2012) Overview of design approach for a sample return capsule. In: 18th AIAA/3AF international space planes and hypersonic systems and technologies conference, 24–28 September 2012, Tours, France, AIAA-2012-5858
13. Project Synthesis Report. RASTAS-AST-D1.3-01, TEA21 n° 052938/10, Ed.1–15 December 2010
14. Pezzella G, Catalano P, Bourgoing A (2012) Computational flowfield analysis of a sample return capsule. In: 18th AIAA/3AF international space planes and hypersonic systems and technologies conference, 24–28 September 2012, Tours, France, AIAA-2012-5818
15. Generic Re-entry Capsule preliminary design, RASTAS-AST-D1.2-01, TEA21 n° 052937/10, Ed.1–15 December 2010
16. Tauber ME, Suttont K (1991) Stagnation-point radiative heating relations for earth and Mars entries. *J Spacecr Rocket* 28(1):40–42
17. PLASMA RADIATION DATABASE PARADE V2.2. Report TR28/96
18. Park C (1993) Review of chemical kinetic problems of future NASA missions: earth entries. *J Thermophys Heat Transf* 7(3):385–398
19. Roberts TP (1995) Modelling gas/surface interaction processes of ablating wall boundaries associated with planetary entry. In: Proceedings of the 2nd European symposium aerothermodynamics for space vehicles, Noordwijk, The Netherlands, 21–25 November 1994, European Space Agency (ESA), Paris, p 311
20. Pezzella G, Buccignani E, Marini M, Ferraris G, Chiarelli C (2009) Computational aero-heating analyses of a capsule in Martian atmosphere. In: 6th European workshop on thermal protection systems and hot structures, 31 March–3 April 2009, University Stuttgart, Germany

# Chapter 8

## Launchers: Present and Future

### 8.1 Introduction

During the development phase, the launchers' needs for aerodynamic characterization are fulfilled by a hybrid approach encompassing wind tunnel testing (WTT) and computational fluid dynamics (CFD) results [1, 2]. The joint use of WTT and CFD is a powerful tool, able to provide high-quality data as input for performance evaluations as well as launcher control and sizing [1].

Aerodynamics for launcher systems focuses on the assessment of the loads the atmosphere determines over the quick moving and accelerating vehicle [2]. These forces are applied through pressure and friction effects on the external launcher surface, thus resulting in a global aerodynamic force and moment [3–5].

The assessment of launcher aerodynamic is fundamental for the determination of the launcher's performances and control software [6]. Indeed, in the motion direction, the aerodynamic drag slows the launcher.

On the other hand, the global aerodynamic force generally does not act at vehicle center of gravity (CoG) location, then the aerodynamic moment exerted at the CoG can lead to stable or unstable behavior of the vector, to account for in the launcher's control software.

Moreover, launcher's structures and protrusions should sustain the aerodynamic loads all along the trajectory. This also should be taken into account in the general loading studies devoted to the launcher sizing.

## 8.2 Launcher Aerodynamic Analysis

### 8.2.1 Aerodynamic Conventions for Launchers

Aerodynamic data for launchers are provided in the body reference frame (BRF) as illustrated in Figs. 8.1 and 8.2 where [1]:

- $V(u, v, w)$  is the CoG speed relative to air
- $O$  is the coordinate system reference point (different from the CoG)
- $X$  is the central revolution body axis: directed from  $O$  to the nose of the launcher
- $Y$  is the transverse axis
- $Z$  is the normal axis built to obtain a direct coordinate system and  $\varphi$  is the roll angle around the  $X$  axis
- $Z_\varphi$  is the transformation of  $Z$  by the  $\varphi$  rotation around  $X$  which contains  $V$
- $\alpha_e$  is the global incidence of the launcher

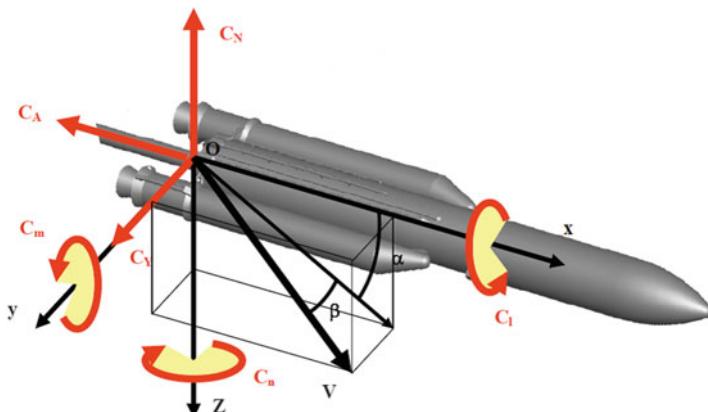


**Fig. 8.1** Conventional body reference frame

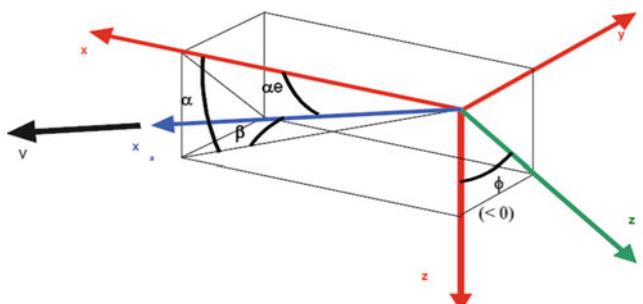


**Fig. 8.2** Rear view of the conventional body reference frame

- $\alpha$  is the angle of attack (i.e., the angle between  $X$  and  $V$  projection in the  $(X, Z)$  plane)
- $\beta$  is the side slip angle (i.e., the angle between  $V$  projection in the  $(X, Z)$  plane and  $V$ )

These conventions come from the ISO norm. 1151 (1988) and are exemplified with Ariane 5 configuration in Fig. 8.1 [1].

It should be noticed that the range of angle of attack is  $-\pi < \alpha < \pi$  with  $\alpha > 0$  if  $w > 0$ , while for the sideslip angle (sometimes also called as yaw angle)  $-\frac{\pi}{2} < \beta < \frac{\pi}{2}$  with  $\beta > 0$  if  $v > 0$ .

The global aerodynamic force  $\vec{F}$  and moment  $\vec{M}$  acting on the launcher are expressed in BRF as follows:

$$\begin{aligned}\vec{F} &= S_{\text{ref}} q_{\infty} (-C_A \hat{i} + C_Y \hat{j} - C_N \hat{k}) \\ \vec{M} &= S_{\text{ref}} L_{\text{ref}} q_{\infty} (C_l \hat{i} + C_m \hat{j} + C_n \hat{k})\end{aligned}\quad (8.1)$$

where:

$C_A$ : axial force coefficient

$C_Y$ : transverse force coefficient

$C_N$ : normal force coefficient

$C_l$ : rolling moment coefficient

$C_m$ : pitching moment coefficient

$C_n$ : yawing moment coefficient

$(\hat{i}, \hat{j}, \hat{k})$  are the reference unit vectors

$S_{\text{ref}}$ : reference surface

$L_{\text{ref}}$ : reference length

$q_{\infty}$ : dynamic pressure

The definition of force and moment coefficients is

$$C_i = \frac{F_i}{\frac{1}{2} \rho_{\infty} V_{\infty}^2 S_{\text{ref}}} \quad i = L, D, Y \quad (8.2)$$

$$C_j = \frac{J}{\frac{1}{2} \rho_{\infty} V_{\infty}^2 L_{\text{ref}} S_{\text{ref}}} \quad j = l, m, n \quad (8.3)$$

with:

$\rho_{\infty}$ : atmospheric density

$V_{\infty}$ : speed relative to air

### 8.2.2 Aerodynamic Coefficients and Vehicle Design

As previously mentioned, aerodynamic coefficients are used at system level for the determination of launcher performances and control as well as for general loading determination.

The launcher control always aims at a null global incidence of the vehicle, except during maneuvers. As a consequence, performances studies use only the axial force coefficient  $C_A$  as the aerodynamic force opposing to the movement [1]. This coefficient should be provided as a function of the Mach number,  $M_\infty$ :

$$C_A = f(M_\infty) \quad (8.4)$$

For the control software which commonly directs the thrust of nozzles in the proper direction, the main aerodynamic parameter is the evaluation of moment at the CoG location. Due to the fact that propellants are continuously consumed along the flight, the CoG location is continuously changing too. As a consequence, aerodynamic moments are provided at a conventional location. For example, for Ariane 5 this location is the main stage nozzle's gimbals point. In flight, given the evaluated location of the CoG, the control software expresses the aerodynamic moment at the CoG with the following expressions:

$$\begin{aligned} \text{In the pitch plane (XOZ)} : \quad A_6 &= \frac{qS_{\text{ref}}}{I} \frac{dC_N}{d\alpha} \left[ X_G - \left( \frac{\frac{dC_m}{d\alpha}}{\frac{dC_N}{d\alpha}} L_{\text{ref}} + X_Q \right) \right] \\ \text{In the yaw plane (XOY)} : \quad A_6 &= \frac{qS_{\text{ref}}}{I} \frac{dC_Y}{d\beta} \left[ X_G - \left( \frac{\frac{dC_n}{d\beta}}{\frac{dC_Y}{d\beta}} L_{\text{ref}} + X_Q \right) \right] \end{aligned} \quad (8.5)$$

The derived aerodynamic coefficients are built from the evolutions of global aerodynamic coefficients (nonlinearized coefficients) as a function of the angle of attack or side slip angle (see Fig. 8.3) [1].

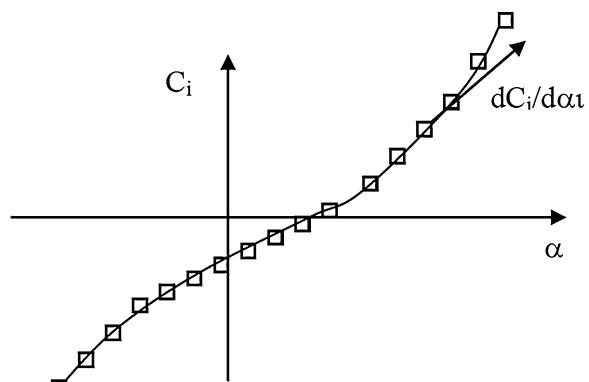
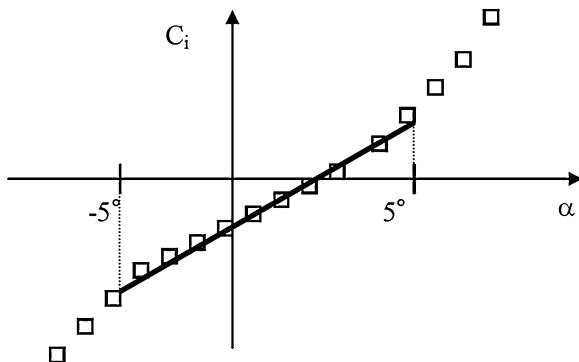


**Fig. 8.3** Example of derived aerodynamic coefficient building

**Fig. 8.4** Example of linear aerodynamic coefficient building



It can be noticed that control software uses also linearized aerodynamic coefficients for frequency analysis, which are determined with the evolution of coefficients in the region of low angle of attack or side slip (see Fig. 8.4). Mean values of global aerodynamic coefficients are used also for temporal analysis in case of wind or gusts. All these formulations should be provided as a function of Mach number.

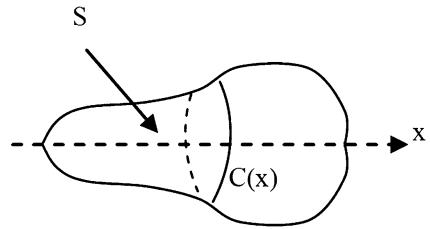
For general loading studies, the main input parameters are the distributed aerodynamic forces and moment coefficients. By distributed coefficients, we mean integration of pressure forces and moments on the surface from the fairing nose down to prescribed body cross sections of interest for general loading studies. Pressure and friction contributions are separated because surface measurements of pressure are easily obtained in wind tunnel testing, whereas friction is not. Moreover, wind tunnel flow conditions are generally not representative of real flight conditions for friction. Indeed, wind tunnel can reproduce the Mach numbers seen in flight on a scaled launcher model, giving access to representative pressure coefficients, but generally cannot reproduce the flight Reynolds number which is necessary to get representative friction contributions. Nevertheless, pressure contributions are the main contributor to the aerodynamic efforts, and generally friction contributions can be neglected except for the axial force. Then the assessment of pressure forces is performed with the following conventions:

For a body-closed external surface, we use the following property (where  $\vec{n}$  is the local normal to  $S$ ):

$$\int_S p_\infty \cdot \vec{n} \, dS = 0 \quad (8.6)$$

Then, the resulting pressure force on the body can be expressed as

$$\vec{F}_p = - \int_S (p - p_\infty) \cdot \vec{n} \, dS \quad (8.7)$$

**Fig. 8.5** Closed body surface

Practically, the integral is computed along cut sections, like  $C$  on Fig. 8.5 [1]:

$$\frac{dC\vec{F}_p}{dx}(x) = -\frac{1}{S_{ref}} \int_{C(x)} C_p \cdot \vec{n} \frac{dS}{dx} dx \quad (8.8)$$

$$\frac{dC\vec{M}_p}{dx}(x) = -\frac{1}{S_{ref}L_{ref}} \int_{C(x)} C_p \cdot \vec{P} \times \vec{n} \frac{dS}{dx} dx \quad (8.9)$$

This finally gives the global force and moment coefficients:

$$C\vec{F}_p = \int_x \frac{dC\vec{F}_p}{dx}(x) dx \quad (8.10)$$

$$C\vec{M}_p = \int_x \frac{dC\vec{M}_p}{dx}(x) dx \quad (8.11)$$

Figure 8.6 gives the example of distributed axial force coefficient obtained along the Ariane 5 booster [1]. The red curve is an integration made thanks to local pressure measurements made in wind tunnel testing, whereas the green curve is obtained in a CFD computation, showing good agreement.

### 8.2.3 Aerodynamic Analysis of Launchers

Classically aerodynamic studies rely on wind tunnel testing and CFD. For launchers the encountered flow regimes begin at null speed on the launch pad and goes up to hypersonic regime in high atmosphere. However, as stated before, aerodynamic studies mainly focus on launcher sizing and control. Then the most sizing part of a launcher trajectory arises when the dynamic pressure is high. As it can be seen

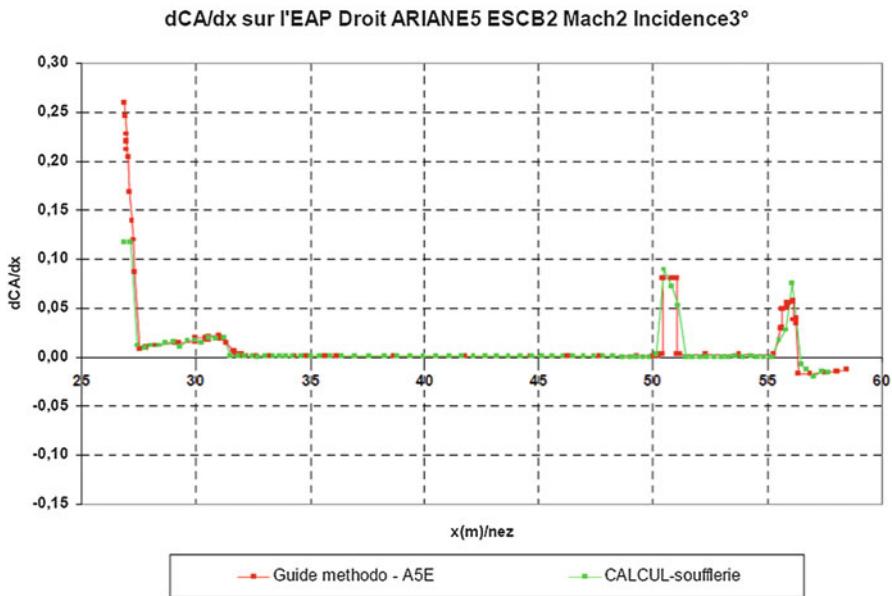


Fig. 8.6 Distributed axial coefficient derivative along A5 EAP right ( $M_\infty = 2$ )

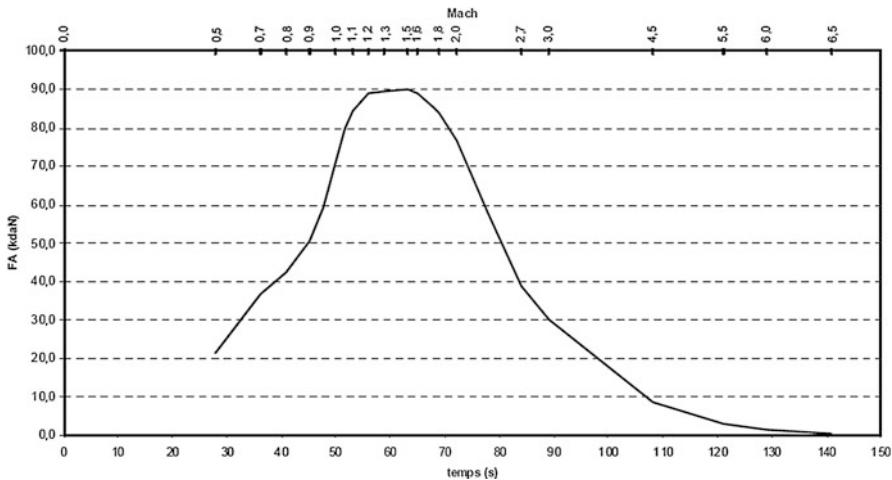
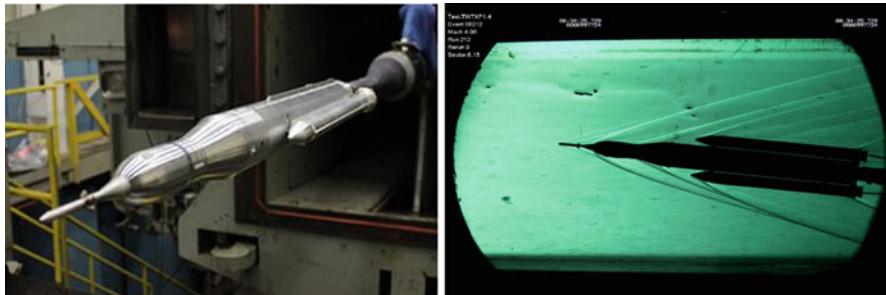


Fig. 8.7 Example of flight domain

on Fig. 8.7, the main part of the needed characterizations is situated in the range  $0.5 \leq M_\infty \leq 3$  [1]. Nevertheless, this remains a quite large domain to be covered, encompassing transonic and supersonic regimes.

Wing tunnel testing consists generally of two kinds of tests. The first one enables measurement of global aerodynamic coefficients of a launcher model like the one



**Fig. 8.8** Space Launch System (SLS) Block I vehicle configuration (SLS-1,000 $\times$ ) at the Boeing Polysonic Wind Tunnel (PSWT) in St. Louis, Missouri

illustrated in Fig. 8.8 [3]. The model is mounted on a sting equipped with six degrees of freedom balance able to measure each of the six previously defined force and moment components. Given the Mach number similarity, the calculated force coefficients can represent the full-scale ones. But, wind tunnel test conditions generally do not fully represent flight flow conditions due to different viscous effects as will be detailed further, and complementary use of CFD is very important to reach fine characterization of the aerodynamic shape.

The second kind of test is devoted to the measurement of local pressures on the model, which are used to determine sizing for local structures or protrusions as well as the distribution along the launcher of the global aerodynamic coefficients. From these kinds of tests, one aims at rebuilding a full mapping of pressure distribution over the launcher, and then pressure sensors should be as numerous as possible. A classical method to build the distributed coefficients from wind tunnel testing involves four types of tests:

- Global weighting with balance for the smooth configuration (without protrusions)
- Local pressure measurements for the smooth configuration
- Global weighting with balance for the full configuration with protrusion
- Local pressure measurements for the full configuration with protrusions

Distributed coefficients along x-axis for the smooth configuration is obtained with the two first tests. Local pressure measurements can be quite numerous, but their number leads to a discretization far less than the one obtained through computation. Then the obtained integration precision is also less. Moreover, even if tests are performed in the same wind tunnel, pressure campaign is not the same as the one for global forces measurements. Then adjustments are performed in order to ensure that distributed coefficient integration gives the measured global coefficients value.

The third testing compared to the first one provides with the global forces due to the addition of protrusions to the launcher.

Generally in the fourth testing, only the main protrusions are equipped with pressure measurements. Once more, the number of available measurements is far less than the number of wall grid points in computations. Moreover, only the protrusions themselves are equipped, then the influence of protrusions presence over the loading distribution on the underlying smooth geometry is neglected. This fourth campaign is used to determine the repartition and magnitude of local loading due to the protrusions. Then hypothesis should be made about integration surfaces around each measurement, as well as about lacking pressure information in high gradients area, for example. Obviously, building of distributed loading with wind tunnel data is not as straightforward as for the global coefficients, and more uncertainties have to be taken into account.

### **8.2.4 Quick Design Approach for External Loading Characterization**

In phase A projects, the work is based on quick conception loops between performances, staging, propulsion, shape design and conception, aerodynamics loading, and control.

For Mach numbers ranging from 0.5 up to 10, aerodynamic characterization of the launcher shape should provide with a database (AEDB) giving:

$$\begin{aligned} C_A &= f(M_\infty) \\ \frac{C_N}{d\alpha} \Big|_{\alpha=0^\circ} &= f(M_\infty) \\ \frac{C_m}{d\alpha} \Big|_{\alpha=0^\circ} &= f(M_\infty) \end{aligned} \quad (8.12)$$

*Spatial derivatives in the axial direction of the previous quantities*

This AEDB should be built quickly and for a lot of launcher variants which are initially envisaged. Order of magnitude for a database building duration is one or two weeks during which tens of computation points should be produced. These needs imply work processes with high level of tool chain automation (meshing, computing, postprocessing). Aerodynamic sensitivity studies related to the geometry can be added (shape design with CFD, e.g., for tail planes). Today these studies are performed before wind tunnel testing and are the reference used for concept selection (i.e., launcher trade-off design). This approach makes wide use of high-performance computers, using meshes made of millions of cells for each computation and managing several computation cases in parallel. One key necessary feature is the automated generation of meshes for each computation case, without which the allocated timeframe would not be sustainable.

In order to get reasonable quality of results, meshes are adapted for each Mach number in order to adequately fit each region with important gradients like

compression, shocks, and expansion. Best compromise for precision versus number of grid cells is generally obtained with hexahedra cells.

Nevertheless, building multiblock structured or hybrid grids is quite an important constraint for this type of complex topologies. An important simplification is obtained by using a CHIMERA approach. Indeed, each simple body or significant part of a body (e.g., tail planes) is gridded separately, making the automation of such gridding quite easy.

Afterward, all these grids are overlapped with adequate relative priority in order to represent the full launcher geometry with all desirable details. These resulting intersected grids are seen as a unique grid by the solver, on which the resolution is performed with finite volume approach (no use of interpolation between grids, which insures conservation in the solution). Moreover, this feature is used also for grid refinement purpose in shock regions, for example, with overlapping grids fitting the shocks. Then, using fitted grid for each Mach number, computations are submitted in parallel on several computers, each computation being also performed in parallel mode on several processors. Post treatment of each computation is also standardized and automated in order to get quickly a synthetic AEDB.

## 8.3 Examples of Quick Aerodynamic Design Analysis of Launchers

Quick appraisal of launcher aerodynamic performance relies on panel method analysis at supersonic/hypersonic speed and Euler CFD analysis carried out considering simplified launcher aeroshape. As example, four design study cases are reported hereinafter for different launcher vehicles, namely, VSB-30, Vega, NGLV, and FLPP concepts [2].

### 8.3.1 *The VSB-30 Launcher*

The VSB-30 vehicle is a two-stage, unguided, rail-launched sounding rocket, consisting of a solid propellant S31 rocket booster, a boost adapter, the second-stage S30, payload, and a recovery and a service system. Motor and payload are connected by an adapter section, and they are separated by pneumatic pistons. The vehicle is designed to fly in a spin-stabilized unguided mode. The spin stabilization is achieved by using canted fins. To reduce impact dispersion, the vehicle is equipped with three spin-up motors, installed in the booster adapter. The fins are arranged in the standard three-fin configuration, and they are nominally set to 18' (S31) and 21' (S30), respectively, causing the vehicle to spin from lift-off through burnout. The basic architecture of VSB-30 is presented in Fig. 8.9, while the flight events sequence is presented in Fig. 8.10 [7].



Fig. 8.9 The VSB-30 launcher

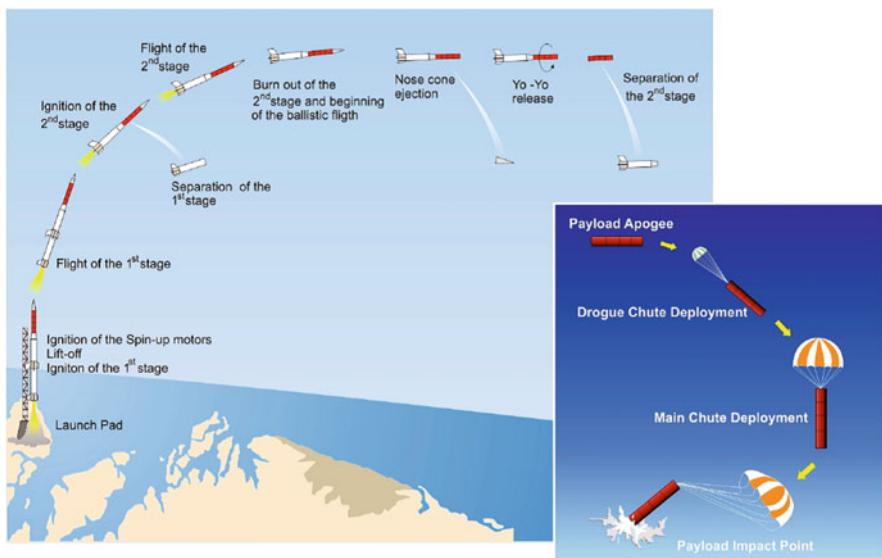


Fig. 8.10 The VSB-30 flight events

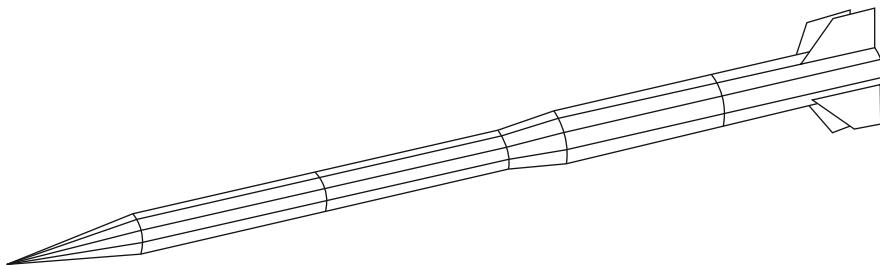


Fig. 8.11 VSB-30 panel mesh

As far as launcher aerodynamics is concerned, the vehicle reference length (for transitional aerodynamic assessment) is the stage diameter  $\varnothing = 0.557$  m, while the reference surface is  $S_{\text{ref}} = 0.075$  m<sup>2</sup> (i.e., stage cross-sectional area).

A typical panel mesh considered for the stage aerodynamic appraisal is shown in Fig. 8.11.

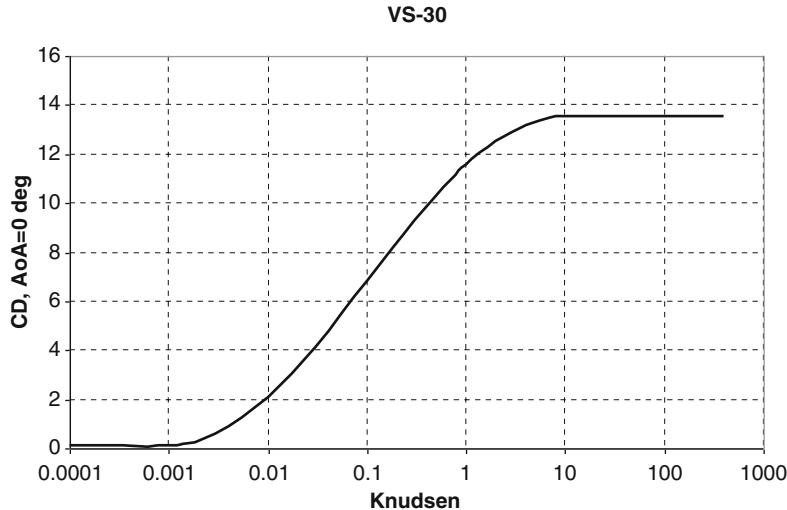


Fig. 8.12 VSB-30 axial coefficient at  $\alpha = 0^\circ$  in the transitional regime

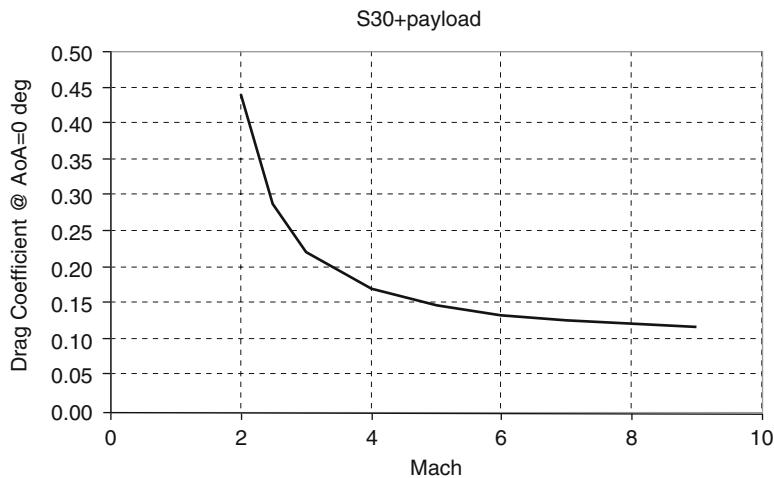


Fig. 8.13 VSB-30 axial coefficient at  $\alpha = 0^\circ$  and different Mach numbers

The axial coefficients, at zero AoA, in the transitional and continuum flow conditions are shown in Figs. 8.12 and 8.13, respectively. Indeed, Fig. 8.12 provides  $C_A$  versus Kn number, while in Fig. 8.13 the axial coefficient is reported as function of Mach number.

### 8.3.2 The Vega Launcher

Vega which is the short form for *Vettore Europeo di Generazione Avanzata* (Advanced Generation European Carrier Rocket) is an expendable launch system in use by Arianespace jointly developed by the Italian Space Agency and the European Space Agency (see Fig. 8.14) [8, 9]. Development began in 1998, and the first launch took place from the Guiana Space Centre on February 13, 2012 [5]. Arianespace has ordered launchers covering the period till at least the end of 2018. It is designed to launch small payloads—300–2,500 kg satellites for scientific and Earth observation missions to polar and low Earth orbits [11, 12]. The reference Vega mission is a polar orbit bringing a spacecraft of 1,500 kg to an altitude of 700 km (see Fig. 8.14). Vega, named after the brightest star in the constellation Lyra, is a single-body launcher (no strap-on boosters) with three solid rocket stages, the P80 first stage, the Zefiro 23 second stage, the Zefiro 9 third stage, and a liquid rocket upper module called AVUM. The technology developed for the P80 program will also be used for future Ariane developments. Italy is the leading contributor to the Vega program (65 %), followed by France (13 %). Other participants include Spain, Belgium, the Netherlands, Switzerland, and Sweden [4].

An example of the panel mesh considered in the launcher aerodynamic appraisal is reported in Fig. 8.15.

The assessment of launcher axial coefficient versus Mach number is provided in Fig. 8.16 for two angles of attack, namely,  $2^\circ$  and  $5^\circ$  [5]. In this figure, more reliable CFD results are also reported. Therefore, the accuracy of panel method can be also inferred.

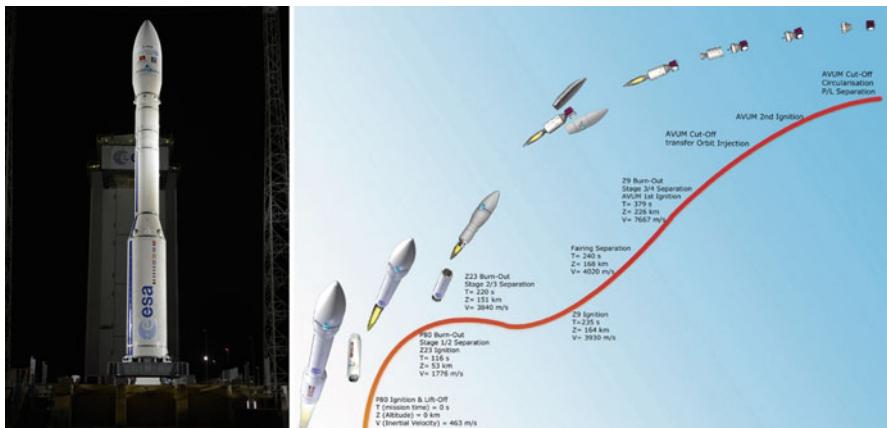


Fig. 8.14 Vega launcher and overview of mission profile

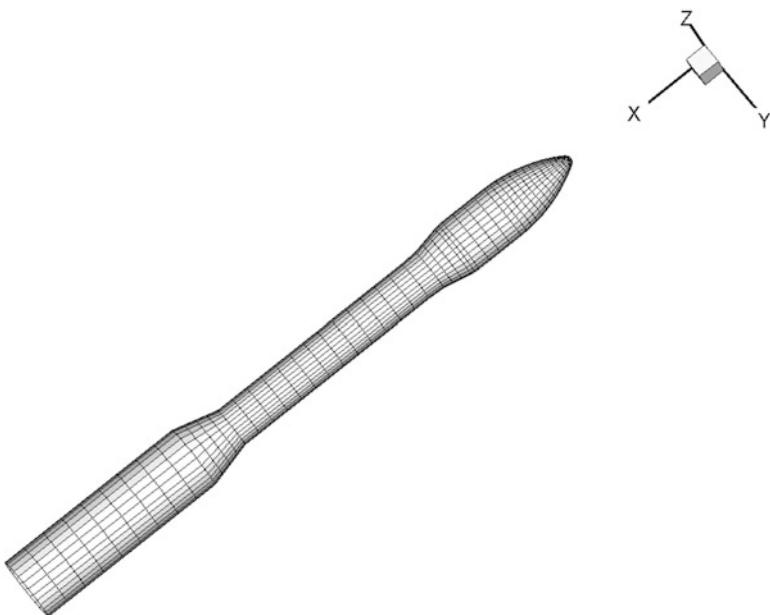


Fig. 8.15 Vega panel mesh

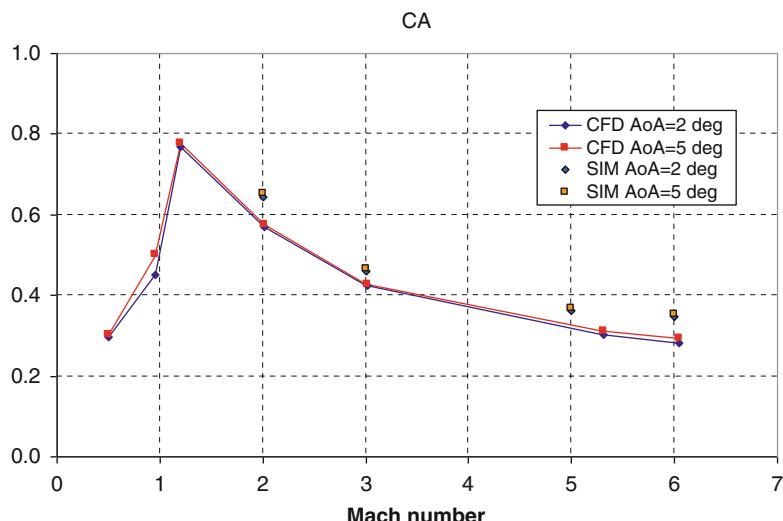


Fig. 8.16 Vega axial coefficient at  $\alpha = 2$  and  $5^\circ$  and different Mach numbers

**Fig. 8.17** The NGLV aeroshape



**Table 8.1** The CFD test matrix

AoA ( $^{\circ}$ )	Mach			
	0.5	1.1	2.5	5
0	E	E	E	E
5	E	E	E, NS	E, NS
7	E	E	E	E

E Eulerian CFD, NS Navier–Stokes CFD

### 8.3.3 The Next-Generation Launcher Vehicle (NGLV)

An example of aerodynamic analysis of a next-generation expendable launcher by means of CFD is provided hereinafter. The aeroshape under investigation features two boosters and a central core stage with hammerhead fairings (see Fig. 8.17). It is close to that expected for Ariane 6 concept.

Launcher aerodynamics has been addressed considering four Mach numbers, namely, 0.5, 1.1, 2.5, and 5, at three angles of attack, i.e.,  $\alpha = 0^{\circ}$ ,  $5^{\circ}$ , and  $7^{\circ}$ , as shown in Table 8.1.

Therefore, Eulerian and Navier–Stokes 3-D CFD computations have been carried out on several unstructured hybrid meshes. An overview of the unstructured mesh domain at  $M_{\infty} = 0.5$  is shown in Fig. 8.18 (left side), where the grid in the launcher symmetry plane is provided.

As one can see, a square brick wide twenty body length upstream, downstream, upward, and downward the launcher is considered to assure farfield unperturbed

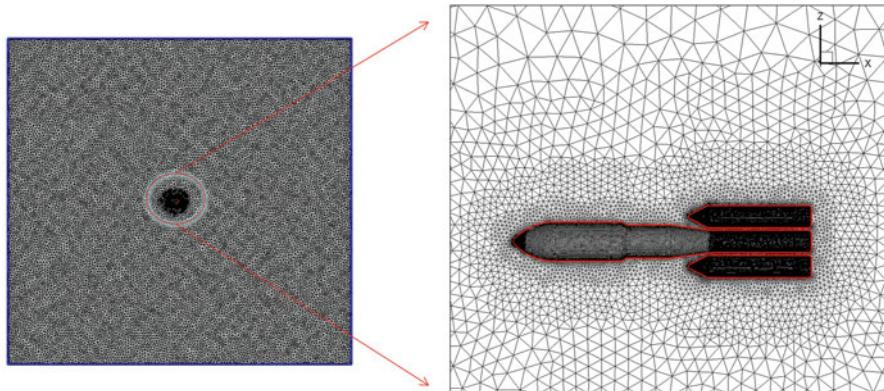
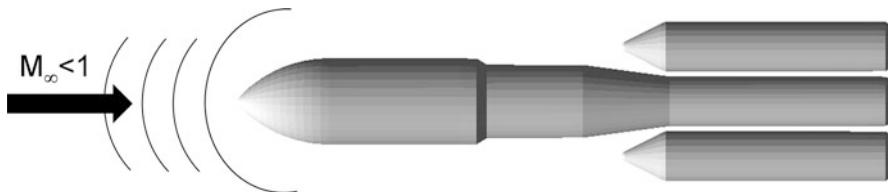


**Fig. 8.18** Overview of the unstructured mesh domain at  $M_\infty = 0.5$  and  $\alpha = 0^\circ$



Disturbance due to the body is propagated upstream via molecular collisions at approximately the speed of sound.

**Fig. 8.19** Propagation of disturbance in subsonic flow

flow conditions. Indeed, in a subsonic (i.e., flow moving slower than the speed of sound) elliptic flow, disturbances due to the body are propagated upstream via molecular collisions at approximately the speed of sound, thus influencing flow everywhere (see Fig. 8.19) [8, 9]. Therefore, the computational domain must be wide enough to avoid interferences between flowfield and farfield boundary conditions [9].

A blow-up of the mesh close and over the launcher is also provided on right side of Fig. 8.18 (see also Fig. 8.20).

The pressure distribution expected on the surface of launcher flying at  $M_\infty = 0.5$  and  $\alpha = 5^\circ$  is provided in Fig. 8.21. Flow compression at stagnation region of launcher fairings and of booster conical forebodies is clearly shown. A recompression zone at the beginning of the cylindrical trunk, just after the fairings, and on that close to the booster forebodies can be also noted.

Numerical investigations at higher Mach number, say  $M_\infty = 2.5$ , have been performed on a narrow grid domain compared to that in Fig. 8.18. An overview of surface mesh on launcher symmetry plane and surface is provided in Fig. 8.22.

Indeed, at supersonic speed, a shock wave appears at launcher leading edge (i.e., hyperbolic flowfield), because when the flow moves faster than the speed of sound,

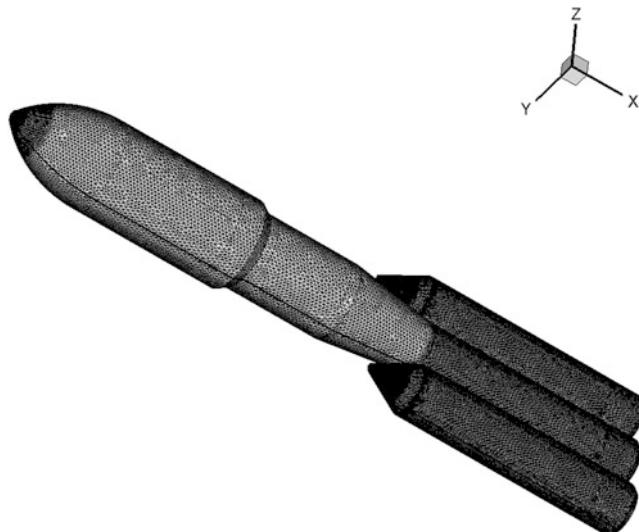


**Fig. 8.20** Overview of the unstructured mesh domain on launcher surface

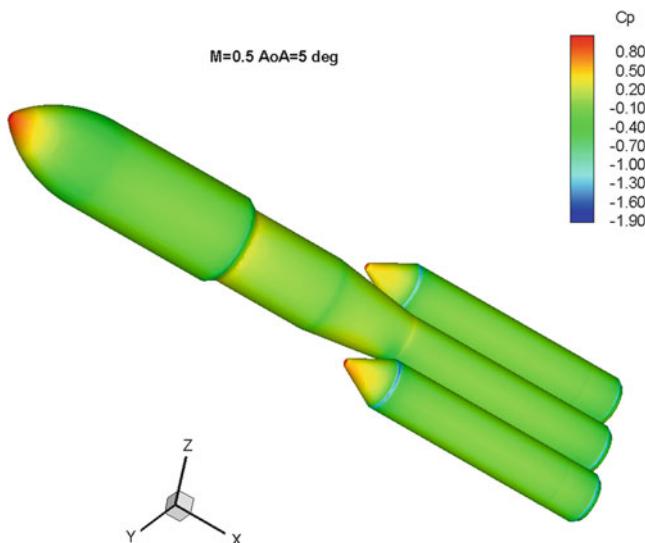


**Fig. 8.21** Pressure coefficient at  $M = 0.5$  and  $\alpha = 5^\circ$

disturbances cannot work their way upstream. As a result, disturbances coalesce forming a standing wave, namely, bow shock (see Fig. 8.23) [10, 11].

The bow shock that takes place when the launcher flies at  $M_\infty = 2.5$  and  $\alpha = 5^\circ$  is shown in Fig. 8.24, where Mach number field is provided on vehicle symmetry plane and pressure coefficient contours on launcher surface.

**Fig. 8.22** Overview of the unstructured mesh domain at  $M_\infty = 2.5$  and  $\alpha = 5^\circ$

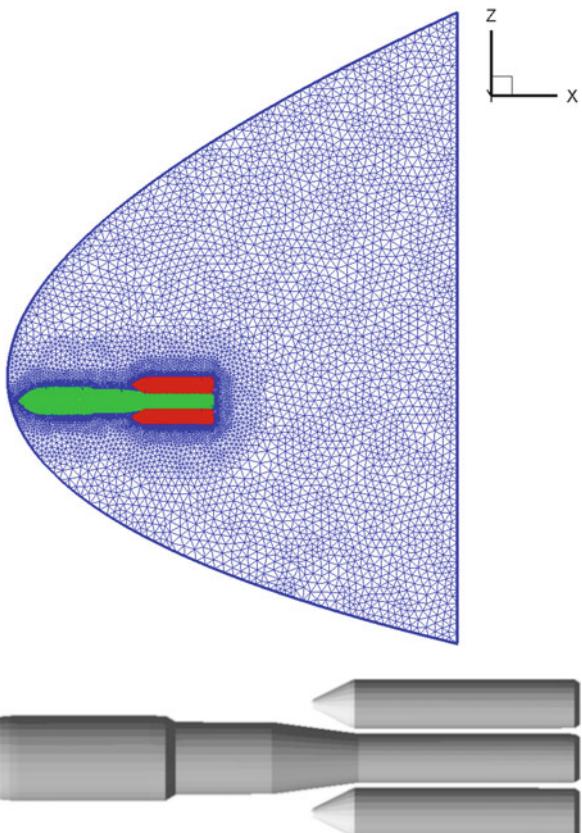


**Fig. 8.23** Propagation of disturbance in supersonic flow

Figure 8.24 highlights also a complex flowfield past the vehicle. For instance, after compression at conical flare of the fairings, the flow undergoes to expansions that align the flow along with the constant cross-section part of fairing. Hence, at the end of fairings, another strong expansion takes place to accommodate the flow to the variation in launcher cross section (i.e., narrow cross section due to fairing boattail). Then a shock wave arises at the beginning of the cylindrical trunk, just after the fairings, to redirect the flow along with the launcher wall. Flow complexity increases further in the region close to the boosters. Here, complex shock–shock and shock-wave–boundary-layer interactions take place. They result in higher thermomechanical loads (i.e., pressure and thermal overshoots) on the launcher wall that must be carefully addressed in vehicle design.

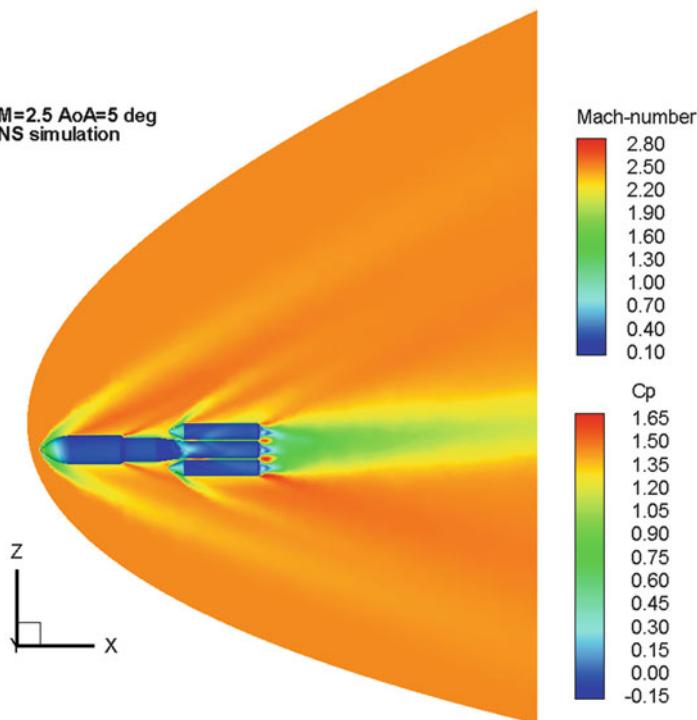


**Fig. 8.24** Mach number field on symmetry plane and pressure coefficient on launcher surface at  $M = 2.5$  and  $\alpha = 5^\circ$

An overview of pressure coefficient distribution on launcher symmetry plane and surface at  $M_\infty = 2.5$  and  $\alpha = 5^\circ$ , with streamtraces, is provided in Fig. 8.25.

The flowfield past the launcher at higher Mach and AoA is shown in Fig. 8.26, where Mach number field on symmetry plane and pressure coefficient on launcher surface at  $M_\infty = 5$  and  $\alpha = 7^\circ$  are provided. The effect of AoA is clearly evident in the Mach number field past the launcher.

As far as aerodynamic coefficients are concerned, NGLV axial force, normal force, and pitching moment coefficients are summarized in Figs. 8.27, 8.28, 8.29, 8.30, 8.31, and 8.32.

For instance,  $C_A$ ,  $C_N$ , and  $C_m$  versus AoA are shown in Figs. 8.27, 8.28, and 8.29, respectively, while Figs. 8.30, 8.31, and 8.32 report the same coefficients but as function of Mach number.

Looking at the axial force coefficient, Fig. 8.27 points out that the  $C_A$  does not significantly change passing from  $0^\circ$  to  $7^\circ$  AoA at each considered Mach number, while the effect of flow compressibility is remarkable, as shown in Fig. 8.30. Regarding normal force coefficient, numerical results in Fig. 8.28 highlight that, for each Mach number,  $C_N$  features a quite linear slope as  $\alpha$  increases up to  $7^\circ$  AoA.

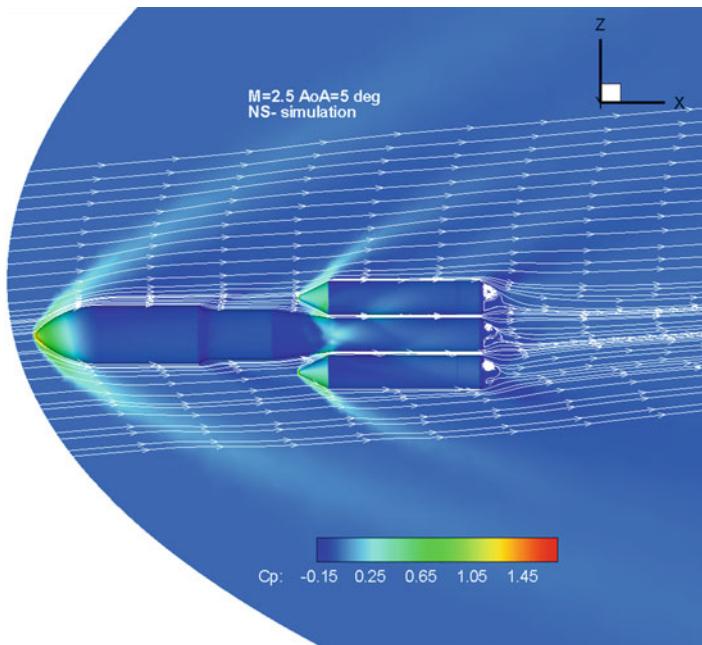


**Fig. 8.25** Overview of pressure coefficient distribution on symmetry plane and launcher at  $M_\infty = 2.5$  and  $\alpha = 5^\circ$ , with streamtraces

Also in this case, compressibility effect influences NGLV normal force by means of different curve slopes for each Mach number case (see Fig. 8.31).

Finally, the vehicle pitching moment coefficient (see Fig. 8.29) features a behavior quite close to that described for the  $C_N$  with a strong pitch down detected for  $M_\infty = 5$ .

Profiles of  $C_A$  in Fig. 8.30 underline the strong increase to which undergoes the axial aerodynamic force when  $M_\infty$  ranges from 0.5 to 5. Indeed, once Mach number crosses a critical value, a shock wave appears in front of launcher, as described in Fig. 8.23. As a result, a new contribution to vehicle aerodynamic drag must be accounted, namely, wave drag. This contribution tends to be less strong as Mach number goes toward hypersonic speed conditions considering that the shock becomes weak due to the streamlined vehicle aeroshape (i.e., high inclined shock to assure a narrow shock layer). This determines the classical peak shape of  $C_A$  versus  $M_\infty$ , summarized in Fig. 8.30. In particular, all curves are very close each other, as suggested by Fig. 8.27.

The variation of  $C_N$  and  $C_m$  in Figs. 8.31 and 8.32 suggest, also for these coefficients, the influence of flow compressibility even in a weaker way. In particular, both  $C_N$  and  $C_m$  at  $\alpha = 0^\circ$  are zero due to the symmetric launcher aeroshape.

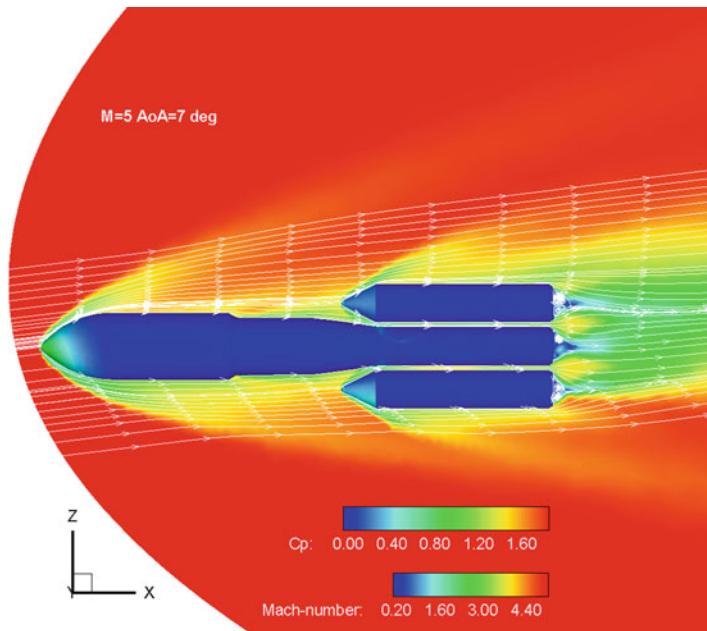


**Fig. 8.26** Overview of Mach contours distribution on symmetry plane and pressure on launcher at  $M_\infty = 2.5$  and  $\alpha = 5^\circ$  with streamtraces

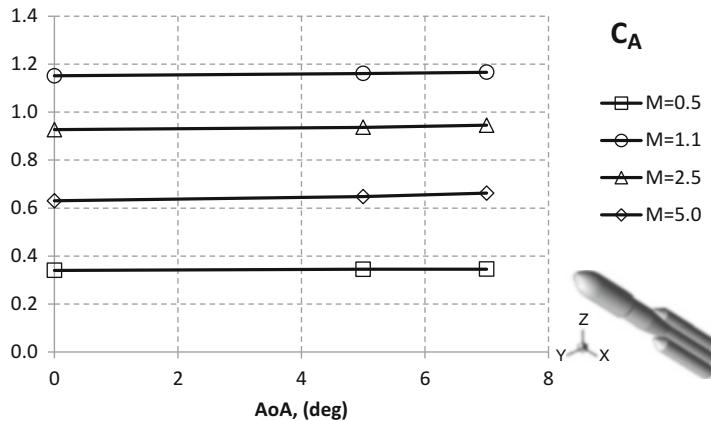


**Fig. 8.27** Axial force coefficient versus AoA at different Mach numbers

### 8.3.4 The Future Launchers Preparatory Program Concepts

In the framework of the Future Launchers Preparatory Program (FLPP), carried out by the European Space Agency (ESA), several reusable launch vehicle (RLV)

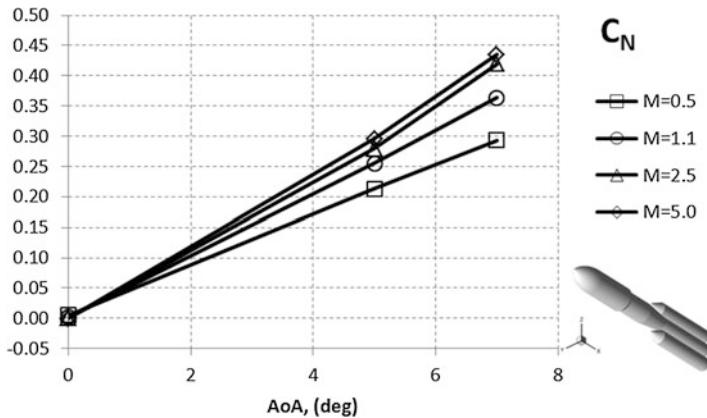


Fig. 8.28 Normal force coefficient versus AoA at different Mach numbers

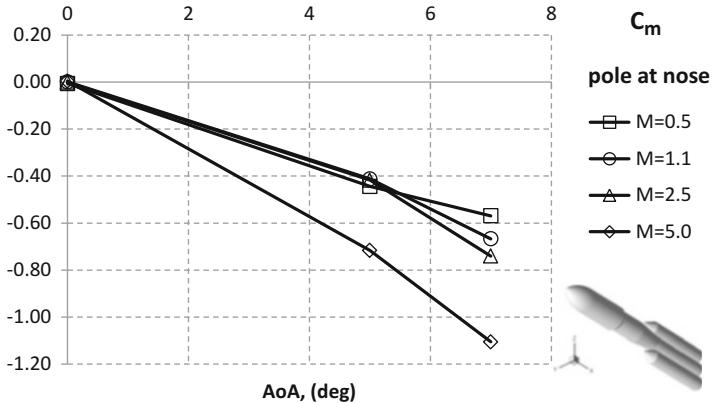


Fig. 8.29 Pitching moment coefficient versus AoA at different Mach numbers

concepts have been investigated [13]. The FLPP program aims to allow Europe to develop a Next-Generation Launcher (NGL) within the next decades [14]. Expendable and reusable concepts have been studied to satisfy a large range of missions. The FLPP has been structured in three successive overlapping periods. Activities of period 1 aimed at the down-selection of RLV system concepts, key technologies development, and associated experimental vehicle concepts for in-flight demonstration. Period 2 activities focused first on the evaluation of expendable launch vehicle (ELV) concepts as well as on the consolidation of RLV ones and, hence, on ELV/RLV trade-off activities [14, 15]. The development to the required key technologies also pursued through ground demonstrations and in-flight experimentation. The last period provided the final recommendation of one NGL concept. In this framework, the paragraph focuses on the RLV concept candidates investigated in the period 1 phase 2. They are the Horizontal Take-Off (HTO)

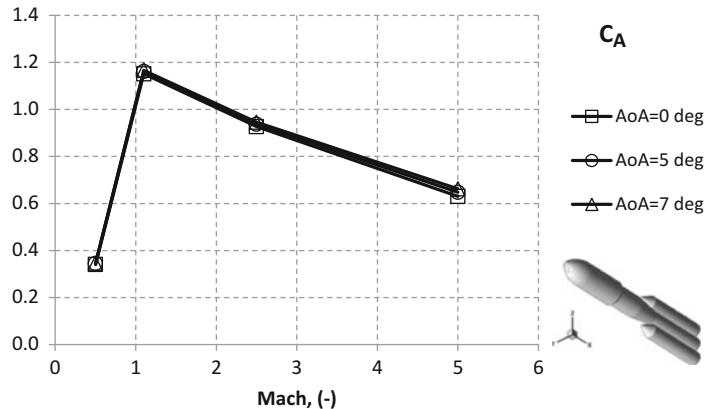


Fig. 8.30 Axial force coefficient versus Mach at different AoA

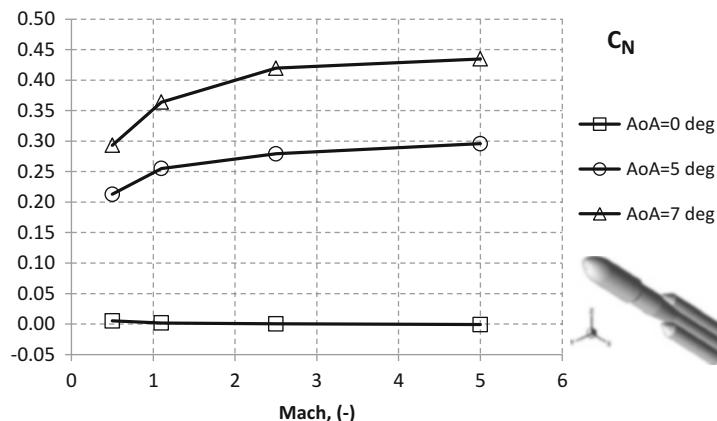


Fig. 8.31 Normal force coefficient versus Mach at different AoA

Hopper, the Vertical Take-Off (VTO) Hopper, the Reusable First Stage (RFS), and the LO<sub>2</sub>/CH<sub>4</sub> Liquid Fly Back Booster (LFBB) shown, in the order as mentioned, from left to right in Fig. 8.33 [8, 15, 16].

Each launcher concept features a reusable winged booster and an expendable upper stage (EUS) to deliver the payload in orbit. These configurations are being investigated and compared within a launcher concept competition aimed to assess the best promising vehicle configuration able to address the FLPP mission requirements. For instance, since the FLPP concept is planned to achieve its operation capability by 2020–2025, a high flexibility of the launch system is requested as far as the set of missions to be covered are concerned [8, 17]. The latest analyses of the commercial and European institutional needs led to define the following *driving* reference missions for single payload launches. For example, future commercial market needs demand 8,000 kg in geostationary transfer orbit (GTO) or equivalent

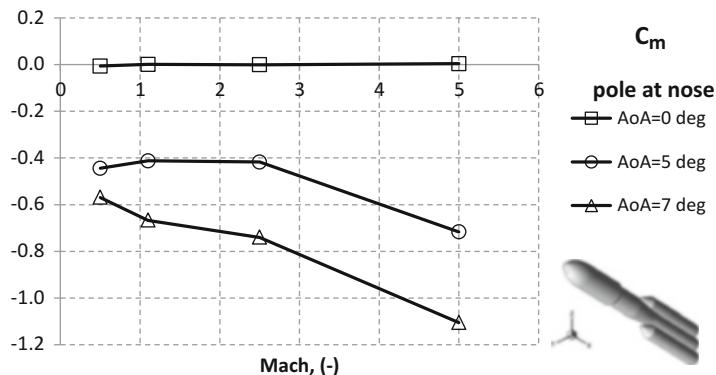


Fig. 8.32 Pitching moment coefficient versus Mach at different AoA

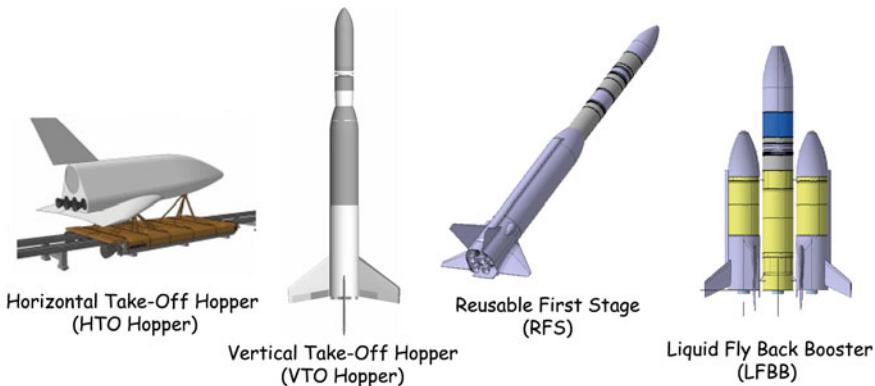


Fig. 8.33 FLPP RLV vehicle concepts overview

as in the case of large telecommunication satellites, whereas European institutional needs require up to 5,000 kg in GTO or equivalent as in the case of meteorology and military telecommunications satellites. Anyway, as RLVs to be economically viable need a high launch rate, aside from the RLV reference mission, presently considered, a very wide range of missions are foreseen as to deliver payload in Sun-synchronous orbit (SSO) for Earth observation, low Earth orbit (LEO) and medium Earth orbit (MEO) servicing as Galileo constellation maintenance, and robotic space exploration (e.g., escape trajectories).

In this framework, this research effort deals with the definition of both the preliminary aerodynamic (AEDB) and aerothermodynamic (ATDB) databases for each reusable booster in re-entry phase (also in ascent phase only for VTO), compliant with a phase A design level. The former (AEDB) is needed for the Flight Mechanics analysis and for guide, navigation, and control (GNC) studies, since it must be verified that the concept aerodynamic performance ensures that the vehicle stays within the load constraints (i.e., pressure, inertial, and thermal loads) during

descent. The latter (ATDB) is needed for thermal protection design analyses; in fact, as booster flies through descent to Guiana Space Center (GSC), its potential plus kinetic energy is converted into thermal energy within the boundary layer close to the vehicle surface, so a thermal shield must be provided to the booster in order to withstand this heat loading. Different design approaches have been addressed. For instance, aerodynamic and aerothermodynamic analyses have been performed starting from engineering-based approach, by using a 3-D panel method code, named SIM,<sup>1</sup> based on the simplified Newtonian approach and local surface inclination methods (SIM). Then, increasing the order of complexity, a number of detailed 3-D Euler and Navier–Stokes computational fluid dynamics (CFD) analysis have been carried out at different Mach numbers and angles of attack, at the most critical flight conditions occurring during the descent trajectory (i.e., trajectory peak heating). A brief description of each vehicle concept is provided herein. In particular concept dimensions are compared to those of US Space Shuttle in order to properly highlight FLPP vehicle features.

The HTO Hopper, designed for horizontal take-off from a sled (see Figs. 8.33 and 8.34), is a conventional wing–body configuration. It is an upscaled version of the DLR Hopper/Phoenix configuration and shows an overall body length of 45.9 m and a wingspan of 26.6 m [13].

The HTO Hopper aerodynamic configuration features a compact body with rounded edge delta-like cross section equipped with a far rear delta planform wing (60° leading edge sweep), a central vertical stabilizer, and a flat-bottomed surface in order to increase the overall vehicle hypersonic performance. The fuselage cross section is large enough to accommodate both propulsion tanks and the EUS bay, which is located at central rear part of the fuselage, just under the vertical tail (see left side of Fig. 8.34) [14].

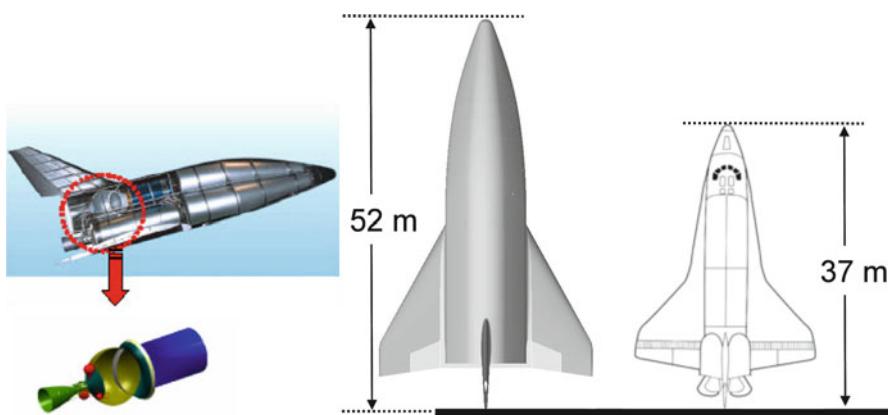


**Fig. 8.34** The HTO Hopper and its EUS. Comparison with US Space Orbiter

<sup>1</sup>SIM is the name of the former version of the HPM code widely used in this book.

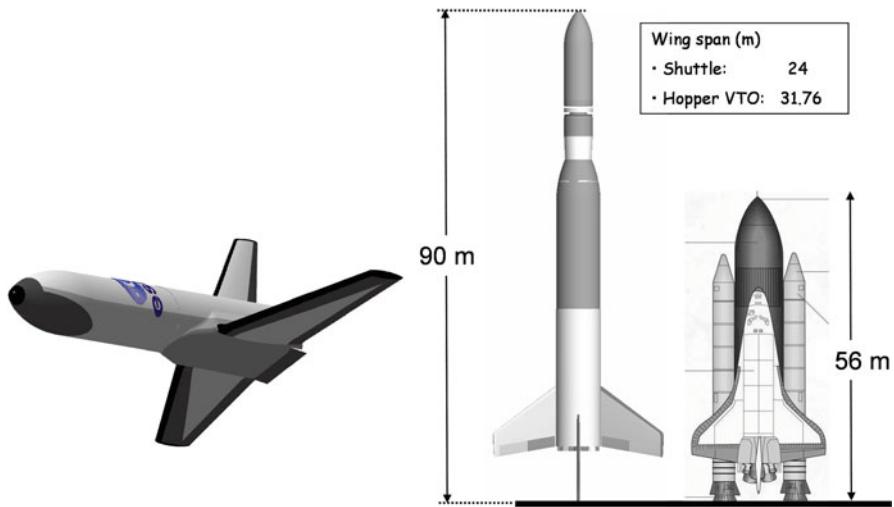


**Fig. 8.35** The VTO Hopper. Reusable booster on the *left*. Comparison with US Space Orbiter

The VTO Hopper launcher concept, designed for vertical take-off, is a two-stage space transportation system concept with a fully reusable booster (see left side of Fig. 8.35) mated on top by an expendable upper stage (see right side Fig. 8.35) [16]. The first stage, designed as a winged re-entry body, will return to Earth to a point downrange of the launch site and land horizontally. It features a rather conventional slender missile-like vehicle with a small delta planform wing ( $37.2^\circ$  leading edge sweep) at very rear position and a central vertical stabilizer. The vehicle architecture shows a circular cross section with a loft fillet on the belly side to accommodate both the wings (blended wing–body interface) and the body flap (see left side of Fig. 8.35) [17].

The Wing geometry data are root/tip chord,  $11.70\text{ m}/4.914\text{ m}$ ; half span  $b/2$ ,  $11.63\text{ m}$ ; wing leading/trailing edge angle,  $37.23^\circ/10^\circ$ ; apex longitudinal position (from the base of the fuselage),  $11.70\text{ m}$ ; angle of incidence (setting) of the wing,  $3^\circ$ ; and dihedral,  $3^\circ$ . With these data, the wing surface is equal to  $193.23\text{ m}^2$ . The aerodynamic controls comprise rudders on the vertical tail, elevons and ailerons on the wings, and a body flap underneath the main engines in order to provide maneuverability and longitudinal stability during atmospheric descent. A surface behind the vehicle center of gravity (CoG) balances the nose-up pitching moment typical of such kind of vehicle configuration at hypersonic speeds. Normalizing the vehicle overall dimensions by fuselage length ( $L_{ref} = 58.8\text{ m}$ ), the VTO Hopper is characterized by the following normalized reference data:

- $B'$  (wingspan) = 0.54.
- $S'$  (reference surface) = 0.056.
- $X'_{MRP} = 0.69$ ;  $Y'_{MRP} = 0$ ;  $Z'_{MRP} = 0$ .

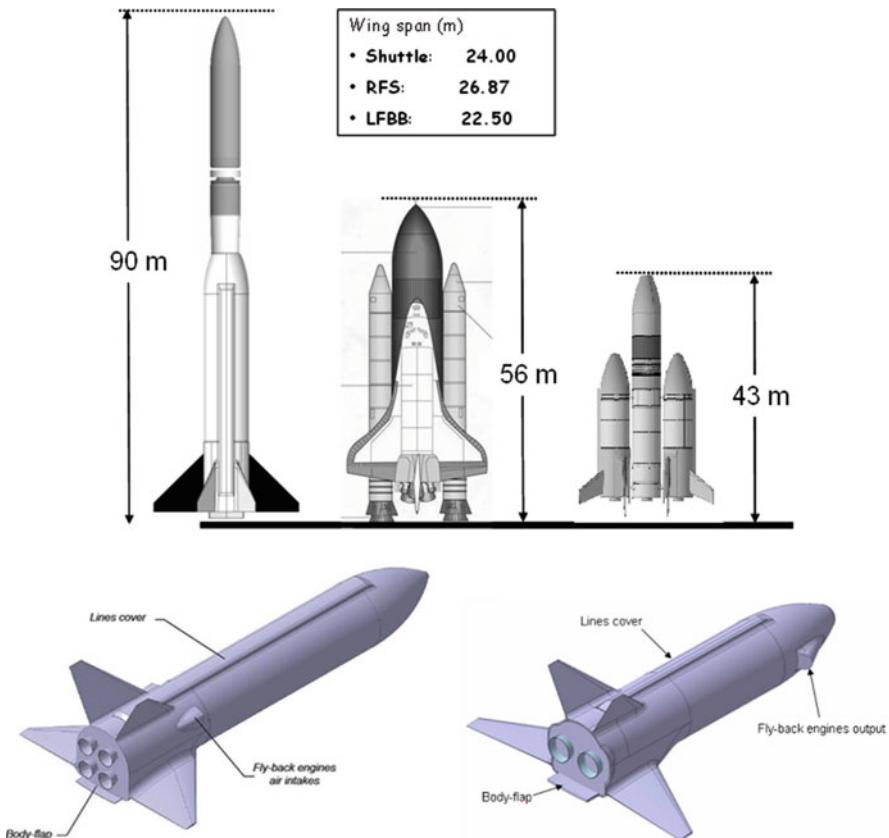


**Fig. 8.36** The RFS and LFBB concepts. At left of the Space Shuttle the complete RFS vehicle, at right the LFBB one. At lower side RFS and LFBB reusable boosters

The RFS launcher (see Fig. 8.36) is a three-stage space transportation system concept featuring a reusable booster mated with two expendable stages in tandem configuration. RFS is launched vertically from GSC. The vehicle architecture in ascent and descent configuration is shown in Fig. 8.36, upper and lower side, respectively [13, 14].

The booster stage carries an EUS and a conventional (Ariane 5-type) fairing hosting the GTO payload. After the separation at high Mach number (e.g.,  $M_\infty = 9$ ), the reusable booster performs a flight back to the launch site by its own means (on board air-breathing turbojet engines) and lands horizontally. The vehicle shape features a fuselage circular cross section adapted to introduce the wing in low position and a body flap. The wing sweep angle at leading edge and trailing edge is equal to  $45^\circ$  and  $0.07^\circ$ , respectively. The two fins (i.e., V-Tail) are mounted so that they form an angle of  $55^\circ$ .

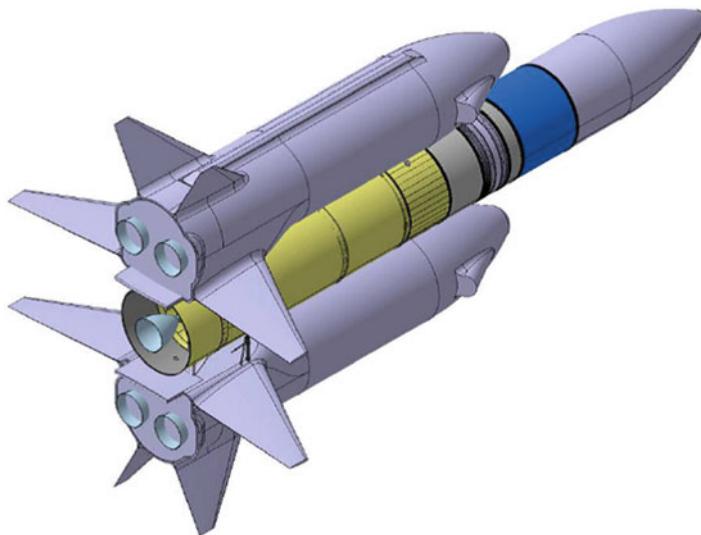


**Fig. 8.37** The LFBB (LO<sub>x</sub>/CH<sub>4</sub>) in ascent configuration

The RFS launcher architecture is quite close to that of the VTO Hopper. However, some differences can be remarked by considering these two concepts. First of all, the VTO Hopper is the most power launcher between them. For example, the mass at take-off of the VTO Hopper is 1.3 times that of RFS. Moreover, the culmination point of the ascent trajectory at which the EUS is ejected together with the payload is about 130 km altitude for the VTO Hopper and close to 60 km for the RFS, whereas the Mach number at staging conditions is about 19 and 9, for the VTO Hopper and RFS, respectively. Therefore, the aerothermal loading of the VTO Hopper is more challenging than the one that the RFS has to face during descent flight, as will be recognized hereinafter [17].

The LO<sub>x</sub>/CH<sub>4</sub> LFBB (see Figs. 8.36 and 8.37) is a vehicle composed of two reusable boosters and a central expendable core stage (configuration similar to the Ariane 5, with the reusable liquid boosters replacing the solid ones). The vehicle architecture for ascent flight is shown in Fig. 8.37 [15, 16].

The forebody is characterized by simple cone–sphere geometry with smooth streamlined surfaces on the upper and lower side of fuselage. Also a body flap is foreseen in order to improve longitudinal stability during descent.

The aerodynamic configuration features a compact body with a circular fuselage cross section and delta planform wing as basic shape. The wing sweep angle is equal to 30°. The two fins are mounted forming an angle of 55°, whereas the vertical tail sweep angle is 45°.

The typical flight scenario foreseen for each FLPP concept consists in performing a suborbital trajectory, in separating at staging altitude, and then in reentering to

GSC, where the reusable booster performs a runway landing. The EUS is ejected together with the payload at the culmination point of the ascent trajectory at an altitude of about 130 km (i.e., staging altitude) for HTO and VTO Hopper and close to 50/60 km for RFS and LFBB ( $\text{LO}_x\text{-CH}_4$ ). After the separation, each reusable booster follows a ballistic arc trajectory and flies back to perform a downrange landing, thus experiencing a rather challenging aerothermal loading environment. The re-entry scenario with the corresponding loading environment for the proposed vehicle concepts is reported and analyzed, starting from the staging altitude.

The HTO Hopper re-entry loading environment is illustrated in Fig. 8.38. As shown, the convective heat flux at fuselage nose reaches about  $500 \text{ kW/m}^2$  [16].

The re-entry scenario of the VTO is shown in Fig. 8.39 [4, 14]. As can be seen, the HTO and the VTO Hopper concepts are characterized by a very similar descent loading environment. The same results apply for the RFS and LFBB concepts (see Fig. 8.40) [5, 14]. LFBB, however, stages at  $M_\infty = 6$ ; hence, its stagnation-point heat flux is expected to be lower than  $40 \text{ kW/m}^2$  [5, 14, 18]. Therefore, the LFBB flight scenario has been omitted for simplicity.

The free-stream conditions of each trajectory peak heating are shown in Table 8.2.

The aerodynamic performance of each concept has been assessed according to the space-based design approach [18]. It dictates the generation of a complete data set as function of a lot of number of independent parameters such as Mach number ( $M_\infty$ ), Reynolds number ( $\text{Re}_\infty$ ), AoA ( $\alpha$ ), and sideslip angle ( $\beta$ ) [19].

On the other hand, the surface heat flux distributions for each booster have been provided according to the trajectory-based design approach which dictates

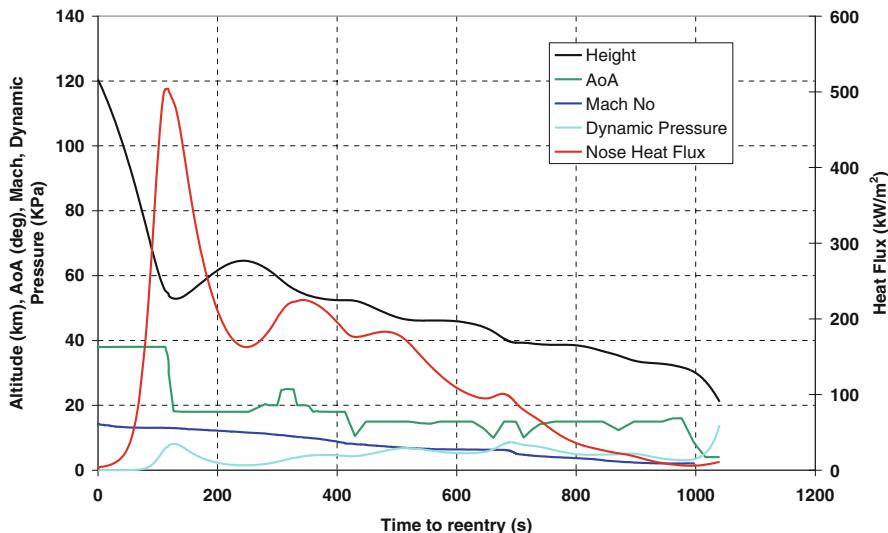


**Fig. 8.38** The HTO Hopper re-entry scenario

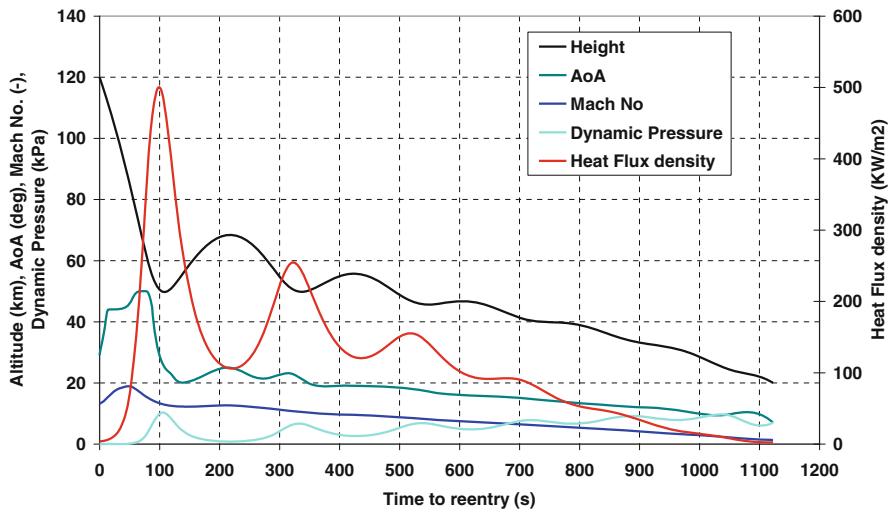


Fig. 8.39 The VTO Hopper re-entry scenario

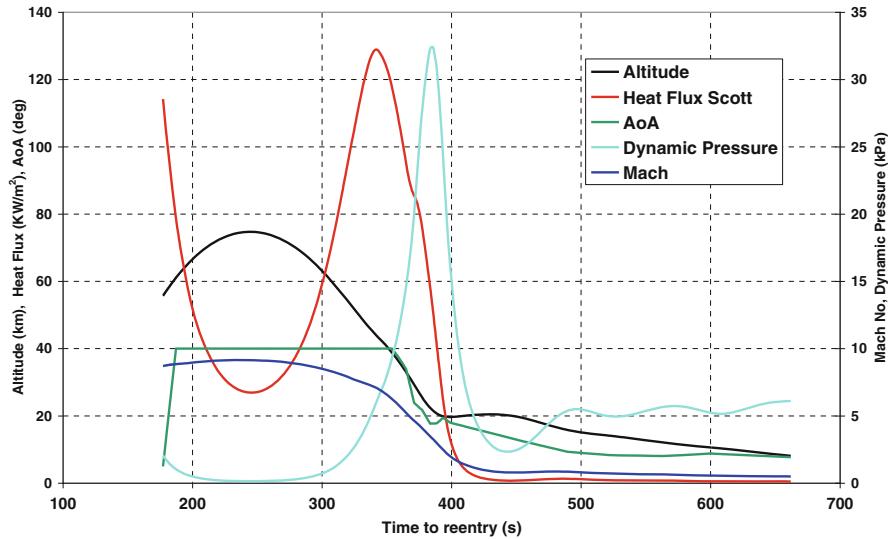


Fig. 8.40 The RFS re-entry scenario

Table 8.2 Peak heating flight conditions

FLPP concept	HTO Hopper	VTO Hopper	RFS	LFBB (LO <sub>x</sub> /CH <sub>4</sub> )
Altitude (km)	49.4	50.8	44.0	40.0
$M_\infty$ (-)	14.3	13.4	7.0	4.7
AoA ( $^\circ$ )	38.0	29.7	40.0	40.0
$q_\infty$ (kPa)	7.3	9.7	32.4	12.0

the generation of a complete aerothermodynamic database by performing the aerothermal computations at a finite number of *critical* points, sampled along the vehicle design trajectory [18].

An accurate aerodynamic and aerothermodynamic analysis for several flight conditions, however, is very complex and time consuming and is not compatible with a phase A design study, in which fast predicting methods are mandatory. Therefore, the evaluation of the vehicle AEDB and ATDB was mainly performed by means of engineering tools, while a limited number of more reliable CFD computations have been performed in order to verify the attained accuracy and to focus on some critical design aspects not predictable with simplified tools.

Concerning flowfield modeling, only continuum regime (supersonic and hypersonic speed ranges) with the air modeled either as an ideal gas or as a chemical equilibrium flow has been considered.

In the present analysis, only continuum regime (supersonic and hypersonic speed ranges) is considered.

It is worth to underline, however, that at high altitudes the rarefaction and real gas effects should be taken into account when the vehicle is flying at high Mach number, being the AEDB and ATDB strongly affected by both these aspects [9]. Therefore, for the prosecution of vehicle design (i.e., phase B and C), more reliable design methodologies are mandatory.

In the following paragraphs, the tools used for the analysis are described.

Vehicle surface meshes for engineering-based analysis are shown in Fig. 8.41 [18].

The pressure acting on each panel is evaluated by user-specified compression-expansion methods derived from Newtonian, modified Newtonian, tangent cone, tangent wedge, and Prandtl-Meyer theories [13, 14].

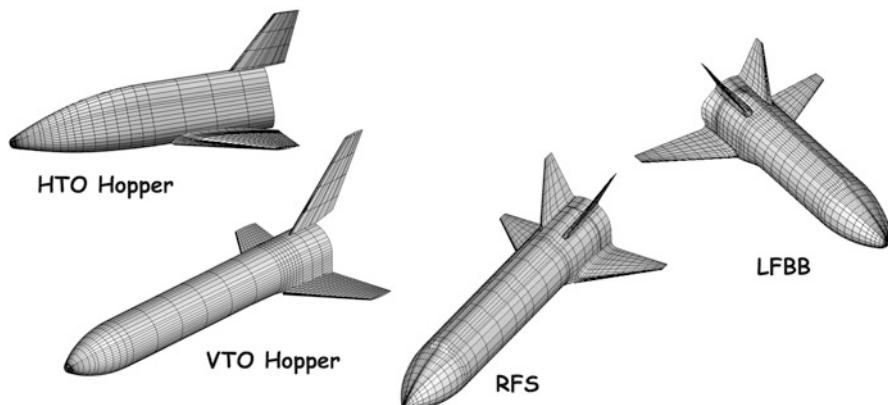


**Fig. 8.41** Example of surface mesh used for engineering-based design analyses

In order to predict viscous contribution to aerodynamic forces and moments, the shear force is determined on each vehicle panel. The skin friction is estimated on the assumption of a laminar or turbulent flat plate as

$$\Delta C_{D,\text{friction}} = C_f \frac{S_{\text{wet}}}{S_{\text{ref}}} \quad (8.13)$$

where  $S_{\text{wet}}$  is the panel wetted area,  $S_{\text{ref}}$  is the reference vehicle's surfaces, and the skin friction coefficient,  $C_f$ , is estimated through reference temperature and enthalpy methods, available for both laminar and turbulent flows [8]. As far as the base drag is concerned, the following simple formula was used [24, 25]:

$$\Delta C_{D,\text{base}} = -C_{P,\text{base}} \frac{S_{\text{base}}}{S_{\text{ref}}} \cong \frac{S_{\text{base}}}{M_\infty^2 S_{\text{ref}}} \quad (8.14)$$

where  $S_{\text{base}}$  is the base vehicle's surface.

The panel aeroheating is evaluated by means of approximate one-dimensional boundary-layer methods (1D BLM) as reference temperature and reference enthalpy ones, which are available both for laminar and turbulent flows [14]. The aeroheating analysis is performed along streamlines, and the results are then interpolated to the panel centroids. The streamlines are generated starting from the inviscid surface velocities generated previously in the aerodynamic analysis phase.

CFD computations have been carried out on multiblock (up to 62 blocks) structured grids similar to that shown in Fig. 8.42 for VTO, RFS, and LFBB concepts. All the mesh domains have an overall number of about  $3 \times 10^6$  cells (half body).

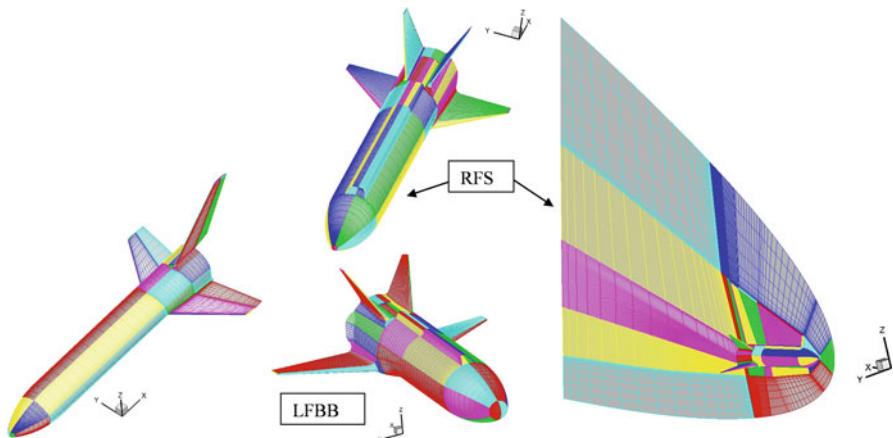


**Fig. 8.42** Multiblock CFD domain. Mesh on symmetry plane and vehicle surface for VTO, RFS, and LFBB concepts

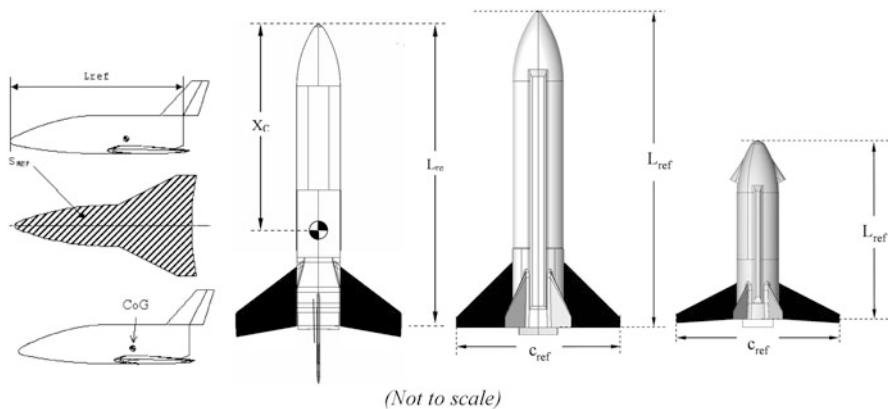


**Fig. 8.43** Vehicle aerodynamic reference parameters

**Table 8.3** Aerodynamic reference parameters

FLPP concept	HTO Hopper	VTO Hopper	RFS	LFBB (LOx/CH <sub>4</sub> )
$S_{ref}$ (m <sup>2</sup> )	602.78 <sup>a</sup>	193.23 <sup>b</sup>	118.20 <sup>b</sup>	60.66 <sup>b</sup>
$L_{ref}$ (m) (Fuselage length)	45.90	58.80	52.48	27.76

<sup>a</sup>Vehicle planform area

<sup>b</sup>Planform area of wetted wing, black in Fig. 8.43

An overview of the aerodynamics and aerothermodynamics of the FLPP concepts, in clean configuration only, is herein recognized by means of several comparisons between engineering and CFD results which allow also to assess the error margins of engineering-based design analyses [26, 27]. The aerodynamic analysis is shown in terms of lift ( $C_L$ ), drag ( $C_D$ ), and pitching moment ( $C_m$ ) coefficients. The reference parameters (see Fig. 8.43) selected in order to make aerodynamic forces and moments nondimensional coefficients are summarized in Table 8.3.

Basing on re-entry flight scenarios summarized in Figs. 8.38, 8.39, and 8.40, the aerodynamic data set has been generated for the following ranges:  $2 < M_\infty < 20$ ;  $0^\circ < \alpha < 50^\circ$ ;  $10^6 < Re < 70 \times 10^6$ ;  $\beta = 0^\circ$ .

They are compliant with the space-based design approach since vehicle aerodynamic performances are evaluated at a number of flight conditions large enough to accommodate or enclose all possible vehicle re-entry trajectories (i.e., trajectory dispersion envelope).

The used aerodynamic reference frames are shown in Fig. 8.44, considering the Hopper concepts. The subscript “b” indicates the body reference frame (BRF), while “w” indicates the wind reference frame (WRF). The origin of both reference systems is in the vehicle CoG [17, 19].

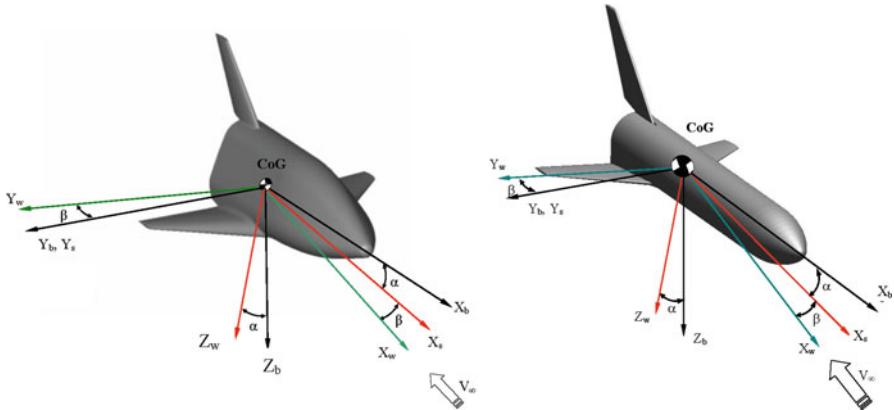


**Fig. 8.44** Hopper aerodynamic reference frames

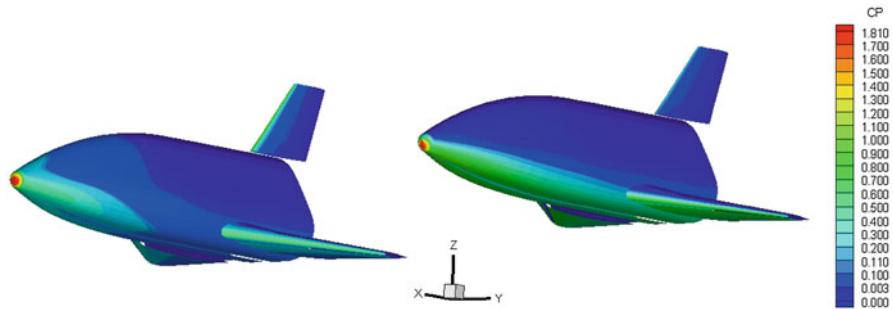


**Fig. 8.45** HTO Hopper. Pressure coefficient contours on the vehicle surface. Comparison between  $\alpha = 10^\circ$  (on the left) and  $\alpha = 30^\circ$  (on the right) at  $M_\infty = 7$

The aerodynamic coefficients are evaluated according to the usually Flight Mechanics convention. Therefore, the longitudinal static stability condition for the vehicle reads

$$C_{m\alpha} = \frac{\partial C_m}{\partial \alpha} < 0 \quad (8.15)$$

Results for the HTO Hopper aerodynamics at  $M_\infty = 7$  are summarized in Fig. 8.45, where the static pressure distribution over the vehicle surface is reported for two AoAs (i.e., 10 and 30°). As shown, when  $\alpha$  ranges from 10 to 30°, the pressure coefficient contours highlight that the flow compression increases on the vehicle flat lower surface, while on the vehicle leeside, the pressure is negligible [14].

As a benchmark evaluation, Fig. 8.46 shows the vehicle lift-to-drag ratio at  $M_\infty = 6$ . Here HTO Hopper aerodynamic efficiency is compared with a preliminary aerodynamic database of the DLR Hopper, evaluated by ASTRIUM [8]

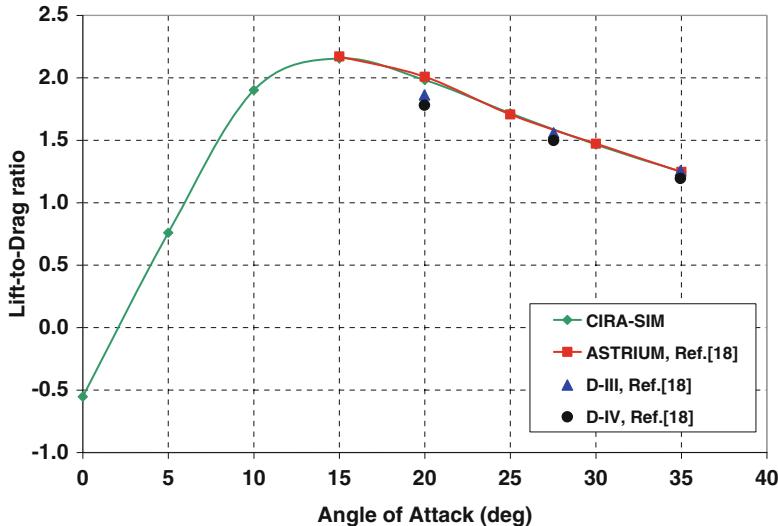


**Fig. 8.46** HTO Hopper. Lift-to-drag ratio at  $M_{\infty} = 6$ . Comparison with Glossner's data

through Newtonian method calculations for an inviscid perfect gas flow. Some experimental results, collected during the Hopper experimental aerodynamic assessment performed in the detonation-driven shock tunnel TH2-D of the Shock Wave Laboratory of Aachen University, e.g., D-III and D-IV, are also reported [28].

As shown, AEDB results provided by SIM and experimental data are in good agreement for all the AoA, especially at  $\alpha = 35^\circ$ .

The aerodynamic performance of VTO Hopper in ascent flight has been carried out starting from the results summarized in Ref. [29] for the French concept RFS. The geometry of RFS launcher configuration with booster, expendable upper stage, and fairing is shown in Fig. 8.47 [29].

As one can see, this vehicle concept is characterized by an aerodynamic configuration very close to the VTO one, except for canard flight control surfaces mounted in front of launcher. Therefore, the preliminary ascent AEDB of the VTO Hopper has been built by properly scaling the RFS's AEDB on the base of VTO aerodynamic configuration features.

For the RFS launcher, with configuration provided in Fig. 8.47 (different from that considered hereinafter), the aerodynamic coefficients are summarized in Fig. 8.48 [29].

Starting from those data, the preliminary AEDB of the VTO Hopper is synthesized in Figs. 8.49, 8.50, and 8.51.

The re-entry scenario of the VTO Hopper launcher is summarized in Fig. 8.52 where the flight profile refers to the altitude–velocity map. Moreover, the Mach and Reynolds numbers grid is also reported in order to characterize the aerodynamic flight scenario of the booster.

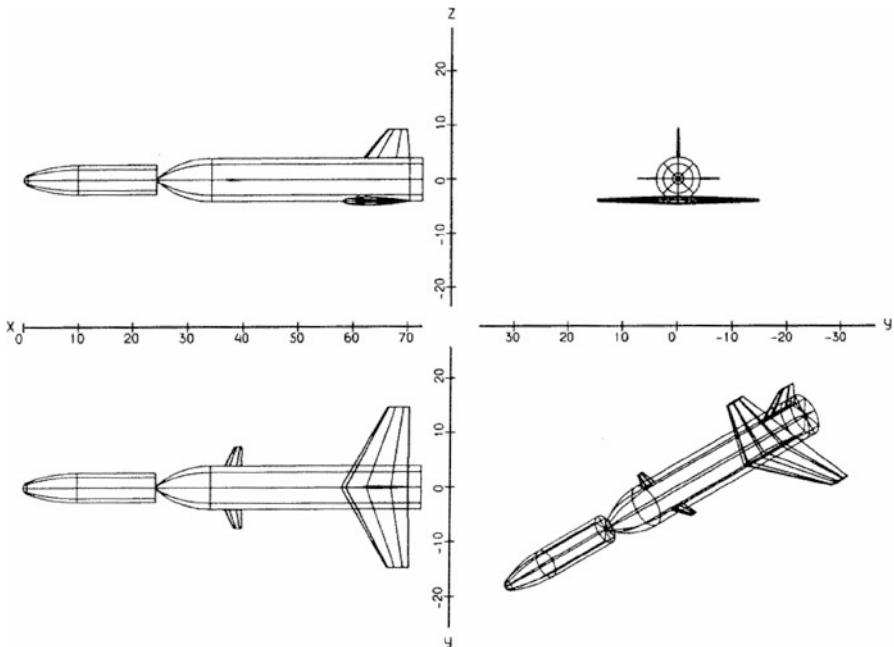


**Fig. 8.47** RFS configuration. Dimensions in [m] (Guédron et al. [29])

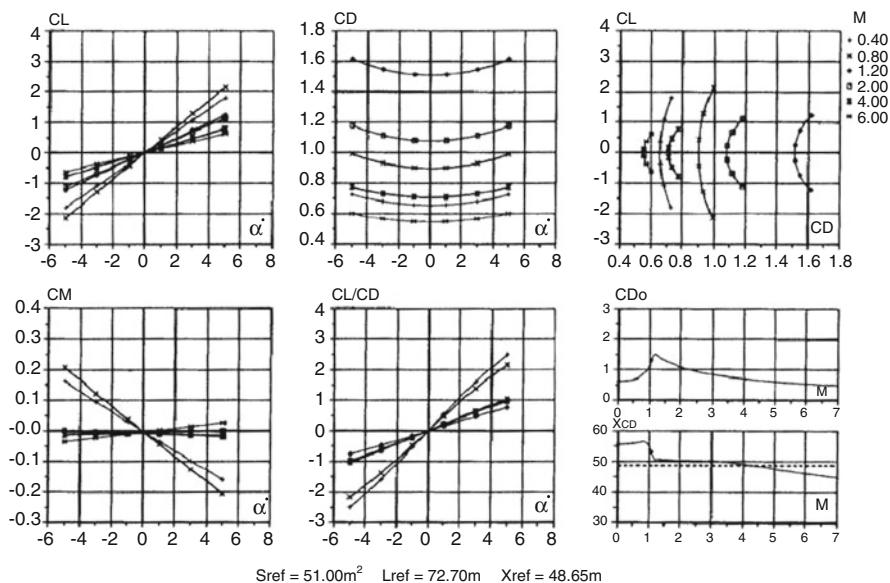


**Fig. 8.48** Aerodynamic coefficients for ascent flight of RFS launcher

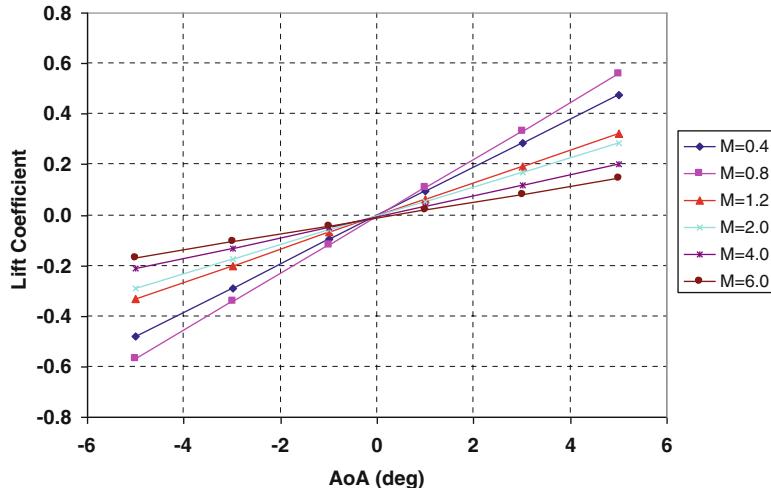


Fig. 8.49 Lift coefficients vs. AoA for ascent flight VTO-Hopper

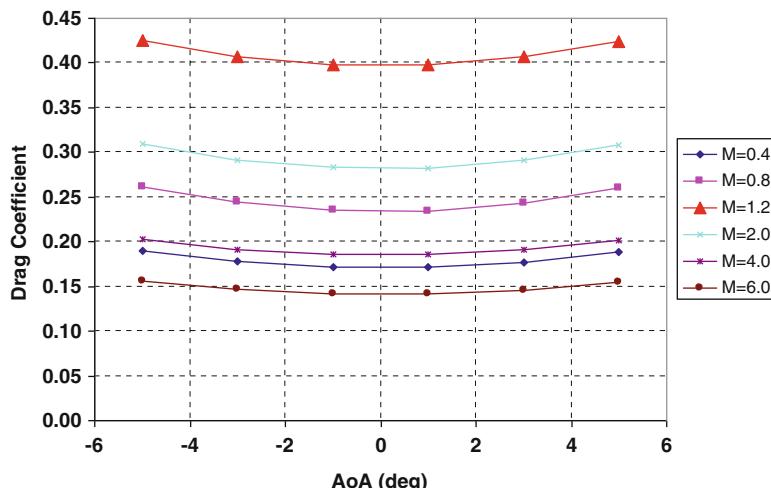
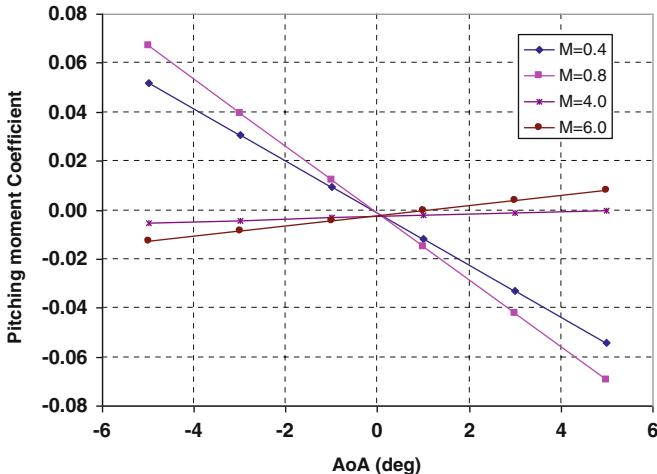
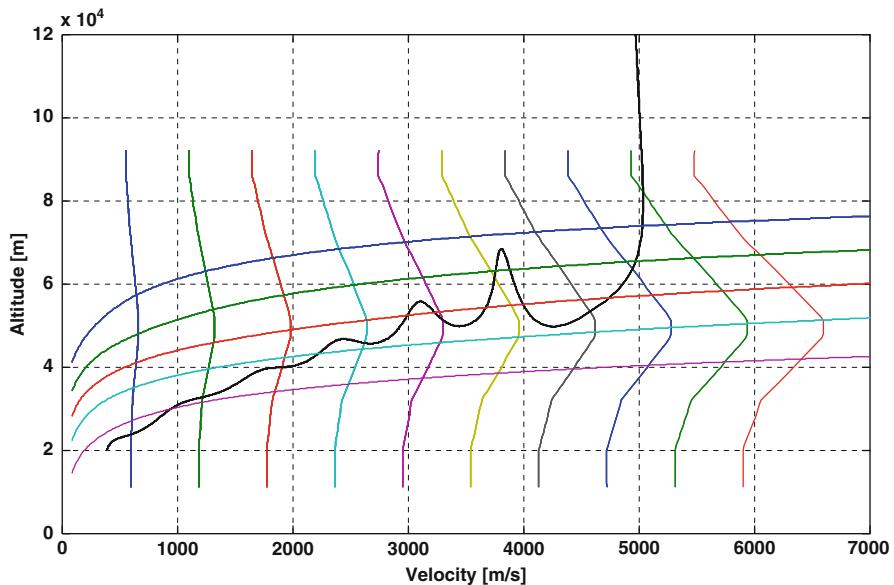


Fig. 8.50 Drag coefficients vs. AoA for ascent flight VTO-Hopper

Mach number ranges from 2 to 20, while five Reynolds numbers (i.e., [1, 3, 8, 20, 70]  $\times 10^6$ ) with respect to  $L_{ref}$  are displayed. It must be noted that the ranges of Mach and Reynolds numbers were chosen in such a way to cover a wide part of the re-entry flight, especially the most critical one from the aeroheating point of view (i.e.,  $M_\infty = 13.4$ ) [18, 21].



**Fig. 8.51** Pitching moment coefficients vs. AoA for ascent flight VTO-Hopper



**Fig. 8.52** The VTO Hopper re-entry trajectory in the altitude–velocity map

Based on re-entry flight scenario summarized in Fig. 8.52, the aerodynamic data set was generated for the following ranges:

$$\begin{aligned} 2 < M_\infty < 20 \\ 0^\circ < \alpha < 50^\circ \\ 10^6 < Re_\infty < 70 \times 10^6 \\ \beta = 0^\circ \end{aligned}$$

$$\begin{aligned} & [2, 3, 5, 7, 10, 15, 19] \\ & [0, 5, 10, 15, 20, 25, 30, 35, 40, 45, 50] \\ & [1, 3, 8, 20, 70] \times 10^6 \end{aligned}$$

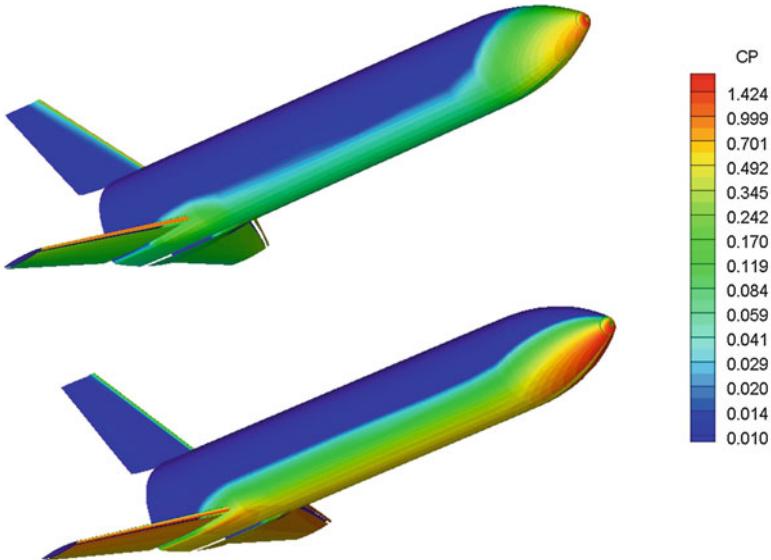


**Fig. 8.53** Pressure coefficient contours on the vehicle surface at  $M_{\infty} = 5$ ,  $\text{AoA} = 10^\circ$  (top) and  $30^\circ$  (bottom)

Neither lateral-directional analysis nor wing and body flap effects have been taken into account in this analysis.

As an example, results for  $M_{\infty} = 5$  are summarized in Fig. 8.53, where the static pressure distribution over the wetted vehicle surface for two angles of attack (i.e.,  $10^\circ$  and  $30^\circ$ ) is reported [19, 22].

Ranging AoA from  $10$  to  $30^\circ$ , as highlighted by pressure coefficient contours, the Hopper configuration must exhibit very different aerodynamic performance. For example, Fig. 8.54 shows that starting from  $\text{AoA} = 0^\circ$ , the booster aerodynamic efficiency straightly increases, reaching the peak of about 1.6 at  $\text{AoA} = 15^\circ$ , and then it decreases up to about 0.7 at  $\text{AoA} = 30^\circ$ .

By conclusion, looking at Fig. 8.55, one can appreciate an overview of booster's aerodynamic efficiency for the whole Mach number and AoA regimes.

Note that lift-to-drag ratio (L/D) is the most important feature of vehicle aerodynamic performance, which has a direct impact on cross-range capability of a re-entry vehicle that reaches its nominal landing site (DLRS) at the end of space mission by unpowered flight [17].

As clearly shown, the Oswatich principle (independence of aerodynamic coefficients to  $M_{\infty}$ ) is satisfied starting already from  $M_{\infty} = 7$  [14]. Moreover, quick aerodynamic assessment is fundamental for concept aeroshape trade-off analysis. For instance, preliminary evaluation of wing planform shape on the booster aerodynamic performance is herein described.

Generally speaking, the wing shape may influence markedly the aerodynamic and aerothermodynamic performance of a launcher [17].

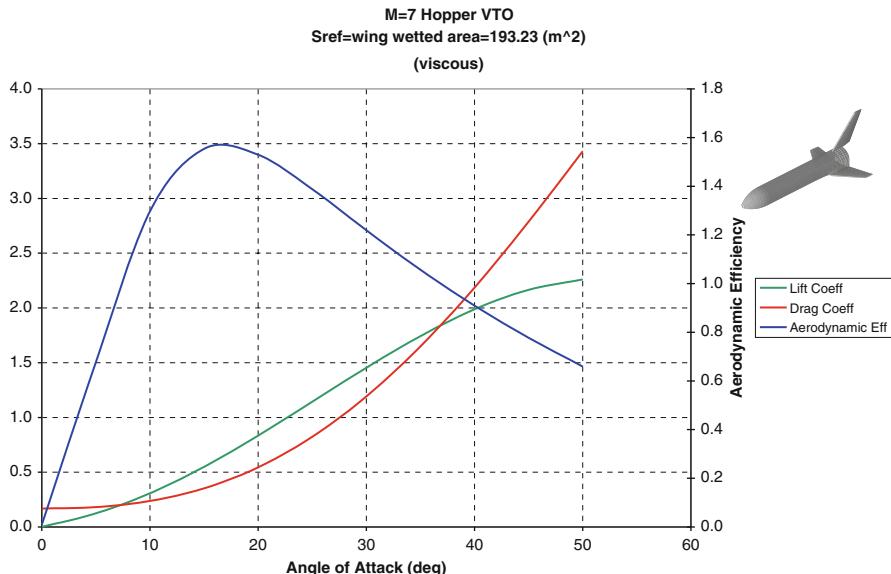


Fig. 8.54 Booster aerodynamic characteristics at  $M_{\infty} = 7$

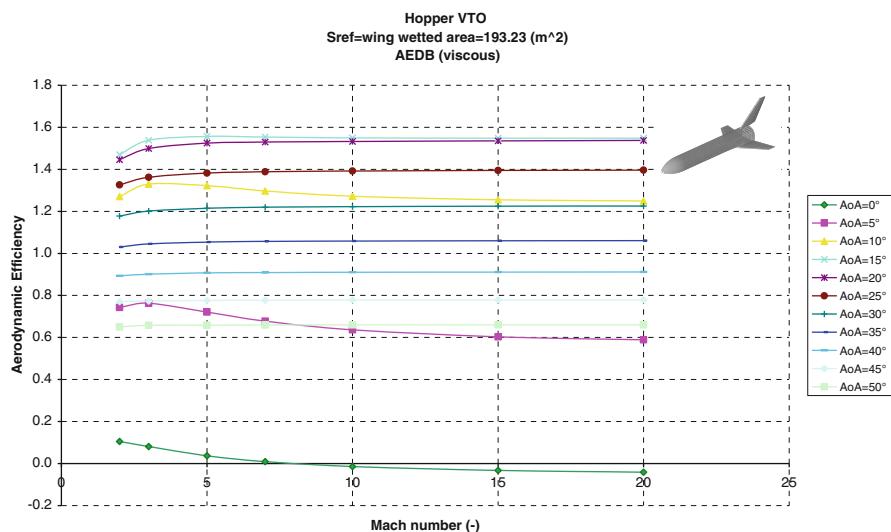


Fig. 8.55 Booster aerodynamic efficiency vs. Mach number, for different AoA

For example, in hypersonic flow conditions, the presence of a wing sweep angle ( $\Lambda$ ) influences both the aerodynamic efficiency ( $E_{ff}$ ) and wing leading edge aeroheating.

**Fig. 8.56** Qualitatively behavior of  $E_{ff}$  vs. wing swept

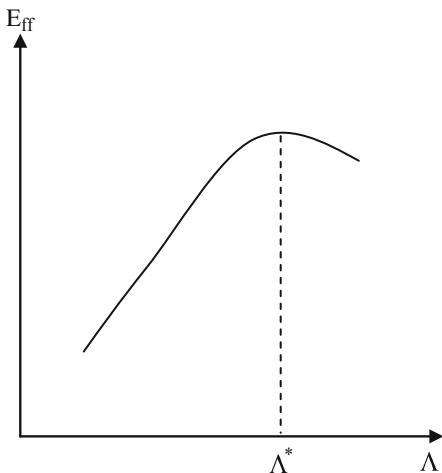


Figure 8.56 shows qualitatively that the more the wing sweep angle ( $\Lambda$ ), the more the aerodynamic efficiency. This is true only up to  $\Lambda^*$  where a reversal occurs and  $E_{ff}$  begins to decrease. Typically  $\Lambda^*$  ranges between  $65^\circ$  and  $75^\circ$ .

Detailed trade-off analyses on wing planform shape are beyond the scopes of this chapter. However, the effect of five different wing planform shapes on whole launcher's aerodynamic efficiency has carried out in a very preliminary analysis. A simplified approach has been used to build the wing. Each of them has been derived by scaling up the baseline geometry, in  $x$  and  $y$  directions, by different factors. An overview of these wing planforms is shown in Fig. 8.57.

The first wing, identified as step #1, has been obtained scaling up the baseline one in  $x$ -direction by 1.5, taking constant  $y$ . The second one (step #2) is characterized by an  $x$ -axis scaling of a factor of two. The wing number three (step #3) differs from baseline one for a  $y$  scaling by a factor of 1.3. Step #4 identifies a wing obtained by  $x$  and  $y$  scaling up the baseline by a factor of 1.5 and 1.3, respectively.

Finally, wing step #5 is obtained by  $x$  and  $y$  scaling the baseline wing by a factor of 2 and 1.3, respectively.

Figure 8.58 shows the comparison between the baseline configuration on the left side of the booster and the modified wing (e.g., step # i) on the right side. Therefore, one can appreciate at same time the wing differences.

The effect of each wing shape is summarized in Fig. 8.59 where is shown the  $\Delta E_{ff}$  (i.e., aerodynamic efficiency with respect the baseline at the same AoA) versus AoA at  $M_\infty = 7$ . Note that this Mach number was chosen as representative of whole hypersonic regime on the base of Oswatich principle. As one can see, a strong effect can be appreciated only around  $AoA = 10^\circ$ . Therefore, if the vehicle re-enters flying at an AoA higher than  $20^\circ$  no matter is the influence of wing planform shape on aerodynamic performance for a configuration as such that of VTO Hopper.

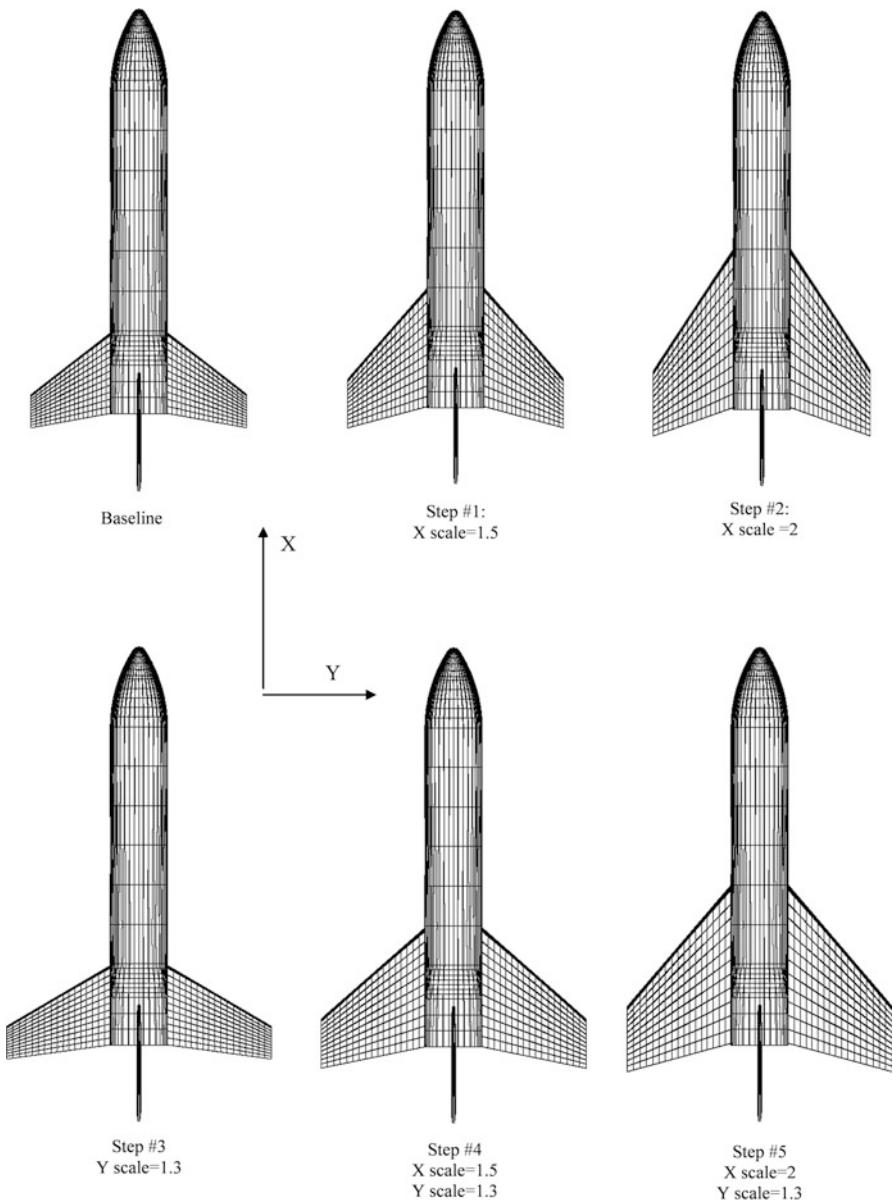


**Fig. 8.57** The VTO Hopper booster with different wing planform shapes

As far as reliability of design activities is concerned, several comparisons are provided between results of present analyses and data provided by more reliable CFD computations.

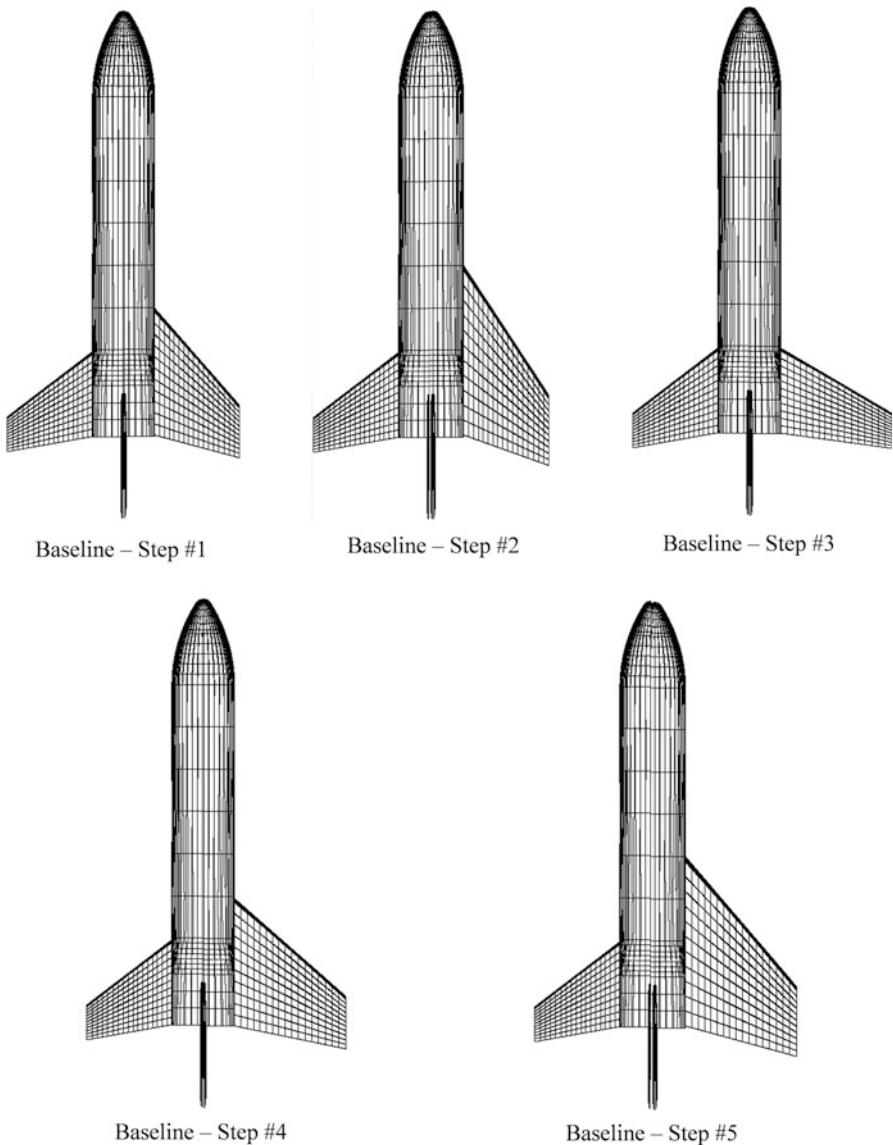


**Fig. 8.58** The VTO Hopper booster with base line wing (*left*) and different wing planform shapes (*right*)

For instance, on the base of the re-entry scenario of VTO Hopper (see Fig. 8.52), a number of flight conditions have been chosen to carry out CFD computations. Those numerical computations will allow anchoring engineering analyses in order to verify the attained accuracy of these simplified analyses and to focus on some

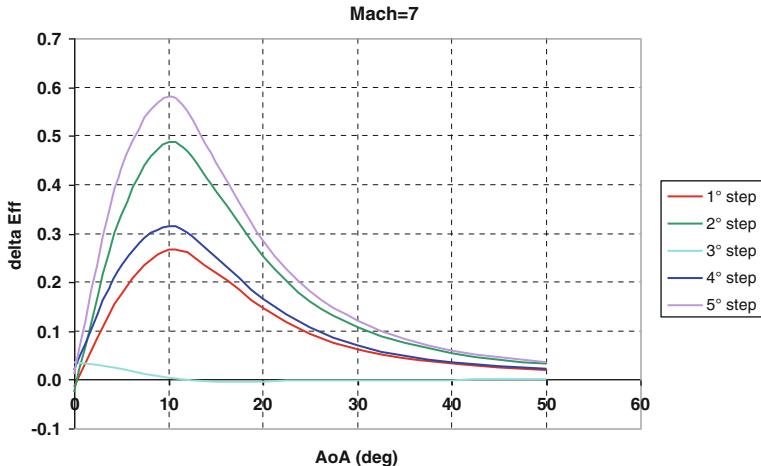


**Fig. 8.59**  $\Delta\text{Eff}$  vs. AoA for each different wing planform shape

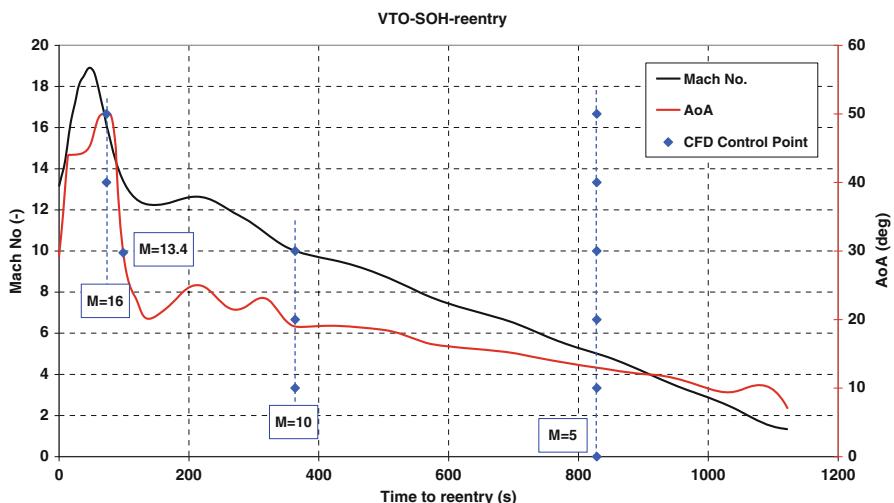


**Fig. 8.60** The VTO Hopper booster re-entry scenario with control points for CFD analyses

critical design aspects not predictable with engineering tools. Those control points are reported in Fig. 8.60, while the CFD test matrix is summarized in Table 8.4.

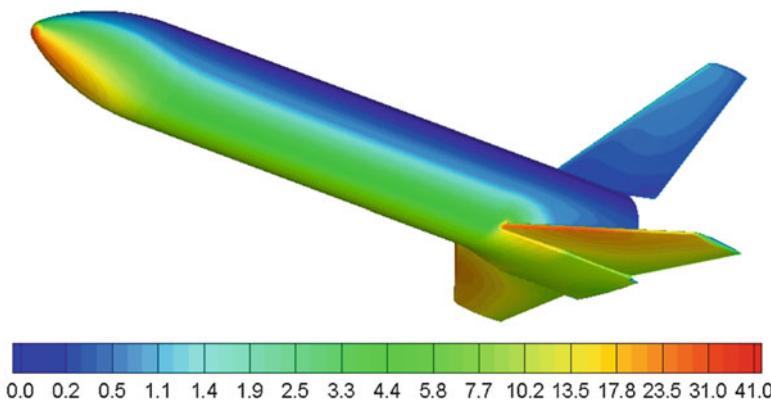
As one can see, each check point lies within the flight scenario foreseen for a typical mission profile of the booster. Therefore, the results of twelve CFD Euler computations were considered within the vehicle preliminary design.

In the following figures, some of the main CFD results obtained for the booster configuration are shown.

For example, Fig. 8.61 shows normalized pressure contour field is shown for  $M_\infty = 5$  and  $\text{AoA} = 20^\circ$ .

**Table 8.4** The CFD test matrix

AoA [deg]	Mach			
	5	10	13.4	16
0	Red	White		
10	Red	Red		
20	Red			
30	Red		Red	
40	Red	White	White	Red
50	Red			Red

**Fig. 8.61** Normalized pressure contours on vehicle surface at  $M_{\infty} = 5$ ,  $\text{AoA} = 20^\circ$ . Euler computation

Further flowfield features can be recognized in Fig. 8.62. It shows the normalized temperature contours field both on the vehicle symmetry plane and booster outer surface when the booster is flying at  $M_{\infty} = 5$  and  $\alpha = 10^\circ$ .

Looking at contour field on the vehicle symmetry plane, one can appreciate the bow shock that occurs ahead of vehicle during descent at these flight conditions.

This shock surface envelopes the vehicle and may impinge on wing leading edge (i.e., shock-shock interaction (SSI)), thus increasing locally the heat flux (overheating) the vehicle thermal shield has to withstand during descent, as shown in Fig. 8.63. This figure provides the Mach number contour field in the cross plane where bow shock impinges over the wing for  $M_{\infty} = 10$  and  $\alpha = 20^\circ$ . Therefore, analyses of SSI with overloads (pressure and heat flux) at impingement are mandatory for a reliable vehicle design [20].

Figure 8.64 reports, for  $M_{\infty} = 10$  and  $\alpha = 20^\circ$ , Mach number contours on both different cross planes (on the left) and vehicle surface (on the right) with 3-D streamtraces [9].

The contour shapes in Figs. 8.63 and 8.64 give an idea of the shape of the bow shock wave that envelopes the vehicle at these flight conditions.

For what concerns aerodynamic coefficients comparisons from Figs. 8.65, 8.66, 8.67, 8.68, 8.69, and 8.70, engineering and numerical results for lift, drag, and

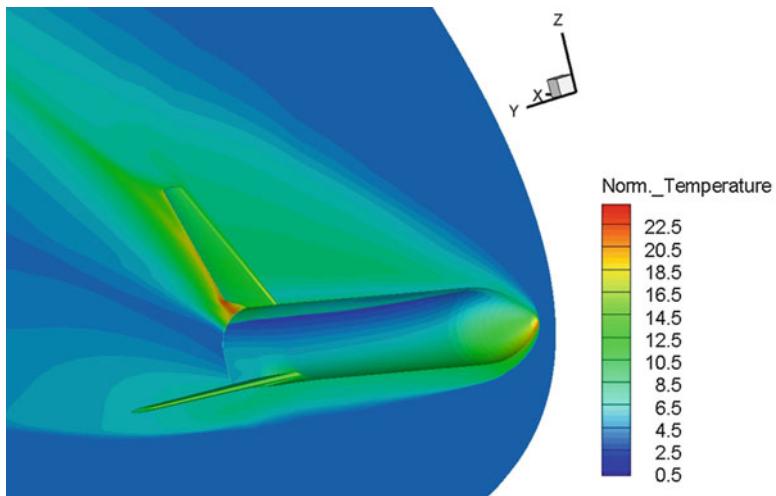


**Fig. 8.62** Normalized temperature contours on symmetry plane and vehicle surface at  $M_{\infty} = 5$ , AoA = 10°. Euler computation

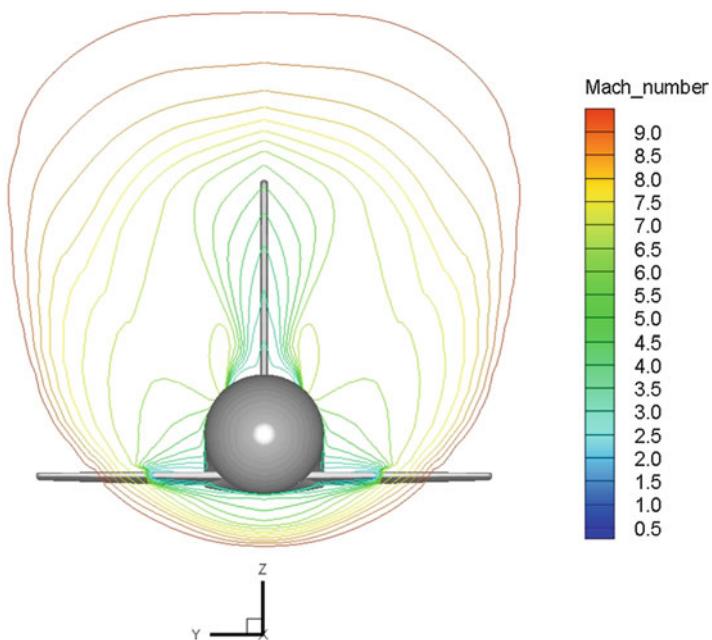


**Fig. 8.63** Mach number contours in the cross plane where bow shock impinges over the wing (SSI) for  $M_{\infty} = 10$  and AoA = 20°. Euler CFD computation

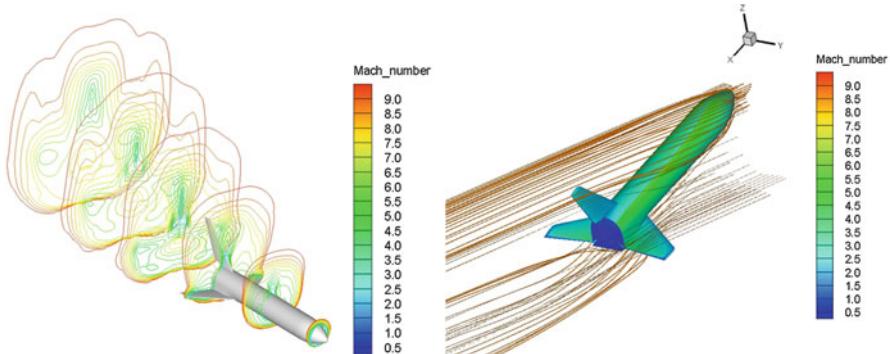


**Fig. 8.64** VTO Hopper. Mach number contours on different cross planes and vehicle surface. Euler computation at  $M_\infty = 10$  and  $\alpha = 20^\circ$

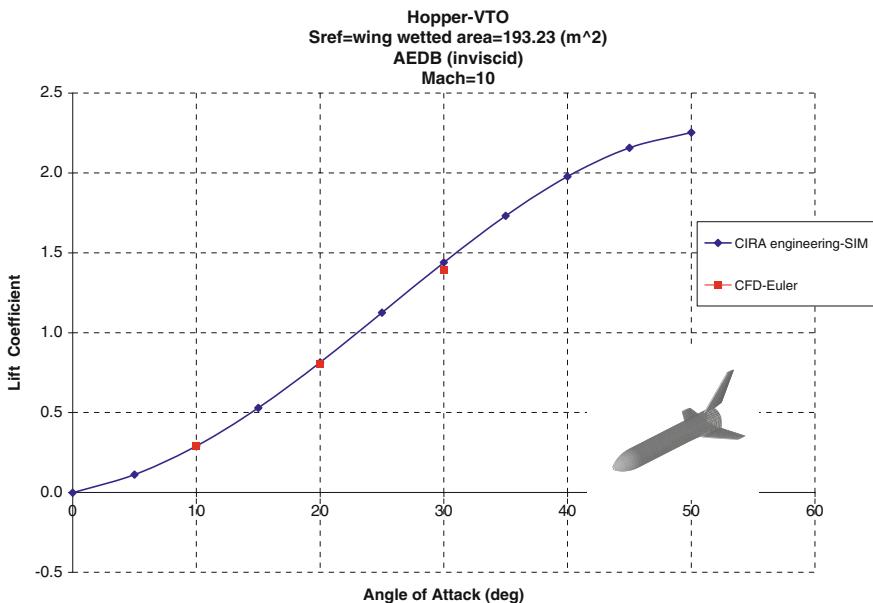


**Fig. 8.65** Lift coefficient vs. AoA. Comparison between SIM and CFD Euler at  $M_\infty = 10$

pitching moment are provided. In particular,  $C_L$ ,  $C_D$ , and  $C_m$  at  $M_\infty = 10$  are shown in Fig. 8.65, 8.66, and 8.67, respectively. The same coefficients but for  $M_\infty = 16$  are summarized from Figs. 8.68, 8.69, and 8.70.

As clearly evident, results of engineering-based approach and CFD computations compare very well at each Mach number and AoA considered. The maximum difference was found at Mach 16 and  $\text{AoA} = 50^\circ$  even if it is comprised within an error bar of 10 %.

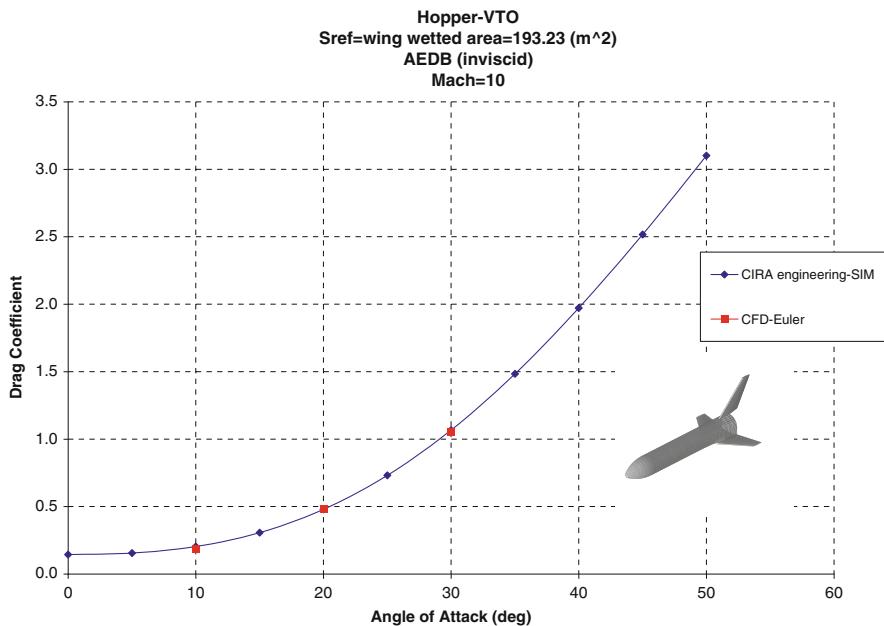


**Fig. 8.66** Drag coefficient vs. AoA. Comparison between SIM and CFD Euler at  $M_\infty = 10$

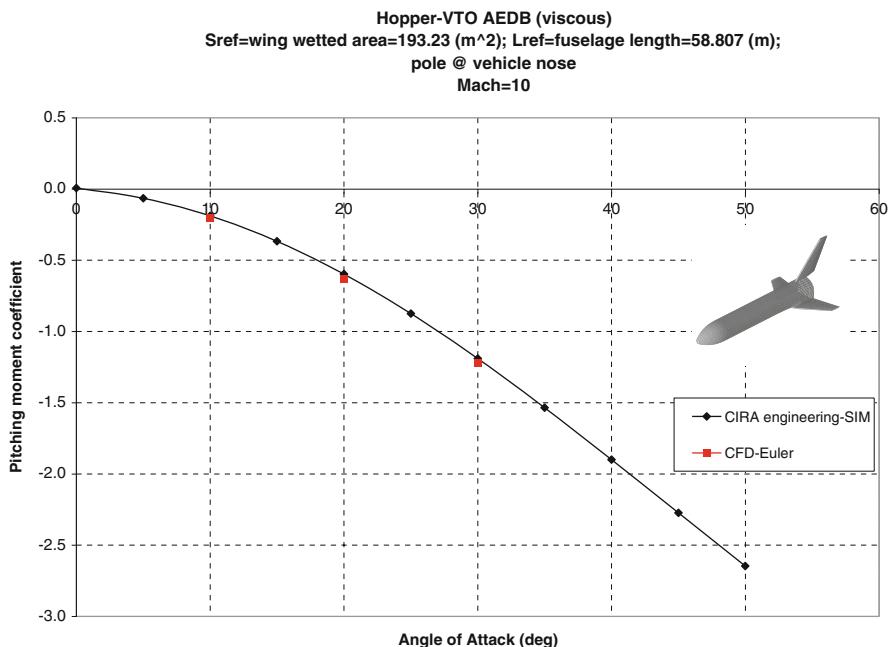


**Fig. 8.67**  $C_m$  vs. AoA. Comparison between SIM and CFD Euler at  $M_\infty = 10$

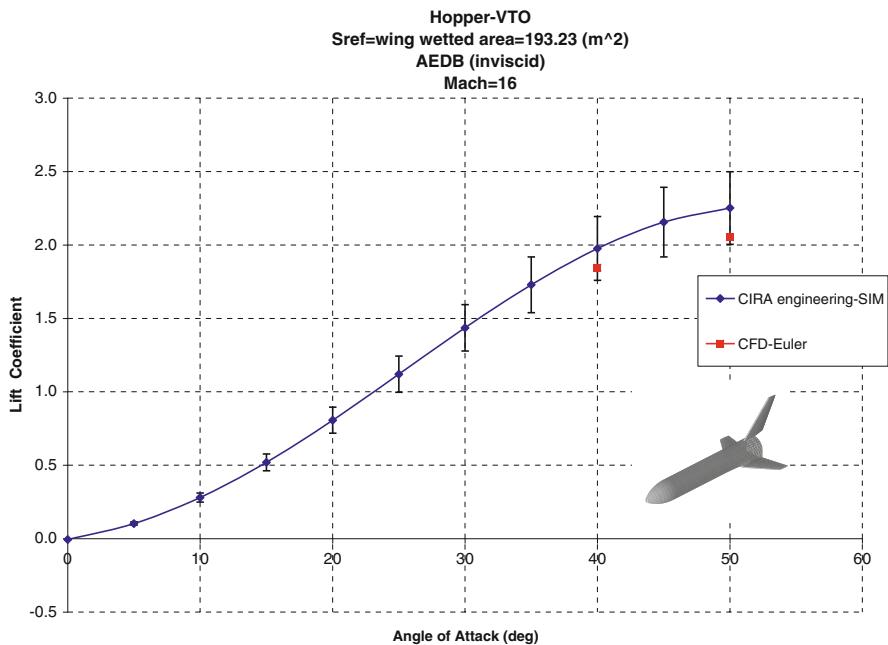


Fig. 8.68  $C_L$  vs.  $\alpha$ . Comparison between SIM and CFD Euler at  $M_\infty = 16$  (error bar for 10 %)

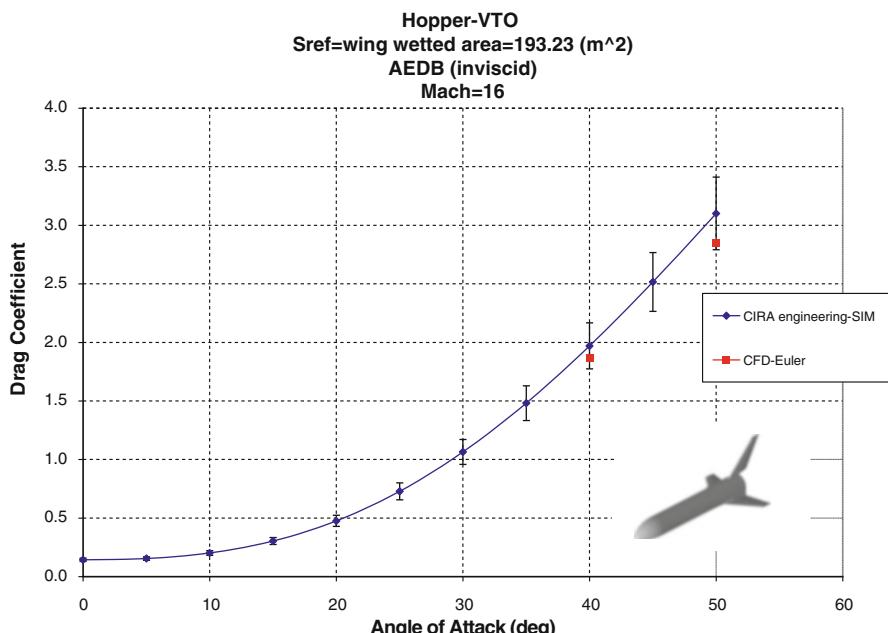
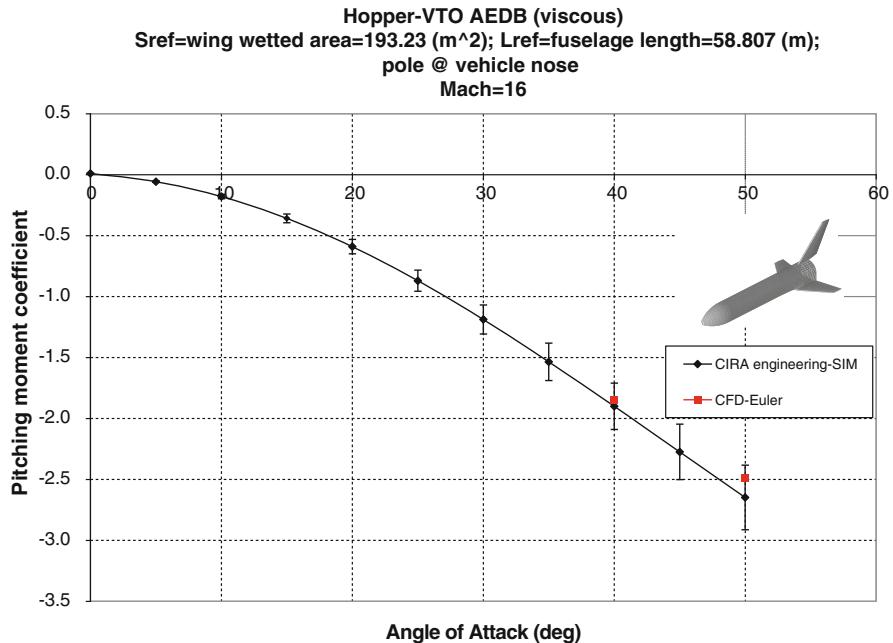


Fig. 8.69  $C_D$  vs.  $\alpha$ . Comparison between SIM and CFD Euler at  $M_\infty = 16$  (error bar for 10 %)



**Fig. 8.70**  $C_m$  vs.  $\alpha$ . Comparison between SIM and CFD Euler at  $M_\infty = 16$  (error bar for 10 %)

CFD results for RFS are reported in Fig. 8.71 for  $M_\infty = 5$  and  $\alpha = 10^\circ$ , where the bow shock as well as the shock in front of pipelines on the vehicle leeside are clearly evident [22].

Flow streamtraces are also reported in the vehicle symmetry plane, thus highlighting the flow vortexes that arise in the wake. CFD results for  $M_\infty = 8$  and  $\alpha = 15^\circ$  are shown in Fig. 8.72.

Looking from two different lines of sight, several flowfield features can be recognized as the volume streamtraces and the static pressure contours field shown over the RFS surface.

Flowfield streamlines highlight the vortex structures which arise from the pipeline over the vehicle leeside. It is worth noting that these vortexes can localize over the RFS leeward dangerous local overheating that must be taken into account for a reliable design of the booster TPS.

The lift-to-drag ratio of RFS at the staging Mach number (i.e.,  $M_\infty = 9$ ) and for inviscid flow is shown in Fig. 8.73 (error bars of 10 %). The pressure coefficient field for the LFBB ( $\text{LO}_x/\text{CH}_4$ ) is reported in Fig. 8.74 for  $M_\infty = 2$  and  $\alpha = 5^\circ$ .

The compression localized on vehicle surface as in front of pipelines on leeside, at wing–body interface, and on the nozzle shields at the side end of fuselage suggests that here local overheating is expected. Finally, when the flow hits the booster at  $M_\infty = 5$  and  $\alpha = 10^\circ$  and sideslip angle AoS =  $8^\circ$ , the pressure distribution over the vehicle surface changes as displayed in the Fig. 8.75.

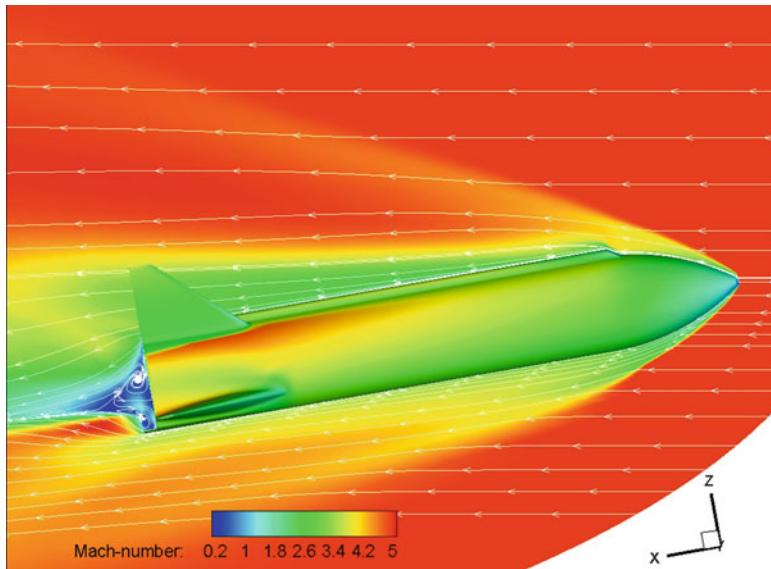


**Fig. 8.71** RFS. Mach number contours on symmetry plane and vehicle surface at  $M_\infty = 5$  and  $\alpha = 10^\circ$ . CFD Euler computation

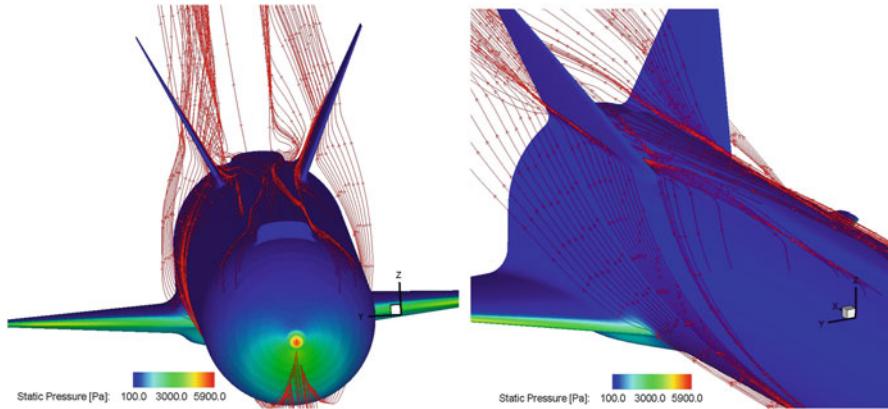


**Fig. 8.72** Contours of static pressure on RFS surface with flowfield streamtraces at  $M_\infty = 8$  and  $\alpha = 15^\circ$

The corresponding AoS effect on LFBB lift, drag, and lift-to-drag ratio is recognized in Fig. 8.76 for  $\beta = 0^\circ, 4^\circ$ , and  $8^\circ$ . As one can see, at  $\beta = 4^\circ$  the vehicle L/D does not change significantly, whereas for  $\beta = 8^\circ$  the aerodynamic efficiency decreases of about 7 % only.

The present aerothermodynamic analysis of each FLPP concept (in clean configuration only) provides vehicle thermal loading by means of surface heat flux

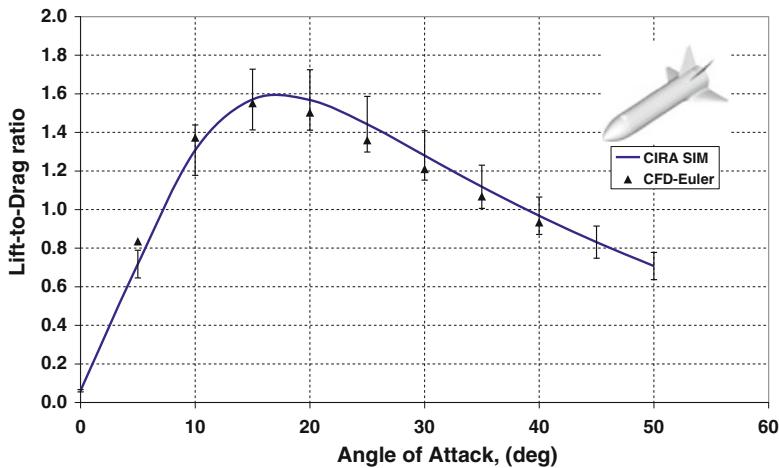


**Fig. 8.73** The RFS lift-to-drag ratio vs. AoA at staging conditions. Comparison between CIRA SIM and CFD Euler at  $M_\infty = 9$ . Error bar of 10 %

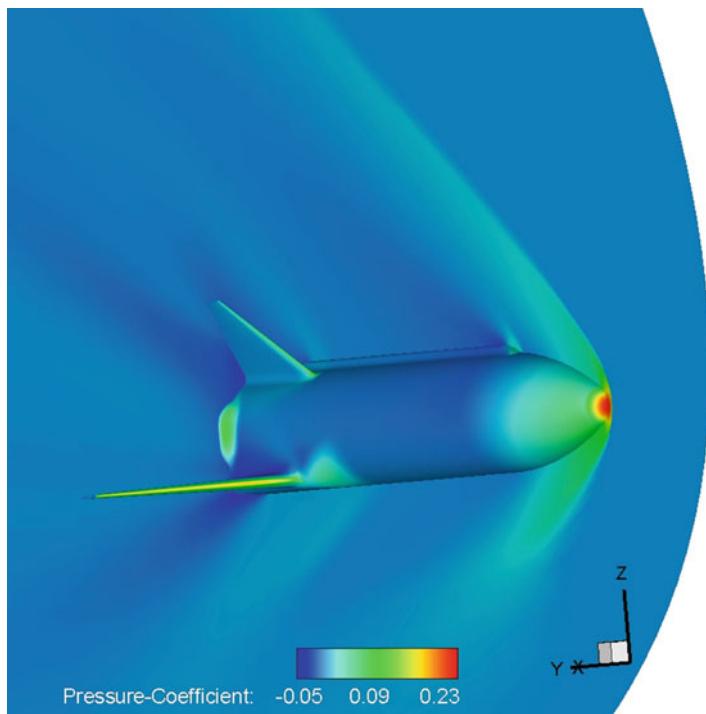


**Fig. 8.74** LFBB.  $C_p$  contours on symmetry plane and vehicle surface at  $M_\infty = 2$  and  $\alpha = 5^\circ$

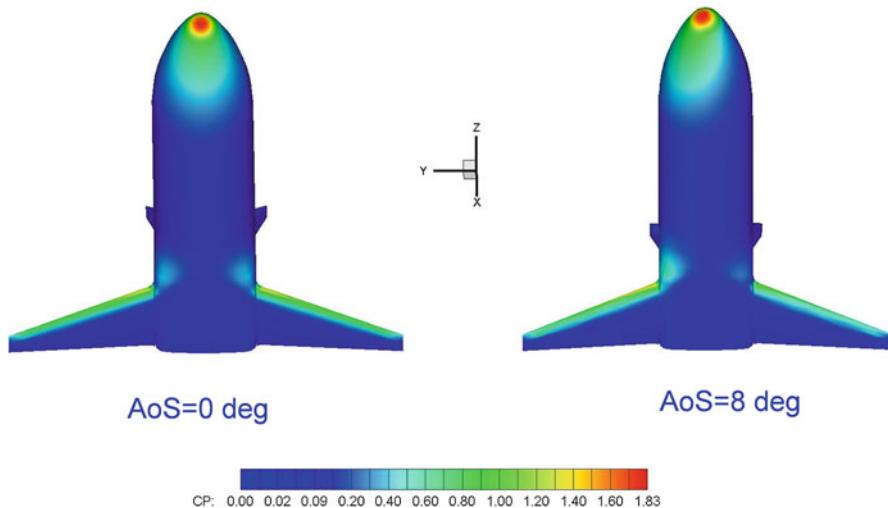


**Fig. 8.75** LFBB. Cp contours on the vehicle surface at  $M_\infty = 5$ ,  $\text{AoA} = 10^\circ$ , and  $\text{AoS} = 8^\circ$ . Comparison between  $\text{AoS} = 0^\circ$  and  $8^\circ$

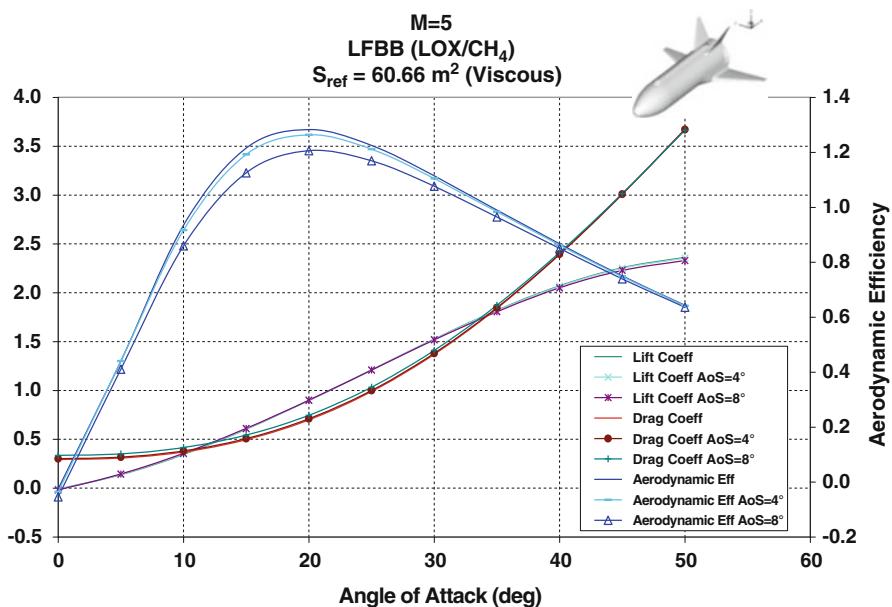


**Fig. 8.76** LFBB aerodynamic characteristics at  $M_\infty = 5$ . Comparison among  $\text{AoS} = 0^\circ$ ,  $4^\circ$ , and  $8^\circ$

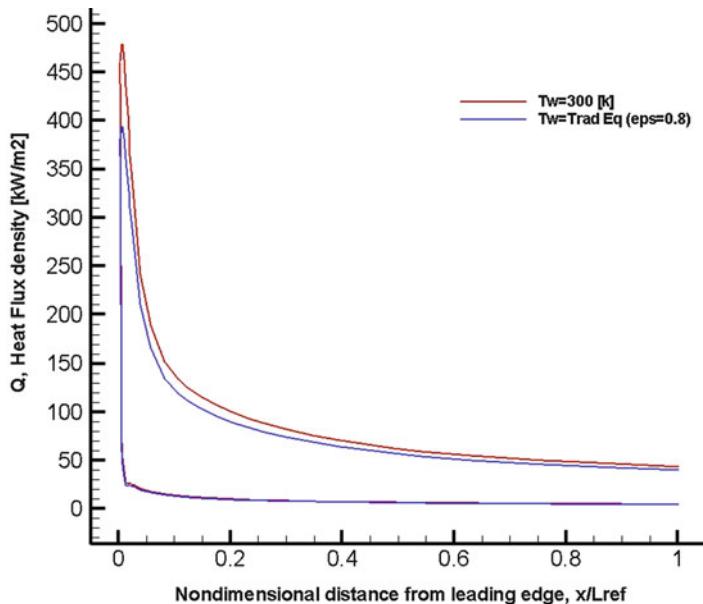


**Fig. 8.77** Heat flux along Hopper centerline at peak heating (Table 8.2). Comparison between cold and radiative equilibrium wall boundary conditions

distributions, computed for cold wall (i.e.,  $T_w = 300 \text{ K}$ ) and radiative equilibrium wall boundary conditions (wall emissivity,  $\epsilon$ , equal to 0.8). The air is modeled either as ideal gas or as a reacting gas mixture in chemical equilibrium, both for laminar and turbulent flow, depending on the trajectory free-stream conditions, of course [30, 31]. For example, Fig. 8.77 shows the heat flux distribution on the HTO Hopper centerline at trajectory peak heating provided by SIM (see Table 8.2). Here, the effect of radiative cooling can be appreciated as fuselage stagnation-point heat flux decreases of about  $100 \text{ kW/m}^2$ .

The heat flux distribution on the VTO Hopper centerline at trajectory peak heating is shown in Fig. 8.78 for turbulent equilibrium flow and cold wall conditions [19].

Note that the CFD heat flux markedly differs from that evaluated with engineering methods, only at about  $x/L_{ref} = 0.2$  and 0.8. This behavior is due to pressure changes related to surface curvature variations induced by blending of the nose and wing sections into the VTO main fuselage (e.g., downstream effects of nose blunting that originate a combining effects of entropy layer and AoA).

The surface distribution of heat flux for the RFS flying at staging conditions, for  $T_w = 300 \text{ K}$  and for equilibrium turbulent flow, is reported in Fig. 8.79, as evaluated by SIM.

As one can see, when the RFS is flying at  $M_\infty = 9$ ,  $\alpha = 5^\circ$ , and  $H = 55.7 \text{ km}$ , also the leeside is exposed to the incoming flow, thus reaching surface heat flux distributions comparable to those of windside. Therefore, particular care demands

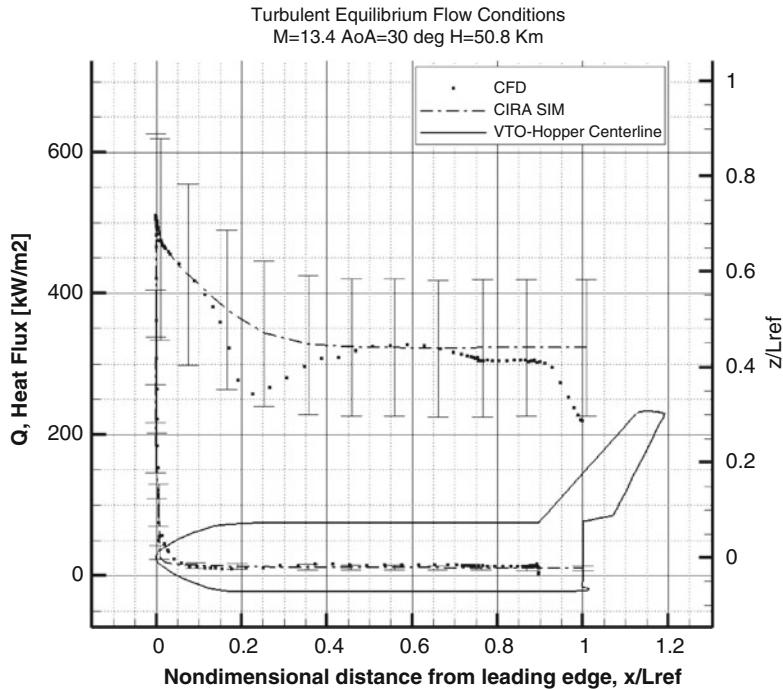


**Fig. 8.78** VTO centerline heat flux at peak heating for turbulent equilibrium flow.  $M_\infty = 13.4$ ,  $\alpha = 30^\circ$ , and  $H = 50.8$  km.  $T_w = 300$  K. Error bar of  $\pm 30\%$

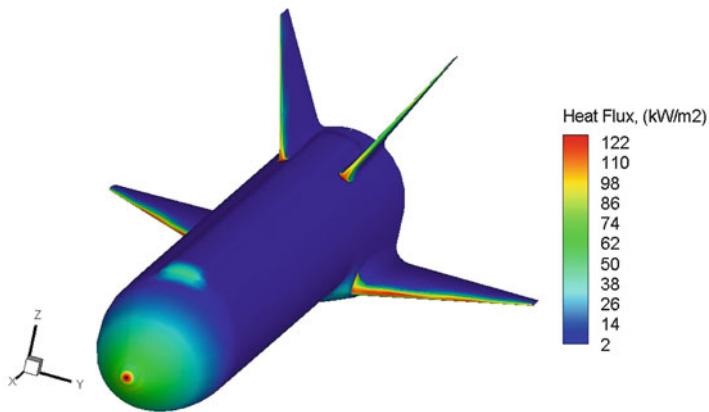


**Fig. 8.79** Surface heat flux distribution at staging conditions for equilibrium turbulent flow.  $M_\infty = 9$ ,  $\alpha = 5^\circ$ , and  $H = 55.7$  km.  $T_w = 300$  K

both the pipeline and wing-fuselage junction thermal shielding as well [23, 32]. The centerline heat flux at trajectory peak heating is shown in Fig. 8.80, both for laminar and turbulent equilibrium flow.

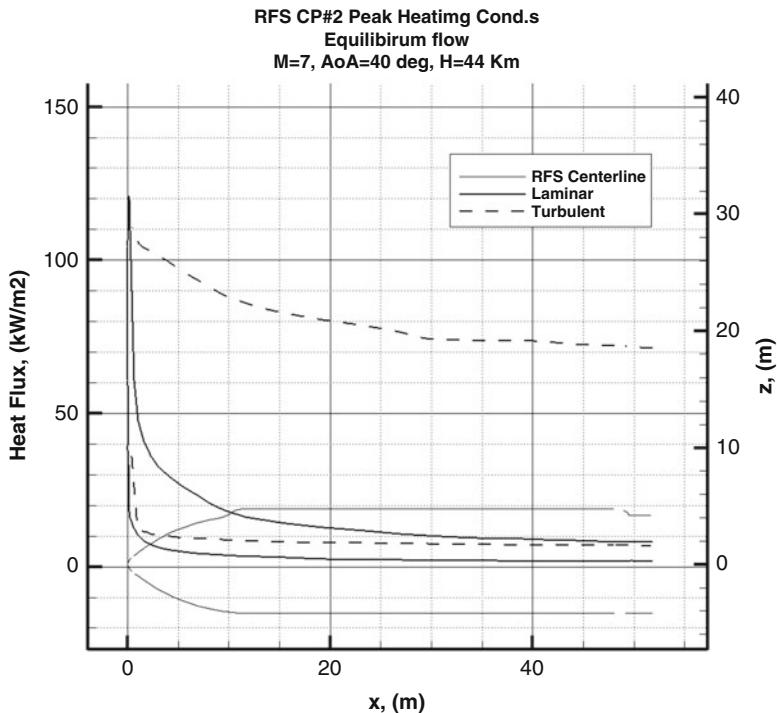


**Fig. 8.80** Heat flux along RFS centerline at peak heating.  $T_w = 300$  K. Comparison between laminar and turbulent flow for equilibrium gas conditions

Then the RFS descent trajectory results in a peak heating at fuselage nose of about  $120 \text{ kW/m}^2$ , whereas the turbulent to laminar heat flux ratio is larger than four [33].

For the LFBB concept, the stagnation-point heat flux does not exceed  $40 \text{ kW/m}^2$ .

For a reliable design, however, the above results must be confirmed by CFD analysis since complex 3-D flowfield interactions phenomena can arise as, for example, shock–shock interaction (SSI) over the wing and fin leading edges.

For example, in Fig. 8.81, it is clearly recognized the pressure spike on the wing leading edge due to SSI when the RFS is flying at  $M_\infty = 8$  and  $\alpha = 15^\circ$  (see left side) and at  $\alpha = 30^\circ$  (right side). As shown, the SSI location depends also on vehicle attitude.

Anyway, above results provide very interesting features to be taken into account for a reliable TPS design for the FLPP concepts. For instance, turbulent equilibrium flow and cold wall conditions result in a conservative estimation of the aerothermal environment that the vehicle has to withstand through descent, as expected.

If the RFS configuration is divided in a number of surface patches, as shown in Fig. 8.82, it is possible to estimate, at engineering level, the heat load and, hence, the integrated heat load that the booster experiences through descent.

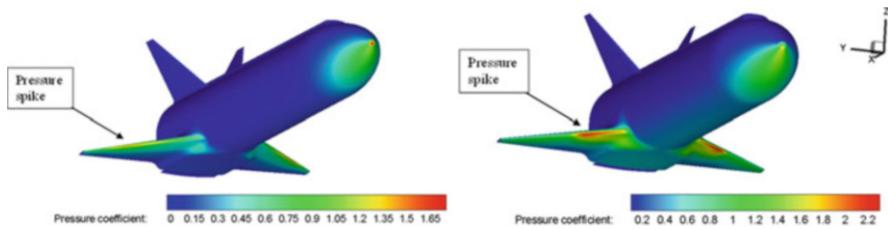
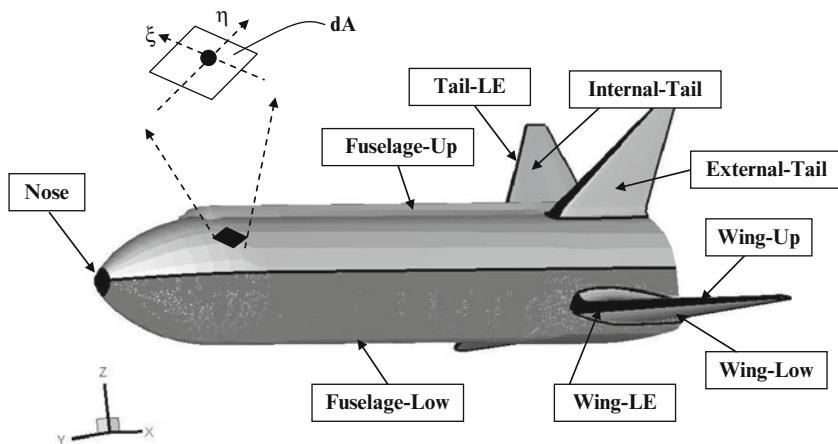


**Fig. 8.81** Pressure coefficient contours on RFS surface for  $M_\infty = 8$ , and  $\alpha = 15^\circ$  (left) and  $\alpha = 30^\circ$



<b>nose</b>	<b>0.81</b>	<b>wing_up</b>	<b>60.52</b>	<b>tail_up</b>	<b>44.00</b>
<b>fuse_up</b>	<b>240.15</b>	<b>wing_low</b>	<b>57.21</b>	<b>tail_low</b>	<b>42.67</b>
<b>fuse_low</b>	<b>434.14</b>	<b>wing_le</b>	<b>6.13</b>	<b>tail_le</b>	<b>5.30</b>
<b>Total Fuse (m<sup>2</sup>)</b>	<b>675.10</b>	<b>Total Wing (m<sup>2</sup>)</b>	<b>123.86</b>	<b>Total Tail (m<sup>2</sup>)</b>	<b>91.97</b>
<b>Total (m<sup>2</sup>)</b>	<b>890.93</b>				

**Fig. 8.82** Surface patches for RFS heat load assessment

Note that such evaluation is mandatory for thermal shield design scopes. In fact, while the peak heat flux determines the TPM and the heat shield layout depends on the heat flux distribution on the whole vehicle surface, the integrated heat load drives the thermal shield thickness.

First, for the generic RFS surface patch, the heat load  $\dot{Q}_{\text{patch}}$ , at the time  $\bar{t}$  during descent, reads

$$\dot{Q}_{\text{patch}}(\bar{t}) = \iint_{\text{patch}} \dot{q}_{\text{patch}}(\xi, \eta, \bar{t}) d\xi d\eta \quad (8.16)$$

where  $\dot{q}_{\text{patch}}(\xi, \eta, \bar{t})$  is the surface heat flux distribution recognized on the RFS patch at the time  $\bar{t}$  (e.g., at each trajectory control point), while each point of patch is identified by the surface coordinates  $(\xi, \eta)$  (see Fig. 8.82). For the sake of simplicity, this surface integral can be approximated by a summation, provided that the surface heat flux is supposed constant at each surface panel  $dA$ :

$$\dot{Q}_{\text{patch}}(\bar{t}) = \iint_{\text{patch}} \dot{q}_{\text{patch}}(\xi, \eta, \bar{t}) d\xi d\eta = \int_{A_{\text{patch}}} \dot{q}_{\text{patch}}(A, \bar{t}) dA \cong \sum_i \dot{q}_{A_i}(\bar{t}) dA_i \quad (8.17)$$

If this relationship is applied to each trajectory control point and for each RFS patch (see Fig. 8.82), one can obtain the results summarized in Fig. 8.83.

As one sees, the lower side of fuselage contributes for the larger part of total RFS heat load, and both vehicle leeside and wing windside represent, essentially, the remaining contribution. Moreover, looking at the fuse low, wing low, and fuse-up curves shape, the effect of AoA can be appreciated as well, since the heat load for fuse and wing low patches increases with a rate larger than that for fuse-up before the heat load peak (e.g., higher AoA). After the peak (e.g.,  $\alpha$  is decreasing), the contribution of RFS leeside to the vehicle heat load increases, of course.

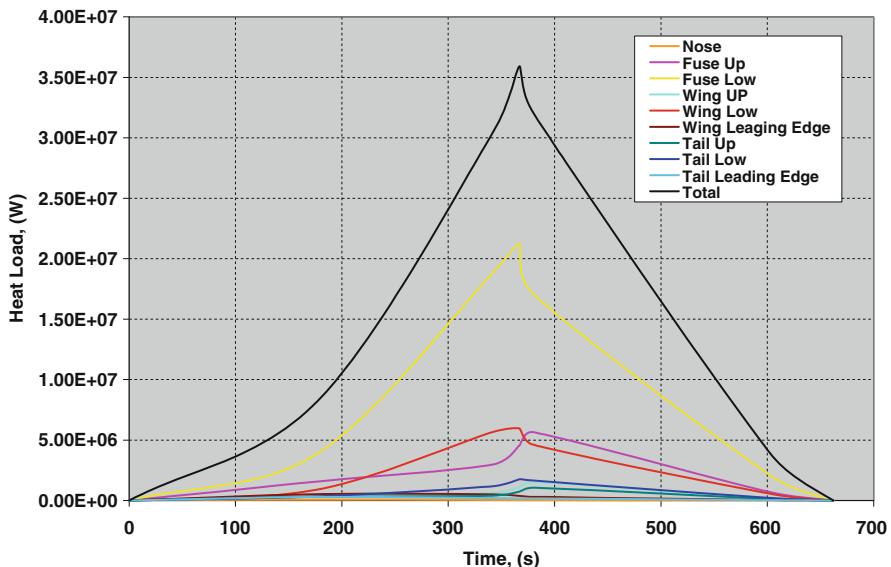


**Fig. 8.83** RFS heat load and its components

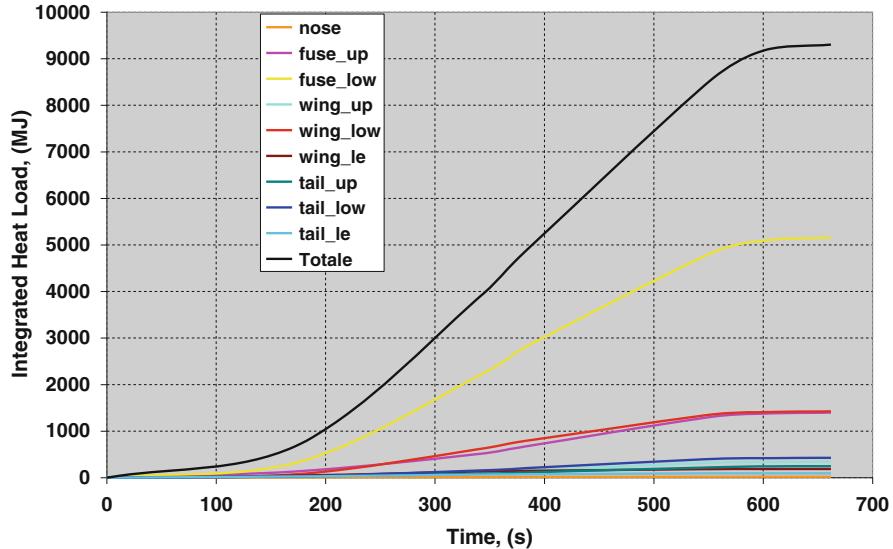


Fig. 8.84 RFS integrated heat load and its components

Once the time history of heat load for each surface patch has been evaluated, the integrated heat load can be straightforward calculated.

For instance, the integrated heat load  $Q_{\text{patch}}$  at the generic vehicle patch reads

$$Q_{\text{patch}} = \int_{t_i}^{t_f} \dot{Q}_{\text{patch}}(t) \, dt \quad (8.18)$$

and is recognized in Fig. 8.84.

## 8.4 Pre-projects Phases: Uncertainties in Databases

Design examples discussed so far highlight that vehicle aerodynamic design analysis improves by using computational fluid dynamics [1, 34, 35]. However, three categories of uncertainties in AEDB for phase A projects based on CFD approach can be identified. They are:

- Uncertainties due to CFD level of physic model and code validation
- Uncertainties due to launcher shape representation in early program phases
- Uncertainties due to limited computation points

### ***8.4.1 Uncertainties Due to CFD Level of Physic Model and Code Validation***

Several levels of CFD model can be used with increasing level of precision and increasing computation cost [1, 38].

Quite quick computations can be obtained with Euler approach, due mainly to reduced grid cells number requirements when compared to other approaches. With this level, viscous effects are not taken into account. The first consequence is that axial force coefficient is underestimated and should be complemented by an evaluation of friction contribution with boundary-layer formulae. Furthermore, in region of intensive expansion (hammerhead fairing or shrinkages between different stages), flow separation is not conveniently determined in pressure level and expansion, leading locally to poor precision of pressure maps. Moreover, viscous spreading of flows interactions on walls in the boundary layer is not simulated, leading to too intensive and too focalized pressure shoots on walls. Nevertheless, the two last inconveniences are quite local and practice shows that Euler approach leads to valuable assessments in quick loops. Critical is the knowledge of WTT reference data on similar configurations in order to build a margin policy relative to the CFD code/physical modeling precision [39, 40].

Navier–Stokes approach can improve CFD results, nevertheless at a much higher computing cost. Indeed, discretization of the boundary layer approximately doubles the requirements in terms of grid cells, versus the Euler approach. Moreover, due to much reduced grid cell sizes near the walls, iteration time step magnitude is also more limited, which also increases the number of time steps needed to reach convergence. Launcher Navier–Stokes computations are always performed with turbulence models, which is justified by high Reynolds number encountered in flight. Improvements obtained versus Euler results are very clear concerning the viscous spreading of flow interaction on walls which provide with much more precise pressure maps. Determination of separated area is also better predicted in terms of expansion of pressure level thanks to more realistic viscous and turbulent models. Nevertheless, this aspect is not fully mastered today with RANS modeling for turbulence. Validity and precision of turbulence models for such or such separated configuration has to be demonstrated case by case with reference test data, which is not satisfactory for new configuration assessment. Then, for the choice of the more convenient RANS turbulence model, some trends are known like, for example, the difficulty to obtain the exact separation point with the K- $\varepsilon$  model if this point is not fixed by a particular edge. On the contrary, separation points are generally well predicted by the Spalart–Allmaras model, but this model is not convenient for the determination of turbulent wake. Today, it seems that the more widely used is the  $\kappa$ - $\omega$  SST model, better performing with the two previously

described inconveniences. However, no RANS model is able to predict every type of separated area even for the mean flow topology.

Difficulties encountered for turbulence simulation with Navier–Stokes approach is due to unsteady nature of this phenomenon, when it can no more be represented by a mean value which is called “turbulent viscosity” in RANS models. This is particularly the case in separated flow area. Numerous attempts to upgrade turbulence simulation by representing its unsteady nature are today investigated in the aerodynamic community. In this case, models should reproduce the generation, transformation, and breakdown of turbulent structures. This leads potentially to a tremendous increase a computational effort, which depends on the necessity to fully resolve all the structures, or (on the contrary) the possibility to model the lower structure scales and resolve only the biggest ones of interest. Very promising results are now obtained with these kinds of approaches; nevertheless, due to the necessity to describe at least big turbulent structures and the necessity to perform an unsteady computation, the computing cost of this approach remains very big today.

Due to the necessity to quickly build an AEDB in phase A, today’s practice is Euler computation with refined grids. The associated margin policy is built through the comparison of some reference results with existing wind tunnel data (over similar shapes, e.g., or some specific testing for the project).

#### ***8.4.2 Uncertainties Due to Launcher Shape Representation in Early Program Phases***

In early phases, quick loops are performed between the following topics: performances, staging, propulsion, structural design, aerodynamics, general loading, and control [1, 2, 39]. Then, launcher shape constraints for aerodynamic inputs come mainly from staging and propulsion studies, and shape details are not defined already. Particularly no clear interbody attachment solutions are defined (e.g., for boosters). Moreover, a quite large number of protrusions emerging from what is called the clean surface are added to the general shape all along the launcher development (for example, RCS systems fairings for upper stages, feeding lines for liquid propellant stages, separation systems fairings, cable ducts, etc.). Certain of these devices can provide with a significant amount of lift, and according to their location versus the center of gravity location, this lift can provide with a significant amount of moments. As a consequence, a specific margin policy must allocate some estimated possible contribution for all these devices according to the anticipated device sizes and locations.

### 8.4.3 Uncertainties Due to Limited Computation Points

None computed attitudes and Mach numbers of the launcher which are necessary in the AEDB should be derived through interpolation or extrapolation between existing points. This leads to a specific uncertainty which should be taken into account [1].

## 8.5 Developments Phases: The Challenges for Precise CFD

For early developments phases (B1/B2), detailed reference aerodynamic databases are required, anchored on detailed wind tunnel testing. Desirable data are the following:

- Force coefficients:

$$C_A = f(M_\infty, \alpha_e, \Phi); C_Y = f(M_\infty, \alpha_e, \Phi); C_N = f(M_\infty, \alpha_e, \Phi); \quad (8.19)$$

*(and derivatives)*

- Moment coefficients:

$$C_I = f(M_\infty, \alpha_e, \Phi); C_m = f(M_\infty, \alpha_e, \Phi); C_n = f(M_\infty, \alpha_e, \Phi) \quad (8.20)$$

*(and derivatives)*

This is needed for ranges in Mach number ( $M_\infty$ ), global incidence ( $\alpha_e$ ), and roll angle ( $\Phi$ ) mapping the flight domain and for all the variants of the launcher. Indeed, the launcher can have a different shape for different missions, different payload masses, and different flight phases. In this phase, CFD is used initially to refine shape design (e.g., the trade-off of fairing shape) and to build the first version of the AEDB. It is also used to define precisely the needs for wind tunnel testing (shape representation, choice of model mounting in test section, identification of main flow features, location of pressure taps, and needs for other measurement techniques) [1]. After wind tunnel testing, CFD contributes to the completion of the AEDB for nontested attitudes and Mach numbers; it provides also with reference data for extrapolation to flight of wind tunnel data, which generally are obtained for too low Reynolds numbers and with a limited geometrical representativeness. As much as possible, computations should be performed over refined geometry definition of the launcher and with RANS turbulence models, in order to obtain the best possible precision according to industrial standards. Indeed, more advanced models with unsteady turbulence simulation remain too expensive for a very wide use. Nevertheless, some specific VLES computations can be envisaged in order to assess potential buffeting problems on a new launcher (e.g., hammerhead fairing or base flow).

## 8.6 Example of Navier–Stokes Computations for a Development Phase

### 8.6.1 Aerodynamic Design of an Ariane 5 Liquid Flyback Booster

In the framework of launcher design development, unstructured Euler calculations and Newtonian aerodynamics provide several interesting engineering insight in vehicle aerodynamic performances both in ascent and descent phases. In fact, these kinds of calculations allow avoiding the time-consuming and complex grid generation process and are sufficient for the prediction of the surface pressure distribution, but of course they neglect the viscous effects. Nevertheless, they are able to provide rather detailed aerodynamic data sets which allow the trim and balance of the vehicle along the complete return flight trajectory and to show the main shock–shock interactions which may be used for the localization of possible hot spots. The regarded partially reusable space transportation system (see Fig. 8.85) consists of two booster stages, which are attached to the expendable Ariane 5 core stage at an upgraded future technology level [34, 36–38].

The vehicle has a length of  $l_{\text{ref}} = 42$  m, a span of  $b = 21$  m, and a planform area of  $A_{\text{ref}} = 360 \text{ m}^2$ . With view to the hypersonic region of the descent trajectory, where the aerodynamic coefficients of the vehicle are dominated by the lower surface, the trapezoidal wing has an airfoil with flat lower surface. Indeed, a detailed analysis of the flowfield interaction for the considered ascent condition points to some regions which have to be considered in more detail during the structural layout of core stage and booster, especially considering that, due to the structural design of the Ariane 5 core stage, the position of the LFBB with regard to the core stage is fixed. The behavior of the booster has to be robust over the complete Mach number



**Fig. 8.85** Ariane 5 liquid flyback booster concept

range, in order to provide sufficient safety with view to the expected aerodynamic uncertainty margins. For instance, after the lift-off, design investigations must focus on maximum dynamic pressure conditions to address structural design issues of the launcher, while after staging reusable booster aerodynamic must be well known in order to safely recover the vehicle by landing on runway. The aerodynamic and flight dynamic simulation applied in the second design loop of the LFBB requires trimmed aerodynamic data sets for the complete flight trajectory between  $0.27 < M_\infty < 7$  and angles of attack of  $5^\circ < \alpha < 35^\circ$ . Within these studies, tight margin concerning longitudinal stability and trim have to be taken into account for the isolated LFBB as well as for the complete system. With view to the structural layout of wing and body, the flight condition with maximum dynamic pressure at  $M_\infty \approx 1.6$  is of special interest. In order to extract all aerodynamic interactions on the structural loads, the isolated LFBB is compared to the Ariane 5 + 2 LFBB combination without and with junctures between rocket and LFBB. The LFBB panel mesh is shown in Fig. 8.86 [34].

Preliminary aerodynamic results are provided in Fig. 8.87 where is reported the elevon deflection angle  $\eta$  needed to pitch trim the booster for  $M_\infty > 2$ . As shown, the trim of this vehicle is only possible for  $M_\infty < 5.6$  and assuming an actually not achievable far backward position of the CoG,  $x_S/l = 0.75$ . The required flap deflections in hypersonic flow are still in the order of  $\eta = 30^\circ$  and more than  $\eta = -10^\circ$  for  $M_\infty < 2$ . These results are obtained with very large wing and

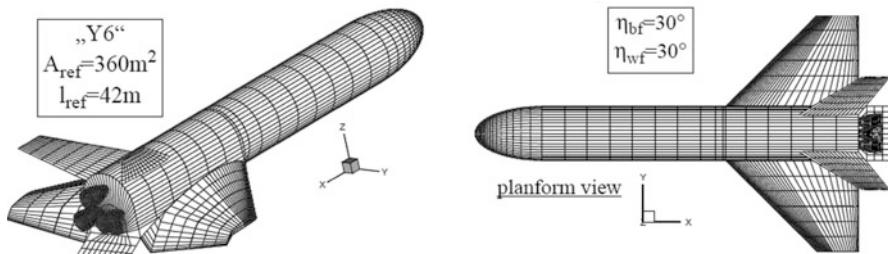


**Fig. 8.86** Initial configuration Y6. Panel mesh

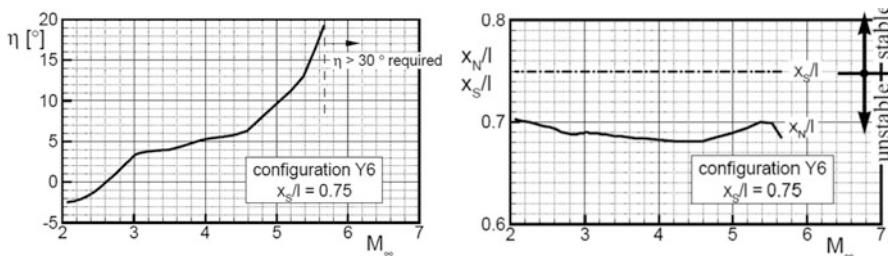


**Fig. 8.87** Trim results for configuration Y6

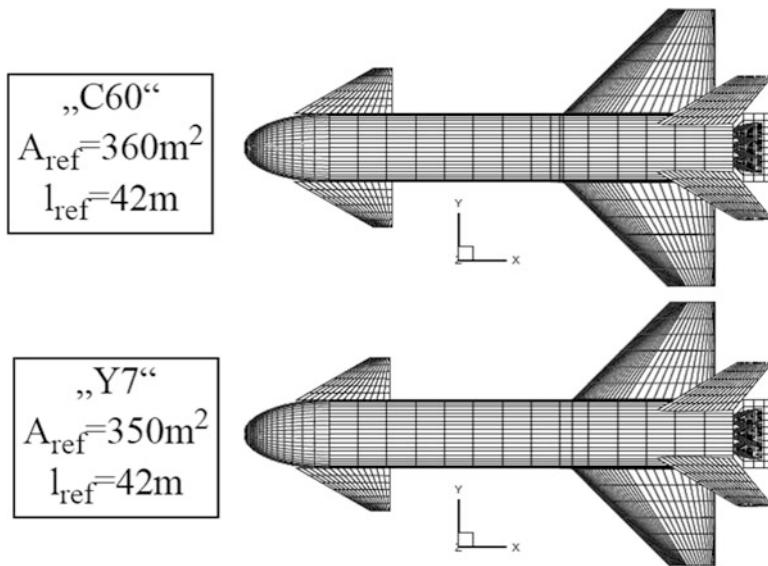


**Fig. 8.88** Geometry of the main canard configurations

body flaps with simultaneous deflection (see Fig. 8.86) [34]. Additionally the configuration is highly unstable, as shown in Fig. 8.87 [34]. Based on these results, it is decided to investigate LFBB configurations with canards. During the design cycle of the canard configuration, a large number of wing planforms and canards are investigated.

Planform views of the initial (C60) and the final configuration (Y7) of this study are given in Fig. 8.88 [34].

All investigated LFBB variants have canards with unswept trailing edges and a leading edge sweep of  $\varphi = 60^\circ$ . With view to the canard efficiency and controllability in subsonic flow, this sweep angle is chosen in order to establish leading edge vortices up to angles of attack for the canards of  $\alpha \approx 15^\circ$ . Even for bursted vortices in the trailing edge region, the maximum lift of the canards is not expected for  $\alpha < 25^\circ$ . The strategy for the application of the control surfaces is to consider a clean wing, a body flap with constant deflection, and variable canard deflection for trim. In order to allow a direct comparison to the LFBB without canard (Y6), the initial canard configuration C60 has an unchanged planform area of  $A_{ref} = 360 \text{ m}^2$ . Therefore, also the wing load is constant. The final configuration Y7 has a slightly reduced planform area of ( $A_{ref} = 350 \text{ m}^2$ ) obtained by minor changes of canard and wing size. This is required because the masses of wing and canard have to be reduced. The body itself has to be kept unchanged due to the tight margins concerning the connection with the Ariane 5 core stage.

The most important trim results are summarized in Fig. 8.89 [34].

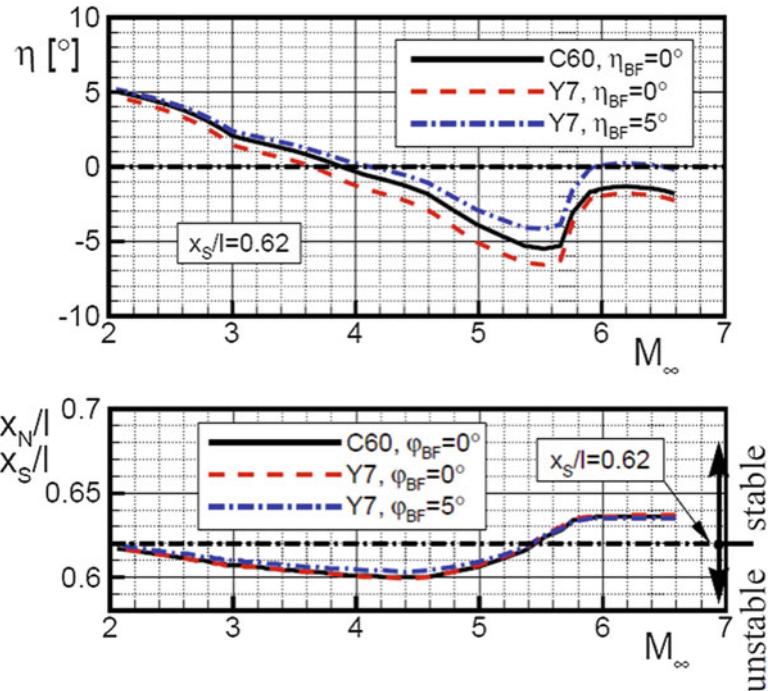


**Fig. 8.89** Trim results of the main canard configurations

It turns out that the configurations C60 and Y7 are very robust even for a realistic position of center of gravity at  $x_S/l = 0.62$ . The obtained canard deflections are always smaller than  $\eta = 5^\circ$ . The configuration is stable for  $M_\infty > 5.5$  and only slightly unstable for  $2 < M_\infty < 5.5$ . Furthermore, other design estimations indicate that the required canard deflections for subsonic conditions are always smaller than  $\eta = 10^\circ$ . An additional assessment of configuration Y7 with a deflected body flap ( $\eta_{BF} = 5^\circ$ ) again reduces the flap deflections and results in a slightly increased longitudinal stability.

Using these results, configuration Y7 is chosen as final LFBB for this design cycle. Additionally, a wind tunnel model of this configuration is shown in Fig. 8.90 [34].

For the analysis of configuration Y7 in subsonic, transonic, and supersonic flow, Euler grids around the configuration with a fixed body flap deflection of  $\eta_{BF} = 5^\circ$  are generated for canard deflections of  $\eta = 0^\circ$  and  $\eta = 10^\circ$  (see Fig. 8.91) [34].

In order to be able to simulate the influence of the leading edge vortices on the canard efficiency, also based on Euler calculations, the original NACA 0008 was slightly sharpened along the leading edge. This approach of course does not allow obtaining the real vortex structure, but it gives a good approximation of the vortex strength, and it also enables to predict a possible vortex bursting. The

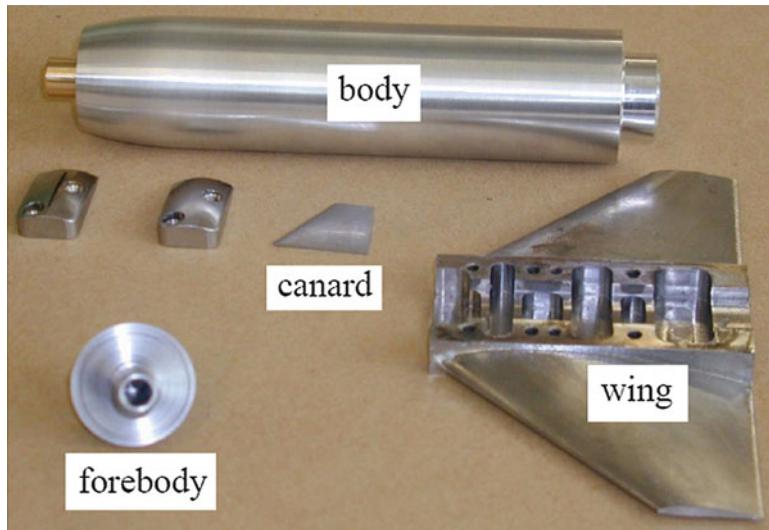


**Fig. 8.90** Already manufactured parts of the Y7 wind tunnel model

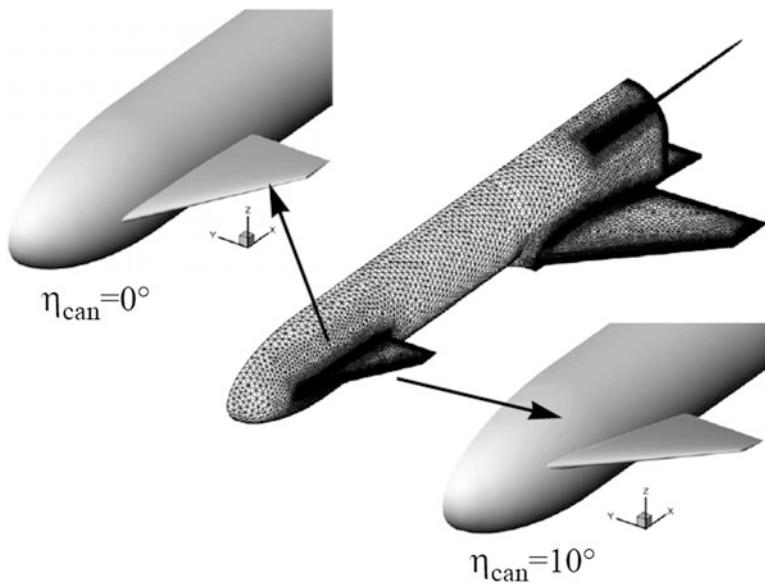


**Fig. 8.91** Surface grids of configuration Y7

goal is to interpolate a trimmed aerodynamic data set for the Mach number range  $0.27 < M_\infty < 2.0$ . The basis for this data set are calculations for 15 Mach numbers, two canard deflections, and four angles of attack for each  $(M, \eta_{\text{can}})$  combination (see Fig. 8.92) [34].

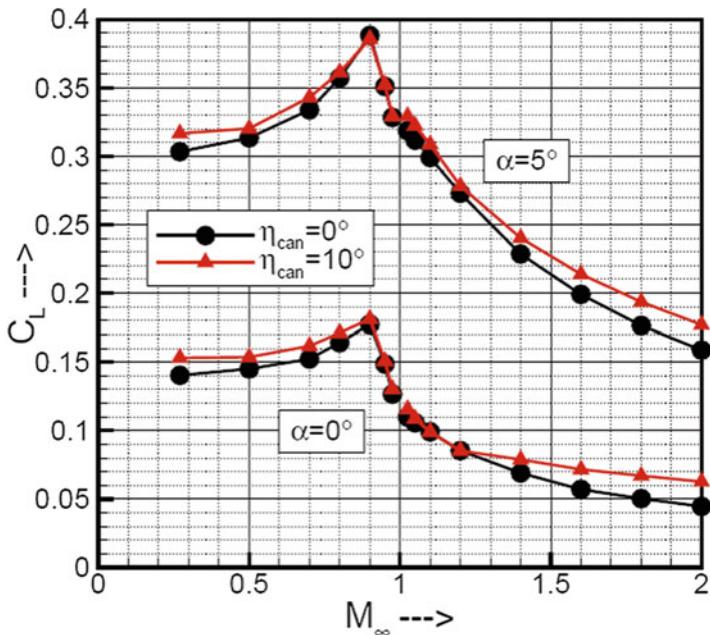


**Fig. 8.92** Euler lift coefficients of configuration Y7

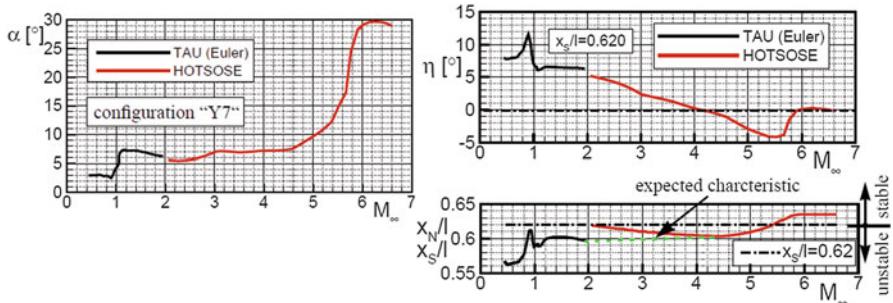


**Fig. 8.93** Trim results along the complete trajectory

For the trim calculations and the definition of the final aerodynamic data set, the lift and pitching moment coefficients are obtained by linear interpolation. For the interpolation of the pressure drag coefficients, quadratic polars are fitted into the Euler results. The skin friction drag is estimated based on the assumption of a turbulent flat plat as

$$C_{D,f} = \frac{A_{\text{wet}}}{A_{\text{ref}}} C_f \quad (8.21)$$

The trim results of this approach are summarized in Fig. 8.93 [34].

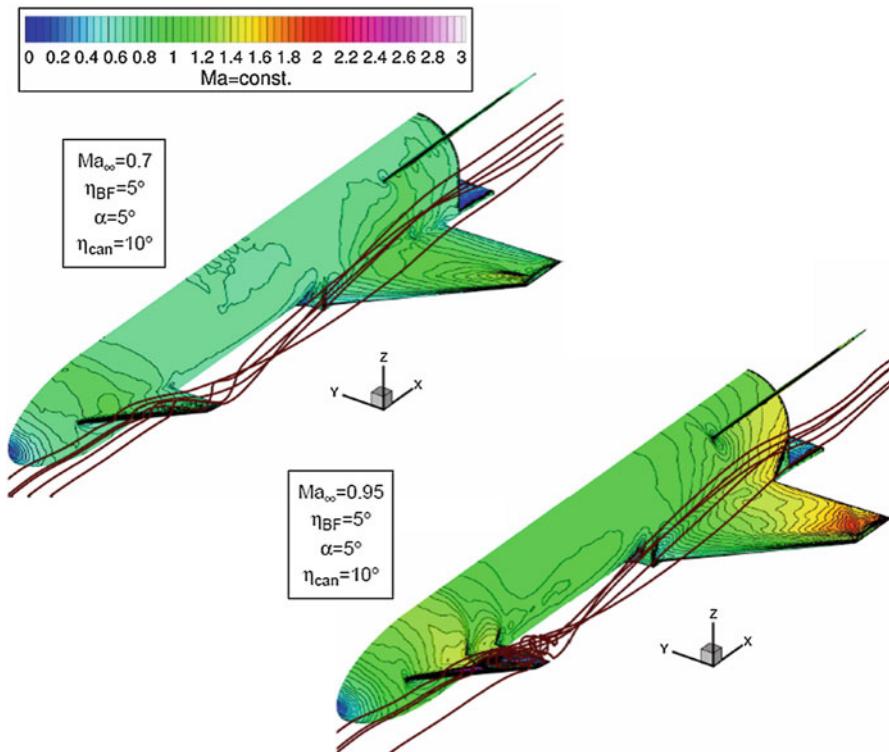


**Fig. 8.94** Flowfields around configuration Y7

The Euler results indicate a slightly unstable behavior for  $M_\infty = 2$ . The HOT-SOSE results are more optimistic and show an indifferent behavior and, therefore, also a slightly reduced canard deflection. Due to the fact that surface inclination methods are known to be sufficiently accurate for  $M_\infty > 4$ , a stability margin of  $(x_N - x_S)/l = -0.02$  can be expected in the range  $2 < M_\infty < 4$  (dotted line in Fig. 8.93) [34]. Considering the flap deflections for subsonic and transonic flight conditions, it turns out that, with the exception of  $M_\infty = 0.95$ , all canard deflections are smaller than  $\eta = 10^\circ$ . This shows that the careful application of handbook methods for estimation of the vehicle behavior in subsonic flow proved oneself. A comparison of the flow fields for  $M_\infty = 0.7$  and  $0.95$  (see Fig. 8.94) explains the increased canard deflections for  $0.9 < M_\infty < 1$  [34]. For  $M_\infty = 0.7$  a vortex is established along the leading edge of the canard. It is responsible for the relatively small canard deflections in subsonic flow because it increases the canard efficiency.

For transonic conditions, it is visible that vortex bursting appears at the trailing edge of the canard. This behavior results in the situation that the lift coefficient in transonic flow is nearly independent of the canard deflection (see Fig. 8.92). Therefore, larger canard deflections are required. A second interesting effect in

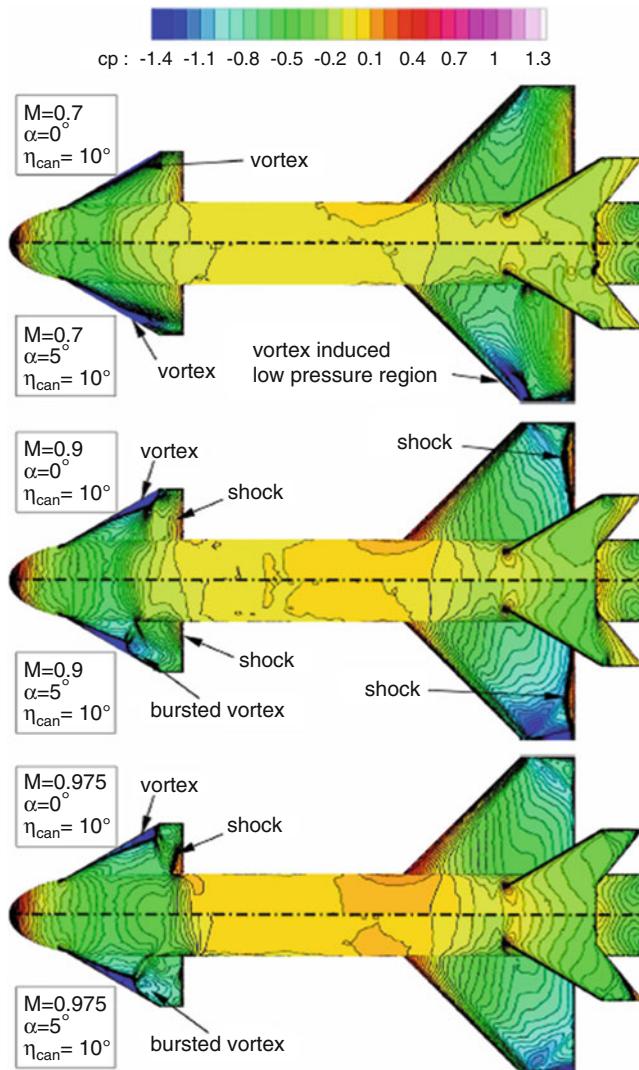


**Fig. 8.95** Upper surface pressure distribution of configuration Y7

transonic flow is the sudden tailward shift of the neutral point for  $0.75 < M_\infty < 0.95$  and the following frontward movement for  $0.95 < M_\infty < 1.025$ . This behavior may be explained with the help of Fig. 8.95 [34].

For the explanation, it has to be recalled that the aerodynamic forces resulting from a change in AoA are acting in neutral point. Therefore, a comparison of the pressure distributions of two angles of attack allows an assessment of the influence of the Mach number on the neutral point position.

First, the upper surface pressure distributions for  $M_\infty = 0.7$  are considered. The comparison of  $\alpha = 0^\circ$  and  $\alpha = 5^\circ$  turns out that the leading edge vortex of the canard is responsible for the increase of the lift force. The vortex strength along the canard leading edge increases, and this vortex also induces a low-pressure region over the outer part of the main wing. If now the results for  $M_\infty = 0.9$  are considered, it is visible that the overall upper surface pressure levels of the canard do not differ significantly for the shown angles of attack. Along the inner part of the leading edge, the vortex strength increases with the angle of attack, but in the trailing edge region, vortex bursting appears.

This effect partly revokes the gain in lift obtained in the inner part of the canard. Additionally, the effect of the canard vortex on the upper surface of the main wing is significantly reduced. A second important effect on the increase of lift results from the influence of the trailing edge shock on the upper surface of the wing. In subcritical transonic flow, a shock moves rearward with increasing Mach number and angle of attack. This is visible if additionally the results for  $M_\infty = 0.975$  are considered. Here the shock already reached the trailing edge. For  $M_\infty < 0.975$ , the shift of the shock position is still possible, and therefore, an increase on AoA results in a rearward extension of the low-pressure region on the upper surface. In summary, regarding the results for the Mach numbers  $M_\infty = 0.7$  and  $M_\infty = 0.9$ , the additional lift resulting from an increased AoA at  $M_\infty = 0.9$  is mainly produced in the wing region, and it is not dominated by the canard vortex. This explains the sudden neutral point shift to a more backward position for  $0.7 < M_\infty < 0.9$ . For  $M_\infty = 0.975$  the same situation appears except that the shock on the upper surface of the wing already reaches the trailing edge. This effect is independent of the angle of attack, and thus, the resulting lift forces acts slightly more frontward. The lack of additional suction force along the trailing edge then leads to the noseward jump of the neutral point for  $0.9 < M_\infty < 1.025$ . Based on the Euler results, the aforesaid discussion about the neutral point position also explains the lack of longitudinal stability ( $(x_N - x_S)/l = -0.05$ ) for the subsonic cruise condition (see Fig. 8.93). This situation would lead to permanently changing canard deflections, and therefore, it is to prefer to obtain a vehicle which has an indifferent or stable behavior. The pressure distributions in Fig. 8.95 show that the strong interaction of the leading edge vortex and main wing is responsible for the given unstable behavior of Y7. The results indicate that the problem can be solved if the wing is defined in a way that the increase of the wing lift with angle of attack is higher than the one of the canard. Additionally, it would help to shift the center of gravity in noseward direction. For a final discussion of this problem, at first the wind tunnel experiments have to be analyzed concerning the existence of a vortex along the leading edge of the main wing which could increase the slope of the wing lift curve. Due to the fact that the leading edge has a large bluntness, the Euler calculations are not able to predict these phenomena.

In order to extract the aerodynamic interactions on the structural loads, the pressure distributions of the isolated LFBB and the Ariane 5 + 2 LFBB configuration without and with junctures between core stage and LFBB are compared for  $\alpha = 0^\circ$  and  $\eta_{BF} = \eta_{can} = 0^\circ$ . At  $\alpha = 0^\circ$  the assessment of the computational grid

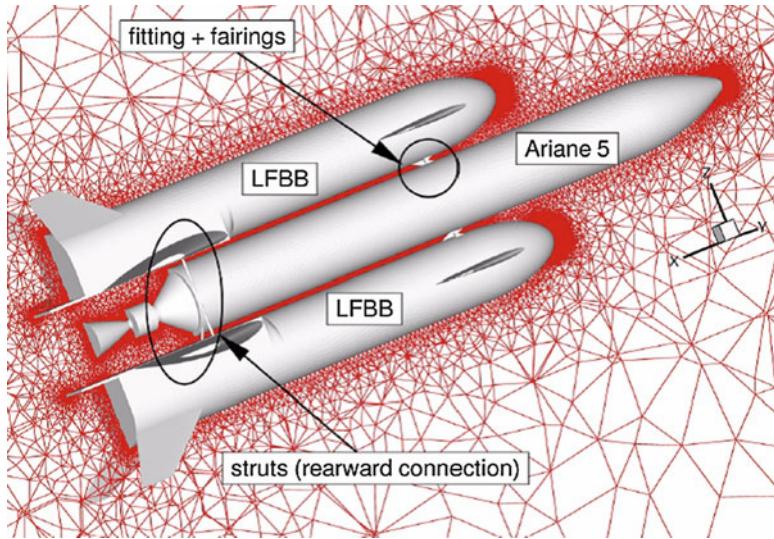


**Fig. 8.96** Ariane 5 liquid flyback booster concept. CFD Euler Grid

around the launcher can take advantage of body symmetry, that is, only half body configuration can be considered. However, due to the fact that the configuration may be asymmetric for small angles of attack or for lateral flow conditions, the complete configuration has to be considered as the worst case. Therefore, whole domain grid, close to that shown in Fig. 8.96, required 10.7 million tetraeders. In the grid are considered also the four connection points (namely, fitting in Fig. 8.96) between the LFBB and the core stage [34].

The grid is tailored for free-stream conditions of  $M_\infty = 1.6$  and 13.2 km altitude which corresponds to the maximum dynamic pressure point along the ascent flight. The overall flowfield is given in Fig. 8.97 [34].

At the ogive nose of the core stage, a detached shock is obtained. Also the two bow shocks in front of the elliptic forebodies of the boosters are visible. As shown, in the enlarged view of Fig. 8.98, they impinge on the shell of the core stage [34].

Reflected shocks are not obtained because the local impingement angle is nearly normal to the core stage. In the  $z=0$  plane of the core stage their shock–shock interaction induces a high-pressure spot. The maximum pressure coefficients in this region are in the order  $C_p = 0.8$ . From the structural point of view, the zone between the forebody of the booster and the fitting on the core stage has to be considered very careful. In this region, the shell of the core stage is very thin because it only protects the engine of the second stage of Ariane 5.

An enlarged view of the fitting is given in Fig. 8.99 [34]. Due to the fact that the thermal loads on the fitting are very high during the re-entry flight, it is protected by a pair of fairings. These fairings will be closed after the separation of the boosters.

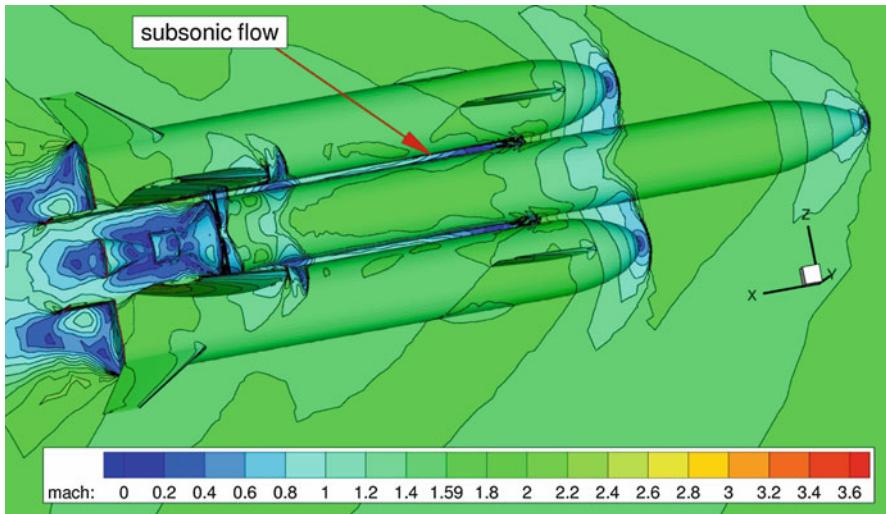


**Fig. 8.97** Flowfield around the Ariane 5 + 2 LFBB configuration ( $M_\infty = 1.6$ ,  $\alpha = 0^\circ$ )

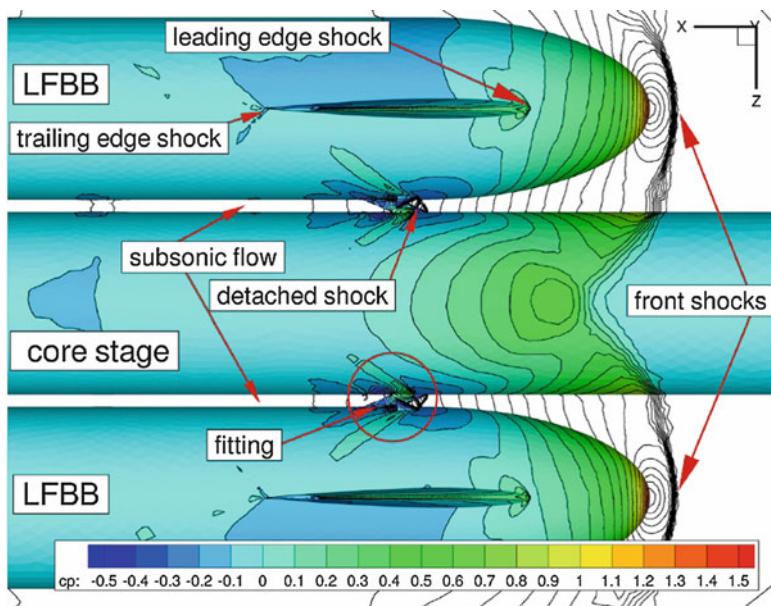


**Fig. 8.98** Pressure distribution in the vicinity of canard and LFBB forebody ( $M_\infty = 1.6$ ,  $\alpha = 0^\circ$ )

The remaining connections are at the end of the core stage, directly in front of the main engine. An enlarged view is given in Fig. 8.100 [34].

For the connection of core stage and the boosters' six struts, each of them with a diameter of approximately  $d = 0.2$  m are used. The struts transmit the very strong

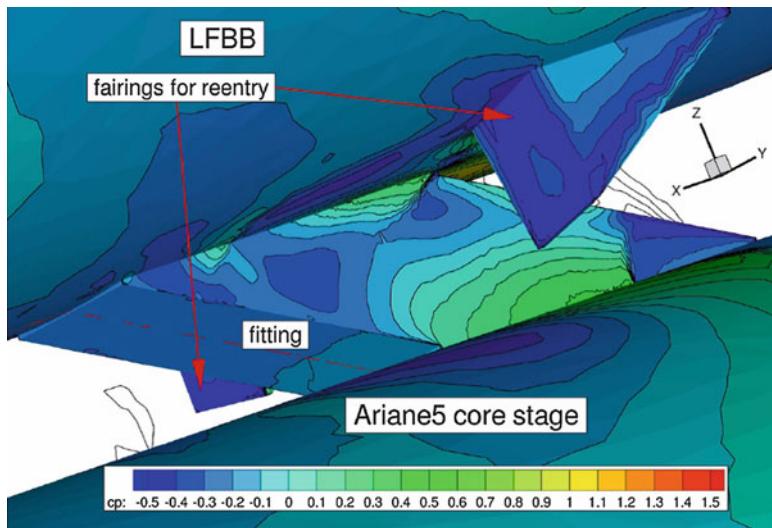


**Fig. 8.99** Pressure distribution in the vicinity of canard and LFBB forebody ( $M = 1.6$ ,  $\alpha = 0^\circ$ )

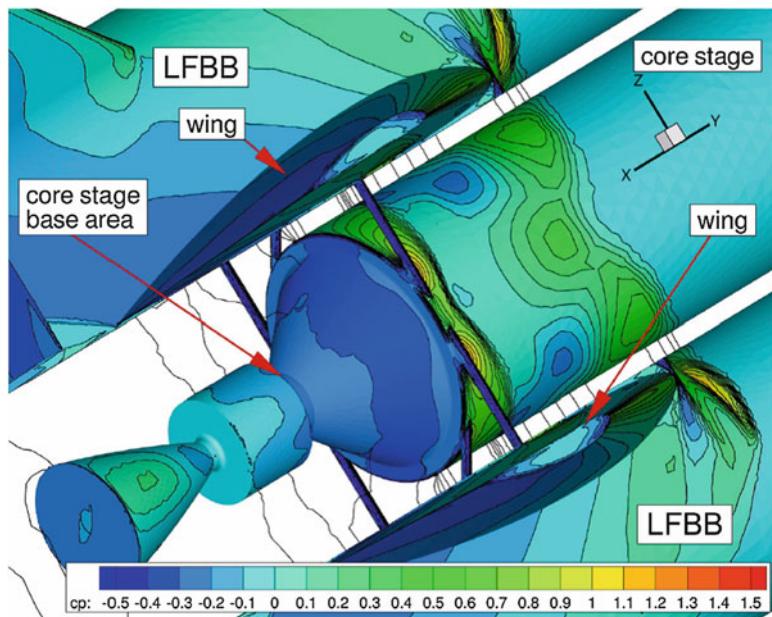


**Fig. 8.100** Pressure distribution in the vicinity of the rearward struts and the wing

radial forces. In particular, the two shorter struts transfer the torque into the core stage. All the struts will be assembled on the booster frame close to wing root. Due to the fact that the fitting (see Fig. 8.99) closes the gap between core stage and booster, a detached shock is found in front of it. The pressure peaks in this region are in the order of  $C_p = 1.1$ . Until a position of 10 m downward, the fitting the gap flow is subsonic (see Fig. 8.97) [34]. Near the x-position of the forward fitting, which is assembled into the attachment ring of Ariane 5, also the canards are visible (see Fig. 8.98). For the ascent flight, they are fixed at  $\alpha = 0^\circ$ . Therefore, their effect on the pressure distribution of the core stage may be neglected. On the LFBB surface, the front shock of the canards and also the trailing edge shock are visible. In Fig. 8.100 the wing region is considered. The wing of the LFBB has a subsonic leading edge and does not generate a shock. But on the upper surface, the supersonic region is visible. If the trailing edge is considered, also the trailing edge shock may be identified on the sidewall of the LFBB. In front of the fillet between circular and rectangular part of the LFBB body, detached shocks are obtained. On the LFBB surface, they result in an increased pressure coefficient of up to  $C_p = 1.3$ . The shocks also impinge on the core stage surface. The resulting shock–shock interaction in the  $z = 0$  plane induces a high-pressure spot ( $C_p \approx 0.7$ ). Also in front of the struts (rearward connection), detached shocks are obtained. They impinge on the surface of the core stage and on the lower side of the wing. On the surface of the core stage, their interaction is visible directly in front of the base area. They also affect the surface pressure distribution on the lower side of the LFBB. For the symmetry plane, this is shown in Fig. 8.101 [34].

By comparison of the isolated LFBB and the Ariane 5 + 2 LFBB configuration, this figure shows the interactions between the core stage and the LFBB. The isolated LFBB has a nearly undisturbed lower surface. The pressure coefficients are in the order of  $C_p \approx 0$ .

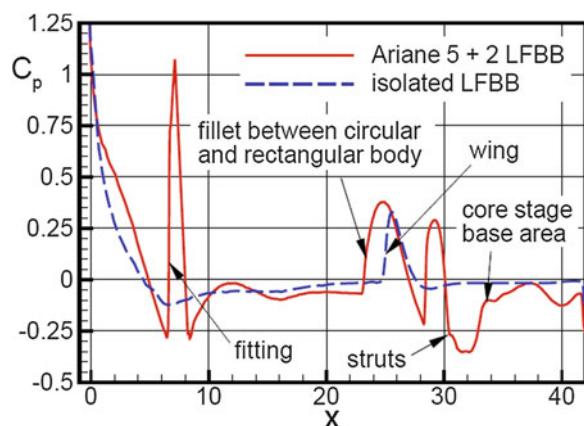


**Fig. 8.101** Surface pressure coefficients on the lower symmetry plane of the LFBB ( $M_\infty = 1.6$ ,  $\alpha = 0^\circ$ )

The only pressure peak is caused by the shock in front of the fillet between the circular and the rectangular part of the body. The first pressure peak induced by the core stage appears at  $x \approx 7$  m. It is caused by the shock in front of the fitting (see Fig. 8.99).

Due to the existence of the core stage, the strength of the shock in front of the fillet is slightly increased ( $x \approx 24$  m), and it is positioned more frontward. The third pressure peak at  $x \approx 28$  m is a result of the detached shock in front of the struts.

Resuming the comparison of the Ariane 5 + 2 LFBB configuration without and with junctures to the core stage, it turns out that the displacement of the struts and the fittings results in 6.8 % additional pressure drag.

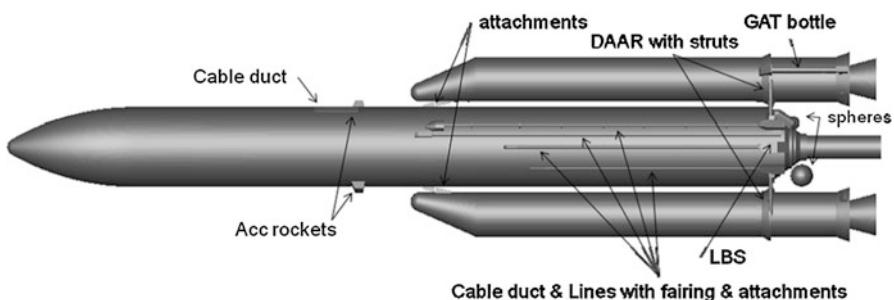
### 8.6.2 The Ariane 5 Geometry for Wind Tunnel Testing

Figure 8.102 shows an Ariane 5 geometry example for wind tunnel testing in development phase [1]. This shape was also used for the tuning of RANS Navier–Stokes approach for development context. Computations were performed for Mach number 2 and  $3^\circ$  AoA in wind tunnel flow conditions at  $Re = 1.38 \times 10^6$  and in flight flow conditions at  $Re = 50 \times 10^6$ . This will illustrate also the interest of extrapolation to flight through CFD.

In order to handle this complex topology, overlapping mesh approach has been used. Indeed, each shape component is gridded in separate mesh boxes, and every box is overlapped by the solver which computes all grids intersections. Some details of the skin meshes can be seen in Fig. 8.103 [1].

Even the quite complex base area can be handled straightforwardly with this kind of approach. In Fig. 8.104, a global view and two more detailed views of the volume mesh in the boosters' plane are shown. Near the boosters' noses, one can observe a specific overlapped box which use is to improve the nose shock fitting in the mesh [1].

Both Navier–Stokes computations were performed on very similar grids as only viscous effects are different. These differences can be observed in the following



**Fig. 8.102** A5 ESCB2 1/40th wind tunnel testing model

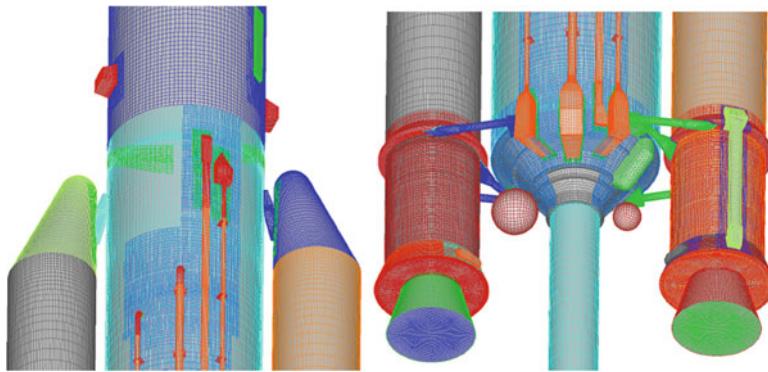


Fig. 8.103 Skin mesh of the A5 model

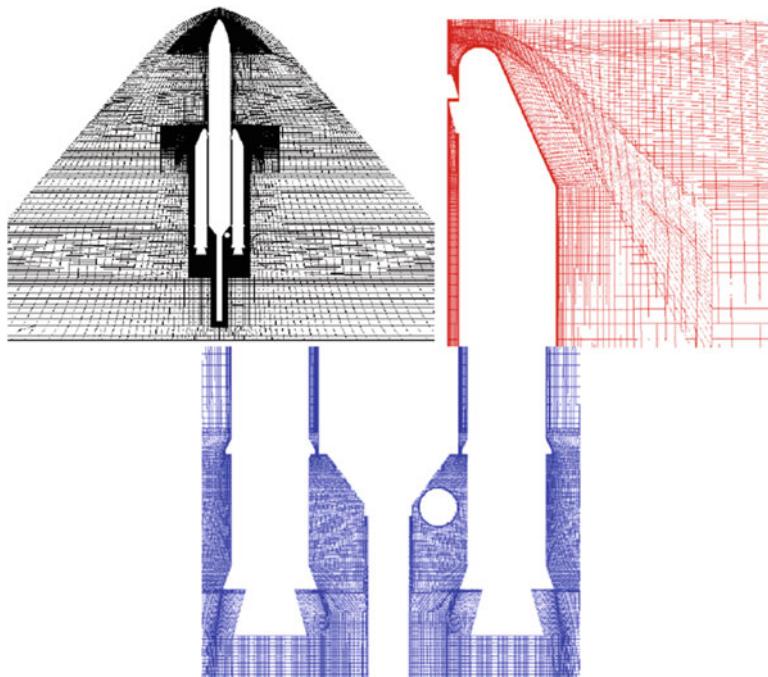
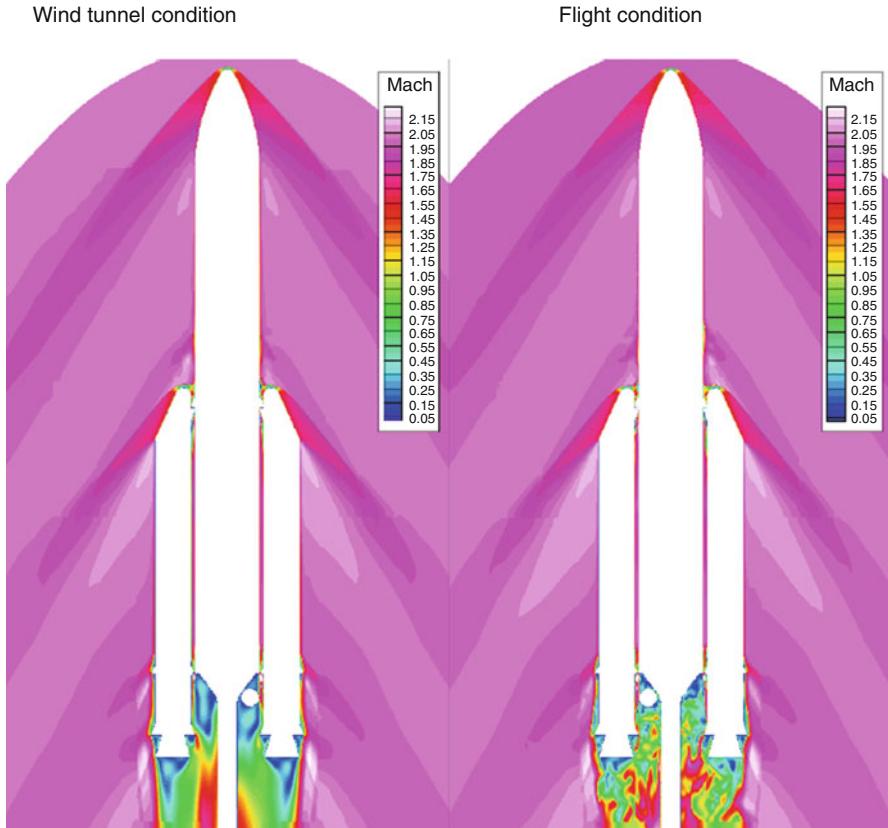


Fig. 8.104 Field mesh of the A5 model in the boosters' plane

figures illustrating the computational results. As shown in Fig. 8.105, the flow in the booster plane is very similar in both cases [1]. Indeed, viscous effects are sensitive mainly near to the body; nevertheless, differences in the wake flow can be observed which illustrates a much more turbulent regime in flight.



**Fig. 8.105** Computed flows in the boosters' plane. Comparison between wind tunnel and flight conditions

Differences are easier to observe on the launcher surface where flow interactions can be illustrated with pressure maps. One can see on Fig. 8.106 that these interactions have not exactly the same intensities, the same locations, or the same shapes [1]. Note that  $K_p$  stands for  $C_p$ .

In fact, this illustrates the effects of higher Re number in flight, and we can identify three consequences:

- The higher level of turbulence leads to thinner boundary layer and lower friction levels on the walls.
- In this thin boundary layer, the protrusions are less protected from the external flow and their pressure loading is higher.

As a consequence of the two previous effects, the loading of the main bodies of the launcher around the protrusions is more intensive and more focalized. These consequences are illustrated more precisely on Fig. 8.107 [1].

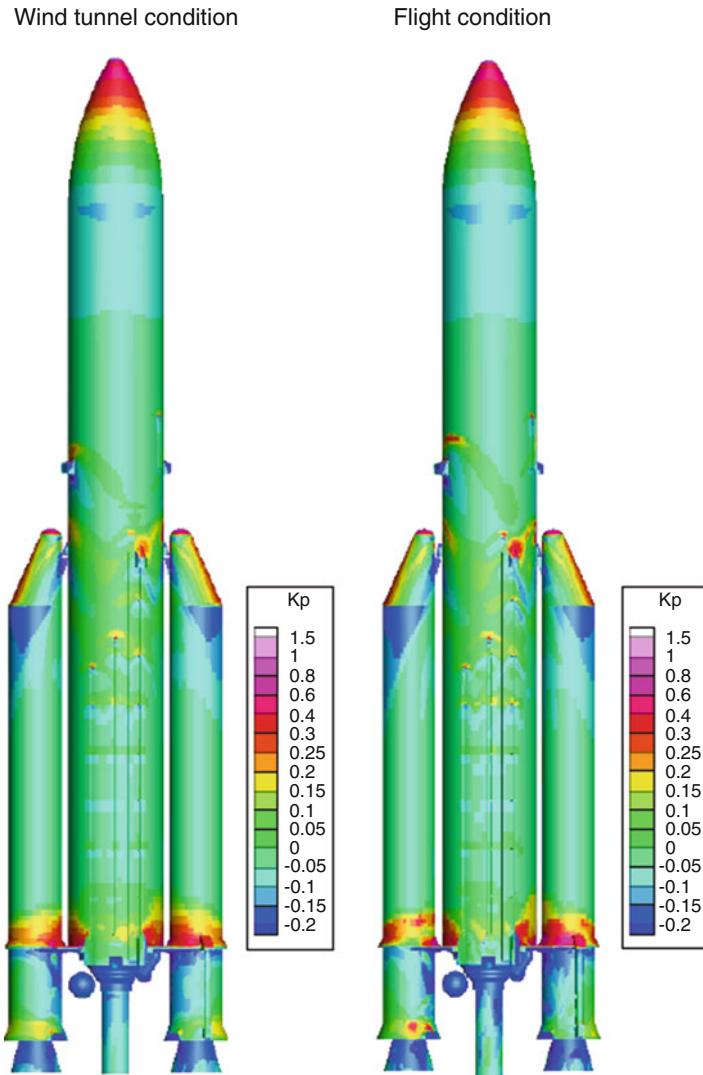


**Fig. 8.106** Pressure maps on the walls. Comparison between wind tunnel and flight conditions –  $K_p$  stands for  $C_p$

### 8.6.3 CFD Contribution to the Aerodynamic Appraisal of the Vega Launcher

CFD represents a fundamental design tool to address launcher aerodynamics when considered in association or in a complementary fashion with respect to the wind tunnel simulations. Indeed, CFD plays a key role in supporting wind tunnel activities (i.e., to better drive the experimental test campaigns) and in providing

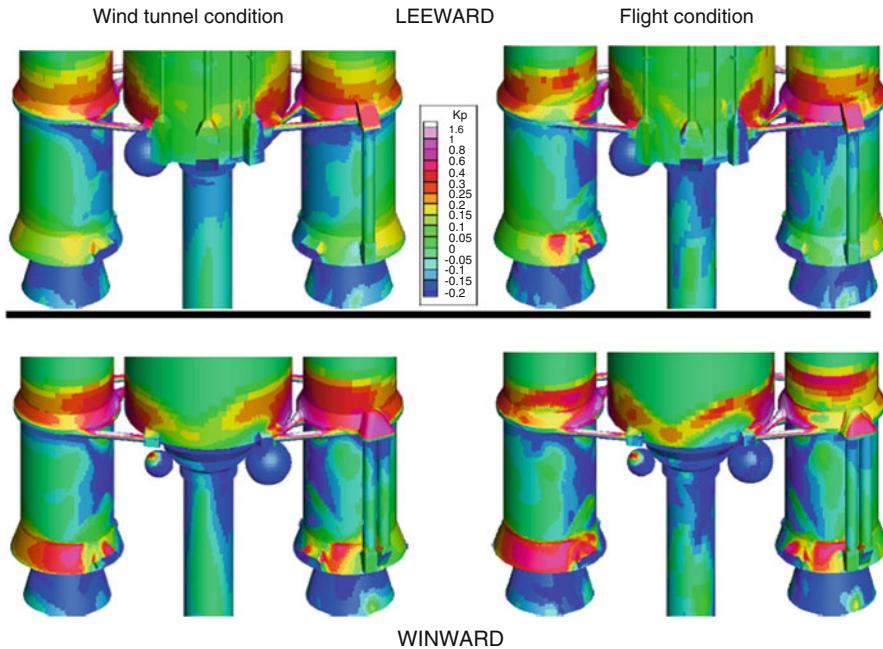


**Fig. 8.107** Comparison of pressure maps on launcher base

data for the determination of extrapolation-to-flight procedure (i.e., a procedure to correct the measured aerodynamic coefficients to the actual flight conditions) [9–12]. In this framework, this paragraph presents the CFD activities performed to simulate the subsonic, transonic, and supersonic flow around the four-stage configuration of the Vega launcher in motor-on conditions. Numerical simulations, complementary to experimental test campaigns, have been performed covering a range of Mach numbers from 0.50 to 3.02, two angles of attack, and three Reynolds numbers[11, 12].

In particular, the engine conditions have been reproduced by a boundary condition that allows to impose density, pressure, and momentum at the nozzle exit section in the hypothesis of ideal gas assumption (i.e.,  $\gamma = 1.4$ ). The mass flow and the ratio between the jet and the free-stream static pressure have been exactly duplicated, whereas the Mach number and the temperature of the jet have been slightly under- and overestimated, respectively [9, 10].

Results provided hereinafter prove that a globally satisfactory agreement between numerical simulations and experiments has been achieved over a wide range of flow regimes, in terms of both local and global properties, and the main flow structures have been well predicted. Therefore, CFD is able to provide important and detailed information on the characteristics and topology of the flow to allow for an improved design effort from the subsonic to the hypersonic regime and to produce a detailed aerodynamic data set.

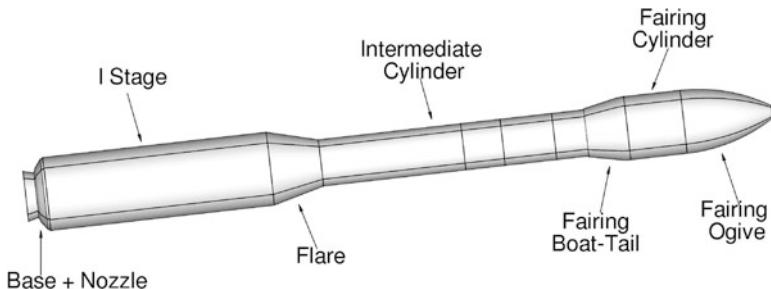


**Fig. 8.108** Vega launcher in flight configuration

For the Vega launcher, wind tunnel test campaigns have been conducted in several facilities to cover the flow regimes experienced by the vector.

The flight configuration, shown in Fig. 8.108, is equipped with a propulsive nozzle where the exit flow conditions of the P80FW engine of the Vega launcher have been imposed. The wind tunnel configurations are 1:30 scaled and are equipped with a device to model the jet exiting from an annular engine. The RANS CFD approach results to be not very computationally expensive and is supposed to provide accuracy sufficient to the goals of the project [9–12].

Drawbacks were expected in the prediction of the base flow. The effect of this issue on the definition of the laws to extrapolate the aerodynamic coefficients to the flight conditions has been addressed by properly analyzing the experimental and numerical data. Typical useful insights of CFD are numerical result, in the form of distributions of the normal and axial force coefficient as function of Mach and Reynolds numbers. Experimental test campaigns have been conducted in the FOI (Swedish Defense Research Agency) T1500 wind tunnel for the subsonic/transonic flow conditions ( $0.5 \leq M_\infty \leq 1.2$ ) and in the DNW (German–Dutch Wind Tunnel foundation) SST for the supersonic regime ( $1.58 \leq M_\infty \leq 3.96$ ). Pressure measurements, global aerodynamic forces and moments, and flow visualizations have been carried out. The 1:30-scaled model of the launcher was equipped with a cold air plume simulator with an annular nozzle to reproduce the effect of the jet plume on the base drag and pressure. The design of the plume simulator was based on the “component” method. The global aerodynamic coefficients were measured by a six-component balance up to  $\alpha = 10^\circ$ . The model was instrumented with 48 pressure taps along a generatrix line. Four taps along a generatrix line plus other six taps to form a semiring were placed on the base. The pressures were acquired by two electronically scanned transducers (ESP) placed inside the model in the payload region and calibrated before each run. To map the pressure field around the overall launcher, the pressures were acquired along seven different generatrix lines, equally spaced of  $30^\circ$  in the azimuthal direction between the lee and the windside. The uncertainty of the measured  $C_p$  is reported in the Table 8.5 [10].

This was estimated from the uncertainties of the wind tunnel test conditions and the uncertainties of the pressure instrumentation used, following the error

**Table 8.5** Uncertainty of the measured pressure coefficients evaluated at  $C_p = 0$

Mach	$C_p$ uncertainty
0.50	$\pm 0.008$
0.80	$\pm 0.003$
0.85	$\pm 0.003$
0.90	$\pm 0.003$
0.95	$\pm 0.003$
1.07	$\pm 0.002$
1.20	$\pm 0.002$
1.58	$\pm 0.003$
1.72	$\pm 0.002$
2.01	$\pm 0.003$
2.50	$\pm 0.003$
3.00	$\pm 0.006$
3.96	$\pm 0.039$

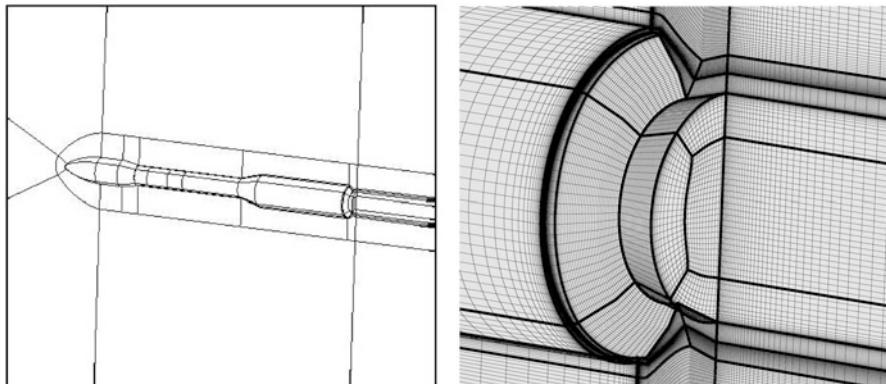


**Fig. 8.109** Grid for flight configuration in subsonic and transonic flow regime. On the *left*, domain decomposition. On the *right*, base and nozzle region

propagation methodology. Oil flow visualizations with  $TiO_2$  were performed at  $M_\infty = 0.90, 1.20, 1.58, 2.01$ , and  $3.0$  at  $\alpha = 2^\circ$  and/or  $\alpha = 5^\circ$ . CFD simulations are carried out on structured multiblock grids for the flight configuration (see Fig. 8.108) and 1:30-scaled model of the Vega launcher. The mesh for the full-scale configuration in the subsonic and transonic flow regimes employs a C-O topology with the farfield boundaries placed at about five body lengths. The total number of points is about 2.81 million and is the result of a compromise between the requirements dictated by the flight Reynolds number and grid details and a reasonable CPU time. Figure 8.109 shows the block decomposition and an enlargement of the mesh in the base and nozzle region [10].

Other two meshes have been generated for the supersonic simulations. The external boundaries have been adapted to the flow regime: the inflow surface has been determined by considering the stand-off distance and a suitable shock shape

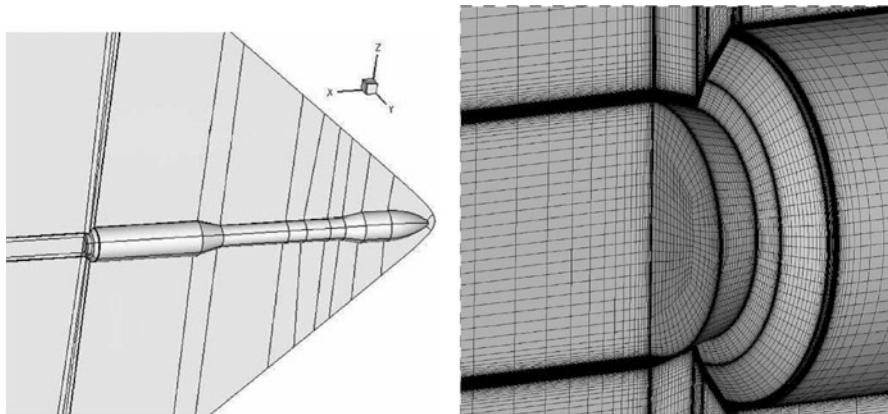


**Fig. 8.110** Grid for flight configuration in subsonic and transonic flow regime. On the *left*, domain decomposition. On the *right*, base and nozzle region

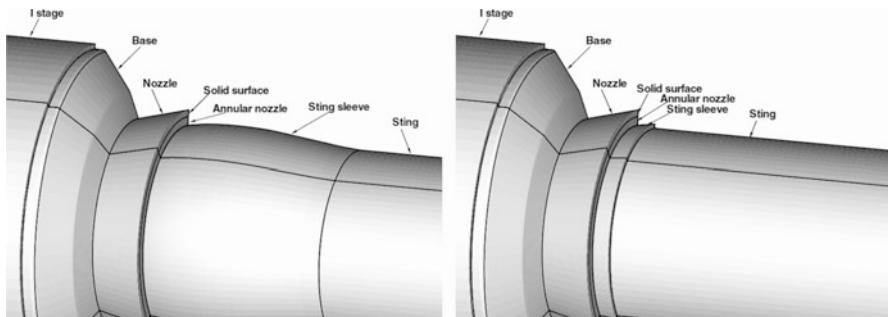


**Fig. 8.111** Wind tunnel plume simulator system. Subsonic/transonic regime, *left*. Supersonic regime, *right*

given by the Billig correlation formulae, whereas the outflow plane has been placed at about three body lengths for  $M_\infty = 2.01$  and one body length for  $M_\infty = 3.02$  [10]. The total number of points is decreased to 2.42 million for  $M_\infty = 2.01$  and 1.47 million for  $M_\infty = 3.02$ .

The block decomposition and an enlargement of the mesh in the zone of base and nozzle are presented in Fig. 8.110 [10].

The model used in the wind tunnel tests is 1:30 scaled with respect to the flight configuration and is equipped with a device to simulate the plume exiting from the engine.

Two different configurations of the plume simulator system, shown in Fig. 8.111, have been designed by FOI: one “shaped” for the subsonic and transonic regimes and another “stepped” for the supersonic tests [10].

It is worth noting that CFD results, achieved during the first phase of the project, have been very useful to analyze the differences between the two configurations.

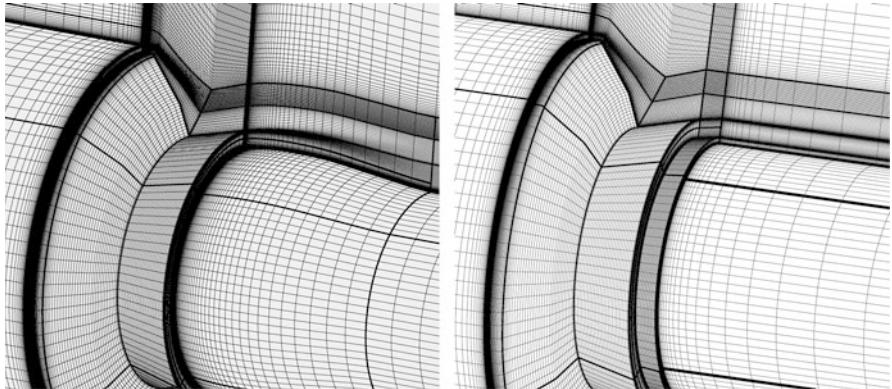


**Fig. 8.112** Grid for wind tunnel configuration. Subsonic/transonic regime, *left*. Supersonic regime, *right*

The operation conditions of the plume simulator system, in terms of Mach number, pressure, temperature, and exit angle, have been provided as a function of the radial coordinate of the model. Numerically averaged values, always in terms of density, momentum, and pressure, have been imposed at the annular ring representing the nozzle exit. The jet angle has been taken into account by properly setting the components of the momentum.

The grids generated for the wind tunnel configurations have been obtained by scaling the meshes generated for the full-scale launcher and by changing the topology in the region of the annular nozzle and sting. Details of the grids used to reproduce the experimental tests are shown in Fig. 8.112 [10].

It is worth to note that the proper geometrical definition of the plume simulator system has required additional blocking and wall stretching, thus in general increasing the total number of points (i.e., at  $M_\infty = 3.02$  from 1.47 to 1.89 million) [10].

The values of the viscous turbulent coordinate of the wall-adjacent layer of cells have been analyzed. The transonic simulations in flight conditions present the highest Reynolds numbers, thus the worst situation. The values are between 4 and 6 along all the launcher with exception of the rear part of the first stage, where there are regions with  $y^+$  about 9. For the subsonic and transonic simulations around the wind tunnel configuration,  $y^+$  ranges between 1 and 2 along the entire configuration. The highest values (about 5) are always obtained on the rear end of the first stage. The situation is quite good for the supersonic regime. The  $y^+$  is less than 1 in the front part of the launcher and remains always lower than 4. However, the turbulence model employed ( $\kappa-\omega$  model proposed by Kok) has the advantage to not have a direct dependence of the eddy viscosity on the distance from a solid surface, and this should allow to relax the requirements on  $y^+$ . The same turbulence model has been used to perform simulations of high Reynolds number flows by employing no-slip boundary conditions and a wall function formulation [10]. The wall-integrated results have shown, in terms of pressure, friction, and global

**Table 8.6** Effect of grid resolution in the transonic regime ( $M_\infty = 0.95$ ,  $\alpha = 2^\circ$ )

Grid level	No. of cells	$C_N$	$C_A$	$C_m$	$X_{CP}/D$
L <sub>1</sub>	41,376	1.2478	0.7314	1.5402	1.2349
L <sub>2</sub>	331.008	0.9884	1.0043	0.9410	0.9525
L <sub>3</sub>	2,648.064	1.0000	1.0000	1.0000	1.0000

**Table 8.7** Effect of grid resolution in the supersonic regime ( $M_\infty = 3.02$ ,  $\alpha = 2^\circ$ )

Grid level	No. of cells	$C_N$	$C_A$	$C_m$	$X_{CP}/D$
L <sub>2</sub>	160,752	1.0260	0.9937	1.0426	1.0163
L <sub>2.5</sub>	735,392	1.0028	0.9997	1.0118	1.0090
L <sub>3</sub>	1,286.016	1.0000	1.0000	1.0000	1.0000

aerodynamic coefficients, a satisfactory accuracy, provided that  $y^+$  does not exceed 10. The effect of the grid resolution on computed results has been analyzed for the flight configuration in motor-on conditions in transonic ( $M_\infty = 0.95$ ,  $\alpha = 2^\circ$ ) and supersonic ( $M_\infty = 3.02$ ,  $\alpha = 2^\circ$ ) regimes. Tables 8.6 and 8.7 report the aerodynamic coefficients  $C_N$ ,  $C_A$ ,  $C_m$  and the normalized center of pressure  $X_{CP} = D$  as a function of the grid resolution, all the values having been normalized to the finest grid level (L<sub>3</sub>) [10].

The coarse grid (L<sub>1</sub>) results for the transonic case (see Table 8.6) have been obtained with laminar flow assumption and motor-off conditions (a strategy used to initialize the complex base flow structure) and then have to be considered only as reference values. The percentage variation between the results of the fine (L<sub>3</sub>) and medium (L<sub>2</sub>) grid levels is 1.17 % for the normal force, -0.43 % for the axial force, 6.27 % for the pitching moment coefficient, and 4.98 % for the position of center of pressure. Concerning the supersonic case (Table 8.7), the coarse level of the grid (L<sub>1</sub>) was not adequate to capture the quite strong bow shock wave around the launcher's nose. An intermediate grid (L<sub>2.5</sub>) between the medium (L<sub>2</sub>) and the fine (L<sub>3</sub>) level of the grid has been then generated to demonstrate the grid independence of the results. For each elementary edge, an intermediate number of points between those of L<sub>2</sub> and L<sub>3</sub> levels have been selected, with the spacing law scaled accordingly. Figure 8.113 shows the aerodynamic coefficients as a function of the parameter  $h = (1/N)^{1/3}$ , where N is the number of cells of a grid level, this number representing the grid resolution (the accuracy of the grid increasing from right to left). The percentage variation between the result obtained on the fine (L<sub>3</sub>) and intermediate (L<sub>2.5</sub>) grid levels is -0.28 % for the normal, 0.03 % for the axial force coefficients, -1.17 % for the pitching moment, and -0.90 % for the position of the center of pressure. The level of convergence of the solution can be estimated by using the Richardson extrapolation method applied to functionals such as the global aerodynamic coefficients [15, 10].

The values of  $C_N$ ,  $C_A$ , and  $C_m$  have been extrapolated to zero grid spacing ( $h = 0$ ), assuming the actual grid refinement ratio and a second order of accuracy. The discretization error of the CFD data has been evaluated looking at the difference between the quantitative results obtained on the fine grid level and the values

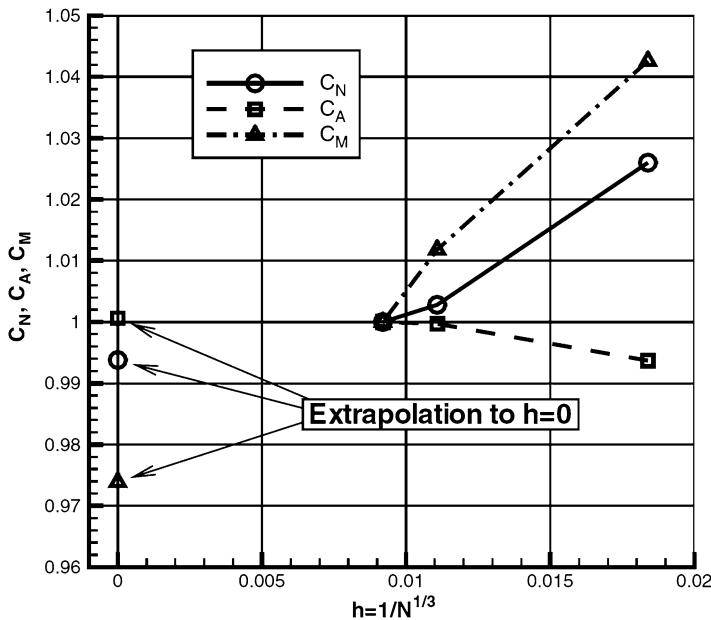


Fig. 8.113 Grid resolution effect in supersonic regime

Table 8.8 Discretization error

Flow regime	$C_N$	$C_A$	$C_m$
Transonic	0.0003	0.0005	0.0057
Supersonic	0.0007	0.0002	0.0099

extrapolated at  $h = 0$  (see Table 8.8) [10]. The error is of order of magnitude  $10^{-4}$  for both  $C_N$  and  $C_A$  and larger for  $C_m$  (the pitching moment coefficient is computed with respect to the nose-tip) [10].

It is possible to affirm that, in the frame of the physical and numerical modeling adopted in the present analysis, the computational grids employed in the simulations in subsonic, transonic, and supersonic regimes provide grid-independent results in terms of global aerodynamic coefficients.

The numerical simulations have been performed by employing a three-level strategy. The block faces of the computational mesh representing the engine have been considered as solid surfaces on the coarse and medium grid levels and as fluid surfaces on the fine level. Then density, pressure, and momentum have been taken from free-stream to the values reproducing the flow conditions at the exit of the engine in several steps. Considering the part of simulations with the actual engine-on conditions applied, the residual of the density equation has decreased of about two orders of magnitude in subsonic, between two and three in transonic, and more than three in the supersonic flow regime. The pressure and friction coefficients have been integrated on the lateral surface of the launcher which is proportional to  $\pi DL$ . The

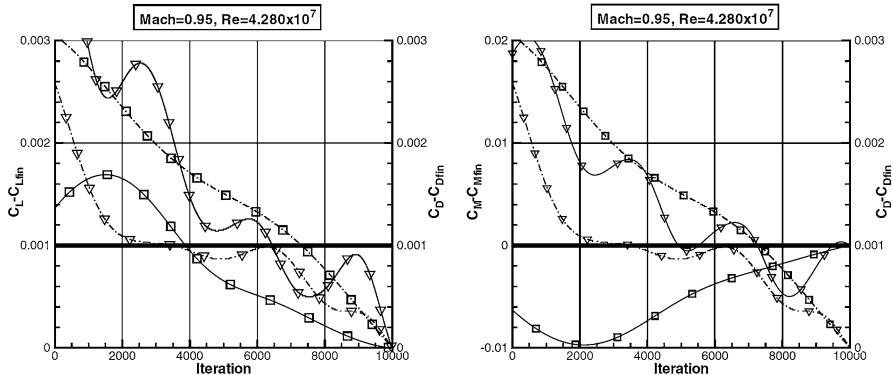


**Fig. 8.114** Convergence of the aerodynamic coefficients in the transonic flow regime:  $\square \alpha = 2.0^\circ$ ,  $\nabla \alpha = 5.0^\circ$ .  $C_L$  (solid line)  $C_D$  (dashed-dotted line).  $C_m$  (solid line),  $C_D$  (dashed-dotted line)

surface used to scale the force and moment coefficients is  $\pi D^2/4$ . The ratio between the integration and reference surfaces is therefore proportional to  $4 L/D$ , a value of about 40 for the Vega four-stage configuration. Based on this consideration and on the fact that an accuracy of order of magnitude of the drag-count can be expected in a CFD simulation, a variation of less than ten drag-counts was decided to be adequate for the convergence of the numerical solutions. This criterion has not been satisfied in the subsonic regime where the drag coefficient has shown oscillations of about 2.5 %. This unsteadiness was essentially attributed to the pressure distribution on the base as confirmed by comparison with the experimental results presented in the following sections. The convergence of lift, drag, and pitching moment coefficients in the last 10,000 iterations is shown in Fig. 8.114 for the transonic flow regime [10].

The aerodynamic coefficients are referred to the values obtained at the end of the numerical simulations. The line representing the adopted criterion is reported in bold. The  $C_L$  changes of less than  $10^{-3}$ , and  $C_m$  less than  $10^{-2}$ . The criterion is fulfilled earlier at  $\alpha = 5.0^\circ$  than at  $\alpha = 2.0^\circ$ . The situation is better in the supersonic regime, in which a variation of 0.05 % for the  $C_D$ , 0.1 % for the  $C_L$ , and 0.1 % for the  $C_m$  has been generally obtained. This means that the  $C_D$  is converged to the drag-count in the supersonic simulations [10].

RANS simulations have been performed at two angles of attack, and the wind tunnel, actual flight, and an intermediate Reynolds number determined as

$$\log_{10} \left( \frac{1}{\sqrt{Re_{INT}}} \right) = \frac{1}{2} \left[ \log_{10} \left( \frac{1}{\sqrt{Re_{WT}}} \right) + \log_{10} \left( \frac{1}{\sqrt{Re_{FL}}} \right) \right] \quad (8.22)$$

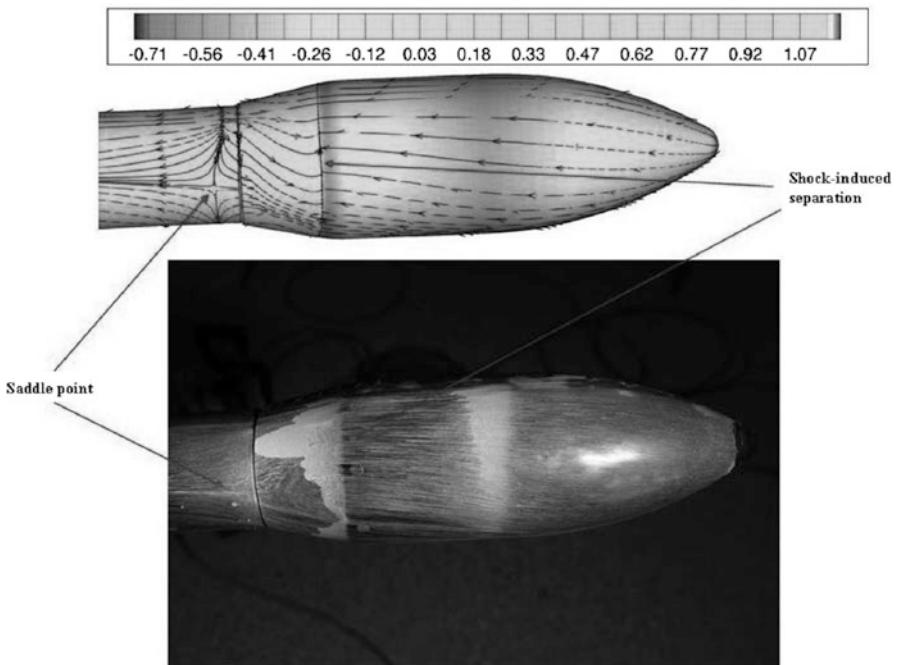
have been taken into consideration.

The complete set of simulations is reported in Table 8.9 [10].

A comparison between numerical (skin friction lines) and experimental (oil flow visualization) surface flow patterns is shown in Fig. 8.115, where the pressure map distribution is also reported for  $M_\infty = 0.95$  and  $\alpha = 5.0^\circ$  [10].

**Table 8.9** CFD test matrix

Mach	Reynolds	$\alpha$ ( $^{\circ}$ )	Configuration	Propulsive characteristics
0.50	$5.382 \times 10^6$	2	1:30	Subsonic/transonic plume simulator (PS) + sting
0.50	$5.382 \times 10^6$	5	1:30	Subsonic/transonic PS + sting
0.95	$7.275 \times 10^6$	2	1:30	Subsonic/transonic PS + sting
0.95	$1.765 \times 10^7$	2	1:1	Motor-on (MO)
0.95	$4.280 \times 10^7$	2	1:1	MO
0.95	$7.275 \times 10^6$	5	1:30	Subsonic/transonic PS + sting
0.95	$1.765 \times 10^7$	5	1:1	MO
0.95	$4.280 \times 10^7$	5	1:1	MO
1.20	$7.108 \times 10^6$	2	1:30	Subsonic/transonic PS + sting
1.20	$7.108 \times 10^6$	5	1:30	Subsonic/transonic PS + sting
2.01	$7.275 \times 10^6$	2	1:30	Supersonic PS + sting
2.01	$7.275 \times 10^6$	5	1:30	Supersonic PS + sting
3.02	$8.846 \times 10^6$	2	1:30	Supersonic PS + sting
3.02	$1.454 \times 10^7$	2	1:1	MO
3.02	$2.388 \times 10^7$	2	1:1	MO
3.02	$8.846 \times 10^6$	5	1:30	Supersonic PS + sting
3.02	$1.454 \times 10^7$	5	1:1	MO
3.02	$2.388 \times 10^7$	5	1:1	MO

**Fig. 8.115**  $M_{\infty} = 0.95$  and  $\alpha = 5.0^{\circ}$ . Comparison between numerical (skin friction lines) and experimental (oil flow visualization) fields. Contour map of pressure coefficient  $C_p$

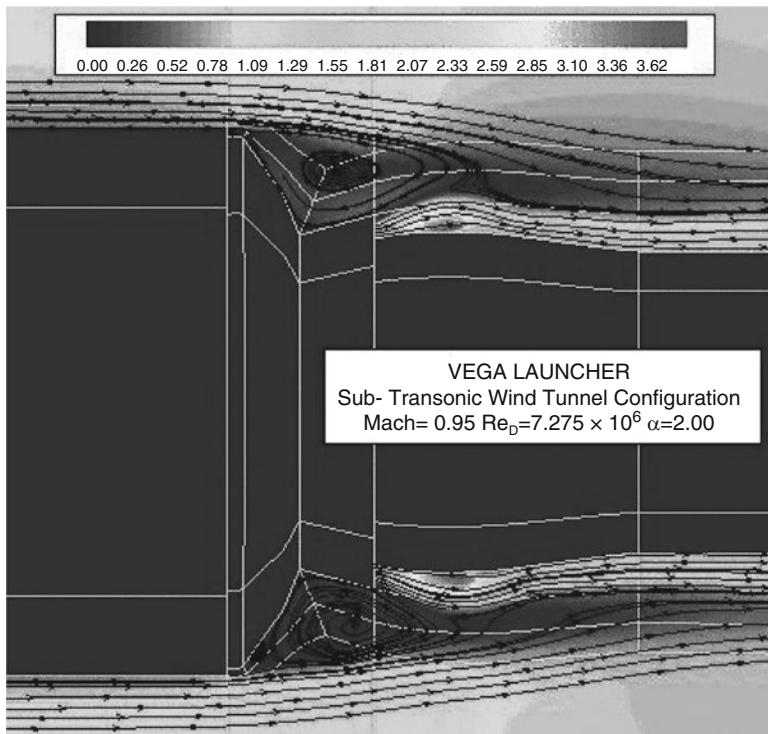


**Fig. 8.116** Base flow in the transonic regime: Mach number distribution and streamlines at  $M_\infty = 0.95$  and  $\alpha = 2.0^\circ$

As one can see, a strong compression is present between the ogive and the fairing, and a shock-induced separation occurs at the junction between the fairing cylinder and the boattail. A saddle point is also visible on the intermediate cylinder on the windside with separation lines and detached eddies departing downstream. The flowfield is reproduced satisfactorily by the numerical simulation. The extension of the separated flow region on the boattail decreases as the Mach number increases and at  $M_\infty = 1.20$  is just a little zone on the leeside. The simulation of the base flow in the transonic, as well as in the subsonic regime is really critical, as recognized in Fig. 8.116 [10].

Recirculation bubbles are present in the region between the base and the nozzle, whereas a supersonic zone exists at the exit of the annular nozzle of the plume simulator. A strong shear layer is formed. The Mach number decreases from free-stream to very low values in the recirculation regions, and then a sudden and strong expansion occurs where the supersonic jet exits from the annular nozzle. The situation is further complicated by the system of detached eddies that contribute to the unsteadiness of the flow. The zone of interaction of the external stream with the jet plume is quite large, about two times the nozzle length, and a significant suction effect, with a consequent increase of the drag coefficient, is produced.

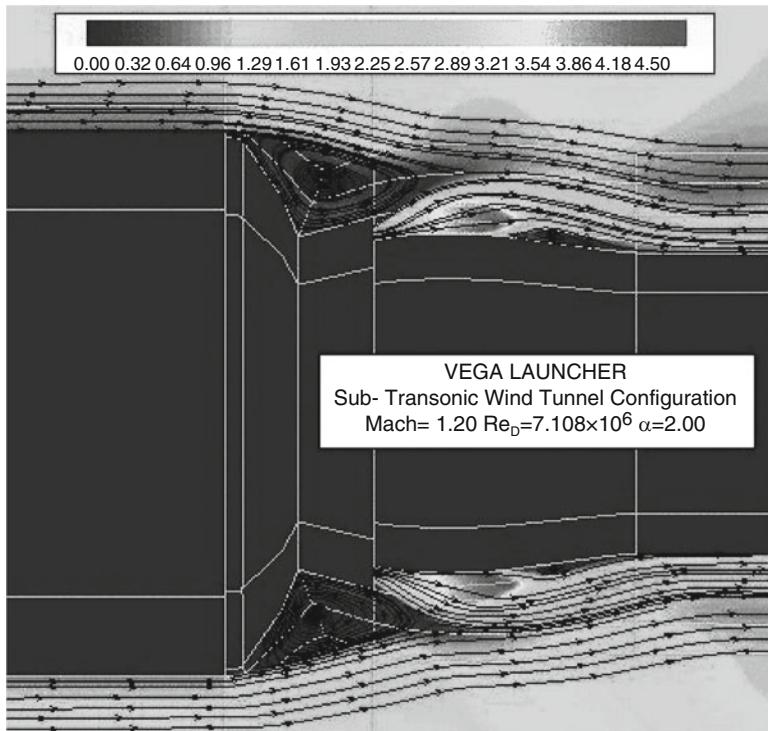


**Fig. 8.117** Base flow in the transonic regime: Mach number distribution and streamlines at  $M_\infty = 1.20$  and  $\alpha = 2.0^\circ$

The zone of interaction between the jet plume and the external stream decreases as the Mach number increases (see Fig. 8.117) and the prediction of the base flow becomes less critical [10].

In the supersonic regime, information on the flow topology can also be derived from the oil flow visualizations taken during the experiments, as those shown in Fig. 8.118 [10].

A separated region with recirculation zones is visible upstream of the flare on leeside at intermediate angles of attack (left plot of Fig. 8.118). This foci-type separation, due to the interaction between the vortex field generated on the intermediate cylinder and the shock wave forming upstream of the flare, is typical of the cylinder-flare configurations in supersonic regime at intermediate angles of attack [10]. The recirculation regions disappear at lower incidence (right plot of Fig. 8.118). The CFD simulations return the same type of flow. The skin friction lines computed at Mach 2.01 are reported in Fig. 8.119 [10]. The foci-type separation is present at  $\alpha = 5.0^\circ$  on the leeside upstream the flare, whereas a “simple” shock-induced separation is obtained at  $\alpha = 2.0^\circ$  (the same can be said for Mach 3.02).

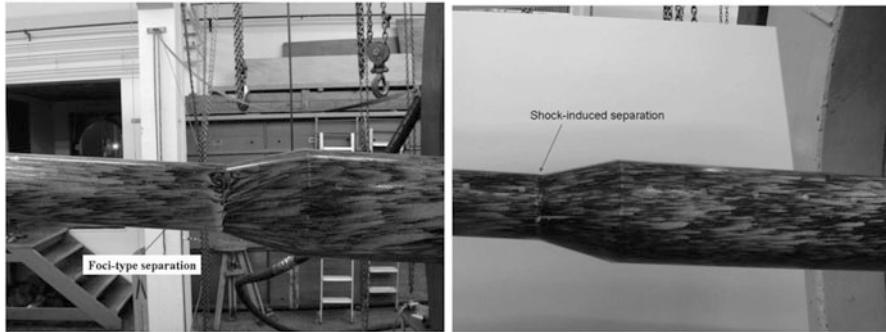


**Fig. 8.118** Oil flow visualizations in the supersonic regime at  $M_\infty = 1.58$  and  $\alpha = 5.0^\circ$  (left) and  $M_\infty = 2.01$  and  $\alpha = 2.0^\circ$  (right)

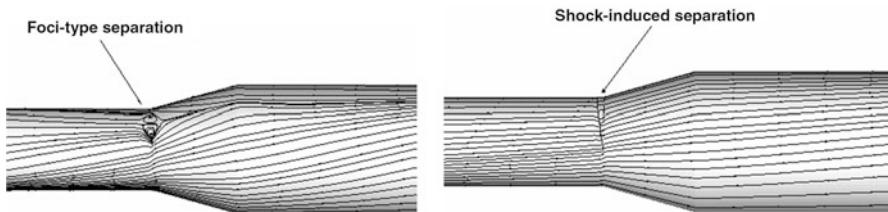


**Fig. 8.119** Skin friction lines in the supersonic flow regime at  $M_\infty = 2.01$  and  $\alpha = 5.0^\circ$  (left) and  $\alpha = 2.0^\circ$  (right)

Laws of extrapolation-to-flight of the global aerodynamic coefficients in the form

$$C_{N,A,m} = a[\log_{10}(\text{Re})]^b \quad (8.23)$$

with  $a$  and  $b$  being functions of  $\alpha$  and  $M_\infty$  have been found. CFD has played an important role in the extrapolation-to-flight procedure adopted [10]. Results at different Reynolds numbers and preliminary trends have been obtained through the numerical simulations. To perform a detailed correlation with the experimental data, the “distributed” aerodynamic coefficients defined as

$$\begin{aligned} C_{N,A}(x) &= \int_0^x \frac{2\pi r(x)C_{n,a}(x)}{S_{\text{ref}}} dx \\ C_m(x) &= \int_0^x \frac{2\pi r(x)C_m(x)}{DS_{\text{ref}}} dx \end{aligned} \quad (8.24)$$

have been computed by integrating the pressure and friction coefficients along the launcher longitudinal axis. Moreover, the integration has been performed on

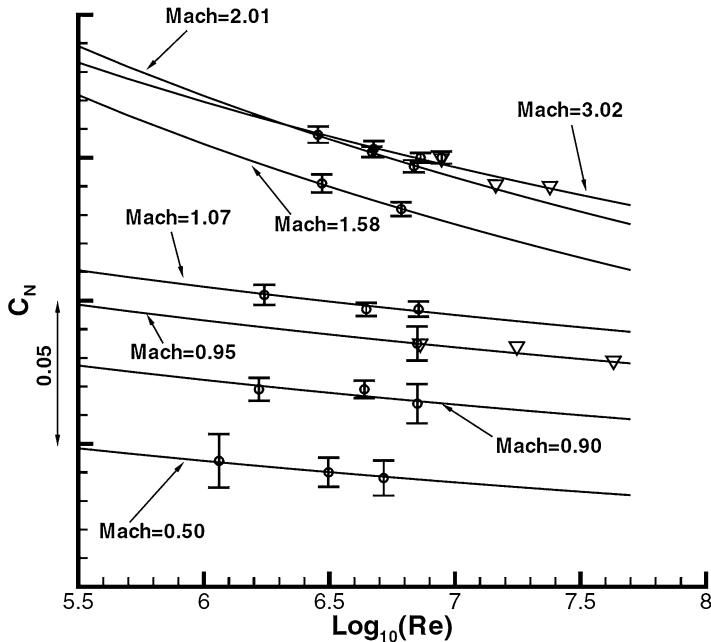


**Fig. 8.120** Normal force coefficient as function of the Reynolds and Mach numbers: *Solid line*, Eq. (8.23);  $\circ$  experimental data + error bars;  $\nabla$  corrected CFD data

the parts in which the launcher has been subdivided, as shown in Fig. 8.108, and the “lumped” coefficients have been obtained. This has allowed to identify the discrepancies between numerical and experimental data and to understand the reasons of the differences. In this way, the preliminary trends with the Reynolds number have been corrected and the functions of Eq. (8.23) determined [10]. As an example of the results achieved, the normal force coefficient at  $\alpha = 5.0^\circ$  as a function of the Reynolds and Mach numbers is reported in Fig. 8.120 [10].

## 8.7 Developments Phases: Uncertainties in Databases

The same kind of uncertainties as described previously for pre-project phases has to be considered in developments [1].

Concerning level of models in CFD, it is to be considered that more use of Navier–Stokes approach in these phases enables to reduce the related uncertainties. This should be quantified through CFD code precision assessment thanks to comparisons to wind tunnel data. Indeed, in development phases, the AEDB should be built with a composite approach involving CFD and wind tunnel testing as

previously mentioned. Wind tunnel data are then considered as anchor points which represent a physical reality. Nevertheless:

- Precision of wind tunnel measurements should be taken into account.
- Extrapolation to flight of experimental data should be performed with Navier–Stokes CFD in order to take into account differences in terms of Re number between experiment and flight, as previously illustrated.
- Base flow and then base pressure are not representative in experiments where no propulsive flow is represented. Base flows would require some specific testing facilities in order to assess the effects on pressure of hot jet gases injected in the recirculating base flows. Indeed this area is generally subjected to 3-D separated flow which provides in transonic regime with highly unsteady shear layers. This separated flow interacts either with some part of the emerging motor (buffet phenomenon) or with the hot propulsive jets. The hot propulsive jet can also feed the separated base flow with hot reducing gases, leading to locally heated flows and recombustion risks. As these aspects are not fully mastered, up to now the precision of launchers' base area pressure loading estimations before flight is quite poor. This affects the precision of predicted axial force coefficient, and it is generally recalibrated after the first flight, with flight measurements.

Concerning precision of shape representation, we can notice that the definition of the launcher is quite detailed in these phases. Then an assessment is performed to decide up to which size a shape detail can be neglected in the aerodynamic loading evaluation. During developments, the launcher shape may still evolve, and some CFD assessments of shape evolutions may be necessary after termination of the full wind tunnel testing plan. Moreover, some margins should be managed in the AEDB to cover foreseen possible limited evolutions. The magnitude of this last point can be illustrated by the following example. The previously detailed Ariane 5 simulation was initially computed with a first version of the forward boosters' attachments (called DAAV). Due to discrepancies in the results with wind tunnel data, it was then recomputed with the exact geometry of the tests. The comparison of local pressure maps is given in Fig. 8.121, and the attachments influence over the global aerodynamic coefficients is provided in Table 8.10; one can observe that this influence is quite sensitive at the global level [1].

As for pre-projects, some uncertainties should also be evaluated for AEDB values which are interpolated or extrapolated between measured or computed data.

### 8.7.1 Local Loading of Protrusions and Interstages Cavities

The protrusion structures and attachments on the launcher wall have to sustain aerodynamic loadings without any damage. Then, these loading exerted locally should be specified for every possible flight conditions. As the number, locations, and shapes of protrusions can evolve all along the launcher life, it is useful to define generic shapes of protrusions as *conception rules* for the design office

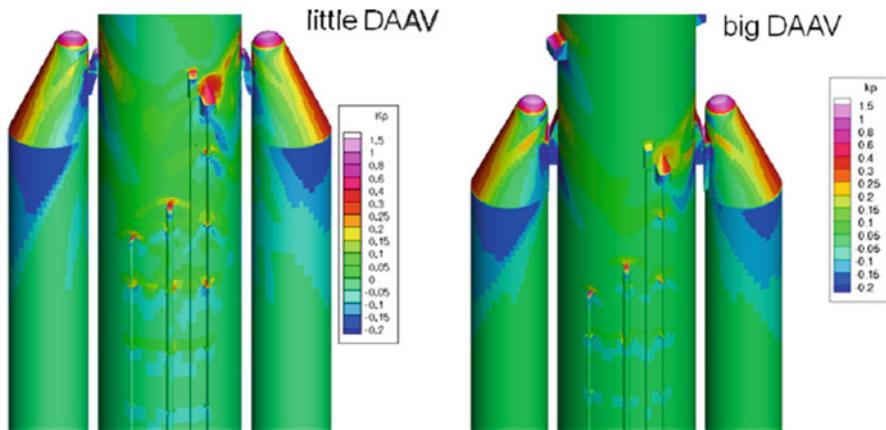


**Fig. 8.121** Local influence of forward boosters' attachments

**Table 8.10** Global influence of forward booster's attachments

Computations	$C_A$	$C_N$	$C_m$
Little DAAV	0.94	0.48	1.23
Big DAAV	0.944	0.513	1.27
Discr. vs. big %	0	6.5	3

and the associated generic loadings of these shapes. These loadings are defined as envelopes of all the possible efforts resulting from possible flight conditions. Indeed, some margins should be applied to the protrusion structures' sizing, in order to avoid very specific and recurrent analyses. Then, generally we distinguish two categories of protrusions, the ones which are specifically characterized for aerodynamic loading, selected for their big size or particular location, and the one which are not specifically investigated and considered as “generic type protrusions”.

In this sizing domain too, both experimental and CFD tools can be used in a complementary manner. The reference data obtained in wind tunnel result from local pressure measurements on the protrusions surfaces. Then due to limited number of measurements in a wind tunnel, limited space on a single protrusion face, important number of protrusions on a launcher, the amount of experimental data obtained for a particular protrusion face is limited. Otherwise, local data obtained in wind tunnel for low Re numbers (compared to flight ones) are not major. As shown above, with thinner boundary layers in flight, flow interaction on protrusions is more intensive. Moreover, due to costs, it is not thinkable to systematically test every evolution of protrusion shapes. Then CFD (possibly recalibrated on reference tests results) can provide with very detailed pressure maps on the protrusions, as well as results in full flight conditions. Moreover, CFD can contribute at the shape conception and localization of protrusions, as well as the determination of their impacts on the

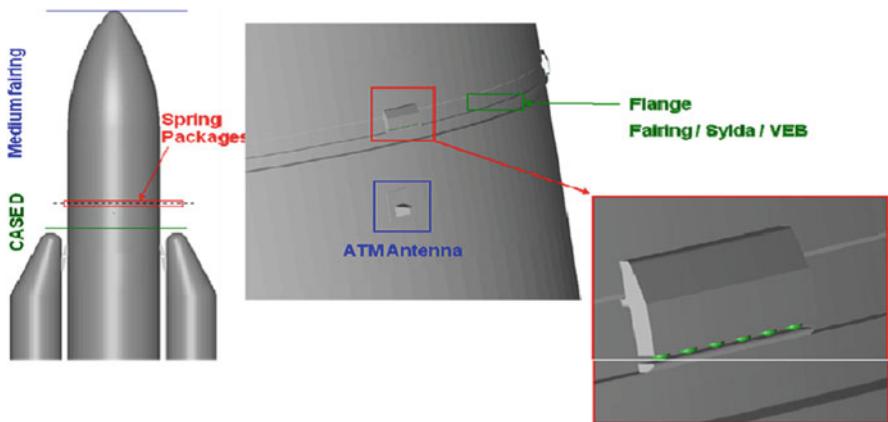


**Fig. 8.122** Location and external shape of the spring package fairing

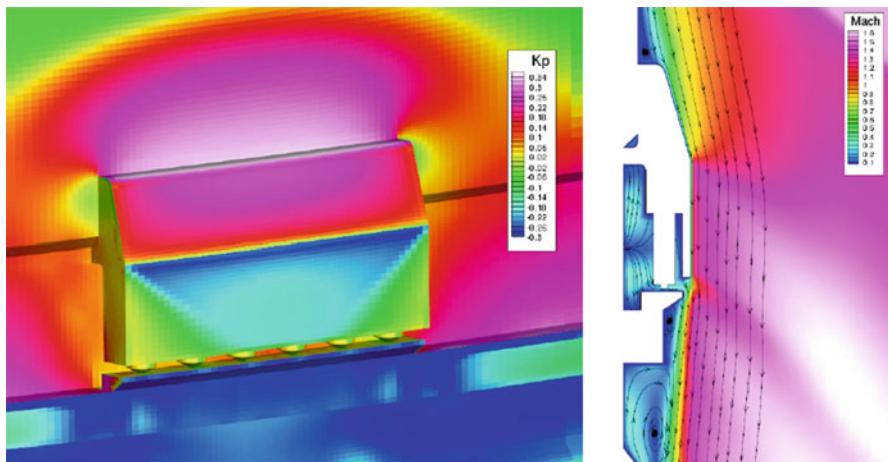


**Fig. 8.123** Local pressure map and flow over the cover at  $M_\infty = 1.5$  and  $\alpha = 3.7^\circ$

underlying launcher surfaces and global forces coefficients. This type of study is exemplified hereafter with the conception of a specific cover package developed for an upgraded implementation of Ariane 5 main fairing jettison. Location of this protrusion is illustrated in Fig. 8.122 [1]. An example of flow computation around the fairing for  $M_\infty = 1.5$  and a  $3.7^\circ$  AoA of the launcher is presented in Fig. 8.123 [1]. Several computations of that sort should be performed in order to build an envelope of the possible loading for each face of the protrusion. Then a loading specification can be built with a simple form as shown on Fig. 8.124 [1].

It is to be noted that external protrusion's shape is generally a fairing. This shape is also loaded with an internal pressure which should be computed. This

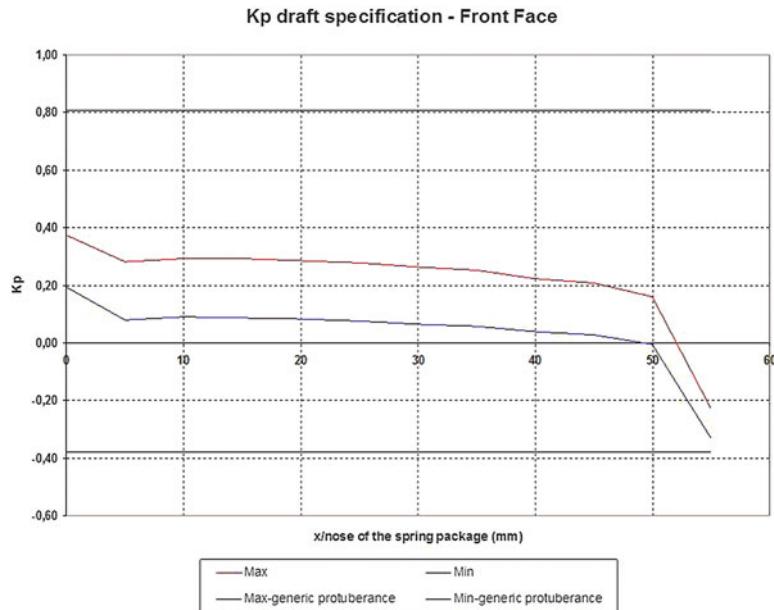


**Fig. 8.124** Example specification of protrusion front face loading, refined through CFD

need is also applicable to all internal launcher cavities and in particular to interstage areas. Depending on the leaks and vent holes between different cavities or with external atmosphere, this internal pressure can result from the full ascent phase depressurization history which begins at lift-off. Then this necessitates the use of specific software for computations of cavity pressures. These algorithms are quite simple and quick to run; nevertheless, they necessitate as input data the values of flow rate coefficients for each vent holes. When located between a cavity and the external flow, these coefficients depend on numerous parameters:

- The whole shape
- Its localization on the launcher
- The local external launcher shape
- The flow regime
- The launcher attitude
- Possible interactions with neighboring protrusions or other holes

All these possible influences cannot be completely characterized for every situation. Nevertheless, they should be sufficient in order to enable reasonable sizing of fairings and interstage walls in order to sustain internal pressure loading. These vent hole specification necessitates also some reference testing and CFD analysis.

## 8.8 Numerical Solution and Grid Convergence Analyses

All the CFD results provided in the chapter refer to both converged and grid-independent computations. In order to assess the numerical solution convergence, the density equation residual, stagnation-point heat flux, and aerodynamic coefficients (i.e.,  $C_L$ ,  $C_D$ , and  $C_m$ ) have been monitored during the iterations. Solution convergence is assumed when equation residual drops more than three orders of magnitude and both the stagnation-point heat flux and aerodynamic coefficients do not vary anymore. For example, the convergence histories of lift, drag, and pitching moment coefficients for the VTO Hopper in the case of  $M_\infty = 5$  and  $\alpha = 0^\circ$  are reported in Fig. 8.125. As one can see, numerical computation is stopped at about 220,000 iterations since each plot curve looks flat.

For each CFD result reported above, grid sensitivity analysis has been carried out by using three levels of the structured multiblock grid ( $L_1$ ,  $L_2$ ,  $L_3$ ). The number of cells of the finest level ( $L_3$ ) is 8 and 64 times that of the medium ( $L_2$ ) and the coarse ( $L_1$ ) levels, respectively.

As a numerical strategy, the single computation is started on the coarsest grid level ( $L_1$ ), and then, once that a satisfying level of accuracy has been reached, the solution is successively interpolated on finer ones and restarted. Convergence analyses have been assessed, according to Richardson extrapolation criteria. Indeed, if the solution is in the asymptotic range of convergence, it is possible, by means of

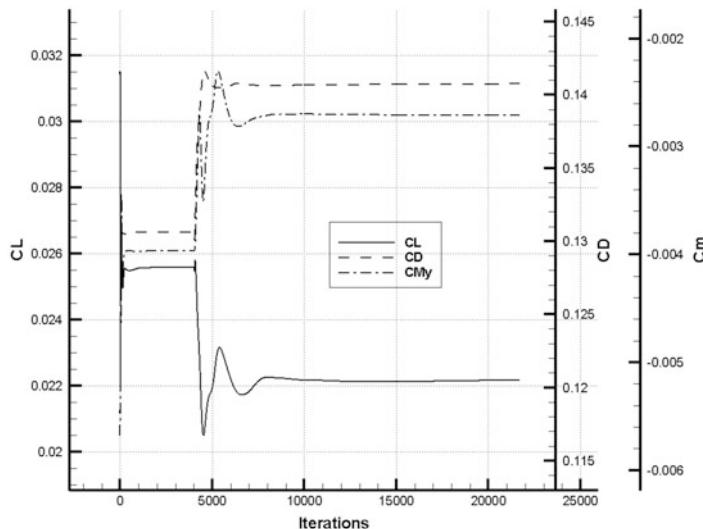


**Fig. 8.125** Convergence histories of lift, drag, and pitching moment coefficients for the VTO Hopper in the case of  $M_\infty = 5$  and  $\alpha = 0^\circ$

the Richardson extrapolation formula, to obtain the value of a global ( $C_L$ ,  $C_D$ , etc.) or a local variable (pressure, heat flux etc.) at virtually zero cell dimension, i.e., at an infinite number of cells [15, 19].

For example, both Figs. 8.126 and 8.127 show the grid sensitivity analysis for the CFD computation at  $M_\infty = 5$  and  $\text{AoA} = 0^\circ$ .

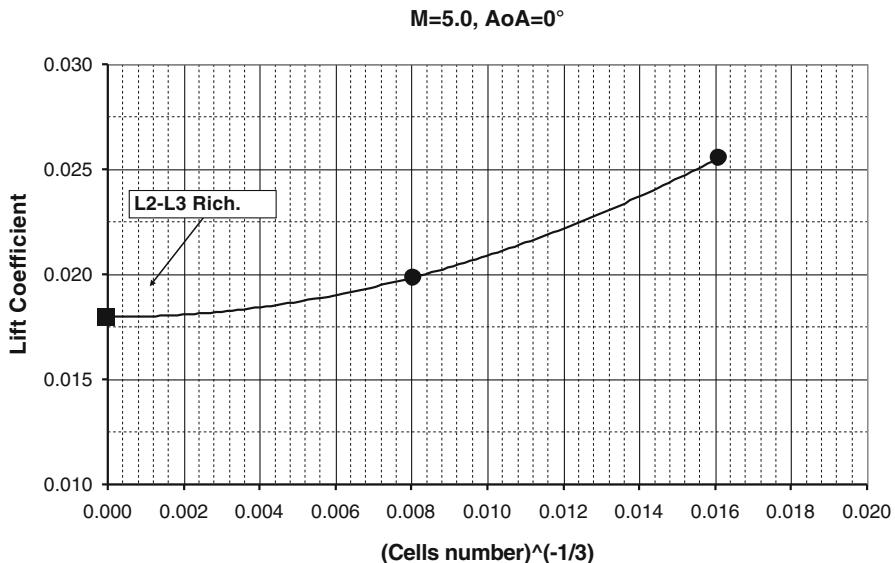


**Fig. 8.126** Grid sensitivity analysis: VTO Hopper lift coefficient

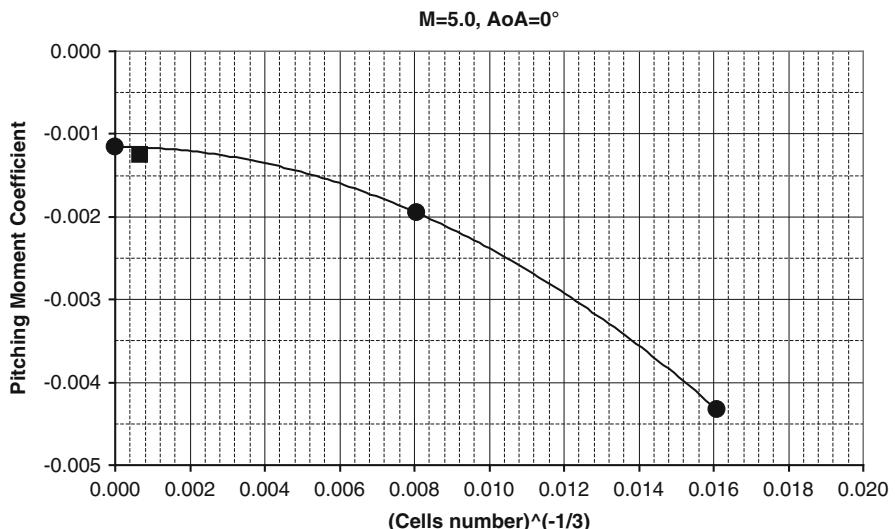


**Fig. 8.127** Grid sensitivity analysis: VTO Hopper pitching moment coefficient

The former figure (Fig. 8.126) reports the case of the lift coefficient  $C_L$  versus the inverse of the cubic root of the number of cells (representative of a mean value of the cell dimension). The values reported are the  $L_2$  and  $L_3$  ones and the extrapolated value (at “zero” cell dimension), that in the hypothesis of a spatial second-order scheme and a grid level ratio equal to 2, can be obtained by means of the following formula:

$$C_L(h=0) = \frac{4}{3} \cdot C_{L,FINE} - \frac{1}{3} \cdot C_{L,MEDIUM} \quad (8.25)$$

Analogous trends can be observed for pitching moment coefficient in Fig. 8.127. As shown in both cases, the  $L_2-L_3$  Richardson extrapolated values (bold square symbol) are in the asymptotic range of convergence. As a conclusion, it must be said that, as a general rule for such complex geometry, the maximum number of cells used was chosen in accordance with an acceptable convergence central processing unit (CPU) time estimation.

## References

1. Pallegoix JF (2014) Launcher aerodynamics. STO-EN-AVT-206
2. Guedron S et al (2004) Future space transportation in Europe: the CNES roadmap proposal. In: ISTS 2004-9-04, Miyazaki – Japan, 30 May–6 June, 2004
3. Sippel M et al. (2003) Technical development perspective of reusable booster stages. In: 12th AIAA int. space planes & hypersonic systems, 15–19 December, 2003
4. Iranzo-Greus D et al (2004) Evolved European reusable space transport (EVEREST) – system design process and current status. In: IAC-04-V.4.07
5. Polti S Reusable first stage vehicle. In: IAC-04-W.2.07
6. Tomatis C, Bouaziz L, Franck T, Kauffmann J (2006) RLV candidates for European future launchers preparatory programme. In: 57th international astronautical congress, 2–6 October 2006, Valencia, Spain. IAC-06-D2.2.07
7. Garcia A, Yamanaka BNB, Bizarria JW, Scheuerpflug F (2011) VSB-30 sounding rocket: history of flight performance, São José dos Campos, September–December 2011. J Aerosp Technol Manag 3(3):325–330. doi:[10.5028/jatm.2011.03032211](https://doi.org/10.5028/jatm.2011.03032211)
8. Kauffmann J (2006) Future European launch systems in the FLPP overview and objectives. In: 57th international astronautical congress, 2–6 Oct 2006, Valencia, Spain. IAC-06-D2.4.05
9. Pizzicaroli A, Paglia F, Lambiase E, Contini C, Barbagallo D (2007) Vega launcher aerodynamics at lift-off. In: 43rd AIAA/ASME/SAE/ASEE joint propulsion conference & exhibit 8–11 July 2007, Cincinnati, OH. AIAA 2007-5850
10. Catalano P, Marini M, Nicolí A, Pizzicaroli A (2007) CFD contribution to the aerodynamic data set of the vega launcher. J Spacecr Rocket 44(1):42–51 January–February 2007
11. Nicolí A, Imperatore B, Fauci R, Pizzicaroli A (2006) Wind tunnel test campaigns of the VEGA launcher. In: AIAA Paper 2006-0257, Jan 2006
12. Catalano P, Marini M, Vitagliano PL, Pizzicaroli A (2005) CFD role in the extrapolation-to-flight procedure of the vega launcher aerodynamic data-base. In: Proceedings of XVIII Congresso Nazionale AIDAA [CD-ROM], AIDAA, Rome, 2005
13. Anderson JD (1989) Hypersonic and high temperature gas dynamics. McGraw-Hill, New York
14. Bertin JJ (1994) Hypersonic aerothermodynamics, AIAA education series. American Institute of Aeronautics and Astronautics, Washington, DC

15. Roache PJ (1998) Verification and validation in computational science and engineering. Hermosa Publishers, Albuquerque
16. Rom J (1992) High angle of attack aerodynamics, subsonic transonic and supersonic flow. Springer, New York
17. Pezzella G (2011) Preliminary aerodynamic and aerothermodynamic assessment of the VTO Hopper Booster. ISRN Mech Eng 2011: 15 pages. Article ID 215785, doi:[10.5402/2011/215785](https://doi.org/10.5402/2011/215785)
18. Pezzella G, Marini M, De Matteis P, Kauffmann J, Dapra A, Tomatis C (2010) Aerothermodynamic analyses of four reusable launchers in the framework of ESA future launchers preparatory programme. Aerotecnica Missili & Spazio (J Aerosp Sci Technol Syst) 89(1), January 2010
19. Pezzella G, Marini M, Roncioni P, Kauffmann J, Tomatis C (2009) Preliminary design of vertical takeoff hopper concept of future launchers preparatory program. J Spacecr Rock. 46(4):788–799 doi:[10.2514/1.39193](https://doi.org/10.2514/1.39193). ISSN 0022-4650
20. Pezzella G, Marini M, Roncioni P, Kauffmann J, Tomatis C (2008) Aerodynamic and aerothermodynamic evaluation of the VTO Hopper Concept in the frame of ESA future launchers preparatory program. In: 15th AIAA international space planes and hypersonic systems and technologies conference, 28 April–1 May 2008, Dayton, Ohio (USA), paper AIAA-2008-2639
21. Pezzella G, Kauffmann J, Dapra A, Tomatis C (2009) An Italian contribution to the next generation launcher in the framework of ESA future launchers preparatory programme. In: XX AIDAA congress, Milan, Italy, 29 June–3 July 2009
22. Pezzella G. et al. (2009) Appraisal of aerodynamics and aerothermodynamics of RFS and LFBB (Lox/CH4) ESA future launchers preparatory program concepts. In: 16th AIAA/DLR/DGLR international space planes and hypersonic systems and technologies conference, 19–22 Oct 2009, Bremen, Germany. AIAA 2009-7340
23. Viviani A, Pezzella G (2009) Heat transfer analysis for a winged reentry flight test bed. Int J Eng 3(3):330–345. ISSN:1985-2312
24. Prabhu DK (2004) System design constraints-trajectory aerothermal environments. In: RTO AVT/VKI lecture series in *Critical Technologies for Hypersonic Vehicle Development*, 10–14 May 2004
25. Moore FG, Hymer T, Wilcox F (1994) Base drag prediction on missile configurations. J Spacecr Rockets 31(5):759–765
26. Kinney D (2004) Aero-thermodynamics for conceptual design. In: 42nd AIAA aerospace sciences meeting and exhibit, Reno, Nevada, 5–8 January 2004 AIAA-2004-31
27. Kinney D (2007) Aerothermal anchoring of CBAERO using high fidelity CFD. In: 45th AIAA aerospace sciences meeting and exhibit, Reno, Nevada, 8–11 January 2007. AIAA-2007-608
28. Glossner CO (2003) Force and moment coefficients of the hopper/phoenix configuration in hypersonic flow. In: 3rd Int. Symposium Atmospheric Reentry Vehicles and Systems, Arcachon, France, March 2003
29. Guédron S, Prel Y, Bonnal C, Rojo I (2003) RLV concepts and experimental vehicle system studies: current status. In: 54th international astronautical congress, 29 September–3 October 2003, Bremen, Germany, IAC-03-V.6.05
30. Srinivasan S, Tannehill JC, Weilmuenster KJ (1987) Simplified curve fits for the thermodynamic properties of equilibrium air. NASA-RP-1181
31. Srinivasan S, Tannehill JC (1987) Simplified curve fits for the transport properties of equilibrium air. NASA-CR-178411
32. Lees L (1956) Laminar heat transfer over blunt-nosed bodies at hypersonic flight speeds. Jet Propuls 26:259–269
33. Tauber ME (1989) A review of high-speed, convective, heat-transfer computation methods. NASA TP-2914, July 1989
34. Eggers T, Bozic O (2002) Aerodynamic design and analysis of an Ariane 5 liquid fly-back booster. AIAA 2002-5197

35. Pezzella G. Aerodynamic and aerothermodynamic trade-off analysis of a small hypersonic flying test bed. *Acta Astronaut* 69(3–4):209–222. doi:[10.1016/j.actaastro.2011.03.004](https://doi.org/10.1016/j.actaastro.2011.03.004). ISSN 0094-5765
36. Burkhardt H, Sippel M, Herbertz A, Klevanski J (2004) Kerosene vs. methane: a propellant tradeoff for reusable liquid booster stages. *J Spacecr* 41(5):762–769
37. Eggers T (2003) Aerodynamic behaviour of a liquid fly-back booster in transonic cruise flight, AIAA-2003-3422. In: 21st applied aerodynamics conference, Orlando, Florida, 23–26 June 2003
38. Eggers T (2004) Aerodynamic design of an Ariane 5 reusable booster stage. In: Fifth European symposium on aerothermodynamics for space vehicles, Cologne, November 2004
39. Tarfeld F (2004) Comparison of two liquid fly-back booster configurations based on wind tunnel measurements. In: Fifth European symposium on aerothermodynamics for space vehicles, Cologne, November 2004
40. Boži O (2004) Flow field analysis of a future launcher configuration during start. In: Fifth European symposium on aerothermodynamics for space vehicles, Cologne, November 2004

# Appendix A: A Manned Space Mission to Mars

## A.1 Introduction

This paper reports about the results of aerodynamic design analyses of two manned braking systems (MBS) entering the Mars atmosphere, with the aim of supporting design studies of a planetary entry system. Two unusual lifting body configurations with rounded edge delta-like cross section have been analyzed. The preliminary aerodynamic analyses have been focused on flight conditions compatible with a manned mission entering the Mars atmosphere. However, neither the mission architecture needed to reach Mars from Earth or neighbor Earth space nor surface explorations have been addressed. All the design analyses have been performed at several levels. Indeed, vehicle aerodynamic assessment has been extensively addressed through simplified design approach as, e.g., hypersonic panel methods (HPM); then, a number of fully three-dimensional computational fluid dynamics (CFD) simulations, both with Euler and Navier–Stokes approximations, of the hypersonic flowfield past the entry vehicle have been performed. The results herein provided have been obtained for a Mars entry scenario compliant with an approach to the red planet both by direct planetary entry and entry after aerobraking [1]. These results may be used to provide numerical data for understanding requirements for the human exploration of Mars [2].

## A.2 The Trip to Mars and Return

Several typical examples of mission scenarios are given below for manned missions to Mars. They also illustrate the influence of mission requirements on determination of aerothermal environment expected for such a kind of mission. Indeed, recent studies of manned exploration missions to Mars have considered four different

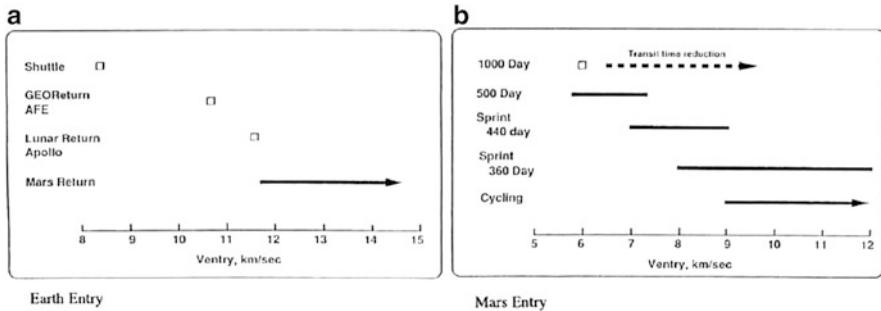


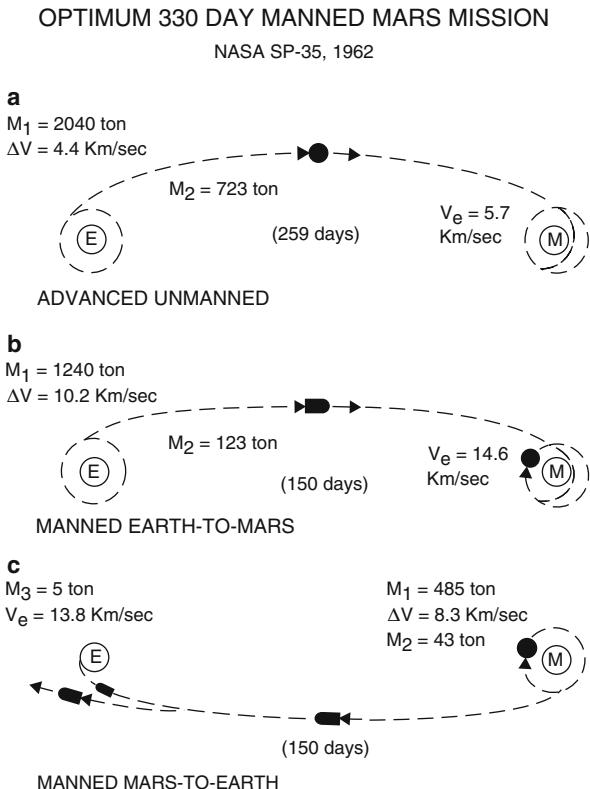
**Fig. A.1** Entry velocity envelopes for Mars mission with return to Earth (a) Earth Entry, (b) Mars Entry

scenarios. These include a short, 330-day, *sprint* mission; a medium length, nominal 500-day mission; a long, nominal 1,000-day mission; and a cycler mission. Each of these missions demands multiple vehicles and will involve entry and aerocapture maneuvers both at Mars and at Earth on the return. Entry velocities both at Mars and at Earth can vary greatly depending on the mission duration and whether the aerocapture vehicle is manned or unmanned. Shown in Fig. A.1 are Mars and Earth entry velocity envelopes for various missions [3].

For Mars aerocapture the highest entry velocities will be experienced by the cycling missions followed by the sprint down to the 1,000-day mission having the lowest approach speeds, which increases as transit time decreases. For the Earth return, all the approach speeds are greater than those for cislunar missions. A sprint mission scenario is illustrated in Fig. A.2 [3].

Here an advanced unmanned vehicle with an initial mass of 2,040 tons is sent on a low-energy trajectory with an initial thrust from Earth orbit of 4.4 km/s, requiring the expenditure of 1,317 tons of fuel. This 723 ton vehicle would arrive at Mars in 259 days with an approach velocity of 5.7 km/s for aerocapture into an orbit around Mars. This vehicle would be followed by a smaller, manned vehicle with an initial mass of 1,240 tons thrust from Earth orbit at 10.2 km/s. This would require 1,117 tons of fuel leaving a 123 ton vehicle approaching Mars 150 days later at a speed of 14.6 km/s. This vehicle will be aerocaptured and docked with the larger unmanned vehicle already in Mars orbit. From this docking orbit, a smaller, manned entry vehicle will be sent to land on the Martian surface. After 30 days the Mars lander would return to the docking orbit in preparation for the return of the crew to Earth. The manned Earth return vehicle will leave the Martian orbit with an initial mass of 485 tons and a thrust of 8.3 km/s, requiring 442 ton of fuel. The 43 ton return vehicle will reach the vicinity of Earth 150 days later, at which time a 5 ton manned capsule will be jettisoned for Earth aerocapture with an entry speed of 13.8 km/s. The remaining unmanned, expendable 38 ton return vehicle would continue on in space.

**Fig. A.2** Sprint mission schematic to Mars (a)  
Advanced unmanned, (b)  
Manned Earth to Mars, (c)  
Manned Mars to Earth



### A.3 Vehicle Configuration Selection

The vehicle concepts, under investigation in this work, are lifting body (LB) configurations and are shown in Fig. A.3. On the left is shown the vehicle named LB-A while on the right that named LB-B.

They represent the best configuration obtained by optimization processes performed at *Dipartimento di Ingegneria Aerospaziale e Meccanica* of Second University of Naples in the framework of a design study of planetary entry systems [3, 4]. The main objective of this study is the searching for the minimum weight configuration taking into account for both the vehicle thermal and the operational constraints, as discussed in Ref. [3] and [4]. Note that, minimizing vehicle weight is an important figure of merit within the optimization processes for the design of a Mars exploration mission.

Each vehicle features an aerodynamic configuration with a compact body with a rounded edge delta-like cross section as shown in Fig. A.4 [3, 4].

The proposed concepts represent a rather conventional configuration characterized by a low nose camber and a flat bottomed surface in order to increase the

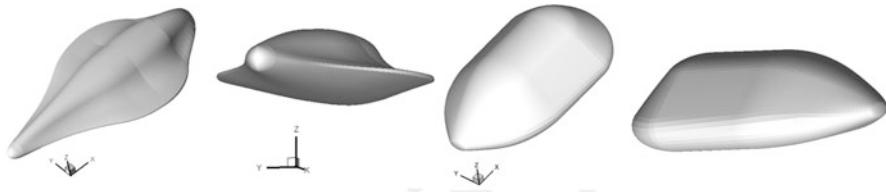


**Fig. A.3** Vehicle configurations LB-A (*left*) and LB-B

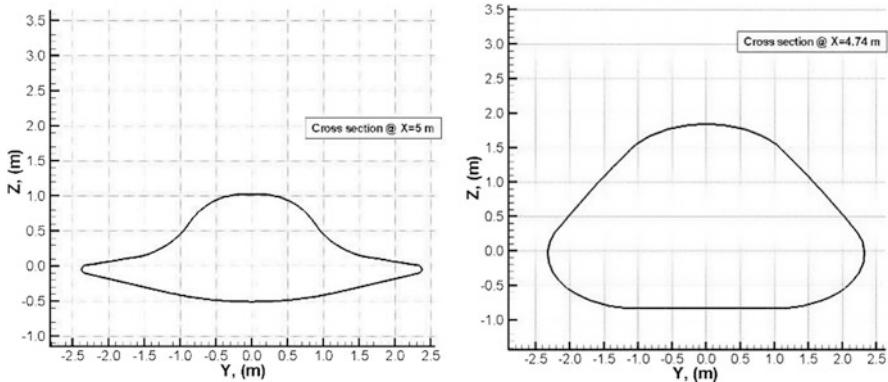


**Fig. A.4** Vehicle cross section [4]

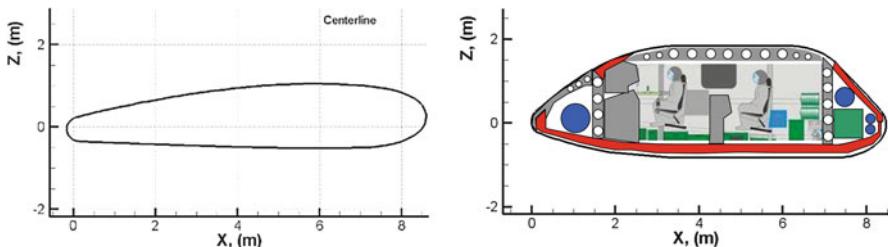


**Fig. A.5** Vehicles centreline with internal layout for the LB-B configuration only

overall vehicle hypersonic performance. The forebody is characterized by simple cone-sphere geometry with smooth streamlined surfaces on the upper and lower side of vehicle (see Fig. A.5).

A very preliminary internal layout for a crew of three/four astronauts is also reported in Fig. A.5 for the LB-B configuration only.

The nose radius of both vehicle concepts reads 0.3 m.

Each vehicle is thought for a little crew entering into the Mars atmosphere from a low orbit and performing a variable angle of attack (AoA) entry trajectory.

For instance, during the entry maneuver, the vehicle experiences a high-speed and high-temperature flow. As a consequence, three main design topics have

been focused for safety and performance: the structural integrity of the vehicle; livable conditions for the crew; the minimization of the vehicle structural weight. Considering that the peaks of both structural and thermal stresses are generally reached during the hypersonic flight, and the low speed flight is assumed being performed by the use of a parachute system, only the flight hypersonic regime has been analyzed.

The pursuit of a feasible and livable minimum weight configuration has preliminarily required the definition of a well-suited parametric model for both the vehicle aerodynamic shape and for thickness distribution of the thermal insulating material.

The structural stresses are considered by the mean of the asymptotic dynamic pressure and the normal load factor peaks, and crew liveability conditions are accounted for by controlling that the inner temperature remains locally below a duly imposed value. An optimization procedure, using Genetic Algorithm (GA), is performed to find the optimal configuration [3]. The vehicle shape is modeled by a suitable parametric model, based on Coons surfaces, and a parametric insulating material distribution is foreseen.

The entry trajectory is calculated by the three degree-of-freedom (3 dof) model for planetary unpowered gliding entry with no bank angle (see Fig. A.7). The shape aerodynamics is performed via HPM and the thermal state of the external surface is determined by means of one-dimensional boundary layer model together with the hypothesis of radiative cooling at vehicle wall. Some other tools, able to evaluate the lifting body entry trajectory and the thermal analysis of the protection shield system, have been also developed. The initial trajectory angle is considered as an optimization parameter. Furthermore, a parametric control of the AoA has been implemented.

A two-people crew has been considered for the LB-A concept. The crew layout into the re-entry vehicle is not a priori fixed, but parameterized and managed by a discrete variable. The internal volume hosting the crew is set by the layout parameter, while the volumetric efficiency is considered in vehicle configuration selection, since, in the first order, thermal protection system and structural weight are a direct function of vehicle wetted area.

Then, the vehicle outer shape is defined in detail by about 30 parameters that perform an affine transformation of a spherical domain into a suitable aerodynamic shape [3]. The latter vehicle feature is an important design topic considering that, in the case of Mars entry, the basic problem is one of decelerating the vehicle sufficiently to allow for the tenuous nature of the atmosphere. As a result, the most significant vehicle requirement is a rather low ballistic coefficient,  $B_C$ .

As a consequence, the vehicle configurations must be very blunt shapes, as in the case of LB-B configuration, in order to maximize vehicle aerodynamic drag,  $C_D$ . Moreover, the vehicle must be also able to provide rather high aerodynamic lift to increase the allowable  $B_C$  and, therefore, payload weight, as in the case of the more streamlined configuration, LB-A [4].

Finally, for Mars entry heating is a determining factor in vehicle configuration. Since manned vehicles are necessarily large, radiant heating becomes dominant for

such entries if simply blunt vehicles are used. To avoid such heating, configurations such as those reported in Fig. A.3 have been proposed considering that the radiative heat flux is linearly dependent on geometrical radius of the vehicle nose [5].

## A.4 Methodology Analysis and Used Tools

This work summarizes a contribution to the planetary exploration concept design dealing with the definition of both the preliminary aerodynamic (AEDB) and aerothermodynamic (ATDB) databases for a manned vehicle entering the Mars atmosphere, compliant with a phase-A design level [6]. The former (AEDB) is needed for the Flight Mechanics analyses, since it must be verified that the concept aerodynamic performance ensures that the vehicle stays within the load constraints (i.e., pressure, inertial and thermal loads) during descent. The latter (ATDB) is needed for the TPS design analyses; in fact, as the vehicle flies through descent to red planet, its internal energy (i.e., potential plus kinetic) is converted into thermal energy within the boundary layer close to the vehicle surface, so that a thermal-shield must be provided to the MBS in order to sustain this heat loading.

In this framework, different design approaches have been adopted. The aerodynamic performance of each concept has been assessed according to the space-based design approach [7].

On the other hand, the surface heat flux distributions for each MBS concept have been provided according to the trajectory-based design approach [7].

An accurate aerodynamic and aerothermodynamic analysis for several flight conditions, however, is very complex and time consuming and is not compatible with a Phase-A design study, in which fast predicting methods are mandatory. Therefore, aerodynamic and aerothermodynamic analyses have been mainly performed by means of engineering-based approach, by using a 3-D panel method code developed by CIRA [8]. Increasing the order of complexity, a number of detailed CFD simulations have been carried out to more deeply characterize the hypersonic aerothermal environment of the vehicles and to focus on some critical design aspects not predictable with simplified tools. Indeed, 3-D Euler and Navier–Stokes numerical flowfield computations have been performed at different Mach numbers and AoA, at the most critical flight conditions occurring during the descent trajectory.

### A.4.1 Engineering-Based Design Analysis

Engineering-based aerodynamic analysis has been extensively performed by using a 3-D Panel Methods code, namely, CIRA SIM, based on the simplified Newtonian approach and local surface inclination methods (SIM). This tool, at high supersonic and hypersonic speeds, is able to accomplish the aerodynamic and aerothermodynamic analyses of a complex re-entry vehicle configuration by using simplified

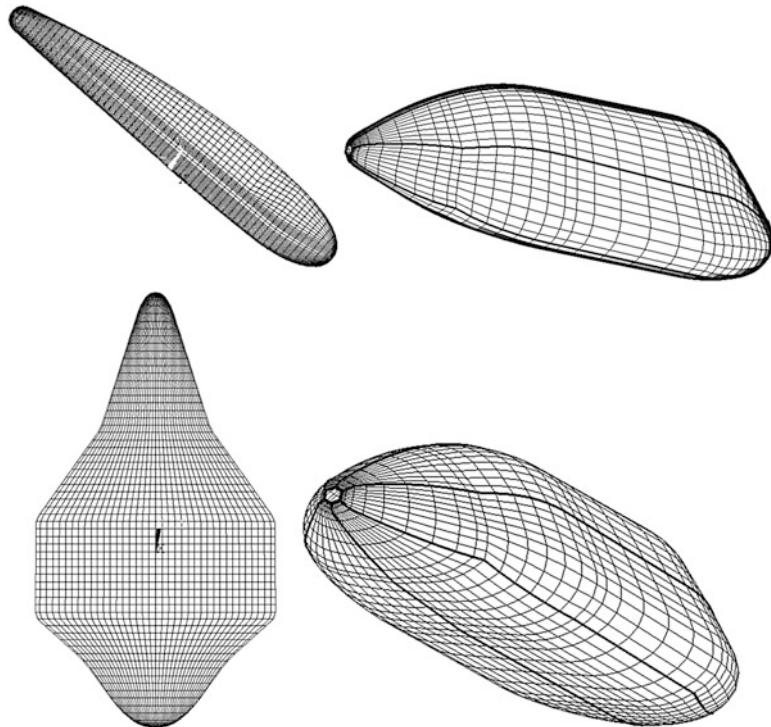


**Fig. A.6** Example of surface mesh used for engineering-based design analyses

approaches as local surface inclination methods and approximate boundary-layer methods, thus avoiding complex grid generation and CFD high time consumption [8]. Typical surface meshes of the MBS, used for the engineering level computations, are shown in Fig. A.6. As shown, the vehicle surface is approximated by a system of planar and leading edge panels; the lowest level of geometry used in the analysis is a quadrilateral element.

The pressure acting on each panel of impact and shadow regions is evaluated by user-specified compression-expansion method. Several methods, typical of hypersonics, are available such as those derived from Newtonian, Modified Newtonian, and Prandtl-Meyer theories [5]. In order to predict viscous contribution to aerodynamic forces and moments, the shear force is determined on each vehicle panel on the assumption of a laminar or turbulent flat plate [9].

In particular, the viscous calculation is performed along with streamlines, and the results are then interpolated at the panel centroids. The streamlines are generated starting from the inviscid surface velocities generated previously in the aerodynamic analysis phase.

Finally, the panel aeroheating is evaluated by means of approximate one-dimensional boundary-layer methods (1D BLM) as reference temperature and reference enthalpy ones, which are available both for laminar and turbulent

boundary-layer assumptions. Indeed, the generic vehicle component may be modeled as either a flat plate or a leading edge by selecting the appropriate boundary-layer model. The Mangler factor is used to transform the solution of two dimensional boundary layers to the axially symmetrical case [9].

#### A.4.2 CFD-Based Design Analysis

CFD design analyses of vehicle concepts have been carried out by using the commercial code FLUENT [10]. A number of user-defined functions (UDFs), developed in order to perform numerical computations with a thermochemical nonequilibrium model suitable for Martian atmosphere are also considered [11, 12]. The code solves the fully Reynolds average Navier–Stokes (RANS) equations on hybrid grids by means of the finite volume approach; it uses a flux difference splitting (FDS) second-order upwind scheme for the spatial reconstruction of convective terms, while for the diffusive fluxes, a cell-centered scheme is applied.

In the present CFD analysis, an alternative way to compute the flux vector is considered by using a flux-vector splitting scheme, namely, Advection Upstream Splitting Method (AUSM). It provides exact resolution of contact and shock discontinuities and it is less susceptible to Carbuncle phenomena. Implicit solver formulation is available and considered in the computations of this work. Indeed, due to broader stability characteristics of the implicit formulation, a converged steady-state solution can be obtained much faster using the implicit formulation rather than the explicit one. Global transport properties of the gas mixture rely on semi-empirical rules such as Wilke’s mixing rule for viscosity and thermal conductivity [5]. The viscosity and thermal conductivity of  $i$ th species is obtained by kinetic theory of gases [5]. For the diffusion coefficient of the  $i$ th species in the mixture the multicomponent diffusion coefficient is applied, where species mass diffusivity is evaluated by kinetic theory [5]. Flowfield chemical reactions proceed with forward rates that are expressed in the Arrhenius form and reaction rate parameters are due to Park [13].

In particular, a number of in-house modifications (i.e., UDF) have been developed to account for both the thermal nonequilibrium in the flow and radiative equilibrium temperature at wall, since both vibrational nonequilibrium and wall radiative cooling boundary conditions are not basic code features. In the UDF vibrational relaxation is modeled using a Landau–Teller formulation, where relaxation times are obtained from Millikan and White, assuming simple harmonic oscillators [5], whereas to account for wall radiative cooling, during numerical simulations, the wall temperature is calculated by Stefan–Boltzmann law.

Finally, in order to assess numerical solution convergence, equation residuals and aerodynamic coefficients (i.e.,  $C_L$ ,  $C_D$ , and  $C_m$ ) have been monitored during iterations. Solution convergence is assumed when equation residuals drop more than three orders of magnitude and the aerodynamic coefficients plots are flat for enough iterations.

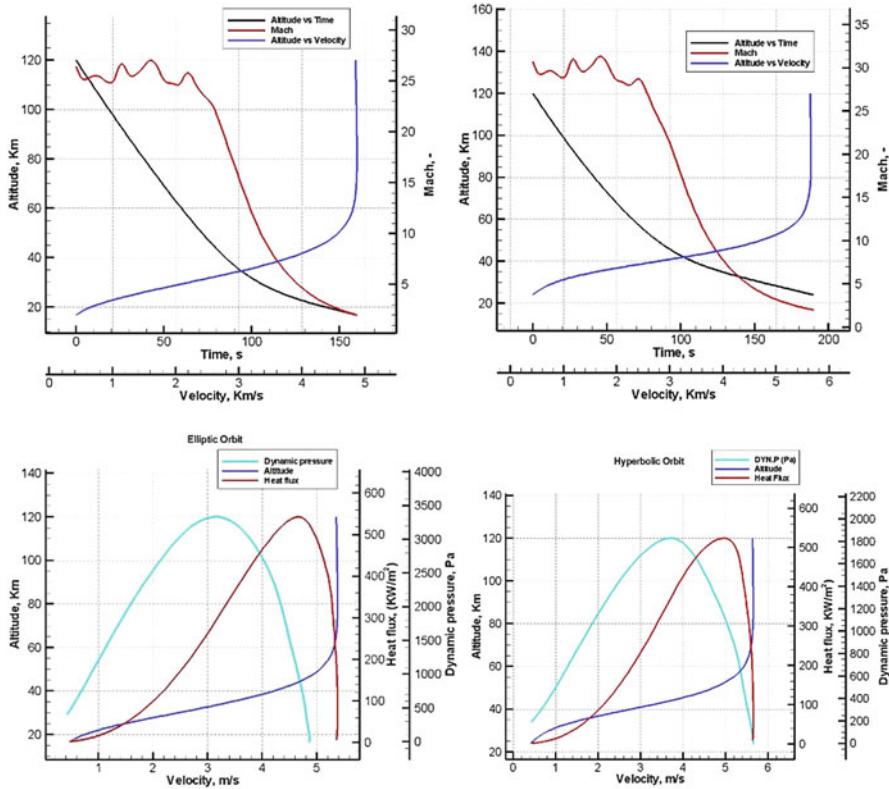


**Fig. A.7** MBS flight scenario, EO on the *left* and HO on the *right*

#### A.4.2.1 Flowfield Analysis

CFD analyses have been performed to assess the aerothermal environment that the MBS experiments during descent, thus evaluating several surface loading distributions (e.g., pressure and heat flux). To this end, several fully three-dimensional numerical computations, both for perfect and chemically reacting gas approximation, have been performed. The flight scenario considered so far is summarized in Fig. A.7. It refers to a vehicle entering the Mars atmosphere both from an elliptic orbit (EO), e.g., planetary entry after aerobraking, and hyperbolic orbit (HO), e.g., direct planetary entry.

In particular, the free-stream conditions considered in the present CFD analysis, according to both space-based and trajectory-based design approaches, are summarized in Table A.1.

Therefore, 21 CFD numerical simulations (both Euler and Navier–Stokes) have been performed both in trajectory-based design approach (i.e., simulation ID 1–7 and 10–17) and space-based design approach (i.e., simulation ID 8, 9, and 18–21)

**Table A.1** CFD free-stream conditions [14]

Simulation ID	Gas model	Mach [-]	AoA [deg]	Altitude [Km]	Pressure [Pa]	Temperature [K]	Density [Kg/m <sup>3</sup> ]
1	Perfect Gas	10	10	10	284.19	227.55	6.50E-03
2		15	40	60	3.16	116.55	1.41E-04
3		20	10	60	3.16	116.55	1.41E-04
4		20	20	60	3.16	116.55	1.41E-04
5		20	30	60	3.16	116.55	1.41E-04
6		20	40	60	3.16	116.55	1.41E-04
7		22	40	60	3.16	116.55	1.41E-04
8		EO PH*	22	40	44.2	13.09	151.63
9		HO PH	26	40	52.1	6.43	134.09
10	Reacting Gas	10	10	10	284.19	227.55	6.50E-03
11		10	20	10	284.19	227.55	6.50E-03
12		10	30	10	284.19	227.55	6.50E-03
13		10	40	10	284.19	227.55	6.50E-03
14		20	10	60	3.16	116.55	1.41E-04
15		20	20	60	3.16	116.55	1.41E-04
16		20	30	60	3.16	116.55	1.41E-04
17		20	40	60	3.16	116.55	1.41E-04
18	EO PH	NCW	22	40	44.2	13.09	151.63
19		FCW	22	40	44.2	13.09	151.63
20	HO PH	NCW	26	40	52.1	6.43	134.09
21		FCW	26	40	52.1	6.43	134.09

\*EO PH (Elliptic Orbit Peak Heating conditions)

HO PH (Hyperbolic Orbit Peak Heating conditions)

NCW (Non-catalytic wall)

FCW (Fully catalytic wall)

[7, 14]. In particular, the latter simulations refer to trajectory peak heating conditions both for EO and HO, needed to address the vehicle TPS design (not reported in this chapter). Preliminary result of vehicle aeroheating analysis can be found in Ref. [15] and [16].

All CFD computations have been carried out considering radiative cooling at vehicle wall (i.e.,  $\dot{q}_{cw} = \sigma\varepsilon T_w^4$ ). For the reacting gas computations, the Martian atmosphere has been considered as a mixture of 95.7 % carbon dioxide, 1.6 % argon and 2.7 % nitrogen. The flow has been modeled as a reacting gas mixture of 9 species (Ar, CO<sub>2</sub>, N<sub>2</sub>, O<sub>2</sub>, CO, NO, N, O, C). Reaction mechanism and chemical kinetics, taken into account in the present work, are due to Park [6, 13].

Nonequilibrium computations have been performed since one of the most challenging problem facing the design of atmospheric entry vehicle is the phenomenon of “real gas behavior.” At hypersonic speeds, the shock wave produced ahead of the vehicle suddenly elevates the gas temperature in the shock layer. So the gas thermal energy may be comparable with the energy associated with a whole range of gas chemical processes such as molecular vibrational excitation; dissociation of atmospheric molecules into their atomic forms; formation of other chemical species through recombination reactions; and ionization of both molecular and atomic species [17]. Therefore, the gas mixture has to be considered in thermal and chemical nonequilibrium.

Finally, CFD analysis of the MBS has been preceded by a code validation phase performed considering the available numerical and experimental data for the Mars Pathfinder probe at entry peak heating conditions, as summarized in Ref. [18–20].

## A.5 Aerodynamic Analysis

The aerodynamic analysis of MBS is shown in term of lift ( $C_L$ ), drag ( $C_D$ ), and pitching moment ( $C_m$ ) coefficients.

The reference parameters  $L_{ref}$  (e.g., longitudinal reference length) and  $S_{ref}$  (e.g., reference surface) are the vehicle length (i.e., 8 m for both configurations) and planform area (i.e.,  $31.7 \text{ m}^2$  for LB-A and  $32.0 \text{ m}^2$  for LB-B). The pitching moment is computed from the vehicle nose (i.e., 0,0,0) and also considering the vehicle CoG at different percentage of vehicle length in order to address a CoG sensitivity analysis as well.

MBS aerodynamic results, provided by engineering-based analysis, cover  $\alpha$  ranging from 0 to  $50^\circ$ .

On the other hand, present CFD computations for the MBS have been carried out on a 3-D multiblock (up to 80 blocks) structured grids similar to those shown in Fig. A.8. In particular, Fig. A.8 shows a close-up view of the 3-D mesh on the vehicle surface and pitch plane (LB-B only).

All the mesh domains have been generated with the commercial software package ANSYS ICEM-CFD® and are characterized by an overall number of about  $1.2 \times 10^6$  cells (half body).

Both computational domains are tailored for the free-stream conditions of Table A.1. The distribution of surface grid points has been dictated by the level of resolution desired in various areas of the vehicle such as the stagnation region and the base fillet one, according to the computational scopes. Grid refinement in strong gradient regions of flowfield has been made through a solution adaptive approach.

Preliminary results of CFD simulations performed so far are summarized hereinafter. For example, Fig. A.9 shows CFD (perfect gas) results for  $M_\infty = 22$  and  $\alpha = 40^\circ$  concerning the configuration LB-A. The left side reports pressure

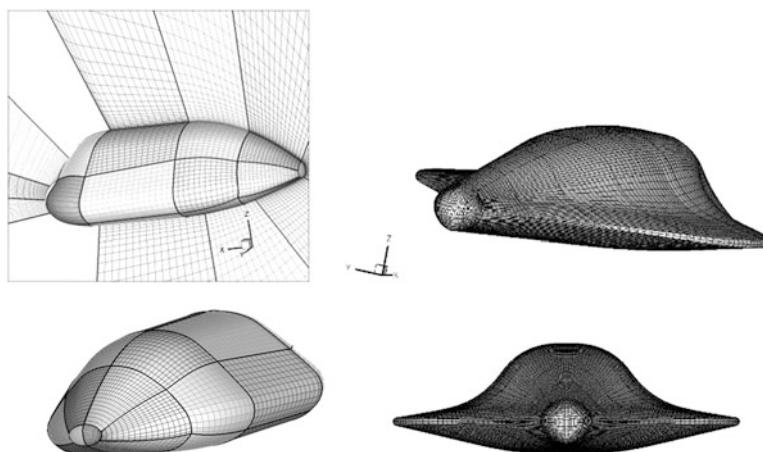


**Fig. A.8** The computational mesh domains for Euler CFD simulations

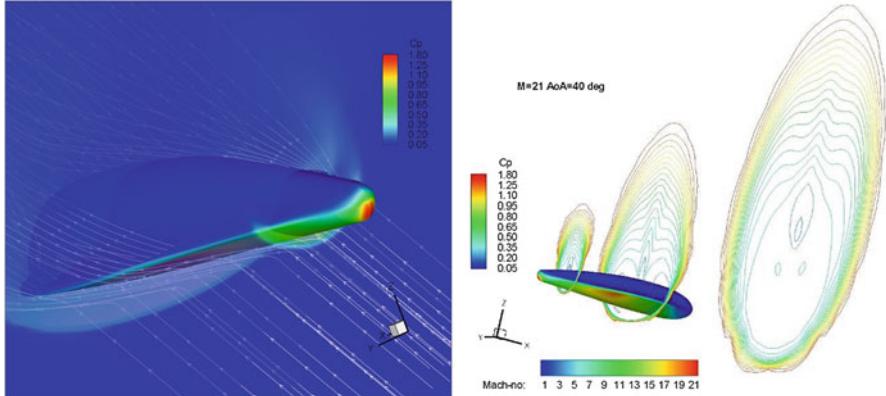


**Fig. A.9**  $M_\infty = 22$  and  $\alpha = 40^\circ$ . (Left) pressure coefficient contours on LB-A surface and on two cross sections; (right)  $C_p$  contours on vehicle surface and Mach contours on three cross sections

coefficient contours ( $C_p$ ) on vehicle surface and on two cross sections, whereas on the right  $C_p$  contours on vehicle surface and Mach number contours on three cross sections have been shown.

Looking at contours field of Fig. A.9, the shock layer that takes place past the vehicle at  $M_\infty = 22$  and  $\alpha = 40^\circ$  can be clearly inferred, as in the case of both Figs. A.10 and A.11. In these figures Mach number contours are shown on a vehicle cross section at  $x = 3.28$  m (from nose) and on a section at  $z = -0.1$  m in order to identify the MBS bow shock also in the vehicle planform plane. Note that those sections allow also assessing the cause of the overpressure that takes place on the vehicle windside highlighted in Fig. A.9. Indeed, results reported in Figs. A.10 and A.11 suggest that those pressure overshoots depend on the belly side shape and not from a shock–shock interaction phenomenon because of the shock shape reported in the vehicle planform plane does not impinge on the vehicle shape.

Figure A.12 shows the static temperature contours on the vehicle (LB-A) symmetry plane and static pressure contours on vehicle surface at  $M_\infty = 20$  and  $\alpha = 20^\circ$ , considering the Mars atmosphere as a reacting gas mixture. As shown, streamtraces are reported to point out flowfield structure past the vehicle at those flight conditions.

At the same free-stream conditions, Figs. A.13 and A.14 report contours of  $N_2$ ,  $CO_2$ ,  $O$ , and  $CO$  mass fractions on the pitch plane of LB-A concept, thus accounting for chemical dissociation of the flow in the shock layer. As a consequence, flow dissociation determines a large density ratio  $\varepsilon$  across the bow shock compared with a flow of the same gas where no dissociation takes place, resulting in a thinner shock layer around the entry vehicle (e.g., lower stand-off distance).

Under conditions where dissociation exists, the aerodynamics of vehicle depends primarily on shock density ratio. In fact, the change of aerodynamic characteristics is the result of change in surface pressure acting on the vehicle forebody [5].

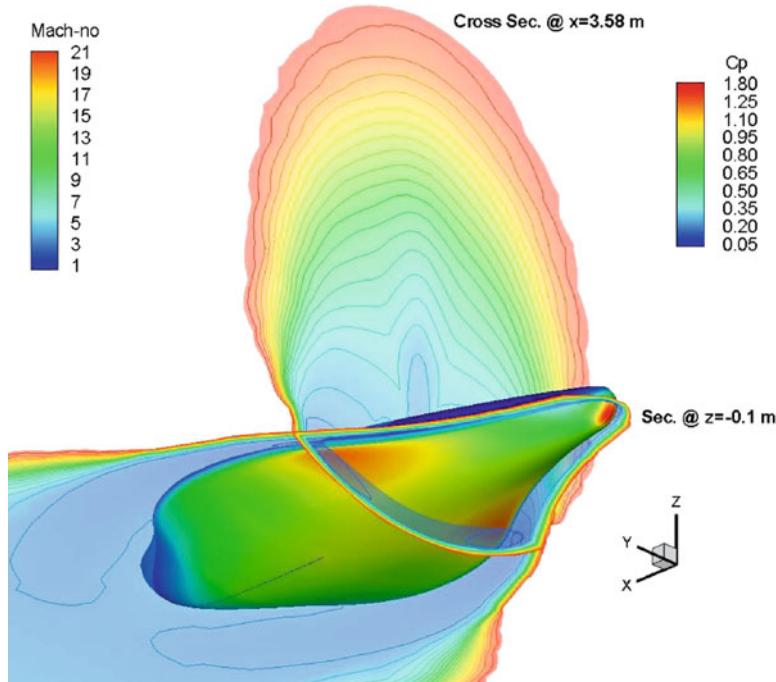


**Fig. A.10**  $M_\infty = 22$  and  $\alpha = 40^\circ$ . Pressure coefficient contours on LB-A surface and Mach number contours on two flowfield sections. Windside view

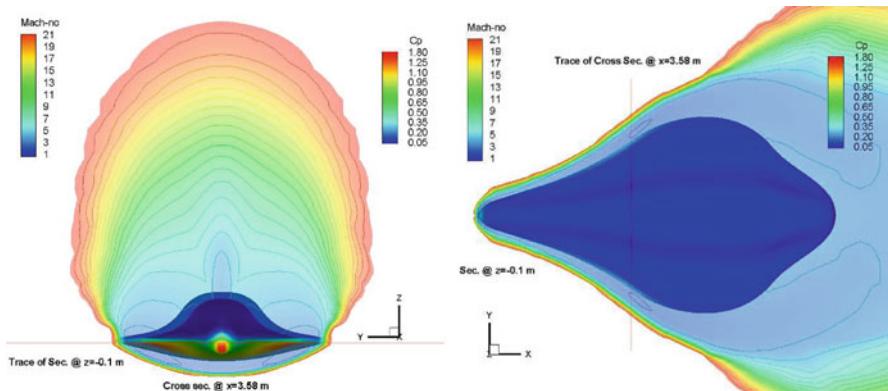


**Fig. A.11**  $M_\infty = 22$  and  $\alpha = 40^\circ$ . Pressure coefficient contours on LB-A surface and Mach number contours on two flowfield sections. Front and up view

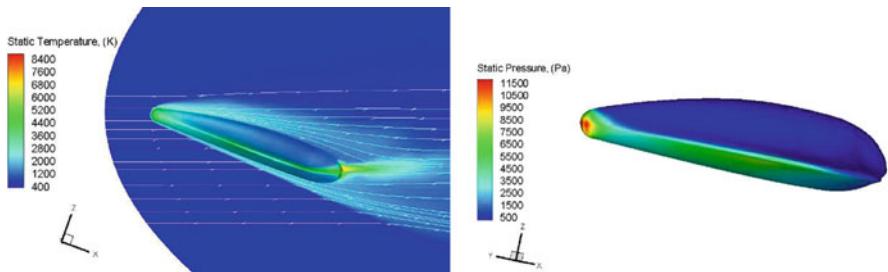


**Fig. A.12**  $M_\infty = 20$  and  $\alpha = 20^\circ$ . (Left) static temperature field on vehicle (LB-A) symmetry plane; (right) static pressure contour on vehicle surface for nonequilibrium reacting gas

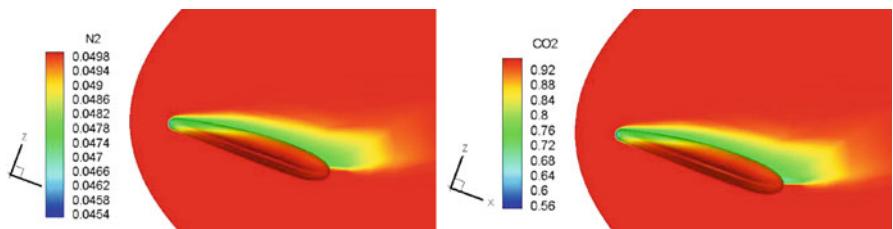


**Fig. A.13**  $M_\infty = 20$  and  $\alpha = 20^\circ$ . Contours of  $N_2$  and  $CO_2$  mass fractions on MBS (LB-A) pitch plane

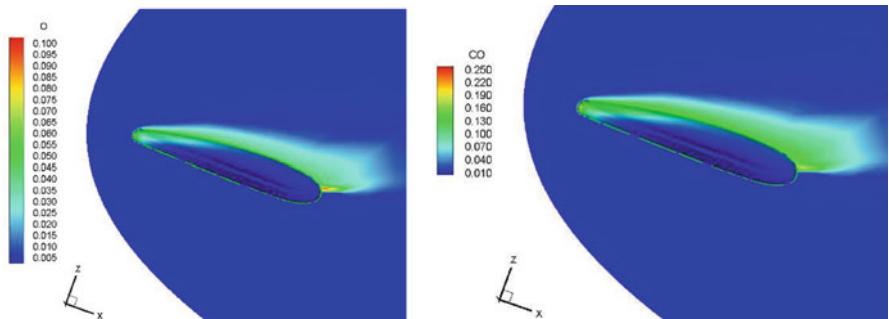


**Fig. A.14**  $M_\infty = 20$  and  $\alpha = 20^\circ$ . Contours of  $O$  and  $CO$  mass fractions on MBS (LB-A) pitch plane

The curves of lift and drag coefficients are shown in Fig. A.15 for  $M_\infty = 20$  and 60 km altitude. Those curves collect MBS (LB-A) aerodynamic coefficients compared with available numerical data both for perfect gas and reacting gas approximations, reported in order to highlight accuracy of both numerical and engineering-based results [16]. As one can see, engineering and numerical data compare very well, thus confirming that engineering-based estimations represent

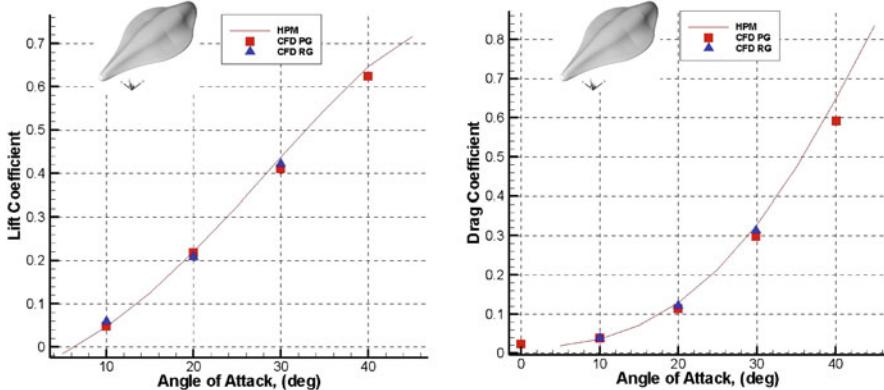


**Fig. A.15**  $C_L$  and  $C_D$  versus  $\alpha$  for  $M_\infty = 20$  and  $H_\infty = 60$  km. Comparison between panel methods and CFD results for perfect and reacting gas approximations

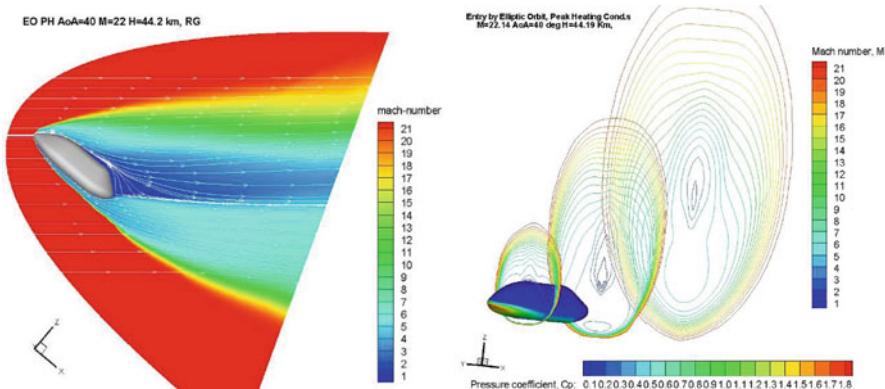


**Fig. A.16** Mach contours on the vehicle pitch plane and three flowfield cross sections at the EOPH conditions

reliable preliminary aerodynamics of a Mars entry vehicle. Moreover, result comparison highlights also that high enthalpy effects increase only slightly both the aerodynamic lift and drag coefficients at those flight conditions due to its high streamlined aeroshape [22].

As far as CFD results for the second configuration (i.e., LB-B) are concerned, Fig. A.16 shows the Mach number contour field that takes place around the vehicle when it is flying at the peak heating conditions of entry by EO (e.g.,  $M_\infty = 22$ ,  $\alpha = 40^\circ$ , and  $H = 44.20$  km). In particular, the left side of Fig. A.16 shows the Mach contour field on the vehicle pitch plane, while the right side of figure gives an idea of the bow shock shape that envelopes the vehicle, since the Mach field is reported on three different flowfield cross sections. As shown, a thin shock layer envelopes

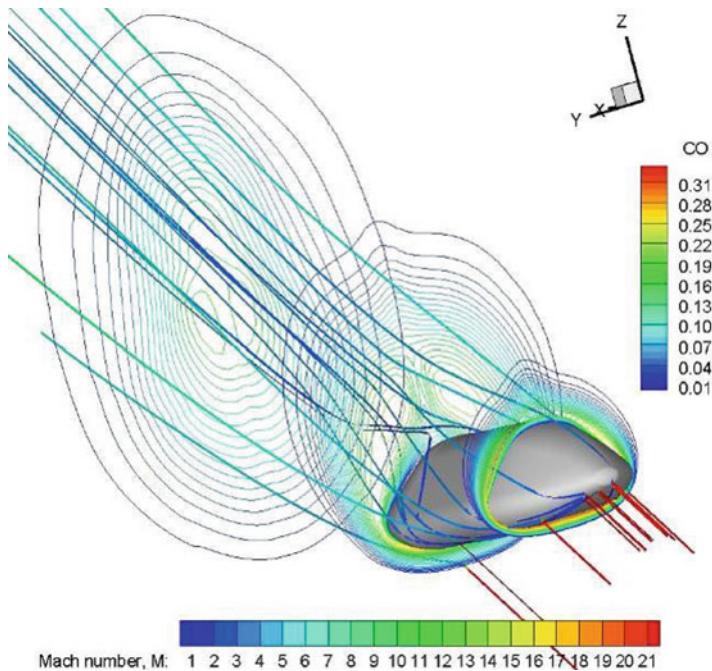


**Fig. A.17** CO mass fraction at the EOPH conditions on three cross sections with streamtraces colored by Mach number

the entry vehicle with a strong expansion that characterizes the windside flow at the end of the vehicle concept [22].

The CO mass fraction field around the vehicle for the same free-stream conditions is shown in Fig. A.17 where some streamtraces colored by Mach number are also reported.

As one can see, the CO concentration reaches its maximum value close to the body and evolves through the vehicle wake flow [21]. Figure A.18 shows the temperature comparison among nonequilibrium flow (right side of pilot) and perfect gas computation, evaluated at three flowfield cross sections ( $x = 1.5, 5.5$  and  $9.5$  m). It is clearly evident how real gas phenomena affect the vehicle shock layer, as discussed above.

Curves of lift, drag, and pitching moment coefficients are shown in Fig. A.19. As shown, high enthalpy effects slightly increase aerodynamic lift, drag, and pitching moment coefficients. Vehicle aerodynamics is also summarized in the Table reported in Fig. A.19.

As far as vehicle aerodynamic performance comparisons are concerned, Figs. A.20, A.21, and A.22 show pitching moment coefficient and aerodynamic efficiency for both MBS concepts.

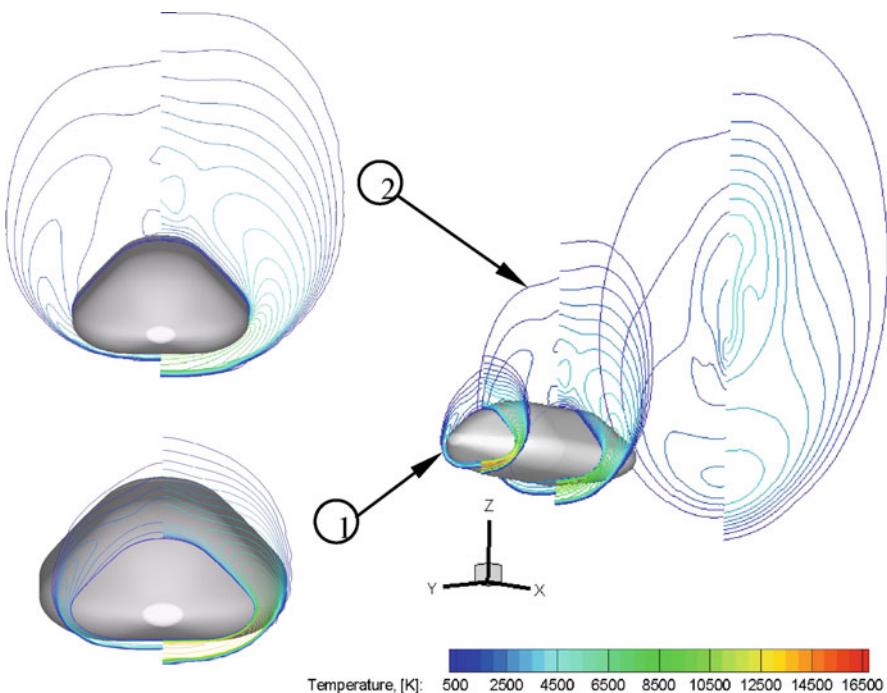


**Fig. A.18** Temperature comparison between nonequilibrium flow (right side of pilot) and perfect gas computation, at  $x = 1.5, 5.5$  and  $9.5$  m flowfield cross sections

Results reported in Fig. A.20 highlight that the concept LB-A is statically stable in longitudinal flight (e.g.,  $C_{m\alpha} < 0$ ) for  $\alpha \geq 20^\circ$  and CoG located up to half of vehicle length, whereas if the CoG is at 55 % of  $L_{ref}$  (maximum allowable CoG excursion), the AoAs must be higher than  $30^\circ$  to guarantee static stability flight conditions. In particular, the AoA at which the moment coefficient about the center of gravity equaled zero (i.e., trim condition) are appreciatively  $20^\circ$  and  $40^\circ$  for CoG at 50 %  $L_{ref}$  and 55 %  $L_{ref}$ , respectively.

On the other hand, Fig. A.21 shows that, at hypersonic speed, the LB-B concept is statically stable in longitudinal flight for  $\alpha \geq 20^\circ$  and CoG located up to 40 % of vehicle length, whereas if the CoG is at 50 % of  $L_{ref}$  (maximum allowable CoG excursion), the AoAs must be higher than  $40^\circ$ . In particular, trim AoAs are appreciatively  $20^\circ$  and  $40^\circ$  for CoG at 40 %  $L_{ref}$  and 45 %  $L_{ref}$ , respectively.

Finally, Fig. A.22 shows the lift-to-drag ratio (L/D) comparison between LB-A and LB-B vehicle concepts. As one can see, the former MBS features a better aerodynamics performance at low AoA (say  $10 \leq \alpha \leq 35^\circ$ ) as expected due to its more streamlined configuration and different aeroshape.

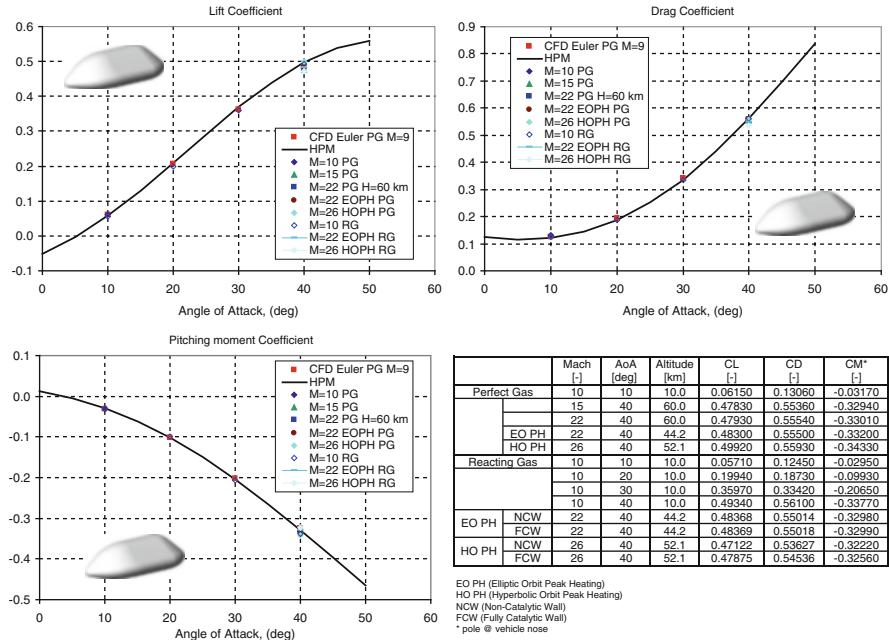


**Fig. A.19** Lift, drag, and pitching moment coefficients versus  $\alpha$ . Comparison between panel methods and CFD results for perfect and nonequilibrium gas computations

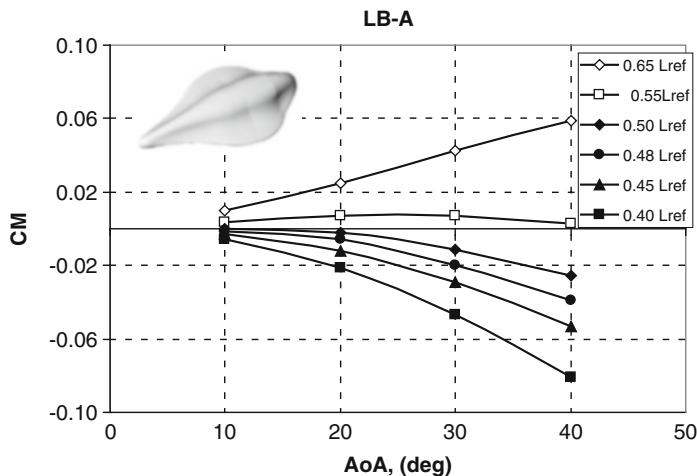


**Fig. A.20** LB-A. Pitching moment coefficients versus  $\alpha$  for CoG position at different percentage of vehicle length and at hypersonic flight conditions

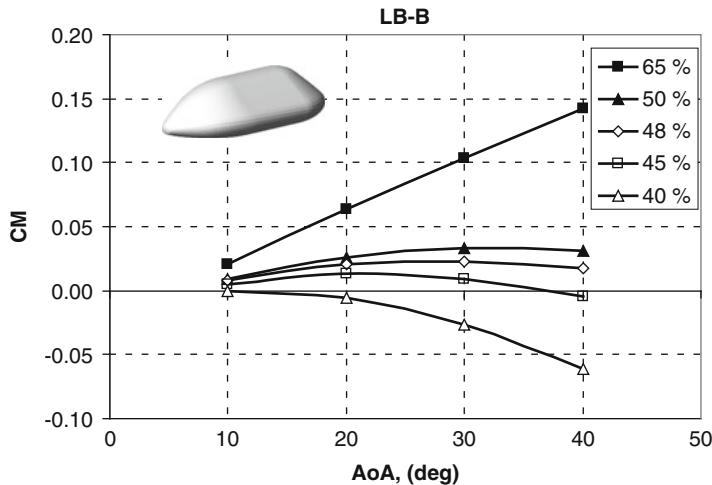


**Fig. A.21** LB-B. Pitching moment coefficients versus  $\alpha$  for CoG position at different percentage of vehicle length and at hypersonic flight conditions

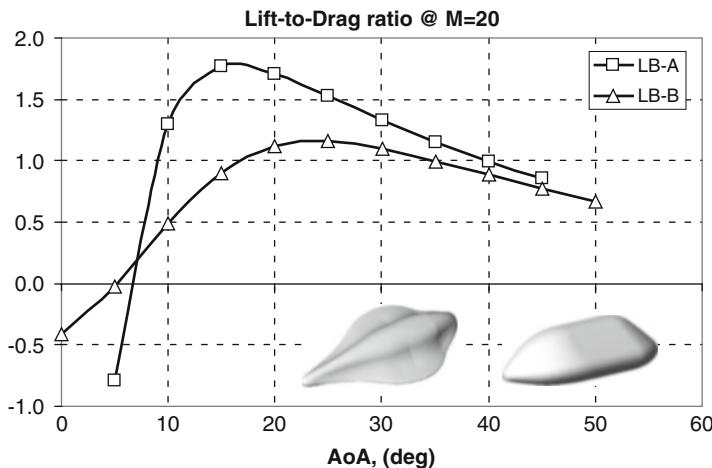


**Fig. A.22** Lift-to-drag ratio versus  $\alpha$ . Comparison between LB-A and LB-B concepts

## References

1. Polishchuk G, Pichkhadze K, Vorontsov V, Pavla K (2006) Proposal on application of Russian technical facilities for International Mars Research Program for 2009–2015. *Acta Astronaut* 59:113–118
2. Viviani A, Pezzella G (2009) Aerodynamic analysis of a capsule vehicle for a manned exploration mission to Mars. In: Sixteenth AIAA/DLR/DGLR international space planes and hypersonic systems and technologies conference, Bremen, October 2009, AIAA-2009-7386

3. Capsule aerothermodynamics. AGARD-R-808. Published May 1997
4. Viviani A, Iuspa L, Lanzillo G, Pezzella G (2011) Preliminary design of minimum weight configurations for a re-entry vehicle. In: The international conference of the European Aerospace Societies, Venice, Italy, 24–28 October 2011, CEAS 2011
5. Hanley GM, Lyon FJ (1964) The feasibility of spacecraft deceleration by aerodynamic braking at the Planet Mars. In: Proceedings of the 1st AIAA annual meeting, Washington, DC, June 29–July 2, 1964, AIAA-64-479
6. Anderson JD (1989) Hypersonic and high temperature gas dynamics. McGraw-Hill Book Company, New York
7. Pezzella G, Viviani A (2011) Aerodynamic analysis of a Mars exploration manned capsule. *Acta Astronaut* 69:975–986
8. Prabhu DK (2004) System design constraints-trajectory aerothermal environments, RTO AVT/VKI lecture series in critical technologies for hypersonic vehicle development, Rhode-st-gen  se, Belgium, 10–14 May 2004
9. Schettino A, Pezzella G et al (2005) USV\_X Phase-A aerodynamic and aerothermodynamic analysis, Capua, Italy, CIRA-CF-06-1393
10. Bertin JJ (1994) Hypersonic aerothermodynamics, AIAA education series. American Institute of Aeronautics and Astronautics, Washington, DC
11. Fuent 12.0 Theory Guide
12. Mack A (2008) CFD validation for CO<sub>2</sub> re-entry applications. In: Second international ARA Days, Arcachon, France, 21–23 October 2008, AA-3-2008-37
13. Hannemann V, Mack A (2009) Chemical non equilibrium model of the martian atmosphere. In: Proceedings of the 6th European symposium on aerothermodynamics for space vehicles, Versailles, France, 3–6 November 2008, ESA SP-659
14. Park C, Howe JT, Jaffe RL, Candler GV (1994) Review of chemical-kinetic problems of future NASA missions, II: Mars entries. *J Thermophys Heat Transf* 8(1):9–23
15. Mars Exploration Program, NASA – JPL, [www.mars.jpl.nasa.gov](http://www.mars.jpl.nasa.gov)
16. Viviani A, Pezzella G, Golia C (2010) Aerodynamic and thermal design of a space vehicle entering the Mars atmosphere. In: The fifth international conference on thermal engineering theory and applications, Marrakesh, Morocco, 10–14 May 2010
17. Viviani A, Pezzella G, Golia C (2010) Aerothermodynamic analysis of a space vehicle for manned exploration missions to Mars. In: Twenty seventh international congress of the aeronautical sciences, ICAS 2010, Nice, France, 19–24 September 2010
18. Kustova EV, Nagnibeda EA, Shevelev YD, Syzranova NG (2009) Comparison of non-equilibrium supersonic CO<sub>2</sub> flows with real gas effects near a blunt body. In: Proceedings of the 6th European symposium on aerothermodynamics for space vehicles, Versailles, France, 3–6 November 2008, ESA SP-659
19. Gnoffo P, Braun R, Weilmuenster K, Mitcheltree R, Engelung W, Powell R (1998) Prediction and validation of Mars pathfinder hypersonic aerodynamic data base. In: Seventh AIAA/ASME joint thermophysics and heat transfer conference, Albuquerque, NM, USA, 15–18 June 1998
20. Gnoffo P, Weilmuenster K, Braun R, Cruz C (1996) Influence of sonic-line location on mars pathfinder probe aerothermodynamics. *J Spacecr Rocket* 33(2):169–177
21. Gupta R, Lee K, Scott C (1996) Aerothermal study of Mars pathfinder aeroshell. *J Spacecr Rocket* 33(1):61–69
22. Mitcheltree RA, Gnoffo PA (1995) Wake flow about the Mars pathfinder entry vehicle. *J Spacecr Rocket* 32(5):771–776

# Index

## A

- Ablative heat shield, 330, 462, 704, 717, 720  
Ablative thermal protection system, 114, 116, 250, 369, 714, 717, 719, 720, 743  
Adiabatic wall temperature, 317–319  
Aeroassisted orbital transfer vehicle (AOtv), 224, 271  
Aeroassisted space transfer vehicle (ASTV), 224, 334–336, 348  
Aeroassist Flight Experiment (AFE), 229, 266, 271, 274–278, 336, 353  
Aerodynamic coefficient, 446, 538, 539, 542, 544, 550, 602, 603, 607, 745, 770, 771  
Aerodynamic control surface, 458, 525, 537, 600, 601, 647  
Aerodynamic damping moment, 282  
Aerodynamic database, 52, 95, 249, 250, 271, 331, 339, 448, 458, 469, 496, 515, 538–542, 589, 600–607, 648, 665, 667, 687–692, 800, 828  
Aerodynamic design, 62, 97–105, 212, 219, 229, 287, 331, 647, 664, 776–825, 829–842, 869  
Aerodynamic performance, 20, 62, 63, 98, 259, 275, 287, 303, 331, 332, 417, 611, 622, 655, 776, 790, 795, 801, 805, 874, 884  
Aerodynamic shape, 50, 57, 59, 354, 478, 480, 681, 774, 873  
Aerodynamic trim, 50, 581, 830, 833  
Aerospace plane, 104, 218, 219  
Aerothermodynamic database, 119, 647, 797, 874  
Aileron, 59, 62, 501–504, 509, 511, 537, 539, 541, 550, 601, 604, 618, 680, 695–696  
Airbreathing propulsion system, 11, 238, 299  
Air chemical non-equilibrium, 586, 729  
Allen, H.J., 4, 238, 239, 264  
Altitude-velocity map, 11, 15, 38, 39, 201, 580, 584, 590, 601, 602, 647, 726, 733–735, 737, 801, 804  
Anandakrishnan, S.M., 15  
Anderson, J.D. Jr., 15, 201  
Angle of attack (AoA), 10, 11, 47, 55, 56, 59, 60, 72, 73, 76, 86, 88, 94, 106, 187, 228, 240, 246, 249, 250, 253–266, 275–277, 280–284, 286, 294, 298, 301, 304–307, 312, 319, 329, 357, 373, 379, 400, 442, 458, 497, 498, 506, 507, 509, 510, 512, 538, 539, 577, 581, 587, 590, 625, 631, 645, 671, 747, 761, 769, 771, 837, 872  
Apollo command module, 146, 148, 182, 183, 428  
Apollo spacecraft, 147, 217, 233  
Approximate methods, 83  
ARD capsule, 377, 446, 485, 572  
ARIANE V, 294, 300, 377, 378, 462–464, 572, 769, 770, 772, 779, 781, 793, 794, 829–845, 859, 861  
Arnold Engineering Development Center (AEDC), 407, 432, 446  
Ascent trajectory, 794, 795  
Atmospheric entry, 40, 95, 127–210, 226, 257, 338, 343, 354, 399, 704, 750  
Atmospheric re-entry, 11, 235, 370, 463, 475, 476, 487, 557, 581, 626, 633

- Atmospheric re-entry demonstrator (ARD), 367, 368, 377, 378, 446–450, 462–464, 484–487, 496, 571, 572, 740
- Axial force coefficient, 53, 60, 267, 451, 642, 769, 772, 785, 787, 789, 826, 847, 859
- B**
- Ballistic parameter, 706
- Ballistic vehicle, 207, 269, 353
- Bank angle, 151, 152, 581, 873
- Base drag, 21, 594, 629, 633, 764, 798, 847
- Base pressure, 21, 859
- Beginning of transition, 584
- Bent bicones, 229, 266
- Binary mixture, 43, 190, 596
- Binary scaling, 364, 365, 405, 513, 514
- Blasius relation, 164, 165, 596
- Blunt bicone, 63, 474
- Blunt body flowfield, 71
- Blunt(ed) cone, 13, 80–82, 187, 243, 256, 395, 712, 763
- Blunt delta wing, 216, 302
- Body flap, 40, 59, 62, 211, 457, 459, 461, 463, 465, 469, 471, 473, 480, 482, 496, 515, 538, 559, 561, 562, 579, 580, 604, 606, 621, 626, 653, 655, 656, 662, 663, 693, 694, 792–794, 805, 831, 832
- Body reference frame (BRF), 50, 538, 598, 600, 768, 799
- Boltzmann distribution, 318, 375, 732, 876
- Boltzmann equation, 21, 22, 348
- Boundary condition, 4, 16, 18, 20, 22, 26, 41, 160, 316–318, 322, 359, 362, 363, 369, 384, 391–392, 394, 396, 398, 436, 439, 441, 442, 516, 527, 595, 627, 741–745, 782, 820, 850, 876
- at wall, 4
- Boundary-layer trips, 171
- Bowcutt, K.G., 309
- C**
- Calorically perfect gas, 23, 41, 170, 171, 177, 190
- Carlo, M., 257, 333
- Carman, R., 213
- Catalytic surface, 469, 721
- Catalytic walls, 189, 190, 198, 199, 251–252, 332, 368, 373, 439, 527, 596, 627, 677, 743
- Centre of gravity (CoG), 50, 418, 423, 480, 535, 536, 539–541, 552, 580, 598, 618, 621, 624, 625, 630, 645, 648, 655, 661, 707, 708, 725, 726, 767, 768, 770, 792, 799, 830, 879, 885–887
- Centre of pressure, 284
- Chapman–Rubensin coefficient, 48
- Chavez, F.R., 104
- Chemical equilibrium, 15, 35, 172, 199, 252, 342, 343, 363, 364, 383, 384, 391, 405, 561, 584, 743, 744, 820
- Chemically reacting boundary layers, 191
- Chemically reacting equilibrium flow, 35, 343, 384, 405, 797
- Circular orbit velocity, 201
- Code calibration, 333
- Code validation, 369, 825–827, 878
- Coefficient of viscosity, 19, 124
- CoG. *See* Centre of gravity (CoG)
- CoG offset, 256–257, 259, 266–267, 270, 377, 708
- Cold wall, 185, 369, 391, 438, 439, 744, 820, 822
- Composition at high temperature air, 438
- Compressibility factor, 41–46, 97, 156
- Compressible flow, 27, 33, 63, 166
- Computational fluid dynamics (CFD), 63, 98, 120, 331–343, 457, 486, 571, 767, 791, 825, 869
- Concentration, 34, 35, 42, 189, 198, 339, 342, 387, 391, 596, 731, 744, 884
- Conduction, 16, 18, 19, 23, 24, 116, 156–158, 193, 239, 317, 319, 373, 383, 439, 441, 519, 596
- Cone flow waverider design, 222, 313–316
- Cone heat transfer, 274
- Continuum flow, 11, 13–50, 204, 344, 345, 347, 348, 353, 354, 361, 385, 457, 514, 542, 543, 547–555, 573, 581, 583, 591, 606, 611–625, 648, 653–671, 729, 738, 740, 761–763, 778
- Convection, 116, 155, 158, 254
- Corner flow, 301
- Crew Return Vehicle (CRV), 367–454
- Crew Transfer Vehicle (CTV), 474
- Cross range, 74, 150–154, 211, 228, 229, 236, 244, 267, 268, 296, 302, 353, 368, 399, 465, 480, 485, 581, 625, 805
- Cylinder drag, 106
- Cylinder/flare, 856
- D**
- Deflection angle, 28, 29, 59, 60, 64, 67, 83, 100, 537, 655, 658, 830
- De Jarnette, F.R., 4
- Density ratio, 113, 179, 369, 371, 422, 880

- Descent trajectory, 11, 39, 399, 401, 581, 586, 726, 791, 822, 829  
Design experience, 571  
Design margin, 484, 627, 671  
Diffusion coefficient, 156, 173, 388, 596, 597, 876  
Diffusion velocity, 156  
Directional stability, 288–293, 481, 578, 579, 616, 618, 621, 695  
Direct simulation Monte Carlo, 333, 348, 384–385, 543, 582  
Drag, 3–5, 21, 40, 50, 52, 55–59, 62, 72–78, 81, 82, 86–88, 90, 92, 94, 95, 102, 105–108, 110, 128, 130, 134–136, 147, 151, 153, 155, 159, 168, 171, 211, 212, 216, 217, 223–226, 229–231, 235–250, 265, 270, 272, 275, 276, 280, 285, 286, 288, 295, 296, 298, 301–310, 331, 348, 353, 354, 356, 367, 401, 406, 414, 417, 421–424, 428–433, 436–438, 448, 452, 453, 458, 465, 480, 492, 503, 505, 535, 539–541, 545–556, 566–568, 577, 579, 581–583, 587, 594, 598, 600, 605, 608–611, 613, 616, 622–625, 628–630, 633, 635, 642, 648, 650–654, 656–658, 668–670, 687, 692, 693, 706, 713, 725, 745, 760–765, 767, 786, 798–803, 805, 811, 814, 816–818, 834, 842, 847, 853, 855, 863, 873, 879, 882–887  
Drag coefficient, 57, 73, 76, 77, 81, 82, 86, 90, 92, 231, 245–247, 250, 272, 275, 285, 286, 295, 422–423, 430–433, 436, 437, 448, 452, 453, 465, 541, 545, 546, 548–549, 551, 553, 555, 567, 568, 609, 611, 613, 615, 622, 623, 628, 629, 651, 652, 654, 669, 670, 692, 706, 745, 762–765, 803, 814, 834, 853, 855, 882, 883  
Drake, H., 213  
Dunn/Kang model for non-equilibrium air, 389, 390, 406, 409, 429, 433, 434, 436, 444  
Dynamic stability, 50, 62, 246, 247, 253, 254, 261–265, 465, 714
- E**  
Earth atmosphere, 110, 272, 463, 577, 684, 719  
Earth diameter, 133  
Earth gravitation, 133  
Earth return mission, 347  
Eckert's reference temperature, 96, 166, 322, 324, 325, 329–330  
Eddy viscosity, 850  
Effective nose radius, 181–183, 319, 349, 383  
Eggers, A.J. Jr., 4, 238–240, 243  
Electronic temperature, 339, 341, 342, 717, 754  
Electron temperature, 33  
Elevator, 281, 481, 501, 503, 509, 510, 537, 539, 540, 542, 555, 579  
Elevon, 59–61, 464, 466, 467, 469, 497, 498, 559, 579, 601, 604, 606, 621, 653, 657, 658, 661, 662, 693, 792, 830  
Emissivity, 318, 320, 382, 391, 402, 515, 718, 820  
Energy equation, 19, 27, 96, 110, 123, 173, 318  
Energy levels, 41, 336, 573  
Enthalpy, 8, 18, 35, 96, 122, 156–159, 173, 175–177, 189, 196, 198, 201, 202, 205, 241, 316, 320–323, 329, 332, 343, 370, 373, 382, 383, 387, 388, 461, 513, 584, 594, 595, 714, 723, 731, 759, 798, 875, 883, 884  
Entropy, 3, 8–9, 29, 63, 184, 196, 345, 429, 679, 704, 747, 755, 820  
Entropy layer, 8, 9, 63, 345, 679, 704, 747, 755, 820  
Entropy layer effects, 679  
Entropy layer swallowing, 755  
Equilibrium chemically reacting flow, 33  
Equilibrium glide trajectory, 143  
Etkin, B., 280, 285  
Euler equations, 20, 25–27, 32  
Expansion waves, 254, 370, 399, 557  
Expendable launch vehicle (ELV), 788  
External forces, 24, 280
- F**  
Fay and Riddell stagnation point analysis, 189  
Fay, J.A., 189, 198, 273, 276, 381, 402, 596  
Fick's Law, 391  
Fire II vehicle, 719  
First law of thermodynamics, 21  
Flat plate aerodynamics, 85, 89  
Flat plate heat transfer, 329  
Flight control system (FCS), 495  
Flight mechanics (FM), 60, 61, 128, 330, 379, 435–437, 580, 582, 590, 602, 684–686, 709, 714, 740, 790, 800, 874  
Flight path angle, 117, 130, 134, 136–138, 140, 144–147, 169, 207, 262, 263, 274, 353, 488, 684, 709, 726  
Flying test bed, 377, 446, 461, 463, 481, 571, 615

- Free molecular flow (FMF), 11, 13, 15, 52, 99, 204, 206, 344, 400, 543, 544, 582, 591, 593, 606–610, 647–649, 652, 738, 748, 760, 762
- Free-stream conditions, 39, 175, 316, 320, 321, 339, 368, 392, 405–407, 436, 441, 446, 492–494, 557, 587, 664, 673, 734–736, 738, 741, 752, 795, 820, 838, 877–880, 884
- Frozen flow, 189, 251, 343, 363, 382, 585
- Fully-catalytic surface, 469
- Future launcher preparatory programme (FLPP), 457, 468, 470, 477, 484, 485, 500, 507, 508, 776, 787–791, 794, 796, 799, 817, 822
- G**
- Gamma (the ratio of specific heats), 6, 171, 176, 341, 342
- Gap flow, 522, 841
- Gas constant, 22, 35, 37, 43, 122, 131, 192, 376, 387, 388, 731, 736
- Gemini capsule, 141, 224
- G-loads, 148, 150, 209, 235–237, 244, 274, 368, 487, 707
- Gnoffo, P.A., 119
- Goddard, R.H., 212
- Grid convergence, 453–454, 863–865
- Gupta, R.N., 375
- H**
- HALIS, 20, 21
- Hawk, K., 212
- Hayes, W.D., 48, 113
- Heat of formation, 189, 368, 373, 382, 596
- Heat shield, 41, 155, 223, 237, 241, 247, 249, 251, 252, 258, 267, 269, 271–275, 277, 278, 319, 330, 331, 335, 339, 340, 347, 367–369, 373–377, 381, 383, 402, 404, 407, 408, 424, 427–429, 438, 442, 443, 462, 515, 704, 705, 714, 717, 719, 720, 723, 726–728, 736, 738, 740, 744, 746, 750, 755, 757–759, 823
- Heat transfer, 3–5, 15, 18, 20, 25, 40, 41, 47, 50, 114, 116–118, 124, 154–162, 164, 166, 167, 171–173, 178–202, 206, 208, 226, 229, 238, 239, 241, 242, 249, 272–278, 285, 294, 298, 317, 319, 320, 322–329, 339, 345, 347, 350, 362, 363, 373, 374, 377, 383, 395, 441, 515, 596, 681, 704, 732, 742
- HERMES, 224, 229, 238, 294–296, 298–302, 461, 462, 464, 469, 484
- High-temperature flow, 33, 40, 872
- High temperature real gas effects, 15, 23, 35, 416, 438, 540, 585
- High temperature reusable surface insulation (HRSI), 375, 377, 442
- Hinge moment, 60, 279, 537, 600
- Hopper, 789, 791, 792, 794–796, 799–801, 804–810, 820, 863, 864
- Horizontal take-off (HTO), 789, 791, 795, 796, 800, 801, 820
- Huygens, 129, 244, 246–253, 257–260, 364, 365, 718, 720
- Hydrogen, 334, 720
- Hyperboloid, 357
- Hypersonic aerodynamics, 1–124, 212, 213, 217, 372
- Hypersonic flow, 2–11, 26, 47, 49, 63, 66, 67, 69, 74, 77–80, 83, 97, 121–123, 159, 177, 182, 221, 291, 293, 312, 313, 315, 393–395, 515, 542, 546, 606, 623, 681, 747, 763, 806, 830
- Hypersonic research airplane, 102, 103
- Hypersonic similarity parameter, 85
- Hypersonic transport (HST), 217–219
- Hypersonic viscous interaction, 296, 583
- I**
- Ideal gas, 23, 114, 131, 176, 562, 769, 797, 820, 846
- Induced drag, 107, 285, 629, 693
- Induced pressure from viscous interaction. *See* Viscous interactions
- Interaction phenomena, 591
- Intermediate experimental vehicle (IXV), 156, 457–459, 468, 470–569, 571, 573
- Inviscid, 8, 9, 16–18, 20, 21, 27, 47, 48, 63, 64, 76, 95, 96, 99, 102, 105, 122, 156, 158, 175, 184, 238, 254, 301, 333, 341, 345, 349, 357, 381, 386, 392, 421, 593, 665, 679, 747, 748, 798, 801, 813, 816, 875
- Isentropic expansion (IE), 429
- J**
- Johnson, D.B., 284
- K**
- Kinetic theory, 15, 206, 344, 384, 388, 389, 435, 543, 582, 597, 647, 738, 876
- Knight, P., 215
- Known unknowns, 690

- Knudsen number, 13, 14, 49, 52, 121, 122, 273, 345–347, 349, 357, 401, 404, 435, 437, 514, 537, 538, 543–547, 582, 602, 603, 606, 608, 610–612, 652–654, 740
- L**
- Laminar flow, 97, 160, 165, 166, 171, 322, 327, 330, 407, 408, 515, 521–523, 560, 587, 595, 596, 678, 851
- Laminar-to-turbulent flow transition, 740
- Lateral stability, 289, 464
- Leading edge, 3–5, 13, 18, 29, 47, 48, 73, 105, 107, 155, 157, 165, 174, 178, 179, 188, 212, 216, 222, 225, 236, 241, 284, 298, 301, 308, 311, 313, 314, 323, 348, 368, 379, 381, 490, 519, 557, 588, 592, 594–597, 612, 621, 626, 631, 633, 635, 636, 644, 645, 666, 671, 673, 675, 676, 678, 680, 681, 683, 782, 791–793, 806, 822, 831, 832, 835, 837, 841, 875, 876
- Lees' formula, 187
- Lees, S.-H., 395
- Lewis number, 121, 172, 173, 189–191, 197, 198, 200, 382, 596
- LFBB. *See* Liquid fly-back booster (LFBB)
- Lift, 6, 40, 50, 52, 55–59, 62, 74, 77, 79, 87, 90, 92, 94, 101, 106, 107, 109, 128, 130, 134–136, 138, 140–143, 145, 148, 150, 151, 207, 209, 211, 216, 219, 221, 225, 226, 228–230, 23, 236, 242–244, 265, 268, 278, 280, 281, 283, 285, 286, 288, 295, 297, 298, 302, 306, 307, 309, 331, 332, 348, 353, 356, 359, 399, 401, 412, 417, 422–424, 427–431, 433, 492, 513, 539, 540, 544, 546, 547, 553, 554, 566, 577, 580, 582, 598, 600, 603–605, 608–610, 622, 623, 625, 629, 632, 652, 837, 853, 864, 882, 886
- Lift coefficient, 74, 283, 295, 296, 306, 427, 430, 540, 544, 546–548, 551, 553, 554, 566, 568, 603, 604, 608–611, 616, 622, 623, 628, 629, 650, 653, 761, 803, 813, 834, 835, 865
- Lifting body, 13, 211, 217, 238, 243, 303–305, 457–569, 573, 691, 869, 871, 873
- Lifting vehicle, 116, 144, 151, 268, 269, 308, 329, 459
- Lift-to-drag ratio, 74, 76, 88, 134, 147, 151, 153, 211, 216, 225, 226, 229–230, 235–238, 244, 296, 298, 302–308, 348, 356, 424, 480, 577, 621–622, 624, 625, 651, 652, 800, 801, 805, 816–818, 885
- Liquid fly-back booster (LFBB), 789, 793–796, 798, 799, 816–819, 822, 829–832, 837–842
- Longitudinal stability, 284, 288, 792, 794, 800, 830, 832, 837
- Low-density effects, 344–345
- Low density flow, 344–345
- Low Earth orbit (LEO), 11, 144, 155, 190, 206, 235, 236, 238, 270, 350, 367–372, 377–385, 389, 405, 463, 484–488, 514, 571, 573, 580, 779, 790
- Lunar return mission, 350
- M**
- Mach number, 1–4, 6–8, 10, 19, 26, 29, 31, 33, 52, 54, 56, 62–64, 70, 71, 80, 83, 95, 112, 121–123, 179, 182, 187, 188, 213, 215, 221, 253, 262, 263, 276, 280, 281, 283–285, 291, 293–296, 299, 308–312, 315, 323, 325, 339, 340, 345, 346, 379, 396, 398, 400, 404, 405, 407, 414–417, 419, 424, 432, 434, 446–450, 458, 468, 481, 492, 497–499, 504, 505, 509, 510, 517, 525, 527, 539, 540, 554–557, 560, 583, 587, 604, 613, 615, 616, 618, 620–622, 628–630, 634–636, 639–641, 653–655, 658, 662, 664–666, 670, 675, 676, 688, 692, 697, 698, 727, 740, 741, 745, 748–751, 757, 761, 764, 770, 771, 774–776, 778–780, 782–786, 794, 795, 797, 803, 805–807, 811, 813, 816, 817, 828, 829, 833, 836, 837, 842, 850, 855, 856, 858, 874, 880, 881, 883, 884
- Mach number independence principle, 79, 629
- Mach-Reynolds map, 13, 120, 583
- Mangler factor, 595, 876
- Manor, D., 284
- Mars, 129, 132, 133, 145, 203, 224, 236, 244, 247, 251, 255, 258, 270, 275, 334–337, 352, 354, 377, 572, 703, 713, 714, 719, 720, 869–887
- Mason, 729
- Mass fraction of  $i$ th species, 23, 387, 731
- Maughmer, M., 102
- MDO. *See* Multidisciplinary design optimization (MDO)
- Mean aerodynamic chord, 13, 53, 289, 598, 697
- Mechanical loads, 154
- Mercury, 2, 129, 136, 139, 141, 216, 224, 229, 231, 238, 330, 331, 713
- Method of characteristics (MOC), 31–33, 85
- Miele, A., 284

- Mixture, 23, 34, 35, 42–46, 156, 173, 189, 190, 370, 385, 387–389, 404, 405, 409, 412, 482, 515, 578, 582, 584, 586, 588, 596, 597, 704, 728, 729, 731, 733–738, 749, 820, 876–878, 880
- Model sale, 342
- Modified newtonian flow, 70–72, 97, 181
- Molecular weight, 37, 42, 43, 45, 46, 173, 192, 387, 731
- Molecular wight of mxtures, 43, 45
- Mole fraction, 45, 46, 388, 723
- Mole species, 736
- Moment of inertia (MoI), 259
- Moment reference point (MRC), 295, 296
- Moore, M., 102
- Multidisciplinary design, 98, 573, 713
- Multidisciplinary design optimization (MDO), 98, 573, 713
- N**
- N. *See* Nitrogen (N)
- National Aeronautics and Space Administration (NASA), 5, 118, 213–217, 219, 232, 235, 244, 303–305, 367, 377, 384, 460, 462, 472
- National Aerospace Plane (NASP), 104, 219, 220, 238
- Natural trim point, 501, 552, 614, 625, 662
- Navier–Stokes equations, 21, 22, 24, 25, 348, 584
- NCW. *See* Non-catalytic wall (NCW)
- Newton, I., 5, 9, 64, 66, 67, 465
- Newtonian theory, 9, 64, 67, 68, 70, 72–74, 77, 79–82, 91, 99, 104, 122, 180, 186, 291–293, 395, 398, 399, 421, 428, 644
- Nitrogen (N), 33–35, 38, 43, 45, 72, 189, 196, 198, 336, 364, 370, 372, 374–376, 389, 395, 396, 404, 405, 407, 408, 412, 413, 427, 436, 514, 515, 578, 585, 596, 635, 649, 720, 733, 737, 749, 752–754, 851, 878
- Non-catalytic surface, 374
- Non-catalytic wall (NCW), 189, 198, 199, 363, 373, 382, 383, 391, 397, 408, 411, 438, 439, 441–444, 527, 530–535, 677
- Non-equilibrium chemically reacting flow, 39, 336, 339, 340, 342, 363, 364, 370, 372–374, 384, 385, 404, 405, 514, 588, 599, 729
- Non-equilibrium real gas effects, 15, 338, 584, 628, 666
- Nonweiler, T.R.F., 311
- Normal force coefficient, 53, 60, 73, 87, 267, 424, 450, 451, 602, 643, 769, 785, 788, 858
- Normal shock wave (NS), 6, 7, 68–70, 72, 175, 176, 193, 196, 315, 321, 355, 362, 383, 384, 705, 733, 756
- Nose-down moment, 632
- Nose-up moment, 580, 626, 792
- No-slip boundary condition at wall, 4, 850
- No-slip condition, 344, 437
- Nusselt number, 96, 121, 157–159, 178
- O**
- Oblique shock, 9, 28, 29, 83, 85, 99, 100, 314, 315, 341, 342, 557
- ONERA, 446, 447, 464, 496–498, 563
- One-temperature model, 390
- Onset of transition, 171
- Orbit, 2, 11–16, 39, 50, 128, 137, 139, 142–144, 146, 150, 154, 155, 190, 201, 204, 207, 209, 212, 218, 219, 224, 228, 267, 270, 275, 295, 350, 352–354, 377, 400, 473, 477, 484, 485, 488, 489, 514, 571, 573, 685, 779, 789, 791, 870, 872, 877, 878
- Orbital-maneuvering system (OMS), 278–279
- Orbital transfer, 207, 271, 275, 350–353
- Osculating cone flow waverider design, 313–315
- Oswatich principle, 80, 614, 629, 653, 805, 807
- P**
- Parabolized Navier–Stokes (PNS) equation, 21, 22, 24, 25, 348, 584
- Park, C., 375, 389, 390, 406, 409, 411, 412, 420, 429, 433, 434, 444, 729, 737, 738, 876, 878
- Park reaction rate model, 389, 390
- Perfect gas (PG), 6, 9, 22, 23, 33, 35, 41, 42, 82, 122, 154–155, 157–172, 175, 177, 178, 189–192, 201, 251, 287, 318, 324, 336, 343, 361, 369, 381, 385, 396, 397, 406, 408, 415, 420, 429, 432–435, 438, 446, 448, 449, 451, 515, 578, 582, 626, 634, 667, 669, 724, 729, 731, 801, 879, 882, 884, 885
- Pitch, 52, 224, 372, 428, 458, 549–555, 580, 708, 769
- Pitch damping, 253, 256, 265, 269
- Pitching moment, 52, 56, 57, 60, 61, 246, 254, 261, 277, 280–283, 287, 295, 331, 332, 372, 416–418, 424, 428, 429, 431–433,

- 435, 446–448, 458, 492, 497, 509, 513, 535, 538–541, 545, 547, 549–557, 559, 566, 567, 569, 578, 580, 600, 603, 605, 608, 612–616, 622, 625, 626, 630, 631, 635, 642, 648, 649, 651–655, 658, 662, 668–670, 693, 694, 697, 760–762, 769, 785, 786, 788, 790, 792, 799, 804, 813, 834, 851–853, 863–865, 879, 884, 886, 887
- Pitching moment coefficient, 56, 57, 60, 61, 246, 261, 277, 281, 287, 331, 332, 372, 416, 428, 429, 431, 432, 447, 448, 458, 492, 497, 509, 538–541, 545, 547, 549–555, 559, 566, 567, 569, 603, 605, 608, 612–616, 630, 642, 648, 649, 651, 652, 654, 658, 662, 668, 697, 761, 762, 769, 785, 786, 788, 790, 804, 834, 851–853, 863–865, 878, 884, 886, 887
- Planar flight, 128–154
- Planetary mission, 128, 275, 350
- Planform area, 289, 598, 616, 799, 829, 831, 879
- Prabhu, D.K., 171
- Prandtl, L., 16, 23
- Prandtl–Meyer expansion, 31, 99, 594, 761
- Prandtl–Meyer flow, 596, 761
- Prandtl number, 157, 158, 163, 164, 172, 191, 595, 596
- Pressure coefficient, 49, 64–68, 71, 73, 93, 95, 99, 273, 325, 326, 395, 398, 399, 419, 420, 424, 447–450, 522–524, 527, 530–532, 560, 595, 620–623, 632, 633, 640, 641, 659, 668, 670, 761, 783, 785, 786, 800, 805, 816, 823, 838, 841, 848, 854, 880, 881
- Pressure distribution, 9, 47, 64, 71, 72, 85, 86, 93, 97, 99, 102, 104, 112, 179, 181, 186, 395, 397, 414, 415, 417, 428–429, 432, 444, 446, 517, 525, 527, 562, 632, 640, 655, 666, 745, 754, 761, 774, 782, 800, 805, 816, 829, 836, 837, 839–841, 853
- Pressure drag, 239, 240, 414, 633, 834, 842
- Pressure loads, 154, 223, 844, 859, 862
- Probstein, R.F., 48, 113, 114, 741
- R**
- Radiating flows, 117
- Radiative heat flux, 204, 249, 274, 277, 331, 339, 519, 714, 715, 720, 723, 724, 726, 728, 732, 733, 754–756, 759, 874
- Radiative transfer equation, 732
- Range, 11, 22, 35, 127, 226, 229, 368, 458, 578, 703, 769
- Rankine–Hugoniot relation, 28
- Rasmussen, M., 95
- Rate equation, 185
- Reaction control system (RCS), 50, 61, 252, 261, 279, 459, 462, 464–466, 469, 481, 483, 486, 491, 538, 578–581, 603, 645, 655, 681, 827
- Reaction-cured glass (RCG) coating, 375, 377, 442
- Real gas, 9, 15, 23, 35, 41, 97, 102, 114, 170, 175, 199, 212, 284, 299, 301, 322, 336, 338, 342, 343, 348, 367, 368, 370, 373, 396, 397, 405, 416, 421, 424, 428, 431, 448, 451, 482, 486, 491, 496, 578, 581, 584–587, 626, 653, 664, 670, 671, 675, 688, 692, 693, 733, 755, 797, 878, 884
- Real gas effects, 15, 23, 35, 41, 97, 114, 170, 199, 284, 299, 367, 369–371, 373, 399, 405, 413, 416, 421, 424, 428, 438, 448, 450, 482, 486, 491, 496, 578, 585, 626, 643, 653, 670, 671, 675, 693, 704, 733, 797
- phenomena, 35, 299, 301, 342, 343, 586, 627, 884
- Recovery factor, 4, 160, 327, 595
- Recovery temperature, 160, 318, 328
- Re-entry flight, 1, 2, 116, 146, 298, 377–385, 399–401, 406, 418, 453, 459, 461, 487, 572, 573, 580, 585, 600, 616, 629, 633, 684–686, 689, 706, 725–728, 799, 803, 804, 838
- Re-entry trajectory, 16, 38, 40, 156, 201, 242, 294, 301, 354, 367, 368, 377, 379, 382, 399, 401, 405, 449, 483, 489, 515, 543, 577, 581, 582, 584, 601, 642, 670, 672, 684–686, 705, 726, 733, 740, 804
- Reference enthalpy, 322, 323, 584, 594, 595, 798
- Reference length, 53, 56, 260, 418, 514, 535, 598, 633, 648, 649, 697, 769, 777, 879
- Reference surface, 56, 79, 260, 598, 769, 777, 792, 853, 879
- Reference temperature, 96, 166, 322, 324, 325, 329–330, 594, 595, 798, 875
- Regan, F.J., 15
- Reid, L.D., 280, 285
- Reusable launch vehicle (RLV), 457, 459, 464, 466, 476, 489, 674, 698, 787, 788, 790
- Reynolds analogy, 96, 162–167, 170, 171, 178, 241, 322, 328, 329, 724
- Riddell, F.R., 189, 190, 198, 204, 206, 273, 276, 381, 402, 596

- RLV. *See* Reusable launch vehicle (RLV)
- Roll, 61, 151, 156, 224, 253, 257–259, 274, 278, 279, 289, 481, 485, 501, 503, 506, 563, 579, 618, 621, 634, 635, 659, 695, 768, 828
- Rolling moment coefficient, 53, 60, 617, 662, 769
- Rosetta, 143, 244, 247, 249–251, 257–259, 268, 271–274, 347, 724
- Rotational flow, 27
- Rotational temperature, 754
- Rudder, 59, 60, 473, 579, 600, 601, 604–606, 662–665, 683, 792
- S**
- Sample return mission (SRM), 271, 703, 708, 713, 728
- Sample return vehicle (SRV), 207, 703–710, 713–721, 725, 726, 728, 732, 733, 735, 738, 740, 743, 745–752, 755, 757, 758, 760–765
- Schmidt, D.K., 104
- Scott, C.D., 172, 201, 202, 215, 375, 402
- Scramjet. *See* Supersonic combustion ramjet (Scramjet)
- Shear layer, 251, 255, 342, 348, 394, 412, 741, 745, 855, 859
- Shock fitting, 516, 842
- Shock layer, 3, 7–9, 34, 35, 41, 66, 84, 91, 112, 114, 116, 117, 175, 190, 193, 204, 248–249, 252, 272, 298, 332–336, 339, 340, 343–345, 349, 355, 357, 359, 364, 370, 371, 397, 408, 409, 412, 441, 519, 583, 626, 640, 679, 704, 714, 716, 718–725, 728, 732, 738, 744, 747, 750–755, 758, 786, 877, 880, 882–884
- Shock–shock interaction (SSI), 491, 498, 516, 560, 594, 621, 626, 627, 636, 666, 784, 811, 812, 822, 829, 838, 841, 880
- Shock stand-off distance, 112, 363, 714
- Shock wave boundary layer interaction (SWBLI), 242, 482, 491, 516, 557, 562, 591, 626, 656, 675, 784
- Side coefficient, 563, 565
- Sideslip angle, 50, 59, 497, 498, 509, 539, 562–564, 590, 635, 769, 795, 816
- Similarity transformations, 332
- Sine-squared law, 64–66
- Single-stage-to-orbit (SSTO), 142
- Skin friction coefficient, 18, 58, 96, 97, 118, 162–167, 178, 298, 594, 595, 755, 757, 798
- Skip trajectory, 143, 168
- Slender bicones, 267, 268
- Slender vehicle, 114, 267, 268, 298
- Slip boundary condition at wall, 850
- Small-density ratio, 113, 369
- Snake flow, 279, 519
- Sonic flow, 431
- Sonic line, 273, 368, 372, 413, 415, 420, 421
- Sound barrier, 110
- Space shuttle orbiter, 15, 87, 88, 102, 103, 234, 235, 238, 287, 303–305, 322, 367, 633, 675, 691, 692, 698
- Specific gas constant, 131, 736
- Specific heat ratio, 369, 370, 429, 582
- Speed of sound, 3, 19, 25, 54, 110, 122, 175, 316, 346, 782–783
- Sphere drag, 40, 275
- SRF. *See* Stability reference frame (SRF)
- SRM. *See* Sample return mission (SRM)
- SRV. *See* Sample return vehicle (SRV)
- SSI. *See* Shock–shock interaction (SSI)
- Stability
- analysis, 465, 618, 655, 661
  - characteristic, 261, 275, 597, 876
- Stability reference frame (SRF), 50–52, 598
- Stagnation point, 4, 12, 41, 65, 68, 70, 71, 82, 95, 105, 112, 118, 119, 123, 155, 174–206, 226, 229, 246, 247, 273, 298, 319–321, 323, 343, 368, 371, 382, 395, 398, 402, 404–406, 419, 422, 442, 443, 449, 452, 453, 482, 581, 586, 596, 631, 671–674, 677, 733, 734, 745, 747, 752, 755, 757, 795, 820, 822, 890
- Stagnation streamline, 112, 349, 357–362, 364, 404, 724, 754, 758
- Standard atmosphere, 131, 177, 190, 191, 202, 399, 434, 651
- Stanton number, 18, 121, 124, 159, 164, 170, 178, 206, 241, 328, 597
- Static margin, 274, 277, 280, 283, 284, 287, 627, 708
- Static stability, 11, 60, 62, 246, 250, 261, 267, 280–283, 288–289, 296, 415, 424, 579, 616, 646, 662, 707, 762, 763, 800, 885
- Steady state conditions, 626
- Stefan-Boltzmann constant, 318
- Streamlines, 8, 17, 27, 32, 64, 66, 67, 96, 112, 165, 175, 183, 184, 275, 312, 322, 323, 340, 349, 357–362, 364, 381, 404, 442, 517, 521, 527, 557, 594, 634, 641, 666, 724, 748, 754, 758, 798, 816, 855, 856, 875
- Strong interaction, 26, 48, 557, 837

- Structured grid, 392, 597, 627, 664, 741, 798, 879  
Suborbital trajectory, 794  
Subsonic flow, 25, 26, 74, 105, 122, 557, 573, 606, 782, 831, 835  
Supersonic combustion ramjet (Scramjet), 2, 10, 102, 104, 212, 218–221, 574–576, 625  
Supersonic flow, 7, 25–26, 28, 30–32, 47, 63, 64, 74, 76, 112, 217, 254, 284, 291, 342, 601, 606, 784, 832, 846, 852, 857  
Supersonic/Hypersonic Arbitrary Body Program (S/HABP), 105  
Surface emissivity, 320, 515  
Surface reaction-rate parameter, 389, 599, 876  
Surface streamlines, 381, 442, 557  
Sutherland's equation, 184, 191, 192, 197, 200, 327, 729  
SWBLI. *See* Shock wave boundary layer interaction (SWBLI)
- T**  
Tannehill, J.C., 171  
Temperature  
    jump, 15, 205, 350, 434, 582  
    sensitive coatings, 272  
Thermal barrier, 110, 112, 242  
Thermal conductivity, 18, 154, 157, 158, 241, 327, 330, 387, 388, 597, 680, 718, 729, 731, 876  
Thermal equilibrium, 39, 330, 390, 405, 409, 410, 412, 578, 581, 586  
Thermal loads, 127, 128, 143, 154, 790, 838, 874  
Thermal protection system (TPS), 114, 116, 118–120, 171, 208, 211, 223, 228, 236, 242, 245, 247–252, 261, 270, 273, 276, 298, 317, 319, 330, 332, 336, 337, 353, 367–369, 373, 374, 377, 379, 381, 391, 401, 404, 407, 439, 442, 461–466, 468, 469, 471, 473, 474, 476–478, 480, 483, 486, 487, 489–491, 573–575, 580, 581, 626, 627, 671, 673–683, 704, 707, 708, 710–712, 714–726, 728, 743, 744, 751, 755, 760, 762, 791, 816, 822, 873, 874, 878  
Thermochemical equilibrium, 191, 252, 405, 754, 755  
Thermocouples, 319  
Thermodynamic properties of air, 96  
Thomas, R., 284  
Three-dimensional results, 29, 313, 562, 589  
Total enthalpy, 8, 122, 157–159, 177, 196, 241, 316  
Total pressure, 70, 72, 384, 499  
Total temperature, 177, 322, 446  
TPS. *See* Thermal protection system (TPS)  
Trailing edge, 58, 59, 102, 525, 579, 632, 634, 792, 793, 831, 837, 841  
Trajectory, 50, 127, 223, 368, 457, 582, 706, 767  
Trajectory constraints, 98, 119, 224, 293, 296, 580, 673, 684  
Transition, 4, 12, 13, 155, 171, 238, 242, 250, 251, 273–274, 294, 299, 336, 337, 344, 401, 407, 413, 469, 482, 491, 497, 498, 508, 510, 515, 525, 543, 574, 587–589, 675, 680, 708, 714, 721, 732, 740  
Transitional regime, 207, 333, 344, 545, 582, 652, 686, 778  
Translational temperature, 339, 341, 359, 408–411, 748, 754  
Transonic flow, 26, 62, 606, 630, 835–837, 848, 849, 853  
Transpiration cooling, 724  
Transport properties, 158, 204, 343, 349, 367, 370, 388–392, 405, 597, 876  
    of air, 343, 367  
Trim  
    angle of attack, 256, 257, 259, 277, 286, 400, 509  
    condition, 284, 423, 431, 581, 630, 631, 885  
Trimmed trajectory, 399, 442, 830  
Turbulent effects, 174  
Turbulent flow, 18, 97, 155, 160, 164, 166, 167, 171, 185, 273, 293, 327, 330, 333, 335, 342, 407, 439, 523, 587, 588, 594–596, 740, 798, 820–822  
Turbulent kinetic energy, 18, 96, 155, 335  
Turbulent Prandtl number, 164, 597, 598  
Turbulent spots, 174, 242, 523  
Turbulent viscosity coefficient, 827  
Two-stage-to-orbit (TSTO), 477  
Two-temperature model, 339, 390, 738
- U**  
Uncertainties, 10, 11, 172, 209, 224, 250, 254, 287, 323, 324, 448, 465, 486, 495, 565–569, 688–700, 825–828, 847, 858–862  
Universal gas constant, 37, 43, 376, 387, 731  
Unknown unknowns, 690

- Unmanned Space Vehicle (USV), 475, 476, 479, 680
- Unstructured grid, 628
- U.S. Standard Atmosphere, 137, 177, 191, 202, 399, 434, 651
- USV. *See* Unmanned Space Vehicle (USV)
- V**
- Van Driest, E.R., 4
- Vega, 457, 464, 465, 467, 473, 484, 485, 487–489, 645, 646, 776, 779–781, 845–858
- Vehicle, 1, 127, 211–365, 457–699, 767
- Venus, 129, 132, 139, 203, 268, 352, 720
- Vertical fin, 648
- Vertical take-off (VTO), 789, 790, 792, 794–796, 798, 801, 804, 807–810, 813, 820, 821, 863, 864
- Vibrational Temperature, 339, 341, 359, 410, 412, 413, 748–750
- Viking, 224, 246, 249–251, 253, 266, 275
- VIP. *See* Viscous interaction parameter (VIP)
- Viscosity effects, 16, 55, 56
- Viscous effects, 3, 16, 18, 23, 298, 309, 312, 339, 345, 418, 581, 656, 657, 774, 826, 828, 842, 843
- Viscous interaction parameter (VIP), 47–49, 583, 584
- Viscous interactions, 3, 7–8, 47–50, 63, 296, 301, 345, 654, 704
- Viscous shock layer, 349, 355
- Vortex interaction, 856
- Vorticity interaction regime, 8
- VSB-30, 776, 777
- VTO. *See* Vertical take-off (VTO)
- W**
- Wake, 16, 21, 105, 108, 212, 223, 253, 254, 335, 341, 348, 350, 392, 394, 414, 632, 634, 638, 708, 741, 748, 764, 816, 826, 843, 885
- Wall, 4, 154, 239, 367, 499, 574, 589, 704, 775
- Wall temperature, 23, 24, 160, 172, 173, 190, 191, 197, 201, 272, 273, 317–322, 330, 356, 357, 384, 391, 402, 434, 439, 445, 544, 596, 607, 651, 743, 744, 876
- Walpot, L., 447
- Waverider, 221, 222, 308–316, 575
- Waverider design, 311, 312, 314, 315
- Weak interaction, 48
- Wedge flow, 29, 311, 315, 316
- Williams, J., 102
- Wind reference frame (WRF), 50, 51, 598, 600, 799
- Wind tunnel, 40, 52, 57, 58, 120, 156, 171, 265, 272, 273, 275, 294, 308, 322–324, 343, 365, 394, 407, 431, 461, 473, 486, 492, 499, 501, 505–507, 512, 513, 552, 561–563, 579, 686, 689–693, 764, 771, 774, 775, 827, 828, 832, 837, 842, 845, 847, 849, 850, 858–860
- HEG, 395
- H2K, 492
- S4ma, 492, 563
- Winged body, 53, 211
- Wing flap, 618, 657
- WRF. *See* Wind reference frame (WRF)
- X**
- X-15, 102, 103, 214, 215, 293, 294, 303–306, 459
- X-33, 538, 589, 590, 693–698
- X-34, 87, 89–92, 538, 605
- X-38, 229, 304, 459, 460, 462, 464, 469, 472, 473, 480, 484, 659
- X-24C, 108
- Y**
- Yaw, 60, 61, 95, 221, 259, 261, 272, 278, 288, 323, 501, 504, 509, 564, 581, 622, 769, 770
- Yawing moment coefficient, 53, 60, 291, 535, 541, 563, 605, 616, 622, 623, 658, 661, 662, 769
- Z**
- Zero-lift drag, 76, 81, 285, 421, 422
- Zoby, 171, 201, 375